

AD-A122 200

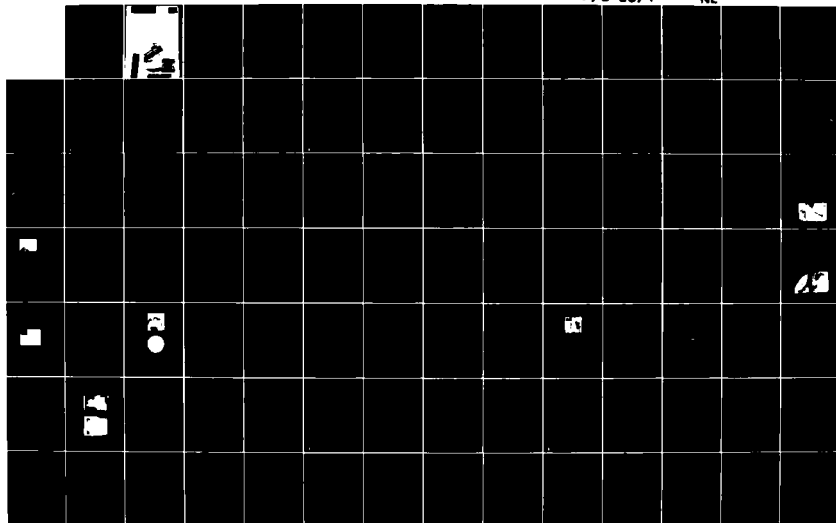
PROCEEDINGS OF THE INTERNATIONAL SYMPOSIUM ON SHOCK
TUBES AND WAVES (13TH. (U) CALSPAN ADVANCED TECHNOLOGY
CENTER BUFFALO NY C E TREANOR ET AL. JUL 81
AFOSR-TR-82-1031 F49629-81-C-0002

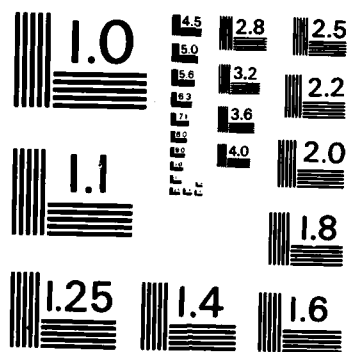
1/10

UNCLASSIFIED

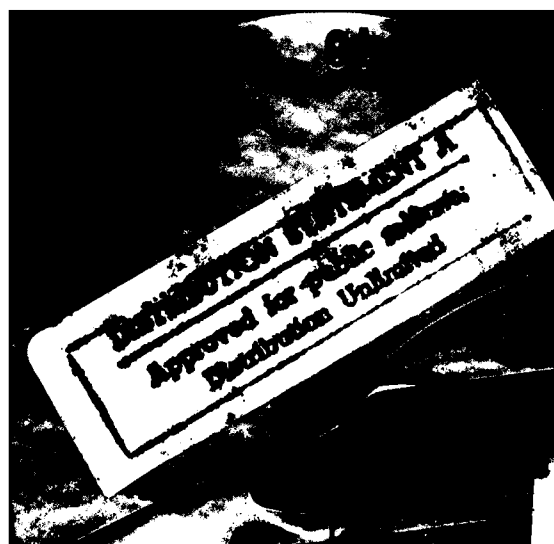
F/O 20/1

NL





MICROCOPY RESOLUTION TEST CHART
NATIONAL BUREAU OF STANDARDS-1963-A



UNCLASSIFIED

SECURITY CLASSIFICATION OF THIS PAGE (When Data Entered)

REPORT DOCUMENTATION PAGE		READ INSTRUCTIONS BEFORE COMPLETING FORM
1. REPORT NUMBER AFOSR-TR- 82-1081	2. GOVT ACCESSION NO. AD-A122200	3. RECIPIENT'S CATALOG NUMBER
4. TITLE (and Subtitle) SHOCK TUBES AND WAVES		5. TYPE OF REPORT & PERIOD COVERED FINAL 1 Oct 80 - 30 Sep 81
		6. PERFORMING ORG. REPORT NUMBER
7. AUTHOR(s) CHARLES E TREANOR J GORDON HALL		8. CONTRACT OR GRANT NUMBER(s) F49629-81-C-0002
9. PERFORMING ORGANIZATION NAME AND ADDRESS CALSPAN CORPORATION ADVANCED TECHNOLOGY CENTER P O Box 400 BUFFALO, NY 14225		10. PROGRAM ELEMENT, PROJECT, TASK AREA & WORK UNIT NUMBERS 61102F 2307/A1
11. CONTROLLING OFFICE NAME AND ADDRESS AIR FORCE OFFICE OF SCIENTIFIC RESEAFCH/NA BOLLING AFB, DC 20332		12. REPORT DATE July 1981
		13. NUMBER OF PAGES 884
14. MONITORING AGENCY NAME & ADDRESS (if different from Controlling Office)		15. SECURITY CLASS. (of this report) UNCLASSIFIED
		15a. DECLASSIFICATION/DOWNGRADING SCHEDULE
16. DISTRIBUTION STATEMENT (of this Report) Approved for Public Release; Distribution Unlimited.		
17. DISTRIBUTION STATEMENT (of the abstract entered in Block 20, if different from Report)		
18. SUPPLEMENTARY NOTES Proceedings of the 13th International Symposium on Shock Tubes and Waves, Niagara Falls, NY, July 6-9, 1981.		
19. KEY WORDS (Continue on reverse side if necessary and identify by block number) SHOCK WAVES SHOCK TUBES SHOCK INDUCED SEPARATION BLAST WAVES CHEMICAL KINETICS SHOCK WAVE STRUCTURE		
20. ABSTRACT (Continue on reverse side if necessary and identify by block number) This volume contains six invited papers and ninety two contributed papers presented at the XIII International Symposium on Shock Tubes and Waves, which was held in Niagara Falls, NY, July 6-9, 1981. Professor I I Glass of the University of Toronto presented the Paul Vieille Memorial Lecture. This paper and five other invited papers form Part I of the Proceedings. The contributed papers are presented in Parts II through VII, divided according to subject matter. The typical broad range of interests associated with shock waves is demonstrated in both the invited and contributed papers, with		

UNCLASSIFIED

SECURITY CLASSIFICATION OF THIS PAGE(When Data Entered)

subject material covering viscous aerodynamics, explosions, chemistry, optics, and energy-related processes. It is intended that this volume provide an up-to-date accounting of international progress in these fields insofar as shock-wave phenomena are involved.



1	2	3	4	5	6	7	8	9	10

UNCLASSIFIED

SECURITY CLASSIFICATION OF THIS PAGE(When Data Entered)

(1)

COMPONENT PART NOTICE

THIS PAPER IS A COMPONENT PART OF THE FOLLOWING COMPILATION REPORT:

(TITLE): Proceedings of the International Symposium on Shock Tubes and
Waves (13th), Niagara Falls, July 6-9, 1981.

(SOURCE): Calspan Advanced Technology Center
Buffalo, NY

D
E
S
DEC 17 1982

TO ORDER THE COMPLETE COMPILATION REPORT USE AD-A122 200. A

THE COMPONENT PART IS PROVIDED HERE TO ALLOW USERS ACCESS TO INDIVIDUALLY AUTHORED SECTIONS OF PROCEEDINGS, ANNALS, SYMPOSIA, ETC. HOWEVER, THE COMPONENT SHOULD BE CONSIDERED WITHIN THE CONTEXT OF THE OVERALL COMPILATION REPORT AND NOT AS A STAND-ALONE TECHNICAL REPORT.

THE FOLLOWING COMPONENT PART NUMBERS COMPRISE THE COMPILATION REPORT:

AD#:	P000 223	TITLE:	Review of Shock Tube and Shock Tunnel Advancements at NAL.
	AD-P000 224		Current Studies at Calspan Utilizing Short-Duration Flow Techniques.
	AD-P000 225		Shock-Induced Flow Separation and the Orbiter Thermal Protection System.
	AD-P000 226		Chemical Kinetics Studied by Vacuum-UV Spectroscopy in Shock Tubes.
	AD-P000 227		Blast Waves Generated by Accidental Explosions.
	AD-P000 228		A Shock Tube Driver with a "Cyclone" Separator.
	AD-P000 229		A New, Diaphragmless, Flexible, Luminous Shock Tube.
	AD-P000 230		A Powder-Injection Shock-Tube Facility.
	AD-P000 231		The Testing in BIA Hypersonic Gun Tunnel.
	AD-P000 232		An Application of the Molecular Beam Time-of-Flight Technique to Measurements of Thermal Boundary Layer Effects on Mass Sampling from a Shock Tube.
	AD-P000 233		Measurement of Dynamic Pressure in Shock Tube by Streak Photography.
	AD-P000 234		Measurement of Temperatures in a Shock Tube by Coherent Antistokes Raman Spectroscopy (CARS).
	AD-P000 235		Temperature Measurement of Detonation Using UV-Absorption of O ₂ .
	AD-P000 236		A Laser-Interferometric Trajectory-Following System for Determining Forces on Freely Flying Models in a Shock-Tunnel.
	AD-P000 237		Shock Tube Simulation of Pulsed Flow Aerodynamic Windows.
	AD-P000 238		Velocity Measurements of Incident and Reflected Shock Waves in Various Gases and in Saturated Water Vapor.
	AD-P000 239		Investigation of the Distortion of Shock-Fronts in Real Gases.
	AD-P000 240		Measurement and Calculation of Shock Attenuation in a Channel with Perforated Walls.
	AD-P000 241		High-Energy Air Shock Study in a Steel Pipe.
	AD-P000 242		Optical Studies of Shock Generated Transient Supersonic Base Flows.

COMPONENT PART NOTICE (CON'T)

AD#:P000 243	TITLE: Amplification of Non-Linear Standing Waves in a Cylindrical Cavity with Varying Cross Section.
AD-P000 244	Cyclic Wave Action in the Stable Operation of a Hartmann-Sprenger Tube.
AD-P000 245	Some Fundamental Aspects of Shock Wave - Turbulent Boundary Interactions in Transonic Flow.
AD-P000 246	Heating-Rate Measurements over 30 deg and 40 deg (Half-Angle) Blunt Cones in Air and Helium in the Langley Expansion Tube Facility.
AD-P000 247	Shock Induced Unsteady Flat Plate Boundary Layers and Transitions.
AD-P000 248	The Boundary Layer Behind a Shock Wave Incident on a Leading Edge.
AD-P000 249	Real Gas and Wall Roughness Effects on the Bifurcation of the Shock Reflected from the End Wall of a Tube.
AD-P000 250	Determination of Shock Tube Boundary Layer Parameter Utilizing Flow Marking.
AD-P000 251	Stability Limits and Transition Times of Wave-Induced Wall Boundary Layers.
AD-P000 252	An Accurate Determination of the Thermal Conductivity of Argon at High Temperatures.
AD-P000 253	Thermal Conductivity Measurement in High Temperature Argon by the Shock Perturbation and Mach Reflection Methods.
AD-P000 254	Temperature Measurements of an Implosion Focus.
AD-P000 255	Boundary Layer Influenced Shock Structure.
AD-P000 256	Influence of Surface Roughness on the Shock Transition in Quasi-Stationary and Truly Non-Stationary Flows.
AD-P000 257	Microscopic Structure of the Mach-Type Reflection of Weak Shock Waves.
AD-P000 258	Weak Spherical Shock-Wave Transitions of N-Waves in Air with Vibrational Excitation.
AD-P000 259	Generation of the Patterns in Gaseous Detonations.
AD-P000 260	Evolution of Shock-Induced Pressure on a Flat-Face/Flat-Base Body and Afterbody Flow Separation.
AD-P000 261	Shock Strength Modification for Reduced Heat Transfer to Lifting Re-Entry Vehicles.
AD-P000 262	Cylindrical Resonators.
AD-P000 263	Propagation of Shock Waves through Nonuniform and Random Media.
AD-P000 264	Shock Wave Diffraction at a Sharp Edge and the Effect of Baffles in a Shock Tube.
AD-P000 265	Propagation of Two-Dimensional Nonsteady Detonation in a Channel with Backward-Facing Step.
AD-P000 266	The Blast-Noise Environment of Recoilless Rifles.
AD-P000 267	Shock-Excited Emission Spectrum of Tungsten Oxide.
AD-P000 268	Rotational Nonequilibrium Influences in CW HF/DF Chemical Lasers.
AD-P000 269	High Gain CO Chemical Laser Produced in a Shock Tunnel.
AD-P000 270	Shock/Ludwig-Tube Driven HF Laser.

AD-P000 271	TITLE: Determination of Absorption Coefficients in Shock Heated Propellant Mixtures for Laser-Heated Rocket Thrusters.
AD-P000 272	Supersonic Flow E-Beam Stabilized Discharge Excimer Lasers.
AD-P000 273	Fluid-Dynamical Aspects of Laser-Metal Interaction.
AD-P000 274	Shockfronts as Model Targets in Laser-Plasma Interaction Experiments.
AD-P000 275	Experimental Study on the Ionization of Argon Gas in a Non-Equilibrium State Behind Reflected Shock Waves.
AD-P000 276	Studies of the Vibrational Relaxation of Diatomic Molecules in a Shock Heated Molecular Beam and Its Application to Ionization by Electron Impact.
AD-P000 277	Discharge Flow/Shock Tube Studies of Singlet Oxygen.
AD-P000 278	Rotational Relaxation of H ₂ in Nozzle Flow.
AD-P000 279	Vibrational Relaxation of Polyatomic Molecules in Gas Mixtures.
AD-P000 280	Vibrational Relaxation and Dissociation Rate Measurements in Polyatomic Molecules.
AD-P000 281	CO + O Chemiluminescence: Rate Coefficient and Spectral Distribution.
AD-P000 282	Resonance Absorption Measurements of Atom Concentrations in Reacting Gas Mixtures. 9. Measurements of O Atoms in Oxidation of H ₂ and D ₂ .
AD-P000 283	Direct Measurements of O-Atom Reactions with HCN and C ₂ H ₂ Behind Shock Waves.
AD-P000 284	The Effect of Minute Quantities of Impurities on Shock Tube Kinetics. The Reaction H ₂ + D ₂ Yields 2HD.
AD-P000 285	Molecular Beam Technique for Recording Chemical Species Behind Incident Shock Waves.
AD-P000 286	Shock Tube Study of the Thermal Decomposition of Hydrogen Cyanide.
AD-P000 287	Decomposition of Hydrogen Azide in Shock Waves.
AD-P000 288	The Relaxation Zone Behind Normal Shock Waves in a Reacting Dusty Gas. Part 1. Monatomic Gases.
AD-P000 289	Shock Wave Structure in Gas-Particle Mixtures at Low Mach Numbers.
AD-P000 290	Cross-Sectional Concentration of Particles during Shock Process Propagating through a Gas-Particle Mixture in a Shock Tube.
AD-P000 291	Motion of Small Particles in a Field of Oscillating Shock Waves.
AD-P000 292	Shock Tube Measurements of IR Radiation in Hot Gas/Particle Mixtures.
AD-P000 293	Study of Binary Nucleation in a Ludwig Tube.
AD-P000 294	Investigations of Homogeneous Nucleation in Fe, Si, Fe/Si, FeO(x), and SiO(x) Vapors and Their Subsequent Condensation.
AD-P000 295	Condensation Kinetics of Iron and Silicon in the Vapor Phase.
AD-P000 296	Shock-Tube Simulation Experiment of Supersonic Condensation Flow Accompanying a Shock Wave.
AD-P000 297	Experiments in Shock Liquefaction.
AD-P000 298	Shock Propagation in Liquid-Gas Media.
AD-P000 299	A Comparison of Measured and Computed Energy Exchanger Performance.

BEYOND THREE DECADES OF CONTINUOUS RESEARCH AT UTIAS
ON SHOCK TUBES AND WAVES

I. I. Glass

Institute for Aerospace Studies, University of Toronto
Toronto, Canada

Analytical and experimental research on nonstationary shock waves, rarefaction waves and contact surfaces has been conducted continuously at UTIAS since its inception in 1948. Some unique facilities were used to study the properties of planar, cylindrical and spherical shock waves and their interactions. Investigations were also performed on shock-wave structure and boundary layers in ionizing argon, water-vapour condensation in rarefaction waves, magnetogasdynamic flows, and the regions of regular and various types of Mach reflections of oblique shock waves. Explosively-driven implosions have been employed as drivers for projectile launchers and shock tubes, and as a means of producing industrial-type diamonds from graphite, and fusion plasmas in deuterium. The effects of sonic-boom on humans, animals and structures have also formed an important part of the investigations. More recently, interest has focussed on shock waves in dusty gases, the viscous and vibrational structure of weak spherical blast waves in air, and oblique shock-wave reflections. In all of these studies instrumentation and computational methods have played a very important role. A brief survey of this work is given with some perspectives on future research.

1. INTRODUCTION

The actual research on shock tubes and supersonic wind tunnels was initiated by Dr. G. N. Patterson when he envisioned and planned the then Institute of Aerophysics in 1948, even though it was not actually available until 1949, and opened officially in 1950 [1]. He became its Founder and first Director. His first three students in the shock-tube field, Bitondo [2,3,4], Glass [3,5] and Lobb [2,6,7], were initially guided by his analysis of shock-tube flows [8] for the design of their facilities and appropriate experiments.

Since this survey is confined to nonstationary flows, it will not be possible to include references to many other gasdynamic flows which were studied then and subsequently throughout the decades by members of the staff and students alike. Dr. Patterson's interests later centred on kinetic theory [9, 10], and when I obtained my Ph.D. in 1950, I assumed responsibility for research and development in nonstationary flows. The present survey then deals with the analytical, numerical and experimental studies in this field from

1948 until the present day.

It should be noted at the outset that this survey is not meant to be exhaustive as far as references are concerned or in the details of the various researches. Here and there a reference from sources other than UTIAS will be called up to assist the reader. Consequently, I hope that many authors will forgive me if their names do not appear, and the readers for the brevity of this presentation. The choice had to be arbitrary in order to fit the limitations of this review.

2. THE FIRST DECADE, 1948-1958

Analytical and experimental work in this decade centred mainly on one-dimensional flows in shock tubes induced by shock waves and rarefaction waves. The various interactions of these waves as well as those with contact surfaces were also of considerable interest. As shown in Figs. 1 to 4, it was soon realized that the diaphragm-breaking process was far from ideal [2,7,11]. This had a serious effect on the flow quality behind the contact region (Figs. 1-4), which originated in the driver section of the shock tube, and was disturbed and made turbulent by the remaining jagged edges of the diaphragm. Consequently, the predicted high Mach number in this cold gas was not achieved [6,12]. On the other hand, the flow Mach number in the region compressed by the shock wave in the channel was in quite satisfactory agreement with analysis at the lower shock strengths [7,12].

As for the velocity of the shock wave, it was soon found that it attenuated [11,12,13] with distance from the diaphragm, increasing shock Mach number, and lowered channel pressures for a given shock-tube cross-section (Fig. 5). The attenuation increased with decreasing cross-sectional area. Some early analyses [14,15,16] showed that the sidewall boundary layers (Fig. 6) induced by the shock wave and rarefaction wave were responsible for the shock-wave attenuation. In addition, the boundary layer caused the contact surface to accelerate [11] (Fig. 7) so that the testing time in the hot region was limited and it was not possible to increase it by going to a longer channel, as inviscid analysis predicted. This situation also caused flow gradients in the hot region, which meant that gasdynamicists, physicists, and chemists had to take these deviations into account in analysing their test results for perfect and imperfect gases with vibrational, dissociational or ionizational excitations.

Subsequently, the shock tube became one of the most versatile and economical test facilities for universities, government, and commercial institutions alike. It soon evolved into several hybrids of shock tunnels, expansion tubes and multidaphragm shock tubes designed to provide high-stagnation temperature and high-Mach number test conditions useful for re-entry heat-shield design of space capsules which were then under development.

At UTIAS however, some emphasis was placed on wave interactions such as the refraction of a shock wave at a contact surface [3,4,17] and through a gas layer (Fig. 8). This work also showed that a shock wave may be tailored through refraction such that only a Mach wave is reflected from the contact surface. This idea led to the reflected shock wave, tailored-interface, shock-tunnel operation, thereby providing a constant-pressure high-enthalpy reservoir of gas for expansion through supersonic or hypersonic nozzles [18,19] (Fig. 9). It was also surmised that a layer of gas, such as hydrogen or helium, might provide a protective barrier for attenuating blast waves. However, it was soon noted that the subsequent overtaking of the transmitted shock wave by the refracted shock wave would quickly diminish the attenuation [17,20] and increase the pressure ratio across the transmitted wave to nearly the original shock strength incident on the layer of helium.

It is worth noting that the overtaking of two shock waves provides the

ideal shock-tube problem after their interaction, that is, a shock wave and a centred rarefaction wave which are separated by a perfect contact surface (Fig. 8). A near-perfect shock-tube problem can also appear at the refraction of a shock wave at an air/helium interface, as shown in Fig. 8, with a very well defined centred rarefaction wave. Breaking a diaphragm in a shock tube does not produce a centred wave. The tail of the wave is usually obscured in schlieren or shadow photographs, showing that sharp gradients are absent (Fig. 2). However, the head of the wave is always visible and provides a gasdynamic means of measuring very accurately the speed of sound in gases [21a]. It is worth noting that only the equilibrium sound speeds were measured from the first characteristic line, even in CO₂-carbon dioxide [21b], and SF₆-sulfur-hexafluoride [21c], as it was not possible to produce an ideal centred wave where the frozen precursor might have been observed [see 52a] near the origin.

Additional interactions were studied, such as the head-on collision of shock waves [22] and of shock and rarefaction waves [22,23]. In the former case, again a perfect contact surface is formed (Fig. 10). The head-on collision of two shock waves also provides a means of studying reflected shock waves without wall-effects by using two shock waves of equal strength. Very high temperatures with real-gas effects can be obtained in this manner. If a wall is used for reflection, the tailored-interface technique mentioned above can be used to provide a gas with very high escape speed, which is also useful for molecular-beam studies.

One-dimensional refractions of rarefaction waves at contact surfaces [24, 25] were also investigated analytically and experimentally using hot-wire anemometry and piezo-pressure gauges. This study showed that rarefaction-wave profiles did not agree with one-dimensional theory and were very much weaker than predicted for a given diaphragm pressure ratio, especially for stronger waves [25]. The so-called Riemann invariants were also not satisfied [12]. Nevertheless, the rarefaction waves as produced agreed reasonably well with the refraction analysis. It can be stated that the various one-dimensional wave interactions studied analytically were verified by experiment. However, in the case of strong shock waves, real-gas effects had to be considered to improve the agreement with analysis [22,12].

With the construction of a 23-cm diameter field of view Mach-Zehnder interferometer [26], many worthwhile problems could now be investigated where quantitative density distributions were important for an understanding of the flows involved. This made it possible to study the transition through a contact front developed in a supersonic nozzle [27]. It was shown that it had a density profile resembling a shock-wave transition. The spiral vortex [28] produced by the diffraction of a plane shock wave over a sharp plate was another interesting problem for optical study (Fig. 11), especially with the interferometer. It has since been investigated by other researchers in greater detail. The interactions of plane shock waves with plane wire screens [29] and plane and oblique perforated plates [30,31] was also a fruitful area of interest (Figs. 12-14). Transmitted and reflected shock waves were formed which were separated by the screen or plate and a contact region. If the flow through the screen or plate was choked then a second, upstream-facing, shock wave was formed near the screen or plate similar to the flow development in a nozzle (Fig. 9). Since the screen or perforated plate produces a new transmitted shock wave and contact region, it is possible to obtain density and pressure measurements behind the new shock wave from measurements of the shock speed and contact surface speed in the (x,t)-plane, using a rotating drum camera. This method is useful for perfect gases. However, for real gases, neither the pressure nor particle velocity is very sensitive to changes in initial pressure for a given shock speed. Consequently, this is not a precise method of measuring real-gas properties behind strong shock waves. There is little doubt that direct measurements of pressure, density, and temperature are required in such cases.

The interaction of a plane strong shock wave with a steady magnetic field [32] is not unlike the interaction with a wire screen. If argon is used as the test gas for example, then it ionizes and the axial components of the ponderomotive force produced on the gas when it interacts with the magnetic field also gives rise to a transmitted and reflected shock separated by a contact surface. A secondary upstream-facing rarefaction wave can also occur. The wave systems are limited by the initial conditions such that all waves may not always occur. A current flow is also produced at right angles to the flow velocity and magnetic field vectors. In essence, this is the principle of all magnetogasdynamic electric-power generators.

It is also worth noting that some theoretical work on various aspects of the collision and penetration of two rarefaction waves [33], and the overtaking of shock waves by rarefaction waves [34], and vice versa [35], was also completed. Although these are interesting problems, they were not investigated experimentally. In the case of the overtaking problems, simplifying assumptions were made by neglecting secondary characteristics resulting from the interaction. This would limit the analyses to weak rarefaction waves.

It may be concluded that the studies of diaphragm rupture, the actual wave system in a shock tube, the effects of sidewall boundary layers, various types of wave interactions or shock-wave collisions with screens, perforated plates or magnetic fields have taught us a great deal about one-dimensional nonstationary flows in shock tubes. The agreement with analyses has been quite satisfactory by and large. Researchers using such facilities can apply corrections to deviating flows, whether they be due to inviscid, viscous, or real-gas effects. However, there are still untested analyses that require experimental verification. In addition, there are unanswered questions about actual flows in rarefaction waves, in the cold-flow region, and the entire flow profiles from the head of the rarefaction wave to the shock wave as functions of time. Undoubtedly numerical methods could help in answering some of these questions supported by better experimental data. However, researchers probably have more interesting, pressing and challenging current problems to solve and would not be interested in the academic resolutions of old problems; yet this is not always the case, as some recent references indicate. A few examples will be of interest, such as the use of the shock tube for transonic-flow testing of airfoils at high Reynolds numbers [36], the collision of shock waves with screens and honeycombs [37], inviscid-flow and viscous boundary-layer interactions [38], and properties of rarefaction waves and compression waves [39a] and their induced boundary-layer flows [39b]. Many additional examples can be found in journals and Proceedings of the recent Shock Tube Symposia.

3. THE SECOND DECADE, 1958-1968

This period is marked by the extension of the investigations to spherical and cylindrical-shock and blast-wave phenomena in gases and underwater. (It should be noted that a fairly complete picture of what was known during this period about planar flows was summarized in the portion of the Handbook of Supersonic Aerodynamics on Shock Tubes [12], which was published in 1959. It soon became out of print. However, photocopies were to be found in many laboratories worldwide and to this day, for example, on a visit to China in 1980, it was ironic to hear it considered as the "bible" for shock-tube research — the term being used by older researchers trained in the West.) Rather simple-type glass diaphragms were utilized for this purpose. Nevertheless, the glass spheres had to be blown carefully by an expert glass blower. The cylindrical diaphragms had optical quality glass discs welded to both ends. The assembly was held between two glass plates to ensure cylindrical flow without end-effects [40].

Our first venture was to study the wave system generated by an exploding pressurized glass sphere [41]. It proved to be a very fruitful avenue of

research. Wave-speed schlieren records of the radius-time (r,t) -plane (Fig. 15) soon showed some remarkable differences with planar shock-tube flows and also similarities. The glass diaphragm-breaking process was similar to that of other diaphragm materials used in a shock tube. Namely, the high-pressure driver-gas was made eddying and turbulent by the glass fragments. Nevertheless, the blast wave soon became spherically symmetrical despite the protuberances in the contact front (Fig. 16). As predicted by analysis [42,43] the shock wave and the contact front decelerated and the rarefaction wave head moved at the constant sound speed. In addition, it was clearly shown, for the first time, how the second shock wave, formed at the tail of the rarefaction wave, imploded on the origin and reflected. Although the reflected implosion could be seen as a second shock following the main blast wave after the contact front in chemical explosions, the implosion phase was always obscured by the dense gases. Similar results were obtained for cylindrical explosions [44] (Fig. 17).

Additional interesting applications involved the collision of spherical shock waves (Figs. 18,19) [45] and underwater explosions (Fig. 20). Unfortunately, glass diaphragms have a limited pressure range in which they can be broken. Consequently, it was not possible to study the spherical shock-wave collision problem experimentally over an adequate range. The underwater explosions were more successful from an analytical viewpoint. It was necessary to solve the hydrodynamic shock-tube problem [46] in order to apply the appropriate boundary conditions at the moment of rupture and then continue with the analysis. The agreement of the experiments with this analysis was very satisfactory [47].

Simultaneous with the foregoing studies, the groundwork was being laid for a number of important analytical and experimental investigations. The concept of using explosive-driven implosions as drivers for shock tubes and hypervelocity projectile launchers was taking shape [48-50]. Some of the analytical work was also being done during this period on the nonequilibrium expansion flows of dissociating and ionizing argon around a sharp corner [51,52]. This was in preparation for conducting several investigations on real-gas effects in the very excellent new shock-tube facility designed, instrumented and tested for this purpose [53]. Concurrently, investigations were performed on magneto-hydrodynamic flow in the boundary layer of a shock tube [54]; in a hypersonic shock-tunnel test-section (generously donated by the Cornell Aeronautical Laboratory, Buffalo) which was coupled to an existing UTIAS shock tube [55,56]; and an initial ionization process in strong shock waves produced in hydrogen and helium in a unique electromagnetic-driven implosion shock tube [57].

It is of interest to look at some of the above projects in more detail. The explosive-driven-implosion research and development is of particular importance as it has continued until the present day. It was not only necessary to understand the spherical combustion and detonation processes [50], but also to develop a means of instantly and simultaneously detonating an explosive hemispherical shell in a safe and reusable facility. Some consultation with U.S. and Canadian explosive-research laboratories made it clear that the current thinking was that it was not possible to detonate a solid explosive with a gaseous detonation wave. However, we felt that not enough was known then (nor is it known now) about the physical processes involved in the micro-second regime during the initiation of a solid explosive and therefore the advice from experts was put aside. A small one-dimensional facility was built to test the initiation of solid explosives by gaseous detonation waves [58]. Many explosives were tried (including some dangerous ones, like lead azide; I am grateful to Dr. R. E. Duff for persuading me by telephone to immediately desist from using such unpredictable and hazardous materials) and PETN was found to be an excellent safe secondary-explosive to be used for making hemispherical shells of explosives to be detonated by the gaseous detonation wave in stoichiometric hydrogen-oxygen mixtures in the reusable hemispherical driver [59]. The implosion on reflection at the geometric centre produced a hot high-

pressure plasma useful for driving projectiles, intense shock waves, the creation of diamonds from graphite and producing fusion plasmas in deuterium. This work will be discussed subsequently in more detail.

The explosive-driven implosion chamber used as a driver for projectiles and shock tubes is shown in Fig. 21. A great deal of analytical, design and experimental work was done to predict and verify its performance [60-65]. Although plans were made to build a much larger launcher (from a 5 mm barrel to a 25 mm barrel; from a 100-mm radius hemispherical cavity to a 300-mm radius cavity; from a few hundred-gram PETN-shell to one of many kilograms), it was soon found on the smaller-scale model that there were no projectile materials available that could withstand the enormous plasma base-pressures and temperatures developed after reflection of an implosion. Consequently, even though very high velocities (20 km/s) were predicted analytically, no more than 5.4 km/s was actually obtained for an 8-mm dia lexan projectile weighing 0.36g [66]. It is possible that such problems would not have existed on the projected full-scale launcher. Nevertheless, the very high cost of producing such a large facility, coupled with several uncertainties such as projectile integrity, the large amounts of explosive to be used, consistent focussing of the implosions and safety aspects associated with a facility of this size discouraged its construction.

It is also worth noting that an alternative scheme for producing explosive-driven implosions was tried by directly initiating a 5-mm thick sheet explosive hemispherical shell by using 91 explosive detonators. This meant that all detonators had to fire within a jitter of two or three microseconds — a formidable task. The method did not prove successful and had to be abandoned [67].

In order to prepare for the interferometric studies of nonequilibrium corner-expansion flows of dissociating oxygen and nitrogen, as well as ionizing argon, it became necessary to determine the refractivities of the component gases in the mixtures [68-70]. This was done successfully with considerable accuracy in the 10cm x 18cm hypervelocity shock tube by means of the 23-cm dia Mach-Zehnder interferometer. Additional analytical work was also done on such flows with coupled vibrational-dissociational nonequilibrium [71]. An initial investigation on dissociating-oxygen corner-flow did not prove to be definitive in its comparison with analysis [72] and therefore would require additional study.

Some preliminary research was also done on oblique shock-wave reflections at a sharp compressive corner and shock-wave diffraction over a sharp expansive corner [73]. In subsequent years this area of investigation was to lead to some important studies with significant results.

Interest was also aroused by the possibility of flying a micrometeoroid-impact gauge designed by NASA on one of NASA's or Canada's rocket experiments. This area of research was at that time of much importance. The safety of astronauts and spacecraft under bombardment from micrometeoroid particles travelling at the escape velocity from earth (11 km/s) up to the escape velocity from the solar system (73 km/s) was still an unsettled question. The gauge was calibrated by dropping glass microspheres under gravity and in a shock-tube flow [74] seeded with the same glass spheres as well as one-micron particles charged electrostatically [75] and accelerated to 7 km/s at the NASA Goddard Space Flight Center. This gauge was not flown on one of the rocket experiments owing to lack of funds and personnel.

4. THE THIRD DECADE, 1968-1978

This decade is marked by efforts to experimentally observe (Fig. 22) and measure actual and physical properties [76] of the focus of combustion and

explosive-driven implosions and to compare them with analytical predictions [77]. Temperatures were measured spectroscopically for combustion runs only [76], and projectile base-pressures were inferred from microwave measurements of the projectile velocity in the launcher barrel [78]. Spectroscopic temperature and pressure measurements [79,80] were reasonably successful and were improved on subsequently.

An important step was taken to apply the explosive-driven implosions as drivers for shock tubes [81]. A 25-mm shock-tube channel was used instead of a launcher barrel [82]. This proved to be a very worthwhile method of producing very strong shock waves (20 km/s) in air [83] (Fig. 23). It also led to the explanation of some anomalous radiation effects in the shock fronts [84] (Fig. 24), which until then defied a reasonably physical interpretation. (One of the reviewers of our paper in complimenting our work noted that this proper explanation had waited for several years and urged us to change our research note to a full paper.) Although this was a very useful driver, far more impressive electrical drivers were developed at JPL [85] and NASA Ames [86]. This made it possible to obtain at JPL shock-wave velocities of 45 km/s, with little attenuation in a 15 cm dia channel with a 4 μ s test-time. Concurrently, an explosive (Voitenko) driver developed at NASA Ames [87], using 30 kg of explosive (about 300-fold greater than the explosive-driven implosion shock tube at UTIAS) yielded velocities of 70-67 km/s in a 3cm x 3.1m long glass tube over a distance of 1 meter in one of the runs (about 3-fold greater than at UTIAS). These experiments had to be done at the Lawrence Radiation Laboratory explosive test site, where the facility was destroyed after each run (except for the instrumentation). This is probably the highest shock-wave velocity obtained, with a modest attenuation, and some test time useful for Jovian entry studies. It should be noted that all of these facilities used very low (0.05 torr \sim 2 torr) channel gas pressures.

Another very important application of the UTIAS Explosive-Driven Implosion Driver was in the production of synthetic diamonds from graphite. By placing graphite in a steel capsule and exposing it to a focussed-implosion and its reflection, thereby generating enormous pressures (megabar range) and temperatures (millions of degrees), the attenuated transmitted shock-wave pressures and temperatures were sufficient to create the phase transition. Industrial-type diamonds of 10-20 μ m were produced with a yield of about 5-10% of the original graphite [88]. Although such diamonds had been produced statically and dynamically before, this technique was quite novel and promising for the manufacture of new materials and in the application to problems in solid-state physics.

The process was transferred to 3M Canada Ltd., as it was felt that it could best be developed by an industrial firm with much experience in related areas. As a result a fairly large group was set up by 3M at UTIAS to further develop and extend the work on the production of industrial diamonds. The success of this initial work (diamonds were produced in the first experiment) [88], led to the concept of using the explosive-driven implosions to produce fusion plasmas and neutrons from deuterium-deuterium reactions. Further consideration will be given to the implosion research in the final section.

This period was also productive in analytical and experimental studies of ionizing-argon flows. Definitive interferometric investigations were made of the shock structure of ionizing argon and krypton at nominal shock Mach numbers of 13 and 16 [70,89,90]. It was found that the shock wave developed nonstationary oscillations (Fig. 25) at the higher Mach numbers (> 14). The oscillations were easily removed by adding small amounts of hydrogen ($\sim 0.5\%$ of the initial pressure), with the consequent reduction of the overall transition length to about one-third of its pure-gas value. The total plasma density and electron-density profiles for pure argon (Fig. 26) and with small amounts of hydrogen added as an impurity, agreed well with analysis. Two questions

remain unanswered to this day: precisely why only a hydrogen impurity removes the oscillations and why the electron cascade-front, where equilibrium ionization occurs, moves towards the translational front as it approaches the wall (Fig. 27). Some analytical work has recently appeared, which attempts to explain this phenomenon [91].

At the same time the laminar shock-tube wall-boundary layer (Fig. 28) and the flat-plate boundary-layer flow (Fig. 29) in the quasi-steady region was studied in ionizing argon analytically and interferometrically for the same shock Mach numbers as the shock structure [92-95]. (It is worth noting that a wall-boundary-layer study at low shock Mach numbers in air had been done many years earlier [96] using the same Mach-Zehnder interferometer with a smaller rectangular shock tube.) It was shown that the wall boundary layer had a profound effect on the shock structure. The smaller the tube hydraulic-diameter the thinner was the shock structure (Fig. 30). This result is of importance when comparing experimentally-measured shock structure with analysis. The properties of both types of boundary layers were compared analytically and experimentally. There certainly are differences between them. A difficulty with any experimental technique is to probe the boundary layer near the wall. Nevertheless, total plasma density and electron-number densities were obtained up to 0.1 mm from the wall. The shock-structure wall-boundary-layer interaction did not appear to affect the flat-plate boundary layer too much at lower shock Mach numbers (~ 13). However at higher Mach numbers (~ 16) radiation losses induced nonuniformities at a given test-section station [95]. Additional analysis should be done on this aspect of the investigation.

Another important area of ionizing-argon flows was the investigation of a quasi-steady corner-expansion [97]. The results agreed reasonably well with an earlier analysis [52c], which was later extended to include radiation losses [98]. Apparently, radiation losses were not too important at the lower shock Mach numbers (where the experimental data was obtained) to affect the corner-expansion. As noted earlier, at higher shock Mach numbers, radiation effects are quite significant and would affect such flows. Further analytical work should be done to settle this question.

A number of analytical and experimental investigations were started on condensation of water vapour cooled by nonstationary rarefaction waves in a shock tube [99-101]. Although the initial work was started in the Fifties in order to see if indeed condensation shock waves do appear in rarefaction waves (Fig. 31), it was not until the Seventies that it was shown analytically (using the method of characteristics) that such waves must occur as a result of the release of the latent heat of condensation [99]. The experimental pressure profiles [101] could be explained on either the analytical basis of homogeneous [99] or heterogeneous [100] nucleation. Which model is correct will have to await a future experimental decision. Unfortunately, this interesting work had to be terminated owing to insufficient financial support. It is also worth noting that in the Seventies a number of excellent facilities such as the wave-interaction tube [11], the shock sphere [40] and a new hypersonic shock tunnel [102] had to be abandoned owing to a lack of funding in these areas of research.

This period also saw a continuation of the research on oblique shock-wave reflections, which culminated in some significant results. The work initially dealt with a number of considerations of real-gas effects [103]. It was later extended to solve once and for all the problem of: given a sharp compressive corner of angle θ_w in a shock-tube channel at specified initial conditions, what type of reflection will occur when it is hit by a plane shock wave at a specified Mach number M_s ? Investigators from a number of countries had tackled this problem since the Forties with only partial success. It was finally solved and verified interferometrically at UTIAS for diatomic [104] and monatomic gases [105]. It was shown that in the (M_s, θ_w) -plane four types of

reflections (regular, single Mach, complex Mach and double Mach) can occur. The regions and their transition boundaries were determined analytically for perfect and imperfect gases including the effects of equilibrium vibration, dissociation and ionization. Recently, it was found that our interferometric results and the optical data from many other researchers agree best with a perfect-gas analysis as far as the various regions and their transition boundaries are concerned. However, real-gas effects become important immediately after the viscous shock waves. Consequently, some areas bounded by the incident, reflected and Mach-stem shock waves may be in nonequilibrium or may achieve equilibrium depending on the various relaxation times. Therefore, in analysing the flow isolines, real-gas effects including rate equations must be considered.

The experimental lines of constant-density (isopycnics) (Fig. 32) showed that despite the many developments in computational methods, all were not capable of accurately predicting the isopycnics of such nonstationary flows [106]. This is now being addressed by a number of computational centres with increasing accuracy [107,108]. Numerical data can now be compared with the available interferometric data for monatomic, diatomic [104-106] and triatomic [125] gases.

It can be expected that more novel and accurate computational methods will evolve in the near future. Such results would be of much assistance to the experimenter in interpreting his optical data not only in the laboratory but in field trials of spherical blast waves. Numerical time-dependent solutions for such problems are yet to be achieved. Once computer codes are verified experimentally, they can produce far more data on physical quantities than it is possible to measure.

In the late Sixties the supersonic transport (SST) became controversial for a number of reasons. Their possible injurious effects on humans, animals and structures were important considerations for Canada, if overflight laws were to be enacted based on facts. Therefore, a number of Canadian establishments and the University of Toronto contributed to the construction of two simulators: a travelling-wave sonic-boom facility and a loudspeaker-driven booth [109]. A great deal of research was conducted in the areas of psychoacoustics, human response, effects on animals, structural response and gas-dynamic analyses [110-117]. Basically, no effects on humans when subjected to sonic booms similar to SST's were observed as far as heart rate changes, temporary threshold shifts and while driving an arduous automobile course. The structural effects on "aged" panels also were found to be negligible. However, small animals like mice, guinea pigs, chinchillas and Rhesus monkeys did tend to suffer physical damage at the basal turn of the cochlea in the form of bleeding which was absorbed in time (or destroyed hair cells). Sonic-boom rise-time, overpressure-amplitude and frequency of exposure were all important factors affecting the bleeding. However, the scaling laws from small animals to humans are unknown. Nevertheless, caution should be exercised against excessive exposure to superbooms.

Since human-startle effects increase with decreasing sonic-boom risetime [118], the question arose why actual sonic booms produced by SST's can be 100 to 1000-fold greater than predicted by planar shock wave analysis. Atmospheric turbulence [119], temperature gradients near the ground, microphone-response limitations and vibrational excitation [120] of the oxygen and nitrogen components of air were all blamed. Consequently, this problem was investigated experimentally using exploding sparks and wires [121]. It now appears that vibrational excitation of oxygen can give rise to extended shock-wave transitions at low overpressures (about one-tenth the usual sonic-boom value of 100 Pascals). Small-scale turbulence would not be significant. However, large eddies of the size of the aircraft might well give rise to rounded booms with large risetimes or spiked booms with short risetimes. Both types are observed

during any overflight past an array of microphones at different altitudes or on the ground.

5. THE FOURTH DECADE, 1978-

Some of the problems discussed in the previous section are being continued and extended. New research is being initiated and conducted in new or forthcoming facilities. The following research areas are being pursued at the present time: implosion-wave dynamics, oblique shock-wave reflections, sonic-boom effects and the new areas of turbulent, swirling, combusting flows (although this does not deal with shock-tube flows, it deserves to be mentioned) and shock waves in dusty gases.

Three aspects of implosion-wave dynamics are of importance, including the spectroscopic measurements of temperature at an implosion focus, which is produced by combustion or with explosives, and the application of the Random-Choice Method [122] to analyse the experimental results. This topic will be presented as a separate paper at this Symposium [123]. Consequently, it will not be dealt with here. The application of explosive-driven implosions to the production of industrial diamonds and other new materials is very active. An improved facility has been built for this purpose which eliminates a good deal of physical labour through mechanization (Fig. 33). The horizontal position of the flat face of the hemisphere during a run has greatly improved the frequency of excellent focussing. The measurement of physical quantities using manganin-wire pressure gauges, X-ray diffraction, electron diffraction and photomicrographs have all proved to be very useful (Fig. 34). A model is being developed to explain how dynamic transitions from graphite to diamond can take place in the submicrosecond regime [124]. Additional solid-state problems will be investigated in the oncoming years.

The use of explosive-driven implosions to produce fusion has not been easy mainly due to a lack of financial support and trained personnel. Nevertheless, neutrons and γ -rays have been generated from D-D reactions at the focus in runs of 54-atm stoichiometric deuterium-oxygen ($2D_2+O_2$) and about 100-g PETN-explosive shells (Fig. 35). Similar results have also been obtained by placing a small hemispherical capsule containing 1.2 atm of pure deuterium covered by a metal diaphragm at the implosion focus (similar to a Voitenko compressor [87]). Experts in the field were skeptical if we would obtain neutrons with so little explosive energy. Our prospects for improving this work and to measure the neutron flux and other radiation properties are not good without adequate financial support. Yet, our ideas have proved to be sound and they await further developments.

The research on oblique shock-wave reflections in monatomic and diatomic gases has been successfully applied to a triatomic gas such as carbon-dioxide [125a], which is already substantially excited at room temperature. Yet, the numerous experiments all agree with the (M_s, θ_w) -plot for a perfect gas with $\gamma = 1.29$ (Figs. 36, 37). Consequently, the shock-wave-reflection process behaves as if the specific heats were frozen in front and immediately behind the shock waves. The flow regions bounded by the shock waves will be in non-equilibrium and if the flow times are long enough equilibrium will finally be attained. The results do not fit the complete vibrational-dissociational-equilibrium model nor any other partial equilibrium model [125a]. The research is being continued in air [125b]. The early dissociation of oxygen with increasing shock strength compared to nitrogen adds some interesting aspects to this problem (Fig. 38). It is, of course, of most interest to experimenters conducting spherical-blast investigations in the field.

It has now been found that some small animals suffer significant hearing impairment (in the entire range or in some part of the high-frequency range) after the blood clots in the cochlea have been absorbed. Since their hearing

range far exceeds that of man (mice hear up to 100 kHz), it is at present not known whether humans also suffer losses and for how long at high frequencies (< 20 kHz) when chronically exposed to sonic booms [126]. This question will be investigated in the near future.

It now appears that the excellent N-waves produced by exploding wires may not be able to exactly simulate SST sonic booms. The Random-Choice Method has been successfully applied to solve this problem by modelling the exploding wire or spark by a blast from a small pressurized sphere. Since this method does not introduce an artificial viscosity it is possible to solve the spherical shock-wave transition. It is thinner than the equivalent plane-wave profile solved by G. I. Taylor. Since this subject is also being presented as a separate paper [127] at this symposium no further details will be given. The work on the structural response of a wood-plaster room subject to sonic boom and its subsequent crack-propagation properties has been completed and is being presented as a separate paper at this symposium [128]. The agreement between pressure and strain measurements and analysis was very good. The agreement of the finite-element crack-propagation analysis and (of necessity) one decisive experiment was very satisfactory. The problem of the pressures generated in two interconnecting rooms by a sonic boom is now being investigated analytically and experimentally.

The design of thermally efficient combustors with a minimum of pollutants for jet engines and home furnaces is a very important field of research in view of our dwindling fossil fuels. Such flows are usually turbulent, swirling and chemically reacting. It is a difficult problem to model analytically [129]. In order to verify such analysis, it is important to measure the turbulence quantities of the flow. This can be done using laser-Doppler velocimetry. It can also be applied to measure fuel-droplet size and distribution. Such a facility has now been developed and will shortly be applied to verify the analytical work [129]. Hypersonic combustion is another area of interest [130-132] and will be continued if financial support is made possible.

The structure of moving shock waves in dusty air is of considerable interest. For this purpose the analysis of a dusty-gas shock tube has been completely investigated using the Random-Choice Method [133]. The nonequilibrium-flow profiles from the head of the rarefaction wave to the frozen shock wave were computed, including the shock-front and the contact-front transitions (Fig. 39). Working curves were determined for frozen and equilibrium shock transitions as functions of the initial conditions, dust concentration and diaphragm-pressure ratio. The regions where only dispersed shock waves eventually occur have also been found (Fig. 40). A new 7.6cm x 20cm shock tube is under construction to validate the analysis and to conduct many new experiments of current interest to the researcher in the laboratory or on field trials.

6. CONCLUSIONS

This brief survey of research on shock tubes and waves at UTIAS over the past 33 years has attempted to give some insight into a unique experience. It is doubtful if any other laboratory has been engaged in this ever-changing field, continuously, over such a lengthy period. A lot of good research and development work was done in a number of specially conceived facilities. It has led to the training of many Ph.D. and Masters graduates, visiting scientists and academics. Numerous UTIAS reports and journal papers were published. The present list of references is by no means complete. Our work over the years has attempted to add to and enlarge mankind's store of scientific and engineering knowledge. The outlook for the future is bright. There are excellent young people at UTIAS to take over and continue this important work on shock tubes and waves for many years to come.

ACKNOWLEDGEMENTS

This paper is dedicated to my students and colleagues everywhere who have made it all possible. In particular, I thank Dr. J. J. Gottlieb and Dr. J. P. Sislian for reading the manuscript, and their helpful discussions.

I am grateful to the Executive Committee for the honour of choosing me as the Paul Vieille Lecturer. This lecture was initiated when I was Chairman of the Seventh Symposium, Toronto, 1969. It is gratifying to see it established now as a tradition in memory of the first known researcher on shock tubes and waves, whose paper appeared in *Comptes Rendus* in 1899 (and in the original and translation in the Proceedings of the Seventh Symposium).

The financial support received over the years from many Canadian (DRB, NRC, NSERC, EMR) and U.S. (AFOSR, NASA, ONR, ARO) government agencies and Canadian (AC, P&W) industry is acknowledged with thanks.

NOTE

Owing to a lack of space it was not possible to include the 40 figures. These may be found in UTIAS Review No. 45, 1981.

REFERENCES

1. G. N. Patterson, *Pathway to Excellence*, UTIAS, 1977.
2. D. Bitondo and R. K. Lobb, "Design and Construction of a Shock Tube", UTIA Report No. 3, 1950.
3. D. Bitondo, I. I. Glass and G. N. Patterson, "One-Dimensional Theory of Absorption and Amplification of a Plane Shock Wave by a Gaseous Layer", UTIA Report No. 5, 1950.
4. D. Bitondo, "Experiments on the Amplification of a Plane Shock Wave", UTIA Report No. 7, 1950.
5. I. I. Glass, "Design of a Wave-Interaction Tube", UTIA Report No. 6, 1950.
6. R. K. Lobb, "On the Length of a Shock Tube", UTIA Report No. 4, 1950.
7. R. K. Lobb, "A Study of Supersonic Flows in a Shock Tube", UTIA Report No. 8, 1950.
8. G. N. Patterson, "Theory of the Shock Tube", NOL Memo 9903, White Oak, Md., 1948.
9. G. N. Patterson, *Molecular Flow of Gases*. John Wiley & Sons, New York, 1956.
10. G. N. Patterson, *Introduction to the Molecular Theory of Gas Flows*. UTIAS, 1971.
- 11a. I. I. Glass, W. A. Martin, G. N. Patterson, "A Theoretical and Experimental Study of the Shock Tube", UTIAS Report No. 2, 1953.
- 11b. I. I. Glass and G. N. Patterson, "A Theoretical and Experimental Study of Shock-Tube Flows", *J. Aero. Sci.*, 22, 2, 1955, pp. 73-100.
12. I. I. Glass and J. G. Hall, *Handbook of Supersonic Aerodynamics*, Section 18, Shock Tubes. Navord Report 1488, Vol. 6, U.S. Government Printing Office, Washington, D.C., 1959.
13. D. W. Boyer, "Effects of Kinematic Viscosity and Wave Speed on Shock Wave Attenuation", UTIA Technical Report No. 8, 1956.
14. Mirels, H., "Attenuation in a Shock Tube due to Unsteady Boundary Layer Action", NACA TN 3278, 1956.
15. R. L. Trimpi and N. B. Cohen, "An Integral Solution to the Flat Plate Laminar Boundary Layer Flow Existing Inside and After Expansion Waves and After Shock Waves Moving into Quiescent Fluid with Particular Application to the Complete Shock Tube Flow", NACA TN 3944, 1957.
16. H. Mirels and W. H. Braun, "Nonuniformities in Shock-Tube Flow due to Unsteady Boundary Layer Action", NACA TN 4021, 1957.

- 17a. C. A. Ford and I. I. Glass, "An Experimental Study of Shock Wave Refraction", UTIA Report No. 29, 1954.
- 17b. C. A. Ford and I. I. Glass, "An Experimental Study of One-Dimensional Shock Wave Refraction", J. Aero. Sci., 23, 2, 1956, pp. 189-191.
18. E. K. Parks, "Supersonic Flow in a Shock Tube of Divergent Cross-Section", UTIA Report No. 18, 1952.
19. G. V. Bull, "Starting Process in an Intermittent Wind Tunnel", UTIA Report No. 12, 1951.
20. G. V. Bull, L. R. Fowell and D. H. Henshaw, "The Interaction of Two Similarly Facing Shock Waves", UTIA Report No. 25, 1953.
- 21a. I. I. Glass, "An Experimental Determination of the Speed of Sound in Gases from the Head of a Rarefaction Wave", UTIA Report No. 9, 1951.
- 21b. I. I. Glass, "On the Speed of Sound in Gases", J. Aero. Sci., 19, 4, 1951, p. 286.
- 21c. I. I. Glass and J. G. Hall, "Determination of the Speed of Sound in Sulfurhexafluoride in a Shock Tube", J. Chem. Phys., 27, 5, 1957, p. 1223.
22. D. G. Gould, "The Head-On Collision of Two Shock Waves and a Shock and Rarefaction Wave in One-Dimensional Flow", UTIA Report No. 17, 1952.
23. C. I. H. Nicholl, "The Head-On Collision of Shock and Rarefaction Waves", UTIA Report No. 10, 1951.
24. I. J. Billington and I. I. Glass, "On the One-Dimensional Refraction of a Rarefaction Wave at a Contact Surface", UTIA Report No. 31, 1955.
25. I. J. Billington, "An Experimental Study of One-Dimensional Refraction of a Rarefaction Wave at a Contact Surface", UTIAS Report No. 32, 1955.
26. J. G. Hall, "The Design and Performance of a 9 Inch Plate Mach-Zehnder Interferometer", UTIA Report No. 27, 1954.
27. J. G. Hall, "The Transition Through a Contact Region", UTIA Report No. 26, 1954.
28. H. F. Waldron, "An Experimental Study of a Spiral Vortex Formed by Shock-Wave Diffraction", UTIA Technical Note No. 2, 1954.
29. W. J. Franks, "Interaction of a Shock Wave with a Wire Screen", UTIA Technical Note No. 13, 1957.
30. W. H. Friend, "The Interaction of a Plane Shock Wave with an Inclined Perforated Plate", UTIA Technical Note No. 25, 1958.
31. H. F. Waldron, "An Experimental Investigation of the Flow Properties Behind Strong Shock Waves in Nitrogen", UTIA Report No. 50, 1958.
32. J. H. de Leeuw, "The Interaction of a Plane Strong Shock Wave with a Steady Magnetic Field", UTIA Report No. 49, 1958.
33. J. A. Steketee, "On the Interaction of Rarefaction Waves in a Shock Tube", UTIA Review No. 4, 1952.
34. I. I. Glass, L. E. Heuckroth and S. Molder, "On the One-Dimensional Overtaking of a Shock Wave by a Rarefaction Wave", UTIA Technical Note No. 30, 1960; see also ARS J., 1961, pp. 1453-1454.
35. G. F. Bremner, J. K. Dukowitz and I. I. Glass, "On the One-Dimensional Overtaking of a Rarefaction Wave by a Shock Wave", UTIA Technical Note No. 33, 1960; see also ARS J., 1961, pp. 1455-1456.
36. W. J. Cook, L. L. Presley and G. T. Chapman, "Shock Tube as a Device for Testing Transonic Airfoils at High Reynolds Numbers", AIAA J., 17, 7, 1979, pp. 714-721.
37. K. O. Tong, C. J. Knight and B. K. Srivastava, "Interaction of Weak Shock Waves with Screens and Honeycombs", AIAA J., 18, 11, 1980, pp. 1298-1305.
38. D. Zeitoun and M. Imbert, "Interaction Between the Unsteady Boundary Layer and Inviscid Hot Flow in a Shock Tube", AIAA J., 17, 8, 1979, pp. 821-827.
- 39a. J. G. Hall, "Studies of Transient Gas Boundary Layer Flows Generated by Unsteady Waves", Proceedings on Unsteady Aerodynamics, edited by R. B. Kinney, University of Arizona, 1975.
- 39b. Y. M. Amr and J. G. Hall, "Stability Limits and Transition Times of Wave-Induced Wall Boundary Layers", 13th Int. Symp. on Shock Tubes and Waves, July 6-9, 1981, Niagara Falls, New York.
40. I. I. Glass, "Aerodynamics of Blasts", UTIA Review No. 17, 1960; see also CASI J., 7, 3, 1961, pp. 109-135.

41. I. I. Glass and J. G. Hall, "Shock Sphere - An Apparatus for Generating Spherical Flows", J. Appl. Phys. 28, 4, 1958, pp. 424-425.
42. D. W. Boyer, H. L. Brode, I. I. Glass and J. G. Hall, "Blast from a Pressurized Sphere", UTIA Report No. 48, 1958.
43. D. W. Boyer, "Spherical Explosions and Implosions", UTIA Report No. 58, 1959.
44. R. Collins, "Some Methods of Generating Cylindrical Explosions", UTIA Technical Note No. 43, 1960.
45. I. I. Glass and L. E. Heuckroth, "An Experimental Investigation of the Head-On Collision of Spherical Shock Waves", UTIA Report No. 59, 1960; see also Phys. Fluids, 2, 5, 1959, pp. 542-546.
46. I. I. Glass and L. E. Heuckroth, "The Hydrodynamic Shock Tube", Phys. Fluids, 6, 4, 1963, pp. 543-547.
47. L. E. Heuckroth and I. I. Glass, "Low-Energy Spherical Underwater Explosions", Phys. Fluids, 11, 10, 1968, pp. 2095-2107; see also UTIA Report No. 96, 1964.
48. A. Benoit, "An Experimental Investigation of Spherical Combustion for the UTIA Implosion-Driven Launcher", UTIA Technical Note No. 71, 1963.
- 49a. A. Benoit, "Thermodynamic and Composition Data for Constant Volume Combustion of Stoichiometric Mixtures of Hydrogen-Oxygen Diluted with Helium or Hydrogen", UTIAS Technical Note No. 85, 1964.
- 49b. A. Benoit, "Specific Heat Ratios and Isentropic Exponents for Constant Volume Combustion of Stoichiometric Mixtures of Hydrogen-Oxygen Diluted with Helium or Hydrogen", UTIAS Technical Note No. 102, 1966.
- 49c. A. Benoit, "Properties of Chapman-Jouguet Detonations in Stoichiometric Hydrogen-Oxygen Mixtures Diluted with Helium or Hydrogen", UTIAS Technical Note No. 104, 1967.
- 49d. A. Benoit, "Equilibrium Thermodynamic Data for the H_2-O_2-He Systems", UTIAS Technical Note No. 128, 1968.
50. A. Benoit and I. I. Glass, "An Experimental Study of Spherical Combustion Waves in a Hemispherical Chamber", Combustion & Flame, 12, 2, 1968, pp. 521-533.
51. I. I. Glass and H. Kawada, "Prandtl-Meyer Flows of Dissociated and Ionized Gases", UTIA Report No. 85, 1962.
- 52a. I. I. Glass and A. Takano, "Nonequilibrium Flows of Dissociated Oxygen and Ionized Argon Around a Corner", Prog. Aero. Sci., 6, 1965, pp. 163-249.
- 52b. I. I. Glass and A. Takano, "Nonequilibrium Expansion Flow of Dissociated Oxygen Around a Corner", UTIA Report No. 91, 1963.
- 52c. I. I. Glass and A. Takano, "Nonequilibrium Expansion Flow of Ionized Argon Around a Corner", UTIAS Report No. 95, 1963.
53. A. G. Boyer, "Design, Instrumentation and Performance of the UTIAS 4 in x 7 in Hypersonic Shock Tube", UTIAS Report No. 99, 1964.
54. J. K. Dukowitz, "A Magnetohydrodynamic Flow in the Shock Tube Boundary Layer with Transverse Magnetic Field", UTIAS Report No. 115, 1966. (This work was supervised by Prof. J. H. de Leeuw.)
55. Y. Y. Chan, R. P. Mason and N. M. Reddy, "Instrumentation and Calibration of UTIAS 11 in x 15 in Hypersonic Shock Tunnel", UTIAS Technical Note No. 91, 1965.
56. N. M. Reddy, "The Use of Self-Calibrating Catalytic Probes to Measure Free-Stream Atom Concentration in a Hypersonic Flow", UTIAS Report No. 121, 1966.
- 57a. A. N. Belozarov, "Study of the Initial Ionization Process in a Strong Shock Wave", UTIAS Report No. 131, 1968. (This work was supervised by Prof. R. M. Measures.) See also A. N. Belozarov and R. M. Measures, J. Fluid Mech., 36, 1969, pp. 695-720.
- 57b. S. P. Kalra and R. M. Measures, "Approach to Ionization Equilibrium and Atomic Cross-Section Measurements in a Helium Shock Wave", Can. J. Phys., 51, 18, 1973, pp. 1956-1965. (This work was supervised by Prof. R. M. Measures.)
58. A. H. Makomaski, "Preliminary One-Dimensional Investigation of the Initiation of Low-Density PETN by Hydrogen-Oxygen Detonation Waves", UTIAS

- Technical Note No. 83, 1965.
59. R. F. Flagg and I. I. Glass, "Explosive-Driven Spherical Implosion Waves", *Phys. Fluids*, 11, 10, 1968, pp. 2282-2284; see also R. F. Flagg, "The Application of Implosion Wave Dynamics to a Hypervelocity Launcher", UTIAS Report No. 125, 1967.
 60. J. D. Watson, "Implosion-Driven Hypervelocity Launcher Performance Using Gaseous Detonation Waves", UTIAS Technical Note No. 113, 1967.
 61. P. Sevray, "Performance Analysis of UTIAS Implosion-Driven Hypervelocity Launcher", UTIAS Technical Note No. 121, 1968.
 62. R. F. Flagg and G. P. Mitchell, "An Optimization Study of the UTIAS Implosion-Driven Hypervelocity Launcher MK II", UTIAS Technical Note No. 130, 1968.
 63. S. K. Garg, "Spherical Elastic-Plastic Waves in Solid Media", UTIAS Technical Note No. 32, 1969.
 64. W. Czerwinski, "Structural Design and Development of UTIAS Implosion-Driven Launcher", UTIAS Report No. 153, 1970.
 65. A. K. Macpherson, "A Preliminary Monte-Carlo Analysis of the Reflection of an Imploding Hemispherical Shock Wave Similar to that Generated in the UTIAS Implosion Driven Hypervelocity Launcher or Shock Tube", UTIAS Report No. 153, 1970.
 66. I. I. Glass, "Appraisal of UTIAS Implosion-Driven Hypervelocity Launchers and Shock Tubes", *Prog. Aero. Sci.* 13, 1972, pp. 223-291.
 67. J. E. Kennedy and I. I. Glass, "Multipoint Initiated Implosions from Hemispherical Shells of Sheet Explosive", UTIAS Technical Note No. 99, 1966.
 68. J. H. B. Anderson, P. J. K. Osborne and I. I. Glass, "Gladstone-Dale Constants for the Oxygen Atom and Molecule", *Phys. Fluids*, 10, 8, 1967, p. 1848.
 69. D. E. Wettlaufer and I. I. Glass, "Specific Refractivities of Atomic Nitrogen and Oxygen", *Phys. Fluids*, 13, 11, 1972, pp. 2065-2066.
 70. M. P. F. Bristow and I. I. Glass, "Polarizability of Singly-Ionized Argon", *Phys. Fluids*, 15, 11, 1972, 2066-2067.
 71. D. Tirumalesa, "Oxygen Corner-Expansion Flows with Coupled Vibrational and Dissociational Nonequilibrium", UTIAS Technical Note No. 120, 1967.
 72. J. E. Drewry, "An Experimental Investigation of Nonequilibrium Corner Expansion Flows of Dissociated Oxygen", UTIAS Report No. 124, 1967.
 73. R. R. Weynants, "An Experimental Investigation of Shock-Wave Diffraction Over Compressive and Expansive Corners", UTIAS Technical Note No. 126, 1968.
 74. M. Gorjup and I. I. Glass, "Laboratory Calibration of a Micrometeoroid Impact Gauge", *CAS J.*, 13, 5, 1967, pp. 197-204.
 75. R. L. Evans and I. I. Glass, "Calibration of a Condenser Microphone Micro-Meteoroid Sensor", *CAS J.*, 16, 9, 1970, pp. 375-379.
 76. D. E. Roberts and I. I. Glass, "A Spectroscopic Investigation of Combustion-Driven Spherical Implosion Waves", *Phys. Fluids*, 14, 8, 1971, pp. 1662-1670; see also UTIAS Technical Note No. 140, 1969.
 77. A. Elsenaar, "A Numerical Model for a Combustion-Driven Spherical Implosion Wave", UTIAS Report No. 144, 1969.
 78. A. Elsenaar, "Microwave Measurements of Projectile Motion in the Barrel of the UTIAS Implosion-Driven Hypervelocity Launcher", UTIAS Technical Note No. 145, 1969.
 79. R. A. Roig and I. I. Glass, "A Spectroscopic Study of Combustion Driven Implosions", *Phys. Fluids*, 20, 10, 1977, pp. 1651-1656.
 80. B. Vasudevan, "Pressure Measurements at the Focus of Combustion-Driven Implosions", UTIAS Technical Note No. 209, 1977.
 81. J. C. Poinssot, "A Preliminary Investigation of a UTIAS Implosion-Driven Shock Tube", UTIAS Technical Note No. 136, 1969.
 - 82a. S. K. Chan, "An Analytical and Experimental Study of an Implosion-Driven Shock Tube", UTIAS Report No. 191, 1973.
 - 82b. S. K. Chan, G. Capelli and W. O. Graf, "Performance Trials of the Eight-Inch Diameter UTIAS Implosion Driven Hypervelocity Launchers MK II and MK III", UTIAS Technical Note No. 161, 1971.

83. I. I. Glass, H. L. Brode and S. K. Chan, "Strong Planar Shock Waves Generated by Explosively-Driven Spherical Implosions", AIAA J. 12, 3, 1974, pp. 367-374.
84. S. K. Chan and I. I. Glass, "Radiative Relaxation Behind High-Speed Shock Waves in Air", Phys. Fluids, 17, 4, 1974, pp. 688-690.
85. W. A. Menard, "A Higher Performance Electric-Arc-Driven Shock Tube", AIAA J., 9, 10, 1971, pp. 2096-2098.
86. R. E. Dannenberg, "Capabilities of Arc-Driven Shock Tubes", in Proc. 11th Int. Symp. on Shock Tubes & Waves, ed. B. Ahlborn, A. Hertzberg and D. Russel, U. of Washington Press, Seattle, 1977, pp. 416-431.
87. D. L. Compton and D. M. Cooper, "Duplication in a Shock Tube of Stagnation Region Conditions on a Jovian Atmosphere-Entry Probe", Proc. 9th Int. Shock Tube Symp., ed. D. Bershader & W. Griffith, Stanford U. Press, Stanford, 1973, pp. 218-329.
88. I. I. Glass and S. P. Sharma, "Production of Diamonds from Graphite Using Explosive-Driven Implosions", AIAA J. 14, 3, 1976, pp. 402-404.
89. I. I. Glass and W. S. Liu, "Effects of Hydrogen Impurities on Shock Structure and Stability in Ionizing Monatomic Gases, Part 1. Argon", J. Fluid Mech., 84, Part 1, 1978, pp. 55-77.
90. I. I. Glass, W. S. Liu and F. C. Tang, "Effects of Hydrogen Impurities on Shock Structure and Stability in Ionizing Monatomic Gases, Part 2. Krypton", Can. J. Phys., 55(14), 1977, pp. 1269-1279.
91. R. G. Fowles, "Stimulated and Spontaneous Emission of Acoustic Waves from Shock Fronts", Phys. Fluids (to be published), 1981.
92. W. S. Liu, B. T. Whitten and I. I. Glass, "Ionizing Argon Boundary-Layers, Part 1. Quasi-Steady Flat-Plate Laminar Boundary-Layer Flows", J. Fluid Mech., 87, Part 4, 1978, pp. 609-640.
93. W. S. Liu and I. I. Glass, "Ionizing Argon Boundary Layers, Part 2. Shock-Tube Side-Wall Boundary-Layer Flows", J. Fluid Mech., 92, Part 3, 1979, pp. 459-496.
94. W. S. Liu, K. Takayama and I. I. Glass, "Coupled Interactions of Shock-Wave Structure with Laminar Boundary Layers in Ionizing Argon Flows", J. Fluid Mech. 96, Part 4, 1980, pp. 735-756.
95. I. I. Glass, W. S. Liu and F. C. Tang, "Radiation-Induced Shock-Tube Flow Nonuniformities in Ionizing Argon", Phys. Fluids, 23, 1, 1980, pp. 224-225.
96. W. A. Martin, "An Experimental Study of the Boundary Layer Behind a Moving Plane Shock Wave", UTIAS Report No. 47, 1957.
97. O. Igra and I. I. Glass, "Corner Expansion Flow of Ionized Argon", in Dynamics of Ionized Gases, Ed. M. S. Lighthill et al, Tokyo U. Press, 1973, pp. 449-460.
98. O. Igra, "Radiation Effects in a Nonequilibrium Corner-Expansion Flow of Ionizing Argon", Phys. Fluids, 23, 8, pp. 1513-1517.
99. J. P. Sislian and I. I. Glass, "Condensation of Water Vapor in Rarefaction Waves: I. Homogeneous Nucleation", AIAA J. 14, 12, 1976, pp. 1731-1737.
100. S. Kotake and I. I. Glass, "Condensation of Water Vapor in Rarefaction Waves: II. Heterogeneous Nucleation", AIAA J. 15, 2, 1977, pp. 215-221.
101. I. I. Glass, S. P. Kalra and J. P. Sislian, "Condensation of Water Vapor in Rarefaction Waves: III. Experimental Results", AIAA J. 15, 5, 1977, pp. 683-693.
102. W. W. Koziak, "Quantitative Laser Schlieren Measurements in an Expanding Hypersonic Laminar Boundary Layer", UTIAS Report No. 173, 1971 (supervised by Dr. P. A. Sullivan, who built the new hypersonic shock tunnel).
103. C. K. Law and I. I. Glass, "Diffraction of Strong Shock-Waves by a Sharp Compressive Corner", CAS Trans., 4, 1971, pp. 2-12.
104. G. Ben-Dor and I. I. Glass, "Domains and Boundaries of Non-Stationary Oblique Shock-Wave Reflexions, 1. Diatomic Gas:", J. Fluid Mech., 92, Part 3, 1979, pp. 459-496.
105. G. Ben-Dor and I. I. Glass, "Domains and Boundaries of Non-Stationary Shock-Wave Reflexions, 2. Monatomic Gas", J. Fluid Mech. 96, Part 4, 1980.
106. G. Ben-Dor and I. I. Glass, "Nonstationary Oblique Shock-Wave Reflexions, Actual Isopycnics and Numerical Experiments", AIAA J. 16, 11, 1978, pp. 1146-1153.

107. D. L. Book, J. P. Boris, A. L. Kuhl, E. S. Oran, J. M. Picone and S. T. Zalesak, "Simulation of Complex Shock Reflections from Wedges in Inert and Reactive Gaseous Mixtures", NRL Memo Report 4333, 1980.
108. M. W. Booen and C. E. Needham, "Two Dimensional Hull Code Simulation of Complex and Double Mach Reflections", Air Force Weapons Laboratory Technical Note NTE-TN-81-001, 1981; also H. M. Glaz, NSWC, Priv.Com. June 1981.
109. I. I. Glass, H. S. Ribner and J. J. Gottlieb, "Canadian Sonic-Boom Simulation Facilities", CAS J. 18, 10, 1972, pp. 235-246.
110. R. Carothers, "Initial Calibration and Physiological-Response Data for the Travelling-Wave Sonic-Boom Simulator", UTIAS Tech. Note No. 180, 1972.
111. J. J. Gottlieb and I. I. Glass, "Recent Developments in Sonic-Boom Simulation Using Shock Tubes", Can. J. Phys. 52, 3, 1973, pp. 207-218.
112. B. R. Leigh, R. C. Tennyson and I. I. Glass, "Aged Plaster Panels Subjected to Sonic Booms", CAS J. 21, 9, Nov. 1975, pp. 352-360.
113. I. I. Glass, K. W. Lips, O. V. Nowakowsky and L. D. Reid, "Sonic-Boom-Startle Effects During Simulated and Actual Driving Tests", CAS J. 22, 2, 1976, pp. 70-88.
114. J. J. Gottlieb, "Sonic Boom Research at UTIAS", CAS J. 20, 5, 1974, pp. 199-222.
115. J. J. Gottlieb, "Simulation of a Travelling Sonic Boom in a Pyramidal Horn", Prog. Aero. Sci. 17, 1976, pp. 1-66.
116. S. Reinis, "Acute Changes in Inner Ears of Laboratory Animals by Simulated Sonic Booms", UTIAS Report No. 211, 1976.
117. N. N. Wahba, "Pressure Inside a Room Subjected to Sonic Boom", UTIAS Technical Note No. 207, 1977.
118. A. Niedzwiecki and H. S. Ribner, "Subjective Loudness of N-Wave Sonic Booms", J. Acoust. Soc. Amer. 64, 6, 1978, pp. 1617-1621.
119. P. E. Tubb, "Measured Effects of Turbulence on the Rise Time of a Weak Shock", UTIAS M.A.Sc. Thesis, 1975 (supervised by Prof. H. S. Ribner).
120. N. H. Johannesen and J. P. Hodgson, "The Physics of Weak Waves in Gases", Rept. Prog. Phys. 42, 1979, pp. 629-676.
121. O. Holst-Jensen, "An Experimental Investigation of the Rise Times of Very Weak Shock Waves", UTIAS Technical Note No. 229, 1981.
122. T. Saito and I. I. Glass, "Application of Random-Choice Method to Problems in Shock and Detonation-Wave Dynamics", UTIAS Report No. 240, 1979.
123. T. Saito, A. K. Kudian and I. I. Glass, "Temperature Measurements of an Implosion Focus", 13th Int. Symp. on Shock Tubes and Waves, July 6-9, 1981, Niagara Falls, New York.
124. K. Kleiman, "Application of Explosive Driven Implosions to Production of Diamonds and New Materials", Ph.D. Thesis in Progress (supervised by Prof. I. I. Glass and Prof. N. Salansky).
- 125a. S. Ando and I. I. Glass, "Domains and Boundaries of Pseudostationary Oblique-Shock-Wave Reflections in Carbon-Dioxide", 7th Int. Symp. on Military Appl. Blast Symp., July 13-17, Medicine Hat, Canada, 1981 (see also UTIAS Technical Note No. 231, 1981).
- 125b. R. L. Deschambault, UTIAS M.A.Sc. Thesis, in progress.
126. S. Reinis, J. W. Featherstone and D. S. Weiss, "The Effects of Sonic Booms on Hearing and Inner Ear Structure", Int. Symp. on Effects of Impulse Noise on Hearing, Aug. 25-27, 1980, Malmo, Sweden.
127. H. Honma, I. I. Glass, Y. Tsumita and O. Holst-Jensen, "Weak Spherical Shock-Wave Transitions of N-Waves in Air with Vibrational Excitation", 13th Int. Symp. on Shock Tubes & Waves, July 6-9, 1981, Niagara Falls, New York.
128. N. N. Wahba, I. I. Glass and R. C. Tennyson, "Response of a Room Subjected to Simulated Sonic Booms", 13th Int. Symp. on Shock Tubes & Waves, July 6-9, 1981, Niagara Falls, New York.
129. J. P. Sislian, "Analysis of Swirling Jet Turbulent Mixing and Combustion", UTIAS Report No. 249, 1981.
130. J. P. Sislian, "Analysis of Turbulent Free-Jet Hydrogen-Air Diffusion Flames with Finite Chemical Reaction Rates", UTIAS Report No. 224, 1978 (also NASA CR Report 3024, 1978).

131. J. P. Sislian, "Equations of Motion and Two-Equation Turbulence Model for Plane or Axisymmetric Turbulent Flows in Body-Oriented Orthogonal Curvilinear Coordinates and Mass-Averaged Dependent Variables", UTIAS Report No. 225, 1978 (also NASA CR Report 3025, 1978).
132. J. P. Sislian, J. S. Evans and I. I. Glass, "Analysis of Turbulent Free-Jet Hydrogen-Air Diffusion Flames with Finite Chemical Reaction Rates", CAS J. 25, 1, 1979, pp. 61-75.
133. H. Miura and I. I. Glass, "A Dusty-Gas Shock Tube", 7th Int. Symp. on Military Appl. Blast Symp., July 13-17, Medicine Hat, Canada, 1981.

SHOCK TUBES AND WAVES

*Proceedings of the 13th International Symposium
on Shock Tubes and Waves*

Niagara Falls, July 6-9, 1981

Edited by

Charles E. Treanor
Calspan Advanced Technology Center

J. Gordon Hall
State University of New York at Buffalo

Editorial Committee

Paul V. Marrone
George Rudinger

William J. Rae
Anthony L. Russo

Walter H. Wurster

**CALSPAN
ADVANCED
TECHNOLOGY
CENTER**



Faculty of Engineering
and Applied Sciences
State University of
New York at Buffalo

STATE UNIVERSITY OF NEW YORK PRESS
ALBANY, NEW YORK

DISTRIBUTION STATEMENT A
Approved for public release;
Distribution Unlimited

Published by
State University of New York Press, Albany

© 1982 State University of New York

All rights reserved

Printed in the United States of America

No part of this book may be used or reproduced in any manner whatsoever without written permission except in the case of brief quotations embodied in critical articles and reviews.

For information, address State University of New York Press, State University Plaza, Albany, N.Y. 12246.

Library of Congress Cataloging in Publication Data

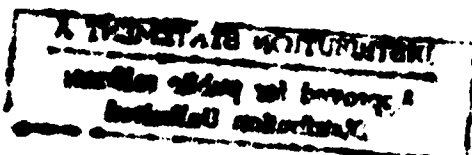
International Symposium on Shock Tubes and Waves (13th :
1981 : Niagara Falls, N.Y.)
Shock tubes and waves.

Sponsored by the U.S. Air Force Office of Scientific
Research.

Includes index.

1. Shock tubes—Congresses. 2. Shock waves—
Congresses. I. Treanor, Charles E., 1924-
II. Hall, J. Gordon. III. Calspan Corporation. Advanced
Technology Center. IV. State University of New York at
Buffalo. Faculty of Engineering and Applied Sciences.
V. United States. Air Force. Office of Scientific
Research. VI. Title.

TL567.S4152 1981 620.1'074 82-3160
ISBN 0-87395-595-1 AACR2



PREFACE

This volume contains six invited papers and ninety two contributed papers presented at the XIII International Symposium on Shock Tubes and Waves, which was held in Niagara Falls, N.Y., July 6 - 9, 1981. Professor I.I. Glass of the University of Toronto presented the Paul Vieille Memorial Lecture. This paper and five other invited papers form Part I of the Proceedings. The contributed papers are presented in Parts II through VII, divided according to subject matter. The typical broad range of interests associated with shock waves is demonstrated in both the invited and contributed papers, with subject material covering viscous aerodynamics, explosions, chemistry, optics, and energy-related processes. It is intended that this volume provide an up-to-date accounting of international progress in these fields insofar as shock-wave phenomena are involved.

The abstracts contributed to this symposium were reviewed and categorized by the Executive Committee and subsequently evaluated by members of the Advisory Committee. On the basis of these reviews, the Executive Committee made the final decisions on paper acceptance. Two hundred participants from seventeen countries were welcomed at the opening session by Professor George C. Lee, Dean of Engineering and Applied Sciences at the State University of New York at Buffalo, Dr. H. Robert Leland, General Manager of Calspan Advanced Technology Center, and the Honorable Michael O'Laughlin, Mayor of Niagara Falls. Professor Charles H.V. Ebert, from the Department of Geography at SUNYAB, addressed the participants after the symposium banquet on the timely subject "Mountains of Fire: The Nature of Volcanoes." At the farewell gathering a narrated movie of the first flight (April 1981) of the space shuttle Columbia was shown, provided by Rockwell International Corporation.

Like its predecessors, the XIII International Symposium on Shock Tubes and Waves has been sponsored by the U.S. AIR FORCE OFFICE OF SCIENTIFIC RESEARCH. Their support and interest is warmly appreciated by all the participants.

The members of the Executive Committee wish to express their gratitude to their organizations, the Calspan Advanced Technology Center and the State University of New York at Buffalo, for their support during the two years of preparation for this meeting. The cooperative efforts of many members of the staff of both organizations are gratefully acknowledged. We especially wish to thank Mrs. Doris Jackson, Mrs. Jann Thomas and Mrs. Bonnie Boskat for their contributions in the organization of the symposium and publication of these proceedings.

CHARLES E. TREANOR
J. GORDON HALL

EXECUTIVE COMMITTEE

Charles E. Treanor (Chairman)
J. Gordon Hall
George Rudinger
Paul V. Marrone
William J. Rae
Anthony L. Russo
Walter H. Wurster

INTERNATIONAL ADVISORY COMMITTEE

B. Ahlborn, Canada	R. Nicholls, Canada
D. Baganoff, USA	H. Oguchi, Japan
S. Bauer, USA	A. Oppenheim, USA
T. Bazhenova, USSR	H. Palmer, USA
D. Bershader, USA	S. Penner, USA
W. Cook, USA	L. Presley, USA
R. Dannenberg, USA	H. Reichenbach, Germany
L. Dumitrescu, Rumania	M. Rogers, USA
R. Emrich, USA	J. Rom, Israel
C. Ferrari, Italy	D. Russell, USA
W. Fiszdon, Poland	P. Savic, Canada
R. Fowler, USA	F. Schultz-Grunow, Germany
K. Fukuda, Japan	R. Sedney, USA
I. Glass, Canada	G. Skinner, USA
W. Griffith, USA	M. Slack, USA
A. Hertzberg, USA	R. Soloukhin, USSR
H. Hornung, Germany	R. Stalker, Australia
I. Hurle, England	J. Stollery, England
A. Kantrowitz, USA	B. Sturtevant, USA
A. Lifshitz, Israel	J. Valensi, France
H. Mirels, USA	J. Wendt, Belgium
R. Narasimha, Japan	J. Whitfield, USA
R. Neumann, USA	

SPONSOR

The U.S. Air Force Office of Scientific Research

TECHNICAL ENDORSEMENT

The American Physical Society
The American Institute of Aeronautics and Astronautics
The American Society of Mechanical Engineers

LOCAL INDUSTRIAL SUPPORT

Bell Aerospace Textron
Bethlehem Steel Corporation
Sierra Research Corporation

CONTENTS

Part I. Plenary Lectures

Paul Vieille Memorial Lecture: BEYOND THREE DECADES OF CONTINUOUS RESEARCH AT UTIAS ON SHOCK TUBES AND WAVES	
I.I. Glass	3
REVIEW OF SHOCK TUBE AND SHOCK TUNNEL ADVANCEMENTS AT NAL	
K. Soga and I. Wada	21
CURRENT STUDIES AT CALSPAN UTILIZING SHORT-DURATION FLOW TECHNIQUES	
M.G. Dunn	32
SHOCK-INDUCED FLOW SEPARATION AND THE ORBITER THERMAL PROTECTION SYSTEM	
S-A. Waiter	41
CHEMICAL KINETICS STUDIED BY VACUUM-UV SPECTROSCOPY IN SHOCK TUBES	
Th. Just	54
BLAST WAVES GENERATED BY ACCIDENTAL EXPLOSIONS	
R.A. Strehlow	69

Part II. Facilities, Techniques and Experiments

A SHOCK TUBE DRIVER WITH A "CYCLONE" SEPARATOR	
R.J. Stalker and R.P. French	81
A NEW, DIAPHRAGMLESS, FLEXIBLE, LUMINOUS SHOCK TUBE	
Y.W. Kim	89
A POWDER-INJECTION SHOCK-TUBE FACILITY	
M.W.P. Cann, J.B. Shin and R.W. Nicholls	98
THE TESTING IN BIA HYPERSONIC GUN TUNNEL	
F.G. Zhuang, M.X. Zhao, B.P. He and X.J. Xu	107
AN APPLICATION OF THE MOLECULAR BEAM TIME-OF-FLIGHT TECHNIQUE TO MEASUREMENTS OF THERMAL BOUNDARY LAYER EFFECTS ON MASS SAMPLING FROM A SHOCK TUBE	
K. Teshima, N. Takahashi and M. Deguchi	116

MEASUREMENT OF DYNAMIC PRESSURE IN SHOCK TUBE BY STREAK PHOTOGRAPHY J.H. Owren and R.E. Dannenberg	124
MEASUREMENT OF TEMPERATURES IN A SHOCK TUBE BY COHERENT ANTISTOKES RAMAN SPECTROSCOPY (CARS) K. Knapp and F.J. Hindelang	132
TEMPERATURE MEASUREMENT OF DETONATION USING UV-ABSORPTION OF O ₂ T. Tsuboi, M. Egawa, H. Kobayashi, T. Hirose, M. Kamei and Y. Teranaka	141
A LASER-INTERFEROMETRIC TRAJECTORY-FOLLOWING SYSTEM FOR DETERMINING FORCES ON FREELY FLYING MODELS IN A SHOCK-TUNNEL L. Bernstein and G.T. Stott	150
SHOCK TUBE SIMULATION OF PULSED FLOW AERODYNAMIC WINDOWS V.A. Kulkarny, J. Schwartz, and R.A. Briones	159
VELOCITY MEASUREMENTS OF INCIDENT AND REFLECTED SHOCK WAVES IN VARIOUS GASES AND IN SATURATED WATER VAPOUR W. Garen, K. Brudi and G. Lensch	167
INVESTIGATION OF THE DISTORTION OF SHOCK-FRONTS IN REAL GASES A.F.P. Houwing, H.G. Hornung and R.J. Sandeman	176
MEASUREMENT AND CALCULATION OF SHOCK ATTENUATION IN A CHANNEL WITH PERFORATED WALLS W. Merzkirch and W. Erdmann	185
HIGH-ENERGY AIR SHOCK STUDY IN A STEEL PIPE H.D. Glenn, H.R. Kratz, D.D. Keough and R.P. Swift	191
OPTICAL STUDIES OF SHOCK GENERATED TRANSIENT SUPERSONIC BASE FLOWS P-Y Liang, D. Bershader and A. Wray	200
AMPLIFICATION OF NON-LINEAR STANDING WAVES IN A CYLINDRICAL CAVITY WITH VARYING CROSS SECTION E. Brocher and M. Elaouazi	209
CYCLIC WAVE ACTION IN THE STABLE OPERATION OF A HARTMANN-SPRENGER TUBE J. Iwamoto and B.E.L. Deckker	216

Part III. Boundary Layers and Heat Transfer

SOME FUNDAMENTAL ASPECTS OF SHOCK WAVE – TURBULENT BOUNDARY INTERACTIONS IN TRANSONIC FLOW G.R. Inger	227
HEATING-RATE MEASUREMENTS OVER 30° AND 40° (HALF-ANGLE) BLUNT CONES IN AIR AND HELIUM IN THE LANGLEY EXPANSION TUBE FACILITY N.M. Reddy	235

SHOCK INDUCED UNSTEADY FLAT PLATE BOUNDARY LAYERS AND TRANSITIONS	
M. Matsushita, T. Akamatsu and K. Fujimura	244
THE BOUNDARY LAYER BEHIND A SHOCK WAVE INCIDENT ON A LEADING EDGE	
B.E.L. Deckker	253
REAL GAS AND WALL ROUGHNESS EFFECTS ON THE BIFURCATION OF THE SHOCK REFLECTED FROM THE END WALL OF A TUBE	
J.R. Taylor and H.G. Hornung	262
DETERMINATION OF SHOCK TUBE BOUNDARY LAYER PARAMETER UTILIZING FLOW MARKING	
Th. Reese, F. Demmig and W. Böttcher	271
STABILITY LIMITS AND TRANSITION TIMES OF WAVE-INDUCED WALL BOUNDARY LAYERS	
Y.M. Amr and J.G. Hall	280
AN ACCURATE DETERMINATION OF THE THERMAL CONDUCTIVITY OF ARGON AT HIGH TEMPERATURES	
A. Hirschberg, P.J. Vrugt, J.F.H. Willems and M.E.H. van Dongen	289
THERMAL CONDUCTIVITY MEASUREMENT IN HIGH TEMPERATURE ARGON BY THE SHOCK PERTURBATION AND MACH REFLECTION METHODS	
A. Caverio, K. Chung and H.N. Powell	297
TEMPERATURE MEASUREMENTS OF AN IMPLOSION FOCUS	
T. Saito, A.K. Kudian and I.I. Glass	307

Part IV. Shock Structure and Propagation

BOUNDARY LAYER INFLUENCED SHOCK STRUCTURE	
F. Seiler	317
INFLUENCE OF SURFACE ROUGHNESS ON THE SHOCK TRANSITION IN QUASI-STATIONARY AND TRULY NON-STATIONARY FLOWS	
K. Takayama, J. Gotoh and G. Ben-Dor	326
MICROSCOPIC STRUCTURE OF THE MACH-TYPE REFLECTION OF WEAK SHOCK WAVES	
Z.A. Walenta	335
WEAK SPHERICAL SHOCK-WAVE TRANSITIONS OF N-WAVES IN AIR WITH VIBRATIONAL EXCITATION	
H. Honma, I.I. Glass, O. Holst-Jensen and Y. Tsumita	342
GENERATION OF THE PATTERNS IN GASEOUS DETONATIONS	
F. Schultz-Grunow	352
EVOLUTION OF SHOCK-INDUCED PRESSURE ON A FLAT-FACE/FLAT-BASE BODY AND AFTERBODY FLOW SEPARATION	
K.K. Yoshikawa and A.A. Wray	358

SHOCK STRENGTH MODIFICATION FOR REDUCED HEAT TRANSFER TO LIFTING RE-ENTRY VEHICLES	
L.H. Townend and R.A. East	367
SHOCK CAPTURING USING FLUX-CORRECTED TRANSPORT ALGORITHMS WITH ADAPTIVE GRIDDING	
M. Fry, J. Tittsworth, A. Kuhl, D. Book, J. Boris and M. Picone	376
CYLINDRICAL RESONATORS	
R.A. Neemeh, J.H.T. Wu and M.N. Elabdin	385
PROPAGATION OF SHOCK WAVES THROUGH NONUNIFORM AND RANDOM MEDIA	
B. Sturtevant, L. Hesselink, B.S. White, V. Kulkarny and C. Catherasoo	392
SHOCK WAVE DIFFRACTION AT A SHARP EDGE AND THE EFFECT OF BAFFLES IN A SHOCK TUBE	
J.M.R. Graham and R. Hillier	402
PROPAGATION OF TWO-DIMENSIONAL NONSTEADY DETONATION IN A CHANNEL WITH BACKWARD-FACING STEP	
T. Sugimura, S. Taki and T. Fujiwara	411
THE BLAST-NOISE ENVIRONMENT OF RECOILLESS RIFLES	
D. Gladstone and E.G. Plett	420

Part V. Chemical Kinetics and Optics

SHOCK-EXCITED EMISSION SPECTRUM OF TUNGSTEN OXIDE	
J.B. Shin, M.W.P. Cann and R.W. Nicholls	431
ROTATIONAL NONEQUILIBRIUM INFLUENCES IN CW HF/DF CHEMICAL LASERS	
S.W. Zelazny, W.L. Rushmore, J.W. Raymonda, and M. Subbiah and L.H. Sentman	438
HIGH GAIN CO CHEMICAL LASER PRODUCED IN A SHOCK TUNNEL	
M. Tilleman and J. Stricker	447
SHOCK/LUDWIG-TUBE DRIVEN HF LASER	
D.A. Russell and G.W. Butler	454
DETERMINATION OF ABSORPTION COEFFICIENTS IN SHOCK HEATED PROPELLANT MIXTURES FOR LASER-HEATED ROCKET THRUSTERS	
R.H. Krech and E.R. Pugh	462
SUPERSONIC FLOW E-BEAM STABILIZED DISCHARGE EXCIMER LASERS	
B. Forestier and B. Fontaine	470
FLUID-DYNAMICAL ASPECTS OF LASER-METAL INTERACTION	
M. Cantello, R. Menin, V. Donati, L. Garifo, A.V. La Rocca and M. Onorato	479
SHOCKFRONTS AS MODEL TARGETS IN LASER-PLASMA INTERACTION EXPERIMENTS	
P. Kolodner and E. Yablonovitch	486
EXPERIMENTAL STUDY ON THE IONIZATION OF ARGON GAS IN A NON-EQUILIBRIUM STATE BEHIND REFLECTED SHOCK WAVES	
K. Terao, M. Hozaka and H. Kaitoh	495

NEW EXPERIMENTAL RESULTS UPON IONIZATIONAL RELAXATION OF A SHOCK HEATED XENON PLASMA P. Valentin, Cl. Thenard and P. Maillot	504
NUMBER DENSITY OF THE 5s STATES DURING THE IONISATION RELAXATION OF SHOCK HEATED KRYPTON Th. Zaengel and W. Böttcher	510
COLLISIONAL EXCITATION AND IONISATION OF NO BEHIND SHOCK WAVES H.P. Richarz, A.E. Beylich and H. Grönig	519
THE INVESTIGATION OF IONIZATION PHENOMENA IN A 800 MM SHOCK-TUBE N. Zhu and X. Li	528
STUDIES OF THE VIBRATIONAL RELAXATION OF DIATOMIC MOLECULES IN A SHOCK HEATED MOLECULAR BEAM AND ITS APPLICATION TO IONIZATION BY ELECTRON IMPACT B. Evans, S. Ono, R.M. Hobson, S. Teii, A.W. Yau and J-S. Chang	535
DISCHARGE FLOW/SHOCK TUBE STUDIES OF SINGLET OXYGEN P. Borrell, P.M. Borrell, M.D. Pedley, K.R. Grant and R. Boodaghians	543
ROTATIONAL RELAXATION OF H ₂ IN NOZZLE FLOW Y. Matsumoto, H. Matsui and T. Asaba	552
VIBRATIONAL RELAXATION OF POLYATOMIC MOLECULES IN GAS MIXTURES H. Teitelbaum	560
VIBRATIONAL RELAXATION AND DISSOCIATION RATE MEASUREMENTS IN POLYATOMIC MOLECULES M. Tyaga Raju, S.V. Babu, Y.V.C. Rao and V. Subba Rao	570
CO + O CHEMILUMINESCENCE: RATE COEFFICIENT AND SPECTRAL DISTRIBUTION A. Grillo and M. Slack	576
RESONANCE ABSORPTION MEASUREMENTS OF ATOM CONCENTRATIONS IN REACTING GAS MIXTURES. 9. MEASUREMENTS OF O ATOMS IN OXIDATION OF H ₂ AND D ₂ K.M. Pamidimukkala and G.B. Skinner	585
DIRECT MEASUREMENTS OF O-ATOM REACTIONS WITH HCN AND C ₂ H ₂ BEHIND SHOCK WAVES P. Roth and R. Löhr	593
THE EFFECT OF MINUTE QUANTITIES OF IMPURITIES ON SHOCK TUBE KINETICS. THE REACTION H ₂ + D ₂ → 2HD A. Lifshitz, M. Bidani and H.F. Carroll	602
MOLECULAR BEAM TECHNIQUE FOR RECORDING CHEMICAL SPECIES BEHIND INCIDENT SHOCK WAVES St. Arndt and A. Frohn	610
SHOCK TUBE STUDY OF THE THERMAL DECOMPOSITION OF HYDROGEN CYANIDE A. Szekely, R.K. Hanson and C.T. Bowman	617
DECOMPOSITION OF HYDROGEN AZIDE IN SHOCK WAVES G. Dupré, C. Paillard, J. Combourieu, N.A. Fomin and R.I. Soloukhin	626

Part VI. Two Phase Flow and Condensation

THE RELAXATION ZONE BEHIND NORMAL SHOCK WAVES IN A REACTING DUSTY GAS. PART 1. MONATOMIC GASES	
G. Ben-Dor and O. Igra	637
SHOCK WAVE STRUCTURE IN GAS-PARTICLE MIXTURES AT LOW MACH NUMBERS	
G. König and A. Frohn	646
CROSS-SECTIONAL CONCENTRATION OF PARTICLES DURING SHOCK PROCESS PROPAGATING THROUGH A GAS-PARTICLE MIXTURE IN A SHOCK TUBE	
E. Outa, K. Tajima and S. Suzuki	655
MOTION OF SMALL PARTICLES IN A FIELD OF OSCILLATING SHOCK WAVES	
G. Rudinger, K.H. Chou and D.T. Shaw	664
SHOCK TUBE MEASUREMENTS OF IR RADIATION IN HOT GAS/PARTICLE MIXTURES	
V.S. Calia, W. Konopka, R.A. Reed and R.A. Oman	673
STUDY OF BINARY NUCLEATION IN A LUDWIG TUBE	
R.A. Zahoransky and S.L.K. Wittig	682
INVESTIGATIONS OF HOMOGENEOUS NUCLEATION IN Fe, Si, Fe/Si, FeO _x , AND SiO _x VAPORS AND THEIR SUBSEQUENT CONDENSATION	
J.R. Stephens and S.H. Bauer	691
CONDENSATION KINETICS OF IRON AND SILICON IN THE VAPOR PHASE	
J. Steinwandel, Th. Dietz, V. Joos and M. Hauser	700
SHOCK-TUBE SIMULATION EXPERIMENT OF SUPERSONIC CONDENSATION FLOW ACCOMPANYING A SHOCK WAVE	
H. Oguchi, K. Funabiki and T. Ito	707
EXPERIMENTS IN SHOCK LIQUEFACTION	
G. Dettleff, G.E.A. Meier, H.-D. Speckmann, P.A. Thompson and C. Yoon	716
SHOCK PROPAGATION IN LIQUID-GAS MEDIA	
T. Fujiwara and T. Hasegawa	724

Part VII. Environmental and Energy Related Applications

A COMPARISON OF MEASURED AND COMPUTED ENERGY EXCHANGER PERFORMANCE	
W.J. Thayer III and J.F. Zumdieck	735
FLOW FIELDS PRODUCED BY PIPELINE EXPLOSIONS	
D.G. Edwards and R.M. Smith	744
STUDIES ON MECHANICAL AND AERODYNAMICAL BLAST-ATTENUATION DEVICES	
L.Z. Dumitrescu, A. Mitrofan and S. Preda	753
RESPONSE OF A ROOM SUBJECTED TO SIMULATED SONIC BOOMS	
N.N. Wahba, I.I. Glass and R.C. Tennyson	762

SHOCK DIFFRACTION COMPUTATIONS OVER COMPLEX STRUCTURES A. Mark and P. Kutler	772
SIMULATION OF BLAST FIELDS BY HYDRAULIC ANALOGY J.L. Stollery, K.C. Phan and K.P. Garry	781
FAST PYROLYSIS OF PULVERIZED LIGNITE IN A SINGLE-PULSE SHOCK-TUBE H.J. Frieske, E. Seelbach and G. Adomeit	790
SHORT RESIDENCE-TIME PYROLYSIS AND OXIDATIVE PYROLYSIS OF BITUMINOUS COALS S.L. Szydlowski, D.C. Wegener, J.F. Merklin and T.W. Lester	800
SHOCK WAVE IGNITION OF PULVERIZED COAL E.A. Ural, M. Sichel and C.W. Kauffman	809
A STUDY ON THE IGNITION OF A FUEL DROPLET IN HIGH TEMPERATURE STAGNANT GAS Y. Yoshizawa, M. Tomita and the late H. Kawada	818
SHOCK INITIATED IGNITION IN HEPTANE-OXYGEN-ARGON MIXTURES A. Burcat, R.F. Farmer and R.A. Matula	826
AN EXPERIMENTAL AND ANALYTICAL INVESTIGATION OF HIGH TEMPERATURE IGNITION OF ETHANOL K. Natarajan and K.A. Bhaskaran	834
A STUDY ON THE HYDROGEN-OXYGEN DIFFUSION FLAME IN HIGH SPEED FLOW S. Takahashi, Y. Yoshizawa, T. Minegishi and the late H. Kawada	843
EXPERIMENTAL INVESTIGATION OF SHOCK INITIATED METHANE-COMBUSTION NEAR A WALL R. Keiper and J.H. Spurk	851
A SINGLE PULSE SHOCK TUBE STUDY OF SOOT FORMATION FROM BENZENE PYROLYSIS S.N. Vaughn, T.W. Lester and J.F. Merklin	860
RATES AND MECHANISMS OF FORMALDEHYDE PYROLYSIS AND OXIDATION J.M. Kline and S.S. Penner	869
TRIBUTE TO JOHN N. BRADLEY	879
SYMPOSIUM PHOTOGRAPHS	880
AUTHOR INDEX	882
PREVIOUS PROCEEDINGS OF THE SHOCK TUBE SYMPOSIA	884

7

Part I: PLENARY LECTURES

63

23

AD P

11

REVIEW OF SHOCK TUBE AND SHOCK TUNNEL ADVANCEMENTS AT NAL

K. Soga and I. Wada

National Aerospace Laboratory

Chofu, Tokyo, Japan

Since it was organized in 1960, the Shock Tube Research Group of NAL has studied the various aerodynamic problems of hypersonic flight at high altitudes using a reflected shock tunnel, electrically heated shock tubes and a gun tunnel. These studies are reviewed briefly in this paper.

In order to construct and operate a large-scale shock tunnel used for project works, a new operational method of short-duration wind tunnels using a large-orifice plate and high speed valves is proposed in this paper. The practicability of this method has been studied using the gun tunnel, and the results of these experiments are shown in this paper. The exclusion of the piston and the use of high speed valves to replace the diaphragms not only enable us to eliminate dust in the flow but also to reduce the tunnel reset time.

INTRODUCTION

Since it was organized in 1960, the Shock Tube Research Group of NAL has studied the various aerodynamic problems of hypersonic flight at high altitudes using a reflected shock tunnel ^{1,2)}, electrically heated shock tubes ³⁾ and a gun tunnel ⁴⁾. The shock tunnel was operated at low pressure and the electron-beam technique was used in order to do research on the transition regime hypersonic flow ^{1,2)}. The gun tunnel was used for preliminary experiments before using the NAL 50 cm diameter hypersonic wind tunnel. In the gun tunnel experiment, aerodynamic characteristics of spherically-blunted cones and heat-transfer problems of the backward-facing steps and shock-impingement were elucidated by the development of techniques for measuring aerodynamic force ⁵⁾, pressure ^{6,7)} and heat-transfer rate ⁸⁾. The gun tunnel was reconstructed as a free-flight experimental facility in 1981 to study the stability of a free-flight projectile.

A short-duration wind tunnel such as the gun tunnel has been used because of its low construction and operating costs. Also, other type tunnels have been developed by several authors, based on new concepts such as the Longshot Free-Piston Tunnel ⁹⁾, the Piston Compression Wind Tunnel ¹⁰⁾ and the Isentropic Light Piston Tunnel ^{11,12)}. Now NAL is planning to construct a large-scale shock tunnel in the near future to be used for such projects as the recovery of rocket payloads.

In the conventional short-duration tunnel, a free-piston and diaphragms are used. But some of its components must be moved between runs to reset the piston

and diaphragms. In the case of a large-scale tunnel, the moving components should be fixed. It is also important to obtain and continue a steady flow for as long as possible. Moreover, elimination of dust in the flow should be considered. To solve these technical problems, we propose that a new operational method using a large-orifice plate and high speed valves should be used. The practicability of this method has been studied using the gun tunnel ⁴⁾.

In former methods, small-orifice plates have been used to stabilize the tunnel stagnation conditions. However, a major problem has been that it takes about a full second to stabilize tunnel conditions and the temperature of the heated test gas decreases as the time of the stabilization increases ^{10~12)}. To overcome this problem an orifice plate with a large area is used in the present method. The test gas in the driven tube is then heated employing shock compression for two or three steps, quickly stabilizing the tunnel stagnation conditions. High speed valves are used to replace the diaphragms. Therefore, we tested the high speed valves in order to determine the valve performance and effects of the valves on the flow in the test section. The subject matter of the experimental study was the measurements of the tunnel stagnation pressure and temperature changing the orifice area with and without a piston; performance test of the high speed valve installed in front of the nozzle; and measurements of pitot pressure and stagnation heat-transfer rate of the cylinder to diagnose the flow established in the test section.

REFLECTED SHOCK TUNNEL AND ELECTRICALLY HEATED SHOCK TUBE

The shock tunnel was operated at low pressure and an electron-beam densitometer was used in order to do research on the free-molecule to continuum, as shown in Fig. 1 ^{1,2)}. The pressure distribution on a flat plate with a sharp leading edge was obtained from the measured density on the basis of constant wall temperature. The pressure distribution against the hypersonic viscous-interaction parameter corrected by wall temperature, χ agrees well with the results of experiments in a low-density wind tunnel at UC Berkeley.

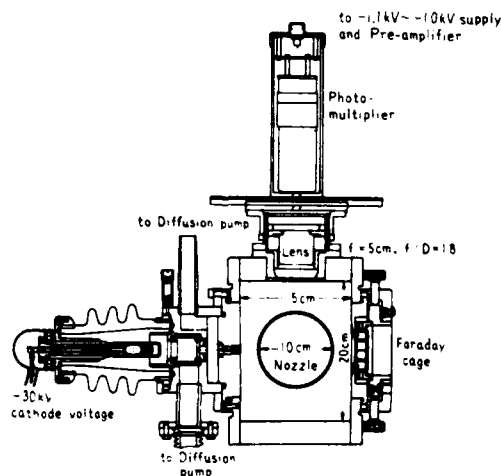


Fig. 1 Arrangement of electron beam densitometer mounted on the wall of the test section of NAL reflected shock tunnel.

The luminous intensity distributions around cylinders and spheres in the electrically heated shock tube with a coaxial gun are similar to these density distributions measured in the shock tunnel under almost identical flow conditions ³⁾ (Fig.2).

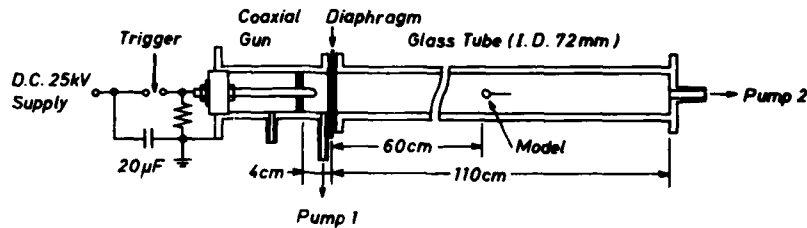


Fig. 2 Schematic of electrically heated shock tube.

NAL GUN TUNNEL

The gun tunnel (in Fig. 3) was used for preliminary experiments before using the NAL 50 cm hypersonic wind tunnel⁴⁾. In the gun tunnel experiment, aerodynamic characteristics of spherically-blunted cones, heat-transfer problems on the backward facing steps and shock-impingement were elucidated by the development of techniques for measuring aerodynamic force⁵⁾, pressure^{6,7)} and heat-transfer rate^{8,13~15)}.

A three-component force balance with semi-conductor strain gages was provided for the force measurement. The axial and normal forces and the pitching moments of spherically-blunted cones with nose bluntness ratios of 0, 0.1, 0.2, 0.3 and 0.5 and half-vertex angles of 12.5°, 16° and 20° were measured at angles of attack from 0° to about 17° and a Mach number of 13.6⁵⁾.

The pressure distribution on a series of spherically-blunted cones having a half-vertex angle of 16°, which were installed in the test section as an axisymmetric condition, were measured in the hypersonic flows produced with contour and conical nozzles. The effect of nose bluntness on the pressure distribution of a blunted cone in inviscid hypersonic flow was clarified by taking into account the viscous induced pressure included in the experimental results. The inviscid pressure coefficient obtained in experiments in the NAL gun tunnel and the NAL hypersonic wind tunnel was correlated with the blast-wave-type parameters $C_p/C_{p, \text{cone}}$ and $(\theta c^2/\sqrt{C_{Dn}}) / (x n/dn)$ in order to compare it with the numerical inviscid flow pressure distributions^{6,7)}.



Fig. 3 NAL gun tunnel.

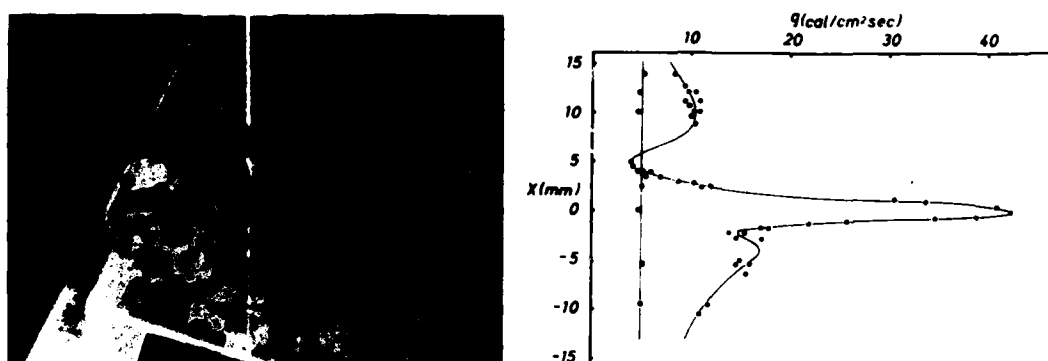


Fig. 4 Heat-transfer rate distribution along stagnation line of cylinder after shock-impingement. (Flow model, Type IV by B. Edney)

It was also found that the pressure distribution on models tested in a flow produced with a conical nozzle was appreciably different from that on models tested in a flow produced with a contour nozzle, but they show good agreement with each other when harmonized by the source flow correction method based on experimental data of pitot pressure distribution in a conical-nozzle-produced flow ^{5,6}).

The heat transfer rate behind backward facing steps in laminar high Mach number flows has been measured and discussed at various laboratories including the NAL. J. Rom summarized these results of the peak in heat-transfer using the ratio of the boundary layer thickness to the step height, $h/\text{Re}_L/L$ ^{13,15}).

A typical example of results obtained in the heat-transfer experiment on shock impingement, which is now being conducted at NAL, is shown in Fig. 4. This is a schlieren photograph corresponding to a flow pattern that a supersonic jet flow almost normally impinges on the surface of a cylinder, that is, Type IV as defined by B. Edney. The peak heating rate nondimensionalized with non-interference one is higher than that in any other flow pattern. The most significant parameters governing the heat-transfer rate distribution and peak value are considered to be the length and width of a supersonic jet in this case. Another flow pattern, where a shear layer impinges on the body surface obliquely with an oblique shock wave, is called Type III. Distributions and peak values of this type are considered to be influenced mostly by the length, angle and turbulence level of the impinging shear layer.

NEW OPERATION METHOD FOR SHORT DURATION WIND TUNNEL

The new operational method using a large-orifice plate and high speed valves is outlined as follows with reference to Fig. 5. The wind tunnel operation is begun by opening the 1st high speed valve (1-H.S.V.), which is installed between the tubes. When using a large-orifice plate, the test gas in the driven tube is heated employing shock compression for two or three steps and stagnation conditions in the wind tunnel are quickly stabilized. After the stabilization, the 2nd high speed valve (2-H.S.V.), which is installed in front of the nozzle, is used to release only the heated test gas into the test section of the tunnel.

Experimental Apparatus

The NAL gun tunnel ⁴) was used to test the practicability of the method. The driver tube of the tunnel is 17 cm in internal diameter and 2 m in length.

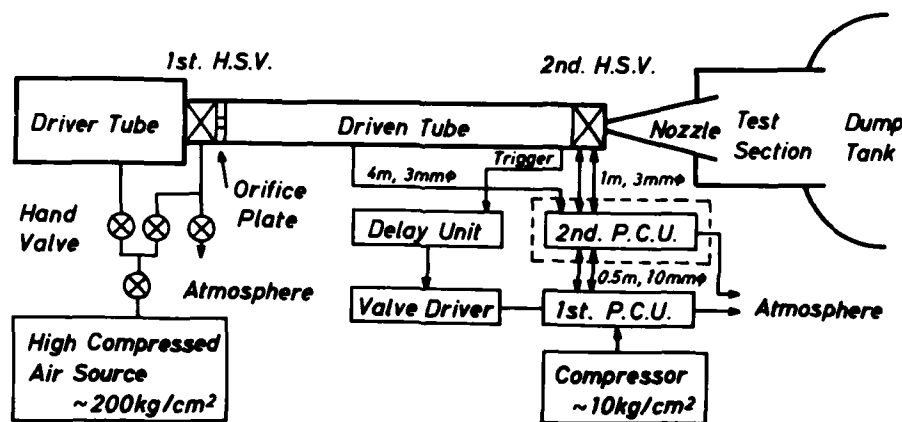


Fig. 5 Gun tunnel and its operating system.

It can withstand up to 200 kg/cm^2 . The driven tube is 7 cm in internal diameter and 7 m in length. A conical nozzle of $M=8$ with a half-angle of $5^\circ 44'$ was used in the present experiment. The throat diameter of the nozzle is 13 mm and the exit diameter is 17.9 cm. A vacuum chamber of 14.5 m^3 in volume, including the test section, is evacuated up to a few μHg by means of a $1,250 \text{ m}^3/\text{hr}$ mechanical booster pump backed by a $6,500 \text{ l/min}$ rotary pump.

While the high speed valve studied by Oguchi, et al ¹⁶⁾, has an auxiliary free-piston and electro-magnetic valve to move the main piston, due to the limited room available and for the sake of simplicity, we chose to use a hand valve to move the piston. The room available for the 1-H.S.V. is 100 mm long with an internal diameter of 140 mm.

While the construction of the valve is complex, the flow path from the driver tube to the driven tube covers only 30% of the cross-sectional area of the driven tube. The sketch of the 1-H.S.V. is shown in Fig. 6.

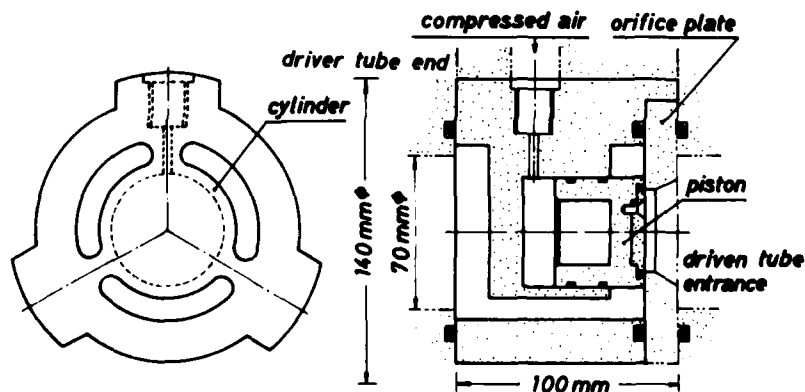


Fig. 6 Schematic of the 1st high speed valve.

The 2-H.S.V. which was manufactured for our test is illustrated in Fig. 7. The valve has a metallic rotor in the same manner as a glass cock used in vacuum instruments and a throat diameter of 15 mm against 13 mm of that of the nozzle. The rotor with a pinion is able to rotate about 90 degree by means of a pressure changeover unit and a piston with a rack. When tunnel stagnation pressure is

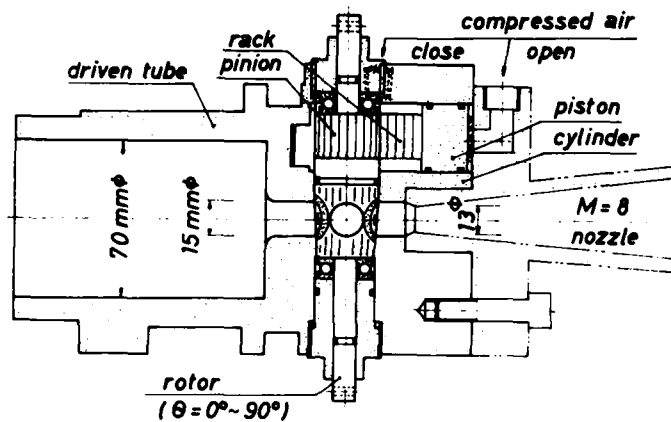


Fig. 7 Schematic of the 2nd high speed valve.

low, the 2-H.S.V. is operated with an electrically controlled pressure change-over unit (1-P.C.U.). The 1-P.C.U. is able to supply compressed air up to 10 kg/cm^2 to one side of the piston with a rack and release synchronously the high pressure air contained in the other side. When the tunnel stagnation pressure is high, the 2-H.S.V. is operated by a 2-P.C.U. backed by the 1-P.C.U. The 2-P.C.U. can supply more highly compressed air, which is led from the driven tube during the tunnel operation.

Stabilization of Tunnel Stagnation Conditions

In this section of our paper, we describe the tests that were made to determine the usefulness of an orifice with a large area. The gun tunnel was operated with the diaphragm as well as the conventional gun tunnel operation and at the initial pressure ratios, $P_4/P_1 = 6 \sim 156$. Dry air at atmospheric pressure and room temperature was used for the initial condition of the driven tube. The nozzle throat was closed during these experiments. Plates having orifices of $0.1A_1 \sim A_1$ area were tested.

Fig. 8 shows the pressure traces which were measured at the end of the driven tube. If we ignore the peak at the beginning of the pressure traces with a piston in Fig. 8-a), there is no substantive difference between those of a) and b) with the same orifice area. The results shown in Fig. 8 were obtained by operating at an initial pressure ratio of 80. Though the initial pressure ratio was changed through a range of 6 to 156, an orifice plate with a constant area produced similar pressure traces for all initial pressure ratios. Even though there were considerable fluctuations in the pressure traces, the tunnel stagnation pressure was stabilized instantly in this wind tunnel when an orifice with an area of $0.6A_1$ was used. The fluctuations depend on the volume ratio between the driver and driven tubes, and decrease as the value of the ratio increases. Therefore, if we use a wind tunnel with a high volume ratio, the tunnel stagnation pressure will be more easily stabilized by employing shock compression for one step using an orifice plate of a suitable area.

The pressure traces obtained using an orifice of $0.3A_1$ were stabilized after two steps and obtained steadier conditions than those for an orifice of $0.6A_1$. When the volume ratio isn't as high as in the present wind tunnel, the fluctuations of the pressure traces can be decreased through the use of a medium-sized orifice such as $A_{or} = 0.3A_1$. In this case, the test gas in the driven tube is compressed for two or three steps, and the time required to reach a stabilized condition increases as the number of steps increases.

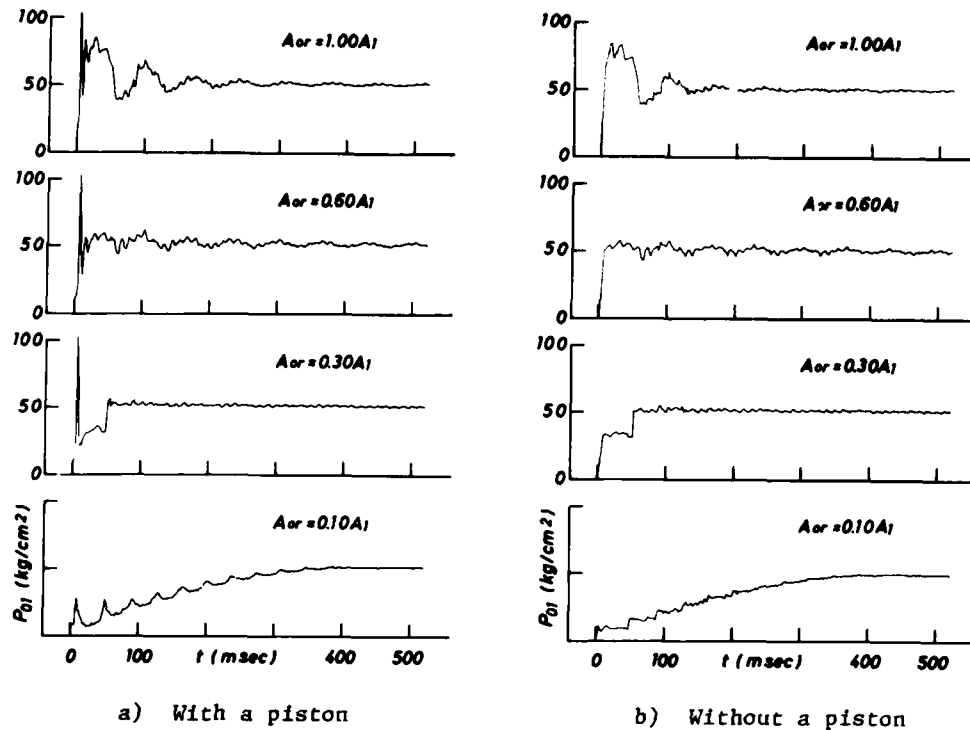


Fig. 8 Effect of the orifice area on the stabilization of the tunnel stagnation pressure.

In the present method using a large-orifice plate, the test gas is compressed and stabilized by employing shock compression for two or three steps. However, if the compression ratio of the test gas isn't so high, the tunnel stagnation pressure and temperature after stabilization can be calculated with the following equations obtained under the assumption of isentropic compression.

$$P_{01}/P_1 = [k/(1+k) \cdot (P_4/P_1)^{1/\gamma} + (1+k)^{-1}]^\gamma \quad \text{.....(1)}$$

$$T_{01}/T_1 = [k/(1+k) \cdot (P_4/P_1)^{1/\gamma} + (1+k)^{-1}]^{\gamma-1} \quad \text{.....(2)}$$

where k is the volume ratio between the driver and the driven tubes, V_4/V_1 . When making the above calculation, we found the experimental values of the tunnel stagnation pressure and temperature to be in fairly close agreement with the calculated values.

Performance Tests of the 2nd High Speed Valve

The wind tunnel was used to conduct performance tests of the 2-H.S.V. Typical traces of physical quantities which show the tunnel and high speed valve performance during the tunnel operation are illustrated in Fig. 9. It shows the result when the tunnel stagnation pressure is low and the 2-H.S.V. is operated by the 1-P.C.U. only as mentioned in the former section of this paper. The dotted lines in Fig. 9 show the voltage supplied to the 1-P.C.U. θ is the turning angle of the rotor of the 2-H.S.V. P_{01} is the tunnel stagnation pressure measured at 40 cm from the end of the driven tube on the upstream side. P_{02} is the pitot pressure of the flow established in the test section of the tunnel.

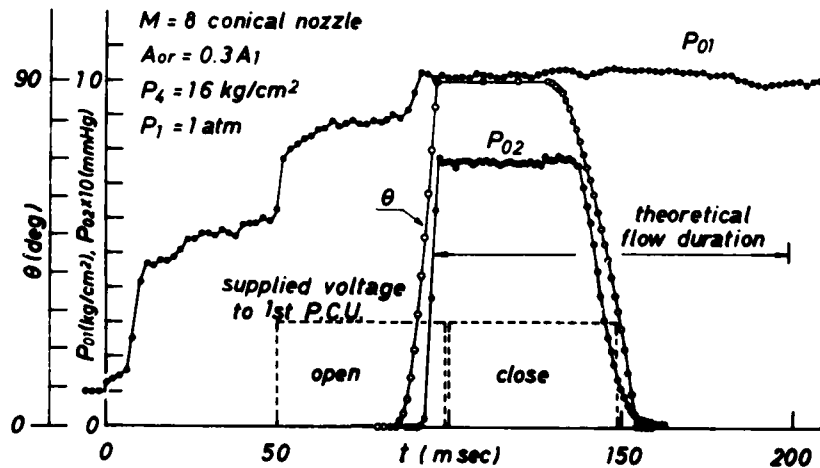


Fig. 9 Typical traces of physical quantities during the tunnel operation.

Opening times of the 2-H.S.V. were measured from rise to the point where pitot pressure and heat-transfer rate reached to steady states, as explained in the next section of this paper. Fig. 10 shows the above opening times for two performance tests. In one of the tests, the 2-H.S.V. is operated by only the 1-P.C.U., and in the other test, the 2-P.C.U. backed up by the 1-P.C.U. is used to operate it. As shown in Fig. 10, the actual opening times are only 4~5 msec in the low pressure range, and even if the tunnel stagnation pressure is high they are below 10 msec. Therefore, the 2-H.S.V. installed in front of the nozzle is of practical use. These values can be reduced by the choice of the suitable internal diameter and length of the high pressure air tube connected to the pressure changeover units.

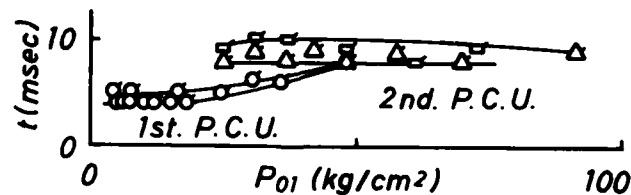


Fig. 10 Opening time of the 2nd high speed valve.

Diagnoses of the Flow Established in the Test Section

As has already been mentioned, typical pitot pressure trace was shown in Fig. 9. The effect of the initial pressure ratio on the pitot pressure of the flow is shown in Fig. 11. The gentle slope in the region of initial pressure ratios in excess of 16 is due to boundary layer growth on the nozzle wall surface. The steep slope in the region below 16 is regarded as the effect of air condensation¹⁷⁾. To confirm this, the flow static pressure and temperature, which were calculated from experimental results, are shown in Fig. 12, in comparison with the onset line for air condensation¹⁸⁾. The solid line, which shows the relation between the static pressure and the temperature, crosses the onset line around $P_4/P_1=16$. Therefore, even if there is a 2-H.S.V. in front of the nozzle, the flow in the test section is considered to be normally established in the tunnel operation without condensation.

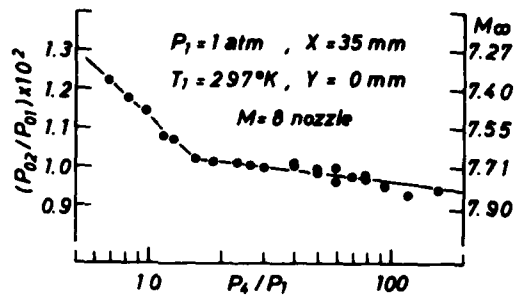


Fig. 11 Effect of the initial pressure ratio on the pitot pressure of the flow.

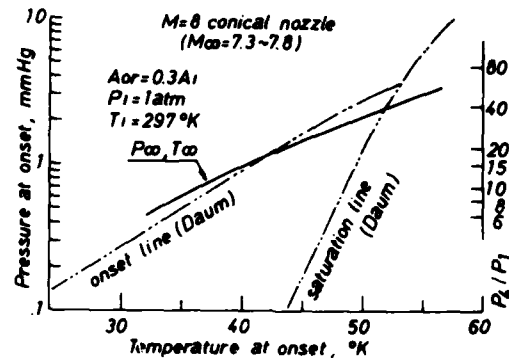


Fig. 12 Air flow condensation.

To diagnose flow stagnation temperature and flow duration, a two-dimensional cylinder, 30 mm in diameter, was installed in the test section. The stagnation point heat-transfer rate of this cylinder was measured with a technique which uses thin-film thermometers and analog networks ¹⁴). Fig. 13 shows a typical record of the heat-transfer rate which was obtained using an orifice plate without a piston.

The heat-transfer rate is explained as follows, referring both to experimental results obtained using a nozzle-like orifice block without a piston and the orifice plate with a piston. The heat-transfer rate trace shown in Fig. 13 is divided into constant, steep and gentle slope regions.

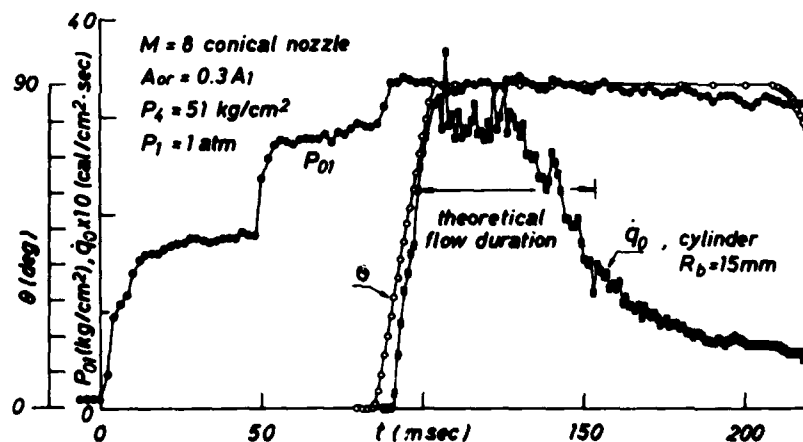


Fig. 13 Typical trace of stagnation point heat-transfer rate of the cylinder.

1) Constant Heat-Transfer Rate Region: The duration of the constant heat-transfer rate region does not depend upon the configuration of the orifice plates and the piston, but only on the operation condition of the tunnel. The tunnel stagnation temperature determined from the heat-transfer measurement

gives almost the same value as the temperature measured directly by the thermocouple.

2) Steep Slope Region: Although the heat-transfer rate traces in all cases are similar to each other, there is a slight difference in gradient. Therefore, the steep decrease of the heat-transfer rate trace is considered to be due to the compression process of the test gas and to the fact that the heated test gas loses some of its heat to the driven tube wall. The effect on the heat-transfer rate of gas mixing between the test gas and the driver gas isn't large in this region.

3) Gentle Slope Region: The gentle slope of the heat-transfer rate trace is due to driver gas, because the value of heat-transfer rate using a piston is zero in this region. Therefore, the heat-transfer rate in the gentle slope region is due to the effect of heat-transfer from driven tube wall to driver gas. In Fig. 14, the flow duration in which a constant heat-transfer rate is maintained is compared with the flow duration that is defined by pitot pressure measurements with a piston.

The flow duration obtained from heat-transfer measurements is about 60~70% of the ideal. Its decrease seems to be due to a compression process of the test gas in the driven tube. The piston did not affect the flow duration in the present experiment.

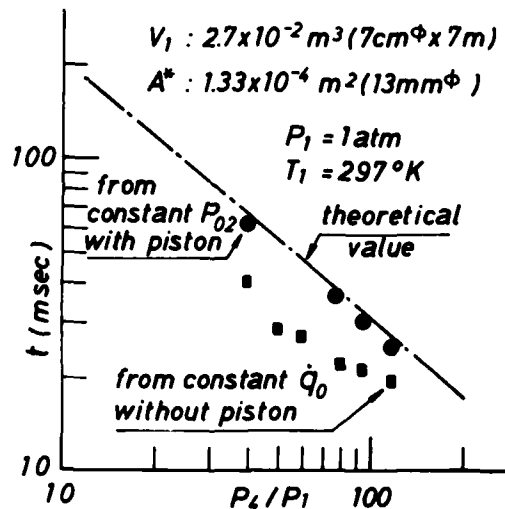


Fig. 14 Flow duration.

CONCLUSION

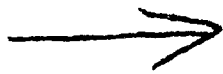
As expected, the results of the preliminary experiment showed that the present method is very useful for construction and operation of a large-scale short duration wind tunnel. The exclusion of the diaphragms and the piston not only enabled us to make a large-scale wind tunnel but also to eliminate dust in the flow. By using a large-orifice plate together with high speed valves, early stabilization of tunnel stagnation conditions and a steady flow in the test section was achieved. The use of high speed valves to replace the diaphragms and the elimination of the piston enabled us to reuse both the states of high pressure in the driver tube and the partially evacuated pressure in the dump

tank after the tunnel operation. Therefore, the tunnel reset time was reduced dramatically. The effect of a piston on the performance of the tunnel was negligible.

On the basis of the above results, we are planning to construct a large-scale shock tunnel to do research on a hypersonic flow having a Mach number of 15. The tunnel will consist of a spherical high pressure chamber of 10 m^3 which can withstand air pressure of 300 kg/cm^2 , an electrically heated driven tube 25 cm in diameter and 20.5 m in length and two spherical vacuum chambers of $1,800 \text{ m}^3$.

REFERENCES

- 1) I. Wada, Proc. of 4th, 5th of Int. Symp. on Rare. Gas Dyn., p.535 (1966), p.1193 (1967)
- 2) I. Wada and K. Soga, Proc. of 4th, 5th Int. Symp. on Space Tech. and Sci., p.251 (1963), p.141 (1965)
- 3) I. Wada and R. Matsuzaki, Proc. of 7th Int. Symp. on Space Tech. and Sci., p.313 (1967), R. Matsuzaki, Jap. J. of Appl. Phys. 6, p.430 (1967) and 7, p.1147 (1968)
- 4) I. Wada, K. Soga and Y. Inoue, NAL TR-556 (1978) (in Japanese)
- 5) K. Soga and I. Wada, Trans. of Jap. Soc. for Aero. and Space Sci. 18, p.167 (1975)
- 6) K. Soga, Proc. of 10th Int. Shock Tube Symp., p.813 (1975)
- 7) K. Soga and T. Yamazaki, J. of Jap. Soc. for Aero. and Space Sci. 25, p.362 (1977) (in Japanese)
- 8) I. Wada, K. Soga and Y. Inoue, Proc. of 9th Int. Symp. on Space Tech. and Sci., p.301 (1971)
- 9) B. E. Richards and K. R. Enkenhus, AIAA Paper No. 69-333 (1969), AIAA J. 8, p.1020 (1970)
- 10) O. Leuchter, ONERA T.P. No. 296 (1965)
- 11) T. V. Jones, D. L. Schulty and A. D. Hendley, Univ. of Oxford, R.M. No.3731 (1973)
- 12) B. Richards and Per-Age Krogstad, Proc. of 10th Int. Shock Tube Symp., p.230 (1975)
- 13) I. Wada and Y. Inoue, HEAT TRANSFER-Jap. Res. 2, 2. p.34 (1973) SCRIPTA pub. Co., Washington, D.C.
- 14) I. Wada and Y. Inoue, Proc. of 10th Int. Symp. on Space Tech. and Sci., p.425 (1973)
- 15) J. Rom, Private Communication
- 16) H. Oguchi, K. Funebiki and S. Sato, Proc. of 10th Int. Shock Tube Symp., p.386 (1975)
- 17) J. F. W. Crane and R. J. Marshall, ARC R. & M., No. 3511 (1968)
- 18) F. L. Daum, AIAA J. 1, p.1043 (1963)



AD P 111 22.1

CURRENT STUDIES AT CALSPAN UTILIZING SHORT-DURATION FLOW TECHNIQUES

Michael G. Dunn

Aerodynamic Research Department
Calspan Advanced Technology Center
Buffalo, New York 14225

A brief review of current shock-wave related research projects within the Aerodynamic Research Department at the Calspan Corporation is given. The subject areas discussed are divided into three basic groups: (1) Application of conventional shock-tube/shock-tunnel techniques to obtain heat-flux distributions on flight vehicles, to study transonic shock/boundary-layer interactions, and to obtain rate-coefficient measurements; (2) Relatively new applications of established shock-tube/shock-tunnel techniques, and (3) Discussion of new techniques specifically developed to improve the accuracy of shock-tunnel simulations.

1. INTRODUCTION

Research utilizing shock-tube/shock-tunnel techniques has been an active area of interest at Calspan for many years. The intention of this paper is to review on-going projects which can be conveniently divided into three groups as noted in the abstract. Included in the discussion of Group 1 is: a description of a shock-tunnel measurement program designed to obtain heat-flux distributions for a pod to be mounted on the top of the space shuttle vertical tail, an experiment that uses a large-scale Ludwig-tube apparatus to obtain data relevant to the fundamental description of the transonic shock/boundary-layer interaction phenomena, and a shock-tube measurement program designed to obtain the reaction rates of the chemical processes in high-temperature reactions involving boron, fluorine, hydrogen and oxygen-bearing compounds.

Two on-going experiments are discussed under Group 2: first, an experiment which uses existing shock-tunnel technology and transient test techniques to obtain heat-flux and pressure distributions for a gas turbine with the wheel rotating at operational speeds; second, a Ludwig-tube program designed to implement a laboratory experiment to obtain fundamental data for the transient response of a turbofan engine when the machine is subjected to a simulated blast-wave environment.

The items composing Group 3 involve new techniques designed to improve the capability for obtaining accurate simulations and measurements in a shock tunnel. These include a description of new heat-transfer gages developed to measure rough-wall heating and a description of a technique to simulate the flow about a highly blowing nose tip.

2. CONVENTIONAL SHOCK-TUBE/SHOCK-TUNNEL INVESTIGATIONS

2.1 SPACE SHUTTLE HEAT-FLUX MEASUREMENTS: NASA plans to mount a scanning

infrared detector on the tip of the vertical tail of a future Space Shuttle Orbiter vehicle. The purpose of this sensor is to measure surface temperatures on the leeside of the orbiter wings and fuselage during entry. Before this experiment can be installed on the Shuttle, the sensor-pod design must be certified as adequate to withstand the aerodynamic forces and heat transfer associated with the entry phase of the Shuttle orbiter. The vehicle will be flying at angles of attack of 40° with the pod in the wake-like flow on the leeside of the vehicle. This flow also contains shock waves generated by the wings and the vertical tail.

A 0.0175-scale model of the orbiter has been instrumented with 92 thin-film heat-transfer gages located on the pod and on the vertical tail, Fig. 1. The hemispherical dome of the pod, although only 0.375-inch diameter, contains 39 miniature gages as shown in Fig. 2. This model is being tested in the 48-inch and 96-inch Hypersonic Shock Tunnels at Mach numbers from 8 to 16, Reynolds numbers from 5×10^4 to 1×10^7 per foot, and angles of attack of 30° , 35° and 40° . The results of this test are currently being analyzed with respect to the pod design. A preliminary correlation of heat-transfer data obtained on the vertical tail with data measured on the first flight of the Columbia show very good agreement.

2.2 TRANSONIC SHOCK/BOUNDARY-LAYER MEASUREMENTS: Serious problems have been encountered in the scaling of transonic wind-tunnel data to full scale when dealing with shock wave/boundary-layer interactions (SBLI). A program of research was initiated at Calspan which centered around a simulation experiment performed in the large Calspan Ludwig Tube¹⁻⁵.

The Calspan Ludwig Tube is a large scale, upstream-diaphragm facility. The supply tube is 60-ft long and has an inner diameter of 3.5-ft. For transonic studies, a perforated nozzle housed within a large dump tank, 8-ft in diameter and 60-ft long, is used. The perforated nozzle is contained within the evacuated dump tank, and during the experiment, sonic outflow through the walls expands the nozzle flow to low supersonic Mach numbers. Selective coverage of some of the perforations permits streamwise variation of the Mach number. A flat-plate shock-holder assembly shown in Fig. 3 completes the apparatus used in the SBLI experiments. This assembly was designed with the objective of simulating the flow through a normal shock wave standing on an airfoil at nearly full-scale Reynolds number. The turbulent boundary layer approaching the shock is developed on the flat plate that spans the transonic nozzle, and the interaction is generated in the shock holder by choking the flow at its exit. In all experiments, an airfoil type pressure history was imposed upon the boundary layer approaching the shock.

The duration of steady test flow in this facility is approximately 95 ms. A steady boundary layer is established in the model after a transient starting process of about 15 ms duration. During the starting process, the choking flap sends a wave system upstream through the shock-holder channel. Stationary shock structures lasting 6 to 25 ms have been obtained. Most of the measurements are made using pressure probes together with fast-response pressure transducers. In addition, skin friction is measured directly by using flowing element balances with a fast-response piezoelectric pick-up. These Calspan-developed skin-friction transducers have a 0.252-inch diameter sensing surface and can measure shearing up to 0.02 psi. The output of all transducers is fed directly to a high-speed data acquisition and processing system⁴ designed to satisfy the specific requirements of short-duration test facilities. Visualization of the shock structure is obtained by schlieren movies and pictures of the flow direction at the model surface are obtained by wool tufts.

2.3 SHOCK-TUBE MEASUREMENTS OF SPECIFIC HBO_2 AND OBF REACTION-RATE

COEFFICIENTS: One goal in the area of high-temperature chemistry research is the development of reliable predictive codes for the chemical processes and subsequent radiation from high-temperature reacting gases. Important input requirements include the chemical kinetic data which govern species production

and removal processes in a reactive environment. For many years, research programs at Calspan have provided a quantitative data base on the spectro-radiometric signatures of molecular species of particular interest within the radiation/kinetics community. Molecular band locations, band shapes and spectral intensities have been measured in such studies⁵.

The objective of the on-going research is to determine selected rate coefficients for selected B-O-H-F species. In particular, radiometric measurements have confirmed the predominant importance of the HBO₂ and OBF band contributions in boron-containing mixtures. The present study comprises reaction-rate measurements for the primary chemical processes affecting the formation and depletion of HBO₂ and OBF. A shock tube is employed, wherein the reactions of interest are monitored behind the reflected shock, using selected initial mixture preparations involving diborane (B₂H₆) and O₂, and boron trifluoride (BF₃) and O₂, in diluent argon. The argon diluent ensures that both isothermal and thin-gas radiation conditions prevail.

The radiometric signatures of selected reactant and product species are monitored in both the short wavelength (<5 μm) and long wavelength (6-10 μm) infrared spectral regions. Three independent optical lines of sight are located at a common station in the shock tube. A schematic of the shock tube and IR instrumentation deployment is shown in Fig. 4. Also included in the figure is an illustrative radiometer record of the detected inband radiance of the 5 μm band of HBO₂ (B=O stretching vibration) in the reflected-shock region. The inband radiation of other reactant and product molecular species is similarly monitored during the experiments, by means of appropriately selected IR filters.

3. NEW APPLICATIONS OF SHOCK-TUBE/SHOCK-TUNNEL TECHNIQUES

3.1 HEAT-FLUX MEASUREMENTS FOR GAS TURBINE ENGINES: The ability to predict accurately the heat-flux distributions for various engine components is an important consideration in gas turbine engine design. Many different facilities are currently being used to perform turbine related studies. The test apparatus currently being used at Calspan (Fig. 5) provides an experimental capability fitting between the well known cascade-type facility and the full-scale engine facility. Heat-flux and pressure measurements have been obtained at Calspan using state-of-the-art shock-tube technology and well established transient-test techniques. These measurements were performed for a full turbine stage of the AiResearch TFE 731-2 engine. This work is an extension of earlier measurements^{6,7}, obtained for a single stator stage in the absence of a rotor.

The modified shock-tunnel apparatus sketched in Fig. 5 consists of a 40-ft long driver tube and a 50-ft long driven tube driving a test-section device mounted near the exit of the primary nozzle. The model containing the turbine stage consists of a forward transition section with a circular opening facing the supersonic primary nozzle flow. The circular opening is followed by a complete 360°-annular passage containing the nozzle stator, the rotor, and the shroud. The orifice plate is used to set the mass-flow rate through the device and thus to set the exit Mach number of the stator nozzle. The stator contains approximately 58 heat-transfer gages, and the rotor airfoil is instrumented as follows: pressure surface (12 gages), suction surface (7 gages), and tip (2 gages). Pressure transducers were installed in the test model from the entrance section to the orifice plate in order to obtain detailed data on the starting process and the stage performance.

The temperature vs time histories obtained from the thin-film heat-transfer gages located on the rotating airfoils (wheel speed is 27,000 rpm at 100% physical speed) are transferred to tape recorders by use of a slip-ring system. The high-frequency data associated with rotor-blade passage through the stator wakes is an important part of this program. The recorder was operated so as to sample at 2 μsec intervals with typical passage times through a stator wake being on the order of 50 to 80 μsec, depending on rotor speed. A 2 μsec sampling rate provided many data points during a typical blade passage⁸.

surface topography of sand-grain roughness. The second type of gage used in this study is a rough calorimeter gage shown in Fig. 9. Both types of gages are employed in the rough-wall heating studies and the results are found to be in excellent agreement.

4.2 MASSIVE BLOWING FROM THE HEAT SHIELD DURING JOVIAN ENTRY: Ablative heat shields have been used successfully to achieve thermal protection for vehicles entering the earth's atmosphere for the past two decades. Convective heating is the principle source of energy and the resulting rate of ablation is such that the nondimensional mass loss from the nosetip ($\dot{m}/\rho_\infty u_\infty$) seldom exceeds 0.3. The high-energy entry into the atmosphere of Jupiter, however, represents a different class of problem. High-speed entry into a H₂/He environment results in extremely large, radiative-heating rates that are combined with relatively small convective-heating levels. Under these conditions, the rate of mass addition from the ablative heat shield is such that mass-addition rates approaching 70% of the mass flux in the free stream can be attained.

A porous nosetip used in the Calspan shock-tunnel massive-blowing studies¹⁵ simulating Jovian reentry is shown in Fig. 10. The injectant was bled into the flow from a large number of slots in the surface of the model that were fed from eight separate reservoirs which were connected through fast-acting valves to eight concentric zones in the nosetip. By adjusting the relative pressure levels in the reservoir, it was possible to control the distribution of injectant from the nosetip. The model was instrumented with thin-film heat-transfer and pressure gages. The model was calibrated to determine the discharge coefficients of each zone of the model for N₂, CO₂, CF₄ and SF₆ injectants. For the test conditions used, it was possible to generate nondimensional blowing rates ($\dot{m}/\rho_\infty u_\infty$) from 0.1 to 1 through the model. Much of the testing was conducted with a CF₄ injectant. Using CF₄ with an 80% H₂/20% He, the freestream closely simulated the molecular weight ratio anticipated for the Jupiter mission. High-speed schlieren photography was also used to examine the structure and stability of the shock layer.

The high Mach numbers in both the test media (80% H₂/20% He) and the driver gas (heated H₂) made the generation of long run times in an impulse facility inherently difficult. To maximize the test time, the shock tunnel was operated with a low incident-shock Mach number ($M_i=2$). After a rapid and clean start, a steady-flow duration of over 4 ms was obtained. The subsequent tests demonstrated that this time was more than two times longer than the duration required to establish steady flow over a highly blowing nosetip. The experimental studies demonstrated that for a given mass-injection ratio, increasing the molecular weight of the injectant increases the stability of the shock layer.

REFERENCES

1. Vidal, R.J., Wittliff, C.E., Catlin, P.A. and Sheen, B.H., "Reynolds Number Effects on the Shock Wave-Turbulent Boundary-Layer Interaction at Transonic Speeds", AIAA Paper No. 73-661, AIAA 6th Fluid and Plasma Dynamic Conference, Palm Springs, CA, 16-18 July 1973
2. Padova, C., Falk, T.J. and Wittliff, C.E., "Experimental Investigation of Similitude Parameters Governing Transonic Shock-Boundary Layer Interactions", AIAA Paper No. 80-0158, AIAA 8th Aerospace Sciences Meeting, Pasadena, CA, 14-16 January 1980
3. Padova, C., "Transonic Separation", Calspan Rept. No. AB-5908-A-1, March 1981
4. Wittliff, C.E., Pflueger, P.G. and Donovan, P.J., "A High-Speed Digital Data Acquisition System for Short-Duration Test Facilities", International Congress on Instrumentation in Aerospace Simulation Facilities, Monterey, CA, 24-26 September 1979
5. Boyer, D.W., "Shock-Tube Measurements of the Band Strengths of HBO₂ and OBF in the Short Wavelength Infrared", JQSRT, Vol. 24, No. 4, pp. 269-282, 1980

3.2 NUCLEAR BLAST RESPONSE OF AIR BREATHING PROPULSION SYSTEMS: A program to evaluate nuclear blast response of airbreathing propulsion systems is an ongoing effort at Calspan. The engine used in the experiments described here was the Williams Research Corporation F107-WR-400.

The basic Ludwig-tube facility, around which this technology program was developed is described in Section 2.2. In order to convert the existing facility to one that could be used to determine the blast-wave response of airbreathing propulsion systems, several modifications were necessary. An important restriction on the generation of shock waves that are to be directed into the engine is that the flow environment must be free of foreign particles. It was thus necessary to modify the facility as shown in Fig. 6 so as to incorporate a driver technique⁹⁻¹¹ consisting of an actuating chamber and a flexible diaphragm in order to create an appropriate shock wave. This chamber is initially pressurized to a static pressure approximately 2 to 5 psi in excess of the Ludwig-tube driver supply tube in order to seal the flexible diaphragm against the shock-tube flange and support grid. The sketch shown in Fig. 6 illustrates that two additional tubes, in addition to the actuating chamber, were added to the facility in order to perform the desired experiments. The shock wave is initiated in the small diameter tube by rapid removal of the flexible diaphragm from the tube entrance. This is accomplished by venting the actuating chamber to the outside away from the engine by rupturing a mylar diaphragm using an air-operated knife. A shock wave is then formed in the 10-inch diameter tube (d) and progresses on to the larger diameter tube (D) where it weakens and is eventually directed into the operating engine. For steady-state operation of the engine prior to initiation of a shock wave, the engine draws its supply air through the annulus bounded by the two tubes of diameters d and D as shown in Fig. 6.

Figure 7 is a sketch of the engine located in the 8-ft test section. In order to utilize the existing shock tubes, it was necessary to design and construct a bypass duct illustrated in Fig. 7. The cross-sectional area of the bypass was maintained constant at the shock-tube value from the inlet entrance to the perforated plate. For these experiments, a forty-probe dynamic-pressure rake was located just upstream of the first-stage fan to determine fan-face distortion. In addition, total-pressure measurements were obtained at approximately 44 other locations within the engine.

Measurements were performed with two inlet configurations and with the engine at 0° and 20° angle of yaw. Experimental results were obtained for equivalent blast-wave overpressures from 1.0 to 2.5 psi. For each of these overpressures, measurements were obtained for engine speeds from 0% to 100% of maximum speed.

4. NEW INSTRUMENTATION AND TECHNIQUES

4.1 SHOCK-TUNNEL INSTRUMENTATION FOR ROUGHNESS EFFECTS IN HYPERSONIC FLOW:

Recent Calspan shock-tunnel studies¹² of the aerothermal effects of surface roughness include detailed measurements of skin friction, heat transfer and pressure on highly-cooled surfaces in high Reynolds-number hypersonic flow. Configurations were chosen to simulate the flow over a nosetip so that boundary-layer transition, entropy swallowing and surface roughness could be studied either separately or in combinations. The studies were conducted at Mach numbers from 8 to 13. Skin-friction measurements were made on both rough and smooth configurations using the skin-friction transducers shown in Fig. 8. The roughness was bonded to the diaphragm of each transducer to form a rough surface in which the particles were packed as closely as possible without creating a multiple layer. A similar surface was molded into two types of heat-transfer gages developed for use in these studies.

A thin film "S" gage has a sensitive element composed of a platinum film that is sputtered uniformly onto a glass substrate which is molded into the

6. Dunn, M.G., and Stoddard, F.J., "Measurement of Heat-Transfer Rate to a Gas Turbine Stator", J. of Engineering for Power, Vol. 101, No. 2, April 1979
7. Dunn, M.G., and Stoddard, F.J., "Development of a Shock-Tunnel Technique for the Measurement of Heat-Transfer Rate to Gas Turbine Components", 11th International Symposium on Shock Tubes and Waves, July 1977
8. Dunn, M.G. and Hause, A., "Measurement of Heat Flux and Pressure in a Turbine Stage", ASME Gas Turbine Conference, Paper No. 81-GT-88, Houston, Texas, March 1981
9. Dunn, M.G. and Rafferty, J.M., "Nuclear Blast Response of Airbreathing Propulsion Systems: Laboratory Measurements with an Operational J-85-5 Turbojet Engine", ASME Gas Turbine Conference, Paper 81-GT-164, Houston, Texas, March 1981
10. Dunn, M.G., Davis, A.O. and Rafferty, J.M., "Nuclear Blast Vulnerability of Airbreathing Propulsion Systems: Laboratory Measurements and Predictive Modeling", Proceedings of the 6th International Military Applications of Blast Simulation, Cahors, France, June 25-29, 1979
11. Muirhead, J.C., "A Review of DRES Studies on the Effect of Blast on Gas Turbine Engines", Suffield Rept. No. 267, DRES, Alberta, Canada
12. Holden, M.S., "Studies of Transpiration Cooling, Surface Roughness and Entropy Swallowing in Transitional and Turbulent Boundary Layers over Nose Tips", XXXth International Astronautical Congress, Munich, Germany, 16-22 Sept. 1979
13. Holden, M.S., "An Experimental Study of Massive Blowing From a Nosetip During Jovian Entry", AIAA 16th Thermophysics Conference, Paper No. AIAA-81-1070, Palo Alto, CA, 23-25 June 1981

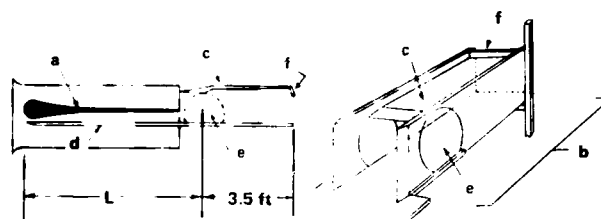
ACKNOWLEDGEMENTS: The author would like to express his appreciation for the contributions made to this paper by his colleagues in the Aerodynamic Research Department, specifically: D. W. Boyer, M. S. Holden, C. Padova and C. E. Wittliff.



Figure 1. Space shuttle vertical tail heat-transfer gage instrumentation

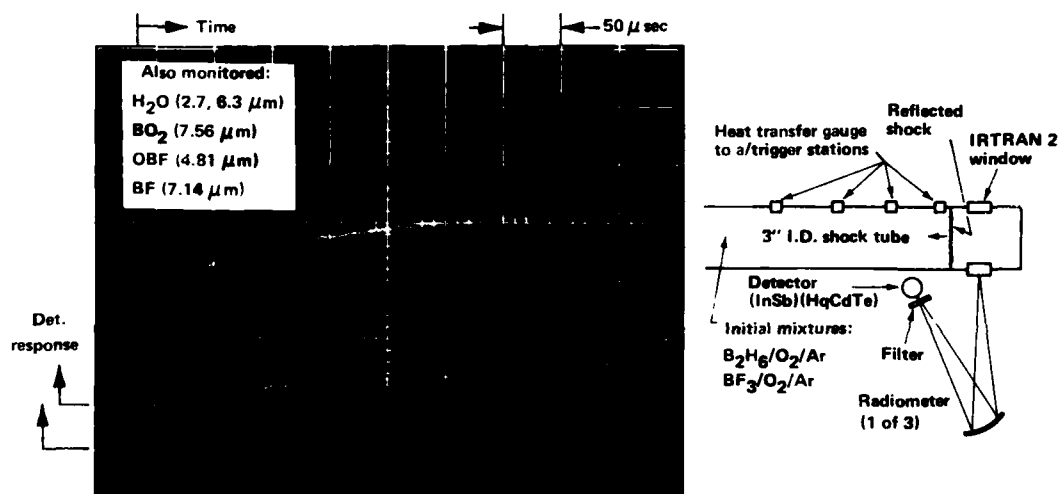


Figure 2. Thin-film gages on dome of pod



(a) Tailored porosity distribution; (b) model (1.08 x 1.31 x 3.42 ft); (c) shock holder top plate; (d) flat plate (L=4.07) (e) observation windows; (f) choking flap

Figure 3. Transonic shock-boundary layer experimental apparatus



Illustrative radiometer record detected in band HBO_2 (4.89-5.05 μm)

Figure 4. Schematic of experimental apparatus and typical data record

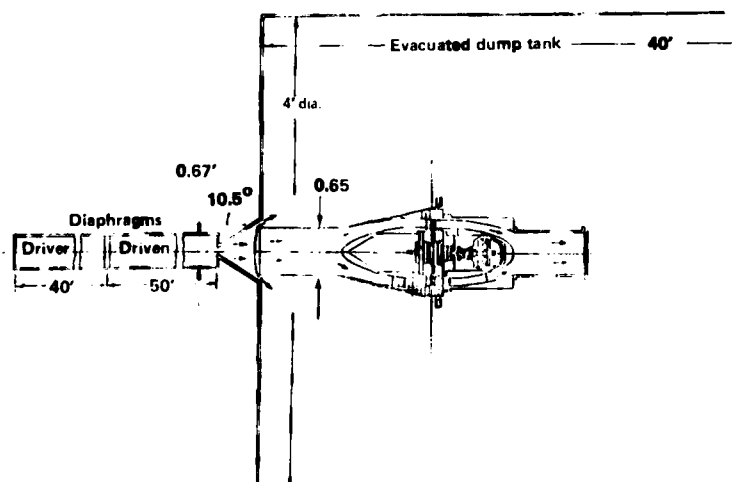


Figure 5. Schematic of turbine heat-transfer experimental apparatus

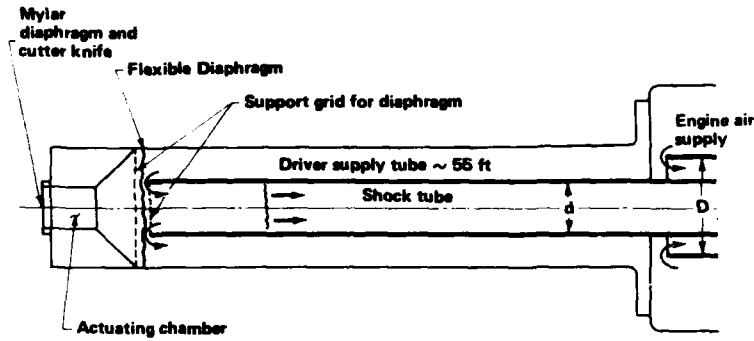


Figure 6. Sketch of apparatus used for blast response experiments

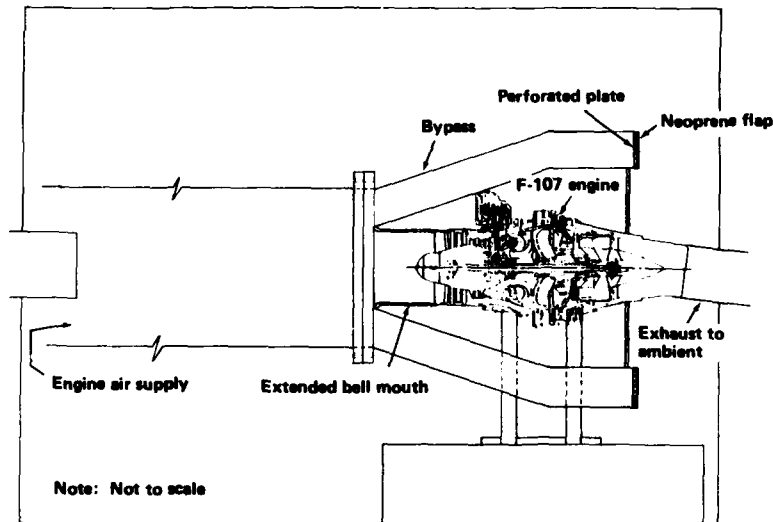


Figure 7. Side-view sketch of engine in Ludwig-tube facility for 0°-yaw configuration with extended bell mouth

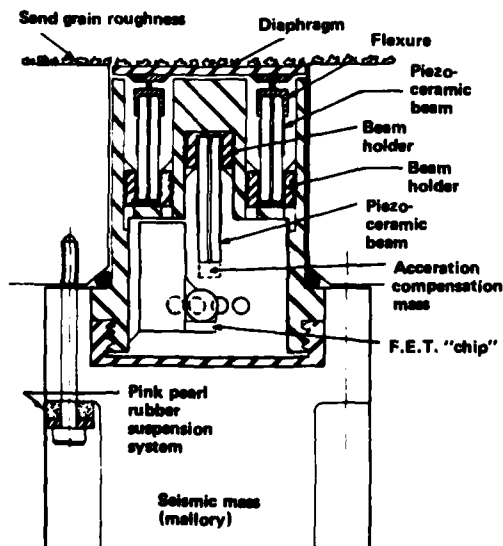


Figure 8. Schematic of skin-friction transducer

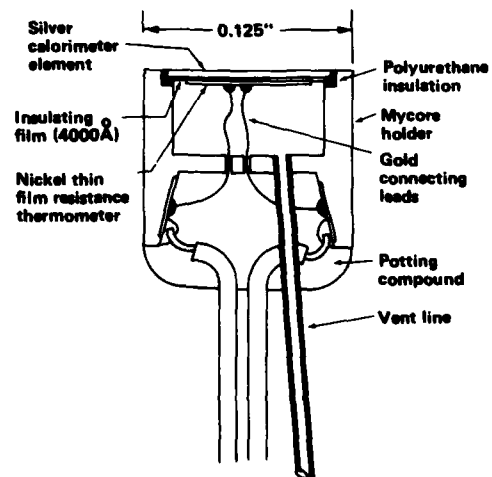


Figure 9. Calspan calorimeter gage

[40]

Dunn

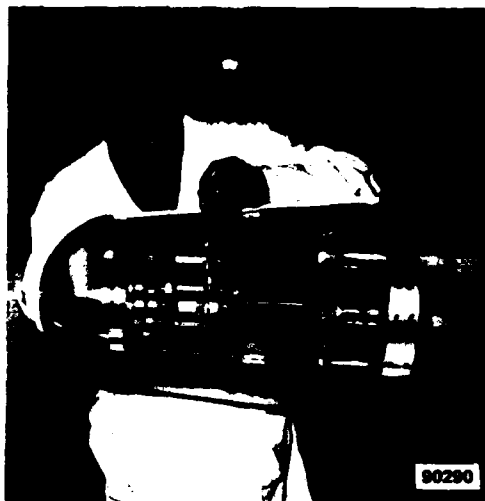


Figure 10a. Model used in Jovian entry studies

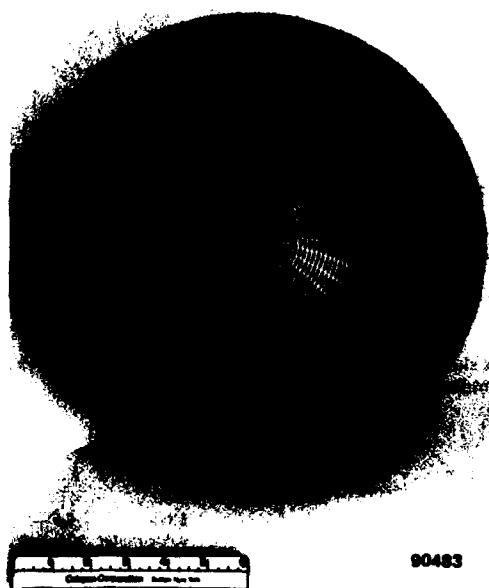


Figure 10b. Instrumented TCNT nosetip



→

SHOCK-INDUCED FLOW SEPARATION AND THE ORBITER THERMAL PROTECTION SYSTEM

Serge-Albert Waiter

Shuttle Orbiter and Integration Division
Space Transportation and Systems Group
North American Space Operations
Rockwell International
Downey, California 90241

AD P 100 225

ABSTRACT

The concept of the Space Shuttle orbiter's thermal protection system (TPS) is based on reusable tiles of various shapes and sizes, but none exceeding 8 inches. The tiles are top-coated, but the sides (edges) are not thermally protected and are susceptible to damage from aerothermodynamic heating. Such a problem occurs when large air-mass flows, created by local pressure gradients, circulate into the tile gaps.

A typical problem is a pressure gradient created during entry by body flap deflection. After a brief description of how the problem affects the Space Shuttle orbiter, a theoretical and experimental review of the phenomenon in which the major parameters involved in gap heating are discriminated and analyzed is presented in Section I. In Section II, a review of well-known classical methods to resolve the gap aeroheating problem in the presence of a pressure gradient is presented, and a few solutions are computed to assess the sensitivity of each one.

Starting with a basic relationship (called "eyeball" because of its simplicity), Section III follows the results obtained up to the most modern engineering approach. It shows that, in all of the cases calculated, there is too little confidence to apply the results to the orbiter without serious structural penalties, such as increased weight from gap fillers used to stop the flow of air into the tile gaps.

Section IV presents the solution obtained by using the most appropriate method, based upon the solution of the Navier-Stokes equations. There is excellent correlation with wind tunnel data. The application to four trajectory time points shows that most of the conservatism introduced because of the uncertainties of the approximate solutions (Section III) can be disregarded. No correlation of this "exact solution" with the simple pre-established relationships has been found, which indicates that more parameters than expected could be involved. However, an after-the-fact, semi-empirical engineering solution that fits the Navier-Stokes solution with good agreement was established.

INTRODUCTION

The TPS of the Space Shuttle orbiter consists of some 35,000 reusable surface insulation (RSI) silica tiles bonded to an aluminum alloy structure. The bonding of these delicate tiles requires extreme precautions, and damage to tiles is to be expected. Furthermore, during flight, friction and convection from the hot and highly energetic flow field surrounding the spacecraft are likely to create severe problems for the TPS system. These two main factors were independently well known when the TPS concept was defined. However, it was not until later that the coupling of the pressure gradient (or skin friction coefficient gradient) with the heat fluxes into the tile gaps was found to be a crucial test for the TPS.

The purpose of this paper is to present the problem for a typical location where high pressure gradients exist during entry, i.e., the bottom fuselage under the influence of body flap deflection. Once the problem is defined, the impact of quick and approximate solutions is assessed, showing a very heavy penalty. A more rigorous solution, whose excellent correlation with experimental data is promising for flight application, is then introduced. The results of the Shuttle's first flight, STS-1, have proven that the heavy burden resulting from the approximate solutions was unnecessary.

I. THE INFLUENCE OF PRESSURE GRADIENT ON TILE GAP HEATING

The Space Shuttle orbiter has a complex geometry, and no exact solutions are presently available to compute the flow field surrounding the vehicle during flight, making it impossible to predict the actual aerothermodynamic environment with a single program code. Instead, a step by step approach is followed using Descartes' methodology. First, an *aeroheating environment* is defined assuming the orbiter is a smooth body (no gaps, steps, or cavities). Then, the influence of "roughnesses" is added on.

Figure 1 shows a typical distribution of orbiter isotherms computed for a smooth surface, and Figure 2 shows the actual orbiter and its tiles. Strong pressure gradients will allow the flow to circulate throughout the many tile cavities and gaps; some of the wall temperatures are already marginal, and, therefore, problems are to be expected.

Figure 3 shows the thermal insulation as it exists and the tolerances presently allowed for gap criteria. Actual size panels of different tile combinations have been tested in NASA's Ames Research Center (ARC) tunnels under pressure gradients similar to those encountered in flight, and a parametric study has shown that it is a combination of pressure and pressure gradients that is producing excessive gap heating. This can be understood when one considers that a driving pressure is necessary to pull the flow through the minigaps of the structure. It should be noted that the pressure gradient can be either positive or negative.

Figure 4 summarizes the analysis and the correlation and its application to the Space Shuttle. A coefficient, G , combining the pressure gradient and the driving pressure has been defined, and its influence on the gap heating with and without pressure gradient is shown in Figure 5 as a function of the gap depth for a 0.030-inch gap width. In the range of interest, the gap heating rates can increase by more than one order of magnitude. Furthermore, since most of the tile sides are not coated, excess heat rates and, thus, heat loads of such an extent will have catastrophic results on the strain isolator pad (SIP) and structure.

II. INFLUENCE OF BODY FLAP DEFLECTION ON FLOW SEPARATION

This section describes the influence of body flap deflection on gap heating. The geometry of the bottom fuselage with its body flap deflected can be compared to a curved plate with a downstream wedge (see Figure 6). Shock waves are generated at separation and reattachment, producing a strong rise in static pressure. Two strong pressure gradients, both positive, are present, separated by a so-called "plateau pressure." Each gradient is driven by a different pressure level and will provide different values for G . The analysis will focus on the determination of the aeroheating pressure coefficient, G , created by such a configuration. It must be remembered that the subgroup $[dp/dx \sqrt{P_{max}}]$ is of interest, and not only the pressure gradient.

Figure 7 shows the sensitivity of the pressure rise $p = (p_2/p_1)$ as a function of a parameter such as wedge angle, Reynolds number, or temperature ratio (wall-to-total) at a given Mach number for a laminar separation. (Laminar flow is studied here because peak heating occurs during this flow regime.) Because of the nature of the parameters playing major roles in the analysis, it was suggested that the boundary layer displacement thickness, δ^* , would be a plausible factor in the calculation of the dx , and an empirical analysis showed that dp/dx could be, for sample cases, approximated by $dp/dx = (p_2 - p_1)/10 \delta^*$. The choice of 10 times δ^* has been determined by empirical analyses based on a significant amount of experimental data for wedges and cones. These data, available upon request, are limited to supersonic Mach numbers below $M_\infty = 6.0$, where no real gas effects behind the shock exist.

III. CALCULATION OF THE AEROHEATING PRESSURE GRADIENT COEFFICIENT

This section presents the results of an approximation of dp/dx . It is assumed that the flow reattaches at the trailing edge of the body flap (see Figure 8). Selecting a given position, X/L , of separation on the bottom fuselage and assuming a 2-D wedge flow, the pressure rise through the shock is easily computed as a function of the body flap deflection angle, and δ^* is obtained by some well-known relationship (see Figure 9).

In the present analysis, the integral technique is used. A computer program for HP 9020 has been written using the aerodynamic parameters derived from Rockwell International's aerodynamic heating program so that the resulting G 's will be consistent with the aeroheating analysis. The results of the integral technique (δ^*) have been compared with finite difference solutions for a few trajectory times and was shown to be adequate for this type of analysis.

Figure 10 presents the variation of the G coefficient for two extreme trajectories vs. entry time for a given location of separation, $X/L = 0.9$. It can be seen that the influence of the trajectory is meaningless. The influence of the separation location ($0.5 \leq X/L (0.9)$) is analyzed next (approximation 1). The flow model is presented in Figure 11. Again, the flow is supposed to reattach at the trailing edge of the body flap, but separation onset is arbitrarily set at given X/L locations. The farther upstream the separation, the weaker is the shock created and the higher is the G coefficient. (In this analysis, large G 's mean weak pressure gradients.)

As expected, the G coefficient is shown to be a significant parameter and its determination could be improved. (That is the reason the results are not presented here but are available on request.) The influence of the body flap deflection angle illustrated in Figure 12 is shown to be insignificant in the range of deflection to be used during entry. Increasing the body flap deflection angle increases the shock strengths and the plateau and reattachment pressures, but the results are hardly noticeable because of the limited deflection range ($14.6 \leq \delta_{BF}^0 \leq 20.6$).

A better approximation (No. 2) is proposed to define more accurately the only unknown as yet, the separation onset location. An iterative process is used, and of the restrictive assumptions included (perfect gases, flat body, etc.) only the peak heating trajectory point was computed

(i.e., $T = 850$ seconds) because of the rather long calculations involved. The results, presented in Figure 13, show that separation onset would occur as early as $X/L = 0.74$, or, to be more specific, all tiles downstream of the main landing gear would experience excess gap heating problems from peak heating to landing as early in flight as $T = 800$ seconds.

Gap filler would be required for several thousand tiles with dramatic consequences such as increased weight, increased labor costs, and significant launch delay. This solution would involve 336 inches of the fuselage's length ($0.26 \times 1,293$), or approximately 72 rows of tiles, most of them on the wing.

This approach was dropped because of the lack of credibility of the assumptions involved. However, the problem was so critical and the flow field mechanics so poorly known that a new approach had to be defined. What was learned in the approximate and sometimes crude analysis is summarized in the following.

1. Trajectory is not influenced. Between the "weak" STS-1 and the design trajectories, the aeroheating pressure gradient coefficients are almost identical.
2. Severe G's are encountered as soon as separation occurs, regardless of the separation angle and the upstream Mach number.
3. In the calculation of pressure gradients, the 10 times δ^* has not been justified for the orbiter boat tail configuration within the range of flight encountered. The comment applies to the 10 as well as the δ^* . All analysis based on these two coefficients have shown severe aeroheating from pressure gradient, causing severe penalties for the TPS.
4. The uncertainty in the prediction of the separation onset is another crucial parameter. The one approximation used in this paper has shown that almost one fourth of the fuselage would require gap filler. However, the assumptions used in the deviation of the analysis are very restrictive and permit the repetition of the conclusions of this approach (cost, weight, delay).
5. A quantitative analysis not presented here has shown that the case of a 2-D flat plate-wedge model was very conservative. It does not appear that the actual geometrical shape could ever be included, but more recent step by step methods could include the boat tail effect, which would significantly minimize the effect of the shock strength.
6. A general conclusion is that, even with the last (less conservative) analysis, pressure gradients could create problems as early as $T = 850$ seconds during entry.

The need for more satisfying methodology is obvious.

IV. CALCULATION OF THE AERODYNAMIC HEATING PRESSURE GRADIENT

The only suitable theoretical approach is to solve the exact Navier-Stokes equations. Many models exist but one of the most satisfying has been developed by NASA ARC. It can be modified to include the boat tail geometry. Only one month was allocated for the analysis so the results could be incorporated in STS-1.

The program was modified very quickly, and its first application was to existing oil flow wind tunnel data (OH 25-B) where separation and reimpingement could be accurately defined. These tests were run in the ARC 3.5-foot tunnel at $M_{\infty} = 7.3$ and several (Re/ft) and angles of attack. A similar pressure test (OH 25-A) was available and provided the input conditions necessary to run

the program. Six wind tunnel cases were analyzed: three angles of attack at 2 (Re/ft) each. Figure 14 presents the results for $\alpha = 40$ degrees (2 Re/ft), and compares theory with experiment. The comparison is excellent for all cases analyzed and gives great confidence for the flight analysis.

Four trajectory time cuts were computed:

$$T = 500, 700, 900, \text{ and } 1,200 \text{ seconds}$$

The starting conditions such as P at X/L , δ^* , M_e were defined theoretically. Convergence to the exact solution should be quick, considering that the starting condition ($X/L = 0.8$) was selected well upstream of the disturbance created by the onset of separation. The results are shown in Figure 15. As expected $[dp/dx \sqrt{p}]$ is a significant function of time.

The very interesting feature of the solution is that separation occurs almost at the hingeline, contrary to the previous approaches. It is assumed that the introduction of the boat tail shape into the solution has provided the significant relief expected. With the present results, only the two rows of tiles upstream of the hingeline are affected by separation.

In order to assess the sensitivity of the parameters of the product $[\sqrt{P_{\max}} dp/dx]$, four different cases were computed for which all input parameters such as δ^* , C_p , C_v were dramatically changed. The results of this error analysis show that the G factor is only affected by ± 7 percent when these parameters are modified (see Figure 16). This can be explained by the extremely fast convergence of the present computer code. Even though the "starting conditions" at $X/L = 0.8$ are voluntarily offrange, the program converges extremely fast to the correct solution, and when separation occurs, the previous history of the flow has been damped and accounted for.

Accordingly, it was decided that only two rows of tiles upstream of the hingeline will be affected by separation and, as a consequence, have their gaps filled. This is a dramatic improvement when compared with the 70 or more rows of tiles previously incriminated.

During the Navier-Stokes analysis, a memo by Jimmy Carter of ARC was discovered and analyzed. In this report, experimental data about pressure distribution on wedges in the separation region at M_∞ up to 6.06 have been collected and plotted. The range of wedge angle is $5 \leq \alpha_w^\circ \leq 11$ and the range of the Reynolds number is $1.35 \times 10^4 \leq Re_x \leq 1.01 \times 10^5$.

After a transformation of variables based on the free interaction model, it is shown that, in the P and X plane (P and X being defined in Figure 17), the scattering is reduced and all data points seem to follow one single curve where a $dP/dX = 1.8$ can be easily identified.

The calculation of the coefficient $G(x)$ can be made and compared with the Navier-Stokes solution previously obtained by writing that

$$dp/dx = dp/dP \cdot dP/dX \cdot dX/dx = 1.8 \frac{dX/dx}{dP/dP}$$

with dX/dx , dP/dP and P and $X = \phi_i [p, x, X, \delta^* \dots]$ according to flight conditions and the free interaction model. The results are presented in Figure 18. The correlation is impressive even though the two logics are so widely different.

Flight test results are shown in Figures 19 and 20. It can be seen that no tile damage is visible upstream of the hingeline. Figure 19 shows the main landing gear door locations. Note the number of rows of gaps to be filled.

V. CONCLUSION

The conclusions are summarized below.

- No correlation has been found between dp/dx and any boundary layer thicknesses. A statistical analysis has been conducted where δ , δ^* , and θ were compared with the dx in dp/dx as predicted by the Navier-Stokes solutions. As of now, no empirical or mathematical relationships have been found. This could be because the various boundary layer thicknesses are not related to the pressure gradient or other parameters (not yet included) should be inserted.
- As for the G coefficient or $[dp/dx \sqrt{p}]$ a good correlation exists between the free interaction model and the solution of the Navier-Stokes equations. A simple computer program has been written that can compute G for any trajectory within a few minutes.
- The location of separation onset is less severe for flight cases than for wind tunnel cases at iso-Reynolds number (per length or per foot). This could be attributed to the fact that the energy level (enthalpy) is much greater in flight than in the wind tunnel.
- Sophisticated solutions predict less severe separation onset and pressure gradient effects than could be predicted by less rigorous analysis. It is assumed that these solutions are based upon experimental wind tunnel data that are, as previously explained, more conservative than flight data.
- It has not yet been possible to correlate quantitatively the flight data to the theoretical predictions because not enough pressure data are available from flight to define a good pressure variation and, thus, a good value of the pressure gradient.
- However, a good qualitative correlation exists for the prediction of the separation location onset.

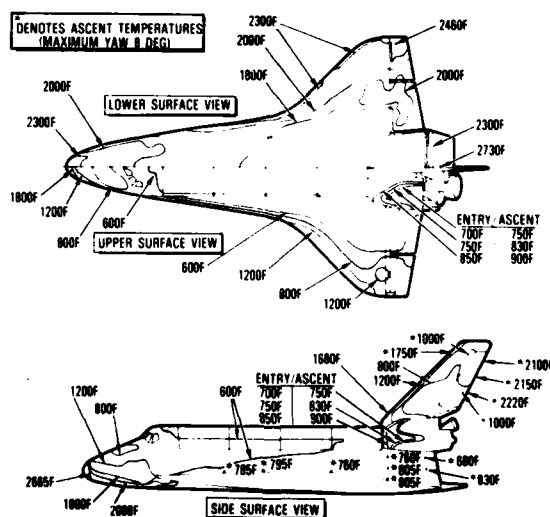


Figure 1. Orbiter isotherms - design trajectory

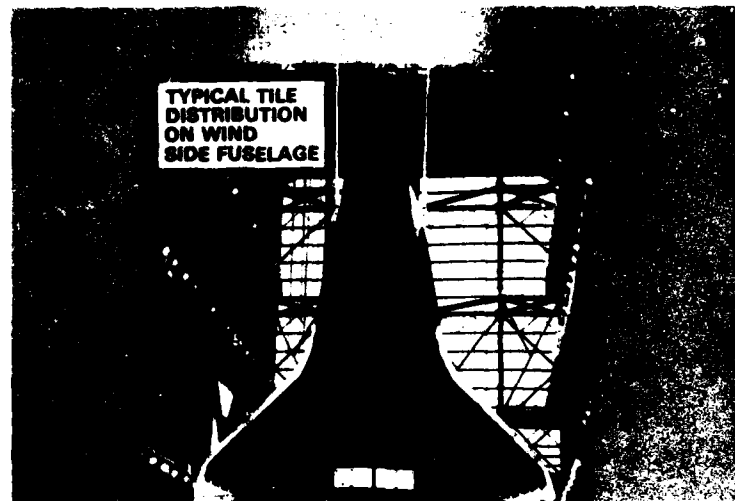


Figure 2. Typical tile distribution on wind side fuselage

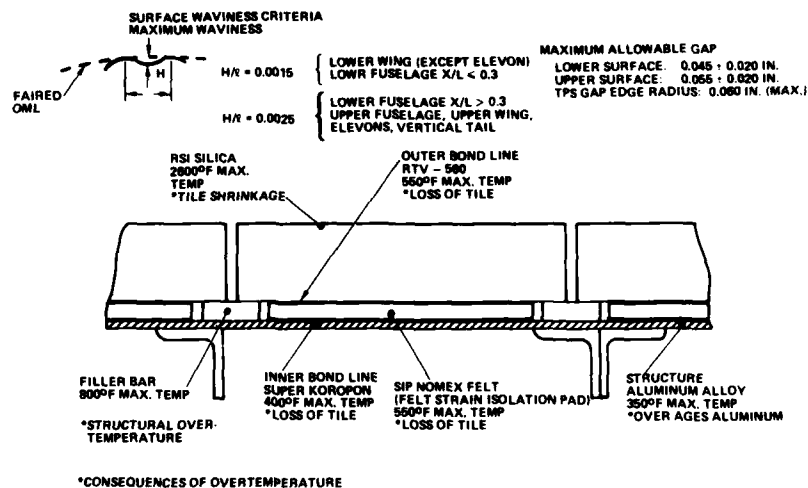


Figure 3. TPS temperature limits

ANALYSIS

- DEVELOP MATH MODEL THAT WILL RELATE GAP HEATING TO PERTINENT PARAMETERS & ALLOW EXTRAPOLATION TO FLIGHT
- PRELIMINARY MODEL BASED ON WING/GLOVE TEST ARTICLE DATA; VERIFY WITH DOUBLE WEDGE TEST ARTICLE DATA
- MATH MODEL TO BE APPLICABLE TO ALL PRESSURE GRADIENT LOCATIONS THROUGHOUT TRAJECTORY

$$\text{CORRELATION} \quad \frac{\dot{q}_{\text{GAP}}}{\dot{q}_{\text{REF}}} \sim \frac{\dot{q}_{\text{CHANNEL}}}{\dot{q}_{\text{LAMINAR FLAT PLATE}}} \sim \frac{(dp/dx)(p)^{1/2}}{(H)^{3/2}}$$

$$\text{BETTER CORRELATION:} \quad \frac{\dot{q}_{\text{GAP}}}{\dot{q}_{\text{REF}}} \sim \frac{(dp/dx)(p)^{1/2}}{(H)^{1/2}}$$

Figure 4. Gap heating data analysis, correlation, and application

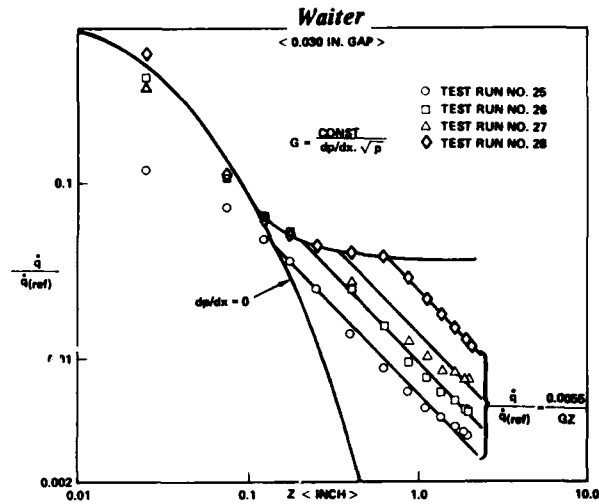


Figure 5. Double-wedge high dp/dx gap heating data correlation

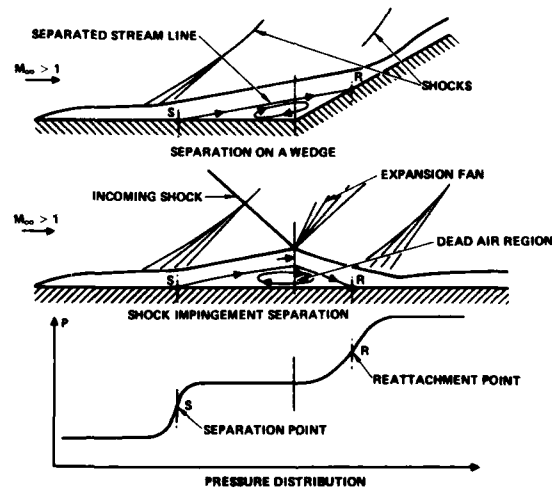


Figure 6. Laminar separation with convective heating

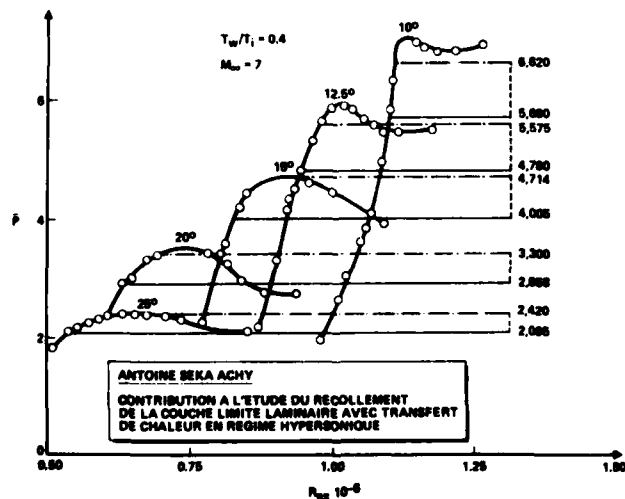


Figure 7. Laminar separation with convective heating

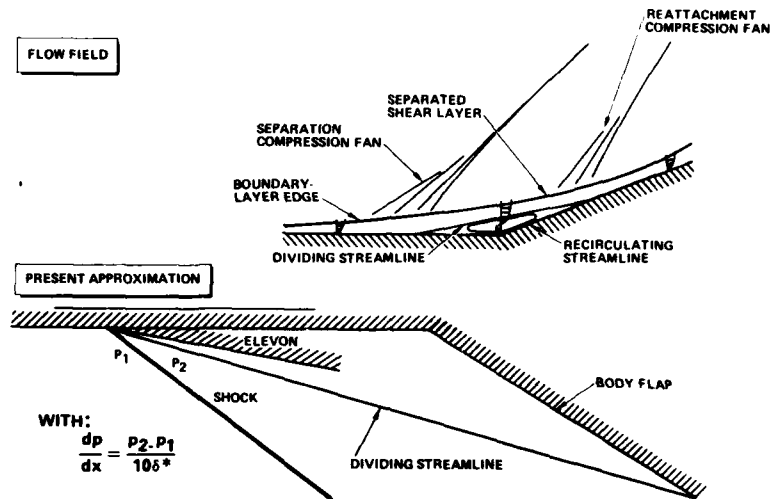


Figure 8. Flow field and approximation

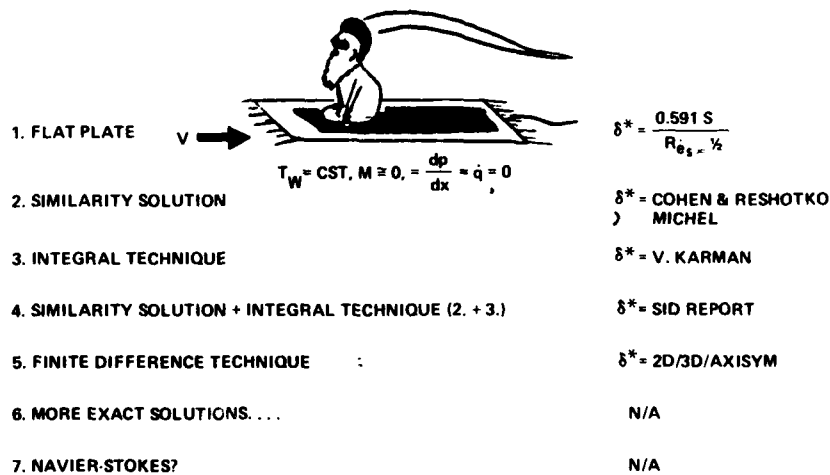


Figure 9. Determination of Δ^*

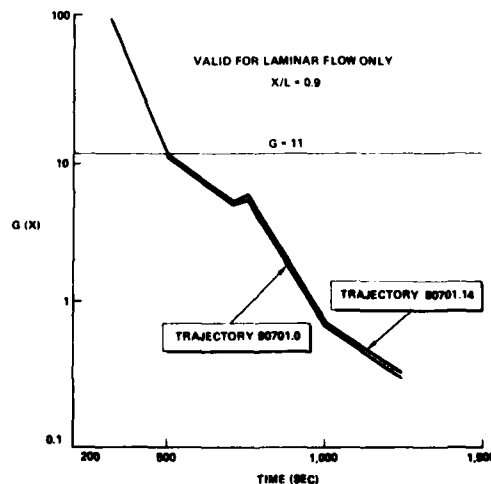


Figure 10. Variation of G due to separation during entry

[50]

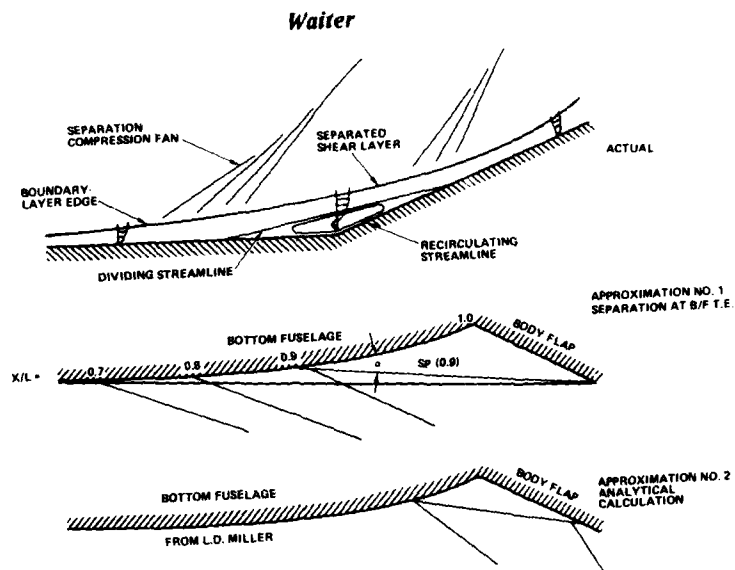


Figure 11. Flow field models

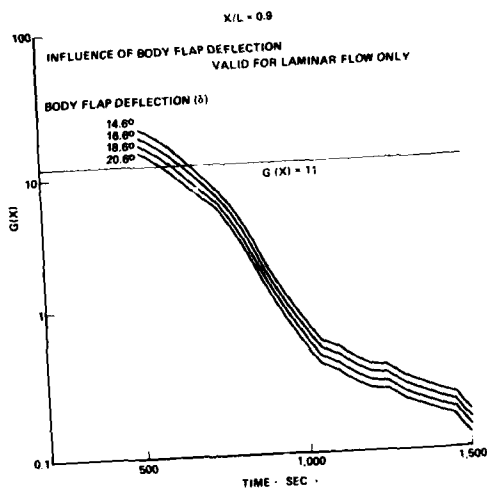


Figure 12. Variation of G due to separation during entry

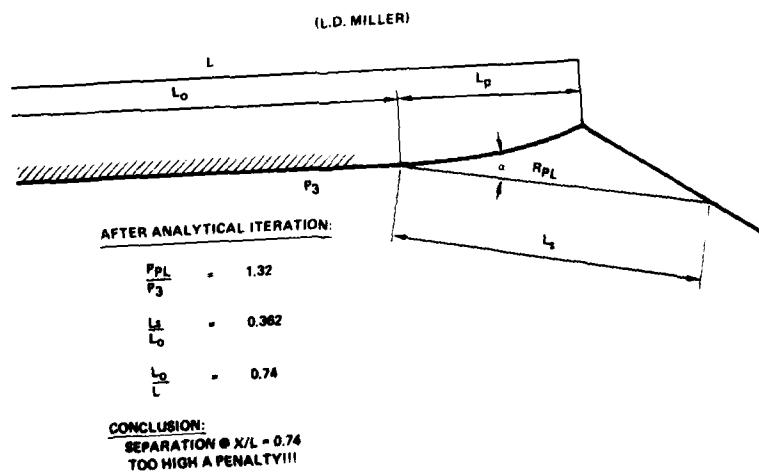
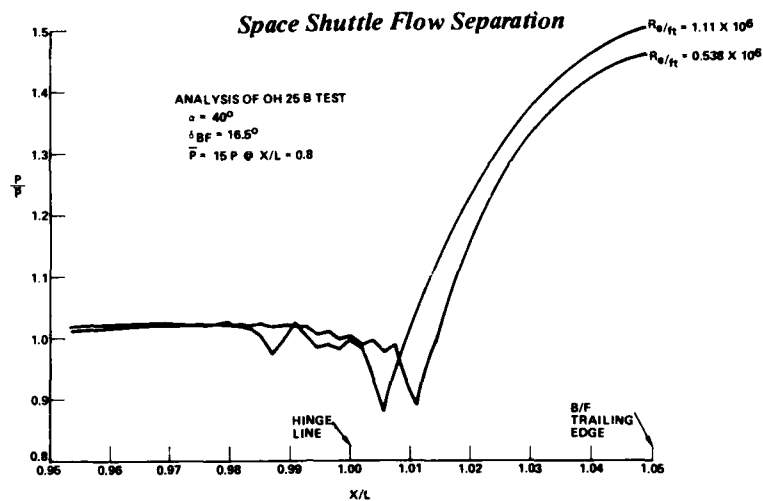


Figure 13. Results of analytical calculations at $T = 850$ sec.



[51]

Figure 14. Analysis of OH 25B test

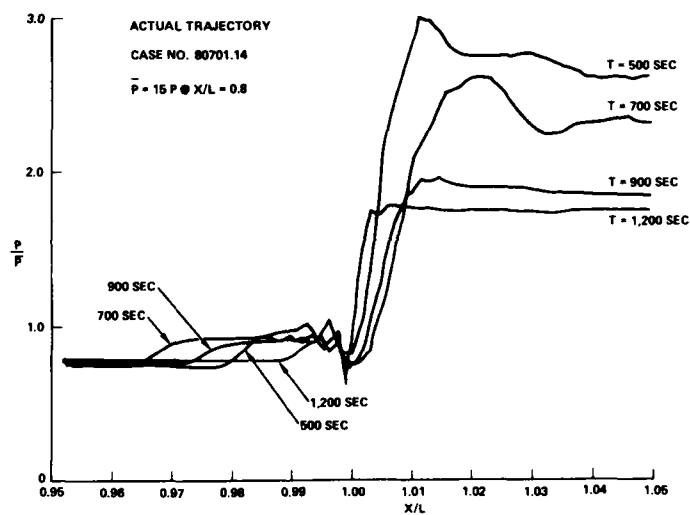


Figure 15. Actual trajectory case no. 80701.14

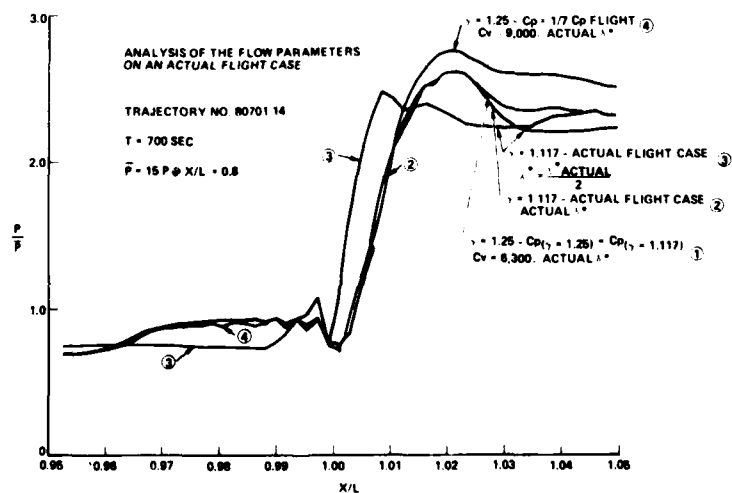
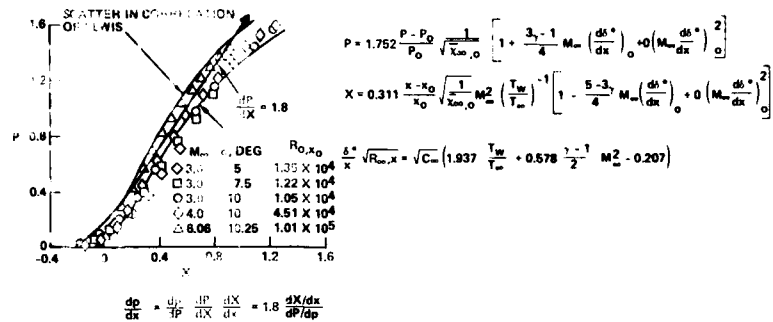


Figure 16. Analysis of the flow parameters on an actual flight case



WITH

$$\frac{dX}{dx} = \frac{d}{dx} \left(0.311 \frac{(x - x_0)}{x_0} \sqrt{\frac{1}{x_{\infty,0}}} M_{\infty}^2 \left(\frac{T_w}{T_{\infty}} \right)^{-1} \left[1 - \frac{5-3\gamma}{4} M_{\infty} \left(\frac{ds^*}{dx} \right)_0 + 0 \left(M_{\infty} \frac{ds^*}{dx} \right)_0^2 \right] \right)$$

$$\frac{dP}{dx} = \frac{d}{dx} \left(1.752 \frac{P - P_0}{P_0} \sqrt{\frac{1}{x_{\infty,0}}} \left[1 + \frac{3\gamma - 1}{4} M_{\infty} \left(\frac{ds^*}{dx} \right)_0 + 0 \left(M_{\infty} \frac{ds^*}{dx} \right)_0^2 \right] \right)$$

Figure 17. Free interaction model

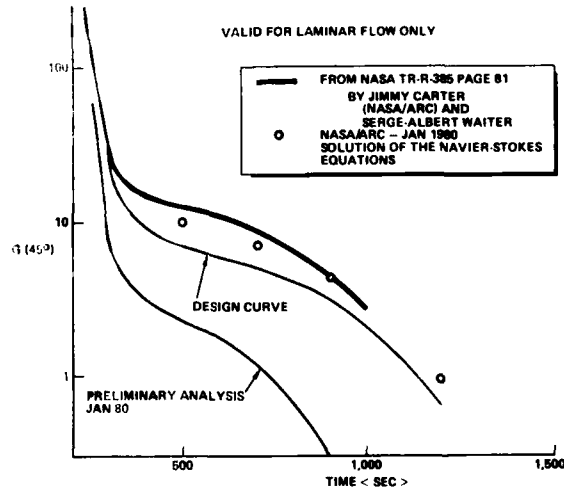


Figure 18. Variation of G due to separation during entry



Figure 19. Bottom fuselage after STS-1

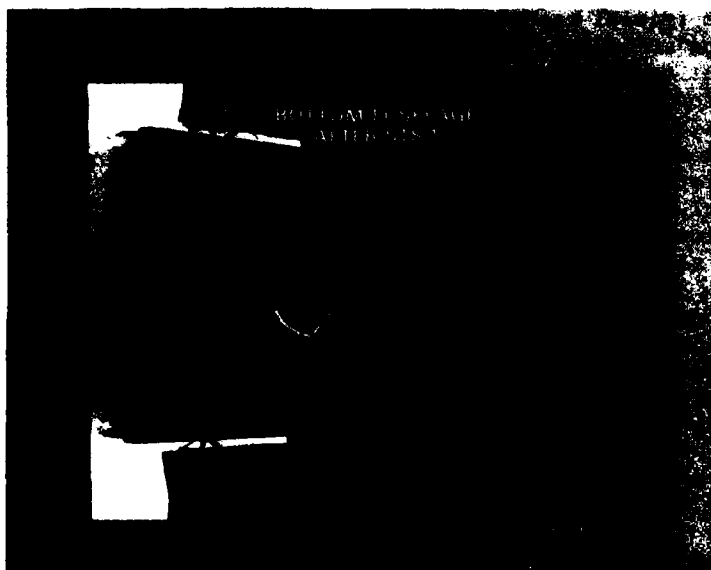


Figure 20. Bottom fuselage after STS-1



AD P000226

CHEMICAL KINETICS STUDIED BY VACUUM-UV SPECTROSCOPY

IN SHOCK TUBES

Th. Just

DFVLR-Institut für Physikalische Chemie der Verbrennung

Pfaffenwaldring 38, 7000 Stuttgart 80

The study of elementary chemical reactions at elevated temperatures is greatly improved when the shock heating of a reactive gas is combined with a very sensitive technique of species detection. Atomic resonance absorption spectrometry, ARAS, is such a technique. For example, it allows the detection of relatively low concentrations of H and O atoms behind reflected or incident shocks.

The generation of the absorption signals with a signal to noise ratio on the order of 10 or better was found to require initial concentrations of only a few ppm of the reacting molecule. The advantages offered by such a low reactant concentration are obvious. The low initial concentration minimizes temperature changes caused by the heat of reaction to a negligible scale. Thus, chemical reactions can be studied under isothermal conditions. In addition, the interpretation of the process under investigation is often greatly simplified. As a result of the low initial concentration, many subsequent radical-radical reactions proceed very slowly during the first 100 to 200 μsec .

The paper includes a discussion of the necessary calibration procedures for H and O atoms, as well as a survey of some results which were obtained by the ARAS method. Finally it contains also some information about the use of strong vacuum-ultraviolet absorption bands of molecules for obtaining additional kinetic information. However, higher reactant concentration levels, on the order of 50 to 200 ppm, are necessary for such experiments.

1. INTRODUCTION

The combination of shock heating of a reacting gas mixture with a sensitive technique for species detection offers great advantages for the study of selected elementary reactions at elevated temperatures. Atomic resonance absorption spectrometry (ARAS) has been known for a long time as a very sensitive technique for concentration measurements in the range of 10^{11} to 10^{14} atoms per cm^3 . To generate these concentrations by chemical reactions, generally at temperatures above 1800 K, initial concentrations of the reactants on the order of 50 to 1 ppm are required.

These low initial concentrations minimize the temperature changes caused by the heat of reaction under study. For example, the temperature behind a reflected shock can be considered as practically unaffected by the chemical process. The initial temperature and its constancy during the utilized measuring time depend solely on the hydrodynamics of the used shock tube.

The carrier gas commonly used in such experiments is Ar with only traces of reactants. Within measuring times of about 200 to 600 μ sec we can expect practically constant temperatures. In a properly designed shock tube typical temperature changes on the order of 1% in Ar were found.

The combined ARAS and shock tube technique is very well suited for studying dissociation kinetics of two-atom molecules for which it was developed first in the past. However, it soon turned out that the advantage of performing experiments with very low initial concentrations is particularly important, when more complex reactions of polyatomic, in particular small hydrocarbon molecules are considered.

For example in pyrolysis experiments the low initial hydrocarbon concentration allows one to distinguish between the primary process of the H-atom abstraction and the secondary reactions of the generated H-atom and radical with the original molecule. In the case of H-atom abstraction we expect for a distinct time interval a linear increase of H-atoms with time.

If the primary step is not a H-atom abstraction, then the system may generate H-atoms in a secondary reaction. In this case we will observe under carefully selected experimental conditions quite a different H-atom profile with $dH/dt = 0$ for $t = 0$. So the two general types of primary dissociation can very easily be distinguished.

Due to the low initial concentration generally the contribution of recombination reactions and of many secondary or tertiary bimolecular radical-radical reactions is minimized in the first 200 to 600 μ sec. The immediate gain is a considerably simplified interpretation of the chemical kinetics of the investigated system.

Since N_2O splits off an oxygen atom very fast at temperatures above 1800 K, mixtures of N_2O with a hydrocarbon can be used to study the primary reactions of oxygen-atoms with the hydrocarbon molecule. In this case measurements of the time dependent profiles of oxygen - as well as hydrogen-atoms - are necessary.

The recording of the H or O-atom profiles needs a vacuum-uv spectrometer. Such an instrument together with suitable light sources enables it also to perform experiments at selected vuv absorption bands of molecules. For example, some hydrocarbons have in the accessible wavelength range of vuv spectrometers fairly strong absorption coefficients on the order of 10^6 to $3 \times 10^7 \text{ cm}^2/\text{mol}$ under standard conditions. This can be exploited for additional experiments in which under favourable conditions information about the sum of all primary decay processes can be gained.

2. EXPERIMENTAL ARRANGEMENTS

Most research groups applied the ARAS or vuv band-absorption technique to reactions which were started behind reflected shocks, since the temperature profile behind reflected shocks is usually of better quality.

2.1. THE SHOCK TUBE

In particular for performing experiments with H or O-atom detection great care has to be taken on the construction of a tight shock tube and auxiliary vessels with clean inner surfaces. Traces of pump oil or organic material from ordinary gaskets cannot be tolerated since these materials can be the source of unwanted and sometimes uncontrollable contributions to the measured H-atom concentrations.

We found an average tightness of 5×10^{-8} torr·liter·sec⁻¹ for the storage tank and about 0.1 to 1×10^{-6} torr·liter·sec⁻¹ for the shock tube tolerable for the application of the ARAS technique.

Facilities for baking the shock tube, storage tank and all connecting tubes are in most cases helpful and in some applications essential. The latter is true for studies with molecules which are adsorbed easily by the walls. Examples are: SO₂, H₂CO, CH₃OH, NH₃, C₄H₂. Further general aspects of shock tube construction in connection with the ARAS-technique are discussed in References (1) to (3).

2.2. GAS MIXTURES

Most important for the ARAS technique is the use of Ar with the highest available purity. Good results can be obtained with Ar which contains less than 0.006 ppm H₂ and hydrocarbons, < 1 ppm of water and 0.4 ppm of air. At densities of about 1×10^{-5} mol·cm⁻³ behind the reflected shock and temperatures of about 2800 K not more than $3 \cdot 10^{11}$ H-atoms cm⁻³ were produced by the residual impurities.

Experiments at higher densities usually require further purification of the Ar. We would propose for experiments under such conditions to pass the Ar through selected molecular sieves at dry ice (CO₂) temperature. Experiments in this direction are presently in progress in our laboratory.

The admixed test gases should be of high purity too. However, here the standards may be somewhat less stringent, since the needed relative concentrations of the test gases is in most cases less than 50 ppm.

2.3. SPECTROSCOPIC ARRANGEMENTS

Windows of MgF₂ near the end flange of the shock tube have proven well suited for the vuv technique. They are little affected by solarization by the high energy quanta in the wavelength range between 1200 to 1400 Å. The transmission of MgF₂ is satisfactory down to 1200 Å with a corresponding transmission of 40% at a window thickness of 1.5 mm.

2.4. LIGHT SOURCES

As light sources for the ARAS technique microwave-driven discharges in He with traces of H₂ or O₂ are well qualified. Typical operation conditions of such lamps are: 5 torr total pressure and microwave power between 50 to 100 W at 2.45 GHz. The discharge tube is usually connected directly to the shock tube window. The He should enter the discharge tube near the shock tube window and should flow slowly in the direction of the microwave antenna. This approach will reduce selfabsorption effects by atoms in the cold layer between the discharge and the shock tube window.

A systematic research in particular on the properties of Lyman-(α)-sources was undertaken by Lifshitz, Skinner and coworkers (4), (5), see also Ref. (3).

When to the carrier gas H₂ traces of N₂, CO₂ or CH₄ are added, we were able to excite a great variety of atomic lines and molecular bands in the spectral range between 1200 and 1700 Å. Selected emissions, which exhibited a good long term stability, were used for vuv band absorption experiments. Excitation of X_e(I) at 1469 Å enabled measurements with SO (8). Excitation of H₂ gave strong emission around 1608 Å which can be used for absorption experiments with C₂H₄(9).

Other light sources for vuv absorption experiments behind shocks were described for example by Patch (6): H₂ Werner transitions around 1150 Å, and by Appleton (7): N₂ transitions around 1176 Å.

2.5. SPECTRAL FILTERING

The use of a vuv spectrometer has many advantages over spectral filters, but one disadvantage is the relatively poor transmission at wavelengths around 1200 Å. For chemical kinetic research in the vuv spectral region a spectrometer is essential, however at the L(α) wavelength a spectral filter can be used favourably. A spectral filter for D(α) radiation based upon a combination of O₂ transmission and the quantum efficiency of the used photocathode was described by Appleton and Appel in Ref. (2). The residual transmission of the filter for radiation other than H(α) or D(α) was reported to be on the order of 2%. This agrees well with our own experience.

The advantage of such a filter is the much higher transmission rate which improves the time resolution or signal to noise ratio of the equipment. However, in studying hydrocarbon reactions it was often found necessary to take into account the time dependent absorption by molecules exactly at the L(α) wave length. This occasional contribution to the measured total absorption is difficult to determine exactly with a simple spectral filter. With a vuv monochromator these important data can be obtained fairly accurately when the absorption of the disturbing molecules is determined at the wave length of the D(α) lines.

In principle a similar method can be used at other wave lengths. For example, when O-atom absorption is studied. No example has been reported up to now. It may be difficult to find in practice a strong emission line which is near enough to the used O-atom triplet around 1306 Å.

2.6. Photo Multipliers

Solarblind detectors with LiF windows have been proven to be well suited for time resolved spectroscopy in the wavelength range between 1150 to 1800 Å.

2.7. SIGNAL TO NOISE RATIO

With a L(α) source driven by 100 W microwave power, a McPherson Model 225-1m spectrometer and a solarblind photomultiplier EMR 541 G-08-18, we obtained a signal to noise ratio on the order of 50 at an electronic band pass of 30 kHz. The time resolution given by the optical arrangement is in our experiments typically about 20 to 25 μsec. This is sufficient for most experiments in a temperature interval between 1600 to 2800 K. When a spectral filter for the H(α) line is used, the time resolution can be improved to a few μsecs at a signal to noise ratio of about 1000. See reference (2).

3. CALIBRATION PROCEDURES

Since it is difficult to determine the exact emitted line profile of a discharge lamp, it is not possible to calculate with good accuracy the needed calibration curves, which connect absorption with concentration. Attempts in this direction have been made. They are reviewed in Ref. (3). Up to now it is necessary to perform separate calibration experiments for H and O atoms.

3.1. HYDROGEN ATOMS

The H_2 -dissociation may be considered as well known in the temperature range between 2500 to 4000 K. Three independent experimental works gave rate coefficients for H_2 -Ar which agree well within 20% deviation between the lowest and the highest value at a given temperature. See: (6), (1), (10). Difficulties arise when calibration at lower temperatures such as 2500 K, becomes necessary. One possible method is to exploit the fast dissociation of N_2O and the production of H-atoms through the reactions: $O + H_2 \rightarrow OH + H$, $OH + H_2 \rightarrow H_2O + H$ by mixtures of N_2O with H_2 .

We prefer mixtures containing about 50 to 200 ppm H_2 and a few ppm N_2O . At temperatures above 2200 K we obtain with such mixtures 2 H-atoms per N_2O molecule. It is therefore possible to check the calibration by H_2 dissociation with this independent simple and very accurate method at $T > 2200$ K. At lower temperatures it is necessary to use computer modeling with known rate coefficients in particular for the N_2O decay. Fortunately, in the temperature range from 2000 to 2500 K these coefficients seem to be known also fairly accurately. However, at present some inconsistencies exist for the N_2O decomposition at temperatures lower than 1800 K. See Ref. 3. We based our calibration on results reported by Olschewski et al (11) and our own measurements (12) which agreed very well with the results of Ref. (11).

In principle it is also possible to use mixtures of large excess of N_2O over H_2 or D_2 . Such mixtures $N_2O > D_2$ for D-atom experiments were used by Appel and Appleton (2). Great care has to be taken when this method is applied to N_2O/H_2 mixtures because here the large excess of generated O atoms may also produce H-atoms by the two fast side reactions with water and OH: $O + H_2O \rightarrow 2OH$, $O + OH \rightarrow O_2 + H$. According to our experience water may be present in our shock tube in relative concentrations in the range between 0.1 to 0.3 ppm. Computed examples for the additional H-atom production are shown in Fig. 1. The coincidence with the measured H-atom profile is good.

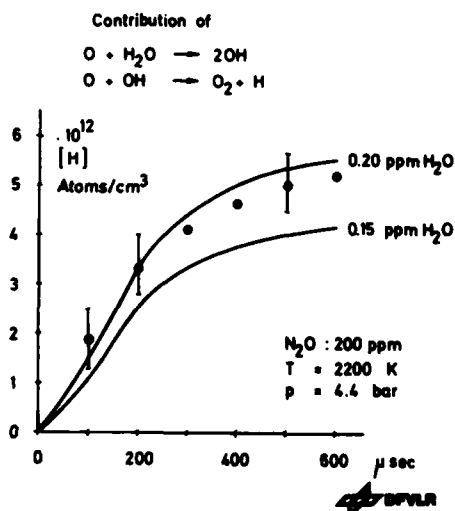


Fig. 1. N_2O in Ar. L(α). Additional H-atom production by $O+H_2O$ reactions. ● measured; — computed with assumed H_2O concentrations. See text.

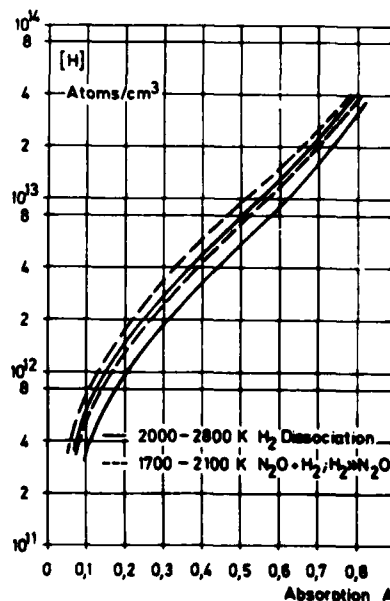


Fig. 2. Typical calibration curves for H-atoms.

In Fig. 2 we show examples of calibration curves obtained by H_2 dissociation and H_2/N_2O mixtures with H_2 in excess.

3.2. OXYGEN ATOMS

At temperatures above 2200 K N_2O dissociation at a typical total density of $1 \times 10^{-5} \text{ mol} \cdot \text{cm}^{-3}$ is so fast that a steady state concentration of O-atoms is achieved within about 200 μsec . At lower temperatures the calibration needs the kinetics of the N_2O dissociation. This is a simple matter under the experimental conditions with a few ppm to about 50 ppm initial relative concentration of N_2O , since subsequent reactions like $O + N_2O \rightarrow N_2 + O_2/2NO$ are known to be slow and are unimportant at such low N_2O concentrations. Recombination of O-atoms can be safely neglected in the typical time scale of 400 to 600 μsec .

3.3. ABSORPTION COEFFICIENTS OF SELECTED MOLECULES IN THE VUV SPECTRAL REGION.

There exist only sparse informations on quantitative data for absorption coefficients of hydrocarbons and other molecules. During the course of our work we had to determine some absorption coefficients which are given in Table 1. Data at $L(\alpha)$ and the O-lines are needed for the proper consideration of molecule absorption at the atomic resonance lines. Other wavelengths were checked in order to find absorption bands of molecules undisturbed by conceivable reaction products. In the cases of N_2O , C_2H_4 , C_2H_2 we found the reported wavelengths in Table 1 at which little or no contributions of reaction products could be observed. We assume that short lived intermediates never reach such a concentration which may be the cause of an interference. This assumption is plausible but in practice sometimes difficult to verify.

Table 1
VUV-Absorption Coefficients in $10^{-17} \text{ cm}^2/\text{molecule}$
Shock-Tube-Measurements by P. Frank

λ	CH_4	C_2H_6	C_2H_4	C_2H_2	C_4H_2	N_2O	O_2	Lamp gas He+y%	Slit width in μ
$L(\alpha)$	2.0/1.9	2.9	2.9	7.3/3.6	2.7	0.5/1.1	a	1% H_2	80 ^b
O-tripl	1.8/1.5	2.8	n.m.	3.1/4.2	4.1	7.5	0.05	1% O_2	80
1282	n.m.	n.m.	n.m.	n.m.	n.m.	9.9	n.m.	2% CO_2	600
1560	0	0.09	2.2/2.2	0.41/0.45	n.m.	n.m.	n.m.	2% CO_2	80
1608	n.m.	<0.01	2.8/2.3	0.18/0.2 ^c	9.5 ^d	n.m.	n.m.	100% H_2	200

Single number: $T = 300 \text{ K}$; when two numbers are given corresponds the first number to $T = 300 \text{ K}$, the second number to $T = 1200\text{--}1700 \text{ K}$.

n.m.: no measurement

a: $7.1 \times 10^{-22} \times T - 6.3 \times 10^{-19}$ for $T: 1200 \text{ to } 2300 \text{ K}$

b: McPherson, Model: 225

c: slit width: 1000 μ d: slit width: 400 μ

The absorption coefficients are given within $\pm 15\%$ or better.

4. CHEMICAL KINETIC RESULTS

Not much has been published on chemical kinetics research using the combination of shock tube and vuv molecular band absorption. R.W. Patch (6) seems to have been the first who has performed such an experiment. He studied the H_2 -dissociation following the absorption of light around 1148 Å (Werner transition). Later Appleton et al (14) published results of the N_2 dissociation, by absorption of N_2 around 1176 Å. A fairly strong absorption band around 1608 Å of C_2H_4 has been exploited by Just et al (9) to investigate directly the total decomposition of C_2H_4 .

Recently the vuv method became more attractive, since Myerson and Watt (1) have demonstrated convincingly the advantages of the ARAS technique in combination with a shock tube.

The much more sensitive technique of atomic-resonance absorption, in particular for H and O atoms, allows the drastic reduction of the reactant gas-concentration. As it was already explained, the utilization of very small initial concentrations simplify markedly the chemical-kinetic interpretation of the experimental results. Under typical experimental conditions of the ARAS technique only primary decay steps and the following reaction of the formed atom and radical with the original molecule in many cases need to be considered. This was first demonstrated by Roth and Just (15) on the pyrolysis of methane at elevated temperatures above 1800 K. The ARAS method appears in particular very well suited for the study of elementary steps of normally complex reactions, as they occur in flames for example.

4.1. RESULTS ON PYROLYSIS OF MOLECULES. $L(\alpha)$ -SPECTROMETRY

The pioneer work of Myerson and coworkers on H_2 (1), O_2 (16) and NO (17) dissociation, the $H + O_2$ reaction (1) as well as the work of Appel and Appleton on D_2 dissociation and the $D + O_2$ reaction (2) will be only mentioned here. For $H + O_2$ and $D + O_2$ see also Chiang and Skinner (18). We will focus our attention on the more complex mechanism of the decay and reactions of polyatomic molecules.

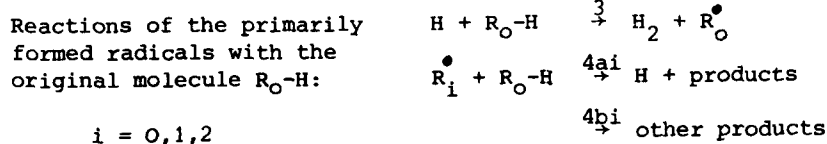
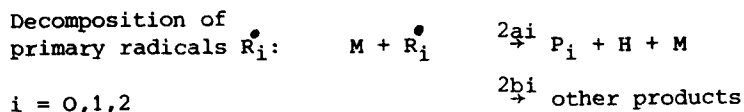
An extremely simple mechanism for the SO_2 decay could be verified by Rimpel and Just (8). At concentrations lower than 200 ppm of SO_2 oxygen atoms were formed only by $SO_2 + M \rightarrow SO + O + M$. All subsequent conceivable reactions turned out to be negligible under the specifically chosen experimental conditions.

At very low reactant concentrations on the order of a few ppm we may in most cases neglect the bimolecular reactions of the original molecule with itself. For example, in $L(\alpha)$ experiments, $2C_2H_2 \rightarrow C_4H_2 + H$ and similar reactions become unimportant as H-producing steps (22).

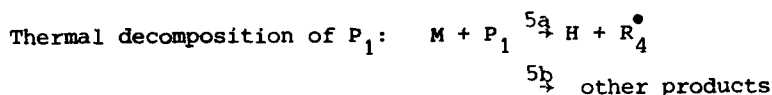
We present for the following discussion a general mechanism, which is typical for a large number of pyrolysis reactions under the conditions of an ARAS experiment. We specify this for the sake of clarity for the decay of a hydrogen containing molecule. R_0-H is the original molecule, P_1 is a stable product, R_1 is a molecular radical. M is an unspecified, nonreactive collisional partner in decay or recombination reactions.



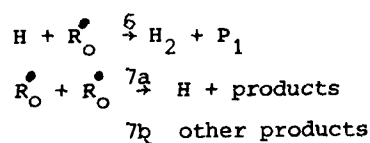
II) Immediate subsequent reactions:



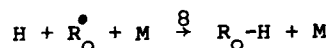
III) Reactions which often can be neglected, or which contribute only at later stages of the reaction:



Radical-radical reactions like:



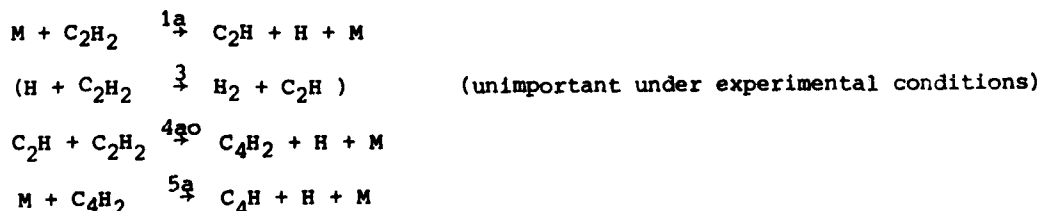
Recombination reactions like:



The general scheme of reactions 1 to 5 describes with excellent approximation the first reaction steps of the following systems:

HCN (19); NH_3 (20, 21); CH_4 (15); CD_4 (18); C_2H_2 (22); C_2H_4 (9); C_4H_2 (22); H_2CO (23); CH_3 (33, 23, and this text).

All these systems have no reaction channel 1c and consequently reactions of R_O-H with R_1^\bullet and R_2^\bullet ($4a_1$, $4a_2$, $4b_1$, $4b_2$) do not appear. In all cases it was possible to find experimental conditions under which only steps 1a and eventually 1b (C_2H_4 ; H_2CO) were dominant through the first 100 or 200 μ secs. At later reaction times and moderate temperatures mainly 3 or 4a with R_O^\bullet were found to contribute to some extent to the H-atom profile, so that these reactions could be additionally determined. Generally at high temperatures an increasing influence of 5a or 6 and 7a could be observed. The systems C_2H_2 and CH_4 are given here as examples:



At temperatures above 2200 K we could interpret the measured H-atom profile only, when reaction 5a was incorporated in the reaction scheme (22). A marked acceleration of the H-atom production through 4a0 could also unambiguously be shown by us (22). For CH_4 (15) we observed in later stages of the reaction at temperatures above 2000 K contributions of reactions 2a0:

$\text{CH}_3 + \text{M} \rightarrow \text{CH}_2 + \text{H} + \text{M}$ and reactions of type 6: $\text{H} + \text{CH}_3 \rightarrow \text{H}_2 + \text{CH}_2$ as well as

7a,b: $2\text{CH}_3 \xrightarrow{\text{a}} \text{C}_2\text{H}_5 + \text{H}$

$\xrightarrow{\text{b}} \text{C}_2\text{H}_4 + \text{H}_2$

However, these reactions may better be studied under specifically selected conditions. See below.

Examples for a strong contribution of 1b additionally to 1a are C_2H_4 and H_2CO . At very low initial concentrations the time dependent profile of the H-atom concentration is practically governed by the combined action of channels a and b. An instructive example is given in Fig. 3, where it is demonstrated that the consumption of H_2CO by channel 1b reduces the formation of $\text{H}(t)$ considerably.

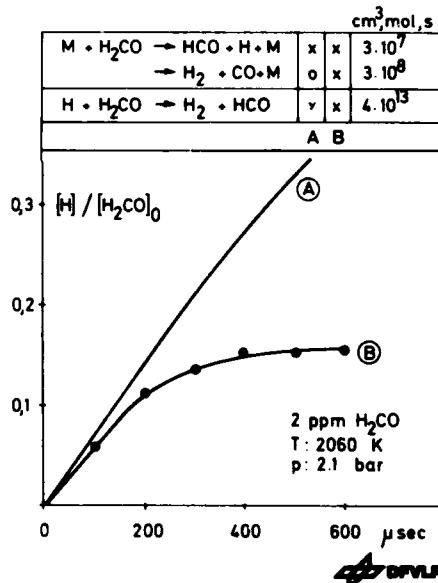
Fig. 3. Decay of formaldehyde.

x: channel is open

o: channel is closed

(A) was calculated without the H_2+CO channel, (B) includes it. HCO decomposes very fast under the experimental conditions.

● measurements.



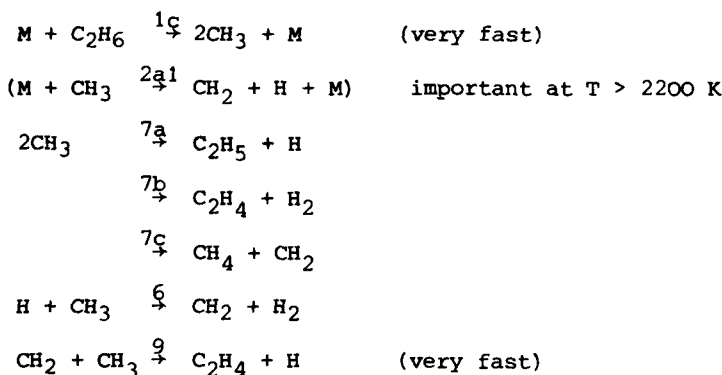
Chiang and Skinner have recently published data on the decomposition of C_3H_8 and C_3D_8 (24). At low concentrations the H-atom profile was solely determined by 1c and 2a2:

$(\text{M}) + \text{C}_3\text{H}_8 \xrightarrow{1\text{c}} \text{CH}_3 + \text{C}_2\text{H}_5 + (\text{M})$ and $\text{C}_2\text{H}_5 \xrightarrow{2\text{a2}} \text{C}_2\text{H}_4 + \text{H}$. Since C_2H_5 -decomposes very fast in the time scale of this experiment, the H-atom profile gives the rate of 1c. As to be expected, 1c was found not far from the high pressure limit, therefore M has been written in brackets.

Now the fairly complex reactions of CH_3 will be discussed a little more in detail, because the potential and the limits of the $\text{L}(\alpha)$ -technique can be demonstrated investigating these reactions.

According to the work of Glänzer et al (25) C_2H_6 decomposition may serve as a fast and clean source of CH_3 radical production at temperatures above about 1800 K. It is easy to predict the decomposition of CH_3 near the low pressure limit, when for example the theory of unimolecular decay for the case of weak collisions is applied. The most useful version was presented by Troe (30). It was calculated that at temperatures lower than about 2200 K and initial concentrations of 1 to 3 ppm C_2H_6 practically no H-atom production should be observed in our apparatus. This was later confirmed by H-atom measurements of the CH_3 decay at very low initial CH_3 concentrations (2 to 4 ppm) and temperatures above 2400 K. (33, 22).

Experiments (26) done between 1800 K and 2200 K showed a fast, and within 400 to 600 μ sec, linearly with the time increasing H-atom production. Further, it was found that the H-atom production rate depended to the square on the initial concentration of CH_3 . This led Roth and Just (26) to the following principle reaction scheme:



The linear increase of H-atoms disregards immediately a mechanism based solely on 7c and 9, since in this case H is a secondary product and therefore dH/dt should start with zero around $t = 0$. Fig. 4. When assuming the back reaction $7c: CH_2 + CH_4 \rightarrow 2CH_3$ as a fast one with a rate coefficient on the order of $2 \times 10^{13} \text{ cm}^3/\text{mol}\cdot\text{sec}$ at 2000 K, then 7c cannot be faster than about $3 \times 10^{11} \text{ cm}^3/\text{mol}\cdot\text{sec}$ at 2000 K. We may compare 7c with a similar H-atom transfer reaction: $O + CH_4 \rightarrow OH + CH_3$, which has around 2000 K an activation energy of about 14 kcal/mol. Then we estimate with $k_{7c} \approx 6 \times 10^{14} \exp(-7000/T)$ and with the help of thermodynamics a value for $k_{7c} \approx 3.5 \times 10^{13} \exp(-9680/T)$. Fig. 4 depicts measurements and some model calculations.

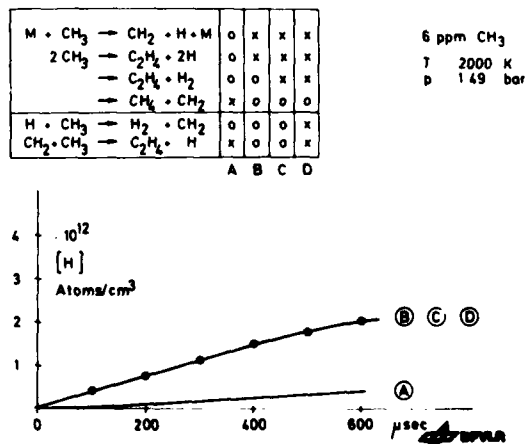
Fig. 4. Reactions of the CH_3 -radical.

x : channel is open

o : channel is closed

$2CH_3 \rightarrow C_2H_5 + H$ with fast decay of C_2H_5 determines the H-atom production. (B)

● measurements.

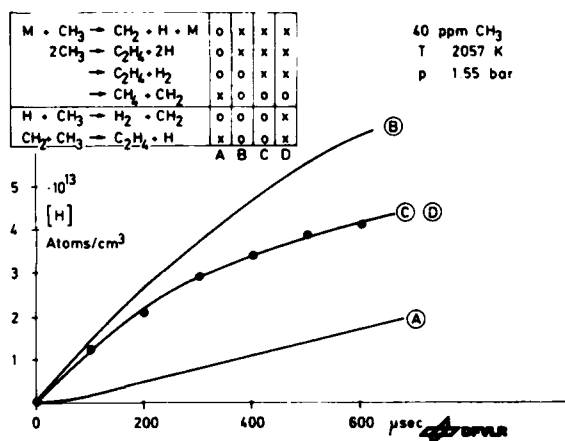


The calculated H-atom profile (A) with reactions 7c and 9 looks rather different from the measured one. Even when increasing the estimated values k_{7c} , k_{9c} by a factor 3 the agreement becomes not better. The main channel for H-atom production must be channel 7a with a fast further decomposition of C_2H_5 into C_2H_4 and H. Channel 7a gives a linear increase of H with time (B). Inserting reactions 6 and 9 in the computer scheme has practically no effect, the same is true for reaction 7b. 9 was measured at room temperature by Laufer and Bass (28), 6 can be estimated according to the similar reaction $H + CH_4$. 7b was approximately measured by Tsuboi (29). Due to the low initial concentration of CH_3 , the additional reactions, 7b, 6, 9 have practically no effect. The computed curve (C) is indistinguishable from (B) in Fig. 4. Results for 7a at low CH_3 concentrations were published by Roth and Just (26).

The situation changes drastically when experiments at higher initial CH_3 levels are performed. Fig. 5 shows an experiment with 40 ppm initial CH_3 .

Fig. 5. Reactions of the CH_3 -radical.

x: channel is open
o: channel is closed
Strong influence of $2CH_3 \rightarrow C_2H_4 + H_2$ can be recognized. (C)
• measurements



Again the mechanism 7c, 9 fails completely to describe the experimental results. When using only rate coefficient 7a, which has been obtained in (26) for low CH_3 -concentrations, for simulating the measured H-profile, curve (B) is calculated. The overshoot demonstrates clearly that for a proper fit of the experimental points some other CH_3 consuming mechanism, which does not produce H-atoms must be active. Inserting a coefficient for 7b, not much different from Tsubois value, results again in a perfect fit of the measured points (C). Thus it was in this case possible to conclude independently from a separate measurement of the CH_3 profile that channel 7b must be open and contributes under these conditions considerably. Finally we are left with the possible contributions of 6 and 9.

It is reasonable to assume that the rate coefficient for 9 would be on the same order at 2000 K as it was found by (28) at 300 K. We assumed for 2000 K $k_9 = 6 \cdot 10^{13}$ which is the value given in (28). k_6 can now be scaled such that in combination with k_9 again the fit with the experiments is perfect. This led us at 2057 K to a value for k_6 of $2.2 \times 10^{13} \text{ cm}^3/\text{mol} \cdot \text{sec}$. We have evaluated experiments with 6 and 40 ppm initial CH_3 concentration between 1850 and 2340 K. All experiments could be simulated with a fairly good fit by the following rate coefficients (units: $\text{cm}^3, \text{mol}, \text{K}$):

$$k_{7a} = 8 \times 10^{14} \exp(-13400/T) \text{ (26)}; k_{7b} = 2.1 \times 10^{14} \exp(-9690/T); k_9 = 6 \times 10^{13} \text{ (28)};$$

$$k_6 = 9 \times 10^{13} \exp(-7600/T); k_{2a} = 6.1 \times 10^{15} \exp(-44910/T) \text{ (23)};$$

$$k_{7c} < 6 \text{ to } 7 \times 10^{11}.$$

The sum of $k_{7a} + k_{7b}$ was measured by Tsuboi (29). Extrapolation to the temperatures which he used, gave maximal deviations on the order of a factor of 1.3 at the upper end of his temperature interval ($T = 2000$ K). The data given here for k_{7b} , k_6 are preliminary values because we have not yet finished our investigation, but the absolute values are very probably correct within less than a factor of 1.5 to 2 in the investigated temperature range.

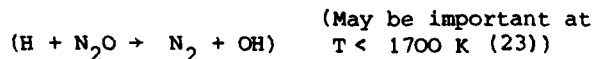
The limits of the ARAS technique are obvious in this example. The channel 7b could be only determined indirectly by changing the initial concentration of CH_3 . Conclusions on 7b would become more reliable, when direct measurements of the CH_3 profile under the same conditions were possible. Tsubois (29) CH_3 measurements, although performed at higher concentrations and lower temperatures, gave us more confidence for our conclusions on 7b. Our model, together with C_2H_6 decomposition, seems to predict his results fairly well.

4.2. EXPERIMENTS WITH ABSORPTION AT $L(\alpha)$ AND THE O-TRIPLET HYDROCARBONS + O.

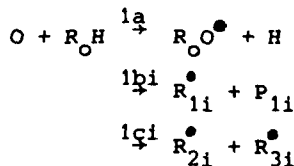
Shock heated N_2O may serve as a fast and clean source of O atoms above about 1500 K. Since $O + N_2O \rightarrow$ products is a slow reaction, we expect under the typical conditions of ARAS experiments with $N_2O < 100$ ppm no interference. However, when H-atoms are formed some influence of $H + N_2O \rightarrow N_2 + OH$ at low temperatures becomes noticeable (23). Roth and Just (27) were the first to use N_2O as a source for O atoms in an ARAS experiment to study a more complex hydrocarbon - O atom reaction. They investigated the reaction: $O + CH_4 \rightarrow CH_3 + OH$. The interpretation of the measured O and H-profiles was straight forward, since only one reaction channel for $O + CH_4$ is to be expected.

The great advantage of the ARAS technique with double measurements of H and O profiles became apparent, when reactions were investigated, which showed a multichannel behaviour of $O +$ hydrocarbon. Again a simple general reaction scheme can be used to facilitate the discussion. Most experiments were performed with $N_2O \approx$ hydrocarbon, or an excess of the hydrocarbon over N_2O . This ensures that in most cases during the first 100 to 200 usecs mainly contributions of $O + R_H$ determine the O and the H-profiles. When $O > R_H$ is chosen, a faster increasing contribution from secondary reactions will be observed.

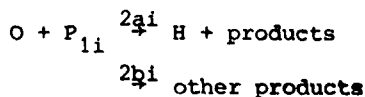
O production:



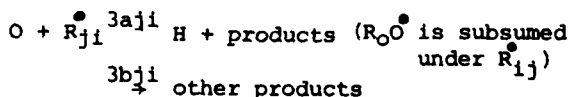
I) Primary attack of
O-atoms :



II) Secondary reactions
with O :



$j = 0, 1, 2, 3$



III) Additional reactions like the thermal decay of R_O-H , P_{11} , R_O^{\bullet} , the reactions of H_2O , molecular radicals R_O^{\bullet} , R_{ji}^{\bullet} with R_O-H etc. have occasionally to be taken into account.

In many cases we will have a multichannel type of reaction 1 to expect. This implies through the multiple secondary reactions 2 and 3 a considerable increase of reaction paths with increasing reaction time. This could make the proper interpretation of the measured H and O profiles in particular for longer reaction times extremely difficult. Therefore experiments must be designed so that the main contribution to the H and O atom profiles is to be expected from reactions 1 and only little from 2 and 3. Extensive computer studies are often unavoidable prior to performing such experiments.

Simple interpretation of experiments was possible with $O + CH_3$ (23). In this case a good fit was obtained assuming only channel 1b: $O + CH_3 \rightarrow H_2CO + H$ to be open. Secondary reactions of type 2a: $O + H_2CO$ and decay of H_2CO had relative little effect on the O and H-atom profiles.

The double measurements of H and O-atom profiles gave interesting results for two recently investigated systems. Roth and coworkers studied $O + HCN$ (31) and $O + C_2H_2$ (32). In both cases one expects a multichannel type of reaction 1. This was confirmed by the comparison of O-atom consumption and H-atom production. In both cases in the early stages of the reaction more O was consumed than H produced. Further, the observed H-atom profile was typical for a direct formation through a reaction of type 1a. Roth and coworkers were able to evaluate rate coefficients for: $O + HCN \xrightarrow{1a} OCN + H$ and the sum for reactions of type 1b and 1c as well as $O + C_2H_2 \xrightarrow{1a} HC_2O + H$ and again the sum of types 1b and 1c. In the latter case Roth et al have assumed that the sum is mainly determined by 1b: $O + C_2H_2 \rightarrow CO + CH_2$ which is known from other experiments. Since CH_2 undergoes fast reactions with O, the computer modeling of the O-atom profiles required the inclusion of reactions of type 3. It was found that a reaction without forming H-atoms gave the best fit in particular for the later parts of the H-atom profiles. Thus it may be that $CH_2 + O$ gives under the experimental conditions mainly products like $CH + OH$ or perhaps $CO + H_2$, and produces only to a smaller percentage H-atoms via $HCO + H$.

4.3. HYDROCARBONS + O_2

Of course, it is possible to investigate reactions with hydrocarbons and O_2 at elevated temperatures behind shocks with the ARAS technique following H- and O-atom profiles. The discussion of the results becomes relatively difficult, since here we can study only secondary reactions, except, when the O_2 -hydrocarbon reaction by chance is a fast one. Very strong influence of $H + O_2 \rightarrow OH + O$ has to be considered (18, 23). Results for $CH_4 + O_2$ (18) and $CH_3 + O_2$ (23) were reported. Some inconsistencies concerning $CH_3 + OH$ were found (23). They are mainly caused by the very complex reaction system CH_3-O_2 . A better designed experiment, starting for example with CH_3OH will probably clarify the problems with $CH_3 + OH$. They are discussed to some extent by Bhaskaran et al in Reference 23.

ACKNOWLEDGEMENT: I thank my colleagues P. Frank, G. Limpel, P. Roth and K. Bhaskaran for many helpful and stimulating discussions on the topics presented in this paper.

REFERENCES

1. A.L. Myerson and W.S. Watt, *J. Chem. Phys.* 49, 425 (1968).
2. D. Appel and J.P. Appleton, 15th Symp. on Combustion (Int.'l), The Combustion Institute, Pittsburgh, 1975, p. 701.
3. Th. Just in: *Shock Waves in Chemistry*, Edited by A. Lifshitz. Marcel Dekker Inc., New York, 1981, p. 279.
4. A. Lifshitz, G.B. Skinner and D.R. Wood, *J. Chem. Phys.* 70, 5607 (1979) and *Rev. Sci. Instrum.* 49, 1322 (1978).
5. C.Ch. Chiang, A. Lifshitz, G.B. Skinner and D.R. Wood, *J. Chem. Phys.* 70, 5614 (1979).
6. R.W. Patch, *J. Chem. Phys.* 36, 1919 (1961).
7. J.P. Appleton, *J. Chem. Phys.* 47, 3231 (1967).
8. G. Rimpel, Th. Just, *Proc. 11th Int. Symp. Shock Tubes and Waves*. p. 226. Seattle, July 11-14, 1977, Univ. of Washington Press, Seattle and London.
9. Th. Just, P. Roth and R. Damm, 16th Symp. on Combustion (Int'l). The Comb. Institute, Pittsburgh 1977, p. 961.
10. E.A. Sutton, *J. Chem. Phys.* 36, 2923 (1962).
11. H.A. Olschewski, J. Troe and H. Gg. Wagner, *Ber. Bunsenges. Phys. Chem.* 70, 450 (1966)
12. P. Roth, Th. Just, *Ber. Bunsenges. Phys. Chem.* 81, 572 (1977).
13. E.D. Schultz, A.C. Holland and F.F. Marmo, GCA Technical Report 62-15-N (1963)
- R.D. Hudson *NSRDS-NBS* 38 (1971)
- G.M. Mount, E.S. Warden and K.W. Moos, *Astrophys. J.* 214, 47 (1977) (CH_4)
- G.M. Mount, H.W. Moos, *Astrophys. J.* 224, 35 (1978). (C_2H_6)
14. J.P. Appleton, M. Steinberg and D.J. Liquornik, *J. Chem. Phys.* 48, 599 (1968)
15. P. Roth, Th. Just, *Ber. Bunsenges. Phys. Chem.* 79, 682 (1975).
16. W.S. Watt, A.L. Myerson, *J. Chem. Phys.* 51, 1638 (1969).
17. A.L. Myerson, 14th Symp. on Comb. (Int'l). The Comb. Institute Pittsburgh, 1973, p. 219.
18. C.Ch. Chiang, G.B. Skinner, *Proc. 12th International Symp. on Shock Tubes and Waves*. p. 629, Jerusalem, 1980, The Magnes Press, The Hebrew University.
19. P. Roth, Th. Just, *Ber. Bunsenges. Phys. Chem.* 80, 171 (1976).
20. M. Yumura, T. ASABA, Y. Matsumoto and H. Matsumi, *Int. J. Chem. Kin.* 12, 439 (1980).

21. M. Yumara, T. Asaba, 18th Symp. on Comb. (Int'l). The Comb. Institute, Pittsburgh (1981), to be published.
22. P. Frank, Th. Just, Comb. Flame 38, 231 (1980).
23. K.A. Bhaskaran, P. Frank, Th. Just, Proc. 12th International Symp. on Shock Tubes and Waves. p. 503, Jerusalem, 1980, The Magnes Press, The Hebrew University.
24. C.Ch. Chiang, G.B. Skinner, 18th Symp. on Comb. (Int'l), The Combustion Institute, Pittsburgh (1981), to be published.
25. K. Glänzer, M. Quack and J. Troe, Chem. Phys. Lett. 39, 304 (1976).
26. P. Roth, Th. Just, Ber. Bunsenges. Phys. Chem. 83, 577 (1979).
27. P. Roth, Th. Just, Ber. Bunsenges. Phys. Chem. 81, 572 (1977).
28. A.H. Laufer, A.M. Bass, J. Phys. Chem. 79, 1635 (1975).
29. T. Tsuboi, Japan. J. Appl. Phys. 17, 709 (1978).
30. J. Troe, J. Phys. Chem. 83, 114 (1979).
31. P. Roth, R. Löhr, H.D. Hermanns, Ber. Bunsenges. Phys. Chem. 84, 835 (1980), see also this book.
32. R. Löhr, P. Roth, Ber. Bunsenges. Phys. Chem. 85, 153 (1981), see also this book.
33. P. Roth, U. Barner, R. Löhr, Ber. Bunsenges. Phys. Chem. 83, 929 (1979).
and:
Proc. 12th International Symp. on Shock Tubes and Waves. p. 621,
Jerusalem 1979, The Magnes Press, The Hebrew University.

AD P000227

BLAST WAVES GENERATED BY ACCIDENTAL EXPLOSIONS

Roger A. Strehlow

Aeronautical and Astronautical Engineering Department
University of Illinois at Urbana-Champaign, Urbana, IL 61801

As a basis for the discussion of the blast waves produced by accidental explosions the structure of the blast wave from an ideal explosion and the mechanisms by which such a blast wave produces damage will be discussed. Next, some general results concerning the manner in which nonideal source behavior produces nonideality of the blast wave will be presented with examples. Finally, accidental explosions will be grouped into nine different types depending upon the nature of the source behavior during the explosion and the events that lead up to the explosion. The nature of the blast wave produced by each of the different types of accidental explosions will then be discussed with examples as appropriate to illustrate how the mechanisms involved in accidental explosions affect the blast waves produced by these explosions.

INTRODUCTION

In the past 10 to 15 years there has been a considerable increase of interest in accidental explosions of all types and the hazards they pose to structures and people in their immediate vicinity (1). This increased interest has led to a considerable amount of activity to characterize the nature of the various accidental explosion processes that can occur and the danger associated with internal explosions, the production of primary and secondary fragments, radiation damage from a fireball and last, but not least, the blast wave produced by the explosion (2). This paper will focus on our current understanding of source behaviors that lead to nonideal blast waves as well as the nature of the blast waves produced by various types of accidental explosions.

IDEAL BLAST WAVES

All free field blast waves whether ideal or not are simple waves traveling away from the source region. Point source, nuclear or bare charge spherical high explosive explosions all produce blast waves which have essentially the same structure at distances from the source where the maximum pressure in the wave is less than about 100 atmospheres (3). These "ideal" waves consist of a lead shock wave followed by a rarefaction fan which causes the pressure to fall slightly below the ambient pressure before it rebounds to the initial atmospheric pressure. Since the wave is simple the

flow associated with the wave is uniquely related to the local pressure in the wave. Specifically, the flow is outward when the pressure is higher than ambient and inward when the pressure drops below ambient.

The three properties of an ideal wave which cause damage are the maximum overpressure, the positive impulse I_+ where $I_+ = \int P dt$ from the time when the shock arrives until the pressure first returns to ambient and the flow velocity associated with the wave (2). Sachs (4) showed theoretically and it has been verified experimentally (5) that the first two of these three properties scale to an energy scaled radius. Specifically, at any distance from the source, R , the quantities $\bar{P} = (P_s - P_0)/P_0$ and $\bar{I} = (I_+ a_0)/(E^{1/3} P_0^{2/3})$ scale to \bar{R} where $\bar{R} = R/R_0$ and $R_0 = (E/P_0)^{1/3}$. Here E is the total energy of the source and P_0 is the local atmospheric pressure.

The mechanism by which a structure is damaged by a blast wave is different for each of the three properties described above. If the duration is very long compared to the response time of the structure, the structural elements are deflected to about twice the extent that they would be if the pressure (now a reflected shock pressure) were applied statically. In this case the strain energy in the structure can be equated to the potential energy stored by the deflection and damage occurs when this amount of energy is sufficient to cause plastic flow and therefore permanent deformation. If the duration is very short relative to the characteristic response time of the structure, the impulse of the wave determines the amount of kinetic energy imparted to the structural elements and this kinetic energy can be equated to the strain energy that will ultimately be stored in these elements. In this impulsive limit the overpressure in the shock has no effect on damage (6).

The third damage mechanism is related to a drag force which first arises because it takes a finite amount of time for the shock wave to reflect, refract and engulf the body and then continues because the body is immersed in a high velocity flow field. Structures that are particularly vulnerable to this type of damage are light standards or unattached bodies like trucks or people. In the latter case, damage is caused by tumbling or gross displacement (2).

NON-IDEAL BLAST WAVES

Most accidental explosions generate a blast wave whose structure is different from the structure of an ideal blast wave. Theoretical, numerical, and experimental work has shown that the differences are directly related to the way that energy is added to or initially distributed in the source region. To illustrate the differences three example spherical source regions will be considered. These are an idealized bursting sphere, the ramp addition of energy (representing a spark) and spherical deflagrative and detonative addition of energy. Additionally, there will be a brief discussion of the effects of non-spherical deflagration in a source region.

The burst of a pressurized frangible sphere containing an ideal polytropic gas has been studied numerically (7) and experimentally (8). All the numerical calculations described here (including that for bursting spheres) used a one dimensional finite difference artificial viscosity computer program in spherical coordinates to follow the flow associated with specific source behaviors (9). For the bursting sphere studies the calculation was started with the source region at a series of high pressures and different temperatures. It was found that when the energy in the sphere was calculated using Brode's (10) formula, $E = (P_s - P_0) V / (\gamma - 1)$, where V is the sphere volume and γ is the heat capacity ratio of the polytropic gas in the sphere, the sphere bursts produced a blast wave whose pressure was never larger than

that calculated using the shock tube bursting pressure equation and decreased monotonically as the shock propagated away from the source. Furthermore, for high pressure sphere bursts the shock pressure asymptotically approached the energy scaled overpressure curve for a high explosive charge. However, for sphere pressures less than about $6 P_0$, the shock overpressure curves did not reach but paralleled the high explosive curve. In other words, far field equivalency in overpressure was lost.

Two other general behaviors of the blast wave from a bursting sphere are 1) positive phase impulse always scales with source energy using Sachs' scaling (this is generally true for all spherical non-ideal explosions) and 2) the negative phase impulse for spheres with low energy density (i.e., with internal pressures below about 100 atmospheres) is always very large when compared to the negative phase for an ideal blast wave. It is in fact more than one half of the positive phase impulse. Furthermore, this negative phase is followed by a relatively strong shock wave whose amplitude is approximately $1/3$ of the amplitude of the initial shock in the blast wave. This is illustrated in Figure 1 which is experimental data obtained from a bursting frangible sphere. A complete set of pressure distance curves for a number of equally spaced times after sphere burst is shown in Figure 2. Notice from Figure 2 the large rarefaction fan propagating to the center, the very large pressure spike produced at the center, and the second shock propagating away from the center. Brode and Chou et al (11) showed many years ago that an extended source such as a bursting sphere exhibits this behavior.

It was also observed that the dimensionless overpressure-scaled distance curves for the different initial sphere conditions paralleled each other when plotted against \bar{R} . Furthermore, dimensional analysis showed (8) that for idealized sphere bursts one must know the sphere source energy, E , the sphere pressure, P_s/P_0 , the internal velocity of sound of the gas in the sphere relative to that of the surroundings, a_s/a_0 , and the heat capacity ratio, γ , of the gas in the sphere to uniquely determine the initial shock pressure and sphere radius on a (\bar{P}, \bar{R}) plot. With this information the (\bar{P}, \bar{R}) nomograph that has been constructed can be used to determine the blast wave overpressure produced by any idealized bursting sphere (7).

Numerical calculations have been performed to study the ramp addition of energy (12). In this case, energy is added in a spatially uniform manner to the entire source region at a rate which is growing exponentially with time until the maximum amount of energy is added. Figure 3 shows that in this case a compression wave is first generated which steepens into a shock wave some distance from the source. Figure 3 also shows the effect of finite source size, because it clearly shows the rarefaction fan propagating towards the center of the source region as energy is being added to the source region. A systematic study of the effect of energy density (defined at $E/C_v T_0$) and dimensionless time of energy addition (defined as a characteristic time for energy addition divided by a characteristic acoustic transit time for the source region, $t_a = r_0/a_0$ where r_0 is the initial radius of the source region and a_0 is the initial velocity of sound in the source region) was performed. This showed that, irrespective of the nonideal behavior of the blast wave close to the source region, source regions which had both a high energy density and a very short dimensionless rate of heat addition exhibited far field equivalency in overpressure and produced a blast wave which was indistinguishable from that produced by an ideal source. However, when energy density dropped to about 8 or 9, and dimensionless rate of energy addition increased to about unity, far field equivalency in overpressure was lost. In other words, the overpressure scaled distance curves were all below those of an ideal explosion with the same total source energy. As in the case of bursting sphere the far field positive impulse was equivalent to that

of an ideal wave on an energy scaled basis.

Numerical (13) and experimental (14) studies have been performed on the blast wave propagating away from a centrally ignited deflagrative or detonative explosion of a gas mixture initially at ambient pressure (15). The calculations have shown that at a radius of about three times the actual combustible sphere radius, the blast wave becomes equivalent to that produced by an ideal explosion, if the initial explosion is centrally ignited and is either detonative or deflagrative with a normal burning velocity of more than approximately 1/8th of the initial velocity of sound. These calculations also show that when the burning velocity drops to approximately 1/16th of the initial velocity of sound, far field overpressure equivalency is lost and the blast wave no longer contains a lead shock wave but instead consists of a simple compression wave propagating away from the source region. This is shown in Figure 4. For lower burning velocities than this, the overpressure in the wave is extremely low and can be modeled by using an adaption of Taylor's (16) original analytical solution for the blast wave produced by a sphere expanding at constant velocity. This behavior is shown in Figure 5.

The blast wave produced by low velocity deflagrative combustion of a non-spherical source has also been studied (17). In this case the acoustic principle first enunciated by Stokes (18) in 1849 has been applied by assuming that the deflagrative combustion can be treated as a monopole source of very low frequency.

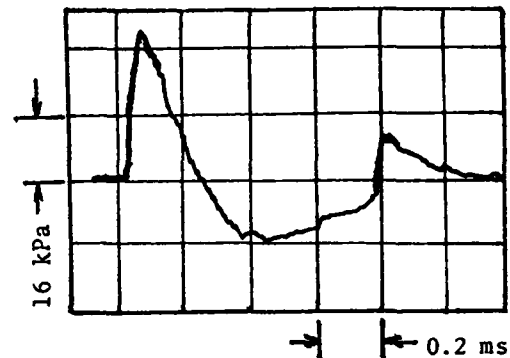


Figure 1

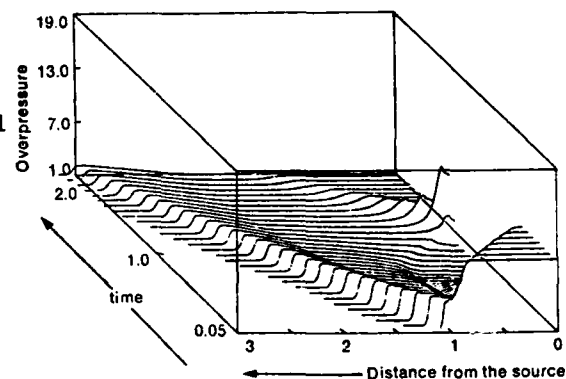


Figure 2

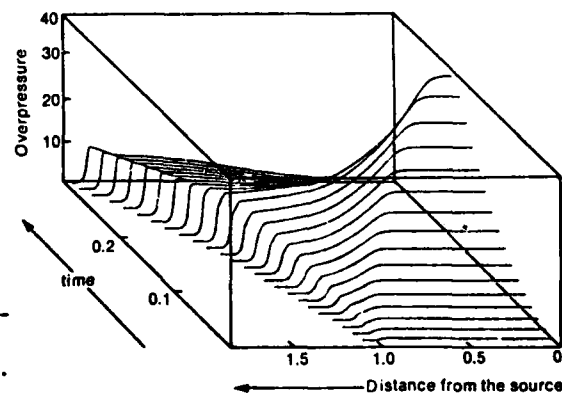


Figure 3

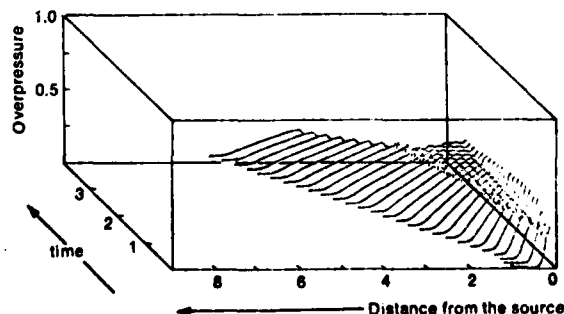


Figure 4

NOTE: Figure captions are at the end of the paper.

When this is done, one finds that the maximum overpressure that one can obtain from deflagrative combustion is a function of the aspect ratio of the source region and decreases very rapidly with increases in aspect ratio. This is shown in Figure 6. This theoretical observation has been verified by experimental studies in which combustion of a spherical soap bubble was initiated near the edge (19). In this case, the acoustic overpressure was considerably lower than the acoustic overpressure when the soap bubble was initiated centrally. The reason why this is true is that in spherical coordinates the maximum overpressure occurs when the product of the burning velocity and flame area exhibit the maximum rate of increase. The theory yields the conclusion that no overpressure is generated in spherical coordinates by a flame of constant area which has a constant burning velocity.

ACCIDENTAL EXPLOSIONS

When accidental explosions are classified by source behavior, one finds that there are nine major types that can occur (1). These are:

1. condensed phase detonations.
2. combustion explosions of gaseous or liquid fuels in enclosures.
3. combustion explosions of dusts in enclosures.
4. boiling-liquid-expanding-vapor-explosions (BLEVEs).
5. unconfined vapor-cloud explosions.
6. explosions of pressurized vessels containing non-reactive gases.
7. explosions resulting from chemical reactor runaway.
8. physical vapor explosions.
9. explosions resulting from nuclear reactor runaway.

The blast waves that are generated by each of these different types of explosions are quite dependent on source behavior and therefore, are different from explosion to explosion. Some general statements can be made, however. In the following each type of explosion will be discussed separately.

Condensed phase detonations produce a blast which is nearly ideal based on the total energy that is available from the source region. If there is considerable confinement, one must take into account the energy impart to the confinement by the explosion and if the explosion occurs at ground level (most do), the energy involved in cratering must be included. Ground level

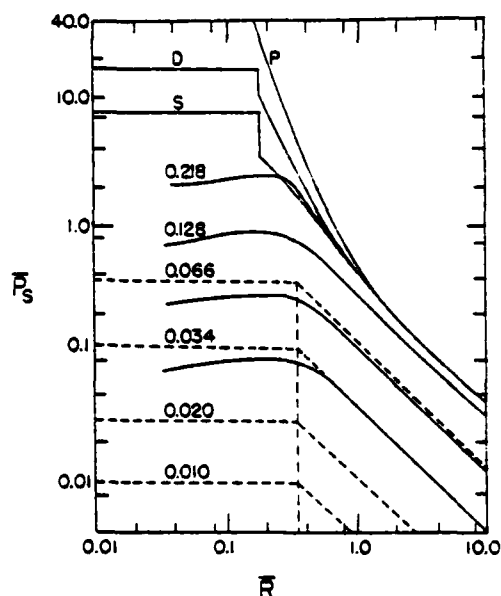


Figure 5

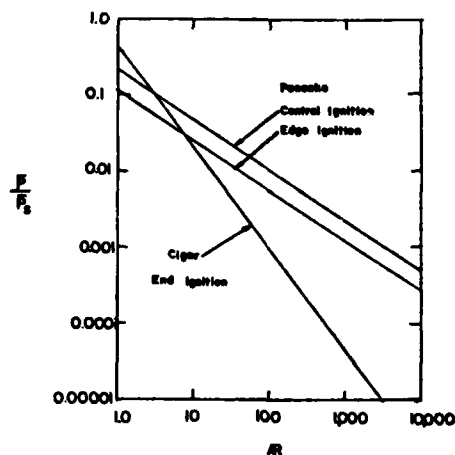


Figure 6

reflection with no cratering would cause the blast wave to appear as if the explosive energy were twice the actual amount of explosive involved. With cratering the usual multiplying factor is taken to be 1.8 (3).

Combustion explosions of gaseous or liquid fuels in enclosures show two distinct limit behaviors. If the enclosure has a low length to diameter ratio ($L/D \leq 6$) and if there are not too many obstacles in the path of the flame, the pressure rise in the enclosure will cause the enclosure to relieve itself at a relatively low overpressure. For example, buildings will fail at 2 to 3 psi overpressure whereas the explosion, if allowed to run its course, would generate at least 90 psi. Under these circumstances, the building is usually completely destroyed by the explosion but pieces are not thrown very far. Also because the source pressure never gets very high the blast wave is minimal. Generally speaking, people close to the source do not hear a blast wave in this case. They simply feel an impulsive flow of air as the explosion process displaces the atmosphere around the explosion source. In the other limit case, when the L/D is large, or when there are many obstacles in the path of the combustion wave, turbulent boundary layer growth and eddy shedding cause flame accelerations to occur which can lead to generation of pressure waves and shock waves in the enclosure. In severe cases the acceleration will be violent enough to actually cause the flame system to make a transition to detonation. In this limit case damage is localized but very severe. Fragments can be thrown large distances and the blast wave that is produced can be quite intense. These are, however, extended source volume explosions (i.e., they have a low energy density) and therefore the blast waves from this source always exhibit a strong negative phase. Because of this it is quite common to see negative phase damage on structures that are close to the source region, when this type of explosion occurs.

Combustion explosions of dusts in enclosures have the same L/D limit behaviors as a combustion explosion of vapors and gases in enclosures and the blast waves that are produced by such explosions are of the same type as those produced by explosions of gases or liquid fuels in enclosures. There is a difference, however, in the way that these explosions occur inside the enclosure. In order for a dust to form a combustible mixture in air, the extinction coefficient of the suspended dust relative to light transmission must be of the order of 30 cm. This is such a high concentration of airborne dust that it could not be tolerated on a continuous basis in the work place. Nevertheless, disastrous secondary explosions do occur in industries that handle organic or metal dusts. These always occur because the work place was allowed to become quite dirty and a primary explosion in a piece of equipment produces a large external fireball and air motion ahead of it which picks up the dust in the work place and propagates the explosion throughout the work place.

Boiling-liquid-expanding-vapor-explosions (BLEVEs) (20) occur when a ductile tank containing a flash evaporating liquid at high pressure is heated externally until the tank tears open. The blast wave in this case is usually not considered to be dangerous. It has been shown experimentally that a bulk quantity of flash evaporating liquid when suddenly exposed to atmospheric pressure evaporates so slowly that the evaporation process cannot contribute to the blast wave (21). Therefore in this case, the blast wave arises only from the vapor space above the liquid in the tank. In this case the maximum blast wave strength can be estimated if one knows the size of that vapor space and treats the explosion as a bursting sphere with the vapor space volume and initial pressure. The real danger in BLEVEs is 1) the flash evaporating liquid can cause rocketing of pieces of the tank to large distances and 2) if the contents of the tank are combustible and catch on fire immediately, a large fireball can be produced, which can injure and kill people by radiation and start new fires some distance from the original fire.

Unconfined vapor-cloud explosions occur when there is a massive release of a combustible hydrocarbon in the atmosphere with delayed ignition (22) (ignition delays from 15 seconds to 30 minutes are common with this type of accident). In this case a large cloud of combustible mixture of the fuel with air is formed and ignition can either lead to a very large fire or a very large fire plus an explosion which causes a damaging blast wave to form. There is mounting evidence that a damaging blast wave occurs only if the initial flame propagation process accelerates until either rapid volumetric combustion or some sort of supersonic combustion or possibly detonation occurs. Recently, it has been shown that one can produce transition to detonation without heating the combustible mixture to the autoignition temperature (23). All that is needed is a sufficiently large hot gas-cold gas mixing region in a flame jet. Furthermore, the acoustic theory for high aspect ratio source regions shows quite conclusively that deflagrative combustion as such cannot produce the damaging blast waves that have been observed as the result of vapor cloud explosions (17).

Explosion of pressurized vessels containing nonreactive gaseous materials produce blast waves which can be treated in a rather straightforward manner using the bursting sphere formulas that were discussed above. One can always assume in this case that the bursting sphere formula will yield the maximum overpressure that one could expect. This is because virtually all pressure vessels are made of ductile material and ductile vessels tear only slowly once failure starts. Thus the high pressure gas will be released at a slower rate than if the vessel were a frangible vessel. If the vessel is frangible there are ways to estimate kinetic energy imparted to the fragments and this energy should be subtracted from the total stored energy in the vessel to estimate the blast wave structure using the bursting sphere formulas described above.

Explosions resulting from chemical reactor runaway occur frequently in the chemical industry. They are due primarily to the fact that the exothermic reaction that is being carried out in the vessel occurs too rapidly either because too much catalyst has been added to the system or because the cooling system for the vessel fails. In either case, the pressure in the vessel rises rather rapidly and if the vessel is not adequately vented, the vessel explodes. In many cases these are ductile tears and the explosion can be assumed to be a BLEVE. In most cases the blast wave, as such, is not severe, but damage to the local environment is because of the fragments that are produced and the danger of a major fire following the explosion.

Physical vapor explosions occur when a hot liquid or solid contacts a cold liquid and causes very rapid vaporization of the cold liquid (24). These explosions occur in the steel and aluminum industry where water is the cold liquid and during the spill of liquid natural gas where water is the hot liquid. They can be quite severe. However, the blast wave that they generate is nonideal because of the extended size of the source region. There has been no experimental study of the structure of the blast wave produced by physical vapor explosions.

Explosions resulting from nuclear reactor runaway fortunately have not yet occurred. A nuclear reactor runaway cannot generate anything like a nuclear bomb detonation. However, it can pressurize the containment vessel to such a pressure that the vessel will burst, releasing its contents to the outside atmosphere. In this case, the discussion of the blast wave and the damage it produces would be moot because the release of long range radio-active material would represent a much more serious catastrophe.

SUMMARY AND CONCLUSIONS

It has been shown that high energy density and high power density sources

produce "ideal" blast waves whose structure is related only to the total energy of the source region. It has also been shown that low energy density or extended sources and sources in which the energy is added slowly produce non-ideal blast waves whose primary deviation from ideality is the lack of far field equivalency in overpressure. It has also been shown that these waves contain a large negative phase following the initial positive phase and that this negative phase is followed by a relatively strong second shock. Interestingly, both theory and experiment have shown that for a spherical source region, positive impulse is always predicted by simple energy scaling, irrespective of how nonideal the source behavior is.

Additionally, accidental explosions have been categorized into nine types, primarily based on the behaviors of the source regions during the explosion process itself. The nature of the blast wave produced by each of these nine types was discussed briefly.

It appears that we currently have sufficient information to either evaluate the potential explosion hazard of any specific situation or to evaluate the nature and course of the explosion after such an incident has occurred. Furthermore, since the principles of blast resistant design are now well understood, such design is being used more and more frequently in locations where the potential for an explosion exists.

It appears that the most important avenue for new research relative to the blast wave from accidental explosions is to study in some systematic manner the effect of the explosion of highly nonspherical source regions on the blast wave produced in the surroundings.

REFERENCES

1. Strehlow, R. A., *Am Scientist*, 68, 420-28 (1980).
2. Baker, W. E., Cox, P. A., Westine, P. S., Kulesz, J. J., and Strehlow, R. A., "A Short Course in Explosion Hazards Evaluation" Southwest Research Institute, San Antonio, Texas, (1979).
3. Baker, W. E., "Explosions in Air," Texas University Press, Austin, Texas (1973).
4. Sachs, R. G., "The Dependence of Blast on Ambient Pressure and Temperature" BRL Report 466, Aberdeen Proving Ground, Maryland (1944).
5. Dewey, J. M. and Sperrazza, J., "The Effect of Atmospheric Pressure and Temperature on Air Shock," BRL Report 721, Aberdeen Proving Ground, Maryland (1950).
6. Newmark, N. M., "An Engineering Approach to Blast Resistant Design," Proc ASCE 79 Separate No. 309 (1953).
7. Strehlow, R. A., and Ricker, R. E., *Loss Prevention* 10, 115-121, (1976).
8. Esparza, E. D. and Baker, W. E., "Measurement of Blast Waves From Bursting Pressurized Frangible Spheres," NASA CR-2843 (May 1977).
9. Oppenheim, A. K., private communication, Berkeley, California (1973).
10. Brode, H. L., *Phys. Fluids*, 2, 217 (1959).
11. Chou, P. C., Karpp, R. R. and Huang, S. L., *AIAA J*, 5, 618-23 (1967).
12. Adamczyk, A. A., "An Investigation of Blast Waves Generated from Non-Ideal Sources," Ph.D thesis, University of Illinois at Urbana-Champaign, (1975).
13. Strehlow, R. A., Luckritz, R. T., Adamczyk, A. A., and Shimpi, S. A., *Comb & Flame*, 35, 297-310 (1979).

14. Lind, D., Loss Prevention, 9, 101-105 (1975).
15. Lee, J. S., Guirao, C. M., Chin, K. W., and Bach, G. G., Loss Prevention, 11, 59-70 (1977).
16. Taylor, G. I., Proc. Roy. Soc., A 186, 273-92 (1946).
17. Strehlow, R. A., Loss Prevention, 14, 145-153 (1981).
18. Stokes, Phil Mag, XXXIV, Ser 3, 52 (1849).
19. Thomas, A. and Williams, G. T., Proc. Roy. Soc., A 294, 449-466 (1966).
20. Walls, W. L., Fire Journal, 72 (6), 46 (1978).
21. Esparza, E. D., and Baker, W. E., "Measurement of the Blast Waves from Bursting Frangible Spheres Pressurized with Flash-Evaporating Vapor or Liquid," NASA CR 2811 (Nov. 1977).
22. Strehlow, R. A., Fourteenth Symposium (International) on Combustion, The Combustion Institute, Pittsburgh, PA, 1189-1200 (1973).
23. Knystant, R., Lee, J. H., Moen, I. and Wagner, H. Gg., Seventeenth Symposium (International) on Combustion, The Combustion Institute, Pittsburgh, PA, 1235-1245, (1979).
24. Reid, R. C., Am Scientist, 64, 146-156 (1976).

Figure Captions

- Fig. 1 An oscilloscope trace of the free field blast wave from a bursting sphere containing air $P_s = 52.5$ Atm. $\bar{P} = 0.40$, $\bar{R} = 0.69$.
- Fig. 2 The blast wave produced by a sphere initially at 9 Atm. pressure.
- Fig. 3 The blast wave produced by the ramp addition of energy.
- Fig. 4 The blast wave produced by a centrally ignited low velocity flame.
- Fig. 5 Scaled overpressure, \bar{P} , versus energy scaled radius, \bar{R} , for detonation (curve D) bursting sphere (curve S) and various centrally ignited flames. Curve P is for Pentolite (ideal wave). Numbers given on the curves are the ratio S_u/a_0 where S_u is the assumed normal burning velocity and a_0 is the initial velocity of sound. The solid lines (except for Pentolite) are the result of numerical calculations. The dashed lines were obtained by using Taylor's analytical solution for an expanding sphere, suitably modified to replace the sphere by a propagating flame. Note the good agreement with theory at $S_u/a_0 = 0.066$ and 0.034 .
- Fig. 6 Effect of the aspect ratio, \mathcal{R} , on the maximum blast wave pressure rise for the deflagrative combustion of pancake and cigar-shaped clouds. Cloud volume, normal burning velocity and observer distance from cloud center are all assumed to be constant from cloud to cloud.

Part II: FACILITIES, TECHNIQUES AND EXPERIMENTS

000228



A SHOCK TUBE DRIVER WITH A "CYCLONE" SEPARATOR

* R.J. Stalker and ** R.P. French

* Department of Mechanical Engineering
University of Queensland, St. Lucia 4067, Australia

** Physics Department, Faculty of Science
Australian National University, Canberra 2600, Australia

An experimental investigation has been made of shock tube operation when the "Cyclone" principle is used to separate diaphragm fragments from the driver gas. For the free piston driver used in these tests, this involved a diaphragm configuration which allowed the driver gas to be injected into the shock tube at right angles to the axis, with a circumferential component of velocity. This greatly reduced the level of model and test section damage due to diaphragm fragments, and thereby extended the practical range of experiments which could be performed in the shock tube. In comparisons made with a conventional diaphragm configuration, it was found that shock speeds were reduced at low diaphragm pressure ratios, but were increased up to values of 16 km sec⁻¹ at high diaphragm pressure ratios. Analysis of pressure records after shock reflection showed that this was associated with entropy increases in the driver gas, arising from the nature of the diaphragm configuration, rather than with the "cyclone" effect. Further tests confirmed that satisfactory shock wave-contact surface separation was maintained, in spite of the circumferential motion of the driver gas. It is concluded that the cyclone effect can be used effectively without in itself significantly reducing the shock tube performance.

INTRODUCTION

Diaphragm fragmentation is a problem particularly related to shock tubes with high pressure drivers. If excessively large fragments are produced when the main diaphragm ruptures, and are projected down the shock tube at high velocities, they may inflict severe damage on models and associated equipment located in the test section.

Such a situation occurred in adapting the free piston reflected shock tunnel T3 at the Australian National University to non-reflected operation. The expansion nozzle was aligned along the shock tube axis and, with a shock tube 76 mm. in diameter and a nozzle entry diameter of 36 mm., it was found that very severe damage was sustained over a series of shots for any model or instrument located in the test section within 18 mm. of the nozzle axis. Whilst this did not constitute a fundamental limitation to use of the non-reflected shock tunnel, it made it difficult to conduct many desirable experiments involving models in the shock tube.

PRECEDING PAGE BLANK

AD-A122 200

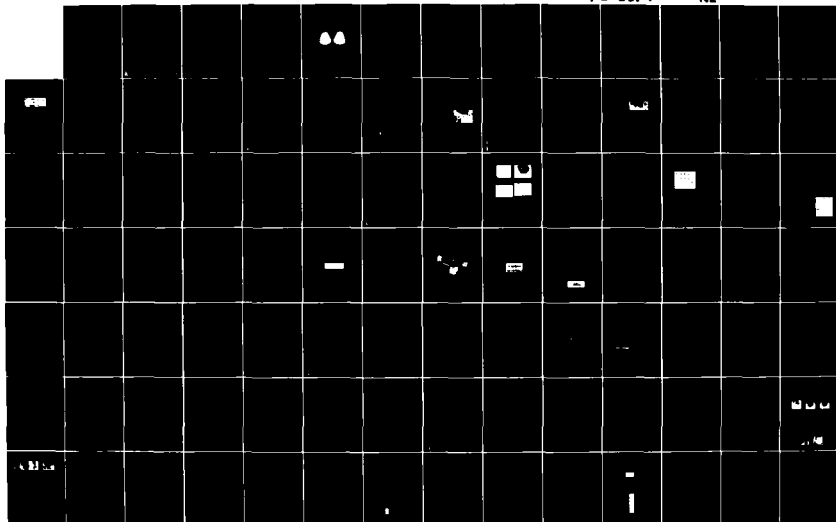
PROCEEDINGS OF THE INTERNATIONAL SYMPOSIUM ON SHOCK
TUBES AND WAVES (13TH. (U) CALSPAN ADVANCED TECHNOLOGY
CENTER BUFFALO NY C E TREANDR ET AL. JUL 81
AFOSR-TR-82-1031 F49620-81-C-0002

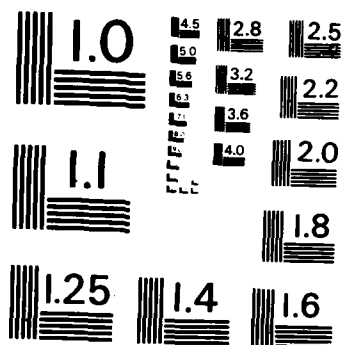
2/10

UNCLASSIFIED

F/G 20/1

NL





MICROCOPY RESOLUTION TEST CHART
NATIONAL BUREAU OF STANDARDS - 1963 - A

000228



A SHOCK TUBE DRIVER WITH A "CYCLONE" SEPARATOR

* R.J. Stalker and ** R.P. French

* Department of Mechanical Engineering
University of Queensland, St. Lucia 4067, Australia

** Physics Department, Faculty of Science
Australian National University, Canberra 2600, Australia

An experimental investigation has been made of shock tube operation when the "Cyclone" principle is used to separate diaphragm fragments from the driver gas. For the free piston driver used in these tests, this involved a diaphragm configuration which allowed the driver gas to be injected into the shock tube at right angles to the axis, with a circumferential component of velocity. This greatly reduced the level of model and test section damage due to diaphragm fragments, and thereby extended the practical range of experiments which could be performed in the shock tube. In comparisons made with a conventional diaphragm configuration, it was found that shock speeds were reduced at low diaphragm pressure ratios, but were increased up to values of 16 km sec⁻¹ at high diaphragm pressure ratios. Analysis of pressure records after shock reflection showed that this was associated with entropy increases in the driver gas, arising from the nature of the diaphragm configuration, rather than with the "cyclone" effect. Further tests confirmed that satisfactory shock wave-contact surface separation was maintained, in spite of the circumferential motion of the driver gas. It is concluded that the cyclone effect can be used effectively without in itself significantly reducing the shock tube performance.

INTRODUCTION

Diaphragm fragmentation is a problem particularly related to shock tubes with high pressure drivers. If excessively large fragments are produced when the main diaphragm ruptures, and are projected down the shock tube at high velocities, they may inflict severe damage on models and associated equipment located in the test section.

Such a situation occurred in adapting the free piston reflected shock tunnel T3 at the Australian National University to non-reflected operation. The expansion nozzle was aligned along the shock tube axis and, with a shock tube 76 mm. in diameter and a nozzle entry diameter of 36 mm., it was found that very severe damage was sustained over a series of shots for any model or instrument located in the test section within 18 mm. of the nozzle axis. Whilst this did not constitute a fundamental limitation to use of the non-reflected shock tunnel, it made it difficult to conduct many desirable experiments involving models in the shock tube.

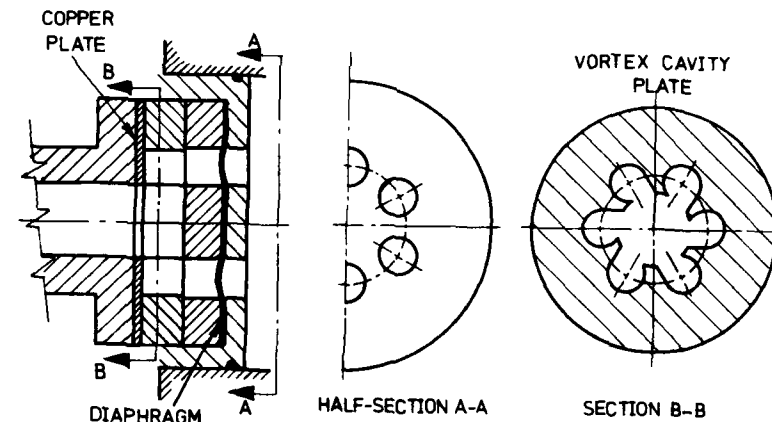
Scored diaphragms were tried but proved unsatisfactory, yielding some residual fragmentation, and displaying unacceptable inconsistency in burst pressure. Presumably, this was due to the rapid loading of the diaphragm which is associated with a free piston driver.

The energy of the diaphragm fragments was such as to suggest that they were being accelerated by the driver gas flow. Thus, in the absence of a satisfactory method of preventing diaphragm fragmentation, some means of removing the diaphragm fragments from the driver gas became necessary. Since the "cyclone" principle has been widely used for particle separation in industry for many decades (ref. 1) it seemed reasonable to attempt to apply it to the present problem.

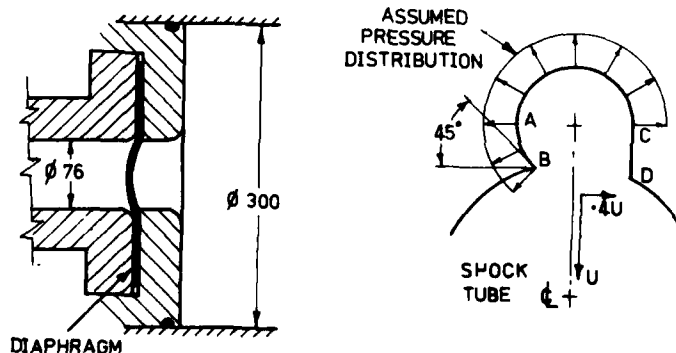
The details of this attempt are reported in this paper. The manner in which the main diaphragm arrangement was modified to allow exploitation of the cyclone principle is described, and a qualitative appreciation of its efficacy in reducing fragment damage is given. Its effect on the gas dynamic behaviour of the shock tube is also discussed.

DIAPHRAGM ARRANGEMENT

The cyclone separator is an inertial separator in which the gas is passed tangentially into a cylinder, yielding a circular gas motion which tends to "centrifuge" solid particles to the walls. In order to realize this effect in the Australian National University shock tunnel - shock tube facility T3 (ref.2) the main diaphragm arrangement was modified as shown in fig.1.



(b) MULTIPLE ORIFICE DIAPHRAGM



(a) CONVENTIONAL DIAPHRAGM

(c) CAVITY FLOW

FIG. 1. MAIN DIAPHRAGM CONFIGURATION

The facility incorporated a large area reduction at the diaphragm, passing from a driver diameter of 300 mm. to a shock tube diameter of 76 mm. In its conventional arrangement, shown in fig. 1(a), a diaphragm was placed at the entrance to the shock tube, and was clamped by a pressure plate. In the modified arrangement, shown in fig. 1(b), the diaphragm was clamped between a pressure plate and a diaphragm backing plate, each of which contained six orifices, 38 mm. in diameter. The orifices were offset from the centreline of the shock tube, and were equally spaced on a pitch circle diameter of 114 mm. The six orifices were aligned with the six deflection cavities in the cavity plate. As shown in section BB of fig. 1(b), these cavities led to the shock tube, with the cavity exits shaped to impart a circumferential component of velocity to the driver gas as it passes from the cavity to the shock tube. The vortex generating cavity plate was followed by a copper striker plate, which was intended to catch any fragments leaving the diaphragm at high velocity as it ruptured.

Some tests were also conducted in a smaller facility, T2, which is a scaled down version of T3, involving a driver diameter of 76 mm. and a shock tube diameter of 22 mm. The same modified diaphragm arrangement was used, with an appropriate reduction in scale.

A rough estimate of the relative magnitude of the circumferential velocity component of the driver gas as it enters the shock tube may be made by reference to Fig. 1(c), where the dimensions of a cavity are shown. It will be noted that the portion CD of the cavity wall is straight and parallel to a line drawn from the centre of the circle forming the rest of the cavity wall to the axis of the shock tube. Assuming that gas enters the cavity with no radial or circumferential component of flow, it follows that the mean flow direction of the gas as it passes into the shock tube is that of the resultant force exerted by the pressure at the cavity walls. The pressure at the walls will be approximately uniform, except over the sections AB and CD, where it will fall as the gas accelerates towards the cavity exit. In order to impart a net clockwise motion to the gas, the pressures along CD must be less than along AB. Therefore, an overestimate of the circumferential component of velocity may be obtained by neglecting the pressure on CD, and assuming that the pressure is equal to the cavity pressure along AB. This yields the result that the circumferential velocity is less than 40% of the radial velocity as the driver gas enters the shock tube.

For consistent operation of the shock tube, it is desirable that the diaphragm open fully on all six orifices, and that diaphragm rupture occur simultaneously at all six. Inspection of multiple orifice diaphragms after rupture indicated that all six orifices opened fully, exhibiting individual rupture patterns which were qualitatively similar to the single orifice diaphragm. A test was also conducted in which the compression tube was fired at conditions producing a peak pressure within 85% of the diaphragm rupture pressure, without actually causing rupture. It was observed that nearly equal yield occurred on all six orifices, with the displacement of the initially flat diaphragm at the centre of each orifice varying by only $\pm 4\%$ about a mean of 0.38 orifice diameters. Comparison of diaphragm kinetic energy and strain energy of deformation during yield at the rate of pressure rise experienced in the test indicated that the diaphragm was essentially statically loaded. Thus, if it was assumed that the diaphragm distorted at each orifice as a spherical surface, and ruptured at a fixed distortion level, then the variation of $\pm 4\%$ at the centre of the diaphragm could be interpreted as a variation of $\pm 1\%$ in the rupture pressure. Since the pressure near rupture was varying at a rate of 1% in 30μ sec., this indicated that rupture was simultaneous to within a time of the order of 60μ sec. During this time, the shock wave travelled only 1m. of the 8m. shock tube length at the highest shock speed tested.

DAMAGE REDUCTION

Use of the cyclone effect has led to marked reductions in the level of damage due to diaphragm fragments. Damage to models mounted on the axis of the shock tube is confined to a mild 'sand-blasting' effect, coupled with an impact by a small diaphragm fragment in every 20 to 30 shots. Fig. 2. demonstrates this improvement, showing the damage sustained by the hardened steel replaceable leading edge insert for the axi-symmetric supersonic-hypersonic expansion nozzle used in non-reflected shock tunnel operation. The insert on the left of the photograph displays the damage sustained in approximately 80 shots with a conventional diaphragm arrangement, whilst that on the right demonstrates the much lower level of damage associated with twice that number of shots using the modified diaphragm arrangement.

In order to confirm that the cyclone effect was an important factor in reducing damage, some experiments were conducted in the T2 facility with the vortex cavity plate replaced by a radial flow cavity plate in which the flow was directed towards the axis of the shock tube i.e. the circumferential component of flow was eliminated.

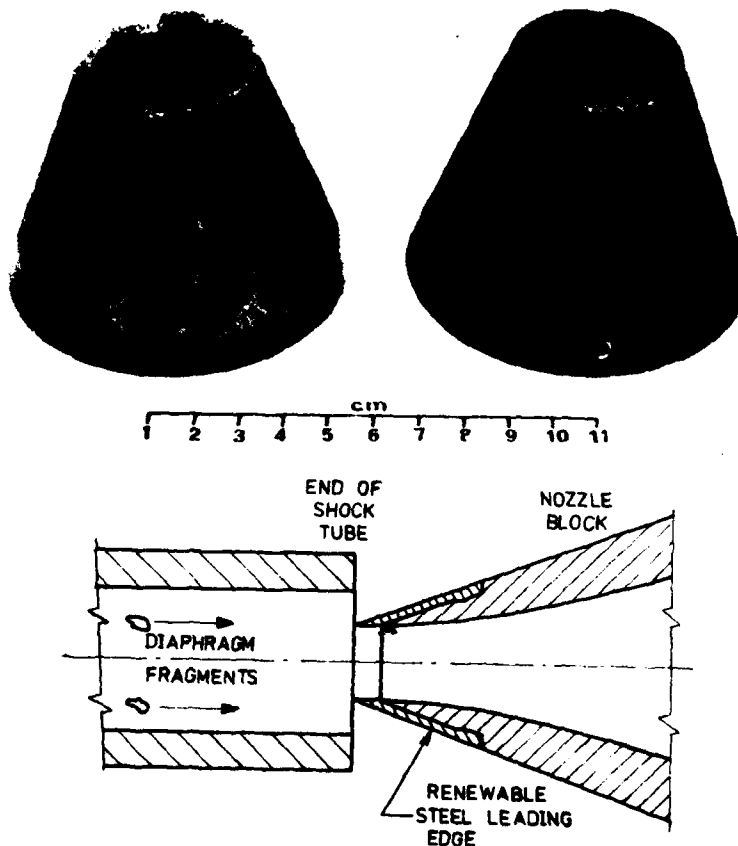


FIG. 2. REDUCTION OF DIAPHRAGM FRAGMENT DAMAGE

A copper disc was placed at the downstream end of the shock tube and, after four shots, was severely pitted by diaphragm fragments. The vortex cavity plate was then replaced and a new copper disc inserted. A further four shots yielded less pitting of the copper disc, with the pitting confined to a region close to the walls of the shock tube. This is consistent with a cyclone effect, which is centrifuging the larger diaphragm particles to the walls of the shock tube.

SHOCK SPEED MEASUREMENTS

Use of the multiple orifice arrangement, involving radial injection of the driver gas into the shock tube, may be expected to produce a strong "vena contracta" effect, and thus act as a throttling orifice at the entry to the shock tube. It may also be expected to generate shock waves, which lead to an entropy rise in the driver gas.

These effects will influence the shock tube performance in a manner which is difficult to model "a priori". However, it is possible to make an overall assessment of their influence by measuring a range of shock speeds for a given driver condition and using these to deduce the driver pressure and speed of sound for an equivalent constant area shock tube - i.e. one which yields the same shock speeds over the range studied.

Results of such measurements in T3 are presented in fig.3. These tests were conducted with a main diaphragm rupture pressure of 750 atm., and a driver gas volumetric compression ratio of 83, as estimated from the ratio of diaphragm rupture pressure to the pressure of the driver gas before compression. The associated speed of sound in the helium driver gas at diaphragm rupture can then be calculated as 5.04 km.s^{-1} . A number of different test gases were used, and so the shock speed is most conveniently plotted against the initial test gas density in the shock tube. The shock speeds were averaged over a distance of 3.5 m to 5.5 m. from the main diaphragm, where the shock speed attenuation was typically 5% per metre. It can be seen that the measurements are consistent with an equivalent driver pressure and speed of sound of 150 atm. and 7.5 km.s^{-1} respectively.

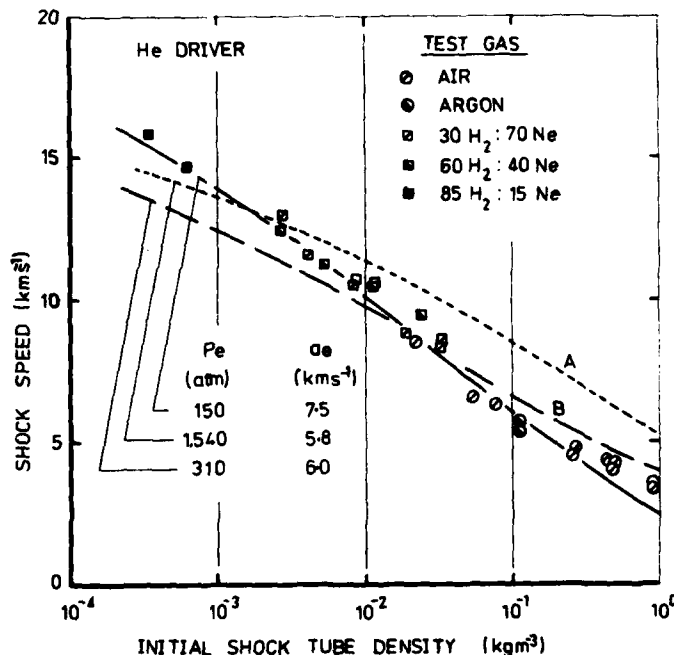


FIG. 3. SHOCK TUBE PERFORMANCE

These results may also be compared with those pertaining to a single orifice diaphragm. For example, the predicted shock speed variation may be obtained for such a configuration by assuming ideal shock tube behaviour, with an infinite area ratio contraction at the diaphragm, and using the diaphragm rupture pressure and speed of sound, as noted above, as driver reservoir conditions. This yields curve A in fig.3. However, as discussed in ref.3, the free

piston driver with a single orifice diaphragm itself does not behave in an ideal manner, and it is convenient to represent its behaviour also in terms of an equivalent constant area shock tube. The appropriate equivalent driver pressure and speed of sound may be obtained by reference to fig.4 of ref.3, where the tailored interface shock Mach number and pressure after shock reflection are plotted against the driver gas volumetric compression ratio. Using the pressure ratio at shock reflection, it is then possible to deduce the conditions in the driver gas at the contact surface and hence, the equivalent driver pressure and speed of sound. For the above diaphragm rupture conditions, this yields values of 310 atm. and 6.0 km.s^{-1} respectively, and leads to curve B on fig.3.

It can be seen that, in comparison with either the ideal or the actual single orifice diaphragm performance, the multiple orifice diaphragm yields shock speeds which are reduced at high initial shock tube densities, and increased at low densities. This is associated with a reduction in the equivalent driver pressure, and an increase in the speed of sound. The reduction in equivalent driver pressure in itself is explicable in terms of an effective area reduction at the entrance to the shock tube, arising from the "vena contracta" effect but, when considered in conjunction with the increase in sound speed, it is clear that it must be associated, at least in part, with an increase in the entropy of the driver gas. Noting that the equivalent driver conditions are related to actual conditions in the driver gas at the contact surface through an isentropic process, it is possible to calculate the entropy change in the driver gas by using the non-isentropic relation (e.g. ref.4).

$$\Delta S/C_v = (\gamma-1) \ln (P_R/P_e) + 2\gamma \ln (a_e/a_R) \quad (1)$$

where P_R and a_R are driver gas pressure and speed of sound at rupture, P_e and a_e are the equivalent driver pressure and speed of sound, ΔS is the entropy change, C_v the specific heat at constant volume, and γ the ratio of specific heats. For the multiple orifice diaphragm in fig.3., this yields $\Delta S/C_v = 2.4$.

The entropy rise in the driver gas was explored further through a series of experiments in T2, in which records were taken of the pressure at the end of the shock tube after shock reflection. As shown in the wave diagram in fig.4. (a), the shock tube was operated in the "equilibrium interface" condition, in which the wave system produced by interaction of the reflected shock with the contact surface is allowed to damp out, leaving the contact surface stationary,

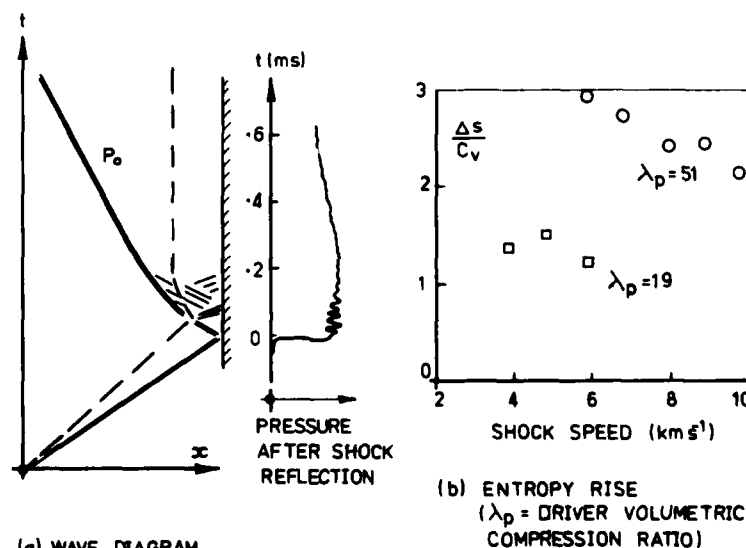


FIG. 4. ENTROPY RISE IN THE DRIVER GAS

with a shock wave propagating upstream in the driver gas to bring the driver gas to rest. In the experiments, a wave passed from the end of the shock tube to the contact surface in less than 50μ sec., a period which, as shown by the typical record of pressure after shock reflection in fig.4(a), is relatively short compared with the period for which pressure remains constant. Thus, by measuring the pressure at 200 to 300μ sec. after shock reflection, a value was obtained for P_0 , the pressure behind the shock wave which brings the driver gas to rest at the equilibrium interface condition. The pressure in the driver gas upstream of this shock wave (i.e. the pressure at the contact surface) could be calculated from the shock speed and the initial shock tube pressure, leading to the pressure ratio across the driver gas shock wave and hence, the driver gas Mach number at the contact surface. In conjunction with the shock speed, this yielded the contact surface velocity and speed of sound and allowed calculation of the equivalent driver pressure and speed of sound. The entropy rise in the driver could then be determined from eqn.(1).

Results are plotted against shock speed in fig.4(b). For a driver volumetric compression ratio of 51, tests were conducted over a range of initial shock tube pressures which allowed the Mach number of the driver gas at the contact surface to vary from 1.0 to 3.2. It can be seen that the entropy rise diminishes as the shock speed increases suggesting that, at least at the higher contact surface pressures, part of the entropy rise is occurring in the shock tube flow of the driver gas. This is consistent with the presence of a strong "vena contracta" effect, and associated flow restriction, at the entrance to the shock tube, preceeding a steady expansion to the shock tube cross-sectional area, followed by recompression of the flow through a moving shock wave system. This is illustrated in fig.5.

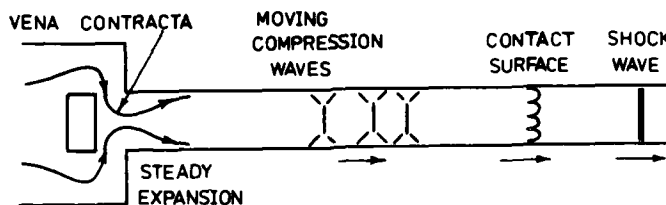


FIG. 5. TENTATIVE MODEL OF DRIVER GAS FLOW

Some tests were also made at a lower driver gas volumetric compression ratio, and are presented in fig.4(b). They serve to indicate that the entropy rise is also influenced by the driver gas volumetric compression ratio, a factor which may, perhaps, be associated with the strong vortex generated by the free piston as it travels down the compression tube (ref.5).

CYCLONE EFFECT ON SHOCK SPEED

As already noted, the circumferential component of velocity in the driver gas as it enters the shock tube is less than 40% of the radial component. Assuming that the gas velocity is no greater than the local sonic velocity, it follows that the kinetic energy associated with the circumferential motion is less than 4% of the stagnation enthalpy of the driver gas, an amount which is unlikely to significantly affect the shock tube performance.

This was confirmed by measurements taken in T2 with the radial flow cavity plate. In comparison with the vortex cavity plate, no detectable difference could be observed in shock speeds or in the magnitude and time dependence of the post reflection pressures at the downstream end of the shock tube.

TEST TIME MEASUREMENTS

To confirm that the driver gas circumferential component of velocity did not significantly influence the development of the contact surface, measurements of test time were taken in T3 whilst it was operating as a non-reflected shock tunnel. Time resolved spectra were taken of the visible radiation emitted from the stagnation region of a hemispherically blunt body in the test section. Tests were made with a mixture of 30% hydrogen and 70% neon as test

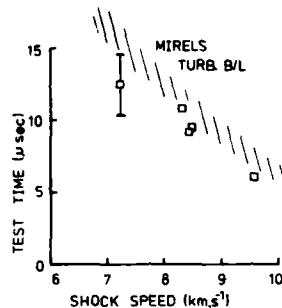


FIG. 6. TEST TIME MEASUREMENTS

Driver : He , Test gas: 30H₂-70He

Distance from main diaphragm = 8m.

gas, operating at shock speeds such that the H_α and H_β lines could be clearly observed during the test period. Arrival of the contact surface was marked by the sudden onset of impurity radiation.

Results are compared with theoretical predictions in fig.6. The cross hatched curve represents the test times estimated by Mirels' theory (ref.6), modified to take

account of expansion nozzle effects, according to method of characteristics calculations of the unsteady nozzle phenomena (ref.7). Assuming that the theoretical times between arrival of the primary shock and the contact surface represent the maximum which can be expected in the presence of shock tube boundary layer effects, it can be seen that the circumferential motion of the driver gas did not grossly affect the shock tube test time.

CONCLUSION

The cyclone effect can be used to separate diaphragm fragments from the driver gas in a shock tube without in itself significantly affecting shock speeds or test times. In the present experiments, it was found that a relatively small circumferential velocity, involving an energy component which was less than 4% of the driver gas reservoir enthalpy, was sufficient to dramatically reduce the level of damage caused by diaphragm fragments. Although changes were observed in the shock speed, it was found that they were associated with the use of a multiple orifice diaphragm. This caused an entropy rise in the driver gas, by virtue of both the complex flow situation at the entrance to the shock tube and the possible recompression shock system in the shock tube.

Although the experiments were conducted in a free piston shock tube, they suggest that the same basic method may be effective in removing diaphragm fragments in more conventional configurations. However, no tests have been conducted to substantiate this view.

ACKNOWLEDGEMENTS

The authors acknowledge the valuable assistance of Mr. V. Adams in the experiments. The facility T3 was constructed and operated with support from the Australian Research Grants Committee.

REFERENCES

1. Marks, L.S. Mechanical Engineers' Handbook 5th Ed. McGraw Hill, New York 1951. p.811.
2. Stalker, R.J. "Development of a Hypervelocity Wind Tunnel" Aeronautical Journal p.374. June 1972.
3. Stalker, R.J. & Hornung, H.G. "Two Developments with Free Piston Drivers" Proc. 7th Int. Sh. Tube Symp. Ed. I. Glass. Univ. of Toronto Press 1970.
4. Liepmann, H.W. & Roshko, A. "Elements of Gasdynamics" J.Wiley & Sons, New York 1967, p.20.
5. East, R.A. & Qasrawi, A.M.S. "A Long Stroke Isentropic Free Piston Hypersonic Wind Tunnel" U.K. Aeronautical Res. Council R & M 3844 Aug. 1978.
6. Mirels, H. "Shock Tube Test Time Limitation due to Turbulent Wall Boundary Layer" AIAA J. 2, p.84. Jan. 1964.
7. Madford, M.R. "Pulsed Nozzle Flows in a Shock Tube" Ph.D. Thesis, Australian National University, Canberra, Australia 1976.

7

→

A NEW, DIAPHRAGMLESS, FLEXIBLE, LUMINOUS SHOCK TUBE

Yong W. Kim

Department of Physics
Lehigh University
Bethlehem, Pennsylvania 18015 U.S.A.

AD P000229

A new pressure-driven shock tube has been designed, incorporating a spring-loaded ball valve in lieu of a diaphragm. One rigid driver section is used to generate shock waves simultaneously in one or more flexible driven sections. Long flexible copper tubings have been used as a driven section with a square cross-section test section. Luminous shocks have been successfully produced in air, argon and xenon for tubings as small as 1.78 mm in inner diameter and well over 1000 in length-to-radius aspect ratio. Furthermore, the tubings have been bent into arbitrary shapes with radius of curvature as small as ten tube radii without measurable degradation of shock tube performance. A large portion of the driver gas is recovered after each shot and the driven section remains free of contamination by exposure to the atmosphere and diaphragms. Coupled with the flexibility and the unprecedented reproducibility, this feature makes the shock tube well suited for a wide range of quantitative spectroscopic applications. A detailed analysis of the exact relationship between the valve characteristics and the shock wave properties is given.

INTRODUCTION

Historically, pressure-driven shock tubes have remained rigid, rectilinear and uniform in crosssection to a high degree of precision. Due to their early successful applications for studies of flows past bodies, the shock tubes are generally large in crosssection and long and consequently, they require large space and command special measures to adapt diagnostic instruments to the peculiarities of a given shock tube. There are also the matters regarding diaphragms: While relatively simple to provide, they are used only once and their rupture characteristics difficult to predict precisely, thus leading to a degree of uncertainty in the reproducibility of given experiments. Diaphragms are also one of the main sources of contamination of the driven section and contribute to poor duty cycle of the experiment. Many ingenious designs for speedier diaphragm changes have been advanced and used but the problems such as diaphragm debris and poor reproducibility remain.

Shifts in the emphasis to the shock tubes as a tool for studies of kinetics can help relax the above requirements of the pressure-driven shock tubes. First of all, the crosssection of the driven section might be reduced drastically and this paves a way to give flexibility to the driven section of a

shock tube. Earlier studies¹ of shock attenuation and shock tube flow duration have established that due to the losses of shocked gas molecules through the boundary layers of the primary shock flow the shock speed decreases substantially below the ideal value and the primary shock flow fails to grow in length linearly with the length of the driven section. This means further that irregular events upstream near the diaphragm have little influence on the uniformity of the shock tube flows near the endwall located far downstream. Placement of a perforated disc immediately downstream of the diaphragm to produce very weak shock waves² is an example of such an implication. Techniques³ of a splitter plate and a cookie cutter represent another such examples.

Following the above reasoning, the concept of a diaphragmless flexible, luminous shock tube has been proposed, and successfully tested by constructing such a shock tube featuring the full concept. The shock tube employs a fast acting ball valve in lieu of the diaphragm and consists of one rigid cylindrical driven section and one or more flexible driven sections, simultaneously driven by the single driver.

Results on hand thus far indicate that the new shock tube will be useful for spectroscopic studies, as non-electric delay lines and for creation of an extended gas dynamic laser medium. Aside from the inherent economy in space and consumables such as the driver gas, the small size and flexibility make it simpler to adapt the shock tube to specialized diagnostic instruments and unusual pressure or temperature environment.

In the following, we describe the construction of the shock tube and the overall performance data. Comments on future improvements are given in the end.

CONSTRUCTION OF THE SHOCK TUBE

The shock tube is equipped with a single cylindrical driven section of 2.22 cm inner diameter and 60 cm in length. The driven section can readily handle high pressure gas of up to 135 atm in pressure and is connected directly to one side of the ball valve. On the other side of the valve a vacuum manifold is connected to handle evacuation and gas mixing requirements. Up to this point the inner diameter of the shock tube is maintained uniformly at 2.22 cm, including the valve in its open position. One or more flexible driven sections are connected to the manifold. Each driven section is terminated with a test section having a flat endwall. The driven section consists of uniform diameter copper tubing, varying in length from 25.4 to 122 cm. Three different tube diameters have been used: 1.78, 4.76 and 7.94 mm. Up to three driven sections have been connected to the manifold for simultaneous generation of up to three shock waves. The overall arrangement is shown schematically in Fig. 1.

These driven sections have been bent into differing shapes, some irregular and another helical, for most of their lengths, except for the last thirty tube diameters or so which remained reasonably rectilinear. No apparent changes in the shock wave characteristics have been observed when the radius of curvature at some point in the driven section was reduced to as small as ten tube radii.

Two different types of test sections have been employed: some of circular crosssection and others of square crosssection. In the latter case, a coupling has been used between the tubing and test section to effect a smooth transformation of the crosssectional profile from a circle to square. All test sections are machined out of plexiglas and polished to a transparent finish.

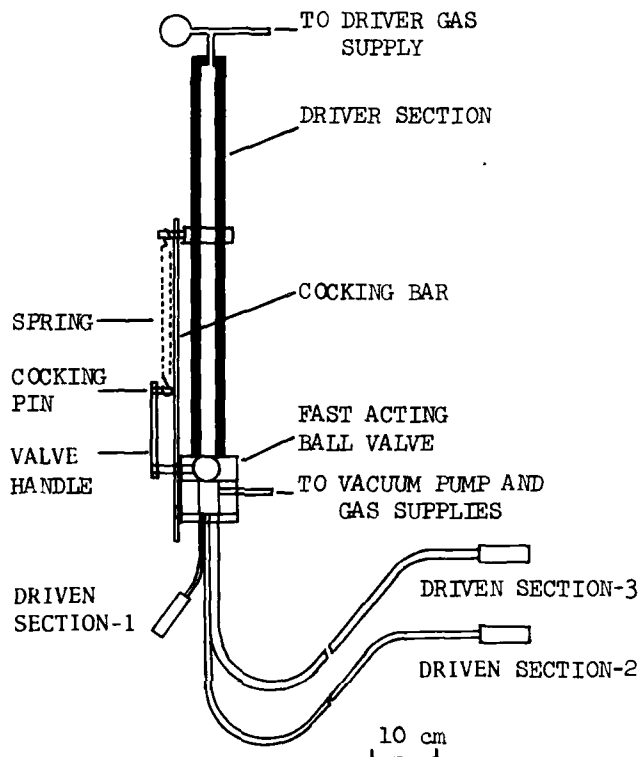


Fig. 1. A schematic diagram of the diaphragmless, flexible, luminous shock tube with three driver sections.

The final and perhaps the most critical element in the design of the shock tube is the fast acting ball valve. The first valve used is the Whitney 7/8" ball valve (Model 60 series) with one change in design. The change entails replacement of two molded gaskets, contoured to fit snugly over the spherical surface of the ball, with two O-ringed flanges. This was done in order to reduce the friction force on the ball and thereby improve on the response of the valve to a sudden application of a torque. The valve handle is linked to one end of an expansion spring and the other end of the spring is anchored at a point along the driver section of the shock tube.

In operation, the valve handle is first armed to a closed position (perpendicular to the driver section) by means of a cocking bar and then fired by releasing the bar. In this manner, the valve is initially given the maximum torque for fast action and settles down to an equilibrium full-open position without requiring any breaking action. We note that in order to insure the reproducibility of the firing action the cocking pin on the valve handle is fitted with a ball bearing sleeve.

The valve has worked well right from the first trial as far as the primary objective of producing luminous shocks in the flexible shock tube is concerned. As the use of the valve continued, the valve opening time began to show an in-

creasing scatter due to a wear on the shaft which links the valve handle to the ball. The original stainless steel shaft is packed only with an O-ring and three plastic washers and gradually developed the wear by coming into contact with the stainless steel body of the valve. Consequently, a modification has been made to the valve by replacing the original shaft with a new shaft which is supported by two ball bearings and sealed with an O-ring. Furthermore, a second shaft of similar design has been added to the opposite side of the ball. In this way, the ball becomes completely supported independently of the two main O-rings mentioned earlier, thus reducing the driver pressure dependence of the valve opening time. Fig. 2 shows schematically the details of

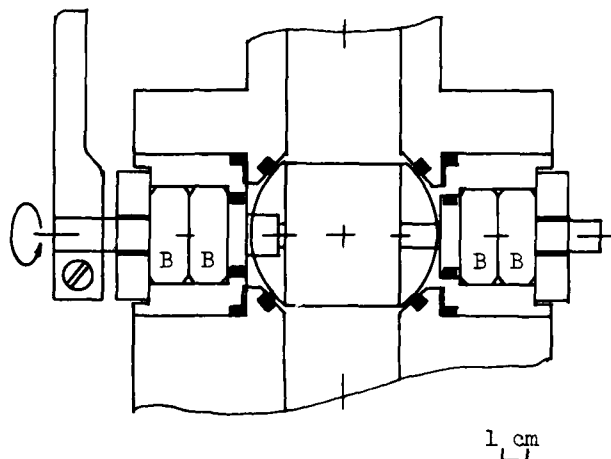


Fig. 2. An exploded view of the fast acting ball valve. B denotes ball bearing sleeves for the shafts supporting the valve ball.

the modified ball valve. This improvement has helped stabilize the performance of the valve, although there still remains some degree of dependence on the driver gas pressure. This aspect is further discussed in the next section.

In operation, the shock tube does not need to be exposed to the atmosphere at all. After each firing, the ball valve is closed by returning the valve handle to the armed position, the driver gas trapped in the driven section released and the driven section evacuated and refilled with a measure of the driven gas. Much of the driver gas is recovered at high pressure, usually better than at 85% of the original pressure, in the process. Due to the small volume of the driven sections, the pumping time for evacuation is short, thus improving the duty cycle of the shock tube immensely.

The initial shake-down period of the shock tube is relatively brief. Several shots loosen up, and bring down to the endwall, the oxide deposits on the inner tubing surfaces. After these are cleaned up once or twice, the test section remains clean for a large number of runs to follow.

PERFORMANCE OF THE SHOCK TUBE

The shock tube has been operated using hydrogen as the driver gas in the pressure range of 30 to 85 atm. Air, argon and xenon have been used as the driven gas in the pressure range of 10 to 30 torr. Observations have been limited to the shocks strong enough to produce high levels of luminosity from the shock heated gases. Fig. 3 shows time integrated white light photographs

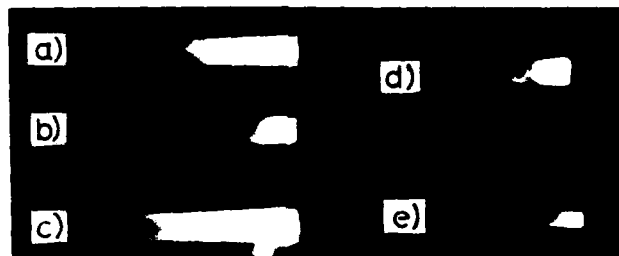


Fig. 3. Time-integrated white-light photographs of the luminous shock tube flows near the end-wall at 22.0 torr driven gas pressure: a) air/68.0 atm H_2 , b) argon/61.2 atm H_2 , c) xenon/49.0 atm H_2 , all in the 7.94 square test section; d) and e) xenon runs in the 7.94 and 4.76 mm dia test sections both driven simultaneously by the single driver section with 30.6 atm H_2 .

of the shock heated gases near the endwall of 122 cm long shock tubes: a), b) and c) show the runs with air, argon and xenon in a 7.94 mm square test section, respectively; d) and e) show the shocked xenon emissions in two cylindrical test sections of 7.94 mm and 4.76 mm dia, respectively, both driven simultaneously by a single charge of hydrogen. In all cases, the test section window is 6.35 cm long and the full width of each test section is left unobstructed for the camera.

Much of the luminosity is due to multiply reflected shocks in each run and consequently some irregular, filamentary emission patterns are visible on the upstream side of the shock-heated gas slug. Rotating drum camera pictures also show that the majority of luminosity originated from the multiply reflected shock region in all of the latest series runs with the modified ball valve design. The above observation is closely related to the fact that the highest shock Mach number in the 122 cm shock tubes has been limited to about 4.5, as determined from some streak photographs and photomultiplier pickups at two different positions near the endwall. We will focus our attention to this aspect later on.

Overall, the luminosity from the multiply reflected shocks lasts for periods far greater than in the conventional luminous shock tubes. For example, the luminosity lasting up to four milliseconds has been observed in the 122 cm long, 7.94 mm dia. driven section containing air initially at 22.0 torr while the time of shock propagation over the entire length of the driven section is only about one millisecond. This feature appears to arise from the fact that the pressure profile upstream of the interface steepens much more sharply here than in the conventional shock tubes due to the large crosssectional disparity between the driver and driven sections and to the characteristic rate of valve opening.

A considerable effort has been exerted to establishment of the exact relationship between the ball valve characteristics and the properties of the shock waves in different diameter driven sections. The relationship plays the central role in explaining the gross features mentioned above, achieving a stable reproducibility regime and also in improving the shock tube performance. In Fig. 4 a summary of runs is given in which the valve opening time,

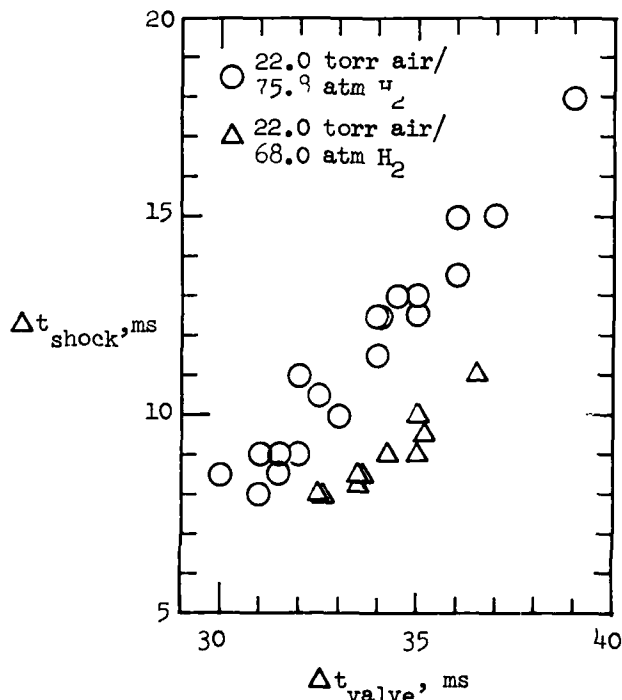


Fig. 4. The shock arrival time, Δt_{shock} , is plotted as a function of the valve opening time, Δt_{valve} , for the 7.94 mm dia test section at two different hydrogen pressures.

Δt_{valve} , as defined by the time for the valve handle to rotate 112° from its initial cocked position, is compared to the shock arrival time, Δt_{shock} , as measured from the moment of valve release to that of the shock arrival at 4.21 cm upstream of the endwall of the 122 cm long, 7.94 mm dia. driven section. All runs were made in 22.0 torr air but driven by hydrogen at two different pressures: 68.0 and 75.8 atm at room temperature.

First, one finds an unmistakably distinct trend that the slower the valve opening time the tardier the shock arrival becomes. A reasonable estimate for the time of shock propagation over the length of the driven section should lie between 0.75 and 1.7 msec, whereas the variation in Δt_{shock} is considerably larger. This points to a role of the valve in the process. Secondly, one sees that at the lower driver gas pressure Δt_{shock} is smaller than that at the higher pressure, again by an amount greater than the possible variation of the shock propagation time. The latter observation also points to the behavior of the ball valve because as the driver gas pressure increases, the load on the ball bearings within the valve increases and consequently the friction force

increases, thus impeding opening of the valve.

We can analyse the time response of the ball valve quantitatively by considering the equation of motion of the valve:

$$I \ddot{\theta} = k(S - S_0) r - f a_0 \quad (1)$$

where I is the moment of inertia of the valve handle/ball system, k the spring constant, f the friction force on the valve shaft and ball and a_0 the effective radius of the shaft/ball system. r is the moment arm length of the valve handle and is given by

$$r = R \cos \theta. \quad (2)$$

where R is the length of the valve handle between the axes of the valve shaft and cocking pin. θ is the angular position of the valve handle with respect to its initial cocked position. S denotes the length of the spring and S_0 the unstretched, equilibrium length of the spring. Denoting by L the distance between the shaft axis and the point where the spring is anchored, we have the following relationship among S , L , R and θ :

$$S^2 = L^2 + R^2 - 2LR \cos(\frac{\pi}{2} - \theta), \quad (3)$$

It is not necessary to determine I , k and $f a_0$ independently in order to solve eq. (1). Instead, eq. (1) is solved self consistently by a numerical method, using the known values of Δt_{valve} , the first turning point (θ_t) of the valve handle following its release and the R/L and S_0/L ratios. For this purpose, we define

$$F \equiv \frac{f a_0}{I} \quad \text{and} \quad K \equiv \frac{kR \sqrt{2LR}}{I}. \quad (4)$$

For $\Delta t_{\text{valve}} = 30$ ms, $R/L = 0.41$, $S_0/L = 0.35$ and $\theta_t = 135^\circ$ we find $F = 2300$ and $K = 12000$ in cgs units. The boundary condition that $\theta(t=0) = \dot{\theta}(t=0) = 0$ has been used, where the time t is measured from the moment of valve release. The solid curve in Fig. 5 gives the full history of the valve opening as a solution of eq. (1) under this condition. The ball valve begins to open at θ_s , which is 12.24° , and this corresponds to $t = 7.2$ ms. The primary shock is detected 1.2 ± 0.3 ms later. This means that the shock wave characteristics are determined by the valve opening process during the period no longer than $500 \mu\text{s}$ beyond θ_s .

It is reasonable to expect that the larger the rate of opening around θ_s the stronger the shock becomes. One might ask them how this rate can be increased. We show three additional calculations involving i) a decrease of the friction by a factor of two (dashed line), ii) a non-zero initial angular velocity of the valve (broken line) and iii) a doubling of the spring constant (dotted line). The decreased friction significantly increases the rate of valve opening about θ_s and this is consistent with the observation made earlier on the driver pressure dependence seen in Fig. 4. Clearly, the most effective avenue is to increase the spring constant, although the long term integrity of the valve shaft must be taken into consideration before exploiting this to the fullest extent. Of course, the ratios R/L and S_0/L will also figure importantly in the optimization effort. It thus appears that the maximum Mach number observed with the present ball valve is due to the present maximum rate of valve opening. With a combined improvement by reducing the friction and increasing the spring constant, the Mach number can be increased substantially.

Finally, the arrival times of two shock waves in two different driven sections (4.76 and 7.94 mm dia.), driven simultaneously by the single driver sec-

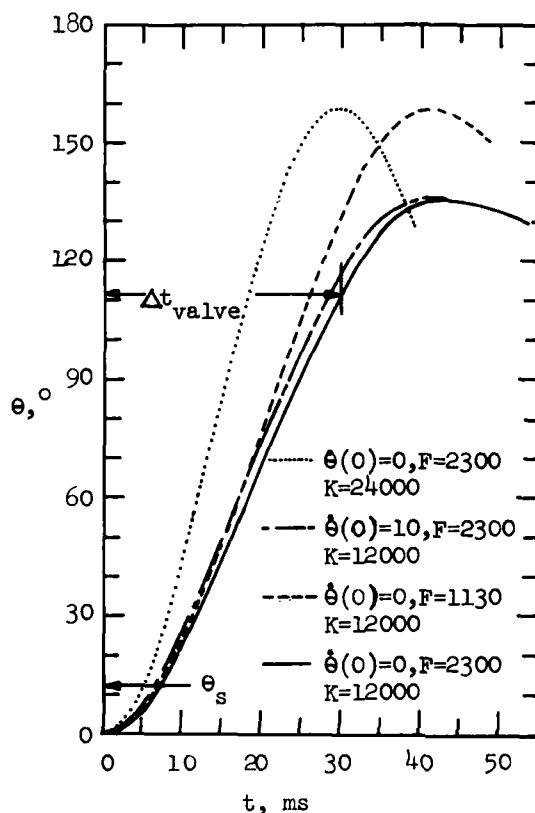


Fig. 5. The angular position of the ball valve is plotted as a function of time from the moment of valve release, as obtained from the numerical solution of eq. (1) (solid line). Other results show the influence of the friction (dashed line), the initial angular velocity (broken line) and the spring constant (dotted line).

tion, are compared in Fig. 6. At each Δt_{valve} value, the two shock arrival times have been measured. The shocks propagate more slowly in smaller diameter tubes due to the increasingly large fraction of the boundary layers present in the primary shock flow. The results of Fig. 6 are indeed consistent with this expectation. We also note that the streak photographs of the runs in air show the reflected shock bifurcation similar to those observed in the conventional shock tubes.⁴

CONCLUDING REMARKS

We have proposed a new concept of the diaphragmless, flexible, luminous shock tube, demonstrated its soundness by constructing such a shock tube and identified the essential relationship between the ball valve characteristics and shock wave properties. Sufficient ground work has been done, and the direction for further development indicated, for establishment of the shock tube as a contamination-free, highly reproducible tool. Especially, the feature that many shock waves can be produced simultaneously with this design offers a broad range of opportunities for application. Some examples are the use of the shock tube as a non-electric delay line, for production of gas dynamic laser media in long narrow channels, for studies of reacting systems with many different relaxation times and for studies of thermodynamic states requiring extreme pressures and temperatures.

The exceptionally long multiply reflected shock regime may or may not be useful, depending on the nature of a particular physics in question. The rather small depth of the shocked gas inherent in the flexible design is in a way a drawback because of decreased luminosity but ready availability of sensitive optical detectors should alleviate this difficulty. It is reasonable

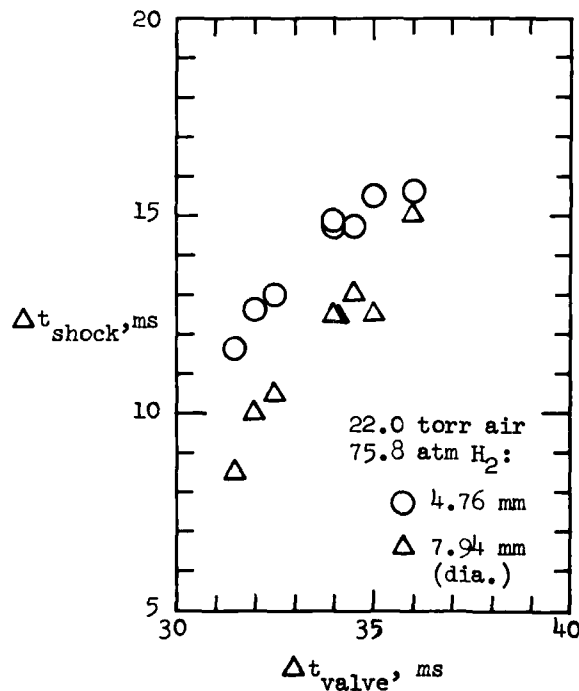


Fig. 6. A comparison is made between the shock arrival times in two simultaneously driven flexible shock tubes of equal length but of different diameters as a function of the valve opening time.

to expect that with further improvement of the valve response in the manner suggested stronger shocks can be readily produced in flexible shock tubes. Much of the diagnostics can be easily improved to bring about more precise descriptions. We believe, however, most of the important features have been unambiguously dealt with and for an experimental tool of a first order design the shock tube has proven to be phenomenally successful. It is hoped that many interested investigators would put the shock tube to varied uses in the near future.

The author acknowledges the assistance of Nick Bigelow in the first assembly of the shock tube.

REFERENCES

1. R. N. Hollyer, Jr., "A Study of Attenuation in the Shock Tube", University of Michigan Engineering Research Institute Report, Project M720-4 (1953); H. Mirels, "Boundary Layer behind Shock or Thin Expansion Wave moving into Stationary Fluid", NACA TN-3712 (1956).
2. Y. W. Kim, unpublished (1973).
3. P. V. Marrone, W. H. Wurster and C. H. Treanor, "Vacuum-Ultraviolet Absorption Measurements of Vibrationally Excited Nitrogen Using a Shock-Tube Splitter-Plate Technique", in *Modern Developments in Shock Tube Research*, ed. by G. Kamimoto (Shock Tube Research Society, Japan, 1975), p. 682.
4. H. Mark, *J. Aero. Sci.* **24**, 304 (1957); R. A. Strehlow and A. J. Cohen, *J. Chem. Phys.* **28**, 983 (1958); Y. W. Kim, *Phys. Fluids* **15**, 1564 (1972).



AD P000230

A POWDER-INJECTION SHOCK-TUBE FACILITY

M.W.P.Cann, J.B.Shin, R.W.Nicholls

Centre for Research in Experimental Space Science

York University, Downsview, Ontario M3J 1P3

Many molecules of spectroscopic interest are best obtained for study in the laboratory by volatilising powdered material. For this purpose a conventional pressure driven shock-tube was modified to include a powder-injection capability. In order to improve reproducibility from one run to the next the injection and firing sequence is automatic and timed. Other features include safety checks, a set-up monitor to reduce bad runs through human error, and several operating options. These options include manual or automatic mode, with one or two diaphragms, overrides on most operations, sequence interrupt on external trigger and remote operation and reset.

INTRODUCTION

Shock-tubes have been used for several decades in, amongst other things, spectroscopy, reaction kinetics, heat transfer studies and in materials research. For the majority of these studies the working medium was a gas but in recent years there has been an increasing need to consider gaseous suspensions of solid material. This is especially true for spectroscopic studies, which provided motivation for the facility described here.

There are many molecules of spectroscopic interest, and of importance in other areas of high temperature research, which do not exist under normal conditions. In many cases these molecules can be generated by heating an appropriate combination of gases, but this usually results in the presence of unwanted molecular species which interfere with the work. An alternative approach is to shock-heat solid material in powder form. This powder is suspended as an aerosol in a gas which includes any other elements needed for the production of the desired molecular species. The powder particles are volatilised behind the shock wave and local thermal equilibrium conditions can be achieved. This then allows one to obtain the chemical composition, temperature and pressure of the gas from chemical equilibrium computer programs, such as

the one by Gordon and McBride (1971), and is why the shock-tube is such a useful facility for spectroscopic research. The powder-injection approach has the advantages of introducing fewer extraneous elements into the shock-tube, and of additional flexibility in the choice of materials, but the disadvantages that it is harder to make quantitative composition measurements and harder to achieve repeatable conditions. Factors affecting reproducibility now include particle size distribution and uniformity of particle densities in the working section of the shock-tube. An important aspect in the design of the powder-injection system was the need to minimise run-to-run variations and to optimise reproducibility.

DESIGN FEATURES

The shock-tube equipped with the powder-injection facility has an internal diameter of 3-inches and diaphragms are ruptured by the helium gas pressure in the driver. Basically the system operates by blowing powder into a settling tank, which contains the working gas to be used, and then admitting the powder suspension into the previously evacuated shock-tube. After a short time delay, to allow the gas to equilibrate, the diaphragm is ruptured and a shock wave initiated. These operations are controlled by a timer or, alternatively, may be effected separately by the user.

Figure 1 shows details of the powder-injection operation. When the shock-tube and powder injection-system are ready for a

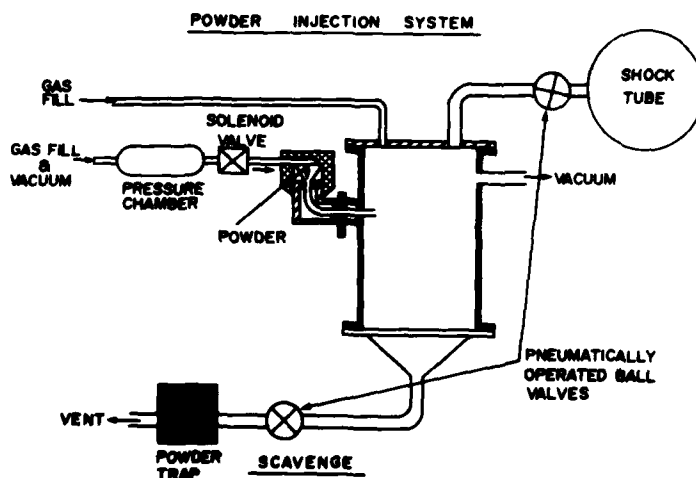


Figure 1.
Diagram of Powder-
Injection System.

run the shock-tube is evacuated, the tank contains the working gas, usually argon, and the pressure chamber contains the same gas at about 45 psi pressure. Powder is placed in the end of a small tube which projects into the tank. Starting the injection operation starts the timer and initiates the following sequence

1. Tank injection. The solenoid valve (Figure 1) is opened and blows the powder into the settling tank.

2. Shock-tube injection. A pneumatically operated valve is opened to admit the gas-powder suspension into the shock-tube.
3. Diaphragm rupture, which is achieved in one of two ways as discussed below.

The times between the above operations, i.e. standing or settling times, and also the length of time that the valves remain open can all easily be changed. The Cramer timer operates a system of cams which, in turn, operate micro-switches. The timer has a synchronous motor which can also be changed. For most of the work with this system a one-minute cycle has proved to be satisfactory, and the timer stops itself after one cycle. The cycle cannot be repeated until the system has been reset.

The Powder Hopper, for introducing powder, is shown in Figure 2. Powder is placed in the tube and the cap replaced. This cap is grooved to direct gas from the pressure chamber down the tube when the solenoid valve is opened.

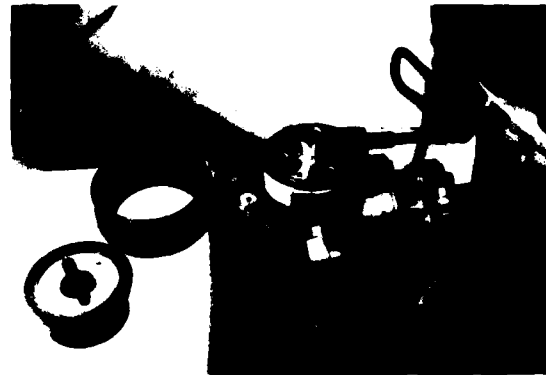


Figure 2. Powder Hopper With Top Removed. Settling tank shows to the right and vertical pipe in foreground carries gas from pressure chamber.

Figure 1 shows a conical base to the settling tank with a scavenge pipe leaving it. The scavenge operation is used to remove excess powder between runs. The tank is pressurised to about 15 psi with nitrogen or argon and the scavenge valve opened, sweeping out the powder which has accumulated at the bottom of the tank. In operation powder accumulates in a number of unwelcome places, including the vacuum valves on the settling tank. This powder damages these valves when they are next operated. So, after a powder-injection operation, internal jets of nitrogen (or argon) blow the powder off the valves before they are opened.

With the cycle timer controlling the various steps in the operation of loading the shock-tube with gas-powder suspension it was desirable that it also controlled diaphragm rupture. Simply opening the fill valve was considered to be unsafe so the signal from the timer arms the line to the fill valve. This then passes control to the operator, who admits more helium to the driver

until diaphragm rupture occurs. An alternative is also offered. The shock-tube may be operated with two diaphragms instead of one. These diaphragms are separated by about six inches. In operation the intermediate chamber is filled to half the driver pressure, such that neither diaphragm is loaded to burst point but that the overall pressure drop across the two does exceed burst pressure. The timer signal now causes the gas in the intermediate chamber to be vented to atmosphere, thus rupturing the diaphragms. Again, the open time of the vent valve can be varied.

The gas handling and powder injection systems are shown in Figure 3, which shows the system of valves used for connecting the driver and intermediate sections for gas filling, test and run operations. It is essential that these valves be connected cor-

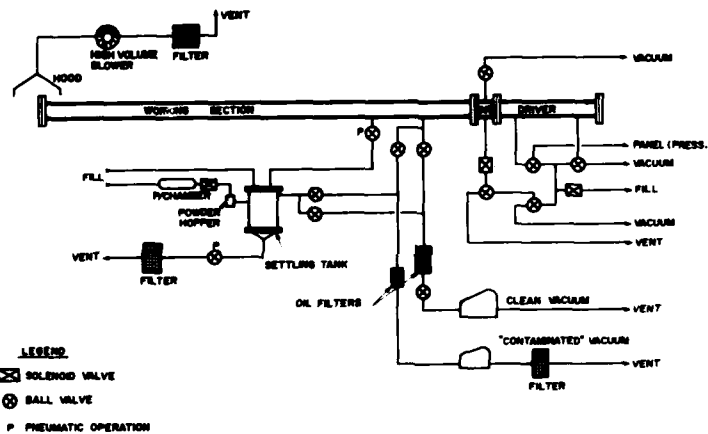


Figure 3. Diagram of Pumping and Gas Handling Systems.

ectly and to avoid accidents they are all fitted with micro-switches which sense their positions. Optical sensors are also placed on all toggle valves on the control panel and also on all vacuum gauge (thermocouple) isolation valves. A control system was constructed for ensuring the safe position of all valves on the shock-tube, and in the powder-injection system, before any gas fill or shock-tube run operation can be implemented.

SAFETY

One aspect of safety has already been considered. The control system ensures that all valves are in a safe position before any gas can be admitted to the driver or intermediate sections, and before the automatic sequence can be started. This protects

the operator and the equipment. Powders may be hazardous to health and it is best to assume that this is the rule. Consequently filters were installed to clean exhaust gases before venting. In addition these gases are mostly vented outside the building. Another hazard occurs when the shock-tube is opened for cleaning and a movable hood is lowered over the end at this time. This hood is connected to a high volume blower and an absolute filter so that there is no danger of a person breathing contaminated air when he opens the shock-tube, see Figure 3.

CONTROL SYSTEM

The control system has three functions,

1. Safety. All valves connecting into the shock-tube must be closed before gas can be admitted into the driver or intermediate sections, or before the automatic sequence can be started. Also the four-way ball valves in the driver gas-handling system have to be set in different positions for the various operations, and the control system ensures that they are correctly set.
2. Automatic operation of the powder-injection and firing sequence. There are several options in this process which are listed below.
3. Set-up and sequence monitoring. During shock-tube preparation there are a number of operations to be performed any of which could easily be overlooked, e.g. loading powder, evacuation of the settling tank, filling tank and pressure chamber. These processes are checked with micro-switches in appropriate places and recorded on a Progress Indicator.

Figure 4 is a block diagram of the elements of the control system, the electronics of which chiefly comprise Transistor-Transistor Logic (TTL) components with LED panel indicators.

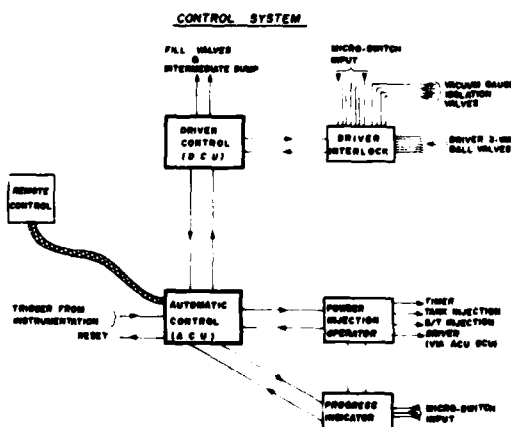
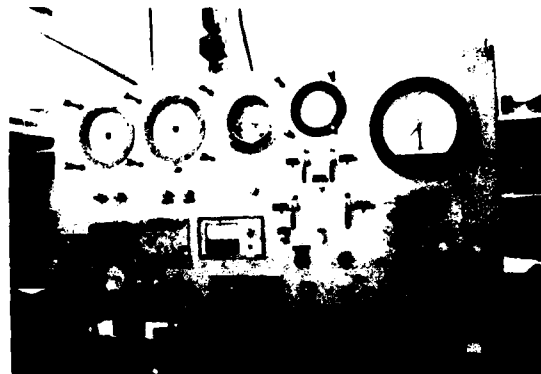


Figure 4. Block Diagram of Shock-Tube Control System.

Wherever possible micro-switches were used on valves that need monitoring but in some situations a photodiode and small incandescent lamp combination was necessary. Figure 5 is a photograph of the control panel showing the elements of the system.

Figure 5. Shock-Tube Control Panel. DCU may be seen on the right, ACU at extreme left and PIU and PIO just left of centre. See text for details.



The functions of these elements are as follows.

- a) Driver Interlock Unit (DIU)
Verifies safe conditions for driver fill, shock-tube run or test conditions. LED panel display indicates status. Verifies that driver three-way ball valves are set correctly: the setting depends on the operation selected.
- b) Driver Control Unit (DCU)
Option selection and driver operation. The options are
 - i) One or two diaphragm operation.
 - ii) Automatic or manual.
 - iii) Test mode. Fill line is routed to the high pressure gauge so that the sequence of operations may be checked without diaphragm rupture.
 - iv) Scavenge of settling tank. This can only be selected when shock-tube is not set to run.
 - v) Pressure switch function. A dual pressure-switch may be used either to set intermediate and driver pressures or for a warning signal and maximum pressure limit control.
- c) Automatic Control Unit (ACU)
Verifies status of driver and powder-injection systems. Issues start, stop and reset commands. Option to switch in automatic stop on receiving input signal from external equipment (e.g. pre-trigger of an oscilloscope or counter). If such a stop occurs any valve in the injection sequence may, optionally, be made to close if open at the time. Re-start issues a reset command to external instrumentation.

d) Powder Injection Operator (PIO)

The sequence of events in the powder-injection operation are

Timer start.

Tank inject. Powder is blown into settling tank.

Shock-tube inject.

Signal to driver. Vents intermediate section with 2-diaphragm operation, otherwise arms fill line for operator.

Signal to driver turned off.

Any of these operations may be performed manually. Also any of them may be switched out of the cycle. Status of each operation is indicated by LEDs.

e) Progress Indicator Unit (PIU)

This unit has five functions.

i) Indicate status of shock-tube preparation and progress in the run sequence with a LED display. Completion of each step is required before the next can be registered and the shock-tube cannot be run until the preparation is complete.

ii) Overrides are provided for most steps.

iii) Manual termination of driver or intermediate section filling, i.e. not controlled by pressure-switch. This is achieved by manually recording completion of the step when the desired pressures (two pressures for 2-diaphragm operation) are reached. Signal of completion is transmitted back to the DCU, necessitating reset of the driver valves before running.

iv) Reset control system for new run.

v) Prevents automatic cycle from repeating even if start button is pressed.

f) Remote Control Unit (RCU)

Attached by cable to ACU this permits remote operation of the shock-tube, with start, stop and equipment reset functions. Some of the indicators of the DCU, ACU and PIU are duplicated.

CONCLUSIONS

This system has been used successfully in spectroscopic studies of metal oxide molecules, an example of which is the work on the spectrum of WO, presented at this symposium by Shin, Cann and Nicholls (1981). The system has proved effective in introducing powders into the shock-tube, increasing safety and in reducing the number of runs failing through human error.

There are a number of variables which affect the performance of the powder-injection operation and the reproducibility of the results. The first of these is the ability to achieve consist-

ently correct pressures in the working section, after expansion from the settling tank. Figure 6 shows that the error here is limited only by the precision of the pressure gauges, Wallace and Tiernen dial gauges in this case. Other variables include the

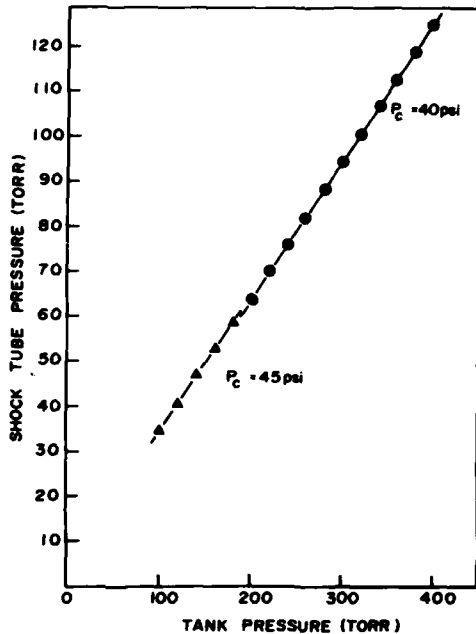


Figure 6. Relationship Between Shock-Tube Pressure and Settling Tank Pressure. Relation is linear to within gauge accuracy.

settling times in the tank and shock-tube as well as the length of time for which the valves are open. All these can be varied quite easily. Optimisation will also depend strongly on the powder itself, and the grinding and filtering processes to which it has been subjected before introduction into the powder hopper. Some studies have been made of these aspects and more are planned. Interested persons may obtain further information from the authors, as it becomes available.

ACKNOWLEDGEMENTS

The authors are much indebted to Dr. W. H. Parkinson, of the Smithsonian-Harvard Observatory, for his advice on the design of this system. The development has been supported by grants to R.W.N. from the National Research Council of Canada, the Defence Research Board of Canada and the Natural Sciences and Research Council of Canada.

REFERENCES

1. Gordon S., McBride B.J., 1971, "Computer Program for Calculation of Complex Equilibrium Compositions, Rocket Performance, Incident and Reflected Shocks, and Chapman-Jouget Detonations", NASA Lewis Research Center, NASA SP-273.
2. Shin J.B., Cann M.W.P., Nicholls R.W., 1981, "Shock-Excited Emission Spectrum of Tungsten Oxide". This symposium.

AD P000231

THE TESTING IN BIA HYPERSONIC GUN TUNNEL

F.G.Zhuang, M.X.Zhao, B.P.He and X.J.Xu

Beijing Institute of Aerodynamics

P.O.Box 7215, Beijing, China

This paper presents the performance of a hypersonic gun tunnel in Beijing Institute of Aerodynamics, describes test techniques and gives several representative experimental results.

The tunnel uses axisymmetrical nozzle with an exit diameter 0.6 meter. The test Mach numbers are from 8 to 15. The test Reynolds numbers are from 1.9×10^6 to 2.6×10^7 per meter. The useful running time is about 25 milliseconds.

This tunnel is equipped with some apparatus developed by ourselves, such as three-component semiconductor strain-gage balance, various types of piezoelectric and strain-gage pressure transducers, thermocouple calorimeters, reservoir thermocouple, thin-film platinum resistance thermometers, schlieren system, and high-speed drum camera, etc.

Several types of measurements can be made in this tunnel: forces, pressures, heat transfer and temperature distributions on a static model, free flight tests, and flow visualization, etc.

In the flow calibration, the reservoir pressure, reservoir temperature and the Pitot pressure were measured. The current operating parameters of this tunnel are tabulated.

Some representative experimental results, such as the free flight tests of standard model HB-2, the force measurements of a 10-degree semiapex angle cone and the heat-transfer distribution on a hemisphere-cylinder model are presented. The given experimental data are compared with theoretical predictions and data from other tunnels. The agreements are fairly well.

GENERAL DESCRIPTIONS OF THE FACILITY

This BIA facility is a light piston hypersonic gun tunnel, its schematic diagram shown in Fig.1. The driver section is 5m long, and the driven section 10m. Both tubes have an internal diameter 130mm. The axisymmetric conical nozzle has a 10-degree semiapex angle, with an exit diameter of 600mm, and three interchangeable throats of diameters 35, 15 and 7.85mm providing nominal Mach numbers 8, 12 and 15 respectively. Two contoured nozzles (for Mach 8 and 12) will be added shortly. The cylindrical test section is 1.8m long, has an internal diameter of 1.2m, with optical glass windows of 450mm diameter on both sides. The capacity of the vacuum tank is 12.5m³. The vacuum pumping system consists of two H150 slide valve pumps, two ZJ-1200 Roots vacuum pumps and one PHB-30 primary air-extracting pump, providing pressures down to about 10⁻³ torr. The compressor system consists of diaphragm compressors G3V and G5Z, providing pressures up to 800 atm.

Prior to a run, the driver section is separated from the driven section by two diaphragms in the double-diaphragm section. The main diaphragm of the double diaphragm section is made of aluminium or stainless steel plate with different thicknesses according to the driver and driven pressures used. The diaphragm is fastened with a hydraulic-auto-holder. The barrel is sealed from the nozzle by an aluminium diaphragm, a plastic diaphragm or a plastic throat-plug. The light piston made of aluminium is placed next to the downstream end of the double-diaphragm section.

This tunnel uses the equilibrium piston technique, that is, the piston weight W_p should be suitably matched with initial pressure ratio of the driver and driven gases P_4/P_1 , so that when the piston comes to rest, no overshoot or intense oscillation would take place. Hence, a substantially constant reservoir pressure could be maintained during useful running time.

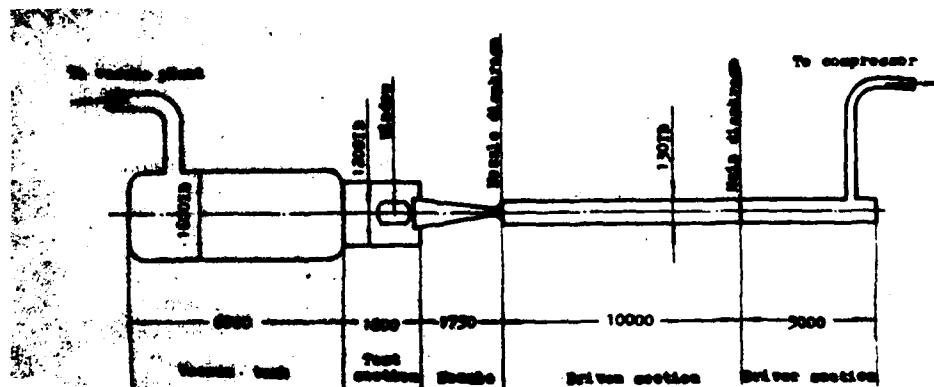


Fig.1 Schematic Diagram of BIA Hypersonic Gun Tunnel

FLOW CALIBRATION

Reservoir pressure was measured by the Institute-developed type AKC-25 piezoelectric pressure transducers, home-built type ZQY-25 and Japan-built type PHF-30W strain pressure transducers. A typical reservoir pressure record trace is shown in Fig. 8. It can be seen from Fig. 8 that the equilibrium condition of the tunnel operation was achieved, and the ratio of the peak pressure \hat{p} to the equilibrium pressure p_e is within the range of $1 \leq \hat{p}/p_e \leq 1.1$. In Fig. 2 the measured reservoir pressure values are compared with the predictions given by the equilibrium piston theory [1,2], indicating that the measured values are about 25% lower than the calculated ones. This discrepancy is supposed mainly due to the clearance leakage between the piston and the barrel internal surface, the friction loss, and the heat loss of the test gas, etc.

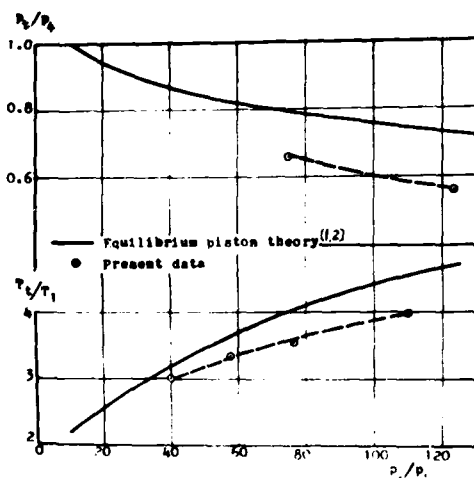
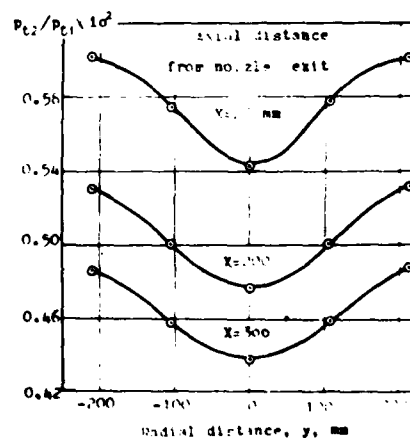


Fig. 2 Reservoir parameter

Fig. 3 Radial pressure distribution, at $M=8$

Reservoir temperature is measured by the Institute-developed chromel-silimel (NiCr-NiSi) thermocouple, which is mounted in the tunnel supply reservoir. Making a compromise between strength and response time we have chosen the thermocouple diameter equal to 0.1mm. In order to protect the thermocouple wire from the impact damage of the compressed dense gas flow, an insulating shielded sleeve made of glass-fiber-reinforced plastic was fitted on the thermocouple. When the reservoir temperatures were measured, a nozzle throat plug was used. The thermocouple temperature reaches its equilibrium value in about 10ms. Since the tunnel useful running time is about 25ms, we have sufficient time which allows to measure the equilibrium temperature in this facility. After data reduction, the variations of the reservoir temperature with the ratio of the driver and driven pressure, p_4/p_1 , were obtained. Fig. 2 shows that the measured reservoir temperatures appear to be 10~15% lower than the predicted values of equilibrium piston theory. Similar to the case of reservoir pressure, these discrepancies are due to the clearance leakage between the piston and the barrel and the friction loss. Besides these, they are also due to the heat loss of the high temperature reservoir gas to the ambient, the heat radiation and heat conduction loss of the ther-

mocouple itself. Nevertheless, the trends either of the measured reservoir pressure or of the measured reservoir temperature variations are in accord with the predicted curves of the equilibrium piston theory.

Pitot pressures in the test section were measured by the Institute-developed type AKC2-23 and AKC2-40 piezoelectric pressure transducers, and type FT foil strain fluctuation pressure transducers. The Pitot rake was equipped with five transducers, with the distance 110mm. Along the axial direction of the test section, surveys were made for three stations, whose axial distances from the nozzle exit were 0, 200, and 300mm, respectively. At each station, both horizontal and vertical Pitot pressure distributions were measured. Typical radial Pitot pressure and axial Mach number distributions are shown in Fig. 3 and Fig. 4. The axial Mach number relative gradients $\Delta M/M$ is about 12% per meter due to conical character of the flow.

The Mach number distributions are calculated from the measured Pitot pressures and the reservoir pressure. After appropriate corrections for real-gas effects, the local Mach number at the measured point can be calculated from the Rayleigh Pitot formula.

The current operating parameters of this tunnel are listed in the Table 1.

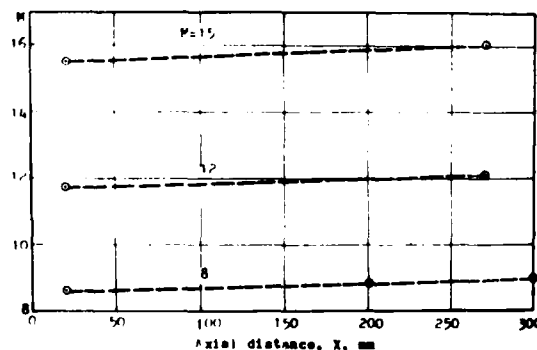


Fig. 4 Axial Mach numbers distribution

Table 1. Operating parameters of the BIA gun tunnel

Nominal Mach number	8		12	15
Nozzle throat diameter, mm	35		15	7.85
Driver pressure, P_4 , kg/cm ²	160	350	160	160
Driven pressure, P_1 , kg/cm ²	1.3	5	1.3	1.3
Piston weight, W_p , kg	0.165	0.50	0.165	0.165
Reservoir pressure, P_t , kg/cm ² predicted measured	116 ~85	280 ~230	116 ~85	116 ~88
Reservoir temperature, T_t , °K predicted measured	1350 ~1150	1120 ~1000	1350 ~1150	1350 ~1150
Test section mean Mach number	8.53	8.52	11.7	15.5
Reynolds number, $Re \times 10^6$, 1/m	7.7	26.3	3.7	1.9
Running time, ms	15	15	25	25

FREE FLIGHT MEASUREMENTS

A constant attitude free-flight measurement technique has been used, in which the model centroid is made to coincide with the center of pressure with a balancing weight, so that the model will move at constant incidence without rotation. Test model, constructed of hard foamed plastics, is initially suspended by thin nylon threads at an angle of attack in test section. When the flow starts, the threads burn away, and the motion of free-flight model can be photographed with multiple-spark recording. About eight distinguishable partially overlapping images can be obtained on the photographic plate. After data reduction, the model accelerations a_x and a_y , along horizontal and vertical direction x and y respectively, can be obtained. Then, the aerodynamic coefficients of the model can be calculated from the given model and flow parameters. The formulas for calculating aerodynamic coefficients are as follows:

$$\text{Drag coefficient, } C_D = \frac{m \cdot a_x}{q_\infty S_r} = \left(\frac{a_x}{a_s} \right) \cdot \left(\frac{W_m}{W_s} \right) \cdot \left(\frac{S_s}{S_r} \right) C_{D_s}$$

$$\text{Lift coefficient, } C_L = \frac{m \cdot a_y}{q_\infty S_r} = \left(\frac{a_y}{a_s} \right) \cdot \left(\frac{W_m}{W_s} \right) \cdot \left(\frac{S_s}{S_r} \right) C_{D_s}$$

where C_{D_s} , a_s , W_s , and S_s are the drag coefficient, acceleration, weight, and the maximum cross-sectional area of the calibration sphere respectively under the same test conditions as that of the model. For a continuum flow, the drag coefficient C_{D_s} of the sphere was assumed to be 0.915. a_x , a_y , W_m , and S_r are the x -directional acceleration, y -directional acceleration, weight, and the reference area of the model, respectively. The axial-force and normal-force coefficients can be calculated from the equations:

$$C_A = C_D \cdot \cos \alpha - C_L \cdot \sin \alpha; \quad C_N = C_L \cdot \cos \alpha + C_D \cdot \sin \alpha.$$

The center of pressure is taken to be at the centroid.

Using the free-flight measurement technique described above, the tests of standard model HB-2 were conducted. The model weight was approximately 10 grams, with centerbody diameter 35mm and total length 171.5mm. The free-stream Mach number, M_∞ , for the tests was 8.5 and the Reynolds number, based on centerbody diameter, was 0.27×10^6 . A set of overlapping images on one photographic plate of the free-flying HB-2 model are shown in Fig. 9. The values of C_N , C_A , and x_{cp}/L obtained are compared in Fig. 5, with force balance and free-flight force data obtained elsewhere. It is observed that the normal-force coefficients obtained here agree with the synthetic curve of AEDC(8) and other test data, the values of pressure center coefficients are somewhat lower than those from the synthetic curve and the ARL test data(4). Part of the reasons for these discrepancies are the effects of the conical flow field. The values of the axial-force coefficients are slightly greater than the data from DVL(6), AEDC(7), and NPL(3).

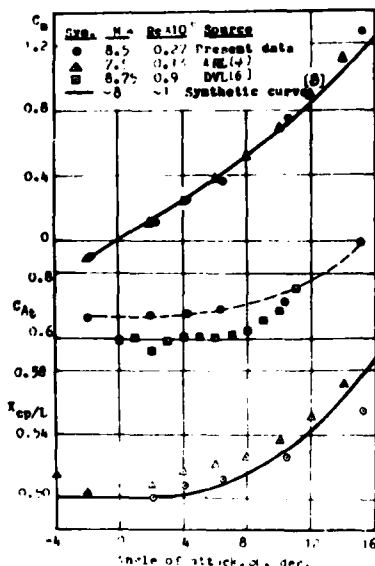


Fig. 5 Force characteristics for Model HB-2

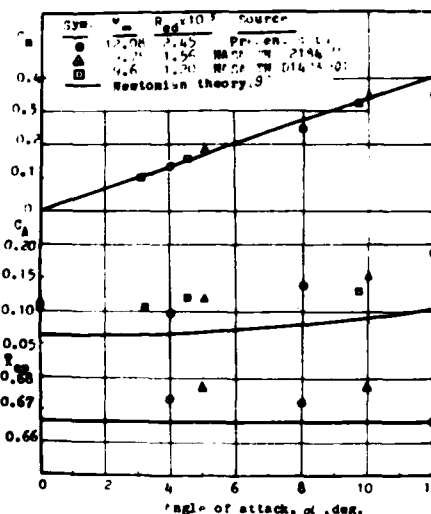


Fig. 6 Force characteristics for a 10° semiapex cone

FORCE BALANCE MEASUREMENTS

Used in the gun tunnel of BIA is the balance TP-B, which is an Institute-developed, inertia uncompensated, three component semiconductor strain-gage balance. The load capacities of the balance are: front normal-force, 2kg; rear normal-force, 2kg; axial-force, 0.5kg.

In an impulse tunnel like this one, it is usually required that the natural frequency of the balance support system should be an order of magnitude higher than the low characteristic frequency of the test flow, so that the high frequency oscillation signals may be filtered out with low-pass filters. But to meet this requirement is difficult. After making some efforts, the lateral and axial natural frequencies of the balance TP-B support system reach 150 and 670Hz respectively. The test cut-off frequency of the low-pass filter was selected as 160–300Hz. If the cut-off frequency is selected too low, it is likely to filter the aerodynamic signal off and make the results distorted. To reduce the impulse effect of the barrel recoil force on the test section, we have designed a flexible connection between the nozzle & test section. The barrel is also fitted with a damping thrust-buffer to absorb the recoil.

To decrease the inertia force withstood by the balance elements, it is necessary to decrease the model weight as much as possible. In one force balance measurements, an aluminium thined shell model was made. It was a 10 degree semiapex angle cone with 70mm base diameter and about 45 grams weight. Typical force balance measured traces are shown in Fig. 10, which indicates that the oscillation of about 150 Hz exists in the normal force waveform, that is caused by the lateral frequency of the balance support systems. In Fig. 6, the measured longitudinal aerodynamic coefficients of the cone model are compared with the Newtonian theory (9) and NASA test data. The test Mach number was 12.08

and Reynolds number, based on diameter, was 2.45×10^5 . In Fig. 6, it can be seen that the measured data give fair agreement with data of NASA (10, 11), and Newtonian theory. The measured values of axial force coefficient are somewhat higher than that predicted by Newtonian theory, this disagreement may be a result of skin-friction effects.

HEAT TRANSFER MEASUREMENTS

The heat transfer rates on test models are measured using the Institute-developed type PM-1 thin-film platinum resistance thermometers, which has a diameter of 3.5mm, and a thin-film thickness of about 0.1 micron. In order to improve accuracy and sensitivity, a Japan-made type DPM-6G dynamic strain amplifier was used in addition to the thin-film thermometers in the heat transfer measuring system. This is suitable to the low heat transfer rate measurements of model surface. To simplify the data reduction of heat transfer rates, a T-shaped thermo-electric analog network was developed according to a scheme proposed by Meyer (12). Thus considering the characteristics of the dynamic strain gage and the analog network used, we arrive at the following expression of the heat transfer rate:

$$q = \frac{2B \times 10^{-6} \cdot R \sqrt{k\rho c}}{\alpha R_0 (R^* \cdot C^*)^{1/2}} \{V_o(t) - V_i(t)\}$$

where R is the precision non-inductive resistance of the dynamic strain-gage bridge box; k, ρ, c , are respectively the coefficients of thermal conductivity, density, and specific heat of the thin film resistance thermometer backing material; α is the resistance thermal coefficient of the thin-film; R^*, C^* are respectively the electrical resistance and the capacitance of the analog network; B is the amplification factor of dynamic strain-gage; and $\{V_o(t) - V_i(t)\}$ is voltage difference on the output resistance of analog network.

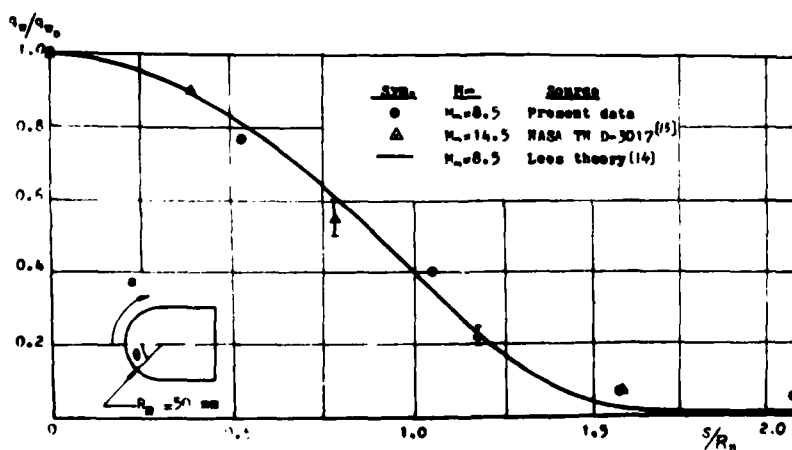


Fig. 7 Heat-transfer on a hemisphere-cylinder

A hemisphere-cylinder model was made for heat transfer measurement. The nose radius of the model was 50mm. The test Mach number was 8.5 and Reynolds number was 0.77×10^6 (based on cylinder diameter). The measured value of the stagnation point heat transfer can be compared reasonably well with the Fay and Riddell's one⁽¹³⁾. The measured value is $9.2 \text{ cal/cm}^2\text{sec}$, and the theoretical calculated value is $9.0 \text{ cal/cm}^2\text{sec}$. The laminar heat transfer distribution of the blunt cone surface at zero angle of attack is calculated by equations of Lees⁽¹⁴⁾. The heat-transfer distribution for the hemisphere-cylinder is plotted in Fig. 7. It can be seen that the present measured data agree closely with the NASA Ames shock tunnel test data⁽¹⁵⁾ and the theoretical curves from the Lees equation.

CONCLUSIONS

At present, the Mach number range of BIA hypersonic gun-tunnel is from 8 to 15, the Reynolds number range is from 1.9×10^6 to 2.6×10^7 per meter, the exit diameter of nozzle is 0.6 meter, and the useful running time is about 25 milliseconds.

From the results of flow calibration, free-flight measurements, force balance measurements, and heat-transfer measurements, it can be concluded that the experimental data from this tunnel agree fairly well with the theoretical predictions and some other corresponding experiments. It was demonstrated that good data could be obtained in the BIA gun tunnel.

REFERENCES

1. R. A. East and L. Pennelegion, ARC CP-607, 1962.
2. L. Davies, J. D. Regan, and K. A. Dolman, ARC CP-982, 1968.
3. L. Pennelegion, R. F. Cash, and M. J. Shilling, ARC CP-934, 1967.
4. A. R. Gilchrist, and M. J. Williams, Note ARL/A346, 1974.
5. K. O. Opalka, BRL-MR 1798 (AD 649254).
6. A. Heyser, W. Wyborny, and H. P. Kabelitz, DLR-FB 66-25, 1966.
7. J. D. Gray, and E. A. Lindsay, AEDC-TDR 63-157, Aug, 1963.
8. J. D. Gray, AEDC-TDR-64-137, (AD 602769), July, 1964.
9. W. R. Wells, and W. O. Armstrong, NASA TR R-127, 1962.
10. C. L. Ladson, and T. A. Blackstock, NASA TN D-1473, Oct. 1962.
11. J. E. Harris, NASA TN D-2184, Nov. 1964.
12. R. F. Meyer, NRC of Canada, Aero. Rept. LR 279, 1960.
13. J. A. Fay, and F. R. Riddell, J. A. S. Vol. 25, No. 2, Feb., 1958.
14. L. Lees, Jet Propulsion, Vol. 26, No. 4, 1956.
15. J. G. Marvin, and C. M. Akin, NASA TN D-3017, Oct., 1962.

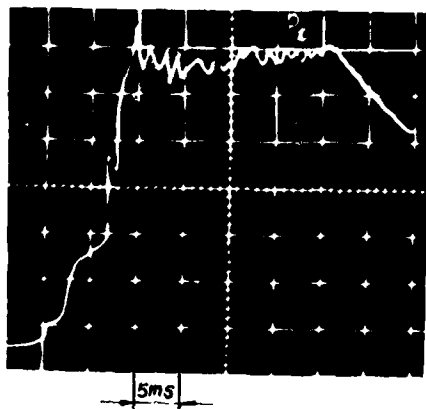
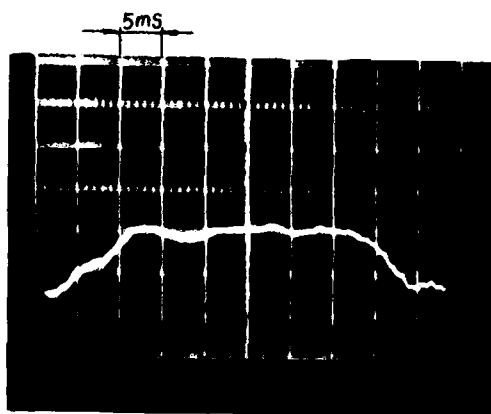


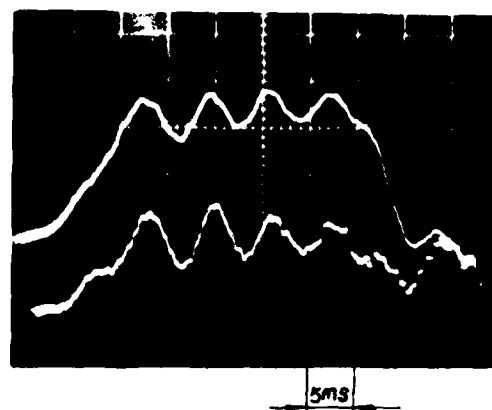
Fig. 8 Reservoir pressure record trace



Fig. 9 HB-2 model multiple spark silhouette



(a) Axial force



(b) Normal force

Fig. 10 Force balance measured trace



AD P000232

AN APPLICATION OF THE MOLECULAR BEAM TIME-OF-FLIGHT TECHNIQUE
TO MEASUREMENTS OF THERMAL BOUNDARY LAYER EFFECTS
ON MASS SAMPLING FROM A SHOCK TUBE

K. Teshima, N. Takahashi and M. Deguchi

Department of Aeronautical Engineering,
Kyoto University, Kyoto, Japan

The conventional time-of-flight (TOF) method was used in shock heated molecular beams. Velocity analyses of TOF signals show that the translational temperature is sufficiently low so that one can assume all the stagnation enthalpy has been converted into the mean mass velocity of the beam molecules, therefore an effective stagnation temperature of the extracted molecules can be calculated using the measured mean mass velocity. For a large extraction orifice (3.2 mm in dia.), it agrees very well with the Rankine-Hugoniot value in a temperature range up to 10,800°K, in case of argon. This technique was applied to measurements of the effective stagnation temperature of sampled gas from a small orifice (50 - 200 μ m in dia.), which is usually used in the shock tube mass sampling and where the gas temperature may be affected during the sampling period by a rapid development of a thermal boundary layer (T_{bl}) at the end wall of the shock tube. An evaluation of the effective stagnation temperature of the sampled gas affected by the T_{bl} growth was made by a simple superposition of an assumed one-dimensional T_{bl} growth and a sampling hemisphere. Comparisons with the experiments show that for appropriate experimental conditions this simple estimation can predict the effective stagnation temperature and its change during the whole sampling period very well.

INTRODUCTION

A shock heated molecular beam (SHMB) is useful for study of the molecular reaction dynamics especially those including internally excited molecules. A time-of-flight (TOF) method to analyze the velocity distribution of the beam molecules can be used to determine their internal states by using the energy conservation and has been used for the conventional molecular beams. For a transient beam like SHMB, other optical methods, e.g. measurements of fluorescences induced by an electron beam or a laser may not be adequate because they need many runs to obtain meaningful data. The use of TOF method in SHMB can give an information about internal energy relaxation process of high temperature gases and can be used to determine their final energy contents in the beam molecules as well as the kinetic energy and its distribution of the beam.

We have used the TOF method in SHMB of argon for a wide range of the source temperature from 1,400 to 10,800°K. For a monatomic gas, the mean mass velocity and its distribution as a parallel translational temperature determined by the measured TOF signal, can give the stagnation temperature using the energy conservation law. Experimental results show that the measured stagnation temperature agrees very well with the Rankine-Hugoniot value, and that the translational temperature of the beam molecules is sufficiently low to assume that all the stagnation enthalpy has been converted into the directional mass motion within 3% error in temperature.

The SHMB is also useful for a shock tube mass sampling, which has been widely used for the study of high temperature reaction kinetics.¹⁾⁻⁷⁾ In this technique high temperature species in the reflected region are extracted into a high vacuum detection chamber through a small orifice (20 - 200 μ m in dia.), so that the detected species may have been subjected to cooling due to a rapid development of a thermal boundary layer (Tbl) at the end wall of the shock tube. A theoretical evaluation of this effect is not easy, because it includes a Tbl growth coupled with an orifice flow and the flow is not one-dimensional near the orifice. Voldner and Trass⁸⁾ have evaluated this effect by numerical works for an orifice flow and by coupling of it with the solution of the Tbl. The application of the TOF technique to such beams extracted from small orifices can give an effective stagnation temperature of the sampled gas as a result of a bulk effect of the Tbl. Experimental results were compared with calculations by a simple superposition of an assumed one-dimensional Tbl growth and a uniform sampling hemisphere surface. Comparisons of these results will be presented and discussed.

TOF TECHNIQUE

A schematic diagram of the apparatus, details of which were reported previously,⁹⁾ and the TOF measurement system is shown in Fig.1. Chopped molecules through a slit on a rotating disk in 47 - 70 μ sec were detected by a quadrupole mass spectrometer and a secondary electron multiplier detector after 104 cm flight. A photocell signal was used to determine the time zero. Argon beams from the reflected region in a wide temperature range from 1,400 - 10,800°K and a pressure range from 1.3 to 6.8 atm were examined. Typical TOF signals

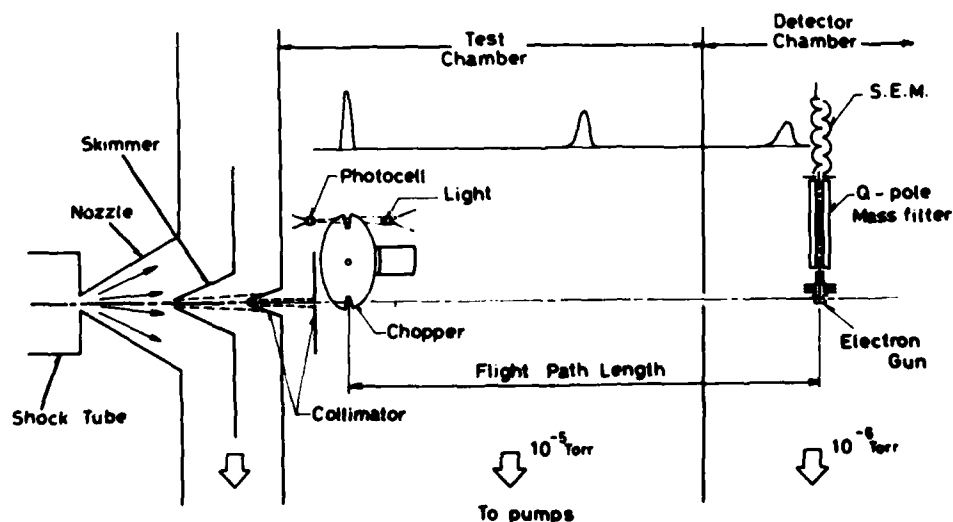


Fig.1 Schematic diagram of SHMB apparatus and TOF measurement system.

are shown in Fig.2 as the lower trace. The upper trace is the photocell signals and the correspondence between them are indicated by numbers. Each TOF signal was fitted to an ellipsoidal Maxwellian in order to determine a translational parallel temperature T_{\parallel} , characterizing the velocity distribution, and was used to determine the mean mass velocity. Although the beam intensity changed for the duration time, the temperature and the mean velocity were almost constant for all TOF signals in a single shot.

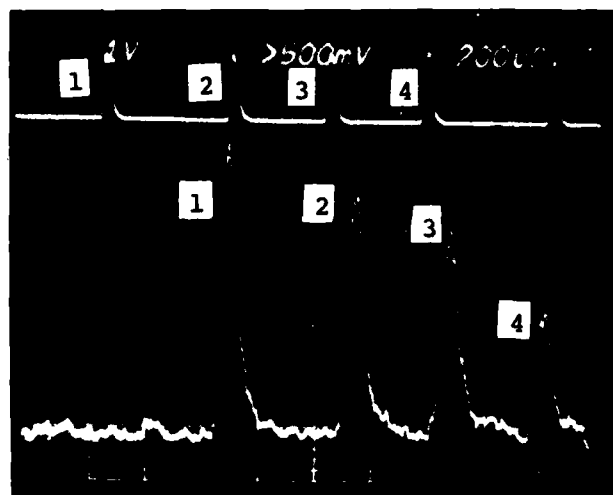


Fig.2
Typical TOF signals (lower trace) and photocell signals (upper trace).
200 μ sec/div.

Fig.3 shows the temperature and the speed ratio of the beam against a scaling parameter which is a measure of the elastic collision effect in the expansion process. A theoretical prediction¹⁰⁾ of the speed ratio for the room temperature monatomic gases is also shown as a solid line. Discussions about the speed ratios of SHMB will be given elsewhere. In Fig.4 the effective stagnation temperature calculated with the measured mean mass velocity and the

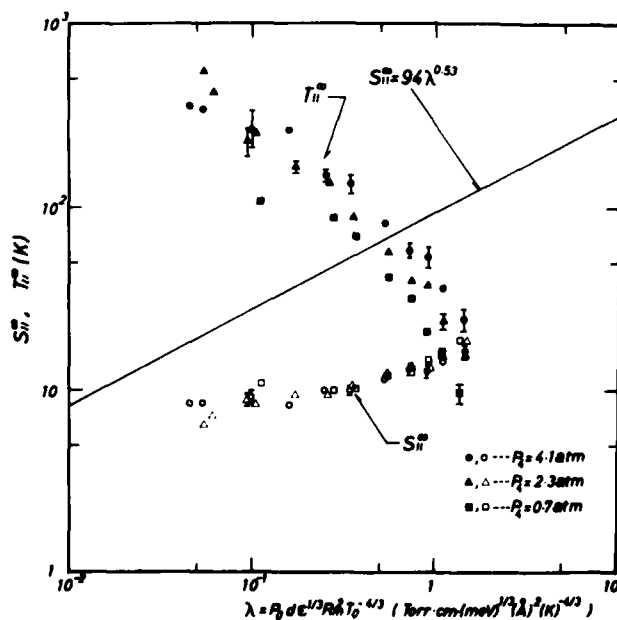


Fig.3
Parallel translational temperature T_{\parallel} , and speed ratio S_{\parallel} of SHMB against a scaling parameter λ , where P_0 is the stagnation pressure, d the nozzle orifice diameter, ϵ and R_m are the potential depth and its location of Lennard-Jones (12-6) potential, respectively and T_c is the stagnation temperature.

translational temperature using the energy conservation, is plotted against the Rankine-Hugoniot values calculated with the measured shock velocities. It can be seen that the measured temperature agrees very well with the ideal frozen temperature up to a high temperature, where the ionization occurs significantly. This is reasonable considering that the ionization relaxation time in our experimental conditions is longer than the beam duration. Experimental results also show that the stagnation temperature can be determined only by the mean mass velocity within a few per cent error. Therefore this technique is applicable to a beam extracted through a small orifice which is usually used in a shock tube mass sampling system, in order to examine the effective stagnation temperature of the sampled gas.

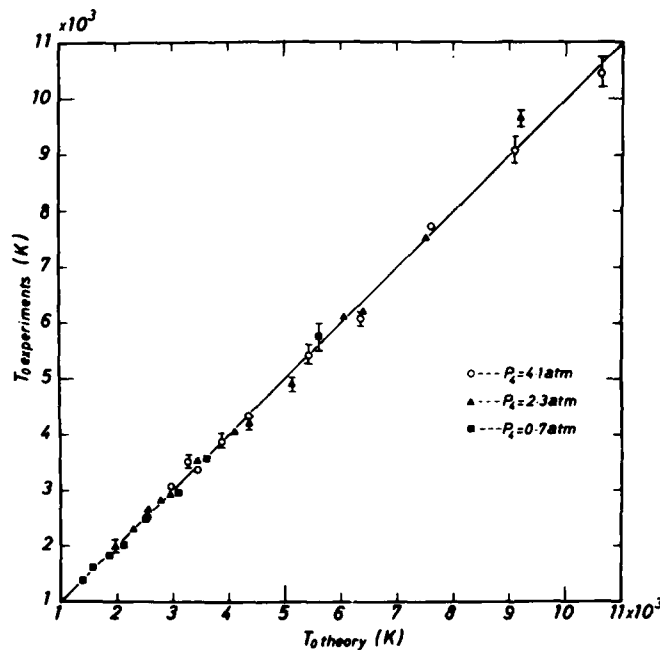


Fig.4
Measured stagnation temperature $T_{0 \text{ experiments}}$ with a large nozzle diameter (3.2 mm) vs the Rankine-Hugoniot value $T_{0 \text{ theory}}$.

SHOCK TUBE MASS SAMPLING SYSTEM

As shown in Fig.5, a small orifice of 50 - 200 μm in its diameter and of 100 μm in its thickness was attached to the end wall of a shock tube to make the surface flush. The expanded flow from the orifice is led to a three stage molecular beam apparatus to make a molecular beam. The first stage, nozzle discharge chamber, was evacuated by a 700 l/sec mechanical booster pump and was kept at a pressure less than 5×10^{-7} Torr when the test gas of 10 - 100 Torr of argon was filled in the low pressure section of the shock tube. The second and third stages, downstream of a skimmer and a collimator, respectively, were evacuated by 600 l/sec oil diffusion pumps and kept at pressures less than 1×10^{-6} Torr. The detector chamber was kept a pressure about 3×10^{-7} Torr. The skimmer was located at a distance of 20 to 100 times of orifice diameter from the orifice so as to obtain a terminal velocity of the expanded flow and also to keep away from disturbances due to the Mach disk of the expanded jet. The molecular beam was chopped into a sequence of short segments by narrow slits on a rotating disk, which was made of 0.1 mm thick and 10 cm diameter stainless steel plate. It had 90 equally spaced, 0.8° width and 10 mm length slits on its periphery and was rotated at 3000 r.p.m., so that it can chop the beam every 200 μsec into a 45 μsec FWHM segment. The disk was manufactured by

a photo-etching technique and the differences in the size of the slits were less than 3 %. The molecules in each segment were detected by the above mentioned detector located at 70.2 cm from the disk. Measurements were made at stagnation temperature ranged from 800 to 4000°K and at pressures from 800 to 1370 Torr. The stagnation pressure was measured at the end wall.

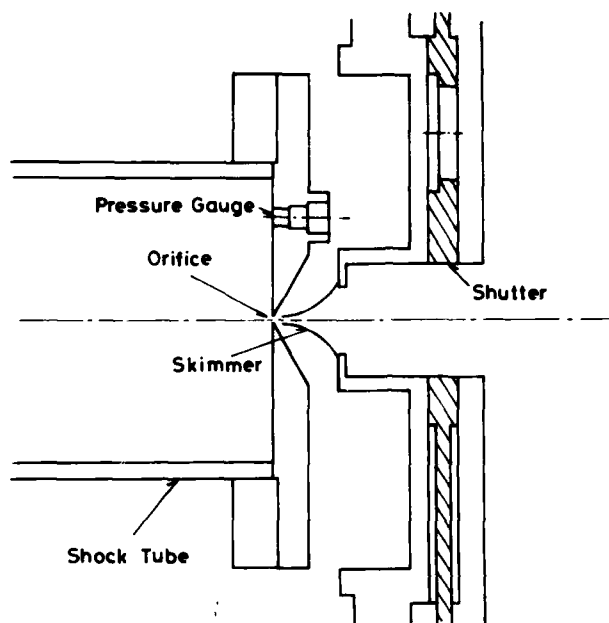


Fig.5
Shock tube mass sampling
apparatus.

EXPERIMENTAL RESULTS

Typical oscillogram traces are shown in Fig.6. The TOF signals are in the middle trace, for which time zeros are shown in the upper trace as the photocell signals. It can be seen that a good agreement between the envelope of the TOF signals and the stagnation pressure history (lower trace). In order to see the correspondencies between the photocell and TOF signals, each fifth slit was masked so as to pass only a part of light through the slit, therefore the TOF signal did not appear for these slits. The correspondence between them is indicated in the figure by circles. From the time difference of these signals and the flight path, the mean mass velocity at each time was obtained. Measurements were made several times for one condition to obtain time dependence of the temperature. The ratio of the measured effective stagnation temperature T to theoretical one T_s are plotted against the sampling time, of which origin is taken as the shock

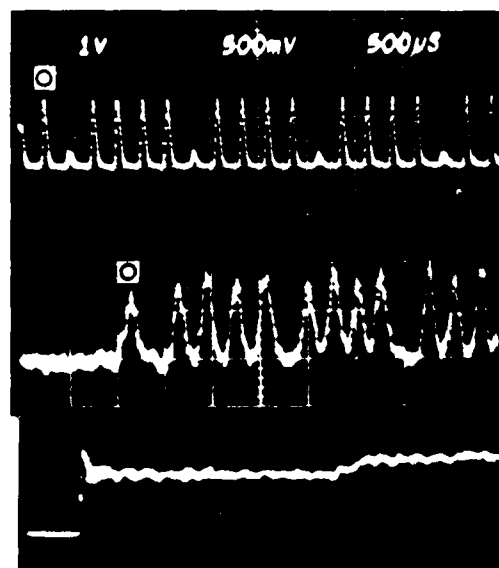


Fig.6 Typical TOF signals (middle) as well as photocell signals (upper) and stagnation pressure (lower). $T_0=1070^\circ\text{K}$ $d=100\text{ }\mu\text{m}$. $500\mu\text{sec/div}$.

arrival time at the end wall, in Fig.7. It shows that for a lower temperature with a larger orifice, the effective stagnation temperature agrees well with the stagnation value for the whole sampling period and for a higher temperature with a smaller orifice, the ratio becomes much smaller than unity and varies with the sampling time. In Fig.8 the effective stagnation temperature at 0.5 msec in the sampling time is plotted against the stagnation temperature for various experimental conditions. It can be seen that for a higher temperature with a smaller orifice the effective stagnation temperature of the sampled gas deviates severely from the true stagnation value.

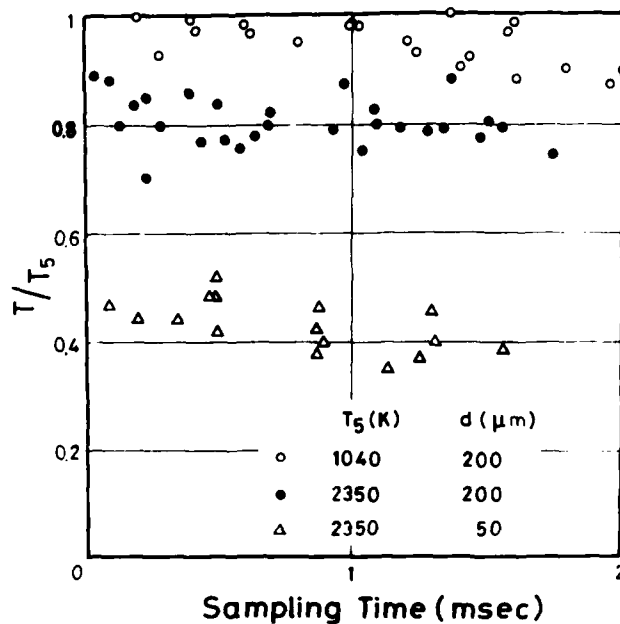


Fig.7
Ratio of the measured effective stagnation temperature T to the Rankine-Hugoniot value T_5 against the sampling time.

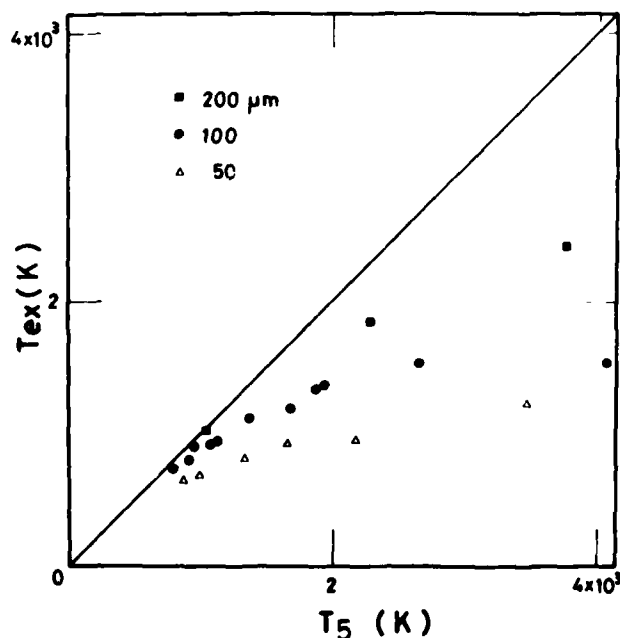


Fig.8
The effective stagnation temperature T_{ex} at 5 msec of sampling time vs the Rankine-Hugoniot value.

COMPARISON WITH A SIMPLE MODEL AND DISCUSSIONS

An exact treatment of the Tbl effect on the sampled gas includes an orifice flow in a Tbl and the numerical method may be realistic only for a very short time after the shock reflection.⁸⁾ If we include the relaxation and chemical reaction process of the species during the sampling process it may become further difficult in the present numerical technique and the computer machine. Here a very simple estimation of the effective stagnation temperature of the sampled gas is made, assuming one-dimensional Tbl growth at the end wall and a uniform sampling from a sampling hemisphere,²⁾ separately. The temperature profiles in the growing Tbl can be calculated using the analysis by Goldworthy¹¹⁾ for a perfect gas with an arbitrary temperature dependence of the thermal conductivity k . We used an empirical relation¹²⁾ of $k = k_w (T/T_w)^{0.682}$, where the suffix w denotes the value at the wall temperature. The radius of the sampling hemisphere can be calculated by the flow rate at the orifice with the stagnation condition at each sampling time. As an effective stagnation temperature of the sampled gas, we take an average surface temperature on this hemisphere immersed in the Tbl whose temperature profile is known, assuming a uniform sampling from the surface.

The calculated temperature are compared with the measured values for several experimental conditions in Fig.9 by solid and broken lines. For a larger diameter orifice at a lower stagnation temperature, the present model can predict the Tbl effect quite satisfactorily for the whole sampling time. But for a smaller orifice at a higher temperature it fails, although the coupling of the Tbl growth with the orifice flow is weak. This seems to be resulted from the assumption of a uniform sampling from the hemisphere surface. For a smaller orifice, cooler gases near the wall flow into the orifice at larger angle than for a larger orifice, then the assumption of the uniform sampling become invalid and underestimate the cooling effect. Therefore the streamline inclination to the wall should be taken into account for such cases, as Voldner and Trass have made.

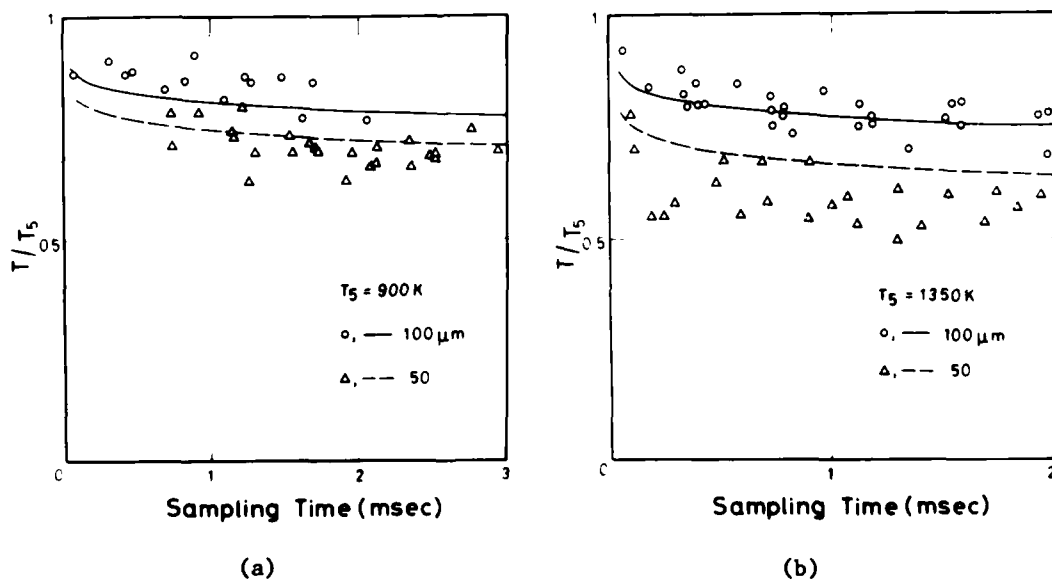
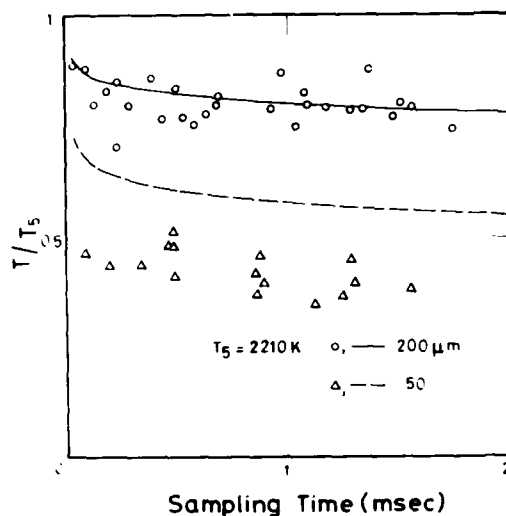
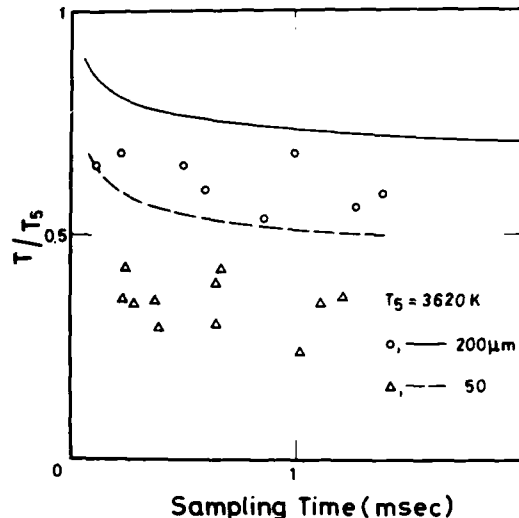


Fig.9 Comparisons of the calculated temperatures with the measured values.



(c)



(d)

REFERENCES

1. J.N. Bradley and G.B. Kistiakowsky, J. Chem. Phys. 35, p.256 (1961). ; ibid. p.264.
2. J.E. Dove and D. McL. Moulton, Proc. Roy. Soc. A 283, p.216 (1965).
3. R.W. Diesen and W.J. Felmlee, J. Chem. Phys. 39, p.2115 (1963). ; ibid. p.2121.
4. D. Gutman, A.J. Hay and R.L. Belford, J. Phys. Chem. 70, p.1786 (1966).; ibid. p.1793.
5. Y. Hidaka, M. Nagayama and M. Suga, Bulletin of Chem. Soc. Japan 51, p.1659 (1978).
6. S.C. Barton and J.E. Dove, Can. J. Chem. 47, p.521 (1969).
7. I. Krizancic, M. Haluk, S.H. Cho and O. Trass, Rev. Sci. Instr. 50, p.909 (1979).
8. E.C. Voldner and O. Trass, Proc. 11th Intern'l Symp. Shock Tubes and Waves, p.490 (1977).; J. Chem. Phys. 73, p.1601 (1980).
9. K. Teshima and N. Takahashi, Proc. Intern'l Symp. Shock Tubes and Waves, p.589 (1979).
10. J.P. Toennies and K. Winkelmann, J. Chem. Phys. 66, p.3965 (1977).
11. F.A. Goldworthy, J. Fluid Mech. 5, p.164 (1959).
12. A. Hirschberg, W.H. von Heugten, J.F.H. Willems and M.E.H. van Dongen, Intern'l J. Mass and Heat Transfer 23, p.799 (1980).

AD P 000233

MEASUREMENT OF DYNAMIC PRESSURE IN SHOCK TUBE

BY STREAK PHOTOGRAPHY

Joseph H. Owren

Marco Scientific, Inc., Sunnyvale, California 94086

and

Robert E. Dannenberg

Kendan Associates, Palo Alto, California 94303

Instrumentation for application of the Mach angle technique to measure dynamic pressure of the stream flow in a shock tube is described. To develop Mach lines suitable for observation, a small conical probe was mounted on axis at the test station. An image converter camera, optics and a standard electronic flash lamp completed the instrumentation. In operation, a Mach cone was generated around the probe following passage of the incident shock wave. Conical flow theory relates the Mach angle to the flow Mach number and dynamic pressure. Photographs of the Mach cone were obtained for framing and streak mode of recording. It was found that a streak record offered the best detail of the flow.

The instrumentation for determining dynamic pressure characteristics was developed for an arc-driven shock tube operating at Mach 7. The test stream flow was to serve as a reference pressure base for the calibration of supersonic total head probes.

INTRODUCTION

When a shock tube is used for a particular study, certain properties of the flow are of primary importance. For example, when calibrating supersonic total head probes, the duration and uniformity of the test gas must be known for proper interpretation of the test results. Calibration or scale factors for the

pressure probes under test are determined by comparison of probe-measured pressures with pressures calculated from normal shock relations based on actual shock speed. It is well known that the shock velocity together with the initial pressure ahead of the shock wave is sufficient to define the equilibrium thermodynamic properties of the shock heated gas. The theoretical normal shock calculations assume a constant level of pressure with time behind the shock (test gas region). In practice, however, the flow velocity may attenuate during the test period and induce changes in the dynamic pressure and, therefore, pitot pressure.

In order that probe calibration studies may be conducted in well understood and characterized flow environments, an experimental technique was developed to measure the time history of the dynamic pressure. The equipment described in this paper was used to evaluate a high pressure test stream of air at Mach 7 ($P_1 = 1 \text{ atm}$) for test time, but more importantly, to measure the uniformity of dynamic pressure for the period between the incident shock and the contact surface.

MACH ANGLE TECHNIQUE

A small conical probe aligned with the flow in a shock tube makes a convenient test fixture. Following the passage of the incident shock wave, a stationary conical shock wave is generated in the stream flow around the probe. Measurement of the angle of the conical shock wave together with the known probe shape will yield the Mach number of the stream flow. For example, Chart 5 in Ref. 1 shows the dependence of shock wave angle on cone semi-vertex angle for various stream Mach numbers. Simplification of the graphical calculations of Ref. 1 is possible if the cone angle is small and the stream Mach number is low, less than approximately 3. Within these limitations, the stream Mach number, M , and the shock wave or Mach angle, θ , are related simply as

$$\frac{1}{M} = \sin \theta \quad (1)$$

Thus for small cones (semivertex angles less than about 6°) variations in stream speed are directly related to changes in the observed Mach angle.

The dynamic pressure, q , is defined as

$$q = \frac{\gamma}{2} P_s M^2 \quad (2)$$

where P_s is the static or side-wall pressure and γ is the specific heat ratio for air. From the measured values of the Mach angle and side-wall pressure, the dynamic pressure can be calculated. For the nominal incident shock Mach number of 7, the flow Mach number was 1.75. The dynamic pressure behind the incident shock was 127.9 atm.

TEST TIME

Prior to the tests to determine the dynamic pressure of the stream flow, a short study was made to evaluate the test time in the shock tube for Mach 7. The instrumentation consisted of an

Imacon (Model 790) image converter camera with its f1.9 spectrograph attachment as indicated in Fig. 1. Measurements were made

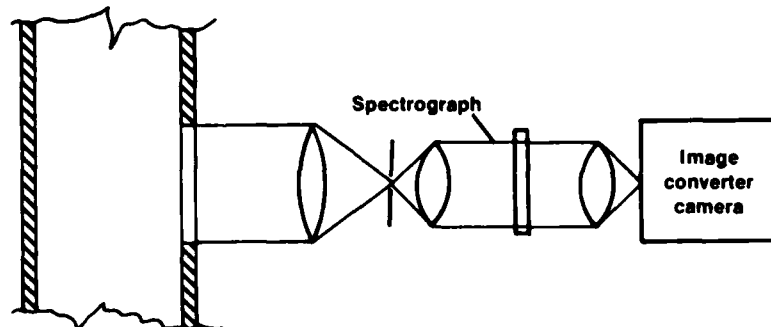


Fig. 1. Time resolved spectrograph.

with the camera operated in the streak mode and with the gas in the shock tube seeded with trace amounts of pure sodium chloride. Streak operation of the camera is discussed later in the text. Photographic records (Fig. 2) of sodium line emission behind

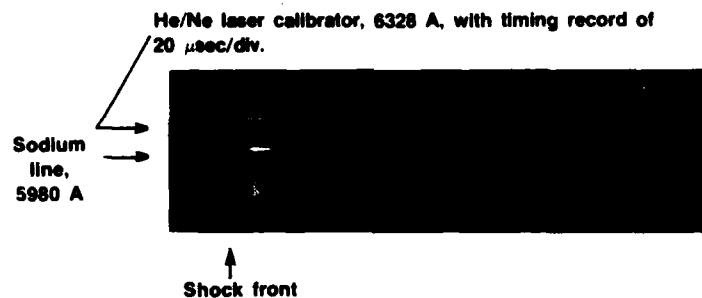


Fig. 2. Spectrograph record.

the incident shock indicated that approximately 95-108 μsec behind the shock front, the radiation extinguished signaling the arrival of the interface region between the test (air) and driver gas.

On the basis of the spectrograph data together with pitot pressure measurements (not shown), it was determined that the overall stream flow was of 160-180 μsec duration. The flow during the first 100 μsec was shocked air followed in the remaining 50-70 μsec by helium which had expanded from the arc chamber. The results dictated that a 200 μsec recording period would cover the flow period of interest in the shock tube.

INSTRUMENTATION SYSTEM

The conical probe and camera system arrangement are suitable for operation for any type of shock tube capable of operation at shock speeds from Mach numbers of about 6 to 20 or more in air. The instrumentation was developed for use with the 10.16-cm diameter shock tube of the arc-driven shock tube facility at NASA-Ames Research Center. Details of the energy storage and arc driver system have been described elsewhere². The shock tube was

operated at Mach number 7 with an initial driven tube pressure of 1 atm of air.

The conical probe had a semivertex angle of 4° with a base diameter of 12.7mm. The general arrangement of the installation in the shock tube is shown in Fig. 3. The test section was

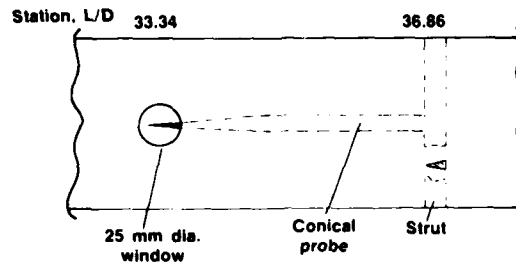


Fig. 3. Test section.

equipped with diametrically opposed ports. The windows mounted in the ports were small, 25mm in diameter, and the interior window surfaces were not contoured to the bore of the shock tube. When installed, the inner surface of the window was mounted flush with the bore (along a meridian diameter) and, therefore, the upper and lower sections of the windows were recessed slightly below the adjacent tube wall by approximately a millimeter. Any waves or disturbances produced by the recessed regions did not appear to cause distortions or interferences in the photographic records. Windows were fabricated from sheets of optical grade Plexiglas. A 20mm thickness was satisfactory for Mach 7 operation. Windows were replaced after every run as their exposed surfaces became crazed and darkened as a result of the shock heating.

The light source for the optics system (Fig. 4) was an ordinary photographic electronic flash, a Sunpak 411. This flash

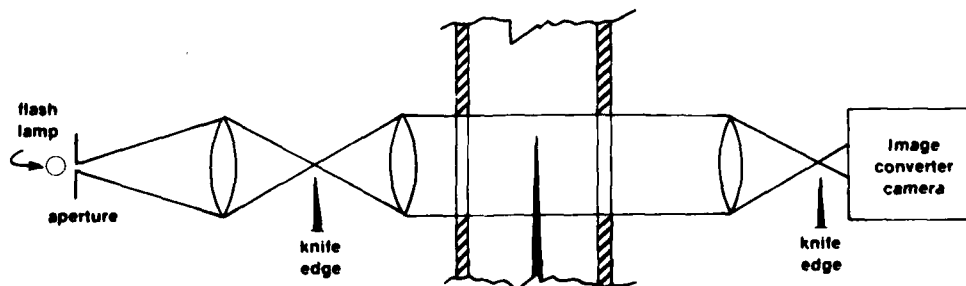


Fig. 4. Optical system.

was selected because it has a reasonably constant level of light output for approximately 250 μ sec. The lamp was masked down with an aperture of approximately 5mm square, and the light was then collected with a 50mm f1.4 lens. This lens was a typical SLR camera lens and was used to image the light to a small spot size where a knife edge was placed. The knife edge was a razor blade. The light was then re-collected with another 50mm f1.4 lens and

collimated to pass through the test section. This system illuminated the needle probe with a uniform field of constant intensity collimated light. A third lens formed an image of the needle at the cathode of the image converter tube. The schlieren system also produced images of shock waves in the field.

The optics and illumination system was designed to take advantage of the unique characteristics of the Imacon camera. The high optical sensitivity of the camera allowed us to use a low powered light source and still provided adequate light for easy adjustment for optimum shock sensitivity. Since the camera provided the shuttering function, we did not have to use short pulse light sources.

The conical shock waves illuminated by the shock sensitive image system were recorded with the camera (Fig. 5) operating in a shuttering or streak mode. The complete optical image is

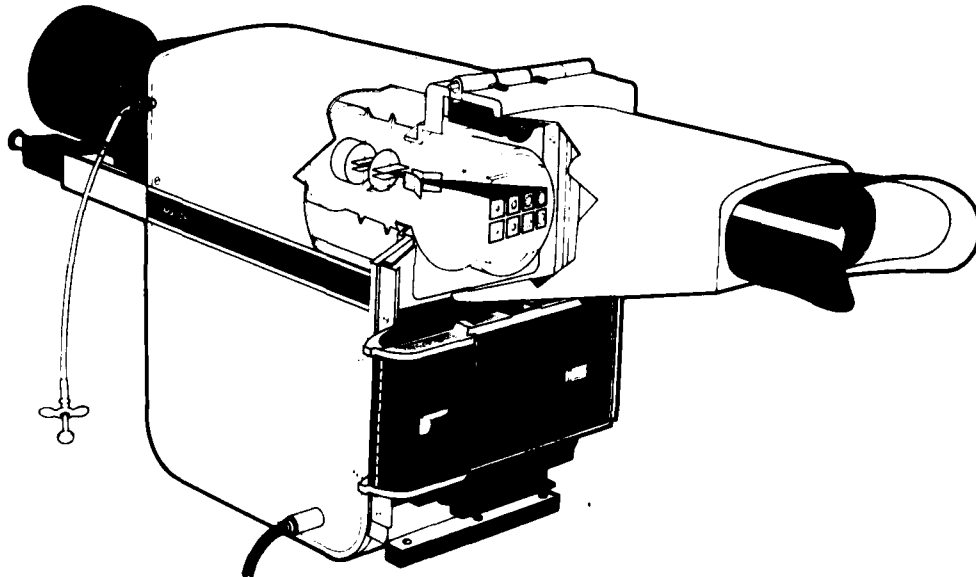


Fig. 5. Imacon 790 image converter camera.

converted into an electron image (by the photocathode) which is transmitted to a phosphor screen where it is again converted into an optical image. The latter image is recorded on Polaroid film. Photographic records were obtained with preset times and selected streak or framing sequences.

In the fast shuttering mode, the camera recorded 8 framing images generally at 5 μsec intervals, each with a 1 μsec exposure time. The equivalent framing rate was 2×10^5 f/s. As the period of the test gas flow was about 200 μsec , and with a camera recording sequence of 35 μsec , several runs were made to detail the entire shock tube flow.

With the streak mode, a single run sufficed to obtain a continuous time history of the flow. For streak operation, the image is optically restricted to a vertical strip by a slit aperture in the primary image plane within the camera. Only a thin slice of the image is observed and swept across the screen

and film at a constant rate. The 200 μsec period of interest for observation was achieved with a streak rate of 2.8 $\mu\text{sec}/\text{mm}$.

The lighting and imaging system was built from common standard components and did not require critical adjustments. Lenses and knife edges were adjusted for optimum resolution and sensitivity without sacrificing too much luminosity. The provision on the Imacon camera for static focusing for picture quality simplified adjustment of the light source and optics on the photocathode of the image converter tube. Both the camera and light source were operated at the times desired by means of adjustable time delay generators. Start signals to the generators were developed from shock detectors located at stations along the shock tube normally used in facility operation to determine the shock velocity.

APPLICATION

Typical framing records of the Mach wave pattern around the probe are shown in Fig. 6. The time that each frame was obtained

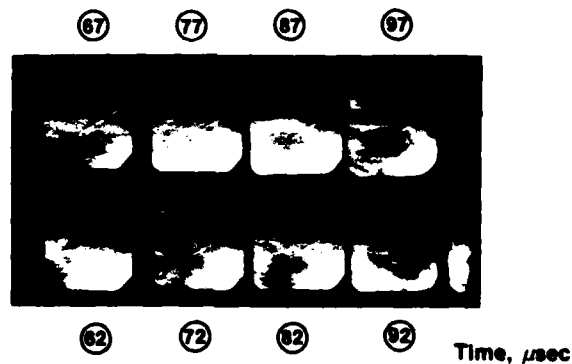


Fig. 6. Framing record.

after the arrival of the incident shock wave at the tip of the probe is indicated on the figure. The sequence of the eight frame recording format was as follows: Frames are read from bottom to top, column by column, from left to right.

Measurements of the Mach angle obtained from framing records are shown in Fig. 7. Several different methods were used to measure the Mach angles. These included enlarging the film, digitizing the wave profile and utilizing various arrangements of protractors and triangles. The most accurate and reproducible measurements were those made directly from the original photographs using an adjustable compass triangle custom scribed with fine reference lines. Measurements were made of the total Mach angle as well as the half-angle. Measurement accuracy was less than $\pm 1^\circ$.

An example of the streak record of the Mach lines is shown in Fig. 8. In this record, the camera was triggered to start

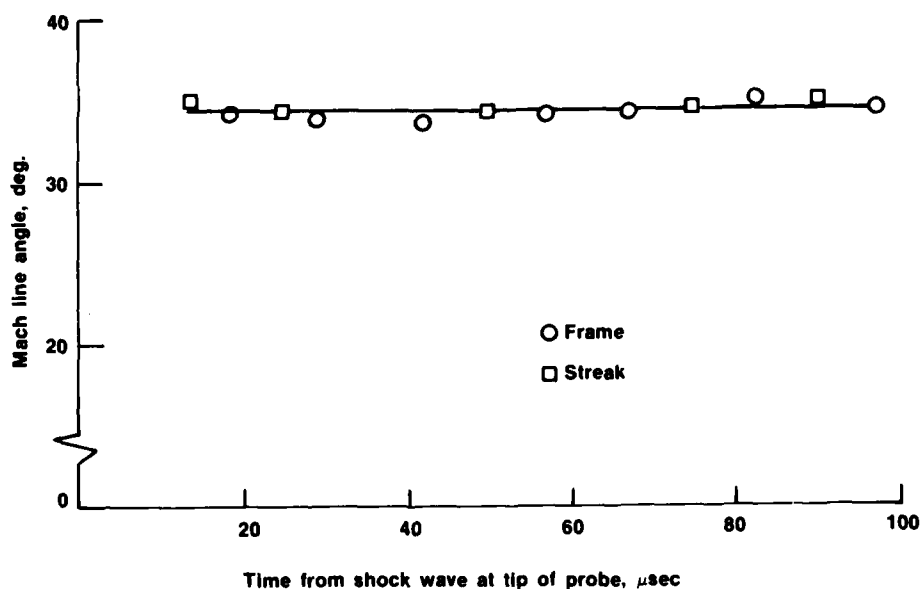


Fig. 7. Mach angle measurements.

recording 20 μsec before the incident shock wave crossed the plane of view. The camera was positioned such that the viewing slit (100 microns wide) was positioned 13mm downstream from the tip of the probe. The streak record displays the two lines representing the sections of the Mach cone (upper and lower edges) intercepted by the viewing slit. A change in the spacing between the lines is indicative of a change in the Mach angle (and dynamic pressure). Measurement resolution was of the order of 0.2mm which corresponded to an angle determination within $\frac{1}{4}$ to $\frac{1}{2}^\circ$.

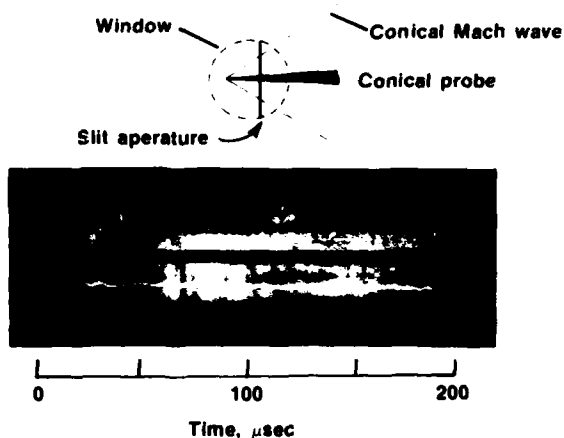


Fig. 8. Streak record.

The spacing between Mach lines measured from streak records indicated that following the development of the Mach cone, the Mach line spacing (and the Mach angle) showed no perceptable change during the remaining period of the test gas flow. It should be mentioned that side wall pressure measurements were also obtained during the run represented in Fig. 8. It will suffice to note here that the (side-wall) measurements agreed with ideal normal shock calculated values and showed no significant variations in magnitude during the test period. Based on the test results, calculations indicated that the dynamic pressure of the test gas stream also was constant.

Mach angles derived from streak records were in good agreement with those obtained from framing records (see Fig. 7). During the analysis of the photographic data, it became evident that one streak record was sufficient to characterize the dynamic pressure of the entire flow field. In addition to providing a representative visual display of the flow on a single record, the effort to obtain dynamic pressure information via streak mode of camera operation was found to require about 1/3 less time (facility runs) than for the framing mode.

CONCLUSIONS

The measurement of Mach angle around a small cone in a shock tube is a useful technique for monitoring and evaluation of the Mach number (and dynamic pressure of the stream flow). The streak type of photograph as obtained with the image converter camera is adequate for data recording. Simple optics and a standard electronic flash lamp complete the instrumentation.

ACKNOWLEDGEMENTS

This work was supported by the Defense Nuclear Agency.

We thank Mr. Frank Kosel, Marco Scientific, for his valuable technical assistance.

REFERENCES

1. Ames Research Staff, "Equations, Tables and Charts for Compressible Flow", NACA TR 1135, 1953.
2. Dannenberg, R. E., "A New Look at Performance Capabilities of Arc-Driven Shock Tubes", Shock Tube and Shock Wave Research, Proceedings of the 11th International Symposium on Shock Tubes and Waves, B. Ahlborn, A. Hertzberg, and D. Russel, eds., University of Washington Press, Seattle, Washington, 416-431 (1978).



AD P000234

MEASUREMENT OF TEMPERATURES IN A SHOCK TUBE
BY COHERENT ANTISTOKES RAMAN SPECTROSCOPY (CARS)

K. KNAPP, F.J. HINDELANG

Fachbereich Luft-und Raumfahrttechnik

Hochschule der Bundeswehr München, 8014 Neubiberg, West Germany

To measure temperatures behind a shock wave the coherent anti-Stokes Raman spectroscopy (CARS) was applied. The optical setup consists of a frequency-doubled, Q-switched Nd-Yag laser, a narrow-band, pulsed dye laser, a colinear optical system and an optical multichannel analyser for recording the scattered CARS beam. The double-diaphragm shock tube is operated with helium and with air as driver gas and air as test gas. The shock wave triggers the laser pulses by means of heat probes and delay electronics at a well defined and reproducible moment. To measure temperatures the wavelength of the dye laser is chosen in such a way that the frequency difference between the two laser beams is identical with a rotational frequency of the ground vibrational state of N₂. The temperature is derived from the intensity ratio of different rotational lines. The experimental results are in good agreement with theoretical data within their error limits of approximately $\pm 10\%$.

INTRODUCTION

The measurement of temperatures in high speed, hot gas flows, especially in the flows behind the shock wave in a shock tube, is a difficult problem. The measuring times are only in the range of microseconds; the known measuring methods are often hindered by strong influences from the flow or the intensities they provide are too small. S. Lederman¹ made an extended review about laser based diagnostic techniques applicable to fluid dynamics and combustion research at the last shock tube symposium in Jerusalem. He also discussed the possibilities of the coherent anti-Stokes Raman spectroscopy (CARS)². Now we have used CARS for the first time as a diagnostic method in shock tube research³.

PRINCIPLES OF CARS

CARS is a nonlinear optical scattering method of laser

light on gas molecules, where the intensity and the wave number of the scattered beam depends on concentration and temperature of the specific gas. The principal experimental setup is quite simple (Fig.1).

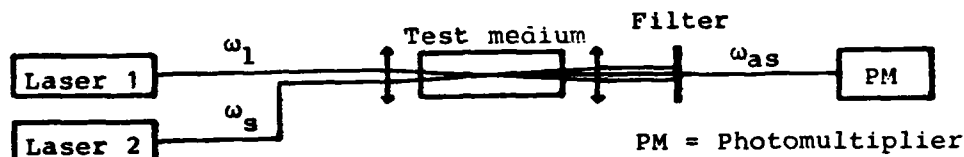


Fig.1: Principal setup for CARS experiments

Two laser beams, the first with a fixed wavenumber ω_1 and the second with a tunable wavenumber ω_s , are focussed simultaneously and colinearly on the test medium. After passing the test cell the two laser beams are separated by filters from the generated, laser-like anti-Stokes beam, which then can be measured by a photomultiplier for example.

The CARS process can be calculated in a semiclassical model by nonlinear frequency mixing of electromagnetic waves (light) within a polarizable medium (gas). The theory yields for the generated CARS intensity I_{as} the following, important dependencies⁴:

$$I_{as} \sim |\chi^{(3)}|^2 \cdot I_1^2 \cdot I_s \quad (1)$$

with

$$\chi^{(3)} \sim \Delta N(v, J) \frac{\omega_{v, J}}{\omega_{v, J}^2 - (\omega_1 - \omega_s)^2 - i \cdot 2\Gamma \cdot (\omega_1 - \omega_s)} \quad (2)$$

$$\Delta N(v, J) := N \left(\frac{N(v, J)}{N} - \frac{N(v', J')}{N} \right) \quad (3)$$

$\chi^{(3)}$ = susceptibility of the 3rd order

I_1, I_s = laser intensities

N = concentration of the specific gas molecules

$\frac{N(v, J)}{N}$ = relative population number of a molecular state with quantum numbers v and J

$\omega_{v, J}$ = wavenumber of a particular transition from $(v, J) \rightarrow (v', J')$

Γ = Raman line width

The following statements can be derived from the above formulas:

- a) The CARS intensity depends on the concentration of the molecules and on the relative population number, which in thermodynamic equilibrium is a function only of the temperature (Boltzmann distribution). CARS is a measuring method for concentration and temperature.

- b) By tuning the laser wavenumber ω_s a CARS spectrum can be generated. In the resonance case, i.e.

$$\omega_1 - \omega_s = \omega_{v,J} \quad (4)$$

or expressed differently

$$2 \cdot \omega_1 - \omega_s = \omega_{as} \quad (5)$$

with ω_{as} = wavenumber of the CARS signal

one gets a peak intensity in the spectrum.

- c) The dependence of the CARS intensity on the cube of the laser intensity leads in comparison with the spontaneous Raman spectroscopy to signal intensities, which are many magnitudes higher.

Fig.2a demonstrates a typical CARS spectrum that we get in experiments in stationary test systems. It shows the N_2 -spectrum of the rotation-vibrational Q-branch, recorded in a premixed propane/air flame.

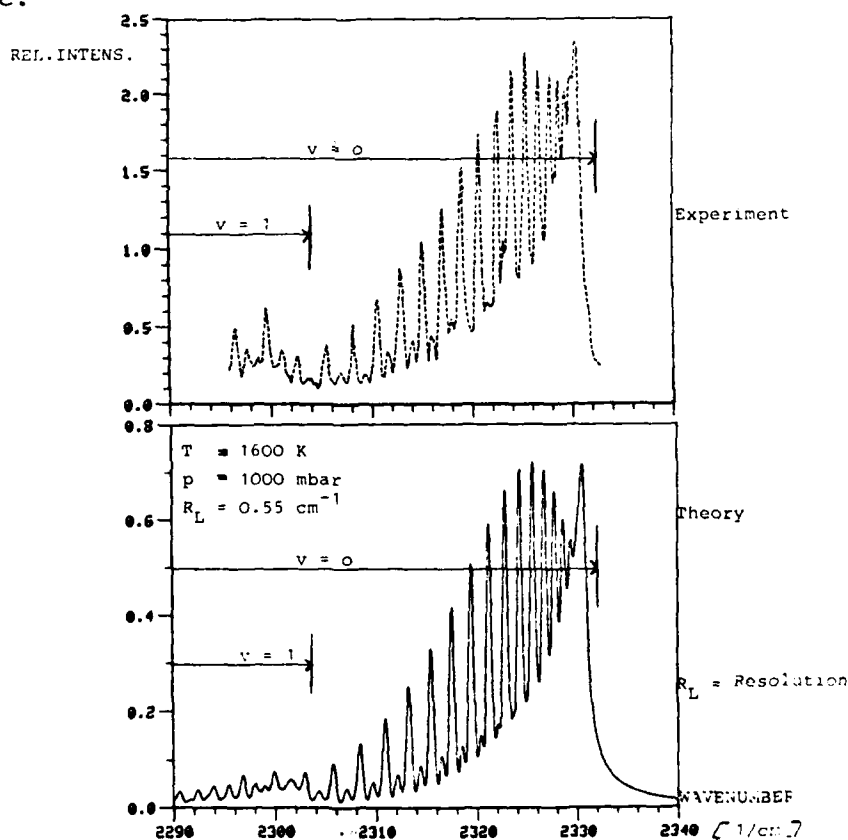


Fig.2: N_2 -CARS spectrum in a propane flame,
(a) experiment, (b) theory

The rotational lines within the ($v=0$)- and ($v=1$)-branch are clearly resolved: a result which cannot be obtained with classical spectroscopic methods because of the poor resolution of the monochromators. With CARS the resolution is given only by the laser line widths. In our experiments the resolution was $R_L = 0.55 \text{ cm}^{-1}$.

To derive the temperature a computer simulation of the CARS spectrum is necessary, a simulation which takes into account the line broadening effects of pressure and temperature and the influence of laser line widths (Fig.2b). By variation of the temperature in the computer program we get for our flame measurements a temperature of $T = 1600 \pm 100$ K. Fig.2 also shows that for the temperature evaluation the measurement of intensity ratios of line maxima is sufficient. This method was used in our shock tube experiments.

EXPERIMENTAL SETUP

The experimental setup for our CARS experiments in the shock tube is shown in Fig.3. It consists of a conventional, double-diaphragm shock tube, a laser system, an optical setup and detection and trigger electronics. The driven tube of the shock tube has a length of 12 m and a tube diameter of 10 cm. Helium and air are used as driver gases, air as test gas. Shock Mach numbers in the range of $3 \leq M_s \leq 6.5$ are obtained. Heat probes (S1-S3) are installed at different points in the tube wall to measure the velocity of the shock wave and to trigger the electronics.

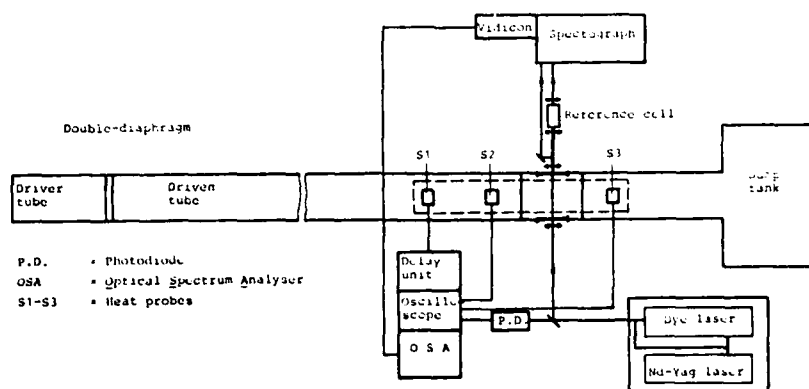


Fig.3: Experimental setup for CARS experiments in a shock tube

The laser system (Quantel Corp., France) consists of a pockelscell-switched Nd-Yag laser with an amplifier and a KDP frequency doubler. The power of the laser is 8 MW for a 15 nsec pulse at a wavelength of $\lambda_1 = 532$ nm. 20% of this output is used as the first beam which is necessary for the CARS process and which has the wavenumber $\omega_1 = 1/\lambda_1$. The main part of the output is used to pump a dye oscillator and amplifier which provides the λ_s beam. The dye laser has a power of 0.7 MW, 15 nsec pulse at $\lambda_s = 550 - 700$ nm and a line width of 0.2 cm^{-1} .

The two laser beams are focussed simultaneously and colinearly on the shock tube. Because of the strong dependence on the laser intensities the CARS beam is generated in a small focal volume

with a diameter of $30\text{ }\mu\text{m}$ and a length of 2 mm , which is an excellent spatial resolution. The CARS signal is reflected by a dichroitic mirror and focussed to the entrance slit of a spectrograph. The two laser beams which pass the mirror are focussed again on a high pressure cell filled with Xenon ($p=5\text{ bar}$). There, a nonresonant, (i. e. independent of wavenumbers) CARS reference signal is generated, which only depends on the laser intensities and fluctuations. The reference beam is also directed to the spectrograph. Different filters and also the spectrograph are used to absorb the laser beams and stray light. With an optical multichannel system (B&M spektronik, West Germany) the CARS and the reference beam are received at the exit slit of the spectrograph and displayed on a screen (Fig.4).

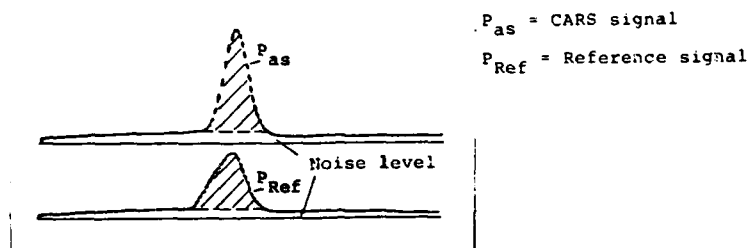


Fig.4: Typical signals on the screen of the optical multichannel system

The ratio between the signals P_{as} and P_{Ref} provides a CARS signal which is nearly independent of laser intensities and fluctuations. Thus, we reduce fluctuations of the CARS intensity from shot to shot to only $\pm 7\%$.

The exact synchronisation of the shock wave and the laser pulse is an important experimental problem, because of the short times which are involved. Fig.5 shows the trigger and delay electronics by which measuring points behind the shock wave can be chosen in such a way as to be reproducible with an accuracy of $\pm 4\text{ }\mu\text{sec}$.

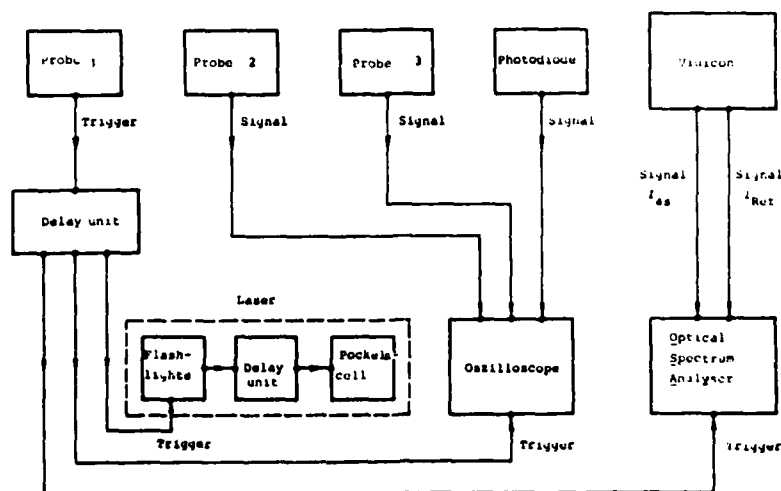


Fig.5: Trigger and delay electronics for the synchronisation of the shock wave and the laser pulse

A shock tube experiment starts with the tuning in the CARS spectrum to the maximum of a rotational line which can be resolved at the test gas pressure ahead of the shock (Fig.6).

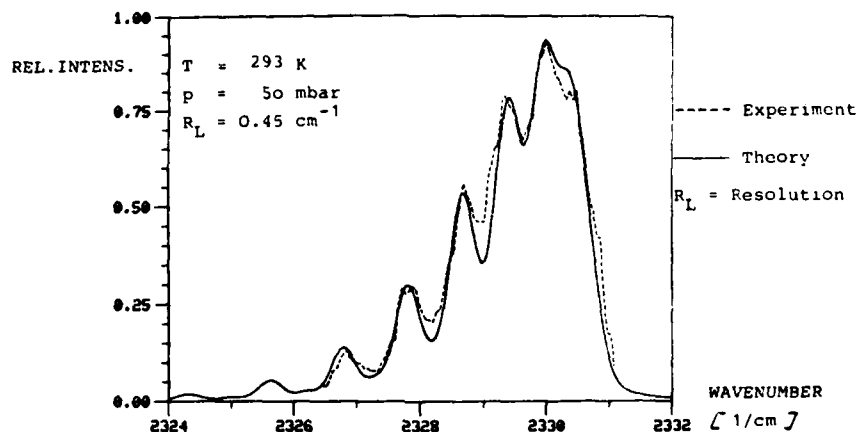


Fig.6: N₂-CARS spectrum at the test gas pressure of 50 mbar

A measuring point with the distance x from the shock wave is preselected by means of the delay electronics. After preparation of all electrical and optical units a shock tube shot is released. For the next experiment another rotational line is chosen.

RESULTS

In such a way we obtained the CARS intensities of different rotational lines in dependence on the distance x behind the shock and on the shock Mach number. We did experiments with three different Mach numbers: $M_s = 3.33, 5.25$ and 6.40 . Fig.7 shows two typical results for the CARS intensities. The intensity values are related to the values ahead of the shock. The measuring points are fitted by an exponential curve.

To derive the temperatures, first the ratios of the line intensities behind the shock are calculated. Therefore the CARS intensities (Fig.7) are divided by each other and corrected with the ratio of the lines ahead of the shock. Fig.8 shows a result which is typical for all our experiment. Within the error limits of $\pm 8\%$ for the CARS intensity ratios at a fixed point x , it follows that the ratio of the line maxima and therefore the rotational temperature behind the shock wave are constant.

The temperature is quantitatively determined by a comparison of the experimentally obtained intensity ratios with the calculated intensity ratios of the line maxima. Fig.9 shows for $M_s = 5.25$ the calibration curve together with the experimental quotient (Fig.8). It provides a mean rotational temperature.

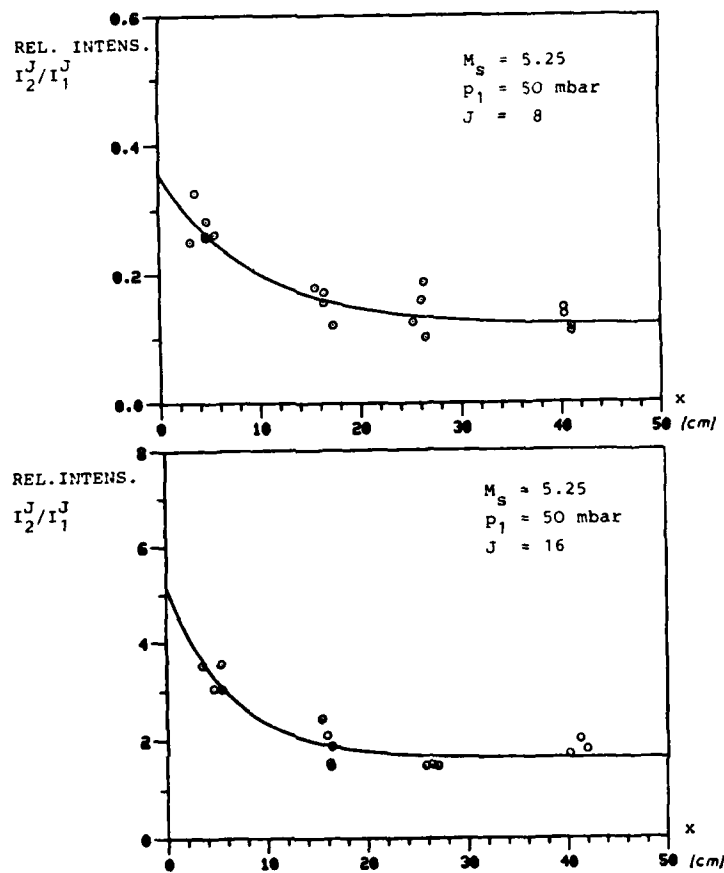


Fig.7: CARS intensities versus distance x behind the shock

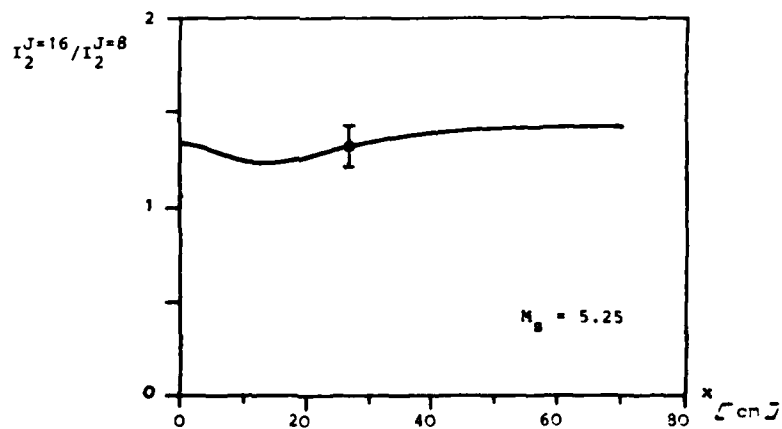


Fig.8: CARS intensity ratios of two rotational lines versus distance x behind the shock

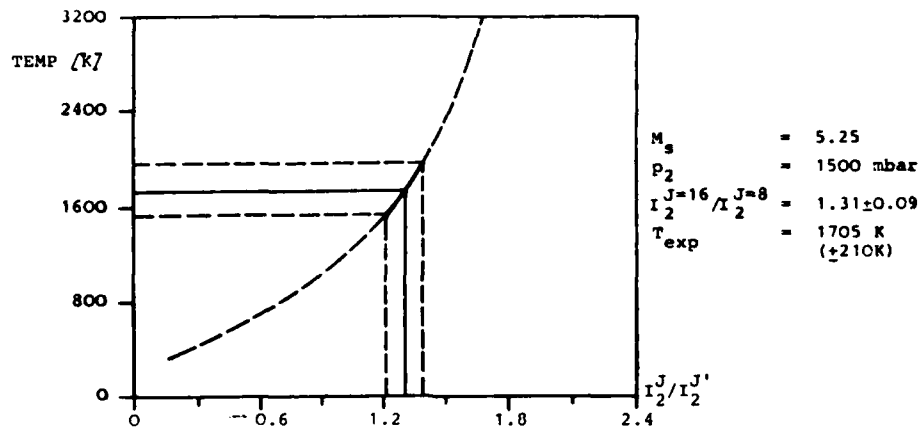


Fig.9: Calculated calibration curve for the temperatures together with the experimental result for $M_s = 5.25$

In a shock wave in air the rotation of the molecules is completely excited within the thin shock front, so that the rotation and translation are in an equilibrium. That means the measured rotational temperature is identical with the gas temperature. Fig.10 shows the experimental results at the tested Mach numbers compared with the calculated temperatures from theories of a plane shock wave with ideal and real gas behavior.

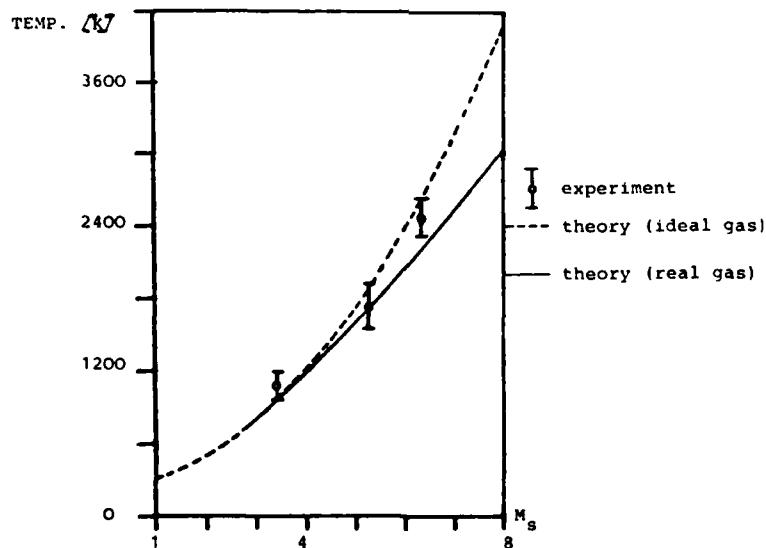


Fig.10: Experimentally derived temperatures in comparison with calculated temperatures

The agreement between experiment and theory is very good within the error limit of approximately $\pm 10\%$ for our temperature measurements.

Finally we have to explain the effect of the strong decay in the CARS intensity behind the shock (Fig.7), which was observed at every Mach number and every rotational line. Because of the

dependence of the CARS intensity on the relative population number (see: (1) - (3)) you could suppose that the strong decay in the intensity is caused by a change in the vibrational population number, that is by vibrational relaxation. But that is not the case because the measured strong intensity decay and the duration of the decay are in no agreement with calculated changes in CARS intensities during vibrational relaxation, and also in no agreement with measured and calculated vibrational relaxation times ⁵.

A comparison with our own interferometric measurements in the increasing turbulent wall boundary behind the shock ⁶ shows a very good agreement between the duration for the building up of a stationary boundary layer and the duration of the CARS intensity decay to a constant signal. Furthermore, if you use some estimations about the defocussing of laser beams in turbulent flows ⁷ and take into account the strong dependence of the CARS intensity on the laser intensities, it is obvious that the increasing boundary layer behind the shock extends the focal volume and therefore reduces the CARS intensity. So we were able to prove for the first time the influence of turbulent structures in flows on CARS measurements which was suspected by several other CARS experimentalists ^{1,8,9}.

The measurement of temperatures by CARS is not influenced by this effect, because temperatures are derived from intensity ratios which are generated under identical experimental conditions, that is with identical boundary layer thickness. The measurement of concentrations is complicated by this effect.

CONCLUSION

With these experiments CARS was successfully applied in a shock tube for the first time. We have been able to demonstrate that CARS is a new promising diagnostic tool for measuring temperatures or relative population numbers of molecular states, which also works reliably in the short time, high speed, hot gas flow in a shock tube. The accuracy of the temperature evaluation reaches + 10%.

REFERENCES

1. S. Lederman: Proc. 12th Int.Symp. Shock Tubes and Waves, Jerusalem 1979
2. J.P. Taran, P. Regnier: Appl.Phys.Lett.23, p.240-246 (1973)
3. K. Knapp: Thesis, Hochschule der Bundeswehr München, 1981
4. N. Bloembergen: Nonlinear Optics, Benjamin, N.Y. 1977
5. J.D. Lambert: Vibrational and Rotational Relaxation in Gases, Clarendon, Oxford 1977
6. K. Knapp, C.-P.Schneider, F.J.Hindelang: Proposed for: ICIASF, Dayton, Ohio, USA 30.9.-2.10.1981
7. N.-S. Hong, A.R. Jones, F.J.Weinberg: Proc.R.Soc.London, A 353, p.77-85 (1977)
8. I.A. Stenhouse, D.R. Williams, J.B. Cole, M.D. Swords: Appl.Opt.18, no.22, p.3819-3825 (1979)
9. A.C. Eckbreth: Comb.Flame 39, p.133-147 (1980)

TEMPERATURE MEASUREMENT OF DETONATION USING UV-ABSORPTION OF O_2

Takao Tsuboi, Makoto Egawa, Hiroshi Kobayashi, Tsuneo Hirose,
Masaki Kamei and Yoshihiko Teranaka

Faculty of Engineering, Yokohama National University
156 Tokiwadai, Hodogaya-ku, Yokohama, 240 Japan

Temperature-dependent molar extinction coefficients of O_2 were measured behind reflected shock waves. Using this temperature dependence of the molar extinction coefficients, the overall temperature profiles of H_2-O_2 detonation were obtained within an error of 10% and with micro-second time resolution. The temperatures measured at C-J point were nearly the same as the calculated. However, the precise observation of the absorption signal showed that the gas temperature fluctuated shortly after the detonation front. In the super detonation zone, the highest gas temperature was much higher than the temperature at the C-J point. There are two methods for this temperature measurement: (1) When the partial pressure of the absorbing species is measured, the temperature profile can be obtained by measuring the absorption profile of one suitable wavelength. (2) When the partial pressure of the species is not obtained, one must observe the absorption profile of two wavelengths.

By using the result that the temperatures of the detonation gas were high, the deformation of a needle was examined in the detonation gas.

INTRODUCTION

In order to know the gas state of detonation, the velocity and the pressure were often measured with various techniques.¹⁻⁴ However, the temperature of the detonation was usually calculated from the velocity using the ZND-model,¹ because there are some difficulties in measuring the temperature directly.

Some groups were successful in measuring the temperature: Soloukhin measured the detonation temperature from the intensities of the two Balmer H-lines and the highest temperature was about 5000 K.⁴ Penzias et al.⁵ obtained the temperature of detonation as well as of shock waves by measuring infrared emission and absorption. They found that the H_2O and CO_2 temperatures agreed

AD P000235

with the temperatures calculated at C-J point. Gaydon et al.⁶ measured the temperatures of the shock-initiated detonation by a spectrum-line reversal method using a chromium line. Terao et al. measured the electron- and gas-temperatures by the double probe method, by the spectrum-line reversal method using argon line, and by the laser light scattering method.^{7,8} They found much higher temperatures than the temperatures at C-J point. These results show that the detonation temperatures are different from each other, probably depending on the species used for the measurement. Therefore, further studies of the temperature of detonation are needed. Recently we proposed a UV-absorption technique for temperature measurement, which has microseconds-time-resolution, and we showed the possibility of measuring the temperature of detonation.⁹

Using this technique the detonation temperatures in C-J condition and other conditions were measured.

METHOD AND THEORY

The light absorption is described by the Lambert-Beer's law. One form of the law is

$$\frac{I}{I_0} = 10^{-\epsilon c l} \quad (1)$$

Here, I_0 is the intensity of the incident light; I is the intensity transmitted through the column of absorbing species of concentration c (mol/cm³); l (cm) is the absorption path length; and ϵ (cm²/mol) is the decadic molar extinction coefficient of the absorbing species at the given wavelength. When one uses the partial pressure P_{partial} (Pa) instead of the concentration of the species, equation (1) can be written as

$$\frac{\epsilon}{T} = \frac{R}{P_{\text{partial}} l} \log_{10} \left(\frac{I}{I_0} \right) \quad (2)$$

Here, the gas constant R is 8.314×10^6 Pa cm³/mol K and the coefficient ϵ depends on the concentration N_i of the lower energy level E_i of light absorption at the given wavelength. From the statistical thermodynamics one obtains for N_i

$$N_i = c \frac{g_i}{Z} \exp(-E_i/RT) \quad (3)$$

where c is the total density of the absorbing species; Z is partition function of the species; g_i is the degeneracy of energy level E_i . The coefficient ϵ is, therefore, temperature-dependent. One can measure the ϵ -values in advance by using shock tube technique. Therefore, when the partial pressure and the ratio I/I_0 can be measured, the temperature for a given species can be obtained by Eq. (2). (Method I)

When one can not measure the partial pressure of absorbing species, one has to measure the ratios I/I_0 at two wavelengths. Namely, one obtains the ratio $\eta(\lambda_1, \lambda_2, T)$ of the decadic molar extinction coefficients $\epsilon(T, \lambda_1)$ and $\epsilon(T, \lambda_2)$ at two wavelengths in advance by using shock tube, then the Equation (2) gives

$$\eta(\lambda_1, \lambda_2, T) = \frac{\epsilon(\lambda_1, T)}{\epsilon(\lambda_2, T)} = \frac{\log_{10}(I_{01}/I_1)}{\log_{10}(I_{02}/I_2)} \quad (4)$$

When one measures the ratios I_{01}/I_1 and I_{02}/I_2 of the absorbing species, he can determine the temperature of the species. (Method II)

RESULTS

Using above mentioned techniques the gas temperatures of H_2 - O_2 detonation were measured. The UV-absorption band of oxygen-molecule was applied to measurement. Figure 1 shows the experimental arrangement of the detonation tube. Figure 2-a gives the decadic molar extinction coefficients of oxygen-molecule. Figure 2-b shows that the total gas density did not influence the molar extinction coefficients. Figure 2-c shows also that the molar fraction of the oxygen in the gas did not influence the molar extinction coefficient. Namely, there was no influence of the pressure broadening of oxygen. The temperature dependences ϵ/T are given in Fig. 3. Figure 4 shows that only the oxygen-molecule absorbs the light at the wavelengths of the UV-range in the H_2 - O_2 detonation, because the wavelength dependences of I/I_0 of the detonation gas and of the oxygen-molecule resemble each other.

Figure 5 shows the observed absorption profile of the

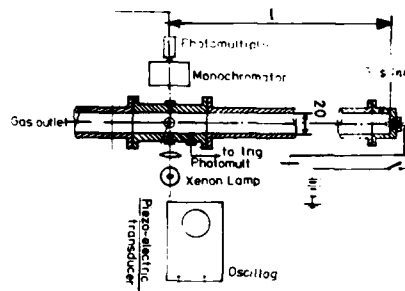


Figure 1. Detonation tube.

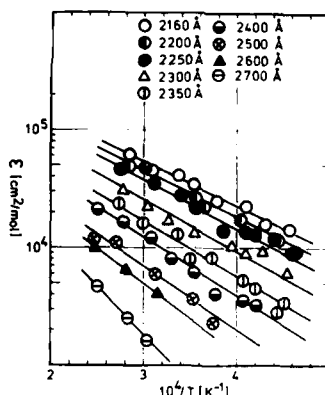


Figure 2-a. Temperature-dependence of decadic molar extinction coefficients of O_2 at various wavelengths.

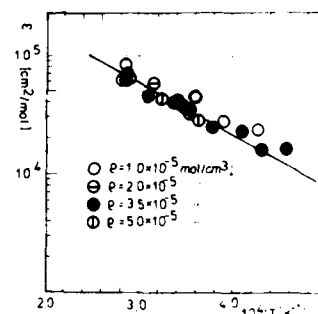


Figure 2-b. Temperature-dependence of decadic molar extinction coefficients of O_2 at various total densities. ($\lambda = 2200 \text{ Å}$)

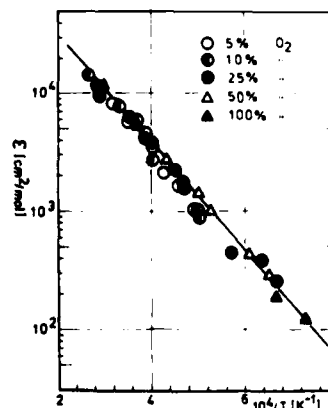


Figure 2-c. Temperature-dependence of decadic molar extinction coefficients of O_2 at various molar fractions of O_2 in argon. ($\lambda = 2400 \text{ Å}$)

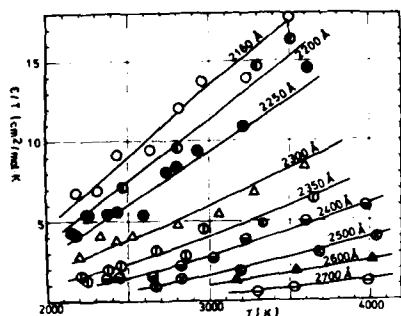


Figure 3. Temperature dependence of ϵ/T at various wavelengths.

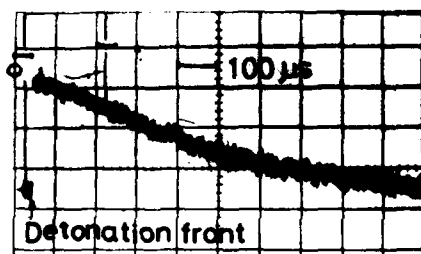


Figure 5. Absorption profile of detonation.

$H_2 : O_2 = 1 : 2$, $\lambda = 2400 \text{ Å}$,
 P_0 (Initial pressure) = 53 kPa,
 Observation place = 3658 mm
 from the ignition point.

detonation and the temperature was calculated for the gas behind the detonation front by using Eq. (2) and Fig. 3. Figure 6 shows the obtained temperature profile. Here, P_{partial} is a partial pressure of the oxygen-molecule in the detonation gas. The pressure was calculated by estimating that the molar fraction $y(O_2)$ of the oxygen-molecule was almost the same as that in the chemical equilibrium under the given conditions. ($P_{\text{partial}} = P_{\text{partial}} \times y(O_2)$) At C-J point the molar fraction $y(O_2)$ are between 0.548 (the initial pressure $P_0 = 40 \text{ kPa}$) and 0.553 ($P_0 = 101 \text{ kPa}$) for the mixture of $H_2 : O_2 = 1 : 2$. It was further estimated that the molar fraction $y(O_2)$ remained almost constant

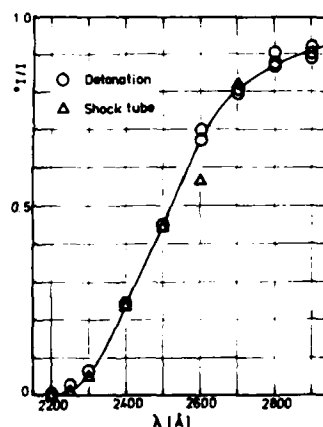


Figure 4. Wavelength-dependences of I/I_0 of H_2-O_2 detonation ($\lambda = 0.25$) in shock waves.

The values of I/I_0 of detonation are the maximum values of light absorption and the values of I/I_0 of shock waves are recalculated for the condition; 3000 K, the light path length of 20 mm, and the oxygen-concentration of $3.5 \times 10^{-5} \text{ mol/cm}^3$, whose values are nearly the same as those at the C-J point.

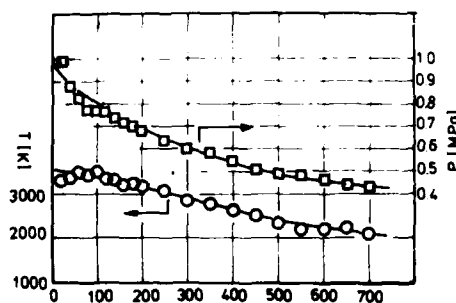


Figure 6. Temperature and pressure profiles of detonation gas.

$H_2 : O_2 = 1 : 2$, $\lambda = 2400 \text{ Å}$,
 P_0 (Initial pressure) = 53 kPa,
 Observation place = 3658 mm
 from the ignition point.

during the observation time (<1 ms). By the other initial mixture ratios the molar fractions $y(\text{O}_2)$ were also estimated to be of the same value as in the chemical equilibrium: i.e. $y(\text{O}_2) = 0.258$ ($P_0 = 40$ kPa) to 0.260 ($P_0 = 101$ kPa) for $\text{H}_2 : \text{O}_2 = 1 : 1$.

	$\text{H}_2 : \text{O}_2 = 1 : 2$		$\text{H}_2 : \text{O}_2 = 1 : 1$		$\text{H}_2 : \text{O}_2 = 2 : 1$	
P_0 (kPa)	T_{CJ} (K)	T_{max} (K)	T_{CJ} (K)	T_{max} (K)	T_{CJ} (K)	T_{max} (K)
40	2948	3200	3321	4500		
47	2962	3400				
53	2974	3300	3364	5000	3538	4000
67	2991	3300	3396	4000		
101	3028	3300	3462	4000		

Table 1. Measured (T_{max}) and calculated (T_{CJ}) temperatures at C-J point.

Table 1 shows the measured (T_{max}) and the calculated (T_{CJ}) temperatures at the C-J point.

Because of the resonant frequency of the pressure sensor (500 kHz) we could not observe the pressure profiles shortly after the detonation front with the time resolution of micro-second. Therefore, the method II was used to measure the temperature just behind the detonation front. Figure 7 shows the absorption profiles at 2500 \AA and 2600 \AA . The absorption increased rapidly at the detonation front. One can not separate the shock front from the C-J point, because many three-dimensional structures exist in our absorption path length (the path length = 20 mm, the slit opening = 2 mm). Therefore, the absorption signal should be considered to be the overall (or mean) absorption intensity. The measured temperature profile is shown in Fig. 8.

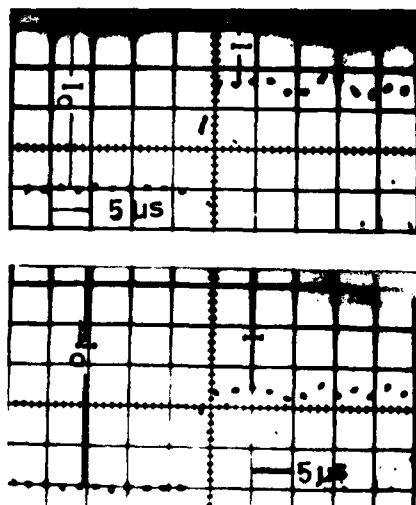


Figure 7. Absorption profiles of detonation at 2500 \AA (upper) and at 2600 \AA (lower).

$\text{H}_2 : \text{O}_2 = 1 : 2$, $P_0 = 101$ kPa,
Observation place = 3658 mm.

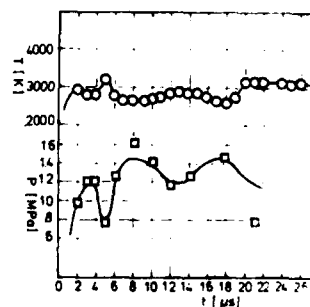


Figure 8. Temperature and oxygen-partial pressure profiles obtained from Figure 7.

$\text{H}_2 : \text{O}_2 = 1 : 2$, $P_0 = 101$ kPa,
Observation place = 3658 mm.

Figures 7 and 8 show that the gas temperature fluctuates behind the detonation front and the amplitude of the temperature fluctuation decreased with increasing distance from the detonation front. Using the method I, the temperatures of the gas were measured at the places of 1088 mm and 1658 mm from the ignition point of the endwall. At these places the stable C-J detonation was not yet formed. Table II gives the temperatures measured at these places. The observed temperatures were higher than those of the stable C-J detonation. The temperatures at 1088 mm, where there was the flame propagation before the shock front, were at first lower (T_i) than that of the above mentioned C-J detonation. ($T_f = 2100$ K, $P_0 = 53$ kPa; $T_f = 2100$ K, $P_0 = 67$ kPa; $T_f = 2300$ K, $P_0 = 101$ kPa).

$H_2 : O_2 = 1 : 2$				
P_0 (kPa)		T_{max} (K)		
		1 = 1088 (mm)	1658 (mm)	3658 (mm)
53	($T_f = 2100$)	3600	4000	3300
67	($T_f = 2100$)	3700	4000	3300
101	($T_f = 2300$)	4000	3500	3300

Table II. Measured maximum temperatures at various observation places from ignition point.

After the flame the shock front came; the temperatures (T_{max}) were higher than that of C-J detonation.

DISCUSSION

There are two possibilities for this temperature measurement technique, i.e. method I and method II. When we measured the temperature with the method I, the partial pressure of the oxygen molecule (i.e. the molar fraction of the oxygen-molecule, $y(O_2)$) was needed during the observation time. The value, $y(O_2)$, at the C-J point was used for the calculation. However, the molar fractions of O_2 behind the detonation front were not those of the C-J point. Furthermore, with decreasing temperature and decreasing total pressure behind detonation front the chemical reactions of the burned gas occurred; most reactions were the recombinations and the related reactions. Then, the molar fraction of the oxygen-molecules changed. In our measurements, however, these influences were not considered (we expected the molar fraction of O_2 to remain constant). Theoretical calculations in the chemical equilibrium show: The molar fraction, $y(O_2)$, which was 0.260 in the C-J condition of $T = 3462$ K and $P = 1.66$ MPa, increased to 0.325 at $T = 2463$ K, $P = 0.648$ MPa for the expanded gas mixture (Initial mixture ratio $H_2 : O_2 = 1:1$, Initial pressure $P_0 = 101$ kPa); $y(O_2) = 0.553$ in C-J condition of $T = 3028$ K, $P = 1.48$ MPa increased to $y(O_2) = 0.598$ at $T = 2028$ K, $P = 0.868$ MPa for the mixture $H_2 : O_2 = 1:2$ of the initial pressure $P_0 = 101$ kPa. These increases of the molar fractions indicate the decrease of about 300 K for the gas temperature at $T = 2463$ K in the mixture $H_2 : O_2 = 1:1$; i.e. the temperatures measured a few hundred microseconds after the detonation front could be about 300 K higher than the true oxygen-temperature; in the mixture of $H_2 : O_2 = 1:2$, about 100 K higher. This change of the oxygen concentration was larger for the stoichiometric mixture ($H_2 : O_2 = 2:1$). The molar fraction of

O_2 , $y(O_2)$, which was 0.049 in the C-J condition of $T = 3675$ K, decreased to 0.033 at 3175 K and to 0.004 at 2675 K. There was another problem for the stoichiometric mixture: When the equivalence ratio of the mixture decreased 10% (i.e. $\phi = 0.91$), the molar fraction, $y(O_2)$, of the oxygen concentration in the C-J condition was already much larger than that of the mixture $\phi = 1.0$; i.e. $y(O_2) = 0.049$ at $\phi = 1.0$ and $y(O_2) = 0.067$ at $\phi = 0.91$. Therefore, the temperature measurement with the method I is difficult for the stoichiometric mixture. From these experiences one can say: Once the partial pressure of the oxygen-molecule is measured, the more exact gas-temperature can be obtained with the method I, since the signal noise ratio, S/N is larger than that of the method II. Nevertheless, the partial pressure can not be obtained easily except for the oxygen-rich (much richer) mixture. Consequently, except the temperature measurement of the oxygen-rich mixture, the method II is more available, though the absorption intensities at two wavelengths have to be measured at one time. Since the temperatures and the densities of unstable species can be measured with this method II, one can observe the gas state in non-chemical equilibrium.

The temperatures measured by this UV-absorption are those of the oxygen-molecules in the detonation gas. When the gas mixtures are in the thermal equilibrium during the detonation process, the measured temperatures are those of the detonation gas. Furthermore, it was expected that the stable C-J detonation was already formed at the place of 3658 mm from the ignition place. The temperatures obtained at this place are nearly the same as the calculated by the ZND-model. Penzias et al.⁵ have also obtained the same temperatures as the calculated. Gaydon et al.⁶ have also obtained uniform temperature profiles behind shock initiated detonations. The observation times of above mentioned groups were the order of a few hundred microseconds. Accordingly, it is probable that the inhomogeneity or the non-equilibrium in the gas phase already vanished.

The temperature profiles with much higher time resolution indicated that there was a fluctuation of the gas temperature. (Fig. 7 and Fig. 8) Saito et al.¹⁰ observed the C_2 and CH emission intensities which were radiated parallel to the tube axis from detonation, and found the oscillations of the emission intensities. They consider that the oscillations are due to the three-dimensional structure of the detonation. These results indicate that there might be the fluctuation of reaction order behind the detonation front.

The measured temperatures were those of oxygen-molecules, as mentioned above. The oxygen-molecule was not the product of combustion reactions. Therefore, the temperatures of the oxygen-molecule did not depend directly on the reaction enthalpy. The temperatures of the oxygen-molecule increase (or decrease) due to the heat conduction from (or to) other species (intermediate products and final products). In this consequence, one can estimate that the temperatures of oxygen-molecule were near the mean value of the gas. When the temperatures of the intermediate products (especially the products activated by the exothermal reaction) are measured, they must be higher than the temperatures of other stable species. Soloukhin⁴ has observed abnormally high temperatures and Terao et al.⁷ also observed much higher electron temperatures. Terao's results also show the fluctuation of the electron temperatures.

Further studies are needed to know whether the fluctuation occurs because of the three-dimensional structure of the detonation front and also to know whether there are some other reasons. It is, however, ascertained that using this UV-absorption measurement, the temperature profile of detonation is obtained with a microsecond time resolution.

The maximum temperatures of the super detonation are higher than the temperature of the C-J detonation (at the places of 1088 and 1658 mm from the ignition place).¹¹ The flame propagation was observed at 1088 mm before the shock wave came. The temperature T_i was much lower than that of the C-J detonation.

Though it was somewhat abrupt, the deformation of the needle was observed in the detonation gas in order to see the high temperature detonation gas from other side.¹² The deformation showed three typical cases: the first was that the top of the needle was melted; the second was that the needle burned; and the third, the needle was broken. (the fourth trivial case was that the needle was not deformed.) These cases of deformation appeared depending on the molar fraction of the mixture and on the setting place of the needle; namely, they depended on the condition of the detonation gas (the temperature, the molar fraction of the gas and the velocity of the burned gas). Melting of the needle occurred in the detonation gas between $\phi = 1$ and $\phi = 0.5$. The melting amount of the top of the needle depended on the diameter of the top. Many of the needles were burned in the detonation gas of the equivalence ratio $\phi = 0.5$ and the needles were broken in the mixture of $\phi = 0.25$. Figure 9 shows the amounts of the needles melted, burned and broken. As seen from this figure, the deformation of the needle depended on the gas condition (i.e. the distance from the ignition place and the mixture ratio). The largest deformation occurred at the places of the super detonation ($l = 1000 - 2000$ mm in our experiments). At these places the temperatures, the pressures and the flow velocities are higher than those at other places.¹¹ As estimated, the flow velocities of the detonation gas influenced the amount of the deformation. Namely, at the endwall of the downstream where the flow velocity of the gas was zero, the needle was not deformed. More precise observation of the melting top of the needle revealed: The top of the needle having a smaller radius, r , melted more and the top whose radius was larger than a certain value ($r = 0.03$ mm at $H_2:O_2 = 2:1$) was not melted.

From this observation one can expect to obtain information on the surface processing of the sharp end of metal¹² or on the form and the place of the detector used for measurements of the high temperature gas. Further details will be published elsewhere.

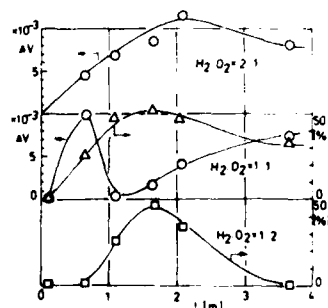


Figure 9. Deformation of needles.

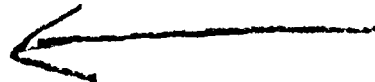
- : amount of melted top in mm^3
 - △ : amount of burned needle in %
 - : amount of broken needle in %
- ($P_0 = 101$ kPa)

CONCLUSION

The temperature profiles of the detonation gas were obtained with microsecond time resolution by the light absorption measurement. The gas temperatures had some fluctuation shortly after the detonation front. By this technique the gaseous temperature and density can be measured with the time resolution of a few microseconds.

REFERENCES

1. B. Lewis, and G. Elbe, Combustion, Flames and Explosions of Gases, Academic Press Inc. (1961)
2. A.G. Gaydon, and I.R. Hurle, The Shock Tube in High-Temperature, Chemical Physics, Ch. 6, 7, 12, Chapman and Hall Ltd. (1963)
3. W.E. Gordon, Third Symposium on Combustion and Flame and Explosion Phenomena, The Williams and Wilkins Co., 579 (1949)
4. R.I. Soloukhin, Shock Waves and Detonations in Gases, Mono Book Corp., 146 (1966)
5. G.J. Penzias, S.A. Dolin, and H.A. Kmeagle, Appl. Optics, 5, 230 (1966)
6. A.G. Gaydon, and I.R. Hurle, Proc. Roy. Soc. A, 262, 38 (1961)
7. K. Terao, T. Neda, K. Nakano, and T. Sato, Japan J. Appl. Phys., 8, 834 (1969)
8. K. Terao, and H. Takasu, Twelfth Symposium on Shock Tubes and Waves, The Magnes Press, 548 (1979)
9. T. Tsuboi, T. Kimura, and K. Yamamoto, Japan. J. Appl. Phys., 14, 1483 (1975)
10. K. Saito, and I. Murakami, Combustion and Flame, 34, 331 (1979)
11. T. Hikita, and K. Akita, Outline of Combustion, Corona Pub. Co. Ltd., 112 (1971) (in Japanese)
12. K.M. Gettelman, Modern Machine Shop ed. by F.W. Vogel, Gardner Publications, Vol. 45, No. 5, 74 (1972)



AD P000236

A LASER-INTERFEROMETRIC TRAJECTORY-FOLLOWING SYSTEM FOR
DETERMINING FORCES ON FREELY FLYING MODELS IN A SHOCK-TUNNEL

Leonard Bernstein & Graham T. Stott

Department of Aeronautical Engineering

Queen Mary College, University of London, U.K.

A prototype, two-point trajectory-following system is described, which uses a pair of simple Michelson interferometers having the same He-Ne laser as a light source. Each interferometer provides a 'measurement arm' which is used to follow the motion of a reference point on the model, a fringe-cycle being generated when the reference point moves a half-wavelength along the beam incident on the model. Each set of frequency-modulated pulse trains is detected by a photodiode and recorded by a transient recorder. The stored information is then played back to a two-pen recorder from which the displacements versus time and hence the accelerations of the reference points can be determined.

The system has been used to follow motions in the pitch-plane of ridge-delta models, allowed to fly under weak restraint in a shock-tunnel. The motions of two models, one of mass 12.7 g, the other 47.6 g were separately followed, each model carrying two corner-cube retroreflectors. Data were obtained from which lift and pitching moment coefficients have been derived. In no case did the model displacement exceed 1 mm in translation or 0.1° in pitch during the test period of 1 ms.

1. INTRODUCTION

To measure aerodynamic forces using a conventional "force balance" in a flow of duration Δt requires a measuring system having a characteristic frequency somewhat in excess of $1/\Delta t$. A force-balance having a high natural frequency is necessarily stiff and consequently insensitive¹. The conventional force-balance is therefore not really suitable for use in shock-tunnels where the test period is less than 5 ms and the nozzle reservoir pressure such that the forces are of order 10 N on a typical model.

Similar problems arise when freely flown models are fitted with accelerometers², because sensitive transducers of high natural frequency and low mass are difficult to design. A hybrid technique in which the response of a low frequency force transducing system is compensated by appropriate accelerometer signals has been reported³, but the calibration and setting-up procedures are elaborate and tedious.

A somewhat different approach involves monitoring the displacement of a freely-flying model. A model of low mass (of order 10 g) is suspended by threads which break as the flow starts. The motion is followed using either a high-speed ciné camera⁴, a multiple-spark exposure of a single photographic plate⁵, or by mounting a flashing light within the model⁶. To derive accelerations, and hence forces, requires double differentiation of the displacement vs time data, so the primary data need to be of high accuracy. In general high-speed ciné-photography results in pictures of small frame size and poor resolution; neither is conducive to high accuracy. The multiple exposure of a single plate is limited by the latitude of the photographic emulsion, which can marginally tolerate ten exposures in which the shadow images of the model overlap. The relative positions of these images can at best be resolved to within 0.1 mm. In the QMC shock-tunnel, the duration of the quasi-steady test flow is about 1 ms and the force levels of order 10 N. A model of mass 10 g is displaced less than 1 mm during a test, so that photographic techniques are clearly unsuitable for resolving the motion.

It is well known that optical interferometry can resolve lengths to within a wavelength of the light used. When a laser is used as the light source, not only is it highly monochromatic, it is also coherent over a length of order metres so that the measurement and reference beam path lengths can be widely different and yet interference can still occur. A low-powered He-Ne laser is very suitable, and with a wavelength of 0.6328 μm , can be used in a Michelson interferometer to resolve displacements to within 0.3 μm .

There is an added advantage in limiting the displacement to small values. When large displacements occur the model also generally rotates, so that its attitude to the oncoming flow changes. Usually models with lateral symmetry are tested at zero yaw, and the problem of ensuring longitudinal stability during a test is an iterative one requiring several runs in which the centre of mass is adjusted from test to test until "flight at constant incidence" is achieved. This problem does not arise when the displacements are limited sufficiently. It would seem therefore that an interferometric technique could be well suited to measuring the small displacements of a model "flown" in the QMC shock-tunnel.

2. SYSTEM SPECIFICATION

The quasi-steady flow in the test-section of a shock-tunnel is preceded by the passage of the starting-waves. The forces acting during this starting process are time-dependent, and difficult to predict, but they are likely to be at most, of the order of those occurring during the test period. For specifying the system requirements it is sufficiently accurate to assume that the acceleration of the model during the starting process is the same as that which it undergoes during the test period. In the QMC shock-tunnel the dynamic pressure can be as low as 1 kN/m^2 , the quasi-steady test period is about 1 ms and the starting process, allowing for the establishment of flow about the model, occupies about 0.7 ms.

To determine accelerations it is necessary to differentiate twice, and experience suggests that at least 10 fringes (data points) are required for reasonable accuracy in the second derivative. To measure force coefficients from 0.01 upwards, we obtain for the "mass loading" required of the model, that $m/S_w < 3.8 \text{ kg/m}^2$. The plan area S_w of the model depends on the size of the test section and the need to mount the reflectors which return the measurement beams to interfere optically with the reference beams of the interferometer. The free-jet test-section of the QMC tunnel has a non-viscous core estimated to be about 200 mm in diameter. A model of length 120 mm with a triangular planform of aspect ratio 1 was chosen, giving $S_w = 0.0036 \text{ m}^2$. Thus $m < 13.7 \text{ g}$ if 10 fringes were to be generated in the "worst" case. Of course, at higher force levels, more fringes would be produced with such a model, or one could tolerate a heavier model.

A symmetrical model at zero yaw will experience only a lift, drag and pitching moment. At least three independent interferometer systems would be needed to follow the motion. Although the model pitches and translates, the beams reflected from the model must be so returned as to interfere with the reference beams at the fringe detectors for the duration of the test. In addition the other components of each interferometer, from the beam splitter to the detector must remain fixed relative to one another, since any relative movement would also give rise to fringes.

Although the design is based on a minimum of 10 fringes being generated during the test period, at higher force coefficients and pressure levels, many more would be produced, perhaps a thousand. At the end of the test period the generation rate would be about 3 MHz. The detection and recording system must have the bandwidth to cope with this if full use is to be made of the available test time.

3. APPARATUS

3.1 *The QMC shock-tunnel*

The driven section of the shock-tube is of square cross-section (76.2 mm) and approximately 9.5 m in length. Cold hydrogen is used to drive shocks in the working gas, nitrogen, the tunnel being operated in the tailored-interface mode, found experimentally to correspond to a shock Mach number of 5.92 at the nozzle entrance. The maximum driver-gas pressure is 100 atm but for safety and economy it is usually operated at lower pressures. A conical nozzle of included angle 20° with interchangeable throat sections exhausts as a free jet of diameter 305 mm into the test chamber, a Melinex diaphragm being used at the throat so that the nozzle, test chamber and dump tank can be evacuated to ensure rapid starting. Side ports in the cylindrical test chamber accommodate windows of diameter 250 mm. The stagnation conditions at the nozzle entrance are determined from measurements of the initial pressure p_1 , and temperature T_1 , of the nitrogen and the speed of the incident shock over the final part of its motion before reflection. The reservoir pressure level and constancy had been previously checked using a Kistler 701A transducer.

3.2 *The model and its mounting*

Although the mass of the model is not to exceed about 14 g, it must carry retroreflectors which return the incident beams along paths parallel to themselves. These retroreflectors, see below, are relatively fragile and expensive and must be protected from damage. Because only small displacements were necessary, it was decided to suspend the model by two threads. Occasionally one of these broke and the model impacted the support, so that protection of the reflectors was felt to be desirable.

The particular layout of the tunnel made it awkward to accommodate an interferometer to follow motion along the stream direction so it was decided to concentrate on the motion due to lift and pitching moment for the prototype system. A lifting-model was therefore necessary, and a simple "ridge-delta" was chosen. The model was fabricated using a thin aluminium alloy plate to form the plane surface, appropriately chamfered to give the sharp leading edges, to which was bonded the upper, ridge portion cast from Isofoam, a closed-cell, polyurethane foam material. Cavities to house the retroreflectors formed part of the cast shape, holes being provided in the alloy plate for lift and moment element blanks.

The retroreflectors are "corner-cube" reflectors, see figure 1. Any beam at incidences up to about 45° is reflected along a path parallel to that along which it came. Moreover, the path length within the glass is independent of the position on the face ABC upon which the beam is incident so that



AB = BC = CA = 7 mm

Fig. 1. Corner cube retroreflector; model suspended on the test-section centre-line from a sting above the flow, using nylon threads. The sting itself was carried on mountings isolated by a system of soft springs from both the tunnel structure and the laboratory¹.

The nominal incidence of the model was set, fairly crudely for these prototype tests, against a protractor attached to the sting.

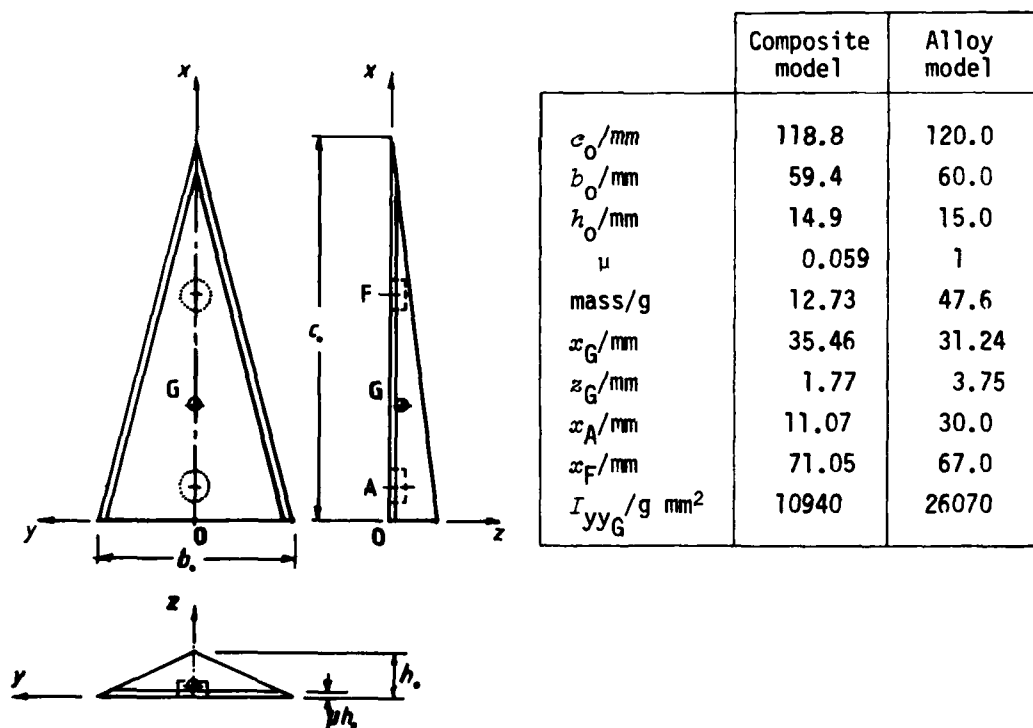


Fig. 2. The main characteristics of the models. G is the centre of mass, A and F denote the centre-lines of the aft and forward retroreflectors.

3.3 The interferometer systems

The decision to concentrate on the lift and pitching characteristics meant that two independent measurement systems were necessary with two incident and two returned light beams passing through the test-section windows. A single He-Ne laser light source was used for both systems, it

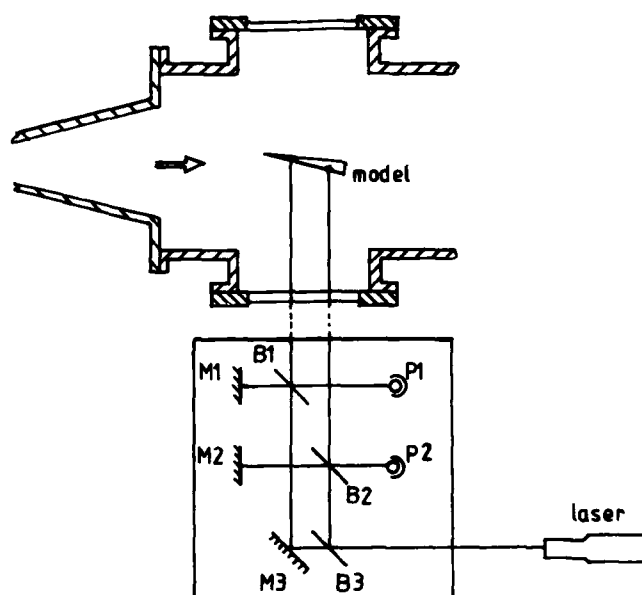


Fig. 3. Schematic diagram of dual interferometers; B, beam splitters; M, plane mirrors; P, photodetectors.

themselves mounted on a plate 405 mm square by 12.7 mm in thickness. This assembly was supported on a heavy tubular pedestal isolated from the laboratory floor by fibre pads. The natural time constant of this system was very long compared with the test period, so that its motion produced less than one fringe during a test, though the laboratory structure and floor responded quite markedly to passing road traffic and underground trains.

The interference fringes were detected by simple photodiodes having a response time of 0.25 μ s. The two signals, essentially frequency-modulated pulse trains, were amplified and recorded using two DATALAB transient recorders having a maximum sampling rate of 5 MHz and a capacity of 1000 points. The recorded signals were then "played back" on a two-pen chart recorder for analysis.

4. THE EXPERIMENTS

The majority of tests were carried out at a nominal nozzle reservoir pressure of about 7.7 atm and a stagnation temperature of 4000 K corresponding to tailored-interface operation of the shock-tunnel at a driven-gas pressure $p_1 = 18$ torr. The nozzle throat was 12.7 mm in diameter. Based on the measurements of references 7 and 8, it is estimated that vibrational freezing of the expanding nitrogen occurs "suddenly" at about 2400 K and that the flow Mach number M_∞ , at the test station is 10.3 with a dynamic pressure of 1.07 kN/m².

Data were obtained over a range of nominal incidences of the model from -20° to 10° (the flat surface is an expansion surface for positive incidences of the model); most cases were repeated several times. The composite model was used for the majority of the tests, but some tests were carried out on the alloy model. At low incidences, when the force levels were also low, data were recorded for the full quasi-steady test period of 1 ms. At higher

being divided into two using a beam splitter B3 after being expanded and collimated to a diameter of about 10 mm. Expansion of the beam was employed to limit the amplitude modulation of the fringe intensity which results from lateral movement of the retroreflectors, the sensitive areas of the photodetectors used being rather small. Each beam was then split into a reference beam and an active beam to form two Michelson interferometers, one impinging on the forward retroreflector on the model, the other on the rearward one, as shown in figure 3. To ensure that fringes were generated only as a result of model motion, all elements of the interferometers apart from the laser and beam expander, and of course the retroreflectors on the model, were mounted rigidly on three optical rails,

force levels, the fringe generation rate was too fast for the transient recorder to be used at one point/microsecond, and "aliasing" of the data was apparent. In such cases each store of 1000 points was filled at 2 MHz or 5 MHz and the effective test period curtailed accordingly; adequate data were produced, even in 200 μ s.

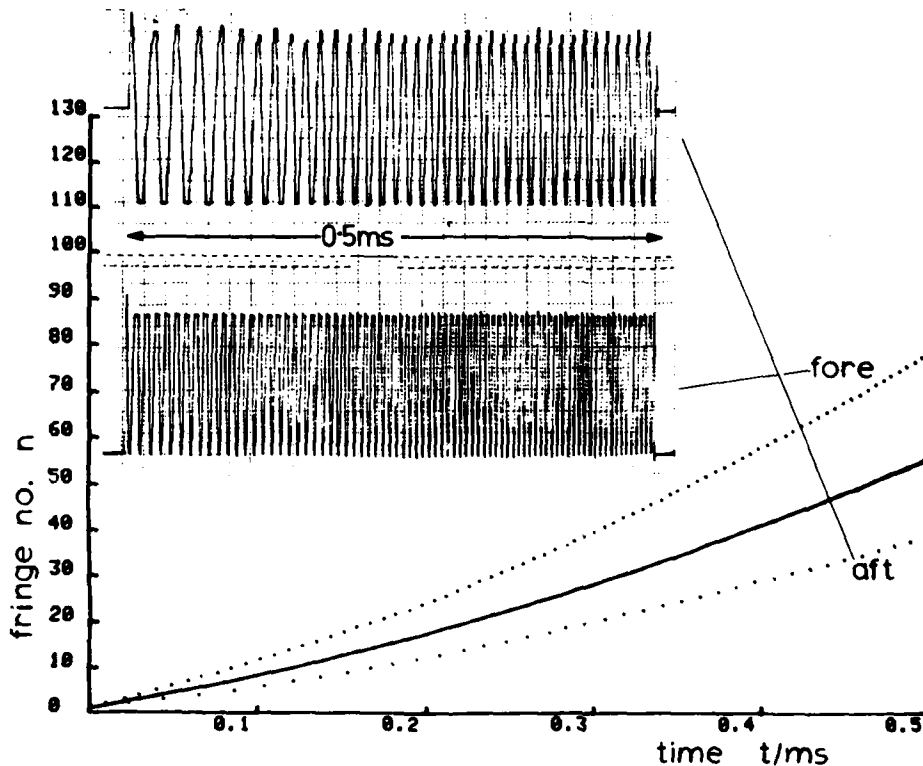


Fig. 4. A typical record. The solid line is the derived motion of the mass centre G.

A typical record is shown inset in figure 4, telescoped along the time-scale to fit the page. In practice the records were spread over a chart length of 0.5 m so that the time of passage of each fringe $t(n)$ could be read to within about 0.1% of the total recorded time. Plots of $n(t)$ for both the fore and aft retroreflectors for the same test run are also shown in figure 4.

5. DATA REDUCTION

Consider two right-handed cartesian frames $O\xi\eta\zeta$ and $G123$ as shown in figure 5. $O\xi\eta\zeta$ is a laboratory-fixed (inertial) frame with $O\xi$ in the stream direction and $O\zeta$ in the direction of the incident laser beams. $G123$ is a body-fixed frame with origin at the centre of mass G of the model, x_1 and x_3 in its plane of symmetry, with $G1$ parallel to the face containing the retroreflectors and directed forward, and $G3$ normal to it, as shown. The angle between $G1$ and $O\xi$ is $\theta(t)$. It may be shown that the component of acceleration $\ddot{\zeta}_G$, of the centre of

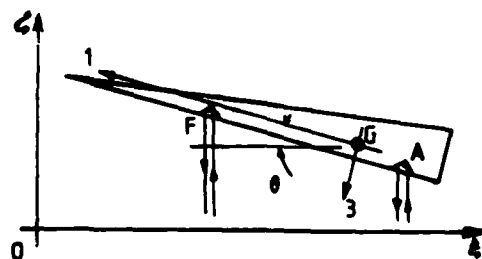


Fig. 5. Inertial and body-fixed co-ordinate frames.

mass, along the direction Oz and the angular acceleration $\ddot{\theta}$ are given by

$$\ddot{\zeta}_G = \frac{(x_{1F} + x_{3F}\tan\theta)\ddot{\zeta}_A - (x_{1A} + x_{3A}\tan\theta)\ddot{\zeta}_F}{x_{1F} - x_{1A}} - x_{3F}\ddot{\theta}^2\sec\theta \dots \dots (1)$$

$$\text{and} \quad \ddot{\theta} = (\ddot{\zeta}_A - \ddot{\zeta}_F)\sec\theta/(x_{1A} - x_{1F}) + \ddot{\theta}^2\tan\theta \dots \dots \dots (2)$$

where x_F and x_A are the position vectors in the frame G123 of the effective fore and aft points of measurement, $\ddot{\zeta}_F$ and $\ddot{\zeta}_A$ are their components of acceleration along Oz and it has been assumed that $x_{3F} = x_{3A}$.

The terms involving $\ddot{\theta}^2$ contribute less than 0.1% in both cases throughout all test runs and have been ignored in the data reduction. Displacements normal to Oz do not affect the path lengths of the laser beams, but rotations of the model do have a small effect. For a "roof-top" prism retroreflector it can be shown that rotations can be accounted for by taking as the effective measurement centre, a point on the intersection of its planes of symmetry a distance ϵL from the face, where L is the distance of the face from the apex. For crown glass, of refractive index 1.5, $\epsilon = 0.88 \pm 0.01$ for $|\theta| < 20^\circ$, and since $x_3\tan\theta \ll x_1$ in all practical cases, $\epsilon = 0.88$ has been used for the corner-cube retroreflectors also, for which $L = 5/\sqrt{3}$ mm. The acceleration components $\ddot{\zeta}_F$ and $\ddot{\zeta}_A$ are then simply $\frac{1}{2}\lambda\ddot{n}_F$ and $\frac{1}{2}\lambda\ddot{n}_A$ respectively. The raw data give the fringe number $n(t)$ for points A and F. By curve-fitting a parabola $n(t) = A + Bt + Ct^2$ using the method of least squares, the second derivative $\ddot{n} = 2C$ may be found, so that $|\ddot{\zeta}| = C\lambda$, where it is implicitly assumed that once in motion the model continues to move in the same general direction. However the signs of the displacements and hence directions of the accelerations remain unknown. Though methods are available for discriminating direction (see ref.10 for example), for simplicity in the prototype system, the present data have been reduced by using internal evidence and plausible argument. For example at large (numerical) values of incidence α , the displacements $\Delta\zeta_A$ and $\Delta\zeta_F$ will both have the same size as α , and since the pressures on each face will be nearly uniform, placing the centre of pressure a distance $c_0/3$ from the base, that is, forward of G, the pitching moment about G will also have the same sign as α . At small values of $|\alpha|$, the situation can be ambiguous but has been resolved by requiring that $\ddot{\zeta}_G$ and $\ddot{\theta}$ be smooth functions of α .

The force F_ζ in the direction Oz and the pitching moment M_G about G2 are respectively

$$F_\zeta = m\ddot{\zeta}_G \quad \text{and} \quad M_G = I_{22G}\ddot{\theta} \dots \dots \dots (3)$$

where in the second equation we have assumed that the squares and products of the roll and yaw rates are negligible. As the model swings at the ends of the threads from the suspension sting, there is a small roll velocity and the direction of the laser beams is not quite that of the lift, because of the manner in which the model is suspended. In consequence there is also a very small yaw, but its effects are negligible. The model is hung by a pair of threads attached close to one of the leading edges, and it must therefore rest initially with the two points of attachment and G in the same vertical plane. On the assumption that the nozzle centre-line is horizontal, the model is also set up with its axis G_1 horizontal. The true incidence therefore differs from that set on the protractor and though it varies slowly with setting angle, the correction is about -0.9° for the composite model and -2.2° for the duralumin model. The correction to the lift because its direction is not quite along Oz is very small, about 1% in the worst case. All these effects are of course avoidable by careful design of the suspension.

The mass m of the model, and of its component parts, were obtained by weighing, to within 10 mg. The position of the centre of mass G was then computed, as also was the moment of inertia I_{22G} about G2. Equation (3) then gives the pitching moment about the centre of mass, which is in a different

geometric position for the two models, figure 2. The moments have therefore been transferred to a common geometric centre, a line $c_0/3$ from the base, corresponding to the position of the centre of pressure, were the pressures uniform over each surface.

In order to derive the coefficients of lift and pitching moment one needs to know the dynamic pressure $\frac{1}{2}\gamma p_\infty M_\infty^2$ of the stream. This is not known with any certainty for the QMC tunnel for two reasons. With relatively low pressure high enthalpy flows, the thermodynamic state of the gas at the test section is uncertain, and with a conical nozzle, the test flow is spatially non-uniform. The data of references 7, 8 and 9, have been used, account being also taken of the small effects due to random variation in the incident shock strength in the shock-tube. The effects of flow conicity remain unaccounted for, but are likely to be smaller than the cone angle of 20° would suggest because of the boundary layer on the nozzle wall.

6. RESULTS

The reduced data, averaged over the test period, for the ridge-delta of aspect ratio 1 and thickness ratio 0.125 are shown in figures 6 and 7. Most of the points represent the means of several tests at the same nominal incidence and hide a scatter of up to $\pm 10\%$ in some cases. This is thought to be due to the rather crude arrangement used for setting the incidence together with the variation in nozzle reservoir pressure which may amount to $\pm 5\%$ during the test period and may also vary from test to test in a random way due to differences in the diaphragm bursting behaviour and shock-wave attenuation.

The fringe count $n(t)$ over the whole test period was fitted by a parabola very well - in all cases the standard deviation was only a fraction of a fringe. Systematic variations attributable to the small differences in final shock velocity in the shock-tube were of course taken into account in the data reduction. The actual measurements yield the lift and moment fairly directly; the derivation of the coefficients, which are based on the plan form area of the delta, depends also on the dynamic pressure as we have noted. However the value used, $0.445p_1$ (normalised at the tailored-interface shock strength) corresponding to sudden freezing of the vibrational mode of the nitrogen differs little from the values obtained assuming full equilibrium flow or fully frozen vibration throughout the nozzle, $0.410p_1$ and $0.440p_1$ respectively.

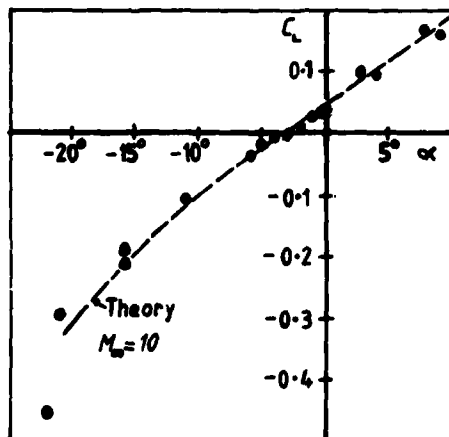


Fig. 6. Lift coefficient vs. incidence;
 $M_\infty = 10.3$

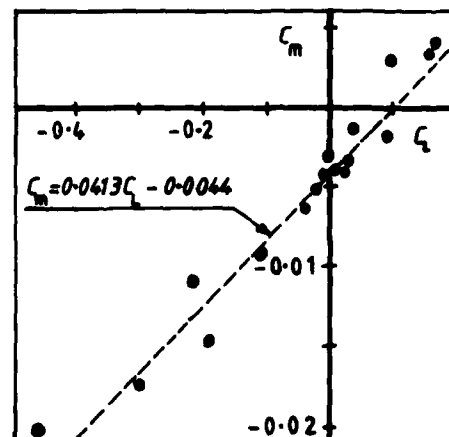


Fig. 7. Pitching moment coefficient
(about line $c_0/3$ from base)
vs. lift coefficient;
 $M_\infty = 10.3$

Also shown in figure 6 is a theoretical curve computed for the compression surfaces using an inviscid, perfect gas theory due to Larcombe¹¹, which assumes that the flow is essentially conical and is an interpolation based on the base areas, between an equivalent cone and a two-dimensional flow. The expansion surface contribution at each incidence has been computed using small disturbance theory (see, for example, reference 12), and is found to provide about 20% of the lift. The base region was assumed to be at the ambient pressure p_∞ . The agreement between theory and experiment is remarkably good but must be regarded as fortuitous.

In these tests for most of which the Reynolds number Re_{C_0} is about 7000 viscous interactions are expected to be significant, and will modify the pressures near the leading edges. It is possible that the effects on the upper and lower surfaces cancel, at least for small incidences, and this may explain the good agreement; at larger values of $|\alpha|$ divergences begin to appear. On the assumption of conical flow, the moment coefficient about the reference line should be zero. A least-squares straight line, see figure 7, suggests that the lift acts about 4% ahead of the reference point consistent with higher pressures in the forward regions than predicted.

7. CONCLUSIONS

The prototype system has been successfully demonstrated and has produced data under conditions in which other methods have so far failed. The extension to the measurement of other force and moment components is one largely of detail.

The main disappointment has been in the rather larger scatter than expected from nominally identical tests. However we feel that this is probably attributable to features other than the acceleration measurement, and until these have been eliminated the full potential of the system will remain uncertain.

The manual data reduction is rather tedious, but readily automated. Once the data are stored in transient recorders, each record could be played back relatively slowly to a system which would measure the times for Δn successive fringes relative to the known overall time of the record. Δn could be controlled by suitable programming of a microcomputer.

REFERENCES

1. Bernstein, L. AGARDograph 214 (1975)
2. Sheeran, W.J. & Duryea, G.R. AIAA Paper No. 69-351 (1969)
3. Beaussier, J. IInd ICIASF, (1966)
4. Richards, B.E. & Clemens, P.L. IVth ICIASF, (1971)
5. Pennelegion, L., Cash, R.F. & Shilling, M.J. ARC CP 934 (1967)
6. Wyborny, W. & Requardt, G. AIAA Paper 74-613 (1974)
7. Lewis, M.J. & Bernstein, L. ARC CP 1294 (1974)
8. Goodchild, R.O. Ph.D. Thesis, Univ. of London, (1968)
9. Bernstein, L. ARC CP 633 (1963)
10. Betz, R.A., Goethert, W.H., & Bomar, B.W. Paper 35 in AGARD CP 174 (1975)
11. Larcombe, M.J. ARC CP 1295 (1974)
12. Shapiro, A.H. Dynamics & thermodynamics of compressible fluid flow, p718. Ronald Press, (1974)

AD P000237

SHOCK TUBE SIMULATION OF
PULSED FLOW AERODYNAMIC WINDOWS*

V. A. Kulkarny, J. Shwartz, and R. A. Briones

TRW Defense and Space Systems Group

Redondo Beach, California 90278

Aerodynamic windows provide pressure and gas species isolation interfaces which are transparent to laser radiation. The feasibility of using a shock tube flow field as a single-shot window for short, high-energy laser pulses was investigated. A primary application of such a window would be for the gas laser driven inertial confinement fusion test facility currently planned by DoE. Experiments were performed to determine the phase aberrations and beam-quality degradations produced by a pulsed-flow window. Holographic interferograms, when interpreted with a densitometer, typically showed an RMS phase aberration of 0.13 rad in tests using He and 1.25 in tests using air, all at the 0.694 μm Ruby wavelength. Scaling relationships developed under this study show that such performance is more than adequate to meet the anticipated fusion laser beam quality requirements.

INTRODUCTION

In the context of high-energy lasers, an aerodynamic window is a gas pressure and species isolation interface generated by a gas stream. Continuous-flow aerodynamic windows have been used now routinely on a variety of high-power CW and pulsed lasers as beam output windows, where the power/energy levels preclude long term operation with material windows. Some examples are CW gas-dynamic (CO_2) and chemical (DF) lasers, and pulsed electric discharge (CO_2) lasers.^{1,2,3,4}

The gas flow rate in such continuous-flow aerodynamic windows is typically proportional to the laser cavity pressure and beam output aperture. For large aperture lasers, such as those currently envisioned for laser fusion applications, the mass flow rate and cost associated with running a continuous-flow aerodynamic window are prohibitively high. However, these lasers operate in a pulsed mode and require only a pulsed-flow aerodynamic window in which the flow is on only for a short time during which the laser pulse is extracted. The flow can then be turned off (and the aperture closed by a non-transparent partition) during the time interval between two pulses, with substantial saving in gas flow rate and recirculation costs.

*Work performed under LASL P.O. No. 4L20-8204K-1.

The operation of a pulsed-flow aerodynamic window which can provide the same pressure and species isolation as a continuous flow window but with only a small fraction of the flow rate was demonstrated at TRW⁵ for single pulse laser fusion applications using a shock-tube simulation technique.

THE PULSED AERODYNAMIC WINDOW CONCEPT

A pulsed-flow aerodynamic window is described schematically in Figure 1. It is essentially a burst-diaphragm shock tube placed at the beam output port of a laser oscillator or amplifier. The window thus becomes an integral part of the laser beam duct.

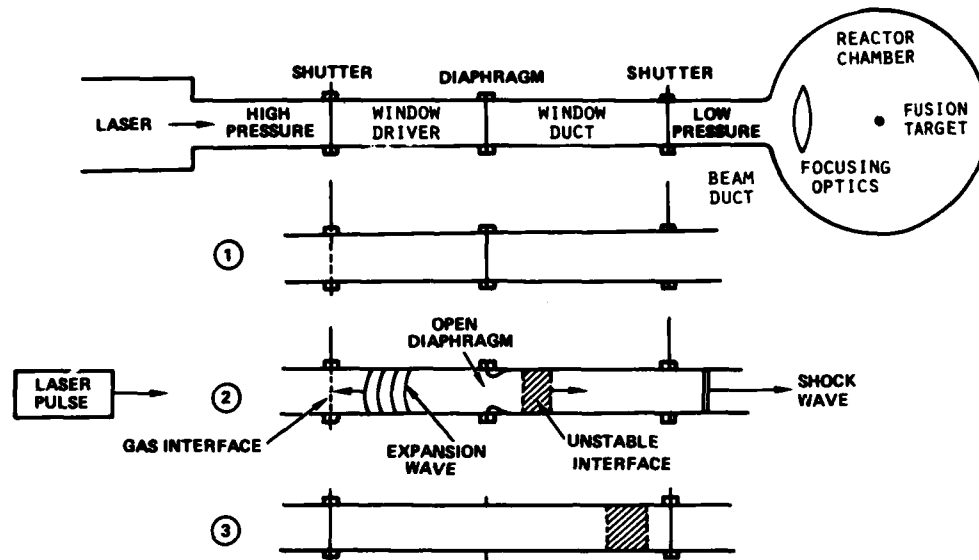


Figure 1. Schematic of a pulsed aerodynamic window and its operation

The portion of the duct to the left of the diaphragm, the window driver, will be typically filled to a pressure which equals the laser pressure. The gas composition there may be different from that of the laser gas to minimize absorption of the laser beam. A shutter can be used to separate the laser gas from the window driver gas. This shutter will then be opened (say, pneumatically) some short time before the laser is fired. The window driver gas should be matched in density and index of refraction to the laser gas to minimize gas mixing and refractive gradients induced by shutter motion. The conditions in the window duct are the same as the beam duct, which depend on the mode of window operation, as will be explained below. A second shutter may be placed downstream of the window duct region to minimize the flow of driver gas into the duct and to minimize pumping required between laser pulses. This shutter too will be opened just before and closed a short time after the laser is fired (see Figure 1, Sequences ① and ③).

The diaphragm opening must be triggered by some external means before the laser is fired. The time delay between triggering the diaphragm burst and transmitting the laser pulse will be of the order of 1 to 10 milliseconds, depending on the window and diaphragm. The diaphragm clears the window aperture and flattens itself against the duct walls (Figure 1, Sequence ②). The resulting gas flow rapidly evolves into the well understood shock tube flowfield:⁶ four uniform regions separated by plane waves and a contact surface. The laser pulse can now be propagated through the window into the beam duct.

The effect of the window flow field on the phase and focusability of the transmitted laser beam is the one major factor which will determine the feasibility and usefulness of this window concept. The major variations in gas properties are along the duct axis, and hence should have little or no effect on the quality of an axially transmitted laser beam. However, lateral variations are also expected to be found in such a duct, particularly next to the "contact surface" which in reality is a turbulent inhomogeneous mixture of gases from regions 2 and 3 of the shock tube flow. The refraction through this region could have a degrading effect on the beam quality of a transmitted laser beam depending on the magnitude of the index variations.

The effects of such lateral disturbances on beam quality can be minimized, with proper choice of conditions in the window duct (or the beam duct). If the beam duct is at very low pressure ($p_1/p_4 \rightarrow \infty$), and the driver gas essentially expands into vacuum then the density of the contact surface is very low and cannot cause significant refraction. If the beam duct is at an intermediate pressure ($p_4/p_1 \approx 0(1)$), then the beam duct gas may be chosen to match the refractive index of the gases in regions 2 and 3 of the shock tube flow.

CONCEPT VERIFICATION TESTS

The experiment utilized a conventional shock tube (3.5" square and 16' long) fitted with optical glass windows at both ends (Figure 2). A scribed aluminum diaphragm was used and the burst was caused by slowly increasing the pressure on the driver side. Phase aberrations caused by the resulting flow field were recorded holographically, using a ruby laser pulse. The gas pressure and composition on the two sides of the diaphragm and the delay time between the diaphragm burst and diagnostic laser pulse t^* , were the test variables.

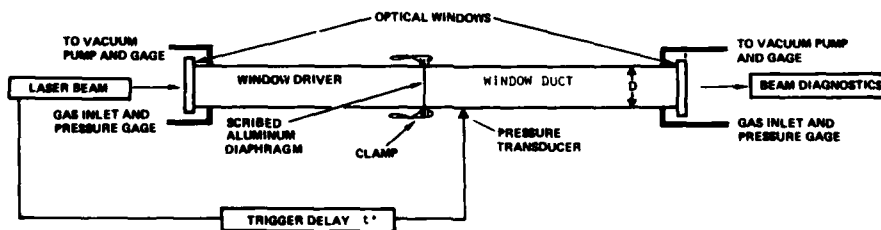


Figure 2. Schematic of test apparatus for pulsed aerodynamic window simulation

The holograms of the shock tube flow event were used in a sandwich mode to obtain interferograms of the medium. This technique allows subtraction of the errors introduced by the measurement optics with the help of a baseline hologram of the evacuated shock tube sandwiched onto the event hologram. Similar in principle to double exposure holographic interferometry, the technique has the additional advantage that the interferogram can be examined under different spacing and direction of the fringes by relative motion of the two holograms, which permits a better evaluation of the phase aberrations and the OPD function.

EXPERIMENTAL RESULTS

Figure 3 shows three interferometric reconstructions of a holographic record, made at different fringe spacings for a case of beam duct at a very low pressure. The driver contained Helium at about 1.2 atm driving into about 0.5 torr of Helium. The three pictures correspond to infinite fringe, coarse fringe and fine

fringe interferograms. There is some crowding of fringes close to the shock tube walls, possibly due to boundary layer effects which are not essential aspects of the window, as discussed later. The central 2" diameter circular portion of the 3.5" shock tube aperture appears to be relatively distortion-free. The flowfield in this medium includes a shock wave of Mach No. 2.8 and expansion waves, none of which are apparent since they are almost parallel to the plane of the picture. The perturbations observed are mostly due to the turbulent contact interface and the wall layers. The time corresponds to about 0.8 ms after the diaphragm burst is initiated. Densitometric evaluation of this and similar interferograms, performed at the Perkin Elmer Co., yielded $(\Delta\lambda/\lambda)_{\text{rms}} \approx 0.02$ for the central 2" circular region after subtraction of tilt and focus.⁷



Figure 3. Sandwich interferograms of axial shock tube flow, $(p_4/p_1) > 10^3$, $p_4 = 1.22$ atm. He., Single event, $t^* = 0.8$ ms.

Figure 4 shows the time-development of the shock tube OPD pattern with a sequence of interferograms made in air with the same gas pressures as above. Here the slower sound speed in air allows more freedom in timing the ruby pulse and also the large refractive index makes the measurement far more sensitive.

Evidently the optical quality of the medium in the central region improves with time, except in the last frame where the shock wave was reflected from the end of the shock tube. A transverse diffraction wave caused during the reflection is seen in the picture. Also, strong light scattering is observed outside the aperture, probably indicating that the reflected shock wave has interacted with the turbulent contact surface and intensified its optical inhomogeneities.

Clearly the central picture on the bottom row provides the best optical quality. In the central 2" region of the 3.5" aperture the maximum optical path perturbation is estimated to be about $\pm \frac{1}{2}\lambda$. The time for this picture, when scaled with the wave velocity and the shock tube dimensions, is equivalent to the time for the pictures in Helium, Figure 3. Accounting for the different refractive indices, 1λ in air corresponds to 0.12λ in He making these results in air consistent with the results obtained in He (Figure 3).





Figure 4. Sequence of interferograms for tests in air with different time delays; $p_4/p_1 > 10^3$, $p_4 = 1.22$ atm. Top: $t^* = 1.0$ and 1.2 ms, Bottom: $t^* = 1.5$, 1.8 and 2.2 ms.

Tests were also made for the case of a beam duct at intermediate pressures. Here He at 1.76 atm was used in the driver and 91.5% He with 8.5% N_2 at 0.59 atm in the driven section ($p_4/p_1 = 3.3$). This gas mixture was selected to match the index of the driver gas after both driver and driven gases are processed by the shock tube waves. The shock Mach No. is roughly 1.3 . Delay times as long as $t^* = 2.4$ ms were examined. The optical quality in the $2''$ central portion of the window was even better in this case as compared to the large pressure ratio cases ($p_4/p_1 > 10^3$), indicating that the shock tube field can have a good optical quality for a wide range of pressure ratios.

Significant degradation of the optical quality is observed next to the shock tube walls throughout this simulation. The observed variations in the optical density in these regions do not correspond to the shock tube flows. The thermal boundary layers on the shock tube walls are typically very thin (≈ 1 mm). In comparison, the observed wall layers are always much thicker (≈ 1 centimeter or more, generally). Interferograms of the shock tube without a diaphragm being pressurized in the same way as the driver section is during a regular test, show density gradients next to the tube walls which bear a striking resemblance to the effects observed in the data. Here the gas in the tube was compressed adiabatically, except near the walls, where the change in gas temperature results in thermal conduction to the shock tube walls. Evidently, this aspect of the data is an artifact of the method used for bursting the diaphragms and is not an essential feature of the shock tube flowfield or of the pulsed aerodynamic window. It will be eliminated if the driver gas can be allowed to come to equilibrium with the walls before bursting the diaphragm by a trigger mechanism.

ANALYSIS AND SCALING OF TEST RESULTS

The properties of the inviscid gas flow in a shock tube are independent of scale when the spatial and time coordinates and the dependent and initial gas properties are properly normalized. Dimensional analysis of the flowfield shows that any gas property "A" is uniquely determined as a function of the scaled space-time variables, with parametric dependence on the normalized initial conditions, in the following form

$$\frac{A}{A_4} \left(\frac{\bar{x}}{D}, \frac{t a_4}{D} \right) = F_A \left(\frac{p_4}{p_1}, \frac{T_4}{T_1}, \frac{M_4}{M_1}, \gamma_1, \gamma_4 \right)$$

When the shock tube is used as an aerodynamic window its most critical property is the variation in the axial optical path lengths across the tube cross-section or window aperture. The relative change of optical path lengths across the window aperture in the (y,z) plane, referenced to any point (y_0, z_0) and at any time can be written as

$$\Delta\lambda(y,z,t) = \int_{-L_4}^{L_1} [\beta(x,y,z,t) - \beta(x,y_0,z_0,t)] dx$$

where x is aligned with the tube (window) axis and β is the local index of refraction minus 1. After normalization, the optical path difference (OPD) function can be written as

$$\frac{\Delta\lambda}{D\beta_4} \left(\frac{y}{D}, \frac{z}{D}, \frac{t a_4}{D} \right) = \int_{-(L_4/D)}^{(L_1/D)} \left[\frac{\beta}{\beta_4} \left(\frac{x}{D}, \frac{y}{D}, \frac{z}{D}, \frac{t a_4}{D} \right) - \frac{\beta}{\beta_4} \left(\frac{x}{D}, \frac{y_0}{D}, \frac{z_0}{D}, \frac{t a_4}{D} \right) \right] d\left(\frac{x}{D}\right).$$

Now since β/β_4 is an invariant for properly scaled devices (identical normalized initial conditions and spatial and time variables), $\Delta\lambda/D\beta_4$ is also invariant.

Thus, given two pulsed aerodynamic windows of different scales but with identical initial conditions, the normalized OPD function will be identical for the two windows provided they are geometrically similar and the time is scaled with the characteristic acoustic period of the device. It should be noted that in the pulsed window typically $T_4/T_1 = 1$. Additionally (β/β_4) depends only weakly upon M_4/M_1 , γ_4 and γ_1 for cases of interest. Thus $(\Delta\lambda/D\beta_4)$, which is the scale invariant performance parameter, becomes mainly a function of the pressure ratio (P_4/P_1) . Also note that the similarity is further contingent on the diaphragms having the same dynamic behavior for the cases being compared. It can be shown, however, that if p_4 and p_1 are the same, and so are the gas composition and diaphragm material, the rupture and overall dynamic behavior of the diaphragm will be similar.

Typical test conditions and test results are presented here in Table 1. Included in the table are two tests with a large pressure ratio (one using He and the other air), and one test for a small pressure ratio (with He in the driver and index matched He/N₂ mix in the driven section). The full window aperture ($D=8.9$ cm) was used in the performance evaluation, assuming that the deleterious wall layers can be completely eliminated with externally triggered diaphragms.

The window beam quality was calculated using the Marechal approximation ($BQ \approx \exp \frac{1}{2} [(\Delta\phi_{RMS})^2]$) for $\Delta\phi_{RMS} \leq 0.5$, whereas an actual "power in the bucket" calculation was performed for cases with $\Delta\phi_{RMS} > 0.5$, using the digitized tilt and focus corrected phase fronts derived from the interferograms. Note that despite the drastic changes in window gas compositions and pressure ratios, the changes in the normalized OPD, the major performance parameter, are rather small, ranging from 2.5 to 4×10^{-3} . This variation may be caused by the change in the normalized pulse delay time, $t^* a_4/D$, as much as by the change in initial conditions. The tests performed were not sufficiently extensive to trace the source of this performance variation.

Table 1. Summary of typical pulsed aerodynamic window test results

TEST CONDITIONS	D(CM)	8.9	8.9	8.9
	Driver Gas	He	Air	He
	P_4 (atm)	1.22	1.22	1.76
	Duct Gas	He	Air	91.5He/8.5N ₂
	P_1 (atm)	10^{-3}	10^{-3}	0.59
	t^* (msec)	0.8	1.8	2.4
	a_4 (m/sec)	1025	344	1025
	λ (μ m)	0.694	0.694	0.694
	β_4	4.4×10^{-5}	3.6×10^{-4}	6.3×10^{-5}
	t^*a_4/D	9.22	6.97	27.5
MEASURED	$(\Delta\lambda/\lambda)_{P-P}$	0.1	1.0	0.06
	$(\Delta\lambda/\lambda)_{RMS}$	0.02	0.2	0.02
	$\Delta\phi_{RMS}$ (rad)	0.13	1.25	0.13
DEDUCED	BQ (at $\lambda = 0.694 \mu$ m)	1.01	2.2	1.01
SCALE INVARIANT PERFORMANCE PARAMETER	$\frac{(\Delta\lambda)_{RMS}}{D\beta_4}$	3.5×10^{-3}	4.3×10^{-3}	2.5×10^{-3}

Table 2 shows projections for pulsed aerodynamic window performance in an ICF system based on our shock tube test results. Two candidate ICF laser drivers are considered: the CO₂ and KrF lasers. Typical laser properties and gas mixes for these two lasers are presented in the table. For the purpose of this performance evaluation it was assumed that the beam duct connecting the laser to the reactor chamber will be under low pressure ($p_1 \approx 10^{-3}$ atm), and therefore only high pressure-ratio windows were considered. Two window apertures were used in this evaluation for each laser candidate: a typical small aperture ($D=10$ cm) window, which would require partial focusing of the laser beam before transmission through the window, and a typical large aperture ($d=100$ cm) window, which matches the laser output aperture and hence requires no beam contraction.

The windows in the ICF system are assumed to be geometrically similar to the window tested in our experiments, and a relatively low value of 10 was assumed for the normalized pulse delay time, t^*a_4/D (t^* being the window rupture to laser beam transmission delay time), to minimize the length of the window (L_1 and L_4). Although the CO₂ and KrF gas mixes were not simulated in our experiments, it was assumed that the gas composition will not have a major effect on the normalized performance parameter, $\Delta\lambda_{RMS}/D\beta_4$, and a conservative value of 4×10^{-3} was used for the performance projections, based on our experiments.

The predicted OPD for the ICF lasers, in terms of $(\Delta\lambda/\lambda)_{RMS}$, can now be determined from the scale-invariant performance parameter, $\Delta\lambda_{RMS}/D\beta_4$, and the scale factor $D\beta_4/\lambda$. The phase variations and beam quality of the transmitted beam can be evaluated by the same procedure used for Table 1.

Included in Table 2 are the beam quality requirements for an ICF laser system. To generate these requirements it was assumed that 1 mm diameter fusion targets will be used, that the beam focusing elements will have a 10 m FL, and that the beam aper-

Table 2. Projections of pulsed aerodynamic window performance for two candidate ICF laser systems.

WINDOW PARAMETERS FOR ICF LASERS	Laser	CO ₂		KrF	
	λ (μ m)	10.6		0.25	
	Laser Mix	He/N ₂ /CO ₂ = .706/.059/.235		Ar/Kr/F ₂ = .95/.045/.005	
	M ₄	14.82		41.92	
	β_4	1.354×10^{-4}		2.613×10^{-4}	
	Driver Mix	He/N ₂ /Ar = .564/.405/.031		Ar/Kr = .9547/.0453	
	λ_4	1.497		1.6576	
	a_4 (m/s)	501.85		314.05	
	p_4 (atm)	1.0		1.0	
	p_2 (atm)	10^{-3}		10^{-3}	
WINDOW INVARIANTS	D (cm)	10	100	10	100
	(p_4/p_1)	10^{-3}	10^{-3}	10^{-3}	10^{-3}
	(t^*a_4/D)	10	10	10	10
	(L_4/D)	10	10	10	10
	(L_1/D)	25	25	25	25
	$(\Delta\lambda/DB_4)_{RMS}$	4×10^{-3}	4×10^{-3}	4×10^{-3}	4×10^{-3}
SCALE FACTOR	(DB_4/λ)	1.28	12.8	104.5	1045
PERFORMANCE PREDICTIONS	$(\Delta\lambda/\lambda)_{RMS}$	0.0051	0.051	0.418	4.18
	$\Delta\phi_{RMS}$ (rad)	0.032	0.32	2.62	26.2
	BQ	1.0005	1.052	8.0	104
ICF REQUIREMENTS	BQ	1.0	4	16	106

ture, before it is focused, is equal to the window aperture. The projected performance of the pulsed windows is clearly within the requirements of the ICF systems considered here.

CONCLUSIONS

A concept for a pulsed aerodynamic window which is compatible with the laser driven ICF Single Pulse Test Facility was developed and tested. Test results, when used in conjunction with similarity and scaling arguments, show that the performance of such windows will meet and surpass the ICF system requirements.

ACKNOWLEDGEMENT

The authors wish to thank Drs. C. Fenstermacher and V. Vishwanathan of LANL for many helpful discussions and suggestions concerning possible implementations of aerodynamic windows in laser fusion systems. They also wish to thank Drs. R. Wuerker and L. Heflinger of TRW for their help in the selection and set up of the optical diagnostics used in these experiments.

REFERENCES

1. E. M. Parmetier and R. A. Greenberg, Supersonic Flow Aerodynamic Windows for High-Power Lasers, AIAA Journal, 11, 7, 1973.
2. E. Zimet, A Transverse-Flow Aerodynamic Window for Chemical Lasers, Naval Ordnance Laboratory, NOL-TR-74-153, August 1974.
3. R. N. Guile and W. E. Hilding, Investigations of a Free Vortex Aerodynamic Window, AIAA Paper No. 75-122, 13th Aerospace Science Meeting, January 1975.
4. H. W. Behrens, G. L. Grohs and C. L. Dailey, Aerodynamic Windows for Chemical Lasers, U.S. Patent No. 4,013,977, March 1977.
5. V. Kulkarny, D. McGregor, J. Schwartz and R. Briones, Pulsed Aerodynamic Windows for Fusion Lasers, TRW Report No. 35659, 101, February 1981.
6. n. Liepman and A. Roshko, Elements of Gasdynamics, John Wiley & Sons, Inc., 1957.
7. P. Mumola, Perkin-Elmer Co., E-O Division, Norwalk, Connecticut (private communication).

AD P 00238

VELOCITY MEASUREMENTS OF INCIDENT AND REFLECTED SHOCK
WAVES IN VARIOUS GASES AND IN SATURATED WATER VAPOUR

W.Garen, K.Brudi, G.Lensch

Fachhochschule Wedel, Germany

Velocity measurements of incident and reflected shock waves have been performed by a four-beam-laserinterferometer. The beam distance for run-time determination was only 3.3 mm, thus insuring an instantaneous velocity measurement obtained by shock-shock reflection (ideal) and by end wall reflection (real). Both investigations have been made in the same tube under the same conditions. Noble gases show a significant deviation of reflected shock velocities between both methods whereas complex gases like CCl_2F_2 are nearly unaffected by end wall influences. Condensation phenomena are also treated. Saturated water vapour has been filled in a perpendicular shock tube and velocity measurements of incident and reflected shock waves have been made. For Mach numbers $M > 1.65$ spontaneous condensation at a copper end wall generates rarefaction waves, which decelerate the reflected shock.

INTRODUCTION

Shock waves reflecting from a co-planar heat conducting wall are influenced by end wall histories. Several investigators have studied such effects on normal stress, temperature¹, density^{2,3} and heat flux to the wall⁴. These measurements have been made at the end wall plate. Theoretical calculations show that besides the above parameters the velocity of reflected shock waves is also obviously influenced by energy exchange, mass absorption and boundary layer effects^{5,6}. Piva et.al² have measured density profiles and velocities (from time marks on scope traces) of reflected shocks for Mach numbers 3, 4 and 6 and for end wall distances between 0.4 and 26 mm. Due to our much smaller shock tube ($40 \times 40 \text{ mm}^2$) we prefer higher pressures p_1 ($38.6 < p_1 < 400 \text{ Pa}$) to prevent undesired boundary layer effects for the tube flow behind the incident shock. The reflected shock is a 'carrier' of end wall histories and brings these influences back from the end wall. Thus it seems to be useful to determine whether careful velocity measurements of incident and reflected shock waves over very small distances demonstrate accommodation effects.

This method requires sufficient space and time resolution and sensitive instrumentation, in particular for low pressures and low Mach numbers. The main goal of part I of this paper is the comparison of reflected shock velocities obtained by shock-shock reflection and by end wall reflection. Both methods have been studied in the same shock tube with similar experimental conditions. Part II of this paper deals in a preliminary way with spontaneous condensation - evaporation - phenomena behind reflected shock waves in saturated water vapour.

Numerical calculations of the Boltzmann equation with the aid of the Krook model⁷ show amongst other things a decrease in reflected shock velocity if on the end wall condensation occurs and an increase in reflected shock velocity if the end wall partly evaporates.

For a first check we have set up a perpendicular shock tube filled with saturated water vapour which is in the state of equilibrium at room temperature. We have used the following 'end walls': a plate of copper or PVC and a plane water surface.

EXPERIMENTAL

Apparatus:

Velocity measurements of reflected shock waves often show an unacceptable scatter caused by various bursting processes of diaphragms and slow deceleration effects for longer distances. Therefore the commonly used diaphragm has been replaced by a quickly opening valve⁸. This method has been successfully applied in several shock tube investigations^{9,10,11}.

The shock tube facility has been described in ref.10. With the help of two identical valves at both ends of a shock tube we have set up a so-called 'double shock wave tube'. Velocity measurements of shock-shock reflections have been presented in 1979 (Symp. on Shock Tubes and Waves, Jerusalem)¹⁰. The present measurements have been performed in the same tube with a cross section of $40 \times 40 \text{ mm}^2$ and a length of 2500 mm.

Measurement technique

Velocities of incident and reflected shock waves have been measured by a laser interferometer in a twofold working mode. The study of shock wave velocities in rarefied gases in a wide range of Mach numbers demands a highly sophisticated measuring technique. A very good temporal and spatial resolution and a high sensitivity (especially for low pressures and low Mach numbers) are required. Fig.1 shows the arrangement of the interferometer. The basic device is a two beam interferometer consisting of two Wollaston prisms¹². The Wollaston prism W_2 splits the laser beam twice with a separating distance of 0.17 mm (middle of shock tube axis). With the aid of the Wollaston prism W_1 the 'two beam interferometer' becomes a 'double two beam interferometer' with a distance of 3.3 mm, i.e. we have two differential interferometers (each with a beam distance of 0.17 mm) and both differential interferometers have a distance of 3.3 mm. By mixing and polarizing the four beams and transforming them to two interfering pairs we get a difference signal from separate photodiodes (PIN-diodes).

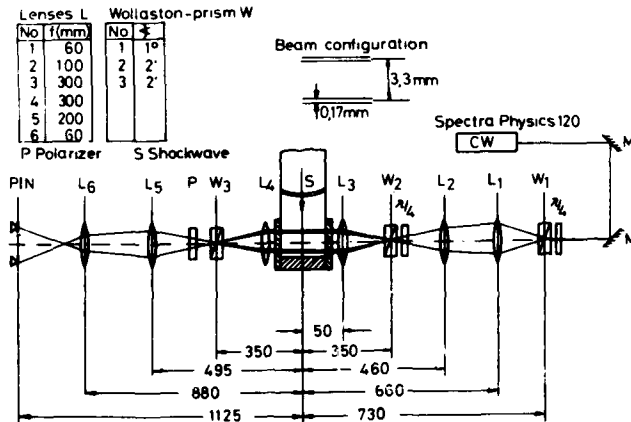


Fig. 1
Laser differential interferometer for velocity measurements.

The diodes are connected inversely, thus the sensitivity is doubled and disturbances (laser power changes, vibration) are avoided. It should be mentioned that the two lenses L_1 , L_2 determine the four beam diameters (at the shock tube axis) as well as the distance of the two corresponding interferometer beams (in this case 3.3 mm). The main advantages of this arrangement are:

- (1) short measuring distance (3.3 mm)
- (2) good spatial and temporal resolution
- (3) high sensitivity
- (4) velocity of the incident and reflected shock wave is measured with the same arrangement, thus the velocity ratio u_R/v_1 is independent of measuring distance d_i .

Fig. 2 shows a typical density trace with a (x, t) - diagram where the x -axis is on a scale of 50:1.

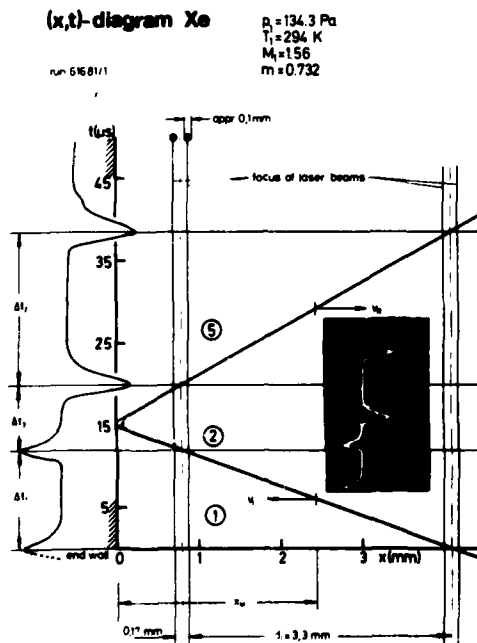


Fig. 2
Typical density trace with (x, t) diagram (x -scale 50:1)

By enlarging the scope pictures, we have calculated the shock Mach number, the velocities of the incident and reflected shock from the time intervals Δt_1 and Δt_2 . The time interval Δt_3 has been used to estimate the position of the end wall relative to the interferometer. This can be done with some measurements of very weak shocks ($M_1 < 1.1$). In the case of an acoustic wave ($M = 1$) the incident and reflected shock wave have the speed of sound.

For $M_1 = 1$, $x_M = \frac{d_i + a_1 \Delta t}{2}$ and we have introduced a dimensionless parameter: $m = x_M/d_i$ thus $0.5 < m < \infty$.

For part I velocity measurements have been made for the values of $m = 0.686$, $m = 0.732$ and $m = 1.376$.

Results (Part I)

Velocity measurements of shock reflection by an end wall plate of aluminium have been performed with the noble gases Ar ($1 < M_1 < 4.1$), Xe ($1 < M_1 < 6.4$) and with the polyatomic gases CO_2 ($1 < M_1 < 5.4$) and CCl_2F_2 ($1 < M_1 < 5.2$).

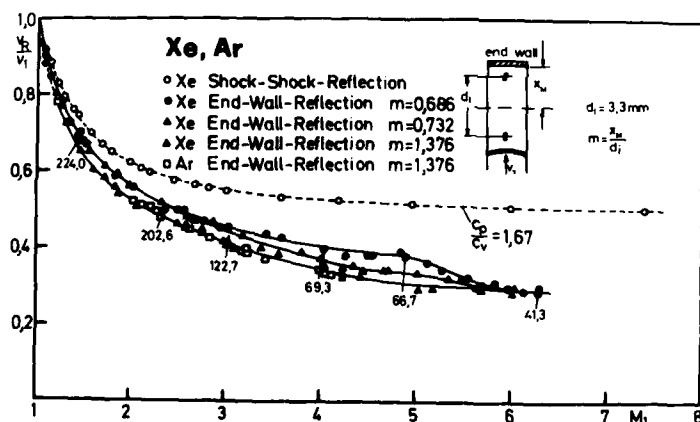


Fig.3
Velocity ratio as a function of Mach number for Xe and Ar. (v_2 : reflected shock velocity, v_1 : incident shock velocity) The parameter values are the initial pressures in Pascal.

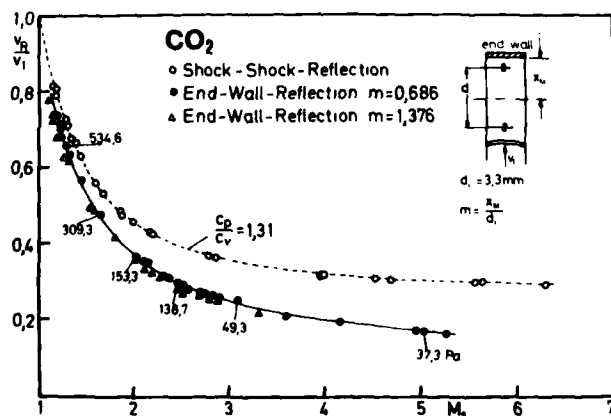


Fig.4
Velocity ratio as a function of Mach number for CO_2 .

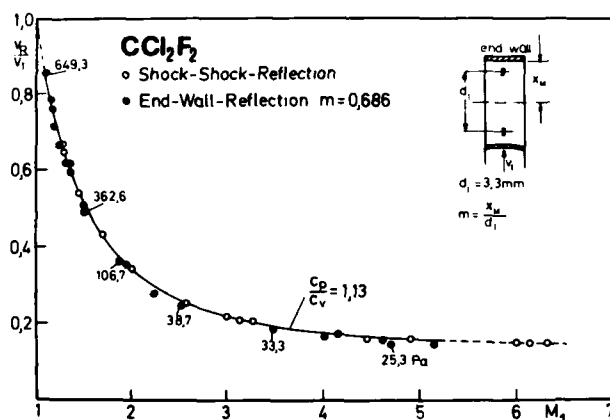


Fig.5
Velocity ratio as a function of Mach number for CCl₂F₂.

Fig. 3,4,5 show velocity measurements of shock waves as a function of the Mach number M_1 . The velocities are normalized by the incident shock velocity v_1 . The open circles are results of shock - shock reflection¹⁰, which have been obtained with the 'double shock wave tube'. In this case the 'end wall' is formed by the collision of two equally strong shocks thus no end wall histories occur ('ideal' reflection). Present results have been obtained with solid end wall plates of aluminium or plastic ('real' reflection). Differences between ideal and real reflection are caused by end wall influences.

The main results are as following:

Velocity measurements of Xe and Ar (especially Xe) depend on measuring position of the interferometer (parameter m) in a certain Mach number range $2.5 < M_1 < 6$ (fig.3). This dependence was not observed for 'ideal' reflection. For instance in the case of 'real' reflection a small displacement of $\Delta x_M = 0.15 \text{ mm}$ ($m=0.686$ to $m=0.732$) changes the normalized velocity v_R/v_1 by a maximum amount of 18% for a fixed Mach number of $M_1 = 5$. On the other hand a displacement of $x_M = 3 \text{ mm}$ ($m=1.376$ to $m=1.41$) doesn't change the reflected shock velocity. This significant change of velocity appears mainly related to the ionisation of Xenon behind the reflected shock wave^{13,14}.

When this paper was submitted for presentation it was expected that numerical calculations⁵ (one - parameter accommodation coefficient) would be available at the time of the Symposium to verify the experimental results above. Unfortunately it was not possible to present calculations which take into account the shock deceleration by ionisation.

Our measurements for CO₂ and CCl₂F₂ are almost independent of displacement m . For CO₂ there is, similarly as for noble gases, an increasing velocity difference between 'ideal' and 'real' reflection (fig.4), whereas in the case of CCl₂F₂ no difference is observed.

Experimental (Part II)

A perpendicular shock tube has been set up for an investigation of the phenomena of condensation and evaporation. Tube and equipment are the same as that mentioned in part I.

Because of the relatively high initial pressures we have connected a cookie cutter made of glass (i.d. 17 mm) to the end of the shock tube. Various 'end walls' (copper, plastic, liquid) can be used for shock wave reflection. Initially the shock tube has been filled with saturated water vapour. This vapour has been obtained from distilled water being thoroughly degassed in advance.

For this system we have measured the incident and reflected shock wave velocities for end walls of copper and plastic. Being dependent on temperature the pressures p_1 were in the range $1064 < p_1 < 3325$ Pa. For driver gas we have used hydrogen up to 19.8 kPa providing Mach numbers $1 < M_1 < 2.5$.

In a second test the solid end wall has been replaced by a plane water surface in order to obtain probable spontaneous evaporation behind the reflected shock wave. Since the measurements were to take place immediately at the water surface, the surface tension had to be avoided.

Therefore, after having moistened the inner surface of the cookie cutter with a solution of silicon oil (2%) and methanol, we have baked the cookie cutter for 24 hours at a temperature of 523 K. Different liquid surface positions (parameter m) can be chosen by varying the level of a small container (communicating tubes). With the help of a TV camera the exact position of the interferometer in relation to the water surface has been measured.

Results:

In the same manner as in part I we have measured the velocities of incident and reflected shock waves as a function of incident Mach numbers. For Mach numbers $M_1 < 1.65$ and saturated water vapour the measured values are identical with those of the polyatomic gas CH_4 , which has the same heat capacity and sound velocity as water vapour.

For Mach numbers $M_1 > 1.65$ there is a sudden decrease of reflected shock velocity (fig.6) and an increase of scatter.

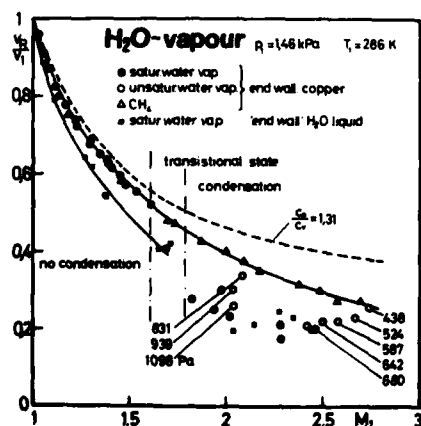


Fig.6
Reflected shock velocity normalized by the incident shock velocity as a function of the Mach number for different 'end walls' in saturated water vapour.

At the cold end wall plate (copper), condensation of water vapour occurs causing rarefaction waves which decelerate the reflected shock wave.

For $M_1 > 1.65$ these rarefaction waves overtake the reflected shock (fixed interferometer position $m=0.5$) effecting the deceleration. Fig.7 shows the density pulses of the incident and reflected shock wave as well as first rarefaction waves.

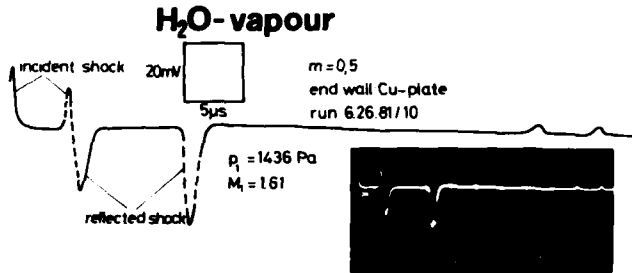


Fig.7
Density trace in saturated water vapour with first rarefaction waves (small pulses at the right side of the figure)

In order to prove the above assumption, and to exclude the observed rarefaction waves coming from the driver section, corresponding measurements with the same pressures have been done with methane ($a_1(\text{H}_2\text{O}) = a_1(\text{CH}_4)$; $c_p/c_v(\text{H}_2\text{O}) = c_p/c_v(\text{CH}_4)$). Fig.6 shows good agreement between water vapour and methane for $M_1 < 1.6$. For a further check, we decreased the initial pressure p_1 to get unsaturated water vapour (the vapour behaves like a real gas) to reduce or avoid condensation. The open circles in fig.6 are measurements which show the increasing reflected shock velocities as a result of decreasing initial pressures p_1 . A few measurements have been made in saturated water vapour with a liquid 'end wall' of water. The measured reflected velocities are all smaller compared to those obtained with solid end walls.

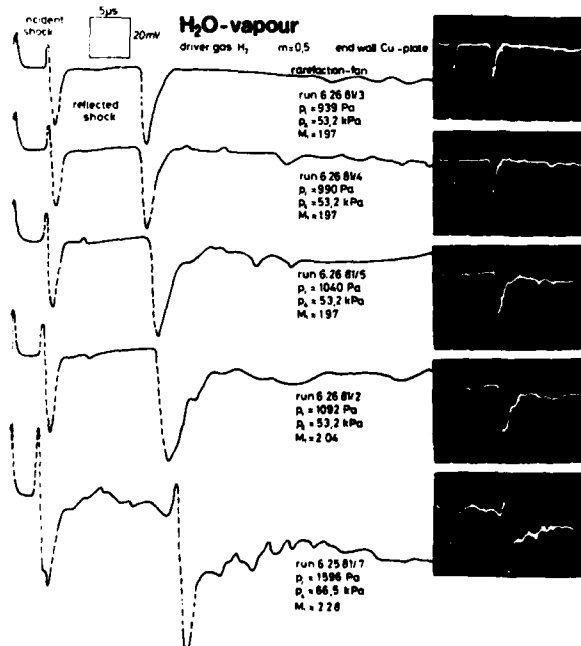


Fig.8
Density traces with increasing initial pressures causing a deceleration of the reflected shock wave by rarefaction waves.

Fig.8 demonstrates condensation effects for a nearly constant Mach number M_1 and different initial pressures p_1 . With increasing pressure p_1 rarefaction waves travel with increasing velocities behind the reflected shock and eventually overtake it.

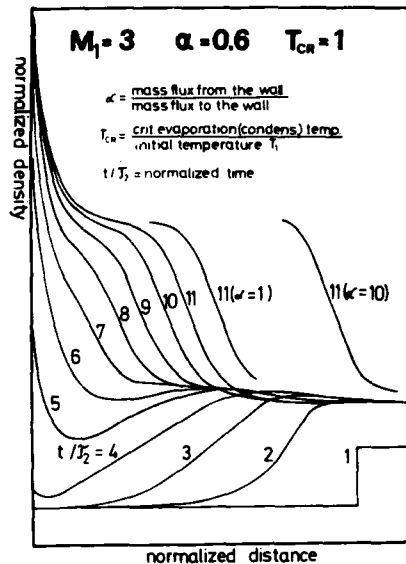


Fig.9

Normalized density calculations as a function of the normalized distance from the end wall with a dimensionless parameter of time.

(condensation: $\alpha < 1$)

'ideal' reflection: $\alpha = 1$

evaporation: $\alpha > 1$)

Fig.9 shows numerical results with the model of ref.7 for the Mach number $M_1 = 3$. Two parameters besides the Mach number can be varied. The ratio of the critical temperature normalized by the initial temperature which is called T_{CR} and the ratio α of the incident and the reflected mass flux to and from the wall. For a value of $\alpha < 1$ condensation (or absorption) occurs and for $\alpha > 1$ the end wall partly evaporates. In the case of $\alpha = 1$ the incident shock will be reflected without end wall influences (ideal reflection). The dimensionless parameter T_{CR} acts as a threshold value.

For instance in a two - phase - system (vapour and liquid end wall' of water) values of $T_{CR} \gg 1$ and $\alpha > 1$ are conditions for evaporation behind reflected shock waves. Spontaneous evaporation behind reflected shock waves are relatively unprobable for small Mach numbers:

1. The pressure increase is much higher than the temperature increase of the vapour.
2. The temperature of the 'end wall' water will differ little from the initial temperature.

On the other hand condensation will be favoured due to the above assumptions. Therefore we have chosen the following conditions in the case of shock wave reflection in saturated vapour:

$$T_{CR} = 1 \quad M_1 = 3 \quad \alpha = 0.6, 1, 10$$

The development of the velocity of the reflected shock wave depending on the value of α is especially interesting (fig.9). Condensation decelerates the reflected shock ($\alpha = 0.6$) and evaporation accelerates it ($\alpha = 10$).

CONCLUSIONS

Velocity measurements for the cases of ideal and real reflection show increasing deviations with increasing Mach numbers as a result of end wall influences. Careful velocity measurements at different positions in front of the end wall plate give more information about the end wall histories and the influences on reflected shock velocity in the boundary layer. The results with Xenon show a non uniformity in reflected shock velocity at a

distance of about 3 mm ($m=1.41$) in front of the end wall. This non uniformity is probable caused by the ionisation of Xenon. The reflected velocity of CCl_2F_2 is equal for both reflection processes, thus there is apparently no energy exchange at the end wall for such complex gases. In all cases of solid end wall measurements no differences in reflected velocities between aluminium, copper and PVC - plastic have been observed.

Reflected shock waves in saturated vapours can be influenced by condensation phenomena. Preliminary results show a strong effect on the reflected shock's deceleration when it is overtaken by rarefaction waves.

A model which specifically takes into account end wall and boundary layer influences as well as the inner degrees of freedom would be very useful for the theoretical interpretation of reflected shock velocity measurements.

This model should also include condensation and evaporation effects in case they occur.

ACKNOWLEDGEMENT

The authors are grateful to Prof.H.Grönig, TH Aachen, for valueable theoretical discussions, and to Vera Ludszuweit in preparing this paper.

REFERENCES

1. R.K.Hanson, Phys.Fluids 16, 369 (1973)
2. H.O.Piva, B.Sturtevant, Rarefied Gasdynamics, Vol.II,381, New York, Academic Press. (1969)
3. H.Meldau, PhD thesis, TH Aachen (1977)
4. D.L.Schultz, T.V.Jones, AGARD No 165, Univ.Oxford, G.Britain (1973)
5. G.S.Deiwert, Phys.Fluids 16, 1215 (1973)
6. D.Hänel, PhD thesis, TH Aachen (1974)
7. F.G.Tcheremissine, Acad.Press, New York, London, 3,417,(1977)
8. W.Garen, R.Synofzik, A.Frohn, AIAA-Journ.12,1132 (1974)
9. W.Garen, R.Synofzik, A.Frohn, G.Wortberg, AIAA-Journ.51 519, (1976)
10. W.Garen, G.Lensch, XII.Int.Shock Tube Symp.,Jerusalem(1979)
11. G.König, A.Frohn, Proc.of the Int.Symp.on Flow Vis, Bochum (1980)
12. G.Smeets, A.George, ISL-Report, 14 (1971)
13. Y.Takano, Y.Shimomura, T.Akamatsu, XI.Int.Shock Tube Symp., Seattle (1977)
14. A.Hirschberg, PhD thesis, TH Eindhoven (1981)

AD P000239

INVESTIGATION OF THE DISTORTION OF SHOCK-FRONTS
IN REAL GASES

A.F.P. Houwing, H.G. Hornung* and R.J. Sandeman

Department of Physics
Australian National University
Canberra, A.C.T., 2601, Australia

Previous experimental work has found that under certain conditions non-planar shock fronts and non-uniform test slugs occur in shock tubes, and suggests that in some instances a Rayleigh-Taylor instability at the contact surface is related to real gas effects of the test gas. For this reason an extension is made of an analysis due to Levine that considers contact surface leakage when embedded in the relaxation region. Also, to elucidate the effect of the post shock boundary layer on possible contact surface instability, a modification of Mirels' boundary layer entrainment theory, to take into account Levine-type mixing across the contact surface, is discussed. Experiments to determine shock shape, test sample uniformity and test slug length are carried out with the use of time resolved differential interferometry and streak shadowgraphy for Ar/SF₆ test gas mixtures. The experimental results suggest that the observed flow non-uniformities depend only weakly on the conditions across the contact surface but depend strongly on test slug conditions.

INTRODUCTION

Distorted shock fronts and non-uniform test slugs have often been observed in shock tubes. Cloupeau¹ showed that under certain conditions in an electromagnetically-driven tube the driver gas did not separate from the test gas to form a well defined contact surface. Evidence obtained by Kelly and Besse² and Levine³ using pressure-driven tubes suggested that this was due to the presence of a Rayleigh-Taylor⁴ instability. In addition Emery and Ashurst⁵ reported non-planar shock fronts and non-uniform test slugs for the heavy test gases SF₆ and C₄F₈ in an explosively-driven shock tube.

In an attempt to understand the cause and nature of test slug non-uniformities and shock front distortions in a free-piston shock tube, experiments were carried out with Ar/SF₆ test gas mixtures, under conditions favourable to Rayleigh-Taylor instability across the contact surface, in the large shock tube facility, T36, by Maddever and Hornung⁷. Experiments using pure SF₆ test gas produced non-planar shock fronts followed by

* Present address: DFVLR, AVA, 3400 Gottingen, West Germany.

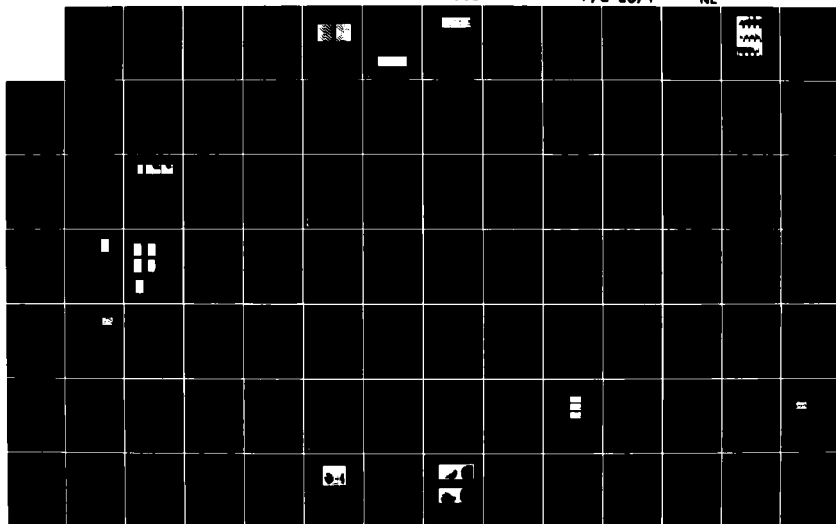
UNCLASSIFIED

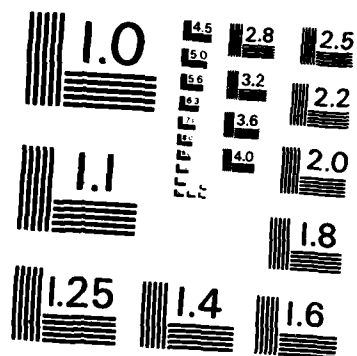
PROCEEDINGS OF THE INTERNATIONAL SYMPOSIUM ON SHOCK
TUBES AND WAVES (13TH. (U) CALSPAN ADVANCED TECHNOLOGY
CENTER BUFFALO NY C E TREANOR ET AL. JUL 81
AFOSR-TR-82-1031 F49629-81-C-0002 F/D 20/1

F/0 20/1

NL

3110





MICROCOPY RESOLUTION TEST CHART
NATIONAL BUREAU OF STANDARDS-1963-A

non-uniform test samples. The addition of sufficient Argon to the test gas produced planar shocks followed by comparatively uniform test slugs, thus suggesting the presence of a Rayleigh-Taylor instability at the contact surface. Because the T3 facility did not allow observation windows to be mounted flush with the circular cross-section inner wall, a square inner-cross-section shock tube was constructed and incorporated into the smaller free-piston shock tube facility, T28. The square section tube allowed windows to be mounted flush with the inner wall, thus enabling the shock tube flow to be visualised without being affected by area changes. These latter experiments undertaken by the present authors employed streak-shadowgraphy for visualisation of the shock, the test slug, and an apparent mixing front which separated the pure test sample from a turbulent region in which the driver and test gas are mixed. These experiments confirmed that pure SF_6 test gas produced distorted shocks and non-uniform test samples. However the addition of only small quantities of Argon produced a planar shock front and a comparatively uniform but short test slug. The use of the heavy noble gas Xenon as the test gas produced planar shocks and very uniform test samples thus suggesting that real gas effects were contributing to the instabilities in the Ar/SF_6 case. For this reason Levine's analysis has been extended to take into account the vibrational and dissociative relaxation behind the Ar/SF_6 shock fronts. In addition, an analysis, to take into account the acceleration field associated with boundary layer mass entrainment, has been used in an attempt to determine the contribution of the boundary layer to instabilities at the contact surface. However both these theories were found to be inadequate in predicting the separation of the mixing front from the shock wave.

THEORY

Levine assumes that the contact surface is a mixing front followed by a region in which the turbulent driver gas and test gas mix. Such a mixing zone can begin during the shock formation process as discussed by White⁹. Levine suggests that this mixing zone consists of "blobs" of mixture, different blobs having different gram fractions, α , of driver gas. Figure 1 shows the varia-

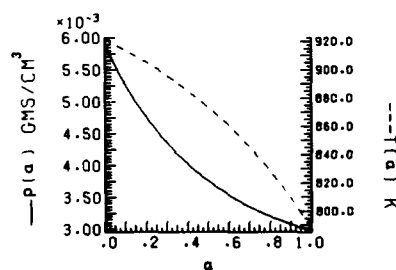


Figure 1(a)

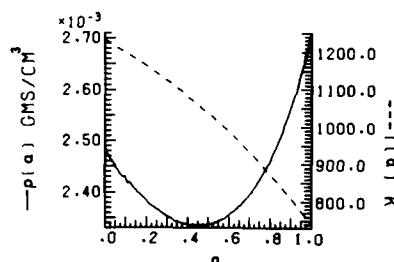


Figure 1(b)

tion of the mixture density $\rho(\alpha)$ on the driver gas gram fraction α for two different experimental conditions. In both situations there exists a particular value of α for which the resultant mixture has a minimum density ρ_{\min} . Thus provided ρ_{\min} is less than the pure test gas density ρ_2 that blob is buoyant in the presence of the pure test gas and will be driven into the test slug if a favourable "pseudo-gravitational" field exists. Note that according to figure 1(b) such a Rayleigh-Taylor instability is possible even if the pure driver gas is more dense than the pure test gas provided that sufficient mixing occurs.

Levine considers the motion of a blob at density ρ_{\min} when the contact surface experiences deceleration on receding from the shock through the relaxation zone in ionizing Argon and suggests a criteria for when the resulting mixing front will not separate from the shock. In the present experimental work temperatures are too low to cause ionisation. However SF_6 has a large number of vibrational energy levels which can be excited at low temperatures and a vibrational-dissociative relaxation zone exists behind the shock. Thus a deceleration field analogous to that considered by Levine can be present in this case. The presence of a boundary layer behind the shock may be a further source of contact surface deceleration through the process of mass entrainment. To elucidate which (if either) of the two possible sources are contributing to the experimentally observed instabilities both possibilities were investigated theoretically. The case for boundary layer mass entrainment is considered first.

According to Mirels and Mullens¹⁰ the density variation due to mass entrainment by the boundary layer behind the shock is small compared to the variation in flow velocity. Mirels¹¹ therefore suggests that if the growth in the thickness of the boundary layer with distance from the shock can be described by a power law, then the velocity profile will be as given in shock-fixed coordinates by

$$u_2(x) = u_2(0) \left[1 - \left(\frac{x}{x_m} \right)^{1-n} \right] \quad \dots(1)$$

where $n = 1/2$ for a laminar boundary layer and $n = 1/5$ for the turbulent case. x_m is the distance at which the post shock free stream velocity, u_2 , becomes stationary when the total mass flux is accommodated through the boundary layer (x_m therefore corresponds to the maximum possible separation of the shock and contact surface). The contact surface recedes from the shock at velocity u_2 which according to equation (1) changes with separation so that the fluid in the contact surface reference frame experiences a "pseudo-gravitational" field

$$g = - du_2(x_c)/dt,$$

where x_c is the separation of the shock and contact surface. Blobs of gas at density ρ_{\min} travelling with the contact surface will be buoyant in the presence of this field and propelled from the contact surface into the test gas. Assuming that the buoyant gas acts like a rigid sphere of sufficiently small size so that viscosity is unimportant it is possible to arrive at an equation of motion. Following Batchelor¹² for the present case we find,

$$\frac{du_b(x_b)}{dt} = k \frac{du_2(x_b)}{dt}, \quad \dots(2)$$

where $R = \rho_2/\rho_{\min}$, $k = \frac{3R}{2+R}$, x_b is the position of the sphere and u_b its velocity. Because the assumption of incompressible flow is valid (see ref. 11) it is possible to integrate with respect to x for steady flow and constant R with the initial condition

$$u_b(0) = u_2(0)$$

to give

$$u_b^2(x_b) - u_2^2(0) = k [u_2^2(x_b) - u_2^2(0)] \quad \dots(3)$$

For the situation where the sphere becomes sufficiently deformed to conform with the enveloping streamlines, the buoyant gas may be considered to behave like a continuum in which case that k is replaced by R . It is important to note that a difference exists between the equation of motion obtained by Levine and that due to Batchelor. In part this can be traced to the fact that

Levine has neglected the virtual mass of the buoyant sphere and to the use of different integration paths.

We assume that x_b becomes the new test slug length in the presence of this Rayleigh-Taylor instability. Further when u_b becomes zero, we assume that the total flux of buoyant gas is accommodated through the boundary layer and the value of x_b at which this occurs becomes the new maximum test slug length S . From equations (3) and (1) this is seen to occur when

$$x_b = S \equiv x_m (1 - \sqrt{1 - 1/k})^{1/(1-n)}. \quad \dots(4)$$

Integration of equation (2) suggests that this limit is reached when

$$\frac{u_2(0)t}{x_m} > 1,$$

where t is the time elapsed since diaphragm rupture. This condition is satisfied in the present work so that in order to compare theory with experiment equation (4) is sufficient.

For the case of buoyant gas travelling through the relaxation zone of length x_r it is necessary to integrate equation (2) taking into account the variation of R through the relaxation zone since the assumption of incompressible flow is no longer valid. Although the profile of $\rho_2(x)$ is easily determined from continuity, evaluating $\rho_{\min}(x)$ contributes a more involved task, and is beyond the scope of this paper. For the present, in order to compare our work with that due to Levine we shall assume that R is constant. Integration then gives equation (2) with $u_2(x)$ now being the profile through the relaxation zone. $u_2(0)$ is then u_{2f} , the frozen post shock velocity. Should u_b become zero inside the relaxation zone the mixing front will remain inside this region. Noting that $u_2(x_r)$ is u_{2e} (the equilibrium post shock velocity) this occurs when,

$$L^2 = \frac{k(u_{2f}^2 - u_{2e}^2)}{u_{2f}^2} > 1 \text{ and } R > 1. \quad \dots(5)$$

This criterion is similar to that due to Levine if his $R-1$ is replaced by our k .

EXPERIMENT

Two separate but related experiments were carried out. The first, undertaken by Maddever and Hornung sought to determine the shock shape and test slug uniformity by producing time resolved differential¹³ interferograms of the flow in the large free-piston shock tube facility T3 using different driver conditions and Ar/SF₆ test gas mixtures. A nitrogen-pumped dye laser having a pulse duration of 5 ns was used as a light source. Shock transit times were measured using thermocouple heat transfer gauges while a pressure transducer located 7.5 cm upstream of the observation windows was used to trigger the laser light source. Flat windows of 4 cm diameter and slightly recessed from the inner wall of the circular cross-section shock tube allowed observation of the flow. Diffraction of the shock and other flow disturbances were caused by the area change at the observation windows and may have contributed largely to uncertainties in classifying the flow condition. However it was still possible in most instances, to discern large non-uniformities of the test slug and distortions of the shock front that appeared to be related to the process of turbulent mixing. Two extreme conditions were observed. The first shown in the interferogram of figure 2(a) is characterised by a planar shock front and undisturbed post shock fringes indicating a

uniform test slug, and was classified as "stable". The second, shown in figure 2(b) and characterised by a badly distorted shock front and chaotic post shock fringe shift depicting a highly turbulent test sample, is classified as "unstable". The extremes shown in figure 2 presented no difficulty in



Figure 2(a)



Figure 2(b)

classification. However under some experimental conditions it was found that a smooth spherically shaped bulge appeared on the shock front while the test slug appeared to be undisturbed. Possibly such an event corresponds to the D'yakov-type^{14,15} instability reported by Griffiths, Sandeman and Hornung¹⁶, although it is outside the criterion for this instability, or could be related to diffraction effects associated with the area change at the observation windows. Care had to be taken in classifying this third condition especially at low densities where the differential interferometer was less sensitive to flow non-uniformities. Because the shock did not have the "bubbly" appearance of that shown in figure 2(b) it was supposed that this latter class was unrelated to the process of buoyantly driven mixing and it was therefore decided to classify such events as "uncertain". Maddever and Hornung's results only allowed the post shock flow to be visualised up to 2 cm behind the shock front before the flow began to interact with the wedge model (visible in figure 2, was used for other purposes and has no significance to the present work) and therefore location of the mixing front was not possible.

Table 1 lists the experimentally measured and theoretically calculated flow conditions for these experiments. Test slug conditions were theoretically calculated from the measured shock speed and shock tube filling pressure by the use of an algorithm that took into account real gas properties but assumed thermodynamic equilibrium. Thermodynamic data for the gases Ar, SF₆, and the dissociation products SF₄, SF₂, S₂ and F₂ were obtained from the data of McBride, Heimerl, Echlers and Gordon¹⁷. The ratio R, was calculated by determining the mixture densities $\rho(\alpha)$ for different values of α by the use of the same computer program until a minimum density was encountered. In evaluating $\rho(\alpha)$ it was assumed that the resulting mixture reached thermodynamic equilibrium isobarically and adiabatically. Two typical plots of $\rho(\alpha)$ are

Table 1.

Ar/SF ₆	P ₁ (torr)	M ₁	Classification	R	L
0	18	11.5	unstable	2.01	1.19
0	5	16.5	unstable	1.92	1.19
1	80	5.5	uncertain	1.78	1.05
1	40	6.9	unstable	2.06	1.10
1	20	8.2	stable	1.52	1.07
1	10	9.7	uncertain	1.34	1.05
1	5	11.6	uncertain	1.31	1.05
2	80	5.4	stable	1.29	0.94
2	35	6.1	stable	1.15	0.92
2	8	7.8	stable	1.07	0.93
6	22	6.2	stable	1.00	0.73

given in figure 1. The flow velocity behind the frozen normal shock, u_{2f} , was simply calculated from (assuming the strong shock limit),

$$\frac{u_{2f}}{u_1} = \frac{\gamma_f - 1}{\gamma_f + 1},$$

where γ_f is the ratio of the frozen specific heats.

The second group of experiments used a square-inner-section shock tube of 3/4" internal width, with observation windows mounted flush with the shock tube walls. A shadowgraph optical arrangement was sufficient to visualise both the shock and the mixing front. Streak photography was used to enable flow visualisation up to 70 μ s behind the shock. A slit focussed into the focal plane of the recording camera allowed a spatial resolution of less than 0.5 mm. Shock transit times were measured using pressure transducers, the closest transducer to the observation windows being used to trigger the streak camera. A cw He Ne laser was used as a light source, and an electronic shutter was necessary to ensure that the high intensity laser light illuminated the photocathode of the streak camera for only a minimum duration. Two typical streak-shadowgraphs are shown in figure 3. Invariably when what appears to be



Figure 3(a)

the mixing front, was observed to be separated from the shock as shown in figure 3(a), the shock wave was found to be plane, while when the apparent mixing front appeared to be not separated the shock was found to be badly distorted as shown in figure 3(b). This suggests that buoyantly driven mixing directly behind the shock may modify the shock strength causing it to



Figure 3(b)

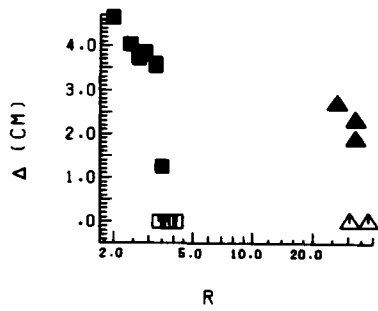
become distorted. Further we did not observe the bulged shock fronts of the previous experiments.

From the shadowgraphs, the streak speed and shock velocity it was possible to measure the separation distance Δ of the apparent mixing front from the shock, while the test slug conditions, the values of R and L were again calculated as previously. S was evaluated from equation (6). x_m was calculated from references 11 and 18 using the real gas properties of the Ar/SF_6 test slug and employing the Sutherland viscosity law. Mirels¹⁹ suggests that an appropriate Reynolds number per unit length for shock tube flow is given by,

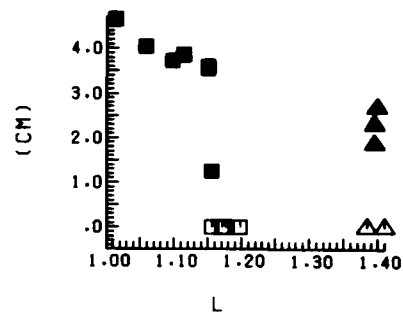
$$\frac{Re}{\ell} = \frac{u_2}{\nu_w} \left[\frac{u_1}{u_2} - 1 \right]^2, \quad \dots(6)$$

where ν_w is the kinetic viscosity measured at the wall. Hartunian, Russo and Marrone (ref. 20) report that the highest boundary layer transition Reynold's number, calculated from equation (6) and experimentally measured values of $\ell = \ell_t$, is approximately 50 million. In the present work Re/ℓ is greater than 100 million/cm and we would expect $\ell_t < 0.5$ cm, consequently the assumption of a turbulent boundary layer appears to be valid. The correlation of Δ with the various parameters is shown in figure 4.

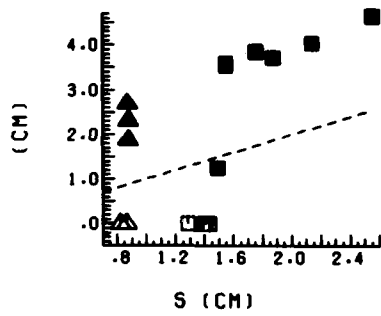
Square symbols correspond to the use of Argon as a driver gas while triangular symbols indicate the use of Helium for the driver gas. The symbols have been filled when the shock front was observed to be plane, but unfilled when distorted. Error bars are approximately the size of the symbol. The results presented were taken over a narrow range of shock Mach number ($6.1 < M_1 < 6.6$) in order to see the consequences of varying the driver gas conditions. The results show a poor correlation with the density ratio R , the modified Levine's parameter and the predicted separation due to boundary layer entrainment, although in the latter case agreement between the two driver gas conditions is improved. It is emphasised that the assumption of constant R could be important in determining the separation as predicted by relaxation effects. The correlation with Reynolds number per centimetre as defined by equation (6) is somewhat better than with the predicted separation S , but the best correlations are obtained with parameters such as the temperature ratio across the shock or the Ar/SF_6 ratio which reflect the thermodynamic properties of the mixture. Noticeable in this correlation is the rapid decrease in the separation of the mixing front from the shock for Ar/SF_6 ratios less than 0.25. Further experiments are in progress to investigate these effects.



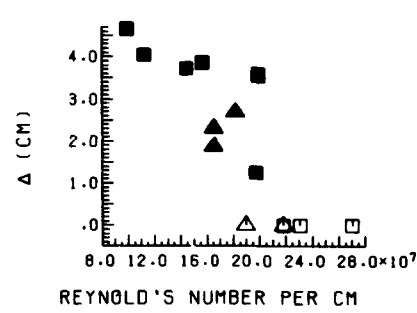
(a)



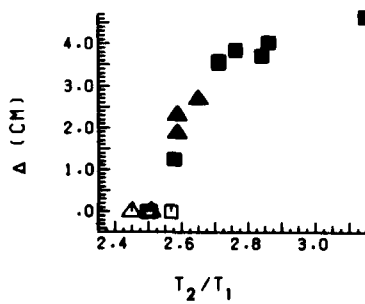
(b)



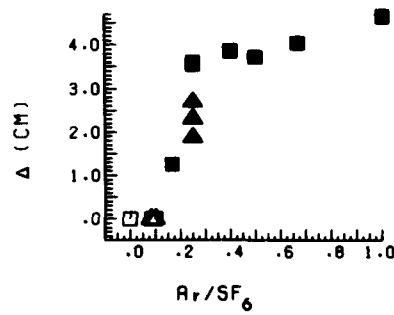
(c)



(d)



(e)



(f)

Figure 4.

CONCLUSION AND REMARKS

The experimental work to date does not support the simple models of Rayleigh-Taylor instability as presented here, although this may be due to the assumption that the ratio R is constant through the relaxation region. The theory is being modified to remove this restriction.

For the second series of experiments no shock distortions were observed where the apparent mixing front was clearly separated from the shock wave, and the separation distance reduced rapidly with increased concentrations of SF_6 in the test gas above a critical value. This is under further investigation and particularly experiments are proposed in which the driver gas density is sufficiently high to reduce the tendency to instability at the contact surface.

ACKNOWLEDGEMENTS

The authors wish to thank Mr. Maddever for the use of his experimental data.

REFERENCES

1. M. Cloupeau, *Phys. Fluids* **6**, 679 (1963).
2. J.G. Kelly and A.L. Besse, *Bull. Am. Phys. Soc.* **12**, 706 (1967).
3. M.A. Levine, *Phys. Fluids* **13**, 1166 (1970).
4. G. Taylor, *Proc. Roy. Soc. (London)* **A201**, 192 (1950).
5. A.F. Emery and W.T. Ashurst, *AIAA J.* **7**, 1731 (1969).
6. R.J. Stalker, *J. Aeronaut. Sci.* **76**, 371 (1972).
7. R.A.M. Maddever, Honours report, A.N.U., unpublished (1980).
8. R.J. Stalker, *AIAA J.* **5**, 2160 (1967).
9. D.R. White, *J. Fluid Mech.* **4**, 585 (1958).
10. H. Mirels and J.F. Mullen, *Phys. Fluids* **7**, 1208 (1964).
11. H. Mirels, *AIAA J.* **2**, 84 (1964).
12. G.K. Batchelor "An Introduction to Fluid Dynamics", page 454, Cambridge University Press (1970).
13. W. Merzkirch, "Flow Visualisation", Ch. 3, Academic Press, Lond. (1974).
14. S.E. D'yakov, *Zh. Eksp. Teor. Fiz.* **27**, 88 (1954).
15. G.W. Swan and G.R. Fowles, *Phys. Fluids* **18**, 28 (1975).
16. R.W. Griffiths, R.J. Sandeman and H.G. Hörnung, *J. Phys. D: Appl. Phys.* **8**, 1681 (1976).
17. B.J. McBride, S. Heibel, J.G. Ehlers and S. Gordon, NASA SP-3001 (1963).
18. H. Mirels, NACA TN-3712 (1956).
19. H. Mirels, *Phys. Fluid* **6**, 1201 (1963).
20. R.A. Hartunian, A.L. Russo and P.V. Marrone, *J. Aerospace Sci.*, August, 587 (1960).

AD P000240

MEASUREMENT AND CALCULATION OF SHOCK ATTENUATION
IN A CHANNEL WITH PERFORATED WALLS

Wolfgang Merzkirch and Walter Erdmann

Institut für Thermo- und Fluidodynamik

Ruhr-Universität, D-4630 Bochum, Germany

The velocity of a shock wave generated in an air/air shock tube with perforated walls is measured by means of an optical Doppler schlieren technique. The attenuation of the shock is measured for perforation ratios varying between 0.1 and 0.5 and over a length of about 40 channel heights. Various numerical models are used to determine the shock attenuation, and these results are compared with the experimental data.

INTRODUCTION

A shock wave propagating in a channel of constant cross section and with perforated walls is continuously attenuated. The perforation causes a loss of the energy or momentum associated to the motion of the shock wave in the channel. As a consequence the shock velocity decreases with time or distance of propagation. The velocity gradient depends on the initial shock strength, expressed e.g. by the shock Mach number M , and on the degree of perforation; i.e. the ratio of the open portion of the wall and the total wall surface. This process has been analyzed by Wu and Ostrowski (ref.1) and by Szumowski (ref.2) who both assume that the mentioned loss of momentum can be described with the momentum flux in stationary gas jets which exhaust from the channel through the perforation after the passage of the shock. The interaction of the moving shock wave with the openings of the perforation is not included in (refs. 1 and 2). As an alternate approach, this interaction can be considered by repeatedly applying one of the various models for the propagation of a shock through a channel with a side-branch, the branches representing the individual openings of the perforation. Three of these models (refs. 3-5) are tested here to predict the attenuation of the shock. The gradient of the shock velocity is measured by applying the optical Doppler-schlieren technique (ref.6) which may deliver the shock velocity with a high degree of local precision. The various theoretical approaches are tested with these experiments for a initial shock Mach number $M_0 = 1.6$ and for values of the perforation ratio $0.1 \leq \eta \leq 0.5$.

EXPERIMENTAL PROCEDURE

Experiments are performed in an air/air shock tube with rectangular

cross section. The perforation consists of parallel, equidistant slits, normal to the tube axis, in the ground and cover plate of the rectangular channel (Figure 1), while the side plates, in the test section, are made of glass so that the interaction of the shock with the openings of the perforation can be photographed.

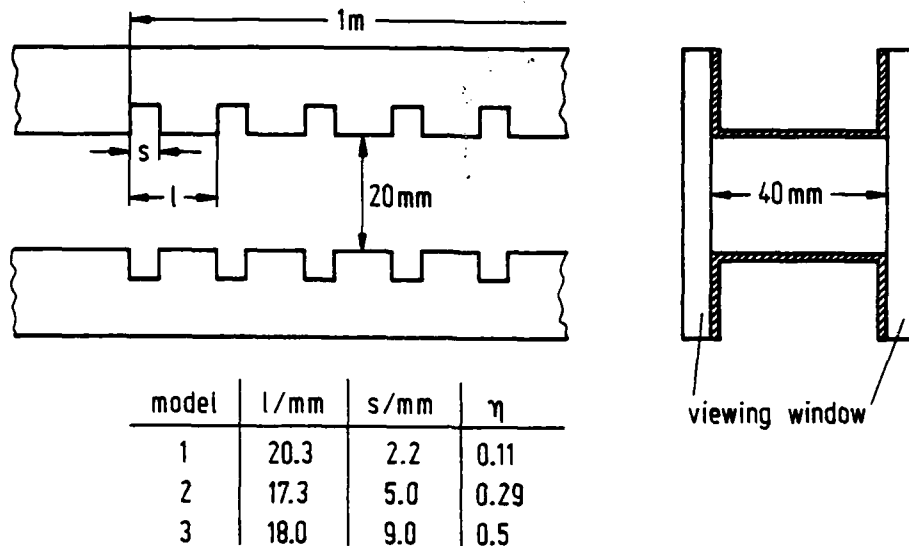


Figure 1: Geometry of the perforation in the ground and cover plate of the shock tube, and definition of the perforation ratio $\eta = s/l$.

Figure 2 is a series of 3 shadowgraphs taken at three different instants of time and showing the shock pattern for the perforation ratio $\eta = 0.5$. Despite the many reflections and refraction processes the front shock remains a relatively plane front. The initial shock Mach number is $M_0 = 1.6$ in all experiments.

The length of the perforated part of the channel is 1 meter. The shock velocity has been measured at various positions along the channel axis (about every 5 cm) with the Doppler-schlieren technique which has been described extensively in ref. 6. With this method the shock velocity is measured while the shock propagates along a distance of only a fraction of a millimeter. Since only one data point can be taken during one test run, a shock tube experiment is repeated many times with the same initial conditions but with different positions of the measurement in order to obtain the decrease of shock velocity or shock Mach number along the perforated channel. The scatter in the experimental data points (Figure 3-5) must be explained with the low degree of reproducibility of the individual experiments. The experimental pattern can be described with a regression curve of the exponential form $y = a \cdot \exp(b \cdot x)$; the constants a and b are determined by a least square fit.

CALCULATION OF SHOCK STRENGTH

Two theoretical models are used here to calculate the decrease of the shock strength along the perforated portion of the channel. The theory of Wu and Ostrowski (ref.1) attributes the decrease in shock strength to the loss of momentum in form of gas jets exhausting through the openings of the perforation. In evaluating this theory equation (22) in ref. 1 which describes the contraction ratio of the gas jet is replaced by equation (2.5) of ref. 7. The numerical result is included in Figures 3 to 5.

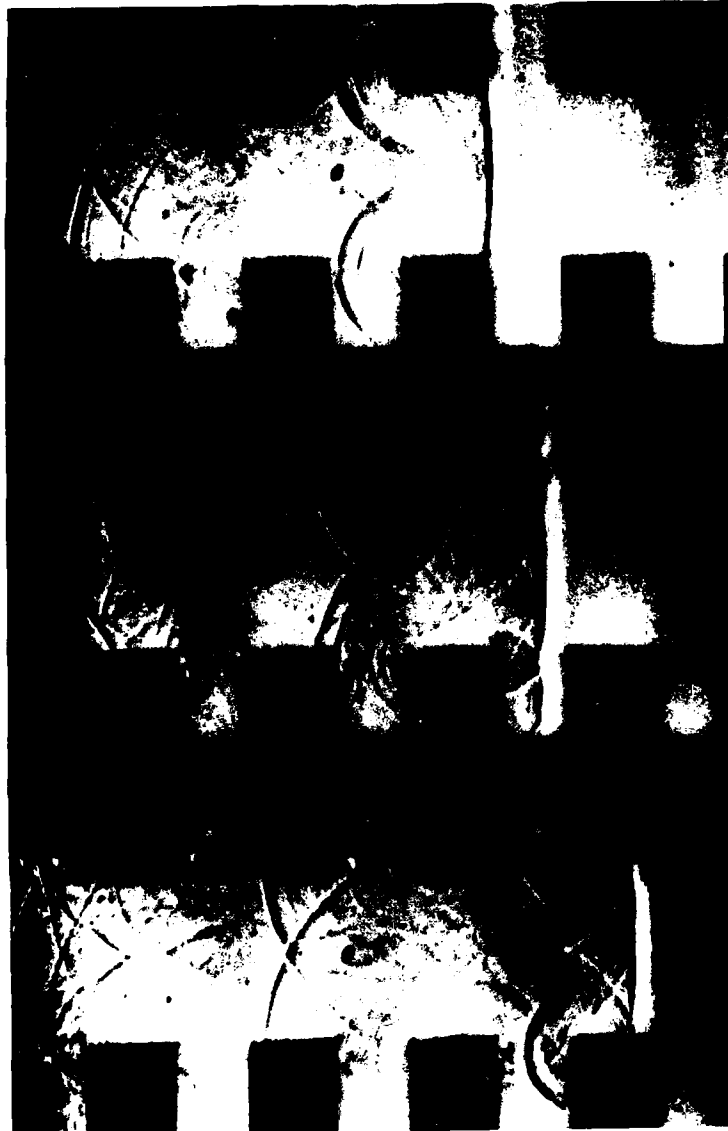


Figure 2: Series of 3 shadowgraphs showing the propagation of a shock wave in a channel with the perforation ratio $\eta = 0.5$. The shock wave moves from left to right and is refracted and reflected at each opening of the perforation.

Figure 2 shows that the shock wave undergoes a refraction process in each individual opening of the perforation. This process is equivalent to the propagation of a shock in a channel with a side-branch. The latter case has been studied by several investigators, and various models are available to calculate the shock strengths in such a configuration. The present case can be analyzed by means of these models if one assumes that the perforation can be represented by a series of side branches in the wall of the main channel. The shock in the main channel which is attenuated after the interaction with the first side branch interacts with the second side branch, etc. and this process is repeated for each slit of the

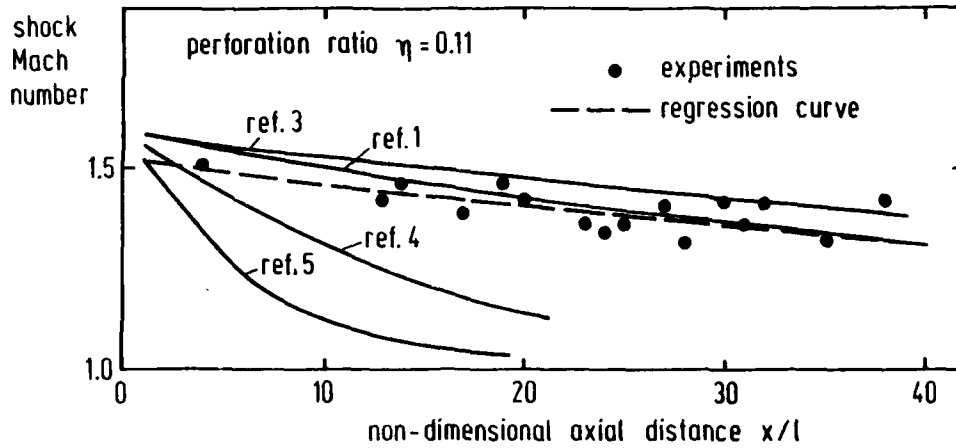


Figure 3: Measured and calculated attenuation of the shock in the perforated channel. Perforation ratio $\eta = 0.11$ (see also Figure 1)

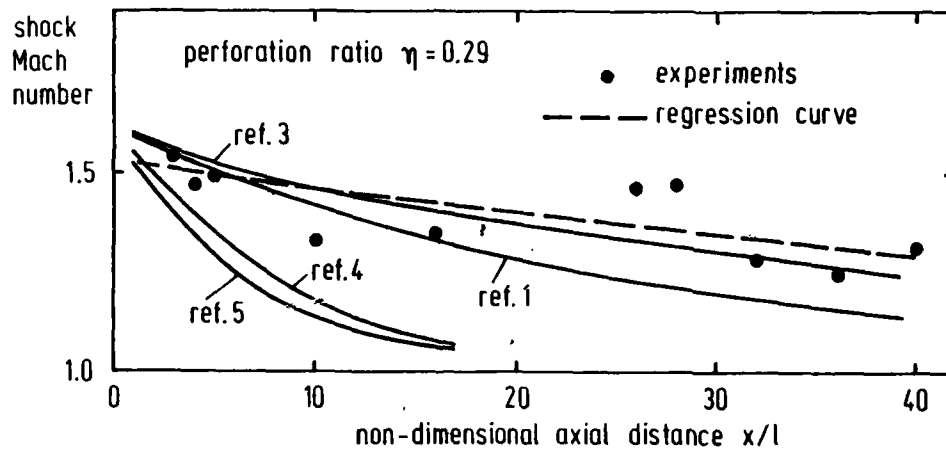


Figure 4: same as Figure 3, $\eta = 0.29$.

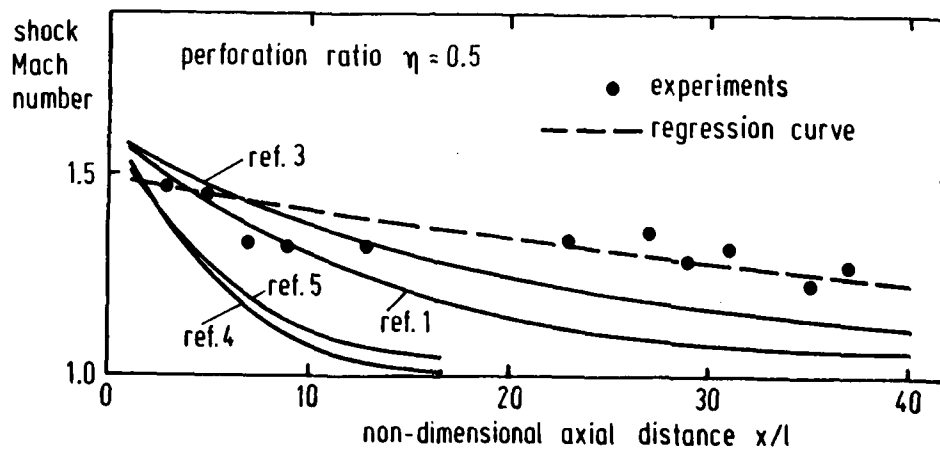


Figure 5: same as Figure 3, $\eta = 0.5$.

used perforation geometry to determine the attenuation of the shock wave in the perforated channel. Three of such branched-tube-models (refs. 3 - 5) are applied here, the direction of the branch is taken at 90° to the main channel axis, and the results of these calculations are also included in Figures 3 to 5.

RESULTS

The numerical and the experimental investigations were restricted to only one value of the initial shock Mach number, $M_0 = 1.6$, because the applied shock tube did not allow for a significant variation of this number. The influence of the shock strength on the results therefore has not been tested. The scatter in the experimental data has two main origins: The low degree of reproducibility has been mentioned above. The second error source is the instantaneous interaction of the shock wave with the openings of the perforation. The shock strength does not decrease smoothly, it experiences rather abrupt changes due to the interactions with reflected and secondary waves as can be seen in Figure 2. The applied method for measuring the shock velocity delivers these local values which might differ considerably from the average value of the decreasing shock strength. It is therefore reasonable to describe the experimental pattern with a regression curve as it has been done in Figures 3 to 5.

The experimental results are described best by the slightly modified theory of Wu and Ostrowski (ref. 1) and by the repeatedly applied branched-tube model of ref. 3. The other two models (refs. 4 and 5) predict a too rapid attenuation of the shock wave in the perforated channel. The numerical results agree better with the experiments for the lower values of the perforation ratio. In the case of the higher perforation ratio (here: $\eta = 0.5$), the wave interactions become dominant, and the numerical models with their included averaging procedures might not adequately describe the real flow situation.

The branched-tube model of ref. 3 which delivers relatively good results is easy to handle because it expresses the shock Mach number to be determined in form of an implicit analytical equation which is simple to evaluate. This model requires the existence of a one-dimensional perforation geometry as used in these experiments (see Figure 2). If one wants to apply this model to a different perforation geometry (e.g. holes in the channel wall instead of slits), it is necessary to assume that such geometry, in the calculation, can be replaced by its one-dimensional equivalent (i.e. the slit geometry) with the same value of the perforation ratio η . No tests have been performed, however, to check the influence of the perforation geometry on the shock attenuation at constant values of η .

ACKNOWLEDGEMENT

This research project has been supported by a grant of the Deutsche Forschungsgemeinschaft (DFG).

REFERENCES

1. J.H.T. Wu and P.P. Ostrowski, Proceed. 8th Int. Shock Tube Sympos., London (1971), 15/1
2. A.P. Szumowski, Proceed. 8th Int. Shock Tube Sympos., London (1971), 14/1
3. F. Peters and W. Merzkirch, Z. Ang. Math. Mech. 55t (1975), 145
4. A. Dadone, M. Pandolfi, F. Tamanini, Proceed. 8th Int. Shock Tube Sympos., London (1971)
5. J.H. Lee, P.P. Ostrowski, J.H.T. Wu, J. Fluid 76 (1976), 675
6. W. Merzkirch and W. Erdmann, Proceed. 10th Int. Shock Tube Sympos., Kyoto (1975), 808
7. V.I. Troshin, J. Appli, Math. Mech. 25 (1959), 1340

AD P000241

HIGH-ENERGY AIR SHOCK STUDY

IN A STEEL PIPE*

H. D. Glenn, H. R. Kratz,** D. D. Keough† and R. P. Swift

Lawrence Livermore National Laboratory

Livermore, California 94550

A modified Voitenko compressor was used to generate a 43 mm/μs air shock in 20-mm-i.d. 6-m long steel pipe containing ambient atmospheric air. Fiber-optic ports provided diaphragm burst time, time-of-arrival data and velocity of the shock front along the pipe. Pressure profiles were obtained at higher enthalpy shock propagation than ever before and at many locations down the pipe. Between 0.10- and 5.0-m from the diaphragm the peak pressure behind the shock front decayed from 3.5- to 0.008 GPa. Over this same interval the velocity of the shock front attenuated from 43- to 1-mm/μs. Postshot measurements indicated 0.34 Kg of entrained wall material condensed out on the walls between 2.5 and 4.35 m from the diaphragm. The value of 0.34 Kg is about an order of magnitude greater than earlier ablation calculations predicted. The scouring model is forwarded as a possible entrainment mechanism to explain this discrepancy. The rapid attenuation of shock velocity (43- to 5-mm/μs) over the first 2 m of propagation is attributed to entrainment of wall material. Beyond 2-m ablation is negligible with heat transfer and friction becoming the dominant attenuating factors.

*Work supported under contract DNA Subtask J24AAXIX955 and auspices of U.S. Department of Energy by the Lawrence Livermore National Laboratory under contract W-7405-ENG-48.

**Systems, Science and Software, LaJolla, CA 92037.

†SRI International, Menlo Park, CA 94025.

INTRODUCTION

For nearly a decade, theoretical studies have indicated that ablation of wall material was the principal attenuation mechanism for high-velocity (>10 mm/μs) air-shock propagation.¹⁻³ This conclusion was primarily based on agreement between calculational and experimental results for time-of-arrival (TOA) of the shock front at specific locations in open pipes containing air at ambient conditions. In the study¹ using the Voitenko compressor,⁴ postshot inspection of the pipe wall clearly indicated that considerable erosion of the surface had taken place. In the Marvel experiment, chemical tracer sections were located in the wall of the Marvel tunnel at specific sites to provide an estimate of ablation thickness. A final distribution of the chemical tracers was obtained from core samples along the tunnel in a postshot drilling program. This final tracer distribution confirmed that significant ablation or mass entrainment in the gas flow occurred.

The term ablation, as related to high-energy flow, is generally confined to the vaporization of wall material and subsequent addition of that vaporized material to the gas flow. However, other processes exist by which wall material may be entrained in the gas flow. For an open pipe in a nuclear explosion the deposition of radiation (x or γ rays, and thermal) ahead of the shock front may vaporize wall material and/or produce a thin melt layer. In addition, a thin melt layer may be produced by high-temperature gases behind the shock front. Then turbulence behind the shock front may scour off this thin liquid layer and add mass to the flow in the form of droplets. This scouring model was first postulated⁵ to explain the results of dynamic ablation measurements associated with plasma flow in a line-of-sight pipe during a nuclear test.⁶ The scouring model has been incorporated into a numerical code for simulating high-energy gas flow in open pipes.⁷ Other considerations for mass entrainment are irregularities in the pipe wall or the wall composition that may result in sizeable wall fragments being entrained in the gas flow. Which of these processes are present depends upon the experiment being considered.

Although considerable evidence exists that ablation plays an important role in the attenuation of high-energy gas flows, the principal uncertainty concerns the rate at which ablation or wall material enters the flow and affects conditions in and behind the shock front. The early computer codes^{1,2} and subsequent modified versions^{7,8} contain parameters to quantify the rate of ablation. Unfortunately, these finite-difference codes lack dynamic experimental data to determine whether the present formulations accurately describe the physical processes of ablation. An accurate measurement of the ablation rate would provide the most direct experimental basis for evaluating the present theory. However, the estimated ablation rate is so small¹ ($<10 \mu\text{m}/\mu\text{s}$) and the typical environment so severe (e.g., pressures >1 GPa, temperatures >1 eV, and wall motion $>0.1 \text{ mm}/\mu\text{s}$) that survival of a credible ablation rate measurement is extremely difficult. Fortunately, other measurements are possible to aid in evaluating the ablation rate and its subsequent effect on conditions behind the shock front.

In the following sections we describe an experiment using a modified^{9,10} Voitenko compressor⁴ to study air-shock propagation. Some of the hardware and diagnostics coverage are common to an earlier experiment.^{1,10} For example, the high-explosives (HE) assembly, compressor section, and first 0.15m of the outlet pipe are identical within tight machine tolerances. The detonated HE drives the stainless-steel plate into the chamber, compressing the 1.1-MPa air (initially in the chamber) to high pressures (>100 GPa), densities ($>1.0 \text{ Mg}/\text{m}^3$), and temperatures (>10 eV) before the diaphragm breaks.^{1,11} The expansion of this compressed air down the exit pipe generates a high-velocity (Mach 130) air shock.

Fiber-optic ports in the outlet pipes transmit luminosity associated with the high-energy air shock to display boards that are scanned by streaking cameras. These optical records are then reduced to give TOA information about air-shock propagation down the outlet pipes. Electronic sensors provide pressure profiles at many locations in this experiment. Figure 1 and Table 1 summarize the physical features and diagnostics coverage of the compressor-outlet pipe assembly. The optical diagnostics employed are similar to previous air-shock¹⁰ and gas-jet^{3,11} studies but will be reviewed for details particular to this experiment.

OPTICAL AND ELECTRONIC DIAGNOSTIC COVERAGE

A framing camera (Model 189B) was focused on the first 0.20 m of the steel outlet pipe to detect the location, duration and extent of possible venting. Since a goal of this study will be to numerically simulate the compressor generation of the air shock and pressure profile for some distance

behind the shock front, a knowledge of venting is crucial. In a previous air-shock study,¹² venting from the HE driver region was observed, but a venting criterion was applied to the numerical simulation which helped to explain the experimental results.

Twenty-one 1.80-m-long light pipes were emplaced along the outlet pipe and divided between two display boards. One end of each light pipe in the first 2.0 m of the outlet pipe was located in the first display board and those beyond 2.0 m were located in the second board. The detonation of bridge wires at predetermined times provided the optical fiducials to correlate air-shock luminosity data for the streaking cameras. The two streaking cameras (Models 132) and the framing camera (Model 189B) were synchronized. No optical filters were used on any of the cameras.

The electronic diagnostics for this experiment consisted of three types of pressure gages, Table 1. A total of 15 bar gages, 4 piezoresistance gages, and 2 PCB quartz gages were installed. Gages similar in design to the bar and PCB quartz gages have been used to measure pressures in other gas flow experiments.¹¹⁻¹³ The bar gages^{14,15} were the primary electronic sensors. The other six gages were installed as an independent check of the pressure profiles obtained with the bar gages. The piezoresistant gages were specifically designed for this experiment. The primary difficulty in obtaining measurements of the flow parameters is in retaining the integrity of the sensor when subjected to high pressures, high temperatures, large displacements, and strain effects.¹⁶

EXPERIMENTAL RESULTS

To correlate the optical and electronic measurements, a common time reference was provided by the electrical pulse that initiated detonation of the plane-wave lens. The time interval between detonation of the plane-wave lens and air shock breakage of the Mylar diaphragm was 58.1 μ s. This time was determined by using a light pipe oriented to view the center of the diaphragm. The above diaphragm breaking time is taken as the new zero time reference for all experimental results in this test.

Optical Experimental Results

The framing camera (Model 189B) gave photographic evidence that no venting of high-energy gases in the outlet pipe occurred for the first 39.3 μ s after breakage of the diaphragm. Although venting after this time would undoubtedly reduce pressures well behind the shock front, it would have negligible effect on propagation of the shock front.

Table 1 summarizes TOA results of the shock front for the fiber optics and pressure sensors. The TOA values given for the fiber optics correspond to the time that the first luminosity peak was recorded at each location. The TOA values for the pressure sensors are the times at which the initial rise for the first pressure peak is very steep. This time was chosen instead of the peak pressure because the pressure sensors have two inherent effects that tend to spread the risetimes and delay the peak. Figure 2 shows a TOA plot for propagation of the shock front in the exit pipe. Differentiation of the TOA curve yielded the velocity for the shock front as a function of distance down the outlet pipe as given in Fig. 3. After a short period of acceleration the shock attains a maximum velocity of 43 mm/ μ s at a distance of \approx 75 mm from the diaphragm. Over approximately the first 2 m, ablation and mass entrainment are considered^{1,3} to be the principal attenuation mechanism. Over this distance the velocity has attenuated to less than 10 mm/ μ s. Beyond the 2.0 m distance the attenuation rate decreases, with the dominant mechanism for attenuation being convective heat transfer and friction.^{3,12}

Pressure Profiles

Figures 4-11 give pressure profiles for this experiment. The pressure records for the bar gages beyond 2.0 m had high noise levels and/or a double trigger of the scope trace. Other than the shock-front TOA value at 2.5 m, no meaningful data reduction was considered feasible for the bar gages beyond 2.0 m. Peak pressures associated with the shock front decayed from 3.5 GPa at 0.10 m to 0.008 GPa at 5.0 m from the diaphragm. The duration of the experimentally measurable flow varies from 50 μ s at 0.10 m (Fig. 4) to over 300 μ s at 5.0 m (Fig. 11). These two positions represent the only locations the scope settings were such that the flow duration could be determined with any certainty. The increase in the duration of the flow can be attributed primarily to the delayed entrainment of wall material to the flow, resulting in a relatively greater attenuation of the flow well behind the shock front. Evidence for this effect is the attenuation of the 3.55 GPa (19 μ s) peak at 0.10 m, to 1.48 GPa (38.6 μ s) at 0.20 m, to 1.14 GPa (50.4 μ s) at 0.30 m and its final disappearance at 0.50 m. The gradual dispersion of the high-energy flow has been observed in jet studies.^{3,17} In those studies the delayed entrainment of wall material was also identified as the primary attenuation mechanism and a major contributor to dispersion.

The piezoresistance gage at 0.10 m suggests the possible presence of a 0.15 GPa precursor before the sharp rise to its 3.5 GPa peak value (Fig. 4). Dispersion in the bar gage will reduce the peak pressure and increase the pulse width of the shock front in addition to masking fine structures such as the precursor. Thus, the results for the piezoresistance and bar gages are felt to be consistent at 0.10 m. The piezoresistance gage at 0.20 m failed within 1 μ s after shock arrival and at 1.00 m not even this datum was obtained. Consequently, the only other location where a similar comparison between these two gage types was at 0.50 m (Fig. 7). Only a hint of a precursor was observed at this distance. The peak pressure appears high with respect to the peak value for the bar gage, even though attenuation of the peak caused by dispersion in the bar gage could be expected, considering the narrow pulse width for the piezoresistance gage. The poor agreement between pressure profiles of the shock front at the 0.50 m is the largest disparity between any gage results at the same axial distance for this experiment.

The large pressure oscillations observed result from axial and radial oscillations of the flow that are induced by an early diaphragm break and radial convergence of the driver gas in the compressor section.¹ The fact these oscillations appear to persist for a substantial distance is confirmed by the pressure profiles obtained with the PCB and bar gages at 2.0 m (Fig. 10). Both gages at 2.0 m give close agreement, in TOA and amplitude, for the first two large pressure peaks. It is not known whether the following two oscillations for the bar gage are factual or a gage related problem. Over all, the pressure profiles are felt to be in good agreement for the duration of the bar gage record. The PCB gage indicates that a flow pressure of ≥ 15 MPa exists well beyond the 55-60 μ s measurement duration of the bar gage record. A more complete record of the duration of the flow is provided by the PCB gage at 5.0 m (Fig. 11). At this distance the rapid oscillations appear to have damped out. Yet the profile is far from that of a classical shock wave, since substantially larger pressures occur well behind the shock front. In addition to damping of the oscillations, a plot of peak pressure in the shock front vs axial distance (Fig. 12) reveals a significant difference. Between 0.10 and 2.0 m the shock-front pressure is fairly well bounded by the two expressions shown in Fig. 12. Extrapolation to 5.0 m would predict a shock-front pressure of approximately an order of magnitude lower than measured. The higher pressures at 5.0 m were partially expected since it has been shown¹² that for shock velocities below 10 mm/ μ s ablation ceases, with only heat transfer and friction remaining as the principal attenuation mechanism.

Radial Expansion

In this and earlier^{3,10,11} experiments the compressor section and first 0.15 m of outlet pipe were machined from a single piece of steel stock. This requirement was imposed¹⁰ to eliminate venting of high-energy gases following diaphragm breakage. The impulse delivered to the compressor by the HE and the high-energy gas flow in the outlet pipe have always been sufficient to highly fragment both the compressor section and first 0.15 m of outlet pipe. In this experiment the remaining 5.85 m of outlet pipe was recovered intact and postshot measurements of the bore diameter were obtained as a function of axial distance from the diaphragm. Results from those measurements are plotted in Fig. 13, showing radial expansion occurred over the first 2.5 m of the outlet pipe. High pressures behind the shock front were the principal factors producing the radial displacement. The other minor contributor is the removal of wall material via ablation and scouring.⁵ The HE transferred significant axial momentum to the first 0.15 m of the outlet pipe, causing it to impact the front end of the 5.85 m section, resulting in flaring of that end of the surviving section. Consequently, measurements of bore diameter over the first 0.05-0.10 m of the surviving section would partially have to be discounted because of the impact and flair effect.

Condensation

Post-shot measurements² and physical observations of wall sections¹ showing the erosional effects of mass entrainment have been documented. The entrainment of mass from the wall contributes to attenuation and cooling of high-energy gases. As this flow propagates, interaction with the cold wall and other energy losses can be expected to further cool the flow. When the flow temperature drops sufficiently, condensation of the entrained wall material will occur. Figure 14 shows a plot of condensation thickness vs axial distance from the diaphragm. Integrating these results indicated that the total entrained mass condensed out over the distance shown was ≈ 0.34 kg.

In an earlier report¹ 8 MJ of energy was calculated to be imparted to the chamber air that exited down the outlet pipe. The value 0.34 kg is more than an order of magnitude larger than those calculations predicted to be entrained in the 0.029 kg of driver and driven gas for that experiment. However, those calculations extended to only 56 μ s following the diaphragm break and were for an outlet pipe of ≈ 1.4 m in length. As a basis for analysis, let us accept 8 MJ as reasonable and assume that all of the chamber air exited down the outlet pipe. The following two options may explain the 0.34 kg of condensed wall material, since the initial experimental conditions and shock TOA results for the earlier experiment¹⁰ are not that different for the first 1.4 m of air shock propagation.

The first option is that the entire 0.34 kg of condensed wall material was vaporized and entrained in the driver (chamber air) and shocked air in the outlet pipe. If only a few grams were entrained in the shocked air and the major fraction was entrained well behind the contact surface, then attenuation effects on propagation of the shock front would be greatly reduced. Approximately 4.25 MJ, 53% of energy in the flow, would be required to vaporize 0.34 kg of steel assuming a specific energy of vaporization (E_v) of 12.4 MJ/kg.¹ Of the remaining 47%, $\approx 14\%$ was calculated¹ to be lost by the gas doing work on the pipe. The value of 14% was based on a pipe length of 1.4 m and flow time of 56 μ s. Figure 13 shows that expansion occurred for a distance of 2.5 m indicating that the 14% value is very conservative. Thus, less than 33% (2.6 MJ) remains in the flow to be partitioned between internal and kinetic energy. Experimental results at 2.0 m for the pressure profiles (Fig. 10) and gross estimates for flow velocities provide estimates for total energy in the flow that are consistent with the 33% value.

The second option is to introduce some latitude to the figures by reducing the energy necessary for mass entrainment in the flow. This can be done by assuming that a melt layer develops which becomes entrained in the flow and is carried along in the form of droplets. This entrainment mechanism, known as "scouring," was first postulated⁵ to account for large dynamic ablation rates⁶ that normal ablation models could not explain. The scouring concept is not a substitute for ablation, but is an additional mechanism of mass entrainment. Scouring may be the dominant entrainment mechanism well behind the shock front where temperatures and specific energies per unit mass in the flow are much lower. Appreciable scouring may occur late in time when HE gases act as a carrier for the droplets.

Numerical simulation of the compressor operation¹⁸ suggests that more than half the air may be trapped in the chamber and may not flow down the outlet pipe. Although those calculations terminated at 10 μ s following the diaphragm break, the predictions were in reasonable agreement with the first two peaks of the pressure profile recorded at 0.10 m. If such a reduction in driver gas is realistic, then significantly less energy than 8 MJ can be expected to be contained in the pipe flow. To explain the 0.34 kg of condensed wall material would require a reduced energy entrainment mechanism for a major portion of the flow. The scouring option is one possible mechanism. For a more detailed discussion of the diagnostics and experimental results than is presented in this paper the reader is referred to Ref. 19.

ACKNOWLEDGMENTS

The authors are grateful to G. W. Ullrich for his advice and support throughout the program and to C. Knowles, B. Hartenbaum, B. K. Killian, K. Pyatt, H. L. Brode, J. Thomsen, and G. R. Abrahamson for their many valuable suggestions that contributed to the design of this experiment. The authors are deeply indebted to A. M. Ban for drafting support, N. W. Stewart for assistance in mechanical assembly, C. H. Dittmore for processing and digital reduction of the films, L. F. Simmons and the 850 bunker crew for their excellent field support, and L. D. Burrow for report preparations.

REFERENCES

1. B. K. Crowley and H. D. Glenn, "Numerical Simulation of a High-Energy (Mach 120 to 40) Air-Shock Experiment," in Proc. Seventh Intern. Shock Tube Symp., Toronto, Canada (23-25 June, 1969), pp 314-342.
2. B. K. Crowley, H. D. Glenn, and R. E. Marks, "An Analysis of Marvel-A Nuclear Shock Tube Experiment," J. Geophys. Res. 76, 3356 (1971).
3. H. D. Glenn and B. K. Crowley, "Comparison of High-Energy Gas Flow Experiments," J. Appl. Phys. 42, 5517 (1971).
4. A. E. Voitenko, "Generation of High Speed Jets," Sov. Phys. Dokl. 9, 860 (1966).
5. H. D. Glenn, J. R. Barthel, and E. A. Day, "Ablation Phenomena Associated with Line-of-Sight Pipes in Nuclear Tests," Defense Nuclear Agency Report, Systems, Science, and Software, La Jolla, CA, DNA-3015T (S/RD) (1972).
6. D. C. Pound, "Measurement of Tunnel Environment and Early Energy," Gulf Radiation Technology, La Jolla, CA, DASA POR 6464 (1971).
7. J. R. Barthel and D. F. Patch, "Condensation Modeling in the FLIP Code," Systems, Science and Software, La Jolla, CA, SSS-R-75-2535 (1975).
8. J. R. Barthel, "A Computational Model for Flow in Line-of-Sight Pipes," Systems, Science and Software, La Jolla, CA, DASA-2554 (1970).
9. D. Sawle, "Characteristics of the Voitenko High Explosive Driven Gas Compressor," in First Intern. Colloq. of Gas Dynamics of Explosions, Brussels (18-21 Sept. 1967).

10. H. D. Glenn and B. K. Crowley, "Optical Technique for Monitoring High Energy (Mach 35-130) Shocks in Steel Pipes Containing Ambient Atmospheric Air," Lawrence Livermore Laboratory, Livermore, CA, UCRL-71007 (1968).
11. H. D. Glenn and B. K. Crowley, "High-Speed (4-6 cm/ μ sec) Gas-Jet Propagation," J. Appl. Phys. 41, 4157 (1970).
12. H. D. Glenn and B. K. Crowley, "An Analysis of a High-Explosive Shock-Tube Experiment," J. Appl. Phys. 42, 2099 (1971).
13. H. R. Kratz, "An Experimental Investigation of the Flow of a High-Velocity, High-Density Iron Plasma in Pipes and Mufflers," Defense Atomic Support Agency Report, Gulf General Atomic, La Jolla, CA, DASA-2319 (1970).
14. A. W. Blackstock, H. R. Kratz, and M. B. Feeney, "Piezoelectric Gauges for Measuring Rapidly Varying Pressures up to Seven Kilobars," Rev. Sci. Inst. 35, 105 (1964).
15. B. Hartenbaum, "A Piezoelectric Transducer for Measuring Sub-millisecond Pressure Pulses with Amplitudes up to 30 Kilobars," Gulf General Atomic Report, La Jolla, CA, GAMD-8474 (1968).
16. H. D. Glenn, "Diagnostics Techniques Improvement Program," Defense Nuclear Agency Report, Systems, Science and Software, La Jolla, CA, DNA 2978T (1972).
17. H. D. Glenn, "High Energy Oxygen Jet Propagation," J. Appl. Phys. 44, 2585 (1973).
18. P. S. Brown and M. L. Lohmann, "Computer Modeling of the Voitenko Tube Generator," in Proc. Sixth Intern. Symp. on Military Applications of Blast Simulations, Cahors, France (25-29 June, 1979).
19. H. D. Glenn, H. R. Kratz, D. D. Keough, D. A. Duganne, D. J. Ruffner, R. P. Swift, and D. Baum, "High-Energy Air Shock Study in Steel and Grout Pipes," Lawrence Livermore Laboratory, Livermore, CA, UCRL-52826 (1979).

Table 1. Diagnostics used and air shock time-of-arrival (TOA) data.

Axial Distance (m)	Diagnostics ^a	Fiber Optics TOA (μ s)	Bar Gage TOA (μ s)	SRI and LLL gage TOA (μ s)
0.	F	0.0		
0.02	F	1.2		
0.05	F	2.1		
0.10	F, B, PM	3.26	3.5	4.0
0.20	F, B, PM	5.9	6.7	6.35
0.30	F, B	8.5	9.1	
0.40	F	11.6		
0.50	F, B, PY	14.4	15.0	16.0
0.75	F	22.6		
1.00	F, B, PY	31.7	32.3	31.8
1.25	F	43.3		
1.50	F, B	57.8	57.3	
1.75	F	77.5		
2.00	F, B, P	103.8	104.5	104.0
2.50	F, B	183.0	185.3	
3.00	F, B	295.0		
3.50	F, B	448.0		
4.00	F, B	611.0		
4.50	F, B			
5.00	F, B, P			1045.
5.50	F, B			
6.00	B			

^aF = fiber optics; B = bar gage (SSS); PM = pressure-manganin (SRI); PY = pressure-ytterbium (SRI); P = LLL 80,000 psi PCB gage 109A (D).

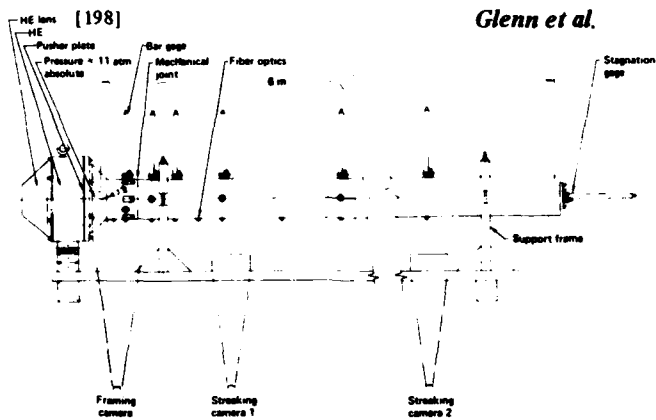


FIG. 1. Compressor assembly, steel outlet pipe, and diagnostics systems for the steel-pipe experiment.

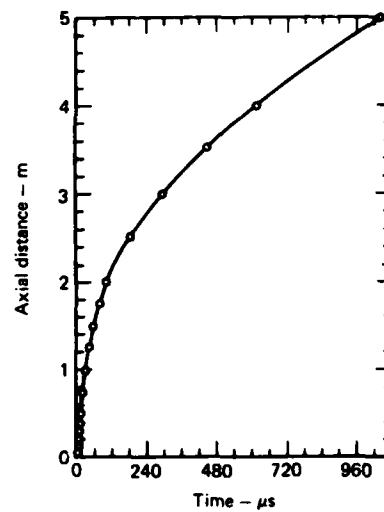


FIG. 2. Air shock TOA data for the steel outlet pipe.

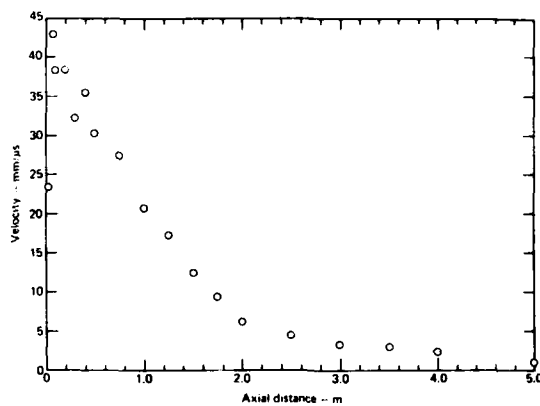


FIG. 3. Shock velocity vs axial distance for the steel shock-tube experiment.

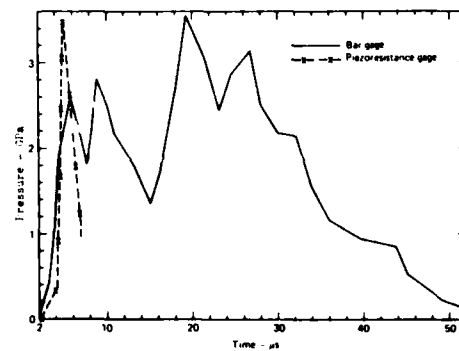


FIG. 4. Pressure profiles at 0.10 m in steel outlet pipe.

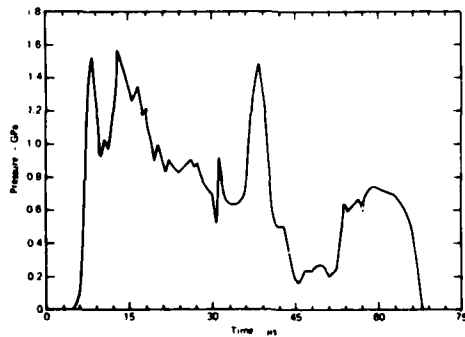


FIG. 5. Pressure profile obtained with a bar gage at 0.30 m from the diaphragm (steel pipe).

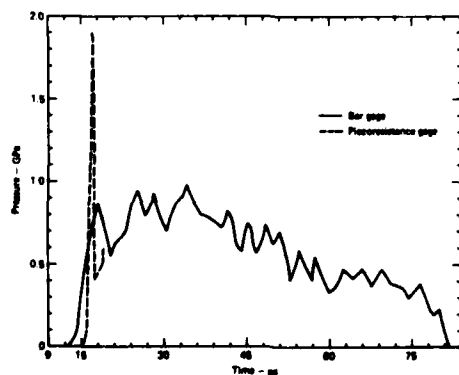


FIG. 7. Pressure profiles at 0.50 m in the steel outlet pipe.

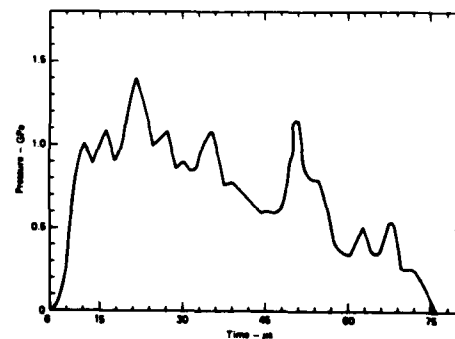


FIG. 6. Pressure profile obtained with a bar gage at 0.35 m from the diaphragm

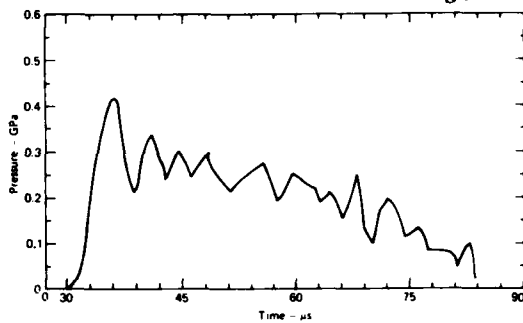


FIG. 8. Pressure profile obtained with a bar gage at 1.0 m from the diaphragm (steel pipe).

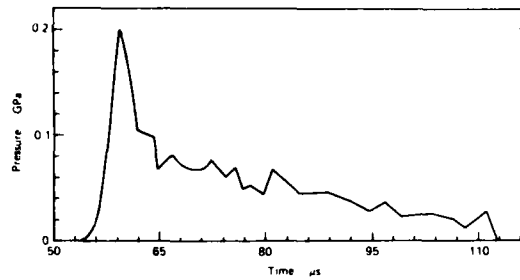


FIG. 9. Pressure profile obtained with a bar gage at 1.50 m from the diaphragm (steel pipe).

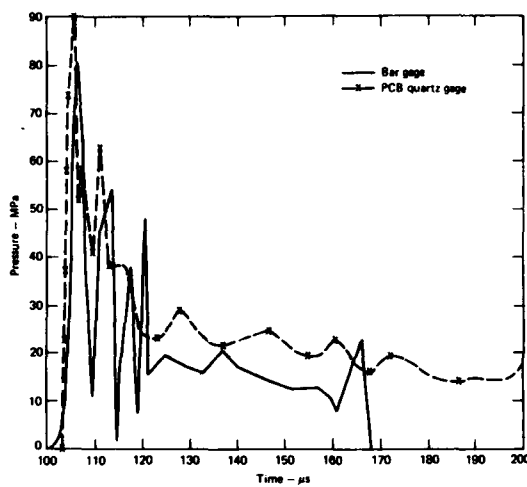


FIG. 10. Pressure profiles at 2.00 m in steel outlet pipe.

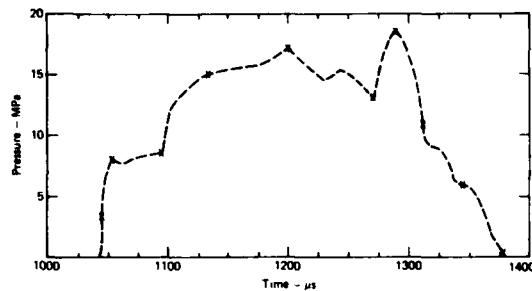


FIG. 11. Pressure profile obtained with PCB quartz gage at 5.0 m in the steel outlet pipe.

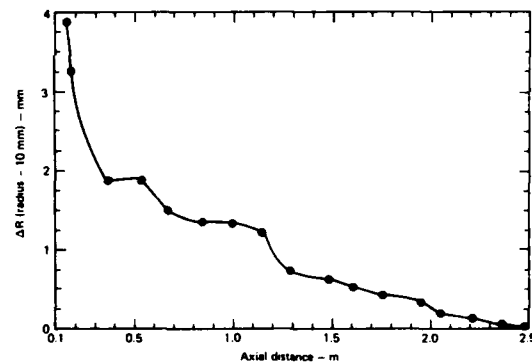


FIG. 13. Radial change vs axial distance from the diaphragm (steel pipe).

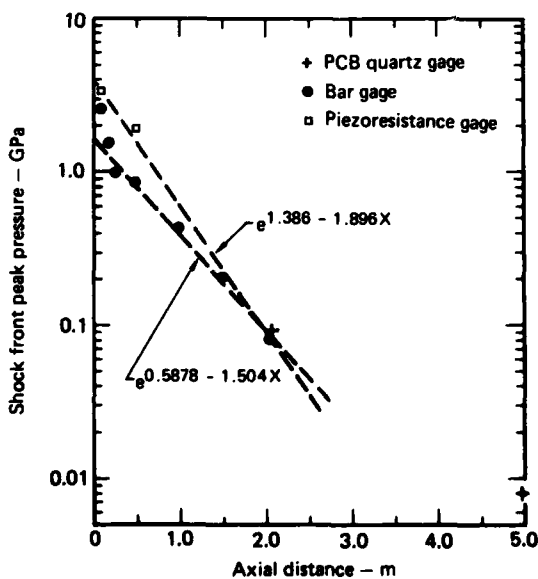


FIG. 12. Peak pressure in the shock front vs axial distance from the diaphragm (steel pipe).

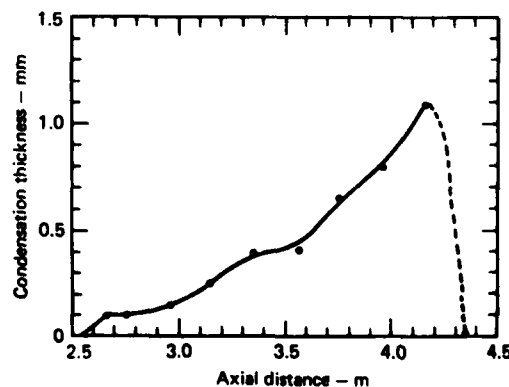


FIG. 14. Condensation thickness vs axial distance from the diaphragm (steel pipe).

AD P000242

OPTICAL STUDIES OF SHOCK GENERATED

TRANSIENT SUPERSONIC BASE FLOWS*

Pak-Yan Liang and Daniel Bershader

Stanford University, Stanford, California 94305

Alan Wray

NASA-Ames Research Center, Moffett Field, CA 94035

Transient base flow phenomena following shock-wave passage over plane bluff bodies were studied in a shock tube using interferometric and schlieren techniques. Two model shapes were examined: a half-circular cylinder and a cylinder with the profile of the Galileo probe. The latter differs from the former aerodynamically in that its forebody flow consists of a weaker expansion than that of the half-circular cylinder, and that the presence of its afterbody provides some boat tailing effects. Both factors result in a higher base pressure for the probe model. The purposes of the present study are two fold: (1) to understand the physics of transition from transient to steady state base flow; and (2) to provide code verification for a computer study with the Illiac IV. The transient base flow interactions included a series of shock diffraction, regular and Mach reflections coupled with boundary layer development, separation and recompression. Underlying these major features are the generation and subsequent transport of vorticity. The Reynolds and Mach numbers enter as scaling factors and thus contribute to configuring the near-wake geometry which is, in turn, related to the base pressure. Quantitative verification of the computer code included comparisons of transient pressure and density fields, near-wake geometries and bow shock stand-off distances. Validity and predictive power of the computer outputs were found to be satisfactory.

INTRODUCTION

Supersonic base flow behind bluff bodies is a much-studied phenomenon (Refs. 1-3) which includes viscous and turbulent flow interactions in the presence of a complex fluid pressure configuration. Extension of existing limited knowledge to the base and wake flows associated with the Galileo Probe as it penetrates the Jovian atmosphere (Ref. 4) introduces still further problems stemming especially from radiative heat transfer and massive ablation. Suitable scaling parameters which serve as guides for experiments cannot be

*Supported in part by NASA Grant NCO 2-10

formulated in any straightforward way. Partly for these reasons a major emphasis of current research consists of advanced computer simulation programs being developed at the NASA-Ames Research Center and other laboratories as well. A goal of the experiments described here was to obtain data for purposes of code verification.

The present study deals with the transient base-flow processes generated by the passage of a strong shock wave over two-dimensional bluff bodies. It includes the asymptotic approach to steady state. Measurement methods were nonintrusive and included both the interferometric and schlieren techniques. The observations and results not only shed light on the relative importance and interrelation of major physical parameters, but the use of a nonsteady flow field also provides a more vigorous verification of the computational formulation in which time is used as an independent parameter again with an asymptotic approach to steady-state. The present paper deals both with a description and assessment of the experimental findings, as well as a comparison with predictions of the numerical code.

EXPERIMENTAL METHOD

The experiments were conducted in a 5cm x 5cm inner cross-section cold helium-driven shock tube. In addition to generating the transient flow patterns desired, the shock tube flow provides some thermal simulation for outer planet entry flows where the heating rate is an important scaling factor. The stagnation enthalpy level of the "free stream conditions" behind the incident shock is of the order of 4 MJ/Kg, much higher than the 0.6 MJ/Kg in typical wind tunnels and the 1 MJ/Kg in free flight tests.

Photographic data are taken with Mach-Zehnder interferometry and schlieren arrangements which make use of a capacitor-charged spark light source triggered through a variable delay circuit. Platinum thin-film heat gauges mounted at the test section measure the incident shock speeds from which free stream equilibrium conditions are deduced. At the benchmark test conditions with nitrogen as the test gas, these conditions are:

$$P_1 = 30 \text{ torr}; P_4 = 1,000 \text{ psi}; M_8 = 5.70; M_2 = M_\infty = 1.836;$$
$$Re_\infty = 4.4 \times 10^4$$

where the partial vibrational excitation of N_2 in the test region has been taken into consideration.

Plane bluff bodies of two different profile shapes are used as test models. One is a half-circular cylinder (herein called the 'half-cylinder'), which represents the geometrically (though not aerodynamically) simplest case. The other is a model with the profile shape of the Galileo probe (Fig. 3). The latter differs aerodynamically from the former in that its forebody flow is less rotational and consists of a weaker expansion around the shoulder than that of the half-cylinder; and the presence of its afterbody gives rise to some boat-tailing effects. As will be discussed in the next section, both factors contribute to a higher base pressure for the probe model, which is about 5% (about 2% for the half-cylinder) of its front stagnation point pressure.

Quantitative density field data are converted directly from fringe-shift measurements of the 2D interferograms. Then, with the help of appropriate assumptions regarding the temperature, the pressure level on the body surface and the wake axis can be deduced. The schlieren records complement the interferograms in flow visualization, and are able to reveal rather unique details of the transient interactions of the wave fronts in the wake. Such semi-quantitative results include measurements of several macroscopic features and geometric properties which provide additional data for comparison with the numerical results.

EXPERIMENTAL RESULTS AND ASSESSMENT OF THE TRANSIENT BASE INTERACTIONS

Figures 1a, b and c are the schlieren records of two typical transient and the asymptotic steady state base flow fields for the half-cylinder, respectively. The complexity of the transient interactions is immediately apparent. In what follows, we highlight a few of the more interesting processes and focus on the physical insight derived from the discussion about them. We shall base our discussion primarily on the half-cylinder model.

When the incident shock front first hits the body it reflects from the surface first in a regular and then in a Mach reflection. The reflected shock then stabilizes to become the bow shock around the forebody in the steady state. When the Mach stem of this triple shock configuration reaches the 90° corner, it veers away from the body in very much a separation-like manner as is the case with the onset of the Mach reflection. Since the initial process is self-similar with no length scales involved, the locus of the triple point Z is a straight line (Fig. 2a). The contact surface marked C.S.1 which evolves directly out of the original contact surface trailing behind the Mach stem, also remains remarkably straight except for its lower portion which is bent backwards due to the streamlines turning inward to "feed" the diffracting shock S_{III} . Note also that the so-called "compression band" C indicated on Fig. 2a is an inherent feature of the shock diffraction process, resulting from the reflection of the shoulder expansion waves from the shock front. It turns out that this compression zone plays the key role in the formation of the most striking features in the flow establishment process -- the strong vortex pairs -- as discussed below.

As we trace the further development of the diffracting shock, the latter eventually collides at the central axis with its counterpart from the other side of the symmetrical flow field. Another regular reflection ensues, this time of two equal cylindrical shocks. The downstream point of reflection also develops into yet another Mach reflection (Fig. 2b) later on. Thus, two and then three more zones are added to the already complex flowfield. Gases in regions 5, 6 and 7 separated by C.S.1 and C.S.2 are in order of decreasing density, as they have been processed by 3, 2 or 1 shocks respectively. Close to the body in region 5a, that part of the reflecting cylindrical shock which passes through the shear layer and attaches itself eventually to the separation point of the shear layer at the shoulder, becoming a weak secondary lip shock. Between regions 5a and 5b is found the 'neck' or recompression zone, where the reflecting shock coalesces with the compression band C to form an even stronger compression wave. The latter straightens out later on to become the trailing recompression shock in the steady state configuration.

Now, a fluid particle in the shear layer carries with it a certain amount of vorticity. As it negotiates the adverse pressure gradient of the recompression zone just mentioned, its vorticity concentration will be increased suddenly. Such behavior is predictable if we consider the RHS terms of the vorticity equation written out for the case of 2D flow with constant viscosity:

$$\frac{D\Omega}{Dt} = \Omega \operatorname{div} \vec{u} + \operatorname{grad} \left(\frac{1}{\rho} \right) \times \operatorname{div} \underline{\underline{\sigma}} + \nu \nabla^2 \Omega \quad (1)$$

where the symbols have their usual meanings and $\underline{\underline{\sigma}}$ is the total stress tensor. Such a process of vorticity concentration is believed to be responsible for the sudden appearance of the big curled-up vortices V1 and V2 in Fig. 2b.

A further insight can be gained from consideration of the global evolution of the vorticity field. As the incident shock passes over the model and the flow is instantaneously started, the forebody surface can be viewed basically as a vorticity generator. Part of this vorticity generated is 'fed' by diffusion through the shear layer, into the recirculating core and then into

the back face of the half-cylinder. The latter is a vorticity sink, i.e., a source of negative sign in relation to the forebody surface. Before reaching steady state, some entrained mass in the shear layer is also turned back at the neck and fed into the growing recirculating core -- mass which carries vorticity with it. In other words, vorticity is being transported from the front surface to the back surface by both diffusion and convection in the transient state and mainly by diffusion in the steady state. The rest of the vorticity generated is convected downstream through the neck and recompression shock. In the transient phase such transport feeds the vortex pair V1, and in the asymptotic state it contributes to the ever-extending inner viscous wake ad infinitum.

One more perspective is yet possible if we trace the vorticity "content" of a fluid element as it traveled its course from the bow shock to the wake. First, let us rewrite eqn. 1 for the 2D case with $\mu = 0$:

$$\frac{D\Omega}{Dt} + \Omega \operatorname{div} \vec{u} - \frac{1}{\rho^2} \frac{\partial \rho}{\partial y} \frac{dP}{dx} = 0 \quad (2)$$

where for simplicity we have assumed that the pressure gradient is only in the x-direction.

Write out also the equation for the mass flux under similar assumptions:

$$\frac{D(\rho u)}{Dt} + (\rho u) \cdot \operatorname{div} \vec{u} + \frac{dP}{dx} = 0 \quad (3)$$

By comparing equations (2) and (3), we recall that Ω is analogous to ρu , the mass flux, in that they are governed by similar transport equations. (Note that adding the viscosity term $\nu \nabla^2 \Omega$ to (2) and $\mu \nabla^2 u$ to (3) does not affect the analogy.)

In the study of 1D supersonic flow such as that in a Laval nozzle, we visualize a tube within which

$$\rho u A = \text{const.} \quad (4)$$

Thus, here we can also visualize a hypothetical "vorticity tube" within which

$$\Omega A^* = \text{const.} \quad (5)$$

Thus a narrowing of the "tube" results in an increase of Ω and vice versa.

The question arises as to what constitutes a "wall" for the vorticity tube. It should be the boundary at which vorticity tends to zero and within which the vorticity of the flow is confined. The outer edge of a boundary layer would be such a line, and so would be lines of symmetry of velocity profiles. A solid surface, however, would not be a vorticity tube boundary but rather a line source of vorticity analogous to a porous wall with blowing or suction in the case of mass flow in a real tube.

Figure 3 is another schematic of the flow field around the Galileo probe model. The dotted line is the "system boundary" of a control volume through which a fluid element of the "entrained mass" will pass. It can be chosen to coincide approximately with the wall of a vorticity tube except that stations 4-5 and 7 must be considered "porous walls" through which vorticity diffuses. As the fluid element proceeds along the vorticity tube, each numbered station locates a physical influence by which the fluid element is "processed", affecting in particular its vorticity content. Any process that "stretches" a velocity profile or thins the shear layer results in an accompanying narrowing of the vorticity tube. Furthermore, a lower Re_∞ means a thickening of the

shear layer and vorticity tube width, and that results in a wider neck. This is indeed what was observed.

Now, a thinning of the shear layer results in an increase of the viscous stress exerted by it on the core. The mass entrainment or scavenging of stagnant fluid from the core, i.e., $(\dot{m})_{scav}$ is thus increased as well. Recalling a useful concept proposed by Chapman (Ref. 5) as summarized in Fig. 4, we view formation of the steady core as a balance between $(\dot{m})_{scav}$ and $(\dot{m})_{rev}$, where $(\dot{m})_{rev}$ is the mass flow rate of the reversed flow in the core. The former is proportional to $\rho_e u_e$ as well as to l_{mix} ; while $(\dot{m})_{rev}$ is proportional to $p_n - p_b$. Now $\rho_e u_e$ and l_{mix} are both large if the base pressure p_b/p_n is higher. Thus $(\dot{m})_{scav}$ and $(\dot{m})_{rev}$ follow opposite trends and their intersection on Fig. 4b represents the equilibrium point. Increasing Ω at the inner edge of the shear layer shifts the \dot{m}_{scav} curve up and results in a lower p_b , a shorter l_{mix} and a larger shear layer angle θ .

Hence, the effects of increasing M_∞ , of increasing Re_∞ , of the replacing of a straight wedge forebody with a circular forebody, and of the removal of boat-tailing are qualitatively equivalent. They all increase the vorticity concentration of the free shear layer. (Increasing M_∞ is equivalent to increasing the rate of vorticity generation.) Note that all these arguments are for the low supersonic range ($1 < M_\infty < 5$) and moderate Reynolds number ($Re_\infty < 10^6$). For hypersonic flow and in a higher Reynolds number range, new mechanisms set in which can reverse the way in which the parameters influence the phenomena (see data in Ref. 2).

VERIFICATION OF THE NUMERICAL CODE

The objectives of this code verification are fivefold; namely, to evaluate

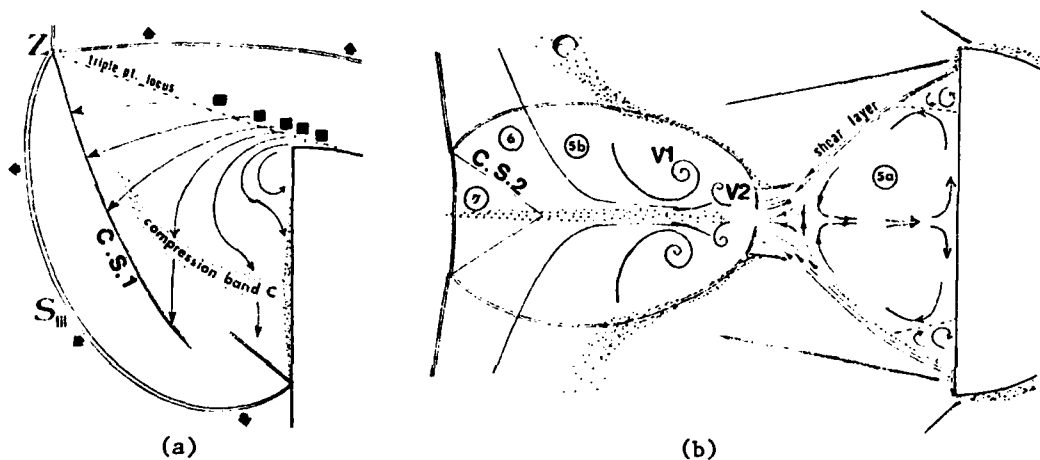
1. the accuracy of the transient solutions vs. the asymptotic state results;
2. the global satisfaction of the governing equations -- the "macroscopic" features;
3. the fine resolution -- the "microscopic" details, e.g., vortex formation;
4. the variation of flow geometries with parameters, hence, the code's predictive power for engineering purposes; and,
5. the actual values of the thermodynamic variables - a test of the fitness of the physical modeling, e.g., the validity of the ideal gas equations, state equations, heat transfer, and viscosity/turbulence model, etc.

The computer code used for this study was developed by Wray (Ref. 6) at NASA-Ames Research Center and is one of the few modern entire flow-field numerical codes that are considered fully developed and operational. The code is flexible in its capability to accommodate reasonably simple body shapes of arbitrary geometry, and in its ability to handle both 2D and axisymmetric cases with or without a sting. The ranges of Mach and Reynolds numbers for which it is most suited also overlap with those of the present experimental setup. The code solves the full Navier-Stokes equations without making any simplifications of the equations such as thin layer approximations, and is thus equally valid in all regions of the flow field. It is, therefore, superior for base flow calculations where many different flow regimes are involved and is superior in its versatility as no fundamental changes are necessary from problem to problem.

Figure 5 shows comparisons of some of the transient geometrical properties of the flow configuration obtained from calculation and experiment, respectively. The bow shock stand-off distance is an extremely sensitive function of the flow Mach number at the low supersonic ranges. The agreement for the half-cylinder case is thus very good. However, at early to intermediate times the



(a) (b) (c)
Fig. 1. Schlieren records of transient and asymptotic steady state flow around half-cylinders. Flow is from right to left.



(a) (b)
Fig. 2. Schematic drawings of the flow fields corresponding to those in Fig. 1a, b.

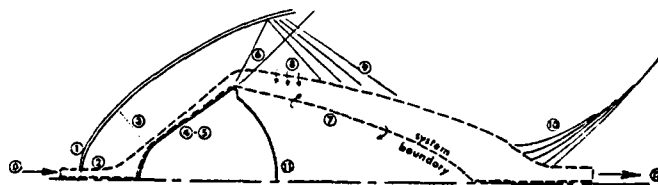
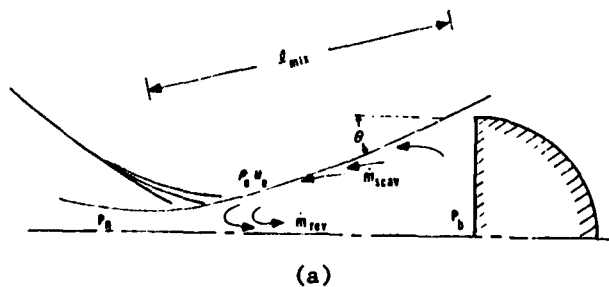
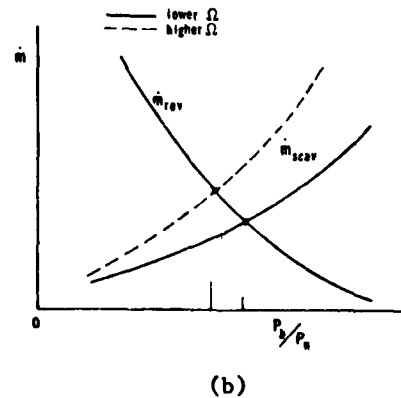


Fig. 3. 'System' view-point for vorticity transport in bluff body flow.



(a)
Fig. 4. Chapman's theory of equilibrium base flow.



(b)

experimental values for δ are higher than the numerical ones because the degree of vibrational excitation in the real gas flow behind the incident shock has not reached equilibrium. I.e., the instantaneous value of the specific heat ratio γ is higher than the steady-state value, $\gamma(t) > \gamma_{ss}$, $M_\infty(t) < M_{\infty,ss}$, and $\delta(t) > \delta_{ss}$. Furthermore, the transient numerical results show that even for values of the nondimensional time $T' > 25$, when the wake features have more or less reached steady state, the bow shock stand-off distance is still growing, but very slowly. This means that for our available test time in the shock tube, the flow has not quite reached steady state for the entire flow field even though the wake features seem to have stabilized. On the same figure, the discrepancy of the curve for the probe model reflects the sensitivity of δ to changes in the forebody shape. The cause of discrepancy may be due to the basic difference in overall forebody shape, or it may be due to inaccuracy in machining the nose radius of the probe model.

The somewhat poorer agreement between computation and experiment in the wake neck geometry is again attributable to real gas effects, a variable γ . The flow in the neck has gone through a strong expansion and then recompression, and the level of vibrational excitation for the gas can be expected to vary to a non-negligible extent from point to point away from the constant free stream equilibrium value assumed for the calculations ($\gamma = 1.354$). The computer code used is capable of accounting for a variable γ in equilibrium without dissociation (but not for nonequilibrium), i.e., due to changes in temperature, and effort is currently underway to adopt this feature into the program.

Figure 6 shows comparisons of the transient density development along the body surface and the wake axis. We note that the overall macroscopic level of the density compares very well. The agreement carries through to the steady state and is true also for the pressure distribution (Fig. 7) thus testifying to the basic validity of the code and the governing equations employed (equation of state, Sutherland's formula for viscosity, etc.). It also proves the correctness of the temperature assumptions in reducing the experimental data (i.e., isentropic for forebody and base surface, and $T = T_{stag}$ for wake axis) to pressure curves. We also see two major discrepancies. Firstly, in localized regions of sharp changes in density gradients (i.e., large second derivatives), especially those that involve a sign reversal of the gradient such as on the back of the half-cylinder, numerical calculations exhibit much overshoot/undershoot in the distribution curves as compared to experimental values. Such disagreement is readily understandable from two facts. Firstly, since no mathematically sharp corner exists in reality, localized discontinuities are always smeared out. Also, the resolution of optical measurements and the manual conversion of photographic data to numerical data tend to smooth out very sharp gradients. On the contrary, such localized disturbances are often exemplified or even amplified in finite difference computations whether they are real or, as is more likely, stem from truncation errors.

The second discrepancy is that the computational results fail to reveal some transient features of intermediate to small size that are easily distinguishable on the photographic records, in particular the big vortex pairs in the transient phase. These vortices, despite their significant size, can be considered 'microscopic' features of the transient flow field and, as previously discussed, trace their origin to the singular point or line sources of vorticity which have been greatly amplified by the physical flow processes. The incapability of the numerical scheme to model such microscopic developments having an infinitesimal origin and their subsequent amplification is typical of finite difference approximations. For instead of a continuum, grid cells of a finite size are used, and local averaging and artificial stabilizing schemes are a necessary part of the mathematical discretization model.

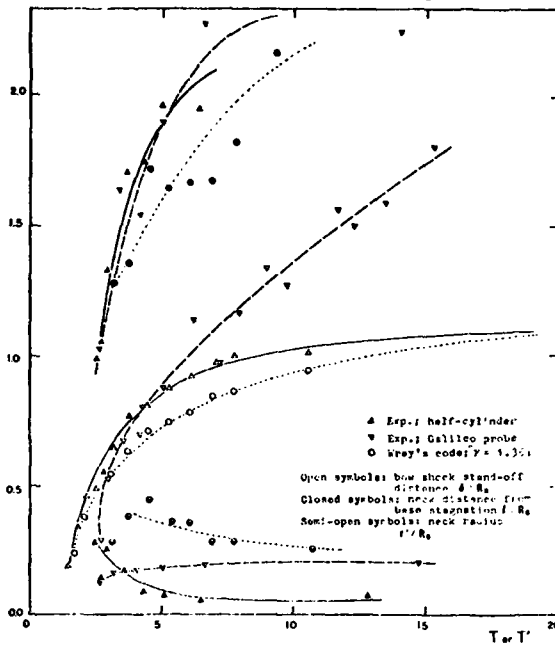


Fig. 5. Geometric properties of transient flow configuration.

$$T = (3.5 + \frac{r}{R_0}) / (\frac{a_2}{C_2}) \text{ and } T' = (2.5 + \frac{r'}{R_n}) (\frac{a_2}{C_2})$$

where r is the distance between the incident shock and the plane of max. diameter and r' the distance between shock and the nose; a_2 is incident shock speed; C_2 is speed of sound in region 2 of the shock-tube flow; R_0 and R_n are the body and nose radii, respectively. Thus, T is the time coordinate for comparing wake features whereas T' is for comparing the body features.

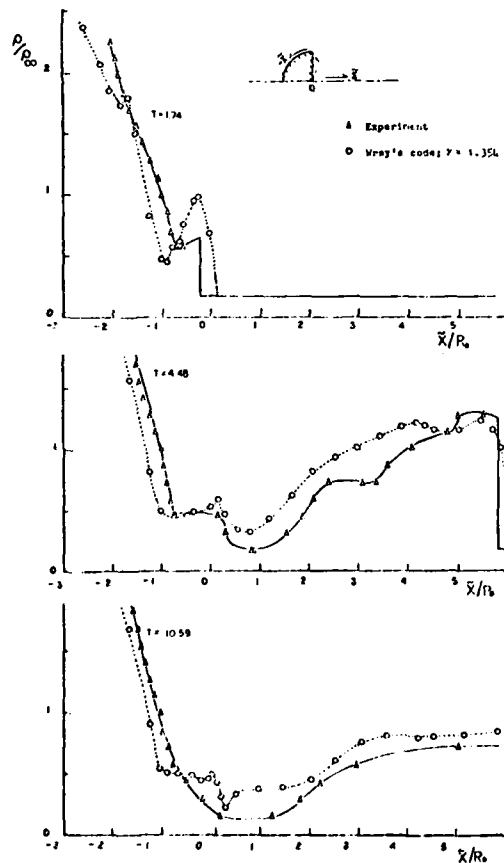


Fig. 6. Comparisons of transient density distributions along body surface and wake axis.

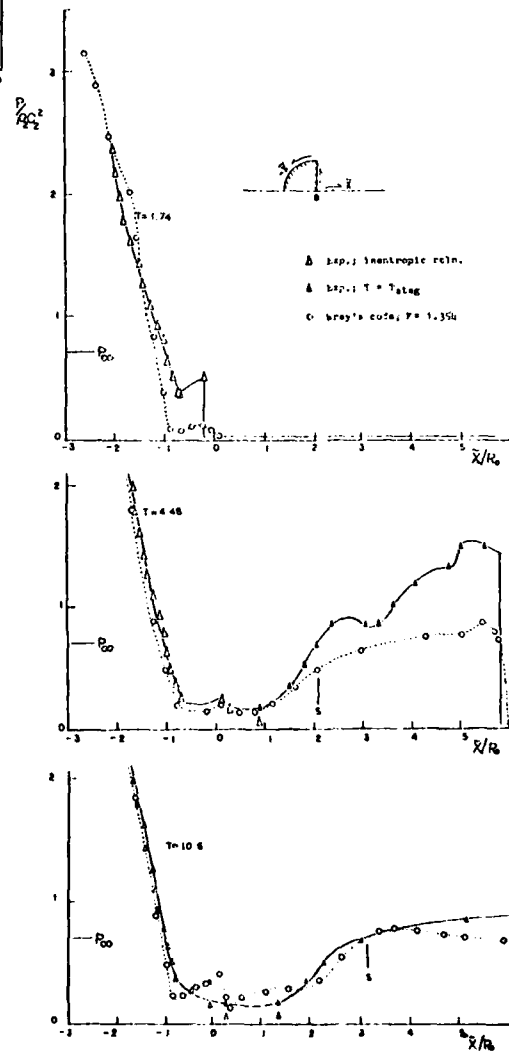


Fig. 7. Comparisons of transient pressure distributions along body surface and wake axis.

The representative density gradient computer map shown in Fig. 8 confirms the remarks just made. The prominent vortices visible in the schlieren records fail to show up in the computational results, though the steady state features such as the bow shock and trailing shock as well as the shear layer are well-modeled. The very weak lip shocks are also absent from the computational results, pointing to the incapability of the numerical code to resolve small localized changes in the thickness of the boundary layer which are believed to be responsible for the formation of the lip shocks. If spatial resolution of the computer code is improved by decreasing the size of the grid cells, or the runs are made at lower Reynolds numbers with correspondingly thicker boundary layers, the lip shock (which has a finite magnitude) may eventually show up in the computational results, although the vortices (which has an infinitesimal origin) still may not.

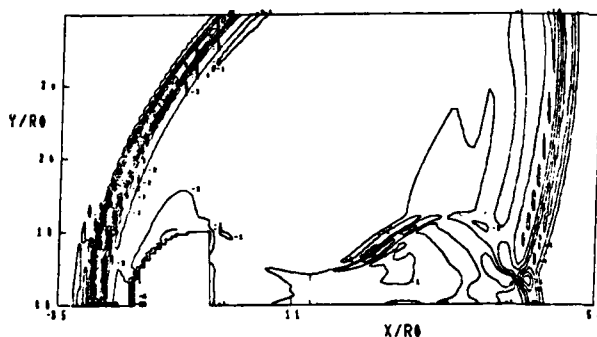


Fig. 8. Typical computer density gradient map

Finally, we note that in the wake the numerical values of density are consistently higher than the experimental ones; i.e., there is less mass entrainment from the core. Again, this is evidently due to a lower real gas value for the specific heat ratio γ in the base region than the constant value assumed for computation, which results in a larger M_∞ and hence density. The calculated pressure on the wake axis, how-

ever, is lower than that deduced experimentally by assuming $T = T_{\text{stag}}$, reflecting the fact that the actual wake axis temperature is somewhat lower than the latter. This situation is only reasonable since heat must have been conducted away from the stagnation streamline whose enthalpy level is correspondingly lowered.

SUMMARY AND CONCLUSIONS

The photographic data obtained in the experimental part of this study shows that the transient base flow establishment process is a complex one involving multiple wave interactions. The influence of all major physical and geometrical parameters on the base and neck pressures, however, can be understood qualitatively in the light of vorticity generation and transport. Though the present studies were done with 2D models to obtain better sensitivity in the optical studies, tests with axisymmetric models can be similarly carried out, preferably with larger shock tubes.

The experimental data also confirm the basic soundness of Wray's code for supersonic flows. Both its global validity in satisfying the governing equations and its time-accuracy have been demonstrated. Some microscopic features fail to be resolved and some unwarranted localized numerical fluctuations are present; they are, however, of secondary significance for engineering purposes. Furthermore, the insight gained from analysis of the transient phenomena enables us to extend the numerical simulation with more confidence to regimes of high Mach number flows, ones that are closer to the actual outer planet entry flight conditions.

REFERENCES

1. S.B. Murphy and T.R. Osborn, Prog. in Astro., 40, 7, (1974).
2. A.I. Shvets, Prog. Aerospace Sci., 18, 177, (1978).
3. J.T. Ohrenberger and E. Baum, Prog. in Astro., 40, 255 (1974).
4. C. Park, AIAA Paper 79-0919 (1979).
5. D.R. Chapman, D.M. Kuehn and H.K. Larson, NACA TN 3869 (1957).
6. K.K. Yoshikawa and A.A. Wray, NASA TP (1980).

AMPLIFICATION OF NON-LINEAR STANDING WAVES IN A CYLINDRICAL CAVITY WITH VARYING CROSS SECTION

E. Brocher and M. Elaouazi

Institut de Mécanique des Fluides

Université d'Aix-Marseille II, Marseille, France

AD P000243

The possibility of amplifying non linear standing waves in a cylindrical cavity, closed at one end, with a sudden change in cross section is studied both theoretically and experimentally. The oscillations are driven by a jet directed towards the open end of the cavity. A simplified wave diagram is constructed which provides a scheme to find the amplification ratio π at large amplitude. In the limiting case of strong shocks, π is found to be $(D_1/D_2)^{2K_\infty}$, where $K_\infty \approx 0.4$ for $\gamma = 1.4$. Agreement between theoretical and experimental values of π is good. A pressure amplitude as high as 28 bars at the cavity end wall has been recorded when the oscillations are driven by an air jet at Mach 2 and with $D_1/D_2 = 6$.

1. INTRODUCTION

At two previous symposia^{1,2}, we have shown the possibilities offered by a new configuration of the Hartmann-Sprenger tube (in short : H.S.-tube), the "needle" generator. This device enables one to obtain oscillations of optimal amplitude in a cavity driven by a jet, both in the subsonic and in the supersonic regime. For a cylindrical cavity of constant cross section, the amplitude of the pressure oscillations is approximately equal to $2\gamma M_1 p_a$, where γ represents the specific heat ratio, M_1 the Mach number of the driving jet and p_a the ambient pressure. For some applications, it is necessary to increase this amplitude by using cavities of varying cross section. This has previously been done with conical, trapezoidal or stepped cavities^{3,4,5}. Here, a new configuration is considered, as shown in Fig. 1.

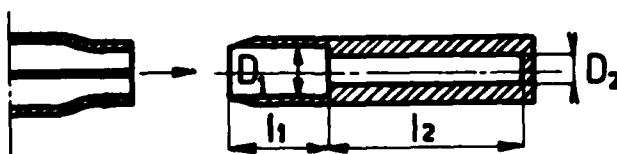


Fig. 1. H.S. tube with sudden constriction

A possible operating mode of the device is one in which the 2 cavities are "tuned", cavity I resonating at a quarter wave-length and cavity II at half wave-length.

The purpose of the present paper is to study both theoretically and experimentally the amplification of the waves due to the change in cross sectional area.

2. THEORY

2.1. Linear theory

By making the usual linear acoustic approximation, the propagating waves in cavity I and II are respectively of the form

$$p^I = A e^{ikz} + B e^{-ikz} \quad (1)$$

$$p^{II} = C e^{ikz} + D e^{-ikz} \quad (2)$$

where z represents the axial coordinate, measured from the step in cross section, and A, B, C, D are constants determined from the boundary conditions. This case has been treated in detail by Elaouazi⁶. It is found that two possible modes exist. The 1st one, with $k\ell_1 = \pi/2$, leads to an amplification ratio of the pressure equal to s_{12}^{-1} ($s_{12} = S_2/S_1$). The 2nd one, with $k\ell_1 = \arctg(1/1 + 2s_{12})^{1/2}$, gives an amplification ratio equal to $(1+s_{12}/s_{12})$.

2.2. Nonlinear theory

When the oscillations are driven by a high speed jet, the pressure amplitude is very important (several bars). It would therefore be useless to start from the acoustic theory, taking higher order terms into account. It is much better to use a simplified wave diagram and the velocity/speed of sound diagram, as was done with success for cylindrical cavities with constant area⁷. Among other things, this approach enables one to show the existence of a limit cycle for the oscillations and to get a good estimate of the pressure amplitude. For the configuration studied in the present paper, a possible simplified, limit cycle is drawn on Fig. 2 for the case $\ell_2 = 2\ell_1$. The shock wave produced by the penetration of the exciting jet in the cavity is reflected at the junction. The reflected shock wave moves towards the cavity mouth and is reflected as an expansion wave which in turn is reflected at the junction. The reflected expansion wave moves towards the cavity mouth and as it arrives there a shock wave is produced by the driving jet and a new cycle begins. From these considerations, it can be said that the wave motion in the upstream cavity is essentially the same as in a conventional H.S.-tube of length ℓ_1 . In the downstream cavity, a shock wave (which originates from the incident shock wave of the upstream cavity in the starting process) moves towards the end wall and is reflected as a shock wave. This reflected shock wave moves towards the junction and arrives there at the same time as the incident shock wave of the upstream cavity does. These two shocks collide and are reflected as shocks. With this possible mode, the junction represents a velocity node and acts like a wall. In the downstream cavity therefore, the waves do not change sign at both ends. This implies that expansion waves should occur between shocks to reduce the pressure between the passage of the shocks. These expansion waves are drawn in the diagram with half-a-period phase shift relative to the shocks. The dotted lines indicate the particle motion and the various fields are numbered. The corresponding velocity/sound-speed diagram for the downstream cavity is shown on Fig. 3.

To study the neighbourhood of the junction in more detail, the cross section is supposed to vary continuously from area S^I to area S^{II} over a distance short compared to the wave length. The wave diagram in this area is sketched in Fig. 4.

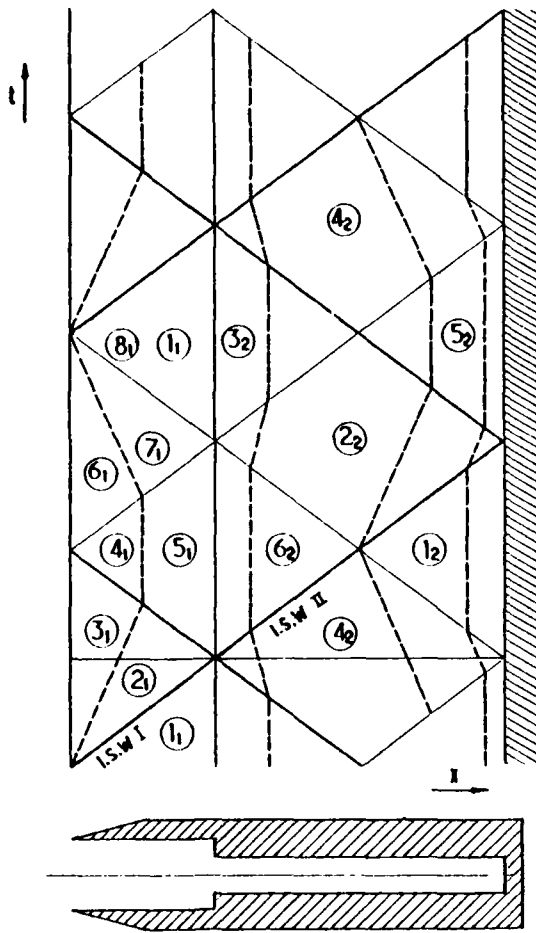


Fig. 2. Simplified wave diagram

i.s.w.: incident shock wave
r.s.w.: reflected shock wave
— : expansion waves
--- : particle displacement

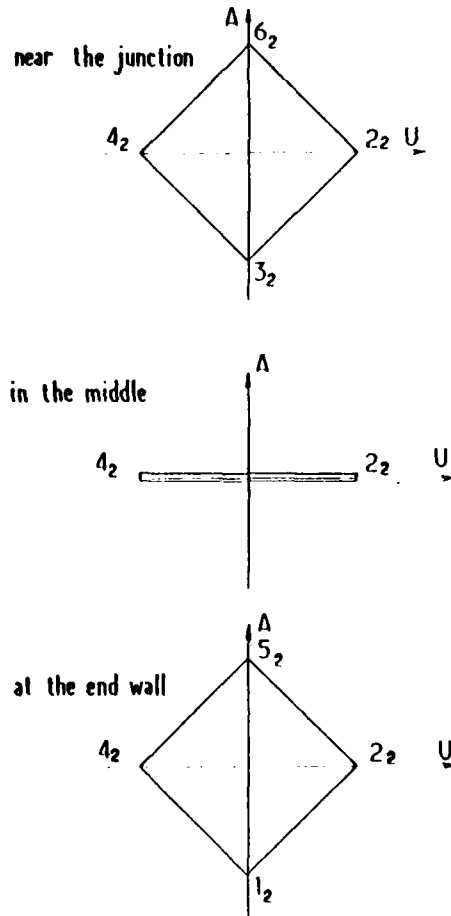


Fig. 3. Gas velocity/speed of sound diagram for the downstream cavity.

$$U = \frac{\gamma-1}{2} \frac{u}{a_0} ; A = \frac{a}{a_0}$$

u = gas velocity
 a = speed of sound
 a_0 = reference speed of sound

The incident shock of the upstream cavity is accelerated by the constriction so that its Mach number increases until it collides with the shock coming from the downstream cavity. The Mach number of this latter shock decreases as it moves through a larger area. Let us denote the flow conditions at the junction by an asterisk. If we require the gas velocity to be zero after the collision of the 2 shocks at the junction, the pressures behind the incident and reflected shocks should be equal, that is

$$p_{2_1}^* = p_{4_2}^* \quad \text{and} \quad p_{5_1}^* = p_{6_2}^* \quad (3)$$

The Mach number $M_{c_1}^*$ and $M_{c_2}^*$ of the colliding shocks should then be equal too.

For strong shocks, the evolution of M in a duct of varying cross section is given by Chester⁸ as

$$M_c \sim D^{-K_\infty} \quad (4)$$

where

$$K_\infty = 2 \left\{ \left[1 + \left\{ \frac{2}{\gamma(\gamma-1)} \right\}^{1/2} \right] \left[1 + \left\{ \frac{2(\gamma-1)}{\gamma} \right\}^{1/2} \right] \right\}^{-1}$$

with $K_\infty \approx 0.4$ for $\gamma = 1.4$.

Using Eq.(3) and (4) it is easily shown that

$$\frac{M_{c2}}{M_{c1}} = \left(\frac{D_1}{D_2} \right)^{K_\infty} \quad (5)$$

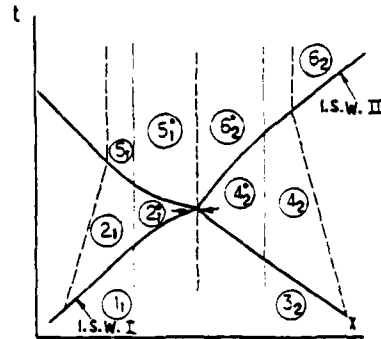
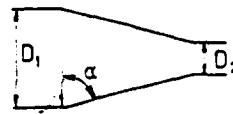


Fig. 4. Wave diagram at the junction

where M_{c1} and M_{c2} represent the shock Mach number in cavities I and II, away from the junction. With the help of various relations for strong shocks, we eventually get for the pressure amplification ratio

$$\pi = \frac{p_{62} - p_{32}}{p_{51} - p_{11}} = \left(\frac{D_1}{D_2} \right)^{2K_\infty} = \left(\frac{1}{s_{12}} \right)^{K_\infty} \quad (6)$$

or

$$\pi \approx \left(\frac{1}{s_{12}} \right)^{0.4} \quad \text{for } \gamma = 1.4$$

It is observed that the theoretical amplification ratio is substantially smaller for high amplitude than for small amplitude waves. (See paragraph 2.1)

3. EXPERIMENTS

3.1. Experimental set-up

The experimental set-up consisted of a nozzle, with a needle mounted on its axis, facing a cavity with a change in cross section (Fig. 5). The length ℓ_2 of the downstream cavity could be changed, so as to vary the parameter ℓ_2/ℓ_1 .

The following dimensions were used in the experiments

D_1 = 18 mm (same as nozzle exit diameter)

D_2 = 9 mm, 6 mm, 3 mm

ℓ_1 = 80 mm

ℓ_2 = 80 to 170 mm

α = 0°, 15°, 30°, 45° (see Fig. 4)

* For the runs with a supersonic exciting jet, the needle was shaped so as to form a converging-diverging nozzle and so as to get a correctly expanded jet.

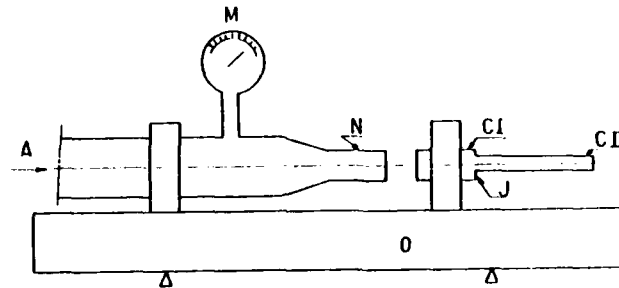


Fig. 5. Experimental set-up

A : pressured air supply ; M : manometer ; N : nozzle ;
O : optical bench ; C_I : upstream cavity ; C_{II} : downstream cavity ;
J : joining section

The pressure was measured at different stations along the cavity as shown on Fig. 6, with Kistler gauges 601 A and piezoceramics.

3.2. Influence of geometrical parameters

A great number of tests were run and are reported in Ref. 6 to determine the influence of several geometrical parameters on the pressure amplitude (distance between nozzle exit and cavity mouth, length ratio l_2/l_1 , angle α of joining section, area ratio S_1/S_2).

3.3. Pressure fluctuations

At low Mach number, the pressure fluctuations at various points in the downstream cavity correspond to the acoustic pressure distribution, that is, a pressure node is observed at midlength whereas pressure anti-nodes are observed just downstream of the junction and at the endwall. The frequencies measured correspond to the 1st solution given by the linear theory.

As the Mach number increases, deviations from the acoustic pressure distribution become larger and larger.

Fig. 6 shows the pressures measured for $M_j = 2$. The pressures were recorded simultaneously so that the wave motion in the cavity can be constructed from this recording. At the end wall (station 1), the pressure fluctuation is similar to the one observed at the end wall of a H.S. tube with constant cross section. At station 2, not far from the point for which a pressure node

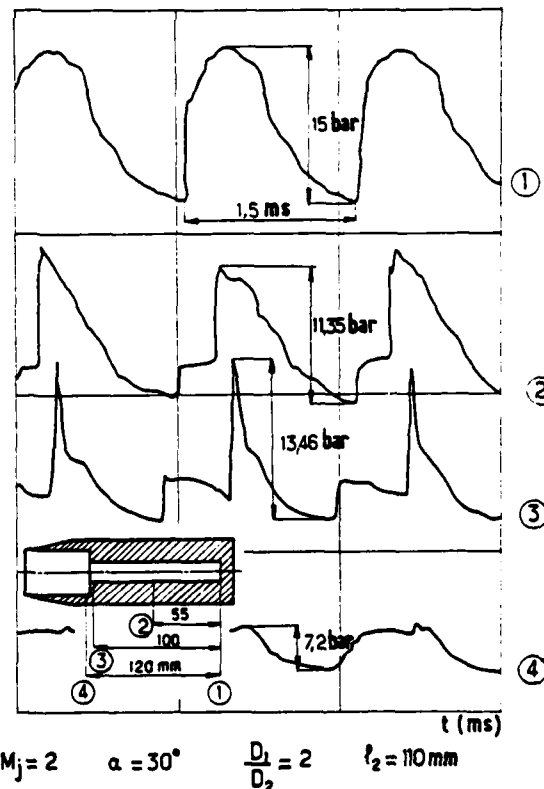


Fig. 6. Pressure fluctuations

At the end wall (station 1), the pressure fluctuation is similar to the one observed at the end wall of a H.S. tube with constant cross section. At station 2, not far from the point for which a pressure node

should occur according to the acoustic theory, the pressure amplitude is 11.35 bars ! This trace also indicates that there is an incident and a reflected shock (in contradiction with the simplified wave diagram, Fig. 2) and this pressure fluctuation is also very similar to the one observed in a conventional H.S. tube at this station. At station 3, these two shocks also exist, the importance of the reflected one being very large. At station 4, just upstream of the constriction, the pressure distribution is similar to that of conventional H.S. tube of length ℓ_1 . It is interesting to note that the strong reflected shock observed at station 3 completely vanishes and does not appear in the upstream cavity.

The largest pressure amplitude measured in our tests at the end wall was 28 bars at $M_j = 2$ with $D_1/D_2 = 6$.

3.4. Pressure amplification ratio π

The main purpose of the present paper was to investigate the amplification of large amplitude standing waves in a cavity with varying cross section. Fig. 7 shows the pressure amplification ratio π as a function of the diameter ratio for 3 values of the jet Mach number. The agreement between theory and experiments is good for area ratios of 4 and 9, whereas the experimental value is 14 % lower than the theoretical one for an area ratio of 36.

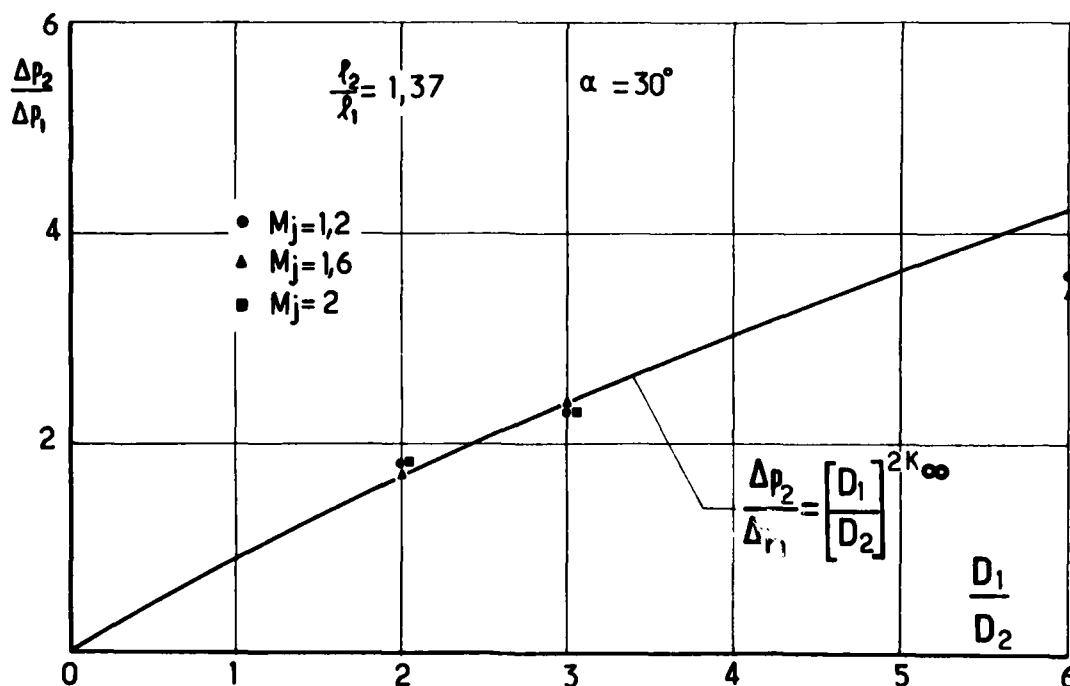


Fig. 7. Amplification ratio $\Delta p_2/\Delta p_1$ as a function of the diameter ratio D_1/D_2

4. CONCLUSION

The present investigation has shown, both theoretically and experimentally, which amplification of standing waves can be obtained in a cavity with a sudden change in cross section. The amplification was found to be smaller for high amplitude waves than for acoustic waves. The agreement between theoretical and experimental values of the amplification ratio is good for the high amplitude waves produced by supersonic exciting jets.

REFERENCES

- 1) E. Brocher, Proceedings of the 11th International Symposium on Shock Tubes and Waves, p.66 (1977).
- 2) E. Brocher, Proceedings of the 12th International Symposium on Shock Tubes and Waves, p.161 (1979).
- 3) B.R. Philips and A.J. Pavli, NASA Technical Note TN D-6354 (May 1971).
- 4) E. Brocher and C. Maresca, C.R. Acad. Sc. Paris, t.273, Serie A, p.1303 (December 20, 1971).
- 5) V.P. Marchese and E.L. Rakowsky, J. Spacecraft, Vol. 10, N°11, p.731 (1973).
- 6) M. Elaouazi, Thèse de Doctorat de Spécialité, Université d'Aix-Marseille II, (Juin 1981).
- 7) E. Brocher and C. Maresca, J.F.M., Vol.43, part 2, p.369 (1970).
- 8) W. Chester, Advances in Applied Mechanics, Vol.VI, p.119, (1960).

AD P000244

CYCLIC WAVE ACTION IN THE STABLE OPERATION OF A HARTMANN-SPRENGER TUBE

J. Iwamoto

Mechanical Engineering Department
Tokyo Denki University
Tokyo, Japan

B.E.L. Deckker

Mechanical Engineering Department
University of Saskatchewan
Saskatoon, Saskatchewan, Canada

The means by which stable oscillation of the air column in a Hartmann-Sprenger tube is initiated and maintained has been explained satisfactorily for the first time. Shadowgraphs of the external flow field obtained by synchronous shadow-photography and the numerical simulation of the flow in the tube have clarified the behavior of the shock wave system in the space between the forcing nozzle and driven tube, and also how its movement is related to flow within the tube. It is shown that the fractions of the periodic time occupied by well defined quasi-steady inflow and outflow phases are about 22 percent and about 32 percent respectively. There are two transient phases that precede quasi-steady inflow and quasi-steady outflow which occupy about 33 percent and 13 percent of a period respectively. The process of inflow is extremely stable, whereas, that of outflow is not always stable. Instability of the outflow has been found to be due primarily to a succession of weak shock waves emerging from the tube as a result of internal wave action obtained between the contact surface on the one hand and the closed end on the other.

INTRODUCTION

The arrangement known as the Hartmann-Sprenger tube (H-S tube) comprises a convergent nozzle aligned co-axially with a tube in which the end further from the nozzle is closed. When an underexpanded sonic jet is directed against the open end, a violent oscillation of the air column in the tube occurs and a high temperature is produced at the closed end. Since Sprenger (1) first published his experimental results in 1954, several investigations have been made into the oscillatory behaviour of the flow and, in particular, into the mechanism by which a stable high temperature is attained; and into the practical application of the temperature effect (2).

It is now well known that the thermal effect is due to irreversible heating by shock waves and by wall friction. However, in order to maintain a constant high temperature, there must be a balance between the heat generated and that removed. In this connection it has been shown in ref. (3), that the exchange of mass in the boundary layer at the contact surface between the, so-called, indigenous fluid and extraneous fluid, is important.

The mechanism by which stable oscillation of the air column in the tube is initiated and maintained has not yet been satisfactorily explained. A theoretical analysis by Kawahashi and Suzuki(4) based on linear theory has shown that it is a self-excited oscillation due to the existence of a negative impedance. The results of experiments and theoretical analysis using a plugged tube or, what has been described as, a Hartmann-Sprenger tube of zero length have been reported by other investigators (5) - (8). With this configuration, also, it is known that a stable oscillation of the flow field occurs when the plugged tube is placed in the underexpanded jet at a critical distance from the convergent nozzle. But in this case also the mechanism by which the stable oscillation is initiated and maintained has not been well established.

In this paper the oscillatory nature of the flow in the space between the forcing nozzle and driven tube has been examined using synchronous shadow photography. The flow is characterized by the presence of a shock-wave pattern, or system. The movement of this shock wave system has been related to the periodic flow within the driven tube by numerical simulation of the flow in the tube using the method of characteristics.

EXPERIMENTAL CONSIDERATIONS

The apparatus used in the experiments is shown schematically in Fig. 1. Dry air is supplied to the plenum chamber in the side of which a convergent nozzle is fitted. The throat diameter, d , of the convergent, or forcing, nozzle is 0.010 m and is equal to the diameter of the driven tube which is 0.170 m long. The tube separation distance, ℓ , is 0.015 m. The forcing nozzle is underexpanded with the ratio of the stagnation pressure p_t to ambient pressure p_0 equal to 4.0.

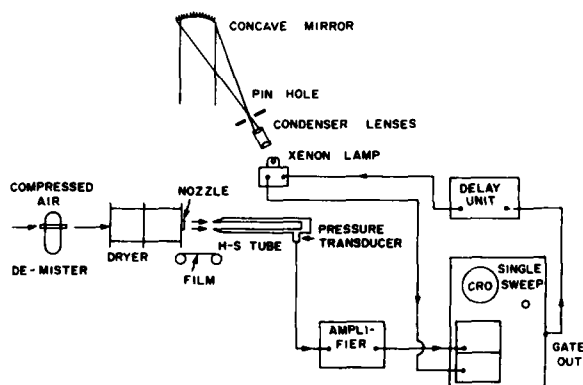


FIGURE 1

The gross structure of the underexpanded sonic free jet is cellular and the cell characteristics are dependent upon the degree of under-expansion, or upon the ratio p_t/p_0 . The variation of the ratio of the cell length to nozzle diameter, λ/d , with pressure ratio, p_t/p_0 , in a free jet is shown in Fig. 2. The spatial periodicity of the cell structure begins to be disrupted at a pressure ratio of about 3.0 and when the ratio is increased to about 4.0 there is a clearly defined Mach reflection at the axis of symmetry in the first cell. The variation of the ratio of the diameter of the Mach disk to nozzle diameter, d_M/d , is also shown in Fig. 2. The shadowgraph of the first cell in a free jet at the pressure ratio $p_t/p_0 = 4.0$, in the present experiments, is shown in Fig. 3. The well known configuration of the Mach reflection consisting of the incident shock wave, or the intercepting shock, the Mach disk and the reflected oblique wave are clearly seen in that Figure.

When the driven tube is placed in the jet of pressure ratio 4.0, and the

The flow in the space between the forcing nozzle and the driven tube has been visualized by synchronous shadow photography. A pressure transducer located in the closed end of the tube is used to trigger the light source and also to give the pressure-time history there. Sequences of the shadowgraphs are obtained at time intervals equal to 0.05 ms throughout one cycle of the oscillation.

EXPERIMENTAL RESULTS

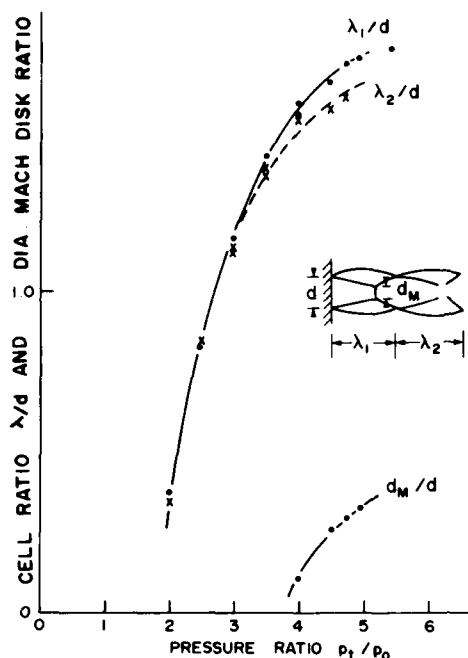


FIGURE 2

to the fundamental resonance frequency of the tube. Typical shadowgraphs which reveal the characteristic features of the flow field between the nozzle exit and open end of the driven tube, in a sequence of events within one such cycle, are shown in Figure 4.

Fig. 4(a) shows the flow field when the nozzle jet is flowing into the tube, the time is $t = 0.04$ ms measured from the instant when the shock wave in the tube reaches the closed end. This shadowgraph clearly shows the slip surface which separates the flow through the Mach disk from the flow through the reflected oblique shock. That part of the flow which goes through the oblique shock is supersonic and another shock is formed in front of the open end so that flow into the tube, inflow, is subsonic. Flow through the Mach disk has the larger entropy rise and larger stagnation pressure drop than the flow through the oblique shock. The flow shown typically in Fig. 4(a) continues for about 22 percent of the period of one cycle. Similarity between this quasi-steady flow pattern and the steady flow pattern which is found when both ends of the tube are open, shown in Fig. 5, is striking.

Fig. 4(b) shows the flow pattern at an instant ($t = 0.62$ ms) during the time that flow into the tube is changing into an outflow. This phase is relatively short and occupies about 13 percent of the period of one cycle. Starting at the end of the inflow phase, Fig. 4(a), at first the subsonic region behind the Mach disk is broadened and the shock wave system, consisting of the Mach disk and oblique shock, moves upstream. Later, the subsonic region in front of the open end of the tube is further broadened and outflow begins suddenly in the region of the axis. Near the rim of the tube, however, the flow is still rightward, that is toward the open end of the tube. In Fig. 4(c) it is seen that a normal shock is formed on the axis of the jet flowing from the tube, which implies that the open end of the tube is choked and that the flow downstream is supersonic and tube-jet underexpanded. As outflow continues and the pressure downstream of the normal shock in the tube-jet increases, the shock wave system associated with the nozzle-jet retrogresses towards the nozzle and in the process becomes nearly normal. It is clear that the two jets are opposed and those parts of the flow that pass through the two normal shocks impinge on one another and are deflected radially. This flow pattern which



FIGURE 3

nozzle-tube spacing adjusted to 0.015 m a violent oscillation of the air in the tube occurs. The nozzle-tube spacing of 0.015 m coincides approximately with the right hand boundary of the first cell as may be seen in Fig. 2. Under these conditions, the observed frequency of the periodic swallowing and disgorging of the nozzle-jet by the tube is 434 Hz., (periodic time 2.30 ms), and is approximately equal

persists for about 32 percent of the period of one cycle is not always as stable as that associated with inflow because the shock waves may oscillate with small amplitude of excursion on the axis.

(a) $t = 0.40$ ms(b) $t = 0.62$ ms(c) $t = 1.30$ ms(d) $t = 1.62$ ms

FIGURE 4

As the outflow weakens with time, the flow pattern begins to change into that for inflow. The nature of the change in the flow pattern is shown in Fig. 4(d) at one instant ($t = 1.62$ ms) during this phase. Toward the end of this phase the shock in the tube-jet is swallowed by the tube and the almost normal shock in the nozzle-jet now moves towards the open end of the tube, changing its configuration as it does so, into that of the characteristic Mach reflection. This transient phase occupies about 33 percent of the period of one cycle and is long compared to the previous transient phase in which flow into the tube changes into an outflow. At the beginning of this transient phase when the flow pattern is changing to that of inflow, a shock is formed near the edge of the jet, between the oblique shock and the open end. Most of the flow through this shock is deflected over the rim of the open end of the tube, and only the subsonic flow behind the Mach disk passes into the tube. In the later stages of this transient phase, the shock system in the nozzle-jet moves closer to the open end of the tube and takes up a stationary position, when most of the nozzle-jet is deflected into the tube. This signals the start of the regime of quasi-steady flow into the tube, the flow pattern being that of Fig. 4(a).

FLOW WITHIN THE DRIVE TUBE

Flow within the tube has been predicted by the method of characteristics, assuming an unsteady one-dimensional flow. The results obtained in this way have been found to be in good agreement with experiment (9). In ref. (10), wall friction, heat transfer and mass exchange at the contact surface in accord with the concepts in ref. (3) have been taken into account in calculating the flow pattern in the tube. The wave diagram, which has been constructed from the results of the numerical simulation of the internal flow using the



FIGURE 5

method of characteristics, is shown in Fig. 6(a). Fig. 6(b) shows the trajectories of the shock waves in the space between the nozzle and open end of the driven tube. The period of one oscillation of the cyclic flow in the tube as calculated by the method of characteristics is $a_t(t/L) = 4.57$, which is in reasonably good agreement with the experimental value of 4.63 (corresponding to $t = 2.30$ ms) obtained by means of the pressure transducer located in the closed end of the driven tube, a_t being the stagnation sonic velocity and L the tube length.

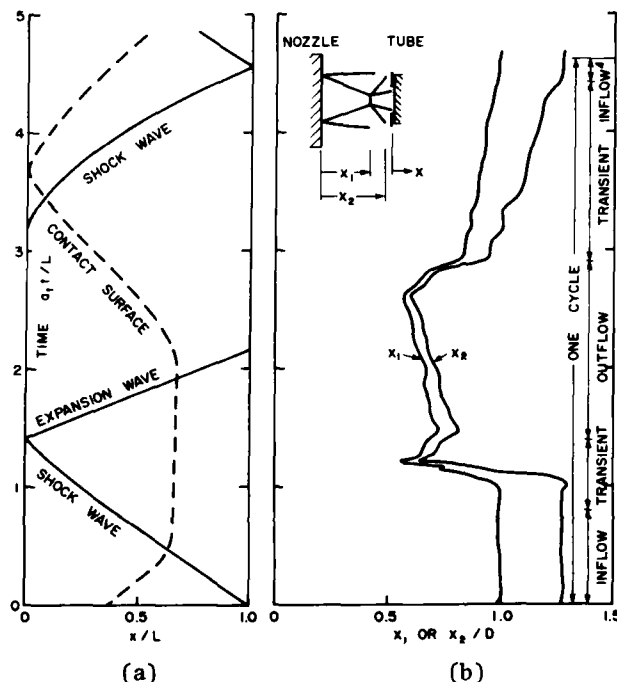


FIGURE 6

From the path of the shock between the nozzle and open end of the tube, Fig. 6(b), it may be inferred that flow into the tube is quite stable. The change from inflow to outflow clearly starts with the sudden movement of the shock system towards the nozzle. The wave diagram, Fig. 6(a), shows that outflow from the driven tube begins when the shock wave in the tube reaches the open end and reflects from it as expansion wave. However, there is a discrepancy between the calculated time at which this occurs and experiment because of the simplifying assumptions underlying the calculation.

Instability of the shock wave system in the space between the nozzle and the open end and the discrepancy in the times noted above during outflow may be explained as follows:

The shock wave reflected from the closed end of the tube interacts with the contact surface in the tube, part of the shock being transmitted through it and the other part being reflected. The partially reflected shock moves towards the closed end and is again reflected from it, interacting with the contact surface and again undergoing partial transmission and partial reflection. The wave action is repeated until the reflected shock becomes sufficiently attenuated for its effect to be negligible. Thus, during outflow, a series of increasingly weaker shock waves arrive at the open end in succession, after the arrival of the first strong shock wave there, and so affects the shock in the jet. This would be of particular significance immediately after the start of the outflow from the tube.

Referring to the wave diagram, Fig. 6(a), as outflow from the tube gradually weakens, a shock wave is formed in the driven tube due to the overtaking of compression waves that are reflected from the open end on first arrival of the expansion wave from the closed end. Other compression waves which are reflected at later times from the open end also catch up with this shock. Meanwhile, the shock wave which initially was stationary in the tube-jet now moves towards the open end as a result of the interaction with the expansion waves that have been partially transmitted from the open end of the tube, and eventually enters the tube. The two shock waves merge somewhere in the tube and travel towards the closed end.

DISCUSSION

The experimental results show, when the tube is driven cyclically, that

the flow pattern in the space between the nozzle exit and the open end during quasi-steady inflow is nearly the same as that for steady flow in the case when both ends of the tube are open. The mechanism that initiates the flow oscillation, may be described in the following way.

As a starting point, the jet from the nozzle may be assumed to be directed against a tube that has both ends open and that the steady state flow pattern of Fig. 5 has been attained. If the right-hand of the open tube is now suddenly closed, the flow pattern in the space between the nozzle and the open end of the tube will change. What has to be considered here is whether, or not, the same flow pattern as that of the original steady flow can be restored after the lapse of a certain time. If the flow pattern reverts to that of the steady state, then a periodic oscillation of the flow could result, since quasi-steady inflow could be one phase of a possible periodic oscillation.

In what follows, the flow is treated for the most part as being one-dimensional, both inside and outside the tube.

Referring to the wave diagram shown in Fig. 7, when the right-hand end of the open tube is closed suddenly, the "hammer wave" (11) which is generated there propagates to the left-hand end (the open end) of the tube. A part of this shock wave is reflected at the open end as an expansion wave so initiating outflow from the tube. The transmitted part of the shock wave moves upstream into the nozzle-jet and merges with the shock system which would be stationary in the jet under the steady state conditions described earlier. Merging of these shock waves results in a single strong shock wave and at the same time gives rise to an expansion wave which moves downstream towards the open end of the tube as shown in Fig. 7.

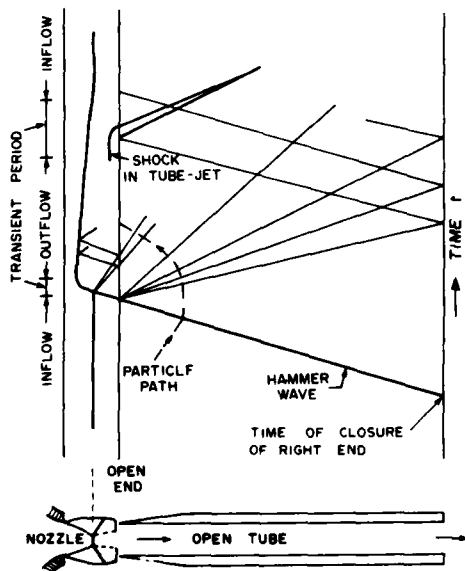


FIGURE 7

expansion wave is relatively weak. When a periodic oscillation has been established, this movement is even smaller because weak shock waves that are transmitted in succession at the contact surface in the tube, as a result of repeated interactions between the reflection at the closed end of the expansion wave, that earlier entered the tube, and the contact surface, arrive at the shock wave in the nozzle-jet and strengthen it. As flow out of the tube continues, the sonic condition is attained at the open end and the tube-jet becomes underexpanded. As a result, the flow pattern shown in Fig. 4(c) is obtained.

The merged shock wave, which is of greater strength than either the shock wave system in the nozzle-jet or the transmitted shock wave, now moves upstream in the underexpanded jet from the nozzle and takes up a position in the jet where the local Mach number is compatible with the strength of the merged shock wave.

In the meantime, the expansion wave which originated when the two shock waves merged, propagates towards the open end of the tube. A part of this wave enters the tube and a part is reflected from its rim, propagating upstream towards the nozzle. The expansion wave so reflected interacts with the stationary merged shock wave in the nozzle-jet and weakens it, causing it to move downstream. This downstream movement is small because the reflected

The expansion wave which originates at the open end when outflow first begins, returns to the open end after being reflected at the closed end. A part of this wave is reflected at the open end as a compression wave which propagates towards the closed end and develops into a shock wave at some position in the tube. The transmitted portion of the expansion wave weakens the shock wave in the tube-jet causing it to move downstream and to be swallowed by the tube. This shock wave then catches up with the shock wave which has already been formed in the tube from the reflected compression wave and gives rise to a single strong shock wave.

At the same time that the shock wave system in the tube jet moves towards the tube and is swallowed by it, the region of impingement between the nozzle jet and the tube jet, which is seen in Fig. 4(c), also begins to move towards the open end of the tube. The condition for inflow is gradually established in this way. The change in the external flow pattern from outflow to inflow takes place very gradually because the expansion fan is broadened as it is reflected from the closed end.

CONCLUSIONS

The oscillatory nature of the flow in the space between the forcing nozzle and the driven tube has been examined using synchronous shadow-photography.

Shadowgraphs of the external flow field and the numerical solution of the flow in the tube by the method of characteristics have clarified the behaviour of the shock wave systems in the nozzle-jet and tube-jet and also how their movements are related to flow within the tube. It has been reported (12) that the inflow and outflow phases occupy about 40 percent of the periodic time. The present work has shown that the fractions of the periodic time occupied by well defined quasi-steady inflow and outflow phases are about 22 percent and about 32 percent, respectively. It has also been shown that there are two transient phases, that is, when the quasi-steady flow into the tube is changing into the quasi-steady flow out of the tube, and vice-versa, which occupy about 13 percent and 33 percent of a period, respectively.

It has been observed that inflow is extremely stable, whereas outflow is not always stable. The instability of the outflow has been found to be due primarily to a succession of weak shock waves emerging from the closed end after interacting with the contact surface in the tube.

These findings have been corroborated by work using a separation distance equal to 0.012 m and pressure ratio, p_t/p_o , of 2.50.

ACKNOWLEDGEMENT

One of the authors (J.I.) would like to acknowledge the financial assistance in the form of the research grant from the Research Foundation of Tokyo Denki University.

REFERENCES

1. Sprenger, H., Mitt. E.T.H., 21 (1954), p. 18.
2. Iwamoto, J., Research Reports from Tokyo Denki University, Dec. 1974, No. 22, pp. 113-125.
3. Brocher, E. and Maresca, C., Int. J. Heat Mass Transfer, Vol. 16, 1973, p. 592.
4. Kawahashi, M. and Suzuki, M., ZAMP, Vol. 30, 1979, pp. 797-810.
5. Moerch, K.A., J. Fluid Mech., 20-1 (1964), p. 141.
6. Kukita, Y1, JSME Preprint, No. 750-16 (1975), p. 229.
7. Iwamoto, J., Research Reports from Tokyo Denki University, Dec. 1969, No. 17, pp. 135-143.

9. Iwamoto, J., Research Reports from Tokyo Denki University, Dec. 1972, No. 20, pp. 79-89.
10. Iwamoto, J. and Deckker, B.E.L., Proceedings of the 7th CANCAM, 1979, p. 585.
11. Rudinger, G., "Nonsteady Duct Flow", 1969, Dover Publications, Inc.
12. Wu, J.H.T. et. al., CASH Trans., Vol. 6, No. 1, March 1973, p. 26.

Part III: BOUNDARY LAYERS AND HEAT TRANSFER

AD P000245

SOME FUNDAMENTAL ASPECTS OF SHOCK WAVE -
TURBULENT BOUNDARY INTERACTIONS IN TRANSONIC FLOW

G. R. Inger

Department of Aerospace Engineering Sciences
University of Colorado, Boulder, Colorado 80309

Transonic normal shock - turbulent boundary layer interactions can significantly influence not only the local viscous flow but also the downstream behavior of the boundary layer on aerodynamic bodies. It is therefore important that fundamentally-based analytical tools be developed for describing and scaling these interaction effects. This paper examines recent progress toward this goal, with emphasis on two aspects. (1) A basic non-asymptotic triple-deck theory of non-separating two-dimensional interactions that is applicable over a wide range of practical Reynolds numbers and boundary layer profile shapes. (2) Its application as a local "interactive module" in the global transonic flow field analysis of wings, including detailed comparisons with experimental data. Also discussed is the adaptability of this theory to treat interactions involving non-adiabatic wall conditions, including the prediction of incipient separation.

1. INTRODUCTION

Shock - boundary layer interaction can significantly influence not only the local transonic flow on missiles, wings and turbine blades but its influence can also extend downstream within the boundary layer and thereby alter the global aerodynamic properties of lift, drag and pitching moment. It is therefore important that these interactions and their Reynolds and Mach number-scaling be properly modeled in engineering flow field prediction methods for supercritical aerodynamic bodies. This paper describes the application of a non-asymptotic triple-deck theory of transonic shock - turbulent boundary layer interaction which provides such a tool for non-separating two-dimensional flows over a wide range of practical Reynolds numbers. Section 2 contains a brief description of the essential features of the theoretical model. Section 3 then describes how this theory is extended to treat the influence of non-adiabatic wall conditions such as may be encountered in Cryogenic Wind Tunnels or on the Space Shuttle. In Section 4 we examine application of the theory as an element in global viscous flow field analyses of supercritical airfoils where the interaction may significantly alter the subsequent turbulent boundary layer behavior for appreciable distances, especially when large downstream adverse pressure gradients are present.

2. BRIEF OUTLINE OF THE LOCAL INTERACTION THEORY

Unlike separated flow, the disturbance flow pattern associated with a nearly-normal shock - boundary layer interaction in the unseparated case pertaining to turbulent boundary layers up to roughly $M_1 \approx 1.3$ has a much simpler type of interaction pattern¹ amenable to analytical treatment. With some judicious simplifications, it is possible to construct a fundamentally-based approximate theory of the problem in the latter case. Consider a known boundary layer profile $M_0(y)$ subjected to small transonic disturbances due to an impinging weak and nearly normal shock. In the practical Reynolds range of interest here ($10^5 < Re_L < 10^8$), it is known that the local interaction field organizes itself into three basic layered regions or "decks" (Fig. 1): (1) an outer region of potential inviscid flow above the boundary layer containing the incident shock and interactive wave systems; (2) an intermediate deck of frozen shear stress-rotational inviscid disturbance flow occupying the outer 90% or more of the incoming boundary layer thickness; (3) an inner shear-disturbance sublayer which accounts for the interactive skin friction perturbations (and hence possible incipient separation) plus most of the upstream influence. The "forcing function" here is thus impressed by the outer deck upon the boundary layer; the middle deck couples this to the response of the inner deck but in so doing can itself modify the disturbance field to some extent, while the slow viscous flow in the thin inner deck reacts very strongly to the pressure gradient disturbances imposed by these overlying decks. Our approach is to employ a non-asymptotic method² that is an extension to turbulent flow of Lighthill's approach³, because of its essential soundness and adaptability to practical engineering problems, similarity to related types of multiple-deck approaches that have proven highly successful in treating turbulent boundary layer response to strong adverse pressure gradients, and the large body of turbulent boundary layer interaction data plus Navier-Stokes numerical studies which support the predicted results (see the survey in Ref. 2). Moreover, this approach provides at realistic Reynolds numbers a treatment of the inner deck pressure gradient terms plus the middle deck $\partial p / \partial y$ and streamline divergence effects, along with simplifying approximations that render the resulting theory tractable from an engineering standpoint.

A very detailed description of the above-mentioned non-asymptotic triple-deck analysis can be found in Ref. 2 and hence will not be given here. The resulting predictions, such as typically illustrated in Fig. 2, describe all the essential global features of the mixed transonic character of the problem including the interactive pressure distribution and upstream influence, displacement thickness and local shape factor, and interactive skin friction up to incipient separation. This interaction theory employs for the incoming turbulent boundary layer velocity profile a very general Composite Law of the Wall - Law of the Wake profile model which is characterized by three parameters (M_1 , boundary layer thickness Reynolds number and the incoming shape factor). The influence of both shock obliquity and wall curvature have also been examined in detail and incorporated into the theory. Extensive parametric studies⁴ and detailed comparisons with experiment have shown that it gives a very good account of the interaction over a wide range of Mach and Reynolds number conditions including the important but heretofore-ignored influence of incoming boundary layer shape factor H_{1i} (hence upstream pressure gradient history).

Although the present theory breaks down at separation, it does yield a useful indication of incipient separation where $C_{f_{min}} \rightarrow 0$, owing to the particular attention paid to the treatment of the local interactive skin friction behavior. In particular one obtains the explicit criterion on the interactive pressure field that

$$C'_{P_w} \left[\frac{2 C'_{P_w}{}^{3/2} / \kappa_{\min}}{3 \int_{-\infty}^x (C'_{P_w})^{3/2} dx} \right]^{2/3} \underset{SEP}{\geq} C(Re_{\delta^*}, M_{e_1}, H_{1_i}) \quad (1)$$

where the RHS constant C is a function of Reynolds number, Mach number and the incoming boundary layer shape factor (see Ref. 2). A parametric study of this was carried out with the results for a normal shock on an adiabatic flat surface shown in Fig. 3, where the shock Mach number above which incipient separation occurs is plotted as a function of the Reynolds number with the shape factor as a parameter. Also shown in the Figure is the approximate experimental boundary determined by an examination of a large number of transonic interaction tests, besides the " $M \sim 1.30$ " criterion for turbulent flow. It is seen that the theoretical prediction of a gradual increase in the incipient separation Mach number value with Reynolds number is in agreement with the trend of the data.

3. EXTENSION TO NON-ADIABATIC FLOWS

Detailed analysis has shown⁵ that the presence of small to moderate heat transfer does not introduce any new terms in the interactive perturbation equations governing either the inviscid or viscous disturbance regions; thus in the leading approximation, the influence of a non-adiabatic wall enters only implicitly through the undisturbed $M_0(y)$, skin friction C_{f_0} , boundary layer thickness δ_0 and the shape factor as given in terms of a prescribed incoming incompressible value H_{1_i} by

$$H_1 = \left(\frac{T_w}{T_e} \right) H_{1_i} + .1145 Me_1^2 \quad (2)$$

This may be readily implemented via a modified Crocco energy equation solution with a recovery factor $r = P_r^{1/3} \approx .89$ for air plus the Eckert reference-temperature method of accounting for the attendant modest compressibility effects.

The typical wall temperature effect on the interaction pressure distribution along the wall is illustrated in Fig. 4 and is seen to be weak; this was found to be true over a range of shock strengths and Reynolds numbers. Increasing wall temperature tends to increase the upstream influence and lower the pressure downstream of the shock. The upstream influence distance over a wide range of conditions has been found to be $\sim \delta_0$ independent of heat transfer; thus, e. g., cooling reduces this influence essentially proportional to the corresponding reduction in δ_0 , as also observed at higher Mach numbers. The corresponding typical interaction-induced growth of the boundary layer displacement thickness is shown in Fig. 5 illustrating the expected thinning out with increasing Reynolds number or wall cooling. The influence of a hot wall $T_w > T_{w,ad}$ is increasingly significant at lower Re_L .

The effect of shock-boundary interaction on the local skin friction is of particular importance in transonic airfoil design and testing, since it bears directly on the downstream boundary layer behavior and its possible separation. Since wall temperature also influences the undisturbed skin friction C_{f_0} , the relative effect on its interactive decrement alone can be shown by plotting the ratio $C_f(x) / C_{f_0}$ as illustrated in Fig. 6. It is seen that the effect of cooling $T_w < T_{w,ad}$, in spreading out the interaction and weakening the interactive pressure gradient, is thus to delay the onset of incipient separation while wall heating has the opposite effect. Judging by comparison with calculations showing the effect of Reynolds number⁴, it would appear that proper wall temperature simulation may be of comparable importance to Reynolds

number as regards skin friction. These results are in qualitative agreement with experimental data on non-adiabatic interactions at supersonic speeds with oblique shocks. However, to the author's knowledge, there exist as yet no experimental data on transonic non-adiabatic interactions in the unseparated case.

4. APPLICATION TO GLOBAL TRANSONIC FLOW FIELD ANALYSIS

Nandanan et al⁶ have carried out a detailed study of interactions on actual supercritical airfoils including experimental comparisons. They developed a global computational method for transonic airfoil flow analysis which incorporates the present analytical solution for near-normal shock - boundary layer interaction into a state-of-the-art viscous-inviscid computation code. Theoretical results obtained with this method were compared to representative data from boundary layer and surface pressure measurements on three transonic airfoils in the DFVLR-AVA (Göttingen) Transonic Wind Tunnel; some examples of these comparisons are shown in Fig. 7. The agreement between theory and experiment in both the boundary layer displacement thickness and the surface pressure distributions was, for all test cases considered, quite good. The associated predictions of the local skin friction variation through the interaction zone also agree reasonably well with the values inferred from the experimental boundary layer profiles via the Ludwig-Tillman relation.

The results of this investigation indicated that treating the shock - boundary layer interaction by conventional boundary layer theory generally leads to a slight underprediction of the displacement thickness immediately downstream of the shock and, due to the amplifying effect of the sustained rear adverse pressure gradients, to an appreciable underestimation of the displacement thickness at the trailing edge. The latter is also clearly reflected in the pressure distributions and aerodynamic coefficients compared. Considering these results, one may conclude that it is generally necessary to include a physically correct treatment of shock wave - boundary layer interaction in the analysis of transonic airfoil flow.

These results show that it is now possible to incorporate as an interactive module within a global flow field analysis the correctly-modeled (and scaled) local shock - boundary layer interaction effects for the non-separating case. The non-asymptotic triple-deck interaction theory involved covers a wide range of practical Reynolds numbers and turbulent boundary layer profile shape factors; moreover, it gives an approximate indication of when incipient separation occurs. Such theory is generally desirable when accurate predictions are desired in the important trailing edge region of rear-loaded supercritical airfoils because the detailed changes across an upstream interaction can significantly alter the subsequent turbulent boundary layer behavior for appreciable distances downstream.

References

- 1 Ackeret, J., F. Feldman and N. Rott, "Investigation of Compression Shocks and Boundary Layers in Gases Moving at High Speed," NACA TN-1113, 1947.
- 2 Inger, G. R., "Upstream Influence and Skin Friction in Non-Separating Shock - Turbulent Boundary Layer Interactions," AIAA Paper 80-1411, Snowmass, Colorado, July 1980.
- 3 Lighthill, M. J., "On Boundary Layers and Upstream Influence, II. Supersonic Flow Without Separation," Proc. Royal Soc. A 217, 1953, pp. 478-507.
- 4 Inger, G. R., "Some Features of a Shock - Turbulent Boundary Layer Interaction Theory in Transonic Flow Field," Proc. AGARD Symposium on Computation of Viscous-Inviscid Interactions, pp. 18-1 to 18-66, Colorado Springs, Colorado, Sept. 1980.

-
- The diagram illustrates the flow structure in a thin shear-disturbance sublayer. On the left, a vertical wall is shown with a velocity profile $M_0(y)$ and a shear stress $\tau_0(y) = \tau_w$. The flow is divided into a 'LINEARIZED SUPERSONIC' region and a 'LINEARIZED SUBSONIC' region by a 'NORMAL SHOCK'. A 'sonic line' is indicated in the supersonic region. The flow is described as 'ROTATIONAL INVISCID FLOW WITH FROZEN TOTAL SHEAR STRESS'. A 'DISPLACED EDGE' is shown as a dashed line. The bottom boundary is labeled 'THIN SHEAR-DISTURBANCE SUBLAYER'.

Figure 1 consists of four sub-graphs (a, b, c, d) showing the variation of flow parameters with normalized distance x/δ_0 for different Mach numbers M_1 (1.10, 1.15, 1.20, 1.25, 1.30) and a fixed Reynolds number $Re_{\delta_0^+} = 3.5 \times 10^4$. The graphs show:

- (a) Pressure coefficient C_p/C_{p0} vs x/δ_0 . The curves show a sharp drop in pressure coefficient as x/δ_0 increases, with the drop being more pronounced for higher M_1 . A box in the graph specifies $H_{iL} = 1.40$ and $Re_{\delta_0^+} = 3.5 \times 10^4$.
- (b) Displacement thickness $\Delta \delta^+/\delta_0^+$ vs x/δ_0 . The curves show a sharp increase in displacement thickness as x/δ_0 increases, with the increase being more pronounced for higher M_1 .
- (c) Skin friction C_f/C_{f0} vs x/δ_0 . The curves show a sharp drop in skin friction as x/δ_0 increases, with the drop being more pronounced for higher M_1 .
- (d) Shape factor H_i vs x/δ_0 . The curves show a sharp increase in shape factor as x/δ_0 increases, with the increase being more pronounced for higher M_1 .

Fig. 2 Typical Interaction Zone Properties (Ref. 4)

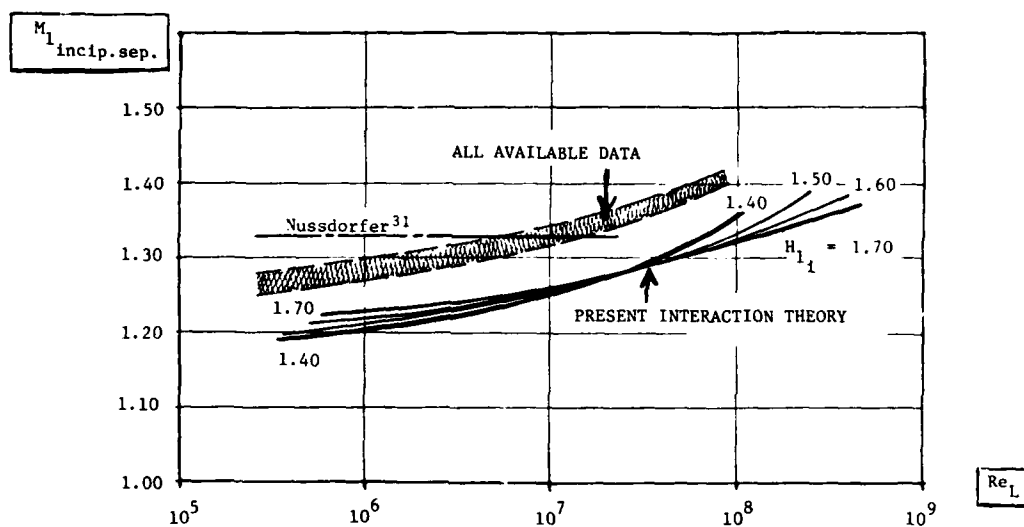


Fig. 3 Incipient Separation Prediction for Adiabatic Wall

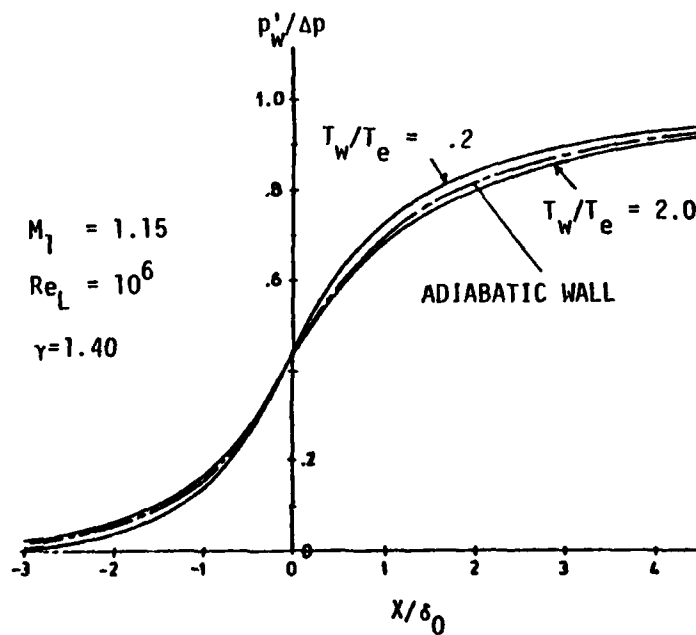


Fig. 4 Wall Temperature Effect on Interaction Pressure

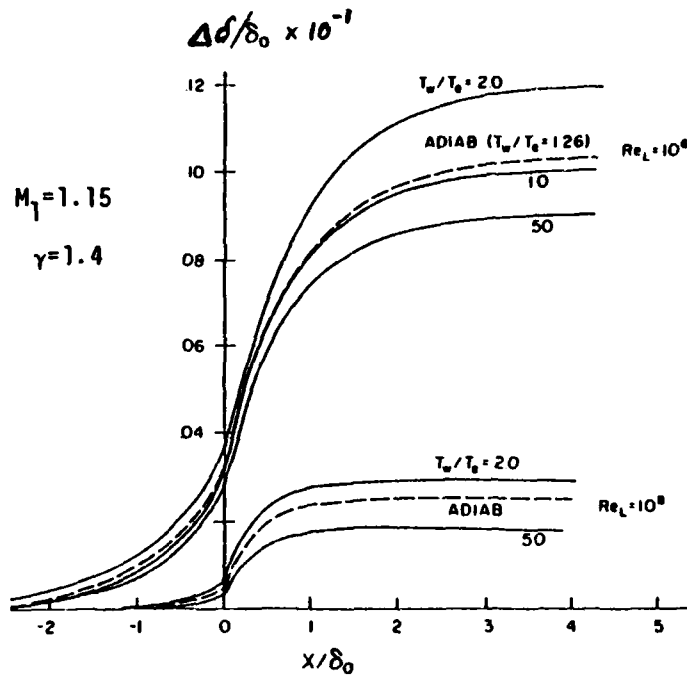


Fig. 5 Wall Temperature Effect on Interactive Displacement Thickness Growth

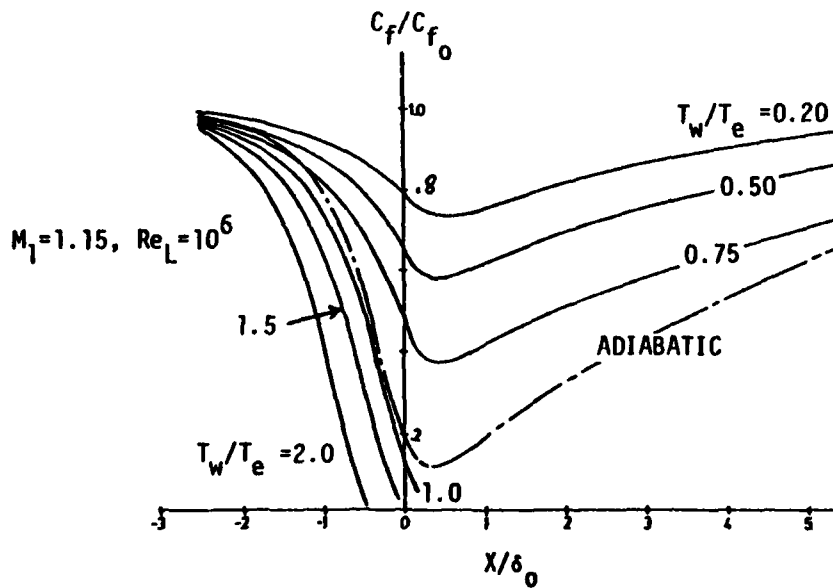
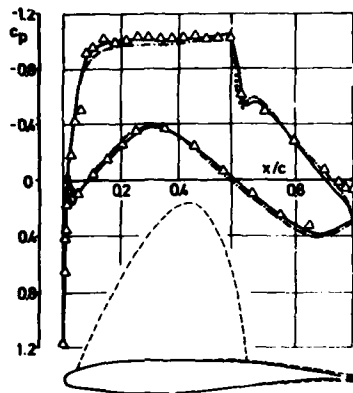


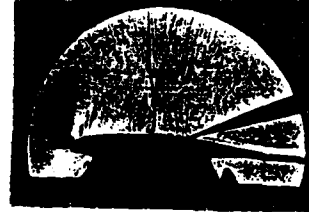
Fig. 6 Wall Temperature Effect on Interactive Skin Friction Distribution



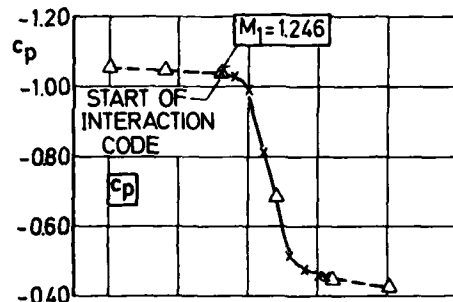
AIRFOIL CAST 7/DOA 1

$M_\infty = 0.765$
 $\alpha_g = 2.4^\circ$
 $Re = 2.4 \times 10^6$
 Transition at $7\%c$
 WIND TUNNEL: DFVLR-TWB

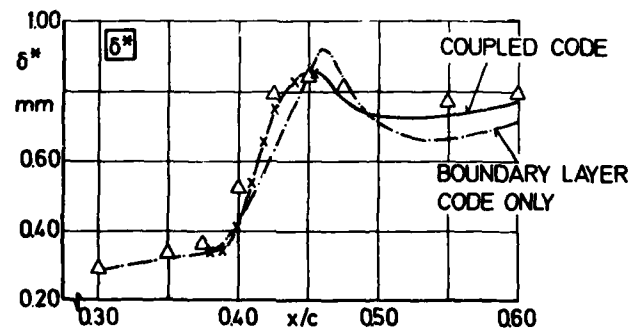
• Surface pressure due to interaction code



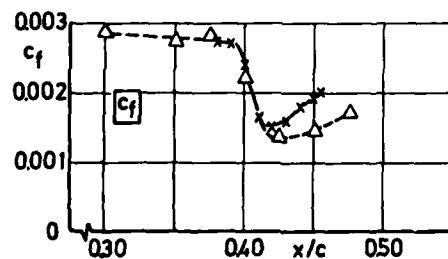
--△-- EXPERIMENT
 --x-- INTERACTION CODE



Pressure Distribution



Displacement Thickness



Skin Friction Distribution

Fig. 7 Comparison of Theory and Experiment for the Interaction Zone on a Supercritical Airfoil (Ref. 6)

HEATING-RATE MEASUREMENTS OVER 30° AND 40° (HALF-ANGLE) BLUNT
CONES IN AIR AND HELIUM IN THE LANGLEY EXPANSION TUBE FACILITY

N. M. Reddy

Department of Aeronautical Engineering

Indian Institute of Science, Bangalore 560 012, India

Convective heat-transfer measurements were made on the conical portion of spherically blunted cones (30° and 40° half angle) in the Langley expansion tube. The test gases used were helium and air: flow velocities were about 6.8 km/sec for helium and about 5.1 km/sec for air. The measured heating rates were compared with calculated results using a viscous shock-layer computer code. For air, various techniques to determine flow velocity yielded nearly identical results, but for helium the flow velocity varied by as much as 8% depending on which technique was used. The measured heating rates were in satisfactory agreement with calculation for helium test gas if the higher flow velocity was used, but for air and for helium assuming the lower flow velocity, the measurements were significantly greater than theory and the discrepancy increased with increasing distance along the cone.

INTRODUCTION

Determination of windward side heating rates during entry of the Space Shuttle Orbiter is very difficult. Analytical methods for calculating flow fields over complex configurations are as yet in a developmental stage, are costly, cumbersome, and limited in scope of variables. The extent of experimental data for such configurations is also limited, particularly for high velocity flow conditions. One approximation which has been made to permit calculation of the windward heating distribution on a vehicle at high angle of attack is to assume the flow along the windward centerline is similar to that of a cone whose half-angle is equal to the vehicle's local slope relative to the velocity vector. Several methods are available to the engineer to calculate the flow and heat-transfer rate for the equivalent blunted cone at zero angle of attack (ref.1). The critical heating rates on windward surfaces of the space shuttle are expected to occur at altitudes between 61 and 76 kilometers (200,000 and 250,000 ft). In an effort to simulate the shuttle flow field, total flow-field calculations for blunt spherical nose cones (half-angle 30° and 40°) have been presented in ref.1. This analysis consisted of defining the complete flow field around blunted cones for assumed equilibrium and react-

AD P000246

ing gas cases and was mainly concerned with delineating in detail the real-gas effects in the boundary layer and their effect on the surface skin friction and heat transfer. Based on the results presented, the authors of ref.1 have concluded that investigations of two types would be required to verify the analytical results, namely (a) basic investigations of boundary-layer profiles combined with skin friction and heat-transfer measurements on relatively simple cylindrical shapes, and (b) aerodynamic heating tests on blunt-cone configurations of the type analyzed in ref.1.

The present investigation measured the heating-rate distributions over a blunt cones of 30° and 40° half-angle in the Langley expansion tube facility with helium as well as air as test gases. The purpose of the present study is to present hypersonic cone heating data at both perfect-gas and real-gas conditions. The measured heating rates have been compared with computed values (ref.2). An attempt has been made to measure heating rates within an accuracy of 4 to 5 percent by using two different and independent methods to deduce heating rates. Based on the results of the present investigation, some conclusions are drawn regarding the accuracy of heating-rate measurements and their comparison with the computed values.

FACILITY AND TEST CONDITIONS

Several papers (refs. 3 to 5) have been published concerning the description and performance estimation of the expansion tube facility at the Langley Research Center. A detailed description of the basic components and auxiliary equipment of the Langley expansion tube is presented in refs.4 and 5. The operating sequence for the expansion tube is shown schematically in Figure 1. The operating sequence starts with rupture of the high-pressure primary diaphragm. This creates an incident shock wave which travels down the intermediate section until it encounters the secondary diaphragm. The low-pressure secondary diaphragm will be ruptured due to impact of incident shock wave. This creates a secondary incident shock wave which propagates into the low-pressure acceleration gas while an upstream expansion wave moves into the test gas. In passing through this upstream expansion wave, which is being washed downstream since the shock-heated gas is supersonic, the test gas undergoes an isentropic unsteady expansion resulting in an increase in the flow velocity and Mach number.

Extensive flow calibration in the expansion tube facility for the case of helium test gas has been completed and reported in ref.4. Pitot pressure profiles at various distances downstream of acceleration tube exit in the case of helium test gas ($p_1=3447$ N/m²; $p_{10} = 16.0$ N/m², $t = 200 \mu\text{s}$), are shown in Figure 2 (taken from ref.4). From this study it was found that for the initial conditions used in the present tests, the pitot survey shows uniform flow region of about 7 to 8 cm in diameter between 1 and 20 cm downstream of the acceleration tube exit. Calibrations for air test gas have shown a similar test core size.

The free-stream flow quantities were computed from the real-gas computer program of ref.5. At least three flow quantities (either predicted or measured) have to be known to obtain other flow quantities. Calculated flow quantities based on test section flow measurements are considered to be superior to those based on initial state variable because of deviations from theoretical

prediction. The usual procedure would be to use the measured wall static pressure and shock velocity near the acceleration tube exit in each run and the measured pitot pressure in the test section in a repeated run as the three required flow quantities to compute the other free-stream flow quantities from the computer program of ref.6. In the expansion tube facility the repeatability of runs as ascertained from the measured shock velocity is good in almost all cases with air and helium as test gases. But the inherent nonideal effects (viscous, real-gas and shock-reflection phenomena at the secondary diaphragm) might affect the flow quantities in the test section significantly in each run. In this sense, the repeatability as ascertained from the measured shock velocity may not be sufficient. Therefore, in the present investigation it was decided to measure simultaneously the pitot pressure in addition to wall static pressure and shock velocity in each run. In the present investigation the pitot pressure was measured by installing a small pressure transducer (2.5 mm dia.) in the blunt nose of each of the heat-transfer cone models. Since the transducer size was very small, the effects on flow over the model due to curvature change near the nose region were assumed to be negligible. The details of the measurement of free-stream static pressure, pitot pressure and free-stream velocity are given in ref.7.

Because of the importance of accurate velocity determination at the test section, an examination was made of the method for determining velocity. The shock velocity between the last two stations (station numbers 27 and 31 which are 1.554 m apart) was deduced by using corresponding counter readings as well as the time interval measured from the oscilloscope film of heat-transfer gage outputs. The wall pressure gage film data between these two stations were also available and velocity was deduced from these data also. It was apparent that the shock velocities obtained by different methods for any given run do not agree with each other. More details can be found in ref.7.

In the case of air test gas, the shock velocities deduced from the counter reading between stations 27 and 31 are believed to be suspect since the output from the heat-transfer gage at station 27 went negative immediately after the shock passage before it recovered back to its normal behaviour and this might have affected the counter reading. The discrepancy noticed between velocities obtained from heat transfer and wall pressure film data is somewhat surprising since the method used is the same. However, it was observed that the heat-transfer gage's response at stations 27 and 31 was much slower than the pressure gage's response at the same stations, which is perhaps due to thick coating on the heat-transfer gages. For this reason, the velocity obtained from the pressure film data between stations 27 and 31 may be of superior value. It was also found that in the case of air, the differences between the velocities obtained from the straight-line fit to the data over the entire tube length and the pressure film data were very small. In the case of helium the differences between velocities obtained from different methods are much more than those obtained in air. The output from the heat-transfer gage at station 27 in the case of helium did not go negative, unlike the case of air, probably due to negligible ionization. But the response was too slow and the signal level was very small which might have affected the counters significantly. Because of these discrepancies, the theoretical heating predictions were computed for both the velocity deduced from the curve fit (U_{average}) and that obtained from the pressure data (U_{27-31}) for helium runs. For air

runs, the difference was not significant so only U27-31 was used to compute heating rates. Flow-state calculations were based on U27-31.

FABRICATION AND CALIBRATION OF THIN-FILM GAGES

Thin-film heat-transfer gages were fabricated by sputtering palladium on quartz substrates. The quartz substrates were fabricated with proper radius of curvature to fit the cone surface. The palladium film was sputtered over the entire top surface of the substrate and then the thin film in a serpentine pattern (Fig. 3) was etched by using a photetching process. The ends of the thin film are joined by a thick film in the sides and wires were soldered to the thick film. During development of this technique it was found that a thin coat of chromium (sputtering time 30 secs) on the substrate before palladium application improved the thin-film adherence to substrate enormously. The sputtering time for palladium film was 5 to 6 minutes. A coat of silicon dioxide (sputtering time 7 to 8 minutes) was sputtered on top of the palladium film to avoid possible shorting across the thin film due to ionization in the test gas. About 14 to 16 gages at nearly 3 mm apart were fabricated on each substrate (Fig. 3). The quality control was such that all the films were identical in their geometrical characteristics: the resistance of each film was within a few percent of each other. The resistance value varied between 75 and 100 Ω for different batches.

Two types of calibrations are required for any thin film to be used as a quantitative heat-transfer measuring device, namely, the temperature coefficient of resistance α and the substrate property $\beta = (K\rho C_p)^2$. The values of α and β were measured for each film by using methods which are described in detail in ref. 7. The measured value of β in the present investigation was 1512.5 W - Sec^{1/2}/m² - °K for all the gages.

BLUNT NOSE-CONE MODELS

Two 40° and 30° semivertex angle cone models with a spherical blunt nose (6.35 mm radius) were fabricated out of stainless steel. The geometrical details of these models are shown in Figure 3. Quartz substrates of 6.35 mm x 6.35 mm cross section were fitted in a slot cut along a single ray in the conical portion of the models as shown in Figure 3. The top surfaces of the quartz substrates were optically ground and polished to match the varying curvature along the cone surface. About 14 to 16 thin-film gages at intervals of 3.2 mm were fabricated on the quartz substrate as shown in Figure 3. The models were tested in the expansion tube facility at zero and positive angles of attack with air as well as helium test gas. The acceleration gas was the same as the test gas in all the runs. The initial conditions used in the intermediate and acceleration sections, as well as the different angles of attack used in all the runs, are given in Table I.

DATA RECORDING AND PROCESSING

The heat transfer rates were measured by using two independent methods namely: (a) by numerical integration of surface temperature data, (b) direct measurement by using electric analogs. Ref. 7 gives all the necessary details. Two types of tests were made to compare the two different methods that have been used in the present analysis for heat-transfer measurements. First, the surface-

temperature history obtained due to incident shock heating in air in the acceleration section was recorded by installing a thin-film gage inside the shock-tube wall. The surface-temperature history was recorded on a scope and the same signal was simultaneously fed into the analog network and the output from the analog was measured in the wave-form recorder. The surface-temperature history was measured from the oscilloscope film using a digitizer and the heating rates obtained by this procedure and those directly measured from the analog are compared in Figure 4. The significant and important observation is that the numerical integration technique does not seem to simulate the fast response of the heating rate immediately behind the shock wave whereas the analog circuit shows a much better response in this region. About 35 to 40 μ secs after the shock passage, the two methods agree within 8 percent.

The heating rates were also deduced using the preceding procedure in the case of stagnation-point heating-rate measurement to a spherical nose of 25.4 mm radius mounted in the expansion tube test section. The test gas was helium and the other conditions correspond to the run number EC 1500 given in Table I. The surface-temperature history was recorded in the recorder at 2.5 μ sec intervals. The numerical integration was performed by using data at two time intervals, namely 2.5 and 5.0 μ secs. The heating rates variation with time is shown in Figure 5. The differences in heating rate by using the two time intervals is negligible. However, the computer time required to perform the integration over a 200 μ sec time period was reduced by 50 percent for 5 sec time intervals. The heating rate obtained from the analog network by feeding the same surface temperature was also recorded in the recorder at 2.5 μ sec intervals and is compared in Figure 5. with the values obtained by numerical integration. In this case also, the numerical integration does not seem to simulate the fast response of the heating rate immediately behind the shock wave. The two methods agree well (differences within 3 to 4 percent, except for a couple of peak values) after an elapsed time period of about 90 to 95 μ secs. This fact was taken into account in the data-reduction procedure adopted for the heating rates over cone models.

The measured heating rates over the cone models should remain constant with time. This ideal situation requires that the free-stream flow quantities are constant with time during the testing period. However, due to several nonideal effects that exist in the operation of the expansion tube facility, the free-stream flow quantities do exhibit some variation with time, especially in the case of helium test gas. Therefore, a time-averaging procedure was adopted to obtain the measured heating rates over the cone models. More details can be found in ref.7. A typical heat transfer rate variation with time is shown in Fig.6.

THEORETICAL HEATING-RATE DISTRIBUTIONS OVER BLUNTED CONES

Theoretical heating-rate distributions have been obtained by using the method developed by Kumar and Graves (ref.2) for the viscous flow over blunted cones at zero and small angles of attack. This method used time-dependent viscous-shock-layer-type equations to describe the flow field between the body and the shock wave. A time-dependent finite difference technique is used to solve the equations in the planes of symmetry of the flow field. Complete details of this method are given in ref.2.

In the present investigation, heating rates over the 30° and 40° sphere cones are computed under perfect-gas approximation for helium test gas and under chemical-equilibrium approximation for air-test gas. The equilibrium mass fractions of various species of air are computed by using the free-energy-minimization technique. The radiative heating terms were also included in the governing equations. In all the cases computed, it was found that the radiative heating rate was almost negligible.

RESULTS AND DISCUSSION

The measured heating rates for the 40° cone at zero angle of attack with helium as test gas are compared with theory in Figure 7. As discussed earlier, the velocity obtained from the pressure film data between stations 27 and 31 was used for the theoretical computations; the other free-stream quantities were the same for both the cases. It is apparent from Figure 7 that the theoretical computation using velocity obtained from pressure film data agrees with the measured values within 6 percent. In Figure 8, the heating rates measured over the 30° cone at zero angle of attack with helium as test gas seem to agree with theoretical values corresponding to a velocity (U_∞) 10 percent more than the one deduced from pressure film data. Considering the uncertainty in the measured flow velocity, the agreement of the measured heating rates over both the cones, with theory is considered satisfactory. More data at angles of attack can be found in ref.7.

In Figures 9 and 10, the measured heating rates over 30° and 40° cones at zero angle of attack with air as test gas are compared with theory. The measured stagnation-point heating rate using a spherical blunt-nose model (0.0254 m nose radius) in a repeated run is also compared with theory in Figures 9 and 10. The measured stagnation-point heating rates agree with theory within 2 percent. However, the measured heating rates over the cone surface for both the models are consistently higher than the computed values, the differences being 5 to 15 percent in the beginning and increase to as much as 50 percent toward the end of the cone surface. The measurements, which are believed to be accurate to about 5 percent thus disagree with the computation by too much to attribute to measurement accuracy. At present no reasonable explanation exists for this discrepancy. It is also noted in ref. 7 that the discrepancy between theory and measurements increase as the effective cone angle increases.

ACKNOWLEDGEMENT

This investigation was carried out at NASA-Langley Research Center, Hampton, Virginia when the author was on sabbatical leave from his institution. The author is grateful to Mr. Jim Jones for his constant encouragement and fruitful discussions the author had with him. The heating rates for the present experimental conditions were kindly computed by Dr. Ajay Kumar, Research Assistant Professor, Department of Mechanical Engineering and Mechanics, Old Dominion University, Norfolk, Virginia.

The financial assistance received from NRC-Washington D.C. is gratefully acknowledged.

REFERENCES

1. Fivel, H.J.; Masak, R.V.; and Mackapetus, L.J., Analytical comparison of hypersonic flight and wind tunnel viscous/inviscid flow fields, NASA Contractor Report, prepared by McDonnell Douglas Astronautics-East, St.Louis, Missouri.
2. Ajay Kumar and Graves, R.A.Jr., Numerical solution of the viscous hypersonic flow past blunted cones at angles of attack. AIAA paper No.77-172, Jan.1977.
3. Trimpi, Robert L., A preliminary theoretical study of the expansion tube, A new device for producing high-enthalpy short-duration hypersonic gas flows. NACA TRR-133, 1962.
4. Shinn, Judy L., and Miller, Charles, G.III: Experimental perfect gas study of expansion tube flow characteristics, NASA Technical Paper 1317, 1978.
5. Moore, John A. Description and initial operating performance of the Langley 6-inch expansion tube using heated helium driver gas NASA TMX-3240, 1975.
6. Miller, C.G.III: Computer program of data reduction procedures for facilities using CO₂-O₂-AR equilibrium real-gas mixtures, NASA TMX-2512, March 1972.
7. Reddy N.M.: Heating rate measurements over 30° and 40° (Half-angle) Blunt cones in air and helium in the Langley expansion tube facility, NASA TM 80207, 1980.

TABLE I INITIAL TEST CONDITIONS

Run number	Test gas Accel.gas	Semivertex cone angle deg	Angle of attack deg	P ₁ (N/m ²)	P ₁₀ (N/m ²)	Remarks
EC 1473	He/He	30	+8	689.5	16.0	Gages on lee-ward side
EC 1475		40	0			—
EC 1476		30	0			—
EC 1491		30	0			—
EC 1499		-	-			} stag. point heat transfer (R _n =25.4 mm)
EC 1500		-	-			
EC 1477	Air/air	40	+12	3447	6.67	Gages on lee-ward side
EC 1478		30	+12			—
EC 1479		40	0			—
EC 1494		30	0			—
EC 1495		40	+4			Gages on wind-ward side
EC 1496		30	+4			} stag. point heat transfer (R _n =25.4 mm)
EC 1497		-	-			
EC 1498		-	-			

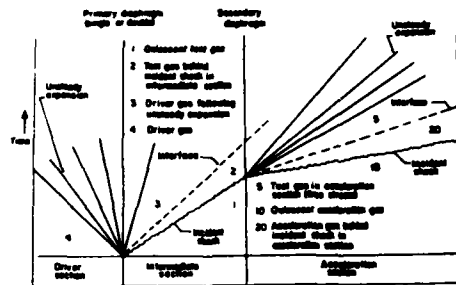


FIG. 1 SCHEMATIC DIAGRAM OF EXPANSION TUBE FLOW REGIMES

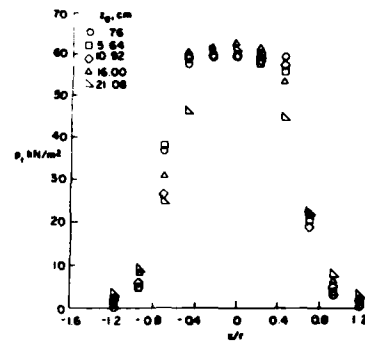
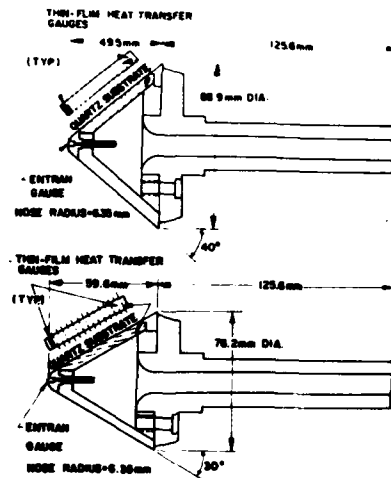
FIG. 2 PYROT PRESSURE PROFILE AT VARIOUS DISTANCE DOWNSTREAM OF TUBE EXIT $p_1 = 3.45 \text{ MN/m}^2$, $p_2 = 16.00 \text{ MN/m}^2$, $t = 200 \mu\text{s}$ 

FIG. 3 DETAILS OF BLUNT CONE MODEL

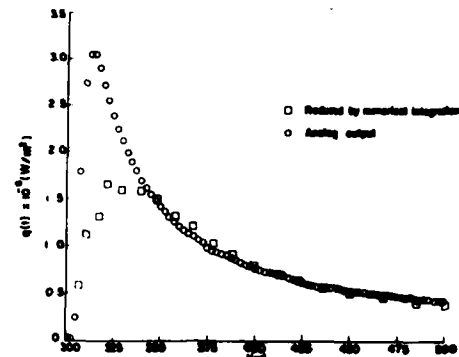


FIG. 4 COMPARISON OF HEATING RATES OBTAINED BY NUMERICAL INTEGRATION OF SHOCK-TUBE WALL SURFACE TEMPERATURE HISTORY WITH RESULTS OF ANALOG OUTPUT

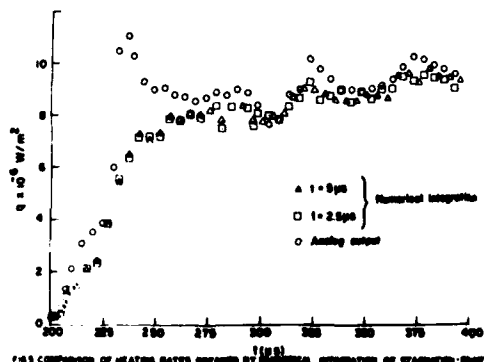


FIG. 5 COMPARISON OF HEATING RATES OBTAINED BY NUMERICAL INTEGRATION OF SHOCK-TUBE WALL SURFACE TEMPERATURE HISTORY WITH RESULTS OF ANALOG OUTPUT

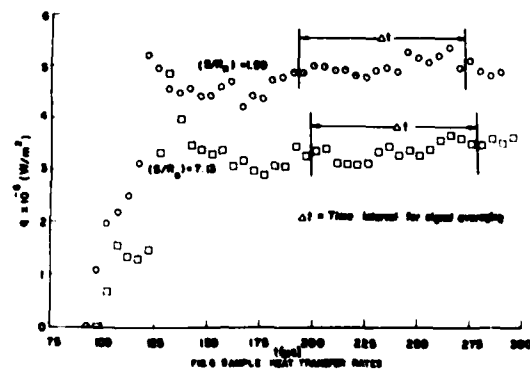


FIG. 6 SAMPLE HEAT TRANSFER RATES

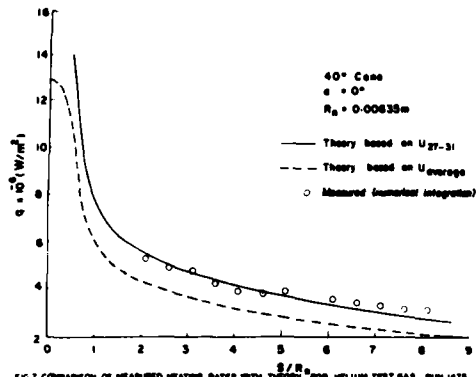


FIG. 7 COMPARISON OF MEASURED HEATING RATES WITH THEORY FOR HELIUM TEST GAS, RUN 1475

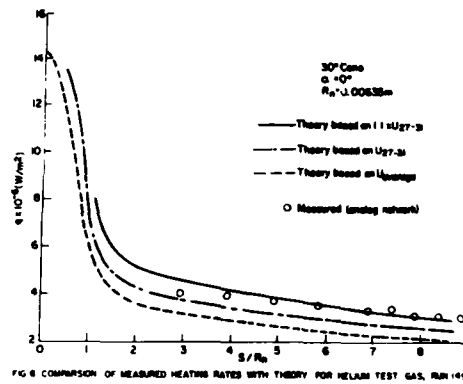


FIG. 8 COMPARISON OF MEASURED HEATING RATES WITH THEORY FOR HELIUM TEST GAS, RUN 1476

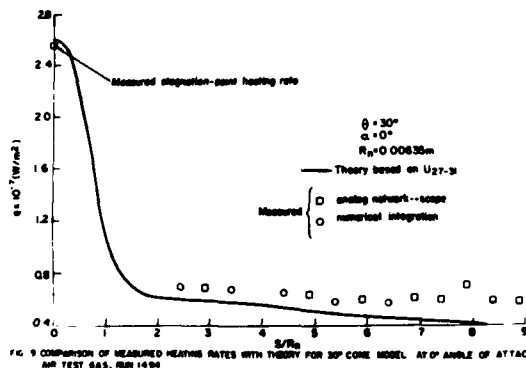


FIG. 9 COMPARISON OF MEASURED HEATING RATES WITH THEORY FOR 30° CONE MODEL AT 0° ANGLE OF ATTACK AIR TEST GAS, RUN 1490

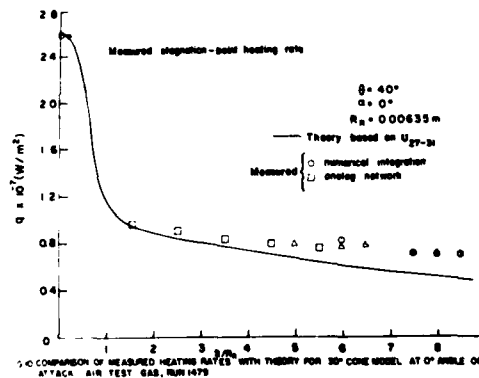


FIG. 10 COMPARISON OF MEASURED HEATING RATES WITH THEORY FOR 30° CONE MODEL AT 0° ANGLE OF ATTACK AIR TEST GAS, RUN 1479

AD P000242

SHOCK INDUCED UNSTEADY FLAT PLATE
BOUNDARY LAYERS AND TRANSITIONS

M. Matsushita, T. Akamatsu and K. Fujimura *

Department of Mechanical Engineering
Kyoto University, Kyoto 606. Japan

* Japan Atomic Energy Research Institute

For the shock-induced unsteady boundary layers over a flat plate installed in a shock tube, the effect of velocity profile, not of surface cooling and compressibility, on the transition into turbulence is estimated by using Wazzan's relation. The locus of the points of instability are drawn on the $x-t$ diagram, where the lowering of instability points is found in the unsteady interaction region. The limiting case that the shock waves become weak correspond to that which the incompressible fluid starts to move impulsively. This flow is achieved in an intermittent liquid tunnel. And the transition of unsteady flat plate boundary layer is observed to take place earlier than the time predicted from the linearized theory.

1. INTRODUCTION

Concerning the shock-induced unsteady boundary layers over a flat plate installed in a shock tube, numerical computations for laminar flows have been performed by Lam and Crocco¹, Akamatsu², Felderman³, Murdock⁴ and Cook⁵. The limiting case that the shock waves become weak corresponds to that which incompressible fluid starts to move impulsively. Studies on this unsteady laminar boundary layer were initiated by Stewartson's analysis⁶. Various theoretical approaches have been tried; analytical^{7,8}, integral^{4,9-11} and numerical ones^{1,3,5,12}.

Experimentally the shock-induced unsteady boundary layer was verified by Akamatsu², Felderman³, Davies and Bernstein¹³, Cook¹⁴ and Dekker¹⁵ et al. Davies and Bernstein traced the transition points on $x-t$ diagram (Fig.12 of Ref.13), where the unsteady transition points are parallel to the path of shock front. The behaviors of transition are not clarified in the merging region of steady and unsteady transition points.

Concerning the transition of quasi-steady boundary layers developed on the side-wall of shock tubes, Morkovin¹⁶ reviewed experimental observations¹⁷⁻¹⁹ including transition structure such as turbulent spots²⁰. Comparison with linearized stability theory of Ostrach and Thornton²¹ indicates that transition takes place precritically, presumably due to finite disturbances.

The present paper aims at predicting theoretically the points of instability and at verifying experimentally the transition points in the liquid flow impulsively started. This liquid flow, which is achieved in a kind of liquid Ludwig tube, corresponds to that of the extremely weak shock and is to reveal the effect of velocity profile only.

2. SOLUTIONS OF UNSTEADY LAMINAR BOUNDARY LAYERS BY INTEGRAL METHOD

When the shock wave passes over a flat plate, as shown in Fig.1, the boundary layer of shock tube-type develops immediately behind the shock wave and the steady boundary layer of Blasius-type develops from the leading edge of the plate. The limiting case that the shock wave becomes weak corresponds to the state that the incompressible fluid starts to move at a constant infinitesimal velocity U in the direction of positive x . For simplicity, let us call the former the case (S) and the latter (R).

Initially, as shown in Fig.2(a), let us mark fluid particles with fine lines, a chain and dotted lines according to the region $x < 0$, $x = 0$ and $x > 0$ respectively. At a time t after impulsive motion, the positions of marked fluid particles are shown in Fig.2(b). Define $\xi = x/Ut$, $\xi = 0$ and 1 indicate the leading edge of the plate and the position of fluid particles initially situated on y -axis respectively. Stewartson⁶ showed that Rayleigh's solution is applicable to the region $\xi \geq 1$. Similarly, Mirels' solution is applied to the region $1 \leq \xi \leq V/U$ in Fig.1, where V and $U (=u_2)$ are velocities of the shock and the flow behind the shock respectively.

As well-known, the boundary layers behind the moving shock waves and expansion waves are regarded as the quasi-steady ones by observing from the coordinate fixed with the wave fronts, where the velocity U_w on the tube wall and U_e in the freestream are expressed as $U_w = V$, $U_e = V - U$. $U_w/U_e = 0$ corresponds to Blasius' boundary layer and $U_w/U_e \leq 1$ the expansion wave-type, Rayleigh's and the shock-type respectively.

Let us take the x - and y -axis as shown in Figs.1 and 2, and take the instant as $t=0$ when a shock wave just arrives at y -axis or that a fluid begins to move.

For two-dimensional compressible fluid past a flat plate the unsteady laminar boundary layer equations are

$$\frac{\partial \rho}{\partial t} + \frac{\partial \rho u}{\partial x} + \frac{\partial \rho v}{\partial y} = 0 \quad (1)$$

$$\frac{\partial u}{\partial t} + u \frac{\partial u}{\partial x} + v \frac{\partial u}{\partial y} = \frac{1}{\rho} \frac{\partial}{\partial y} \left(\mu \frac{\partial u}{\partial y} \right) \quad (2)$$

where ρ , u , v and μ are density, x - and y -components of velocity, and viscosity coefficient respectively. Assuming that Chapman-Rubensin's factor $C = \rho \mu / \rho_w \mu_w$ is constant, that is, μ is proportional to temperature, the momentum equation becomes independent of the energy equation.

The boundary conditions are

$$\begin{aligned} y=0; \quad u=v=0, \\ y=\infty; \quad u=U (=u_2), \end{aligned} \quad (3)$$

Introduce the variable Y in place of y .

$$Y = \int_0^y \frac{\rho}{\rho_w} dy \quad (4)$$

The compressible boundary layer equations (1) and (2) reduce to the incompressible one.

$$\frac{\partial u}{\partial t} + u \frac{\partial u}{\partial x} + v \frac{\partial u}{\partial Y} = \nu \frac{\partial^2 u}{\partial Y^2} \quad (5)$$

where ν is a kinematic viscosity and $\nu = C \nu_w$. The present paper is concerned with the effect

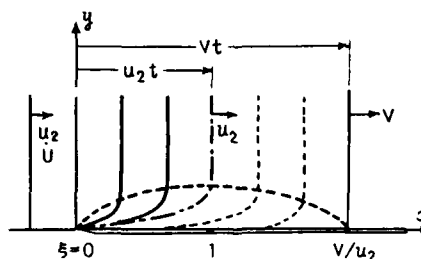


Fig.1

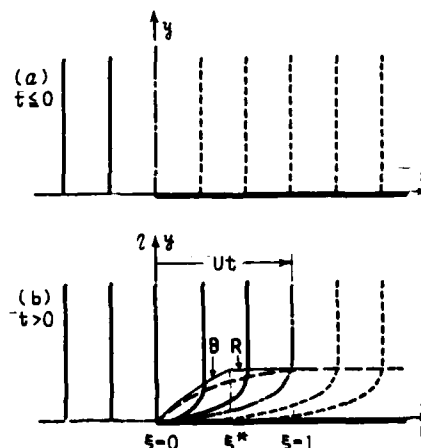


Fig.2

only of the velocity profile, not to the combined effects of surface cooling and compressibility. So that, the energy equation is disregarded.

Let us solve the partial differential equation (5) by an integral method which modifies Tani's method¹⁰ for unsteady boundary layers.

$$\text{Momentum Integral:} \quad \frac{\partial}{\partial t}(U\delta_1) + \frac{\partial}{\partial x}(U\delta_2) = \frac{\tau_w}{\rho} \quad (6)$$

$$\text{Energy Integral:} \quad \frac{\partial}{\partial t}(U\delta_2) + U^2 \frac{\partial \delta_2}{\partial t} + \frac{\partial}{\partial x}(U^3 \delta_3) = \frac{2D}{\rho} \quad (7)$$

where $U(t,x)$ is freestream velocity and δ_1 , δ_2 and δ_3 are displacement, momentum and energy thickness respectively. The wall shear stress τ_w and energy dissipation D are defined as follows:

$$\tau_w = \mu \left(\frac{\partial u}{\partial y} \right)_{y=0}, \quad D = \mu \int_0^\infty \left(\frac{\partial u}{\partial y} \right)^2 dy \quad (8)$$

Assuming that the velocity profiles are expressible by a family of exact solutions of Falkner-Skan's flow, the following three nondimensional quantities composed of the variables appearing in Eq.s (6) and (7) are evaluated and shown in Fig.3 as the functions of shape factor $H = \delta_1/\delta_2$.

$$G = \frac{\delta_3}{\delta_2}, \quad Q = \frac{2\delta_2}{\mu U^2}, \quad A = \frac{2\delta_2 \tau_w}{\mu U} \quad (9)$$

The present method is generally applicable even to the unsteady separated flows, when the velocity profile is expressed with a family of quartic polynomials. The equations (6) and (7) are rewritten in terms of unknown variables δ_2 and H :

$$\frac{\partial}{\partial t}(H\delta_2) + \frac{\partial}{\partial x}(U\delta_2) = \frac{A}{2\delta_2} \quad (10)$$

$$\frac{\partial}{\partial t}[(H+1)\delta_2] + \frac{\partial}{\partial x}(UG\delta_2) = \frac{Q}{\delta_2} - \frac{2\delta_2}{U} \frac{\partial U}{\partial t} - 2G\delta_2 \frac{\partial U}{\partial x} \quad (11)$$

(i) The quasi-steady boundary layer behind the incident shock waves

By introducing the shock-fixed coordinates (X,T) , $X=Vt-x$, $T=t$, the Eq.s (10) and (11) are rewritten.

$$\frac{d}{dX}(\delta_2^2) = \frac{A}{VH-U} = \frac{2Q}{V(H+1)-GU}$$

A, G and Q being expressible with H , the above middle and right hand equation determines H for a given shock Mach number. Consequently the momentum thickness is expressed:

$$(\delta_2)_S = \sqrt{A_S X / (VH_S - U)}$$

(ii) The Rayleigh-type boundary layers

By putting, $\partial U / \partial t = 0$ ($t > 0$), $\partial / \partial x = 0$, the Eq.s (10) and (11) are rewritten,

$$\frac{d}{dt}(\delta_2)^2 = \frac{A}{H} = \frac{2Q}{H+1}$$

Similarly, H_R and $(\delta_2)_R$ are determined.

$$(\delta_2)_R = \sqrt{A_R t / H_R}$$

(iii) The unsteady boundary layers ($0 < \xi < 1$)

The partial differential equations (10) and (11) are solved by a finite difference scheme: the forward-difference for the time derivative and the backward difference for the spatial derivative. The boundary conditions are

$$x = 0; \quad \delta_2 = 0, \quad H = H_B \quad (\text{specified})$$

$$x = Vt \quad (X=0); \quad \delta_2 = 0, \quad H = H_S \quad (\text{specified})$$

The computation proceeds by setting the following initial conditions at the first mesh points of $t = \Delta t$.

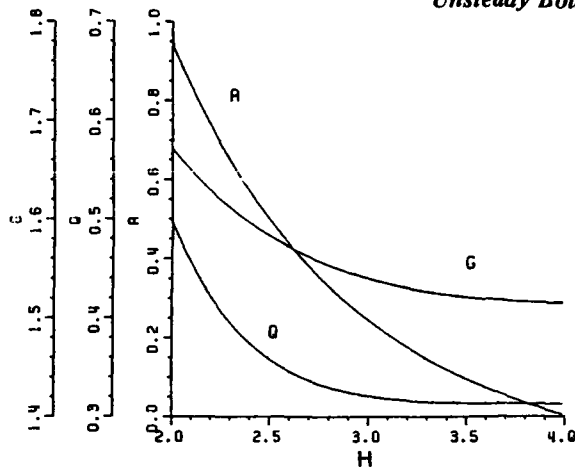


Fig.3 Relations of A,G,Q versus H in Falkner-Skan's flow

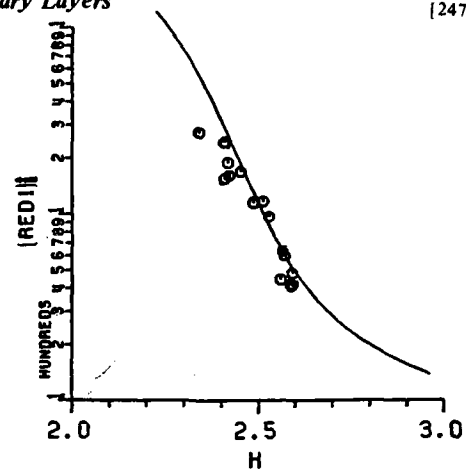


Fig.4 Wazzan's relation of instability Reynolds number versus H

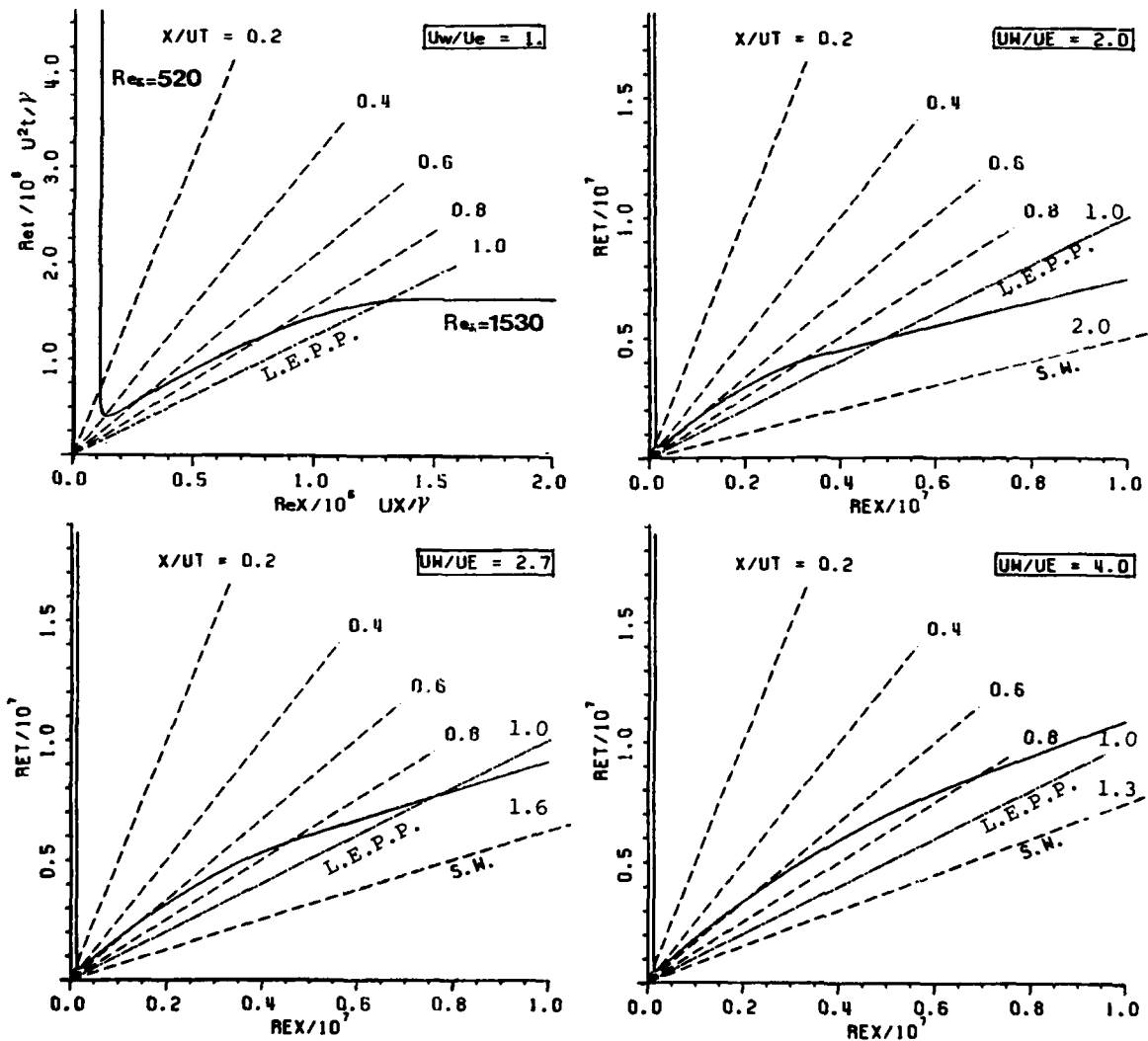


Fig.5 Locus of points of instability on x-t diagram (continued)

For the case (S), $x = 0$; $\delta_2 = 0$, $H = H_B$
 $x = V\Delta t - x$ ($X=\Delta x$); $\delta_2 = \sqrt{\frac{A_S x}{VH_S - U}}$, $H = H_S$
 $x = V\Delta t$ ($X=0$); $\delta_2 = 0$, $H = H_S$

For the case (R), $x = 0$; $\delta_2 = 0$, $H = H_B$
 $x > 0$; $\delta_2 = \sqrt{A\Delta t/H_R}$, $H = H_R$

It is well known that the solutions should be expressible in a similarity form, that is, $\xi = x/Ut$, $\eta = Y\sqrt{U/C_W}x$. Therefore the accuracy of computation is checked by examining whether δ_2/\sqrt{x} and H are universally expressed with $\xi = x/Ut$ only, or by comparing with the exact solutions in the specified regions ($\xi \approx 0$ or $\xi > 1$). Employing of finitedifference scheme is specially favorable for the case of time-dependent freestream.

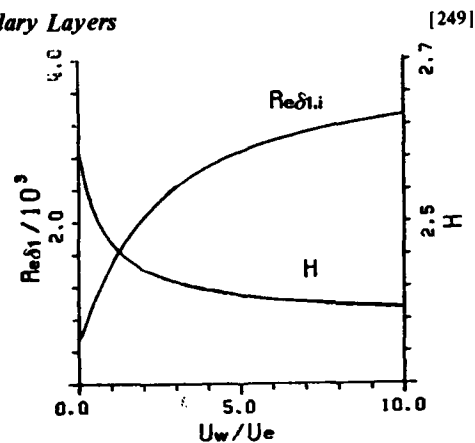
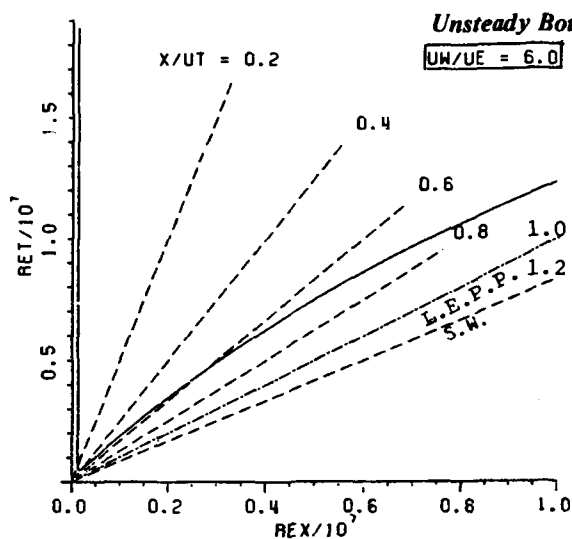
3. PREDICTIONS OF POINTS OF INSTABILITY

As a next step, let us predict the time and location of the point of instability. Assume that the Wazzan's relation²² of instability Reynolds number $(Re\delta_1)_i$ versus the shape factor H , shown with the solid lines in Fig.4, are applicable to the present unsteady flow. This relation is derived from the linearized stability theory of parallel flow for Falkner-Skan boundary layer. The displacement thickness δ_1 and the shape factor H can be easily evaluated by the above mentioned integral method. Subsequently the points at which the local Reynolds number $Re\delta_1$ just attains the instability Reynolds number $(Re\delta_1)_i$ are surveyed on $x-t$ diagram. The loci of instability points are indicated with solid lines in Fig.5. The coordinates are non-dimensional time $Ret (=U^2t/\nu)$ and distance $Rex (=Ux/\nu)$. The lowering of instability points is found in the unsteady interaction regions ($0 < \xi < 1$). This predicts the possible earlier transition to turbulence in actual flows. The instability Reynolds number $(Re\delta_1)_i$ and the shape factor H in the unsteady interaction regions are indicated as functions of $\xi = x/Ut$ in Fig.6. The same tendency, as shown in Fig.5 and 6, is recognized in the unsteady Couette flow²³ (independent variables are t and y only and the distance of two parallel denoted as s), if x/Ut in Fig.6 and Rex in Fig.5 are replaced by δ_1/s and $Res (=Us/\nu)$ respectively.

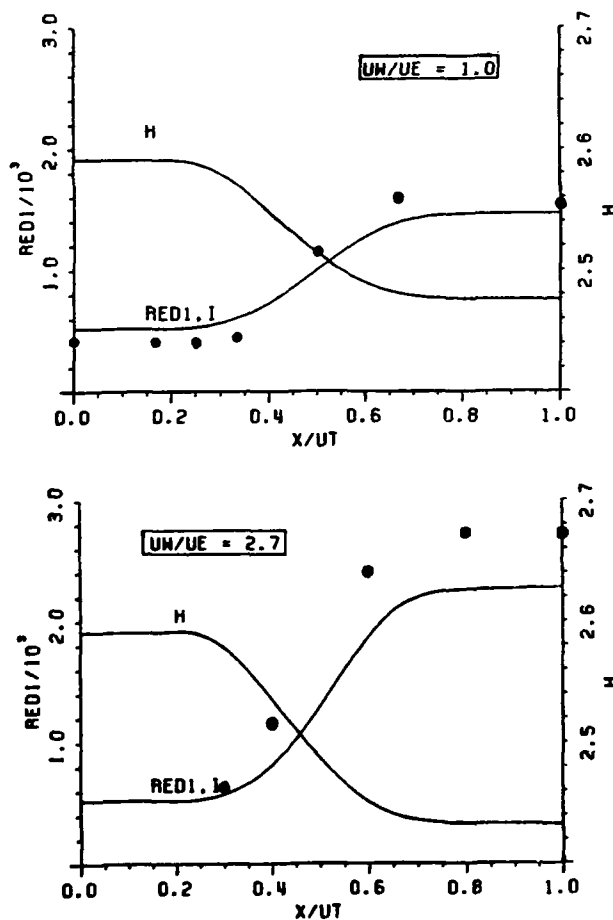
Fig.7 shows the relations $(Re\delta_1)_i$ versus H for the quasi-steady boundary layers related to shock tube wall. The instability Reynolds number of Blasius' boundary layer is the lowest among all the related boundary layers. The instability Reynolds number increases monotonically with shock strength. Ostrach et al²¹ calculated $(Re\delta_1)_i$ following the two-dimensional linear stability theory including the effect of velocity profile as well as the surface cooling and the compressibility. They found that the flow for $U_w/U_e = 2.94$ ($\gamma=1.4$) is infinitely stable. However such a trend is not observed in the present prediction considering only the effect of velocity profiles.

By applying the conventional linearized stability theory, the instability Reynolds numbers are calculated for the velocity profiles of unsteady boundary layers in the interaction region, which are evaluated by Lam¹ (Case S) and Hall¹² (Case R). These results are shown with circles in Fig.6 and 7, and their coincidence with Wazzan's relations shows that these relations are widely applicable to the present unsteady boundary layers.

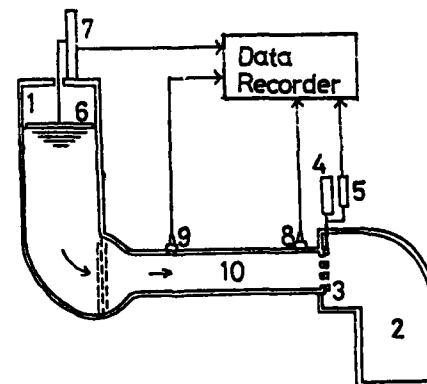
Ostrach et al²¹ showed that the observed transition data of boundary layers on the shock tube side wall do not follow the trends theoretically predicted, and that the transition Reynolds number are orders of magnitude below the computed instability Reynolds number. However, in Fig.2 of their paper, this discrepancy is found to be small for the weak shock. This is attributed to experimentally the comparatively weak disturbances and theoretically the least stabilized effects of cooling and compressibility. Then we try to achieve, in an intermittent liquid tunnel, the Rayleigh-type unsteady boundary layers.



Instability Reynolds number for quasi-steady shock-type boundary layer



Estimated instability Reynolds number and shape factor in unsteady interaction region
Circles; predicted from linearized stability theory



1. High Pressure Chamber
3. Sliding Valve
- 5,7. Potentiometer
- 8,9. Pressure Gauge
2. Low Pressure Chamber
4. Air Cylinder
6. Float
10. Test Section

Fig.8 Structure of unsteady intermittent liquid tunnel

4. EXPERIMENTS AND RESULTS

The unsteady intermittent liquid tunnel is an apparatus²⁴ which gives a rapidly accelerated liquid flow starting from rest and attaining a final steady flow velocity within a short period of time. As shown in Fig.8, it is composed of two chambers separated by a sliding plate valve; one is filled with pressurized liquids and the other with low pressure gases. The sliding plate valve being opened quickly by the air-cylinder, the liquid is ejected into the low pressure gas chamber. The test section is made of a P.V.C. pipe of 460 mm long and 50 mm inside diameter and a P.V.C. flat plate of 3 mm thick inserted in the pipe. The apparatus is made of P.V.C. plastics which is inert in the presence of electrolytic solution. Under the pressure difference between the two chambers $\Delta p = 500$ Torr, the attainable final freestream velocity U is about 1.5 m/s and the rise time τ is about 15 msec. When a divergent nozzle (10 cm in diameter), equipped with the larger sliding valve, is attached to the end of the test section, $U \approx 4$ m/s, $\tau = 50$ msec for $\Delta p = 500$ Torr.

This apparatus looks like a kind of Ludwig tube. Its operational principle is described in the previous proceedings²⁴. In the conventional Ludwig tube, the cold gas flow behind the incident expansion waves are utilized until the reflected expansion waves run back to the test section. On the contrary, in the present apparatus the liquid flow is accelerated gradually, owing to its high density, by the waves propagating back and forth.

The velocity-time history can be given either by the differentiation of a measured displacement of the float, by the integration of pressure difference between the two points in the test section or by a hot film velocity meter. The wall shear stress is detected by electrodes (electrochemical method) or a hot-film flush mounted on the wall.

In the electrochemical method to detect a wall shear stress, the diffusion limited current of electrolytic reaction is measured between a small cathode flush mounted on the wall and an anode of much larger surface area. Under the condition of limiting current, electrode current I is related to a wall shear stress τ_w : $I = \alpha \tau_w^{1/3}$, where α is a calibration constant.

The test electrodes are composed of five rectangular nickel electrodes of 0.1 mm long 10 mm wide. The counter electrode is made of a nickel pipe installed downstream. The test fluid consist of 0.1 molar potassium ferricyanide ($K_3Fe(CN)_6$), potassium ferrocyanide ($K_4Fe(CN)_6$) and one molar potassium hydroxide (KOH) as a supporting electrolyte. The voltage applied by the potentiostatt is 0.7 v and the probe circuit current is approximately 100 μA .

Fig.10 is an example of the numerical calculation of the growing boundary layer over the flat plate corresponding to the observed freestream. It shows the time varying profiles of the displacement thickness δ_1 and the shape factor H . Developing independently of x (Rayleigh-type) at the early stage in the region far from the leading edge, the boundary layer gradually changes into the steady Blasius-type from the leading edge. The shape factor H , in the region of uniform displacement thickness far from the leading edge after $t = 8$, is equal to that of the Rayleigh-type boundary layer ($H=2.48$) and also gradually changes into the values of Blasius-type ($H=2.59$). The low value of H , in the uniform region ($x>3$) at early time $t=4$, means that the freestream has not attained the final steady state.

Fig.11 shows the observed freestream velocity U , the electrode current observed I_m and calculated I_c , and the predicted shape factor H . I_c and H are predicted from the present integral method for the observed $U(t)$. Increasing at the initial stage, the value of shape factor H remains constant for a while corresponding to Rayleigh flow and then gradually increases to the value of Blasius flow. The electrode current increases at the initial stage accompanied by the acceleration of freestream and then decreases by the development of the boundary layer of Rayleigh-type. Finally it settles down to the constant value corresponding to the Blasius-type boundary layer. Compared with I_c , I_m is delayed to rise at initial stage and then it suddenly rises again owing to the transition into turbulence. Later it proved to be enhanced by disturbances generated at the intersecting point of the edge of the flat plate and the side wall. Thereafter, the flat plate was installed with clearance between the side-

walls. Consequently, the transition did not take place any more for the same flow conditions.

In order to achieve the higher Reynolds number flow in which the transition is expected to occur, the final freestream velocity was raised from 1.4 m/s to 3.4 m/s. The experimental results are shown in Fig.11. The rise time of the freestream velocity U is prolonged under the limited pressure difference. Here the wall shear stress is measured by a hot-film instead of the electrodes. Before the shape factor H reaches that of Rayleigh-type, the transition takes place. This is indicated by the abrupt change of observed output E_m from the hot-film. The output of hot-film E_c theoretically predicted from the observed freestream velocity U is shown for comparison.

The observed transition points are shown with closed circles on the Rex-Ret diagram in Fig.12. The solid curves denoted as $\alpha = 1$ is the locus of the points of instability. The curves denoted as $\alpha = 0.5$ and 0.2 correspond to the loci of $Re\delta_1 = 0.5(Re\delta_1)_i$ and $0.2(Re\delta_1)_i$ respectively. The transition takes place earlier than the predicted time of instability. This is attributed to the external disturbances; the observed turbulent intensity is about 0.3 % in the freestream. The curve denoted as $\xi = 1$ shows a trace of freestream fluid particles initially situated on the leading edge of the flat plate. The transition points are found to move downstream with almost the same velocity of freestream.

5. CONCLUSIONS

For the shock-induced unsteady flat plate boundary layers, including its limiting case, the effects of velocity profile on the transition were investigated theoretically and experimentally.

(1) By one parameter integral method, unsteady laminar boundary layer equations were reduced to the partial differential equations in terms of the momentum thickness and the shape factor. Employing a finite difference scheme make it feasible to apply this method to the case of time-dependent freestream.

(2) Assuming that Wazzan's relations of instability Reynolds number versus shape factor, the locus of the points of instability were drawn on the $x-t$ diagram. The lowering of instability points is found in the unsteady interaction region.

(3) In the liquid flows almost impulsively started, the transition of unsteady flat plate boundary layer was observed to take place earlier than the time predicted from the linearized stability theory. This early transition may be attributed to the external disturbances. This resembles to the experimental observations of the boundary layers on the shock tube side wall.

Now we intend to construct a new intermittent unsteady liquid tunnel with freestream of lower turbulent intensity and of higher Reynolds number, by which behaviors of transition and turbulent structure of unsteady boundary layers will be investigated.

6. REFERENCES

- 1) S.H.Lam & L.Crocco; Princeton Univ. Rep.428 (1958), Rep.480 (1959), J.Aero.Space Sci. 26,1 (1959)54
- 2) T.Akamatsu & H.Yoshioka; Proc.7th Japan Nat.Congress Appl.Mech.(1967)254
- 3) E.J.Felderman; Iowa State Univ. Ph.D.thesis (1966), J.AIAA 6,3(1968)408
- 4) J.W.Murdock; Aerospace Corp.Rep.TR-0158(S3816-62) 2 (1968)
- 5) W.J.Cook & G.T.Chapman; Phys.Fluids,15,12, (1972)2129
- 6) K.Stewartson; J.Mech.Appl.Math.4,2 (1951)182,Advances in Appl.Mech.6(1960)1
- 7) T.Akamatsu; Bull.Japan Soc. Mech. Engrs.10,40 (1967) 641
- 8) S.H.Smith; J.Fluid Mech.42,3 (1970) 627
- 9) T.Akamatsu; Bull. Japan Soc. Mech. Engrs. 11,48 (1968) 1091
- 10) I.Tani & J.J.Yu; Proc.IUTAM Symp. Unsteady Boundary Layer (1971) 886
- 11) S.J.Koob & Abott; *ibid.* p270
- 12) M.G.Hall; Proc.Roy.Soc.A310 (1969) 401, Ingenger-Archiv. 38 (1969) 97

- 13) W.R.Davies & L.Bernstein; J.Fluid Mech. 36,1 (1969) 87
- 14) W.J.Cook; Phys. Fluids 17,5 (1974) 900
- 15) B.E.L.Dekker & M.E.Weeks; Proc.Instn.Mech.Engrs. 190,11 (1976) 287
- 16) M.V.Morkovin; AFOSR Themis R71-2 (1971)
- 17) W.A.Martin; Univ. Toronto Inst. Aerophys. Rep.47 (1957)
- 18) R.A.Hartunian, A.L.Russo & P.V.Marrone; J.Aero.Space Sci.25 (1960) 587
- 19) H.Mark & M.J.Mirtich; Phys. Fluids 10 (1962) 251
- 20) W.P.Thompson & R.J.Emrich; Phys. Fluids 10 (1967) 17
- 21) S.Ostrach & P.R.Thornton; J.Aero.Space Sci.29 (1962) 289
- 22) A.R.Wazzan, T.T.Okamura & A.M.O.Smith; McDonnell-Douglas Co.Rep DAC-67086
- 23) H.Schlichting; Annalen der Physik 5, 14 (1932) 905 (1968)
- 24) T.Akamatsu; Proc.11th Int.Symp.Shock Tubes & Waves (1978) 24

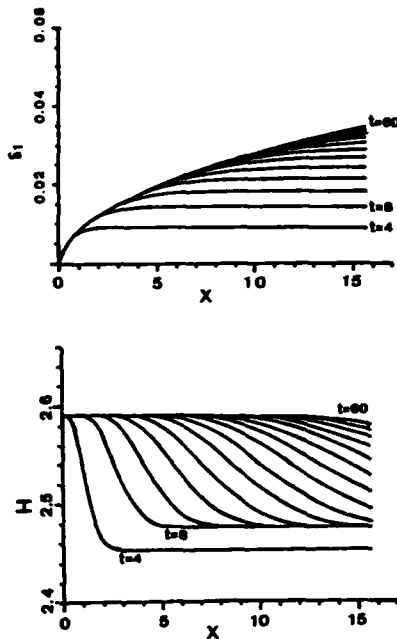


Fig.9 Growing boundary layer over a flat plate inserted in a liquid tunnel

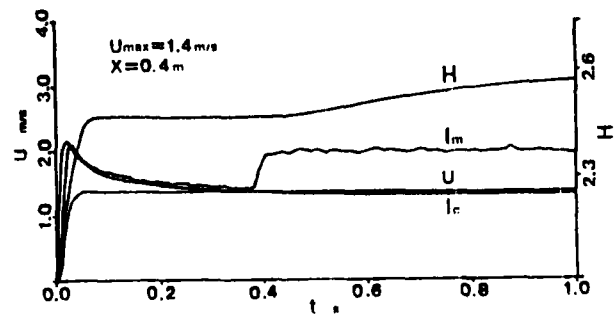


Fig.10 Experimental observation of U, H, I_m, I_c (τ_w measured by electrochemical method)

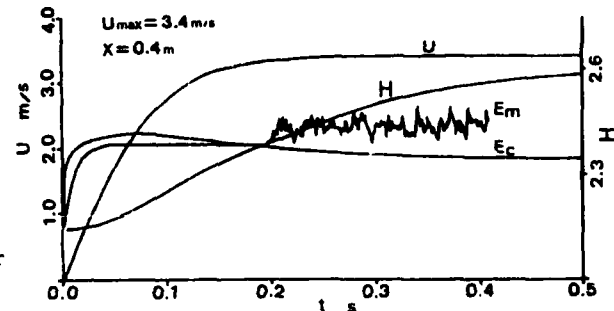


Fig.11 Experimental observation of U, H, E_m, E_c (τ_w measured by hot-film)

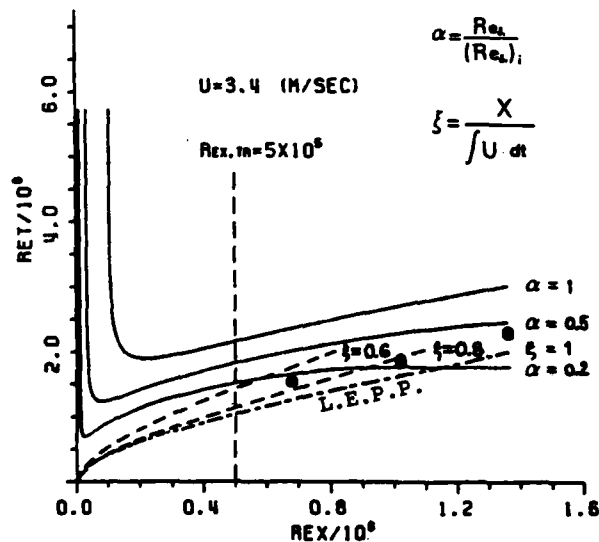


Fig.12 Predicted instability points and observed transition points on $x-t$ diagram

AD P000248

The Boundary Layer Behind a Shock Wave
Incident on a Leading Edge

B.E.L. Deckker

Mechanical Engineering Department, University of Saskatchewan
Saskatoon, Canada S7N 0W0

Boundary layer growth at a leading edge behind three shock waves of strength $M_s = 1.11, 1.19$ and 1.44 have been followed by schlieren photography. Thicknesses measured by optical comparator at $x/10$ have shown that initial growth rates of the laminar portion of the boundary layer exceed that predicted by Mirels' theory. It would appear that a pseudo-turbulent regime is initially set up. In the other two cases after the initial stage the rate of growth is in fair agreement with theory. From the average speed of the interface between the shock-induced and quasi-steady boundary layers it has been concluded that the theoretical velocity at the edge of the boundary layer is attained. There is no evidence for growth of the quasi-steady boundary layer except for the final thickness. However, this is reproduced satisfactorily using well-tested empirical equations for skin friction and the velocity distribution given by the wall law and velocity defect law. An attempt has been made to reproduce the characteristic lengths of the laminar and turbulent boundary layers, matching the final thickness and that at the critical length. Schlieren photographs show the structure of the turbulent boundary layer to be made up of discrete inclined features which may be hairpin vortices.

INTRODUCTION

Interest in boundary layer effects behind moving shock waves in a shock tube stems from the need to predict conditions at a section where measurements are being made. In this connection the many contributions made by Mirels (1) need no recapitulation here. However, there are few publications concerned primarily with the basic problem of the growth of the shock-induced boundary layer and verification of Mirels' theoretical treatment of it. Attempts have been made by Martin (2) and Gooderum (3) to measure boundary layer growth indirectly by interferometry; Davis (4) has confirmed Mirel's theory indirectly by heat transfer measurements.

Deckker and Weekes (5), (6), have attempted to measure boundary layer growth behind weak shock waves directly from schlieren photographs in a shock tube of cross-section $0.051\text{m} \times 0.076\text{m}$, aspect ratio 0.72 . Their results showed that while there was some measure of agreement between Mirels' theoretical treatment and their experiments, the boundary closed on the centre line in a time that was less than the running time of the shock tube. They also found in

one experiment with a shock wave of strength $M_s = 1.22$ that the velocity and temperature distributions were not uniform behind the shock wave and, in particular, that the velocity profile did become fully developed until the shock wave was about 27 hydraulic diameters downstream of the reference station. Specific reference to boundary layer closure has been made by Gooderum (3) but Bazhenova et al. (7) make no reference to the possibility of boundary layer closure nor to non-uniformity of the kind encountered in ref (6) in discussing the distribution of flow properties behind moving shock waves. In references (2), (5) and (7) the shock tubes were of comparable cross-section. In ref (3) the cross-section of the tube was greater, 0.102m x 0.191m, aspect ratio 0.63, but the results obtained were in fair agreement with that of ref (5) for roughly the same wave strength.

Hubbard and de Boer (8) found theoretically that there was significant departure from uniformity close to the shock front but that the flow was one-dimensional further downstream. The non-uniformity described in ref (6) was evidently due to contact-surface irregularities in spite of the use of "petalling" diaphragms. It would appear that the use of such diaphragms does not, in itself, secure uniformity of the flow. In ref. (5) boundary layer thickness on the floor of the shock tube was measured at a reference station located 3.9m from the diaphragm. In the experiments described in this paper, measurements were made at the same distance from the diaphragm but after the shock wave had impinged on the leading edge of a splitter plate 0.13m from the reference station.

EXPERIMENTAL CONSIDERATIONS

The experimental equipment has been described in some detail in ref (5) and ref (9) and only the main features are given here.

The cylindrical compression chamber 0.2m diameter and 2.6m long was joined to the rectangular expansion duct 0.051m x 0.076m by a transition section. The length of the expansion duct from the diaphragm to the reference station in the test section was 3.9m and the overall length from the diaphragm to the open end was 6.9m.

The test section, 0.74m over flanges, was made of aluminium plate and its internal surfaces were ground and polished to match those of the expansion duct. The latter were in two lengths, one on each side of the test section. They were made of timber reinforced on the outside by steel angle-bars and lined internally with a hard smooth plastic. The windows in the test section were of optical quality glass (surface finish 546Å).

A splitter plate 0.75m long and 0.013m thick was fitted across the span of the test section, with its upper surface 0.02m above the floor so making the upper portion of the test section 0.031m x 0.076m. The splitter plate had a slender forebody formed by chamfering the under surface of the plate at an angle of approximately 6 deg. to provide a sharp leading edge.

A single-pass schlieren system with two parabolic front-surface mirrors (surface finish 546Å), 0.305m diameter and 2.44m focal length was used. Illumination was provided by an argon jet spark-source of duration 0.2 μ s and rise-time 0.04 μ s. The spark was triggered by the arrival of the shock wave at a fixed position in the test-section but after the signal had passed through a variable delay circuit. The sensitivity of the optical layout was estimated to be sufficient to resolve density gradients in the test section near to unity (10).

Schlieren photographs were taken at successive intervals of about 0.5ms, after first arrival of the shock wave at the reference station, using single exposures during the course of an experiment. Negative images of these

photographs were used to measure boundary layer thickness by means of an optical comparator at $\times 10$, the resolution of the comparator being better than $2 \times 10^{-5} \text{ m}$. To ensure repeatability of the incident shock wave its speed was checked between measuring stations 0.61m apart.

The diaphragms were of laminated cellophane sheets, the topmost sheet being bonded to an acetate sheet $8 \times 10^{-5} \text{ m}$ thick. Cruciform lines were incised diametrically in the latter to a predetermined depth. These diaphragms were installed with the acetate face on the low pressure side and rupture initiated by piercing the intersection of the cruciform lines with a solenoid driven needle. The diaphragms invariably "petalled" on rupture.

RESULTS AND DISCUSSIONS

The results of experiments with three shock waves of strength $M_s = 1.11$, $M_s = 1.19$ and $M_s = 1.44$ are presented and discussed here. These shock waves were selected because they were expected to give shock-induced boundary layers that were, respectively, almost wholly laminar, transitional and almost wholly turbulent.

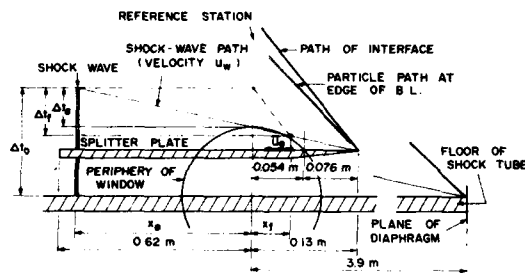


FIGURE 1

Referring to Fig. 1, when the incident shock wave clears the leading edge, simultaneously two boundary layers are formed, the one growing from the foot of the shock and the other from the leading edge. The latter is formed from air particles that have already been set in motion by the shock and being relatively remote from the walls of the tube ideally are in steady, uniform motion so that the boundary layer conforms to the classical model. Growth of the shock-induced boundary layer, measured from the instant the shock wave arrives at the reference station, is concomitant with the arrival of air particles that initially were on, or in the vicinity of, the plate and have been set in motion by the shock wave. These particles have been subjected to viscous effects over increasing lengths, x_f , and for corresponding times, Δt_f , depending upon the distance, x_e , of the shock wave from the reference station. The time corresponding to x_e is Δt_e , measured from the time the shock wave was initially at that station. The maximum thickness of the shock-induced boundary layer is attained when particles in the quasi-steady boundary layer growing from the leading edge first arrive at the reference station. By definition, thereafter the boundary layer thickness at this station remains constant for the running time of the shock tube. In the present experiments, the duration is limited by the time when wave-action at the trailing edge of the plate begins to influence conditions at the reference station.

Shock-induced boundary layer

For each shock wave, boundary layer thickness, measured at the reference station in the manner already described, has been plotted as a function of the time Δt_e in Fig. 2(a), 2(b) and 2(c). Also shown is the boundary layer thickness measured at the right-hand edge of the window at 0.054m from the reference station, (Fig. 1).

The steep fronts in Fig. 2(a) and Fig. 2(b) signal the arrival of the interface between the shock-induced and quasi-steady boundary layers at the reference station. In Fig. 2(c) the interface is not immediately apparent but after careful scrutiny of the curve the time of arrival is believed to be

indicated. The distance travelled by the interface from the leading edge to the reference station is 0.13m so that the average speed may be determined. In each case schlieren photographs of the advancing fronts at the times indicated are also shown.

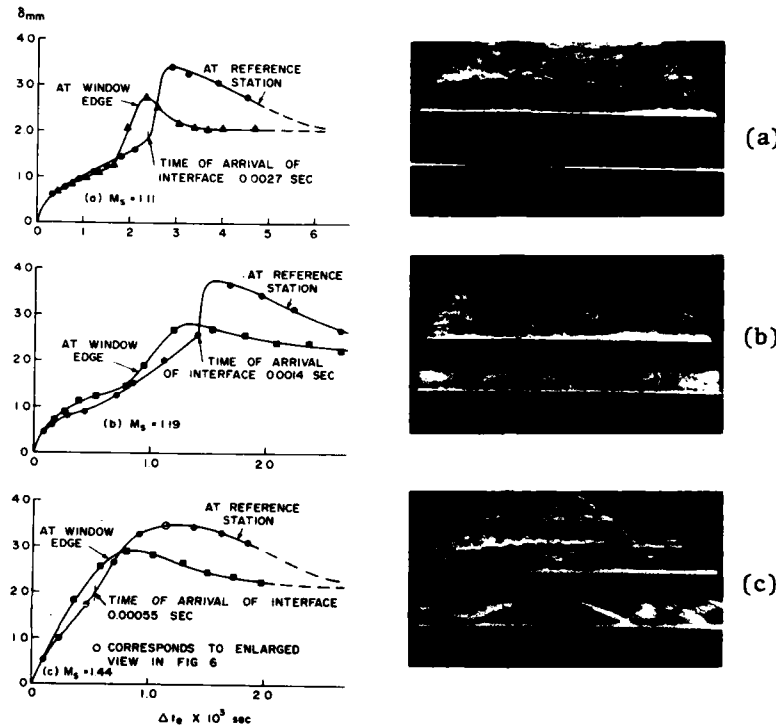


FIGURE 2

270m/s respectively, which are as close as can be expected to the theoretical values in measurements of the kind that have been made. Such close agreement must be regarded as fortuitous.

shock strength M_s	u_w m/s	u_e m/s	\bar{u}_e m/s	T_e K	T_m K	$v_e \times 10^5$ m ² /s	$v_m \times 10^5$ m ² /s	θ/δ	δ^*/δ
1.11	384	322	62	318	307	1.74	1.645	-0.0258	-0.0339
1.19	413	309	104	333	315	1.88	1.718	-0.0493	-0.1221
1.44	497	215	282	380	343	2.38	1.977	-0.1201	-0.1271

Table 1. Theoretical properties and mean values used in calculations.

θ , δ^* are the momentum and displacement thickness of boundary layer;

δ is the thickness corresponding to $u/\bar{u}_e = 0.99$; $u_e = (u_w - \bar{u}_e)$, the particle velocity in shock-fixed co-ordinates.

If the abscissae in Fig. 2 are transformed to flow length x_f using the relationship implicit in Fig. 1 namely, $x_f = u_w \Delta t_e / (u_w / \bar{u}_e - 1)$ and the theoretical values of \bar{u}_e and the wave speed u_w , then the curves will be stretched. But when the abscissae are scaled appropriately to 0.13m, spatial growth of the boundary layer appears as in Fig. 3(a), 3(b) and 3(c), the temporal growth

If it is assumed, as Mirels has done (11), that the velocity distribution in the growing shock-induced turbulent boundary layer conforms to the one-seventh power law, the average speed of the interface would be $0.88 \bar{u}_e$, \bar{u}_e being the particle velocity at the edge of the boundary layer. Theoretical values of this velocity are given in Table 1. The measured average speeds of the interface are 54m/s, 93m/s and 236m/s for the three shock waves, and the corresponding values of \bar{u}_e are 62m/s, 106m/s and

being also shown in those Figures. It is clear that there is a large discrepancy between theoretical and experimental laminar growth rates. Since it has been shown that \bar{u}_e at the edge of the boundary layer is equal to the theoretical value and, also, since u_w has been maintained essentially constant throughout the experiment, differences between theory and experiment are most likely to reflect differences in physical behaviour. It may be noted that in each case the discrepancy arises in the very early stages of growth during which, what appears to be, a pseudo-turbulent regime is temporarily established but which in the case of the weakest shock wave, $M_s = 1.11$, cannot be maintained at further distances from the foot of the shock.

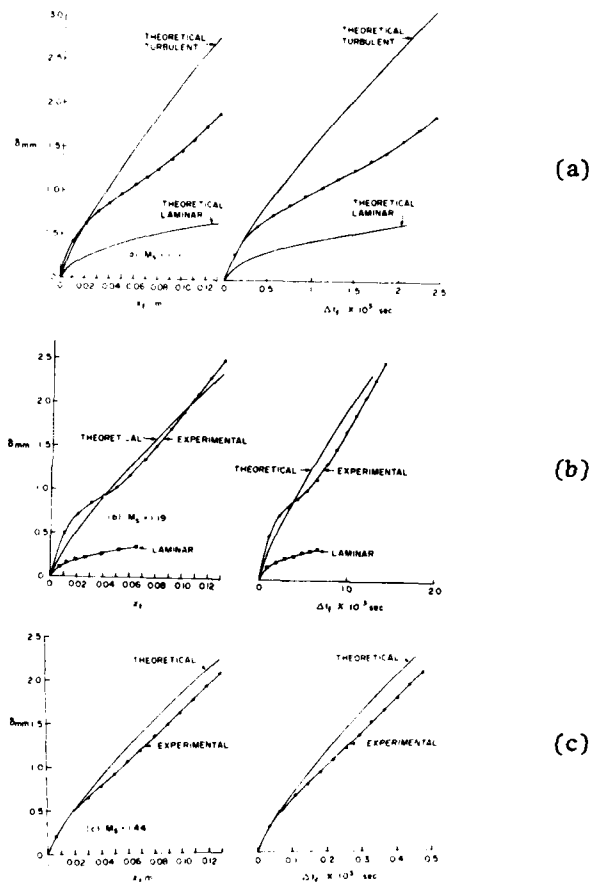


FIGURE 3

Quasi-steady boundary layer

Boundary layer thickness measured at the right-hand edge of the window, 0.054m from the reference station, during the passage of a shock wave over the splitter plate is shown in Fig. 2(a), 2(b) and 2(c). Except for the weakest shock wave, $M_s = 1.11$, the final quasi-steady boundary layer thickness could not be measured at the reference station because the splitter plate downstream of it was short enough (0.62m) to allow the wave reflected at the trailing edge to affect the boundary layer at that station.

Also, the boundary layer growing between the leading edge and the right hand edge of the window, a distance of 0.076m, could not be observed and, therefore, no experimental evidence for the manner in which that boundary layer grows is available. Nevertheless an attempt has been made to reproduce the

In Fig. 3(b), as in Fig. 3(a), after the initial stage the rate of growth is more nearly in accord with theory, bearing in mind that there is a trend to boundary layer closure.

Fig. 3(c) shows the spatial and temporal growth rates for the strongest shock wave, $M_s = 1.44$. There is evidence of a short length of laminar boundary layer which also suffers from the limitation observed in the other two cases, otherwise the rate of growth conforms well to that predicted theoretically. In particular, the trend to boundary layer closure is less well marked but this is also a function of Δt_f (0.48×10^{-4} sec) which is only a fraction of that for $M_s = 1.11$ ($\Delta t_f = 24 \times 10^{-4}$ sec) and for $M_s = 1.19$ ($\Delta t_f = 14 \times 10^{-4}$ sec).

overall characteristics of the steady boundary layer using well tested empirical equations.

For the incompressible turbulent boundary layer growing from the leading edge in zero pressure gradient, which is a reasonable assumption in the experiments described, a number of equations are available for predicting local and average skin friction coefficients. As a matter of convenience three of these were selected, namely:

$$c_f = 0.370/(\log R_x)^{2.58} \text{ (Schultz-Grunow)} \quad (1a)$$

$$c_f = 0.059/(R_x)^{0.2} \text{ (Power Law)} \quad (1b)$$

$$\bar{c}_f = \{0.427/(\log R_\ell - 0.407)^{2.64}\} - A/R_\ell \text{ (Schultz-Grunow-Prandtl)} \quad (1c)$$

where c_f , \bar{c}_f are local and average friction coefficients, respectively, and R_x , R_ℓ the corresponding length-Reynolds numbers.

Implicit in the use of these friction coefficients are the velocity distributions given by the law of the wall and, in the outer reaches of the turbulent layer, the velocity-defect law. The two equations for the velocity are:

$$\text{For } y/\delta < 0.15, u/u_* = 5.6 \log (u_* y/\nu) + 4.9 \quad (2a)$$

$$\text{and for } y/\delta > 0.15, (\bar{u}_e - u)/u_* = 8.6 \log (y/\delta) \quad (2b)$$

Where \bar{u}_e is the velocity at the edge of the boundary layer at a distance δ from the plate; $u_* = (\tau_o/\rho)^{1/2}$ is the friction velocity, the shear stress τ_o being equal to $\frac{1}{2}c_f\rho\bar{u}_e^2$; u is the velocity at a distance y from the plate. In keeping with the approximate nature of the calculation, and in the spirit of Mirel's theoretical treatment of the turbulent boundary layer, mean property values (Table 1) calculated as in ref (11) were used for the density and kinematic viscosity in the above equations.

The results obtained using equations (1) and (2) above are shown in Fig. 4(a), 4(b) and 4(c) for values of \bar{u}_e and v_m behind the shock waves. It is clear that the thickness of the steady boundary layer predicted by these equations is in good agreement with that estimated experimentally having regard to the fact that in the experiments there are side-wall effects and that the boundary layer is not turbulent from the leading edge.

The relative distribution of turbulent and laminar skin friction over length ℓ from the leading edge may be deduced from the transition equation, eqn. 1(c), in which the expression in braces is the average turbulent skin friction over length ℓ from the leading edge and the term A/R_ℓ is a correction for the effect of laminar skin friction over the critical length, x_{crit} . A is related to the critical length Reynolds number, R_{crit} . Daily and Harleman (12) have published data for this relationship in the range $3 \times 10^5 < R_{crit} < 10^6$. When these data are plotted it has been found that, while the relationship between A and R_{crit} is approximately linear over the entire range of critical Reynolds numbers, it is linear in the lower range $3 \times 10^5 < R_{crit} < 5 \times 10^5$. Using the steady boundary layer thickness at the reference section which has been shown to be in accord with well tested empirical equations, the corresponding skin friction coefficient can be calculated by trial and error. Substitution for \bar{c}_f in eqn. 1(c) then yields a value for A/R_ℓ from which A is determined. The corresponding value of R_{crit} is found from the linear relationship referred to above, whence x_{crit} may be calculated for mean property values. Alternatively, on the basis of the linear relationship, a value of A may be found by trial and error to give the appropriate \bar{c}_f directly from eqn. 1(c) which will yield the required value of boundary layer thickness. Pairs of values of A and R_{crit} which satisfactorily reproduce the steady boundary layer thickness are given in Table 2.

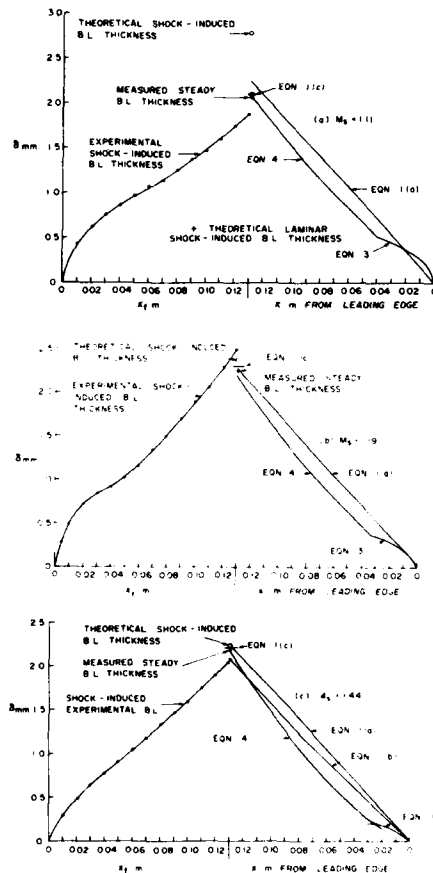


FIGURE 4

Shock strength M_s	Velocity at edge of b.l. \bar{u}_e m/s	A	R_{crit}	x_{crit} m
1.11	62	510	1.5×10^5	0.040
1.19	104	760	2.2×10^5	0.036
1.44	282	1390	3.9×10^5	0.027

Table 2. Relationship between A and R_{crit} in Eqn. 1(c).

Shock strength M_s	Velocity at edge of b.l. \bar{u}_e m/s	exponent n	
		at x_{crit}	at ref. station
1.11	62	0.092	0.173
1.19	104	0.083	0.151
1.44	282	0.070	0.132

Table 3. Values of exponent n in Eqn. (4).

The laminar boundary layer profile from the leading edge can be obtained from the Blasius equation, $\delta = 5x/(R_x)^{1/2}$ so that the thickness at x_{crit} may be determined. The skin friction coefficient over the critical length is easily found from:

$$c_f = 0.664/(R_x)^{1/2}, \quad (3)$$

or in terms of mean property values,

$$c_f = 0.664 (\nu_m/\bar{u}_e)^{1/2}/x^{1/2}.$$

The power law, eqn. 1(b), when averaged over the critical length gives a value of \bar{c}_f (turbulent) which is too small to match the thickness of the laminar layer at that position. Similarly, at the reference station $\ell = 0.13m$, when the net average \bar{c}_f is taken as \bar{c}_f (turbulent) - \bar{c}_f (laminar), that is,

$$\bar{c}_{f_{net}} = .074(\nu_m/\bar{u}_e)^{0.2}/\ell^{0.2} - 0.664 (\nu_m/\bar{u}_e)^{1/2}/\ell^{1/2}$$

the value of $\bar{c}_{f_{net}}$ is too small to reproduce the boundary layer thickness there.

However, if a modifying factor, which is a function of the distance from the leading edge, is introduced into Eqn. (3) so that it may be written as:

$$\bar{c}_{f_{net}} = \bar{c}_f \text{ (turbulent)}/x^n - \bar{c}_f \text{ (laminar)}, \quad (4)$$

then the exponent n may be found by matching the turbulent boundary layer thickness to the laminar thickness at x_{crit} and to the experimental thickness at the reference plane. A linear variation of the exponent between those stations may be assumed. The boundary layer profile calculated in this way is shown in Fig. 4(a), 4(b) and 4(c). Values of n at the two stations for the three shock waves are given in Table 3.

Boundary layer structure

Head and Bandyopadhyay (13) have recently published the results of their flow visualization studies of the structure of turbulent boundary layers on the floor of a wind tunnel. In the light of their conclusions it is of interest to present in Fig. 5 schlieren photographs of two typical turbulent boundary layers taken simultaneously

on the splitter plate and on the floor of the shock tube. The photograph has been magnified $\times 10$ approximately, corresponding to which measurements of thickness have been made by optical comparator as described earlier. Only the central section, approximately 0.006m wide, has been reproduced in the photograph, since the inclined features seen in that Figure have been rotated in opposite directions at further distances from the vertical axis due to aberration arising from the off-axis mirror system. The shock wave strength is $M_S = 1.44$.

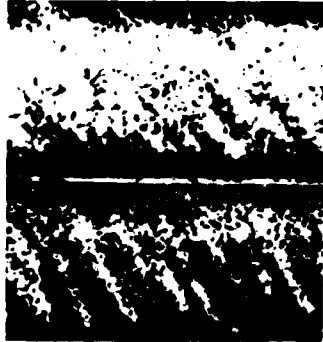


FIGURE 5 The upper boundary layer in Fig. 5 is that induced behind the shock wave on the splitter plate and is formed from particles of air that were initially well removed from the shock tube walls. The lower boundary layer is also shock-induced but is on the floor of the shock tube. It has been formed from air particles that have been subjected to viscous effects for a longer time than those in the upper boundary layer. The Reynolds number of the flow behind the wave is 10^7 , calculated according to ref (11).

CONCLUSIONS

Growth of shock-induced boundary layers behind weak shock waves of increasing strengths, $M_S = 1.11$, $M_S = 1.19$ and $M_S = 1.44$ have been measured directly from schlieren photographs.

There is evidence of a laminar boundary layer in each case but the rate of growth is different from that predicted by Mirels' theoretical treatment. However, the difference appears to arise only in the very early stages of growth and later the rate of growth in the case of the stronger shock waves conforms reasonably well with Mirels' theory. Better agreement between experiment and theory is apparently subverted by the initial differences in growth. There is also evidence that the boundary tends to close on the centre line of the flow passage.

The quasi-steady boundary layer growing from the leading could not be observed except near the reference station and the final thickness at that station has been estimated from experimental measurements. The final thickness is in reasonable agreement with values calculated from empirical equations for the friction coefficient, the wall law and velocity defect law, using mean property values.

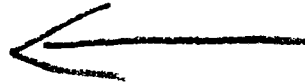
An attempt has been made to predict the characteristic spatial distribution of the laminar and turbulent boundary layers between the leading edge and reference station, using the Schultz-Grunow-Prandtl equation. On this basis the spatial rate of growth of the boundary layer has been calculated using well established empirical equations but introducing a modifying factor based on distance from the leading edge. Boundary layer profiles obtained in this manner are like those measured experimentally when there is boundary layer closure.

Schlieren photographs of the turbulent boundary layers in this investigation show discrete features that are inclined in the flow direction. The angle of inclination is generally different from that reported in ref (13) but may be

a Reynolds number effect.

REFERENCES

1. Mirels, Eighth Intl. Shock Tube Symp., 1971, p. 6.
2. Martin, W.A., UTIAS, Report No. 47, 1957.
3. Gooderum, P.B., NACA TN 4243, 1958.
4. Davis, W.R. and Bernstein, L., J. Fluid Mech., Vol. 36, Pt. 1, 1969, p. 87.
5. Deckker, B.E.L. and Weekes, M.E., Proc. 1, Mech. E. (Lond), 190 41/76, 1976, p. 287.
6. Deckker, B.E.L. and Weekes, M.E., Proc. 1, Mech. E. (Lond), 190 41/76, 1976, p. 437.
7. Bazhenova, T.V., Nabako, I.M. and Nemkov, R.A., Seventh Intl. Shock Tube Symp. 1969, p. 60.
8. Hubbard, E.W. and de Boer, P.C.T., Seventh Intl. Shock Tube Symp. 1969, p. 109.
9. Deckker, B.E.L., Intl. Symp. Flow Visualization, 1980, p. 555.
10. Holder, D.W. and North, R.J., Notes on Applied Science No. 31, HMSO, 1963.
11. Mirels, H., NACA TN 3712, 1956.
12. Daily, J.W. and Harleman, D.R.F., Fluid Dynamics, Addison-Wesley Publ. Co., 1966, p. 240.
13. Head, M.R. and Bandyopadhyay, P., AGARD Conf. Proc. 271, 1979, p. 25-1.



AD P000249

REAL GAS AND WALL ROUGHNESS EFFECTS ON THE BIFURCATION OF THE SHOCK REFLECTED FROM THE END WALL OF A TUBE

J. R. Taylor and H. G. Hornung^{*}

Australian National University, Canberra, Australia

^{*}DFVLR-AVA, Göttingen, Federal Republic of Germany

Several aspects of the interaction between the boundary layer on the shock tube side wall and the shock reflected from the end wall were investigated experimentally in the free piston shock tube T3. The experiments were conducted at sufficiently high shock speed to produce vibrational excitation and dissociation in the case of nitrogen and carbon dioxide, while the experiments in argon were restricted to the ideal gas range. Numerical calculations were made with the model of Mark (1958) which was extended to account for equilibrium real gas effects. The numerical as well as the experimental results show clearly, the real gas effect on the angle of the bifurcated foot is very significant. The modified Mark model is in fair agreement with N_2 results, but shows large discrepancies with weakly bifurcating (Argon) and strongly bifurcating (CO_2) gases. The growth rate of the bifurcation configuration is initially linear and rapidly reduces to zero for N_2 and CO_2 . In argon, for which no bifurcation is predicted, a small bifurcation was observed. For N_2 , increased wall roughness caused the bifurcation to continue to grow linearly well beyond the asymptotic scale on a smooth wall.

INTRODUCTION

The phenomenon of shock bifurcation is illustrated in figure 1. The configuration shown is brought about when a plane "incident" shock travels into uniform gas at rest in a tube and is reflected off an end wall, which is parallel to the incident shock. The reflected shock then interacts with the boundary layer generated by the incident shock on the side wall of the tube. Under some conditions the reflected shock may cause the boundary layer to separate, so that an oblique shock precedes the normal reflected shock as the front leg of the bifurcation, and a short rear leg causes the gas to be deflected back to-

wards the wall behind the separation bubble which is carried along by the bifurcation.

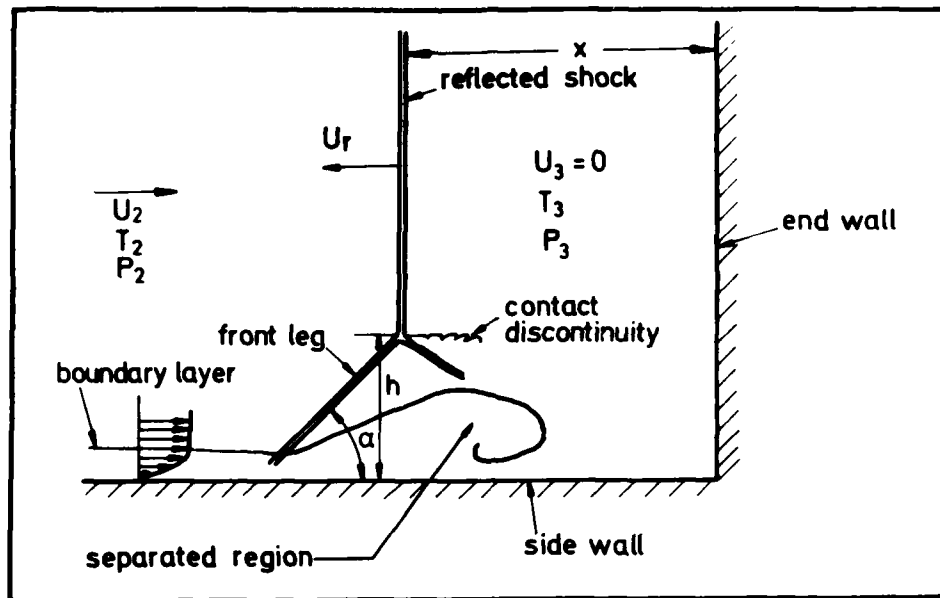


Fig. 1: Schematic sketch of reflected shock bifurcation

A number of authors have attempted to make models of this process. By assuming the boundary layer to consist of test gas at the wall temperature T_1 and at post incident shock pressure p_2 with no velocity gradient, Mark¹ (1958) was able to define Mach number regions where the reflected shock would bifurcate. He assumed that the gas in the boundary layer would be brought to rest relative to the reflected shock. If the stagnation pressure in the boundary layer is smaller than the post reflected shock pressure p_3 he assumed the boundary layer would separate, forming a separation bubble shaped like a double wedge of cold fluid which caused the free stream to be deflected through a double oblique shock system.

One of the most sensitive measures of the success of bifurcation models is the angle α of the front leg of the bifurcation. Mark's analysis, which is restricted to a thermally perfect gas predicts a large rise of α with incident shock Mach number M_1 for $\gamma = 1.4$ (ratio of specific heats). This has not been observed to occur. The failure of the model at higher Mach numbers was pointed out by Davies (1969) who questioned the assumption of the basic model, that properties of the boundary layer feed gas should determine the pressure under the bifurcated foot and hence the foot angle α .

Byron and Rott (1961) also pointed to the existence of a minimum Mach number in the boundary layer at a finite distance from the side wall. They showed that if the boundary layer stagnation pressure is calculated with this Mach number, the rapid increase of α with increasing M_1 is avoided.

Extensive calculations made by Honda et al. (1975) taking into account dissociative real gas effects in equilibrium, showed that these effects also reduce α , and hence that bifurcation would continue to occur in regions where Mark's analysis suggested it would not be possible. For this paper, we have made similar calculations for nitrogen, carbon dioxide and argon, for the

first two gases making calculations of α , so that direct comparison with experimental results is possible.

Near the end wall, the bifurcation configuration grows linearly with distance from the end wall. The growth rate loses this self-similarity however, as it proceeds away from the end wall. Eventually it stops growing and an asymptotic height h_0 may be defined. This behaviour was first observed by Strehlow and Cohen (1959). Matsuo et al. (1974) have proposed a model to describe this phase, in which the boundary layer fluid is not trapped but a separation bubble of fixed size is carried along with the reflected shock. In this model, the determining length scale for h is the boundary layer thickness. In the present experiments it was hoped that the growth of h , and possibly h_0 , could be influenced by deliberately changing the boundary layer thickness through increased wall roughness.

REAL GAS CALCULATIONS

The model for our calculations is basically the same as that of Mark (1958). In accordance with the assumption that the boundary layer gas is at wall temperature and is brought to rest relative to the reflected shock, the boundary layer stagnation pressure is calculated with the Mach number $M_{b.l.} = U_r/a_1$, where a_1 is the speed of sound in the undisturbed test gas. The stagnation pressure is then computed with the Rayleigh supersonic pitot pressure formula with the important proviso that the specific heat ratio for the boundary layer was taken to be that after the incident shock, γ_2 , rather than γ_1 , the value in the undisturbed gas.

At the conditions of interest in our experiments, i. e. $4 < M_1 < 9$, significant real gas effects occur both across the incident and the reflected shock. The front leg of the bifurcated foot does not cause a significant change in the composition and it turns out that this shock can be calculated reasonably accurately by assuming γ_2 to be constant across it. The gas model allows for vibrational excitation according to the harmonic oscillator model, as well as dissociation, electronic excitation and ionization. The results of these calculations are discussed in a later section.

EXPERIMENT

The facility used in the experiments was the large free piston shock tube T3 at ANU. The driver gas in this device is heated by adiabatic compression with a heavy piston driven by compressed air. The temperature of the driver gas is continuously adjustable by choosing the initial pressure in front of and behind the piston and the diaphragm burst pressure. This provides the very convenient feature (not needed in the present experiments) that initial shock tube pressure p_1 and M_1 can be varied independently and continuously over wide ranges.

In the present experiments a sharp-nosed cookie cutter of square cross section (4.45 x 4.45 cm) and 36 cm length was fixed at the exit plane of the circular shock tube (7.6 cm diameter). The cookie cutter has window positions such that the reflected shock can be photographed at the end wall and approximately 2.5 and 4.5 test section heights from the end wall. The window diameter is approximately 6 cm, so that it overlaps top and bottom walls of

the cookie cutter.

One of the main difficulties of observing high speed shocks with window contact is that the high temperatures encountered, especially in reflected shock work, make it necessary to use a glass of low thermal expansion coefficient such as quartz or one of the new ceramic-glass mixtures used for high quality telescope mirrors. Since high pressures also occur, the windows also need to be very thick and thus they become very expensive. Moreover, the modern ceramic materials are poor in transmission and are therefore only useful where thin windows suffice. To avoid high cost, the windows were made by gluing a thin sheet (2 mm) of quartz onto a thick (60 mm) piece of Bk7 glass. Since the windows are only exposed to high temperatures for a short time this thin layer of quartz was sufficient to avoid excessive thermal stress, and the windows served their purpose very well. Windows with ceramic materials of a suitable thickness are now being constructed and were not available in time for our experiments. These would enable the Mach number to be increased considerably beyond our range.

The flow was observed by either a differential interferometer or a shadow-graph system, in which the light source was a dye laser pumped by a nitrogen laser. To avoid complicated alignment difficulties as well as to remove the troublesome spatial coherence of the light, the output of the dye laser was conducted to the focus of the input lens of the optical system by means of a glass fibre light conductor.

RESULTS

The experiments were conducted with a fixed driver condition at three different initial shock tube pressures in carbon dioxide and nitrogen and at a single condition in argon.

Testgas	M_1	p_1 (Torr.)	Reynolds No. Length = $d/2$
N_2	6.9 ± 0.3	10	2.5×10^5
	5.5 ± 0.3	20	3.9×10^5
	4.8 ± 0.3	40	6.7×10^5
CO_2	8.4 ± 0.4	5	6.5×10^5
	7.4 ± 0.4	10	9.0×10^5
	6.1 ± 0.4	20	1.2×10^6
Ar	7.5 ± 0.3	10	7.5×10^4

Table 1: Experimental Conditions

Table 1 lists the conditions of the experiments. The argon shots were chosen in such a way that no significant ionization occurs. The shot to shot variation is indicated in table 1 by the error in the Mach number. This caused considerable shot to shot variation particularly in the scale of the bifurcation. The angle α was affected to a much smaller extent.

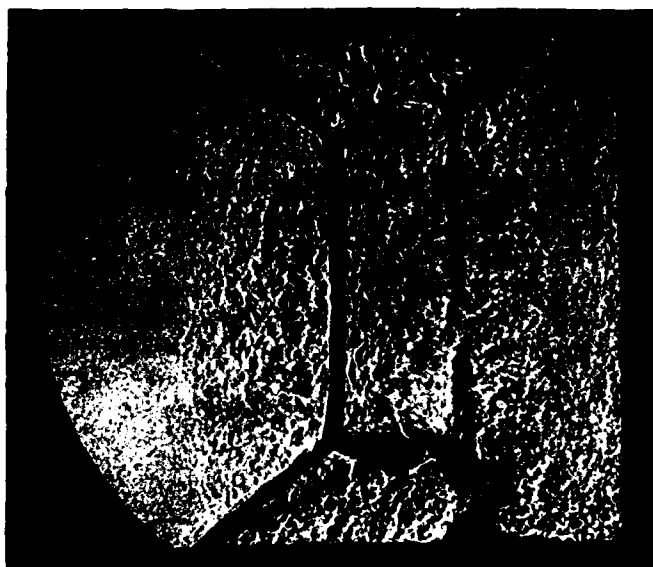


Fig. 2: Shadowgraph of bifurcated shock in CO_2 . $M_1 = 6.1$, $p_1 = 20$ Torr.,
 $x = 0.54 d$ (d = test section height).

Figure 2 shows a shadowgraph of the flow in carbon dioxide at a stage where the reflected shock is approximately half a test section height from the end of the square tube. Although the shock system is somewhat disturbed by the large scale turbulence behind it, the photograph shows clearly the bifurcation with long front leg, short rear leg, contact discontinuity, separation bubble and central normal shock. The bifurcation also occurs on the window, of course, so that the light that passes through the centre of the testsection in front of the reflected shock has to pass through the front leg of the bifurcation on both windows. This is the reason for the turbulent appearance of the flow in that region.

Figure 3 shows the calculated and measured values of the angle α . For nitrogen, vibrational relaxation behind the incident shock is slow, so that for $M_1 < 4$ the vibrational degrees of freedom may be expected to remain frozen. Relaxation effects may be expected to become significant, however, at least near the end wall when $4 < M_1 < 6$. Beyond $M_1 = 6$, the relaxation distance (at our density) becomes very small. The experimental results reflect this behaviour nicely, inasmuch as they drift from the calculated curve for vibrationally frozen incident, equilibrium reflected shock towards that for equilibrium incident and reflected shock as M_1 is increased. No change of α with distance from the end wall could be observed. This leads to the conclusion that α is only insignificantly affected by relaxation. The experimental values are averages over photographs taken at different axial positions in the tube.

Similar good agreement could not be observed in carbon dioxide. The experimental points lie very significantly above the equilibrium curve in figure 3, though at our conditions the vibrational relaxation lengths are very small, and

no significant dissociation occurs. With the strong bifurcation occurring in carbon dioxide, it may well be that the structure of the boundary layer, which is not accounted for by Mark's analysis, is important.

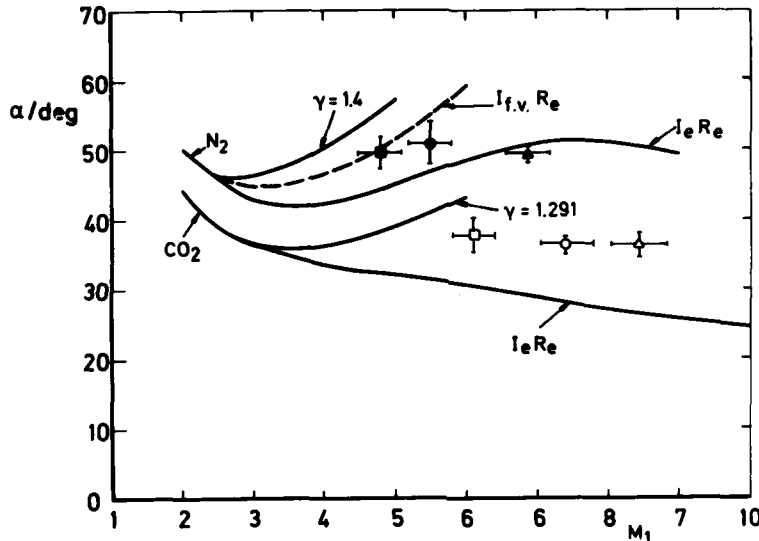


Fig. 3: Comparison of calculated and measured bifurcation angles. Notation: I - incident shock, R - reflected shock, e - equilibrium, f.v. - frozen vibration. Ideal gas curves are labelled with $\gamma = 1.4$ or 1.291 . $\blacksquare, \bullet, \blacktriangle$, - Nitrogen, $p_1 = 40, 20, 10$ Torr. $\square, \circ, \triangle$, - CO_2 , $p_1 = 20, 10, 5$ Torr.

The most interesting calculations were those made for argon. No calculations of α are possible because the criterion for bifurcation is not satisfied for $5 < M_1 < 12$. Bifurcation has been observed in argon by Kuiper and Bershader (1969) and by Takano et al. (1979), and its occurrence was explained by ionization after the reflected shock. Kuiper and Bershader also observed the onset of bifurcation to coincide with the passage of the reflected shock through the ionization front behind the incident shock. No bifurcation was observed in the ideal gas.

Although the real gas effects in the calculations for our experimental conditions were insignificantly small, definite evidence of separation can be observed in our experiments in argon. This is shown in figure 4b close to the end wall and figure 4a at 3 test section heights from the end wall. At this condition, the "boundary layer stagnation pressure" is $2.7 p_3$. Mark's model can therefore certainly not be considered adequate to describe this case.

Figures 5a and 5b show two shadowgraphs taken with nitrogen. 5b shows the reflected shock configuration close to the end wall and 5a shows it at 5 test section heights from the end wall. The most striking feature of figure 5a is the considerable asymmetry of the bifurcation. This is brought about by a slight wall roughness in the form of a triangular ripple on the upper wall of the test section. Small shocks can be seen to emanate from these ripples. This experiment was conducted in order to examine whether the scale of the bifurcation could be influenced by changing the character and the scale of the boundary layer encountered by the reflected shock. Clearly, this is the case. Results of a number of other experiments of this type are shown in figure 6 as

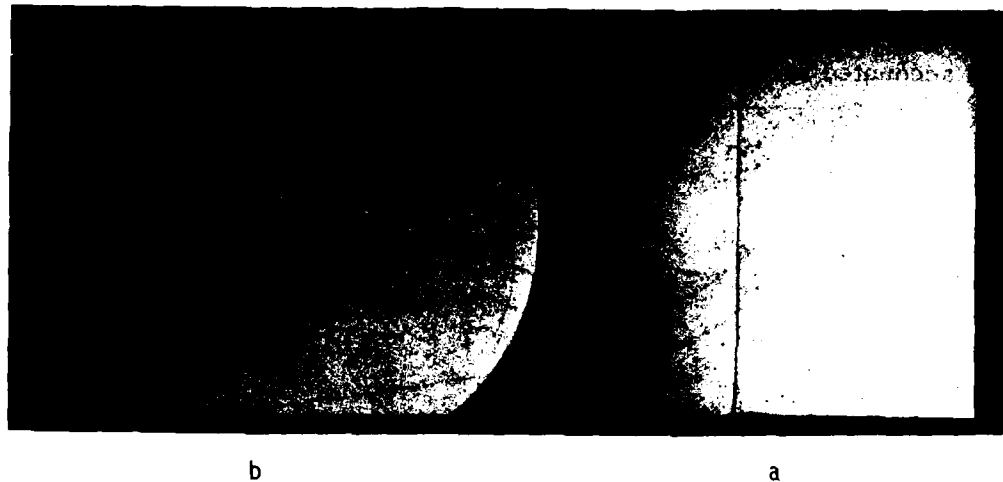


Fig. 4: Shadow graphs of reflected shock in ideal gas argon. $M_1 = 7.5$, $p_1 = 10$ Torr. a) $x/d = 0.61$, b) $x/d = 3.09$
Note clear evidence of boundary layer separation.

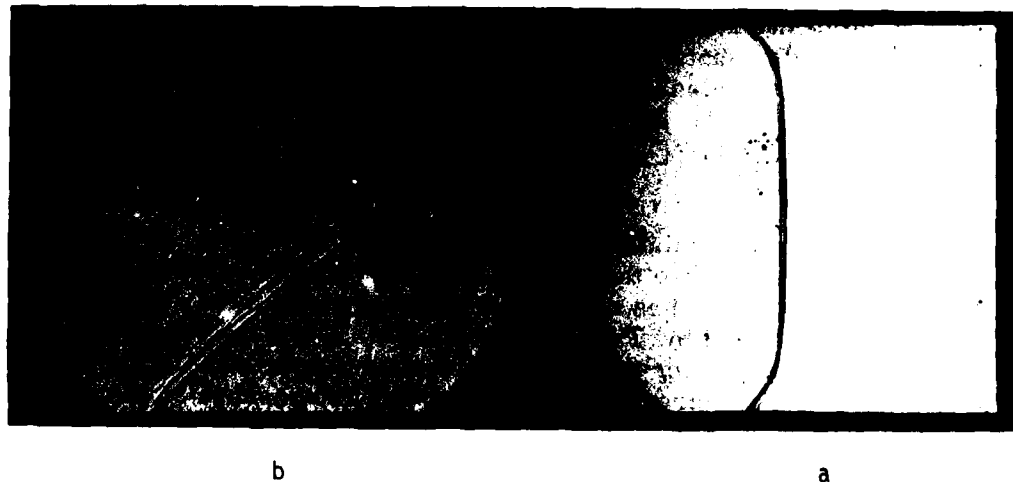


Fig. 5: Shadowgraphs of reflected shock in nitrogen.

$M_1 = 6.9$, $p_1 = 20$ Torr.

a) $x/d = 0.57$, smooth walls.

b) $x/d = 4.9$, lower wall roughened with triangular ripple, pitch and height 1.2 mm. Note asymmetry caused by roughness.

a plot of bifurcation size versus distance of the reflected shock from the end wall. This shows very clearly the initial growth and asymptotic constant value of h for the smooth wall, contrasting with the continued linear growth in the case of the rough wall.

Similar experiments in carbon dioxide show a different behaviour, see figure 7. Initially, the growth of the bifurcation on the rough wall is slower than on the smooth wall, but far from the wall, the rough wall bifurcation reaches an asymptotic value slightly larger than the smooth wall value. The growth is

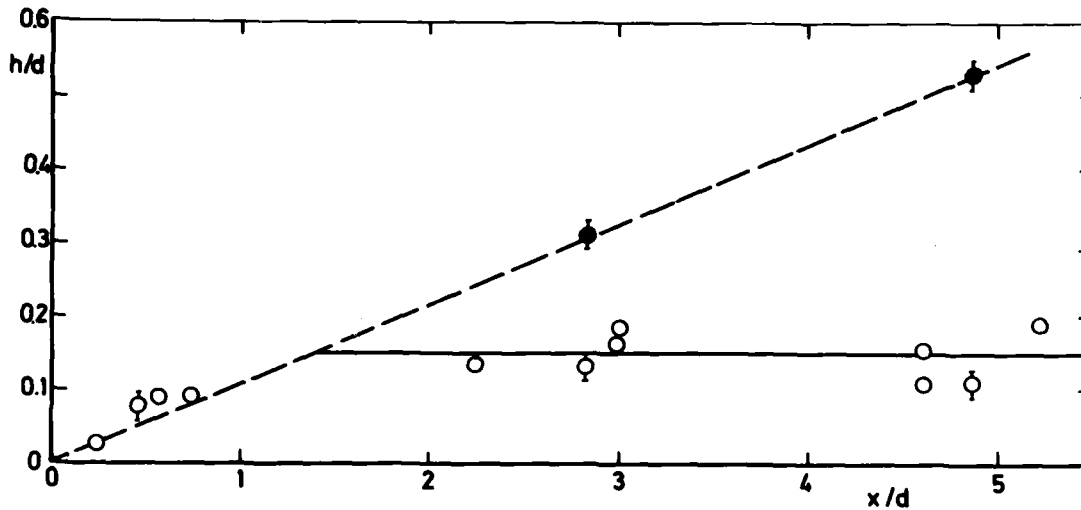


Fig. 6: Growth of bifurcation in nitrogen $M_1 = 6.9$, $p_1 = 20$ Torr.
O - smooth wall, ● - rough wall.

not linear in x . The evidence of these experiments seems to confirm the suggestion of Matsuo et al. (1974) that the asymptotic size of the bifurcation is proportional to a length scale pertaining to the boundary layer, but the mechanism which causes the change from the linear growth to a steady state is not clear.

CONCLUSIONS

1. Real gas effects modify reflected shock bifurcation significantly.
2. The simple model of Mark with real gas modification gives good predictions for bifurcation of intermediate strength (e.g. N_2).
3. For monatomic ideal gas, where theory predicts no bifurcation, definite evidence of it can be observed in our experiments.
4. Strongly bifurcating situations (e.g. CO_2) are poorly predicted by the Mark model.
5. Wall roughness can have a dramatic effect on the growth and asymptotic height of the bifurcation, but the mechanism of the transition from linear to small growth rate is not understood.

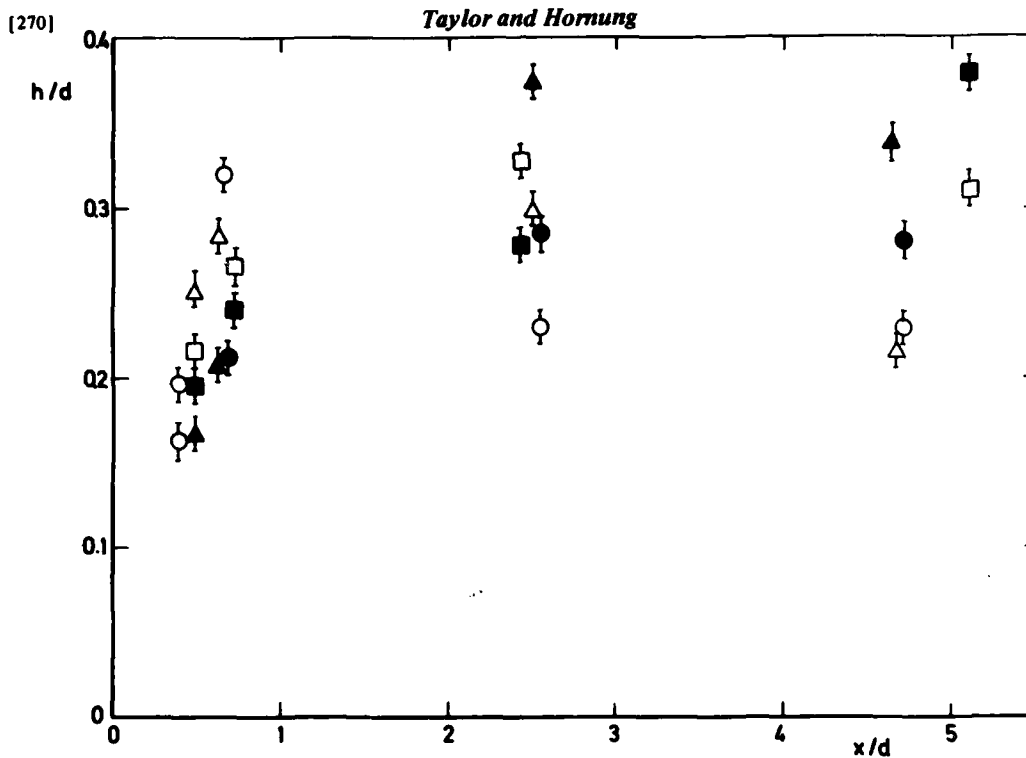


Fig. 7: Growth of bifurcation in carbon dioxide. \square , \circ , \triangle , - $p_1 = 20$, 10, 5 Torr., smooth wall. Filled symbols - rough wall.

ACKNOWLEDGEMENTS

The financial support of the Australian Research Grants Committee is gratefully acknowledged.

REFERENCES

- S. Byron and N. Rott (1961) Proceedings, 1961 Heat Transfer and Fluid Mechanics Institute.
- L. Davies and J. L. Wilson (1969) Phys. Fluids Supplement 13
- M. Honda, K. Takayama, O. Onodera and Y. Kohama (1975) Proceedings, 10th ISTS, Kyoto.
- R. A. Kuiper and D. Bershader (1969) AIAA J. 7
- H. Mark (1958) NACA TM 1418
- K. Matsuo, S. Kawagoe and K. Kage Bull. J.S.M.E. 17 no, 110.
- R. A. Strehlow and A. Cohen (1959) J. Chem. Phys. 30
- Y. Takano, S. Miyoshi and T. Akamatsu, (1979) Proceedings, 12th ISSTW, Jerusalem

AD P000250

DETERMINATION OF SHOCK TUBE BOUNDARY LAYER

PARAMETER UTILIZING FLOW MARKING

Th. Reese, F. Demmig, W. Böttcher

Institut für Plasmaphysik
Universität Hannover
Callinstr. 38, D-3000 Hannover, FRG

In shock tube flow a fluid particle is marked by laser-induced breakdown. The marking is detected about 15 cm downstream by a schlieren arrangement. The error in distance and time is less than 2 percent. The particle paths are influenced by both wall boundary layers and attenuation, the latter being known from a shock path measurement with high accuracy. Thus flow marking provides a method to check the shock tube boundary layer models and to determine the value of a parameter characterizing the mass loss term of the free stream. The marking measurements are compared with numerical computations of the nonequilibrium flow starting from the actual shock path. If the flow is marked in the initial zone where the influence of chemical reactions on the flow velocity is negligible simple analytic formulae can be used instead. For our shock tube with $5.2 \times 5.2 \text{ cm}^2$ cross section we find that the parameter K of Yu. A. Dem'yanov has to be enlarged by a factor of 1.8, the error being 15 percent. In chemical kinetics studies this enlargement clearly has a considerable influence on the reaction rates. Measuring the particle path, flow marking appears to be the most reliable method to determine the boundary layer parameter.

INTRODUCTION

As is well known, chemical kinetics in shock tube flow is influenced by boundary layers and flow non-uniformity. As a consequence, the temperature is substantially different from its ideal value, a situation which all the more applies to the reaction rates. While the variation of the shock velocity can be measured with high accuracy by recording the passage time of the shock front at several laser beams (see fig. 1) one usually has to resort to theoretical predictions of the influence of boundary layers.

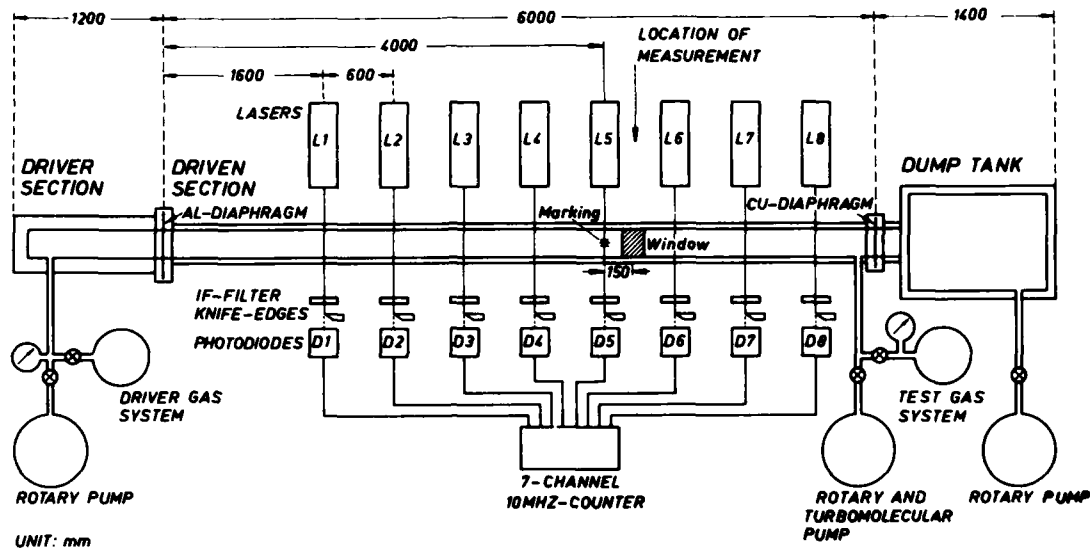


Fig. 1 - Schematic of the shock tube and the arrangement for shock speed measurement and flow marking. L 1 through L 6 are the lasers monitoring the shock front passage. The fluid particle is marked at the position of L 5 and is detected by a schlieren photograph through the window 15 cm downstream (see also fig. 2).

In the case of laminar boundary layers the commonly used similarity model (e. g. refs. 1-8) yields the familiar square root dependence of the boundary layer thickness on the distance to the shock front. The effect of the boundary layers on the free stream can be represented by a mass loss term at the right hand side of the continuity equation

$$\frac{D\rho}{Dt} + \rho \frac{\partial u}{\partial x} = R = -\beta \rho u (dRe[x_s - x])^{-1/2}, \quad (1)$$

where ρ , u , d , Re , and x_s are the density, flow velocity, shock tube diameter, Reynolds number, and shock front coordinate, respectively. β is a numerical parameter slightly different in value for different theories. For atomic gases Yu. A. Dem'yanov¹ gives $\beta = 2.72$ while P. J. Musgrove and J. P. Appleton² find $\beta = 2.94$. Following H. Mirels^{3,4}, a steady free stream is often represented by its quasi one-dimensional analogue (varying cross section).

To take into account the influence of boundary layers on the history of a fluid particle we used the mass loss term R of equation (1) with the value of β still to be determined. This seems to be a reasonable assumption since several authors^{9,10,11} came to the conclusion that more realistic boundary layer flows than the original equilibrium flow nevertheless could be approximated quite well by a similarity law as far as gas density and velocity are concerned. The influence of shock attenuation is fully accounted for by measuring the shock path with a laser beam deflection method.

Our investigations in ionization relaxation showed that the effect of boundary layers is larger^{12,13} than given e. g. by Yu. A. Dem'yanov¹ (H. Mirels^{3,4} theory does not apply since maximum plug length is not attained). This is not surprising because the similarity model is based on idealized assumptions as for instance a circular cross section of the shock tube with a large diameter and non-ionized boundary layers. Since the enlargement of the parameter β was inferred mainly from comparison of computed electron density profiles with n_e -values measured in the relaxation zone of shock waves, we wanted to control this finding by a direct measurement.

To this purpose, we marked a fluid particle by a laser-induced gas breakdown and detected this small cloud of excess ionization some ten centimeters downstream by a schlieren arrangement. The result is a value of the mean flow velocity. In case the experiment is performed entirely within the initial relaxation zone (heat bath region) it can be evaluated utilizing an approximate formula for the particle path to yield the value of the boundary layer parameter β . Otherwise numerical computations^{12,13} of the unsteady flow under the influence of the boundary layers represented by equation (1) have to be carried out.

APPROXIMATE FORMULA FOR PARTICLE PATHS UNDER THE INFLUENCE OF BOUNDARY LAYERS AND SHOCK ATTENUATION

In order to determine the boundary layer parameter β of equ. (1) by flow marking one has to calculate particle paths. In principle, this has to be done by numerical computation since the unsteady non-equilibrium flow equations comprising the rate equations^{12,13} are far too complicated to have solutions in closed form. If, however, the marking point * and the detection point \odot (see fig. 2) are within the initial relaxation zone where the influence of the chemical reactions on the flow is negligible simple approximate formulae can be used instead. For ionization relaxation in krypton this heat bath region extends to ionization degrees of some 10^{-3} , that is to about one third of the relaxation time for Mach 10 shock waves.

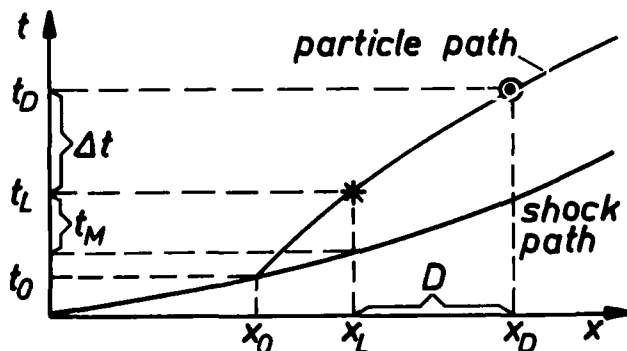


Fig. 2 - x-t-diagram of flow marking (curvature exaggerated)
 *, marking by laser-induced breakdown
 \odot , detection of marked fluid particle.

In the approximate formula (3) the coordinate x is given as a function of the particle time

$$\tau = t - t_0, \quad (2)$$

which is the time elapsed from the instant the particle entered the shock front at the point x_0 (see fig. 2). Mathematically speaking this function is not analytic since the expansion does

not proceed in integer powers of τ , which is due to the structure of the boundary layer term R of equ. (1),

$$x = x_0 + u_0 \tau + \frac{2}{3} A_1 \tilde{\beta} \tau^{3/2} + \frac{1}{2} (A_2 \tilde{\beta}^2 + A_3 \tilde{\alpha}) \tau^2 \quad (3)^\dagger$$

u_0 denotes the flow velocity at the point (x_0, t_0) of entry and has to be calculated by means of the Rankine-Hugoniot relations from the shock velocity u_{s_0} at this point. The shock velocity is determined from the shock path which in turn is based on the passage times of the shock front at eight laser beams (see fig. 1). For the evaluation of flow marking experiments it is sufficient to find a local parabola passing through the laser deflection stations L 4, L 5, and L 6, and to determine the value of a local attenuation coefficient $\tilde{\alpha} = (du_s/dx)/u_s$, measuring the instationarity of the shock path. The influence of the boundary layers is represented by the parameter

$$\tilde{\beta} = \frac{\beta}{\sqrt{dRe}} \quad (4)$$

which is part of the mass loss term in equ. (1).

The coefficients A_1 , A_2 , and A_3 have to be calculated from u_0 , u_{s_0} , the density ρ_0 , and the sound speed a_0 at the entering point (Rankine-Hugoniot values),

$$A_1 = (u_{s_0} - u_0)^{1/2} A \quad \text{with} \quad A = \frac{4}{\kappa+1} \frac{a_0^2}{u_{s_0} - u_0} \quad (5)$$

$$A_2 = 3 \frac{\kappa-1}{\kappa+1} a_0^2 + \frac{1}{6} \left(1 - 3 \frac{u_{s_0}}{u_0} \right) A^2 \quad (6)$$

$$A_3 = \frac{1}{\kappa+1} \frac{u_{s_0}^2}{u_0} \left(A \frac{u_{s_0}^2 + a_1^2}{u_{s_0}^2} + \frac{8\rho_1}{\kappa+1} \frac{u_{s_0}}{\rho_0} \right) \quad (7)$$

$\kappa = c_p/c_v$ denotes the ratio of specific heats, ρ_1 and a_1 are the density and the sound speed ahead of the shock.

Our method to determine the boundary layer parameter β by flow marking can now be made clear; marking * and detecting \odot means to fix two (x,t) -positions of a fluid particle on its path (see fig. 2). Each position has to fulfill the equ. (3) for the particle path. The corresponding two equations serve to determine the following two unknowns,

- 1) the time t_0 of shock front entry,
- 2) the boundary layer parameter $\beta = \sqrt{dRe} \tilde{\beta}$.

This approach is in a sense complementary to that of refs. 15 through 17 where the shock path is predicted by an ab initio calculation of the shock tube flow. For vanishing boundary layers ($\tilde{\beta} = 0$; only shock attenuation) equation (3) is in conformity with the shock expansion theory of H. Mirels⁴ and also with the corre-

[†] Details of the derivation and related physical quantities will be published elsewhere⁴.

AD-A122 200

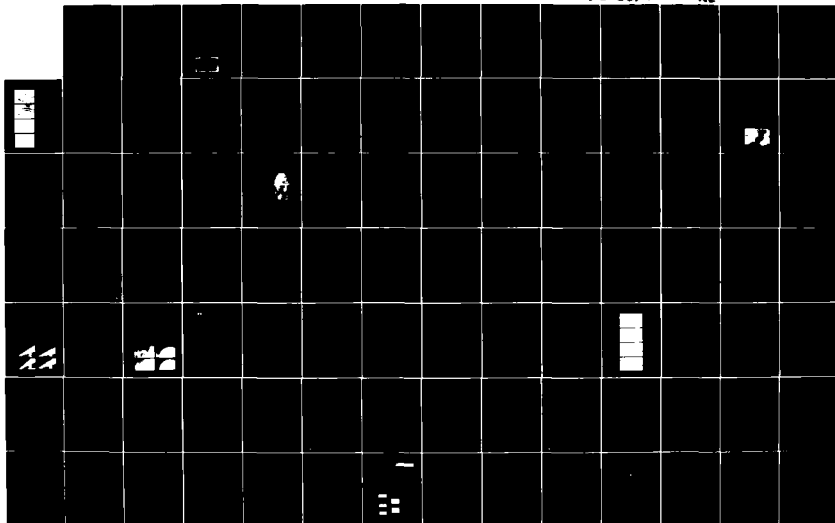
PROCEEDINGS OF THE INTERNATIONAL SYMPOSIUM ON SHOCK
TUBES AND WAVES (13TH. (U) CALSPAN ADVANCED TECHNOLOGY
CENTER BUFFALO NY C E TREANOR ET AL. JUL 81
AFOSR-TR-82-1031 F49629-81-C-0002

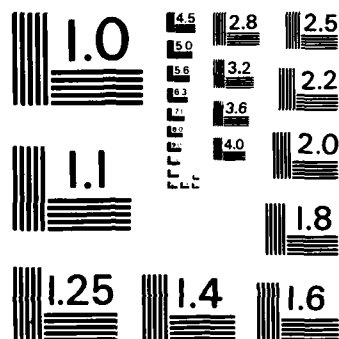
4/10

UNCLASSIFIED

F/O 20/1

NL





MICROCOPY RESOLUTION TEST CHART
NATIONAL BUREAU OF STANDARDS-1963-A

sponding exquations of P.C.T. de Boer and J.A. Miller⁶. Since H. Mirels' boundary layer expressions apply to the case of constant plug length only, which we do not assume, merely asymptotic agreement can be stated.

PRINCIPLE OF MEASUREMENT

In the shock tube plug a fluid particle is marked by a laser-induced gas breakdown. The resulting small cloud of excess ionization travels with the flow and can be made visible by a schlieren arrangement some tube diameters downstream due to the change in the refraction index. The flow is marked at the station x_L at the time t_L (see fig. 2). At time $t_D = t_L + \Delta t$ the marked fluid particle is detected at a distance D downstream at the station x_D by a schlieren photograph (compare fig. 3, too). The particle path between these two stations cannot be visualized. As has been shown in the preceding paragraph, however, two points of the particle path are sufficient to determine the boundary layer parameter.

By varying the time t_M relative to the passage time of the shock front at x_L the flow can be marked at arbitrary distances behind the front. In this way mean values $\bar{u} = D/\Delta t$ of the flow velocity can be measured at different parts of the plug. For steady shock waves one should be able to check the limitation of the similarity assumption for the boundary layers, too.

FLOW MARKING IN SHOCK TUBES

The shock waves are generated in a hydrogen-driven diaphragm shock tube of 6 m length and a quadratic cross section of $52 \times 52 \text{ mm}^2$ (see fig. 1). Before filling it with test gas it is evacuated to a rest gas pressure of about $6 \cdot 10^{-6}$ Torr.

The shock path is measured by a laser beam deflection method. Eight equidistant beams of He-Ne lasers cross the shock tube perpendicular to the flow direction and will only illuminate the photodiodes if the beam is deflected by the shock front passing. The amplified signals of the diodes start and stop a 7-channel 10 MHz counter, displaying the times Δt_i between two successive pulses. The maximum error in the determination of a single time interval is $\pm 0.2 \%$. The distance between two laser beams can be determined with an error $\leq 0.1 \%$.

For our numerical computations of the ionization relaxation^{12,13} we fit a polynomial to these data, since for relaxation times of about 100 μs values of the shock velocity enter the computation belonging to a running distance of about 2 m. Usually a polynomial of degree 3 or 2 gives the best fit, as might have been expected, because the shock front first accelerates due to the finite opening time of the diaphragm and then decelerates due to friction. For the evaluation of flow marking experiments, being locally confined, however, we use a parabolic interpolation between the laser stations L 4, L 5, and L 6 (see fig. 1). The error of the shock speed is $\pm 0.3 \%$, its attenuation coefficient $\tilde{\alpha}$ is typically $2 - 3 \%$ m^{-1} .

As has been mentioned in the previous paragraph the flow marking is achieved by a gas breakdown which is generated at the shock tube axis by focussing the radiation of a q-switched 100 MW ruby laser (see fig. 3). Part of the laser light illuminates a photodiode which starts a 10 MHz counter. The counter is stopped by the

signal of another photodiode which detects part of the light emitted by a second q-switched ruby laser. This laser is the background light source of a sensitive schlieren arrangement by means of which the marked volume is photographed about 15 cm downstream of the breakdown. The two laser pulses have a half width time of 30 ns.

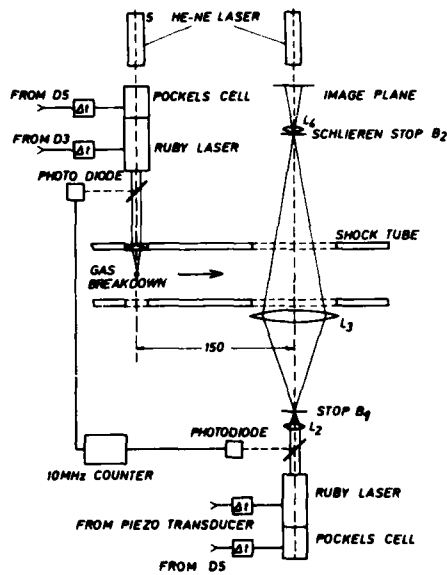


Fig. 3 - Shock tube section with marking by laser-induced gas break down and detection of marked fluid particle by a schlieren arrangement. For the location of the shock tube section see fig. 1.

Measured data are the time Δt between the two laser pulses and the distance D covered by the marked fluid particle which is obtained from the schlieren photo (see fig. 4). The maximum error for Δt is about $\pm 0.5\%$ while D is measured with an error of about $\pm 2\%$. The investigations were carried out with krypton at a test gas pressure of 10 through 20 Torr and Mach numbers of 8 through 11. In a series of measurements the flow was marked at labtimes t_m ranging from 6 to 250 μs (see fig. 2). Only in case the flow is marked near the shock front the latter will be photographed together with the marked fluid particle, as is shown in fig. 4.

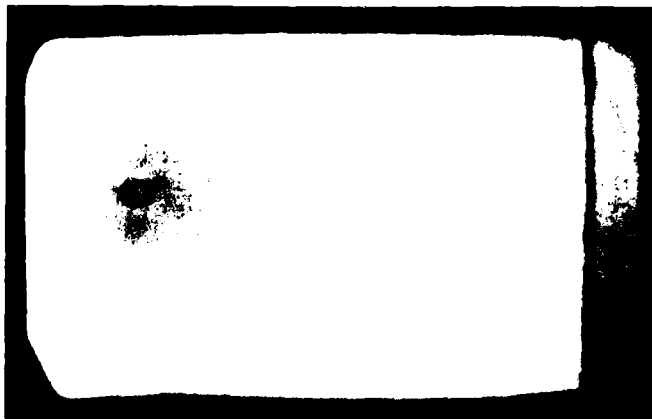


Fig. 4 - Schlieren photograph of the shock tube flow behind the shock front which is to be seen as a narrow line. The schlieren image of the marked fluid particle is on the left hand side.

RESULTS

Fig. 5 gives an overview of ten successive marking experiments with test gas pressure of 12.0 Torr (numbers 1532 through 1541). The Mach number M_s at the station x_L of the marking laser varied only by $\pm 0.5\%$. The diagram shows the measured mean flow velocity $\bar{u} = D/\Delta t$ normalized to the shock velocity u_s vs. the time t_M elapsed between shock front passage and marking at the station x_L (compare fig. 2). For comparison the broken line indicates the normalized value of the flow velocity u_2 immediately behind the shock, calculated by means of the Rankine-Hugoniot relations. Clearly, the flow velocity deviates substantially from the value it would have without the influence of boundary layers and shock attenuation.

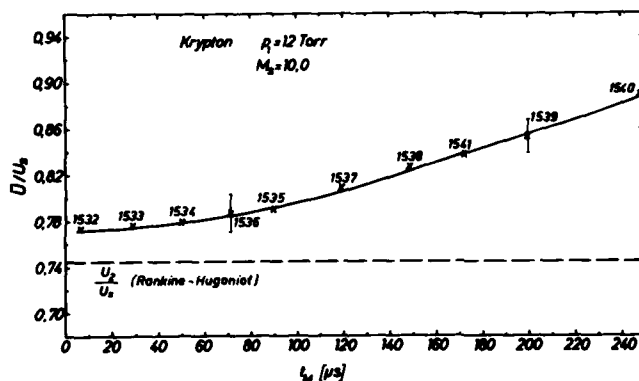


Fig. 5 - Measured values of the normalized mean flow velocity \bar{u}/u_s vs. time t_M after shock front passage. Plotted are 10 successive experiments, all at test gas pressure of 12 Torr and practically equal Mach number 10.0 at laser 5. For comparison, the broken line gives the normalized flow velocity immediately behind the shock front.

This deviation is large for marking experiments far off the shock front and tends to a constant value for marking near the shock front. The reason therefore is that the mean velocity is determined over approximately the same time interval Δt of about 80 μs for all shots. If it were possible to mark the flow immediately behind the shock front the resulting asymptotic mean velocity would be $\frac{1}{2} \{u_2 + u(\Delta t)\} > u_2$ since $u(\Delta t) > u_2$ due to boundary layer influence.

Because we measure mean velocities and the flow is unsteady the upper curve of fig. 5 cannot be viewed as the velocity graph of one fluid particle. For the evaluation of a marking experiment one has to determine the time t_0 at which the marked fluid particle originally entered the shock front (see fig. 2). One can imagine that even this partial result depends on the curvature of the shock path, i. e. the attenuation. For experiments within the heat bath region of the flow the evaluation can be carried out with equation (3) for the particle path (compare second paragraph). If the experiment extends to a region where the chemical reactions have a marked influence on the flow velocity numerical computations of the non-equilibrium flow with different values of the boundary layer parameter β have to be performed, instead. Since the shock path is already determined the value of β is varied in order to find a particle path through the points *

and © of fig. 2. For the details of the numerical computation of ionization relaxation see refs. 12 and 13; radiation cooling is now accounted for, too¹⁸.

The present measurements allow the conclusion that in a shock tube of conventional surface quality the actual boundary layers are thicker than predicted by existing similarity models. For our shock tube we find a value of the boundary layer parameter β of 4.8, the error being 15 per cent. This finding agrees with a conclusion we draw from relaxation measurements in shock heated krypton. In order to achieve agreement between model computations and measured values of e. g. the electron density a boundary layer parameter of about the same value had to be taken. The corresponding theoretical value of Yu. A. Dem'yanov¹ is $\beta = 2.72$, i. e. smaller by a factor of 1.8. P. J. Musgrove and J. P. Appleton² use a different velocity profile and predict $\beta = 2.94$ which is smaller by a factor of 1.6. - Experiments which extend to a larger range of parameters are in preparation.

CONCLUDING REMARKS

Possible reasons for the stronger influence of the shock tube boundary layers on the free stream may be the uneven surface of the tube wall and the remaining small irregularities of the tube ($< 50 \mu\text{m}$) due to the windows. Also, the similarity model of the boundary layers is based on idealized assumptions as for instance a circular cross section of the shock tube with large diameter, equilibrium and steady flow.

The side wall boundary layers of a shock tube can be determined under unsteady non-equilibrium conditions by taking into account also plasma processes. The drawbacks of wall irregularities, a quadratic cross section (well suited for diagnostics), residual gas, impurities, and a possibly curved shock front etc., however, cannot be overcome totally and limit the accuracy with which the free stream properties can be predicted. Therefore, it seems to be appropriate to accept the form (3) of the mass loss term as a practical approximation and to use a tube specific value of the boundary layer parameter.

ACKNOWLEDGEMENT

We would like to thank the members of the shock tube group of our institute for numerous discussions.

REFERENCES

1. Yu. A. Dem'yanov, R. A. E. Library translation No. 796 (1959).
2. P. J. Musgrove and J. P. Appleton, Appl. Sci. Research 18, 116 (1967).
3. H. Mirels, Phys. Fluids 9, 1907 (1966).
4. H. Mirels, Proceedings of the 8th International Shock Tube Symposium, Lecture 6 (1971).
5. Y. Enomoto, J. Phys. Soc. Jap. 35, 1228 (1973).
6. P. C. T. de Boer and J. A. Miller, Proceedings of the 10th International Shock Tube Symposium, p. 796 (1975).
7. H. Ezumi et al., J. Phys. Soc. Jap. 43, 1060 (1977).
8. S. P. Vaguin et al., Rev. Phys. Appliqu., 399 (1978).

9. G. Smeets and A. George, Proceedings of the 9th International Shock Tube Symposium, p. 429 (1973).
10. J. J. Bertin et al., Proceedings of the 10th International Shock Tube Symposium, p. 595 (1975).
11. W. S. Liu and I. I. Glass, J. Fluid Mech. 91, 679 (1979).
12. F. Demmig, Proceedings of the 11th International Shock Tube Symposium, p. 119 (1977).
13. R. R. Ritter and F. Demmig, Computer Phys. Commun. 18, 205 (1979).
14. F. Demmig, J. Meissner, and M. Einsel, to be published.
15. L. Z. Dumitrescu et al., Proceedings of the 9th International Shock Tube Symposium, p. 439 (1973).
16. R. Brun and M. Imbert, Proceedings of the 10th International Shock Tube Symposium, p. 415 (1975).
17. D. Zeitoun et al., Proceedings of the 12th International Symposium on Shock Tubes and Waves, p. 180 (1979).
18. D. Krauss and F. Demmig, to be published.

AD P000251

STABILITY LIMITS AND TRANSITION TIMES OF WAVE-
INDUCED WALL BOUNDARY LAYERS

Yehia M. Amr

Heat Transfer Group, Research Division
Carrier Corporation, Syracuse, NY 13221

J. Gordon Hall

Dept. of Mechanical and Aerospace Engineering
State University of New York at Buffalo, Amherst, NY 14260

The study concerns theoretical analysis of stability and experimental investigation of transition for laminar wall boundary layers developed within plane expansion waves and behind shock waves traveling into gas at rest. The stability analyses involved approximate methods for critical stability Reynolds numbers, numerical integration of the Orr-Sommerfeld equation, and a multiple-scales perturbation technique for unsteady boundary layers. In the experiments several techniques were used to detect transition. Expansion-wave transition times measured are typically five times larger than reported by previous investigators. Shock-wave transition times are generally in close agreement with previous results. Most of the transition times are less than critical stability values from linear theory.

1. Introduction

Transition time data for the shock-wave boundary layer have been obtained by a number of previous investigators (e.g. 1-5). All shock-wave transition Reynolds numbers of past investigations are below the critical stability values calculated by Ostrach and Thornton (6) from linear stability analysis. Boundary layer transition within the expansion wave (Fig. 1) has apparently been previously studied by only two investigators (1,7). Chabai (1) used thin-film surface thermometers and Mack (7) used an interferometer to detect transition. Transition times measured could not be correlated with any particular Reynolds number.

The present paper presents experimental results for expansion-wave and shock-wave boundary-layer transition obtained using thin-film surface thermometers, surface hot-film anemometers, and a hot-wire anemometer within the boundary layer. Also presented are results of a stability analysis of the expansion-wave boundary layer.

A more detailed account of the work is given in Ref. 8.

2. Stability Analysis of Expansion-Wave Boundary Layer

The expansion-wave wall boundary-layer is assumed to be a thin, laminar, two-dimensional, unsteady, compressible, perfect-gas boundary layer developed within an ideal centered expansion wave which is plane and isentropic. Previous theoretical analyses (9-13) and experiments (1,12,13) confirm this base-flow model except for non-centered wave effects (11-13) herein neglected. The inviscid perfect-gas flow then depends only on the similarity variable $S = 1 + (x/a_0 t)$ where a_0 is the sound speed of the initial gas at rest (Fig. 1). For conditions considered the wall temperature change is very small and can be neglected (10). The mean boundary-layer flow is then described in terms of S and a normal similarity coordinate η defined by

$$\eta = (v_0 \tau)^{-1/2} \int (\rho/\rho_0) dy$$

where $v = \mu/\rho$ is kinematic viscosity, $\tau = St$ is the time after wavehead arrival at station x , and y is normal distance from the wall. Solutions for streamwise velocity u (along x) and temperature T in the boundary layer are given in Refs. 9, 10, and 13.

The preceding base flow model is inherently unsteady as well as nonparallel in space. The usual approach to stability analyses of such unsteady flow is to assume the stability is quasi-steady, i.e. that the disturbance field depends only on the instantaneous velocity profile etc. of the mean flow and not on the mean flow time derivatives. This requires disturbance characteristics times to be much smaller than the time characterizing changes of the mean flow. It is shown (8) that the expansion-wave boundary layer is near quasi-steady for stability over a wide range of conditions. Accordingly, the present stability analyses mainly assumed a quasi-steady, quasi-parallel (QSQP) model.

Close to the expansion wavehead S is small (S increases from 0 at the wavehead to 1 at $x = 0$) and the flow is essentially incompressible. Assuming a two-dimensional Tollmien-Schlichting disturbance field the governing equation for the linear stability of this QSQP model is then the classical Orr-Sommerfeld equation (8,14). The associated eigenvalue problem was solved numerically (8) to obtain the neutral stability curve for $S = 0$, i.e., at the expansion wavehead. The boundary-layer in this case is identical to the initial boundary layer on a semi-infinite flat plate undergoing constant acceleration from rest. The mean velocity profile at $S = 0$ is given by (10)

$$\frac{u}{u_e} = 1 - \left(1 + \frac{\eta^2}{2}\right) \operatorname{erfc} \left(\frac{\eta}{\sqrt{2}}\right) + \frac{\eta}{\sqrt{\pi}} e^{-\frac{\eta^2}{4}}.$$

The numerical method used (8) integrated inward from outside the boundary layer to the wall, and orthonormalization was necessary. Neutral stability eigenvalues were calculated for chosen values of $Re_{\delta^*} = u_e \delta^*/\nu_e$ where δ^* is the local displacement thickness and subscript e denotes local inviscid flow conditions. The resulting neutral stability curve is shown in Fig. 2. The critical or minimum Reynolds number Re_{δ^*cr} for stability is found to be 25,488.

Obtaining the entire neutral stability curve is unnecessary if only Re_{δ^*cr} is required. For Re_{δ^*cr} only, an approximate method

developed by Lees (15) for compressible boundary layer flows was used (8) for the QSQP model. Figure 3 shows the calculated variation of critical Reynolds number $Re_{\theta_{cr}}$ based on momentum thickness θ with similarity variable S . For $S = 0$, Lees' method gives $Re_{\theta_{cr}} = 26609$, $k_{cr} = .4039$ and $\omega_{cr} = .0728$. These values compare well with the numerical Orr-Sommerfeld values of $Re_{\theta_{cr}} = 25,488$, $k_{cr} = .4022$ and $\omega_{cr} = .0773$ (k and ω are dimensionless wave-number and angular frequency eigenvalues).

The preceding stability analyses assume a QSQP base flow. The nature of the expansion-wave boundary layer permits perturbation to obtain more accurate results for small departures from the limiting QSQP model (8). The method used (8) extends the method of multiple scales used in Ref. 16 to account for spatial non-parallel effects. In the present study both slow time and streamwise space variations of the mean flow are included. Numerical application of the analysis is presently underway.

3. Experimental Apparatus and Program

The apparatus used is a 1.5 x 5 inch internal cross-section tube sealed by a diaphragm from the surrounding room air. For expansion waves the tube was pressurized above atmospheric or room pressure. In this case the tube flow discharged to the room, usually through a sonic-flow orifice plate. For shock waves the tube was partially evacuated and functioned like a shock tube of infinite area ratio with a driver pressure of one atmosphere. All experiments used dry bottled air. The tube walls are steel, Kanogen nickel plated, and relatively massive to minimize transient vibrations (wall thickness 5/8 inch). The interior surface roughness is less than 20 μ -inch rms. The transition experiments were done using the boundary layer developed on the 5-inch sidewalls of a special 4-foot test section having 3.5 ft of polished surface free of any inserts or steps.

Transition was detected mainly with surface or flush mounted hot-film anemometers (Disa 55A90) consisting of a nickel film on the plane end surface of a .187-inch diameter quartz rod. Confirming transition data were obtained with a hot wire (Thermal Systems Inc.) immersed in the boundary layer. The surface hot-film anemometer was found to give a much more sensitive indication of transition for expansion-wave flows than a surface thin-film resistance thermometer. Local surface static pressures were measured with Kistler 603A piezoelectric transducers. The transition instrumentation was located within 6 inches of one end of the 4-foot test section. One 5-inch sidewall contained two hot films, flush mounted in .187-inch diameter holes, with one film mounted 1.75 inches off the centerline (.75 inches from the corner) to observe possible corner effects or transverse variations of transition. The opposite wall contained a 2-inch diameter plug, machine ground and plated in position, which carried the hot wire probe on the wall centerline.

For the expansion-wave boundary layer, transition times were obtained at distances of 2.17, 4.60, and 8.17 feet from the diaphragm over a range of initial air pressure p_0 from 35 to 145 psi. For the shock-wave boundary layer, transition times were measured at 7.5 feet from the diaphragm over a range of p_0 from 1 to 7 psi.

4. Experimental Transition Results for Expansion-Wave Flow

Figure 4 shows typical oscilloscope recording of outputs from the flush hot-film anemometer (FHFA) on the wall centerline and the hot-wire anemometer (HWA) located at $y = .022$ inches from the opposite wall centerline for the expansion-wave boundary-layer flow at 4.6 ft from the diaphragm. The initially smooth hot-film output undergoes a large and near step-like increase when transition occurs because it essentially responds to the local surface shear stress or skin friction (8). Following this step-like increase the initially smooth hot-film trace has a pronounced random fluctuation indicative of turbulent flow. Coincident with the sharp increase in the hot-film output at transition, the hot-wire output decreases, which is attributed to a reduced local mean velocity due to sudden thickening of the boundary layer on transition. The two transition times (obtained on opposite walls) are obviously in very close agreement, which was typical.

Figure 5 shows oscilloscope recording of outputs from the two flush hot-film anemometer probes, one located on the wall centerline and the other .75 inches from the corner, for the expansion-wave flow at 8.17 feet from the diaphragm. Transition occurs earlier at the corner probe location. This behavior was typical at the higher pressures used (p_0). At the lower pressures, both probes indicated essentially the same transition times. The reason for this transverse difference in transition times at higher pressures is not understood, but it is noted that the 1.5-inch top and bottom walls of the test section are significantly rougher than the polished 5-inch sidewalls.

Another feature of the corner probe is that at certain conditions it showed early transition followed by relaminarization before indicating permanent transition to turbulent flow. This behavior, which was generally not observed on the wall centerline, is illustrated in the record of Fig. 6. The occurrence of this turbulent "slug" followed by laminar flow was very reproducible. It occurred only at intermediate pressures, depending on the x location, and the second laminar region rapidly shrank and disappeared as the pressure level was increased.

Table I gives typical measured transition times for the expansion-wave boundary layer obtained from the centerline and corner hot-film probes. Occurrence of the relaminarization phenomenon is so noted. The observed transition times increase with distance x_s from the diaphragm and decrease with increasing initial pressure p_0 . The particle path lengths to transition for most of the experiments are less than the 3.5 feet of clear polished surface of the test section. The transition times at $x_s = 4.6$ feet are almost constant for $p_0 < 55$ psi. This is possibly due to the particle path length for "natural" transition being larger than 3.5 feet for these conditions, and transition thus possibly being initiated by the inevitable small step or discontinuity at the junction of the test section and the adjoining tube section (all such steps at section junctions were less than .002 inch). For $x_s = 8.17$ feet and $p_0 < 92$ psi transition did not occur until shortly after the reflected wave had reached the probe station. In general, the transition times observed are about five times greater than those reported in Ref. 1 for nitrogen.

Figure 8 illustrates the expansion wave transition data for the wall centerline in terms of local Reynolds number $Re_{\delta_*} = u_e \delta_* / \nu_e$

at transition versus similarity variable S . The calculated critical stability curve for Re_{δ^*CR} (from Fig. 3) is also shown. Most of the experimental points lie below the stability curve and tend to show an opposite trend with S .

5. Experimental Transition Results for Shock-Wave Flow

The shock-wave boundary-layer experiments were limited to weak shocks and were done primarily for comparison with previous studies as a basic check on the experimental technique and apparatus. The oscilloscope record of Fig. 7 shows outputs from the two hot-film probes at 7.5 feet from the diaphragm for a shock Mach number of 1.18. Transition is identified as the second steplike increase (the center probe also shows a brief early transition and relaminarization in this record). It will be noted that the corner probe in this case indicates a later transition than the centerline probe. This behavior was typical, and is just the opposite of what was observed for expansion-wave flow. The present centerline data and those of previous investigators are summarized in Fig. 9 which shows transition Reynolds number Re_{xTR} as a function of T_w/T_e = wall to free stream temperature ratio. Re_{xTR} is based on the distance of transition from the shock wave and on local inviscid velocity and kinematic viscosity, the velocity being that for shock-fixed coordinates. The critical stability curve for Re_{xCR} (Ref. 6) is also shown. Most of the data fall below the stability curve. The present data agree rather closely with the results of Thompson and Emrich (5) and tend to show the opposite trend of Re_{xTR} with T_w/T_e than indicated by the stability limit.

6. Concluding Remarks

The present study has analyzed theoretically the linear stability of the expansion-wave boundary layer and experimentally determined transition occurrence in both expansion-wave and shock-wave boundary layers. Transition times measured for the expansion-wave flow are much greater than values reported by previous investigators. However, most of the transition times are still less than the calculated critical stability limit. The present shock-wave transition data are in close agreement with previous data of Thompson and Emrich (5), but mostly the transition Reynolds numbers are again less than the calculated stability limit. For both shock and expansion-wave boundary layers it thus appears that transition is determined by effects or mechanisms not accounted for in the linear stability analyses which have been done.

7. References

1. Chabai, A.J.; Inst. of Res. Tech. Rpt. 12 and Ph.D. Thesis, Lehigh Univ. 1958.
2. Gooderum, P.B.; NACA TN 4243, 1958.
3. Asbridge, J.R.; Inst. of Res. Tech. Rpt. 14, Lehigh Univ. 1959.
4. Hartunian, R.A. et al.; J. Aerosp. Sci. 27, 587, 1960.
5. Thompson, W.P. and Emrich, R.J.; Phys. Fluids, 10, 17, 1967.
6. Ostrach, S. and Thornton, P.R.; J. Aerosp. Sci. 29, 289, 1962.
7. Mack, J.E.; Inst. of Res. Tech. Rpt. 4, Lehigh Univ. 1954.
8. Amr, Yehia, M.; Ph.D. Thesis, State Univ. of New York at Buffalo, 1979.
9. Cohen, N.B.; NACA TN 3943, 1957.

10. Hall, J. Gordon; AIAA Jour., 10, 499, 1972.
11. Hall, J. Gordon, et al.; AIAA Jour., 11, 1770, 1973.
12. Hall, J. Gordon, et al.; AIAA Jour., 12, 724, 1974.
13. Srinivasan, G. and Hall, J.G.; Proc. 10th Inter. Shock Tube Symp., Kyoto Univ., p. 102, 1975. Also, Srinivasan, G.; Ph.D. Thesis, State Univ. of New York at Buffalo, 1974.
14. Shen, S.F.; J. Aerosp. Sci. 28, 397, 1961.
15. Lees, L.; NACA Tech. Rpt. 876, 1947.
16. Saric, W.S. and Nayfeh, A.H.; Phys. Fluids, 18, 945, 1975.

8. Acknowledgement: Financial support for this study was received from the U.S. Air Force Office of Scientific Research under Grant 74-2719.

	$x_s = 2.17$ ft		$x_s = 4.6$ ft		$x_s = 8.17$ ft	
P_o (psi)	CENTER PROBE	CORNER PROBE	CENTER PROBE	CORNER PROBE	CENTER PROBE	CORNER PROBE
45	11.15	11.25	13.8	13.0	16.9	15.25
65	8.85	4.65	10.9	Relam.* 5.75/10.3	15.65	14.90
85	5.7	3.75	8.0	5.0	12.15	6.50
105	4.9	Relam.* 1.90/3.5	6.2	4.9	7.50	5.75
115	5.0	1.80	6.05	4.6	Relam. 5.75	5.45
125	3.25	1.90	5.95	4.5	4.75	
145	3.1		5.3	4.35	4.4	

TABLE I. TYPICAL EXPANSION-WAVE TRANSITION TIMES (MILLISECS).
* INITIAL TIME/FINAL TIME

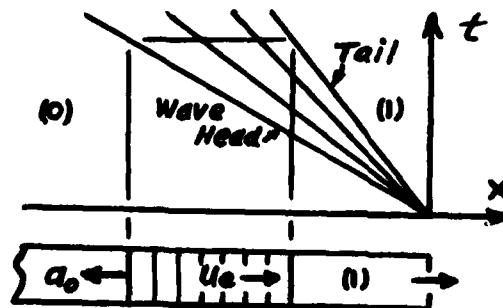


Fig. 1 Centered Expansion-Wave Flow

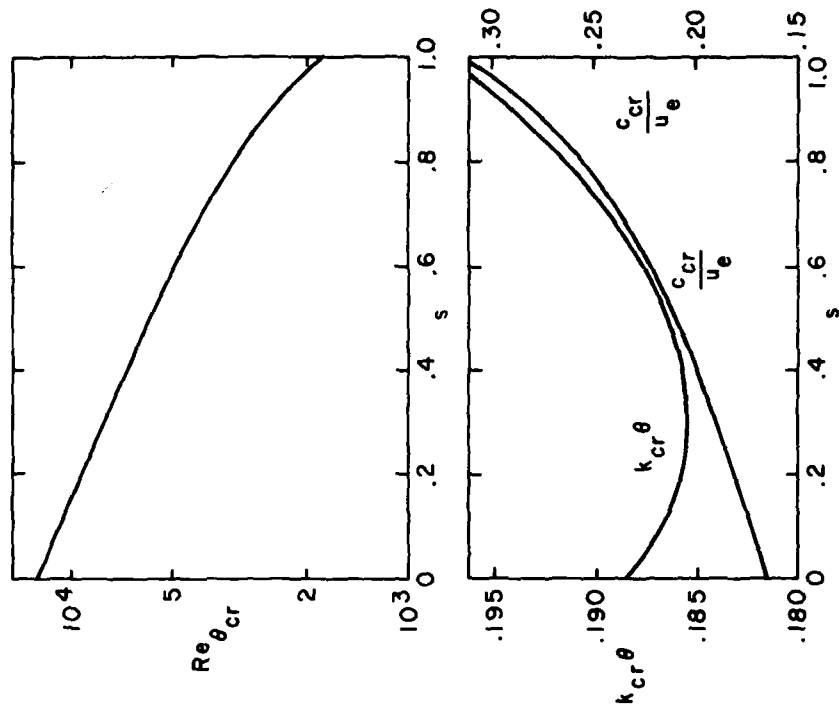


Fig. 3 Critical Re_{θ} , k , and Phase Velocity versus S for Expansion-Wave Boundary Layer

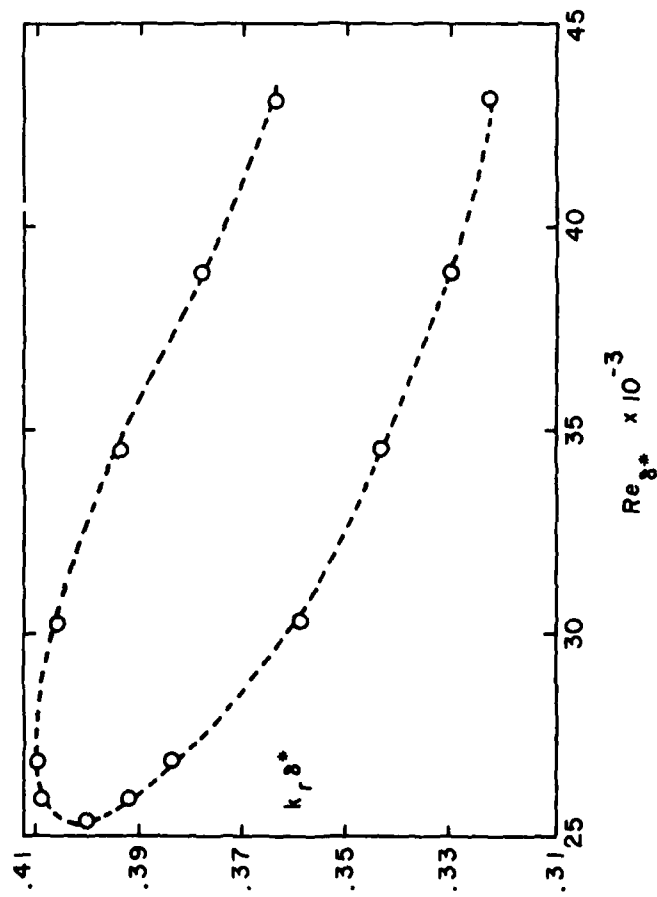


Fig. 2 Neutral Stability Curve for Expansion-Wave Boundary Layer at $S = 0$. Circles are Calculated Points.

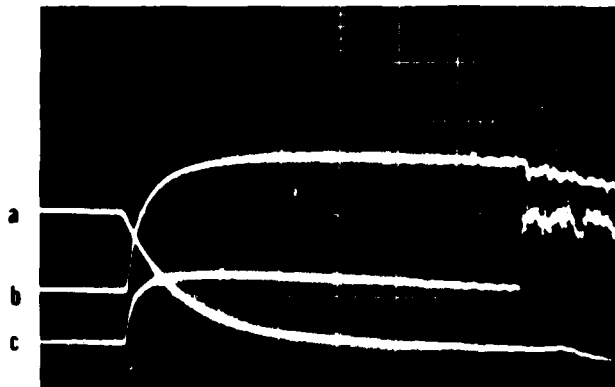


Fig. 4
Expansion-Wave Boundary Layer
Record. $p_0 = 45$ psi, $x_s = 4.6$
ft. (a) pressure, 10 psi/cm,
2 ms/cm (b) HWA at $y = .022$ in,
2 v/cm, 2 ms/cm, $R_0 = 6.95\Omega$,
 $a = .5$ (c) FHFA at center, .5
v/cm, 2 ms/cm, $R_0 = 13.1\Omega$, $a =$
.5. (x_s = diaphragm distance,
 a = overheat ratio).

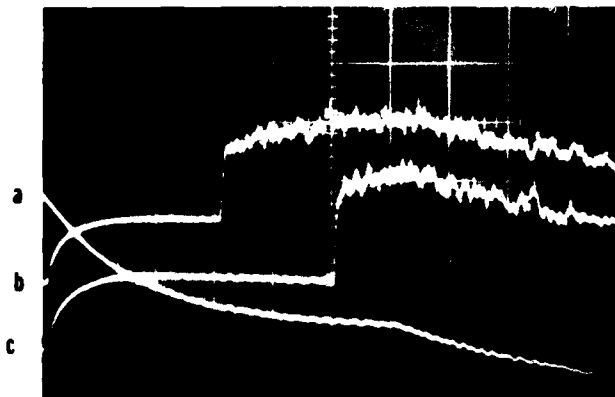


Fig. 5
Expansion-Wave Boundary Layer
Record. $p_0 = 95$ psi, $x_s = 8.17$
ft. (a) pressure, 20 psi/cm,
2 ms/cm (b) FHFA at corner, .5
v/cm, 2 ms/cm, $R_0 = 11.12\Omega$, $a =$
.2 (c) FHFA at center, .5
v/cm, 2 ms/cm, $R_0 = 13.1\Omega$,
 $a = .2$.

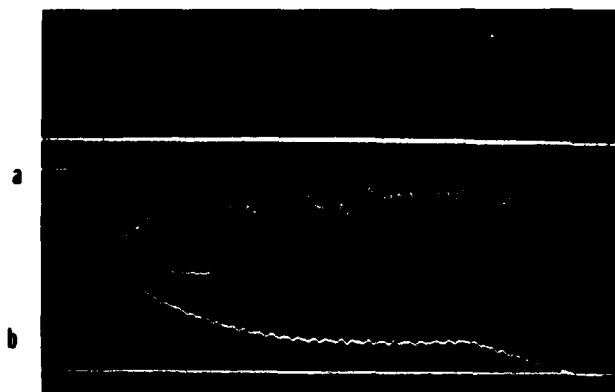


Fig. 6
Expansion-Wave Boundary Layer
Record. $p_0 = 65$ psi, $x_s = 5$ ft.
(a) pressure, 10 psi/cm, 2
ms/cm (b) FHFA at corner, .5
v/cm, 2 ms/cm, $R_0 = 15.4\Omega$,
 $a = .5$.

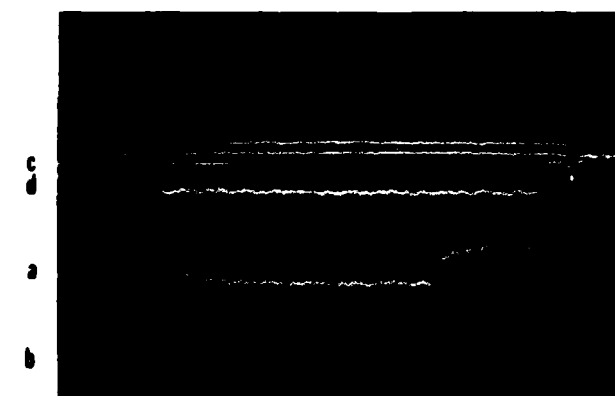


Fig. 7
Shock-Wave Boundary Layer
Record. $p_0 = 377$ mmHg, $x_s =$
7.5 ft, $M_s = 1.18$. (a) FHFA
at corner, (b) FHFA at center,
(c), (d) pressures at $x_s =$
10.58, 7.63 ft. FHFA .1 v/cm,
 $a = .2$. pressures 4 psi/cm.
Sweeps 1 ms/cm.

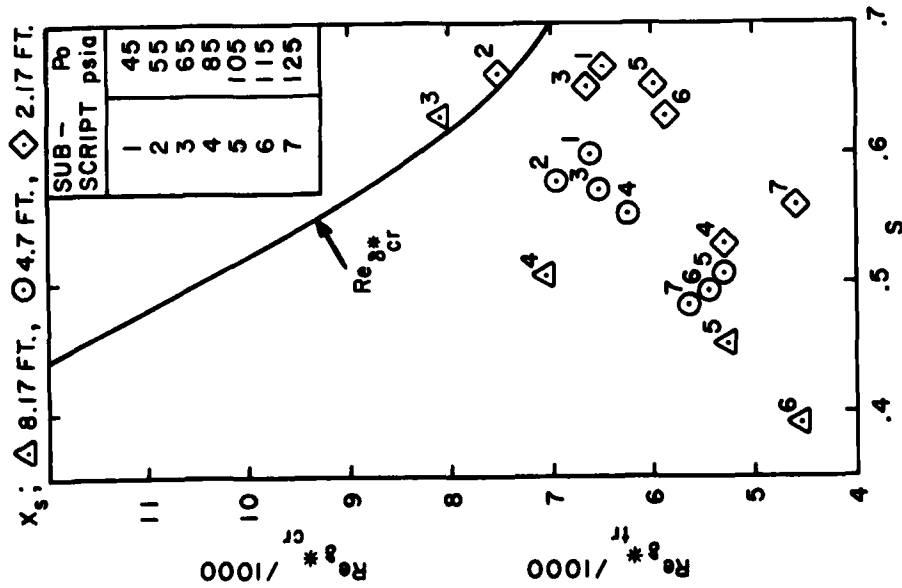


Fig. 8 Re_{δ^*} for Transition and Critical Stability Limit for Expansion Wave

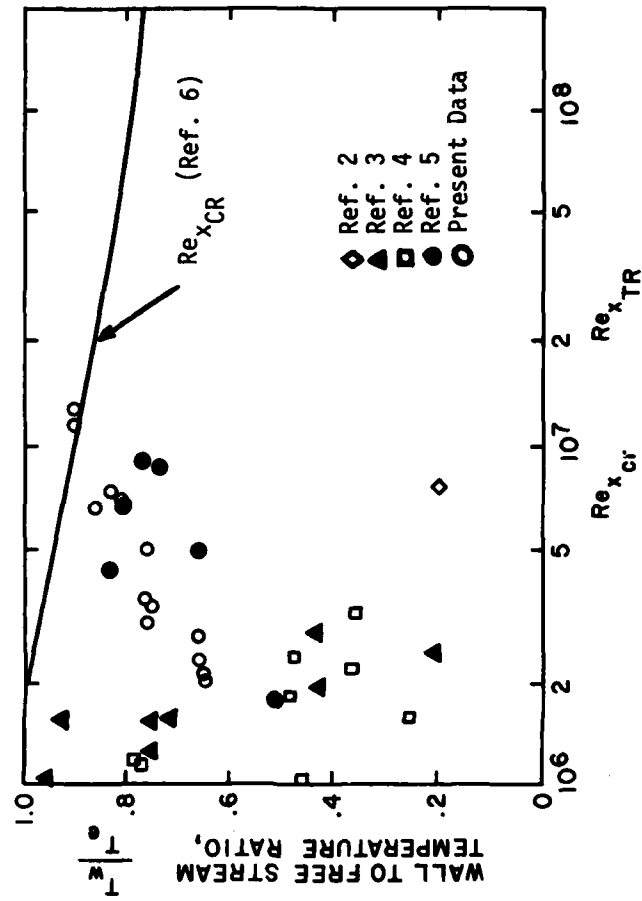


Fig. 9 Re_x for Transition and Critical Stability Limit for Shock Wave

AD P000252

AN ACCURATE DETERMINATION OF THE THERMAL CONDUCTIVITY
OF ARGON AT HIGH TEMPERATURES.

A. Hirschberg*, P.J. Vrugt, J.F.H. Willems, M.E.H. van Dongen
*Laboratory for Fluid Dynamics and Heat Transfer, Department of Physics
Eindhoven University of Technology, Eindhoven, The Netherlands*

A method is described to obtain the thermal conductivity of a gas from laser-schlieren measurements of the density gradient in the end-wall thermal boundary layer of a shock tube. The pressure increase after shock reflection is taken into account. Attention is given to the contribution of higher order derivatives of the refractive index to the schlieren signal. Data on the thermal conductivity of argon are presented for temperatures from 1500-2100 K and from 5000-6500 K. They appear to be about 3% lower than the values based on the intermolecular potential of Aziz and Chen, which is attributed to the influence of side-wall boundary layers.

INTRODUCTION

In the past many attempts have been made to obtain quantitative information on the heat conductivity of non-ionized gases by means of shock tube experiments. Such studies are based on the investigation of the end-wall thermal boundary layer. This boundary layer is induced by the heat flux from the hot gas in the reflected shock region to the wall. The analysis of the flow is simplified by the fact that viscous effects are negligible. The boundary layer structure is well described by a one-dimensional model if the tube cross section is large enough compared to the boundary layer thickness.

Two different approaches have been followed in order to obtain thermal conductivity data from shock reflection studies. The first one was based on measurements of the heat flux to the wall by means of thin metal film temperature gauges. From reviews by Saxena¹ and Vrugt² one can conclude that measurements of this type will not yield thermal conductivity data at high temperatures within error bounds less than 15%.

The alternative approach, initiated by Smeets³ and Bunting and Devoto⁴, is to determine the boundary layer structure itself by optical means. Although the method is much more promising as has been shown by Kuiper⁵, Ewald and Grönig⁶ and Vrugt², their results have inaccuracies not less than 10% so far.

Much progress has been made in the knowledge of thermal transport properties of the noble gases in particular for temperatures below 2500 K⁷.

* present address: Shell International Research, Rijswijk, The Netherlands

Above that temperature the shock tube is still the only possible source of data so that it is worthwhile to improve the shock tube method.

PRINCIPLE OF THE METHOD

In order to find the thermal conductivity, we followed the procedure of determining all terms of the energy equation, as proposed by Ewald and Grönig⁶. It appears to be sufficient, for a given shock Mach number M and for initial conditions (p_1, T_1) to measure the density gradient in the outer part of the boundary layer and the time-dependent end-wall pressure. In a previous paper⁸ laser-schlieren measurements of the density gradient for moderate Mach numbers and argon as testgas were found to be in good agreement with theoretical values based on the accurate thermal conductivity data of Chen and Saxena⁷, when the pressure increase of about 10% within 1 ms was taken into account.

We start from the assumptions, that the gas is monatomic and behaves calorically perfect; the boundary layer approximation is assumed to be valid, so that the pressure depends only on time. Temperature T_∞ and density ρ_∞ outside the boundary layer vary isentropically with pressure p , starting from the ideal Rankine-Hugoniot values just after shock reflection. Then, the conservation laws of mass and energy can be brought in the following form:

$$\frac{1}{T} T_t + \frac{u}{T} T_x = \frac{1}{p} p_t + u_x \quad (1)$$

$$\frac{1}{T} T_t + \frac{u}{T} T_x = \frac{2}{5} \frac{1}{p} p_t - \frac{2}{5} \frac{1}{p} q_x \quad (2)$$

where subscripts t and x denote differentiation with respect to time and space, and with q denoting the heat flux, which equals $-\lambda T_x$, λ being the thermal conductivity. An explicit expression for the velocity u can be found by equating the right hand sides of eqs. (1) and (2) and integrating the resulting expression with respect to the space coordinate x starting from the wall at $x = 0$:

$$u = \frac{2}{5} \frac{\lambda}{p} T_x + \frac{2}{5} \frac{q_i}{p} - \frac{3}{5} \frac{1}{p} p_t x \quad (3)$$

Subscript i is used here to indicate the interface between gas and wall. The next step is to substitute the velocity of eq. (3) into the energy equation (2) which is somewhat rearranged to give:

$$\lambda \left(\frac{T_{xx}}{T_x} + \frac{T}{\lambda} \frac{d\lambda}{dT} \frac{T_x}{T} - \frac{T_x}{T} \right) = \frac{5}{2} \frac{p}{T} \left(\frac{T_t}{T_x} \right) + \frac{2}{5} \frac{q_i}{p} - \frac{3}{5} \frac{p_t}{p} x - \frac{2}{5} \frac{p_t}{p} \frac{T}{T_x} \quad (4)$$

Since the temperature itself cannot easily be measured it is advantageous to rewrite eq. (4) in terms of p and ρ . With the notation ν for $T/\lambda \, d\lambda/dT$, and using the isentropic relation $\frac{1}{p} p_t = \frac{5}{3} \frac{1}{\rho_\infty} \partial \rho_\infty / \partial t$, we finally obtain:

$$\lambda = \frac{5}{2} \rho R \frac{[(\rho - \rho_\infty)_t / \rho_x + \frac{2}{5} q_i / p - \frac{3}{5} p_t / p (x + (\rho - \rho_\infty) / \rho_x)]}{[\rho_{xx} / \rho_x - (1 + \nu) \rho_x / \rho]} \quad (5)$$

This expression is used as the basis for the determination of λ . Nearly all terms can be determined experimentally. The a-priori unknown exponent ν can be found by means of an iterative procedure. In practice, however, an approximate knowledge of ν is sufficient, because ρ_{xx} appears to be the dominant term in the denominator for the outer part of the boundary layer.

The effect of the time dependent pressure is most pronounced in the leading density term. The time derivative of the pressure appears to give a minor contribution to λ , at least for our experimental conditions. The experimental determination of the density and pressure terms is described in the next section. The heat flux q_i has not been measured, but has been evaluated

theoretically. This is possible, because the heat flux q_i is mainly determined by the thermal conductivity in the cold gas region close to the wall, where the thermal conductivity is very well known. The q_i/p term is of equal importance as $(\rho - \rho_\infty)_t/\rho_\infty$. The influence of the time-dependent pressure on the heat flux was taken into account by applying a local similarity approach, which is described in appendix B.

EXPERIMENTAL PROCEDURE

Most experiments were performed in a $10 \times 10 \text{ cm}^2$ shock tube at an initial testgas pressure of 667 Pa, which was measured by means of a micro-manometer with an accuracy better than 2 Pa. The impurity level of the argon testgas, mainly caused by leakage and outgassing, was less than $2 \cdot 10^{-4}$. The end-wall pressure was measured by means of a piezo-electric transducer (Kistler 603 B), which was calibrated dynamically.

The boundary layer structure was determined by means of the laser-schlieren system of figure 1. The laser beam (Spectra-Physics, helium-neon laser model 120.) is positioned

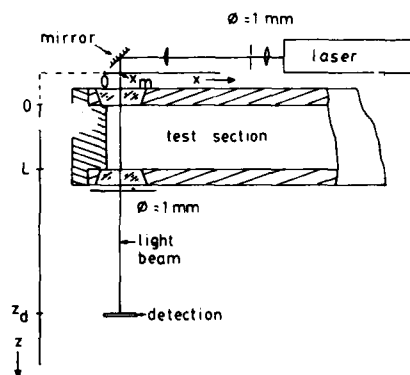


Fig. 1. Sketch of the laser-schlieren set-up and definition of the reference frame.

parallel to the end wall with a possible uncertainty in position of $\pm 6 \mu\text{m}$. The beam undergoes a schlieren deviation ϕ which is in first order proportional to the density gradient: $\phi = K \rho_x L$, K being the Gladstone-Dale coefficient and L the width of the test-section. For K the value of $1.582 \cdot 10^{-4} \text{ m}^3 \text{kg}^{-1}$ was taken. This schlieren deviation is measured by means of a photodetector consisting of two semi-circular sensitive areas positioned at $z = z_d$. Before each experiment, the system was calibrated by moving the detector in the x direction.

Several precautions were taken in order to reduce the contribution of the higher order derivatives of the density to the signal. The laser beam was imaged in the test

section, and the laser beam waist w_0 , i.e. beam width between the e^{-1} points at its smallest cross-section, has been chosen such that

$$\left(\frac{1}{3}\right)^{1/4} < w_0 \left(\frac{k_0}{L}\right)^{1/2} < 1,$$

k_0 being the wavenumber of the laser light. The upper bound corresponds to a minimum laser beam width at the entrance and exit windows, and the lower bound to a minimum width averaged over the test-section. Further, the position of the waist was chosen at a distance $L/6$ in front of the shock tube axis. As is shown in appendix A, the contribution of the second density derivative to the signal is then made as small as possible. The contribution of the higher order density derivatives to the signal was estimated by means of a wave optics analysis¹³, the result of which can also be found in appendix A.

RESULTS AND DISCUSSIONS

The heat conductivity data were obtained from two series of experiments, each consisting of seven runs. The temperature range covered by the first

series was chosen between 1500-2000 K, so that the thermal conductivity values could be compared with the independent accurate data of Chen and Saxena in order to investigate the reliability of the method. The second series should yield new data in the range of 5000-7000 K. For both series, the distance of the laser beam to the wall was varied approximately between 0.6 and 1.4 mm. The initial testgas pressure was 667 Pa. The recorded end-wall pressures for both series of experiments are shown in figure 2.

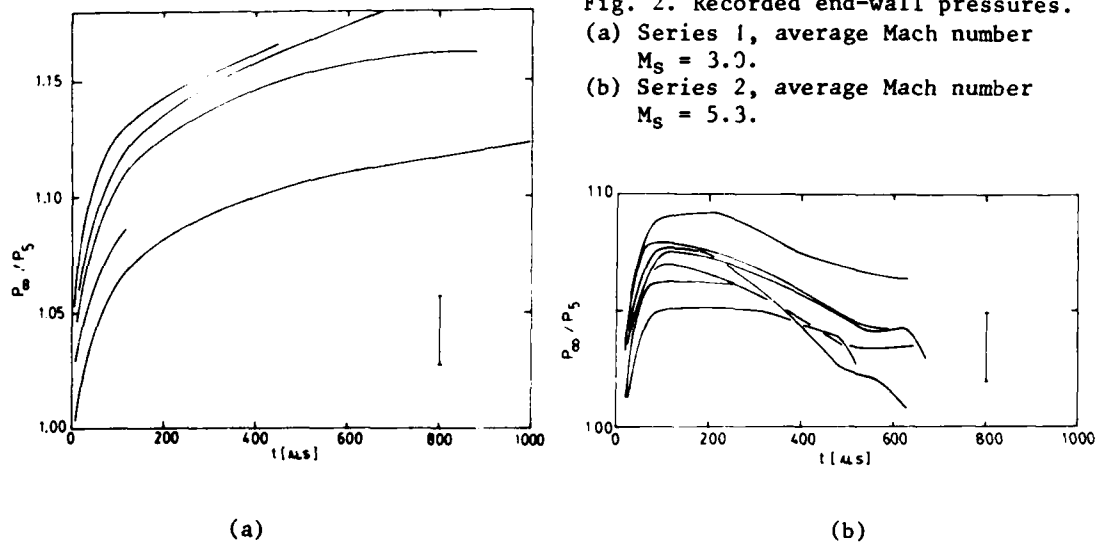


Fig. 2. Recorded end-wall pressures.

(a) Series 1, average Mach number

$M_s = 3.0$.

(b) Series 2, average Mach number

$M_s = 5.3$.

The data on the density gradient as a function of time and space were reduced by introducing a boundary layer coordinate s , and a reduced density gradient F defined by:

$$s = x_m / (a_5 t)^{1/2}, \text{ and } F = \rho_x (a_5 t)^{1/2} / \rho_5$$

where a_5 and ρ_5 are the thermal diffusivity and the density evaluated at the ideal Rankine-Hugoniot state behind the reflected shock wave. To calculate $a_5 = \lambda_5 / \rho_5 c_p$ the following expression for λ_5 was used: $\lambda_5 = \lambda_{\text{ref}} (T_5 / T_{\text{ref}})^{0.68}$, with $\lambda_{\text{ref}} = 0.0568 \text{ Wm}^{-1}\text{K}^{-1}$, and $T_{\text{ref}} = 1500 \text{ K}$.

The data of each series appeared to show a selfsimilar behaviour; all experiments within one series could be well represented by a single curve. By linear regression, a 6th order polynomial in s^{-1} was fitted to the $F(s)$ data of each experiment. Then corrections were made for the 3rd order derivative of the density by substituting this polynomial into eq. (A6). In fig. 3, the final average $F(s)$ curve is shown for series 1, together with the result of a single experiment without and with correction for the third derivative of the refractive index η_3 . It should be noted, that the example given here is a rather extreme one, the distance to the wall being 0.4 mm, while the beam width is approximately 0.2 mm. Once the corrected $F(s)$ curve is found, this relation is used to evaluate the relevant terms of eq. (5), which can be rewritten in the form

$$\lambda = \lambda_5 \frac{\rho}{\rho_5} \frac{[-s/2 + \frac{2}{5} \frac{q_i}{p} (\frac{t}{a_5})^{1/2} - \frac{3}{5} \frac{t}{p} p_t (s + I/F)]}{F_s / F - (1 + v) F \rho_5 / \rho} \quad (6)$$

$$\text{with } I = \int_0^s F ds, \quad \frac{\rho}{\rho_5} = (\frac{p}{p_5})^{0.6} + I, \quad T = p / \rho R, \quad F_s = \frac{dF}{ds}$$

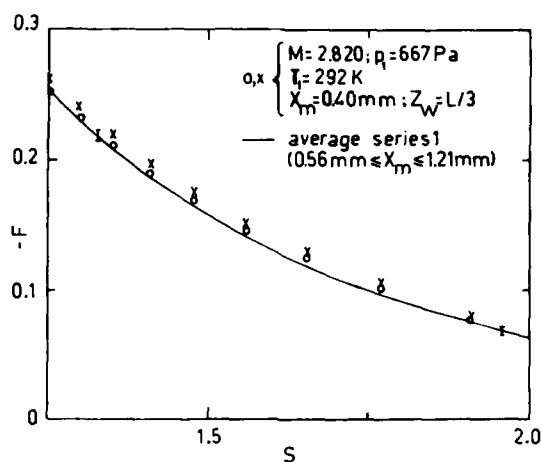


Fig. 3. Illustration of the self-similarity of the boundary layer structure, and of the influence of η_3 on the signal.

The results are depicted in figure 4, together with the handbook values for the thermal conductivity by Touloukian et al.¹⁰, and the theoretical data of Aziz¹¹, which are based on the intermolecular potential of Aziz and Chen¹². The latter can be considered to be the best possible representation of a great variety of experimental data. In Touloukian's data, the contribution of the electrons and ions to the thermal conductivity of atmospheric argon is included and causes the steepening of the slope above 6000 K. Aziz' data are valid only for the monatomic frozen gas. Our thermal conductivity values are on the average 3% lower than that of Aziz, which can be verified by inspection of the detailed results given in Table I. This implies that our results are also 3%

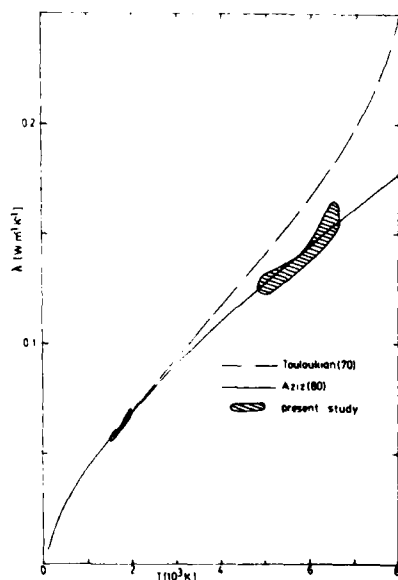


Fig. 4. Thermal conductivity versus temperature.

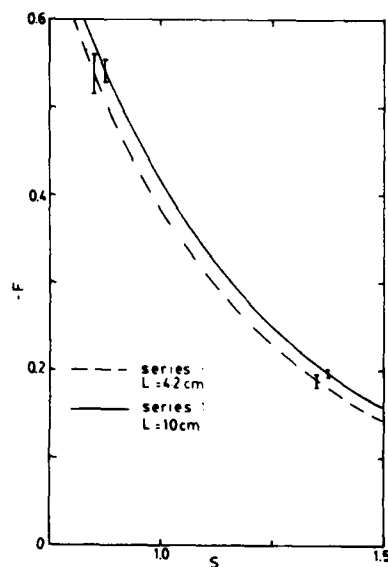


Fig. 5. Comparison of the schlieren data obtained in shock tube I ($L = 10$ cm) with data obtained in shock tube II ($L = 4.2$ cm).

TABLE I

T	λ	σ_λ	λ_{th}	T	λ	σ_λ	λ_{th}
(K)	(W/mK)	(W/mK)	(W/mK)				
1550	5.86	0.27	5.813	5000	0.127	0.04	0.1279
1600	5.80	0.25	5.938	5200	0.129	0.03	0.1313
1650	5.89	0.18	6.062	5400	0.131	0.04	0.1348
1700	5.98	0.12	6.184	5600	0.134	0.03	0.1382
1750	6.09	0.10	6.305	5800	0.137	0.02	0.1415
1800	6.17	0.06	6.425	6000	0.140	0.02	0.1449
1850	6.29	0.08	6.544	6200	0.145	0.04	0.1482
1900	6.47	0.22	6.661	6400	0.149	0.06	0.1515
1950	6.40	0.07	6.778				
2000	6.53	0.11	6.894				
2050	6.75	0.21	7.009				
2100	7.09	0.42	7.123				

Comparison of thermal conductivity λ obtained by means of the present method with the theoretical data of Aziz¹¹. σ_λ is the standard deviation obtained on the basis of 4 to 6 experiments.

lower than the results of Chen and Saxena obtained by means of a thermal diffusion column method. They claim to have a possible error of 1.5%, so that our results seem to have a small but significant systematic error. A possible reason for such an error could be found in the influence of the boundary layers along the side walls of the tube disturbing the one-dimensional character of the boundary layer structure. This effect should be dependent on the shock tube dimension. Therefore, a third series of experiments was carried out in a smaller shock tube (II) with a test-section width of 4.2 cm. Indeed, the density gradient found in the smaller tube is significantly lower than that of series I, as is shown in figure 5. A further improvement of the present method can be expected when this influence of the side wall boundary layer is better understood. Then, an accuracy comparable with that of the thermal diffusion column method ($\pm 1.5\%$) should not be beyond the possibilities.

Appendix A. THE LASER SCHLIEREN METHOD

The gas density is related to the refractive index by the Gladstone-Dale law, $N = 1 + K\rho$. Assume, that the refractive index profile can be represented by

$$\eta = \frac{1}{2} + \eta_1(x - x_0) + \frac{1}{2}\eta_2(x - x_0)^2; \quad 0 < z < L \quad (A1)$$

where $\eta = \frac{1}{2}N^2/N_0^2$, N_0 being the refractive index at the position of the undisturbed central ray of the beam x_0 , and $\eta_i = (d^i\eta/dx^i)_{x=x_0}$. From geometrical optics it is found, that the trajectory of the central ray satisfies the ray equation.

$$\frac{d^2x_r}{dz^2} = \frac{d\eta}{dx} \quad (A2)$$

Combining Eqs. (A1) and (A2) with the initial conditions $x_r(0) = x_0$ and $(dx_r/dz)_{x=x_0} = 0$, yields the trajectory of the central beam:

$$x_r(z) - x_0 = \frac{\eta_1 z^2}{2} \left(1 + \frac{\eta_2 z^2}{12}\right); \quad 0 < z < L \quad (A3)$$

$$\text{and } x_r(z) = x_r(L) + (z - L)\eta_1 L \left(1 + \frac{\eta_2 L^2}{6}\right); \quad z > L \quad (A4)$$

The signal measured by the photodetector V is proportional to $x_r(z_d)$ and to the light intensity $I(o)$ of the beam center at $z = z_d$. In order to evaluate the latter, it is important to realize that owing to the presence of η_2 , the boundary layer acts as a thin lens (in first approximation) with a focal length f of $(-\eta_2 L)^{-1}$. If the beam is focused at a distance d behind the lens at $z = L/2$, the aperture of the outgoing beam will be increased by a factor $(1 + d/f)$. Then the beam intensity I_o will be proportional to $(1 - d/f)$ if $|d/f| \ll 1$, and consequently the signal varies according to

$$V \sim (z_d - L)\eta_1 L \left(1 + \frac{\eta_2}{6} L^2\right) \left(1 - \frac{d}{f}\right) \sim \left(1 + \frac{\eta_2}{6} L^2\right) (1 + \eta_2 L d) \text{ for } z_d \gg L \quad (A5)$$

Obviously, if the laserbeam is focused at $d = -\frac{1}{6}L$, the terms linear in η_2 vanish.

The correction for the higher order derivatives on the signal has been obtained by means of scalar wave optics. We only give the results here, derived for the situation that the laserbeam is focused on the shock tube axis. The details of the calculations are given by Hirschberg¹³.

$$V \sim \left(z_d - \frac{L}{2}\right) \left[\eta_1 L + \frac{\eta_3}{6} w_o^2 L + \frac{\eta_1 \eta_2 L^3}{6} + \frac{\eta_2 \eta_3 L^3 w_o^2}{96} \left(7 + \frac{3}{5} \left(\frac{L}{k_o w_o^2}\right) + \frac{1}{21} \left(\frac{L}{k_o w_o^2}\right)^4 + \dots\right)\right] \text{ for } \eta_1 L < \frac{2}{k_o w_o}, z_d \gg L \quad (A6)$$

For a quadratic medium, this result is equivalent with the geometrical optics solution (A3-4), for $z_d \gg L$.

Appendix B. HEAT FLUX AT THE WALL

In order to evaluate the heat flux at the wall, the following approximation for the thermal conductivity was used, expressing all quantities in S.I. units:

$$\lambda = 0.0172(T/290)^{0.8}, \quad 290 < T < 500; \quad \lambda = 0.0172(500/290)^{0.8} (T/500)^{0.7}, \quad T > 500 \quad (B1)$$

The energy equation (2) is rewritten by introducing the following set of variables:

$$\xi = \int_0^x \rho dx', \quad \bar{T} = T/T_\infty, \quad \lambda = \lambda_\infty \bar{T}^\nu, \quad \tau = \int_0^t (\rho_\infty \lambda_\infty / c_p) dt' \quad (B2)$$

The mathematical problem then becomes:

$$\bar{T}_\tau = \frac{\partial}{\partial \xi} (\bar{T}^{\nu-1} T_\xi) \quad \tau = 0, \xi > 0: \bar{T} = 1; \xi \rightarrow \infty: \bar{T} \rightarrow 1; \xi = 0: \bar{T} = T_i/T_\infty \quad (B3)$$

where for T_i the initial wall temperature can be used. When T_∞ is constant, the problem can easily be solved numerically, and the solution can formally be written as:

$$\bar{T} = f\left(\frac{\xi}{T_\infty^{1/2}}; \frac{T_i}{T_\infty}\right) \quad (B4)$$

The heat flux at the wall then is:

$$q_i = -\lambda_i \frac{P_\infty}{RT_i} f_\xi(0; \Gamma_i/T_\infty) / \tau^{1/2} \quad (B5)$$

The heat flux found in this way is in good agreement with experimental results reported by Saxena¹.

The isentropic variation in time of the state outside the boundary layer is taken into account by stretching the time scale according to (B2) and by substituting the instantaneous values of T_i/T_∞ in eq. (B5). The validity of this so-called local similarity approach was confirmed by analytical model calculations for $\nu = 1$ and experimentally by means of measurements of the wall surface temperature using a Pt-film gauge.

REFERENCES

1. Saxena, S.C., High temperature science, 4 (1972) 517;
2. Vrugt, P.J., Ph.D. thesis, T.H. Eindhoven (1976);
3. Smeets, G., Z. Naturforschung, 20a (1965) 683;
4. Bunting, J.D. and Devoto, R.S., SUDAAR No. 313, Stanford (1967);
5. Kuiper, R., SUDAAR No. 353, Stanford (1968);
6. Ewald, R. and Grönig, H., AIAA J., 9 (1971) 946;
7. Chen, S.H.P. and Saxena, S.C., Molecular Physics, 29 (1975) 455;
8. Hirschberg, A., Heugten, W.H.H. van, Willems, J.F.H. and Dongen, M.E.H. van, Int. J. Heat Mass Transfer, 23 (1980) 799;
9. Lauver, M.R., Phys. Fluids, 7 (1964) 611;
10. Touloukian, Y.S., Siley, P.E. and Saxena, S.C., TPRC Data Series on Thermophysical Properties of Matter, 3, Plenum Press (1970);
11. Aziz, R.A., Private communication (1980);
12. Aziz, R.A., Chen, H.H., J. Chem. Ph, 67 (1977) 5719;
13. Hirschberg, A., Ph.D. thesis, T.H. Eindhoven (1981).

ACKNOWLEDGEMENT

The authors are indebted to prof. G. Vossers, prof. P. Schram and prof. D. de Vries for their stimulating interest. The experimental and technical assistance of mr. H.J. Jager and mr. E.J. van Voorthuisen, and the editorial support of mrs. E. van der Steen is also gratefully acknowledged.

AD P000253

THERMAL CONDUCTIVITY MEASUREMENT IN HIGH TEMPERATURE
ARGON BY THE SHOCK PERTURBATION AND MACH REFLECTION METHODS[†]

A. Cavero, K. Chung and H.N. Powell*

Department of Mechanical Engineering

University of Wisconsin, Madison, Wisconsin 53706

Two methods of thermal conductivity measurement have been developed and applied to argon in the range from 3000 to 5400 K. The shock perturbation method (SPM) employs a set of small carefully spaced grooves in the wall of the shock duct. The resulting weak acoustic disturbances generate a set of weak thermal (or "entropy") waves behind the shock which decay with time. Schlieren-photodiode detection and rapid transient digital storage of the signals permit the decay of these waves to be analyzed to yield the thermal conductivity. In the Mach reflection method, (MRM) the shock impinges on a small angle ramp. High speed (10 ns) interferograms of the resulting tangential thermal and vorticity diffusion zone permit the conductivity to be calculated from the relevant compressible flow equations in which use is made of the Ilingworth variable. In the weak tangential flow regimes of interest, the conductivity measurement is independent of the viscosity value. Least square fits of $K(T)$ by both methods to a power law, gives

$$K = K_0 (T/T_0)^{\nu} \quad \text{SPM: } \nu = 0.697 \pm 0.004; \quad \text{MRM: } \nu = 0.700 \pm 0.017$$

in which $K_0 = 4.25 \times 10^{-5}$ cal/cm-s-K at $T_0 = 300$ K. The advantages and difficulties of each method is discussed and compared with those of other methods.

BACKGROUND

A variety of methods have been used to measure the thermal conductivity, K , of gases. References 1a,b contain an extensive critique of all previous methods as well as an extensive bibliography of high temperature (>1500K) measurements through 1977. No attempt will be made to describe these methods, but their limitations will be summarized:

- (a) *Thermal Column Method*: simple and elegant for non-oxidizing gases, limited by radiation effects to $T < 1500$ K.
- (b) *Reflected Shock Method*: data reduction requires the a priori assumption of a power law, $K \sim T^{\nu}$, which restricts applicability to monatomic gases; the value of ν is rather insensitive to the measured variable, leading to substantial discrepancies between different workers for the same gas.

*Professor of Mechanical Engineering, University of Wisconsin.

†The support of the National Science Foundation by Grant ENG-76-10760 is gratefully acknowledged.

- (c) *Confined Arc Method*: restricted to ionization and near ionization temperatures; $K(T)$ evaluations depend heavily on collateral information on electrical conductivity and spectral emittance.
- (d) *Ultrasonic Absorption*: restricted to monatomic gases for which a precise value of the Prandtl number is independently known.

Against this background, let us establish criteria for an "ideal" thermal conductivity measurement method for the range between the thermal column and confined arc methods, i.e., from 1500K to ionization:

- (a) It must be applicable to any gas, monatomic, polyatomic, etc., regardless of oxidation-reduction chemistry.
- (b) The evaluation of a K and T data pair should not only be mutually independent, but independent of all other K , T pairs; no functional $K(T)$ relation should be needed.
- (c) The evaluation of K should have a minimum dependence on other properties. While thermodynamic properties are known with great precision, the capability of specifying other properties, viz., viscosity, radiation emittance, etc. is likely to be much poorer than the K value being sought.
- (d) It should be applicable to chemically dissociated gases with sufficiently long residence times to assume local chemical equilibrium.

In this paper the authors present two new methods, which while not without problems of their own, do satisfy all the above criteria. To establish the validity of the methods, argon was chosen as the test gas because of the extent of previous work. Comparisons of present and previous results are given at the end of the paper.

All shocks were generated in a large bore, 11.75 cm wide by 9.20 cm high, combustion driven shock tube which incorporated a number of novel design features (3,4). Shock speeds were routinely predicted to $\pm 1\%$ which was crucial for the proper setting of timing sequences.

THE SHOCK PERTURBATION METHOD (SPM)

When a moving planar shock impinges a small localized irregularity in the shock duct wall which is oriented parallel to the front, a weak acoustic disturbance is created which expands cylindrically behind the shock. If the post shock flow is supersonic, the irregularity is the seat of a Mach wave which blends into the cylindrically expanding wave as shown in Fig. 1. According to the geometry of the wall perturbation, if the acoustic wave has the exact local acoustic velocity, a_2 , linearized perturbation analysis (5) shows that no "record" of the interaction of the acoustic wave with the shock front is left along the dotted line shown in Fig. 1, a conclusion confirmed in earlier work (6). However if the wall perturbation, even though very small, contains discontinuities, the acoustic wave will also contain discontinuous higher order terms, and a narrow thermal and vorticity disturbance (also called "entropy wave") is left in the gas along the dotted line position; it is clearly visible in schlieren photographs. Despite the implied shock like nature of the acoustic wave, no wave velocity in excess of a_2 has ever been detected in argon, as is not the case with more recent work in oxygen.

Therefore, with known pre-shock T_1 , P_1 , ρ_1 data, a single schlieren photograph taken at a known time t after the shock passed the wall perturbation, yields a wealth of information for confirming theoretically calculated post shock states. Failure to do so in one instance revealed air leak contamination and in subsequent oxygen work has identified non-equilibrium post shock conditions in

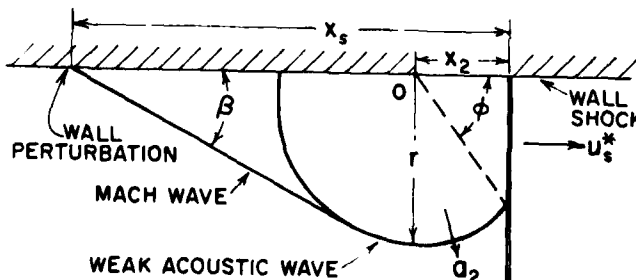


FIG. 1 Thermal wave generation by a wall perturbation.

certain cases. An asterisk identifies quantities defined in laboratory coordinates while those without are in shock coordinates. Therefore, with the Fig. 1 definition of x_s , x_2 , r , ϕ and β and the aid of the continuity, gas law and acoustic velocity equations for ideal gases, we have:

$$U_s^* = x_s / t \quad (1) \quad M_2^* = U_2^* / a_2 = (\sin \beta)^{-1} \quad (4)$$

$$\rho_2 / \rho_1 = (P_2 / P_1) (T_1 / T_2) = x_s / x_2 \quad (2) \quad M_2 = U_2 / a_2 = \cos \phi \quad (5)$$

$$T_2 = (m / \gamma R) (r / t)^2 \quad (3) \quad U_2^* = (1 - \rho_1 / \rho_2) U_s^* \quad (6)$$

in which ρ , P , M , m , γ and R have their conventional meanings.

Experimentally, U_s^* was measured from the shock transit time (to $\pm 0.1 \mu s$) over two 50 cm intervals. The accuracy was then about $\pm 0.04\%$ and decelerations were generally less than the $0.4 \mu s$ needed to be significant. With a carefully adjusted 1:1 magnification ratio and a photographic reading accuracy of about $\pm 2\%$, no discrepancies between post shock states calculated from U_s^* and the photographs were detected (1c). Thus it was possible to calculate and verify T_2 data independently of K evaluations.

If, instead of a single wall perturbation, there are twenty with a spacing λ_w (cm), then a family of twenty parallel thermal waves is generated with a period and frequency:

$$\lambda_{2x} = \lambda_w (\rho_1 / \rho_2) \quad (7) \quad f^* = U_s^* / \lambda_{2x} = U_s^* (\rho_2 / \rho_1 - 1) \lambda_x \quad (8)$$

Following t - x plane analysis, (1d) photodiode schlieren detectors were located to electronically detect this wave family without interference from either the primary or reflected acoustic wave families. A nitrogen laser schlieren photograph of such a wave field is shown in Fig. 2 including mirrors of the two photodiode detectors. Their data was recorded before the reflected acoustic waves reached the level shown in Fig. 2; illumination was from an intense xenon flash source.

Much of the earlier work used a "rounded saw tooth" perturbation profile which promoted a much more rapid boundary layer thickening than evident in Fig. 2. Also early thermal waves interacted with later perturbations to generate a secondary superposed "ghost wave" family. Both these problems were solved by using a narrow "v" groove geometry (45° included angle, 0.63 mm depth) which rapidly filled with stagnant boundary layer gas and presented minimum disturbance to the post shock wall flow. They extended over the central 1/2 of the 11.75 cm duct width.

The heat conduction equation for analysing the decay of the $\delta T(x, y, t)$ thermal wave perturbations at uniform pressure, in the general and expanded forms (in shock coordinates) is:

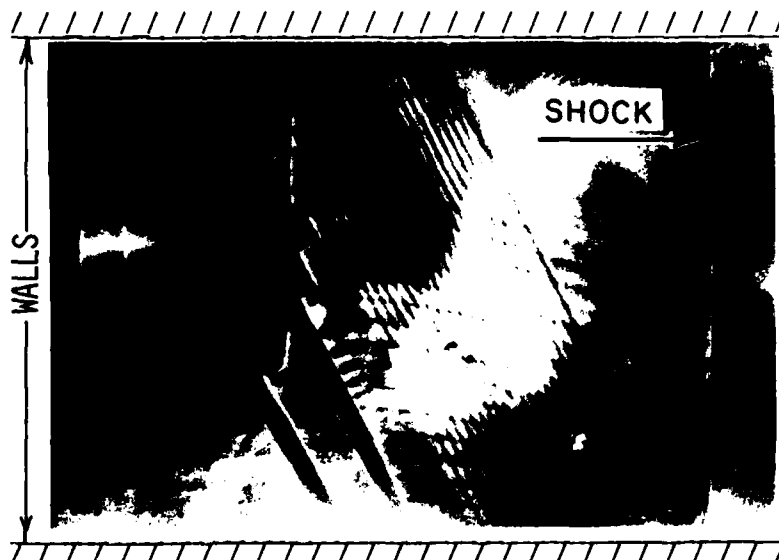


FIG. 2 Schlieren photograph (10 ns) of a thermal and acoustic wave field Run No. 144.

$$\frac{\partial \delta T}{\partial t} + \vec{U}_2 \cdot \nabla \delta T = \frac{1}{c_p \rho_2} \nabla \cdot K \nabla \delta T \quad (9a) \quad \frac{\partial \delta T}{\partial t} + U_2 \frac{\partial \delta T}{\partial x} + \delta \vec{u}_2 \cdot \nabla \delta T = \alpha_2 \left[\nabla^2 \delta T + \frac{\nu}{T_2} (\nabla \delta T)^2 \right] \quad (9b)$$

in which $\alpha_2 = K/C_p \rho_2 (\text{cm}^2 \cdot \text{s}^{-1})$ is the thermal diffusivity; $\nu = (\partial \ln K / \partial \ln T)_p$ the power law exponent; $\delta \vec{u}_2$ = perturbation velocity. The dot product in Eq. (9b) vanishes because of the orthogonality of $\delta \vec{u}_2$ and $\nabla \delta T$. For periodic perturbations, if $\delta T/T_2 \ll 1/\nu$, the last term may be neglected as is easily justified since $\delta T \text{ max} \approx 60\text{K}$ and $\nu = \text{order unity}$.

To solve Eq. (9b), let the solution domain be the $x \geq 0, y \geq 0$ quarter plane in which $x = 0$ defines the shock position and $y = 0$ defines the wall, neglecting boundary layer effects; the gas flow is in the $+x$ direction. Except for the δT and $\delta \vec{u}_2$ perturbations, T_2, P_2, ρ_2 and U_2 are everywhere uniform and the physical finite thermal wave field is taken to be a subset of an infinite wave field extending to $y = \infty$. The associated boundary conditions are:

$$x = \infty, y \geq 0, \delta T = 0 \quad (10a) \quad x = 0, y \geq 0, \delta T \text{ is uniformly periodic} \quad (10b)$$

While strength of the exciting acoustic waves must clearly diminish with increasing y , the extreme uniformity of the wave structure with y at constant x as seen in Fig. 2 indicates the effect is very weak and would not affect wave decay, hence Eq. (10b). See Ref. (1d) for a more formal justification.

Let a particular solution to Eq. (9b) be expressed as a complex wave equation,

$$\delta T_n = \delta T_{s(n)} \exp\{-k_r^{(n)} x + i n [\vec{k}_i \cdot \vec{r} - \omega t]\} \quad (11)$$

in which $n = 1, 2, 3 \dots$ is the harmonic number and $\delta T_{s(n)}$ is the associated amplitude at $x = 0$. If $(k_r^{(n)})^2 \ll K_1^2$ one finds that $k_r^{(n)} = n^2 k_r^{(1)} = n^2 k_r$. After dropping the imaginary part, the particular solution which satisfies the Eqs. (10a,b) boundary conditions, simplifies to:

$$\delta T_{(n)} = T_{s(n)} \{\exp(-n^2 k_r x)\} \cdot \{\cos n(k_{ix} x + k_{iy} y - \omega t)\} \quad (12a)$$

in which

$$k_r = (\alpha_2/U_2)(2\pi/\lambda_{2x})^2 (\sin \phi)^{-2} \quad (12b) \quad k_{ix} = 2\pi/\lambda_{2x} = \omega/U_2 \quad (12c) \quad k_{iy} = 2\pi/\lambda_{2y} = k_{ix} \cot \phi \quad (12d)$$

In the general solution consisting of a sum over all n , the n^2 term in the exponent causes the higher harmonics to die out very rapidly. Furthermore, Ref. (1e) describes an "optical tuning" of the photodiode schlieren detector which causes a complete suppression of all even order, $n = 2, 4, \dots$ harmonics from the detected signal. Therefore, $n = 1$ is the only experimentally relevant solution, as indeed was borne out by spectral analysis of actual signals.

It now only remains to transform Eq. (12a) with $n = 1$ from shock attached coordinates to one which is detected by a photodiode detector fixed in laboratory coordinates. If t is the time since the shock passed the detector, $x = U_2^* t$, so that Eq. (12a) becomes:

$$\delta T = \delta T_s e^{-t/\tau^*} \cos(\omega^* t + \theta) \quad (13)$$

in which, by Eqs. (12b, 5, 7, 8)

$$1/\tau^* = k_r U_s^* = [K/(C_p \rho_1)] (2\pi/\lambda_w)^2 (\rho_2/\rho_1)^2 / (1-M_2^2) \quad (14)$$

$$2\pi f_{th}^* = \omega_{th}^* = k_{ix} U_s^* - \omega = (2\pi U_s^*/\lambda_w) (\rho_2/\rho_1 - 1) \quad (15)$$

$$\theta = k_{iy} y = \text{a constant since } y \text{ is fixed} \quad (16)$$

Except for K itself, $1/\tau^*$ and ω_{th}^* are all expressed entirely in terms of the initial state ρ_1 , the known wall spacing λ_w , and quantities which are accurately calculable from the measured U_s^* . Since for strong shocks in a monatomic gas M_2 and ρ_2/ρ_1 are essentially constant, the only parameters for adjusting $1/\tau^*$

are ρ_1 and λ_w . A lower limit on ρ_1 is imposed by the schlieren detector sensitivity.

The two detected signals were stored sequentially in a Nicolet Model 1090 AR digital storage oscilloscope. Typically $f^* \approx 0$ (1 Mhz) so that at a sampling rate of 100 ns per point, each wave was represented by a nominally adequate 10 points (8 bits each). The signal was transferred by a modem to a central computer where a standard least square subroutine fitted the data to:

$$S = A(\exp(-t/\tau^*)) \cos(\omega^*t + \theta) + b_1 + b_2t + b_3t^2 \quad (17)$$

Best fit values for A , ω^* , θ , b_1 , b_2 and b_3 , together with their associated standard deviations were calculated. b_1 absorbs any dc bias to the signal and b_2 and b_3 allow for any low frequency drift; frequently b_2 and b_3 were too small to be statistically significant. A fit of the least square fit (solid line) is shown to the actual digital data in Fig. 3 for the same run as Fig. 2. Because of end effects the first and last two waves were excluded from the analysis.

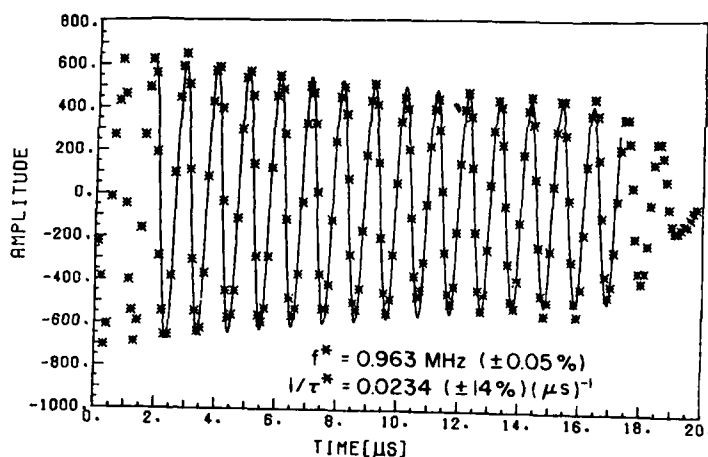


FIG. 3 Fit of least square fitted function (solid line) to digitally recorded thermal wave signal. (Run 144)

Table I summarizes the results of 18 independent evaluations of K together with other data. Those entries with a repeated M_s^* value indicate independent contributions from the two detectors. The next column gives the total number of digital data points actually contributing. The next gives the least square evaluation of f^* , while the next column gives the ratio f^*/f_{th}^* in which the theoretical f_{th}^* was calculated by Eq. (15) from the U_s^* and λ_w . While the general agreement is excellent, a systematic departure from unity is apparent which is appreciably larger than the percent standard deviation shown for f^* . Reference (1f) considers several explanations but concludes it is probably due to radiation cooling, especially since the deviation of the second detector is always larger than the first in the same run. Therefore to account for the apparent decrease from the calculated T_2 , an empirical correction, ϵ , was introduced:

$$f^*/f_{th}^* = [(\epsilon \rho_2/\rho_1 - 1)]/[(\rho_2/\rho_1 - 1)], T_2' = T_2/\epsilon \quad (18)$$

K was evaluated from $1/\tau^*$ (Eq. (14)), using the $(\epsilon \rho_2/\rho_1)$ group instead of (ρ_2/ρ_1) . While the largest ϵ correction decreased T_2 by only 3%, the scatter of $K(T_2')$ was appreciably reduced. The K data in the last column have the same standard deviation as that for $1/\tau^*$.

Two least square fits of the Table I $K(T_2')$ data to a power law were made. First, using $K_{ref} = 4.25 \times 10^{-5}$ cal/cm ks at 300K as a reference gave:

$$K = K_{ref}(T/T_{ref})^\nu \quad \nu = 0.697 \pm 0.004 \quad (19)$$

Secondly, when both K_{ref} and ν were allowed to "float", the high temperature data predicted an increase of K_{ref} at 300K by 5% and a decrease in ν by 3%. This is perhaps the first experimental proof of the validity of the power law for argon in this temperature range, in contrast to previous workers who assumed it a priori. A graphical presentation is given in Fig. 8 and a comparison with other worker's results in Table III.

TABLE I: SPM Results

Run	M_s^*	n data pts.	f^* [Mhz]	f^*/f_{th}^*	P_2 [ATM]	T_2 [K]	T_2' [K]	$1/\tau^*$ [1/ μ sec]	K [$\frac{\text{cal}}{\text{cmKsec}} 10^{-4}$]
138	5.846	147	0.8549($\pm 0.11\%$)	1.024	4.500	3408	3349	0.0217($\pm 28\%$)	2.390
		185	0.8731($\pm 0.07\%$)	1.044	4.500	3408	3302	0.0211($\pm 18\%$)	2.255
140	5.821	134	0.8382($\pm 0.08\%$)	1.010	4.460	3381	3355	0.0212($\pm 18\%$)	2.392
		143	0.8659($\pm 0.06\%$)	1.021	4.460	3381	3328	0.0198($\pm 19\%$)	2.195
141	5.841	116	0.8521($\pm 0.09\%$)	1.022	4.464	3403	3350	0.0226($\pm 24\%$)	2.488
		154	0.8610($\pm 0.04\%$)	1.033	4.464	3403	3323	0.0205($\pm 12\%$)	2.214
144	6.416	123	0.9490($\pm 0.09\%$)	1.017	5.424	4052	4002	0.0232($\pm 25\%$)	2.516
		152	0.9637($\pm 0.05\%$)	1.032	5.424	4052	3959	0.0234($\pm 14\%$)	2.488
145	6.687	108	0.9845($\pm 0.11\%$)	1.005	5.895	4381	4365	0.0250($\pm 30\%$)	2.728
		106	0.9761($\pm 0.14\%$)	1.007	5.895	4381	4358	0.0267($\pm 33\%$)	2.935
148	6.625	124	0.0090($\pm 0.06\%$)	1.019	5.749	4344	4274	0.0240($\pm 17\%$)	2.564
150	6.874	100	1.0618($\pm 0.12\%$)	1.044	6.230	4656	4510	0.0263($\pm 32\%$)	2.695
153	7.454	108	1.1297($\pm 0.08\%$)	1.018	7.284	5360	5290	0.0309($\pm 21\%$)	3.266
154	7.309	78	1.1044($\pm 0.09\%$)	1.018	3.502	5165	5096	0.0585($\pm 11\%$)	3.092
		98	1.1050($\pm 0.09\%$)	1.016	3.502	5165	5104	0.0551($\pm 12\%$)	2.921
155	6.867	123	1.0174($\pm 0.11\%$)	1.008	3.089	4588	4561	0.0522($\pm 14\%$)	2.836
156	5.659	138	0.8356($\pm 0.11\%$)	1.034	4.188	3198	3121	0.0205($\pm 27\%$)	2.254
158	5.432	126	0.8278($\pm 0.06\%$)	1.006	3.856	2965	2952	0.0173($\pm 18\%$)	1.993

While the present authors regard the SPM as conceptually and experimentally superior to any previous method for this temperature range, it is not without its own problems. Viewing the thermal wave field as a weak sinusoidal temperature distribution, distributed uniformly in depth across the center of the shock duct, it is evident that any local, non-uniform disturbance causes a misregister of the waves as seen by the schlieren photodetector *with an inherent decrease in signal amplitude*. Extraneous waves were in the test gas and were easily traced to the most minute joint imperfections in the shock duct. For some, elimination would require rebuilding the entire installation. Fortunately, they were visible in the schlieren photographs, (Fig. 2), and were highly predictable in location. Depending on M_s^* , it was many times possible to avoid them by proper location of the detectors, e.g., run 144. At some M_s^* values this was not possible and the "joint waves" caused a severe localized "pinch effect" in the recorded wave train. When the pinch occurred close to an end, truncation could salvage the usable part; if it came in the middle the whole signal had to be abandoned which explains the several single entry runs in Table I.

Subsequent work has lead to substantial improvements, but it is nevertheless a problem which makes severe demands of aerodynamic perfection for its avoidance.

THE MACH REFLECTION METHOD (MRM)

When a planar shock encounters a small angle ramp a "Mach reflection" process occurs as shown in Fig. 4, for the case of a sufficiently large M_1^* . Figure 1 is seen to be a special case, $\delta_w \rightarrow 0$ limit, of the Fig. 4 flow field. Reference (2a) reviews the many reported types of shock-ramp encounters and gives special emphasis to the results of Ref. (17).

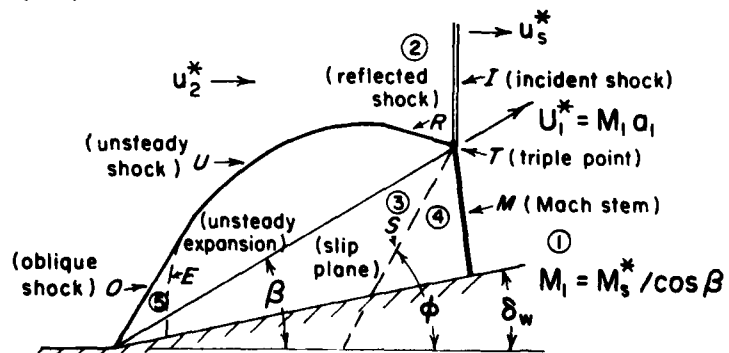


FIG. 4 Mach reflection of an incident shock by a small angle ramp.

In Fig. 4 the I , R and M (perpendicular to the ramp) shocks are all planar and constant velocity in laboratory coordinates; thus the T intersection also has constant velocity, $U_1^* = M_1 a_1 = [M_2^*/\cos \beta] a_1$. U is an unsteady shock bridging the moving R and steady oblique O ; E is an unsteady rarefaction.

Thus a Gallilean transformation from laboratory to T attached coordinates, with a subsequent rotation, leads to the *steady state* representation shown in Fig. 5a. For MRM analysis, T attached coordinates are analogous to the shock attached coordinates for SPM analysis, except that as MRM data reduction is from an interferogram, no inverse transformation is needed.

In Fig. 5a the uniform 3 and 4 flow fields are separated by a slip plane, S , implying that $P_3 = P_4$ and $U_3 \parallel U_4$. However as gas particles from the same 1 state enter 4 by one shock and 3 by two, we note $T_3 \neq T_4$ and $U_3 \neq U_4$. We therefore wish to determine the (T_3, U_3) and (T_4, U_4) states to serve as boundary conditions for a viscous and heat conducting slip flow analysis in the region of S .

The evaluation of the 3 and 4 states is easily represented graphically from plots of standard $P/P_1 - \delta$ shock functions, (Fig. 5b). The curve 1 IMN represents the locus of every (P, δ) state attainable from a specified M_1, P_1 state by varying the wave angle from the Mach angle to a normal shock. It must therefore contain both the (P_2, δ_2) and (P_4, δ_4) states which are attained from the same (P_1, M_1) . Therefore, the intersection of a second polar curve for R with an origin at 2, determines where $P_3 = P_4$ and $U_3 \parallel U_4$ since from the diagram, $\delta_4 = \delta_2 - \delta_3$. In Fig. 5b the R curve is located for pictorial clarity; in reality it is quite close to the sonic point. Thus in T coordinates 2, 3 and 4 are a patchwork of near sonic flows and it is unlikely that a stable steady state fulfillment of Fig. 5a is possible. Once $P_3 = P_4$ and δ_4 are known, standard oblique shock relations generate all other desired data including (T_3, U_3) and (T_4, U_4) . Table II shows the percentage difference in photographically measured S wave angles, ϕ_m , and the three shock theory calculated ϕ_c (from M_2^* and δ_w); the validity of the latter is confirmed.

Because of space limitation, the derivation, Ref. (2b), of the slip flow equations will only be summarized. With the x axis now parallel to the direction of flow, Fig. 6 shows the momentum, δ_m , and thermal, δ_T , thicknesses in relation to the boundary conditions. The objective now is to express δ_T as a function of x , K and known parameters.

The usual boundary layer approximations are applied to the momentum equation with $\nabla P = 0$. A similarity transformation then expresses the dimensionless stream function, $f(\eta)$, Eq. (20), in terms of the independent Illingworth variable, η , Eq. (22) to allow for varying ρ and T . The standard Blasius equation results, Eq. (24), in which $f' = df/d\eta$ etc. The similarly transformed energy equation expresses a dimensionless temperature, g , Eq. (21) in terms of η , f and the Prandtl number, $Pr = C_p \mu / K$, Eq. (25), in which $g' = dg/d\eta$, etc.

$$\psi \equiv \sqrt{\xi} f(\eta) \quad (20) \quad \eta \equiv (U_3 / \sqrt{2\xi}) \int_0^y \rho dy^* \quad (22)$$

$$g \equiv (T - T_3) / (T_4 - T_3) \quad (21) \quad \xi \equiv (\rho_3 \mu_3 U_3) x \quad (23)$$

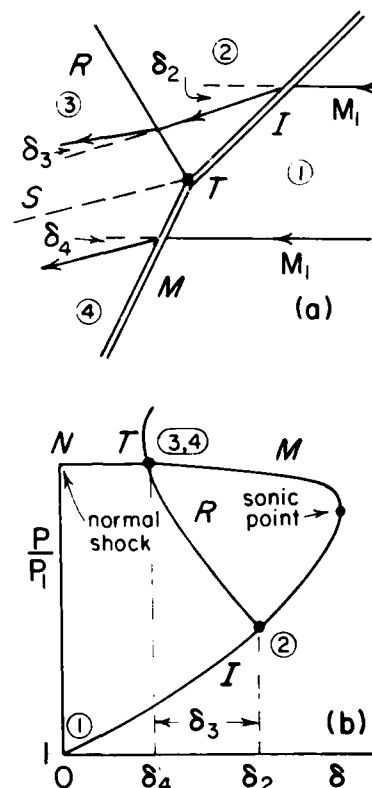


FIG. 5 Steady state representation of the triple point region in the (a) physical and (b) P - δ planes.

$$f''' + ff'' = 0, \quad \text{BC: } \begin{cases} \eta \geq 0, & f'(+\infty) = 1, & f(0) = 0, & f'(0) = f' \\ \eta \leq 0, & f'(-\infty) = U_4/U_3, & f(0) = 0, & f'(0) = f' \end{cases} \quad (24)$$

$$g'' + (\text{Pr})fg' = 0, \quad \text{BC: } \{g(+\infty) = 0, g(-\infty) = 1\} \quad (25)$$

Equations (24), (25) imply several simplifications as justified by the near unity experimental $U_4/U_3 \approx T_3/T_4 \approx 0.96$, namely; the neglect of viscous dissipation, placing $\rho\mu/\rho_3\mu_3 = 1$, and constant C_p , K and μ over the range of varying T . f_0' is iteratively chosen to be that value which smoothly joins the two half plane solutions along $\mu = 0$. It is noteworthy that K appears only in the Prandtl number, Pr .

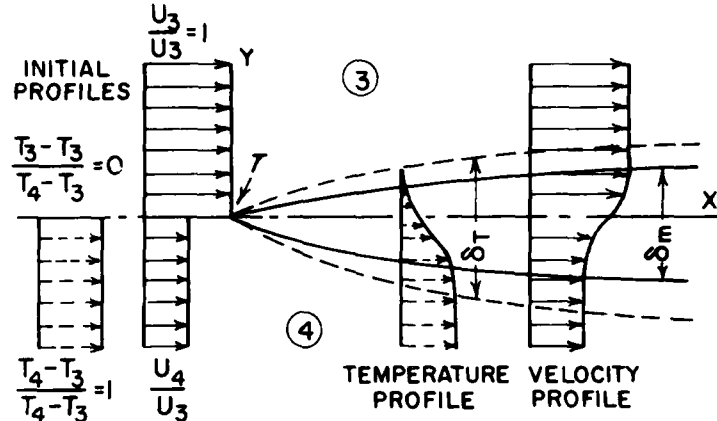


FIG. 6 Slip flow region showing momentum, δ_m , and thermal, δ_T , thicknesses.

In the $U_4/U_3 = 1$ limit, $f = \eta$ and Eq. (25) is easily integrated:

$$g = (1/2)(1 - \text{erf}[(\text{Pr}/2)^{1/2}\eta]) \quad (26a) \quad \text{or,} \quad \eta = (\text{Pr}/2)^{-0.5} \text{erf}^{-1}(1-2g) \quad (26b)$$

If the dimensionless thermal thickness, δ_T^* is associated with the $\Delta\eta$ between the conventional $g = 0.01$ and 0.99 limits, then Eq. (26b) gives the (a) result below:

$$\delta_T^* = \begin{cases} 4.653 \text{ Pr}^{-0.5000} & U_4/U_3 = 1 \\ 4.705 \text{ Pr}^{-0.5002} & U_4/U_3 = 0.96 \\ 4.813 \text{ Pr}^{-0.518} & U_4/U_3 = 0.80 \end{cases} \quad \begin{matrix} (27a) \\ (27b) \\ (27c) \end{matrix}$$

A general numerical integration of Eqs. (24), (25), Ref. (2a) for the (b) and (c) U_4/U_3 values shown shows that δ_T^* is very insensitive to U_4/U_3 in the unity range. As most of the applications were near 0.96 the Eq. (27b) formula with a 0.500 exponent was adopted. Using Eq. (22) to formulate δ_T^* gives

$$\delta_T^* = U_3/\sqrt{2\xi} \int_{\eta(g=0.01)}^{\eta(g=0.99)} \rho d\eta \approx U_3/\sqrt{2\xi} [(\rho_3 + \rho_4)/2] \delta_T \quad (28)$$

in which δ_T (mm) is the corresponding physical thickness. Elimination of ξ by Eq. (23) and δ_T^* between Eqs. (27b) and (28) gives the desired expression for K , upon recalling that $\text{Pr} = C_p\mu/K$;

$$K = (C_p/177.09)(\rho_3 U_3/x)(1 + \rho_4/\rho_3)^2 (\delta_T^*)^2 \quad (29)$$

The μ from Pr cancels the μ in ξ so that the $K(x, \delta_T)$ is independent of μ in the range of near unity U_4/U_3 ratios.

Interferograms of the slip flow region were obtained with a Michelson interferometer in the Twyman-Green (double pass) form; illumination was by nitrogen laser giving a 10 ns flash at $\lambda = 337.1$ nm, Fig. 7. A 14.0 nm bandpass filter at this λ was used to block extraneous radiation. The magnification was 2.20:1 and reference (no flow) interferograms were taken for each shot.

The molar refractivity of argon at 337.1 nm was calculated by the one term Cauchy formula (2d,7) to be $N = 4.376$. The percent difference of measured, ΔS_m , and calculated ΔS_c fringe shifts are given in Table II and validated both the value of the molar refractivity and the three shock analysis used to

TABLE II: MRM Results

Run No.	M_s^*	$\frac{\phi_m - \phi_c}{\phi_m}$ (%)	$\frac{\Delta S_m - \Delta S_c}{S_m}$ (%)	δ_T^{\dagger} {mm}	x {mm}	T {K}	K^*
341	6.617	-0.37	-7.45	0.259	46.68	4479	2.675
342	6.953	+0.48	-4.59	0.284	46.15	4909	3.231
343	7.259	+0.26	-3.48	0.257	42.38	5329	3.098
345	6.361	+0.40	-0.51	0.281	50.95	4146	2.690
346	6.013	-0.63	+2.00	0.271	48.52	3733	2.458
348	6.730	+0.55	-0.99	0.291	50.33	4616	3.023

*K(10⁻⁴ cal/cm⁻¹ s⁻¹ K⁻¹)

denominator. Measurements were made with an uncertainty of about ± 0.02 mm. From the known position of the reference wire across the interferogram the x distance to T was calculated from triple shock theory. The resulting δ_T^{\dagger} , x and K data are presented in Table II. Least square fits of the $K(T)$ data to a power law gives:

$$K = K_0 (T/T_0)^{\nu} \quad \nu = 0.700 \pm 0.017 \quad (30)$$

The authors regard the excellent agreement with the SPM results as possibly fortuitous due to the small number of data and the inherent uncertainties in evaluating K from small fringe shifts. Nevertheless, the agreement does lend powerful support to both the $\nu = 0.70$ value and the basic validity of both methods. Figure 8 presents the superposed SPM and MRM results and Table III gives the present ν results in relation to those of others.

The MRM has the marked advantage of being much less sensitive to stray

calculate ΔS_c . Instead of using the difficult to locate $g = 0.01$ and 0.99 contours to measure δ_T , a different δ_T^{\dagger} was identified with the more accurately locatable $g = 0.50$ and 0.95 contours. In Eq. (29), δ_T^{\dagger} then replaces δ_T and 21.975 replaces 177.09 in the



FIG. 7 Laser interferogram (10 ns) of slip flow region, 2.20:1 mag.

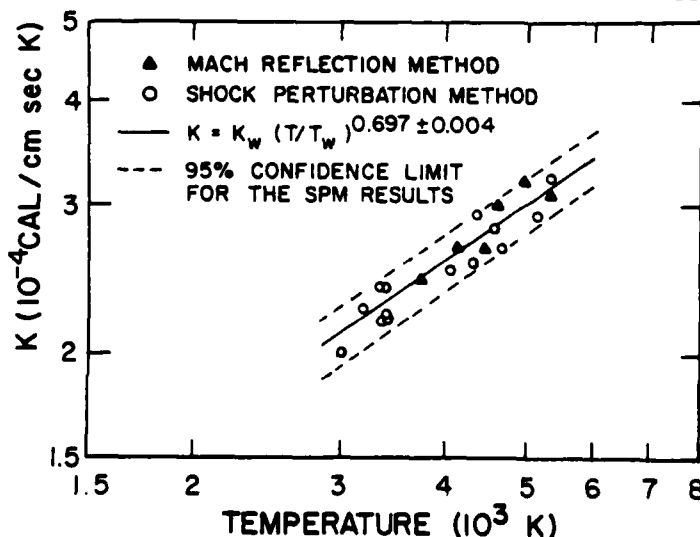


FIG. 8 Comparison of SPM and MRM $K(T)$ results for argon.

disturbances than the SPM. It is also applicable to any gas since only the constancy of μ , K and C_p from T_3 to T_4 was assumed; no specific value of for Pr was needed or assumed. All the difficulties of the MRM as developed here, stem from the interferometric data acquisition and the resulting analysis uncertainties. The authors feel that if continuous high speed data acquisition could be used, like that for the SPM, the MRM would likely be the best method to date.

TABLE III: Comparison of Present ν Values with Others.
TCM (Thermal Column Method; RSM (Reflected Shock Method).

Investigator(s)	Method	Temperature Range	Exponent
Present Results	SPM	2900-5400K	0.697±0.004
	MRM	3700-5350K	0.700±0.017
Saxena & Saxena (8)*	TCM	350-1500K	0.731±0.008
Saxena (9)	RSM	1500-6000K	0.800
Matula (10)	RSM	1500-4800K	0.680±0.010
Bunting & Devoto (11)	RSM	2500-9200K	0.668±0.020
Kuiper (12)	RSM	2500-9200K	0.750±0.010
Willeke (13)	RSM	2100-16400K	0.749±0.023
Collins & Menard (14)	RSM	1500-5000K	0.703
Poliakov & Spirin (15)	RSM	2500-10000K	0.700
Smiley (16)*	RSM	1100-3300K	0.688±0.005

*Fitted by present authors

REFERENCES

1. CAVERO, A.E., PhD Thesis, U. of Wis. (1978) "Thermal Conductivity Measurement of Argon by the Shock Perturbation Method", (a) p. 4; (b) pp. 18,20,132; (c) pp. 84,89; (d) p. 74; (e) p. 63; (f) p. 115.
2. CHUNG, K. PhD Thesis, U. of Wis. (1978) "Thermal Conductivity Measurement of Argon by the Mach Reflection Method", (a) p. 19; (b) p. 43; (c) pp. 50,53; (d) pp. 83,87.
3. CHAMPOMIER, F., MS Thesis, U. of Wis. (1972) "Some Design and Performance Aspects of the New Wisconsin Shock Tube".
4. CHUNG, K. MS Thesis, U. of Wis. (1974) "Operational Aspects of the Wisconsin Shock Tube".
5. MOORE, F.K., NACA TR-1165 (1954).
6. CHU, A.C., PhD Thesis, U. of Wis. (1970) "Thermal Conductivity Measurement of Air by the Shock Perturbation Method", p. 28.
7. ALPHER, R.A. and WHITE, D.R., *Phys. Fluids*, 162, 2 (1959).
8. SAXENA, V.K. and SAXENA, S.C., *Chem. Phys. Letters*, 2, 44 (1968).
9. SAXENA, S.C., "Determination of Thermal Conductivity of Gases by Shock-Tube Studies", *High Temperature Sci.*, 4, 517 (1972).
10. MATULA, R.A., "High Temperature Thermal Conductivity of Rare Gases and Gas Mixtures", *J. of Heat Trans.*, 90, 319 (1968).
11. BUNTING, J.O. and DEVOTO, R.S., NASA CR88360 (1967).
12. KUIPER, R.A., *SUDDAR NO. 353*, Stan ord U. (1968).
13. WILLEKE, K. and BERSHADER, D., *AIAA J.*, 7, 11 (1969).
14. COLLINS, D.J. and MENARD, W.A., *J. Heat Trans.*, 88, 52 (1966).
15. POLIAKOV, Y. and SPIRIN, G.G., *Teplofiza Sovistva Gazov*, 3rd (1968).
16. SMILEY, E.F., "The Measurement of the Thermal Conductivity at High Temperatures with a Shock Tube; Experimental Results in Argon at Temperatures Between 1000 K and 3000 K", PhD Thesis, Catholic U. of America Press, Washington, D.C. (1957).
17. LAW, C.K. and GLASS, I.I., *C.A.S.I. TRANSACTIONS*, 2, Vol. 4, No. 1 (1971).

AD P000254

TEMPERATURE MEASUREMENTS OF AN IMPLOSION FOCUS*

T. Saito, A. K. Kudian** and I. I. Glass

Institute for Aerospace Studies, University of Toronto
Toronto, Canada

Spectroscopic temperature measurements were made at the focal point of imploding shock waves in the UTIAS implosion chamber, which has a 20-cm diameter hemispherical cavity. The chamber was filled with a stoichiometric H_2-O_2 gas mixture at different initial pressures ($14 \sim 68$ atm). The mixture was ignited at the origin by an exploding wire generating an outgoing detonation wave which reflected at the chamber wall as an imploding shock wave (gas-runs). Additional experiments where an explosive shell of PETN was placed at the hemispherical wall were also conducted. The shell was detonated by the impact of the reflected gaseous detonation wave at its surface, thereby generating an intense implosion wave (explosive-run). The temperatures were measured at the implosion focus using a medium quartz Hilger spectrograph with an eight photocell polychromator attachment over the visible wavelength range. The measured radiation intensity distributions were fitted to blackbody curves. The temperatures were $10,000 \sim 13,000$ K for gas runs, and $15,000 \sim 17,000$ K for explosive runs. The continuous spectra from photographic film and the measured emissivities, which were very close to unity, confirmed that the plasma was a blackbody. Numerical studies using the random choice method (RCM) and classical strong-shock theory were used to analyse the flows in the entire range of the implosion process. Real-gas effects and radiation losses were also considered. The results were compared with the experimental data and good agreement was obtained.

1. INTRODUCTION

The UTIAS explosive-driven implosion chamber has been used in several research areas since it was conceived by Glass (Ref. 1) in the early 1960's. The extremely high pressures and temperatures generated at the focus of implosions were utilized for driving projectiles to hypervelocities (Ref. 2), as a shock-tube driver (Ref. 3), and to produce diamonds (Ref. 4). Currently, experimental studies were done on deuterium-deuterium fusion reactions and

*This work was supported by the Canadian Natural Sciences and Engineering Research Council, the U.S. Air Force under Grant AFOSR-77-3303, and the U.S. Army Research Office.

**Senior Physicist, Fraser Papers Inc., Thorold Division, Thorold, Ontario.

measurements of the resulting neutrons and gamma rays (Ref. 5).

The conditions produced by imploding spherical shock waves were first obtained by Guderly (Ref. 6). His self-similar solutions, however, deal only with very strong shock waves. They do not allow for any characteristic lengths, such as the chamber radius in the present problem. Consequently, in the present study, the conditions in the chamber were calculated by combining the numerical results of the RCM and solutions using strong-shock theory.

The principle of operation of the UTIAS 20-cm dia implosion chamber can be understood by referring to Fig. 1. The hemispherical chamber is filled with a $2\text{H}_2+\text{O}_2$ mixture at high pressure (14 ~ 68 atm for pure gas runs and 27 atm for explosive runs). The gas is ignited by exploding a fine nickel wire (0.13 mm dia x 1 mm long) at the origin of the hemisphere creating an outgoing detonation wave which is reflected at the hemispherical-chamber wall and then converges on the origin as an imploding shock wave. For an explosive run, a PETN explosive shell bonded against the wall of a copper-carrier liner is ignited upon reflection of the detonation wave and further reinforces the imploding shock wave. The imploding wave is again reflected at the origin leaving behind an extreme high-pressure-temperature region. The objective of the present work was to measure the peak temperature of this region and compare the data with analysis.

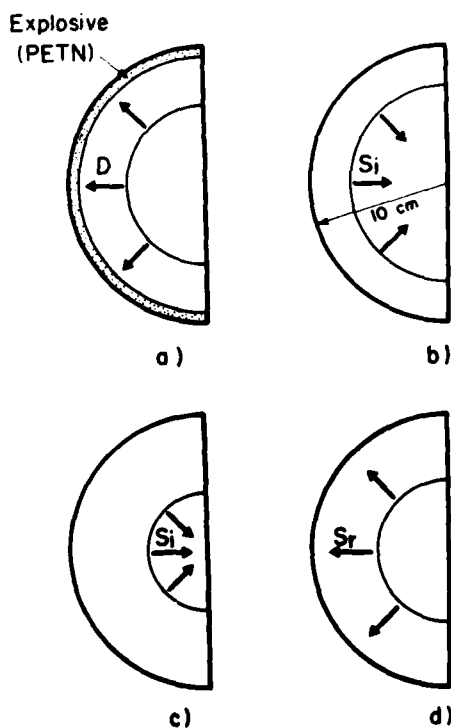


Fig. 1 Schematic of implosion chamber wave dynamics.

- (a) Outgoing detonation wave in $2\text{H}_2+\text{O}_2$ mixture.
- (b) Detonation wave reflects as a shock wave (or initiates the hemispherical PETN liner when used).
- (c) Implosion phase onto the origin when the converging shock becomes very strong.
- (d) Implosion reflects as an exploding shock wave leaving behind a high-pressure-temperature region.

In previous experiments, time-integrated (Ref. 7) as well as time-resolved colour-temperatures of the implosion focus made with large observing areas (3 x 9 mm) were found to be surprisingly low (4000 to 5000 K) (Ref. 8). In the present work, a much smaller observing area (0.55 mm dia) was used and time-resolved simultaneous measurements were made at eight wavelengths covering the visible region. Our temperature measurements are more precise (Ref. 11) and are in better agreement with expected values. Also, the emissivity of the radiating plasma was evaluated for the first time.

2. EXPERIMENTAL ARRANGEMENTS

The UTIAS implosion chamber consists of two massive front and rear plates held together by 32 large bolts (Ref. 9). A 20-cm dia hemispherical cavity is machined in the rear plate supporting a hemispherical copper liner. An explosive PETN package is manufactured on the inner surface of the copper liner for explosive runs. The barrel, which holds the Plexiglas observing window, the gas inlet and the exploding wire are installed in the front plate. For explosive runs, a 20-degree conical liner plate is added to the front plate to guard the chamber from any serious mechanical damage due to off-focus implosions (Ref. 10).

A 0.13-mm dia x 1-mm long nickel wire is exploded at the geometrical centre of the chamber by discharging a 1- μ F capacitor charged to 21 KV. All spectroscopic observations were made with a Hilger medium-quartz spectrograph. For photographic work Kodak Plus-X pan film was used. For time-resolved photoelectric recording a photomultiplier attachment enabled simultaneous measurements at eight wavelengths (3900, 4128, 4391, 4710, 5123, 5629, 6328 and 7525 Å). The time-response of the system was about 0.1 μ sec. The calibration of the photomultipliers was done in the conventional manner using a calibrated tungsten ribbon strip lamp.

For gas runs, a $2H_2+O_2$ gas-mixture was filled at different pressures (13.6, 27.2, 40.9, 54.5 and 68.1 atm). Thickness of 1.6 mm and 3.2 mm PETN explosive shells were used with a $2H_2+O_2$ gas-mixture of 27.2 atm initial filling pressure for explosive runs. These explosive shells weighed approximately 40g and 80g, respectively.

3. EXPERIMENTAL RESULTS

Pictures of the radiation spectrum of the first implosion pulse were taken to investigate the characteristics of the radiation with a rotating-disk shutter. Details of the operation of the shutter can be found in Refs. 7 and 11. It was found that the spectrum was completely continuous suggesting that the temperature of the radiating gas at the implosion focus can be determined by finding a blackbody curve of a certain temperature which fits best to the experimental data. The temperature measurements were carried out photoelectrically with the experimental set-up shown in Fig. 2. A brass mask with a small hole (0.55 mm dia) at the centre was placed on the window surface. The observing area was determined by the hole size and the width of the entrance slit of the spectrograph.

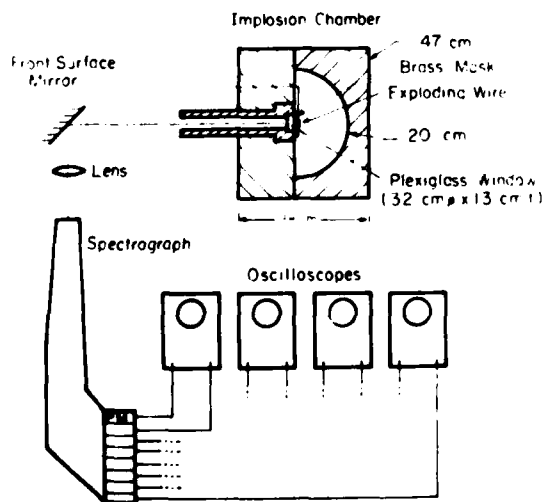


Fig. 2 Schematic diagram of experimental facility to study spherical implosions.

A typical oscillogram of a time-resolved measurement for a gas run is shown in Fig. 3. The recordings are strongly disturbed by the electromagnetic pick-up from the discharge system of the exploding wire. The interference disappears in about 30 μ sec and the radiation intensity stays at a quite constant value until the first implosion wave comes back to the origin. The implosion time (the time between the ignition and the arrival of the implosion shock wave at the centre) was approximately 75 μ sec for gas runs and 59 μ sec and 56 μ sec for explosive runs of 1.6 and 3.2 mm PETN layers, respectively. In gas runs some subsequent implosion pulses were observed although the radiation intensities were much lower than the first implosion pulse. The window broke about 500 \sim 700 μ sec after ignition for gas runs and about 16 μ sec after the first implosion pulse for explosive runs.

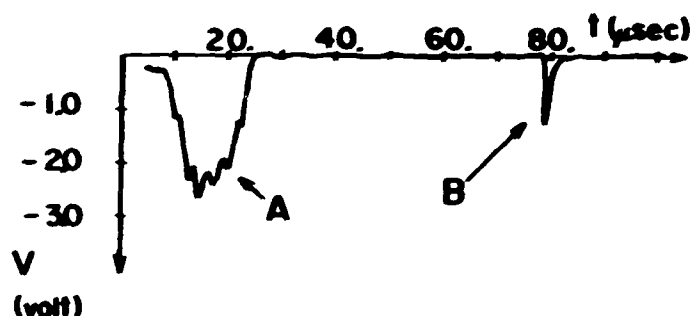


Fig. 3. Typical output signal from photomultiplier for a gas run.
 $P_0 = 27.2$ atm, $\lambda = 5125\text{\AA}$.

A: Noise from discharging system + radiation from exploding wire.

B: Implosion pulse.

The radiation intensities at eight different wavelengths which cover the whole visible radiation range were measured for each run to eliminate the run-to-run fluctuation due to the variation in the degree of focussing.

The radiation intensity of a graybody at a given temperature T and wavelength λ_i is expressed as

$$I_{\lambda_i} = E \cdot B_{\lambda_i}(T) \quad (1)$$

where $B_{\lambda_i}(T)$ is the Planck law,

$$B_{\lambda_i}(T) = \frac{C_1}{\lambda_i^5} \frac{1}{\exp(C_2/\lambda_i T) - 1} \quad \frac{\text{erg}}{\text{cm}^2 \cdot \text{sec} \cdot \text{ster}} \quad (2)$$

with $C_1 = 1.191 \times 10^{-5} \text{ erg} \cdot \text{cm}^2 \cdot \text{sec}^{-1}$ and $C_2 = 1.4388 \text{ cm K}$; E is the emissivity of the radiating gas. Under the condition $\exp(C_2/\lambda_i T) \gg 1$, $B_{\lambda_i}(T)$ can be replaced by the Wien approximation,

$$B_{\lambda_i}(T) \approx \frac{C_1}{\lambda_i^5} \exp\left(\frac{-C_2}{\lambda_i T}\right) \quad (3)$$

Substituting Eq. (3) into Eq. (1) results in

$$\ln\left(\frac{C_1}{I_{\lambda_i} \lambda_i^5}\right) = \frac{C_2}{T} \frac{1}{\lambda_i} - \ln E \quad (4)$$

Obtaining the intensities I_{λ_i} ($i = 1, 2, \dots, 8$) experimentally, the temperature can be determined from the slope of the line which goes through the data points of a plot of the values of the left-hand side of Eq. (4) against the wave number ($1/\lambda_i$). The emissivity can also be evaluated from the values at the intersection of the line with the vertical axis. However, after evaluating

some experimental data, it was found that the temperature range obtained at the implosion focus was above 10,000 K and the accuracy of Wien's approximation was poor. Therefore, in practice, the temperature and emissivity were varied to minimize the sum of the squares of deviations in the experimentally obtained intensities from the intensities given by Eq. (2). Typical results of a gas run and an explosive run are shown in Fig. 4. The results are presented taking advantage of Eq. (4), namely, the solid lines are drawn in such a way that their slopes and their intersections with the ordinate represent the temperature and emissivity obtained by using Planck's law and the data points are correspondingly corrected by a factor

$$F_{\lambda_i}(T) = 1 - \exp \frac{C_2}{\lambda_i T} \quad (5)$$

which is simply the ratio of Planck's law to Wien's approximation.

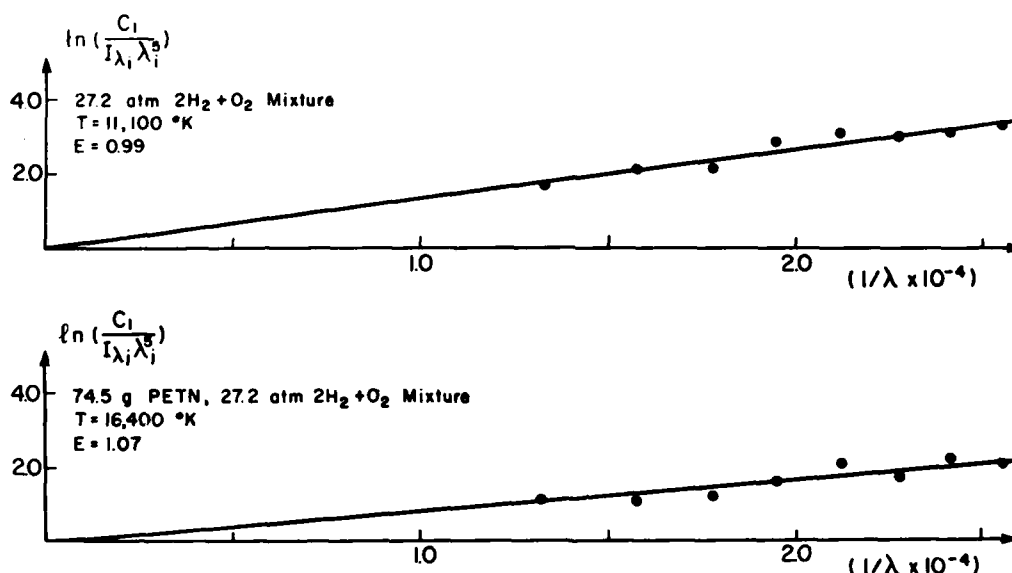


Fig. 4. Experimental results for a gas run and an explosive run.

It was found that the emissivity of the radiating gas was very close to unity except for the low initial pressure gas runs ($p_0 = 13.6$ and 27.2 atm) where the emissivities have a range of $0.7 \sim 0.9$.

4. ANALYTICAL PREDICTIONS

In the present study, the RCM was employed to calculate the imploding stage. Details of the RCM are available in Refs. 12 to 15. In the RCM, the waves are propagated statistically and the discontinuities such as shocks and contact surfaces appear as perfectly sharp fronts without any smearing, unlike finite-difference schemes using artificial viscosity. Self-similar solutions for constant speed spherically expanding Chapman-Jouguet (C-J) detonation waves in the detonation stage were calculated to give the initial conditions for the imploding stage (Ref. 16). The details of the numerical results from the RCM and strong-shock theory for gas runs and explosive runs are given in full in Ref. 11.

5. COMPARISON OF EXPERIMENTAL RESULTS AND THEORY

Figure 5 compares the experimental results and the expected average tem-

peratures over a 0.55-mm dia circular area at the origin. The calculated temperature depends on the position of the imploding shock wave. When the wave radius is larger than the radius of the observing area only the wave front can be seen through the window. When the imploding shock wave comes inside the observing area, not only the wave front but also the region behind the imploding shock wave is seen and the averaged temperature becomes lower than the temperature at the wave front. This arises from the rapidly falling temperature behind the implosion wave. As a result, the averaged temperature has a maximum when the radius of the imploding shock wave is slightly smaller than the radius of the observing area. The imploding shock radius at which this occurs is called R^* , as shown on Fig. 5. In other words, there is a certain maximum observable temperature for a certain size of observing area no matter how small the imploding shock wave converges. This maximum temperature and the temperatures which are expected to be observed when the imploding waves are at different radii from the centre are also shown in Fig. 5. In principle, if it were possible to place the observing area exactly at the focus of the implosion then higher temperatures would be measured with decreasing mask hole size. However, in practice the size of 0.55 mm dia was found to be an optimum limit considering the time resolution of the present measuring system.

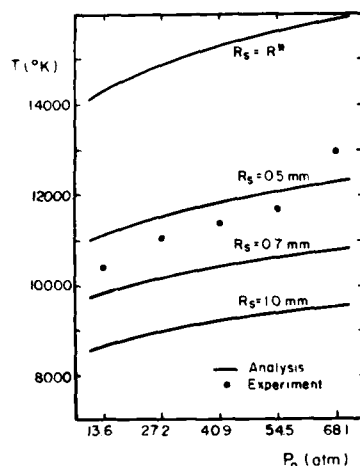


Fig. 5(a). Comparison of experimental results with analysis for gas runs.

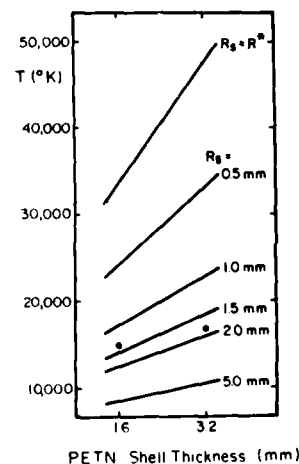


Fig. 5(b). Comparison of experimental results with analysis for explosive runs.

For gas runs the dependence of measured temperatures on the initial filling pressures agreed quite well with the analytical predictions although the absolute values of the temperatures were somewhat ($\sim 20\%$) lower than the expected maximum temperatures. The lower values of the measured temperature can be attributed to the fact that the temperature behind the imploding shock front decreases rapidly. When the temperature is measured in a radial direction from a certain point ahead of the wave front, it would be lower than the front temperature. It would probably be a kind of averaged temperature of the region between the shock front and a certain point behind the front by about the same distance as the radiation mean free path. It has been calculated that, when the imploding wave radius R_s has converged to R^* (~ 0.25 mm, in Fig. 5), the temperatures at points 5 and 63 μ behind the shock front are, respectively, 90 and 60% of the shock-front temperature.

For the explosive runs, the measured temperatures were much lower than the expected temperatures. Also the increase in the measured temperatures for increased PETN thickness was small compared with the analytical prediction.

Considering the much higher temperatures in explosive runs at the shock front than in gas runs, the so-called "screening effect" of the preheated gas layer ahead of the shock front (Ref. 17) is probably the reason for this phenomenon.

Although the measured maximum temperatures were relatively low and corresponding to large analytical radii for the imploding waves in explosive runs, the pressures obtained in explosive runs are much higher than in gas runs even for the highest initial gas pressure ($p_0 = 68.1$ atm) as the window breaks much faster in explosive than in any gas runs. The final size of the implosion focus which gives the measured temperature obtained analytically is about 1.5 mm radius. The final pressure that would be obtained in an explosive run for this focal size corresponds to the pressure which would be obtained in a gas run of $p_0 \sim 54$ atm when it converged to about 0.6 mm radius. However, the window breaks nearly 20-fold faster in the explosive runs, producing a pressure far beyond what can be produced in a gas run of 54 atm initial pressure. Despite the fact that the observed temperature remains at a low value, owing to the preheating of the gas ahead of the shock wave and becomes opaque with a surface temperature of about 17,000 K, the actual implosion focus continues to decrease to much smaller values (from the 1.5 mm radius). However, this has no effect on the measured temperatures as the preheated gas is opaque.

Although an appropriate perfect-gas analysis ($\gamma \sim 1.14$) was used throughout the present work, the approach appears quite reasonable. Flagg (Ref. 10) has shown that the isentropic exponent of the gas scarcely changes during the implosion and reflection stages ($\gamma \sim 1.14$) after investigating the numerical results of Brode (Ref. 18) who used an equation of state for a real gas for a burnt $2H_2+O_2$ mixture. The equilibrium compositions of the $2H_2+O_2$ system were calculated separately in the present study using the method of minimizing Gibbs' free energy (Ref. 19). It was noted that the effects of increasing temperature and pressure on dissociation and ionization compensate each other and no significant change in the composition occurred.

The radiation loss has also been estimated and it was found that the order of the loss compared to the energy flux into the shock-wave region due to the converging geometry, i.e., the inhomogeneous term of the energy equation in the lossless basic equations was negligibly small ($10^{-2} \sim 10^{-6}$), owing to the very high pressure and particle velocity ($p \sim 1.4 - 5.8 \times 10^4$ atm and $u \sim 12-24$ km/sec at $R_s = 0.1$ mm). Therefore, the radiation loss is not important for the present work.

In the most recent experiments (Ref. 5), where deuterium was used instead of hydrogen, production of neutrons and γ -rays from D-D reactions were observed. If this is the case then the final focus of the implosions could be very small, say the order of 10μ .

6. CONCLUSIONS

The continuous radiation spectra and the measured emissivities showed that the hot gases at an implosion focus from gas and explosive drivers radiate as blackbodies. The temperatures at the focal point of an imploding shock wave were measured spectroscopically in the visible region. For gas runs, the effect of the initial filling pressures on the temperature was small and 10,000 \sim 13,000 K were measured when the initial pressure was increased from 13.6 to 68.1 atm. This dependence of the temperature agreed very well with analytical results. For explosive runs, the observed temperatures were 15,000 K for a 1.6-mm and 17,000 K for a 3.2-mm shell of PETN explosive. The measured temperatures in explosive runs were limited to 15,000 \sim 17,000 K owing to the screening effect of the preheated layer ahead of the shock front, even though the imploding shock wave continued to converge. A high degree of

convergence was obtained despite the possible existence of bifurcation of the imploding shock waves due to the boundary layer developed on the flat surface and some of the unavoidable geometrical roughness of the chamber around the origin (which is not small, if we talk about a final focus in the micron range). It is even more remarkable if neutrons and γ -rays can be obtained (Ref. 5). Many additional investigations are still needed to settle the question of the actual final focal size and the physical conditions which exist there. Further details can be found in Ref. 11.

REFERENCES

1. I. I. Glass, "Appraisal of UTIAS Implosion-Driven Hypervelocity Launchers and Shock Tubes", in Prog. in Aerospace Sci., edited by D. Kuchemann, Vol. 13, pp. 223-291, Pergamon Press, Oxford and New York, 1972.
2. R. F. Flagg and I. I. Glass, "Explosive-Driven Spherical Implosion Waves", Phys. Fluids, 11, 10, pp. 2282-2284, 1968.
3. I. I. Glass, H. L. Brode and S. K. Chan, "Strong Planar Shock Waves Generated by Explosively-Driven Spherical Implosions", AIAA J. 12, 3, pp. 367-374, 1974.
4. I. I. Glass and S. P. Sharma, "Production of Diamonds from Graphite Using Explosive-Driven Implosions", AIAA J. 14, 3, pp. 402-404, 1976.
5. I. I. Glass and D. Sagie, "Application of Explosive-Driven Implosions to Fusion" (to be published).
6. G. Guderley, "Strong Spherical and Cylindrical Shock Waves in the Neighbourhood of the Center of the Sphere or the Axis of the Cylinder", Luftfahrtforschung, 19, 9, pp. 392-412, 1942.
7. D. E. Roberts and I. I. Glass, "Spectroscopic Investigation of Combustion-Driven Spherical Implosion Waves", Phys. Fluids, 14, 8, pp. 1662-1670, 1971.
8. R. A. Roig and I. I. Glass, "Spectroscopic Study of Combustion-Driven Implosions", Phys. Fluids, 20, 10, pp. 1651-1656, 1977.
9. W. Czerwinski, "Structural Design and Development of UTIAS Implosion-Driven Launchers", UTIAS Report No. 153, 1971.
10. R. F. Flagg, "The Application of Implosion Wave Dynamics to a Hypervelocity Launcher", UTIAS Report No. 125, 1967.
11. T. Saito, "An Analytical and Experimental Study of the Temperatures at Implosion Foci Produced by Combustion and PETN-Explosives", University of Toronto Ph.D. Thesis, in progress.
12. J. Glimm, "Solution in the Large for Nonlinear Hyperbolic Systems of Equations", Comm. Pure Appl. Math. 18, pp. 697-715, 1965.
13. A. J. Chorin, "Random Choice Solution of Hyperbolic Systems", J. Comp. Phys. 22, pp. 517-533, 1976.
14. G. A. Sod, "A Numerical Study of a Converging Cylindrical Shock", J. Fluid Mech. 83, 4, pp. 785-794, 1977.
15. T. Saito and I. I. Glass, "Applications of Random-Choice Method to Problems in Shock and Detonation-Wave Dynamics", UTIAS Report No. 240, 1979.
16. J. H. Lee, R. Knystautas and G. G. Bach, "Theory of Explosions", McGill University, MERL Report 69-10, 1969.
17. Ya. B. Zel'dovich and Yu. P. Raizer, "Physics of Shock Waves and High-Temperature Hydrodynamic Phenomena", Vols. I and II, Academic Press, 1967.
18. H. L. Brode, "Theoretical Description of the Performance of the UTIAS Hypervelocity Launcher", Astronautica Acta. 15, pp. 301-309, 1970.
19. C. W. Stroud and K. L. Brinkley, "Chemical Equilibrium of Ablation Materials Including Condensed Species", NASA TN D-5391, 1969.

Part IV: SHOCK STRUCTURE AND PROPAGATION

AD P000255

BOUNDARY LAYER INFLUENCED SHOCK STRUCTURE

F. Seiler

German-French Research Institute Saint-Louis
Saint-Louis, France

The region of a shock wave close to a wall is subject to theoretical and experimental investigations. For the theoretical description of the flowfield the direct Monte Carlo simulation method is used. The theoretical results are compared with experimental data, obtained with a multi-beam laser differential interferometer in a low density shock tube. The influence of the wall boundary layer on the shock structure and the shock curvature will be discussed as a function of the shock strength, the intermolecular potential and the accommodation coefficient at the wall.

INTRODUCTION

A shock wave, moving along an infinite wall, develops a two-dimensional structure in the region close to the wall. Figure 1 gives an impression of the flowfield of interest. The quiescent gas initially ahead of the shock wave is set in motion by the

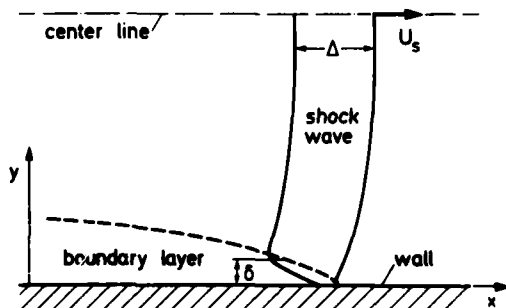


Figure 1. Shock-surface interaction

shock and is accelerated to high speeds within a distance of a few mean free path λ_1 of the quiescent gas. This acceleration is accompanied by a rise in temperature, pressure and density for the

gas. Due to the boundary conditions, the moving gas downstream of the shock wave is slowed down at the wall and the gas temperature equals the temperature at the wall. Where the shock touches the wall a shear layer develops, which is the beginning of the boundary layer downstream of the shock. This shear layer is subject to the theoretical and experimental investigations.

THEORY

The direct Monte Carlo simulation method, as developed by Bird (ref. 1) is used to describe the flow in the region of interest. The physical model to apply the simulation technique to this two-dimensional problem is shown in Figure 2. The simulated

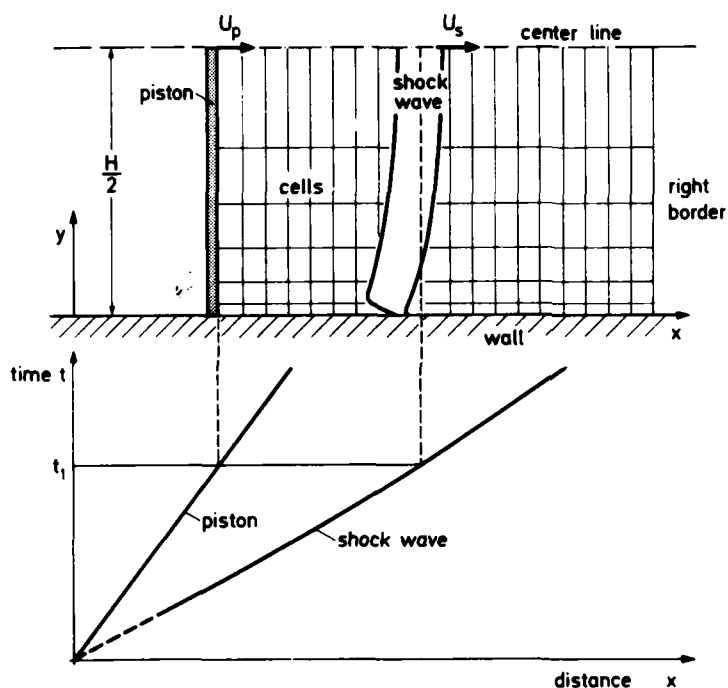


Figure 2. Simulation model

flowfield is bounded by a piston, a center line, a right border and a solid wall. This region is subdivided into about 1600 cells. The flow in front of the piston is modeled in terms of about 15000 model molecules. The shock wave is generated by the piston, which is suddenly set in motion and moves with constant velocity u_p into the gas.

The simulation procedure starts with molecules having a Maxwellian velocity distribution corresponding to thermodynamic equilibrium in the quiescent gas at temperature T_1 . These molecules are uniformly distributed in space. The simulation proceeds in discrete time steps. During these steps, the molecules move according to their individual velocities and are reflected at the flow boundaries. At the solid wall, the molecules are reflected according to a wall accommodation coefficient α , the free other boundaries (right boundary, center line, piston) reflect the molecules specularly ($\alpha = 0$). At each time stop, collision pairs are selected randomly in each cell according to their relative speed. The collision process is calculated classically with a

given intermolecular potential.

The macroscopic quantities, for example density, temperature, pressure and others can be extracted by sampling and averaging over appropriate molecular quantities in each cell. Because the model number density is small, the fluctuations in the macroscopic quantities are significant. The fluctuations are reduced by repeating the simulation process several times and averaging the flow properties.

EXPERIMENT

The experiments are carried out in a low density shock tube of 150 mm inner diameter. At the end of the driven section a 90×90 mm square test section (Figure 3) was attached in which a

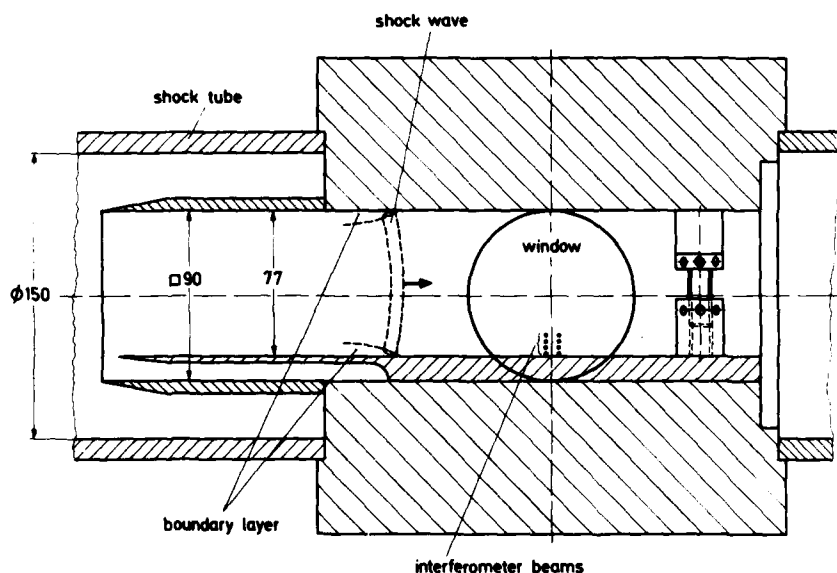


Figure 3.
Test section

flat plate (aluminium) was inserted for the measurements. The local gas density has been measured with a multi-beam laser differential interferometer. The interferometers are stacked perpendicular to the plate at wall distances from 0.15 mm to 1.5 mm. Figure 4 shows the arrangement for one of these interferometers. The measurements are obtained in argon and nitrogen at an initial pressure of 0.13 mbar and for shock Mach numbers between about three and nine. At this pressure, the mean free path λ_1 is about 0.5 mm.

The effective beam diameter in the test section was 0.19 mm and the distance between the beams of one interferometer was 3.3 mm. This combination provided sufficient resolution in time and space for the density measurements in the region of interest.

The test section was arranged sufficiently far downstream of the diaphragm that the flow is fully developed at the location of the density measurements.

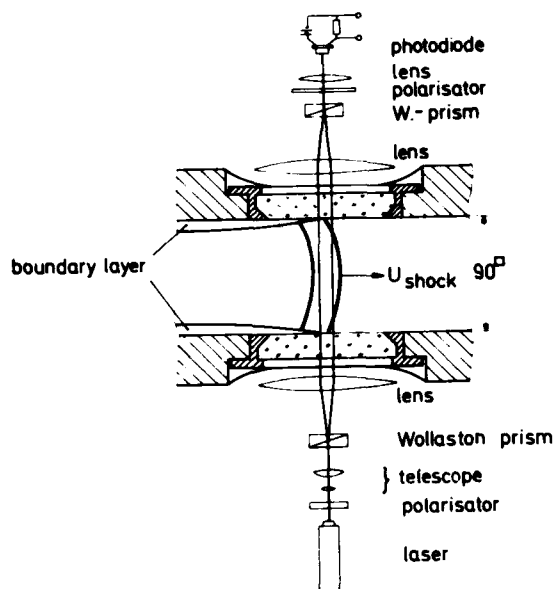


Figure 4. Laser differential interferometer

RESULTS

In Figures 5 through 7, the experimental density profiles closest to the wall ($y/\lambda_1 = 0.28$) in argon are compared with Monte

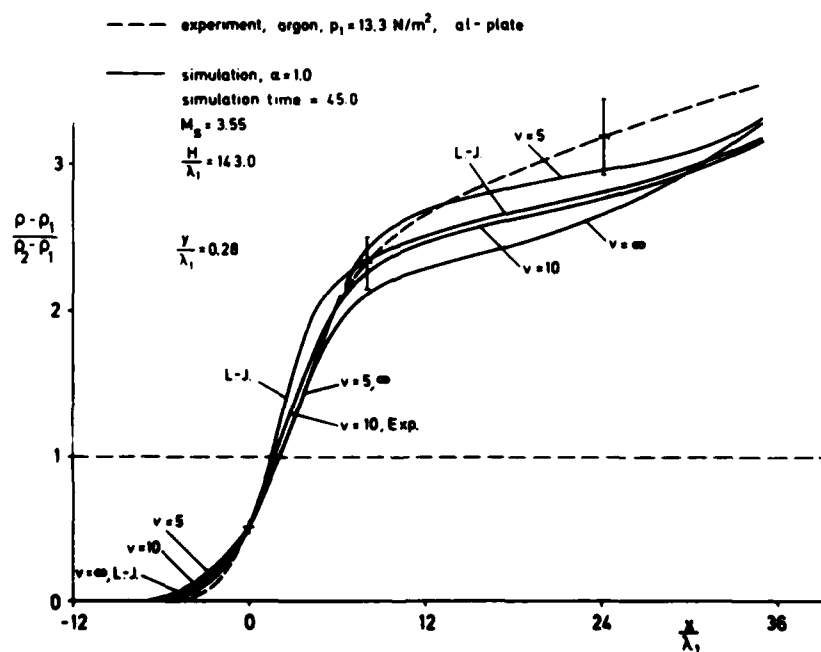


Figure 5. Numerical and experimental results

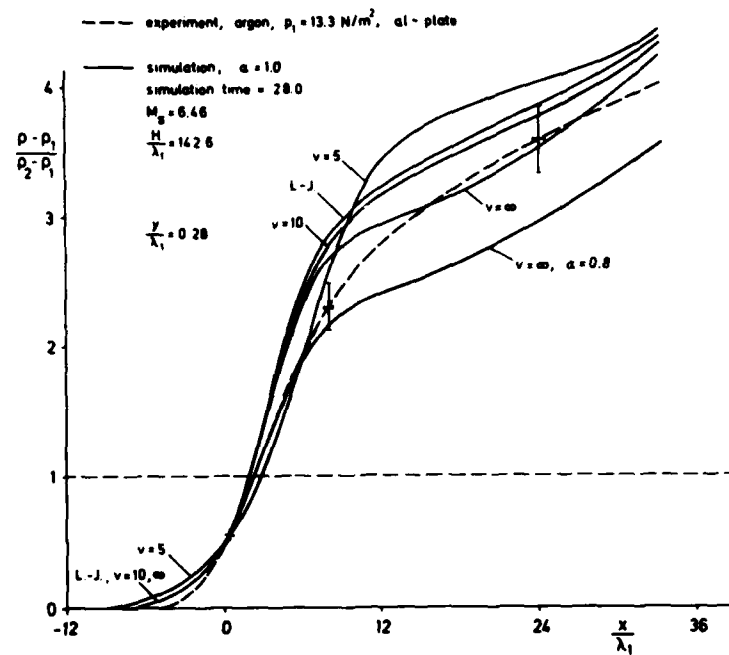


Figure 6. Numerical and experimental results

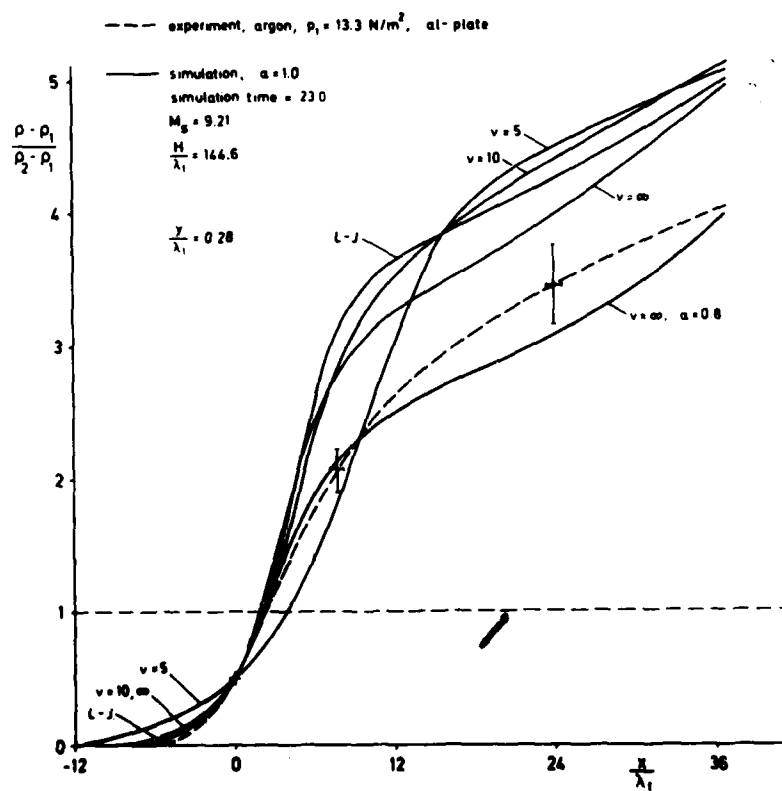


Figure 7. Numerical and experimental results

Carlo calculations. The axes are the normalized density and the normalized distance along the wall. The density is normalized with ρ_1 , the density upstream of the shock and ρ_2 , the theoretical density rise downstream of the normal shock wave. For the simulation calculations, the Lennard-Jones (12-6) potential, the repulsive potential proportional to $1/r^{v-1}$ with $v = 5$ and 10 and the hard-sphere model ($v = \infty$) are assumed.

For comparing together different density profiles, these are crossed at $(\rho - \rho_1)/(\rho_2 - \rho_1) = 0.5$. The statistical scatter of the Monte Carlo results is eliminated by fairing curves through the points representing the sampling results for the individual cells.

The comparison for $M_s = 3.55$ (Figure 5) shows that the experimental profile downstream of the shock is above the calculated ones. The deviation between experiment and simulation cannot be an effect of the accommodation coefficient α , because full accommodation ($\alpha = 1$) at the wall is assumed. A reduced value for α increases the difference between theory and experiment. The repulsive potential with $v = 5$ gives better agreement than the repulsive potential with $v = 10$, the Lennard-Jones potential and the hard-sphere model. This indicates, that for this shock strength a weak potential, that is the repulsive potential with $v = 5$, with an accommodation coefficient of $\alpha = 1$ is good. Perhaps a modified repulsive part of the Lennard-Jones potential is required to improve agreement with the experimental data. Perhaps a (9-6) instead of (12-6) potential.

In Figure 6 density profiles for $M_s = 6.46$ are presented. In contrast to the data for $M_s = 3.55$ the experimental density value is now below the simulation calculations with the repulsive potential with $v = 5$ and 10 , the Lennard-Jones potential and an accommodation coefficient $\alpha = 1$. The hard-sphere model now is in the range of the experiment. Lowering the accommodation coefficient to about $\alpha = 0.9$ and calculating with the repulsive potential with $v = 10$ or the Lennard-Jones potential, results in a better agreement between experiment and theory than calculating with the hard-sphere model and $\alpha = 1$. This confirms the well-known fact that the Lennard-Jones potential is more realistic than the hard-sphere model. From these considerations it can be concluded that the accommodation coefficient α is now below unity.

The experimental result for $M_s = 9.21$ (Figure 7) is fully below the calculated ones. Good agreement, relative to the shape of the profiles and the density values, can be reached with the repulsive potential with $v = 10$ or the Lennard-Jones potential by reducing α to about 0.8 .

In Figure 8 and Figure 9 experimental and calculated density profiles in nitrogen are shown. The simulation calculations are done with the "energy sink model" using the repulsive potential with $v = 10$ and an energy transfer factor $t_f = 0.054$, corresponding to a relaxation value $Z_R = 4$. In argon the repulsive potential with $v = 10$ has given good results with a minimum of computing time needed, wherefore this intermolecular potential has been chosen for the calculations in nitrogen.

In these figures three wall distances - $y/\lambda_1 = 0.3, 1.11, 2.28$ - are presented. It can be seen that close to the wall the density rises considerably above the value for a normal shock wave, $(\rho - \rho_1)/(\rho_2 - \rho_1) = 1$. The large gradients in the flow proper-

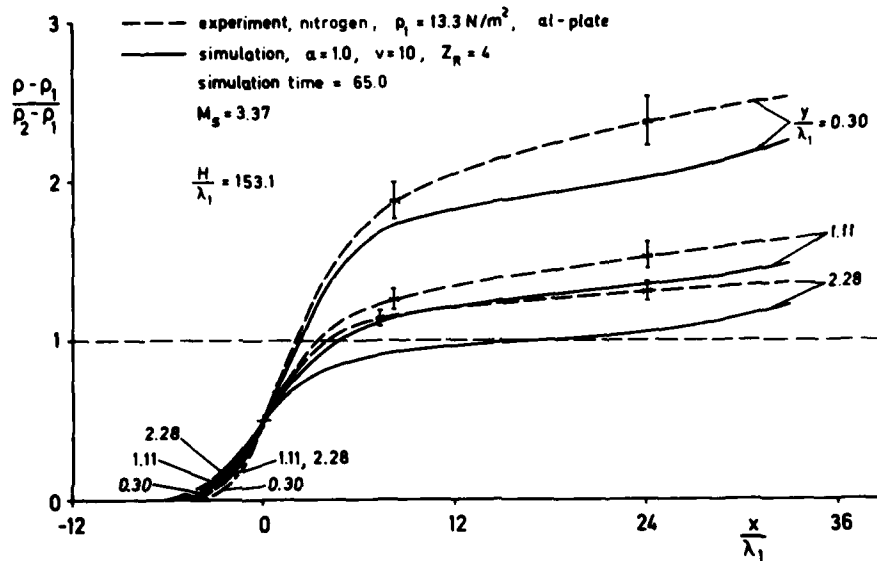


Figure 8. Numerical and experimental results

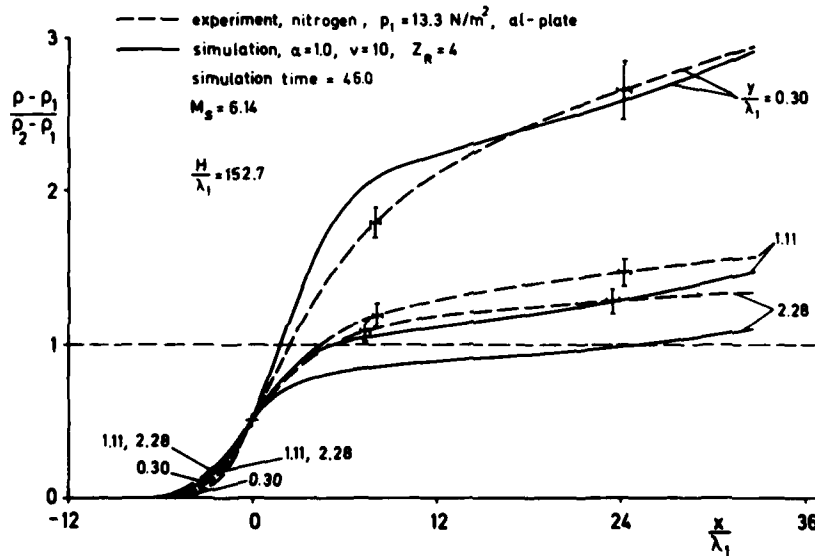


Figure 9. Numerical and experimental results

ties perpendicular to the wall are limited to a few mean free path distances from the wall and therefore the most interesting density profile is the one closest to the wall.

Regarding the profiles closest to the wall in Figure 8 and Figure 9 together with the profiles in Figures 5 through 7 some conclusions about the accommodation coefficient can be obtained. For weaker shocks ($M_s = 3.37$) the experimental density profiles in nitrogen are above the calculated ones, whereas for stronger shocks ($M_s = 6.14$) the experimental profile for $y/\lambda_1 = 0.3$ is in the range of the calculated one. This means that relative to the

accommodation coefficient, the results in nitrogen are similar to these in argon. In both gases the experimental density profiles closest to the wall are above the calculated ones for weak shocks and in the range or below the calculated ones for increasing shock strength. This result indicates a decreasing accommodation coefficient at the wall with growing shock Mach number, equivalent to an increasing temperature difference between the temperature at the wall and the freestream. In first approximation it is assumed that the temperature of the wall remains at constant temperature T_1 .

Furthermore the intermolecular potential influences the shape of the shock and the density level downstream. For lower Mach numbers ($M_s < 4$) the comparison between experiment and simulation in argon shows that the repulsive potential with $v = 5$ gives a good fit. For stronger shocks, the repulsive potential with $v = 10$, the Lennard-Jones potential and the hard-sphere model gives better results than the pure repulsive potential with $v = 5$. With the Lennard-Jones potential the best results for all shock Mach numbers are obtained, although it seems that the repulsive part of the Lennard-Jones potential is too hard and a weaker part would give better results.

An interesting picture develops for the shock curvature. The direct Monte Carlo simulation calculations allow the determination of lines of constant density and of constant temperature. These lines of constant density (Figure 10a) shows an inflection point at the front part of the shock wave and turn forward. Downstream the lines are less spaced closer to the wall, due to the large density rise in this narrow region. In contrast to the forward foot of the lines of constant density, the lines of constant temperature (Figure 10b) are only bend backward.

The difference in the density and temperature flowfield can be explained gaskinetically. The fast molecules, coming from the freestream, are slowed down when they come into contact with the

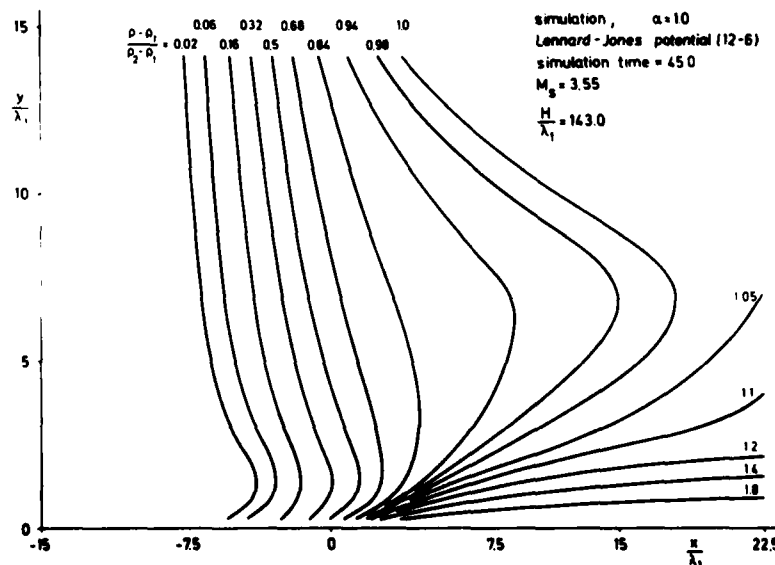


Figure 10a. Lines of constant density

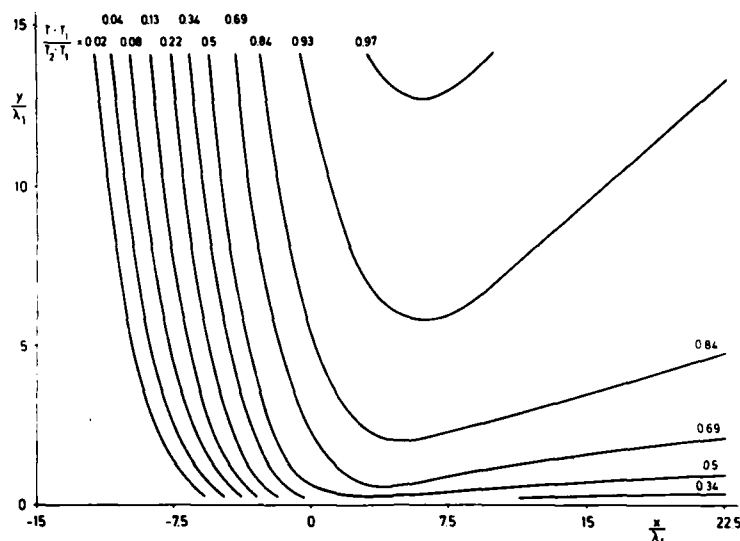


Figure 10b. Lines of constant temperature

solid wall. These molecules adopt the temperature of the wall, become slower and accumulate near the wall. This results in a density rise. In contrast, the translational energy, or macroscopically the temperature, changes gradually with growing distance from the wall by the action of molecular collisions.

The influence on the curvature of the lines of constant density and constant temperature by varying the intermolecular potential is smaller than by changing the accommodation coefficient. A decreasing accommodation coefficient (from $\alpha = 1$ to $\alpha = 0$) vanishes the curvature of the density and temperature flowfield. $\alpha = 0$ produces a normal, one-dimensional shock wave with lines of constant density or temperature perpendicular to the wall.

Lines of constant density, obtained from the measured density profiles, are also bent forward as can be seen for the calculated data in Figure 10a. Previous curvature measurements (ref. 2), done with an array of thin film gauges, don't agree with the present results. The reason for this can be explained with the response of thin film gauges. These respond to the heat flux into the surface. The heat flux is proportional to the gas density and the temperature difference. The laser differential interferometer responds to density only. The fact that the temperature flowfield shows no forward bend, allows an explanation for the difference and it is understandable to miss a forward facing in the curvature as measured with thin film gauges.

REFERENCES

1. G. A. Bird, *Molecular Gas Dynamics*, Oxford University Press, London, 1976
2. B. Schmidt, *Archives of Mechanics*, 28, 809, Warsaw, 1976



AD P000256

INFLUENCE OF SURFACE ROUGHNESS ON THE SHOCK TRANSITION IN
QUASI-STATIONARY AND TRULY NON-STATIONARY FLOWS

K. Takayama and J. Gotoh

Institute of High Speed Mechanics
Tohoku University, Sendai, Japan

G. Ben-Dor

Department of Mechanical Engineering
Ben-Gurion University of the Negev, Beer Sheva, Israel

The effect of surface roughness on the shock transition over flat wedges in quasi-stationary flows and concave and convex wedges in truly non-stationary flows is examined experimentally. For flat wedges saw-toothed roughnesses were used. For the curved wedges, as surface roughness a mesh No. 40 sand paper and a mesh No. 320 sand paper were used. Experiments were conducted on the Institute of High Speed Mechanics 40 mm x 80 mm shock tube equipped with a double exposure holographic interferometer. The incident shock Mach number range was 1.04 to 4.0 for nitrogen or dry air. In the case of curved wedges, the shock transition angles were determined by means of streak camera technique with curved slits. It was found that the shock transition angles become smaller with increasing surface roughness. For flat wedge of 0.8 mm surface roughness, the transition angle was 10° smaller than that of a smooth flat wedge for stronger shocks. The experimental result was very well explained by using a shock polar. In the case of curved wedges with mesh No. 40 roughness, the Mach to regular transition takes place at 54° (for a smooth concave wedge, it occurs at 65°) while the regular to Mach transition takes place at 27° (40° for a smooth convex wedge).

INTRODUCTION

The reflection of oblique shock waves is a nonlinear problem which has been investigated analytically and experimentally by many researchers. The recent publications concerning this problem have indicated that in general the phenomenon of shock wave reflection should be divided into three cases, according to the types of flow, i.e., 1) steady flow, 2) quasi-stationary flow, and 3) truly non-stationary flow.

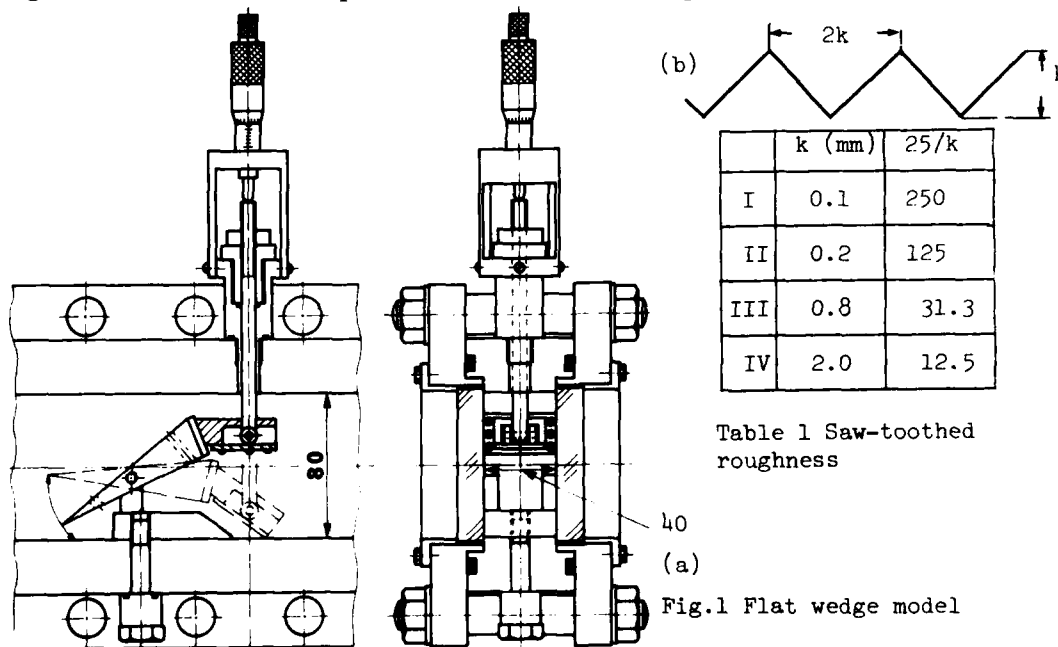
The reflections possible in each type of flow as well as the appropriate transition criteria between them are described by Ben-Dor and Glass (ref.1 and 2) for a quasi-stationary flow, Ben-Dor (ref.3) for a steady flow and Ben-Dor

Takayama and Kawauchi (ref.4) for a truly non-stationary flow. Ben-Dor and Glass (ref.1 and 2) hypothesized that in a truly non-stationary flow the RR (regular reflection) \rightarrow MR (Mach reflection) transition need not be the same as the MR \rightarrow RR transition. They assume that once RR or MR is formed and then the wedge angle θ or the incident shock Mach number M_s is changed gradually to cause transition to MR or RR, the original reflection (RR or MR) will terminate only when physically it becomes impossible for it to exist. Observing the shock transition over a concave or a convex wedge, Ben-Dor, Takayama and Kawauchi (ref.4) have experimentally shown that in truly non-stationary flows (i.e., flows which cannot be made quasi-stationary) the transition angle of RR \rightarrow MR is different from that of MR \rightarrow RR. Schultz-Grunow (ref.5) has observed that in a shock transition over corrugated wedges at $M_s = 1.5$ and 2.7, the transition wedge angle becomes smaller than that over a smooth flat wedge owing to surface irregularity.

In the course of the study on the shock transition, it is of primary importance to investigate the effect of surface roughness on the shock transition over a flat wedge with surface roughness or on the MR \rightarrow RR or RR \rightarrow MR transition over a concave or a convex wedge. Therefore the purpose of the present paper is to examine this effect on the shock transition over flat wedges with surface roughness and the MR \rightarrow RR and the RR \rightarrow MR transition over the curved wedges with surface roughness. It is found that the shock transition angle is decreased with increasing surface roughness in both quasi-stationary and truly non-stationary flows. In the case of the flat wedge with surface roughness, the experimental result is very well interpreted by using a shock polar.

EXPERIMENTS

For the flat wedge with surface roughness, the saw-toothed surface roughness of height $k = 0.1, 0.2, 0.8$ and 2.0 mm was set on a flat wedge the apex angle of which is arbitrarily variable from 10° to 50° , as shown in Fig. 1(a). Figure 1(b) shows the shape of the saw-toothed roughness.



Each concave or convex wedge was investigated with three different surface roughness: 1) smooth surface, 2) mesh No. 320 sand paper, and 3) mesh No. 40 sand paper. Practically, a sand paper of mesh No. X has the average grain size of $25.4/X$ mm. Therefore the average roughness of a mesh No. 320 sand paper

is 0.08 mm and 0.64 mm for a mesh No. 40 sand paper. The thickness of each sand paper is 0.3 mm for a mesh No. 320 sand paper and 1.3 mm for a mesh No. 40 sand paper. The sand papers were carefully pasted upon the the curved wedge surface with epoxy resin. Two types of curved wedges were used: In the concave cylinder with radius $R = 50$ mm, the wedge angle changes from 0° to 90° , and in the convex cylinder with $R = 40$ mm, the wedge angle changes from 90° to 0° . Consequently, the $MR \rightarrow RR$ transition takes place over the concave wedge, the $RR \rightarrow MR$ transition occurs over the convex wedge. Each model is shown in Fig.2.

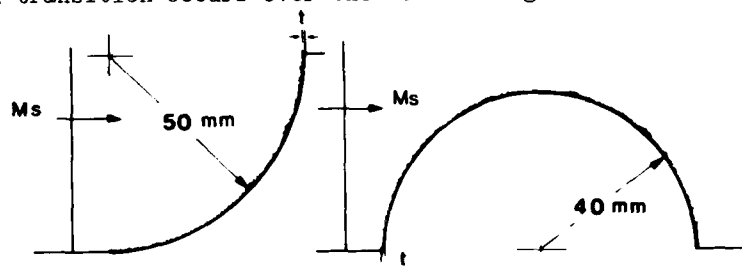


Fig. 2 Concave and convex wedges with surface roughness

Experiments were conducted on the Institute of High Speed Mechanics, Tohoku University 40 mm X 80 mm shock tube. Incident shock Mach number range was from 1.04 to 4.0 for nitrogen or dry air as test gas at initial pressure of $3 < p_0 < 760$ torr. Ben-Dor (ref.6) has shown that in the range $M_s < 6$ the initial pressure does not influence the $RR \rightarrow MR$ transition. Consequently, the initial pressure could be considered practically constant. The initial temperature T_0 was 293 K throughout the present study. The shock velocity was measured with pressure transducers (Kistler 606L) placed 120 mm apart just ahead of the test section. The output signal was displayed on electronic counters or a transient recorder (Iwatsu DM 901). A very good repeatability was obtained, i.e., the errors of shock Mach numbers thus obtained were $\pm 0.5\%$ for $M_s < 3.0$ and $\pm 0.7\%$ for $M_s > 3.0$. (for details see ref.7).

The non-stationary phenomena were recorded using a 300 mm dia. double exposure holographic interferometer or mainly to the flat wedge cases direct shadowgraph technique. A giant-pulse ruby laser with light pulse width of about 20 nsec was used as an instantaneous light source. In the case of the flat wedge, the shock transition angles were determined from the sequential shadowgraphs taken under the same initial conditions and only by changing the wedge angle. This method is completely powerless to the truly non-stationary flow. Instead an Ima-Con High Speed Camera (John Hadland Model 790) was used in the streaking mode. In the streak mode operation, a curved slit of 0.6 mm wide was accurately placed on the test section window in a direction that coincides exactly with the curved wedge surface. Especially for a convex wedge, a curved slit of 0.7 mm wide was used. These slits were used only for the curved wedges with smooth surface or mesh No. 320 surface roughness. However, for mesh No. 40 surface roughness, a wider slit was used due to the larger surface irregularity. Consequently, measured transition angles included uncertainty of $\pm 1.0^\circ$ for a smooth or a mesh No. 320 roughness and $\pm 1.5^\circ$ for a mesh No. 40 roughness. It should be mentioned here that in order to obtain the best spacial resolution for determining the transition point by means of streak camera technique with curved slits, an image rotator should be inserted between the objective lens and the camera.

SHOCK POLAR IN QUASI-STATIONARY FLOWS

It is of particular interest to apply an analytical method using a shock polar valid in quasi-stationary flows (ref.6) to predicting the shock transition angle over a flat wedge with surface roughness. As sketched in Fig.3, the influence of the surface roughness is confined only within the region (2) for RR as shown in Fig. 3(a) and the regions (2) and (3) for MR in Fig.3(b).

In incompressible pipe flows, the coefficient of resistance in rough pipes is given as a function of the Reynolds number $Re = ud/\nu$, and roughness k where

u , d and ν are mean velocity, diameter of the pipe, and kinetic viscosity, respectively. However, if the roughness is so large that all protrusions reach outside the laminar sub-layer, the coefficient of resistance depends only on the roughness, ref.8. Huber and McFarland (ref.9) have investigated boundary-layer growth and shock attenuation in a shock tube with pyramid-shaped surface roughness and obtained a reasonable agreement between the experimental result and the analysis using this relationship. In the non-stationary shock tube flow surface roughness brings about increase of not only the additional wall skin friction but also the wave drag. However, the mechanism of momentum loss or others is still far from being completely understood.

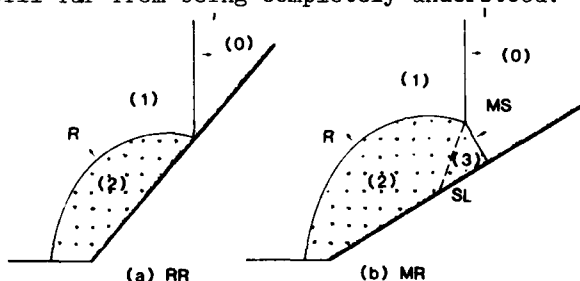


Fig.3 Sketch of shock diffraction over a flat wedge with surface roughness

Therefore, for simplicity it is assumed here that the influence of surface roughness is independent of Re and the total pressure loss Δp due to surface roughness is described $\Delta p = f(k, \xi)(p_1 - p_2)$ where $p_{1,2}$ are pressure ahead of and behind the shock waves, respectively, and ξ is the inverse pressure ratio. This relation is combined with the R-H relations for oblique shock waves to the regions (2) in Fig.3(a) RR and (2,3) in Fig.3(b) MR. $f(k, \xi)$ will be determined from the experimental data and is assumed as follows;

$$f(k, \xi) = \lambda(1 - \xi)^n \quad (1)$$

where $\lambda = \lambda(k)$ is a constant showing a magnitude of surface roughness, and n is also a constant to be determined from the experimental data. The R-H relations for the incident shock I are common with Eqs. (2.1)-(2.4) or Eqs. (2.17)-(2.20) of ref.6.

For reflected shock R:

$$\rho_1 \tan \phi = \rho_2 \tan(\phi - \theta) \quad (2)$$

$$\rho_1 U \sin \phi = \rho_2 U \sin(\phi - \theta) \quad (3)$$

$$p_1(1-f) + \rho_1 U^2 \sin^2 \phi = p_2(1-f) + \rho_2 U^2 \sin^2(\phi - \theta) \quad (4)$$

$$h_1 + \frac{1}{2} U^2 \sin^2 \phi = h_2 + \frac{1}{2} U^2 \sin^2(\phi - \theta) \quad (5)$$

For Mach stem MS:

$$\rho_0 \tan \phi_3 = \rho_3 \tan(\phi_3 - \theta_3) \quad (6)$$

$$\rho_0 U \sin \phi_3 = \rho_3 U \sin(\phi_3 - \theta_3) \quad (7)$$

$$p_0(1-f) + \rho_0 U^2 \sin^2 \phi_3 = p_3(1-f) + \rho_3 U^2 \sin^2(\phi_3 - \theta_3) \quad (8)$$

$$h_0 + \frac{1}{2} U^2 \sin^2 \phi_3 = h_3 + \frac{1}{2} U^2 \sin^2(\phi_3 - \theta_3) \quad (9)$$

where h_i , U_i , ρ_i , θ_i , and ϕ_i are enthalpy in region (i), flow velocity in region (i), density in region (i), deflection angle from its original direction while entering region (i), and incident angle between shock and flow in region (i), respectively. The boundary conditions are as following:

$$\theta_2 = -\theta_1 \quad \text{for RR in Fig.3(a)} \quad (10a)$$

$$p_2 = p_3, \theta_2 = \theta_1 \pm \theta_3 \quad \text{for MR in Fig.3(b)} \quad (10b)$$

For an ideal and perfect gas, Eqs.(2)-(5) can be reduced to the following

$$\tan \theta_2 = \frac{1 - \xi}{\gamma \xi M_1^2 + (1-f)(\xi-1)} \left[(1-f) \frac{2\gamma \xi M_1^2 \{1 + (\gamma-1)f\} - 2\gamma(1-f) - (1-f)^2(\gamma-1)(\xi-1)}{2\gamma + (1-f)(\gamma-1)(\xi-1)} \right]^{\frac{1}{2}} \quad (11)$$

where M_1 is Mach number in region (1) which was defined by Eq.(2.12) of ref.6. Eqs.(6)-(9) can also be reduced to Eq.(11) if the variables are changed as $M_1 \rightarrow M_0$, $\xi \rightarrow p_0/p_3$, and $\theta_2 \rightarrow \theta_3$. As a matter of course this equation can be reduced to Eq.(2.11) of ref.6 for a smooth wedge, $f = 0$.

Drawing an incident shock polar I (ref.6) and then a reflected shock polar with Eq.(11), one can immediately determine all the variables in region (2) of RR or those in regions (2) and (3) of MR. Consequently, for a given surface roughness, i.e. $f(k, \xi)$ or $\lambda(k)$ is known, the shock transition criteria, i.e. the detachment criterion by Von Neumann (ref.10) and mechanical equilibrium criterion by Henderson and Lozzi (ref.11) can be calculated. It is found from Eq.(11) that with increasing roughness, i.e., $\lambda \rightarrow 1$, and the pressure ratio being kept constant, the deflection angle is decreasing. This indicates that the critical shock transition angle becomes small with increasing roughness.

RESULTS AND DISCUSSIONS

Typical examples of the shock diffraction at $M_\infty = 1.44$ and $\xi = 0.44$ over flat wedges with various surface roughnesses are shown in Fig. 4(a) and (b) for $k = 0.2$ mm and in Fig. 4(c) and (d) for $k = 2.0$ mm; (a) MR at $\theta_w = 32.3^\circ$, (b) RR at $\theta_w = 40.6^\circ$, (c) MR at $\theta_w = 25.6^\circ$, and (d) RR at $\theta_w = 31.6^\circ$.

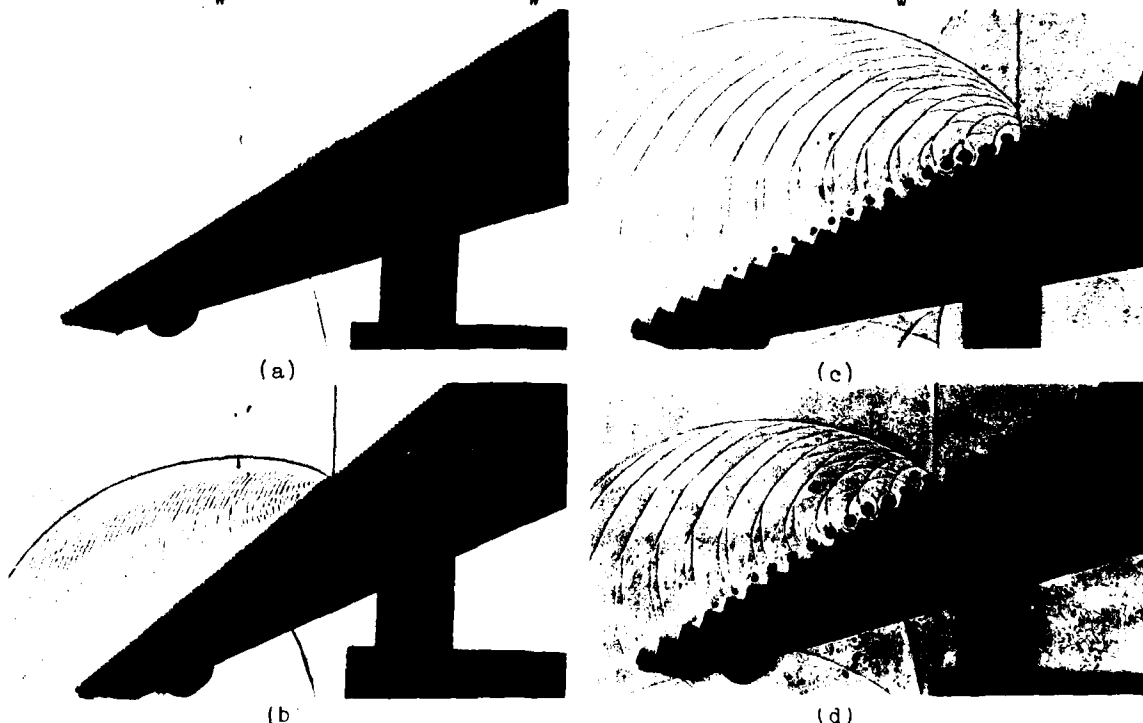


Fig.4 Direct shadowgraphs of shock diffraction over flat wedges with surface roughness, (a), (b); $k = 0.2$ mm, (c), (d); $k = 2.0$ mm.

In Fig.4 (a),(b), growth and development of wavelets in regions (2), (3) are clearly visible. Since the flow in the regions is subsonic the reflected shock is a simple Mach reflection and growth and decay of the vortices at the edges of the saw-toothed roughness are seen. These effects thicken the boundary layer displacement thickness or the momentum thickness etc. and then encourage the pressure loss in regions (2), (3). In Fig.4 (c), (d), since the height of roughness is much larger than the boundary layer displacement thickness, $k = 2.0$ mm, edges of roughness act as a step exposed to a subsonic flow and detached shock waves are observable. These shock waves are accumulated into the reflected shock. The triple point configuration is still a simple Mach reflection. For stronger shock waves a complex or a double Mach reflection configuration can be seen at much smaller angles. It should be mentioned that wavelets generated with smaller surface roughness are good indicators of disturbance propagation in regions (2), (3).

The critical shock transition angle θ_{crit} is determined experimentally by taking direct shadowgraphs for slightly different θ and comparing the triple point trajectory angle χ against θ_w in the similar manner as Smith, ref.12. A typical example is shown in Fig.5 for $M = 5.3$ ($\xi = 0.05$) and 4.2 (0.03), $\theta_{crit} = 42.0 \pm 1.0^\circ$. The result is shown in Fig.6 together with analytical results using a shock polar. θ_{crit} is shown against ξ . Two criteria, detachment and

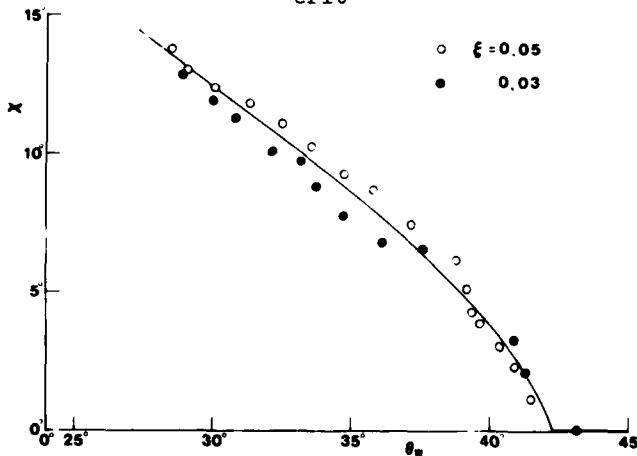


Fig. 5 Variation of the triple point trajectory angle χ vs. θ_w for stronger shock waves, $\xi = 0.05$ and 0.03. Surface roughness is 0.2 mm (model II of Table 1).

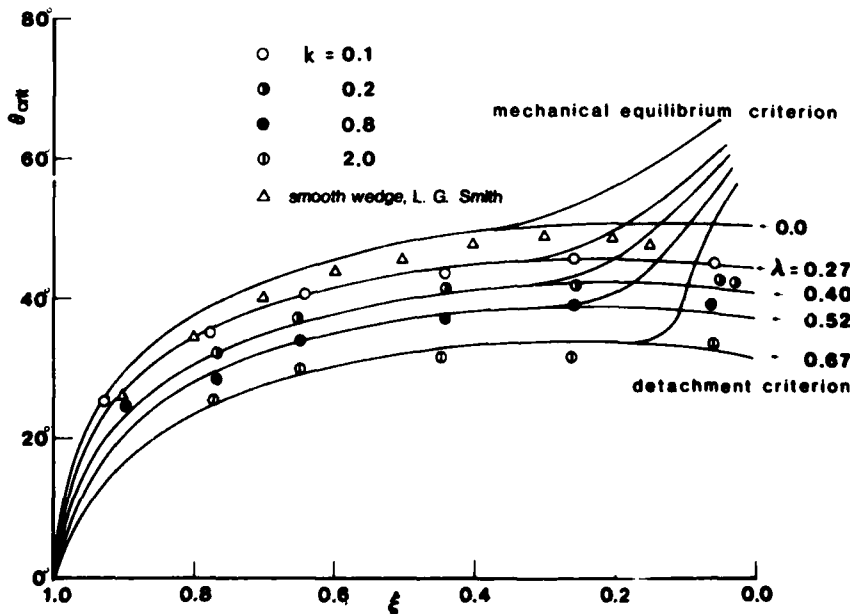


Fig.6 Experimental results of the shock transition over flat wedges with surface roughness in (ξ, θ_{crit}) -pl. Solid lines are detachment and mechanical equilibrium criteria for $\lambda = 0.0, 0.1, 0.2, 0.8,$ and 2.0 mm.

mechanical equilibrium criteria, are calculated for each roughness. n and $\lambda(k)$ representing a magnitude of roughness in Eq.(1) are obtained from best fit with the experimental data for each k . It is found that $n = 7/9$ independent of k and a good agreement is obtained for each roughness except for very weak shock waves. Triangles designate Smith's experiments for a smooth flat wedge, ref.12. In conclusion, the critical shock transition angles become smaller with increasing surface roughness, and in the case of 0.8 mm roughness, for example, θ_{crit} for stronger shock waves is about 10° smaller than that for a smooth flat wedge. The result is tabulated in Table 2.

M_s	ξ	Re 10^5	θ_{crit} (degree)			
			I	II	III	IV
1.04	0.92	0.80	27.5	25.0	24.7	23.1
1.12	0.77	2.50	35.2	32.1	28.3	25.3
1.21	0.65	3.40	40.5	37.2	34.0	29.6
1.44	0.44	2.70	43.7	40.1	37.2	31.1
1.86	0.26	0.06	45.8	42.3	38.8	31.5
3.77	0.06	0.03	44.9	41.9	39.3	33.8

Table 2 Critical shock transition angles.

Typical holography interferometric photographs for $M_s = 1.4$ ($\xi = 0.4$) and mesh No.40 roughness are shown in Fig.7, (a); MR, concave wedge, (b); RR concave wedge, (c); RR convex wedge, (d); MR convex wedge. Figure 7(a) is an infinite fringe width interferometric photograph while the others are finite fringe width interferometric photographs. Due to large roughness, $k = 0.64$ mm, the flows behind the reflected shock waves are strongly disturbed. The critical shock transition angle for concave wedge is 53.5° , and 27.0° for convex wedge. It should be mentioned that in Fig.7(b), a normal shock wave still exists behind the regular reflected shock wave and this fact indicates that the MR \rightarrow RR transition over a concave wedge with mesh No.40 roughness obeys the process of inverted Mach reflection, see ref.13. θ_{crit} for the curved wedge cases can be determined easily and accurately by using streak camera technique with curved slits. Typical examples are shown in Fig.8, (a); $M_s = 1.4$, concave wedge with mesh No.320 roughness, (b); $M_s = 1.3$, convex wedge with mesh No.320 roughness, where I, R, MS, and SL designate incident shock wave, reflected shock wave, Mach stem and slip line, respectively.

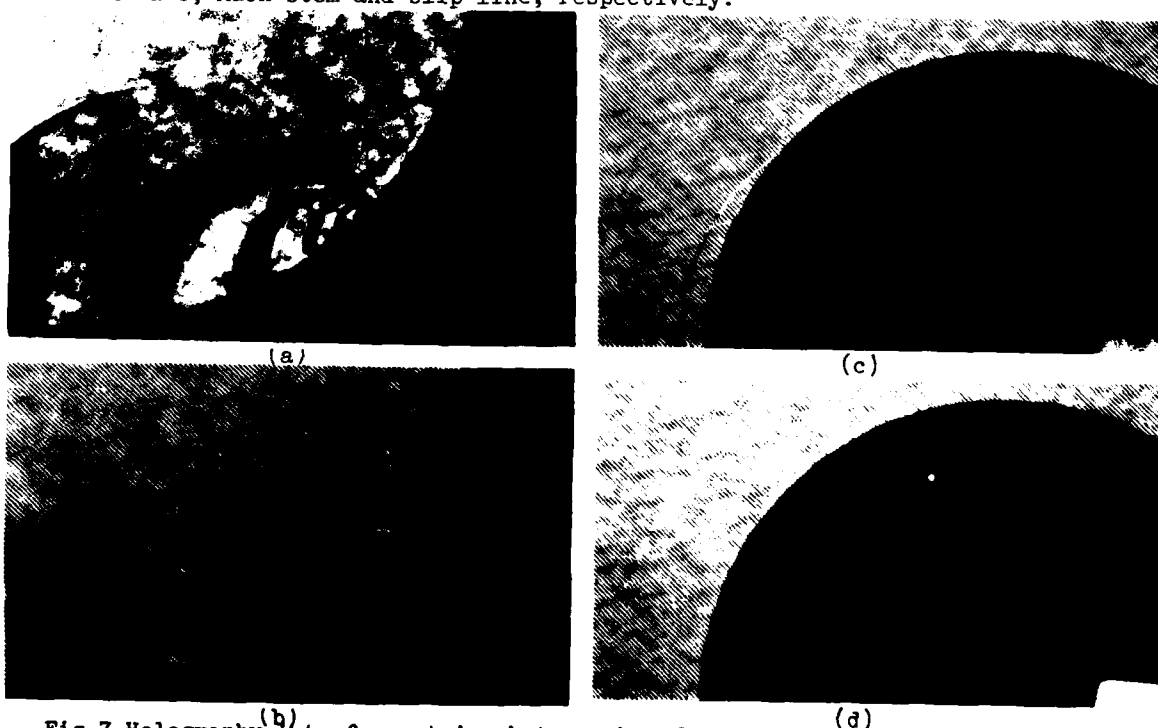


Fig.7 Holography interferometric photographs of shock transition over a concave or a convex wedge with mesh No. 40 roughness.

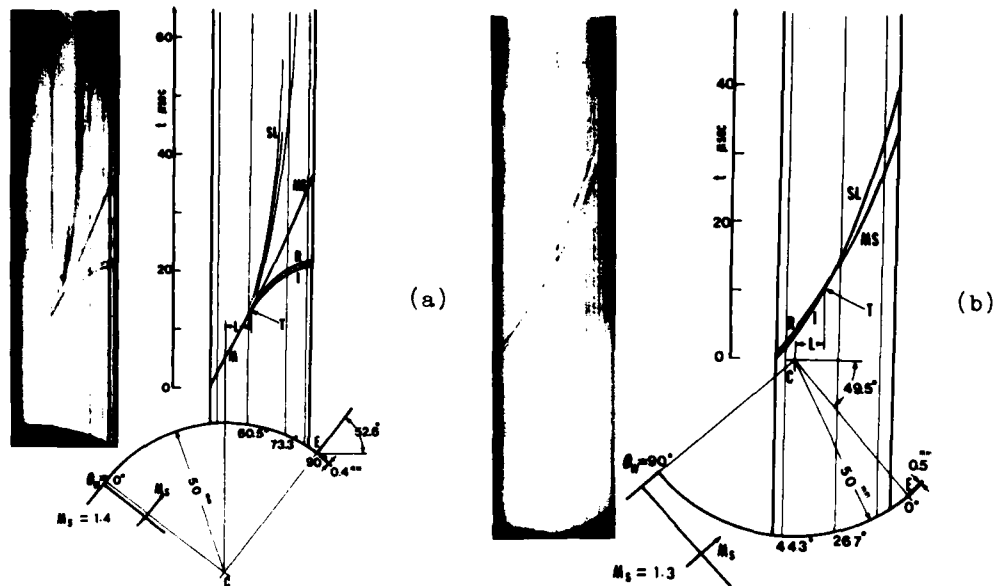


Fig.8 x-t diagrams of MR → RR or RR → MR transition over a concave or a convex wedge with mesh No. 320 roughness, (a); concave wedge, (b); convex wedge.

If the shock diffraction process is observed through a curved slit, it can be easily seen that in the MR → RR transition the trajectory of the first Mach stem M splits into those of I, R, MS, and SL at the transition point T, while in the RR → MR transition the trajectories of I and R intersect at T and turn into MS and SL at T. Therefore, the transition point T can be easily recognized; for more details see ref.4. The influence of mesh No.320 roughness is almost unnoticeable while as seen in Fig.7, mesh No.40 roughness has a significant effect on the flow behind the reflected shock wave, i.e., on the shock transition angle.

Figure 9 represents the present experimental result. The solid line A and B correspond to RR → MR and MR → RR criteria, detachment and mechanical equilibrium criteria, respectively. Dashed line A' and B' also correspond to those of imperfect nitrogen, $p_0 = 15$ torr and $T_0 = 300$ K, ref.1. Solid line C and D represent the result for quasi-stationary flows with $k = 0.2$ mm and 0.8 mm,

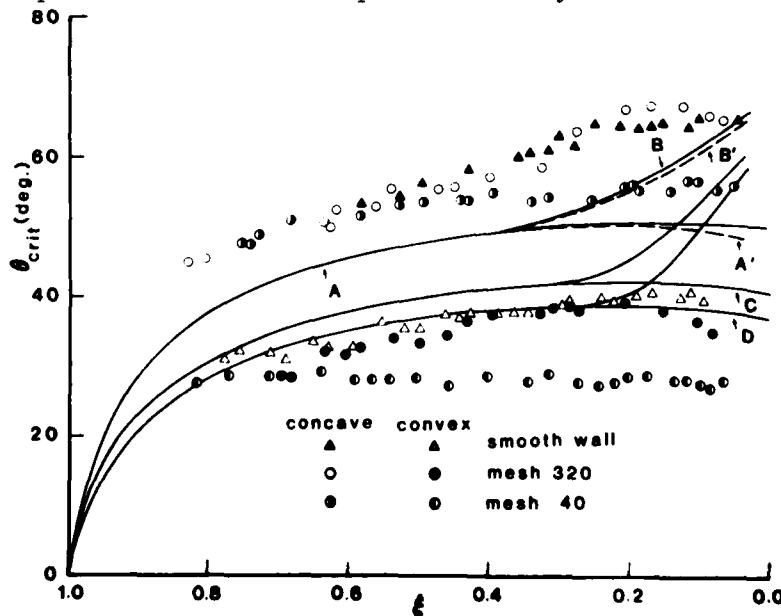


Fig.9 Present experimental results of the MR → RR and RR → MR transition in (ξ, θ_{crit}) - pl. Solid line A,B; detachment and mechanical equilibrium criteria, respectively, dashed line A',B'; the same criteria in imperfect nitrogen and solid line C and D; the same criteria for flat wedges with 0.2 mm and 0.8 mm saw-toothed roughness.

as shown in Fig. 6, respectively. Since the equivalent saw-toothed roughness is given by $k_s = 1.33k$, ref. 9, solid lines C and D correspond to $k_s = 0.27$ mm and 1.07 mm, respectively. Experiments were conducted with three cases, smooth surface, mesh No. 320 roughness, and mesh No. 40 roughness. The result for mesh No. 320 roughness is almost the same as that for a smooth wedge for all the shock Mach numbers. However, the shock transition angle for mesh No. 40 roughness is much smaller than that for a smooth surface or mesh No. 320 roughness, except for very weak shock waves. It is expected that the analytical curve which corresponds to mesh No. 40 roughness in quasi-stationary flows exists between curves C and D. In conclusion, the shock transition angles for both concave and convex wedges are decreased with increasing surface roughness and this tendency is prominent for stronger shock waves. For example, at about $M_s = 4.0$ ($\xi = 0.05$) the transition angles for mesh No. 40 roughness are about 10° smaller than those corresponding to a smooth surface, and the MR \rightarrow RR transition takes place at 54° (65° for a smooth concave wedge) while the RR \rightarrow MR occurs at 27° (40° for a smooth convex wedge).

CONCLUSIONS

An experimental investigation of the shock transition over flat wedges with surface roughness in quasi-stationary flows and the MR \rightarrow RR and RR \rightarrow MR transitions over concave and convex wedges with surface roughness in truly non-stationary flows revealed that:

- 1) As the surface roughness increases, for a given incident shock Mach number the wedge angle at which the shock transition takes place decreases in both quasi-stationary and truly non-stationary flows.
- 2) For mesh No. 40 roughness, it seems that the transition angle becomes independent of the incident shock Mach number, i.e.,
 - a) MR \rightarrow RR transition occurs at $\theta_w = 54^\circ$.
 - b) RR \rightarrow MR transition takes place at $\theta_w = 27^\circ$.
- 3) An analysis taking into account the effect of surface roughness and using a shock polar can explain the shock transition phenomena in quasi-stationary flows.

ACKNOWLEDGEMENTS

The authors would like to express their appreciation to Professor M. Honda of the Institute of High Speed Mechanics, Tohoku University for his encouragement throughout the course of the present study. Gratitude is also expressed to Professor I. I. Glass of the Institute for Aerospace Studies, University of Toronto for his stimulating discussions of this problem. The authors are indebted to Mr. O. Onodera for his help in conducting the experiments.

REFERENCES

1. G. Ben-Dor and I. I. Glass, *J. Fluid Mech.*, **92**, 459 (1979).
2. G. Ben-Dor and I. I. Glass, *J. Fluid Mech.*, **96**, 735 (1980).
3. G. Ben-Dor, *AIAA J.*, **18**, 1143 (1980).
4. G. Ben-Dor, K. Takayama and T. Kawauchi, *J. Fluid Mech.*, **100**, 147 (1980).
5. F. Schultz-Grunow, *Bericht Ernst-Mach Institut*, Nr. 7/72.
6. G. Ben-Dor, UTIAS Report No. 232 (1978).
7. K. Takayama, M. Honda, O. Onodera, and T. Kawauchi, *Mem. IHSM*, **44**, 1 (1980).
8. H. Schlichting, *Boundary Layer Theory* 7th ed., 615 (1979).
9. P. W. Huber and D. R. McFarland, *NACA TN*, **3627**, (1956).
10. J. von Neumann, *Collected Works of J. von Neumann*, 6 Pergamon Press (1963).
11. L. F. Henderson and A. Lozzi, *J. Fluid Mech.*, **68**, 139 (1975).
12. L. G. Smith, *OSRD Report No. 6271*, (1945).
13. K. Takayama and W. Watanabe, *Mem. IHSM*, **45**, 33 (1980).

AD P000252

MICROSCOPIC STRUCTURE OF THE MACH-TYPE REFLECTION OF WEAK SHOCK WAVES

Zbigniew A. Walenta

Department of Fluid Mechanics, Institute of Fundamental
Technological Research, Polish Academy of Sciences
00-049 Warsaw, ul. Swietokrzyska 21, Poland

The purpose of the present work was to investigate the microscopic structure of the three-shock interaction region generated in a low-density shock tube during the Mach-type reflection of a weak shock wave. The experimental conditions corresponded to the case when Von Neumann's theory fails to predict the existence of reflection while Guderley's theory predicts the presence of a rarefaction wave behind the reflected shock. The experiment shows that under such conditions the Mach-type reflection does exist, and no rarefaction wave is present. A possible reason for this disagreement is the influence of viscosity, neglected in Von Neumann's and Guderley's theories.

INTRODUCTION

The purpose of the present work was to investigate experimentally the Mach-type reflection of weak shock waves (Fig. 1).

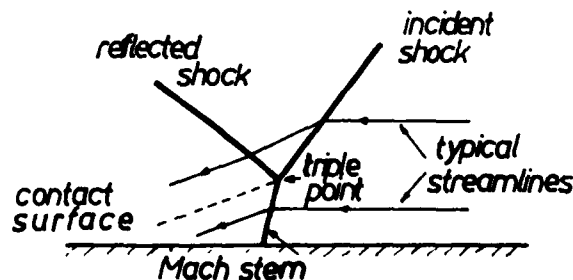


FIG. 1 MACH-TYPE REFLECTION

For strong shocks this phenomenon is reasonably well understood in terms of the theory proposed by Von Neumann (ref. 1). In this theory the steady flow of an ideal gas is considered. Thus the shock waves are considered as discontinuities. Assuming that the shocks are planar, the Rankine-Hugoniot conditions are obeyed and the flow in regions between the shocks is uniform. The slipstream generated behind the triple point is thin and there is no pressure

difference across it.

The solution of the Mach reflection problem is conveniently illustrated on the polar diagram in $p - \theta$ coordinates (Fig. 2) where p is pressure ratio across the shocks and θ is the flow deflection angle.

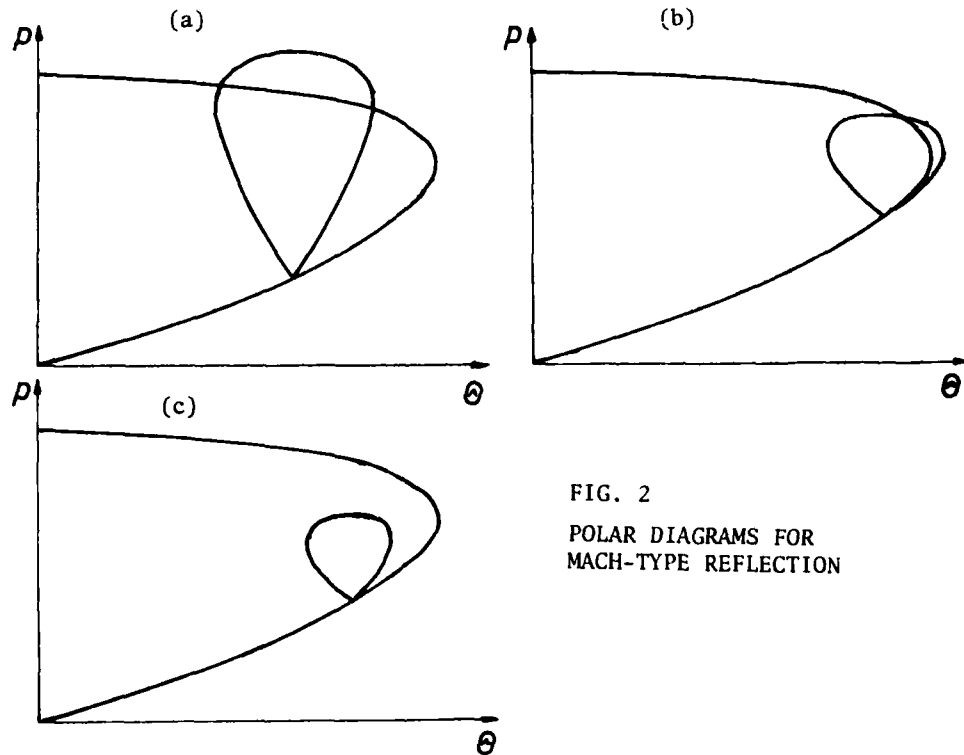


FIG. 2
POLAR DIAGRAMS FOR
MACH-TYPE REFLECTION

Since at both sides of the slipstream behind the triple point the pressures and flow directions are the same, the solution is given by the point of intersection of the shock polars for the incident and reflected shocks.

When, as shown in Fig. 2a, there are two points of intersection, the theory fails to predict which one gives the proper solution. Experiments show that the point on the left hand side is the proper one. If the Mach number is decreased, only one intersection point may exist (Fig. 2b). If it is placed at the right-hand side of the reflected shock polar the theory predicts that the reflected shock wave is inclined upstream as shown in Fig. 2b.

For even weaker shocks there may be no intersections of the shock polars at all, and according to Von Neumann's theory there should then be no Mach reflection (Fig. 2c). For this situation Guderley (ref. 2) proposed a solution assuming that behind the reflected shock a rarefaction wave was generated, thereby equilibrating the pressures at both sides of the slipstream. The reflected shock in this case should also be inclined forward and strongly curved in the vicinity of the triple point. The above mentioned rarefaction wave as well as the forward inclined reflected shock wave have not been observed experimentally. It was suggested that they should not be noticed with the conventional optical techniques because of the small dimensions. However, some investigators (ref. 3) argues that no rarefaction or strong shock curvature actually would exist at low densities since all such effects would

be masked by viscous effects. To know the actual situation it was necessary to perform suitable experiments under low density conditions, with the linear scale expanded sufficiently so that the necessary details of the triple point region were visible.

EXPERIMENT

The experiments were performed in a low-density shock tube 250 mm in diameter and 17 meters long (ref. 4). The ordinary diaphragm was replaced by a steel plate with a 20-mm opening closed by an electromagnetically driven valve. The valve required about four milliseconds to open completely. This device made it possible to generate very weak shocks since the driver pressure could be made arbitrarily low. To measure the velocity of very weak shocks two electron guns working on the beam attenuation principle were used. The first electron gun was also used to trigger the measuring equipment, while the second was used for the actual recording of the density profiles. With this equipment it was possible to study shocks down to Mach number $M_s = 1.1$ at the initial pressure of 0.2 mm Hg in Argon.

To maintain the planarity of the flow, a rectangular "cookie cutter" was placed in the test section of the tube (Fig. 3).

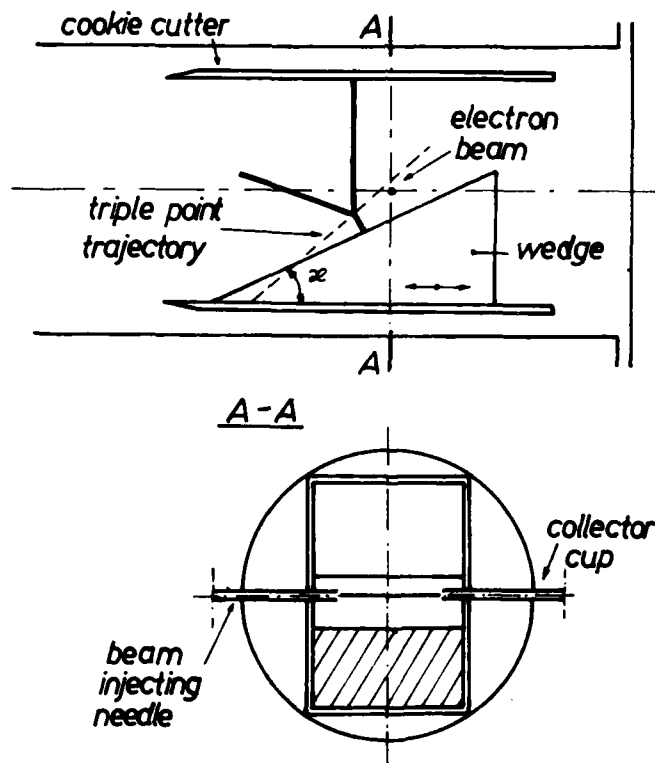


FIG. 3 TEST SECTION OF THE SHOCK TUBE

Inside this cookie cutter a 25-degree wedge was placed. The wedge could be shifted in the direction parallel to the tube axis. The density measuring electron beam was perpendicular to the tube axis and parallel to the wedge surface. To avoid the influence of the sidewall boundary layer, both the beam injecting needle and the collector cup protruded deep into the test section. In order to

obtain the reference time a laser differential interferometer was used, placed perpendicular to the electron beam in the test section. The signal from this interferometer was recorded simultaneously with the signal from the electron gun.

In a single run it was possible to obtain the density distribution along a straight line parallel to the trajectory of the triple point (Fig. 5). To obtain the whole density field it was necessary to superimpose the results taken from several runs at various positions of the wedge. Such a superposition was possible due to very good repeatability of the runs. The scatter of the shock speed was $\pm 1\%$. To obtain the triple point trajectory angle, for each Mach number two sets of runs were taken with the beam placed at two different positions with respect to the tube axis. The conditions of the experiments are summarized in Table I.

Table I

Experiment	I	II
Test gas	Argon	Argon
Initial pressure	0.250 mm Hg	0.250 mm Hg
Initial mean free path	0.218 mm	0.215 mm
Driver gas	Nitrogen	Nitrogen
Driver pressure	200 mm Hg	100 mm Hg
Shock Mach number	1.28	1.14
Wedge angle	25°	25°

The experimental conditions correspond to the case of no intersection of the shock polars. Hence the rarefaction wave and the strongly curved reflected shock, inclined forward, should be present.

RESULTS

The results of the experiments are presented in Figs. 4-6. Figures 4 and 5 show the positions of the inflection points of the density distribution curves inside the shocks for Mach numbers $M_s = 1.28$ and $M_s = 1.14$, respectively. For $M_s = 1.28$ the reference time was taken from the interferometer. For $M_s = 1.14$ the position of the incident shock was taken as the reference point since the signal from the interferometer was too weak in that case. From these figures it is evident that in the cases studied:

1. in the vicinity of the triple points no curvature of the reflected shock can be noticed.
2. the reflected shocks are inclined backwards, contrary to the prediction of Von Neumann's and Guderley's theories.

Figure 6 shows four oscilloscope traces taken in Experiment II at the beam locations indicated in Fig. 5. Figure 6a shows the incident and reflected shocks separated by a relatively long plateau. Figure 6b shows both shocks very close to each other. Figure 6c shows only the Mach stem. None of these records shows any indication of rarefaction waves.

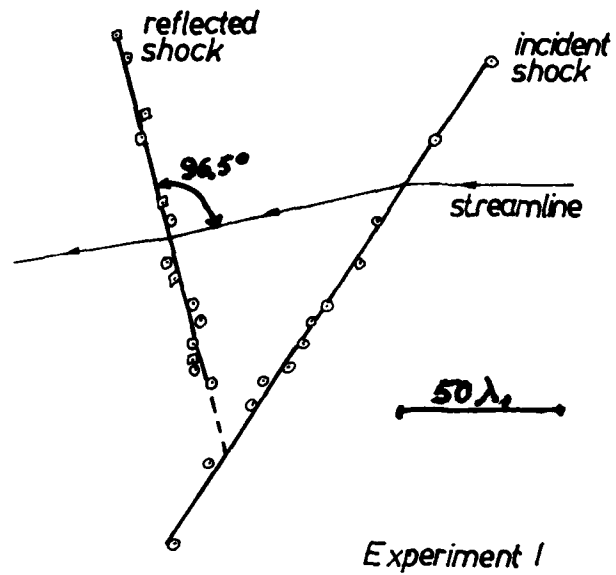


FIG. 4 POSITION OF THE INFLECTION POINTS OF THE DENSITY DISTRIBUTION CURVES

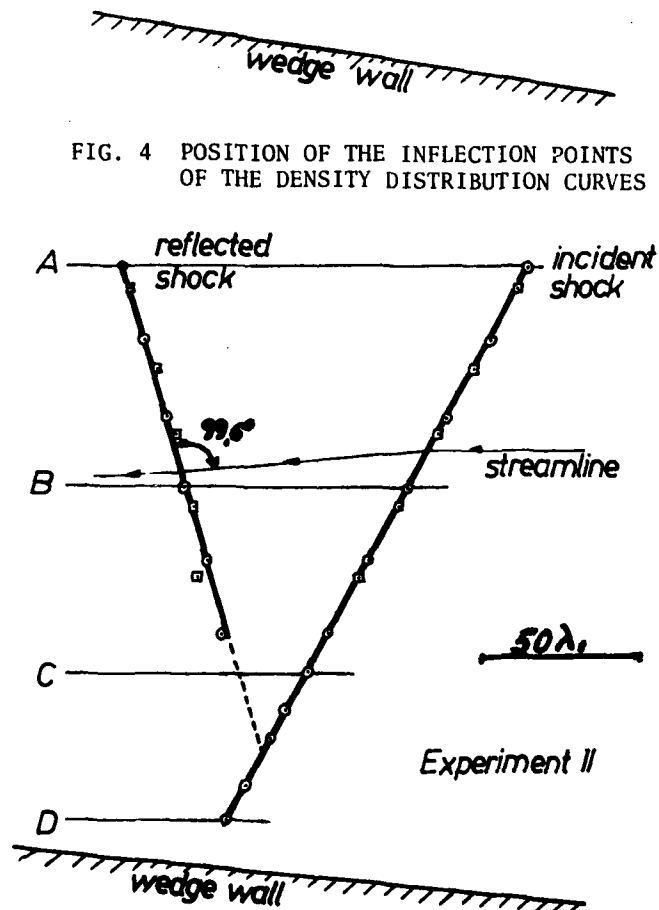


FIG. 5 POSITION OF THE INFLECTION POINTS OF THE DENSITY DISTRIBUTION CURVES

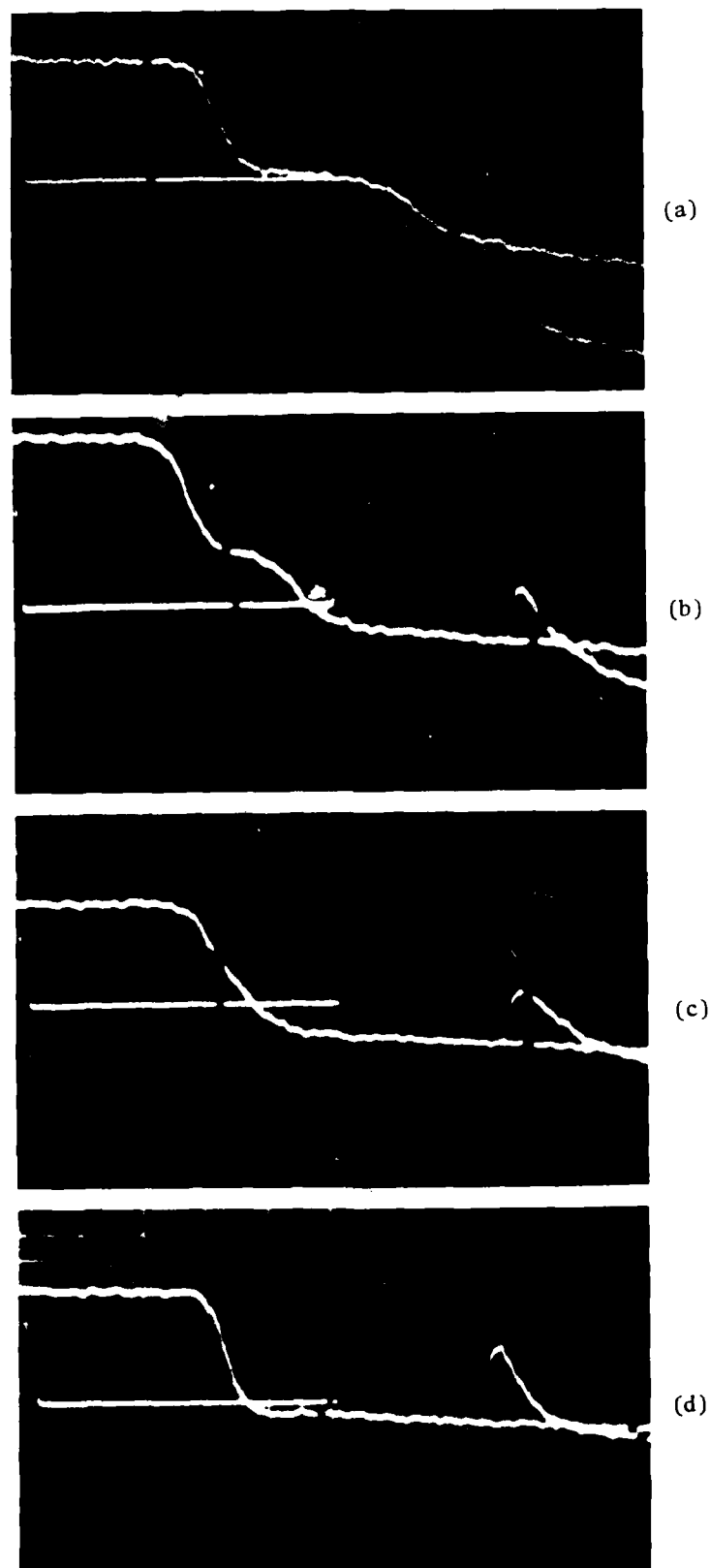


FIG. 6 DENSITY DISTRIBUTIONS ALONG THE LINES A,B,C,D IN FIG. 5

CONCLUSIONS

The reported experiments give some insight into the details of the flow in the region of interaction of three shocks in Mach-type reflection for weak incident shocks. The results are contrary to the predictions obtained on the basis of Von Neumann's theory (reflected shock inclined forward) and Guderley's theory (rarefaction wave behind the reflected shock). A possible explanation is that both theories assume inviscid flow, while viscosity probably has strong influence on the flow in the vicinity of the triple point at low Mach numbers. An adequate theory of the phenomenon is still lacking.

REFERENCES

1. J. Von Neumann, Collected works, 6, Pergamon 1963.
2. K.G. Guderley, Theorie schallnaher strömungen, Springer-Verlag, Berlin, Göttingen, Heidelberg, 1957.
3. J. Sternberg, Triple Shock Wave Intersection, Phys. Fluids, 2, 2, 179-206, 1959.
4. Z. A. Walenta, Arch. Mech., 32, 5, 819-825, 1980.

AD P000258

WEAK SPHERICAL SHOCK-WAVE TRANSITIONS OF N-WAVES
IN AIR WITH VIBRATIONAL EXCITATION*

H. Honma,† I. I. Glass, O. Holst-Jensen and Y. Tsumitat

Institute for Aerospace Studies, University of Toronto, Toronto, Canada
and

†Department of Mechanical Engineering, Chiba University, Chiba, Japan

The effects of vibrational excitation on shock-wave transitions of weak spherical N-waves were investigated for overpressures below 100 Pa. The spherical N-waves were generated by using sparks and exploding wires as sources in a still-air dome of 40-m diam. The pressure profiles of the N-waves were observed by using high-frequency microphones, which were located at several positions (10-30m) from the source. It was found that the measured risetimes of the N-waves for overpressures of 5-30 Pa and half-duration of 50-120 μ sec were much shorter than the risetimes estimated from the theory of plane, fully-dispersed waves with vibrational excitation of oxygen. In order to clarify the real-gas effects on the risetimes of weak spherical N-waves, the compressible Navier-Stokes equations were solved numerically, including vibrational-relaxation relations for oxygen, using a pressurized air-sphere explosion as a model. By employing the random-choice method (RCM) with an operator-splitting technique, the effects of artificial viscosity appearing in finite-difference schemes were eliminated and accurate profiles of shock transitions were obtained. A slight randomness in the variation of the shock thickness remains. It is shown that a computer simulation is possible by a proper choice of the initial parameters to obtain the variations of the N-wave overpressure and half-duration with distance from the source. The calculated risetimes are also shown to simulate both spark and exploding-wire data. It was found that both the duration and the attenuation rate of a spherical N-wave are important factors which control its risetime, in addition to the vibrational relaxation times of oxygen.

INTRODUCTION

The pressure waves generated by supersonic transport aircraft (SST) and from explosions in air are often observed as weak N-waves far from the source. Such pressure waves are heard as sonic booms. The loudness of these waves

*This work was supported by the U.S. Army Research Office and the USAF under Grant AFOSR-77-3303 and the Natural Sciences and Engineering Research Council of Canada and the Japan Society for the Promotion of Science.

depend on their maximum overpressures and risetimes (Ref. 1). The N-waves with short risetimes are perceived as louder and more startling than the ones with long risetimes. As a consequence N-wave risetimes were investigated extensively (Refs. 2,3,4). However, the observed SST risetimes were found to be larger than those which were estimated from classical theory for viscous shock structures of steady, plane waves (Ref. 5).

This discrepancy was attributed mainly to the effects of atmospheric turbulence (Refs. 6,7,8) and real-gas effects arising from the vibrational excitation of the oxygen and nitrogen air molecules (Refs. 9,10). However, the decisive factor for this increased risetime was still in question. Consequently, the effects of vibrational excitation on shock-wave transitions of weak spherical N-waves were investigated for overpressures below 100 Pa from both experimental and analytical considerations. The pressure profiles of spherical N-waves, which were generated by sparks and exploding-wires in a still-air dome (Ref. 11) were compared with numerical results, which were obtained by solving the compressible Navier-Stokes equations with vibrational-relaxation relations for oxygen. For this purpose the random-choice method (RCM) was used with an operator-splitting technique.

The risetime is defined as the time interval for the overpressure to vary from 10% to 90% of its peak value. Figure 1 illustrates the definition of N-wave risetime t_r and its half-duration t_d .

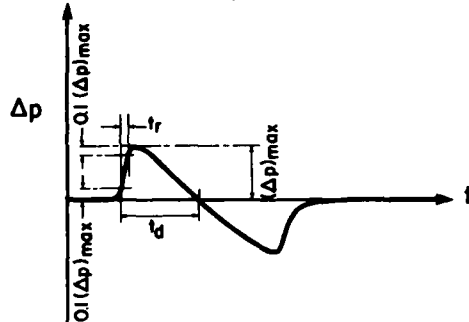


Figure 1. Definitions of N-wave risetime t_r , half duration t_d , and overpressure Δp as functions of time t .

SPARK AND EXPLODING-WIRE EXPERIMENTS

The purpose of these experiments was to generate weak, fully-developed N-waves with overpressures below 100 Pa in air, which would have interference-free shock fronts. This was accomplished by using sparks and exploding wires (Ref. 11). The dome containing the UTIAS air cushion vehicle (ACV) circular-track facility was used as a still-air reservoir for part of the experiments. Its major internal diameter is about 42.7m. This provided waves free from interference with walls and other objects.

For detecting weak shocks in the overpressure range 5-100 Pa, a condenser microphone was used [Bruel & Kjaer (B&K) 4135 free field 6.3mm (1/4in) diam]. Amplification of the microphone signal was provided by a preamplifier B&K 2619, and a power supply B&K 2807. The response of the microphone system was tested in the UTIAS Travelling-Wave Sonic-Boom Simulator (Ref. 12). When measuring without its protective grid at zero angle of incidence, the microphone has an approximate minimum risetime $t_r = 2.9 \mu\text{sec}$. The oscilloscopes used were Tektronix types 555 and 535 with a type D plug-in that has a bandwidth better than 300 KHz. The microphone was calibrated with a B&K Pistophone type 4220, which gives a sound pressure level at 250 Hz of 124 dB.

In the first series of experiments, sparks were used as a source of N-waves. The sparks were generated by the energy release from a charged 7.5 μF capacitor. The maximum charging voltage was 8 KV and the discharge device was a thyatron. A microphone was placed ahead of the measuring microphone in parallel to get the trigger signal for the oscilloscope. The source and the

microphones were set up at 1.8m above the floor to avoid distorted recordings by the measuring microphone due to reflected signals.

Fairly extensive measurements were done by using sparks at temperatures of 273-277 K and relative humidities of 50-73%. Six source-receiver distances, 4.1m, 4.9m, 9.8m, 15.6m and 21.6m, were employed with four different charging voltages of 4.4 KV, 5.0 KV, 5.4 KV and 6.0 KV. This series of measurements is termed Series-I. Another series of measurements (Series-II) was also done at a temperature of 289 K and the relative humidity of 50% for the distance range of 11.8 - 19.0m and a charging voltage of 4.4 KV.

Exploding wires were used to produce N-waves by replacing the resistor in the spark circuit by a thin nickel wire 0.125 mm diam and optimum length of 5 cm (Ref. 11). The sudden discharge of energy vapourized the wire. The expansion of the metal vapour generated an N-wave in the far field. The measurements were done at two conditions for Series III ($T_1 = 277$ K, RH = 75%, R = 27.6m, S = 4.6 KV, 6.0 KV), and for Series IV ($T_1 = 280$ K, RH = 87.5%, R = 24.3m, 29.3m, S = 4.6 KV, 6.0 KV), where T_1 is the room temperature, RH the relative humidity, R the distance from the source and S the charging voltage.

The vibrational relaxation times for oxygen and nitrogen were evaluated by using the empirical relation obtained from the absorption of sound waves by Bass and Shields (Ref. 13), as tabulated in Table 1. The vibrational relaxation times at room temperature strongly depend on the absolute humidity of the atmosphere.

Table 1. Vibrational relaxation times for oxygen (τ_O) and nitrogen (τ_N).

Series		T_1 (K)	RH (%)	τ_O (μ sec)	τ_N (msec)
I	SPARK	273-277	50-73	14-17	1.05-1.22
II	SPARK	289	50	5.8	0.52
III	E.W.	277	75	9.1	0.75
IV	E.W.	280	87.5	5.7	0.52

Representative oscillograms from sparks and exploding wires are shown in Fig. 2. It can be seen that both spark and exploding-wire sources make it possible to produce well-established N-waves far from the source. In the exploding-wire experiments, the N-waves were much cleaner than those generated by a spark, especially with regard to the rear shock. It was found that the wire length L plays a significant role in shaping the rear shock pressure profile. After testing several wire lengths, a wire length $L = 5.0$ cm proved to generate the most symmetrical N-waves, and was used in all subsequent runs. The microphones were set up normal to the wire to minimize any line-source effect.

The measured risetimes of the N-waves for overpressures of 5-30 Pa and half-duration of 50-120 μ s were much shorter than the risetimes estimated from the theory of plane, fully-dispersed waves with vibrational excitation of oxygen (Refs. 9,10). (The vibrational excitation of nitrogen can be neglected, since its relaxation time is much longer than the duration of the N-waves, as shown in Tables 1 & 2.) In order to clarify the effects of vibrational excitation on the risetimes of weak spherical N-waves it was essential to do a numerical analysis.

NUMERICAL ANALYSIS FOR WEAK SPHERICAL SHOCK WAVES

The problem of an explosion of a pressurized air sphere with low pressure ratio in atmospheric air was used as a model to generate weak shock waves. The

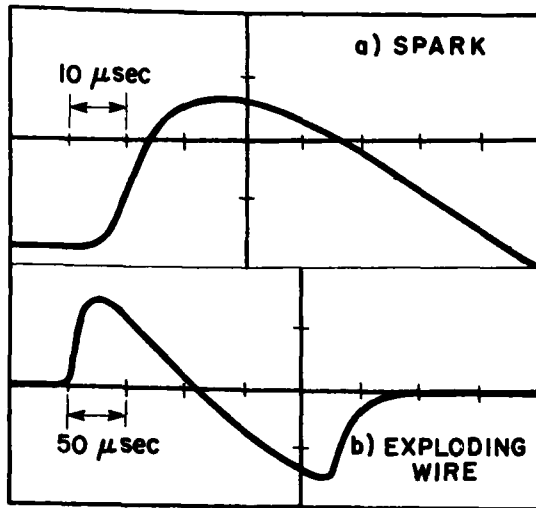


Figure 2. Spark and exploding-wire generated N-waves.

(a) Series-I: Spark, $S = 6.0$ KV, $R = 21.6$ m; $(\Delta p)_{\max} = 8.2$ Pa, $t_d = 72$ μ s, $t_r = 11.9$ μ s.

(b) Series-IV: Exploding-wire, $S = 6.0$ KV, $R = 29.3$ m; $(\Delta p)_{\max} = 20.2$ Pa, $t_d = 122$ μ s, $t_r = 15.2$ μ s.

Table 2. Data for the N-waves exhibited in Fig. 3 and the curves plotted in Figs. 4-7

Curves in Fig. 3	Curves in Figs. 4-7	Series No.	Source Type	P_{41}	R_o (cm)	R (m)	$(\Delta p)_{\max}$ (Pa)	t_d (μ s)	t_r (μ s)	
(a)	A	II	SPARK	1.2	1.8	22.4	5.0	71	6.5	Perfect, viscous
(b)	-	I	SPARK	1.2	1.8	22.4	4.7	85	7.9	Real, inviscid
(c)	C	I	SPARK	2.44	1.15	22.4	8.0	83	10.3	Real, viscous
(d)	D	II	SPARK	1.8	1.15	22.4	5.0	72	19.1	Real, viscous
(e)	E	IV	E.W.	3.3	1.8	30.0	13.5	132	20.0	Real, viscous

(P_{41} : Initial pressure ratio of the pressurized air sphere

R_o : Radius of the initial sphere)

analysis aims at simulating the spark and exploding-wire experiments in order to clarify the effects of the vibrational relaxation on the shock structure of weak blast waves in air. The analysis is based on the following assumptions.

(a) The flow is a nonstationary one-dimensional (plane or spherical) viscous, compressible flow. (b) The viscosity μ and the thermal conductivity λ are assumed to be constant. (c) The gas is air, and only the vibrational relaxation of oxygen is taken into account; the vibrational excitation of nitrogen can be neglected. (d) the bulk viscosity due to the rotational relaxation is assumed to be $\mu_v = (2/3)\mu$.

Then, the basic flow equations can be written as

$$\frac{\partial U}{\partial t} + \frac{\partial F}{\partial r} - \left(\frac{\partial^2}{\partial r^2} + \frac{\alpha}{r} \frac{\partial}{\partial r} \right) C + \alpha(H_I + H_V) - H_R = 0 \quad (1)$$

$$U = \begin{bmatrix} \rho \\ \rho u \\ E \\ \rho \sigma \end{bmatrix}, \quad F = \begin{bmatrix} \rho u \\ \rho u^2 + p \\ (E+p)u \\ \rho u \sigma \end{bmatrix}, \quad C = \begin{bmatrix} 0 \\ 2\mu u \\ \lambda T + \mu u^2 \\ 0 \end{bmatrix},$$

$$H_I = \frac{1}{r} \begin{bmatrix} \rho u \\ \rho u^2 \\ (E+p)u \\ \rho u \sigma \end{bmatrix}, \quad H_V = \frac{1}{r^2} \begin{bmatrix} 0 \\ 2\mu u \\ 0 \\ 0 \end{bmatrix}, \quad H_R = \begin{bmatrix} 0 \\ 0 \\ 0 \\ \rho[\sigma_e - \sigma]/\tau_o \end{bmatrix},$$

$$p = \rho RT, \quad E = \rho \left(e + \frac{1}{2} u^2 \right), \quad e = \frac{5}{2} RT + \sigma$$

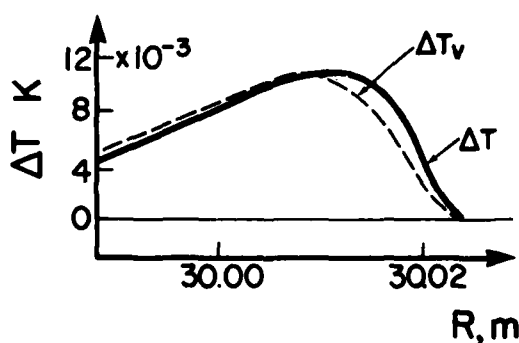
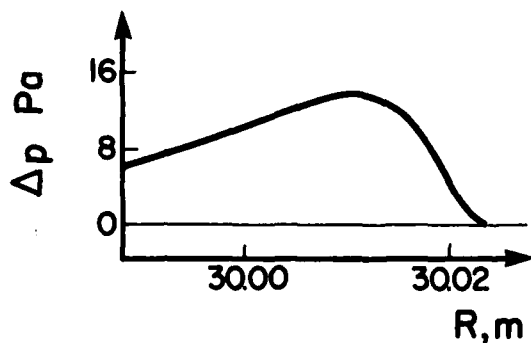
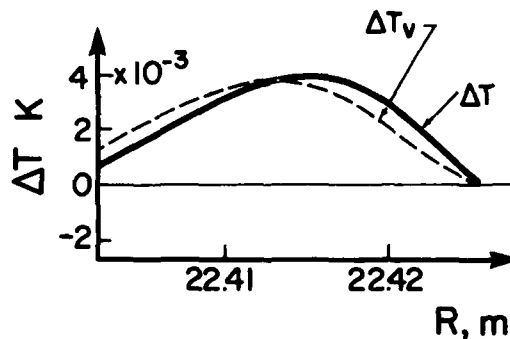
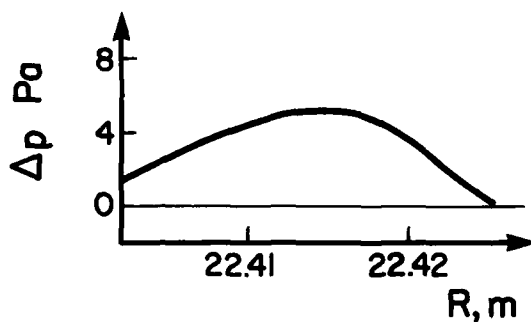
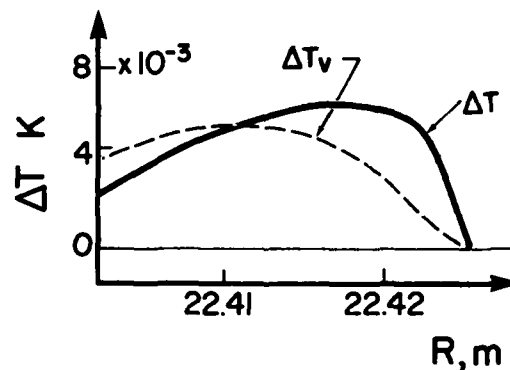
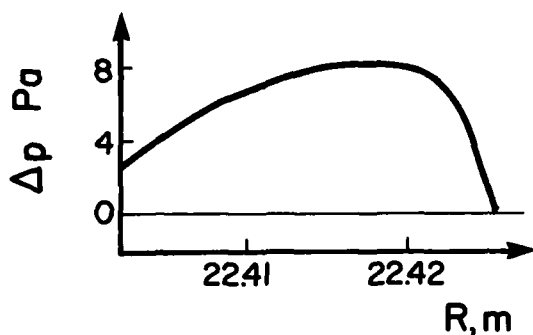
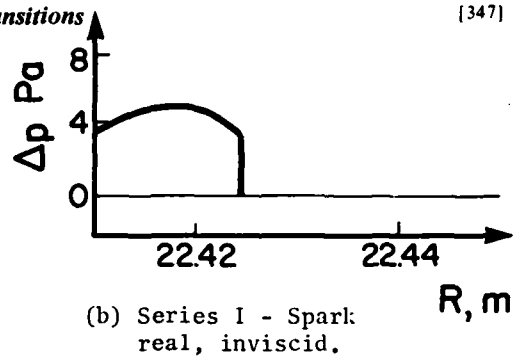
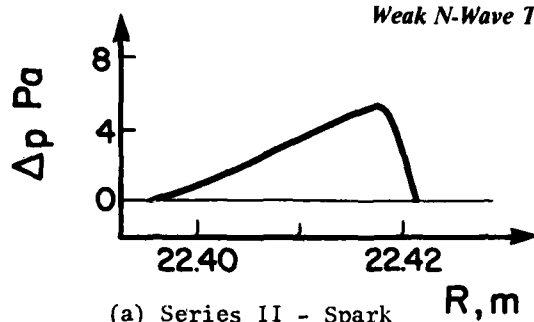
where $\alpha = 0$ for plane flows and $\alpha = 2$ for spherical flows, ρ - density, u - velocity, p - pressure, T - temperature, E - total energy, e - internal energy, R - gas constant, σ - vibrational energy for oxygen, σ_e - equilibrium vibrational energy for oxygen, τ_0 - vibrational relaxation time for oxygen. The harmonic oscillator approximation is applied to the vibrational energy level.

An operator-splitting technique is applied to Eq. (1). The calculation is carried out for each spatial mesh in each time step using the following procedure: (a) the hyperbolic equations are solved for an inviscid frozen plane flow $\partial U_1 / \partial t = -\partial F / \partial r$. (b) The spherical corrections are made by using the values of the physical properties evaluated in the step (a) $\partial U_2 / \partial t = -\alpha(H_1)_1$. (c) The viscous diffusion equations are solved by using the values of the physical properties evaluated in the step (b) $\partial U_3 / \partial t = [\partial^2 / \partial r^2 + (\alpha/r) \partial / \partial r] C_2 - \alpha(H_V)_2$. (d) The vibrational relaxation equation is solved by using the values of the physical properties evaluated in the step (c) $\partial U_4 / \partial t = (H_R)_3$. The final solutions are obtained in the step (d).

The RCM is applied to the step (a), and the explicit method of finite difference is applied to the steps (b)-(d). If one step is passed over among the steps (b)-(d), we could have a solution for a plane flow, an inviscid non-equilibrium flow or a viscous frozen flow, respectively. These are termed as a plane solution, a real, inviscid solution and a perfect, viscous solution, respectively. The full solution including both effects of vibrational excitation and viscosity is called a real, viscous solution.

It is noted that RCM is a numerical method developed by Glimm (Ref. 14), Chroin (Ref. 15) and Sod (Ref. 16) for one-dimensional flow problems including shock waves. In this method, a Riemann problem is solved for each spatial mesh in each time step, and then one of its solutions is chosen at random as a solution for the next time step by using a random sampling technique. It has the great advantage that shock waves and contact surfaces appear as discontinuous surfaces without spreading by implicit or explicit artificial viscosity inherent in finite-difference methods. The algorithm developed by Saito and Glass (Ref. 17) was used in the present study. As a check on the method, perfect, viscous, numerical solutions for an impulsive step wave were compared with Lighthill's analytical solutions (Ref. 18). Very good agreement was obtained thus lending confidence to the subsequent calculations.

Figure 3 illustrates typical pressure and temperature profiles of spherical N-waves, which were computed to simulate the spark and exploding-wire data. The initial conditions $P_{4,1}$ and R_0 , the radius of spherical front R , the overpressure $(\Delta p)_{\max}$, the half-duration t_d and the risetime t_r are shown in Table 2. Figures 3(a) and (b) correspond to the viscous, perfect solution and the real, inviscid solution, respectively. Figure 3(c)-(e) correspond to the real, viscous solution. Figure 3(a)-(d) exhibit the spark simulation and Fig. 3(e) shows the exploding-wire simulation. It should be noted that the shock-transition profiles differ. The profile of the perfect, viscous transition [Fig. 3(a)] is not similar to either profile of the steady, plane wave (Taylor, Ref. 5), the unsteady, plane wave (Lighthill, Ref. 18) or the N-wave for moderate Reynolds numbers (Lighthill, Ref. 18). Figure 3(b) indicates that the wave is a partly dispersed wave with a discontinuous front, even though the steady plane wave becomes a fully dispersed wave with a smooth transition for the corresponding overpressure (Refs. 5,9,10). Figures 3(c) and (d) illustrate the effects of the oxygen vibrational excitation. It can be seen in Fig. 3(c) that the shock transition is mainly controlled by viscous dissipation owing to the long vibrational relaxation time. In Fig. 3(d), the wave front becomes a fully dispersed wave for nearly the same distance and overpressure as in Fig. 3(c), since the 3(d) relaxation time is shorter than the 3(c). In Fig. 3(e), the wave front is also a fully dispersed wave.



(e) Series IV - Exploding wire, real, viscous.

(ΔT_v - vibrational temperature difference)

Figure 3. Computer simulated N-waves.

The risetimes of these waves are much shorter than the risetimes evaluated from the theory of steady, plane waves for viscous or dispersed shocks. They are affected considerably by the duration of the N-waves and the attenuation rate of the maximum overpressure, which is especially important. In blast waves, the maximum overpressure decreases with distance from the source. The rate of change of the maximum overpressure depends on the distance from the source and the energy of explosion. However, the shock thickness increases with decreasing maximum overpressure. The rate of change of this thickness is finite and depends on the maximum overpressure, becoming increasingly small as the shock is weakened. If the attenuation rate of the maximum overpressure is very large, the change of shock thickness cannot follow the change of the overpressure, and the shock thickness or risetime remains short regardless of the maximum overpressure. This can be designated as the nonstationary effect and it complicates the problem. The transient behaviour of shock transition must be evaluated for each case. This is the basic reason why numerical simulation is required for weak spherical N-waves in order to evaluate their risetimes.

COMPARISON WITH EXPERIMENTAL DATA

The computer simulation was carried out by adjusting the radius R_0 of the pressurized sphere and the diaphragm pressure ratio P_{41} to fit the experimental data for the maximum overpressure $(\Delta p)_{\max}$ and the half-duration t_d of the N-wave against the distance R from the source. Several trial calculations were required to obtain curves A-E in Figs. 4 and 5. The initial conditions of these curves are tabulated in Table 2. It can be seen from Figs. 4 and 5 that one can simulate the change of $(\Delta p)_{\max}$ and t_d against R by a proper choice of R_0 and P_{41} . The pressure and temperature profiles in Figs. 3(a), (c), (d) and (e) exhibit the properties to be found on curves A, C, D and E, respectively, in Figs. 4-7.

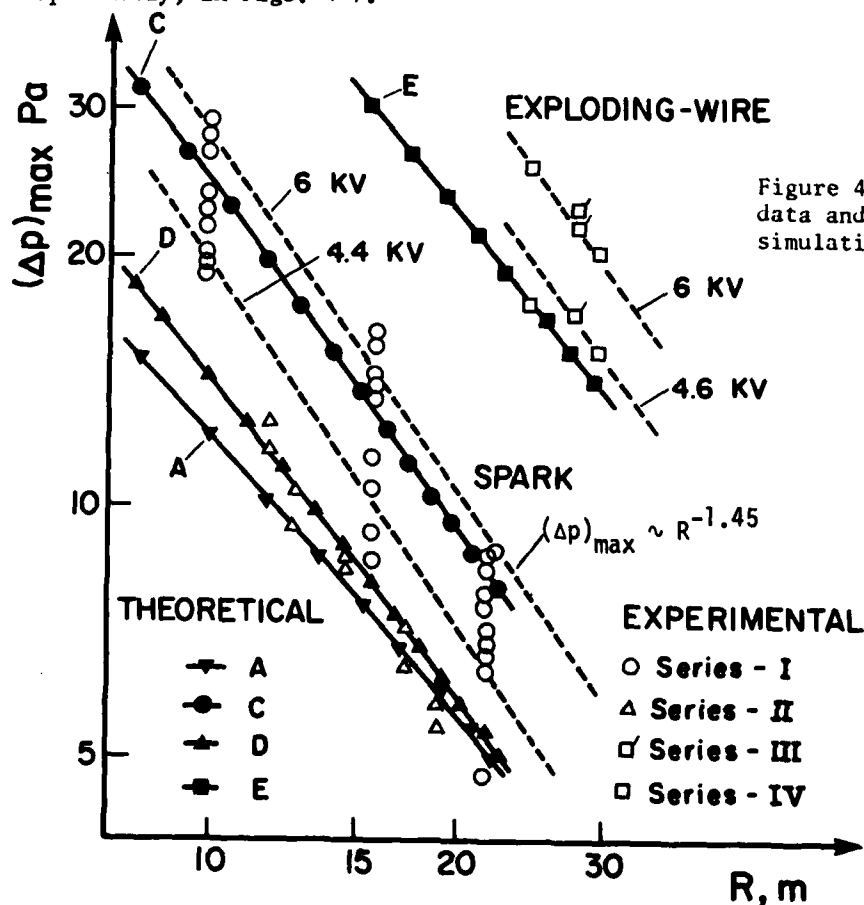


Figure 4. Overpressure data and their computer simulation.

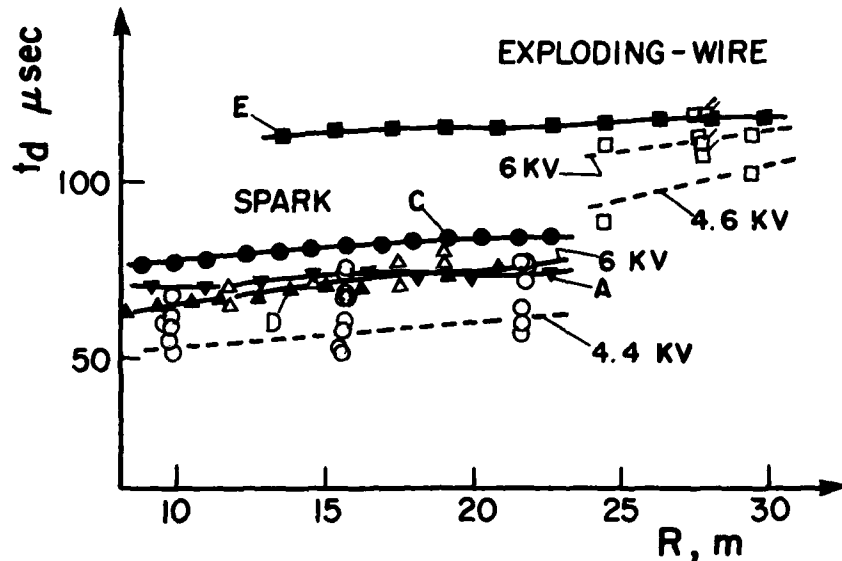


Figure 5. Half-duration data and their computer simulation.

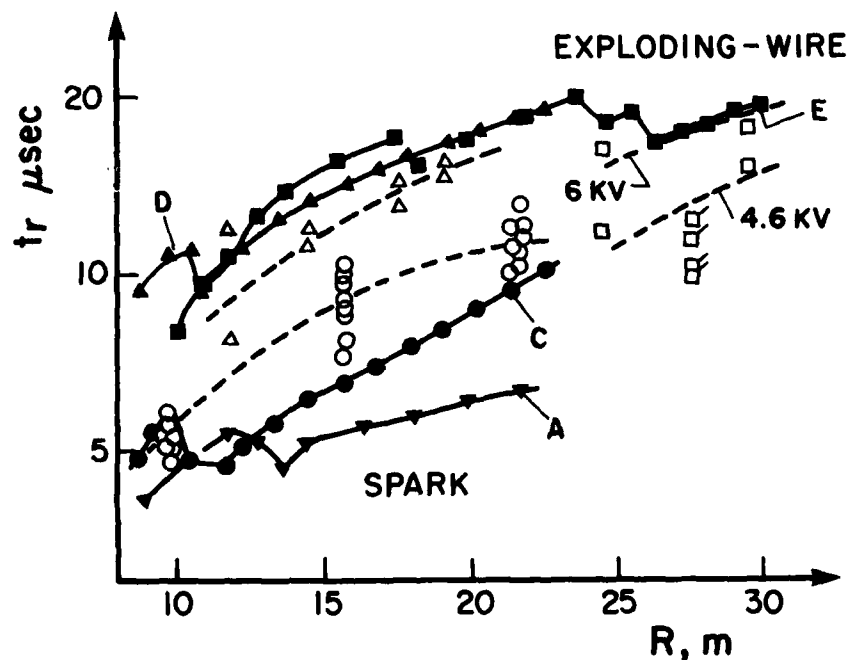


Figure 6. Risetime as a function of distance from source.

In Figs. 6 and 7, the risetimes are plotted against R and $(\Delta p)_{\max}$, respectively. Curve A indicates that the perfect, viscous solution cannot simulate the unsteady behaviour of the risetime. Curves C, D and E indicate that the real, viscous solutions simulate the experimental results reasonably well, when one considers the complexities of the discharge types. Curves C, D and E almost simulate the data for Series I, II and IV, respectively.

The general features of the results can be summarized as follows. (1) The maximum overpressure initially attenuates inversely proportional to the radius of spherical front (Fig. 4). However, the attenuation rate increases with increasing radius for weak waves of overpressures below 100 Pa. It is

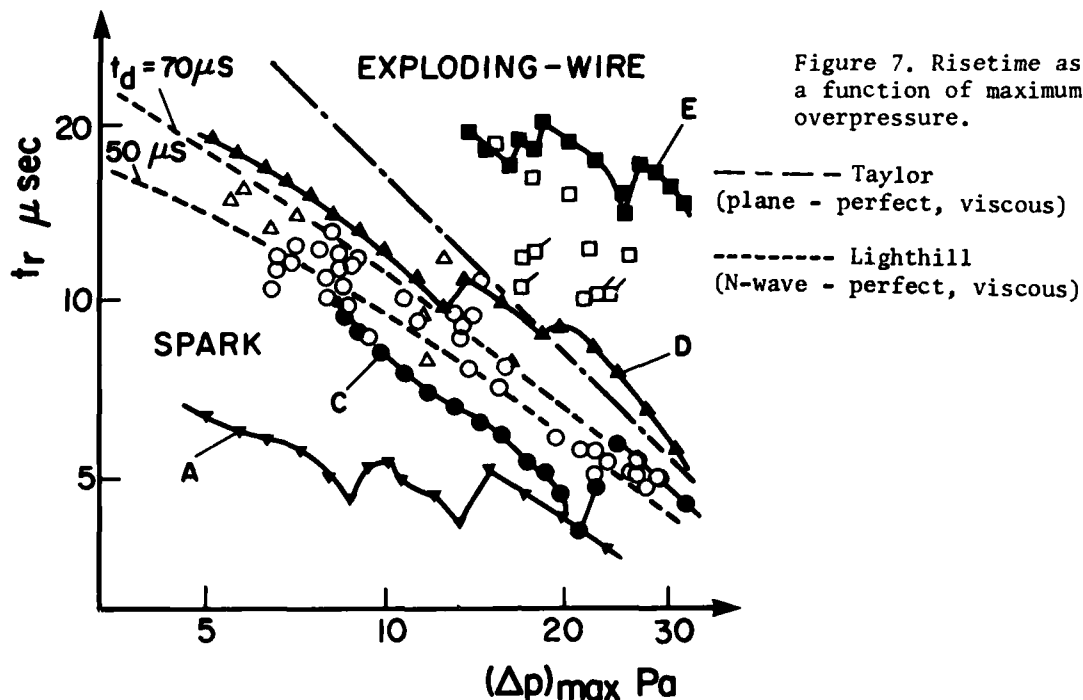


Figure 7. Risettime as a function of maximum overpressure.

mainly controlled by the energy dissipation due to vibrational excitation of air molecules. The shorter the vibrational relaxation time, the faster is the attenuation. The two series of spark experiments illustrate this tendency. (2) The half-duration t_d increases with radius R (Fig. 5). Its rate of increase is about $1.0 \mu\text{sec/m}$, which also simulates the experimental data. The increase in t_d is also attributed to real-gas effects, as the perfect gas solution does not give such an increase in t_d . It may be attributed to the difference in the sound speeds between the front and the middle of the N-wave. (3) The spark data and their simulation for risetime (Fig. 7) show that the shorter relaxation time gives the longer risetime and the longer relaxation time gives the shorter risetime. This tendency is due to the nonstationary effect. The long relaxation time gives the slow rate of change of the shock thickness, so that the risetime remains short even for weak waves. (4) The exploding-wire data and their simulation show by comparison with the spark data that the stronger explosion and the longer duration give the longer risetime for the same overpressure (Fig. 7). This is again due to the nonstationary effects. The strong explosion gives a slower rate of change of the maximum overpressure for the same overpressure (see Fig. 6) so that the risetime has enough time to increase. Furthermore, a longer duration provides a margin for increasing the risetime.

CONCLUSIONS

It has been shown that the real, viscous solutions for the risetimes of weak spherical N-waves can simulate the spark and exploding-wire data obtained in a still-air dome. The random-choice method (RCM) with an operator-splitting technique is an excellent means of analysing shock-wave transitions, including the effects of viscosity and oxygen vibrational excitation. It was shown that the duration and the attenuation rate of a spherical N-wave are factors which control its risetime, in addition to the vibrational relaxation times of the air molecules. Furthermore, it was found that the duration and the attenuation rate are also affected by the vibrational excitation. The present results on the transient behaviour of spark and exploding-wire generated N-waves are applicable to all types of blast waves and sonic booms. The data will provide a basis for studying the attenuation and the risetime of weak blast waves and

sonic booms. Finally, it is doubtful if sparks or exploding wires can accurately simulate the risetime of actual SST-generated N-waves.

REFERENCES

1. A. Niedzwiecki and H. S. Ribner, J. Acoust. Soc. America, 64, 1617, 1978.
2. D. A. Hilton and J. W. Newman, J. Acoust. Soc. America, 39, 1966.
3. D. J. Maglieri, D. J. Huckel and H. R. Henderson, NASA TN D-6823, 1972.
4. J. W. Reed, J. Acoust. Soc. America, 61, 39, 1977.
5. G. I. Taylor, Proc. Roy. Soc., 34, 371, 1910.
6. K. J. Plotkin and A. R. George, J. Fluid Mech., 54, 449, 1972.
7. A. D. Pierce and D. J. Maglieri, J. Acoust. Soc. America, 51, 702, 1972.
8. J. E. Ffowcs-Williams and M. S. Howe, J. Fluid Mech., 58, 461, 1973.
9. J. P. Hodgson, J. Fluid Mech., 58, 187, 1973.
10. N. H. Johannesen and J. P. Hodgson, "Report on Progress in Physics", 42, 639, 1979.
11. O. Holst-Jensen, UTIAS TN 229, 1980.
12. I. I. Glass, H. S. Ribner and J. J. Gottlieb, CASI J., 18, 235, 1972.
13. H. E. Bass and F. D. Shields, J. Acoust. Soc. America, 62, 571, 1977.
14. J. Glimm, Comm. Pure Appl. Math., 18, 697, 1965.
15. A. J. Chorin, J. Comp. Phys., 22, 517, 1976.
16. G. A. Sod, J. Fluid Mech., 83, 795, 1977.
17. T. Saito and I. I. Glass, UTIAS Rep. 240, 1979.
18. M. J. Lighthill, "Survey in Mechanics", Eds. G. K. Batchelor and R. M. Davies, p. 294, 1956.

AD P000259

Generation of the patterns in gaseous detonations

F. Schultz-Grunow

Institute for Applied Mechanics, RWTH Aachen

Aachen, West-Germany

The problem is the mode of formation of the first initial regular pattern and its spacing in a detonation front. It is generally accepted that these patterns are due to a selfsustaining process of formation of Mach stems by colliding blast waves and blast waves by secondary local explosions initiated by these Mach stems whilst the reason for the very first explosions and their spacing is not known. It is shown that this is caused by temperature perturbations as they are introduced with any kind of ignition. A steady mode of perturbation is derived which initiates the first local explosions at the very end of the combustion zone. They substitute the unrealistic asymptotic decrease. The concept is in agreement with measurements of the reaction time and of the spacing of soot patterns.

Numerous publications deal with the regular patterns observed in detonations as corrugated fronts leaving behind regular patterns of striae, as well as cellular patterns drawn by detonations sweeping along sooted walls. According to the common view the triple points of Mach stems draw the soot patterns. The Mach stems are caused by blast waves which had been produced by pointwise secondary explosions initiated by Mach stems. The production of the Mach stems is a selfsustaining process. With this view agreement could be achieved [1] with the numerous observations using high speed photography or sooted walls.

Yet one is not able to see the reason for the mode of formation of the initial pattern and for the specific scale of these patterns which is quite independent of the geometry; that means it occurs in ducts or in cylindrical and spherical detonations [1]. Looking at the experimental results [1,2,3,4] with sooted walls one notices an interesting dependence on the inverse pressure what points to an influence of the order of reaction. Indeed, on reasons of nondimensionality the spacing l should be $\sim \sqrt{\lambda \tau}$, $\sqrt{D \tau}$ resp. with coefficient of diffusion D , heat conductivity λ and reaction time τ . D , λ depend inversely on the pressure p and so does τ in a second order reaction. Thus l is $\sim 1/p$. The second order was proved by Kistia-kowsky and Kydd [5] for H_2 -, O_2 -mixtures. They are used in the following.

Whilst it is no problem to produce perfectly homogenous gas mixtures, the methods of ignition produce perturbed temperatures. This suggests to superpose perturbations ψ to the main C.J.-temperature T_2 . As will be seen these perturbations especially are of influence at the end of the combustion zone. There the rate of reaction is practically constant [5] compared with the time intervals considered here and the main temperature as well because of the asymptotic decrease.

For small perturbations ψ one is therefore inclined to apply the equation of heat conductivity for incompressible media with c_v instead of c_p in kcal/m³°K owing to the rapid changes to be considered. A term for the heat production by reaction has to be added, $Uc_v\psi$, where U is the time factor and $c_v\psi$ the heat release. Thus

$$(1) \quad c_v D^2 \psi / dt = \lambda \Delta \psi + U c_v \psi$$

Since the combustion is bound to a surface the operator Δ refers to the plane with coordinates x, y . The solution is

$$(2) \quad \psi = \psi_0 \sum_{\alpha} \sum_{\beta} \sin(\alpha x \pm \beta y) \exp - [(\alpha^2 + \beta^2) \lambda - U c_v] t / c_v$$

To have equally distant triple points they must form equally sided triangles. Then $\alpha/\beta = \tan 60^\circ = 1.734$ and $\alpha^2 + \beta^2 = 1.33 \alpha^2$ with $\alpha = 2\pi/l$. There exists a steady solution if

$$(3) \quad 1.33 \alpha^2 \lambda = U c_v$$

It relates the steady wave length to the heat release.

During the main part of combustion where U is large the corresponding steady wave lengths are so extremely small that they are irrelevant. Approaching the end of the combustion zone, however U becomes small enough that l may correspond to the spacing of the soot patterns. A 1% perturbation amplitude raises the Arrhenius factor by 10% at the end of the combustion zone when the activation energy is 57 kcal/mole [5] and the temperature 3300°K. This is equivalent to a 5% richer mixture. Thus the perturbations in fact can act as initial centers of secondary explosions the blast waves of which form by collision the first Mach stems. It even makes no difficulty to see why in cylindrical and spherical detonations the specific spacing is maintained although the reacting surfaces expand. The perturbations exist as long as combustion lasts and correspondingly new explosion centers can be formed if the spacing gets too large. Thus the unrealistic asymptotic end of the combustion zone is replaced by such secondary explosions which use up the rest of unburnt gas.

By applying eq.1 one should be aware that the presence of water vapour reduces the heat capacity ratio γ so that small temperature perturbations may not need to mean small density deviations. These however occur rapidly enough to act mainly as enhancement of the secondary explosions.

The question arises why the steady wave length is predominant since solution (2) admits also smaller and larger wave lengths. The method of Fourier expansion shows that only smaller wave lengths are superposed. Thus the steady spacing eq.3 excludes lower harmonics.

This concept will be proved with stoichiometric H_2 - O_2 -mixtures diluted with A because there exist for them once measurements of the spacing l of soot patterns [3,4], secondly because of kinetic results on the C.J.-state [6] and finally on account of the said measurements of the reaction times ([5] s. Fig.7). These experiments use Xe as diluent but it was proved that the percentage of Xe has not the least influence furtheron the use of A or He makes no difference according to experiments [4], so that they also may be used when A is the diluent. The measurements are presented for a partial O_2 -pressure $p_{O_2} = 20$ Torr and times at which 75% are burnt. Then for stoichiometric mixtures as here considered $p_{H_2} = 40$ Torr. On account of the second order reaction these times can be reduced to any specific C.J.-state.

The time factor U is determined by the reaction rate

$$(4) \quad U = - D[H_2]/dt$$

Brackets mean concentrations in kmole/m³. With this dimension the term Uc_v in eqs.1,2,3 has to be replaced by UC_v . The rate equation is

$$(5) \quad D[H_2]/dt = - 2K[H_2][O_2]$$

If the mole fraction μ of the burnt gas is introduced and indices 0 mean initial quantities one becomes

$$(6) \quad U = -[H_2]_0 D(1 - \mu)dt = + 2K[H_2]_0[O_2]_0 (1 - \mu)^2$$

where K means the reaction rate constant. To avoid unnecessary long calculations which would exceed the experimental exactness, the mole change is neglected. This introduces by 70% A a deviation of 5%. The solution of eq.6 then is

$$(7) \quad \frac{1}{1 - \mu} = 2[O_2]_0 K\tau$$

This equation enables to compute K with the experimental data, if τ is reduced by the inverse pressure relation to the specific C.J.-state. Correspondingly to the said meaning of τ one has to introduce $(1 - \mu) = 0.25$. In table I one finds the C.J.-states, reduced times τ and K.

Table I

C.J.-states, corresponding reaction times τ and reaction rate constants K.

Mixture	$2H_2+O_2+0.775A$	$2H_2+O_2+0.7A$	$2H_2+O_2+0.5A$
p_1 (atm)	1	1	1
T_1 (°K)	298,2	298,2	298,2
ρ_1 (Kg/m ³)	1,38	1,29	1,06
p_2 (atm)	15,31	16,87	18,75
T_2 (°K)	2833	3056	3355
ρ_2 (Kg/m ³)*)	2,22	2,13	1,72
D_d (m/s)	1540	1680	1920
C_{v_2} (kcal/kmole, °K)*)	4,91	5,55	6,24
γ_2 *)	1,404	1,385	1,32
c_2 (m/s)*)	959	1012	1169
$\lambda_2 \cdot 10^4$ (kcal/m, s, °K)	0,47	0,43	0,65
$[O_2]_0$ (kmole/m ³) at C.J.	0,00494	0,0067	0,011
τ (μ s)	0,7	0,53	0,316
$K \cdot 10^{-6}$ ($\frac{m^3}{kmole \cdot s}$)	578	565	574

*) without ionization and dissociation

It is of interest to determine the fraction μ of unburnt gas and the time τ^* at which the continuously burning transforms to the point like burning. This is done in table II. With the observed spacing l the left hand side of eq.3 is determined and consequent-

ly U_{c_v} . Then with eq.6 $(1 - \mu)$ can be determined. It shows to be of the order 0,04 so that, as expected, the change to point like burning occurs at the very end of the combustion zone. τ^* is determined by eq.7 and table I. The last column is shown for completeness, where the assumption of constant mole number introduces an approximation of 17%. τ^* fits to the measured density profile [5].

Table II

Calculation of μ .

Mixture	$2H_2+O_2+0.775A$	$2H_2+O_2+0.7A$	$2H_2+O_2+0.5A$
l (mm)	3,0	1,7	0,9
$1,33 \alpha^2 \lambda (\text{kcal/m}^3, \text{s}, ^\circ\text{K})$	274	771	4216
$1 - \mu$	0,03	0,037	0,05
$\tau^* (\mu\text{s})$	6	4	2

A Mach stem is produced if the two intersecting shocks of finite strength form an angle of 80° [1]. This means that the points of intersection should gather on lines which have an inclination of 50° to the direction of propagation. Actually they always gather on lines with 30° inclination [1]. The same inclination is obtained if one superposes transversally the C.J. speed of sound c_2 to the detonation velocity D_d [1] what shows that the point like burning should be an explosion rather than a detonation.

An inclination of 30° instead of 50° means that the explosion does not occur at the point of intersection but with a time lag so that the intersecting waves can form the wanted angle (s. Fig.1). In fact, it cannot start at the intersection point in default of compressed mass. There exists moreover a time lag of combustion which is difficult to estimate. A "rise time" of $0.7 \mu\text{s}$ [5] was observed behind a detonation front with $2H_2+O_2+0.5Xe$ at $p_1=90$ Torr. This gives with 1 atm a time lag of $0.083 \mu\text{s}$. With an inclination of 30° the longitudinal spacing (s. Fig.1) is $l_2 = 1.7$ l. To have an angle of 80° between the crossing shocks the explosion center must have a distance $h = 0.45$ mm (s. Fig.1) from the intersection if $l = 1$ mm. To cross this distance in $0.083 \mu\text{s}$ which surely is too small for the present geometry a velocity of 5400 m/s is wanted. The velocity of sound with which the gas flows off is 1170 m/s (s. table I). The propagation velocity of the Mach stem therefore should be $5.6 c_2$. This corresponds to the considerable pressure ratio 36 at the Mach stem and 13 at the blast waves which surely are too large. At least one sees that the Mach stem can catch up the detonation front and make it undulated. Another fact may still be noted. The 30° inclination means that all of the intersections as well as of the explosion centers have the same distance. This looks like a plausible geometric confirmation. In space this means that adjacent explosion centers form octaedrons [1].

To the last estimation it may be remarked that $\gamma = 1.4$ was assumed, whilst the real γ is smaller. This decreases h and therefore the estimated Machstem velocity which is needed for a specific rise time.

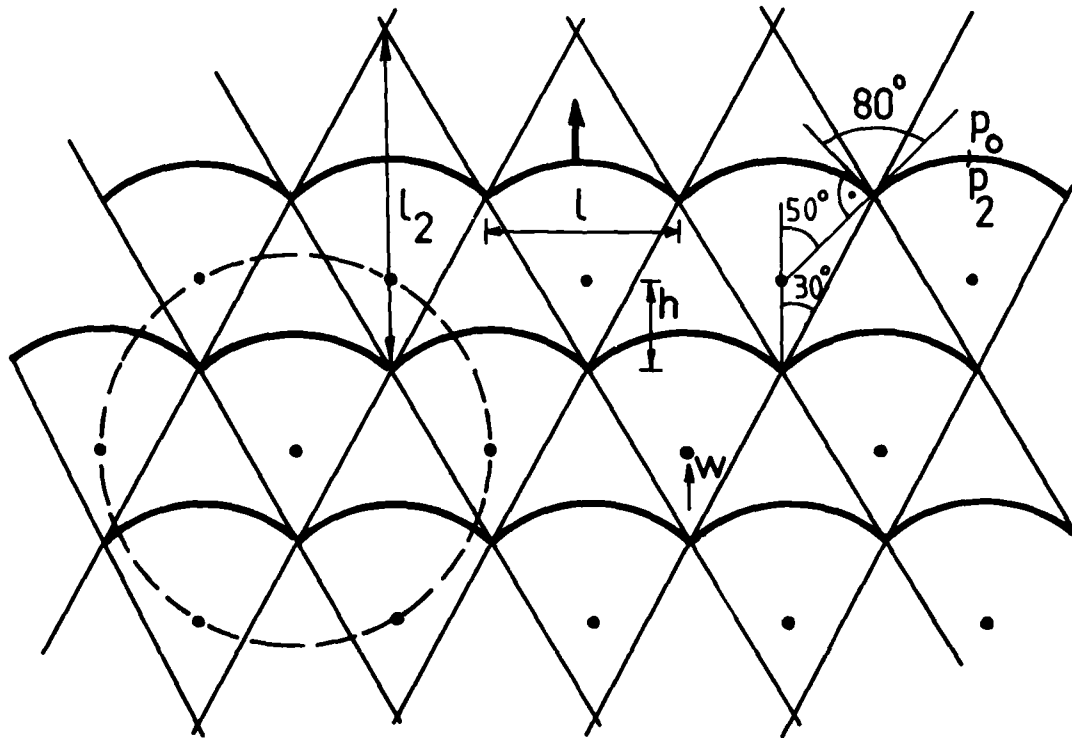


Fig. 1

Sequential secondary fronts in the moment of Mach stem initiation.

References

- 1 Schultz-Grunow, F.: Microstructure of Gaseous Detonation Waves. Rep. 6/71, Ernst Mach Institute, Freiburg i. Br., W.-Germ., Eckerstr. 4.
- 2 Strehlow, R.A., Engel, C.D.: Transverse Waves in Detonations II, AIAA J. Vol. 7 (1969), 323-328.
- 3 Strehlow, R.A., Maurer, R.E., Rajan, S.: Transverse Waves in Detonations I, AIAA J. Vol. 7 (1969), 323-328.
- 4 Schultz-Grunow, F., Struck, W.G.: Cell Structure in Detonation Waves, Rep. 51/69, Ernst Mach Institute, Freiburg i. Br., W.-Germ., Eckerstr. 4.
- 5 Kistiakowsky, G.B., Kydd, P.H.: Gaseous Detonations. IX. A Study of the Reaction Zone by Gas Density Measurements. J. Chem. Phys., Vol. 25 (1956), 824-835.
- 6 Schaefer, J.H.: Detonation and Deflagration in Explosive Gas Mixtures, Rep. 3/73, Ernst Mach Institute, Freiburg i. Br., W.-Germ., Eckerstr. 4.

AD P000260

EVOLUTION OF SHOCK-INDUCED PRESSURE ON A FLAT-FACE/FLAT-BASE BODY AND AFTERBODY FLOW SEPARATION

Kenneth K. Yoshikawa and Alan A. Wray

Ames Research Center, NASA

Moffett Field, California 94035

The time-dependent, compressible Reynolds-averaged, Navier-Stokes equations are applied to solve an axisymmetric supersonic flow around a flat-face/flat-base body with and without a sting support. Important transient phenomena, not yet well understood, are investigated, and the significance of the present solution to the phenomena is discussed. The phenomena, described in detail, are as follows: the transient formation of the bow and recompression shock waves; the evolution of a pressure buildup due to diffraction of the incident shock wave in the forebody and afterbody regions, including the luminosity accompanying the pressure buildup; the separation of the flow as influenced by pressure buildup; the location of the separation and the reattachment points; and the transient period of the shock-induced base flow. The important influence of the nonsteady (transient) and steady flow on the aerodynamic characteristics, radiative heat transfer, and, thus, on the survivability or safeguard problems for an aircraft fuselage, missile, or planetary entry probe at very high flight speeds is described.

INTRODUCTION

The aerodynamic characteristics of nonsteady supersonic flow, especially transient phenomena in turbulent shock-induced flow, passing over a blunt body are not well understood, even though good high-speed photographic techniques have been applied (refs. 1-7). Flow fields generated by shock tubes, blast waves, and detonations are examples of these shock-induced flows. Shock-wave analogy and blast phenomenology have become important subjects of investigation, and scientific interest in the effects of aerodynamics and heat transfer on space vehicles and missiles has been renewed (refs. 8-11). Nonsteady phenomena, such as the development of bow and afterbody recompression shock waves, impact pressure generated by a diffracted shock wave, and the evolution of separation and recirculation at the base, have long been subjects of scientific interest. In particular, the initial formation of the separation bubble, which triggers the base recirculation, has been a controversial subject for several decades (refs. 4-5). Most authors conjecture that the separation originates near the shoulder. Extensive theoretical and experimental efforts, however, have failed to explain the separation phenomenon. In addition, there are characteristics of nonsteady flow (e.g., flow test time and transient period) that are not well understood.

Recent high-speed computer solutions of the fluid dynamic equations provide detailed insight into the physics of these complex unsteady phenomena. Computer simulations reveal new explanations of poorly understood experimental results; these simulations have demonstrated, for the first time, the detailed evolution of shock-induced pressure and afterbody flow separation. This paper introduces and describes some of the new results of the present numerical simulations. A better understanding of the separation and reattachment processes may make it possible to control (e.g., delay or eliminate) the recirculation wake, which is a viscous flow problem of significant scientific

and practical importance. Turbulent flow is assumed throughout the analysis since a conservative estimate for the Galileo probe is one of our immediate applications (refs. 12, 13).

NUMERICAL SIMULATION

Flow Schematic. Nomenclature and a sketch of the initial shock wave passing over a flat-face/flat-base body supported by a sting are shown in Figure 1. A part of the primary shock wave at Mach number M_∞ impacts with and reflects from the flat front surface of the blunt body. The rest of the shock wave passes over the cylinder, diffracts at the shoulder and base stagnation point, and moves toward the downstream direction, leaving a turbulent shear layer in the wake. The reflected shock wave, interacting with the upstream flow, eventually forms the bow shock wave ahead of the blunt body.

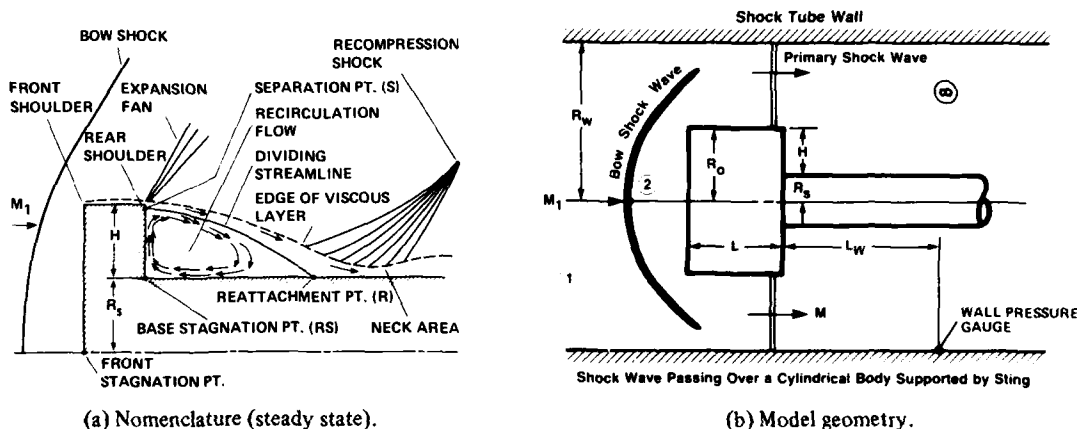


Figure 1. Shock-induced flow schematic.

Computational Method. The computational code for afterbody flow (ref. 9), using the compressible Reynolds-averaged Navier-Stokes equations, has been modified to calculate the entire fore-and-afterbody flow fields; the code is explicit and is second-order accurate in space and time (unsplit, Richtmyer and Morton method). Front, side, base, and sting surfaces are assumed adiabatic. Slip-flow is assumed on the shock-tube wall. A simple physical model with ideal gas, constant eddy viscosity, and unit Prandtl number ($Pr = 1$), has been incorporated in the calculations to see the qualitative effect of the parameters on the flow-field solutions. The appropriate value used for the constant eddy viscosity is discussed in detail in ref. 9.

RESULTS AND DISCUSSION

Transient Flow (Nonsteady). Essential features and results of the present calculation are described in the following sections and shown in Figures 2 through 11.

Formation of the bow shock wave— Evolution of the shock-induced flow around the blunt body is shown in Figures 2(a-d). Density contours, pressure distribution on the centerline, flow velocity on the afterbody axis, and base vorticity distribution at four different times are plotted. The top row of Figures 2(a-d) shows the computed density contours for dimensionless times of $t/(R_0/c_1) = 0.57, 1.12, 1.5,$ and 19.5 , where c_1 is the upstream speed of sound. The dotted lines in the density plots represent the location of the shock front. The effects of compression ahead of the body, expansion around the front and rear shoulders, recompression near the base stagnation point (due to the reflected shock wave impinging on the base line and bouncing back), and the impact pressure induced by the diffraction of the incident shock wave can be visualized through the density and pressure figures (discussed in following sections).

Induced peak pressure— The transient pressure along the centerline ahead of the flat face and behind the flat base are also shown in Figures 2(a-d) for the same dimensionless times as the density contours. As the incident shock wave reflects from the forebody face, the impact pressure at the forebody stagnation point reaches instantaneous values far above the steady-state pressure p_2 . The diffracted shock wave reaches the rear centerline at $t = 1.12$ (Fig. 2b), and the pressure builds up due to the impact of the axisymmetric shock wave with itself at the axis (shock reflection), while the pressure in the forebody shock layer reduces to its asymptotic value. Note the significantly high peak

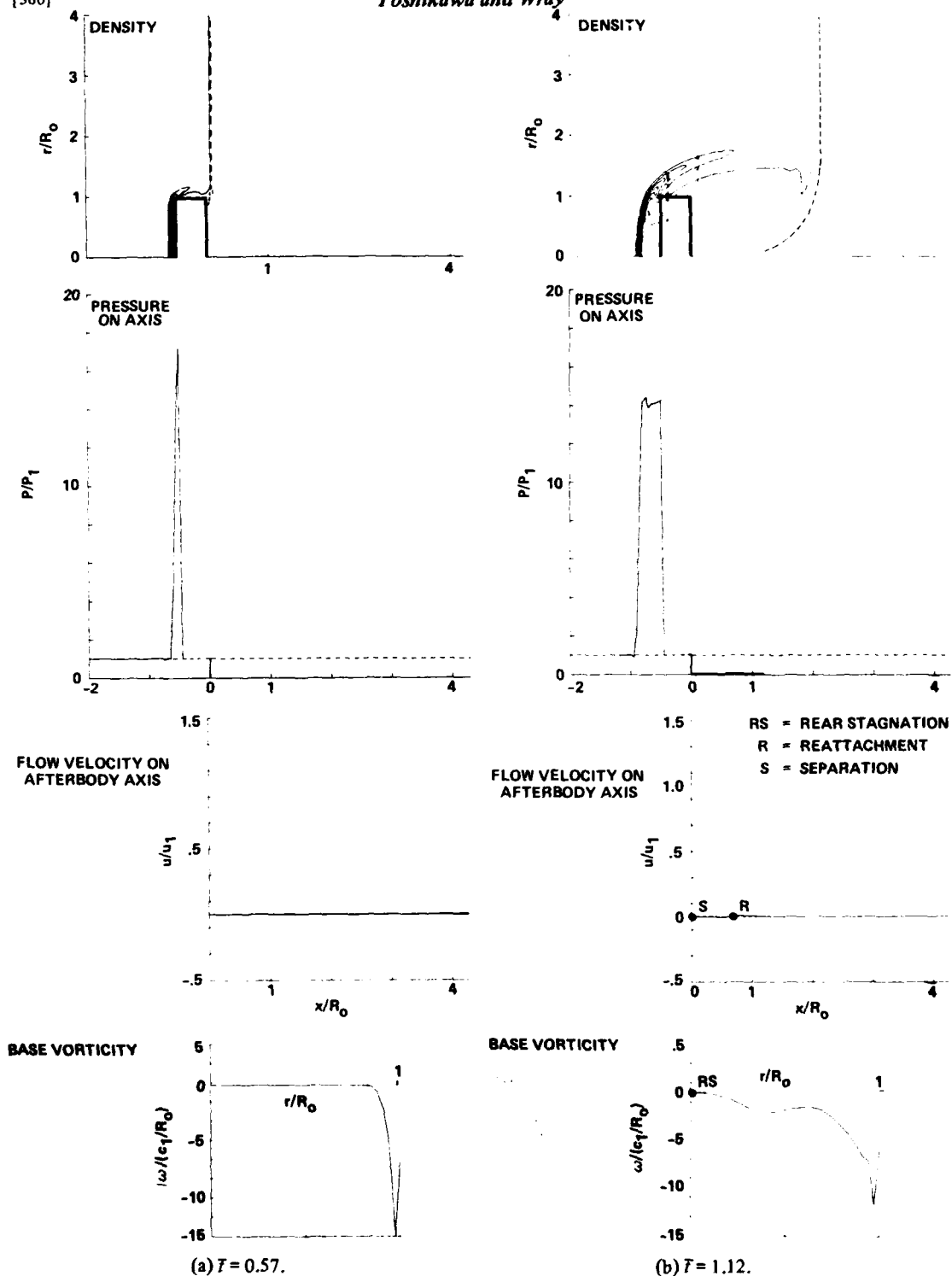


Figure 2. Evolution of the shock-induced flow: density contours, pressure distributions and afterbody flow velocity on the axis, and base vorticity. $M_\infty = 14.5$, $\gamma = 1.15$, $R_g/R_0 = 0$, $L/R_0 = 0.5$, and $R_w/R_0 = \infty$.

pressure behind the base (Fig. 2c). The peak pressure reaches its maximum value at $t \cong 1.5$ (this corresponds to $t \cong 1.0$ of ref. 9) and then decreases as it propagates downstream.

Formation of the separation bubble— To study the transient formation of the base recirculation, time-accurate solutions of the Navier-Stokes equations are necessary. Shown also in Figures 2(a-d) are the flow velocity (u) on the centerline behind the body and the vorticity distribution (ω) on the base. Since the vorticity is zero at the base stagnation point (RS), at the separation point

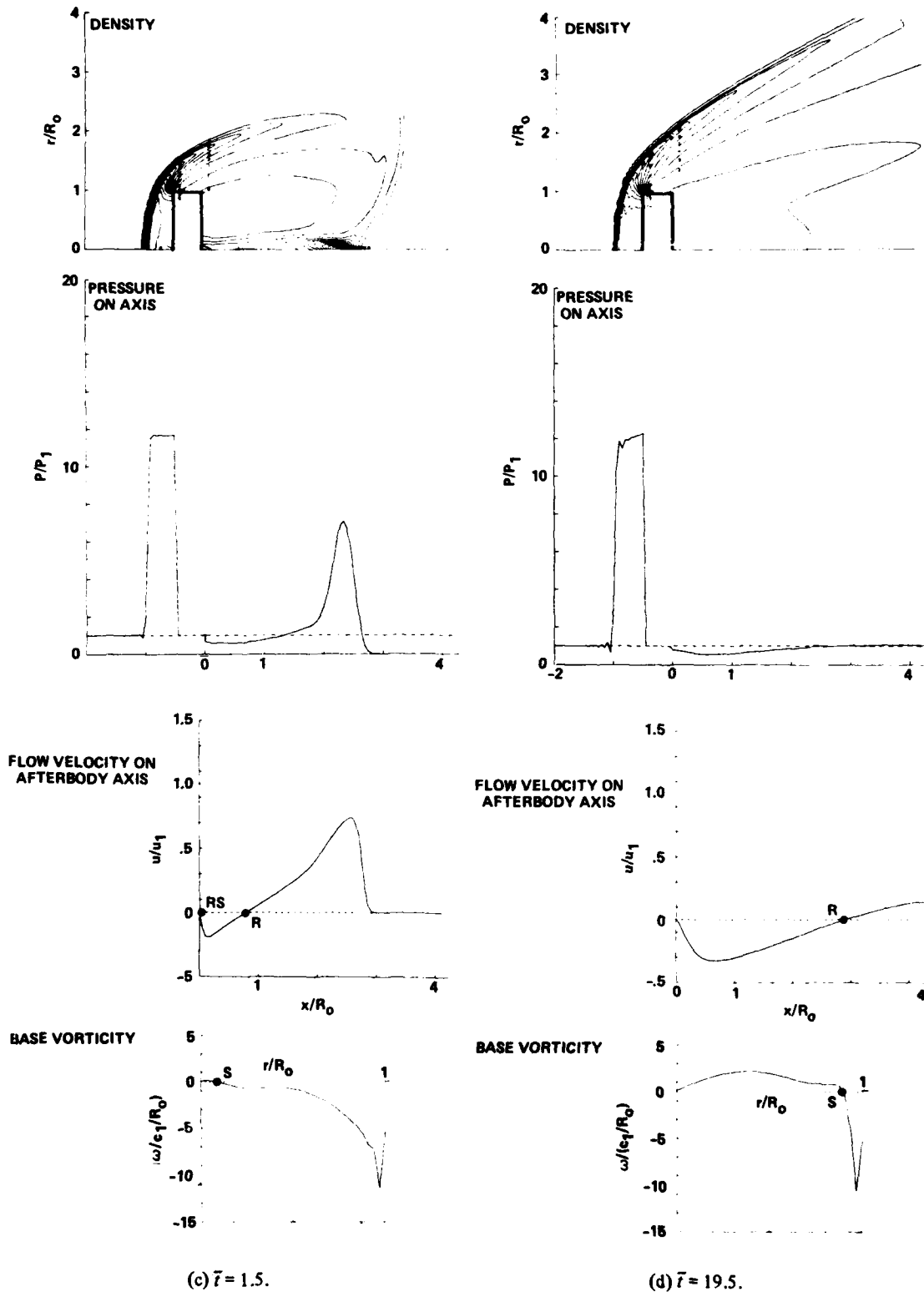


Figure 2. Concluded.

(S), and at the reattachment point (R), its variation can be used to indicate initial formation of recirculation. However, the vorticity along the flow axis behind the body is zero; hence the axial flow velocity is plotted to determine the flow direction, magnitude, and the stagnation or reattachment point.

No variation appears in the velocity plot at $t = 0.57$ because the incident shock front has not reached the flow axis, and the vorticity at the upper portion of the base is suddenly increased because of the diffraction and expansion of the shock wave at the shoulder. As the shock front reaches the centerline the pressure builds up, with the peak pressure initially located at the stagnation point R where the flow is divided into the forward and reverse directions. This point is at some distance away from the base because the shock front passing over the base surface is slightly retarded by the boundary layer (see Fig. 2 and ref. 9). A separation bubble originating at the centerline of the base (S), and reattaching at the base stagnation point (RS), is shown in the velocity figure for $t = 1.12$. As the shock front moves downstream of the body, the location of the peak pressure also moves downstream. The separation bubble expands outward rapidly as the base pressure builds up and, following the upstream propagation of the reflected shock wave, reaches its steady-state position slightly below the shoulder. The reattachment point (R) remains essentially unchanged (see velocity profiles for $t = 1.12$, and 1.5) until the separation bubble reaches this point and then approaches its steady-state position, as shown in the velocity plots of Figures 2(a-d). Note that the vorticity along the base surface is positive and the axial velocity inside the recirculation region is negative. The major source of recirculation is on the centerline behind the body where the incident shock is first reflected. The present result (Fig. 2) does not show that separation originates from or near the shoulder. It should be noted here that some of our recent calculations predict the occurrence of a small and slow-growing separation bubble below the shoulder (ref. 16). This bubble is, however, quickly absorbed by the major bubble from downstream.

Growth of separation bubble (separation and reattachment length)— Shown in Figure 3 are the transient separation and reattachment lengths (\bar{x}_S and \bar{x}_R). The plot of \bar{x}_R that indicates the stagnation point of the incoming flow remains unchanged for a short time. The separation point, on the body, also remains unchanged until the base pressure reaches its maximum value due to shock diffraction. The separation bubble then rapidly expands to its steady-state position. The reattachment point gradually approaches its asymptotic position as the base pressure increases from a minimum to a steady-state value. The dashed line indicates estimated bubble size.

Base and axial pressure— Figure 4 shows the transient pressure histories at the axial locations $\bar{x} = 0, 1.0$, and 2.0 . The sharp rise at the beginning of each figure is caused by shock-wave diffraction behind the base. As shown, the asymptotic approach of each transient pressure is different, depending on its location. The results also show similar behaviors without regard to either its length or the sting-to-body ratio. Relatively uniform variation of base pressure history is particularly useful because flow stability time τ can be defined from the result (Fig. 4a) by $p_B(\tau)/p_B(\infty) \cong 0.9$. An empirical relation for the flow stability time has been obtained previously (ref. 9); however, a universal correlation of this time is not yet well established.

The peak pressure at various locations (described above) has been clearly observed in blast-wave and shock-tube experiments (e.g., refs. 9-10). For certain conditions the afterbody peak pressure is as high as the forebody stagnation pressure, which indicates the base region is a strongly affected area. A computed result for this case is shown in Figure 5.

Experiment: luminosity from the shock induced flow— Transient phenomena for shock-induced flow produce unusually high impact pressures and, thus, high temperatures in the regions ahead of and behind the blunt body. Under these conditions, strong luminosity can be expected from these areas. Typical frames from an unpublished film taken during a shock-tube test (ref. 14) are shown in Figure 6. Even though the model tested was different from that simulated in the present calculation, the transient phenomena are qualitatively substantiated by these films. The driven shock-tube gas was oxygen; the arc chamber gas was helium; the Mach number of the incident shock wave was about

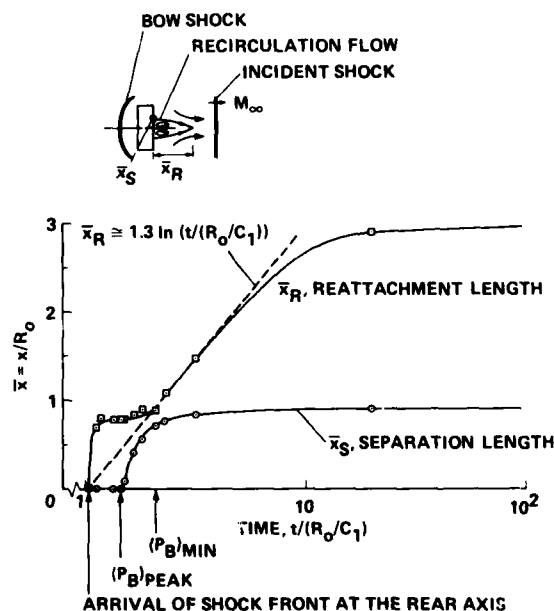


Figure 3. Growth of separation bubble.

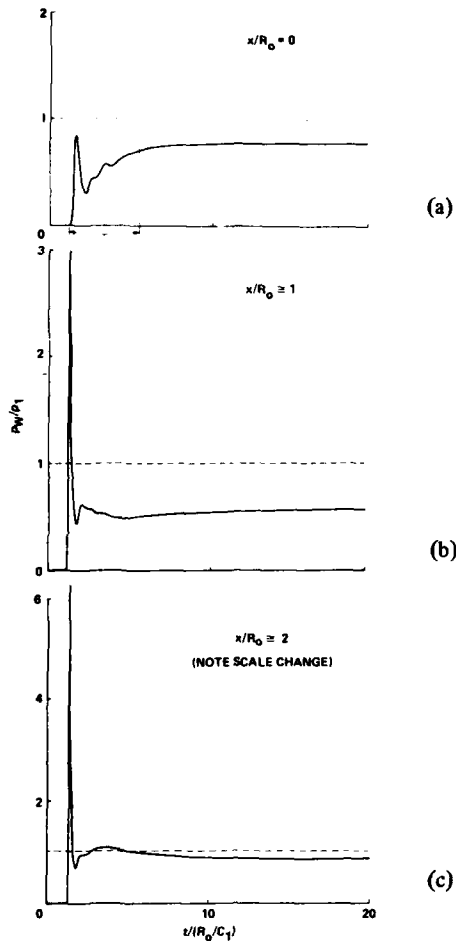


Figure 4. Transient pressures on the afterbody axis.

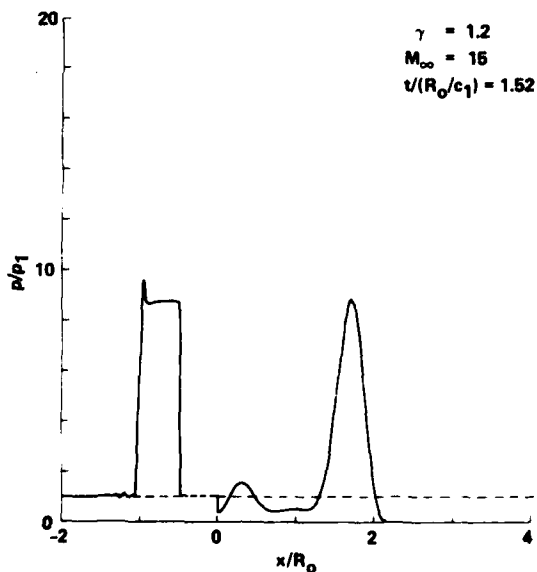


Figure 5. Afterbody impact pressure compared with forebody stagnation pressure.

$M_\infty = 2.8$; and the time between frames was about $33 \mu\text{sec}$. Very narrow, but highly intense luminosity from the strongly compressed gas in the forebody shock layer is clearly shown in Figure 6a. This picture closely corresponds to the conditions described in Figure 2a. A reduced luminosity, but increased shock-layer thickness, ahead of the body, and a bright luminous zone far behind the body, are noted in Figure 6b. These effects can be explained by the phenomena discussed in relation to Figure 2c. As the shock front moves farther away from the body, accompanied by highly compressed gases, and the high temperature in the forebody shock layer decreases toward the steady-state condition, the luminosity in the entire flow field changes significantly, as illustrated in Fig. 6c. The luminosity decreases in the forebody gas layer are partly attributed to the transient heat transfer to the body. Figure 6d shows the luminosity from the entire flow around the body in nearly steady state conditions (comparable with those in Fig. 2d). Strong radiation from the gas-cap area and sizable luminosity from the recompression zone are identifiable in the color film.

Experiment: transient afterbody pressure— Typical results of a shock-tube experiment are shown in Figure 7. Again, the purpose is to demonstrate the general trend of unsteady flow, especially in the afterbody region. The test model is a blunt body supported by a sting; the ratio of sting radius to body radius is $R_s/R_0 = 1/3$. The test facility is the 24-in. Electric Arc Shock Tube (ref. 15) at Ames Research Center; the test gas is air at a shock-wave Mach number $M_\infty = 15$. Transient pressures at the shock-tube wall, and at several locations on the sting surface ($x/H = 0, 1.0, 2.0$, and 4.0) are shown in Figure 7. Air at this test condition is partially dissociated and numerical results obtained for specific heat ratio of $\gamma = 1.2$ are appropriate for qualitative comparison. The sharp pressure spikes that appear at the beginning of each photograph in Figure 7 result from the diffraction of the incident shock wave; the pressure fluctuates around the asymptotic value in a way similar to that described in Figure 4. The test results (wall pressure in Fig. 7a and the other test probes) show that the contact surface (or contaminated gas) arrives approximately $250 \mu\text{sec}$ after the initial shock, thus defining test time interval. Because the flow stability time is longer (about $300 \mu\text{sec}$) the test may never reach steady state before gases contaminate the flow field.

Formation of recompression shock wave— As noted before, the diffracted shock wave at the flow axis triggers reverse flow. The separation below the shoulder is usually

accompanied by a lip shock wave; the reattachment of the flow is always accompanied by a strong recompression shock wave. The evolution of the recompression shock wave in the present simulation (Fig. 2), is not clearly seen because of a restricted computing domain in the afterbody region. Another reason a sharp recompression shock is not formed near the reattachment point is turbulence. However, the formation of the recompression shock can be well demonstrated if the flow-field solution covers only the afterbody region, as shown in refs. 9 and 16. A recompression shock wave appears inside the computing zone when the Mach number ahead of the body is a low supersonic value.

Steady-State Flow. Important computed steady-state results, including the influence of the forebody on the afterbody flow, will be discussed in this section.

Pressure on the body surface and flow axis— Steady-state surface pressure is shown in Figure 8; the free-stream conditions are the same as those given for Figure 2. The origin of the figure is arbitrarily located at the base stagnation point. Negative distance is taken along the body surface and then upstream of the body; positive distance is downstream of the base. The bow shock wave is located at about $s/R_0 = -3.1$, and the maximum pressure is at the forebody stagnation point ($s/R_0 = -2.5$). Surface pressure is lowest at the forebody shoulder ($s/R_0 = -1.5$) and exhibits a local minimum at the afterbody shoulder ($s/R_0 = -1.0$). As pointed out in the discussion of Figure 2, pressure in the base region ($-1.0 \leq s/R_0 \leq 1.0$) is not even nearly constant for a body *without* sting, as can be seen in Figure 8. This result may be significant in that the radiation from the surrounding gases makes a major contribution to the base heating, in addition to the radiation from the recompression wake region. Note that the pressure in the far-wake region overshoots ($p > p_1$), showing a peak near the neck area, and then recovers to the upstream pressure p_1 . The formation of the pressure peak, however, depends on the upstream Mach number, as will be shown in the next figure.

Forebody flow effect on the afterbody pressure— There is noticeable pressure overshoot for a long cylindrical base flow, but not when short forebodies are used (e.g., refs. 9, 17-19). However, the

present calculations show that the pressure overshoot also depends on the upstream Mach number. Shown in Figure 9 are pressure distributions along the base and sting surface (p_W) and pressure distributions along the dividing streamline (p_D) for various flow Mach numbers. The ratio of the sting radius to body radius is $R_s/R_0 = 1/3$. No significant pressure overshoot appears below Mach number 3.0. At Mach numbers greater than 3.0, large overshoots result. In contrast to the steady-state results shown in Figure 2, the pressure is nearly constant in the base region when a sting is present. Pressure near the afterbody shoulder is low due to the sudden expansion around the corner, but it increases noticeably as the boundary-layer separation occurs.

Vorticity distributions— The vorticity along the dividing streamline (ω_D) and along the base-sting surface (ω_W) is presented in Figure 10. Very large

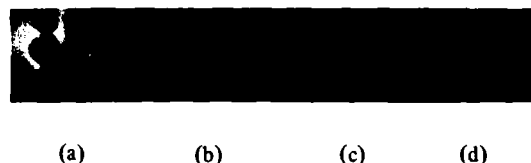


Figure 6. Luminosity from transient flow: shock-tube experiment. (a) $t = +0 \mu\text{sec}$; (b) $t = +33 \mu\text{sec}$; (c) $t = +100 \mu\text{sec}$; (d) $t = +165 \mu\text{sec}$.

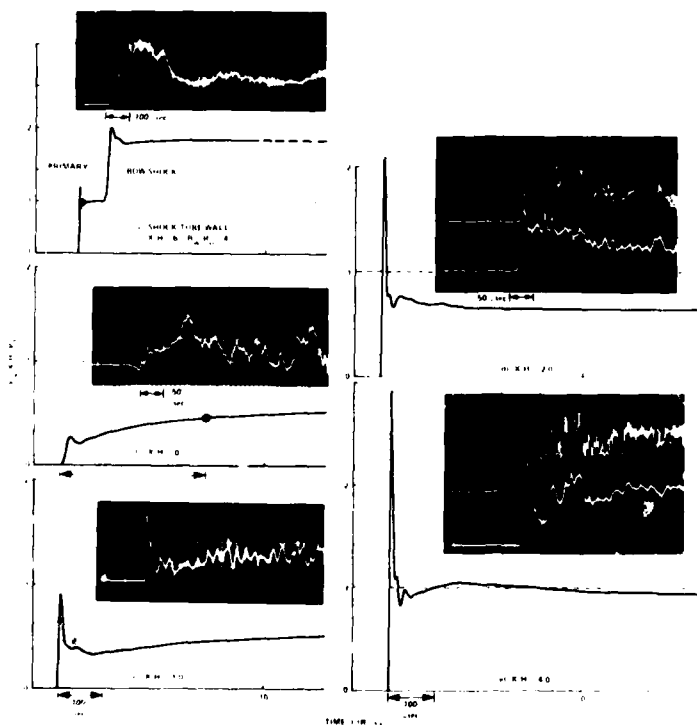


Figure 7. Afterbody pressure: shock-tube experiment.

vorticity is generated around the corners. Three locations of zero vorticity – at the separation, rear stagnation on the base, and reattachment points – are indicated. Positive vorticity indicates recirculation or reversed flow. The vorticity distributions, ω_D and ω_W , are identical before flow separation and after reattachment. The dotted line in the figure shows an interpolation of the calculated data. The vorticity ω_W , for a body without sting, is identically zero on the flow axis because of the flow symmetry.

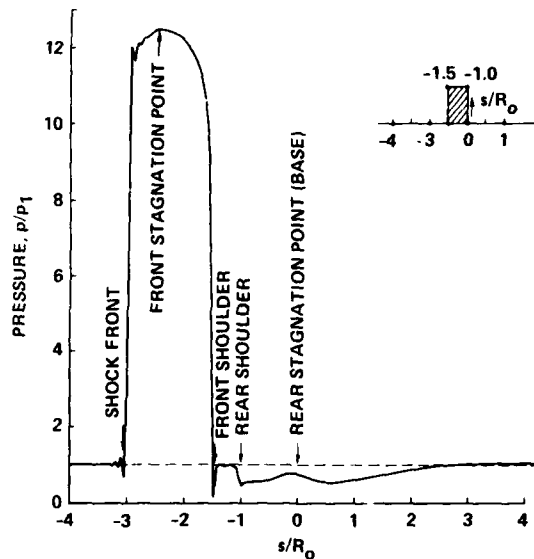


Figure 8. Axial and surface pressures.

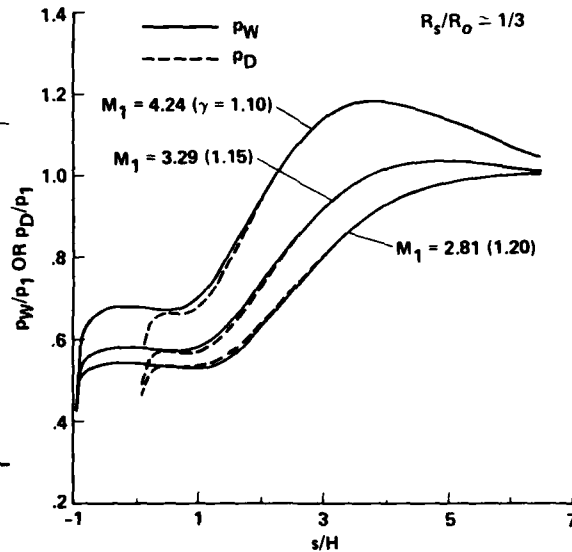


Figure 9. Effect of upstream Mach number on after-body pressure distribution.

Forebody step flow recirculation— Density contours of the forebody flow recirculation are shown in Figure 11. The model is a cylindrical shell (radius R_s), with sharp leading edge, supported by a larger sting (radius of R_0). The shock wave inside the shell is assumed to be swallowed. The separation bubble develops in the same manner as described in the previous cases, except that this time the bubble originates on the frontal face and then expands onto the shell surface, advancing toward the leading edge. The present simulation provides a detailed description of the complex interactions between the oblique shock, separation shock, expansion wave, recompression shock, and reflected shock wave from the wall, including the initial pulsation of the separation jet (ref. 16).

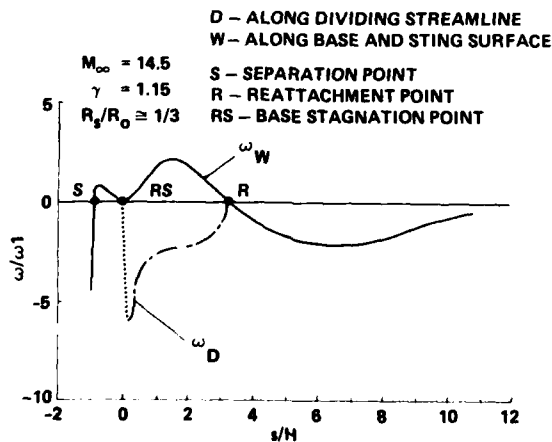
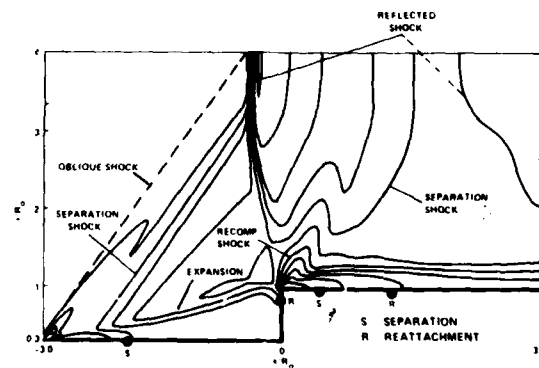


Figure 10. Vorticity along the dividing streamline and afterbody surface.

Figure 11. Forebody step flow (density contours):
 $M_\infty = 3.0$, $\gamma = 1.4$, $R_s/R_0 \approx 1/3$, $L/R_0 = 3$,
 $R_W/R_0 = 4$.

CONCLUDING REMARKS

Solution of the Navier-Stokes equations for nonsteady supersonic turbulent flow passing over a blunt body has been obtained under simple flow model assumptions. The emphasis of the study was on finding the characteristics of the solution essential to understanding the relation between transient pressure and boundary-layer separation, which leads to recirculation. The following conclusions are derived from the solutions for the chosen geometry (a flat-face/flat-base body) and highly turbulent flow accompanied by a strong shock wave. For transient flow:

1. The reversed flow induced by the reflected shock wave on the rear flow axis triggers the main recirculation. Separation from the shoulder is considered slow growing and minor. 2. A separation bubble is generated by the reflected shock wave interacting with the boundary layer on the base and propagates toward upstream direction (it is, therefore, possible to control separation by eliminating the reflected shock wave). 3. The transient stagnation pressure on the forebody can be far greater than the steady-state value and is a function of forebody shape. 4. The transient pressure behind the body is significant and, in some instances, it becomes as great as the forebody stagnation pressure. Thus, the base region is a strongly affected area. 5. The calculated transient phenomena are substantiated by shock-tube measurements of transient pressure and luminosity.

For steady-state flow: 1. The appearance of the pressure overshoot on the afterbody flow axis depends on the forebody length and upstream Mach number, i.e., the overshoot disappears as the forebody length decreases (from infinitely long cylinder to flat-plate disc). The overshoot, however, reappears as the flow Mach number increases. 2. Delayed separation below the shoulder can be readily recognized from the vorticity distribution curves. 3. Radiation heating from the highly recompressed wake region can be significant. 4. The base stagnation pressure for the body *without* sting is much higher than the pressure in the base region. This will yield higher radiation heating to the base.

Body structures, buildings, sensitive instruments imbedded in a model, and heat shields on a probe can be seriously damaged by the blast phenomenology. Additional study of the base flow, using improved models – for example, real gas and variable turbulent viscosity – is essential to the accurate prediction of radiation heat from the wake and plume for very high speed entry vehicles such as the Galileo probe and various missiles.

REFERENCES

1. H. Reichenbach, 7th IST Symp., p. 5 (1967).
2. W. Bleakney, D. R. White, and W. C. Griffith, *J. App. Mech.* 12, p. 439 (1950).
3. H. Oguchi, K. Funabiki, and S. Sato, 10th IST Symp., p. 386 (1975).
4. Raymond J. Emrich, 6th IST Symp., p. 740 (1969).
5. L. Z. Dumitrescu and S. Preda, 10th IST Symp., p. 369 (1975).
6. K. Bracht and W. M. Erzkich, 12th ISP Symp., p. 712 (1979).
7. Koichi Oshima, 10th IST Symp., p. 480 (1975).
8. H. Mirels, Report SAMSO-TR-77-166, The Aerospace Corp. (1977).
9. Kenneth K. Yoshikawa and Alan A. Wray, NASA TP-1769 (1981).
10. Harold L. Brode, 12th IST Symp., p. 31 (1979).
11. Nobuyuki Satofuka, 10th IST Symp., p. 304 (1975).
12. C. Park, Paper 79-0039, 17th AIAA Aerospace Science Meeting (1979).
13. D. E. Nestler and D. N. Brant, Paper 78-862, 2nd AIAA/ASME Thermophy and Heat Trans. Conf. (1978).
14. H. Shirai and C. Park, Paper 79-0038, 17th Aerospace Science Meeting (1979).
15. R. E. Dannenberg, 11th IST Symp., p. 416 (1978).
16. K. Yoshikawa (to be published).
17. A. Roshko and J. C. Lau, *Heat Trans. and Fluid Mech. Inst.*, p. 157 (1965).
18. A. Roshko and G. J. Thomke, *AIAA J.*, 4, p. 975 (1966).
19. C. H. Weng and W. L. Chow, *AIAA J.*, 16, p. 553 (1978).

AD P000261

SHOCK STRENGTH MODIFICATION FOR REDUCED HEAT TRANSFER TO
LIFTING RE-ENTRY VEHICLES

L.H. Townend* and R.A. East†

*Ministry of Defence (UK) †Department of Aeronautics & Astronautics

University of Southampton, Southampton, Hampshire, UK.

Experiments at typical lifting re-entry conditions ($6 < M_0 < 22$ and $250^\circ < \alpha < 700^\circ$) confirm theoretical predictions that delta wings and related vehicle configurations having wholly or partly concave undersurfaces (that is regions of undersurface anhedral) produce higher C_{Lmax} and higher C_L at given L/D , than flat wings of identical planform. This enhanced aerodynamic performance derives from the strengthening of the lifting surface shock wave which results from flow containment. Theoretical reasons underlying the predictions are already published¹. In this paper, the importance of shock wave stand-off angle is explained by reference to its relationship to heat transfer rates and selected shock and force data from hypersonic wind tunnel tests are presented for a wide range of model planform and anhedral distribution. Available measurements showing heat transfer to concave undersurfaces are presented. Configurations based on the Space Shuttle orbiter and concepts for S.S.T.O. are described. For the Shuttle orbiters, wind tunnel tests on a low wing model (LWO) with moderate dihedral and a high wing model (HWO) with pronounced anhedral show the latter to offer 20% higher C_{Lmax} at $M_0 \approx 10$. Configurations with anhedral on the lower surface but offering higher values of $(L/D)_{max}$ are outlined and experiments to measure shock wave geometry, re-entry force data and re-entry stability for variants of the basic high- L/D shape are presented.

INTRODUCTION

When selecting configurations for lifting re-entry vehicles, the designer may face conflicting demands for high lift-to-drag ratio and high maximum lift coefficient. For given wing loading, the latter choice gives high $C_L/(W/S)$ and will alleviate heat transfer, but at the expense of reducing L/D and re-entry cross-range. The former will allow long range and low deceleration, but at a given speed and wing loading, it demands a reduced altitude; it therefore aggravates the heating problem in both duration and intensity. What is required is a body which offers an unusually high L/D at high C_L together with as high C_{Lmax} as possible.

*This paper expresses the opinions of the authors and does not necessarily represent the official view of the UK Ministry of Defence.

Since recent American work in lifting re-entry has been largely concerned with the Space Shuttle, some of the more basic research results have originated in Europe and reflect different conceptual approaches, for example¹, that in which "flow containment" is used to reduce lateral spillage of undersurface flows and the consequent loss of lift beneath a re-entry vehicle. This use of flow containment at lifting re-entry conditions (high Mach number and high angle of attack) is known¹ to produce increased C_L at given lift-to-drag ratio and to increase the value of C_{Lmax} for a wing or lifting body of given planform. For example, a typical set of data points is shown in Figure 1, in which increasing the outboard anhedral on wings of trapezoidal planform

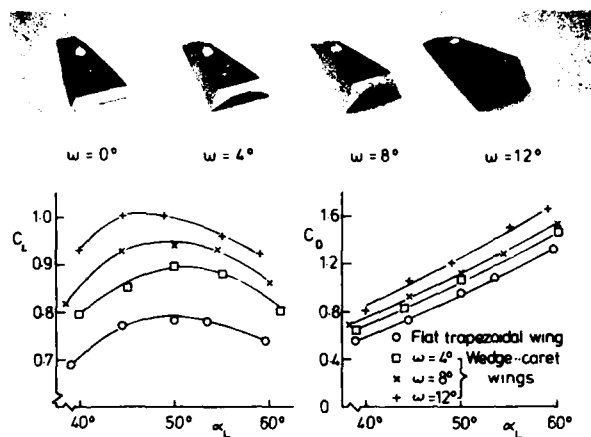


FIG 1. Force measurements on wings of trapezoidal planform
($M_\infty = 9.7$, $Re = 4 \times 10^5$)

improves both C_L per unit L/D and the value of C_{Lmax} by about 0.02 per degree rise in ω ; indeed if no constraint is placed on anhedral or planform (and for some applications this is permissible) the half-elliptic planforms in Figure 2 give lift coefficients as high as 1.15, some 50% higher than the value Newtonian aerodynamics would predict as the maximum possible (See footnote*), and 20% higher than the previous published "record" obtained by Penland². For wings of pure delta planform, realistic sweep ($\Lambda = 75^\circ$) and moderate anhedral (an implied limit of $80^\circ < \omega < 100^\circ$), that is for wings which are

representative of realistic aircraft, it is still found that the flat delta ($\omega = 0^\circ$) cannot match the aerodynamics of its waverider counterpart. Figure 3 shows the aerodynamic superiority of the concave delta wing at Mach numbers ranging from 8 to infinity, ³⁻⁷ that is through the re-entry speed range.

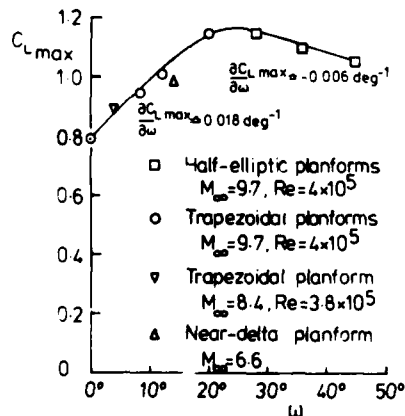


FIG 2. Force measurements on wings of half-elliptic trapezoidal and near-delta planform

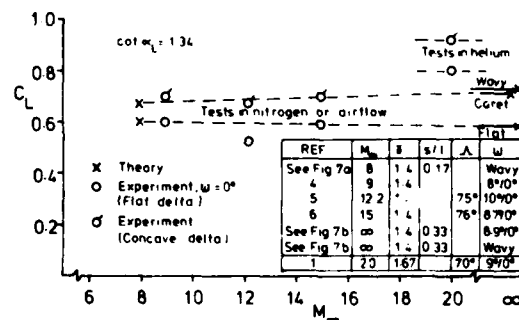


FIG 3. Lift forces on delta wings at reentry conditions
($8 < M_\infty < \infty$, $\alpha_L = 36.7^\circ$)

* A caret wing (of rather extreme shape, i.e. $\omega \approx 20^\circ$) gives $C_L \approx 1.0$ at $L/D_p \approx 1.0$, prior to shock detachment. A flat delta obeying the Newtonian expressions for two-dimensional flow (lift and drag coefficients given by $2 \sin^2 \alpha_L \cos \alpha_L$ and $2 \sin^3 \alpha_L$ respectively) gives a C_{Lmax} of only 0.755.

The most immediate advantage of increasing re-entry C_L would be to reduce at a given flight speed the rates of heat transfer (1) at stagnation points (and on sides and upper surfaces) due to the increase in flight altitude (at given wing loading) and (2) under the entire heat shield due to reduced under-surface local velocities. Alternatively, and subject to low speed considerations, an improved C_L per unit L/D would permit a reduction in wing area, and hence in vehicle weight.

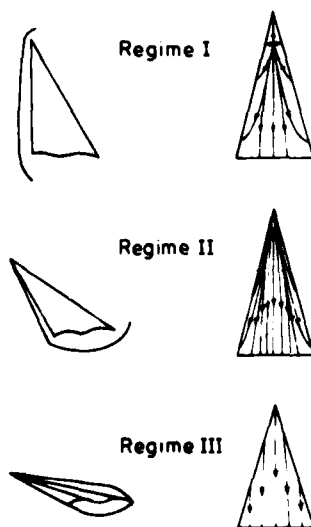
The importance of reducing heat transfer rates and thereby the weight of the thermal protection system (TPS) can be gauged from the fact that the Shuttle orbiter TPS contributes more than 10 per cent to the orbiter's empty weight; this is some 25 per cent of the maximum launch payload and about 50 per cent of the maximum re-entry payload. Again, for currently projected SSTO designs⁸ a 25% reduction in structure mass per unit area has been assumed but TPS mass per unit area has been taken as the same as for the Space Shuttle; TPS therefore assumes great importance in the calculation of SSTO economics, since every kilogram of TPS mass represents payload foregone.

FLows, FORCES AND HEAT TRANSFER ON SIMPLE SHAPES

The flows and pressures beneath flat delta wings at re-entry conditions have been studied for at least twenty-five years, notably by Bertram and Henderson⁹. It was shown that the centre-line pressure ratios are significantly below two-dimensional values, and that the shock waves are weaker (even at their strongest point) than a wedge would produce - one may regard this shortfall in lift as an inefficiency in flat delta aerodynamic performance, and seek to close the gap by examining delta wings having various forms of undersurface concavity to reduce spillage, i.e. to enhance "flow containment", and so to preserve as strong a shock wave as possible.

The Significance of Shock Wave Stand-off Angle.

In Figure 4, three distinct flow regimes are shown, in one or other of which a sharp-edged conical body or wing will operate at supersonic speeds. At hypersonic Mach numbers, thin shocklayer theory seems reasonably accurate in the second and third regimes, and shows that, for a body of prescribed conical shape, the curvature of the shockwave as it crosses a plane of symmetry determines not only the shockwave stand-off angle, but also the pressure, density and velocity anywhere in that plane.



If the initial shockwave curvature is given as $y_s''(0) = -a$, Roe¹⁰ shows that shock stand-off distance and the postshock pressure rise are

$$y_s - y_b = \frac{1 - a + a (\ln a)}{(1 - a)^2}$$

$$\text{and } p_s - p_b = \frac{a^4 - 6a^3 + 3a^2 + 2a + 6a^2 (\ln a)}{2(1 - a)^4} \quad (1)$$

in which equations y and p are related to physical quantities (i.e. actual distance \bar{y} and actual static pressure \bar{p}) as follows:-

FIG 4. Flow regimes under a conical wing in supersonic flow

$$\left. \begin{aligned} \bar{y} &= \bar{x} \varepsilon \tan \alpha \cdot y \\ \bar{p} &= \bar{p}_\infty + \bar{\rho}_\infty U_\infty^2 \sin^2 \alpha (1 + \varepsilon p) \\ \varepsilon &= \frac{\gamma-1}{\gamma+1} + \frac{2}{(\gamma+1)M_\infty^2 \sin^2 \alpha} \end{aligned} \right\} \quad (2)$$

α = inclination of a reference plane lying close to the shock layer.

These equations are especially accurate at those Mach numbers and shock strengths for which heating will be most severe (i.e. at re-entry conditions) and the parameter $(\bar{p})^{\frac{1}{2}} (\bar{u})^{\frac{1}{2}}$ is known¹⁷ to indicate the rate of laminar heat transfer if cooling is by radiation only; thus in the above notation,

$$\left. \begin{aligned} (\bar{p}_b)^{\frac{1}{2}} (\bar{u}_b)^{\frac{1}{2}} &= (\bar{\rho}_\infty)^{\frac{1}{2}} U_\infty^{\frac{3}{2}} \sin^{\frac{1}{2}} \alpha \cos^{\frac{1}{2}} \alpha (1 + \varepsilon \left(\frac{3}{16} - \frac{\tan^2 \alpha}{2} \right) y_s \\ &\quad + \frac{y_b - 1}{16}) \end{aligned} \right\} \quad (3)$$

This formula contains a Newtonian part plus a first order correction term, the latter producing effects which are strongly related to the angle of attack. For CL_{\max} (that is, for $\tan^2 \alpha = 2$ or $\alpha \approx 55$ degrees according to Newtonian theory), the correction becomes equal to $\left\{ 1 - \varepsilon(13y_s - y_b + 1)/16 \right\}$ which depends much more on y_s than on y_b , so that for a high value of α , and for a given free-stream, surface temperatures will be reduced by any measure which increases the shock wave stand-off angle.

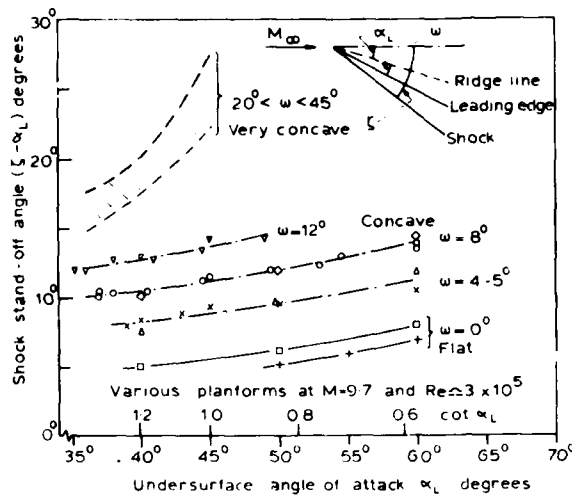
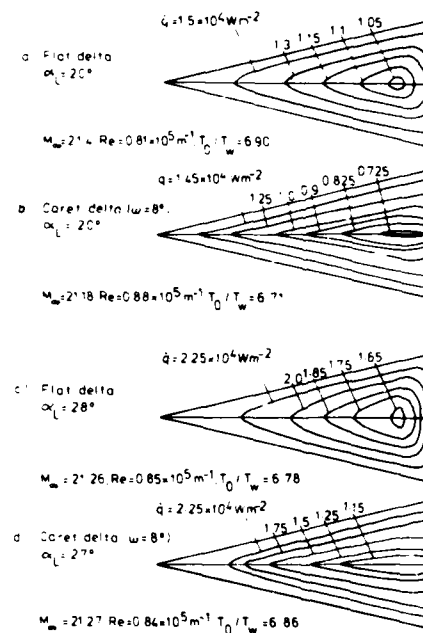
In addition, if two vehicles are of the same wing loading, but at given re-entry L/D and cross range performance they produce different CL values (for example, since one is concave), then in equation (3) the value of $\bar{\rho}_\infty$ will be lower for the vehicle with the higher CL . Thus where heating is a dominant consideration, the CL_{\max} of re-entry gliders should be maximised by appropriate aerodynamic design to provide large shock stand-off on condition that configurations so produced do not suffer unacceptable weight penalties due to special shaping.

In Figure 5, data at Mach number 9.7 confirm that larger shock stand-off occurs for caret and other concave wings than for flat wings of like planform. Some of these planforms (and anhedral distributions) were selected for special applications and are unrealistic for aircraft designs; others, however, were actually related to vehicle designs and concepts, and still demonstrate the aerodynamic merits of flow containment.

A clear indication that moderately concave delta wings will provide not only higher CL (as shown in Figure 3) but reduced heat transfer has been provided¹¹ by Galloway, Jeffery and Harvey, who tested a caret and a flat delta wing at $M_\infty \approx 21$ in the Imperial College Nitrogen Tunnel. As seen in Figure 6, q - values on the caret undersurface fell to significantly lower levels than those beneath the flat delta; in addition the caret wing will have been producing a higher CL at given angle of attack and so, if compared with the flat delta at the same implied wing loading (i.e. equal $R_\infty CL$), would be even less severely heated than Figure 6 suggests.

Some Effects of Varying Anhedral Distribution

For realistic application of flow containment, anhedral distribution is apparently very important since, if the central parts of the vehicle under-surface are progressively filled in, (1) the volumetric efficiency is greatly

FIG 5 Shock wave stand-off angles at $M_\infty = 9.7$ FIG 6 Heat transfer distributions on delta wings (data by Galloway, Jeffery & Harvey¹¹)

improved in structural terms; and (2) if the "pot belly" forces the shock wave outwards in the plane of symmetry, y_s and CL_{max} can be increased while concavity elsewhere on the undersurface preserves relatively higher values of local L/D and so permits an overall improvement in CL per unit L/D .

Squire has studied¹³ the performance of delta wings as aspect ratio and anhedral distribution varied, for Mach numbers 3, 5 and 8 and at angles of attack to some 60 degrees. Aerodynamic gains of concave wings are significant at both Mach numbers (see Figure 3 for $M_\infty = 8$ results).

Results were also obtained for the "wavy wing" of Figure 7(a) where the "filling in" of central regions has greatly improved the configurational acceptability of the lifting surface. Data were obtained for Mach number 3.5 only, but a typical result was quoted as $CL = 0.62$ and $L/D = 1.5$, which represents a gain in CL of 0.08 when compared with a flat delta of aspect ratio 2/3. This comparison of shapes producing identical aerodynamic performances shows the geometric advantage offered by the wavy wing but prompts the question as to whether such advantages are retained at Mach numbers at which lifting re-entry would occur.

Calculations by Roe⁷ suggest that, at infinite Mach number, a form of wavy wing can offer the same L/D_p as a caret wing while presenting a substantial reduction in concavity (see Figure 7(b)), but a shock wave of increased y_s and hence a higher CL . For $\gamma = 1.4$, the wavy wing and the caret wing produce CL values of 0.72 and 0.71, while a flat delta would produce only 0.58. It is encouraging to find experimental confirmation from Houwink and Richards¹² that partly concave undersurfaces provide substantially better aerodynamic performance at high Mach number and high angles of attack than is obtainable with flat undersurfaces of the same planform. For Mach number 15 and $Re = 2 \times 10^6$, a cone of 9 degrees semi-angle, fitted with delta wings of pronounced anhedral (but with wing tips no lower than the belly of the cone) produces a CL_{max} of about 0.8, considerably more than that of a flat delta of similar planform even though as seen in Figure 7(c) the undersurface flow is only partly contained.

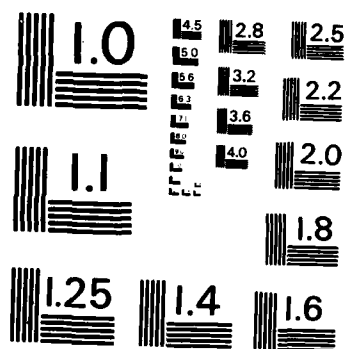
UNCLASSIFIED

PROCEEDINGS OF THE INTERNATIONAL SYMPOSIUM ON SHOCK
TUBES AND WAVES (13TH.) CALSPAN ADVANCED TECHNOLOGY
CENTER BUFFALO NY C E TREANDER ET AL. JUL 81
AFOSR-TR-82-1031 F49629-81-C-0002

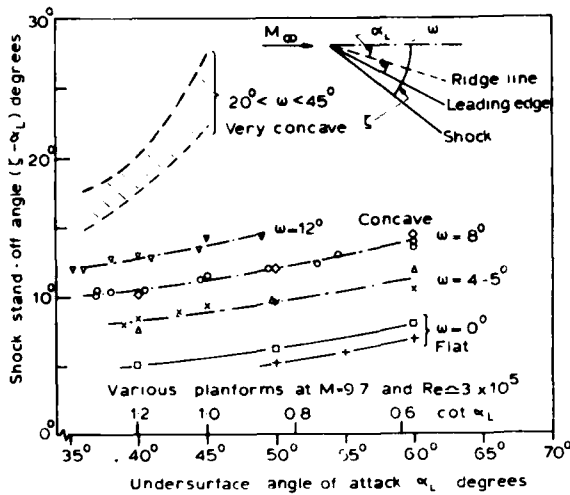
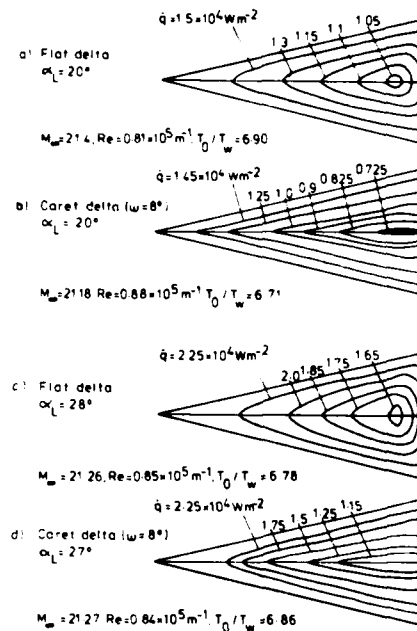
Ni

F/9 20/1

Ni



MICROCOPY RESOLUTION TEST CHART
NATIONAL BUREAU OF STANDARDS-1963-A

FIG 5 Shock wave stand-off angles at $M_\infty = 9.7$ FIG 6 Heat transfer distributions on delta wings (data by Galloway, Jeffery & Harvey¹¹)

improved in structural terms; and (2) if the "pot belly" forces the shock wave outwards in the plane of symmetry, y_s and CL_{max} can be increased while concavity elsewhere on the undersurface preserves relatively higher values of local L/D and so permits an overall improvement in CL per unit L/D .

Squire has studied¹³ the performance of delta wings as aspect ratio and anhedral distribution varied, for Mach numbers 3, 5 and 8 and at angles of attack to some 60 degrees. Aerodynamic gains of concave wings are significant at both Mach numbers (see Figure 3 for $M_\infty = 8$ results).

Results were also obtained for the "wavy wing" of Figure 7(a) where the "filling in" of central regions has greatly improved the configurational acceptability of the lifting surface. Data were obtained for Mach number 3.5 only, but a typical result was quoted as $CL = 0.62$ and $L/D = 1.5$, which represents a gain in CL of 0.08 when compared with a flat delta of aspect ratio 2/3. This comparison of shapes producing identical aerodynamic performances shows the geometric advantage offered by the wavy wing but prompts the question as to whether such advantages are retained at Mach numbers at which lifting re-entry would occur.

Calculations by Roe⁷ suggest that, at infinite Mach number, a form of wavy wing can offer the same L/D_p as a caret wing while presenting a substantial reduction in concavity (see Figure 7(b)), but a shock wave of increased y_s and hence a higher CL . For $\gamma = 1.4$, the wavy wing and the caret wing produce CL values of 0.72 and 0.71, while a flat delta would produce only 0.58. It is encouraging to find experimental confirmation from Houwink and Richards¹² that partly concave undersurfaces provide substantially better aerodynamic performance at high Mach number and high angles of attack than is obtainable with flat undersurfaces of the same planform. For Mach number 15 and $Re = 2 \times 10^6$, a cone of 9 degrees semi-angle, fitted with delta wings of pronounced anhedral (but with wing tips no lower than the belly of the cone) produces a CL_{max} of about 0.8, considerably more than that of a flat delta of similar planform even though as seen in Figure 7(c) the undersurface flow is only partly contained.

$$M_\infty = 3.5$$

$$s/l = 0.17$$

$$L/D = 1.5$$

$$C_L = 0.62$$

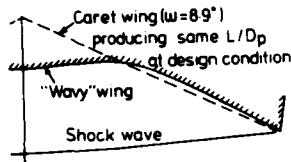


- a) Anhedral distributions for delta wings with similar performance (calculations by Squire³)

$$M_\infty = \infty$$

$$s/l = 0.33$$

$$L/D = 1.34$$

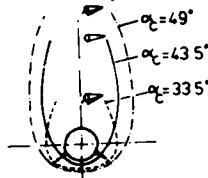


- b) Optimised anhedral distribution for 'wavy' delta wing for infinite M_∞ (calculations by Roe⁷)

$$M_\infty = 15$$

$$s/l = 0.26$$

$$Re = 2 \times 10^6$$



- c) Shock wave envelopes for cone and winged cone (experiments by Houwink & Richards⁶)

FIG 7 Effects of anhedral distribution on the lifting performance of delta wings and cones

Aerodynamic Stability and Control

The design of complete waverider configurations is often based on combining component bodies and flows which are individually understood and which, having aerodynamically sharp leading edges with attached shock waves, operate in aerodynamic isolation from each other, at least when near design conditions. However, at lifting re-entry conditions waveriders should sometimes operate, on both heating and stability considerations with shock waves detached from their leading edges¹⁵, and Hillier has shown¹⁶ that the associated flows may be predicted and that the sideflows can contribute to yaw and roll stability.

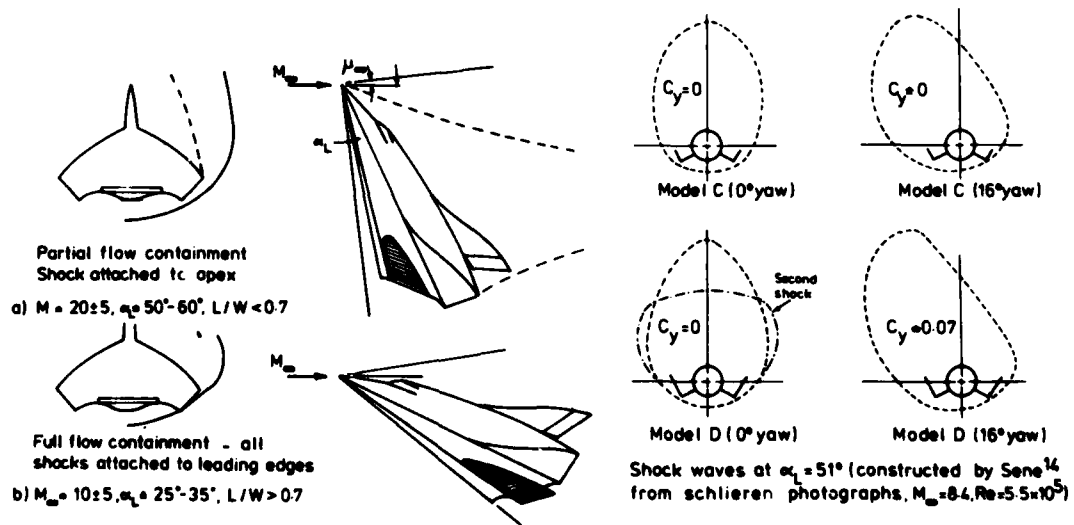


FIG 8a & b. High cross range waverider

FIG 8c. High cross range waverider shock envelopes

A vehicle in which high re-entry C_L and moderate L/D may combine with some inherent stability in roll, pitch and yaw^{1,7} is shown in Figs. 8(a) & (b); experiments by Sene¹⁴ on a simplified variant have confirmed (see Figure 8(c))

These tests are particularly valuable since they were performed in the VKI Longshot Tunnel and conditions were thus fully representative of an orbiter trajectory.

The design of partly concave undersurfaces as pursued by Roe, Squire, Richards and Houwink probably represents the most promising approach to the achievements of realistic undersurface shapes for lifting re-entry vehicles intended to exploit the aerodynamic advantages of flow containment.

that shock waves form as anticipated^{1,7} and that the side force can be "tuned" by altering the sideplate area. For model D, and conditions near CL_{max} , sideforce coefficients (see Figure 9) are positive for angles of yaw up to 30° (at least) and would result in positive yaw stability as compared with model C and model A (no sideplates) for which, at 16° of yaw, C_y values are zero and -0.18 respectively.

With regard to lift and drag, Figure 9 shows that Model D returns a lower value of CL than does Model A, but this is largely due to the inclusion of sideplate projected planform in Model D's reference area. There is no

evidence that the sideplates reduce the lift of the under-surface or that flow containment is affected. On the other hand, sideplates convert yaw instability to yaw stability and greatly enhance the volumetric efficiency of related vehicles.

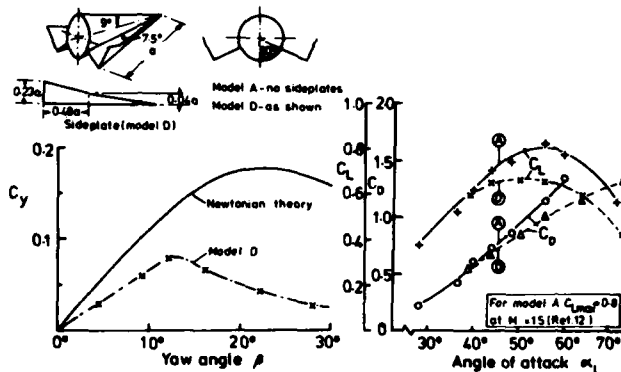


FIG. 9. Lift C_L , drag C_D and sideforce C_y coefficients for a high cross-range waverider with and without sideplates ($M = 8.4$, $Re = 5.5 \times 10^5$ Ref. 14)

FLows AND FORCES ON SHUTTLE-LIKE CONFIGURATIONS

For the Space Shuttle orbiter, insistence on large cylindrical cargo dimensions has enforced the use of a large diameter fuselage which is mounted on a low wing. However, a high-wing configuration can still contain the cargo and can also permit substantial anhedral without increasing the under-carriage length or reducing wing tip ground clearances at given landing attitude (see Figure 10). In comparison with low-wing configurations, the total panel area can actually be reduced¹ and although the proportion allotted to heatshield area will have risen, an improved re-entry CL would moderate heat transfer rates at given wing loading and flight speed. It was therefore thought worthwhile to consider the design and to conduct wind-tunnel tests on a model of a "high-wing orbiter" (HWO). The orbiter selected for modification was the NASA-MSC/O40A, which was based on the use of external, expendable tankage and quite closely resembles the Space Shuttle. For this orbiter, the under-carriage was mounted just outboard of the fuselage and for the high-wing orbiter it was decided that, for the given leg length and given wheel positions, the skin and major load-bearing members should remain in the same position so that leg length would not be changed. Also, for given landing attitude (17 degrees) and for given clearance between wing tips and runway, the wing tips of the modified orbiter were kept at the same position as with the unmodified O40A. Between the wing-tip and the under-carriage leg, concavity was introduced, permitting the partly concave contour shown in Fig. 10.

Both models were tested at hypersonic speeds by Davies and Townsend¹⁸ ($M_o = 8.4$, $Re = 3 \times 10^5$) and by East ($M_o = 9.7$, $Re = 4 \times 10^5$), in the Gun Tunnel at Southampton University but using different balances. Davies and Townsend (1972) measured CL -values only and showed that the HWO produces significantly greater lift than the LWO at given angle of attack¹. The data obtained more recently (1976) show that, for angles of attack between 40° and 50° and at Mach and Reynolds numbers of 9.7 and 4×10^5 , the HWO produces some 20 per cent more lift than the LWO, both CL_{max} and the value

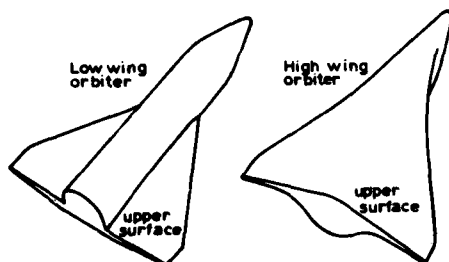
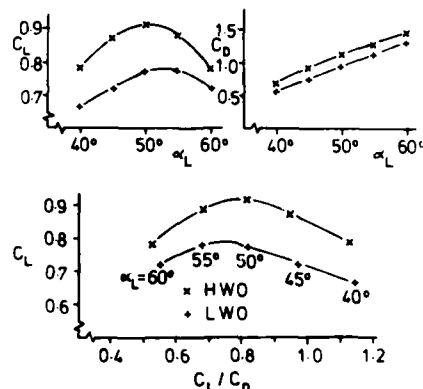


FIG 10. Low-wing and high-wing orbiters

FIG 11. Force measurements on space shuttle orbiters (HWO and LWO) at $M_\infty = 9.7$, $Re = 4 \times 10^5$

of C_L per unit L/D being greatly enhanced by anhedral (see Figure 11).

It is considered that this approach would also be applicable to the design of a re-useable external tank¹ for the Space Shuttle or to an SSTO vehicle derived from those of Ref.8.

CONCLUSIONS

1. Lift coefficients at least 50 per cent greater than the maximum predicted by Newtonian theory are possible if concavity is introduced on the undersurface of delta and related wings.
2. For delta wings of realistic anhedral distribution and planform sweep, concavity enhances $C_{L_{max}}$ and C_L per unit L/D by up to some 25 per cent throughout the re-entry Mach number range ($8 < M_\infty < \infty$).
3. Undersurface heat transfer rates are substantially reduced by concavity beneath delta wings in nitrogen flows of Mach number 21.
4. Regions of convexity in primarily concave undersurfaces improve re-entry aerodynamics and volumetric efficiency.
5. High wing variants of the Space Shuttle orbiter give at least 20 per cent higher $C_{L_{max}}$ at Mach numbers of about 10.
6. High cross-range waveriders may be possible in which volumetric efficiency and aerodynamic stability are improved by appropriate design of sideflows.

ACKNOWLEDGEMENTS

The authors wish to thank Mrs. J.M. Gibbons and Miss P. Willson for their assistance in preparing the typescript for this paper.

REFERENCES

1. L.H. Townend Research and design for lifting re-entry. Prog. Aerospace Sci., 19, 1-80, Pergamon, 1979.

2. J.A. Penland A study of the aerodynamic characteristics of a fixed geometry paraglider configuration and three canopies with simulated variable canopy inflation at a Mach number of 6.6. NASA TN D-1022, 1962.
3. L.C. Squire The effects of recessed lower surface shape on the lift and drag of conical wings at high incidence and high Mach number. Aeronautical Quarterly, 26, 1, 1-10, February 1975.
4. R.W. Jeffery The aerodynamics of wings in low density hypersonic flow. Ph.D. Thesis, University of London, 1975.
5. C.J. Carr Force measurements on caret and delta wings over the incidence range $27^\circ \leq \alpha \leq 55^\circ$ at $M_\infty = 12.2$. Imperial College Aero. Rept. 71-22, October 1971.
6. B.E. Richards
R. Houwink An experimental study of space vehicle configurations with high lift during re-entry. VKI TN 117, 1976.
7. L. Davies
P.L. Roe
J.L. Stollery
L.H. Townend Configuration design for high-lift re-entry. AIAA 72-132. Presented at AIAA Annual Meeting, San Diego, 1972.
8. D.C. Freeman, Jr.
A.W. Wilhite Effects of relaxed static longitudinal stability on a single-stage-to-orbit vehicle design. NASA Technical Paper 1594, December 1979.
9. M.H. Bertram
A. Henderson, Jr. Recent hypersonic studies of wings and bodies. ARS J, 31, 8, 1129 - 39, August 1961.
10. P.L. Roe Private Communication
11. E.M. Galloway
R.W. Jeffery
J.K. Harvey Heat transfer to a delta wing and two waverider wings in a rarefied hypersonic flow. Imperial College Aero. Rept. 76-04, September 1976.
12. R. Houwink
B.E. Richards Experimental study of a high lift re-entry vehicle configuration. AIAA J, 11, 5, 749 - 751, May 1973.
13. L.C. Squire A comparison of the lift of flat delta wings and waveriders at high angles of incidence and high Mach number. Ing. Archiv., 40, 5, 339-352, 1971.
14. K. Sene Lateral force measurements on a cone based Space Shuttle configuration at $M_\infty = 8.4$ B.Sc. Dissertation, University of Southampton 1979.
15. W.H. Hui
H.T. Hemdan Unsteady hypersonic flow over delta wings with detached shock waves. AIAA J, 14, 4, 505-511, 1976.
16. R.J. Hillier Hypersonic flow over conical wing-body combinations. Aeronautical Quarterly, 29, 285-304, 1978.
17. T.R.F. Nonweiler Conduction of heat within a structure subjected to kinetic heating. Aircraft Engineering, 28, 383-387, November 1956.
18. L. Davies
J.E.G. Townsend Private communication. 1972.

SHOCK CAPTURING USING FLUX-CORRECTED
TRANSPORT ALGORITHMS WITH ADAPTIVE GRIDDING

M. Fry and J. Tittsworth
Science Applications, Inc.
McLean, Virginia, 22102, USA

A. Kuhl
R and D Associates
Marina del Rey, California, 90291, USA

D. Book, J. Boris and M. Picone
Laboratory for Computational Physics
U. S. Naval Research Laboratory
Washington, D.C., 20375, USA

A numerical technique has been developed for capturing complex, nonsteady shock structures in multidimensions. The technique relies on moving the computational mesh with the shock wave so that the features of principal interest appear approximately stationary. The method has been implemented using coordinate-split Flux-Corrected Transport (FCT) algorithms which allow the mesh to evolve arbitrarily with respect to the fluid in each coordinate. The grid may thus be optimized in response to the needs of a given problem. Synchronizing the grid and fluid motions permits significant reduction of numerical transients and eliminates numerical diffusion. Shocks develop naturally, with no fitting. The method is illustrated by calculating complex, two-dimensional Mach reflection phenomena associated with airblasts and shock diffraction on wedges. The numerical results are in good agreement with available experimental data.

INTRODUCTION

Numerical solution of transient multidimensional gas dynamics problems is always nontrivial. When, in addition, the problem involves reflecting supersonic flows, large variations in length scales in both space and time, or phenomena for which neither analytic solutions nor detailed experimental observations are at hand, the state of the computational art is challenged. Such a problem arises in calculating the oblique reflection of shocks from solid surfaces in planar geometries (e.g. shock tube experiments) or axisymmetric geometries (e.g. airblasts). The complications arise mainly from the presence of Mach reflections which occur when a shock front impinges on a reflecting surface at angles of incidence sufficiently far from normal. The formation of a Mach stem and, consequently, of a slip surface intersecting the triple point (the confluence of the incident, Mach, and reflected waves) results from the requirement that the flow behind the reflected shock be parallel to the reflecting surface, which cannot be achieved through regular reflection.

Attempts to calculate the properties of the flow in Mach reflections date back at least to von Neumann¹ and the research which grew out of the wartime explosive studies²⁻⁴. For the simplest problem, that of a planar shock

reflecting from a plane surface, Jones, Martin, and Thornhill⁵ noted that it is possible to reduce the number of independent variables to two by transforming to the similarity variables x/t , y/t , a device that was also used by Kutler, et al⁶. Ben-Dor⁷ developed a theory which used shock polars to explain some of the features of this problem, and solved the system of algebraic equations obtained by combining the jump conditions across the various discontinuities (Courant and Friedrichs)⁸ to describe the flow in the neighborhood of the triple point. To date, no satisfactory treatment of the complete flow field has been published, although some features (like the shape of various waveforms) are quite easy to model.

In connection with studies of both chemical and nuclear explosions there have been many attempts to model a spherical blast wave reflecting from the ground, the so-called height-of-burst (HOB) problem. The hydrodynamic phenomena in the two cases are identical, although nonideal effects (primarily explosive afterburn in the first instance and radiation preheating in the second) are different. Previous attempts to model two-dimensional complex shock reflection have suffered from restriction to describing part of the system, the use of a special assumption like that of self-similarity, or less than satisfactory agreement with experimental data.⁹

The calculations discussed here represent a step forward in overcoming these difficulties. They differ from previous numerical work in incorporating two important computational developments: Flux-Corrected Transport (FCT)¹⁰ and an adaptive regridding procedure, called "sliding rezone",¹¹ which optimizes the mesh point distribution and hence the resolution of surfaces of discontinuity.

FCT is a finite-difference technique for solving the fluid equations in problems where sharp discontinuities arise (e.g. shocks, slip surfaces and contact surfaces). It modifies the linear properties of a second- (or higher) order algorithm by adding a diffusion term during convective transport, and then subtracting it out "almost everywhere" in the antidiffusion phase of each time step. The residual diffusion is just large enough to prevent dispersive ripples from arising at the discontinuity, thus ensuring that all conserved quantities remain positive. FCT captures shocks accurately over a wide range of parameters. No information about the number or nature of the surfaces of discontinuity need be provided prior to initiating the calculation.

The FCT routine used in the present calculations, called JPBFACT (an advanced version of ETBFCT)¹², consists of a flexible, general transport module which solves 1-D fluid equations in Cartesian, cylindrical, or spherical geometry. It provides a finite difference approximation to the conservation laws of the general form:

$$\frac{\partial}{\partial t} \int \phi dV = - \int \phi (\underline{u} - \underline{u}_g) \cdot d\underline{A} + \int \tau dA \quad (1)$$

where ϕ represents the mass, momentum, energy or mass species in cell $\delta V(t)$, \underline{u} and \underline{u}_g represent the fluid and grid velocities, respectively, and τ represents the pressure/work terms. This formulation allows the grid to slide with respect to the fluid without introducing any additional numerical diffusion. Thus, knowing where the features of greatest interest are located, one can concentrate fine zones where they will resolve these features most effectively as the system evolves (Fig. 1).

In the next section we describe the computational techniques used to solve the wedge problem and present the results of four simulations carried out to reproduce experimental results of Ben-Dor and Glass.¹³ In Section III we present a parallel discussion for a HOB calculation. Finally, in Section IV we summarize our conclusions.

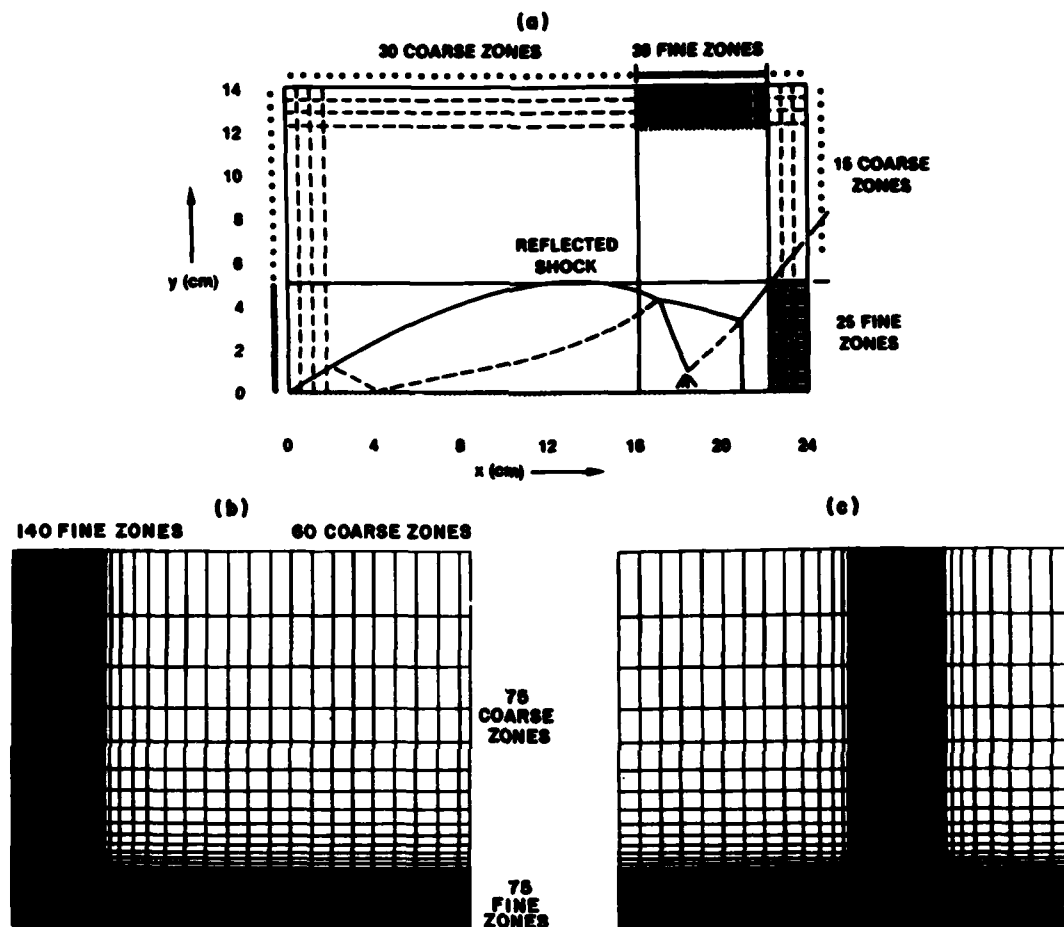


Fig. 1. Adaptive grids for a) planar shocks on wedge (double Mach shock features are indicated); b) and c) HOB problem initially and at transition point (grid lines in fine-zone region are indistinguishable).

SHOCK-ON-WEDGE CALCULATIONS

The JPBFACT algorithm was used in a 2-D Cartesian version of the FAST2D code to model the reflections of planar shocks from wedges of 20° to 60° and varying shock strengths. Four general classes which include regular, single, complex and double Mach reflection were calculated (referred to as cases a,b,c,d respectively). The bottom of the mesh, treated as a reflecting boundary, modeled the surface of the wedge. Quantities on the right hand boundary and on the top were set equal to the ambient values. The remaining boundaries were treated as permeable. In the single, complex, and double Mach reflection cases, the mesh was anchored on the left, essentially at the wedge tip where the incident shock first strikes, while the zones were stretched by a scaling factor proportional to t as soon as the reflection region filled a substantial portion of the grid. In case (d), the double Mach reflection case, the opening angle is so small that the incident shock has to traverse many zones before the Mach stem has grown large enough to be well resolved. For this reason, the problem was solved on a uniform mesh in the frame of reference fixed to the reflection point, with stretching being initiated after the first Mach stem reached ~ 20 cells in length. The timestep was recalculated at every cycle with a Courant number of 0.5.

Figure 2 shows the pressure and density contours and the velocity field for

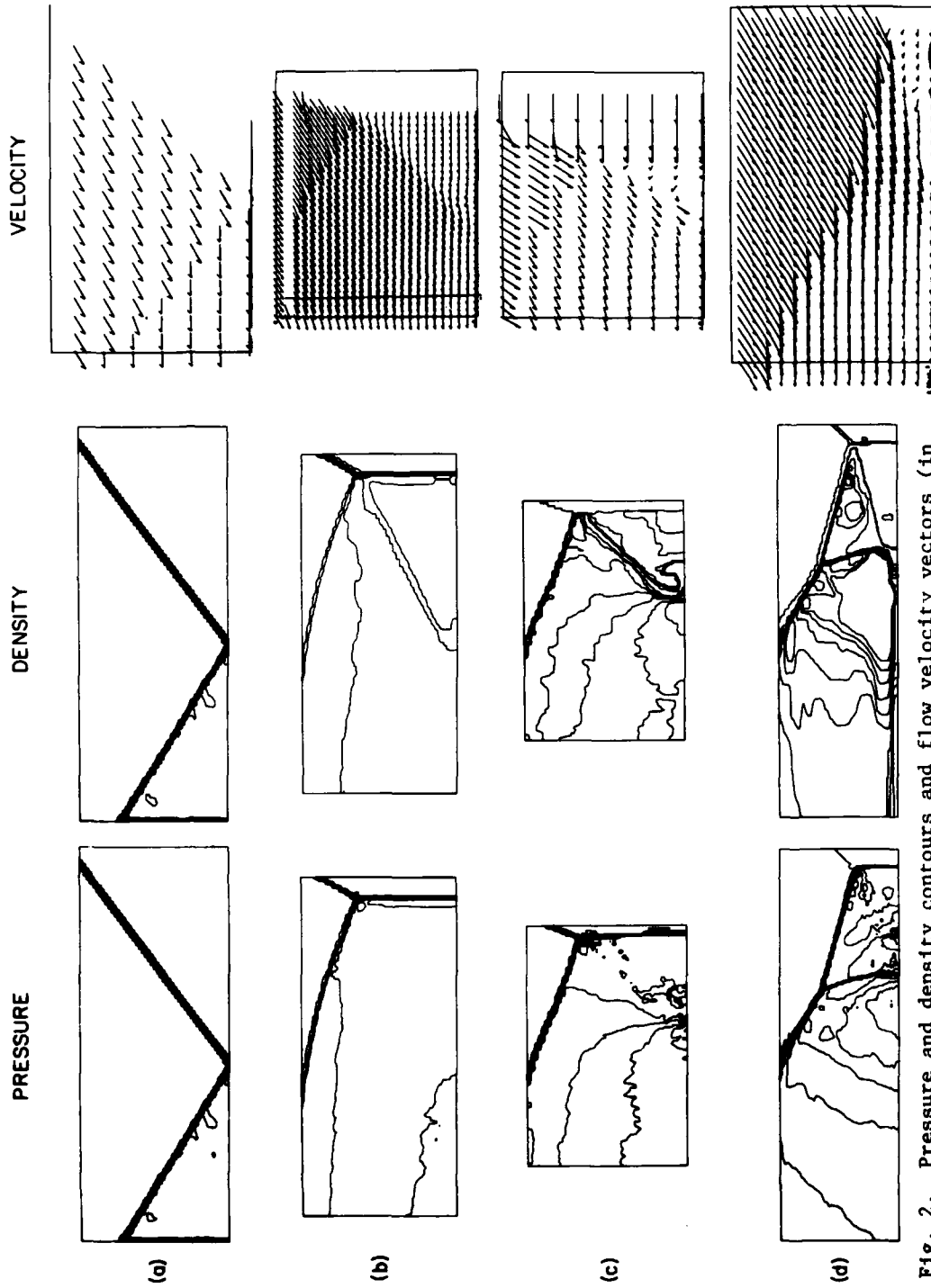


Fig. 2. Pressure and density contours and flow velocity vectors (in frame of reflection point) for planar waves with Mach number M reflecting from wedges with angle θ for (a) $M=2.03$, $\theta=60^\circ$; (b) $M=2.82$, $\theta=20^\circ$; (c) $M=5.29$, $\theta=30^\circ$; (d) $M=7.03$, $\theta=50^\circ$.

cases a,b,c,d. The pertinent shock phenomena can be easily identified: incident shock, contact surface, first and second Mach stems. As shown in Fig. 1, the zoning is particularly sparse except for the region of interest. Adequate resolution of the key surfaces (contact and second Mach stem) is obtained with 5 zones in each direction. The accuracy can be evaluated by comparing the experimental density distributions along the wall (Fig. 3).

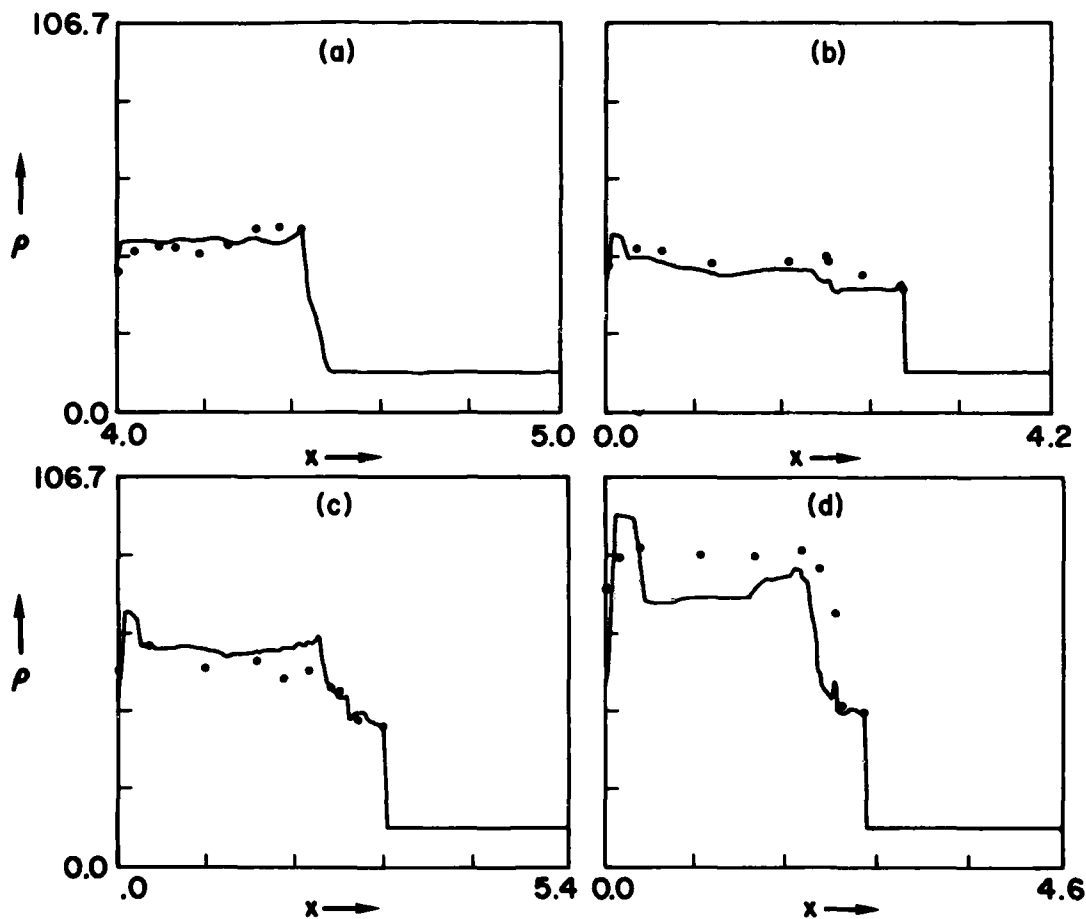


Fig. 3. Comparison of density (in units of ambient density ρ_0) for cases (a), (b), (c), (d) of Fig. 2 vs. distance from corner. Points are measured values reported in Ref. 13.

HEIGHT OF BURST CALCULATIONS

Next, we performed a numerical simulation of a 1KT nuclear detonation at 31.7 m HOB, a case which could be readily compared with high explosive data. A constant ambient atmosphere was used with a density of 1.22×10^{-3} g/cm³ and pressure 1.01×10^6 dynes/cm². To relate the energy and density to the pressure, a real-air equation of state (EOS) was used. This table-lookup EOS was derived from theoretical calculations by Gilmore^{14,15} for equilibrium properties of air and has been vectorized for the Advanced Scientific Computer¹⁶. The internal energy density used in the call to the EOS is found by subtracting kinetic from total energy; this can be negative due to truncation (phase) errors. When this occurred, the value of the pressure was reset to zero.

The transition from regular reflection to double Mach reflection occurs at a ground range approximately equal to the HOB. The size of the mesh should

therefore be roughly twice the HOB in both directions. The upper boundary should be far enough away from the blast front to be non-interfering. We chose boundaries of 55 m for the radial direction and 103.5 m for the axial direction. The fine grid in the radial direction contained 140 out of 200 total zones, each 5 cm in length. The rightmost zones were 80 cm in length, and a smoothing involving 40 zones was performed between the regions to guarantee that the zone sizes varied slowly. In the axial direction the fine grid contained 75 out of 150 total zones, each 5 cm in length. Beyond that region the zones were geometrically increased by a factor of 1.112.

Placement of the fine grid at the origin of the mesh (ground zero, the point at which reflection first occurs) was determined to be optimum for capturing peak pressure in the airblast wavefront. Thus, as the expanding wave moves along the ground surface, the fine grid is always locked to it and each point along the blast front encounters the same spatial gridding as it approaches the ground. By treating each point of the incident front in the same manner, we insure that the calculation is internally consistent and that the computed transition point is accurate to within the limits of the resolution.

The initialization provides a strong shock with approximate Mach number $M=12$. This speed and the need for restart capability led to the choice of 200 timesteps as an interval for the spatial display (snapshots). The dump interval that resulted was $\Delta t \sim 0.3$ milliseconds (ms). These dumps were stored on magnetic tape and post-processed.

A fit to the 1-D nuclear blast flow field (Ref. 17) was used to initialize the energy and mass density and velocity field at 3.76 ms. The corresponding peak overpressure was 113 bars. After the 1 KT flow field was laid down inside a radius of 31.6 m, the fine-zone grid was activated to follow the peak pressure as it moved along the ground surface, modelled as a perfectly reflecting boundary. This region comprised 140 zones, and a switch was set to keep 40 of these zones ahead of the reflection point. Permeable boundary conditions are used on the top and right edges of the mesh, i.e., density, pressure and velocity are set equal to ambient preshock conditions. Reflecting conditions were applied to the left and bottom. The total elapsed physical time in the 2-D calculation, 7.6 ms, required 5600 cycles. Times are referred to $t=0$ at the start of the calculation.

The numerical simulation begins just before the shock first reflects from the ground. Fig. 4a indicates the pressure and density contours and velocity vectors at time 3.18 ms. In Fig. 4b the reflected shock is shown moving upward, the outward flow begins to stagnate at the ground (transition). Fig. 4c, $t=5.99$ ms, shows an enlargement of the shockfront, and the development of the Mach stem, slip surface and second Mach stem. The angle of the shock front with respect to the ground is increasing with time, so that the effective wedge angle is decreasing. From Ben-Dor and Glass¹⁸ one expects a transition to double Mach stem to occur at approximately 45° . The angle in Fig. 4b is about 45° and the shock front has entered the transition phase. Figure 4d shows the fully developed shock structure at 7.79 ms. Clearly visible is the second Mach stem and a vortex region behind the first Mach stem. Toeing out of the first Mach stem can be also seen in the contours of Fig. 4d and occurs as the fluid rolls forward where the slip line would otherwise intersect the ground. The velocity field in Fig. 4d also shows this detail.

One should also note the reflected shock properties. The reflected shock propagates rapidly through the high temperature fireball, due to the high local soundspeed. The shape of this reflected wave is a primary difference between the HOB case and the wedge case¹⁹. The other major difference, of course, is the spherically expanding blast wave which decreases in strength approximately proportional to r^{-2} .

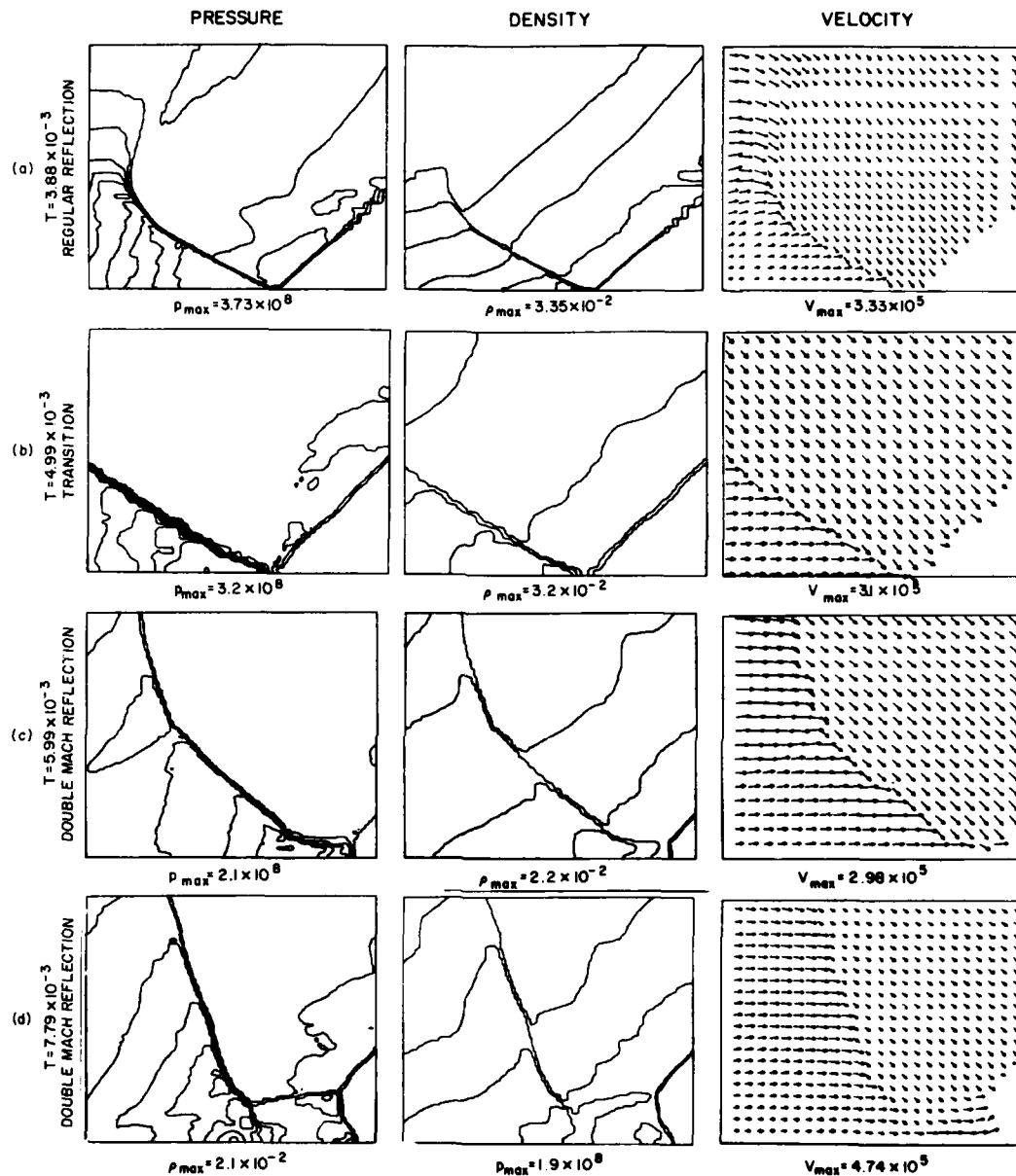


Fig. 4. Pressure, density, and velocity fields for HOB calculation (a) in regular reflection stage; (b) at transition to Mach reflection; (c) shortly afterward, when second peak has become larger than first; and (d) fully developed (note toe at base of first Mach stem).

Finally we consider the pressure/distance relation for the HOB case. In Fig. 5 we compare the results of the numerical simulation with the data of Carpenter and with empirical analysis. Carpenter's data are based upon careful HOB experiments with 8 lb PBX9404 spheres. The empirical analysis was based on a 1 KT nuclear free air curve and HOB construction factors. The calculated values in the regular reflection regime are 20% low and may be attributed to a combination of FCT clipping, the resolution of the grid, and inaccuracies in the initialization of the flow field. During and after Mach reflection, the peaks remain low until the Mach stem structure has grown large enough to be resolved on the mesh. By the time it occupies a region of 15 cells high and 35 cells wide, the peak pressures are in good agreement with the HE data and the empirical analysis.

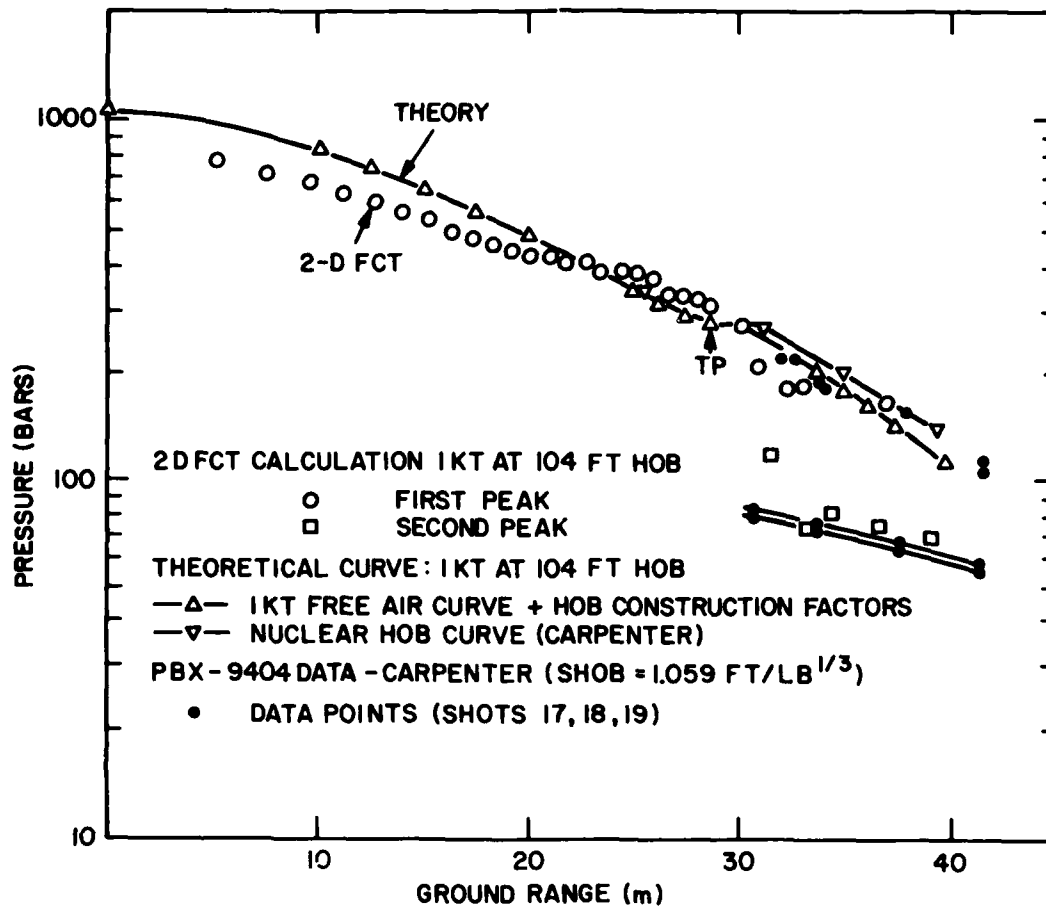


Fig. 5. Pressure-range curves for first and second (after transition - denoted by TP - to double Mach reflection) peaks.

SUMMARY AND CONCLUSION

The complex 2-D Mach reflection phenomena associated with shock diffraction on wedges and height-of-burst explosions have been modeled with the FAST2D computer code. Four wedge cases—regular, single, complex and double Mach reflection—have been calculated and the results compared to experiments. A nuclear detonation (1 KT at 31.7m HOB) was also simulated. The results give insight into the formation and subsequent evolution of the Mach stem, the triple point and the contact discontinuity. The transition from regular reflection to double Mach reflection is predicted. Excellent agreement with Ben-Dor's data is obtained. We suggest that the first signal for transition is the appearance of a second peak behind the shock front due to stagnation in the flow. Calculated first and second pressure peaks versus distance in the HOB case agree both with the HE data and analysis to within 20%.

The use of the adaptive regridding procedure, called "sliding rezone", along with the FCT algorithm allows one to accurately predict the nonsteady shock structures in two dimensions for diffractions on wedges and HOB cases. Comparison with data for both wedges and HOB yields the best results obtained to date.

ACKNOWLEDGEMENT

This work was supported by the Defense Nuclear Agency under Subtask Y99QAXSG, Work Unit 0001, Work Unit Title "Flux-Corrected Transport."

REFERENCES

1. Von Neumann, J., "Oblique Reflection of Shocks", Explosive Research Report No. 12, Navy Department, Bureau of Ordinance, Re2c, Washington, D.C. (1943).
2. Taub, A. H., "Refraction of Plane Shock Waves", Rev. Mod. Phys., Vol. 21, p. 51 (1947).
3. Bleakney, W., and Taub, A. H., "Interaction of Shock Waves", Rev. Mod. Phys., Vol. 21, p. 584 (1949).
4. Lighthill, M. J., "On the Diffraction of Blast I", Proc. Roy. Soc., Vol. 198, p. 454 (1949), Vol. 200, p. 554 (1950).
5. Jones, D. M., Martin, P. M., and Thornhill, C. K., "A Note on the Pseudo-Stationary Flow Behind a Strong Shock Diffracted or Reflected at a Corner", Proc. Roy. Soc., Sec. A, Vol. 205, p. 238 (1951).
6. Shankar, V., Kutler, P., and Anderson, D., "Diffraction of a Shock Wave by a Compression Corner - Part II, Single Mach Reflection", AIAA Journal, Vol. 16, No. 1 (1977).
7. Ben-Dor, G., and Glass, I., "Nonstationary Oblique Shock Wave Diffractions in Nitrogen and Argon - Experimental Results", UTIAS Tech Note (1978).
8. Courant, R., and Friedrichs, K. O., "Supersonic Flow and Shock Waves", Interscience Publishers, New York (1948).
9. Booen, M., and Needham, C., "Two-Dimensional Hull Code Simulation of Complex and Double Mach Reflections", AFWL NTE TN 81-001 (1981).
10. Boris, J., and Book, D., "Flux-Corrected Transport: I SHASTA, A Fluid Transport Algorithm that Works", J. Comp. Phys., 11, 38 (1973).
11. Oran, E. S., Young, T. R., Jr., and Boris, J. P., "Applications of Time-Dependent Numerical Methods to the Description of Reactive Shock", Proc. 17th Symposium (International) on Combustion, The Combustion Institute, Pittsburgh (1979).
12. Boris, J. P., "Numerical Solution of Continuity Equations", NRL Memo Report 3327 (1976).
13. Ben-Dor G, and Glass, I., "Domains and Boundaries of Non-Stationary Oblique Shock-Wave Reflections, II Monatomic Gas", J. Fluid Mech., 96, p. 735 (1980).
14. Gilmore, F. R., "Equilibrium Composition and Thermodynamic Properties of Air to 24,000°K" RAND Corp, RM-1543 (24 August 1955).
15. Gilmore, F. R., "Equilibrium Thermodynamic Properties of High Temperature Air", Lockheed Missile and Space Co., DASA 1917-1 (April 1967).
16. Young, T. R., (Private Communication 1981).
17. Needham, C., et. al., Nuclear Blast Standard, AFWL TR-73-55, Air Force Weapons Laboratory (April 1975).
18. Ben-Dor, G., Glass, I., "Domains and Boundaries of Non-Stationary Oblique Shock-Wave Reflections Diatomic Gas", J. Fluid Mech., Vol. 92, part 3, p. 459 (1979).
19. Book, D., et. al., "Two-Dimensional FCT Model of Low Altitude Nuclear Effects", NRL Memo Report 4362 (1980).
20. Carpenter, H. J., "Height of Burst at High Overpressures", 4th International Symposium on Military Applications of Blast Simulation (1974).

AD P000262

CYLINDRICAL RESONATORS†

R.A. Neemeh, J.H.T. Wu and M.N. Elabdin

Department of Mechanical Engineering

Concordia University, Montreal, Canada

ABSTRACT

Due to its ability to produce repeated cylindrical imploding-exploding shock waves, the cylindrical resonator may reach high temperatures. The present investigation was undertaken to improve the performance of the resonator so that it can produce highly symmetrical shocks for a wide range of jet stagnation pressures. This was achieved by increasing the number of inlets to the plenum chamber and by introducing a step into the jet stream to maintain the oscillations in the subsonic jet range. Using two dimensional tubes, it was found that the strongest oscillations were created by using a nozzle of at least 5 mm in width. When maximum pressure amplitude was obtained by varying both the step size and the width of the cylindrical cavity, spark schlieren photographs were taken of the flow in the cylindrical resonator at various time intervals. Results showed the presence of converging cylindrical shock waves possessing a high degree of circular symmetry. During the explosion phase, two pairs of vortices were seen trailing behind the expanding shock as a result of its interaction with the transverse waves formed during implosion. By insulating the disc with commercial asbestos, a temperature of 500°C was obtained with a jet stagnation pressure (P_{oj}/P_a) of 2.04. Higher temperatures may be reached by using different gases in the resonator or by improving the insulation around the disc.

† This work was supported by the Natural Sciences and Engineering Research Council Canada Under Grant No. A-4206

INTRODUCTION

The cylindrical resonator was first introduced in 1974 by Wu et al.¹ and consists of a cylindrical cavity excited by a circumferential under-expanded sonic jet. Its mechanism of oscillation is similar to that of a Hartmann tube² which is characterized by alternate periods of inflow and outflow but produces converging cylindrical shocks as compared to plane shocks produced in a simple Hartmann tube. Once it is recognized that the internally generated shocks are the main heat production mechanism, the potential of achieving higher temperatures in a cylindrical resonator is excellent since it can provide stronger shocks especially near the center of collapse. This was not, however, well demonstrated with the model proposed earlier mainly because of the asymmetry present in the converging shocks which were observed only at a jet pressure ratio of 3.76. The present work proposes an alternate model which operates at a wide range of jet stagnation pressures and produces converging shock waves possessing high degrees of circular symmetry. Its operation is similar to that of a Sprenger tube³ and therefore operates under subsonic and supersonic jet conditions. The detailed dimension assembly of the resonator used in the present work is shown in Figure 1. It consists of a cylindrical plenum chamber supplied

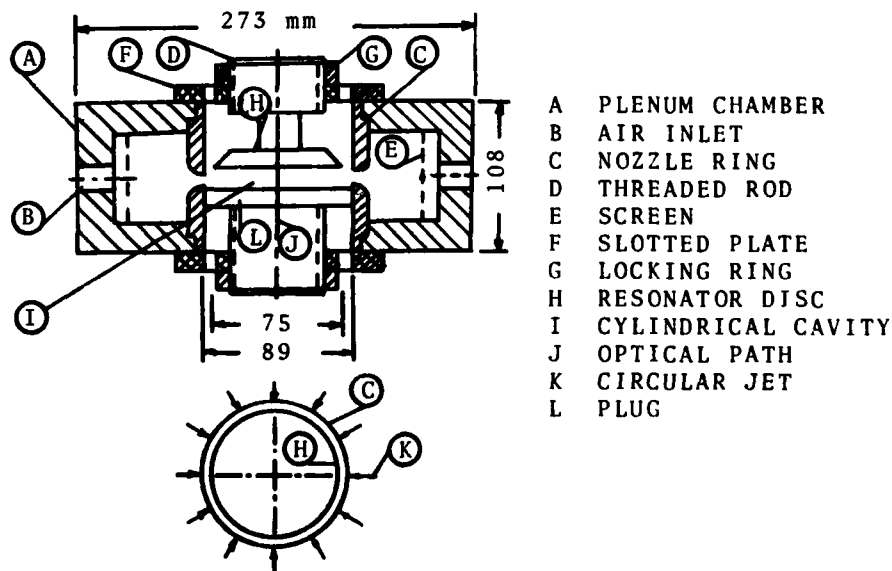


Fig. 1 Schematic of cylindrical resonator

by twenty one-inch diameter inlets connected to a 6 m³ tank filled with air at 830 kPa pressure. A narrow slit with a 6 mm rounded entrance in the inner wall serves as a nozzle. The nozzle jet is surrounded on one side by a disc with a 30 degree chamfer and on the other side by a plug. The position of the disc and the plug may be adjusted by threaded rods so as to control the width of the cylindrical cavity. In the present apparatus, the plug acts as a trip wire (in the case of the Sprenger tube) to weaken the jet close to its surface so that the outflow and the oscillations can be maintained at subsonic jet conditions. Since little experimental data was available

for tubes having a similar configuration it was therefore first necessary to conduct two dimensional tests to determine under what geometric conditions maximum pressure amplitudes prevail and plane shock waves are produced.

Two Dimensional Tests

The two dimensional apparatus used in all tests is presented in Figure 2. It consists of a tube having a rectangular cross section (5.1 x 25.4 mm) and a nozzle with the same exit dimensions. One tube nozzle side wall was constructed from a single aluminum plate and the opposite side wall was chamfered 30 degrees at the tube's open end. Spark schlieren photographs were obtained of the flow inside and outside the tube and piezoelectric pressures were measured at the closed end of the tube.

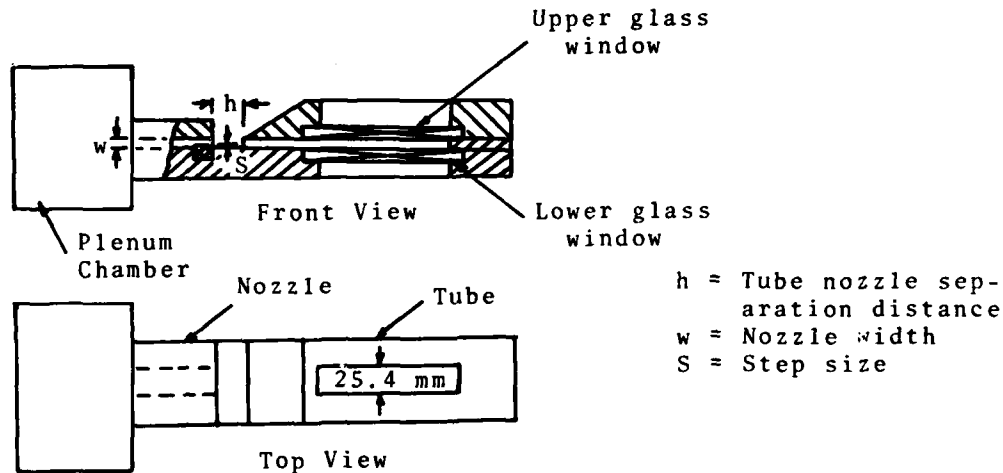


Fig. 2 Schematic of the 2-D tube

For pressure measurements three series of tests were conducted for a jet pressure ratio ($1.1 \leq P_{0j}/P_a \leq 2.5$). The first series was carried out with variable step sizes, the second with variable tube-nozzle separation distance and the third one with a smaller tube-nozzle internal dimensions. The results obtained from these tests indicated that in order to achieve maximum operating conditions with the two dimensional tube presented in Figure 2, the step size S must be greater than 5% of the nozzle width, the tube-nozzle separation distance h/w must be within the 3 and 4.2 values and the nozzle width must be greater than 5 mm otherwise smaller pressure amplitudes will be obtained. At optimum operating conditions the present two dimensional model is found to produce larger pressure amplitudes than those obtained before with square⁴ and round⁵ tubes.

Spark schlieren photographs of the flow interaction outside the tubes are presented in Figure 3 for a jet pressure ratio of 1.82. Photograph a shows the inflow phase as nearly the entire nozzle jet is captured by the tube. The transition from inflow to outflow takes place when the internal shock leaves the tube as shown in photograph b. Photograph c shows that during the outflow phase the nozzle jet is diverted to the outside of the tube owing to the weakness in the jet downstream of the step.

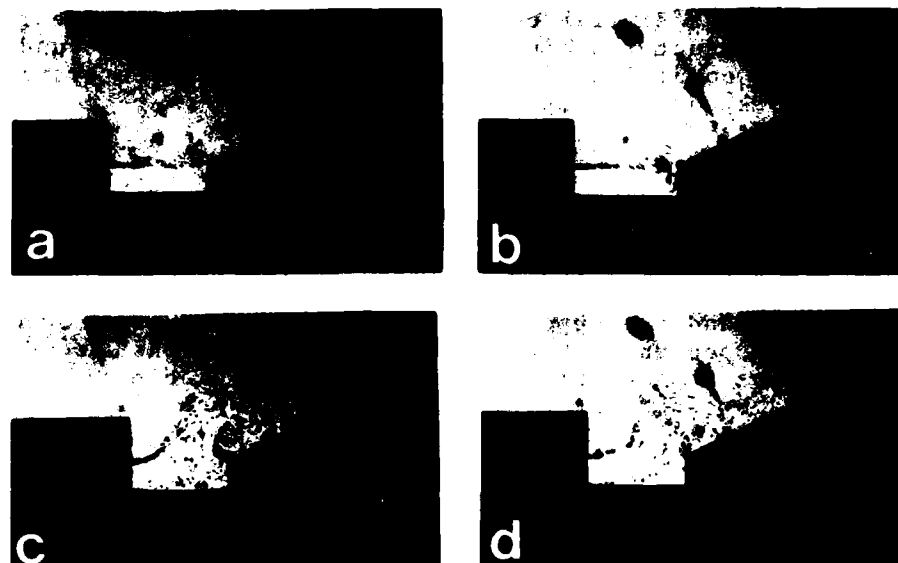


Fig. 3 Spark schlieren photographs of the flow interaction outside the tube.

Photograph d illustrates the transition to inflow which occurs when the tube jet eventually weakens. Another set of schlieren photographs of the flow inside the tube is presented in Figure 4. These photographs show clearly the presence of a moderate strength shock which maintains its plain shape as it propagates in and out of the tube.

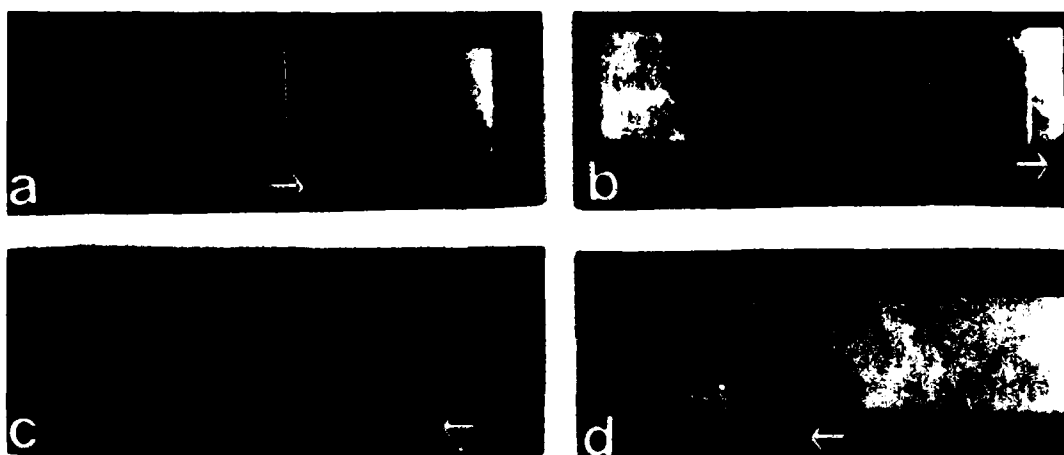


Fig. 4 Spark schlieren photographs of the plane shock in the 2-D tube.

From the two dimensional test results it was concluded that the present geometric configuration produces strong oscillations, similar to or even better than those achieved with any conventional tube shape, and that an axisymmetric model such as proposed in Figure 1 should, in principle, yield symmetrical converging cylindrical shocks for both subsonic and supersonic jets.

Tests on Cylindrical Resonators

These tests consist of pressure measurements, schlieren photography and temperature measurements.

i) Pressure Measurements

All pressure measurements were carried out at the geometric center of the cylindrical cavity by means of a Pcb piezoelectric pressure transducer (sensitive element 5.3 mm in diameter) and were undertaken to determine optimum nozzle width and disk diameter. Optimum step size and cylindrical chamber width were obtained by moving the plug and disk simultaneously in the axial direction until maximum pressures were reached. Figure 5 shows the pressure

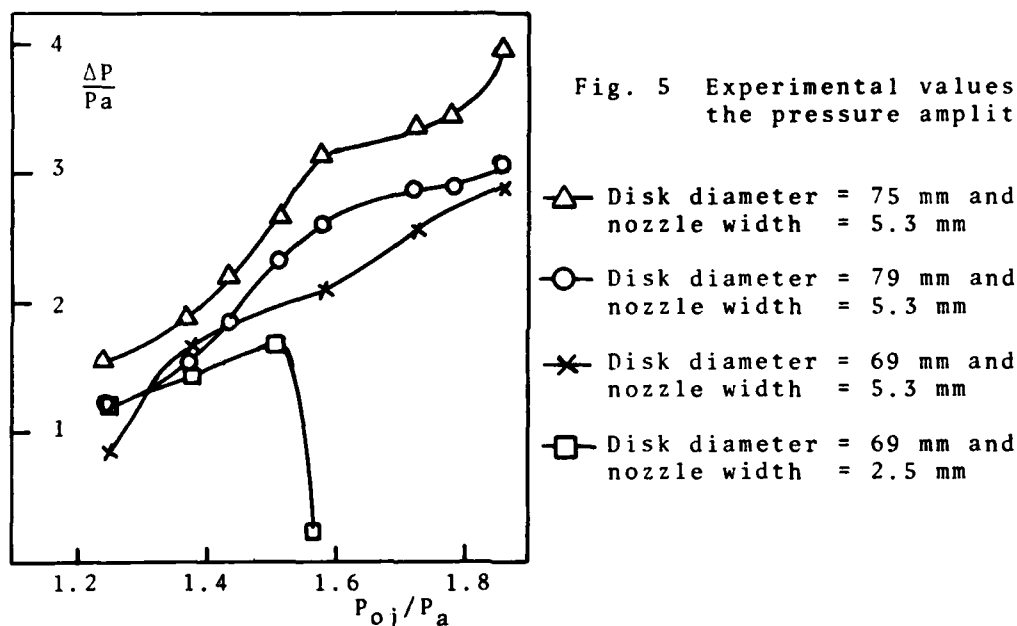


Fig. 5 Experimental values of the pressure amplitude

amplitude variation with jet stagnation pressure for a selected value of nozzle widths and disk diameters. For a nozzle width of 5.3 mm, the pressure amplitude is found to increase continuously with jet stagnation pressure. The maximum recorded values are found to occur with a disk diameter of 75 mm. Smaller or larger disks are found to produce weaker oscillations. For a given disk diameter, the highest pressure amplitudes were recorded for a nozzle width equal to or greater than 5.3 mm. From the results presented in Figure 5, it was concluded that the optimum disk diameter is 75 mm and the optimum nozzle width is 5.3 mm and were therefore adopted in all the following tests.

ii) Schlieren Photography

The schlieren system used for flow visualization in the cylindrical cavity, consists of a double headed parabolic mirror, a 2-KV spark-delay unit, a knife edge and a camera. A set of schlieren photographs of the flow inside the cylindrical cavity is presented in Figure 6. Photographs a and b show the converging cylindrical shock with a good degree of circular symmetry.

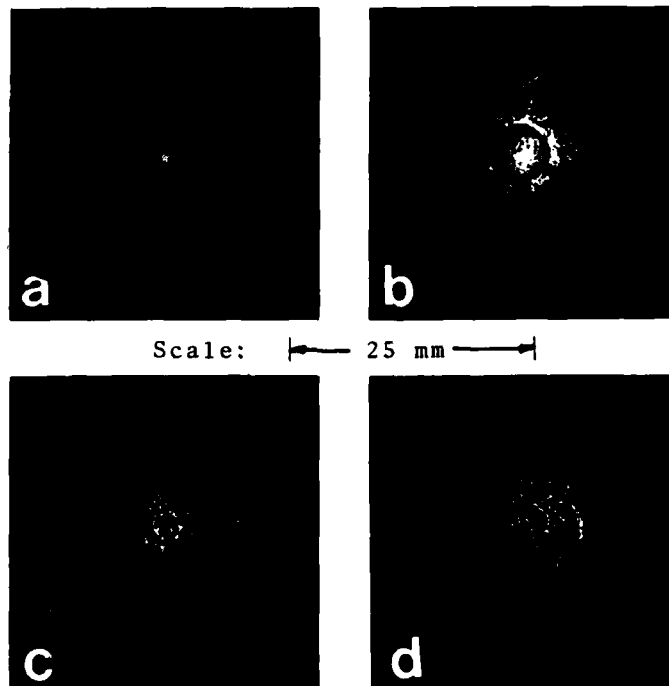


Fig. 6 Spark schlieren photographs of the cylindrical shock

Photographs c and d taken during the explosion phase, show 2 pairs of vortices trailing behind the shock, indicating the unavoidable and eventual breakdown in the shock front curvature and the appearance to triple shocks during the converging phase of the shock motion.⁶

iii) Temperature Measurements

To determine the heat generation capability of the resonator, the central part of both the disk and the plug were insulated with commercial asbestos. A 0.13 mm Chromel-Alumel thermo-couple connected to a digital temperature indicator (Omega Model 2809C) was used to measure the maximum steady state temperatures achieved at the geometric center of the cylindrical cavity for jet stagnation pressures ($1.3 \leq P_{oj}/P_a \leq 2.1$). The recorded values are presented in Figure 7 and shows a steady increase in temperature as the jet pressure ratio increases to its maximum possible reliable limit ($P_{oj}/P_a = 2.1$). For jet stagnation pressures ($1.43 \leq P_{oj}/P_a \leq 2.1$), the following linear empirical equation was obtained

$$T = 230 + 444 (P_{oj}/P_a - 1.43) \text{ } ^\circ\text{C} \quad (1)$$

At higher pressures the cylindrical resonator is expected to yield higher temperatures as suggested by the above equation. This was not verified experimentally, due to the difficulties encountered in maintaining the jet pressures long enough to obtain a temperature reading.

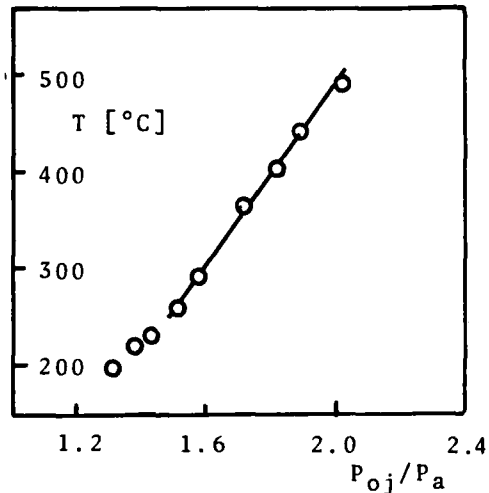


Fig. 7 Equilibrium temperature at the geometric center of the cylindrical cavity

○ Experiment

— Equation

CONCLUDING REMARKS

The present study has shown that, it is possible to produce symmetrical converging shocks in a cylindrical resonator provided that optimum disk diameter and nozzle width are employed. In the present case, the highest pressure amplitude was achieved with a disk diameter of 75 mm and a nozzle width of 5.3 mm. By employing a plug, the resonator was found to operate at subsonic jet conditions thus eliminating its dependence on the jet stagnation pressure. For a given jet pressure, temperatures higher than those obtained with tubes made with same insulation material were achieved. Further tests may be carried out in the future to determine the maximum attainable temperature with a properly insulated plug and disk using Helium as the jet fluid.

REFERENCES

- 1) Wu, J.H.T., Ostrowski, P.P., Neemeh, R.A. and Lee, P., "Experimental Investigation of a Cylindrical Resonator", AIAA Journal, Vol. 12, No. 8, August 1974, p.p. 1076-1078.
- 2) Hartmann, J., "On the Production of Acoustic Waves by Means of an Air of Velocity Exceeding that of Sound", Phil. Mag., Vol. 2, 1931, p.p. 329-334.
- 3) Sprenger, M., "Veber Thermische Effecte in Resonanzrohren", Mitt. Inst. Aerodynamik, Zurich, No. 21, (1954) p.p. 18-35.
- 4) Brocher, E., Maresca, C., "Condition de Fonctionnement d'un jet Subsonique", C.R. Acad., Sci., Paris, Serie A, (1969).
- 5) Wu, J.H.T., Neemeh, R.A. and Ostrowski, P.P., "Subsonic Jet-Driver Resonance Tube", CASI Transaction, Vol. 8, No.1, March 1975, p.p. 29-34.
- 6) Wu, J.H.T., Neemeh, R.A. and Ostrowski, P.P., "Experiments on the Stability of converging Cylindrical Shock Waves", AIAA Journal, Vol. 19, No. 3, March 1981, p.p. 257-258.

AD P 000263

PROPAGATION OF SHOCK WAVES THROUGH NONUNIFORM AND RANDOM MEDIA

B. Sturtevant, L. Hesselink, B.S. White, V. Kulkarny and C. Catherasoo

California Institute of Technology

Pasadena, California 91125

A study of the propagation of shock waves through random media, which was described in the 12th International Shock Tube Symposium, has been continued. A diagnostic technique is described in which shadowgraph motion pictures of the mixing process induced in a random medium by passage of a plane shock wave can be used to study the changes that occur in the distribution of spatial scales in the medium. The growth of large fluctuations in the amplitude of acoustic shocks has been studied theoretically with a new stochastic formulation of geometrical acoustics. Numerical calculations have been made of ray trajectories in a computer-generated two-dimensional random medium in order to check the predictions of the analytical theory and to calculate special parameters for comparison to experiment. Whitham's theory of shock dynamics has been generalized to treat the effects of fluid non-uniformity on the propagation of strong shocks.

I. INTRODUCTION

The propagation of waves through randomly inhomogeneous media is a fundamental problem of interest in a wide variety of scientific and technological fields. Waves refract and scatter from the nonuniformities, and, consequently, large and random fluctuations can develop in the intensity and phase pattern of the waves as they travel through the medium. The propagation of acoustic waves through random media has been studied in detail, as have the analogous problems of propagation of electromagnetic waves in dielectric substances and of stress waves in solids. However, the nonlinear behavior of finite-amplitude shock waves propagating through random media has not received as much attention. The propagation of shocks through fluids with randomly varying properties is particularly significant because coupling between the wave propagation and the fluid motion can be very strong. For example, the vorticity field generated by the passage of a shock wave through a fluid in which entropy (e.g., density or temperature) fluctuations occur can greatly increase mixing in the fluid. In addition, the stability of plane shock waves strongly affects the behavior of the scattered wave field. In this work we present new results, both theoretical and experimental, from an investigation of shock wave propagation in random media first described at the 12th International Shock Tube Symposium (ref. 1). In the experiments, relatively weak shock waves ($M_g = 1.007 - 1.1$) propagate through a volume containing two incompletely mixed gases in which 6% rms sound speed fluctuations occur with a homogeneous, random distribution.

Because shock waves are nearly discontinuous and the present experiments involve relatively weak shock waves, it is instructive and convenient to treat this problem in terms of geometrical arguments, namely with the theory of geometrical acoustics as a first approximation for weak waves and with the theory of shock dynamics to account for the effects of gasdynamic nonlinearity. In particular, the view of scattering that is adopted in this work, heavily influenced by previous work at this laboratory (ref. 2) and by suggestions of Pierce (ref. 3) and Kravtsov (ref. 4), is that the random medium acts like a random array of lenses, focusing and defocusing the waves, creating a random distribution of foci and thereby causing the wave amplitude locally to become very large. At the foci the occurrence of infinite amplitude is prevented by diffraction and nonlinearity. The large-amplitude waves at the foci may interact strongly with the medium, generating more inhomogeneities. Thus, both the effect of the random medium on the waves (scattering) and the effect of the waves on the medium (turbulence production) are of interest. In this paper a survey is given of research directed at both aspects. Reference is given to more complete descriptions to appear in future publications. In §2 the experimental apparatus and some recent results obtained from an optical technique for measuring the statistical properties of the random medium are described. In §3 a stochastic acoustic theory which analyses the occurrence of foci in a random medium is briefly outlined. In §4 numerical calculations tracing wave fronts and rays through a computer-generated two-dimensional random medium are described, and results are presented and compared with the stochastic theory and with the experiments. Finally, in §5 an approximate theory to treat the nonlinear propagation of finite-amplitude waves through random media, based on Whitham's shock dynamics, is described.

2. EXPERIMENTAL

The apparatus used in these experiments, shown in Figure 1, is mounted at the end of the 43 cm dia shock tube at GALCIT* (ref. 5). Its function is to generate a 26.7 cm square by 35 cm long rectangular volume of two incompletely mixed gases immediately prior to a run. The apparatus consists of an array of fine jets, alternately of helium and dichlorodifluormethane (CCl_2F_2 , hereafter referred to as fluorocarbon), arrayed in a checkerboard pattern on 6.3 cm centers behind coarse grids on opposite vertical sidewalls of a box which acts as the test section of the shock tube. The grids are rapidly retracted flush with the sidewalls just before the shock tube is fired. The top and bottom walls of the box are fitted with 15 cm dia optical windows for diagnostics, and the vertical upstream and downstream walls of the box are "shutters", which can be opened rapidly just before shock arrival. The operation of the jets, the grids and the shutters is automated. The gas mixture has the same density as air, so the mean interface between the scattering region and the uniform gas in the shock tube remains parallel to the plane of the incoming wave during a run. The mean speed of sound of the mixture is also matched to that of air to minimize reflection of the shock from the upstream and downstream interfaces. The mixture which yields these properties contains 80% helium by volume, and the mixture in the test section at the time of shock arrival has 6% rms sound-speed fluctuations. A typical length scale of the fluctuation field in the random medium is 1.5 cm. Shadowgraph and schlieren photographs are used to visualize the random medium and the shock wave propagating through it. An argon-ion laser is used as the light source. Quantitative information about the development of the statistical properties of the random medium is obtained from shadowgraph images obtained either from still photographs or with a high-speed motion picture camera operating at a framing rate of 50,000 fps. Figure 2 shows selected frames from a shadowgraph movie which have been digitized on a microdensitometer and re-photographed with a laser printer.+

* Graduate Aeronautical Laboratories, California Institute of Technology

+ The authors are indebted to Mr. D. Madura of the Medical Image Analysis Facility, Jet Propulsion Laboratory, for his aid in this effort.

Information about the statistical properties of the random scattering medium is obtained using the method of Hesselink and White (ref. 6) for processing images on shadowgraph photographs. Assuming homogeneity and isotropy, the (two-dimensional) power spectral density function $S_I(k)$ of the light intensity fluctuations in the observation plane recorded on film is related to $S_3(k)$, the three-dimensional spectrum of the index of refractions, by a perturbation analysis of the wave equation in the limit of vanishingly small optical wavelength and fluctuation amplitude,

$$S_3(k) = \frac{6\pi S_I(k)}{[1 + 3\delta(1 + \delta)]D^3k^4}, \quad (1)$$

where k is the magnitude of the wave vector, $\delta = \hat{D}/D$, D is the thickness of the slab, and \hat{D} is the distance between the entrance plane of the medium and the location of the film plane.

The spectrum of the shadowgraph has been computed and averaged from the digitized images of eleven still photographs (Figure 3a). From the two-dimensional power spectrum of the image, the three-dimensional spectrum of the medium is calculated using equation (1) (Figure 3b). For comparison, two lines with slopes $-11/3$ and -9 are shown on the figure. Kolmogorov similarly suggests that in homogeneous turbulence the power spectral density function in the inertial subrange should follow a $-11/3$ behavior, while empirical data suggest that in the viscous dissipation range a -9 slope is appropriate. The intersection between the two straight lines occurs at a wavenumber $k = 5.3$ cycles/cm which corresponds to a length scale of 1.9 mm. This scale is known as the microscale.

3. STOCHASTIC THEORY OF FOCUSING

The growth of large fluctuations in the amplitude of high-frequency acoustic waves or acoustic shocks has been studied with a new stochastic formulation of geometrical acoustics (ref. 7). Nonlinear terms which represent focusing have been retained in the theory, so the inapplicability of previous theories when amplitude variations become large and when propagation distances are large has been avoided. The coordinate system used in the analysis is arranged so the coordinates (α, β) lie parallel and normal to the wave fronts. The ray direction $\beta = \text{const}$ lies at an angle θ , the flow deflection angle, to the x coordinate. (So far only two-dimensional problems have been treated.) Introducing stretched longitudinal coordinate s and transverse coordinate η ,

$$ds = c d\alpha \quad (2)$$

$$d\eta = A d\beta \quad (3)$$

the equations of geometrical acoustics can be written

$$\theta_s = -c_\eta/c \quad (4)$$

$$K \equiv \theta_\eta = A_s/A \quad (5)$$

$$\frac{A_{ss}}{A} = -c_{\eta\eta}/c \quad (6)$$

or

$$K_s + K^2 = -c_{\eta\eta}/c \quad (7)$$

where c is the sound speed, K is the wavefront curvature, and A is the ray tube area. The essential tendency to focus can be illustrated by examining the behavior in a uniform medium ($c_\eta = c_{\eta\eta} = 0$). In that case the solution to equation (7) is

$$K = \frac{K_0}{1 + K_0 (s - s_0)}, \quad (8)$$

where K_0 is an initial curvature at the initial station s_0 . For $K_0 > 0$, $K \rightarrow 0$ as $s \rightarrow \infty$, while, for $K_0 < 0$, $K \rightarrow -\infty$ as $s - s_0 \rightarrow 1/|K_0|$, the former case corresponding to an initially diverging wave tending toward a plane wave and the latter to an initially converging wave collapsing to a focus. Thus, K always decreases, but it approaches different limits depending on whether the wave is converging or diverging. On the other hand, for small fluctuations the stochastic term involving the sound speed in equation (7) is small and therefore important only near $K = 0$. The significant effect of this term is to cause the curvature of diverging waves to pass the limit $K = 0$ by random walk, and therefore to become converging waves which then focus. Thus, there is an inevitable tendency to focus, and, as a detailed analysis (ref. 7) shows, focusing occurs in a finite distance with probability = 1. Therefore, fluctuations of wave amplitude grow exponentially and the focal length f has a characteristic magnitude

$$f \sim a\sigma^{-2/3}, \quad (9)$$

where a is the correlation length of the index of refraction fluctuations in the medium and σ is their rms amplitude.

4. NUMERICAL RAY-TRACING CALCULATIONS

Computer calculations have been made of ray trajectories in a computer-generated two-dimensional field of index-of-refraction fluctuations. The results of these calculations serve as a check on the validity of the above stochastic theory of focusing and as an indication of the departures that may occur when the amplitude of the sound-speed fluctuations is larger than the range of validity of the analytical theory. Furthermore, calculation of special parameters for comparison with experiment can easily be made. The numerical calculations are carried out for wave propagation through a random medium of the same properties (in particular, rms amplitude and correlation length) as the fluid mixture used in the experiments.

The computer turbulence is computed by convolving a set of nearly normally distributed random numbers with a prescribed weighting function derived from the specified correlation function of the fluctuation field. In the present calculations a Gaussian correlation function with zero mean, variance a^2 and maximum amplitude σ^2 is assumed. The ray paths through the random medium are computed using the ray equation of geometrical acoustics, written this time in characteristic form (ref. 8),

$$\begin{aligned} \frac{d}{ds} \nabla \alpha &= - \frac{\nabla c}{c^2} \\ \text{on} & \\ \frac{dx}{ds} &= c \nabla \alpha \end{aligned} \quad (10)$$

where α is the phase ($d\alpha = ds/c$, as before) and \underline{x} is the position vector of a point on the ray. An incident plane wave is assumed with rays parallel to the x axis.

A photograph of the computer-generated medium is shown in Figure 4. The gray scale represents the level of the sound speed, a high sound speed being black and a low sound speed white. Results of the ray-tracing calculations for waves incident normally on each of the four sides of the medium of Figure 4 are indicated in Figure 5. The wavefronts at five different stations along the path of propagation are also indicated. The strong tendency for the waves to focus in this medium is clearly seen; in some cases multiple focusing occurs. Since the amplitude and scale of the sound-speed fluctuations has been chosen to be similar to that in the experiments, the behavior should be typical of those which occur in the laboratory-generated random medium. In particular, station 4 corresponds to the position of the window in the experiments, which is about three focal lengths (cf. equation 9) from the upstream boundary of the random medium. It is interesting that this distance is of the same order of magnitude as the corresponding normalized propagation distance through the earth's turbulent boundary layer of a typical sonic boom generated by a supersonic transport, assuming that a relevant scale in that case is about $10/k_s$, where k_s is the wave number of the dissipating eddies (ref. 9), that the amplitude of the relevant fluctuations of sound speed equals 0.005 (ref. 10) and that the propagation distance is 2km.

From the data of Figure 5 a histogram has been constructed of the distance to first focus along representative rays. This quantity, normalized to a probability density function, is plotted versus a nondimensional propagation distance (ref. 7) in Figure 6. The solid curve is the prediction of the theory of §3. It is seen that the agreement between the numerical calculations and the stochastic theory is very good.

A procedure has been established for comparing the rise time of the initial disturbance incident upon pressure transducers at the downstream end of the test section with the predictions of the numerical calculations. It is assumed, in keeping with the implications of geometrical acoustics theory, that initially discontinuous wavefronts remain discontinuous, and that any particularly slow rise time recorded by a transducer must be due to tilting of the wave front. The envelope representing the leading disturbance on the wavefront at station 5 in Figure 5 is constructed and a row of simulated pressure transducers, scaled to the diameter of the transducers used in the experiments, is aligned side by side, parallel to the plane of the incident wave front. The slope of the segment of the wavefront envelope incident upon each transducer is taken to be the quantity determining the rise time of that transducer. A histogram of such rise times is presented in Figure 7. Also shown in the figure is the histogram of the experimental results. Agreement between these two results is satisfactory.

5. SHOCK DYNAMICS IN NONUNIFORM MEDIA

Distortions of shock fronts caused when, for example, the fronts pass over curved boundaries, as in shock diffraction over a wedge, has received considerable attention in the past. It is now possible to treat diffraction over bodies with exact numerical calculations or with approximate theory. The approximate theory, known as shock dynamics, is due to Whitham (ref. 8). Shock propagation through nonuniform media has not received as much attention, despite the fact that refraction and diffraction of shock waves in turbulence and in substances of varying sound speed occur in many applications. There does not exist an approximate method for calculating such flows that properly preserves the sharpness of discontinuities, except for the method of characteristics for fully two- or three-dimensional nonsteady flow. In the work reported here, Whitham's theory of shock dynamics has been generalized to treat the effects of non-uniformities in the undisturbed fluid ahead of shock waves. Shock dynamics is the nonlinear analogue of geometrical acoustics. It treats the distortion of wave fronts in the coordinate system of §4 in terms of disturbances propagating transversely, carrying changes of shock strength M and ray inclination θ along the fronts.

The formulation (ref. 11) of the theory follows that of Whitham (ref. 8), and the resulting characteristic equations are the same as in that theory,

$$d\theta \pm d\omega(M) = S(\theta, M, \partial a_0/\partial x, \partial a_0/\partial y), \quad (11)$$

where $\omega(M)$ is a function given by equation 8.72 of ref. 8, except that a source term S , which depends on the variation of sound speed in the medium, appears on the right-hand-side, reflecting the fact that disturbances are formed on the wave fronts even in the absence of nearby curved surfaces. The function S is given in ref. 11. Discontinuities of M and θ can form on shock fronts in this theory, just as in uniform media. These discontinuities are the manifestation of triple-shock intersections in Mach reflection and refraction. In the class of problems studied here another discontinuity may occur; namely, a discontinuity in fluid properties (contact surface) in the fluid ahead of the shock. Thus, jump conditions equivalent to Snell's law must be developed for the changes of θ and M across contact surfaces. These, together with the shock-shock jump conditions, are fitted into the solutions of the characteristic equations.

In order to examine the properties of this theory in simple analytical examples, the problem of shock refraction from a plane contact interface has been studied. The geometry considered is that of two plane interfaces intersecting at an obtuse angle on the x -axis, the portion in the lower half plane being parallel to the incident shock and the portion in the upper half plane lying at an angle δ to the x -axis. Figures 8 and 9 show the results of calculations for two cases. The contact surfaces, shock-shocks, characteristics and a typical wave front are indicated in the figures.

The most interesting result of the analysis is the demonstration that the theory naturally provides a criterion for the transition from regular to Mach refraction, in contrast to the diffraction of shock waves over wedges where the theory only predicts Mach reflection. In this case, when the leading characteristic in the upper half plane falls above the contact surface a shock-shock forms and irregular refraction is predicted (Figure 9), but when the leading characteristic falls below the contact surface regular refraction results (Figure 8). Figure 8 gives the results for the regular refraction of a shock of strength $M = 5.0$ by a sound speed ratio of 1.35 at an angle $\delta = 45^\circ$. Figure 9 gives similar results for irregular refraction with sound speed ratio 1.5 and $\delta = 10^\circ$.

ACKNOWLEDGMENT

This work was supported by the National Science Foundation under Grant CME-7822089.

REFERENCES

1. B. Sturtevant, L. Hesselink, J-F. Haas. Shock Tubes and Waves; Proceedings of the 12th International Symposium on Shock Tubes and Waves. (ed. A. Lifshitz and J. Rom) The Magnes Press, Jerusalem, 1980.
2. B. Sturtevant and V.A. Kulkarny. J. Fluid Mech. 73, 651. 1976.
3. A.D. Pierce. J. Acous. Soc. Am. 44, 1052. 1968.
4. Yu. A. Kravtsov. Sov. Phys JETP 28, 413. 1969.
5. L. Hesselink and B. Sturtevant. "Propagation of Shock Waves Through Random Media". To be published.
6. L. Hesselink and B.S. White. "Digital Image Processing of Flow-Visualization Photographs". To be published.
7. V.A. Kulkarny and B.S. White. "Focusing of Waves in Turbulent Inhomogeneous Media". To be published.
8. G.B. Whitham. "Linear and Nonlinear Waves" John Wiley & Sons, New York. 1974

9. A.A. Townsend. "The Structure of Turbulent Shear Flow" Cambridge Univ. Press, Cambridge. 1976.
10. S.C. Crow. J. Fluid Mech. 37, 529. 1969.
11. B. Sturtevant and C.J. Catherasoo. "Shock Dynamics in Nonuniform Media". To be published.

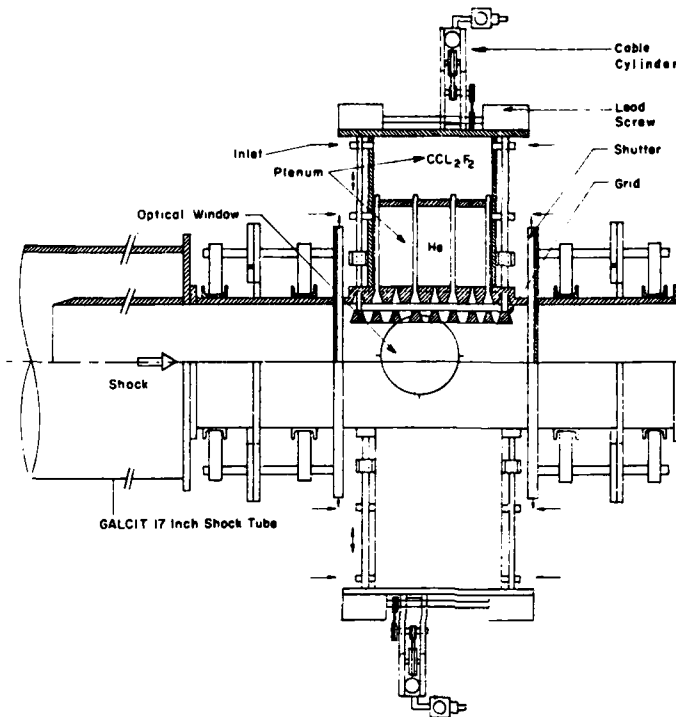


Figure 1. Schematic view of the shock-tube test section.

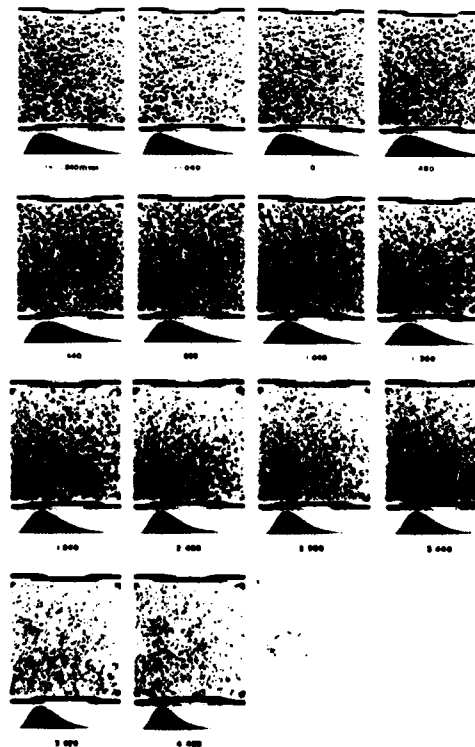


Figure 2. Selected frames from a high-speed shadowgraph movie. $t = 0$ corresponds to the time the shock passes the viewing window.

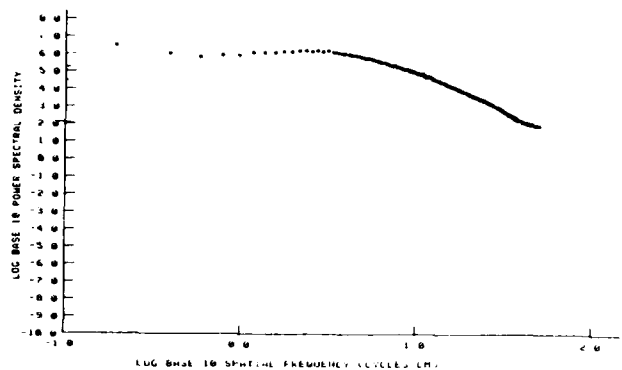


Figure 3. Representative spectra from still photographs. a) 2 - dimensional spectrum of shadow-graph image. b) 3 - dimensional spectrum of random medium calculated from a).

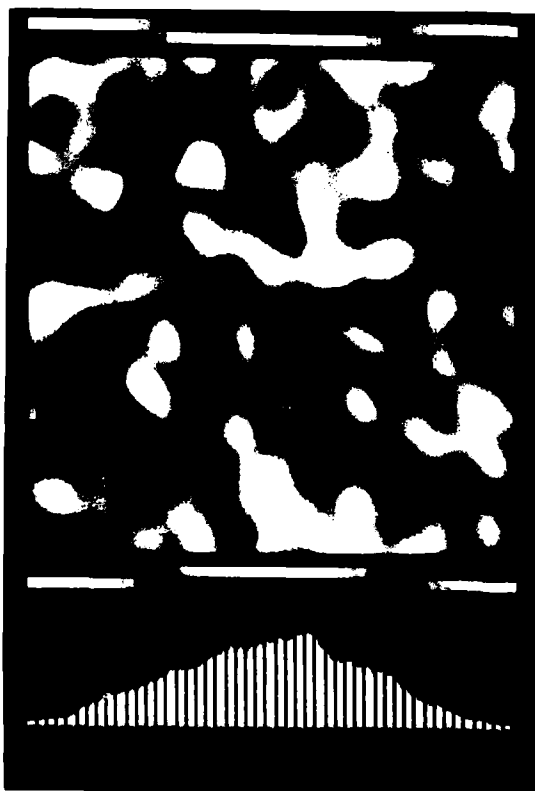
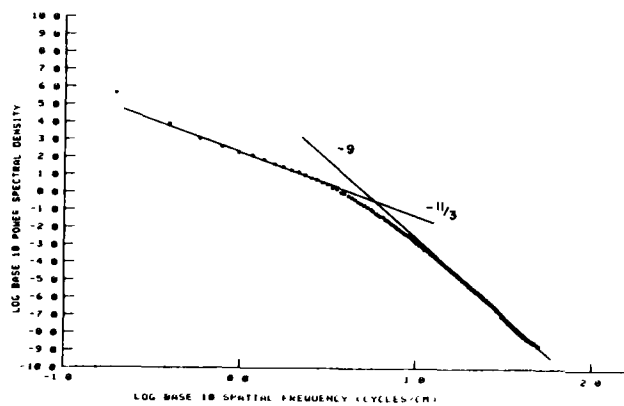


Figure 4. Photograph of computer-generated 2 - dimensional random medium. White = low sound speed. Black = high sound speed.

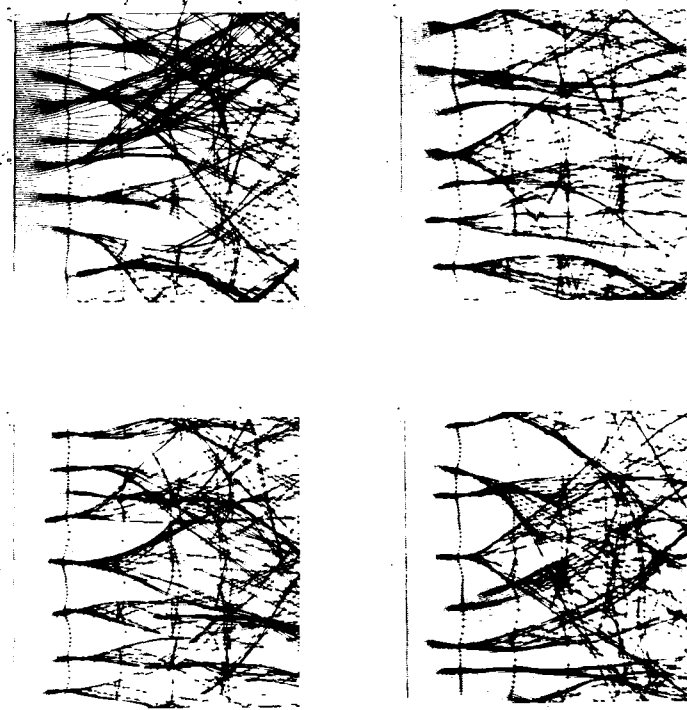


Figure 5. Acoustic ray paths and wave fronts in computer-generated random medium.

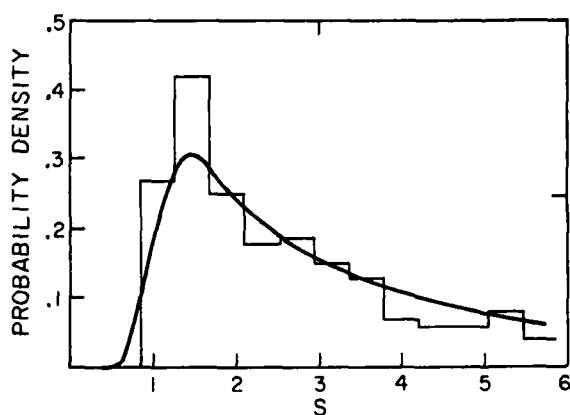


Figure 6. Probability density of distance to first focus.

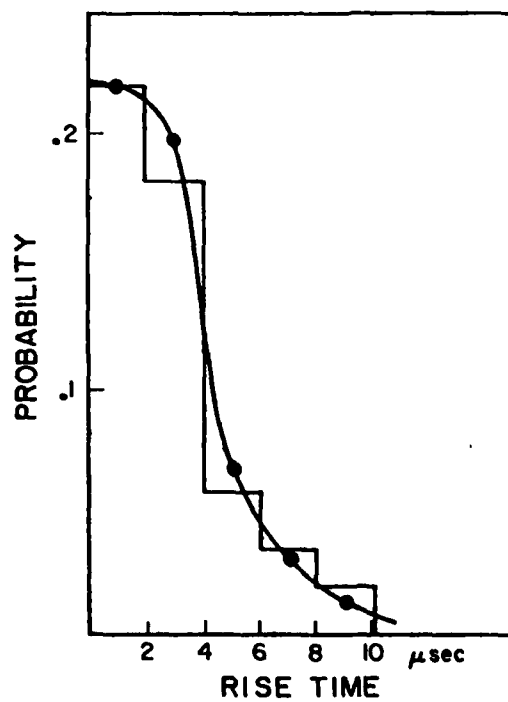


Figure 7. Histogram of transducer rise times.

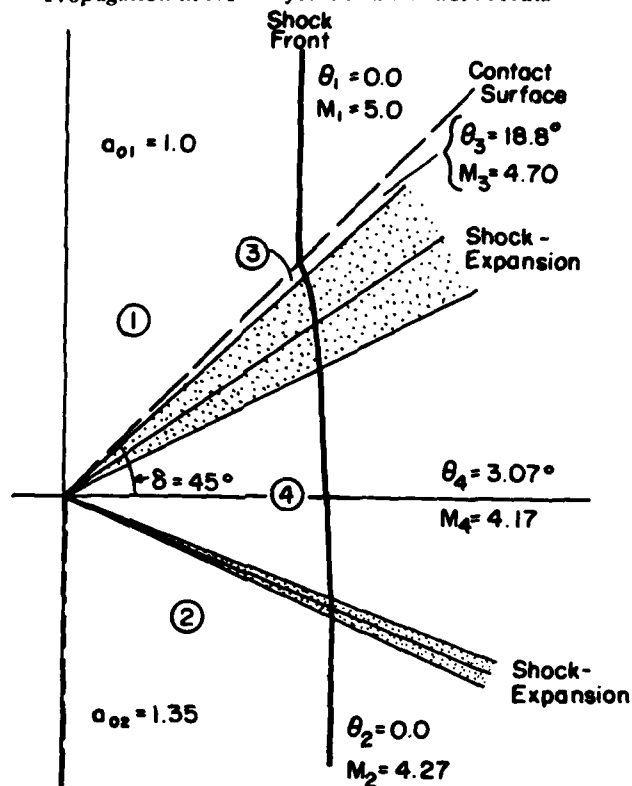


Figure 8. Shock dynamics calculation of regular refraction.

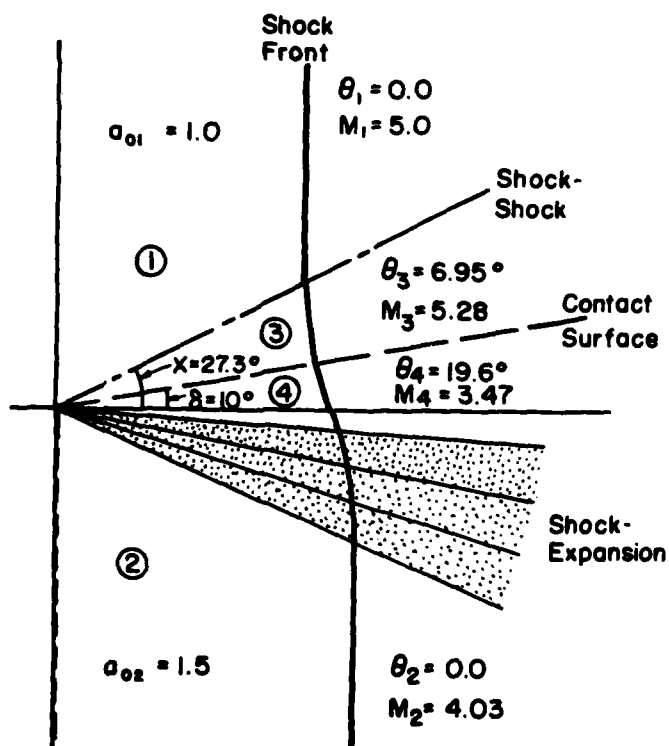


Figure 9. Shock dynamics calculation of irregular refraction.

AD P000264

SHOCK WAVE DIFFRACTION AT A SHARP EDGE
AND THE EFFECT OF BAFFLES IN A SHOCK TUBE

J.M.R. GRAHAM and R. HILLIER

Department of Aeronautics

Imperial College, London SW7, England

The diffraction of a shock wave round a sharp two-dimensional edge is studied numerically using a Fluid-in-Cell method with flux corrected transport. The alternative possibility of a shock fitting technique to this problem in order to reduce numerical diffusion is also discussed briefly. In the case of shocks with subsonic post-shock flow comparisons are made with an isentropic weak wave diffraction theory including the effect of the vorticity shed from the edge. When this vorticity is included, good agreement is obtained between the two different methods of solution for the weaker shocks. Numerical results are also presented for strong shocks, with supersonic post-shock flow. In this case some comparison with quasi-steady theory is possible. These comparisons are presented as a validation of the general numerical technique in dealing with diffraction type problems.

The paper also deals with the propagation of a shock wave through a succession of axisymmetric orifice plates in a long tube. Results of numerical computations of the internal flow fields are presented indicating how the rate of attenuation of the shock wave depends on the relative geometry of the orifice plates. The results are considered in the light of the diffraction results presented in the first part of the paper and are used to discuss the effectiveness of internal baffles which are a common feature of silencer design.

INTRODUCTION

An important aspect of the interaction between shock-waves and solid bodies is the diffraction which occurs at the edges of the body. It is frequently important, for example, to calculate the attenuated shock which propagates into the shadow region. Classical analysis of diffraction usually ignores the flow separation at the edge and even in the absence of separation there is no exact analysis for the diffraction of strong shock waves.

Because of an interest in calculating the attenuation of a propagating shock by a sequence of baffles, we have chosen to look in detail at the diffraction of a plane shock at the edge of a semi-infinite plate. The numerical results presented in this paper have been computed using a finite difference method to solve the inviscid Euler equations. The scheme used was the Fluid-

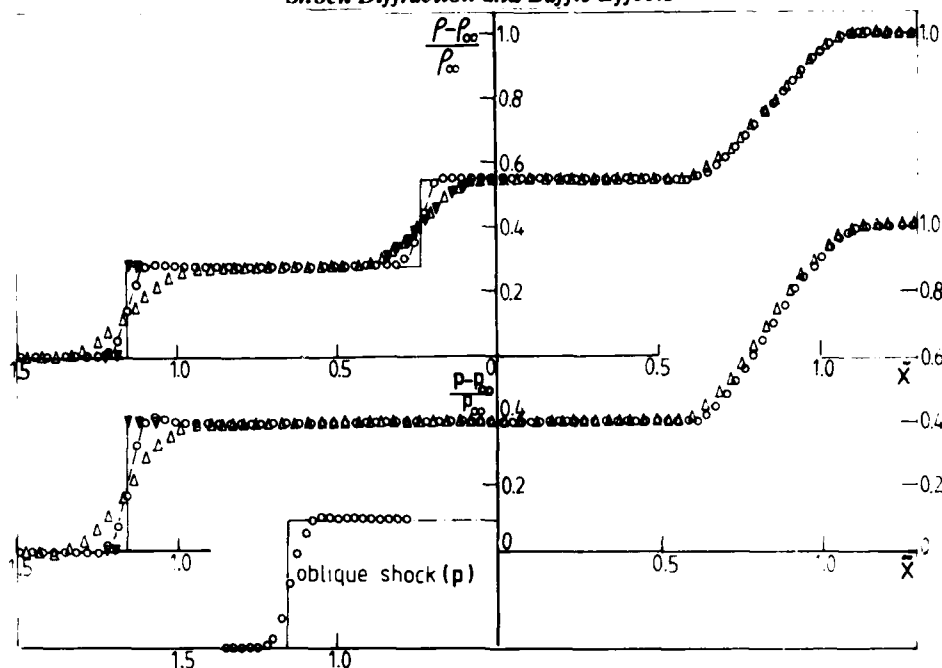


FIGURE 1 Shock Tube Calculations. One-dimensional propagation: Δ Donor Cell, \circ Flux Corrected Transport, ∇ Donor Cell + Shock Fitting, — True position of shock and contact surface. Oblique propagation \circ , computed on different mesh lines.

In-Cell (FLIC-Donor Cell) technique, as described by Gentry, Martin and Daly (1966). This method is a first order scheme which is very stable due to the large amount of numerical diffusion inherent in it and also the incorporation of artificial viscous pressures. However the numerical diffusion results in considerable smearing of shocks and contact surfaces. This can be seen in Figure 1 in which the results of a one-dimensional shock-tube calculation are presented. The non-dimensionalised pressure and density are plotted here against the pseudo-stationary coordinate $\tilde{x} = x/at$ where a is the ambient speed of sound.

The Donor Cell method can be improved to second order accuracy with considerable reduction of the numerical diffusion by incorporating a 'flux corrected transport' (FCT) algorithm as suggested by Book, Boris and Hain (1974). This technique removes the numerical diffusion except where it must still be retained for stability and leads as in Figure 1 (FCT curve) to shock capturing over about three or four meshes of the numerical grid. However we have found that for this particular code the degree of sharpening obtained as the anti-diffusion is increased must be balanced against a slight loss of accuracy (in the form of an overshoot) just behind the shock heralding the onset of instability. This problem is most critical for very weak shock waves ($\Delta p_s/p_\infty \sim 1\%$).

Shock capturing over a single mesh however can only be obtained by techniques of shock fitting or by Random Choice Methods, for example Saito and Glass (1980). The result of performing the shock-tube calculation using the basic FLIC program combined with a shock fitting algorithm is also shown in Figure 1. In this case the shock which is tracked and treated separately by solving a Riemann wave problem across the two adjacent meshes to the shock, is represented more or less perfectly to within a positional accuracy of one mesh, but the contact surface not so treated is still smeared by the numerical diffusion. All three methods predict the mean positions of the shock contact surface and expansion quite accurately for this one-dimensional problem.

TWO-DIMENSIONAL SHOCK DIFFRACTION

We have not applied the shock fitting technique to general two-dimensional problems so far because of the difficulty of tracking compression waves with complete unambiguity. However the FCT version of the Donor Cell technique can be extended to two space dimensions without any great difficulty. In the present case a regular rectangular mesh has been used and the flux corrected anti-diffusion applied in the two directions sequentially by operator splitting. This type of two-dimensional technique can sometimes lead to problems for discontinuities propagating obliquely to the axes of the mesh. As a test of this the result of computing a plane shock propagating at 45° to the mesh is also shown in Figure 1 to be captured with the same resolution as the one-dimensional shocks.

One of the important questions arising from the use of finite difference schemes for diffraction problems is the accuracy with which they cope with flow near the sharp edge. Diffraction at the edge of a flat plate (180° edge) is likely to be most critical for this aspect of the method.

WEAK SHOCK DIFFRACTION AT A SEMI-INFINITE PLATE

In the case of a very weak shock (or acoustic pulse) it is possible to construct an analytical solution for the flow field as a check of the accuracy of the numerical method.

We consider the case of a plane weak shock propagating at the ambient sound speed along a semi-infinite plate past its edge as shown in the inset diagram in Figure 2. The classical attached flow solution for the diffracted acoustic pressure field was given by Friedlander (1958) for this case as:

$$\left. \begin{aligned} p_d &= p_\infty + \Delta p_s \left\{ 1 - \frac{1}{\pi} \tan^{-1} [\operatorname{cosec}(\theta/2) \cdot 1/\sqrt{2} (1/\tilde{r} - 1)^{1/2}] \right\} & y > 0 \\ &= p_\infty - \frac{1}{\pi} \Delta p_s \tan^{-1} [\operatorname{cosec}(\theta/2) \cdot 1/\sqrt{2} (1/\tilde{r} - 1)^{1/2}] & y < 0 \end{aligned} \right\} \quad (1)$$

in the diffraction region, $\tilde{r} < 1$, where Δp_s is the strength of the pressure jump across the shock wave. The diffracted wave front forms a circular boundary to this region. Outside it, $p = p_\infty$ in the undisturbed region (1) and $p = p_\infty + \Delta p_s$ behind the shock (region 2). However this solution has a singularity in the velocity at the edge which is suppressed in reality by the shedding of a vortex sheet from the edge. Rott (1956) has shown how the strength of the shed vorticity is related to the shock strength through the application of the Kutta-Joukowski condition at the edge. The vortex sheet rolls up into a self-similar spiral vortex, and in the case of weak shocks, the local flow field associated with the vortex may be calculated asymptotically from Laplace's equation for an inner incompressible flow in the neighbourhood $\tilde{r} \ll 1$ of the edge.

By matching such an inner solution to the outer diffracted flow, using here for simplicity the Brown and Michael (1955) model for a concentrated rolled up vortex (see Graham, 1977) we obtain:

$$\Gamma(\text{vortex strength}) = 2^{4/3} \pi^{-1/3} \Lambda^{4/3} a^2 t \quad (2)$$

$$\text{and } \tilde{x}_v, \tilde{y}_v \text{ (vortex centroid)} = (0, -2^{4/3} \pi^{-2/3} \Lambda^{2/3}) \quad (3)$$

where Λ is the shock strength parameter $\Delta p_s / \rho a^2 (= \Delta p_s / \gamma p_\infty)$. This shed vorticity induces an acoustic pressure field which modifies the pure diffraction field p_d given by equation (1). The result to lowest order in the shock strength parameter as $\tilde{r} \rightarrow 1$, the wave front, is:

$$p = p_d + 2^{-5/6} \cdot 3 \pi^{-5/3} \Lambda^{2/3} \Delta p_s \sin \theta / 2 (1/\tilde{r} - 1)^{1/2}. \quad (4)$$

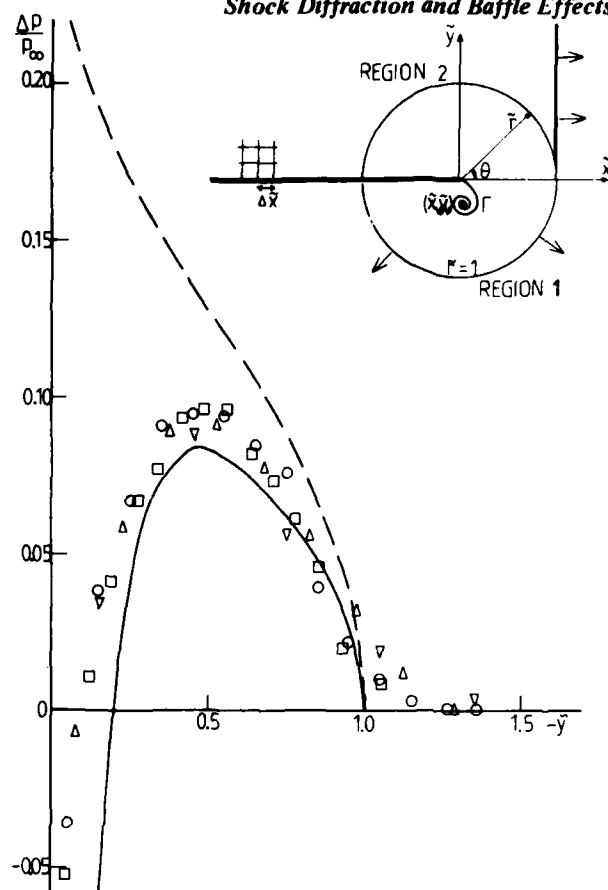


FIGURE 2 Weak Shock Diffraction.

Flux corrected transport numerical calculations: ∇ : $\Delta\tilde{x} = 0.30$,
 Δ : 0.15, \circ : 0.10, \square : 0.075. ---- Theory, pure diffraction
 (eqn 1), — Theory, diffraction + vortex.

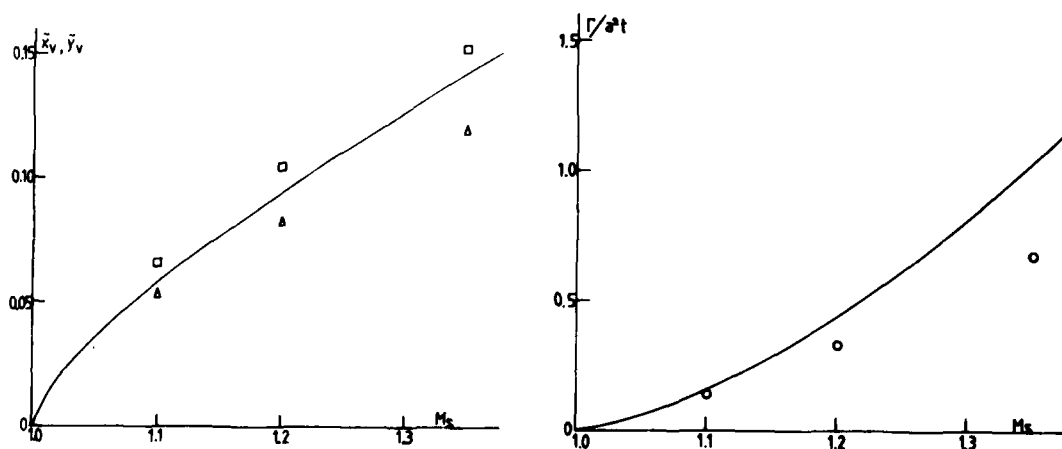


FIGURE 3 Vortex Strength and Position.

F.C.T. calculated position of vortex centroid $\square \tilde{x}, \Delta \tilde{y}$ and
 \circ strength. — Theory, diffraction + vortex.

The pressure field over the whole diffracted flow region $\tilde{r} \leq 1$ can be obtained as a more lengthy expression by similarly adding the vortex and diffraction fields.

The result of this calculation is compared in Figure (2) with the numerical computation for a shock propagating initially at a Mach number $M_s = 1.2$ ($\Lambda = 0.365$). This shows good agreement between the numerical calculation for the pressure field along the $\theta = -90^\circ$ axis and the analytical result including the effects of vortex shedding. The small pressure rise running ahead of the wave front, most noticeable for small elapsed times (large mesh size), is caused by the residual diffusion in the FCT method. The pure diffraction result is also plotted in the same figure and it is clear that the presence of the vortex has a large effect on the pressure in the shadow region. Figure 3 shows a plot of the vortex strength and position against shock strength (expressed as M_s here). The numerical computation of the inviscid Euler equations sheds about the correct amount of vorticity from the edge showing that the numerical viscosity is forcing a Kutta condition to apply. The y-coordinate of the vortex centroid is also in reasonable agreement with the asymptotic theory, but the streamwise position is overestimated. Not all of the vorticity generated by a diffracting shock comes from the edge, some being associated with fluid processed by the curved shock front. However the latter contribution is very small for weak shocks ($O(\Lambda^3)$). Bloor and Evans (1978) have similarly analysed the diffraction of a plane weak shock at a baffle in a channel using a multi-point representation of the vortex, but they did not derive the contribution of the vortex to the radiating acoustic field.

The dependence of the pressure field on the shock strength parameter Λ to the $2/3$ power indicates a monotonic reduction with increasing Λ of the peak value of $(p - p_\infty)/\Delta p_s$ in the shadow region. However the numerical results show that for M_s above about 1.5 the asymptotic weak shock theory starts to overestimate this reduction considerably.

The above problem is the simplest shock diffraction problem. The next simplest is the closely related normal flat plate problem for which a reflected shock is also generated. Similar analysis including the effect of the shed vortex has been carried out for this case also, and indicates a similar magnitude and sign of the effect.

STRONG SHOCK DIFFRACTION

Once the incident shock-wave is sufficiently strong that the post-shock flow is supersonic, the subsequent diffraction must be accompanied by a rarefaction fan centred upon the edge. This is illustrated by the sketch in Figure 4 (plotted in the pseudo-stationary coordinates \tilde{x}, \tilde{y}) where the limits of the diffraction field are marked by the reflected acoustic wave propagating back into the post-shock fluid (AE) and by the diffracting shock (EF). Within this region the existence of various disturbances can be postulated or have been identified experimentally (e.g. Skews, 1967a, 1967b; Bazhenova et al., 1971). The initial expansion is a truly steady region, turning the fluid to the appropriate separation angle for the vortex sheet at A. The precise boundary between this region and the pseudo-steady flow is unclear but is located in part at the secondary rearward-facing shock BC which accommodates the accelerated flow from the expansion fan to the slower fluid behind the diffracting shock. This secondary shock will also interact with the vortex sheet and vortex D.

Computations have been confined to one shock Mach number ($M_s = 2.5$, post-shock Mach number = 1.193) and were terminated once the shock reached a boundary of a 50×50 square cell grid. Figure 5 shows the predicted variation in the pressure rise at the diffracted shock (pressure rise normalised by the value behind the initial incident shock, angle θ measured relative to the

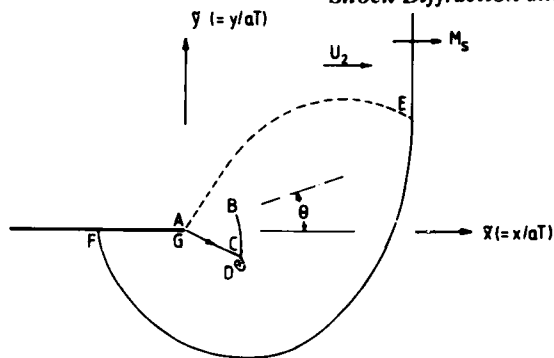


FIGURE 4 Schematic for Strong Shock Diffraction.

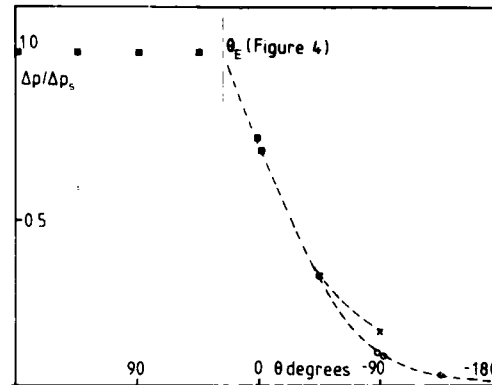


FIGURE 5 Angular Variation of Pressure at Shock.
 $M_s = 2.5$. (\circ , 180° diffraction; \times 90° diffraction).

diffraction edge) for deflection angles of 90 degrees and 180 degrees. The position $\theta = 26.6$ degrees is the exact angle for the intersection between the reflected acoustic wave and the diffracted shock (position E of Figure 4) in both cases; for angles less than this the pressure rise at the edge of the diffraction field should then simply be given by the post incident shock value. The computations appear to represent this limit quite well, the departure associated with numerical diffusion and with a weak pressure overshoot at the shock still only being slight for these FLIC calculations. For the 90° diffraction case the computed pressure rise at the wall ($\theta = -90^\circ$) of 15.8% of the incident shock strength compares favourably with the value of 19.5% inferred from shock speed data in Skews' (1967a) experiments so that it appears that the relative attenuation of the blast from its initial value is well modelled numerically. For the 180° diffraction the final shock strength ($\theta = -180^\circ$) is less than 1% of the initial incident shock strength, relatively a much more significant attenuation than occurs in the weak shock examples (e.g. 8% computed for $M_s = 1.2$).

One feature which differentiates the strong shock from the weak shock examples is the increased contribution to the vorticity field expected from the shock system in addition to that generated by separation from the edge. The total vorticity for the 180° diffraction case is given simply by the contour integral of the tangential component of velocity around the circuit GAEFG of Figure 4. The contribution from the shock segment EF is zero since the shock moves normal to itself, and neglecting the velocity along the segment FG (which is justifiable for this large diffraction/strong shock problem) gives a good approximation to the total vorticity as simply the product of the post incident shock velocity (U_2) and the projection, in the x-direction, of the segment AE. In suitable dimensionless form this gives

$$\tilde{\Gamma}_T \approx \frac{M_s U_2}{a},$$

or

$$\tilde{\Gamma}_T \approx \frac{2}{\gamma+1} (M_s^2 - 1).$$

For $M_s = 2.5$ this gives $\tilde{\Gamma}_T = 4.37$ compared with a computed value of 4.47 obtained by integrating the vorticity over the whole computational field, the small difference reflecting either the neglect of the wall velocity or slight errors associated with the numerical diffusion of the diffracted and reflected wave fronts. For the 90° deflection the computed value of $\tilde{\Gamma}_T$ is 4.01, the difference compared with the 180° case arising now from a significant increase in wall velocity or shock strength. Figure 6 presents computed contours of vorticity indicating that this is still primarily associated with the vortex/vortex sheet rather than being generated by the shock system. It is difficult, unambiguously, to identify that vorticity associated specifically with the flow separation ($\tilde{\Gamma}_v$). A computed value of 3.5 (for $\tilde{\Gamma}_v$) was obtained for the

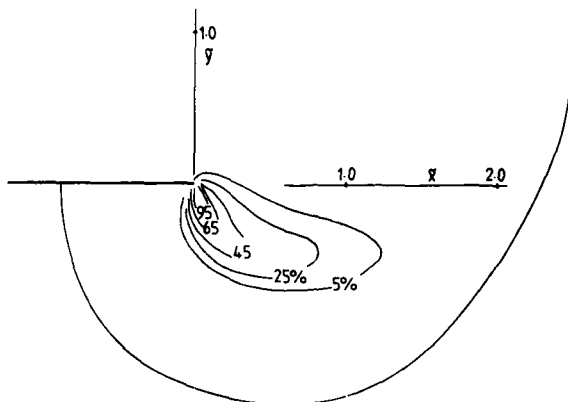


FIGURE 6 Constant Vorticity Contours (% of maximum).

$M_s = 2.5$, 180° diffraction.

region within the 5% contour which agrees well with the simple assumption that the vortex sheet is fed by fluid at the velocity (U_3) appropriate to the downstream side of the Prandtl-Meyer expansion (assuming expansion of the fluid down to ambient pressure). This gives

$$\tilde{\Gamma}_v \approx \frac{1}{2} U_3^2 / a^2$$

or that $\tilde{\Gamma}_v = 3.81$ for $M_s = 2.5$, supporting the computed predictions. This simple model always implies, in fact, that the flow separation provides the dominant contribution, as shown in Table 1, although in practice it will be somewhat reduced since the initial flow will almost certainly not accelerate fully to the ambient pressure and, more importantly, the interaction of the secondary (rearward-facing) shock with the slipstream can generate vorticity of the opposite sign.

M_s	$\tilde{\Gamma}_v / \tilde{\Gamma}_T$ (theory)
2.2	0.89
2.5	0.87
4.0	0.85
6.0	0.85
∞	1.0

Table 1 Variation of $\tilde{\Gamma}_v / \tilde{\Gamma}_T$ with M_s .

SHOCK WAVE DIFFRACTION BY A SEQUENCE OF BAFFLES

The earlier examples demonstrate an ability to predict realistically the diffracted shock strength. This next problem applies the FLIC program (without antidiffusion) to the problem of the attenuation of an initially plane shock wave ($M_s = 2.5$) propagating through a sequence of 'baffles' or 'orifice plates' into a gas with ambient speed of sound a ($\gamma = 1.403$). The axisymmetric geometry shown in Figure 7 and 8 was employed, starting the computation at time $T = 0$ with the shock emerging from the tube shown at position $X = 0$.

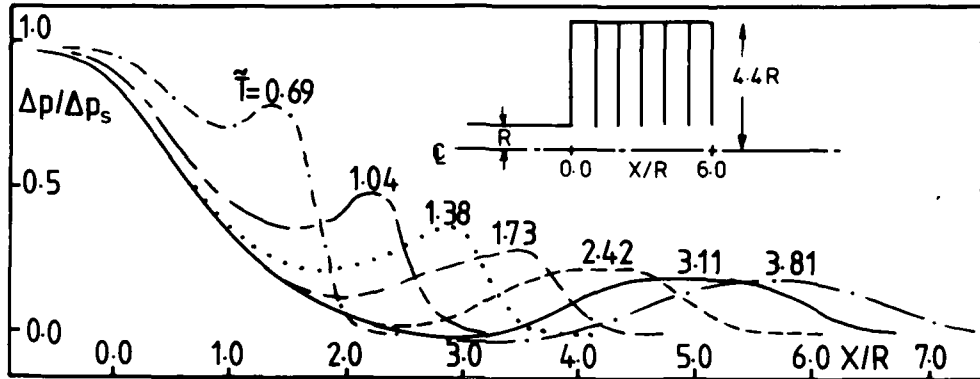


FIGURE 7 Shock Propagation through Sequence of Baffles. Large calibre, shock moving from left to right.

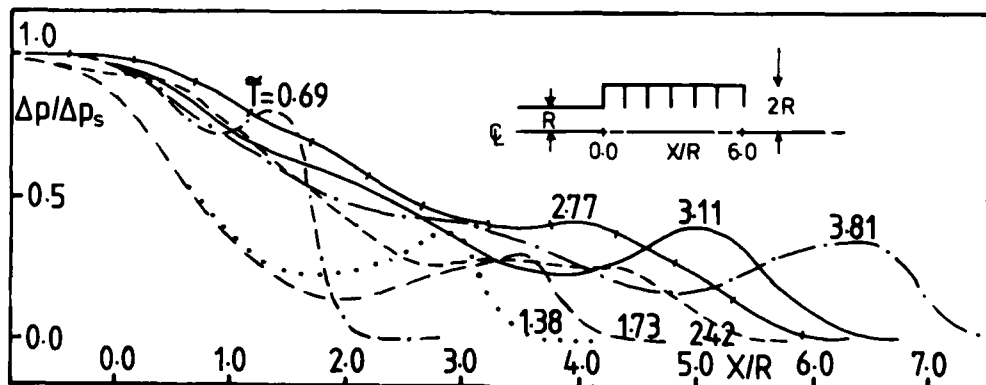


FIGURE 8 Shock Propagation through a Sequence of Baffles (2R calibre).

The computations were conducted on a square cell mesh, with 5 cells to the tube radius, and with both the baffle spacing and orifice radius fixed equal to R . Figures 7 and 8 present pressure distributions along the centre-line at various times ($T = Ta/R$), for configurations with outer radii of $4.4 R$ and $2.0 R$ respectively, the computations being continued until the incident shock wave had passed 6 baffles (in what can be regarded as effectively an infinite sequence). During this time, the larger radius case behaves effectively as if it were infinite, since there is insufficient time for the shock wave propagating into each cavity to reflect and return to the mainstream. Hence the incident shock motion is governed by diffraction alone, each baffle in turn attenuating the shock so that the distributions of Figure 7 show a monotonic

decay of strength with distance or time. Behind the shock wave an increasing extent of steady flow develops, as steady inflow becomes established to successive cavities, indicated by the progressive correlation with time of an ever increasing extent of the pressure distribution. The slight upstream influence from $X=0$ represents numerical diffusion of the initial expansion wave, similar to the increased spreading of the rarefaction wave noted for the shock tube problem in Figure 1.

With the 2.0 R outer radius the subsequent motion is more complex (although this might be the more realistic situation practically), being influenced by the relatively rapid filling of the cavities between baffles and the subsequent reflection of disturbances back into the main flow. Figure 8 shows that initially (up to the distribution for $\tilde{T}=1.73$) the flow follows the same development as in Figure 7, the baffles behaving as if of infinite capacity and a corresponding short steady flow region forming ($0 < X/R < 1.0$). After this time, however, this first cavity has been filled so that the pressure rises again from the initial steady value sending further compression waves after the initial shock to strengthen it again. The subsequent pressure distributions then show considerable departure from those in Figure 7, the shock pressure first rising to remain then more or less constant as the attenuating effect of baffles is compensated by the arrival of compression waves associated with the filling of further cavities.

CONCLUDING REMARKS

The diffraction calculations provide accurate pressure rises at the shock front (both weak and strong shock calculations) and appear to model realistically the effect of the shedding of vorticity from the diffraction edge. Resolution of the finer structure of the flow field is difficult, because of the numerical smearing of shock waves and contact surfaces over several cells, but can be improved by decreasing mesh sizes and by further development of anti-diffusion and discontinuity tracking algorithms.

ACKNOWLEDGEMENT

This work was sponsored by RARDE, UK MOD.

REFERENCES

- Bazhenova, T.V., Gvozdeva, L.G., Komarov, V.S. and Suchov, B.G. 1971. Proc. 8th International Shock Tube Symposium.
- Book, D.L., Boris, J.P. and Hain, K. 1975. Journal Comp. Phys. Vol. 18, 243.
- Bloor, M.I.G. and Evans, R.A. 1979. AIAA Jnl. Vol. 17, 1046.
- Brown, C.E. and Michael, W.H. 1955. NACA Tech. Note 3430.
- Friedlander, F.G. 1958. 'Sound Pulses', Cambridge Monographs on Mechanics and Applied Mathematics, C.U.P.
- Gentry, R.A., Martin, R.E. and Daly, B.J. 1966. Journal Comp. Phys. Vol. 1, 187.
- Graham, J.M.R. 1977. Imperial College Aero Dept, Report 77-06.
- Rott, N. 1956. Journal Fluid Mechanics, Vol. 1, 111.
- Saito, T. and Glass, I.I. 1980. Paper J5(2), XVth ICTAM Toronto.
- Skews, B.W. 1967a. Journal Fluid Mechanics, Vol. 29, 297.
- Skews, B.W. 1967b. Journal Fluid Mechanics, Vol. 29, 705.

AD P000265

PROPAGATION OF TWO-DIMENSIONAL NONSTEADY DETONATION
IN A CHANNEL WITH BACKWARD-FACING STEP

T. Sugimura
Department of Transport Machine Engineering
Meijo University, Nagoya 468, Japan

S. Taki
Department of Mechanical Engineering
Fukui University, Fukui 910, Japan

T. Fujiwara
Department of Aeronautical Engineering
Nagoya University, Nagoya 464, Japan

Re-establishment or quenching of a detonation at a corner is conceivably caused by the interaction of numerous triple shock waves contained in the frontal structure of the detonation; a combined effect of Prandtl-Meyer expansion and the disappearance of collision partner triple shock waves.

In this study, such processes are numerically simulated by allocating a rectangular blockage in a $b=7.4$ cm channel, where attention is focused on the behavior of the detonation in the vicinity of a backward-facing step. First, a stable detonation with periodical structure having two triple shock waves is worked out for a stoichiometric oxyhydrogen at $P_0=0.1$ atm. Then, the collision of one triple shock wave with the forward-facing step and the interaction of the other triple shock wave with the Prandtl-Meyer expansion from the backward-facing step are studied.

The effect of strong Prandtl-Meyer expansion causes the disappearance of the triple shock wave as a result of development of the decoupling between a leading shock wave and reaction. Two kinds of blockages are used; (1) 1.24 cm height (1/6 channel width) \times 2.48 cm length and (2) 3.7 cm height (1/2 channel width) \times 2.48 cm length.

The expansion effect from the backward-facing step in Case(2) is naturally more remarkable where the triple shock wave completely disappears. In contrast, the detonation in Case(1) is re-established, following a temporary decoupling lasting only during its passage of four channel width $4b=30$ cm.

INTRODUCTION

It is usually observed in the experiment that when a detonation propagates along a channel with rectangular corner, the number of existing triple shock waves decreases due to the Prandtl-Meyer expansion from the inner corner while the re-establishment occurs due to the wave reflection from the outer corner. Similar phenomena are observed when a steady detonation is subjected to sudden expansion of channel width.

Bach et al. (ref. 1) and Korobeinikov et al. (ref. 2) investigated the coupling or decoupling phenomenon between the leading shock wave and the flame front, using one-dimensional analysis.

In the present study, the behaviour of the triple shock waves in a 7.5 cm-channel with a blockage were numerically analysed for a two-dimensional non-

steady detonation. In order to obtain an initial condition, a detonation with periodical structure having two triple shock waves was carefully constructed by running the computer code from the starting condition; three concentration inhomogeneities in front of a plane one-dimensional C-J detonation. The parameters of the gas mixture were selected to agree with a stoichiometric oxyhydrogen mixture at $P_0 = 0.1$ atm (refs.3,4).

The calculation was made for the two blockages; (1) 1.24 cm height (1/6 channel width) x 2.48 cm length and (2) 3.7 cm height (1/2 channel width) x 2.48 cm.

EXPERIMENTAL

Fig.1(a) shows an open-shutter photograph of an equi-molar oxyacetylene detonation obtained in a 20 mm x 4 mm tube with rectangular corners at $P_0 = 4 \times 10^3$ Pa (30 Torr). The mesh-pattern in this figure depicts the emission trajectories of the numerous triple shock waves at the detonation front. When the detonation is subjected to a sudden change of its direction at the two corners, a transient process appears where some of the triple shocks clearly disappear and quenching nearly dominates, followed by the re-establishment of detonation each time.

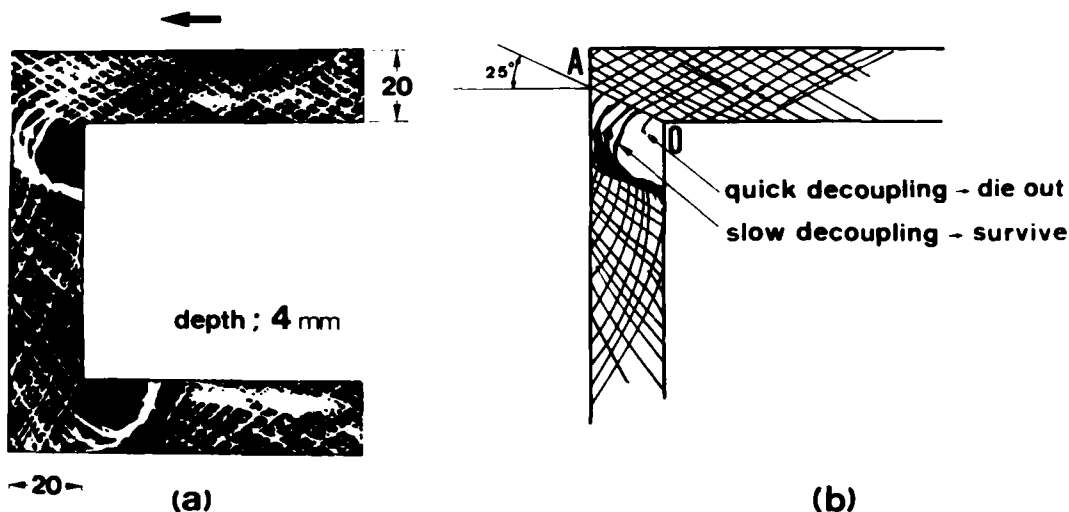


Fig.1 Open-shutter photograph of the emission from equi-molar oxyacetylene detonation in a channel with corners.
(a) photograph, (b) sketch.

Fig.1(b) is the schematic of Fig.1(a), showing the gradient 25° of the segment OA, the envelope of triple shock waves unaffected by the Prandtl-Meyer expansion from the corner. This approximate diffraction angle 25° can be obtained by considering a supersonic flow over a 90° corner. An inert shock wave having the propagation Mach number $M_0 = 8$ produces the trajectory OA the angle of which is 22.8° for the flow Mach number $M_1 = 1.8$, according to the Skews's theory (ref. 5). In the case of the oxyacetylene detonation the propagation Mach number of which is $M_0 = 8.0$ at $T_0 = 300$ K and $P_0 = 0.1$ atm, on the other hand, the induced supersonic flow is $M_1 = 2.68$ which is supposed to yield the diffraction angle 22.4° , fairly close to the observed angle 25° . It is noted that the limiting diffraction angle becomes 22.2° for $M_0 = \infty$, almost unchanged for a wide range of M_0 . On the line OA, numerous triple shock waves are simultaneously exposed to the Prandtl-Meyer expansion. At a closer distance along the line OA from the corner, the rate of expansion is more rapid and the decoupling between the shock and reaction fronts presumably occurs more severely. And therefore the triple shock waves disappear immediately after the expansion comes into effect. At a distance from the corner, in contrast, the

decoupling slows down and the triple shock waves can survive, as shown in Fig. 1 (b). The paths of the survived triple shock waves are curved due to the combined effects of inertia and expansion. When the Prandtl-Meyer expansion ends, the survived triple shocks start interacting each other and become strong enough to ignite the compressed gas and accordingly a coupled wave appears.

Aiming at studying the essential behavior of a detonation near a right-angled corner, the phenomena close to the backward-facing step of a blockage in a channel are experimentally and numerically observed and compared. Fig. 2 shows

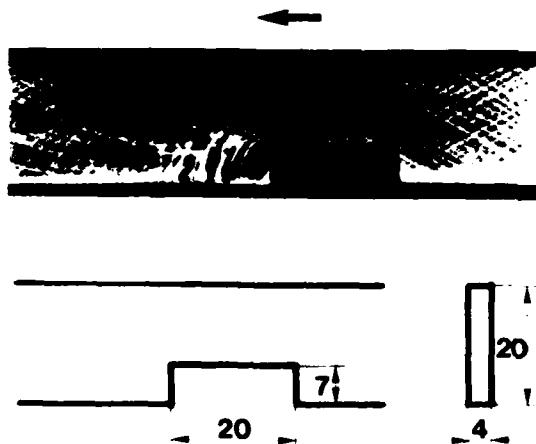


Fig. 2 Propagation of a detonation in a channel with a blockage. mixture: $C_2H_2 + O_2$, initial pressure $P_0 = 39.8$ Torr.

a typical example of the experimental results using the equi-molar oxyacetylene detonation at $P_0 = 5.2 \times 10^3$ Pa (39.8 Torr).

NUMERICAL ANALYSIS

The details of the present numerical method are identical to the one used by Taki and Fujiwara (refs. 3,4), which treated the development of a detonation into a periodical and multi-headed structure starting from a plane one-dimensional C-J one.

(1) Fundamental equations.

It is assumed that a gas mixture is perfect with constant specific heat and constant mean molecular weight, non-viscous and non-heat-conducting. Regarding the chemical reaction, complexity due to numerous elementary reactions is avoided by utilizing a two-step-reaction model originally worked out by Korobeinikov et al. (ref. 2). The parameters are selected to agree with stoichiometric oxyhydrogen reaction at $P_0 = 0.1$ atm. Thus, two-dimensional nonsteady reactive gasdynamic equations can be expressed as

$$\frac{\partial f}{\partial t} + \frac{\partial F}{\partial x} + \frac{\partial G}{\partial y} + \phi = 0 \quad (1)$$

$$f = \begin{bmatrix} \rho \\ \rho u \\ \rho v \\ \rho e \\ \rho \beta \\ \rho \alpha \end{bmatrix} \quad F = \begin{bmatrix} \rho u \\ \rho u^2 + p \\ \rho uv \\ \rho u \{e + (p/\rho)\} \\ \rho u \beta \\ \rho u \alpha \end{bmatrix} \quad G = \begin{bmatrix} \rho v \\ \rho vu \\ \rho v^2 + p \\ \rho v \{e + (p/\rho)\} \\ \rho v \beta \\ \rho v \alpha \end{bmatrix} \quad -\phi = \begin{bmatrix} 0 \\ 0 \\ 0 \\ 0 \\ \rho w \beta \\ \rho w \alpha \end{bmatrix} \quad (2)$$

$$p = \rho RT \quad (3)$$

$$e = RT/(\gamma - 1) + \beta q + 1/2(u^2 + v^2) \quad (4)$$

where u , v , p , ρ , T , q and R denote the velocities in x - and y -direction, the pressure, the mass density, the temperature, the exothermicity per unit mass and the gas constant, respectively. The detailed forms of reaction rates are

$$w_\alpha = \frac{d\alpha}{dt} = \frac{-1}{\tau_{ind}} = -k_1 \rho \exp(-E_1/RT) \quad (5)$$

$$w_\beta = \frac{d\beta}{dt} = -k_2 p^2 \{ \beta^2 \exp(-E_2/RT) - (1-\beta)^2 \times \exp(-\frac{E_2 + q}{RT}) \} \quad (6)$$

where α is the progress variable for the induction reaction, starting from 1 at the shock front decreasing down to 0, when β the progress variable for the exothermic reaction begins to decrease from 1 to its equilibrium value, and the reaction parameters are as follows:

$$k_1 = 3.0 \times 10^{11} \text{ cm}^3/\text{g}/\text{sec}, \quad k_2 = 1.5 \times 10^{-7} \text{ cm}^4/\text{dyn}^2/\text{sec}, \quad (7)$$

$$q = 4 \times 10^{10} \text{ erg/g}, \quad E_1/R = 9800 \text{ K}, \quad E_2/R = 2000 \text{ K}, \quad \gamma = 1.4.$$

(2) Dimensionless forms.

The fundamental equations (1) through (6) can be written in dimensionless forms, utilizing the following three characteristic quantities: ℓ^* , ρ_0 and q , where ℓ^* indicates the induction distance associated with the Neumann spike defined by

$$\ell^* = \frac{u_N}{k_1 \rho_N} \exp(E_1/RT_N). \quad (8)$$

In other words, the quantities used for non-dimensionalization are ℓ^* , ρ_0 , q , $t^* = \ell^*/\sqrt{q}$, $T^* = q/R$, $u^* = \sqrt{q}$ and $p^* = \rho_0 q$.

(3) Finite difference equations.

The differential equation (1) can be approximated by the first-order, central difference method originated by Van Leer (ref. 6):

$$f_{\ell,m}^{n+1} = f_{\ell,m}^n - (\lambda/2) [(F_{\ell+1} - F_{\ell-1})_m + (G_{m+1} - G_{m-1})_\ell]^n - \Delta t \phi_{\ell,m}^n \\ + (\lambda^2/2) [(\phi_{\ell+1/2} - \phi_{\ell-1/2})_m + (\phi_{m+1/2} - \phi_{m-1/2})_\ell]^n \quad (9)$$

$$\phi_{\ell+1/2,m}^n = (a^2)_{\ell+1/2,m}^n (f_{\ell+1,m}^n - f_{\ell,m}^n) \quad (10)$$

$$\phi_{\ell-1/2,m}^n = (a^2)_{\ell-1/2,m}^n (f_{\ell,m}^n - f_{\ell-1,m}^n)$$

$$(a^2)_{\ell+1/2,m}^n = 1/2 [(a^2)_{\ell+1,m}^n + (a^2)_{\ell,m}^n] \quad (11)$$

$$a = \sqrt{\gamma RT} + \sqrt{u^2 + v^2} \quad (12)$$

$$\lambda = \frac{\Delta t}{\Delta x} = \frac{\Delta t}{\Delta y} \quad (13)$$

where (ℓ, m, n) denote a lattice point in x - y - t space, and $\Delta x = \Delta y$ and Δt are the difference steps in space and time. The $n+1$ -th time step Δt_{n+1} is determined by the stability condition:

$$\Delta t_{n+1} = 1 / \max \left\{ a \sqrt{\frac{1}{(\Delta x)^2} + \frac{1}{(\Delta y)^2}} \right\}_{\ell, m, n} \quad (14)$$

(4) Initial and boundary conditions.

First, the characteristic parameters for the C-J detonation are found from the reaction parameters in Eq.(7). A periodical two-dimensional non-steady detonation is numerically produced (refs. 3,4) by positioning several pairs of concentration inhomogeneities in front of a steady plane detonation.

Utilizing the channel width $b=20\lambda^* = 7.4$ cm, a detonation with final periodical structure having two triple shock waves was constructed; starting initially from giving three pairs of concentration inhomogeneities in front of a plane one-dimensional C-J detonation, and requiring to run seven channel widths or 215 μ sec. A blockage was positioned in front of this well-developed two-dimensional nonsteady detonation; additional 9 μ sec was needed before the detonation arrived at the blockage.

Boundary conditions were satisfied by assuming a reflection on both the channel and blockage surfaces, because of non-catalytic and non-viscous walls.

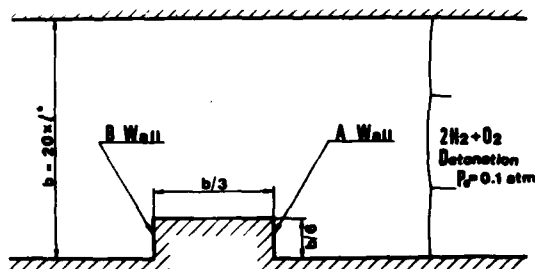


Fig.3 A detonation prior to interaction with a short blockage.

NUMERICAL RESULTS AND DISCUSSIONS

(1) Validity of difference scheme: The present method was applied to a plane one-dimensional shock wave at a right-angle corner, in order to check its appropriateness from quantitative point of view. A shock wave was initiated from a discontinuous step profile and did not encounter the corner until the profile settled into a steady finite-rise one.

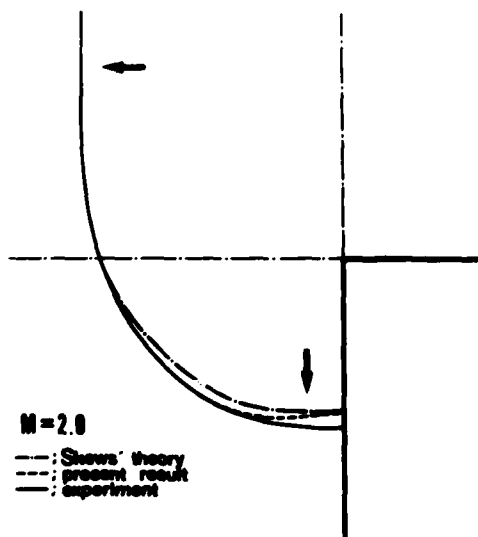


Fig.4 Validity of difference scheme: Application to inert shock diffraction at a corner.

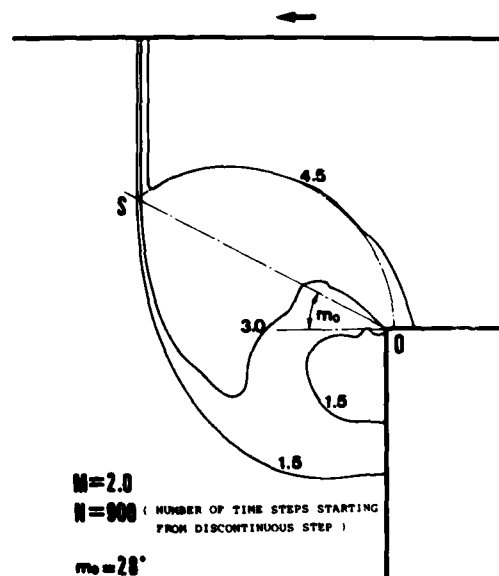


Fig.5 Pressure profile of an inert shock wave near backward-facing step. Solid and chain curves denote the isobaric curves, and the reflected sound wave, respectively. S: the starting-point of shock curvature.

An example of shock diffraction result at a corner is shown in Fig.4. The numerical result shows a generally good agreement with the experimental observation (ref. 5), except near the wall where it approaches the Skews' theory (ref. 5). As a result, the shock wave exhibits an overhang near the backward-facing step, as often indicated in the case of higher Mach numbers.

A snapshot of the pressure distribution near the corner is typically illustrated in Fig.5. It shows the domain of Prandtl-Meyer expansion, where rapid attenuation and deceleration of the shock wave are noted. Quantitatively speaking, the calculated diffraction angle 28° and a spherical reflected sound wave are in exact agreement with the Skews' theoretical results, which implies that this method can be most appropriately applied to the present

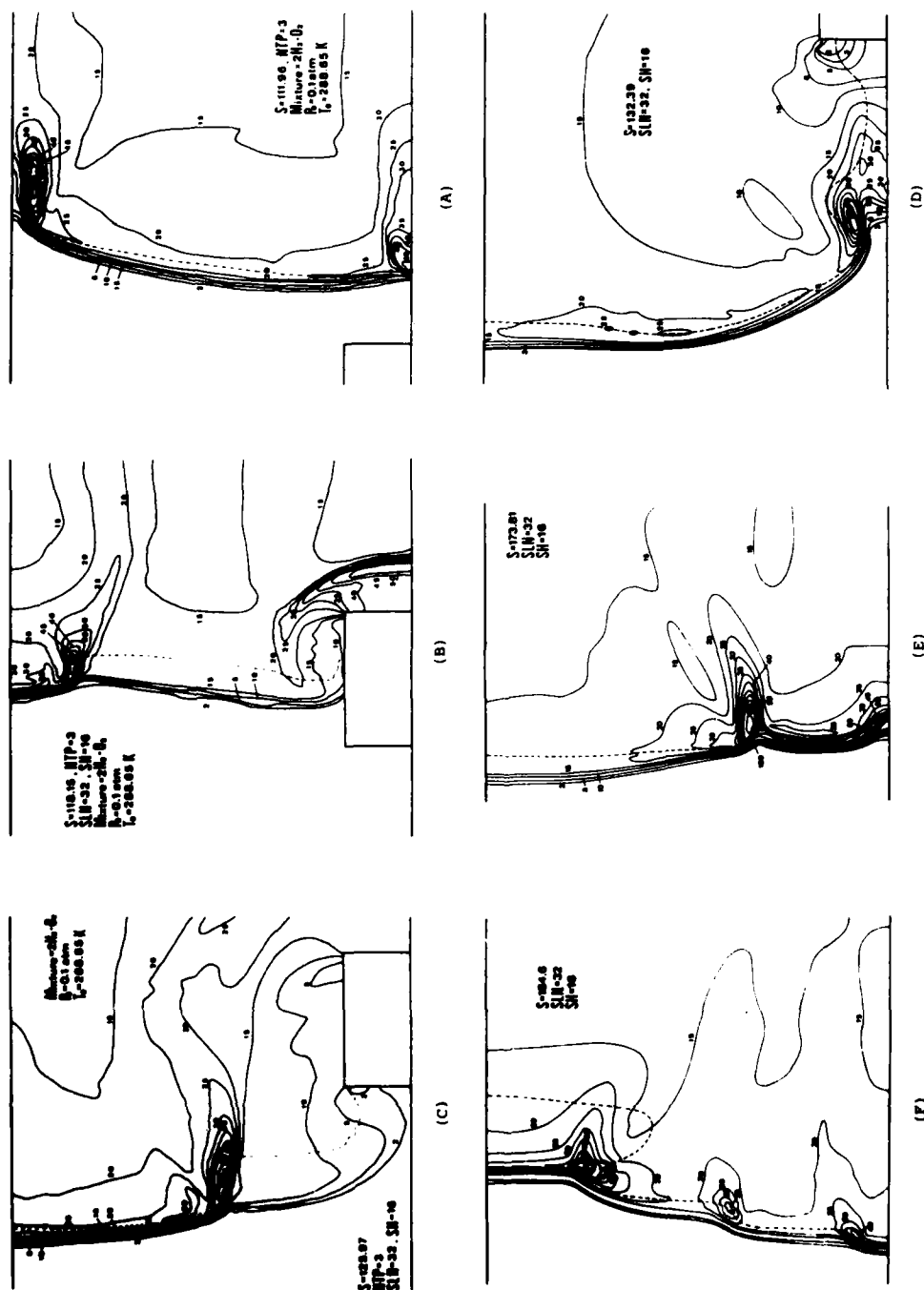


Fig.6 Interaction with a short blockage.

$2H_2 + O_2$ detonation: $M_{C-J} = 4.8$, $P_0 = 0.1$ atm.

Blockage: 2.47 cm length x 1.23 cm height ($h/b = 1/6$).

detonation diffraction at a corner.

(2) Detonation over a short blockage: First, the calculation was carried out for a short blockage: height $b/6 = 1.24$ cm x length $b/3 = 2.48$ cm. Figs. 6(A)~(F) show a sequence of interaction between a detonation and the blockage, where the behavior of the detonation is illustrated by the isobaric curves (solid lines) and the reaction front (broken line).

Fig. 6(A) shows a well-established two-dimensional detonation prior to the encounter with the blockage. It contains two developed triple shock waves travelling upward and downward. These triple shocks eventually collide with the channel walls, as shown in Fig. 6(A), and then start interacting with the blockage. Since the lower triple shock directly interacts with the forward-facing surface of the blockage, as shown in Fig. 6(B), this triple shock disappears after it forms a strong reflected shock in the inert burnt gas (Fig. 6(C)). Meanwhile the healthy upper triple shock is moving downward by the time when the bottom detonation front comes by the rear corner of the blockage. Throughout Figs. 6(B)~(D), an appreciable decoupling exists between the leading shock and reaction front, in particular, behind the blockage, as shown in Fig. 6(D). Later on, however, such a wide unburnt region is wiped out and a single-triple-shock structure prevails until the second and the third triple shocks emerge in Figs. 6(E) and (F). Thus, it can be concluded that although the disappearance of one out of two triple shocks is triggered by the interaction with a short blockage, this lasts only temporarily and returns to a multi-headed structure after propagating about three channel widths.

Such temporary decoupling and re-establishment are more explicitly shown in Figs. 7(a) and (b). According to Fig. 7(b), in particular, decoupling is

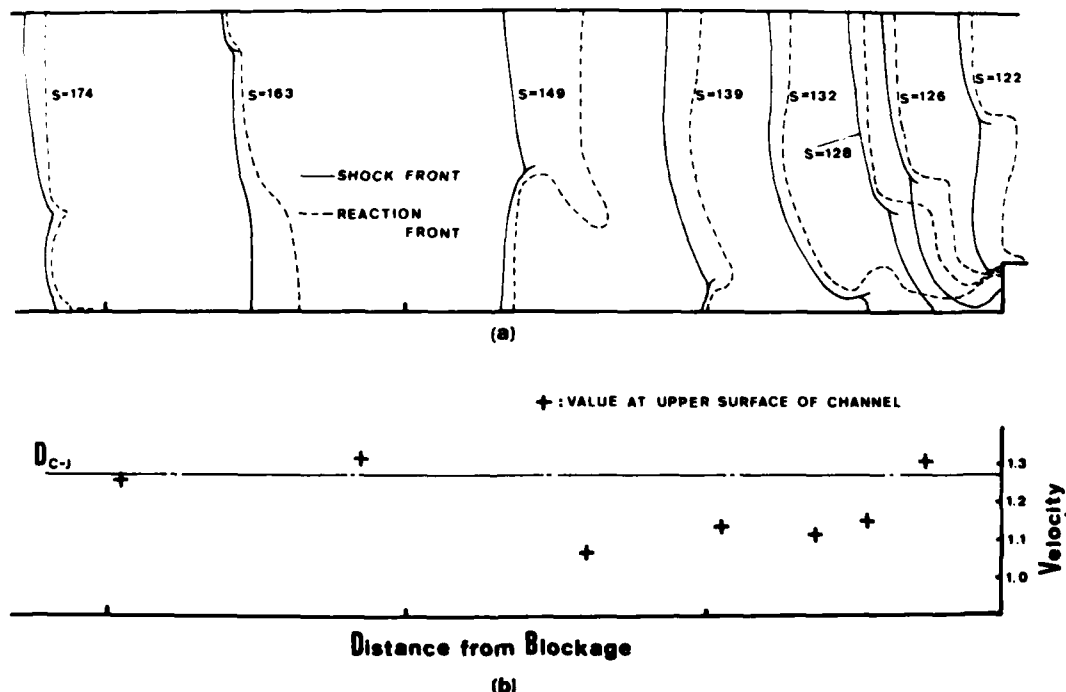


Fig. 7 Short blockage: (a) Coupled detonation after interaction.
(b) Propagation velocities at two typical places on detonation.
 D_{C-J} (dimensionless) = 1.27.

clearly the result of one triple shock disappearance, causing the wavelength of propagation velocity pulsation about two channel widths, twice as long as in the case of two triple shocks. Accordingly, the survival of at least one triple shock is essential from the viewpoint of detonation re-establishment.

(3) Detonation over a tall blockage: A tall blockage, height $b/2 = 3.7$ cm

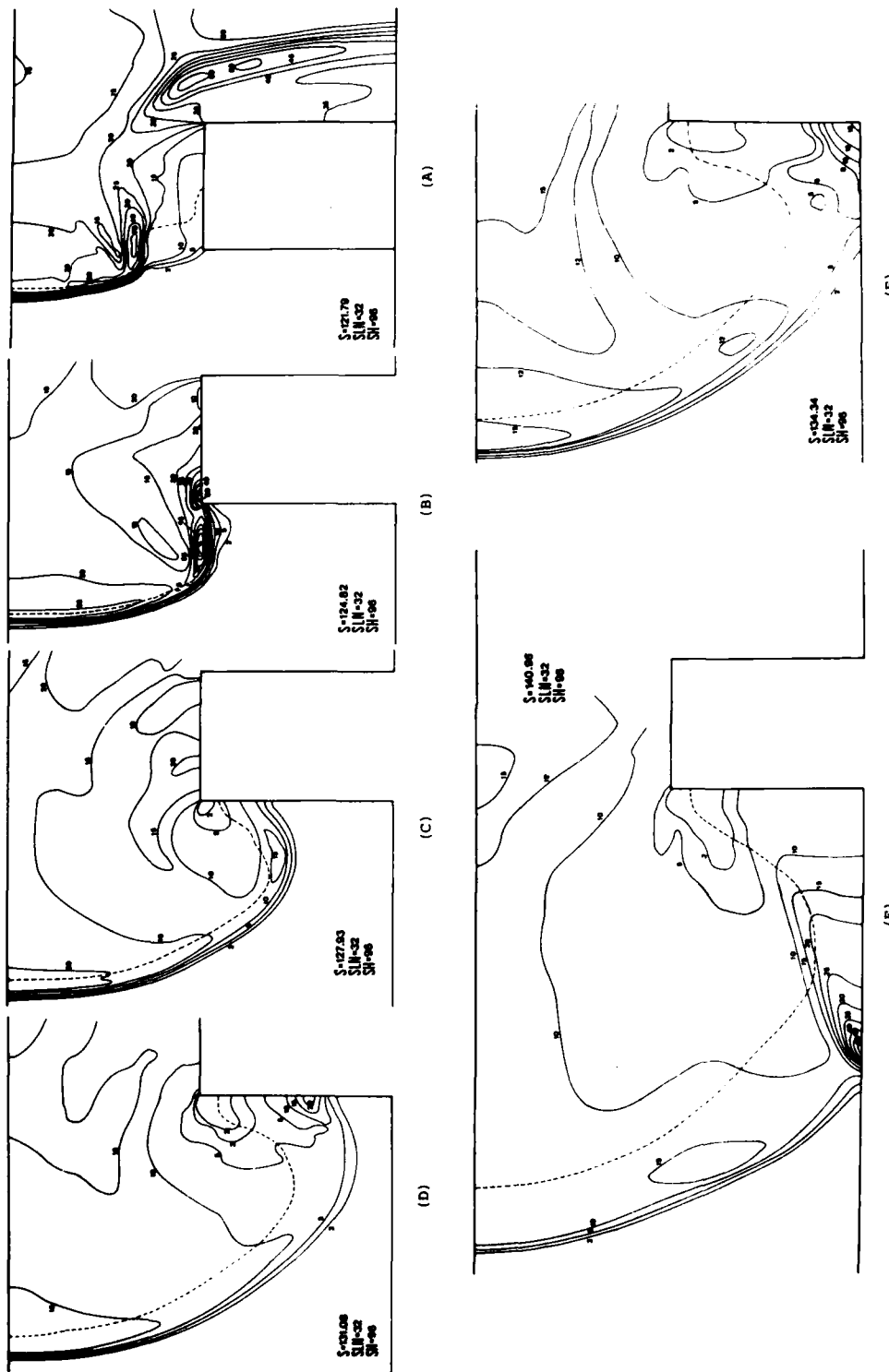
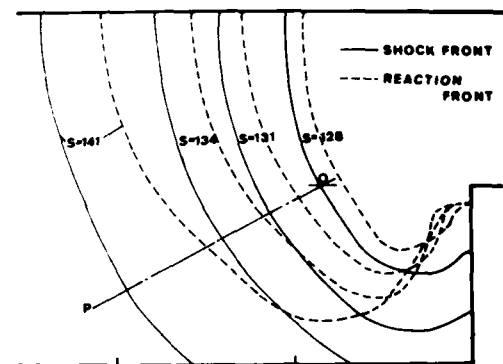


Fig.8 Interaction with a tall blockage ($h/b = 1/2$). Channel width: $b = 7.4$ cm.
 $2H_2 + O_2$ detonation: $M_{C-J} = 4.8$, $P_0 = 0.1$ atm.
 Blockage: 2.47 cm length x 3.7 cm height.

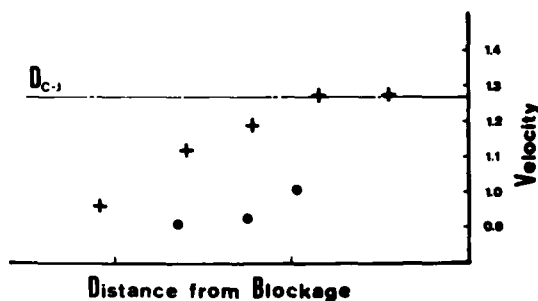
x length $b/3 = 2.48$ cm, is utilized to observe a stronger influence on the temporary behavior. The initial unperturbed detonation is identical with the one shown in Fig.6(A). As illustrated in Fig.8(A), only one triple shock remains intact when the detonation front reaches the rear corner. In Fig.8(B), this survived triple shock is just about entering into the influence of the

Prandtl-Meyer expansion. As seen in Figs.8(B) and (C), the strongly coupled shock and reaction throughout the wave front, in particular, at the triple shock, separate and weaken. In fact, the gas behind the blockage remains unreacted during the simulation, although in Fig.8(F) a newly-formed triple shock is seen; it is generated by the Mach reflection on the lower channel wall.

The decoupling characteristics are shown in Figs.9(a) and (b). In particular, the deceleration due to decoupling becomes maximum 30 % of the C-J propagation velocity, which would cause a complete quenching in additional simulation, unlike the previous short-blockage case.



(a)



+ : VALUE AT UPPER SURFACE OF CHANNEL
o : VALUE ON SEGMENT OP

(b)

Fig.9 A tall blockage: (a) Decoupled detonation after interaction. (b) Propagation velocities at two typical places of detonation. D_{C-J} (dimensionless)=1.27.

CONCLUDING REMARKS

(1) The effect of the Prandtl-Meyer expansion on the quenching and re-establishment of a detonation can be controlled by changing the height of a blockage in a channel.

(2) The decoupling between the shock and reaction fronts takes place rapidly by the strong Prandtl-Meyer expansion from a corner, generating the disappearance of the triple shock.

(3) The reduction of the detonation velocity in normal direction becomes 30 % of the C-J value, when the decoupling reaches most conspicuous at the end of simulation.

References

1. G. G. Bach et al., 12 th Sympo. (Intern.) on Combustion, 853(1969)
2. V. P. Korobeinikov et al., *Astronautica Acta*, 17, 529(1972)
3. S. Taki and T. Fujiwara, *AIAA J.*, 16, 73(1978)
4. S. Taki and T. Fujiwara, 18 th Sympo. (Intern.) on Comb., in press, (1981)
5. B. W. Skews, *J. Fluid Mech.*, 29, 297(1967)
6. R. A. Strehlow et al., *Astronautica Acta*, 17, 509(1972)
7. B. Van Leer, *J. Comp. Phys.*, 3, 473(1969)
8. G. B. Whitham, *Linear and Nonlinear Waves*, Wiley-Interscience, 1974.

AD P000266

THE BLAST-NOISE ENVIRONMENT OF RECOILLESS RIFLES

D. Gladstone

Defence Research Establishment
Valcartier
Courcellettes, Quebec, Canada

E.G. Plett

Department of Mechanical and
Aeronautical Engineering
Carleton University, Ottawa,
Canada

The blast-noise environment of recoilless rifles is a complicated three-dimensional flowfield which must be understood before impulse noise levels in the operator's position can be reduced. Both breech blast (produced by a unsteady, underexpanded jet of hot propellant gas behind the weapon) and muzzle blast (produced by exit of gas both ahead of and behind the projectile) are important. A short survey of some of the experimental and numerical studies of both the breech blast and muzzle blast problems is presented here, followed by a description of the experimental approach used at DREV. Several of the pressure vs time profiles which were obtained are presented with the data for the operator's position appearing to indicate the occurrence of breech and muzzle blast interaction.

These data are compared with the results of two one-dimensional finite-difference models for the breech blast (one assuming spherical, the other cylindrical symmetry). The models are described in general terms with the key boundary conditions being emphasized. It is noted that they are first-order approximations and hence useful for preliminary and qualitative analysis. For quantitative analysis a three-dimensional model is needed and the approach being taken in developing such a code is described.

1.0 INTRODUCTION

Recoilless rifles use a supersonic nozzle behind the breech to vent propellant gas which is designed such that the momentum of the escaping propellant gas equals that of the projectile being fired, thus eliminating the need for a heavy recoil absorbing system. As a consequence of the unsteady flow through the nozzle, and the under-expanded jet formed behind it, a complex unsteady three-dimensional flowfield is formed around the weapon, whose major practical consequences are very high impulse noise levels in the weapon operator's position and a large danger area to the rear of the weapon. As a further complication, it is important to note that while the flow through the nozzle (termed breech blast in the remainder of this paper) is the main contributor to the blast-noise environment, the muzzle blast (produced by the exit of gas both ahead of and behind the projectile) is

also important, especially in the operator's position.

The literature shows a good deal of interest in the flowfields produced by both the breech and muzzle blasts, the major applications being a reduction of the peak noise level in the operator's position, limiting the impulsive loads on nearby structures, and muzzle blast effects on the projectile trajectory. Various approaches have been used including extensive experimental measurements, correlations of experimental data, theoretical analyses based on ideal blast wave theory, and numerical predictions.

Plett et al¹ and Schmidt² give good surveys of the breech blast and muzzle blast problems, respectively. While in both cases we are looking at the flowfield produced by an unsteady underexpanded jet, the pressure-time histories and boundary conditions are, however, different enough to warrant separate studies of each problem. Basic experimental data on breech blast is provided by Baker, Westine, and Bessey³, Clayden and Hillman⁴, and Pennelegion and Grimshaw⁵. Baker et al used a 57 mm recoilless rifle in their tests and also present data obtained for other recoilless rifles. Clayden and Hillman, while concentrating on the blast-noise environment of impulsive rockets, present an interesting overpressure contour plot for the 84 mm Carl Gustaf recoilless rifle. Pennelegion and Grimshaw used a blast simulator in their study, thus allowing more control of the gas parameters and more sophisticated instrumentation.

Detailed experimental surveys of the muzzle blast around small-calibre weapons have been performed by Schmidt and Shear⁶, Schmidt et al⁷, and Klingenberg⁸, amongst others. All are excellent studies of the problem with Ref. 6 presenting a series of high-quality photographs showing the development of the flow structure. Overpressure contour plots at various time intervals are presented as well as relations for the mach-disc and free-air blast trajectories (see Fig. 1 for a schematic diagram).

Correlations of published and unpublished experimental data are given by Baker et al³ for breech blast and Westine⁹ for muzzle blast. In their text, Baker, Westine and Dodge briefly discuss their correlation work, and present the highlights, including a scaled plot of overpressure directly behind the breech, the overpressure directly behind the breech, the overpressure being normalized using P_c , the peak chamber pressure and the distance behind the breech being normalized using the weapon calibre. Also presented is a plot of scaled overpressure 90° from the muzzle vs scaled distance. Further work in this area has recently been reported on by Westine and Ricker¹⁰. Although useful, these correlations are inadequate since they cannot be used to predict the peak noise levels in the operator's position and, further, provide only the barest indications of which physical processes and factors are important.

Given the trouble, expense, and uncertainty involved in obtaining experimental data, and the limitations of correlations, much effort has been expended, as in other areas of fluid dynamics and engineering, in numerical modelling of the breech blast and muzzle blast problems. Numerical analyses of the breech blast have been provided by Chiu et al^{11, 12} and Edwards and Hillman¹³. Adequate comparisons of these analyses with experimental data has yet to be carried out, however.

Finite-difference based numerical analyses of muzzle blast have been published by Schmidt and Shear⁴, Erdos and Del Guidice¹⁴, and Taylor and Lin¹⁵, amongst others. In general, fairly good agreement with experimental data is obtained in the region of the muzzle. No

predictions of far-field overpressures are presented and three-dimensional effects resulting from the presence of the ground-plane are not taken into account.

To summarize, while a good deal of work has gone into probings of the breech and muzzle blast problems, both are far from solved for engineering purposes, with the muzzle blast, however, being somewhat better understood.

2.0 EXPERIMENTAL WORK

Extensive data has been obtained at DREV in the last year in an attempt to define the major elements of the blast-noise environment of a typical recoilless rifle, the Swedish 84 mm Carl Gustaf. Fig. 2 gives a general schematic diagram of the configuration, the operator's position being, of course, just behind the aiming sights. While all recoilless weapons produce very high impulse noise levels in the operator's position, the Carl Gustaf is especially noisy because of the relatively high peak chamber pressure (the result of using erosively-burning propellant in a relatively small combustion chamber), the proximity of the operator to the muzzle, and the absence of any noise-reduction features. DREV has measured a reflected overpressure level of 6.3 psi on the operator's head, this value being equivalent to an impulse noise level of 186.7 db.

In an attempt to define the factors responsible for this high noise level the overpressure levels at several locations around a Carl Gustaf proof launcher (a thick-walled launcher equipped with pressure ports) were measured, along with the combustion chamber pressure, all on the same time scale. Three cartridge variants and two launcher heights were used, in order to examine the influence of the interior ballistics and ground-plane, respectively. In this paper only a small portion of this data will be presented for use in comparing with the two numerical models. The experimental data will be fully presented in a DREV report which is currently in preparation.

Fig. 3 shows the experimental set-up. Note that the pencil blast-pressure gauges and the lead head were mounted at the same height as the launcher, with the lead head being mounted in the operator's position and the pencil gauges being pointed at the nozzle exit plane.

Fig. 4 presents four of the pressure vs time traces (all with the same origin) which were recorded using a standard round of ammunition fired from a launcher 40 ins (15.7 cms) from the ground. The projectile exit-time which is indicated on the combustion chamber trace was obtained using a calibrated interior ballistics computer code. The three overpressure vs time traces provide an indication of the number of phenomena involved in producing the blast-noise environment. Sufficiently far behind the nozzle a classical blast wave is produced as shown in Fig. 4 (b). Ahead of the nozzle a comparatively strong shock-wave propagates towards the operator. Fig. 4 (d) shows, however, that not only the pulse of Fig. 4 (c), but the muzzle blast and ground-plane reflections play an important role in determining the overpressure level in the operator's position.

3.0 NUMERICAL MODELLING

Theoretical Considerations

The theoretical development used here is intended to represent, to a first order approximation, the processes involved in generating

the pressure pulse observed in the near field of the breech exhaust.

In this near field region, one could imagine that the jet is approximately cylindrical. Far from the breech, the source may appear more as a spherically symmetric flow than as a cylindrical flow, but near the jet, the cylindrical geometry is an appealing simplification.

The flow field has been treated as a cylindrically symmetrical flow and as a spherically expanding plane being pushed back by the expanding jet. The jet expands laterally as the nozzle exit-plane pressure increases. This in turn is caused by the pressure in the combustion chamber, rising as the propellant burns. A relationship between the jet expansion and the exit pressure could be developed analytically. Instead, an empirical relationship, based on experimental data is used, as follows for the cylindrical jet:

$$R_j/R_e = (p_e/p_j)^{\beta} \quad (1)$$

where R_j and R_e are the jet and exit plane radii, respectively, and p_e is the back pressure experienced by the jet at its outer boundary. This configuration is represented in Fig. 5. With this approach, the jet expands as the combustion chamber pressure increases and contracts as the chamber pressure decreases.

The numerical scheme used is a Lax-Wendroff two-step scheme¹⁸ in which the equations of mass, momentum and energy conservation are solved. A cylindrical grid with radial steps of 1 cm was used. The time increments were chosen during any step based on the maximum value of $(u + c)$ computed in the previous step, where u is the local particle velocity and c is the local sound speed. Then $dt = 0.5 \times dr/(u + c)_{\max}$ was used in each step, to ensure a reasonably rapid computation with a stable solution. An artificial viscosity was used, to enhance numerical stability. This has the effect of smearing a shock wave slightly.

The boundary conditions can be assigned to be as realistic as desired. At solid boundaries, there can be no flow through the boundary and the velocity adjacent to the boundary must assume the boundary velocity. At outer boundaries, conditions must be continuous; that is, the flow variables have zero gradient.

The jet-plane boundary in this problem was treated as a membrane through which there could be no flow but across which the pressure was continuous. As this membrane moved outward (inward), the abutting cell was compressed (rarefied) generating outward (inward) flow. After each two-step sequence, the computational grid was moved to provide regular sized cells everywhere; the flow variables in each cell were recalculated for the new positions-using interpolative conservation relations based on the values at adjacent points of the previous cell position.

Cylindrical Model

Figure 5 schematically shows the model parameters. The driving force for the generation of the blast field comes from the rapid expansion of an assumed cylindrically shaped jet. The relationship between the jet radius and the chamber and external pressures was given earlier in Eq. 1. From experimental data, the value of β was given by 0.633. Several chamber pressure profiles were tried to observe the effect of pressurization rate on the peak overpressures in the blast field.

Figure 6 shows the computed pressure profiles at various time intervals during the chamber pressure cycle. The rapid jet expansion rate at the initial time causes a large pressure increase at the jet surface. Since the jet expansion rate decreases thereafter, the pressure adjacent to the jet surface decreases, and the peak propagates radially outward, decreasing in amplitude due to the radial area increase effect. As the pressure adjacent to the jet surface continues to fall, an N-wave type profile develops.

Figure 7 shows the decay of the peak overpressure with radial distance for the case plotted in Fig. 6 as well as for two other chamber pressure profiles. As the rate of pressurization of the chamber is decreased, the jet radial velocity is correspondingly decreased resulting in smaller overpressures in the field surrounding the jet. This qualitative relationship between chamber pressurization rate and maximum blast overpressures has been observed in rocket firings. Therefore, the analysis has produced results which explain qualitatively what has been observed before, and has provided a means of predicting the relationship between these two phenomena, at least for an assumed simple geometric configuration.

Spherical Model

The size of the bubble is determined by the cumulative mass flow from the nozzle, and is given as follows:

$$4\pi \int_{R_{j0}}^{R_j} \rho_b r^2 dr = \left[\frac{\gamma}{R_g} \left(\frac{2}{\gamma+1} \right)^{\frac{\gamma+1}{\gamma-1}} \right]^{\frac{1}{2}} \int_0^{\tau} A^* p_c T_c^{-1/2} dt \quad (2)$$

The bubble growth rate is calculated by differentiating this expression, and given by:

$$\frac{dR_j}{dt} = \left\{ \left[\frac{\gamma}{R_g} \left(\frac{2}{\gamma+1} \right)^{\frac{\gamma+1}{\gamma-1}} \right]^{\frac{1}{2}} \frac{A^* p_c}{\sqrt{T_c}} - 4\pi \int_{R_{j0}}^{R_j} \frac{\partial \rho_b}{\partial t} r^2 dr \right\} / 4\pi \bar{\rho}_b R_j^2 \quad (3)$$

where $\bar{\rho}_b$ is the average density in the bubble and ρ_b is obtained by applying the conservation of mass and energy principles to the flow exhausting from the nozzle. This bubble growth rate is the driving effect for generation of the blast flow field.

Again, only near field pressures have been computed, due to the length of computation time required to reach the far field. Fig. 8 gives the plot of the resulting pressure pulses at various times after ignition. An initial peak is observed which propagates outward and decays due to area expansion effects. This is followed by a second rise, probably due to the nature of the chamber pressure variation.

4.0 DISCUSSION

A rough check of our experimental data is available by plotting the measured maximum free-field overpressure 10 m behind the nozzle exit-plane on Baker et al's correlation plot for recoilless rifles of maximum overpressures on a line 0° to the breech. In our case:

$$L/C = 10/0.084 = 119$$

and

$$P/P_c = 120/60,000 = 0.2 \times 10^{-3}$$

As can be seen from their plot³ this value falls near the best-fit line through the data.

A comparison of the numerical predictions with the experimental data is difficult to carry out given the somewhat different chamber pressure histories in the two cases and the availability of only one near-field overpressure profile, that of Fig. 3 (c). Some preliminary investigations have been carried out using the chamber pressure profile of Fig. 3 (a) as an input to the cylindrical model. These give results similar in form to Fig. 6, though the overpressures are, as might be expected, higher. Also the jet surface locus extends out to a considerably greater distance. At a radial distance of 1 m these preliminary results give a peak overpressure of approximately 20 psig, the measured peak overpressure from Fig. 3 (c) being approximately 10.3 psig. The cylindrical model appears to be valid as a first-order approximation. For quantitative predictions, the jet separation and blast-wave diffraction effects around the nozzle must, however, be taken into account.

In general, reducing the peak in the chamber pressure profile reduces the peak overpressure value in the environs of the weapons and also, because of the weaker shocks, delays the arrival of the pulse at a given location.

5.0 CONCLUSIONS

Various approaches to describing and analysing the blast-noise environment of recoilless rifles have been described and some recent experimental data presented. Two 1-D finite difference models have also been presented, along with some typical results. As the experimental data shows, one-dimensional models are clearly inadequate and better representations of the 3-D phenomena are required if reliable predictions of the peak overpressure are to be achieved.

ACKNOWLEDGEMENTS

Messieurs G. Audet, M. Savard, and R. Arsenault, as well as many others, helped obtain the experimental data. Part of the work reported on here was supported by DSS Contract No. 25D81-00017.

REFERENCES

1. E.G. Plett, H.H. Chiu, M. Summerfield, and C.W. Nelson, Blast-Noise Environment of Recoilless Rifle and Impulsive Rocket Firings Part I - Review of the State-of-the-Art, BRL R 1846, 1975.
2. E.M. Schmidt, Survey of Muzzle Blast Research, Proc. 5th Symposium on Ballistics, 1980.
3. W.E. Baker, P.S. Westine, R.L. Bessey, Blast Fields About Rockets and Recoilless Rifles, Southwest Research Institute, 1971, AD 885 260.
4. W.A. Clayden and A. Hillman, Some Recent UK Work on Noise from Shoulder-Launched Recoilless Weapons, Proc. 4th Symposium on Ballistics, 1978.
5. L. Pennelegion and J.F. Grimshaw, The Diffraction of the Blast Wave Emerging from a Conical Nozzle Driven by Compressed Gas, Proc. 12th Symposium on Shock Tubes & Waves, 1980.
6. E.M. Schmidt and D.M. Shear, The Flow Field About the Muzzle of an M-16 Rifle, BRL R 1692, 1974.

7. E.M. Schmidt, E.J. Gion, and K.S. Fansler, Analysis of Weapon Parameters Controlling the Muzzle Blast Overpressure Field, Proc. 5th Symposium on Ballistics, 1980.
8. G. Klingenberg, Investigation of Combustion Phenomena Associated with the Flow of Hot Propellant Gas, Combustion and Flame, Vol. 29, 1977, pp 289-309.
9. P.S. Westine, The Blast Field About the Muzzle of Guns, The Shock & Vibration Bull., No. 39, Part 6, 1969.
10. P.S. Westine and R.E. Wicker, Empirical Procedures for Estimating Recoilless Rifle Breech Blast Overpressures, Proc. 49th Shock & Vibration Symposium, 1978.
11. H.H. Chiu, E.G. Plett, M. Summerfield, and C.W. Nelson, Blast-Noise Environment of Impulsive Rocket Firings, AIAA Paper 74-48, 1974.
12. H.H. Chiu, H.H. Chiang, E.G. Plett, and M. Summerfield, BRL CR 274, 1975.
13. D.G. Edwards and A. Hillman, Computations of Rocket Blast Fields, Proc. 5th Symposium on Ballistics, 1980.
14. E.M. Schmidt and D.D. Shear, The Formation and Decay of Impulsive Supersonic Jets, AIAA Paper 74-531, 1974.
15. J. Erdos and P. Del Guidice, Calculation of Muzzle Blast Flow Fields, AIAA J., Vol. 13, No. 3, 1975.
16. T.D. Taylor and T.C. Lin, A Numerical Model for Muzzle Blast Flow Fields, AIAA Paper 80-0273, 1980.
17. Vick, A.R., Cabbage, J.M., and Andrews, E.H., Jr., "Rocket Exhaust-Plume Problems and Some Recent Related Research," The Fluid Dynamics Aspect of Space Specialists Meeting, Marseilles, France, April 20-24, 1964.
18. Lax, P.D. and Wendroff, B., "Systems of Conservation Laws," Communications of Pure and Applied Mathematics, Vol. 13 No. 2 (1960), pp. 217-237.

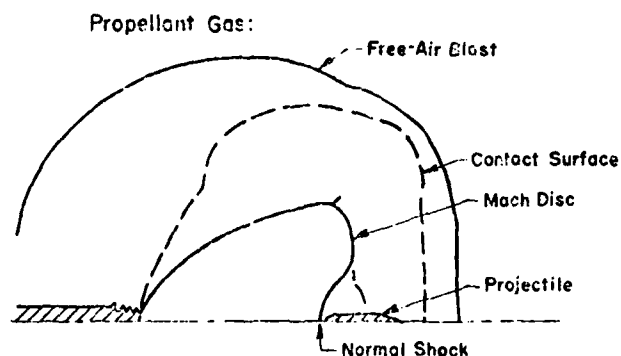


FIGURE 1 - Schematic of Muzzle Blast Flow Field (Ref. 14)

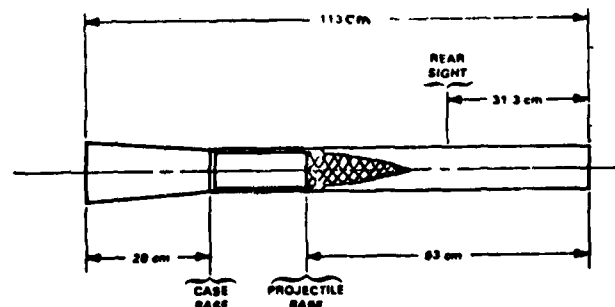


FIGURE 2 - Schematic Diagram of Carl Gustaf Recoilless Rifle

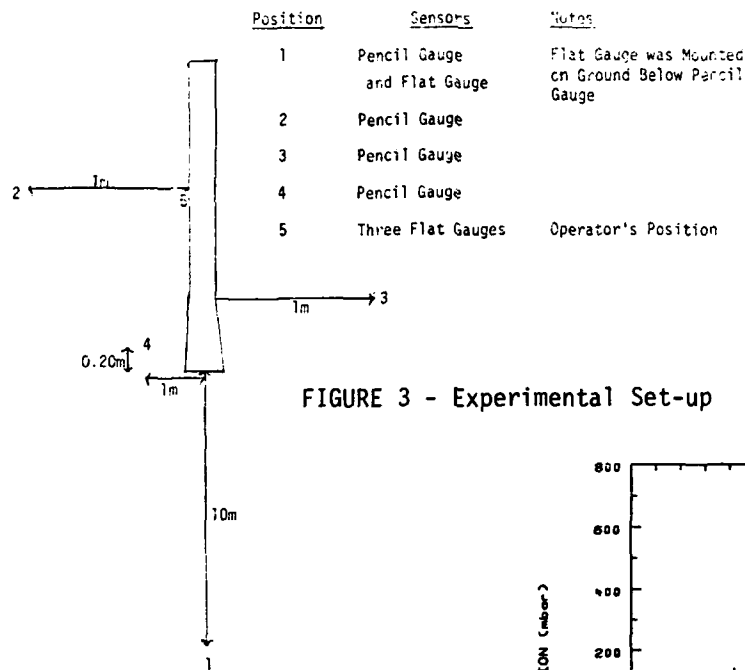


FIGURE 3 - Experimental Set-up

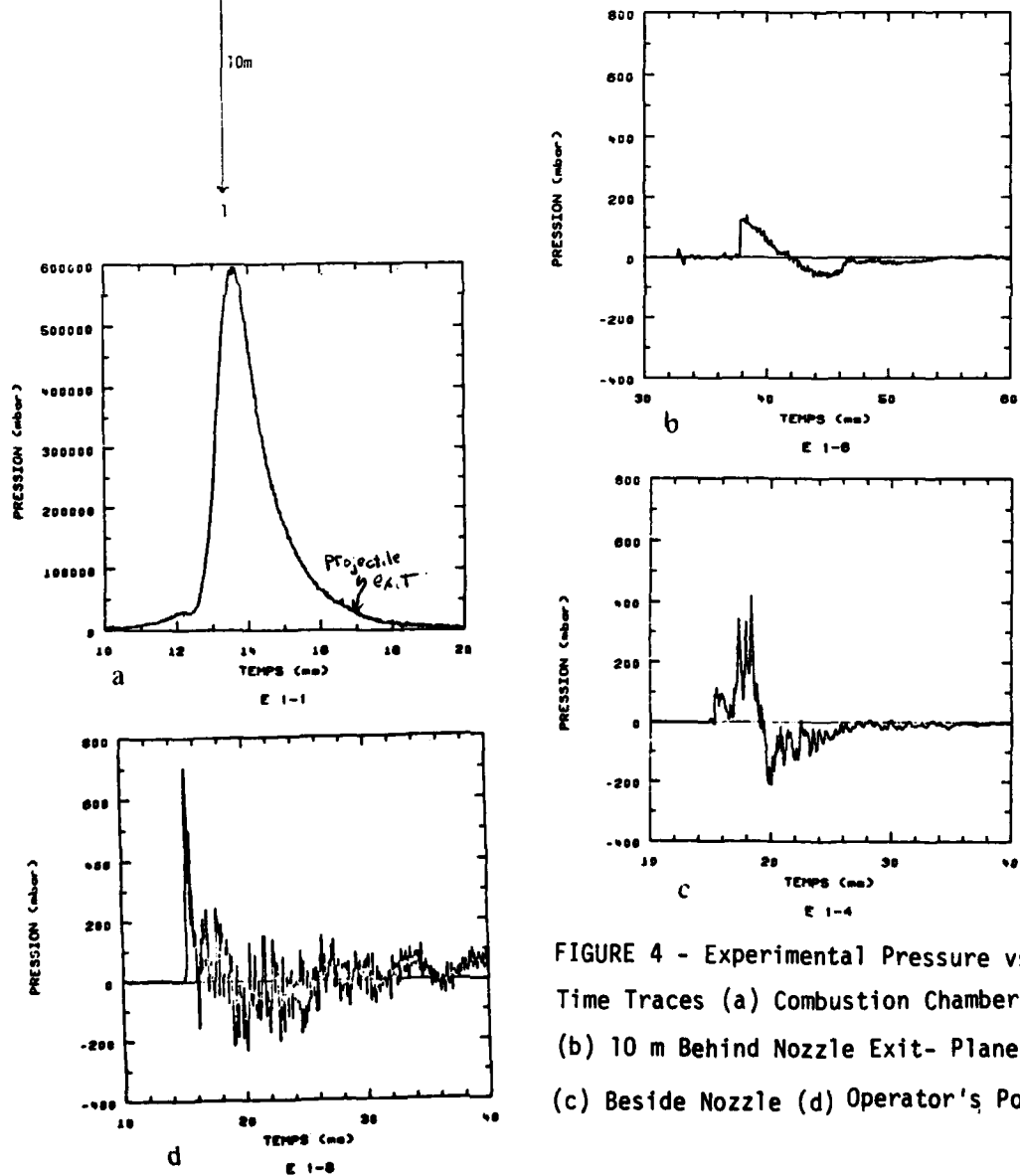


FIGURE 4 - Experimental Pressure vs Time Traces (a) Combustion Chamber (b) 10 m Behind Nozzle Exit-Plane (c) Beside Nozzle (d) Operator's Position

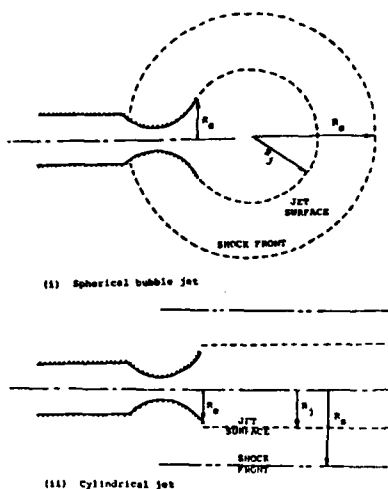


FIGURE 5 - Schematic of the numerical models

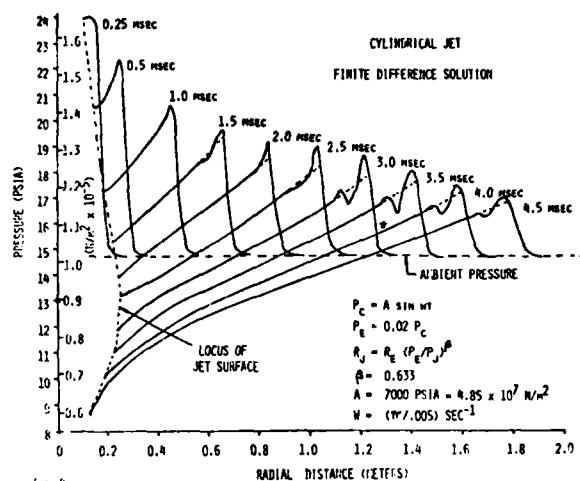


FIGURE 6 - Overpressure vs radial distance for a series of times - cylindrical model

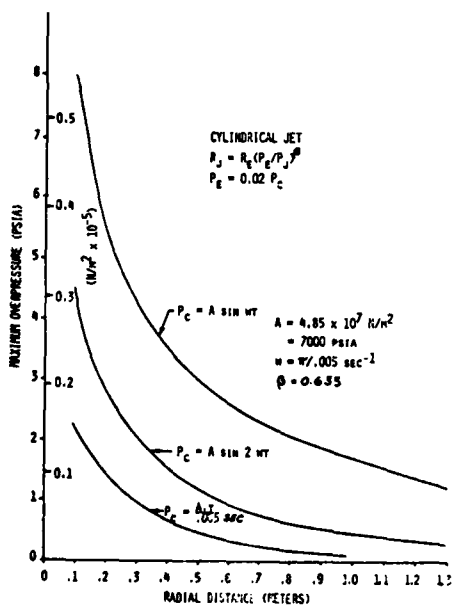


FIGURE 7 - Overpressure vs radial distance for three chamber pressure profiles - cylindrical model

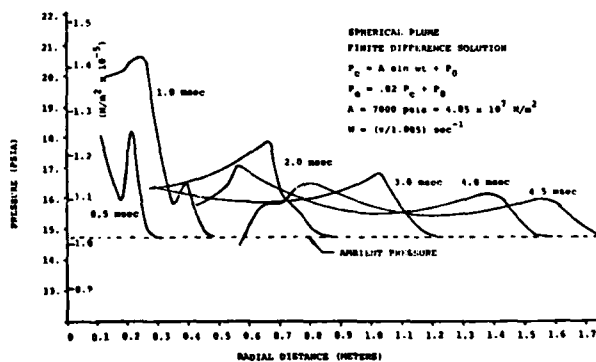


FIGURE 8 - Overpressure vs radial distance for a series of times - spherical model

Part V: CHEMICAL KINETICS AND OPTICS

AD P000267

SHOCK-EXCITED EMISSION SPECTRUM OF TUNGSTEN OXIDE

J.B. Shin, M.W.P. Cann and R.W. Nicholls

Centre for Research in Experimental Space Science
York University
4700 Keele St., Downsview, Ontario, Canada M3J 1P3

The spectrum of WO was studied as part of a continuing investigation of the shock-excited spectra of astrophysically important molecules. A 3-inch i.d. steel-copper shock tube was used to shock-excite tungstic anhydride powder to temperatures between 3800 and 4500K. The resulting extensive emission spectrum of WO was recorded photographically between 3400Å and 8900Å. 119 bands of WO were excited of which 99 were observed for the first time. A preliminary vibrational analysis has been made of the "D" system and vibrational constants are given.

INTRODUCTION

The high dispersion and high resolution study of molecular spectra, such as wavelength analysis and the precise determination of molecular structure constants, is one area of spectroscopy which is not normally associated with shock-excitation studies. The duration of useful light emission in shock tube spectroscopy is usually less than one millisecond, which is far shorter than normal exposure times required by slow, high resolution spectrographs. Nevertheless the shock tube is a most useful spectroscopic light source for the high temperature excitation of many metallic oxide band-systems of astrophysical importance, which are normally difficult to excite in the gas phase without use of sustained high temperatures (Nicholls et al. 1963). Because of the thermal excitation of high vibrational and rotational levels, more vibrational bands and rotational lines are usually observed in the shock excited spectra than low temperature spectra (Shin and Nicholls 1977a,b).

In this paper we report a study of the shock-excited WO spectrum at moderately high resolution using a computer processing of spectral data to aid in the analysis. The rich WO emission spectrum is characterized by many systems of overlapping bands (as yet mainly unassigned) extending throughout the near ultraviolet, visible and near infrared spectral regions. Because of the complexity of the WO spectrum, previously excited in arcs, there have been virtually no attempts to analyze it. Two short notes were published by Gatterer and Krishnamurty (1952) and Vittalachar and Krishnamurty (1954). The last authors propose four band systems with the (0,0) bands at 743, 7060, 6220 and 4710Å. Gatterer and Krishnamurty (1952) proposed two systems with (0,0) bands at 4806 and 4459Å, with a possible third one at 4710Å. Wavelength measurements on 25 WO band-heads have been presented by Gatterer et al. (1957), but the spectrum was not analyzed. In addition, a provisional

Deslanders array was obtained from a low-dispersion shock-excited WO spectrum by Nicholls and Tyte (1965). In this study, all of the observed bands were assigned to one system. The paucity of the published result shows that the WO spectrum has not yet been properly characterized. Difficulty also occurs because of numerous perturbations existing between various energy states and as well as to the great complexity of a typical heavy metal oxide spectrum.

The study of absorption spectra in neon and argon matrices by Weltner and McLeod (1965) reveals that there are seven electronic transitions (A to G systems) in the wavelength range 3500 - 6000Å. There exist very extensive perturbations particularly between systems A and B and also between E and F. Of all the systems of Vittalachar and Krishnamurty (1952) and Gatterer and Krishnamurty (1954) only one at 4807Å, appears in absorption in the neon matrix experiment of Weltner and McLeod (1965).

The purpose of the present study was to obtain a WO spectrum with more bands than have been observed hitherto and to apply computer assisted techniques in the analysis. With these techniques, it is hoped to relate bands to several electronic systems and to obtain the molecular constants describing their energy levels.

EXPERIMENTAL

The spectra of WO were produced by thermally exciting powdered tungstic anhydride (WO₃; purity 99.9%) in a 3-inch(i.d.) steel-copper shock tube with powder-injection system described elsewhere (Cann, Shin and Nicholls 1981). The temperatures of gases behind the reflected shock wave, as estimated from the initial shock speed, were 3800 - 4500K. The emission spectra of WO were photographed at several temperatures from the near UV to the near infrared spectral regions. Emission spectra in the near UV and the visible regions (3400 - 7000Å) were recorded in first order on a Baird Atomic 3-meter grating spectrograph with a reciprocal dispersion of 2.5 Å/mm, and in first order on a Bausch and Lomb 1.5-meter grating spectrograph with a reciprocal dispersion of 15 Å/mm. Spectra for the near infrared region (6700 - 8900Å) were recorded also in first order, with a Czerny-Turner 0.65-meter spectrograph having a reciprocal dispersion of 12.7 Å/mm. The number of shocks required to produce an adequate spectrum on Kodak 2475 film and Kodak high speed infrared film varied between one and thirty, depending on the band intensities in the wavelength region and the speed of spectrograph used. A schematic diagram of the optical arrangement is displayed in Figure 1.

The spectrographic films were measured and digitized with a Perkin Elmer Model 1010A PDS Microdensitometer and PDP8E computer (at the David Dunlap Observatory, University of Toronto). The digitized spectra were measured with an increment of 0.0005 cm and were stored on magnetic tape. Subsequent processing of the tape including wavelength calibration using prominent tungsten atomic lines, was conducted on York University's ITEL AS/6 mainframe computer. In order to reduce noise and enhance the visibility of the bands the digitized spectra were processed by signal averaging, with rectangular functions of various widths. Figures 2(a) - 2(d) show the computer-reproduced Bausch and Lomb spectra without or with averaging. This method enhanced the visibility of the bands and was especially valuable for identifying many weak bands.

The wavelength measurements of band heads were carried out on spectra which were plotted on the CALCOMP drum plotter with wavelength scales chosen to facilitate the measurements. By this means 119 band heads of the shock-excited WO spectrum were observed in the spectral range 3400 - 8900Å. Among these, 99 of the bands have not been reported previously, in particular the band systems in the near infrared region. The infrared bands may be hot bands due to the high temperatures of shock excitation.

SPECTRAL FEATURES

The band head wavelengths, vacuum wavenumbers of all the bands observed in this study, with the vibrational quantum assignments for bands in D-system are displayed in Table 1. The probable observational error in wavelength measurement is about $\pm 0.5 \text{ \AA}$ in the near UV and visible regions and about $\pm 1 \text{ \AA}$ in the near infrared region. The band heads designated by an asterisk are those which have been previously reported in the literature. Otherwise the remaining 99 bands are new. An examination of the spectrum shows that most of the observed bands are degraded to the red. Figures 3 and 4 are the low dispersion WO spectra taken with the Bausch and Lomb and the Czerny Turner(JH) spectrographs.

Because of the high density of bands which remain to be assigned and the strong perturbations between systems described by Weltner and McLeod (1965), only the D-system has been vibrationally analyzed at present.

VIBRATIONAL ANALYSIS AND MOLECULAR CONSTANTS OF THE D-SYSTEM

The head of the (0,0) band of D-system lies at 4805.9 \AA (20801.9 cm^{-1}) and transitions to the higher vibrational levels, up to the $v' = 5$ and $v'' = 3$ are observed. The (0,0) band is the strongest but the (1,0) and (2,0) sequences are well developed.

A set of molecular vibrational constants was determined from a least squares fit to measured band head wavenumbers, giving

$$\begin{aligned} \nu_H = 20833.5 &+ 995.3(v'+0.5) - 5.941(v'+0.5)^2 \\ &- [1062.4(v''+0.5) - 3.975(v''+0.5)^2]. \end{aligned}$$

This set of vibrational constants is the first to be published for the WO molecule.

Table 2 shows the Deslanders table for wavenumbers, wavelengths, Franck-Condon factors, r-centroids, and the first differences between progressions of D-system bands. A set of provisional approximate Morse Franck-Condon factors and r-centroids were calculated from the following input data $\mu_A = 14.7153823 \text{ a.m.u.}$, $\omega_e' = 995.3 \text{ cm}^{-1}$, $\omega_e x_e' = 5.941 \text{ cm}^{-1}$, $\omega_e'' = 1062.4 \text{ cm}^{-1}$, $\omega_e x_e'' = 3.975 \text{ cm}^{-1}$, ($r_e' = 1.74 \text{ \AA}$) and ($r_e'' = 1.69 \text{ \AA}$). Because no r_e values are available in the literature (Huber and Herzberg 1979) (for no rotational analyses have been done) we adopted r_e'' of the ground state of the very similar TaO molecule for which $\mu_A = 1.68669 \text{ \AA}$, and used Birge's rule $\omega_e r_e = \text{const.}$ to estimate r_e' . There is good agreement between the Franck-Condon factor values and the proposed band assignments in Table 2.

DISCUSSION

The above results are preliminary and the work continues on assignments and analyses of the other bands. Spectra obtained with the powder-injection shock tube yield a rich array of bands far more numerous than hitherto reported in the literature. The WO spectrum is complex and its variation with shock temperature, together with study of the absorption spectrum can be expected to assist in relating vibrational bands to particular electronic systems. The computer processing of digitized spectra has been a powerful tool in this work. Filtering by the Fast Fourier Transform methods has also been used for noise removal and extension of this method in future work will be profitable. In addition to the vibrational bands, the rotational lines within some of the stronger bands appear quite clearly on some of the films as well as in the computer generated plots. Further work (including some rotational analyses) is expected to yield many more band assignments and the

corresponding molecular constants.

REFERENCES

1. R.W. Nicholls, W.H. Parkinson, and E.M. Reeves, *Applied Optics* 2, 919 (1963).
2. J.B. Shin and R.W. Nicholls, *Proc. 11th Intern. Symp. on Shock Tubes and Waves*, ed. by Ahlborn et al. 140, Seattle, Wash. (1977a).
3. J.B. Shin and R.W. Nicholls, *Spectroscopy Letters* 10, 923 (1977b).
4. A Gatterer and S.G. Krishnamurty, *Nature* 169, 543 (1952).
5. V. Vittalachar and S.G. Krishnamurty, *Current Sci. India* 23, 357 (1954).
6. A Gatterer, J. Junkes, E.W. Salpeter, and B. Rosen, *Molecular Spectra of Metallic Oxides*, Vatican Press, Vatican City (1957).
7. R.W. Nicholls and D.C. Tyte, *Proc. 5th Intern. Shock Tube Symposium*, 111, Silver Springs, Maryland (1965).
8. W. Weltner and D. McLeod, *J. Mol. Spectrosc.*, 17, 276 (1965).
9. M.W.P. Cann, J.B. Shin and R.W. Nicholls, *Proc. 13th Intern. Symp. on Shock Tubes and Waves* (1981).
10. K.P. Huber and G. Herzberg, *Molecular Spectra and Molecular Structure*, IV. Constants of Diatomic Molecules, Van Nostrand Reinhold, New York (1979).

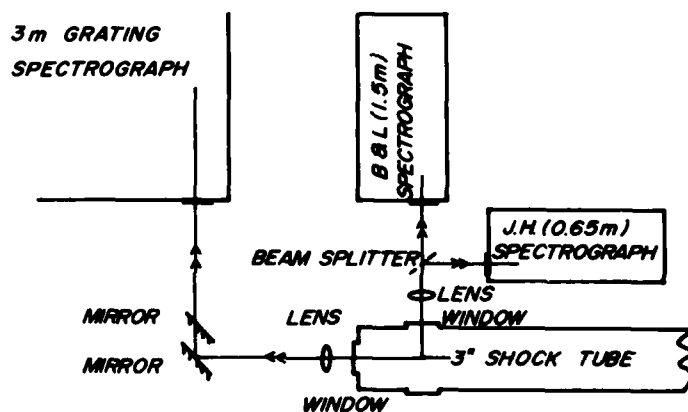


Figure 1. The schematic diagram of optical arrangement.

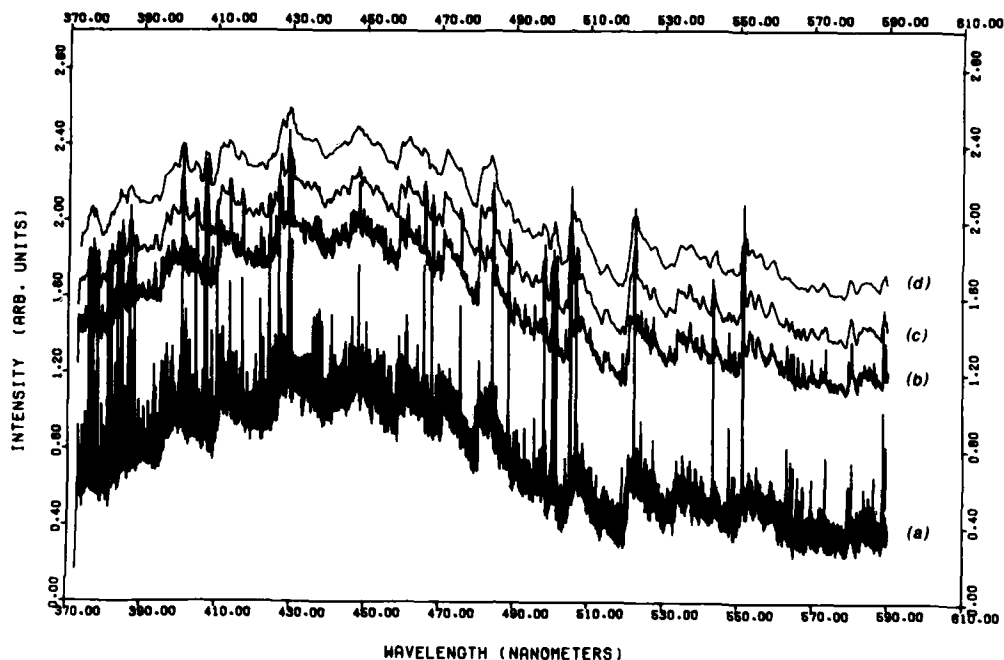


Figure 2. The computer-reproduced Tungsten oxide spectra; (a) spectrum without averaging, (b) spectrum averaged with rectangular function of $HW=2\text{\AA}$, (c) of $HW=8\text{\AA}$, (d) of $HW=16\text{\AA}$.

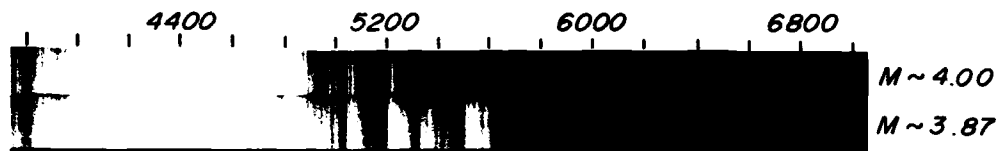


Figure 3. The shock excited WO spectrum in the visible region (photographed with a Bausch and Lomb spectrograph).

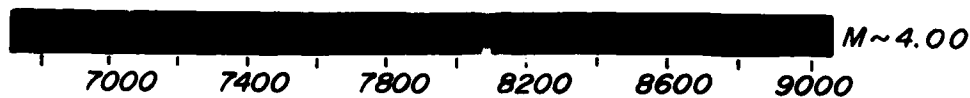


Figure 4. The shock excited WO spectrum in the near I.R. region (photographed with a Czerny-Turner spectrograph).

TABLE 1 BAND HEADS OF THE SHOCK EXCITED NO SPECTRUM

λ_{air} (Å)	ν_{vac} (cm^{-1})	Transition v', v''	λ_{air} (Å)	ν (cm^{-1})	Transition v', v''	λ_{air} (Å)	ν_{vac} (cm^{-1})	Transition v', v''	λ_{air} (Å)	ν_{vac} (cm^{-1})	Transition v', v''
3590.2	27845.7		*4709.3	*21228.6		5440.0	18377.2		6026.3	18590.2	
3682.3	27149.2		4724.5	21160.3		5503.2	18166.2		6040.1	18551.4	
3697.5	27037.6		4738.1	21099.6		5512.8	18134.6		6048.2	18529.3	
3791.5	26367.3		*4805.9	20801.9	D(0,0)	5550.3	18012.0		6063.7	16487.0	
3880.2	25764.6		*4823.0	*20728.2	D(1,1)	5578.7	17920.3		6082.6	16435.8	
3961.5	25235.8		4833.4	20683.6		*5587.2	17893.1		6090.5	16414.5	
3978.0	25137.5		4852.4	20602.6		5614.6	17805.8		6125.5	16320.7	
4082.7	24607.2		4877.0	20498.7		5658.5	17667.6		6172.4	16196.7	
4108.7	24331.8		*4901.3	20397.1		5687.6	17577.2		6177.5	16183.3	
*4164.8	24004.0		4930.4	20276.7		5721.0	17474.6		6194.3	16139.4	
4182.5	23902.4		4955.7	*20173.2		5734.1	17434.7		6202.5	16118.1	
4217.9	23701.8	D(3,0)	4998.4	20000.8		5746.3	17397.7		6257.3	*15976.9	
4271.4	*23404.9		5051.8	19789.4		5794.7	17252.4		6400.9	15618.5	
*4338.3	*23044.0		*5063.7	*19742.9	D(0,1)	5798.0	17242.5		6412.3	15590.7	
*4394.5	*22749.3	D(2,0)	5080.6	*19677.2	D(1,2)	5821.2	17173.8		6451.8	15495.3	
4414.8	22644.7	D(3,1)	5141.3	19444.9		5831.7	17142.9		6454.6	15488.5	
4435.2	22540.6	D(4,2)	5152.4	19403.0		5837.5	17125.9		6473.3	15443.8	
4458.0	22425.3	D(5,3)	*5209.2	19191.5		5854.9	17075.0		6482.4	15422.1	
4472.3	22353.6	D(6,4)	*5228.4	19121.0		5863.2	*17050.8		6504.3	15370.2	
4491.4	22258.5	D(7,5)	5244.7	19061.6		5888.4	16977.8		6566.8	15223.9	
4521.9	*22108.4		5267.8	18978.0		5900.5	*16943.0		6587.6	15175.8	
4562.7	21910.7		5317.1	18802.0		5925.6	16871.3		6599.9	15147.6	
*4590.6	*21777.6	D(1,0)	5337.4	18737.5		5938.6	16834.3		6619.6	15102.5	
4608.5	*21693.0	D(2,1)	5372.9	18606.7		5969.2	16748.0		6661.3	15007.9	
4627.8	21602.5	D(3,1)	5404.1	18499.7		6007.3	16641.8		6745.7	14820.2	

*Indicate the bands previously reported

Emission Spectrum of WO

[437]

TABLE 2 BANDS OF THE WO D-SYSTEM

v'	v''	0	1	2	3
0		20801.9	19742.9		
		4805.4	5063.7		
		(1059)			
		4.8966 -1	3.7536 -1		
1		1.7181 0	1.7589 0		
		(976)	(985)		
		21777.6	20728.2	19677.2	
		4590.6	4823.0	5080.6	
2		(1049)	(1051)		
		3.1735 -1	3.7387 -2	3.4509 -1	
		1.6801 0	1.7359 0	1.7643 0	
		(971)	(964)		
3		22749.3	21693.0		
		4394.5	4608.5		
		(1056)			
		1.2961 -1	2.2497 -1		
4		1.6473 0	1.6871 0		
		(952)	(951)		
		*23701.8	22644.7	*21602.5	
		4217.9	4414.8	4627.8	
5		(1057)	(1042)		
		4.3896 -2	1.9280 -1	7.7994 -2	
		1.6193 0	1.6527 0	1.6983 0	
				(938)	
6				*22540.6	
				4435.2	
				1.6670 -1	
				1.6592 0	
LEGEND: Wavenumber (ν) in cm^{-1}					
Wavelength (λ) in \AA					
Franck-Condon Factor					
r-Centroid					
First differences in cm^{-1} (in bracket)					*22425.3
					4458.0
NOTE: * indicate newly observed bands					9.5931 -2
					1.6678 0

AD P000268

ROTATIONAL NONEQUILIBRIUM INFLUENCES IN CW HF/DF CHEMICAL LASERS

S. W. Zelazny, W. L. Rushmore, J. W. Raymonda, and M. Subbiah
High Energy Laser Technology Directorate
Bell Aerospace Textron Division of Textron Inc.
Buffalo, New York 14240

and

L. H. Sentman
Department of Aeronautical and Astronautical Engineering
University of Illinois
Urbana, Illinois 61801

A theory is presented which considers either rotational equilibrium or non-equilibrium rate processes in continuous wave (CW) hydrogen fluoride (HF) or deuterium fluoride (DF) lasers. The theory is used to predict zero power gain and power spectral distributions and comparisons are made with experimental observations. The DF reaction kinetics model was found to give predictions of zero power gain which were closely correlated with experimental data. However, the HF reaction kinetics were found to produce radically different zero power gains than experimentally observed. Modifications to the reaction rates of certain vibrational-translational and vibrational-vibrational energy exchange processes were found to remove the discrepancy between the measured and predicted zero power gains. The rotational non-equilibrium theory was used to predict the power spectral distributions for HF and DF lasers and results were found to be consistent with experimental data.

I. INTRODUCTION

Interest in chemical lasers and, in particular, continuous wave (CW) hydrogen fluoride (HF) and deuterium fluoride (DF) continues to be maintained at a high level after more than a decade since their first demonstration. Such devices, see Figure 1, operate at high chemical efficiencies and do not require any nonchemical energy for their operation, thereby providing a source of high-level coherent radiant energy from a relatively low weight compact system. Considerable literature describing experimental and theoretical investigations of chemical lasers has appeared since 1964, including the Handbook of Chemical Lasers¹ and the recent review by Cool².

Insight into the dominant physical processes that control CW HF/DF laser performance has been gained through the development and application of theoretical models. Emanuel, in Chapter 9 of the Handbook of Chemical Lasers¹, has reviewed the numerical modeling techniques used to model both CW and pulsed chemical lasers. As shown by Emanuel¹ and others, one of the major elements in the theoretical model of chemical HF/DF lasers is the description of the chemical kinetics. Early analyses, which employed the assumption of rotational equilibrium, were found to be unable to predict accurately the experimentally observed spectral distribution of energy. In an early study of rotational nonequilibrium phenomena, Sentman³ showed that several rotational transitions within a given vibrational band lase simultaneously and most of the power is contained in those rotational transitions that are preferentially populated by the pumping reaction. In a later study⁴, the idealization of a Fabry-Perot resonator was replaced with a more realistic unstable resonator model. It was found⁴ that power spectral distributions obtained with the Fabry-Perot model and the unstable resonator were almost identical as were total power levels (differed by less

than 6%). It was also shown⁴ that the unstable resonator power would fluctuate on lines whose saturated gain did not fill the resonator. These results^{3, 4, 5} showed qualitative agreement with experimentally observed trends but could not be compared quantitatively because of the simplified chemical-fluid dynamic model employed.

A cost effective rotational nonequilibrium model which is capable of predicting results that are quantitative is desirable in order to aid the laser designer and test engineer in test plan preparation and data interpretation. Two theoretical models which satisfy the cost efficiency requirement have been reported by Sentman⁶ and Raymonda et al⁷. Quantitative comparisons between theory and data for the power spectral distributions have been recently reported by Sentman for two classes of lasers.^{5, 6} Comparisons between experimental and theoretical power spectral distributions have shown good agreement for an arc driven CW HF laser, whereas significant discrepancies between theory and data were found to exist for a combustion driven device⁶. The inability of the theory to predict the power spectral distribution in the latter case has been argued to be attributed to an inaccurate prediction of the local translational temperature.

In this study, we continue to expand the data base over which rotational nonequilibrium models have been evaluated in terms of their ability to predict experimental observations. Data characterizing the two types of laser cavity injectors shown in Figure 2 were theoretically modeled. The cavity injector configuration determines the rate of mixing between the lasant and oxidizer streams and, consequently, the local temperature and concentrations in the reaction zone. The theory used to predict the zero power gain or power spectral distributions is given in Section II where the three major elements of the model are described, i.e., (1) the conservation equations, (2) chemical kinetics, and (3) the optics. Comparisons between theoretical projections and experimental data are given in Section III and conclusions are given in Section IV.

II. GOVERNING EQUATIONS

A. Gas Medium Conservation Equations

The conservation equations for the mixing, chemically reacting, and lasing gas medium are reduced to a quasi one-dimensional form by averaging across the mixing zone coordinate. The details of this procedure have been reported previously^{8, 9} and will not be repeated here. The equations may be expressed in a form which applies to rotational equilibrium or nonequilibrium reaction rate formulations and to an arbitrary optical configuration. The specific form of the model for the rate of change of each specie concentration due to chemical reaction, the X_{ch_i} expression, will vary with the reaction rate model. The radiative flux distribution, which appears in the model for the rate of change of a specie concentration due to simulated emission, will implicitly reflect the specific resonator configuration being employed. Earlier modeling efforts⁹ of the resonator were restricted to two plane-parallel mirrors satisfying the gain equals loss condition in the geometric optics limit. This limitation has now been removed in our current models for rotational equilibrium, the BLAZE-II code, and rotational nonequilibrium, the NORO II code.

B. Chemical Kinetics

The DF and HF chemical kinetic models¹⁰⁻¹³ used to compute the X_{ch_i} expression appearing as a source term on the right hand side of the species continuity and energy equations are described in this section. Within the rotational equilibrium approximation, it is only necessary to solve for the total population in each vibrational state, n_v , and determine the rotational distribution, $n_{v,J}$, from the Boltzman distribution function. Hence, an expression for $X_{ch_i}(v)$ is required. Generalizing to the rotational nonequilibrium condition will result in treatment of distinct vibrational and rotational population levels, $n_{v,J}$, and here expressions for the chemical reaction source term are of the form $X_{ch_i}(v, J)$.

The types of reactions can be divided into two general classes: (1) those involving generalized collision partners and (2) those where vibrational energy is exchanged or pumping to a vibrational level occurs. The equilibrium DF rate model used in this study has been described and used previously by Zelazny et al⁹ to examine the sensitivity of predictions of laser power to key assumptions used in the theory. The increase in the number of dependent variables (n_v replaced by $n_{v,J}$) when considering rotational nonequilibrium effects results in a significant increase in computer solution time (in some cases up to a factor of ten). It was of interest to examine the rotational

equilibrium model being employed to minimize the number of reactions and dependent variables without significantly affecting predictions of specie profiles, total power and the vibrational power distribution. Computational experimentation with the model showed that for the DF system where the cold reaction is dominant, it was only necessary to retain $DF(v)$ for $v = 0, 1, 2$ and 3 without significantly changing the predicted power spectral distribution. This is shown in Figure 3. The rotational nonequilibrium model evolved from this reduced reaction set.

When rotational nonequilibrium is considered, it is necessary to specify reaction rates that are dependent on both the vibrational and rotational states. The rotational nonequilibrium reactions may be divided into five classes (1) pumping, (2) collisional decomposition, (3) collisional deactivation, (4) rotational relaxation, and (5) V-V transfer reactions. The form of the reaction rates and the rotational nonequilibrium DF reactions considered in the model are given in Table 1. The rotational equilibrium reaction rates used for the HF system have been modified¹¹⁻¹⁴ from those used in our earlier study⁹. These updated reaction rates are given in Table 2, and the rotational nonequilibrium rates are given in Table 3.

C. Optics Model

The conservation equations are coupled to the optical field through stimulated emission processes which are represented by the χ_{rad} term appearing in the energy and species conservation equations. The constant gain approximation for a Fabry-Perot cavity (two plane parallel mirrors) yields an equation for the threshold gain expressed in terms of the mirror reflectivity and length of the active medium. This approach to close the governing equation system was used in this study.

III. COMPARISONS BETWEEN THEORY AND EXPERIMENT

The experimental data base for combustion driven CW HF and DF lasers has grown considerably over the past eight years. These data include measurements of (1) total outcoupled laser power in stable and unstable resonator configurations, (2) sensitivity of output power to optical axis location, (3) zero power gain rotational temperature distributions as obtained from chemiluminescence data, (4) temporally and spatially resolved output power spectral distributions, (5) sensitivity of output power to the output coupling ratio, (6) zero power gain distributions, (7) saturated gain distributions, and (8) spectrally and spatially resolved intracavity intensities. Hence, it is now possible to assess in some detail the ability of theoretical models to predict quantitatively these experimental observations. As was reviewed by Zelazny et al⁹, there are numerous assumptions that are required before a theoretical model can be constructed which lends itself to solutions that are reasonable in terms of computer core and time requirements. The following paragraphs describe results of a broader study¹⁴ directed toward evaluating the accuracy of the CW laser models developed by Driscoll¹⁵ and Raymonda et al⁷.

A. Zero Power Gain

Rotational relaxation effects are slower than stimulated emission rates and hence including rotational nonequilibrium in a theoretical model to predict power spectral distributions is important. In the absence of a radiation field, a rotational equilibrium theory is sufficient to characterize the dominant reaction processes and allow for an evaluation of the ability of the theoretical model to predict zero power gain distributions in the laser cavity. A comparison of the zero power gain predicted using the rotational equilibrium and nonequilibrium models are shown in Figure 4 where as, stated, only slight differences are observed in the rotational distribution of the gain. Implicit in the exercise of comparing measured and predicted zero power gain is a test of the theoretical prediction of the mixing rate of the primary and secondary streams (which has a first order influence on specie concentrations, pressure, temperature, velocity, and density). Therefore, one of the first tests of a laser performance model is in its ability to predict the zero power gain distribution in the laser cavity.

DF Laser with a Slit Nozzle Array: The model was used to predict the zero power gain generated downstream of a two-dimensional nozzle array. For this device, the combustor pressure was in excess of ten atmospheres and the combustor temperature was sufficiently high to assure greater than 90% dissociation of the F_2 molecule. Comparisons between data and theory, Figure 5, show that the model correctly predicts the peak gain levels and the location at which the medium enters absorption.

HF Laser with an Axisymmetric Nozzle Array: The HF kinetic rates given in Table 2 were used in the model to predict the zero-power gain distribution downstream of an axisymmetric nozzle array. The gains on the $v = 1-0$ transition did not go into absorption until about 4.0 or more centimeters downstream compared to the experimentally observed distance of 2.5 or less centimeters. Similarly, the theoretical prediction for the distance at which the $v = 2-1$ transition enters absorption is greater than the experimentally observed distance, Figure 6. Possible sources for the cause in this discrepancy between theory and data could be due to a combination of errors in estimating the initial conditions, the mixing rates, the average cavity pressure and the reaction rates. However, calculations were made for cases where the only difference in the laser conditions was a change in the D_2 and H_2 species to produce either lasing on HF or DF. It was found that good agreement between predicted and measured zero-power gain was obtained for the DF laser. Hence, it is likely that the source of error is associated with the HF reaction rates. With this in mind, theoretical calculations were made to examine the sensitivity of predictions of the zero-power gain to vibrational-translational deactivation and vibrational-vibrational energy exchange reaction rates. It was found that two types of modifications to the reaction rates could significantly improve the agreement between data and theory. The first type of modification required increasing the fast V-T reaction rates for the HF, DF, and H collisional partners by factors of 2.0, 2.0, and 5.0. The second type of modification, which gave a better correlation between theory and data than the first modification, was to increase the rate of V-V exchange between H_2 and HF by a factor of 4.0 over the value given in Table 2. These comparisons between theory and data are shown in Figure 6a. The uncertainty in the V-V reaction rates is greatest for $v > 1$; however, the accuracy of the rates for $v = 1-0$ exchange are known reasonably well¹¹. When the $v = 2-1$ rates for the H_2 -HF exchange increased by a factor of 4.0, the correlation between data and theory was found to be very poor as shown in Figure 6b. The results illustrated in Figure 6 lead us to conclude that our current rate model for the HF system is questionable. Whether the error is in the H_2 -HF V-V exchange rate, or in a combination of various rates cannot be determined from the type of test data examined in this study.

B. Power Spectral Distribution

Rotational equilibrium and nonequilibrium analyses were conducted for the axisymmetric and two-dimensional nozzle configurations. Comparisons were made between measured and observed power spectral distributions. The power spectra for a two-dimensional combustion driven DF laser has been shown to be divided between the $v = 1-0$, $2-1$ and $3-2$ levels by the percentages of 31%, 45%, and 24% distributed over fourteen rotational lines. This result was obtained with an unstable resonator with an on axis threshold gain of $0.46\% \text{ cm}^{-1}$. Using the rotational equilibrium model and a Fabry-Perot optics idealization resulted in a prediction in the vibrational power distribution which was in excellent agreement with the data as shown in Table 6. However, the limitation of the rotational equilibrium model is that it results in a prediction of lasing on only one rotational level for each vibrational level^{3,4}. Hence, the rotational nonequilibrium model, NORO II, was used to predict the experimentally observed power spectral distributions. The prediction of the observed power spectra for a DF laser is shown in Figure 7. It is concluded from the comparison shown in Figure 7 that the model is capable of predicting to within one to two rotational lines, the major lasing lines and the total number of lasing lines to be anticipated for DF combustion driven lasers using two-dimensional nozzle arrays.

Predictions were made of the power spectral distributions in a laser cavity downstream of the axisymmetric nozzle array shown in Figure 2. The experimental data was obtained with a stable resonator configuration where the beam was sampled by output coupling through a small hole located on the optical axis. Two sets of mirrors were used, a 99-99% and 91-76% mirror reflectivity pairs, to examine the effect of the threshold gain on the spectra. The theory predicted those lines which contained the greatest proportion of energy to within a single rotational level for both the high and low reflectivity case. Power was observed on the $v = 1-0$ and $2-1$ transitions with the $v = 1-0$ transition containing 56% of the energy for the 99-99% reflective mirrors and 67% of the energy for the 91-76% mirror pair. The theoretical prediction of the power split between the $v = 1-0$ and $2-1$ levels was found to be insensitive to the reduced reflectivity, i.e., the predicted percent of power changed from 51% to 50% for the $v = 1-0$ level. This result indicates that the theory predicts a higher degree of saturation than experimentally observed. Comparisons between the theoretical predictions and experimental data are shown in Figures 8 and 9.

IV. CONCLUSIONS

An investigation was conducted to evaluate the two theoretical models for CW HF/DF lasers in terms of their ability to predict zero power gain and power spectral distributions. Two

types of laser nozzle configurations were examined - the axisymmetric and slit nozzle arrays. The main conclusions were:

- The zero power gain for the DF lasers was accurately predicted in terms of peak gain and location at which the medium enters absorption. These results indicate that the DF reaction model has no significant shortcoming.
- The HF laser modeling showed a significant shortcoming in our ability to predict observed zero power gains. The discrepancy between theory and data could be minimized by increasing the V-V energy exchange rate between H_2 and HF. These results suggest that the uncertainty in the HF reaction rate model is significantly greater than in the DF reaction rate model.
- The rotational nonequilibrium predictions of power spectra for both the HF and DF lasers are in good agreement with experimental data. Rotational equilibrium models can not predict lasing on more than one rotational level per vibrational band.

ACKNOWLEDGEMENT

This work was conducted by the Bell Aerospace Textron Independent Research and Development Program.

REFERENCES

1. R.W.F. Gross and J.F. Bott. Handbook of Chemical Lasers (John Wiley and Sons, New York, 1976)
2. T.A. Cool. Chemical Lasers in Physical Chemistry of Fast Reactions. Vol. 2. Reaction Dynamics. I.W.M. Smith Ed. (Plenum Press, New York and London, 1980).
3. L.H. Sentman. J. Chem. Phys. 62, 3523 (1975)
4. L.H. Sentman. Applied Optics 17, 2244 (1978)
5. L.H. Sentman. Applied Optics 15, (1976)
- 6(a) L.H. Sentman and W.L. Rushmore. Computational Efficient Nonequilibrium CW Chemical Laser Model. AIAA, J. accepted for publication, April, 1981
- 6(b) L.H. Sentman. Journal de Physique. Colloque C9 Supplement AU N° 11 Tome 41, Novembre, 1980, P. C9-17
7. J.W. Raymonda, R. Subbiah, J.T. Schimke, S.W. Zelazny, and L.H. Sentman, "Advanced HF and DF Chemical Laser Performance Modeling: Vol I, The CNCDE/BLAZE-II Rotational Equilibrium Code. Vol. II, The NORO-II Rotational Nonequilibrium Code," MIRADCOM Report DRCPM-HEL-CR-79-7 (Bell Aerospace Textron, Buffalo, New York, 1979).
8. L.H. Sentman, M. Subbiah, and S.W. Zelazny. "BLAZE-II. A Chemical Laser Simulation Computer Program". MICOM Report H-CR-77-8 (Bell Aerospace Textron, Buffalo, New York, 1977).
9. S.W. Zelazny, R.J. Driscoll, J.W. Raymonda, J.A. Blauer, and W.C. Solomon. AIAA J. 16, 297 (1978)
10. J.C. Polanyi and K.B. Woodall. J. Chem. Phys. 57, 1574 (1972); 1563 (1972)
11. N. Cohen and J. Bott, Aerospace Corporation, private communication, May 1976
12. S.C. Korzius. MICOM Report RK-CR-75-31, June 1975
13. L. Rapagnani and T. Slankas. Air Force Weapons Laboratory, private communication, April 1977
14. W.L. Rushmore and S.W. Zelazny. "CW, HF and DF Chemical Lasers - Comparisons between Theory and Experiment". Bell Aerospace Textron Report 9500-920375 (Bell Aerospace Textron, Buffalo, New York, 1980)
15. R.J. Driscoll. AIAA J. 14, 1571 (1976)

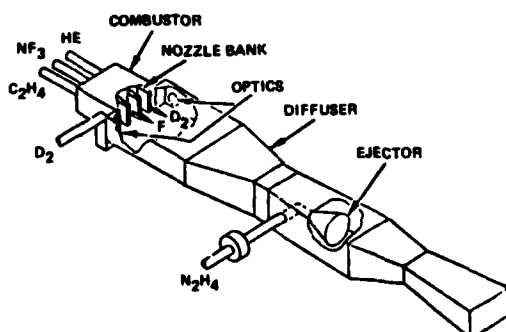


Figure 1. Schematic of Major Elements of a HF/DF Combustion Driven Laser

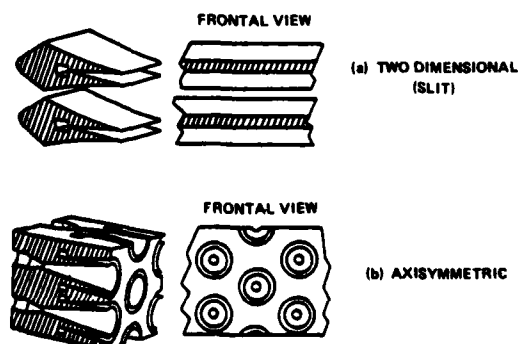


Figure 2. Two Types of Chemical Nozzle Geometries

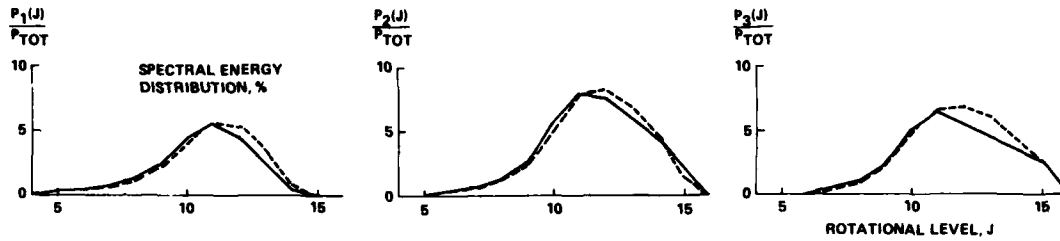


Figure 3. Effect of Using a Reduced DF Reaction Rate Model on the Predicted Power Spectral Distribution for a DF Laser.
(— Full Rate Package, --- Reduced Rate Package)

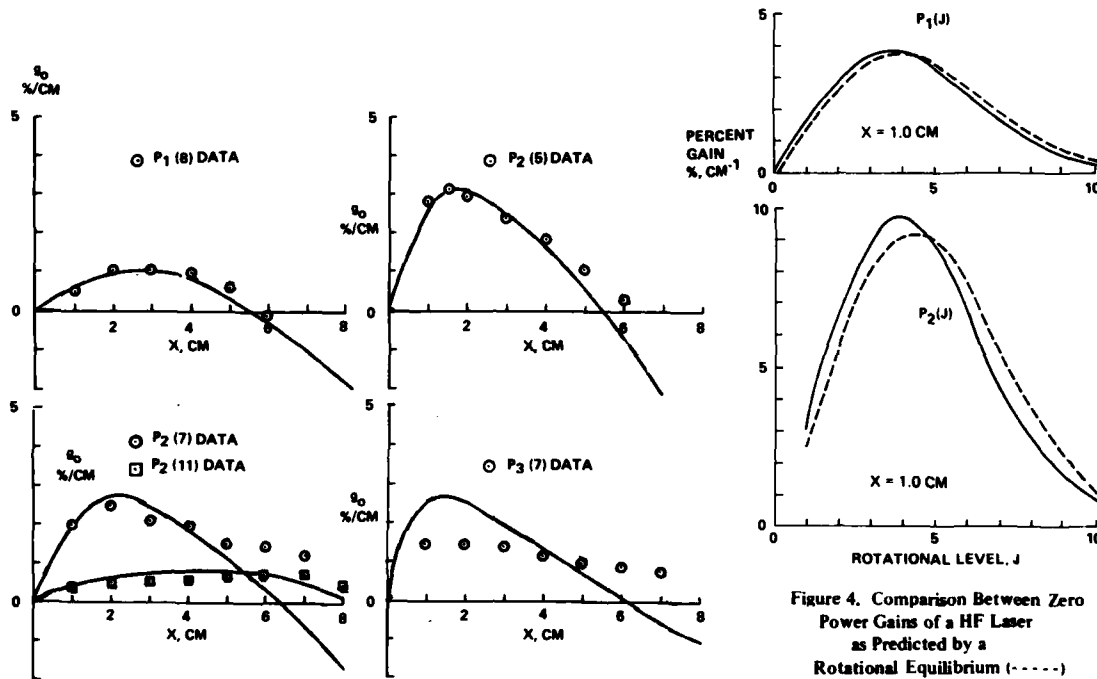


Figure 5. Experimental and Theoretical Zero Power Gains for a DF Laser Using a Two-Dimensional Nozzle Array

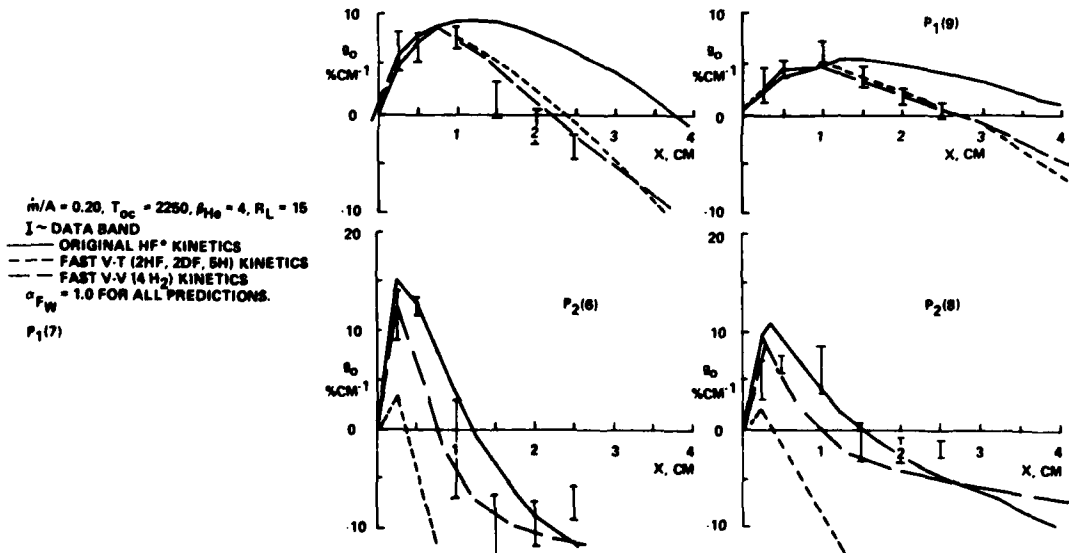


Figure 6(a). Experimental and Theoretical Zero Power Gains for a HF Laser Using an Axisymmetric Nozzle Array Showing Effects of Changes to Select Rate Constants - F₂ Oxidizer

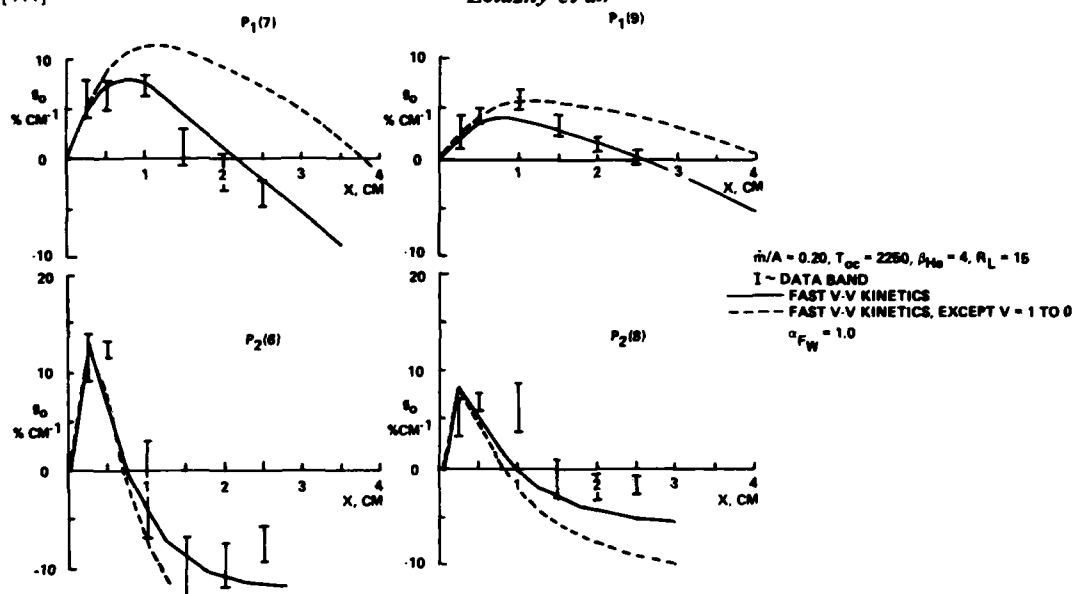


Figure 6(b). Experimental and Theoretical Zero Power Gains for a HF Laser Using an Axisymmetric Nozzle Array Showing Effect of Changing All V-V Rates and All But the $V = 1$ to 0 Rate for the $H_2(V) - HF(V)$ Exchange Reaction

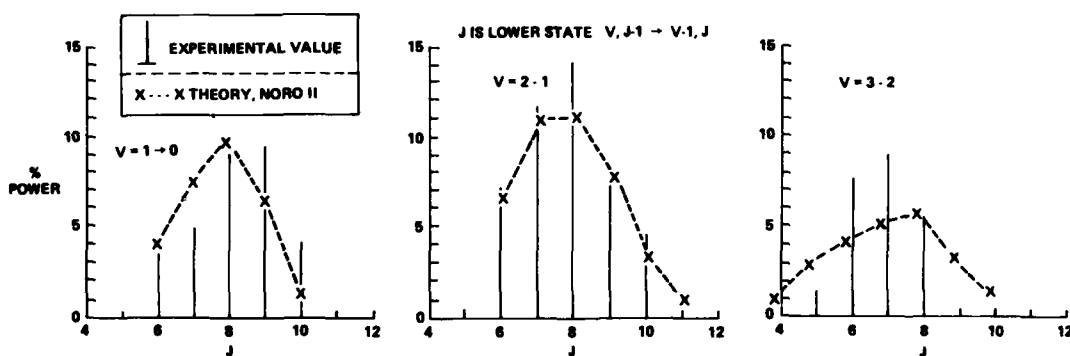


Figure 7. Experimental and Theoretical Power Spectral Distribution of a DF Laser Using a Two-Dimensional Nozzle Array

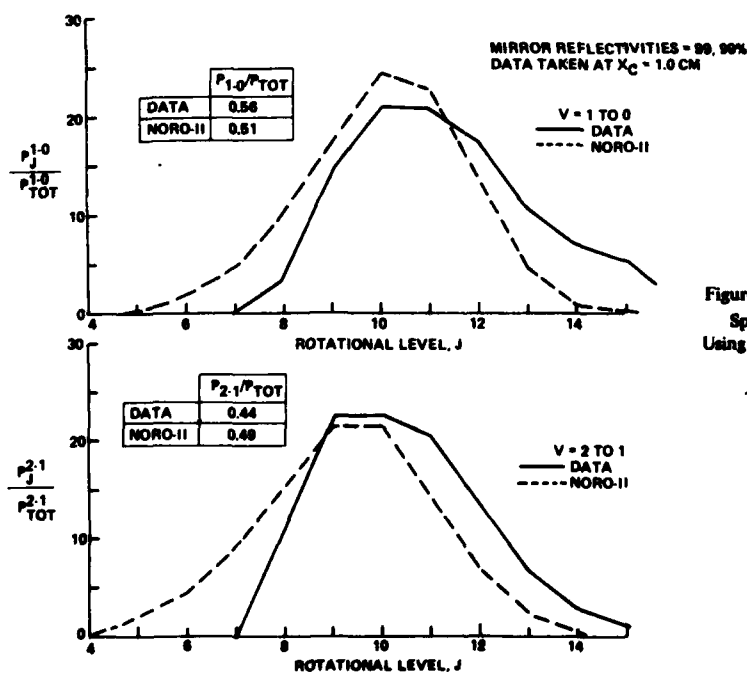


Figure 8. Experimental and Theoretical Power Spectral Distributions for a HF Laser Using an Axisymmetric Nozzle Array with High Reflectivity Mirrors.

Threshold Gain Equals $0.05\% \text{ cm}^{-1}$

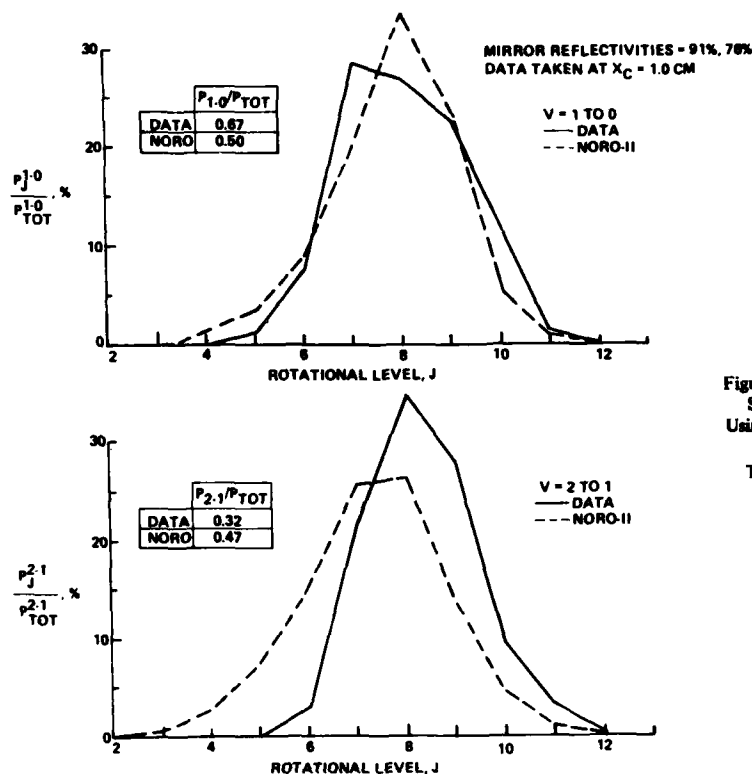


Figure 9. Experimental and Theoretical Power Spectral Distributions for a HF Laser Using an Axisymmetric Nozzle Array with Low Reflectivity Mirrors. Threshold Gain Equals $0.92\% \text{ cm}^{-1}$

Table 1a. Reaction Rate Data for DF System Involving Generalized Collision Partners: Rotational Nonequilibrium

Reaction	Type	M	A	N	E(kcal)	C ₁	C ₂	Comments
1) DF(v) = DF(v')	CDA	DF, 1.58HF	$1.2v \cdot 10^{14}$	-1.0	0	48.3v	0	1cv<3, 0cv'<v; Low Temp Form
2) DF(v) = DF(v-1)	CDA	HF, DF	$1.4v \cdot 10^{12}$	2.96	0	$5.6v \cdot 10^{-11}$	0	v<3, High Temp Form
3) DF(v) = DF(v-1)	CDA	D ₂ , 5CF ₄	55.v	3.0	0	$v \cdot 10^{-11}$	0	1cv<3
4) DF(v) = DF(v-1)	CDA	F ₂ , 2He	$7.8v \cdot 10^{-7}$	5.0	0	$2.44 \cdot 10^{-19}$	0	1cv<3
5) DF(v) = DF(v')	CDA	D	$4.8f(v) \cdot 10^{15}$	-0.75	3.38	(a)	(a)	1cv<3, 0cv'<v, f(v) = v ² /Δv
6) DF(1) = DF(0)	CDA	D	$2.4 \cdot 10^{11}$	0	1.22	0.046	0.147	-
7) DF(2) = DF(1)	CDA	D	$4.5 \cdot 10^{12}$	0	1.38	0.882	0.172	-
8) DF(2) = DF(0)	CDA	D	$2.3 \cdot 10^{12}$	0	1.38	0.406	0.084	-
9) DF(3) = DF(2)	CDA	D	$8.3 \cdot 10^{12}$	0	1.38	1.63	0.177	-
10) DF(3) = DF(1)	CDA	D	$4.2 \cdot 10^{12}$	0	1.38	0.75	0.087	-
11) DF(3) = DF(0)	CDA	D	$2.8 \cdot 10^{12}$	0	1.38	0.49	0.057	-
12) D ₂ (v) = D ₂ (v-1)	REG	700, 5D ₂	$1.8v \cdot 10^{-4}$	4.3	0	-	-	1cv<3
13) D ₂ (1) = D ₂ (0)	REG	D	$5.9 \cdot 10^{11}$	0.17	2.5	-	-	-
14) D ₂ (v) = D ₂ (v')	REG	D	$f(v, v') \cdot 10^{14}$	-0.9	2.4	-	-	f(2,1) = 4.5, (2,0) = 2.3, (3,2) = 70, (3,1) = 57, (3,0) = 34

(a)

v	1	2	3	3	3
v'	0	1	0	2	1
C ₁	2,410	9,700	4,170	22,100	9,250
C ₂	0.41	0.82	0.21	0.43	0.21

Table 1b. Reaction Rate Data for DF System for Exchange and Pumping Reactions: Rotational Nonequilibrium

Reaction	Type	A	N	E(kcal)	C ₁	Comments
1) F + D ₂ (v') = DF(v) + D	PUM	$4 \cdot 10^{13}$	0	1.97	-	k = 1.76, 4.0, 10.4 for v = 1, 2, 3; 0cv'<2 f ₁ (J) = 7±0.0, 0.013, 0.062, 0.065, 0.097, 0.13, 0.143, 0.169, 0.143, 0.117, 0.065, 0.007, 3±0.0 f ₂ (J) = 5±0.0, 0.008, 0.039, 0.064, 0.097, 0.125, 0.152, 0.169, 0.152, 0.122, 0.089, 0.003, 9±0.0 f ₃ (J) = 3±0.0, 0.014, 0.041, 0.067, 0.093, 0.126, 0.152, 0.161, 0.135, 0.106, 0.072, 0.032, 7±0.0 f(J) = 2±0.0, 0.016, 0.069, 0.082, 0.131, 0.18, 0.151, 0.121, 0.085, 0.066, 0.049, 0.036, 0.016, 7±0.0
2) D + F ₂ = F + DF(3)	PUM	$6.73 \cdot 10^{13}$	0	2.46	-	-
3) DF(v) + DF(v') = DF(v+1) + DF(v'-1)	VVE	$6.0 \cdot 10^{15}$	-1	0	2,420	1cv<2, v'<v
4) DF(0) + D ₂ (v) = DF(1) + D ₂ (v-1)	VVE	$5.4 \cdot 10^{11}$	0	0	0.106	1cv<3
5) DF(1) + D ₂ (v) = DF(2) + D ₂ (v-1)	VVE	$1.73 \cdot 10^{12}$	0	0	0.331	1cv<3
6) DF(2) + D ₂ (v) = DF(3) + D ₂ (v-1)	VVE	$5.4 \cdot 10^{12}$	0	0	1.06	1cv<3

Table 2a. Reaction Rate Data for H₂-F₂ Systems, Reactions Involving Generalized Collision Partners

Reaction	M	A	N	E(kcal)	Comments
1) $H + H \rightarrow H_2(0)$	π/OH	$6.2 \cdot 10^{17}$	-1.0	0.0	-
2) $H + H \rightarrow H_2(0)$	$2OH$	$9.4 \cdot 10^{16}$	-0.6	0.0	-
3) $F + F \rightarrow F_2$	$\pi/2.4F_2, 2.4F$	$4.7 \cdot 10^{15}$	-1.0	-1.3	-
4) $H_2(V) + H_2(V-1)$	$\pi/OH_2, OH$	$2.5V \cdot 10^{-4}$	4.3	0	$V = 1, 2$
5) $H_2(V) + H_2(V-1)$	H_2, H	$1.0V \cdot 10^{-3}$	4.3	0	$V = 1, 2$
6) $H_2(V) + H_2(V-1)$	H	$2.0 \cdot 10^{13}$	0.0	2.7	$V = 1, 2$
7) $HF(V) + HF(V-1)$	$HF, 0.5 DF$	$3.5V \cdot 10^4$	2.3	0	$1 \leq V \leq 7$
8) $HF(V) + HF(V-1)$	$HF, 0.5 DF$	$3.0V \cdot 10^{14}$	-1.0	0	$1 \leq V \leq 7$
9) $HF(V) + HF(V-2)$	$HF, 0.5 HF$	$7.5(V-1) \cdot 10^{14}$	-1.0	0	$2 \leq V \leq 7$
10) $HF(V) + HF(V-3)$	$HF, 0.5 HF$	$0.5(V-1) \cdot 10^{15}$	-1.0	0	$3 \leq V \leq 7$
11) $HF(1) + HF(0)$	H	$4.5 \cdot 10^{11}$	0.0	0.7	-
12) $HF(2) + HF(V)$	H	$8.4V \cdot 10^{12}$	0.0	0.7	$V' = 1, 0; V = 2, V'$
13) $HF(3) + HF(V)$	H	$1.57V \cdot 10^{13}$	0.0	0.7	$V' = 2, 1, 0; V = 3, V'$
14) $HF(4) + HF(V)$	H	$1.81V \cdot 10^{14}$	0.0	0.7	$V' = 3, 2, 1; V = 4/(V'+1)$
15) $HF(V) + HF(V)$	H	$1.81 \cdot 10^{14}$	0.0	0.7	$V = 5, 6, 7; V' = V-1, V-2, V-3$
16) $H(V) + HF(V-1)$	$AR, F_2, 2He, 2N_2, 2CF_4$	$7.7V \cdot 10^{-7}$	5.0	0.0	$1 \leq V \leq 7$
17) $HF(V) + HF(V-1)$	H_2	$6.0V \cdot 10^7$	1.0	0.0	$1 \leq V \leq 7$
18) $HF(V) + HF(V)$	F	$4.8g(V) \cdot 10^{14}$	-0.75	3.6	$V \leq 7, V \leq 3, g(V) = V^2/V$

Table 2b. Exchange and Pumping Reaction Rate Data for H₂-F₂ Systems

Reaction	A	N	E(kcal)	Comments
1) $F + H_2(V) \rightarrow HF(V) + H$	$g(V) \cdot 10^{13}$	0.0	1.6	$V' \leq 2, g(V) = 2.72, 8.79, 4.48$ for $V=1, 2, 3$
2) $H + HF(4) \rightarrow H_2(V) + F$	$3.7 \cdot 10^{12}$	0.0	0.46	$V \leq 1$
3) $H + HF(5) \rightarrow H_2(V) + F$	$3.9g(V) \cdot 10^{12}$	0.0	0.51	$g(0) = 1, g(1) = 1.78$
4) $H + HF(6) \rightarrow H_2(V) + F$	$4.2 \cdot 10^{12}$	0.0	0.58	$V \leq 1$
5) $H + F_2 \rightarrow HF(V) + F$	$1.2g(V) \cdot 10^{14}$	0.0	2.4	$g(V) = 0.08, 0.13, 0.35, 0.44$ for $V=3, 4, 5, 6$
6) $HF(V) + HF(V') \rightarrow HF(V-1) + HF(V'+1)$	$3.0 \cdot 10^{15}$	-1.0	0.0	$V = V' - V \leq 3, V \leq V' \leq 6$
7) $H_2(V) + HF(V) \rightarrow H_2(V-1) + HF(V+1)$	$8.3g(V) \cdot 10^{11}$	0.0	0.0	$g(V) = 1, 3.3, 10, 23, 46, 90$ for $V=0, 1, 2, 3, 4, 5, 6$

Table 3a. Reaction Rate Data for HF System Involving Generalized Collision Partners: Rotational Nonequilibrium

Reaction	Type	M	A	N	E(kcal)	C ₁	C ₂	Comments
1) $HF(v) + HF(v-1)$	CDA	$HF, 0.5DF$	$3.5v \cdot 10^5$	2.3	0.0	$1.9v \cdot 10^{-8}$	0.0	$1 \leq v \leq 3$
2) $HF(v) + HF(v-1)$	CDA	$HF, 0.5DF$	$3.0v \cdot 10^{14}$	-1.0	0.0	156v	-	$1 \leq v \leq 3$
3) $HF(v) + HF(v-2)$	CDA	$HF, 0.5DF$	$7.5(v-1) \cdot 10^{14}$	-1.0	0.0	$402(v-1)$	0.0	$2 \leq v \leq 3$
4) $HF(3) + HF(0)$	CDA	$HF, 0.5DF$	$1.0 \cdot 10^{15}$	-1.0	0.0	536	0.0	-
5) $HF(1) + HF(0)$	CDA	H	$4.5 \cdot 10^{11}$	0	0.7	0.0786	0.0618	-
6) $HF(2) + HF(1)$	CDA	H	$8.4 \cdot 10^{12}$	0	0.7	1.47	0.0646	-
7) $HF(3) + HF(2)$	CDA	H	$1.57 \cdot 10^{13}$	0	0.7	2.75	0.0676	-
8) $HF(2) + HF(0)$	CDA	H	$4.22 \cdot 10^{12}$	0	0.7	0.714	0.0316	-
9) $HF(3) + HF(1)$	CDA	H	$7.83 \cdot 10^{12}$	0	0.7	1.32	0.0330	-
10) $HF(3) + HF(0)$	CDA	H	$5.22 \cdot 10^{12}$	0	0.7	0.873	0.0215	-
11) $HF(v) + HF(v-1)$	CDA	H_2	$6.0v \cdot 10^7$	1.0	0.0	$1.2v \cdot 10^{-5}$	0.0	$1 \leq v \leq 3$
12) $HF(3) + HF(2)$	CDA	F	$4.34 \cdot 10^{16}$	-0.75	3.6	$2.8 \cdot 10^8$	0.348	-
13) $HF(2) + HF(1)$	CDA	F	$1.93 \cdot 10^{16}$	-0.75	3.6	$1.2 \cdot 10^8$	0.332	-
14) $HF(1) + HF(0)$	CDA	F	$4.82 \cdot 10^{15}$	-0.75	3.6	$3.0 \cdot 10^7$	0.318	-
15) $H_2(v) + H_2(v-1)$	REG	$\pi/OH_2, OH$	$2.5v \cdot 10^{-4}$	4.3	0.0	-	-	$1 \leq v \leq 2$
16) $H_2(v) + H_2(v-1)$	REG	H_2, H	$1.0v \cdot 10^{-3}$	4.3	0.0	-	-	$1 \leq v \leq 2$
17) $H_2(v) + H_2(v-1)$	REG	H	$2.0 \cdot 10^{13}$	0	2.7	-	-	$1 \leq v \leq 2$

Table 3b. Reaction Rate Data for HF System Involving Generalized Collision Partners: Rotational Nonequilibrium

Reaction	Type	A	N	E(kcal)	C ₁	Comments
1) $F + H_2(v) \rightarrow HF(v) + H$	PUM	$4 \cdot 10^{13}$	0	1.60	-	$0 \leq v \leq 2, 1 \leq v' \leq 3$ $k = 2.27, 8.79, 4.48$ for $v' = 1, 2, 3$ $f_{v'}(J)$ as follows: $f_1(J) = 4^{*0}, 0.010, 0.043, 0.115, 0.191, 0.201, 0.168, 0.120, 0.086, 0.048, 0.019, 7^{*0}$ $f_2(J) = 2^{*0}, 0.012, 0.049, 0.094, 0.127, 0.151, 0.154, 0.139, 0.103, 0.071, 0.049, 0.031, 0.015, 0.004, 6^{*0}$ $f_3(J) = 0.048, 0.226, 0.294, 0.232, 0.132, 0.055, 0.015, 14^{*0}$ $f(J) = 3^{*0}, 0.028, 0.068, 0.102, 0.141, 0.181, 0.169, 0.141, 0.113, 0.059, 9^{*0}$
2) $H + F_2 \rightarrow F + HF(3)$	PUM	$1.24 \cdot 10^{14}$	0	2.4	-	
3) $HF(0) + H_2(v) + HF(1) + H_2(v-1)$	VVE	$3.32 \cdot 10^{12}$	0	0	0.652	$1 \leq v \leq 2$
4) $HF(1) + F_2(v) + HF(2) + H_2(v-1)$	VVE	$1.09 \cdot 10^{13}$	0	0	2.156	$1 \leq v \leq 2$
5) $HF(2) + H_2(v) + HF(3) + H_2(v-1)$	VVE	$3.32 \cdot 10^{13}$	0	0	6.52	$1 \leq v \leq 2$

Table 4. DF Laser Power Spectral Distribution: Theory and Data

Level	Data	Rotational Equilibrium Theory
$v = 1-0$	31%	32%
$v = 2-1$	45%	43%
$v = 3-2$	24%	25%

AD P000269

HIGH GAIN CO CHEMICAL LASER

PRODUCED IN A SHOCK TUNNEL

M. Tilleman and J. Stricker

Department of Aeronautical Engineering

Technion - Israel Institute of Technology, Haifa 32000, Israel

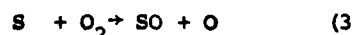
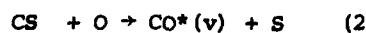
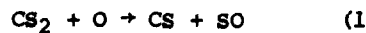
Experimental and theoretical results of small signal gain, in CO chemical laser produced in a shock tunnel, are presented. Thermal dissociation of CS₂ into CS+S is accomplished by a reflected shock wave. The dissociated products, diluted in Ar, expand through a supersonic nozzle with an area ratio of 40 into a combustion chamber. Molecular oxygen is supersonically injected at the nozzle exit. The two streams mix and combustion takes place in which vibrationally excited CO is produced by the CS+O→CO*(v)+S reaction.

Gain measurements of P₇(14) line were made at distances of 5.5 and 11.5 cm downstream of the oxygen injection point, with stagnation pressure of 25 atm. Stagnation temperatures were varied in the range of 2500-4600°K and mixtures of CS₂:Ar between 5:95 and 30:70 were tested. A maximum gain of 8% cm⁻¹ was observed for CS₂:Ar=20:80 at stagnation temperature of about 4000°K at a distance of 11.5 cm.

A semiempirical model, describing the fuel-diluent expansion through the supersonic nozzle and the fuel-oxidizer mixing process, was developed. The good agreement found between the experimental and computational results enables the utilization of the mathematical model for better understanding of the processes involved in laser operation. Maximum gains, in the mixing zone, of 16 and 17% cm⁻¹ were calculated for v=12→11 and v=20→19 lines, respectively. Considerable gain was obtained for v=1→0 transition. The calculations indicate that gains remain positive through large distances downstream from the injectors.

INTRODUCTION

The conventional CO chemical laser operates on the reaction sequence:



Fueling the laser directly with CS, which means elimination of reaction 1, has the advantage of a reduced oxygen atoms requirement. The CS fueled CO lasers have been studied extensively, both theoretically and experimentally¹⁻⁷.

Jeffers, et al.¹⁻² demonstrated the effectiveness of a CS fueled laser over a similar CS₂ fueled laser. The CS was produced by dissociation of CS₂ in a microwave discharge, which could supply a limited amount of CS. The requirement of oxygen atoms supply and the low values of CS:CS₂ obtained (~0.5) limited the laser performance. The development of a thermoelectric CS gas generator enabled the laser operation with CS:CS₂ values up to 1.6 and with reduced atomic oxygen supply. Maximum output power of about 94W, maximum specific power of 67 kJ/lbm and maximum small signal gain (s.s.g.) of $1.3\% \text{cm}^{-1}$ were obtained.

In 1978, Richardson and Wiswall³⁻⁵ first operated a supersonic combustor-driven chemical CO laser. In this laser, the combustor is fueled with NF₃-CH₄-H₂-CS₂ and produces a mixture of CS₂, CS and S with side products of HF and N₂. The mixture is supersonically mixed with O₂. Due to the high values of CS/CS₂ and S/CS achieved (5 and 0.05 respectively), O atom supply was not necessary; the chain reaction between CS and O₂ was initiated by S atoms. Maximum power of 700 W with specific energy of 4.5 J/gr was obtained. A comparison between the power observed and power predicted by a computational model, indicated that the laser performance could be greatly improved by eliminating the presence of the HF molecules and by further increasing both CS/CS₂ and S/CS ratios.

This work presents an experimental and theoretical investigation of a gasdynamical-driven CO chemical laser operated with very high CS-to-CS₂ and S-to-CS ratios. Diluted in argon, CS₂ is thermally dissociated by a reflected shock wave in a shock tube. The dissociated products are preserved by supersonic expanding through a nozzle into a combustion chamber where molecular oxygen is supersonically injected. The numerical model developed describes the fuel-diluent mixture expansion through the supersonic nozzle and the supersonic mixing. The model includes chemical reactions, vibrational-rotational-translational (V-R-T) energy transfer processes and radiation emission. Since a precise modeling of the mixing zone is very complicated a simplified semi-empirical approach was adopted.

EXPERIMENTAL

The pressure driven shock tube has been described previously in Ref. 8. The tube, 8 cm I.D., ends with a two-dimensional contoured supersonic nozzle, shown schematically in Fig. 1. The nozzle, of 0.8 mm throat and area ratio of 40, is separated from the low pressure chamber by a thin Mylar diaphragm which bursts upon arrival of the incident shock wave.

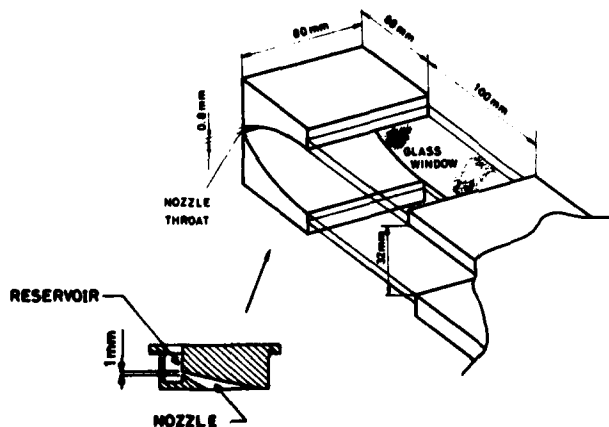


Fig. 1. Schematic description of the main and injection nozzles (lower part of the figure).

Three pairs of 5 cm I.D. ports are located on the nozzle side walls at distances of 28, 88 and 148 mm downstream of the nozzle throat. In the first pair, two convergent-divergent injection nozzles, shown in Fig. 1, are installed. The throat of the injection nozzle is of 1 mm width and of a height equal to the main nozzle outlet height. The divergent section of the injectors open with a constant angle of 20° to area ratio of 3 at the exit. The nozzles are inclined to the tunnel axis by an angle of 20° . The second and third ports serve as windows both for gain and for lasing experiments. A pair of 8 x 10 cm crystal glass windows, shown in Fig. 1, are mounted on the upper and lower walls of the constant area chamber following the nozzle. These windows were used for schlieren measurements and combustion layer photography. The main nozzle is exhausted into a 500 liter dump tank.

The single-mode single-line electrical CO probe laser as well as the experimental set-up for small signal gain measurements have been described previously.

Shock speed measurements were made by means of two platinum films located at a distance of 10 and 50 cm from the end of the low pressure section. The gauges are connected through a pulse amplifier to a counter. Stagnation pressures were measured with a Kistler 603A piezoelectric transducer, located close to the end of the low pressure chamber. The high pressure is achieved both by the reflected shock wave and by the exothermic dissociation of the CS_2 . The pressures were also calculated by solving the shock conservation and the thermochemical equations. The agreement between measurements and calculations was within 10%. The stagnation temperature was determined from the same calculations.

Prior to each experiment the shock tube was evacuated to 10^{-4} torr and the nozzle and dump tank to about 0.1 torr. After the CO electrical laser was tuned to a selected line, the low pressure chamber was filled up with a prepared testing mixture. Finally, the oxygen jet supply was actuated and the high pressure chamber was continuously pressurized up to the bursting pressure of the diaphragm.

The materials used in these experiments were: Herzlia Argon 99.5% pure, Merck CS_2 99.5% pure, I.B. Miller O_2 and N_2 99.5% pure. Airco pure helium was used as the driver gas. The materials were dry and contained impurities of N_2 and O_2 in atmospheric proportions.

NUMERICAL MODEL

In this section the numerical model is briefly presented. A detailed description of the model and further computational results are given in Ref. 6.

The model describes the expansion of the $\text{CS}_2/\text{S}/\text{Ar}$ mixture through the supersonic nozzle and the mixing between this flow and the injected oxygen. The model includes chemical reactions, V-R-T energy transfer processes and radiation emission processes occurring in the mixing region. In the present analysis each of the 20 CO vibrational levels considered is treated as a separate species, in rotational equilibrium. Since the precise modeling of the mixing zone is very complicated, a simplified semi-empirical approach was adopted. The boundaries of the mixing zone as well as the effects on the main flow of the injected oxygen have been determined experimentally. The size of the mixing zones was measured directly by photographing the combustion zone; a typical picture is shown in Fig. 2. In the figure the light area shows the luminous reaction zones where the dark area represents the flow region of the unreacted fuel.

The overall effects of the shear layer, separating the fuel and oxidizer

flows and of the oblique shock waves resulting from flow compression, were estimated by measurements of the variation of the main flow Mach number downstream from the injection points. This was done by measuring the angles of oblique shock waves generated in the flow by a two-dimensional wedge inserted into the test section. The shock waves were visualized by schlieren photography. These measurements were performed with either N₂ or Ar in the main flow (so that no chemical reactions occur) and repeated with different oxygen injection flow rates.

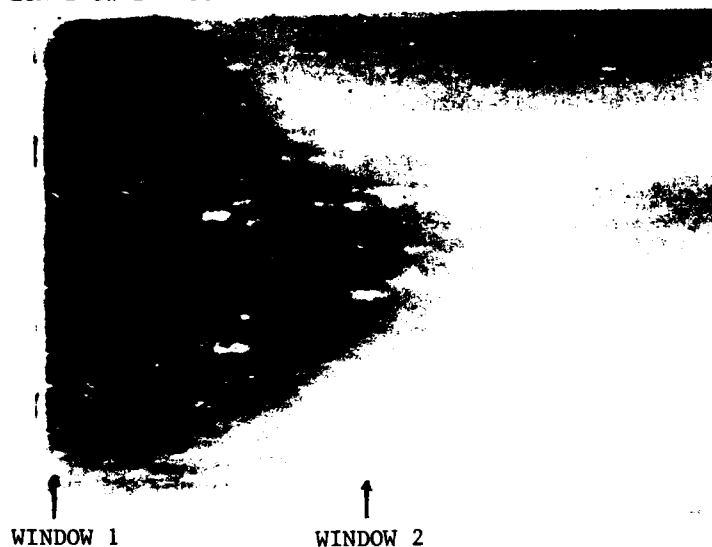


Fig. 2: Photograph of combustion layer. Stagnation conditions: 4100°K, 27 atm., CS₂:Ar = 20:80.

Calculations of the mixing zone properties were based on the following assumptions:

- (i) The flow is uniform on planes transverse to flow axis.
- (ii) The unreacted flow region is divided into a number of stream layers. It was assumed that on crossing the mixing zone boundaries, each of the streams mix instantaneously with the reacting flow in the mixing zone.
- (iii) The new stream quantities are determined by integrating the generalized one-dimensional flow equations (including heating and area variations), simultaneously allowing chemical reactions, V-V and V-T energy transfer processes and spontaneous emission.

The computed quantities, i.e., temperatures, pressures chemical composition and vibrational-rotational distribution of CO molecules, were used for s.s.g. calculations. Average s.s.g. values, over the whole optical path of the probe laser, were also calculated to compare directly with experimental results. Details of chemical reactions considered, chemical rate constants, V-V and V-T energy transfer and spontaneous emission rates are given in Ref. 6 and 8.

RESULTS AND DISCUSSION

Gain measurements were made at a distance of 11.5 cm downstream from the O₂ injection points, at window number 2, for P₇(14) line corresponding to $\lambda = 5.1886 \mu\text{m}$. The small-signal gain, γ , was determined according to:

$$\gamma = \frac{1}{L} \ln(I/I_0)$$

where L is the nozzle width, I_0 is the incident intensity of the probe laser and I is the instantaneous laser intensity during the test. All experiments were performed with a stagnation pressure of 25 ± 3 atm. and with a CS₂:O₂

volumetric ratio of 1:1. It has to be emphasized that the measured gain coefficients are average values over the mixing non-zero gain regions and the unreacted-fuel zero gain region.

Fig. 3 shows s.s.g. variation of $P_7(14)$, as a function of stagnation temperature, for different $\text{CS}_2:\text{Ar}$ concentrations. The figure indicates a fairly good agreement between experimental and calculated results. Maximum gain of $\sim 2\% \text{ cm}^{-1}$ was observed at stagnation temperature of 4500°K for $\text{CS}_2:\text{Ar} = 5:95$, $\sim 6\% \text{ cm}^{-1}$ at 4000°K for $\text{CS}_2:\text{Ar} = 10:90$, $\sim 7.5\% \text{ cm}^{-1}$ at 3900°K for $\text{CS}_2:\text{Ar} = 20:80$ and $\sim 7.5\% \text{ cm}^{-1}$ at 3400°K for $\text{CS}_2:\text{Ar} = 30:70$. Two competing effects, resulting from increasing stagnation temperature, are responsible for these maxima. On the one hand, high temperatures enhance formation of excited CO by accelerating the chemical reactions, while on the other hand, as temperatures rise, de-excitation of vibrationally excited CO by collisions becomes more and more significant.

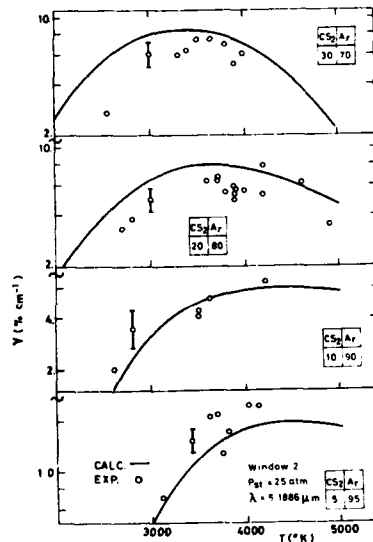


Fig. 3: Small signal gain of $P_7(14)$ line vs. stagnation temperature for $\text{CS}_2:\text{Ar} = 5:95$, $10:90$, and $30:70$.

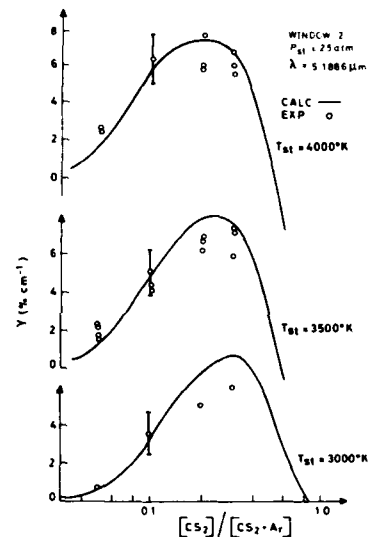


Fig. 4: Small signal gain of $P_7(14)$ line vs. initial CS_2 concentration for $T_{st} = 3000$, 3500 and 4000°K .

Fig. 4 shows experimental and theoretical gains for $P_7(14)$ vs. initial CS_2 concentrations. Results are shown for three values of stagnation temperatures: 3000 , 3500 , and 4000°K . This shows that up to CS_2 concentrations of about 25% gain increases, whereas for larger values of CS_2 concentrations a sharp drop in s.s.g. occurs. Maximum gain of $8\% \text{ cm}^{-1}$ was observed for $\text{CS}_2:\text{Ar} = 20:80$ at the stagnation temperature of 4000°K . This value is relatively very high for CO chemical lasers^{2,3,7}. In the low CS_2 concentration region, gain rises since the more CS_2 available the more CO is produced. The sharp drop in gain at higher CS_2 concentrations is caused by two effects: a) Enhanced CO vibrational relaxation due to increase in COS and SO_2 concentrations, while Ar concentration is being reduced (COS and SO_2 are known as very efficient vibrational energy relaxing molecules). b) The enhanced vibrational relaxation process affects the flow over longer distances downstream of the injectors since the consumption of CS (or formation of CO) becomes very fast and is completed close to the oxygen injectors.

S.s.g. profiles for $\text{CS}_2:\text{Ar} = 10:90$ and different stagnation temperatures are shown in Fig. 5.

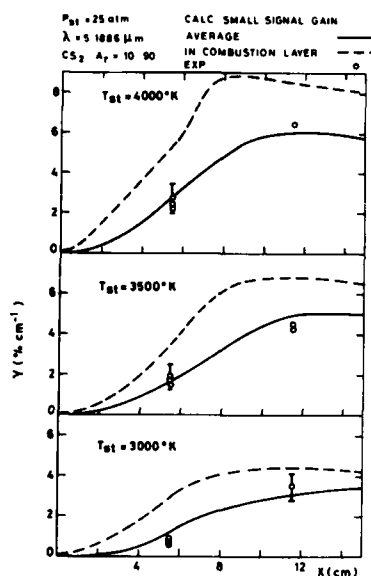


Fig. 5: Small signal gain of $P_7(14)$ line vs. distance along the nozzle. The oxygen injectors are located at $x=0$. The solid lines and the broken lines represent theoretical results for average gain and combustion zone gain, respectively.

The solid lines present, as before, the calculated average s.s.g. while the broken lines show the calculated s.s.g. in the combustion layer. The experimental results shown in the figure are measured at distances of 5.5 and 11.5 cm downstream from the injectors. From the figure it can be seen that both the average gain profile and the combustion-layer gain profile reach a maximum. The higher the stagnation temperature the shorter the distance where the maximum occurs. Once the maximum is reached the relaxation of gain is quite slow.

The quantitative good agreement found between the numerical and experimental results suggests the use of the model for additional investigation of gain mechanism⁶. Fig. 6 shows calculated maximum gains (with respect to rotational levels) vs. vibrational level at various locations downstream of the flow.

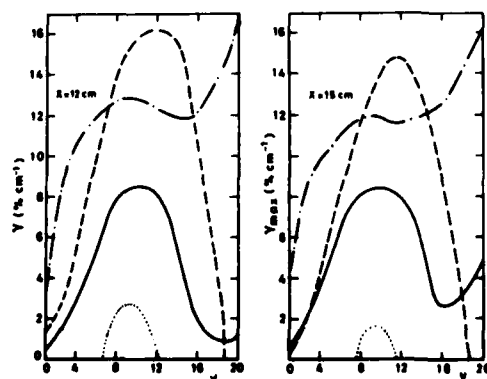


Fig. 6: Calculated maximum gains (with respect to rotational levels) vs. vibrational level at 12 and 15 cm downstream from the injectors. $T_{st} = 4000^\circ\text{K}$, $P_{st} = 25$ atm.,
— $\text{CS}_2:\text{Ar}=5:95$; --- $10:90$
- · - $30:70$ and ···· $60:40$.

The curves shown are those calculated in the combustion zone. It is seen from the figure that very high gains are attained further away from the injectors, mainly for $v=8-14$. It is interesting to note that significant gains are also obtained in the $1 \rightarrow 0$ transition for CS_2 mole fractions of 10-30%.

SUMMARY

The main results of the present investigation are as follows:

- a. High gains were measured for stagnation temperatures of 3500 to 4000°K and for CS_2 :Ar concentrations of 20:80 to 30:70. The maximum gain observed for $P_7(14)$ line was $8\% \text{ cm}^{-1}$ at $T_{st} \approx 3800^\circ\text{K}$ and CS_2 :Ar = 20:80. Gains of the order of $16\% \text{ cm}^{-1}$ were calculated in the combustion zone for $v=12 \rightarrow 11$ and $v=20 \rightarrow 19$ transitions.
- b. The existence of relatively high gains through large distances downstream of the O_2 injectors, indicates that the excited CO molecules undergo quite a slow relaxation. This makes the CO chemical laser attractive compared to the HF chemical laser⁹.
- c. The fairly good agreement between experiments and calculations indicates that the set of chemical rates and energy transfer rates used in this study is quite accurate.
- d. Significant gains were calculated for $v=1 \rightarrow 0$ lines.

ACKNOWLEDGEMENTS

We thank Dr. A. Burcat for helpful discussions. We are also grateful for the technical assistance of Mr. E. Wardnikov and Mr. D. Porat.

REFERENCES

1. W.Q. Jeffers, C.E. Wiswall, J.D. Kelley and R.J. Richardson, Appl. Phys. Lett., 22, 587 (1973).
2. W.Q. Jeffers, H.Y. Ageno and C.E. Wiswall, J. Appl. Phys., 47, 2509 (1976).
3. R.J. Richardson and T.J. Menne, Laser Focus, p. 50, June 1978.
4. R.J. Richardson and C.E. Wiswall, Appl. Phys. Lett., 33, 296 (1978).
5. R.J. Richardson, H.Y. Ageno, H.V. Lilenfeld, T.J. Menne, J.A. Smith and C.E. Wiswall, J. Appl. Phys., 50, 7939 (1979).
6. M. Tilleman, D.Sc. Thesis, Technion - Israel Institute of Technology (1980).
7. S. Wakabayashi, T. Arai and T. Fujioka, J. Appl. Phys., 50, 6155 (1979).
8. M. Tilleman, J. Stricker and A. Burcat, Proceedings of the 12th International Symposium on Shock Tubes and Waves, Jerusalem, p. 644 (1979).
9. K.T. Yano and H.M. Bobitch, IEEE J. Quant. Elect., QE-14, 12 (1978).

AD P000270

SHOCK/LUDWIG-TUBE DRIVEN HF LASER

David A. Russell and George W. Butler

Aerospace and Energetics Research Program

University of Washington, Seattle, Washington 98195, USA

A laboratory facility has been constructed for study of the highly-coupled cw HF/DF chemical laser. F₂/diluent oxidizer gases are heated at the end wall of a rectangular shock tube and expanded through a screen nozzle to the test section. Unheated H₂ fuel is simultaneously supplied to the screen nozzle from a Ludwig tube. The supersonic streams mix and react downstream, and multimode power is extracted by a simple cavity. The power is repeatable and shows some agreement with a quasi 1-D model under development. Operating features and capabilities of the facility are discussed, and its usefulness for systematic study indicated.

INTRODUCTION

The HF/DF chemical laser is one of the most powerful cw systems known, with a maximum vibrational energy storage of $2(10)^3$ J/gm of initial F₂ burned in the cold reaction. The F₂ oxidizer and H₂ or D₂ fuel are typically expanded in separate streams, and mixed and reacted to produce a population inversion in the product state. Supersonic expansions are used to control the upstream extent of the reaction, to provide proper lasing conditions, and to rapidly remove waste heat and deactivating products. The buildup of the latter limits the axial extent of the lasing zone and leads to the use of fine-scale multi (screen) nozzles. These in turn introduce boundary layers, wakes, base regions, and flow-turning shock-systems into the shear layer environment. The layers thus have complex initial and external flow sources, in addition to being transitional in nature. Energy release within the layers causes a displacement effect leading to a system of "reaction shock" that further modify the entering gas. The energy release is large; indeed, extra gas flow and/or cross-sectional area relief are needed to prevent choking. The kinetics of the lasing process are thus intimately coupled to the fluid flow.

A recent paper (ref. 1) provides an excellent overview of the actual performance of the HF/DF chemical laser. State-of-the-art lasers are complex to build and expensive to run, while theoretical modelling will usually lag behind physical insight. This paper discusses a laboratory facility for studying the HF/DF laser that is flexible, safe, and inexpensive to operate. The facility was first reported at the previous symposium (ref. 2). The present paper updates that work to include power extraction measurement from a screen nozzle designed for the study of shear layer performance. The facility, screen nozzle, and optical system are described in the next section, followed by a discussion of operating conditions and test times available. A section on methods then

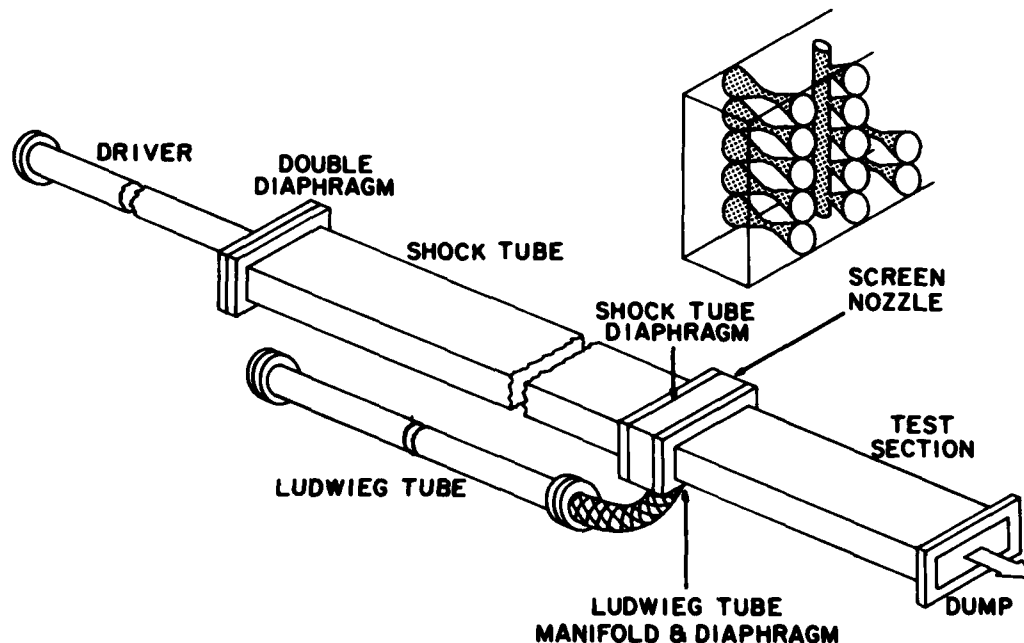


Figure 1. Shock/Ludwig-tube facility (insert shows screen nozzle schematic)

precedes one on typical measurements. Finally, there is a discussion of shear-layer power output, in which a quasi 1-D model currently under development (ref. 3) is used to aid interpretation of the measurements.

THE FACILITY

General Description

Figure 1 shows the shock/Ludwig-tube facility in the configuration used for the present study. The gas mixture containing the oxidizer is shock heated in the 5x20x750 cm tube. Reflection of the shock ruptures a thin prescribed Al diaphragm and the partially dissociated gas expands through the screen nozzle to a 5x20x90 cm long test section. Unheated fuel is simultaneously supplied to the screen nozzle and test section from the 7.5 i.d. x 600 cm Ludwig tube. Synchronization is accomplished by using a double diaphragm to start the shock tube and an electronically delayed, solenoid-operated cutter to break a Mylar diaphragm in the Ludwig tube. The supersonic fuel and oxidizer streams mix and react downstream of the nozzle and exit to a 2.5 m³ dump tank. Beginning at a juncture at 10 cm, the top and bottom walls of the test section are diverged at 1/4° to compensate for turbulent boundary layer growth. The driven tube, screen nozzle and test section are constructed of aluminum, the driver and Ludwig tube of stainless steel. Regular buna-N "O" rings are used throughout.

A screen nozzle was manufactured with individual 10° conical half-angle expansions of area ratio 10 and exit diameter of 0.5 cm. Ten degree conical relief was applied to the subsonic side, leaving throat regions one throat-diameter long. The expansions are close packed in the nozzle, with column spacing of 0.45 cm resulting in an effective downstream base-to-exit cross-sectional area ratio of 0.10. The ten oxidizer expansions in each column are fed directly by the shock tube, whereas the nine fuel expansions in adjacent columns are connected through a manifold to the Ludwig tube (see insert). An extra fuel column is provided next to the side walls to reduce window etching;

altogether the screen nozzle produces 42 equivalent 2-D oxidizer/fuel mixing layers downstream.

Piezoelectric pressure transducers are used to time the initial shock wave, and to measure the pressure 8.3 cm upstream of the screen nozzle and in the fuel manifold. Figure 2 is a schematic of the cavity showing its major components. Two 5.5-cm i.d. x 0.6-cm thick CaF_2 flats were fitted to the test-section side-walls with O-ring seals and a metal mask to provide 2-cm high rectangular windows which extend 4-cm downstream of the screen nozzle exit. The optical cavity is formed by a 5-cm dia 10-m Au-coated mirror and a 5-cm Ge-flat output coupler separated by ~ 75 cm. Power output is focused by a 10-cm CaF_2 lens to a ~ 0.5 cm spot size on the face of a Gentec ED-200 pyroelectric calorimeter. A fast-response PbSe photo-conductive cell is offset to receive a reflected signal from the calorimeter face in order to monitor the temporal behavior of the output. The entire optical system is isolated from the shock tube on a translating platform suspended from the laboratory ceiling.

Operating Conditions

The reduced cross-section driver and a square cross-section diaphragm receiver/transition section cause secondary waves upstream of the contact surface with predicted real-gas shock-tube performance as shown on Figure 3. Here P_4 and P_1 are the initial driver and driven tube pressures, while P_{01} and T_{01} are the oxidizer total pressure and total temperature after shock reflection. The solid lines indicate P_4/P_{01} values while dashed curves represent P_4/P_1 . The calculations (ref. 4) were for N_2 driving into a mixture of 5% F_2 in A, and for He into 5% F_2 in He. With the exception of pure A honesty runs, these were the gas combinations used for the present study. P_{01} was chosen at a nominal 2.8 atm for the A and 1.5 for the He gas mixtures, with nominal T_{01} of 1100°K and 1200°K in A and 1100°K in He. The actual P_4 required was found to be ~ 2 times that given by the figure, the difference presumably due to viscous losses. Note that higher values of T_{01} could exceed gas bottle and driver pressure capability, requiring use of a lighter driver gas and/or more efficient geometry. The Ludwig tube was unheated and thus operated at a nominal T_{02} of 300°K. It was filled with a pure H_2 fuel at an initial pressure (essentially P_{02}) of 2.7 and 1.0 atm for the A and He diluent oxidizers, respectively. This resulted in calculated mixed nozzle-exit fuel-to-oxidizer static-pressure ratios of 1.9 and 1.1.

Wave diagram calculations predict a nominal shock-tube test-time of 0.2 L/a_1 before a re-reflected wave from the contact surface arrives at the end wall. Here L is the length of the driven tube, and a_1 the speed of sound in its initial gas charge. The wave is a relatively strong shock and it reflects back and forth some 5 times to more than double P_{01} before the test gas is exhausted at $\sim 1.0 L/a_1$. The secondary waves in the driver gas are comparatively weak and are not expected to contribute significantly to this process. The test gas slug is $\sim 0.3 L$.

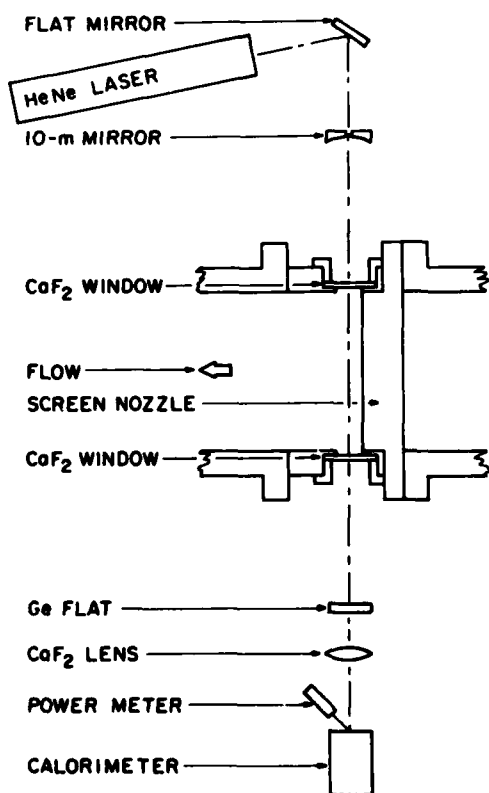


Figure 2. Cavity optics

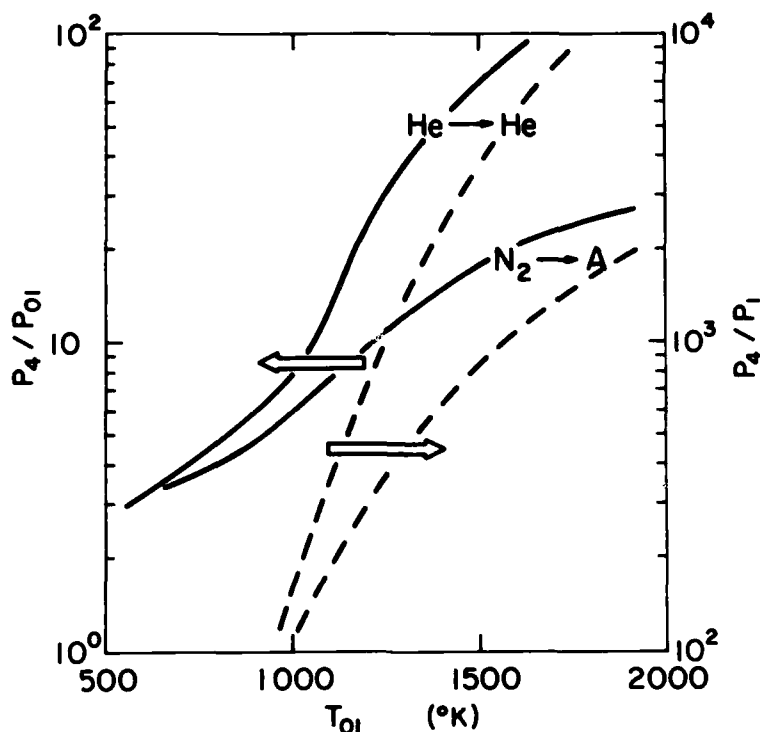


Figure 3. Shock-tube performance; solid lines P_4/P_{01} , dashed P_4/P_1 ($A_4/A_1 = 0.44$; $A_{\text{diaph}}/A_1 = 0.26$; $A_{\text{extract}}/A_1 = 0.05$; $X_{F_2} = 0.05$; $T_1 = 300^\circ\text{K}$)

long, and expands to a length of ~ 1.4 L after passage through the screen nozzle. Viscous effects (ref. 5) are calculated to reduce all of these times and lengths by a factor of ~ 2 . The test time for each pressure plateau in the Ludwig tube is ~ 2.0 times the L/a_j appropriate to it. Nozzle and cavity starting times are expected to be short compared to the test times available.

The optical cavity has a Fresnel number of ~ 40 , and thus should operate multimode with the full gas volume participating. It was nominally centered 1.2-cm downstream of the nozzle exit for the A-runs and 1.4-cm for the He-runs, this being midway between the power on and off points given by calculation (ref. 3) to be discussed later.

EXPERIMENTS

Methods

Commercially-prepared oxidizer mixtures were used which had HF impurity listed as $\leq 0.2\%$ of the F_2 present. The A and He diluents and the H_2 fuel were stated pure to within 10 ppm, except for He in the H_2 . The tubes and dump tank were pumped through LN_2 cold traps to $\sim 10^{-3}$ and $\sim 10^{-2}$ torr respectively. For most of the runs the oxidizer was processed through a commercial HF trap and the fuel through a LN_2 cold trap. Outgassing rates of $\leq 1\mu/\text{hr}$ were maintained for the tubes and for the dump tank by minimizing time open to the atmosphere. The shock tube and screen nozzle were carefully passivated to insure against F_2 depletion to the walls. By storing no more than 10 atm of F_2 in the laboratory, a minimum of 10 ppm HF worst-case spill standard could be met.

The optics were aligned prior to each run using the HeNe laser reflected

through the 2-mm hole in the 10-m mirror (Figure 2). The optical table was first adjusted so that this beam passed through the same location on each CaF_2 window. The Ge-flat was then adjusted to center the reflected spot back on the laser exit pinhole. A mylar film placed in front of the flat would then show an image of the 2 mm-mirror hole. Alignment was completed by adjusting that mirror to center the image on the main reflection. The calorimeter was calibrated using a cw HF laser, a cw power meter (Coherent Radiation Laboratories Model 201), and an electronic shutter. Measured response was $12 \text{ V/J} \pm 10\%$, with no dependence on pulse length detectable for power on times up to $2(10)^{-3} \text{ sec}$. The transmissivity of the combined Ge flat and CaF_2 window was measured to be 0.31. Assuming 59% reflection and 10% absorption, with 95% reflection and 5% absorption at the mirror, the power fraction coupled out was calculated (ref. 6) to be 0.71.

An accelerometer at the double diaphragm station was used to provide a delayed signal for the Ludwig tube cutter when A-diluent test gases were used; however, it was found necessary to delay directly from the double-diaphragm solenoid signal for the He-runs because of the increased speed of the shock wave. Facility operation was very repeatable. The use of substantial over pressure and impulse typically resulted in clean diaphragm breaks, with measured shock speed variation for a given run condition $<0.5\%$.

Measurements

Representative plenum pressure traces are shown on Figure 4. The left-hand figure is from an A-diluent run, the right-hand a He-run. Note that both Ludwig tube (P_{02}) pressures exhibit a $9(10)^{-3} \text{ sec}$ plateau before return of the expansion, in agreement with the predicted $2 L/a_j$. While the amplitude is reduced for the He-run in proportion to the initial charge pressure, the traces are identical in character.

The figure shows initiation of the oxidizer flow just past the midpoint of the fuel flow in both cases. Expanded scale traces of P_{01} show the initial jump is followed by a substantial dip before the approximately constant level is established. This dip is due to the diaphragm opening process and its effects may carry through to the power traces as discussed below. The P_{01} plateau lasts for $2-3(10)^{-3} \text{ sec}$ ($\sim 0.1 L/a_j$) for the A-run, after which compression waves from the shock interaction with the contact surface reflect back and forth to double the pressure by the time the unadulterated test gas is exhausted. This is expected at $10-15(10)^{-3} \text{ sec}$ ($\sim 0.5 L/a_j$), and it is followed by the arrival of

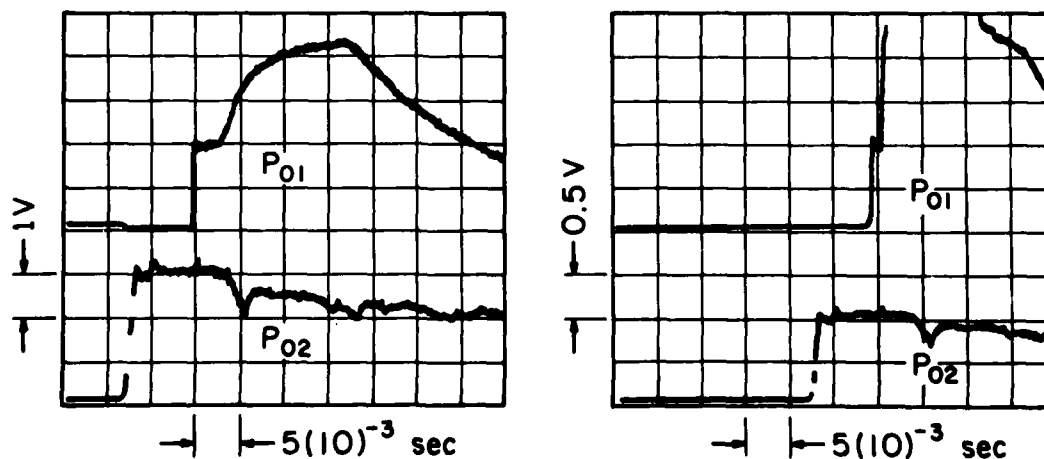


Figure 4. Representative plenum pressure histories ($T_{01} = 1100^\circ\text{K}$; left traces for A-diluent, right for He-diluent)

the reflected driver expansion-wave and subsequent reduction of P_{01} . The initial speed of sound is increased by 2.7 for the He-run, reducing the initial oxidizer plateau to $\sim 10^{-3}$ sec. Strong reflections follow which raise P_{01} by a factor of 4 before the expansion wave returns from the driver, these events now also occurring at a compressed time.

Open-shutter chemiluminescent photographs have been taken looking down on the cavity flow (ref. 2). These show orange light from overtone HF emissions produced by the burning of the H_2 and F in each shear layer. The layers remain distinct and separate for this screen nozzle, and the 42 burning interfaces are clearly visible.

Figure 5 reproduces PbSe detector power traces taken during the runs of Figure 4. The vertical scale was calculated by equating the integral of the profile to the calibrated calorimeter output. Note that substantially more power is produced for the He-diluent case. The power typically starts with a spike. This is most likely due to an initial burst of oxidizer accelerated through the nozzle as the shock-tube diaphragm opens, but it may also be associated with a burning-front starting-process in the cavity. Figure 5 shows that the interval associated with it scales inversely with a_1 , as would be expected in either case. The spike is followed by a power pulse of a duration in approximate agreement with the P_{01} plateau. Indeed, earlier cavity wall-pressure measurements clearly identify the start of the rapid pressure rise with the power fall off. While model calculations (ref. 3) predict total power increases as the P_{01} and T_{01} rise, the width of the lasing zone in the flow direction is expected to decrease by over a factor of 4. As discussed below, this could explain the rapid power fall off.

Honesty runs for which pure A was substituted for the oxidizer mixture produced no power. Further, no effects of increased gas purity, i.e., use of diffusion pumps, repassivation or double flushing before a run, were evident. While no direct check of F_2 content was available, runs with separately ordered bottles and with a locally mixed bottle showed no mixture trends. F_2 dissociation in the shock-heated gas was calculated to have characteristic times on the order of 10^{-4} sec, so that equilibrium chemistry predictions were considered valid. A concern about possible backflow of fuel through the oxidizer nozzles prior to shock-tube diaphragm burst led to experiments in which the cavity and dump tank were initially filled to ~ 10 torr with pure He. While starting processes were sped up for the A-runs, there was no effect on overall performance.

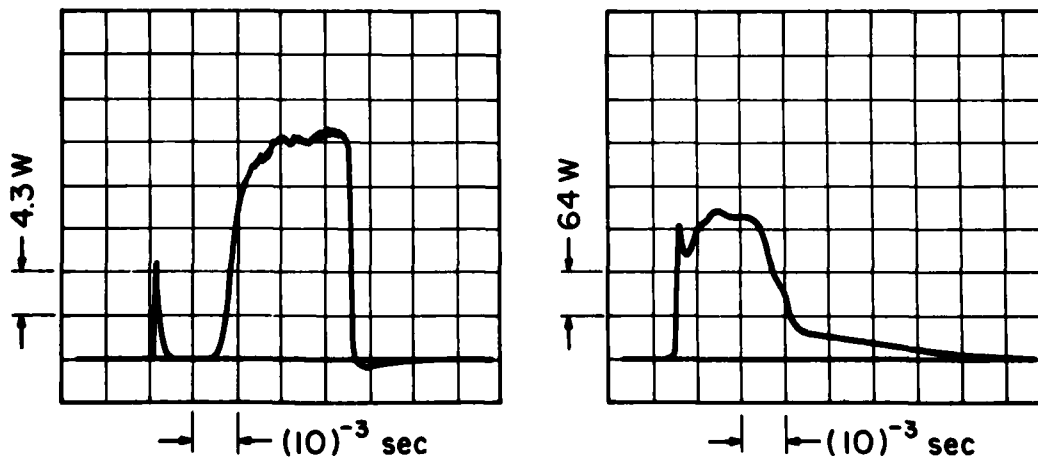


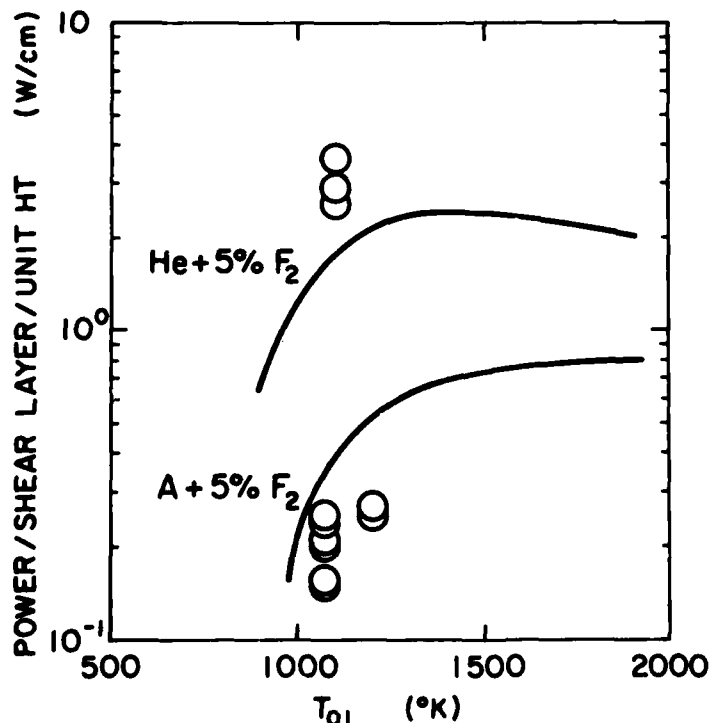
Figure 5. Representative power histories (runs of Figure 4)

The location of the cavity center was found to be important when the lasing zone was predicted to be of small axial extent. In such cases mirror curvature could cause the beam to wander from the gain path into a high-loss region of the flow. This was particularly true for the higher temperature A-runs where the combination of fast kinetics and low velocities reduced predicted lasing length to a small fraction of a centimeter. Avoiding uncertainties associated with such narrow gain regions, power repeatability appeared to depend primarily on the precision of cavity alignment.

DISCUSSION

The calibrated power output from runs such as those of Figure 5 was divided by the number of shear layers (42), by the cavity height (2 cm), and by the fraction of power outcoupled (0.71) and plotted on Figure 6. T_{01} was obtained by real-gas calculation from the measured shock velocity and pressure ratio, P_0/P_1 . There is some uncertainty in the data due to errors in integrating the power curve and losses and calibration error in the calorimeter. Thus accuracy of the order of the symbol size is expected. Some low power runs with erratic power profiles have been excluded. The scatter of the data on Figure 6 is a maximum of $\pm 25\%$ from the mean at each of the three nominal run conditions. There is a trend toward increased power with T_{01} for the A-runs, while the He-runs show over an order-of-magnitude increase in power output.

Calculations by a new quasi-1-D model of the HF laser are shown for comparison on Figure 6. This model (ref. 3) includes non-ideal expansion losses, base flow regions, exit pressure imbalance, and entrainment into layers that grow linearly until merging, and have instantaneous mixing and heat release. The lasing model of Broadwell (ref. 7) is used, which assumes three excited vibrational-states for HF with rotational levels in translational equilibrium. Reservoir inputs to the calculation are the fuel and oxidizer compositions and values of P_0 and T_0 ; expansion inputs are the wall angles, exit diameters,



and area ratios of the expansions, a wall recombination parameter, and the base area; and finally, cavity parameters are the 2-D height of the base flow recompression zone and its axial location, the degree of base flow combustion, the entrainment half angle, and the ratio of entrainment angles of the two streams. For the present calculations recombination was neglected, the recompression zone height and axial location taken to be 0.1 and 1.5 times the effective 2-D base width respectively, base combustion was set to zero, the entrainment half angle to 0.5° , and the ratio of entrainment angles to 1.

Figure 6. Closed cavity power (comparison with theory of reference 3).

Increasing T_0 increases the dissociation of F_2 which approaches 90% at 1500°K. The laser runs primarily on the cold reaction ($F + H_2 \rightarrow HF^* + H$) with an overabundance of fuel present. Thus power depends strongly on the concentration of F . Although the pumping rate constants increase with T , the increased local concentration of ground-state HF enhances deactivation and begins to reduce power at higher T_0 . The mass flux difference between the oxidizer and fuel streams results in large mixing losses when A-diluted oxidizers are used. These losses increase local T and P , and thus speed up the reactions and shut off the process before much gas can be entrained into the shear layer. Heavier oxidizer mixtures travel slower and this also compresses the lasing zone. The predicted effects are large and are seen to be more than borne out by the experiments.

While all fluids-related parameters can significantly influence laser performance (ref. 3), the entrainment angle is particularly important. Increases in this quantity move the laser towards premixed performance, reducing the relative importance of deactivation collisions and allowing larger nozzle scales for efficient use of the flow cross-section. Lasing is predicted to turn on at ~ 1 expansion exit diameter downstream and turn off at ~ 5 diameters or 2.5 cm for the conditions of the He-runs. Less than 10% of the available gases will have been entrained by this distance downstream. The shear layers are thus far from merged by the time lasing is completed. Changes in the entrainment rate should, therefore, directly effect the total power or power-per-shear-layer on Figure 6.

While the 0.5° used is reasonable (ref. 3), it was chosen only as a first approximation. Indeed, the layers are most likely laminar in nature, requiring a parabolic rather than linear entrainment rate in the calculation. Further, the growth rate of a laminar He-diffusion layer is almost double that for A. These facts may partially explain why the He-diluent prediction is a factor of ~ 2 below the experiments while that for A is almost a factor of 2 above. Various attempts to enhance the mixing through increased diffusion-layer surface area have been reported in the literature.

It is concluded that the present facility provides a versatile and inexpensive means of exploring the fundamentals of cw HF/DF laser performance over a wide range of conditions and configurations. Preliminary power measurements have been repeatable to $\pm 25\%$, and it is expected this can be increased with refinement of timing and alignment procedures. Converting to tailored operation offers the prospect of 4-5 times larger test times. Further work is needed on cavity positioning, particularly when narrow lasing zones are predicted, before a systematic study is undertaken of shear layer mixing enhancement and other fluid phenomena important to this laser.

ACKNOWLEDGEMENTS

The authors would like to acknowledge contributions from Robert E. Breidenthal. This work was supported by the United States Office of Scientific Research, Contract F49620-79-C-0020.

REFERENCES

1. L.E. Wilson, J. de Physique, Colloque C9, Suppl. 11, 41, C9-1 (1980).
2. G.W. Butler and D.A. Russell, Shock Tubes and Waves, 655 (1979).
3. G.W. Butler and D.A. Russell, AIAA Paper 80-1401, (1980).
4. D.A. Russell, Phys. Fluids 5, 4, 499 (1962).
5. H. Mirels, Shock Tube Research, 611 (1971).
6. R.W.F. Gross and J.F. Bott, Handbook of Chemical Lasers, Wiley, NY (1976).
7. J.E. Broadwell, Applied Optics 13, 962 (1974).

AD P000271

DETERMINATION OF ABSORPTION COEFFICIENTS IN SHOCK

HEATED PROPELLANT MIXTURES FOR LASER-HEATED ROCKET THRUSTERS

Robert H. Krech and Evan R. Pugh

Physical Sciences Inc.

Woburn, MA 01801

A series of shock tube experiments were performed to determine the temperature dependence of the absorption coefficient of water vapor at high temperatures on the P(16), P(18) and P(20) 10.6 μ CO₂ laser transitions. Measurements were made behind both incident and reflected shock waves encompassing a temperature range from 600 K to 3700 K at pressure from 1 to 40 atmospheres in 2, 5, and 10 mole percent water vapor in argon gas mixtures; a limited number of runs were conducted using 10 mole percent mixtures of water vapor in hydrogen or nitrogen. Conditions at several temperatures were sufficiently varied to investigate the effects of broadening on the absorption coefficient. Within the narrow spectral range from 944 to 948 cm^{-1} covered in the measurements, no significant variation in the absorption coefficient was observed as a function of laser wavelength, water concentration, total pressure, or collision partner. These observations suggest that the water lines are sufficiently broadened to act as a continuum absorber under conditions to be found in a laser-heated rocket thruster. The measured laser high temperature absorption coefficients are 50 percent lower than the value obtained from the Ludwig empirical curve fit to low resolution data.

INTRODUCTION

A laser-heated rocket-thruster converts laser energy, beamed from a remotely stationed laser, into thrust by using the laser radiation to heat the propellant. This technique provides a distinct advantage over conventional chemical rocketry by yielding a high specific impulse (greater than 1000 s^{-1}) vs. approximately 500 s^{-1} for chemical rockets) at high thrust levels (potentially greater than 1000 lb); however, significant technological advances in the design and development of high power laser facilities, pointing and tracking systems, and collection optics will be required before laser-heated thrusters leave the laboratory. Either pulsed or continuous wave (CW) lasers can be used as the radiation source. To obtain the highest specific impulse for a given temperature, hydrogen is the propellant of choice.¹⁻⁴ A 10.6 micron CO₂ laser is a potential candidate as the source of the laser radiation.

The only absorption mechanism for pure hydrogen at this wavelength is inverse bremsstrahlung, which requires the presence of electrons. Ionization of

the hydrogen and the production of electrons is initiated only at temperatures between 7000 K to 11,000 K, depending on the pressure. Thus, pure hydrogen must be heated to absorb the laser energy.

In a pulsed laser propulsion system, this heating is accomplished by focusing the laser beam to create a laser-induced breakdown. The hot, rapidly expanding plasma drives a laser-supported detonation (LSD) wave into the surrounding cool hydrogen. This gas is heated to extremely high temperatures (around 20,000 K), ionizes, and the electrons generated behind the LSD wave absorb the laser energy to sustain the propagation of the wave. The propagation of the wave continues until the intensity of the laser beam drops below the level required to sustain the wave or until the pulse ends. The heated gas then expands in the rocket nozzle creating thrust. Laboratory scale proof of concept experiments at 10.6 μ yielding specific impulses over 1000 s^{-1} , have been conducted at PSI and have demonstrated the feasibility of this system.^{5,6}

CW laser-heated thrusters with pure hydrogen propellant operate in a similar manner. In this thruster, when laser radiation is focused into a plasma, a laser-supported combustion (LSC) wave is created. If the gas flow velocity into the thrust chamber is matched to the wave velocity, then a stationary "flame" front is created. Hydrogen passing through the flame front is heated and ionized. The electrons generated by the ionization absorb by inverse bremsstrahlung, and sustain the wave. One problem with this type of thruster is that there may be severe radiative heating of the chamber walls by the stationary 20,000 K plasma. Seeding the hydrogen with an easily ionizable substance, such as cesium, has been proposed as one method to lower the operating temperature of the thruster and therefore reduce the heat load on the walls. If the hydrogen is seeded with a molecule that absorbs at low temperatures then the system is simplified. First, no LSC wave need be sustained to heat the hydrogen, allowing greater flexibility in the setting of gas flow rates. Second, and perhaps more important, the operating temperature is substantially lower and thus the heat load on the chamber walls is reduced. The problem is to find a low molecular weight, low temperature absorber that will not decompose to any significant degree below 3500 K to 4500 K, the temperature range of a thruster operating with specific impulses between 1000 s^{-1} and 2000 s^{-1} .

Water and/or ammonia have been proposed as possible candidates for absorbers at 10.6 μ . Water is particularly attractive since significant dissociation does not occur until the temperature exceeds 3500 K. Low resolution, broad band spectra of water vapor in flames indicated that the absorption coefficient at high temperature near 10.6 μ would be acceptable for a thruster. However, the high energy levels in the water molecules are not well known; thus it was necessary to conduct measurements on the 10.6 μ laser transitions P(16), P(18), P(20) found in high power CW CO₂ lasers to determine if there was any wavelength dependence on the absorption coefficient.

EXPERIMENTAL

The experimental absorption coefficient measurements were performed behind both incident and reflected shocks. The shock tube has a five foot long by 1.5 inch i.d. driver and a 15 foot long by 1.5 inch i.d. driven section. The optical measurements are made through anti-reflection coated zinc sulfide windows mounted one inch from the end wall in a five foot long by 1.31 inch square test section coupled to the driven section with a three inch long constant area transition piece. Shock pressure is measured by four piezoelectric transducers located at one foot intervals along the test section. The shock velocity is determined by the time of arrival of the shock wave at successive stations. The last transducer is located at the optical port to allow for a direct correlation of the optical signal with total pressure.

The shock heated gas mixtures consisted of 2 to 10 mole percent H₂O in

either Ar, H₂ or N₂. Extreme care went into the preparation and loading of the water vapor/gas mixtures to insure that the H₂O would not condense out and change the gas composition. The tube and all associated hardware were maintained at 320 K to permit the loading of up to 0.1 atm of H₂O vapor without condensation. (In actual practice, no more than 0.05 atm of H₂O vapor was loaded into the system.) Fresh gas mixtures were made for each run. The system was evacuated only to a vacuum of 1-10 μ to avoid removing the monolayer of water on the walls. Typically, the system was exposed to water vapor by filling and evacuating the tube several times just prior to the final fill before the shock to further stabilize the walls. No changes in pressure with time were observed either after making a mix and storing it in the mixing tank or after loading the gas in the shock tube prior to a test. Degassed, deionized water was stored in a flask attached to an end of the mixing tank as the source of water vapor. Typical H₂O partial pressures ranged from 16 to 30 torr depending on the mixture desired. The fill pressure was monitored by a Validyne pressure transducer with a 0.2 torr sensitivity. Other gases were taken directly from the cylinder without further purification.

The stated minimum purities were: Ar, 99.996%; H₂, 99.995%; N₂, 99.99%. To insure good mixing in the mixing tank, the diluent gas was injected into the mixing tank through a spray bar running down the center of the tank. Twenty 0.040" holes on the bar at three inch intervals created swirling to promote rapid mixing.

A single-mode line-tuned CW CO₂ laser was used as the source of the laser radiation. The output beam was split into two components by a salt beam splitter. About 90% of the beam was directed to a salt diffuser located in front of the entrance window. This diffuser was employed to increase the sensitivity of the detection system by reducing Schlieren effects. Radiation from the exit window was collected by a germanium lens, and focused on an HgCdTe detector through a narrow band 10.6 μ interference filter (FWHM 0.15 μ). The filter was used to block out water emission at all but the laser wavelengths. No emission was observed within the laser bandpass when the laser was turned off as long as the filter was in front of the detector. The basic sensitivity of the absorption system is estimated to be around 0.2% for a 1:1 signal to noise level.

The remaining 10% of the laser radiation is sent through a 10 cm path-length absorption cell and into a Scientech laser power meter to determine the laser wavelength. The room temperature laser absorption coefficients of ethylene have been accurately measured,⁷ and by measuring the ethylene absorption coefficients it is possible to identify the laser transition without using a spectrometer.

The absorption coefficient α was determined using the measured optical transmission, I/I_0 , total pressure P , path length, L , the initial mole fraction of H₂O, X_{H_2O} , and the calculated fractional dissociation at the equilibrium temperature, f_T by the following equation:

$$\alpha_{\text{cm}^{-1}\text{-atm}^{-1}}^{\text{eq}_{H_2O}} = \frac{\ln(I_0/I)}{f_T X_{H_2O} P_{\text{atm}} L_{\text{cm}}}$$

Temperatures behind the incident and reflected shocks were determined using the measured incident shock velocity, the initial pressure and gas compositions as input parameters to the PSI full equilibrium real gas shock program. Agreement between the calculated and measured shock pressure ratios was excellent.

Experimental data are collected and stored in a computer-controlled CAMAC

based data acquisition system. The system is built around two LeCroy Waveform Digitizers. Each unit can simultaneously sample four analog signals at a 1 MHz rate, and has a 10-bit 32 K word memory that will store eight milliseconds of data. After a test, the data is transferred to a PRIME 400 computer for immediate preliminary analysis and storage.

RESULTS

The majority of the tests were conducted using argon as the diluent gas instead of hydrogen, since it is much easier to drive a shock into a heavier gas. Measurements were made behind both incident and reflected shocks encompassing a temperature range from 600 K to 3700 K at pressure from 1 to 40 atm in 2, 5 and 10 mole percent water vapor in argon gas mixtures. At the lowest temperatures, little or no absorption was observed, particularly behind the incident shock where the pressures are low. At the highest temperatures, one third of the laser radiation was absorbed by the hot gas in the 3.31 cm path-length.

At several temperatures the total pressure behind the shock, and the partial pressure of water in the gas was varied sufficiently to assess the effect of pressure and water vapor concentration on the absorption coefficient on each of the three laser transitions of interest. For example, there was no change in the value of the absorption coefficient for total pressure ranging from 5 to 40 atm at 2250 K on any of the laser transitions (see Fig. 1). At the same temperature, plots of $\ln I_0/I$ vs. $P_{H_2O}L$ have a constant slope indicating that the absorption depends solely upon the line density of molecules in the laser path. No significant variations in the H_2O absorption coefficient were observed among the three laser transitions for a given temperature within experimental uncertainty. (See Fig. 2.)

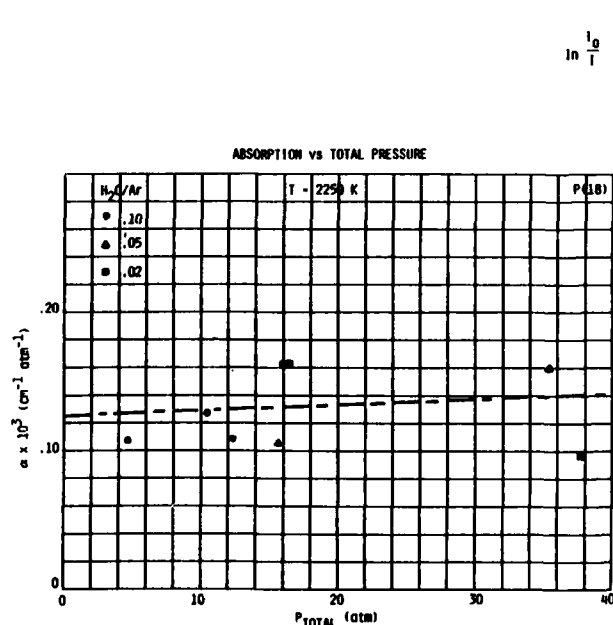


Figure 1 Plot of absorption coefficients vs. total pressure at 2250 K on P(18) laser transition for H_2O/Ar mixtures.

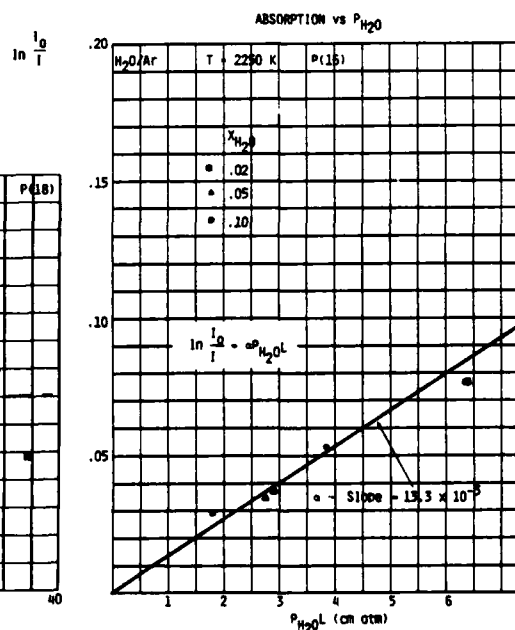


Figure 2 Plot of $\ln I_0/I$ vs. $P_{H_2O}L$ at 2250 K on P(16) transition for H_2O/Ar mixtures.

Nine tests were conducted using 10% H₂O/H₂ gas mixtures between 600 K and 1400 K. These H₂O absorption coefficients fall within H₂O/Ar data collected in the same temperature range. Two tests with 10% H₂O/N₂ gas mixtures were also conducted on the P(18) CO₂ transitions and these also overlap the H₂O/Ar data. All the data collected along with the Ludwig empirical curve fit is plotted in Fig. 3.

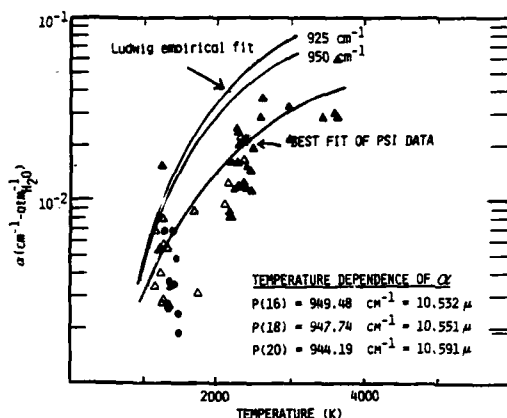


Figure 3 Experimental absorption coefficients vs. temperature - includes H₂O/Ar, H₂O/H₂, and H₂O/N₂ data for all three laser transitions.

DISCUSSION

The experimental observation that changes in total gas pressure, the partial pressure of the water, or the collision partner with small changes in the laser wavelength do not significantly change the value of the absorption coefficient of H₂O vapor/gas mixtures over the ranges of pressures and temperatures encompassed by these measurements is not surprising.

A continuum absorption will be obtained at any temperature if the lines involved in the absorption are broadened into each other. As the temperature rises the density of states increases so that the degree of broadening required to complete the overlap decreases.

The positions of the high temperature water lines are not known with sufficient accuracy to allow a line by line calculation of the absorption coefficient. There are enough low resolution data available to make a reasonable estimate of the absorption coefficient at a given wavelength and temperature. Ludwig and his coworkers have conducted many measurements of water vapor emission from plumes and flames,⁸ empirically correlated all available low resolution spectra,^{9,10} and obtain an expression for the temperature and pressure dependence of the absorption coefficient averaged over a 25 cm^{-1} spectral range.

The band model used by Ludwig determines an average rotational line spacing vs. temperature.¹⁰ His equation for the average spacing as a function of temperature is $d(T) \text{ cm}^{-1} = \exp(-0.00106 T_K + 1.21)$. The primary broadening mechanism under the experimental conditions is collisional broadening. The collisional broadening parameters for all the species of interest are known at room temperature,¹¹ and using these values it is a simple matter to determine the pressure required to broaden a line to an extent that the linewidth equals the average line spacing. Above this pressure the absorption will be a continuum. These plots for the gases tested in this study are shown as Fig. 4.

For the pressure conditions required in the operation of a CW laser-heated thruster, this simple approach predicts sufficient broadening to assume

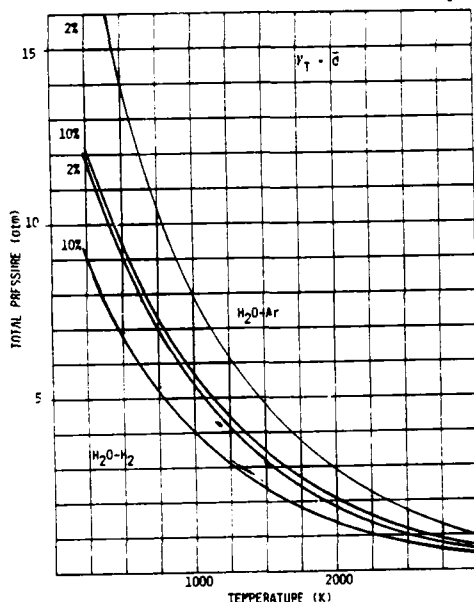


Figure 4 Total pressure required to collisionally broaden lines to the average line spacing vs. temperature.

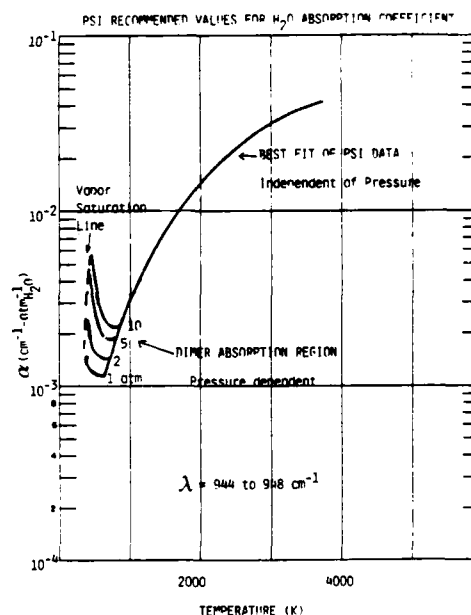


Figure 5 Recommended values for temperature dependence of H_2O absorption coefficient.

a continuum absorption mechanism. Our data closely approximates a curve 50% lower than Ludwig's empirical fit. This is not unexpected either since there is some structure in the high temperature water spectra in the 10.6 micron region. Low resolution spectra recorded in the $944-948 \text{ cm}^{-1}$ region of the spectra appear to be slightly below Ludwig's averaged value.

No absorption was observed below 1000 K. This results from a combination of short path length, low pressure, and low absorption coefficients. In several other measurements it has been observed that the absorption coefficient increases quadratically with increasing pressure and is independent of wavelength. This continuum-like phenomenon has been attributed to absorption by water dimers. The weakly bound complexes dissociate as the temperature increases, and their dissociation is suppressed by increasing pressure. The functional form of the low temperature absorption has been described by Roberts and his coworkers.¹⁴ Combining our high temperature experimental measurements fitted to a value 50% of Ludwig's predictions, and Roberts low temperature observations, a plot of the temperature dependence of the absorption coefficient of H_2O can be generated for all possible operating regimes of a CW laser-heated thruster. This plot is shown in Fig. 5.

CONCLUSIONS

No significant variation in the absorption coefficient was observed as a function of laser wavelength, water concentration, total pressure, or collision partner within the narrow spectral range from 944 to 948 cm^{-1} covered in the measurements. These observations suggest that the water lines are sufficiently broadened to act as a continuum absorber under conditions to be found in a laser-heated rocket thruster. The laser-measured high temperature absorption coefficients are 50 percent lower than the value obtained from the Ludwig empirical curve fit to low resolution data.

For a practical CW laser-heated thruster it is estimated that a propellant

AD-A122 200

PROCEEDINGS OF THE INTERNATIONAL SYMPOSIUM ON SHOCK
TUBES AND WAVES (13TH. (U) CALSPAN ADVANCED TECHNOLOGY
CENTER BUFFALO NY C E TREANOR ET AL. JUL 81

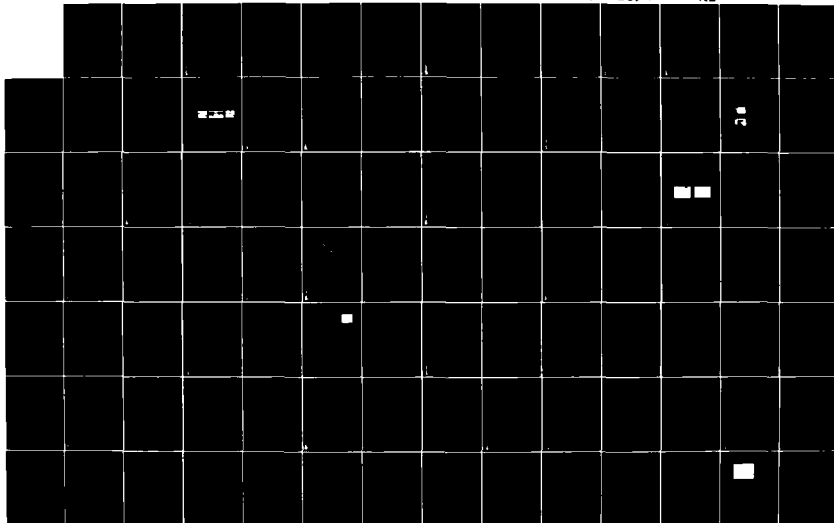
6/10

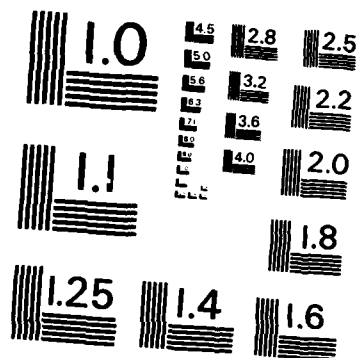
UNCLASSIFIED

AFOSR-TR-82-1031 F49629-81-C-0002

F/O 20/1

NL





MICROCOPY RESOLUTION TEST CHART
NATIONAL BUREAU OF STANDARDS-1963-A

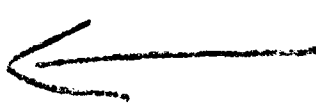
absorption coefficient of $10^{-2} \text{ atm}^{-1} \text{ cm}^{-1}$ will be required.^{3,4,15} The absorption coefficient of water vapor does not reach this value when the gas temperature exceeds 1500-1700 K. High temperature operation will not present problems, but there could be a potential start-up problem for a simple $\text{H}_2\text{O}/\text{H}_2$ propellant system, and other low temperature absorbers may be required.

ACKNOWLEDGMENT

The authors wish to thank G. E. Caledonia, B. D. Green, P. Nebolsine, A. Pirri, and D. Rosen of PSI for their help on this work and Curt Selph of the Air Force Rocket Propulsion Lab and Lee Jones of NASA Marshall Space Flight Center for supporting it.

REFERENCES

1. Caledonia, G. E., Wu, P. K., and Pirri, A. N., "Radiant Energy Absorption Studies for Laser Propulsion," Physical Sciences Inc., PSI TR-20 (NASA CR-134809), 1975.
2. Huberman, M., Seller, J.M., Benson, R., Davenport, W., Davidheiser, R., Mulmud, P., and Glatt, L., "Investigation of Beamed Energy Concepts for Propulsion," TRW Final Report, Contract F04611-76-C-003, AFRPL-TR-76-66, Vols. I and II and AFRPL-TR-76-07, Vol. III (Confidential), October, 1976.
3. Kemp, N. H., Root, R. G., Wu, P. K., Caledonia, G. E., and Pirri, A. N., "Laser-Heated Rocket Studies," Physical Sciences Inc., PSI TR-53, (NASA DR-135127), 1976.
4. Fowler, M. C., Newman, L. A., and Smith, D.C., "Beamed Energy Coupling Studies," Final Technical Report for Contract No. F04611-77-C-0039, AFRPL-TR-79-51, September, 1979.
5. Nebolsine, P. E., Pirri, A. N., Goela, J. S., Simons, G. A., and Rosen, D. I., "Pulsed Laser Propulsion," Paper VI-2, AIAA Conference on Fluid Dynamics of High Power Lasers, Cambridge, MA, 1978 (also PSI TR-142).
6. Weiss, R. F., Pirri, A. N., and Kemp, N. H., Astronautics and Aeronautics, March, 1979, pp. 50-58.
7. Patty, R. R., Russwurm, G. M., McClenny, W. A., and Morgan, D. R., "CO₂ Laser Absorption Coefficients for Determining Ambient Levels of O₃, NH₃, and C₂H₄," Applied Optics, Vol. 13, No. 12, December 1974, pg. 2852.
8. Ludwig, C. G., "Measurements of the Curves-of-Growth of Hot Water Vapor," Applied Optics, Vol. 10, No. 5, May 1971, pp 1057-1073.
9. Ferriso, C. C., Ludwig, C. B., and Thomson, A. L., "Empirically Determined Infrared Absorption Coefficients of H₂O from 300 to 3000 K," J. Quant. Spectrosc. Radiat. Transfer, Vol. 6, pp 241-273, Pergamon Press Ltd., 1966, Great Britain.
10. Ludwig, C. B., Ferriso, C.C., Malkmus, W., and Boynton, F. P., "High-Temperature Spectra of the Pure Rotational Band of H₂O," J. Quant. Spectrosc. Radiat. Transfer, Vol. 5, pp 697-714, Pergamon Press Ltd., 1965, Great Britain.
12. Penner, S. S. and Varanasi, P., "Spectral Absorption Coefficients in the Pure Rotation Spectrum of Water Vapor," J. Quant. Spectrosc. Radiat. Transfer, Vol. 7, pp 687-690, Pergamon Press Ltd., 1967, Great Britain.

13. Varanasi, P., Chou S., and Penner, S. S., "Absorption Coefficients for Water Vapor in the 600-1000 cm^{-1} Region," J. Quant. Spectrosc. Radiat. Transfer, Vol. 8, pp. 1537-1541, Pergamon Press Ltd., 1968, Great Britain.
 14. Roberts, R. E., Selby, J. E. A., and Biberman, L. M., "Infrared Continuum Absorption by Atmospheric Water Vapor in the 8-12 μm Window," Applied Optics, Vol. 15, No. 9, September 1976, pp 2085-2090.
 15. Kemp, N.H. and Krech, R. H., "Laser-Heated Thruster, Final Report," Physical Sciences Inc., TR-220, September 1980.
- 

AD P000272

SUPERSONIC FLOW E-BEAM STABILIZED DISCHARGE

EXCIMER LASERS

B. FORESTIER and B. FONTAINE

Institute of Fluid Mechanics, Marseille II, University

Marseille, FRANCE

Use of very fast flow play a leading part in the development of high repetition rate high average power ultraviolet lasers. Moreover the very low temperature achievable by use of adiabatic expansion permits a strong increases of the laser or fluorescence optical power available for numerous systems.

The aim of the paper is to present new results on ultraviolet and visible laser and fluorescent emissions obtained with the supersonic flow e-beam excitation and supersonic flow e-beam sustained or assisted discharge excitation I.M.F.M. device (Ludwig tube type blowdown).

Particular emphasis will be made on the possibilities of the e-beam assisted discharge for the development of very fast flow high average power XeCl laser ($\lambda = 3080 \text{ \AA}$) whom potential applications are numerous noticeably in the fields of selective photochemistry, energetics and long-range communications.

INTRODUCTION

Interest for high average power ultraviolet or visible laser development is rapidly growing up owing to numerous potential applications such as selective photochemistry and isotope separation, long-range atmospheric and underwater communications, etc. In the table I are summarized some of the potential applications of this class of lasers. The rare gas excimer and mercury halide lasers are presently by far the most powerful and efficient among U.V. and visible high power lasers⁽¹⁾.

When high average power high efficiency lasers are considered ($\bar{P} > 1 \text{ kW}$, $\eta_e > 1 \%$) optimization of active medium characteristics (temperature, pressure, mixture) is needed. Moreover use of fluid mechanics techniques is necessary to rapidly carry away heat and waste products and damp strong acoustic waves generated by the energy suddenly deposited into the gas medium. These problems, already present in the case of infrared lasers, are much more critical in the case of high average power ultraviolet and visible lasers.

TABLE I-Some potential applications of high average power U.V. and visible lasers

A) Photochemistry	D) Surface interactions
. Isotope separation	. Product marking
. Selective chemical purification	. Annealing
. Chemical reaction catalysis	. Photo lithography
B) Excitation of other lasers	E) Inertial confinement fusion
. Dye laser pumping	. Raper - Lawrence Livermore Lab.
. Raman shifting	. Plasma diagnostics
C) Long range energy transfer	F) Spectroscopy
. Strategic communications	. excited state generation
. Laser interactions with targets	. Harmonics to V.U.V.

This paper underlines first the problems related with the control of operating conditions and the homogeneity of the flowing active medium in high average power U.V. and visible lasers. In a second part are summarized the results achieved at I.M.F.M. on supersonic flow low temperature e-beam and e-beam stabilized discharge excimer lasers and on intensity increase of some interesting fluorescent emissions when lowering the temperature. In a last part are presented recent results concerning the possibilities to excite the active medium by means of a high repetition rate electric discharge assisted by an electron or X-rays beam in order to fully take profit of the fast flow in the frame of high average power excimer laser development.

AERODYNAMIC CONTROL OF LASER OPERATING CONDITIONS

In the case of electronic molecular transition lasers and more particularly when high average power is considered, the active medium temperature control is a serious constraint. The active medium temperature may control on the one hand the excited species quenching and absorption losses⁽²⁾ and on the other hand the rate and the branching ratio of useful specific reactions and consequently the laser gain. Recent results have shown that active medium heating leads to an efficiency increase for some excimer lasers⁽³⁾. For other excimer systems, noticeably trimers (Xe_2Cl , Kr_2Cl) strong cooling favours production of upper state level population² and may lower the absorption losses⁽⁴⁾. In any case owing to the complexity of the excimer kinetic scheme, experimental studies in a large temperature range are useful and it seems very interesting to take benefit of fluid dynamic techniques, of which use is already justified by simple reasons of energy balance, as reported hereafter, and to explore very low temperature conditions permitted by adiabatic gas expansion.

In a high average power laser system thermal problem results because about 90 % of the input electrical energy used to excite the active medium is converted into thermal energy. This resultant heat must be removed from the laser gas before it may be efficiently excited again. Fluid mechanics techniques will considerably increase this thermal energy removal. This method has been already successfully used in the case of high average power infrared laser⁽⁵⁾. When short wavelength lasers are envisioned some constraints are much more severe challenging new studies in the fluid dynamics field⁽⁶⁾⁽⁷⁾.

These specific constraints are related to the influence of aerodynamic disturbances on the laser beam quality. The far field laser intensity variations I depend on large scale density variations $\frac{\Delta \rho}{\rho}$ and the relation between these two parameters

$$\frac{\Delta \rho}{\rho} = \frac{\lambda}{4 \pi s L} \times \frac{1}{n-1} \times \ln \frac{(I+\Delta I)}{I}$$

with n : refractive index
 s : turbulence scale
 L : active medium length
 λ : laser wavelength

depends on the laser wavelength. It follows that it is much more difficult to obtain good laser beam quality at U.V. and visible wavelengths than in the infrared.

The results obtained at I.M.F.M. (cf. next part of this paper) have demonstrated that it is possible to obtain U.V. laser emissions from a high density active medium in supersonic flow in which relative density variations are about 10^{-2} on a 1 cm scale. However for some applications (for instance, long range communications) a much higher flow quality ($\frac{\Delta \rho}{\rho} < 10^{-4}$) must be achieved and maintained.

Two points have to be considered : - first, the initial quality of the flow (before any excitation) must be very good, - second, the gas flow, strongly perturbed following electrical excitation, must recover its initial quality before a new excitation pulse occurs.

Transient phenomena due to excitation processes are very strong. The initial processes are described schematically for one dimension flow approximation, on the (X, τ) diagram of Fig. 1. In a high average power excimer

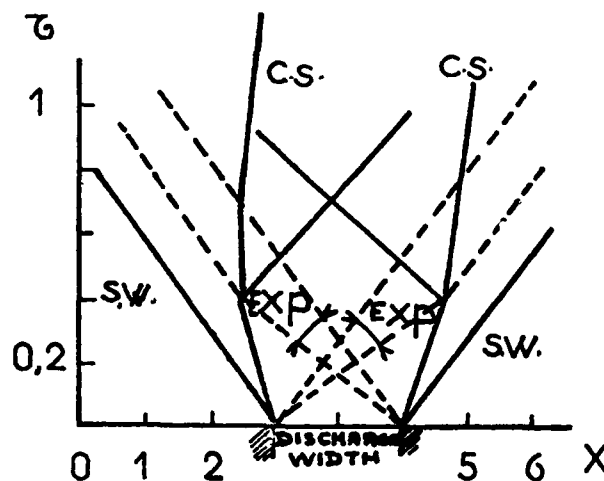


Fig. 1. Typical configurations of longitudinal Shock-Waves (S-W) ; Expansion waves (Exp.) and Contact Surfaces (S.C.) following sudden medium excitation

laser system energy deposited in the active medium during less than one microsecond for each pulse is of the order of several hundred joules by liter - amagat. That represents several tens percent of flowing gas internal energy. It follows that values of $\frac{\Delta \rho}{\rho}$ as high as ten per cent may be induced in the flow immediately after excitation. A damping of longitudinal and transverse acoustic waves inside the laser cavity by a factor above one hundred in 0.1 to 1 millisecond is needed and represents a very difficult problem to resolve. This problem may be of interest for shock tube and waves scientific community. Studies in this field are active in different laboratories in U.S.A. and

Europe and special closed cycle subsonic circulators well fitted to excimer laser studies are currently developed ⁽⁸⁾⁽⁹⁾. Such a subsonic loop will be available at I.M.F.M. in few months⁽¹⁰⁾

It is very likely that use of such subsonic loops will permit reaching near U.V. laser output power above 1 KW in a few years.

Apart from potentiality of a supersonic flow system if the laser efficiency may be strongly favored by very low temperature, as for the well known infrared CO laser, such a system with its ability to very rapidly clear the flow, may be of high interest for applications where very high repetition rate (≈ 10 KHz) is needed and very high beam quality is not required. In such a future system the average electrical power added to the flow would be above 100KW and then the power needed to maintain supersonic flow in the laser cavity could be only a reasonable fraction of the total needed power.

LASER AND FLUORESCENT U.V. AND VISIBLE EMISSIONS FROM AN ELECTRICALLY EXCITED SUPERSONIC FLOW

The results obtained at I.M.F.M. on a supersonic blowdown of Ludwig tube type which has been previously described⁽¹¹⁾⁽¹²⁾ are briefly presented next.

The device mainly consists of a high pressure tank followed by a Laval nozzle initially isolated from it by an aluminium diaphragm. The nozzle is followed by a constant area channel made with permaglass (fiberglass and epoxy) and by a dump tank. The channel is 3 cm high and 16 cm wide. Flow starts with diaphragm opening and the duration of quasi-stationary flow is generally a few milliseconds. Various nozzle profiles permit to achieve in the channel a flow with the following characteristics : Mach number equal to 1.75, 2.5 or 3 ; temperature equal to 120, 80 or 65 K ; density up to 2 amagats. The gas mixture is excited by an electron beam ($j = 20 \text{ mA} - 20 \text{ A cm}^{-2}$; $v_{e.b.} < 300 \text{ KeV}$; $\Delta t \approx 0.4 - 2 \mu\text{s}$) or by a discharge (0 - 10 KV) stabilized or assisted by means of an e-beam or e-beam induced X-rays. Anode and cathode of the discharge are flush mounted in the upper and lower wall of the channel to reduce to a minimum the aerodynamic disturbances.

In table II are presented the main characteristics of supersonic flow high density and low temperature laser emissions achieved at I.M.F.M. gas mixture, wavelength, transition, assignment, specific energy, efficiency and excitation mode are given in this table. The specific extracted energy of XeCl laser is comparable with that obtained elsewhere⁽¹⁾⁽¹³⁾ with various excitation processes and is compatible with the development of a class of U.V. or visible lasers emitting average power at the kilowatt level.

Table 2 Main characteristics of supersonic flow high density and low temperature lasers achieved at I.M.F.M.

Gas mixture	Wavelength	Assignment	Specific energy and efficiency	Excitation
Ne/Xe/NF ₃	many lines $\lambda \approx 3500 \text{ \AA}$	XeF (B \rightarrow X)	0.05 j/l in 0.4 μs	e.beam
Ne/NF ₃	3378, 23; 3481, 95 \AA	NeII		e.beam
Ar/Xe/HCl	3079 ; 3082 \AA	XeCl (B \rightarrow X)		e.beam e.b.+discharge
Ne/Xe/HCl	3079 ; 3082 ; 3084 \AA	XeCl (B \rightarrow X)	1.0 j/l in 0.5 μs $\eta = 2.5 \%$	e.beam e.b.+discharge

In Table III are presented fluorescent systems where an increase in fluorescence intensity was observed at I.M.F.M. following a strong lowering of the temperature. In this table are given gas mixture, wavelength, assignment and fluorescence enhancement factor when low and room temperature fluorescence emission intensities are compared. These results were obtained in the case of e-beam excitation. Arrows in table III point out the systems whose specific behaviour at very low temperature seems interesting for development of high average power and short wavelength lasers. The broad band very intense fluorescence of Kr_2F^* and Xe_2Cl^* excimers are the most promising. It has already been possible to obtain very recently elsewhere⁽¹⁶⁾⁽¹⁷⁾, for room temperature conditions, laser emissions on these systems. It is note-

Table 3 Main U.V. and visible fluorescence intensities enhancements observed in supersonic flow high density and low temperature e-beam excited gas mixtures

Gas mixture	Wavelength	Assignment	$I_T/I_{300\text{ K}}$
Ar/Xe/Oxygène donneurs	5200-5600; 3200 Å°	$\text{XeO}_{1\text{S}} \rightarrow \text{XeO}_{1\text{D}}$	50 at 120 K
		$\text{XeO}_{1\text{S}} \rightarrow \text{XeO}_{3\text{P}}$	300 at 80 K
Ar/Xe	3295 Å°	$\text{Ar}^+_{\text{Xe}} \rightarrow \text{Ar Xe}^+$	10 at 120 K ; 30 at 80K
Ar/COS	2985 Å°-3560 Å°	?	Very high at 120 and 80 K
Ar/Xe/NF ₃	2600 Å°	$\text{XeF}^* (\text{D} \rightarrow \text{A})$	= 1,5 to 2 at 120 and 80 K
	3805 Å°	$\text{ArXeF}^* \rightarrow \text{ArXeF} (?)$	Very high at 120 and 80 K
	4700 Å°	$\text{XeF}^* (\text{C} \rightarrow \text{A})$	= 1,5 to 2 at 120 K
Ar/Kr/NF ₃	→ 4100 Å°	$\text{Kr}_2\text{F}^* \rightarrow \text{Kr}_2\text{F}$	High at 80 and 120 K
Ar/Xe/HCl	3260 Å°	$\text{ArXeCl} \rightarrow \text{ArXeCl} (?)$	Very high at 120 K
	3500 Å°	$\text{XeCl}^* (\text{C} \rightarrow \text{A})$	1,5 at 120 K
	→ 4800 Å°	$\text{Xe}_2\text{Cl}^* \rightarrow \text{Xe}_2\text{Cl}$	High at 120 K
	→ 5100 Å°	$\text{Xe}_2\text{Cl}^* \rightarrow \text{Xe}_2\text{Cl} (?)$	Very high at 120 K
Ar/Kr/HCl	→ 3300 Å°	$\text{Kr}_2\text{Cl}^* \rightarrow \text{Kr}_2\text{Cl}$	High at 120 K

worthy that, for these trimers, laser wavelength could be varied in a large spectral range at wavelengths useful for long range energy transfer. An interferometric study of aerodynamic field in the I.M.F.M. supersonic blowdown device before and after the excitation pulse has been undertaken and results have been previously reported⁽⁴⁾⁽¹²⁾. Two main facts to underline are : first, possibilities to achieve a laser emission from a flowing active medium where initial density fluctuations were about 10^{-2} on one centimeter, and, second the efficient clearing of laser cavity by the supersonic flow leading to a very fast damping of the strong acoustic waves induced by the fast electrical pulse.

POSSIBILITIES OF HIGH REPETITION RATE EXCITATION BY E.BEAM OR X-RAY ASSISTED DISCHARGES

The development of high average power excimer lasers, either with subsonic or supersonic flow, requires at the opposite to the well known fast flow infrared CO_2 electrical lasers, a large amount of preionisation to permit a stable deposition of electrical energy in the active medium. This fact is in a large part due to the electronegativity of usual excimer laser mixtures. This limitation led recently to the development of new excitation schemes.

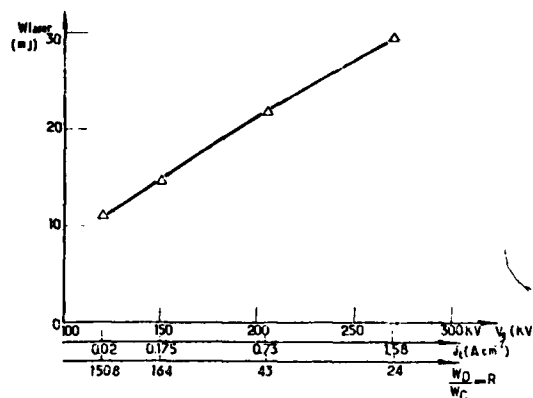
A well known method of excimer laser excitation uses a very fast avalanche discharge (50 - 100 ns duration) preionised by U.V. radiation. This method allows very high repetition rates and has permitted very recently to reach ⁽¹⁶⁾ 250 Watts average laser power at $\lambda = 3080 \text{ \AA}$ (XeCl) laser from a subsonic loop. However U.V. preionisation methods do not permit to preionise efficiently large volumes, need very low circuit inductance and allow only relatively low specific laser energy ($\approx 2 \text{ J/l}$). At last, the very high instantaneous power driven by the thyristors switching the discharge is deleterious for them and so the viability of these switches is not good at the present time.

Very high power electron beams are also frequently used to excite directly the active medium or to stabilize efficiently an electrical discharge during a fraction of microsecond. However when high average power, and so high repetition rate conditions are considered, very strong technological difficulties appear both with very high voltage switch viability and with dissipation of heat absorbed by the very thin window separating the laser cavity and the electron gun. One way to overcome these two limitations is to increase as strongly as possible the ratio between energy deposited homogeneously in the active medium by means of the main discharge and preionisation energy originating from the gun. Some very promising results have been achieved very recently in this way in different laboratories for the case of XeCl laser at $\lambda = 3080 \text{ \AA}$ ⁽¹⁷⁾⁽¹⁸⁾⁽¹⁹⁾.

An experimental study has been performed at I.M.F.M. in order to determine conditions favouring generation of long pulse high repetition rate high average power XeCl laser emission. The current density of the transmitted preionisation electron beam has been varied from 20 mA cm^{-2} to 1.6 A cm^{-2} by changing the Marx generator charging voltage. The constant parameters for these experiments were as follows : discharge capacitor charging voltage (10 kV) ; Ne/Xe/HCl mixture (5300/190/10) ; pressure (1430 Torr), temperature (300 K), coupling mirror transmission coefficient (0.20). On figure 2 are shown the variations of laser energy versus Marx generator voltage. Two scales are added to the voltage scale : one indicates the corresponding transmitted electron beam current density j_t , while the other gives the ratio $R = W_D/W_G$ between discharge and e-beam energies absorbed by the active medium. This figure shows that conditions exist where energy deposited in the active medium originates essentially from the discharge whilst maintaining high laser efficiency. Laser energy undergoes only a threefold decrease when preionisation e-beam energy is decreased by a factor 60. Nearly constant specific energy and peak power of respectively 150 J/l and 500 MW/l were added to the mixture by means of the discharge

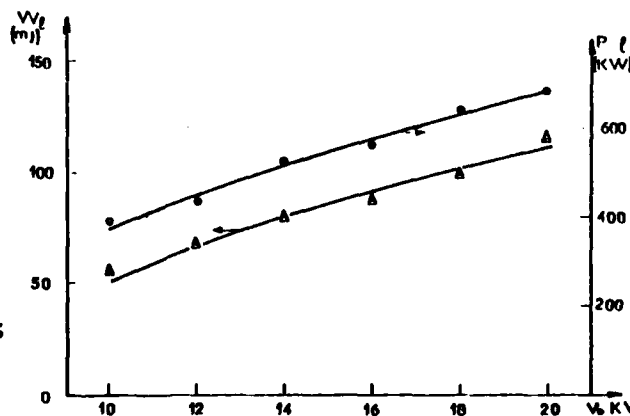
during these experiments. Intrinsic laser efficiency varied from 2 to 0.7 % and seems to have been limited mainly by the short gain length (16 cm) of the present device. The results obtained compare favourably with those obtained from experiments where the ratio R was lower than $10^{(18)}$.

Fig. 2. Laser energy versus maximum Marx generator voltage. In the abscissas are also given the transmitted e-beam density and the ratio R between discharge and e-beam absorbed energy before lasing termination. Ne/Xe/XCl (5300/190/10) ;
 $p = 1430$ torrs, $T = 300$ K ;
 $V_{\text{discharge cap.}} = 10$ kV ;
 $T_{\text{mirror}} = 0.20$.



The slow decrease of laser energy when the beam current density was strongly lowered could indicate the existence of another mechanism controlling preionization at very low e-beam electron density. Very recently S.C. Lin has shown, with very different experimental conditions, the ability to efficiently preionize an excimer laser active medium with X-rays⁽¹⁷⁾. A second set of experiments has been performed with a new device where gain length was increased to 30 cm. The preionization was made by means of an X-ray beam produced by the interaction of e-beam with a tantalum foil fitted just under a thick (1,5 mm) aluminium foil which absorbs electrons. Though preliminary, these experiments have enabled the achievement of laser action from XeCl excimer when Ne/Xe/HCl mixtures at a temperature of 300 K and a pressure of 1 atmosphere were excited by an X-ray assisted avalanche discharge. It is to note that lasing was achieved with X-rays induced by electrons with energy as low as 100 KeV. Fig. 3 shows, as an example, the variations of laser energy

Fig. 3. X-ray assisted discharge XeCl laser energy versus charge voltage of the main discharge. Ne/Xe/HCl (5300/190/10) ;
 $p = 800$ torrs ; $T = 300$ K ;
 Laser volume :
 $2.3 \times 1.2 \times 30$ cm³ (80 cm³) ;
 $V_{\text{gun}} = 210$ KV.



and power versus main discharge voltage. As shown in the figure, a specific energy of 1.5 J/l/bar was obtained in these experiments. This result, obtained with a device not particularly adapted, is interesting because the possibility to use X-rays can strongly facilitate the development of high repetition rate high average power large volume laser systems : a) X-rays penetration range is much higher than the electrons one and could permit homogeneous excitation of large volumes even with relatively low gun voltage ; b) difficulties associated with gun window heating could be strongly reduced. At last it has been possible, very recently during preliminary experiments with the same device but for the case of an electron beam assisted discharge and comparable other experimental conditions, to extract a laser energy of 300 mJ in 200 ns (3 J/l/bar). This result represents only a two fold increase in entrained energy compared to conditions of X-rays preionisation.

CONCLUSION

It has been possible to study at I.M.F.M. effects of very low temperature on excimer systems behaviour, and to obtain single pulse, high power U.V. laser emissions from a high density supersonic flow. The excimer laser systems investigated, in particular XeCl^* at $\lambda = 3080 \text{ \AA}$ seem to fulfill conditions permitting a scaling up to high average power and high efficiency. However very challenging fluid dynamics and electrical excitation problems must be solved. It is very likely that strong progress will appear in these two fields during the next few years. At I.M.F.M., studies of fluid dynamics and kinetics problems will be pursued with the supersonic blowdown and also with a new device including a closed cycle subsonic circulator and various excitation systems.

ACKNOWLEDGEMENTS

The authors gratefully acknowledge the expert technical assistance of E. RODRIGUEZ. This research was supported by French D.R.E.T.

REFERENCES

- (1) C.A. BRAU, Rare gas halide lasers, in EXCIMER LASERS, C.K. Rhodes Editor, (Springer-Verlag, Berlin) 1979.
- (2) W.R. WADT, D.C. CARTWRIGHT and J.S. COHEN, Appl. phys. lett. 31, p.672 (1977).
- (3) J.C. HSIA, J.A. MANGANO, J.H. JACOB and M. ROKNI, Appl. phys. lett. 34, p.208 (1979).
- (4) B. FORESTIER, B. FONTAINE and P. GROSS, A.I.A.A. Paper n°80-1432, A.I.A.A. 13th Fluid and Plasma Dynamics Conference, July 1980, Snowmass, Colorado.
- (5) W.H. CRISTIANSEN, D.A. RUSSEL and H. HEPP BERG, Ann. Rev. Fluid Mech. 7, p.115, (1975).

- (6) M.L. BHAUMIK, 2nd Symposium on Gas-Flow and Chemical Lasers (G.C.L.), Sept. 1978, Rhodes St Genese, Belgium, proc. p.49 (1979), unpublished.
- (7) C.J. KNIGHT, A.I.A.A. 14th Fluid and Plasma Dynamics Conference, Palo Alto, June 1981.
- (8) J.L. MILLER, J. DICKIE, J. DAVIN, J. SWINGLE and T. KAN, Appl. phys. lett. 35, p.912 (1979).
- (9) P.E. CASSADY, G. MULLANNEY and S.R. BYRON, A.I.A.A. 14th Fluid and Plasma Dyn. Conference, Palo-Alto, June 1981.
- (10) M. SENTIS, B. FORESTIER et B. FONTAINE, Note Technique I.M.F.M. N.L. 1981-2, Janvier 1981.
- (11) B. FORESTIER and B. FONTAINE, Rev. Scient. Instrum. 50, p.421 (1979).
- (12) B. FORESTIER and B. FONTAINE, 12th International Symposium on Shock Tubes and Waves, Jerusalem, July 1979, proceedings p.147 (The Hebrew University, Jerusalem) (1980).
- (13) L.F. CHAMPAGNE, Appl. phys. lett. 33, p.523 (1978).
- (14) F.K. TITTEL, W.L. WILSON, R.E. STICKEL, G. MAROWSKY and W. ERNST, Appl. phys. lett. 36, p.405 (1980).
- (15) F.K. TITTEL, M. SMAYLING, W.L. WILSON and G. MAROWSKY, Appl. phys. lett. 37, p.862 (1980).
- (16) T.S. FAHLEN, I.E.E.E. J. Quantum Electronics, QE16, p.1260 (1980).
- (17) S.C. LIN, Bao Zhi Xiang, GongGuang-Yuan, Huo Yun-Sheng, Shu Ju-Ping, Tang Shi-Quing, Wei Gun-Rong, Zhen Chen-Ien, Appl. phys. lett. 38, p.328 (1981).
- (18) W.L. NIGHAN and R.T. BROWN, Appl. phys. lett. 36, p.498 (1980).
- (19) B. FORESTIER, B. FONTAINE et Th. SOLENNE, J. Physique Lettres 42, p. 211, (1981).

AD P000273

FLUID-DYNAMICAL ASPECTS OF LASER-METAL INTERACTION

M. Cantello R. Menin
R.T.M. Vico Canavese, Torino

V. Donati L. Garifo
C.I.S.E. Segrate, Milano

A.V. La Rocca
FIAT Auto, Torino

M. Onorato
Politecnico di Torino

During the interaction of a high-power laser beam with a material surface many fluid-dynamical phenomena arise. The produced flow field interacts with the beam and affects the thermal coupling between the laser energy and the target metal. In this paper the fluid-dynamical aspects of these phenomena are discussed and new experimental results are illustrated. The experiments have been performed in conditions of interest for industrial laser processes with a 15-kW CWCO₂ laser. The developing and the motion of bright clouds ignited from metal targets at incident laser power up to 11.6 kW, using an f/18 focusing system, have been studied by high speed photographic records. The properties of the cloud have been examined by spectroscopic analysis and absorption measurements.

INTRODUCTION

The interaction of a high-power laser beam with a target material in an atmospheric environment has been a subject of intensive study during the past few years.

At low laser intensity, the radiation interacts with the material by direct absorption. Most theoretical and experimental research, in this intensity range, has been devoted to determine the fraction of energy coupled to the surface (the thermal coupling coefficient) as a function of the laser wavelength and the target material.

As the laser intensity is increased new phenomena occur, such as target heating, target mass removal, vaporization and plasma formation, which influence strongly the thermal coupling coefficient. At 10.6 μ wavelength and intensity greater than 10^4 w/cm² the laser-surface interaction is dominated by the formation of absorption waves in the metal vapor or in the air above the material which attenuates significantly the laser intensity incident on the surface.

The purpose of this paper is to describe the fluid-dynamical aspect of the interaction and to illustrate new experimental results obtained by the authors in conditions of interest for industrial laser processes. The interest will be focused to the case of metal target irradiated in an atmospheric environment by infrared CW laser beams, having intensities less than 10^7 w/cm².

As a consequence of the material heating by the laser radiation, the surface starts to emit vapor that expands away from the target. The moving vapor acts as a piston and drives a shock wave into the ambient air. The properties of the developing flow will depend on the initial condition of the emitted vapor. Recently Knight (ref.1) has developed a physically realistic theoretical model for the rapid surface vaporization into surrounding ambient atmosphere. The case of a process involving a phase change from solid to liquid and then liquid to gas is considered. It is assumed that local thermodynamic equilibrium exists in the liquid, as it will be expected if the laser intensity is less than 10^7 w/cm^2 . Near the phase interface, where the vapor pressure is larger than the ambient pressure, the vaporization rate being large for the laser intensities of interest, the vapor is not in translational equilibrium. Few particle mean free paths are required to establish, in a Knudsen layer region, the translational equilibrium. This very thin region is treated by Knight as a gasdynamic discontinuity across which jump conditions expressing conservation of mass, momentum, and energy are applied. The result of the Knight analysis is that the properties of the emitted vapor, that is considered as a perfect gas outside the Knudsen layer, can be predicted, for a given material, as a function of the laser intensity and the ambient pressure. If the vapor pressure is large compared to the ambient pressure, the vapor flow Mach number at the layer exit becomes sonic. For an aluminum target, irradiated by $10.9 \mu\text{m}$ wavelength laser beam, at external air pressure of one atmosphere, the vapor is sonic if the intensity is greater than $2 \times 10^5 \text{ w/cm}^2$.

An extension of the Knight model to the case in which a crater-like formation is present on the material at the laser incident region, has been more recently proposed by M.Germano and M.S.Oggiano (ref.2). The emitted vapor acts as a jet from an orifice into still air. Because of the rather high vaporization temperature and low ionization potential (respectively 2750 K and 6 eV for aluminum), this vapor contains initially a significant population of free electrons, even at the low laser fluxes. For this reason the vapor starts to absorb the incident radiation by inverse bremsstrahlung. If the heating rate by this mechanism exceeds the rate of cooling by gasdynamic expansion, the flow temperature will rise. At temperatures near the vaporization temperature the absorption coefficient is so low that a very thick vapor layer would have to be built up to attenuate the incident energy significantly. However, at very high fluxes, the electrons acquire laser energy faster than they can cool by competing processes. As a consequence, a fast nonequilibrium process arises, collisional ionization of atoms by these energetic electrons produces an electron avalanche in which the electron density grows exponentially in time. The vapor becomes then opaque to the laser beam and its temperature increases fast. By simple analysis of characteristic times of the competing processes, Thomas (ref.3) has given an expression for the characteristic laser intensity

$$I_c = 10^5 (10.6/\lambda)^2 (T_v/2750) (27/A) \text{ w/cm}^2 \quad (1)$$

that separates the equilibrium and nonequilibrium regimes; if $I < I_c$ the vapor will remain in LTE, if $I \gg I_c$ nonequilibrium effects become dominant. Equation (1) is normalized with respect to CO_2 laser wavelength ($\lambda = 10.6 \mu$) and to aluminum vapor properties: the vaporization temperature T_v and the vapor atomic weight A .

Thomas, in the same reference (ref.3), gives the results obtained solving numerically the one dimensional equations governing the phenomenon, giving a detailed description of the vapor heating and of the consequent formation of a laser absorption wave in the air adjacent to the vapor. The numerical procedure accounts for gasdynamics and radiative transport in the gas and for heat conduction within the target. When, for the case of titanium-alloy target, the vapor reaches a temperature near 20,000 K, approaching a state of radiative equilibrium with the incident laser flux, thermal radiation emitted by the hot vapor is absorbed in the adjacent air. Once the air reaches a temperature of about 8000 K, the air is sufficiently ionized to begin absorbing laser radiation directly by inverse bremsstrahlung. The air temperature starts to rise very fast and a so-called laser supported combustion wave (LSC) propagates subsonically, by thermal radiation

transport, toward the laser beam. Thomas shows that the computed results agree with the experiments of Klosterman (ref.4), in which LSC waves have been observed to form on titanium-alloy targets irradiated by a CO₂ gas laser at intensities of $10^5 - 10^6$ w/cm², pulse duration of 1 - 5 m sec, and irradiated spot diameters of 0.5 - 1.3 cm.

Analytic solutions for the time for LSC wave ignition as a function of laser intensity, material, spot size and wavelength have been presented by A.N. Pirri (ref.5) for either one-dimensional planar or two-dimensional axisymmetric flow. This analysis is based on existing possibility for a range of intensities that the vapor properties up to the time for LSC wave ignition can be calculated uncoupling the heating from the gasdynamics. Starting from the vapor properties at the surface, Pirri models first the unheated vapor flowfield and then by a perturbation technique takes into account the thermal effects. In the case of aluminum or titanium target irradiated by infrared laser beam, for intensities less than 2×10^5 w/cm² the vapor exit Mach number is subsonic, for intensities larger than 2×10^5 w/cm² sonic condition arises. In the first case the jet is subsonic and consists of a conical inner core of uniform flow by a growing turbulent mixing flow region (fig.1).

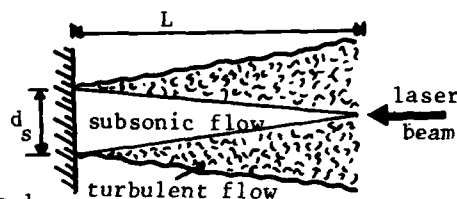


Fig.1

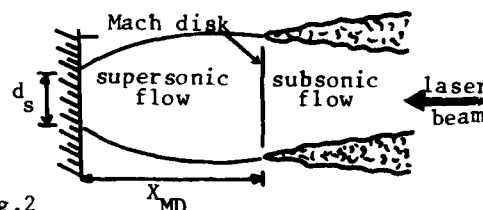


Fig.2

The length of the uniform flow inner core, L , is approximately nine times the spot radius. When the vapor exit velocity is sonic, after leaving the surface the vapor expands supersonically. Because the flow tends to over-expand, a Mach disk forms and shocks the vapor back to ambient pressure (fig.2). The position, X_{MD} of the Mach disk is given to good accuracy by

$$X_{MD}/d_s = 0.67(p_{VS}/p_\infty)^{1/2} \quad (2)$$

where p_{VS} is the stagnation pressure of the vapor at the surface and p_∞ is the ambient external air pressure. For aluminum target and laser intensity of 4×10^5 w/cm², $p_{VS}/p_\infty = 5$ and $X_{MD}/d_s = 1.5$.

The main results obtained by superimposing on the described flow field the perturbation technique is that LSC wave ignition in a subsonic vapor jet can occur only in the center core of jet and in a supersonic jet only downstream of the Mach disk. The calculated time for LSC wave ignition correlates with good accuracy with the Klosterman experimental data (ref.6).

The results of the experimental study described (ref.7) by Fowler and Smith provide considerable insight to the ignition and maintenance of subsonic plasma waves. A 15 kW, CWCO₂ laser radiation, focused with different focal diameters on steel and aluminum targets is used for the experiments in atmospheric pressure air. They measured the dependence of the LSC wave ignition threshold intensity I_i and the plasma maintenance threshold intensity I_m on the focal spot diameter, showing I_i and I_m decrease for increasing beam diameter. For focal spot diameters less than 0.1 cm the values of I_i and I_m were found to be essentially the same. Moreover it was found that for weakly focused systems with f-numbers larger than about 10, LSC waves could not adjust to fluctuations quickly enough and typically are unstable and became extinguished after reaching a maximum propagation length from the focal point. On the contrary, in more sharply focused systems, with f-numbers less than 4, LSC waves could be maintained as long as desired. For a 6 kW laser beam, focused by a f/14 mirror, the LSC wave lifetime was 13 msec, the initial wave propagation was 16m/sec and the maximum distance propagated was 3.9 cm. Results from two-wavelength laser interferometric technique are also presented in ref. 7. For incident power of 6.2 kW an electron number density of

$2.1 \times 10^{17} \text{ cm}^{-3}$ was measured. By assuming local thermodynamic equilibrium within the plasma, for the same incident power, a maximum temperature of 17,000 K was evaluated and an absorption coefficient of 0.7 cm^{-1} . Most of the main results in ref. 7 are in good agreement with the theoretical predictions of Raizer (ref.8).

As it has been said before, the present study is focused on incident laser beam intensities lower than 10^7 W/cm^2 . For higher intensities it may be expected that the shock wave driven by the vapor jet is strong enough to heat the air downstream at a temperature so high that the air layer behind the shock becomes absorbing. In this case a supersonic laser-supported detonation-wave (LSD) originates, travelling toward the laser beam.

In this section an attempt has been made to describe some of the fluid-dynamical phenomena that occur when a focused continuous laser beam irradiates a metal target. A complete review of the subject is reported in ref. 9.

PRESENT EXPERIMENTS

The experiments here reported have been performed in conditions of interest for industrial laser processes. An AVCO continuous CO_2 laser capable of output powers up to 15 kW at $10.6 \mu\text{m}$ wavelength was used. A f/18 focusing system concentrates about 90% of the total power in a focal spot diameter of 1.6 mm. Targets of different materials were irradiated; results for steel (AISI 304) and aluminum (Al 6061) targets are here reported. To simulate conditions of interest for industrial applications, during the interaction the targets were kept in motion with speed varying from 0.6 to 2.3 m/min. Three diagnostic procedures were adopted; high-speed photographic records, absorption measurements and spectroscopic analysis.

A rotating prism camera capable of 20,000 frames per second was used for recording the motion of the absorption wave that originates at short distance from the target and travels toward the laser beam. No special arrangements are needed for this recording procedure. The brightness of the wave is sufficiently high to permit very short exposures.

Absorption measurements were performed using a continuous $10.6 \mu\text{m}$ wavelength, 3 watt, CO_2 laser. The beam of this source was used as a probe traversing the plume in direction parallel to the target. Time integrated attenuation of the beam was measured using a thermopile detector. The whole interaction zone was scanned to measure, at different distance from the target, the spatial averaged along the probe beam absorption coefficient. In fig. 3 the schematic diagram of the diagnostic system is shown.

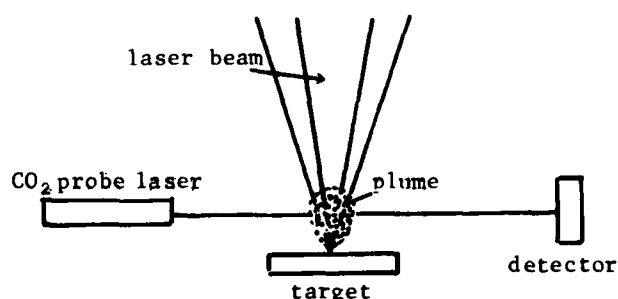


Fig.3
Schematic diagram of the experimental apparatus for absorption measurements.

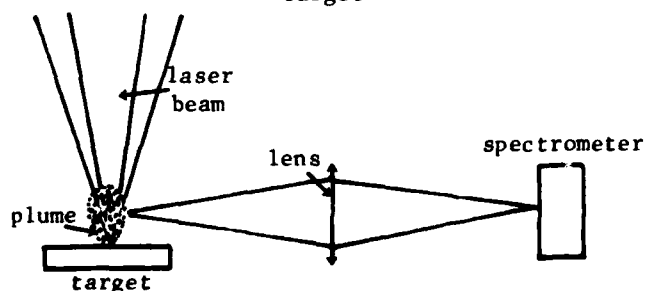


Fig.4
Schematic diagram of the experimental apparatus for spectroscopic analysis.

For spectroscopic analysis a typical Ebert-type spectrometer was used, having a 0.6m focal length mirror. The interaction region was observed in the direction normal to the incident laser beam. Spectral resolution at first order was 0.8 Å. In fig. 4 the experimental setup is shown. The spectroscopic measurements are time integrated and are in the spectral region between 2500 and 6000 Å.

RESULTS AND COMMENTS

From high-speed photographic recording much detailed information can be deduced about the phenomena occurring during the interaction. As an example, the developing of an absorbing wave ignited from a steel target (AISI 304) at an incident laser power of 11.6 kW, using a f/18 focusing system is shown in fig. 5. The focal spot diameter is about 1.6 mm and the workpiece speed is 2.3 m/min. The luminous cloud visible in the picture propagates along the laser beam as far as 5-6 cm from the target, partially decoupling the laser radiation from the target surface. This is evidenced by the strongly reduced brightness of the spot on the surface, as it is shown in the left side of fig. 5a. Subsequent to the disappearance of the luminous cloud a new bright zone is visible at the interaction point and a new cloud is ignited which leaves the workpiece. In fig. 5b the luminous cloud is seen to stand at a distance of about 4-5 cm from the target for few msec and then becomes extinguished, fig. 5c. The frames shown in fig. 5 are selected from high speed 12,000 frames per second photographic records. From one figure to the next there is no continuity in time. This repetitive phenomenon has been observed for all cases in which a plume originates during the interaction.

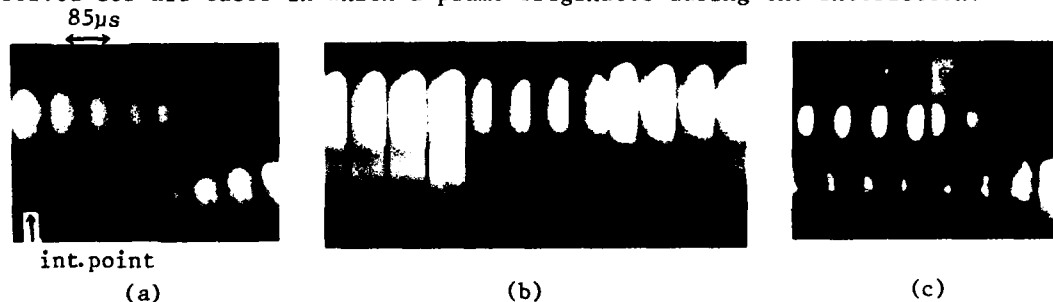


Fig. 5 Ignition and propagation of bright clouds from steel target at 11.6 kW

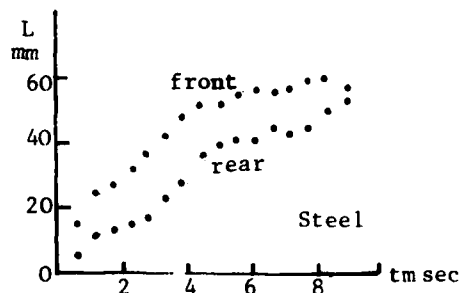


Fig. 6 Temporal variation of the cloud boundaries.

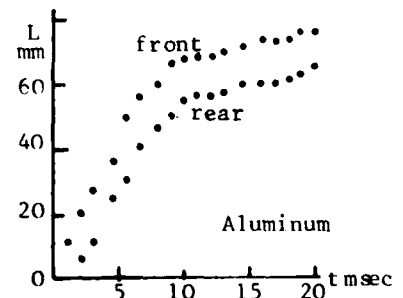


Fig. 7 Temporal variation of the cloud boundaries.

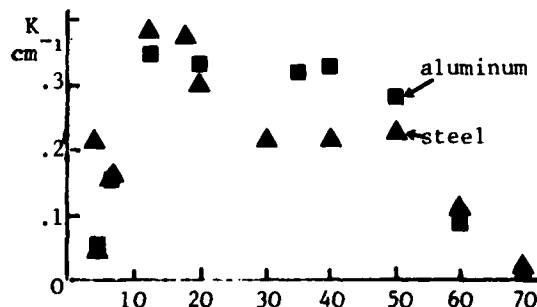


Fig. 8 Time averaged absorption coefficient as a function of the target distance.

From the analysis of the frames, the curves representing the position of the front and the rear boundaries of the bright cloud as a function of time have been obtained. In figs. 6 and 7 results are shown respectively for steel and aluminum targets. For both cases the incident laser power was 11.6 kW. The workpiece velocity was 2.3 m/min for steel and 0.6 m/min for aluminum. At the target velocity of 2.3 m/min plume formation was not observed for aluminum, because of its high surface reflectivity.

TABLE I

	cloud front initial velocity m/sec	cloud extinction distance mm	cloud life time ms
Aluminum 6061	10	70	21
Steel AISI 304	25	55	9

In Table I the main data for aluminum and steel are compared. The values reported have been averaged for many events. Besides material properties and incident laser power, the values of the quantities shown in Table I depend on focal spot diameter and focusing system.

Results from absorption measurements give for both materials maximum values of the absorption coefficient, k , of $0.35 - 0.40 \text{ cm}^{-1}$. The values of k are time integrated and spatially averaged along the probe beam direction. In fig. 8 k is displayed as a function of the distance L from the target. The lateral distribution at constant L shows that the absorbing zone is slightly wider than the beam diameter.

Spectroscopic analysis has been made for steel only. The data referring to the interaction zone near the target show that the emitted spectra consist mainly of lines characteristic of target vapor neutral atoms. This result indicates that the plume temperature, computed by line-ratio method, in the region investigated, is near $6000 - 7000 \text{ K}$.

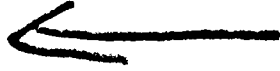
These estimated temperatures are consistent with the absorption coefficient measurements if we assume that absorption is due to inverse bremsstrahlung and the plume is in local thermodynamic equilibrium at atmospheric pressure.

CONCLUSIONS

Measurements on plumes produced by irradiating aluminum and steel targets by CO_2 high power CW laser beams have been reported. Results related to the motion of the observed absorbing and emitting plume are in agreement with data reported in literature. Temperatures evaluated by spectroscopic analysis and confirmed by absorption measurements are lower than temperatures measured during other interaction experiments. This disagreement is due to the peculiar conditions adopted for the present study. Conditions of interest for industrial material processing, primarily welding, were simulated. During the experiments the target was kept in motion and measurements were taken after many cycles of bright cloud developments. In these conditions the target material and the external region close to the interaction point are affected by complex thermal phenomena that can influence strongly the developing plume. In comparing data from different experiments beam quality must be taken also into account.

However, the observed bright clouds may be interpreted as weak laser supported waves traveling toward the incident beam.

For a better understanding of the phenomena, experiments will be repeated in different conditions, and time resolved absorption measurements and spectroscopic analysis will be performed.

1. C.J.Knight, *Theoretical Modeling of Rapid Surface Vaporization with Back Pressure*, AIAA Journal, vol.17 n.5 (1979)
 2. M.Germano;M.S.Oggiano, *Gasdinamica dei prodotti di vaporizzazione superficiale dovuta ad intensa radiazione termica*, VI Congresso Nazionale AIDAA, Roma (1981)
 3. P.D.Thomas, *Laser Absorption Wave Formation*, AIAA Journal, vol. 13, n.10 (1975)
 4. E.L.Klosterman;S.R.Byron, *Experimental Study of subsonic Laser-Absorption Waves*, AFWL - TR - 74 - 003, Mathematical Sciences NW,Inc.,Seattle,Wash(1973)
 5. A.N.Pirri,*Analytic Solutions for Laser-Supported Combustion Wave Ignition above Surface*, AIAA Journal, vol.15, n.1 (1977)
 6. E.L.Klosterman, *Experimental Investigation of Subsonic Laser Absorption Wave Initiation from Metal Targets at 5 and 10.6 μ m*, MSNW - 75 - 123 - 2, Mathematical Sciences Northwest Rept. Seattle, Wash (1975)
 7. M.C.Fowler;D.C.Smith, *Ignition and Maintenance of Subsonic Plasma Waves in Atmospheric Pressure Air by CWCO₂ Laser Radiation and their Effects on Laser Beam Propagation*, Journal of Applied Physics, vol.46, n.1 (1975)
 8. Y.P.Raizer, *Subsonic Propagation of a Light Spark and Threshold Condition for the maintenance of a Plasma by Radiation*, Soviet Physics- JETP vol.31, n.6 (1970)
 9. R.G.Root, *Laser Interaction: Thermal and Mechanical Coupling to Targets*, 3th International Symp.on Gas Flow and Chemical Lasers, Marseille (1980)
 10. E.L.Klosterman, *Measurements of Subsonic Laser Absorption Wave Propagation Characteristics at 10.6 μ m*, Journal of Applied Physics, vol.45, n.11 (1974)
- 

SHOCKFRONTS AS MODEL TARGETS IN
LASER-PLASMA INTERACTION EXPERIMENTS

Paul Kolodner

Bell Laboratories, Murray Hill, NJ 07974 USA

Eli Yablonovitch

Exxon Research and Engineering, Linden, NJ 07036 USA

We have used a shockfront, produced in a small, electrothermal shocktube filled with 40-60 torr D₂, as a model target for studies of the interaction of intense laser light with hot, dense, inhomogeneous plasmas. The CO₂ laser pulse ($\lambda=10.6 \mu\text{m}$; 100-500 psec FWHM; typical energy 100 mJ) is tightly focussed, at an oblique angle, onto the shockfront axis, and a laser-Schlieren shockfront detection system fires the laser at the instant the Mach-5 shockfront passes into focus. The shockfront, whose motion is negligible on the time scale of the laser pulse, is ionized by optical breakdown. When the laser pulse and the shockfront are properly synchronized, we observe energetic electrons (40-140 keV) to be emitted in a narrow cone centered on the shocktube axis. Our measurements of the angular distribution and energy spectrum of these electrons are in agreement with the predictions of the theory of resonance absorption of laser light by plasmas.

INTRODUCTION

In schemes for laser-driven fusion, a target is ionized by a short, intense pulse of laser light. An understanding of the mechanisms by which intense light interacts with the resulting hot, dense plasma is surely a prerequisite to using this process to drive efficient thermonuclear explosions. One of the most important laser-plasma interaction mechanisms is known as resonance absorption (RA).¹ The theory of RA depends critically on the propagation of a lightwave into a plasma density gradient. Thus a controlled experimental study of this mechanism requires a laboratory plasma with a reproducible density profile of the correct geometry and density. For this purpose, we have found shockfronts, ionized by optical breakdown, to be ideal model targets. We will begin this paper with a summary of the theory of RA and conclude with a description and interpretation of our experiments.

The electronic part of the dielectric function of a collisionless fluid plasma may be written $\epsilon = 1 - (\omega_p^2/\omega^2)$, where ω is the laser frequency, and the electron plasma frequency ω_p depends on the plasma density, n : $\omega_p^2 = 4\pi n e^2/m_e$. Thus ϵ is a function of density and may be written in terms of a "critical density" $n_{cr} = m\omega^2/4\pi e^2$ as $\epsilon = 1 - n/n_{cr}$. A plasma may be classified as underdense or overdense by virtue of the relation between its density, n , and n_{cr} . For CO₂ laser light ($\lambda=10.6 \mu\text{m}$), $n_{cr} = 10^{19} \text{ cm}^{-3}$, corresponding to fully ionized hydrogen gas at 150 torr. The critical layer is the region of an inhomogeneous plasma where $n = n_{cr}$ or $\epsilon = 0$.

The plasmas typically encountered in laser-interaction experiments are collisionless, inhomogeneous, and overdense. Let us model this as a plasma filling the half-space $z \geq 0$ with a density which varies only with z and which passes from 0 at the plane $z = 0$ through n_{cr} at the plane $z = L$. In

AD P000274

this case, the density-gradient vector $\vec{\nabla}n$ is parallel to \hat{z} . A ray of light incident from $z = -\infty$ on this plasma at any angle θ from $\vec{\nabla}n$ will eventually encounter a layer of density $n = n \cos^2\theta \leq n_{cr}$, from which it should be totally reflected, by the laws of geometrical optics. Outside this layer, collisional absorption is negligible, and so it was initially somewhat of a mystery that such plasmas actually absorb light quite strongly.

In 1972, the theory of resonance absorption (RA) was applied to the laser-plasma interaction. In RA, a light wave incident on an inhomogeneous plasma tunnels past the layer of total reflection, reaching the critical layer in the form of an evanescent wave. At the critical layer, where $\epsilon = 0$ (except for a small imaginary part), the resonance between laser light and plasma oscillations builds the electric field up to such high levels that substantial collisional absorption can take place, even in the limit of vanishing collision frequency. The strength of the resonance depends on the distance through which the evanescent wave must tunnel to get to the critical layer. This, in turn, depends on the experimental geometry, giving RA a discernible experimental phenomenology, which we will describe.

In a plasma, where there are no free charges, we must have $\nabla \cdot (\epsilon \vec{E}) = 0$ or

$$\nabla \cdot \vec{E} = - \frac{\vec{E} \cdot \vec{\nabla} \epsilon}{\epsilon} \approx - \frac{\vec{E} \cdot \vec{\nabla} n}{\epsilon}, \quad (1)$$

where $\vec{\nabla}n$ is the plasma density-gradient vector. Equation (1) allows us to estimate the longitudinal component of the electric field; this is what drives longitudinal plasma oscillations. In particular, in the critical layer ($\epsilon=0$), $\nabla \cdot \vec{E}$ is singular; this is the resonance (dissipation prevents a true singularity). Equation (1) also allows us to deduce the effects of experimental geometry, as reflected by the scalar product $\vec{E} \cdot \vec{\nabla}n$. In order for this product not to vanish, the polarization of the light must lie in the plane of incidence. This polarization dependence is a distinguishing feature of RA. A dependence on the angle of incidence is also characteristic: there must be a component of \vec{E} parallel to $\vec{\nabla}n$. Thus at normal incidence, when the light wave travels parallel to $\vec{\nabla}n$, $\vec{E} \cdot \vec{\nabla}n = 0$, and there can be no resonance. As the angle of incidence increases, however, the layer of total reflection, given by $n = n_{cr} \cos^2\theta$, moves away from the critical layer ($n=n_{cr}$), increasing the distance through which the light must tunnel to reach the resonant region. At sufficiently large angles, this diminishes the resonance. Clearly, there is an angle, θ_m , at which the effect is maximized; theory² predicts that $3k_0 L \sin^3\theta = 1$, where L is the scale length of the density step, and k_0 is the vacuum wave vector of the laser light. For $L = \lambda/3$ (a typical, sharp laser-plasma density-gradient length), $\theta_m = 30^\circ$.

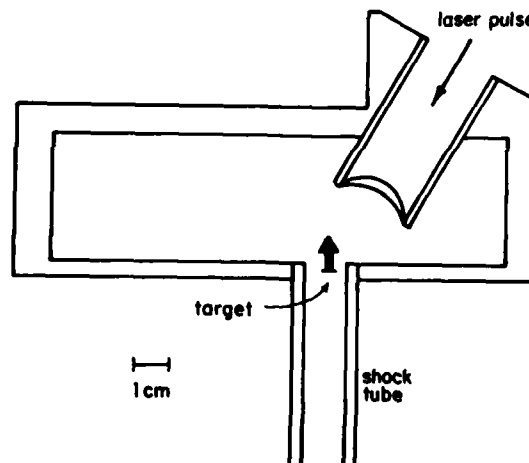
An intimate part of RA is the acceleration of high-energy electrons out of the target in a direction parallel to the plasma density-gradient vector.³ This comes about as the plasma waves formed in the critical layer roll down the density gradient, accelerating electrons in this direction as they go, by the process known as Landau damping or wavebreaking. This electron emission provides a direct probe of the plasma density structure. The angular distribution depends on the orientation of the density gradient, and the energy spectrum depends on the scale length: One can imagine the electrons to be accelerated over the scale length L by the enhanced electric field in the critical layer, which is given by⁵ $E_d = 1.2E_0/(2\pi k_0 L)^{1/2}$; E_0 is the vacuum electric field of the laser. Thus the emitted electron energy is $\epsilon_e = eE_d L \propto I^{1/2} L^{1/2}$, where $I \propto E_0^2$ is the laser intensity. In practice, the emitted electrons are not monoenergetic but rather thermalize to form a "suprathermal tail" on the plasma electron energy distribution; the slope of the "tail" on a semilog plot is given by a "temperature" T_h which coincides with ϵ_e .

One last bit of physics to be added to this description is that, at the extreme laser intensities encountered here, the ponderomotive force, or radiation pressure, is so strong that the underdense plasma in front of the critical surface is pushed away early in the laser pulse. Thus, no matter what the original density-gradient scale length was, the dominant laser interaction is with a steeper density profile whose scale length is observed in computer simulations⁵ to follow $L \propto I^{-\alpha}$, with $\alpha = 0.22 - 0.38$. (Typically, the scale length of the steepened profile is less than an optical wavelength). Thus the hot-electron electron temperature, T_h , should scale with laser intensity as

$$T_h \propto I^\beta, \text{ with } \beta = (1-\alpha)/2 = 0.31 - 0.39. \quad (2)$$

We have already experimentally verified⁴ that resonantly accelerated electrons produced by optical breakdown of H_2 are emitted only in the plane of laser polarization, and only at oblique angles of incidence near θ_m . In the present experiment, our goal is to study the energy spectrum of the resonant electron emission. We use optical breakdown of a shockfront in D_2 to create a reproducibly oriented plasma density step, as confirmed by measurements of the angular distribution of the electron emission. The heart of the experiment is drawn to scale in Fig. 1. We irradiate the shockfront with

Figure 1. Experimental concept. The laser pulse, polarized in the plane of the drawing, is fired at the shockfront as it reaches the end of the shock tube. RA causes fast electrons to be emitted along the density-gradient vector of the shockfront (drawn as heavy arrow).



p-polarized light incident at an oblique angle θ near our estimate of θ_m . With this geometry, we then expect to see strong electron emission along the shockfront density gradient, with an energy spectrum, the temperature of whose "tail" scales with laser intensity as in (2) above. Our expectations of success in this endeavor is based on the realization that, at the laser intensities and pulse durations used here, ionization of a neutral shockfront density profile produces a plasma with an identical profile, because, in H_2 and D_2 at least, ionization proceeds via a "laser-driven breakdown wave"¹⁶ which moves through the laser focus too fast for ionic motion to distort the density profile. So let us now describe an experiment in which shockfronts have been used as laser targets for studies of electron emission in RA.

EXPERIMENTAL APPARATUS

Laser System

Laser-produced plasmas are typically so hot⁷ that they disassemble on a subnanosecond time scale. If this plasma expansion is to be negligible, one is restricted to picosecond laser pulse widths. We used the ultra-short-pulse CO_2 laser system designed by Kwok and Yablonovitch.⁸ The output is a

10.6- μm , single-mode pulse of energy ≤ 150 mJ, rise time 200 psec, and FWHM 500 psec. The repetition rate is 16 shots per minute. The laser pulses are focussed onto the target with an f/1 lens, producing a typical peak intensity of 10^{14} W/cm². Our experimental results appear to be dominated by interactions taking place during the first 100 psec of the laser pulse.⁹ We have also performed experiments with much shorter pulses (100 psec FWHM); these are described elsewhere.⁹

Shocktube System

The shock tube is constructed of quartz tube of 12.7 mm i.d. and 3 mm wall thickness. The tube is 230 mm long and is joined in a Tee at one end to a 46-mm long section of the same tubing. Tungsten electrodes are soldered into copper plugs which are inserted into and seal against the two openings of the Tee; this results in an electrode spacing of about 10 mm. A spark gap discharges a 3.5- μF energy storage capacitor, charged to 10-12 kV, across these electrodes. Our emphasis in the discharge circuit design has been on low inductance, reproducibility, and reliability. Measurements of the discharge waveform are consistent with a circuit inductance of 65 nH and resistance of 20 m Ω . Assuming that half the discharge energy is lost in the spark gap, 20% of that energy should be dissipated in the shock tube during the first ring of the discharge. At 10 kV, the circuit can drive a shock with $M = 5$ in 50 torr D₂, consistent with energy balance at this efficiency.

This discharge apparatus is laid horizontally in a copper box, which provides electromagnetic noise shielding. A pickup coil mounted in the roof of the box provides an electrical timing signal synchronous with the breakdown of the electrode gap. This apparatus can produce a Mach-5 shock in 50 torr D₂ every few seconds. The shot-to-shot fluctuations in M are $\pm 3\%$ and are partially correlated with drifts in pressure and charging voltage. Very low levels of acoustic and electrical noise are produced. The gas is flowed, filtered, and cold-trapped.

In the regime of pressure and Mach number in which we work, it has been established¹⁰ that the acoustical disturbance we observe at the end of the shock tube is indeed a clean, planar shockfront. In D₂, rotational relaxation takes place well downstream of the translational shockfront, so we can calculate the initial density jump from the theory of one-dimensional shocks in a monatomic gas¹²: $\rho_2/\rho_1 = 4M^2/(M^2+3) = 3.57 \pm 0.02$ for $M = 5.0 \pm 3\%$. For shocks with $M = 5$ in 50 torr D₂, the density of electrons bound to the molecules on the high-density side of the shockfront is $2\rho_2 = 1.2 \times 10^{19}$ cm⁻³, just above the critical density for CO₂ laser light. From the argon data of Ahlsmeyer,¹³ we calculate that the density-gradient scale length in the translational shockfront is $L = 8$ μm in 50-torr D₂; this number is very insensitive to fluctuations in Mach number near $M = 5$. This scale length lies in the range of interest ($L \lesssim \lambda$) for studies of RA with CO₂ lasers.

The experiment is performed by irradiating the shockfront, at an oblique angle from the direction of its density step, as it reaches a point near the end of the shock tube. This is accomplished in the aluminum target chamber shown in Fig. 1, which mates the end of the tube with the laser focusing lens. The optical and shock-tube axes intersect at an angle of 30°, the optimum angle for RA by a density-gradient scale length of ~ 5 μm . The focal spot diameter of the lens is claimed to be 17 μm . Laser pulse energy monitoring is performed on each shot by a calibrated Ge:Ga detector, onto which is focussed a small fraction of the incident laser pulse. This is illustrated in Fig. 2, which shows the target chamber in relation to the rest of the experiment.

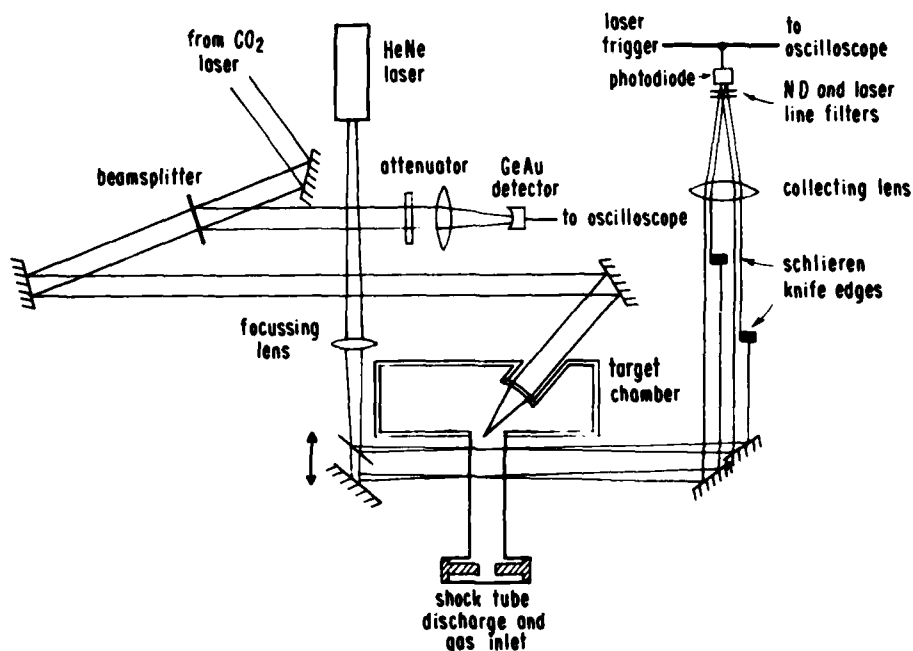


Figure 2. Layout of the experiment, showing shocktube/target chamber, laser-pulse diagnostics, and two-beam laser-Schlieren shockfront detector.

In order to fire the laser at the instant that the shockfront passes into focus (it remains in focus for <10 nsec), laser triggering is performed by a two-channel laser-Schlieren shockfront detection system shown in Fig. 2. Each of the two HeNe laser beams is deflected past the knife edge and into the photodiode as the shockfront passes down the tube. The two short output spikes from the photodiode are fed directly to the laser's trigger circuits and are recorded for calculations of the position of the shockfront. The laser trigger delay is set so that the shockfront and the laser pulse arrive at the laser focus simultaneously. This happens only once in every ~ 20 shots. The shockfront position can be determined to within ± 75 μm .

MEASUREMENTS

Apart from laser pulse diagnostics, shockfront timing, and background plasma characterization, we made a number of experimental observations:

Total electron emission was measured by placing inside the target chamber, next to the focusing lens, a Si surface-barrier detector which looked at the laser focus along the shock tube axis. The detector is masked by a $13\text{-}\mu\text{m}$ thick aluminum foil; incident electrons come to a stop in the foil, producing Al k-x-rays which are sensed by the detector. The detector signal is sent to a charge-integrating preamplifier and recorded on an oscilloscope along with shockfront timing information. In this way, we can measure the total charge emitted during each shot, as a function of shockfront position.

The angular distribution of electron emission was measured by replacing the Si surface-barrier detector with a small piece of Kodak No-Screen x-ray film, wrapped in $13\text{-}\mu\text{m}$ thick Al foil. An image of the electron emission is created on the film by Al k-x-rays produced when fast electrons are stopped in the foil.

The energy spectrum of electron emission was measured with a simple magnetic spectrometer. RA predicts that electrons should be emitted along the plasma density gradient vector, and we expect this to lie parallel to the shocktube axis if the shockfront is in proper focus. Indeed, emission was found only in a narrow cone centered along this direction (see below). This quasi-unidirectional emission allowed us to construct a spectrometer with reasonable focusing properties by placing the target chamber between the faces of a small, permanent magnet. This provided energy dispersion and focussed the electron emission onto a plane which was perpendicular to the shocktube axis and which nearly coincided with the target-chamber wall. There, we placed an array of charge collectors which consist of copper pads etched onto a printed circuit board. Each collector is heavily tinned to assure that the incident electrons are stopped in the conductor. The energy width of each collector was chosen to be 30% of its center energy, so as not to exceed the geometrical resolution of the spectrometer, which is largely determined by magnetic field inhomogeneities and the finite cone-angle of electron emission. Since the energy spectrum is bound to fall off at higher energies, this geometry enhances the signal due to high-energy electrons, resulting in wide dynamic range. The energy range spanned is 14-140 keV. The collectors are connected to cables of different lengths which are connected to the same oscilloscope input. Thus the signals from all the collectors arrive at the oscilloscope in sequence, allowing a complete spectrum to be recorded in a single shot.

RESULTS

As a gross test of the effect of using a shockfront as a laser target, we first measured the total electron emission as the shockfront was moved in and out of focus, using a Si surface-barrier detector as described above. Fig. 3 shows the electron signal as a function of the position Δx of the

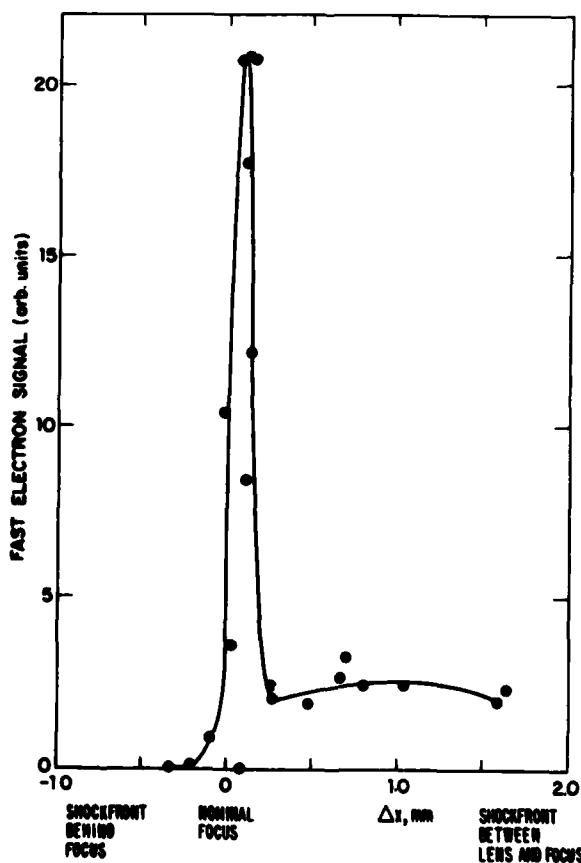


Figure 3. Si surface-barrier detector signal vs. shockfront position Δx , for shockfronts with $M=5.1$ in 43 torr D_2 . Each point is from a single laser shot. The enhancement achieved when the shockfront is in focus ($\Delta x=0$) is the sign that the critical surface is reproducibly oriented near the optimum angle θ_m for electron emission in RA.

shockfront along the shocktube axis, measured relative to the laser focus. These data were produced by laser pulses whose energies lay in a $\pm 20\%$ window. This graph has a simple interpretation. The points on the left of the graph ($\Delta x < 0$) result from shots in which the shockfront had not yet reached the laser focus when the laser pulse arrived ("late" shockfronts). The breakdown thus took place in the low-density gas ahead of the shockfront, in which even total ionization could not produce the critical density needed for resonance absorption. No signal was produced. On the right of the graph ($\Delta x > 0$), the breakdown took place in the overdense gas behind an "early" shockfront. The shockfront found itself in a region of weak laser intensity and played no role. Its position was irrelevant, and the signal strength was similar to that produced in an unshocked, homogeneous gas.⁴ But when the shockfront was in correct focus ($\Delta x = 0$), the signal was enhanced by a factor 10.

Further insight into the details of the interaction is gained from measurements of the angular distribution of electron emission from shockfront targets. For this experiment, the electronic detector was replaced by x-ray films wrapped in Al foil. In Fig. 4, two such films are presented as seen by

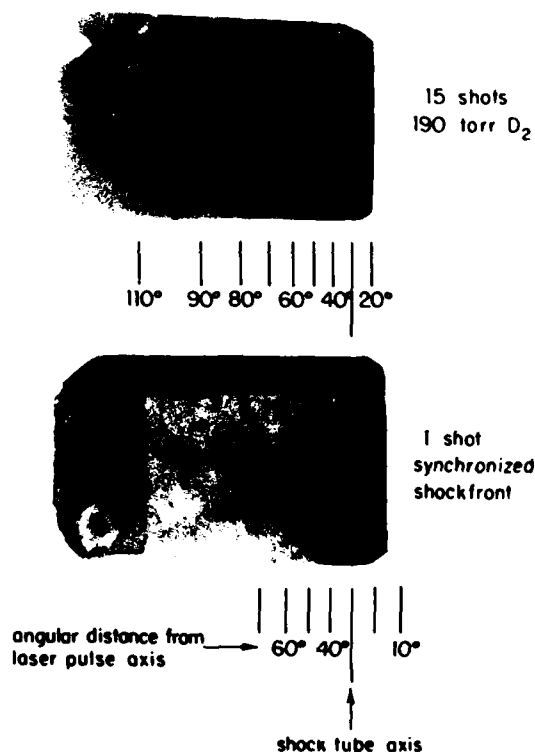


Figure 4. X-ray film exposure by fast electrons emitted in RA. In both films, the plane of polarization intersects the film in a horizontal line which passes through the spot of exposure. Homogeneous gaseous targets (top) emit electrons in the plane of polarization, but the angle of peak emission varies widely from shot to shot, because the direction of \vec{v}_n is not reproducible. In shockfront targets (below), \vec{v}_n points along the shock-tube axis, and this is the direction of strongest electron emission. The shockfront moved at $M = 4.8$ in 43 torr D_2 .

the target. The plane of polarization intersects each film in a horizontal line which passes through the center of the spot of exposure. The upper film was produced in homogeneous gas and is included for comparison. Here, unreproducible emission in the plane of polarization and into a wide range of oblique angles is seen, in accordance with theory and as described in a previous publication.⁴ "Early" shockfronts produce similar patterns of exposure. "Late" shockfronts produce no exposure. As seen in the lower film, however, properly focussed shockfronts emit electrons predominantly in a cone of half-angle $20^\circ - 25^\circ$, centered on the shock-tube axis. Since electrons are emitted along the plasma density-gradient vector, this observation proves that the orientation of the shockfront density gradient has been imposed on the breakdown plasma.

Figs. 3 and 4 prove that breakdown of a shockfront produces a reproducibly

and optimally oriented target for studies of electron emission in RA. Our observation has been that the hot-electron temperature of the electron energy spectrum of such emission is quite reproducible. A typical spectrum, shown in Fig. 5, exhibits a characteristic "bi-Maxwellian" shape with a thermal component ($T_c \approx 2$ keV) below 40 keV and a suprathermal component ($T_h = 36$ keV) above. The scaling, with peak laser intensity, of the suprathermal electron "temperature" is shown in Fig. 6. We see that $T_h \propto I^\beta$, with $\beta = 0.32 \pm 0.03$,

Figure 5. A typical hot-electron energy spectrum. The dark bars along the horizontal axis represent the energy widths of the charge collectors. The spectrum has a distinct "cold" component below $\epsilon = 40$ keV and a suprathermal "tail" due to electron acceleration in RA.

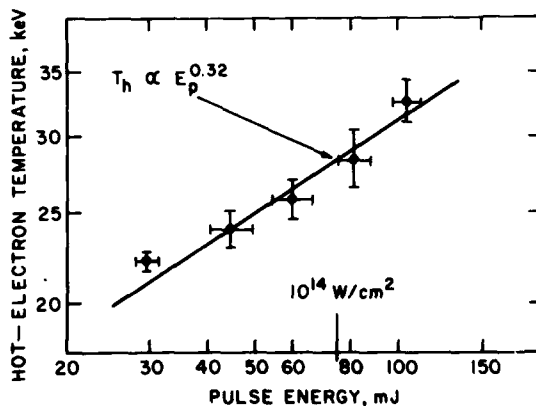
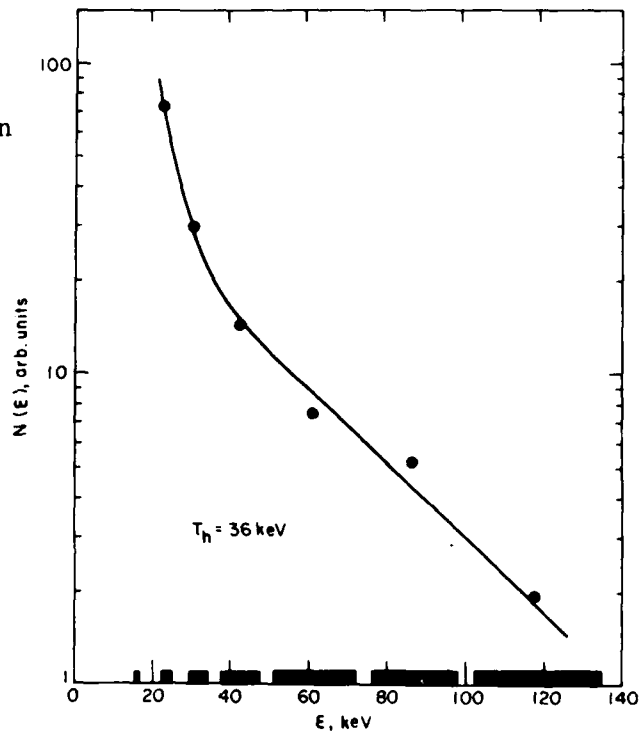


Figure 6. Scaling of hot-electron temperature, T_h , with laser pulse energy, E_p . A tick mark calibrates the horizontal axis with peak laser intensity. Data from 45 laser shots were averaged in groups of from 3 to 13 to produce this graph. The scaling exponent, 0.32 ± 0.03 , is in agreement with the theory of steady-state profile modification by the pondermotive force.

in good agreement with the predicted value of $\beta = 0.31 - 0.39$. This constitutes the first direct confirmation of this important theoretical prediction.

To summarize, we have demonstrated that shockfronts, ionized by intense laser pulses, produce plasma targets that are ideal for the study of electron emission in resonance absorption. We have observed such emission from shockfronts and have directly verified for the first time that the electron energy spectrum scales with laser intensity as predicted by models of profile

steepening by radiation pressure.

This work was performed at Harvard University and was supported by Department of Energy contract number DE-AC02-76DP40018.A001 (formerly ED-78-S02-4631).

REFERENCES

1. J. P. Friedberg, R. W. Mitchell, R. L. Morse, and L. I. Rudsinski, *Phys. Rev. Lett.* **28**, 795 (1972).
2. D. V. Giovanelli and R. P. Godwin, *Am. J. Phys.* **43**, 808 (1975).
3. J. Albritton and P. Koch, *Phys. Fluids* **18**, 1136 (1975).
4. P. Kolodner and E. Yablonovitch, *Phys. Rev. Lett.* **37**, 1754 (1976).
5. D. W. Forslund, J. M. Kindel, and K. Lee, *Phys. Rev. Lett.* **39**, 284 (1977); K. G. Estabrook and W. L. Kruer, *Phys. Rev. Lett.* **40**, 42 (1978).
6. Yu. P. Raizer, *Zh. Eksp. Teor. Fiz.* **48**, 1508 (1965) [*Sov. Phys. JETP.* **21**, 1009 (1965)].
7. E. Yablonovitch, *Phys. Rev. Lett.* **35**, 1346 (1975).
8. H.-S. Kwok and E. Yablonovitch, *Rev. Sci. Instr.* **46**, 814 (1975).
9. P. Kolodner and E. Yablonovitch, *Phys. Fluids* **24**, 759 (1981).
10. G. Pert, *J. Appl. Phys.* **39**, 5932 (1968); H. Brinkschulte, *Z. Naturforsch.*, **22a**, 438 (1967).
11. G. Lensch and H. Gronig, in *Proceedings 11th International Symposium on Shock Tubes and Waves*, Univ. Washington Press, Seattle (1978) p. 132.
12. J. N. Bradley, *Shock Waves in Chemistry and Physics*, Methuen and Co. Ltd., London (1962).
13. H. Ahlsmeyer, *J. Fl. Mech.* **74**, 497 (1976).

AD P000275

EXPERIMENTAL STUDY ON THE IONIZATION OF ARGON GAS IN
A NON-EQUILIBRIUM STATE BEHIND REFLECTED SHOCK WAVES

K.Terao, M.Hozaka and H.Kaitoh

Department of Mechanical Engineering

Yokohama National University, Yokohama, Japan

The electron temperature, the density and the ion temperature in argon gas behind reflected shock waves were measured by a laser light scattering method, while the gas temperature was measured by the spectroscopic method. The values of these three temperatures are different from each other during a certain period after arrival of the reflected shock front. Both the electron and ion temperatures are much higher than the theoretical gasdynamic temperature. The ionization rate is also much higher than that in the equilibrium state, but the measured gas temperature is lower than the theoretical one.

These results suggest that the argon gas is in a non-equilibrium state during the first period. This is supported by the fact that the induction period of light emission in argon behind reflected shock waves fluctuates with a definite probability which depends on the physical state of the gas. The phenomena are explained as an irreversible process in which the association, the ionization and the recombination of argon atoms take place.

INTRODUCTION

At an irreversible process from a stable state to another stable state, an entropy increase is observed according to the second law of thermodynamics. As both the initial and final states have a maximum entropy, the process must pass a minimum entropy state at least once. On the other hand the entropy is expressed as a product of the Boltzmann constant and the logarithm of the probability of the state. The probability of the minimum entropy state therefore must be less than that of the initial state as well as the final state. That is, the irreversible process must pass through some non-equilibrium states and the probability of the irreversible process is less than both those of the initial and final states and the process must fluctuate more than the initial and final states.

We have observed such fluctuations and non-equilibrium states in some combustion phenomena, for example, fluctuation of the induction period of ignition and electron temperature in flames and detonation waves much higher than the mean gas temperature (ref.1, 2 and 3).

Similar fluctuations and non-equilibrium states should also be observed in the ionization of gases behind shock waves, because this kind of ionization proceeds very rapidly and consists of some irreversible processes. We therefore measured the electron, ion and gas temperatures as well as the induction periods of light emission in argon gas behind reflected shock waves. These three temperatures are different from each other and the induction periods fluctuate, too. The measured results and their explanations are reported in this paper.

EXPERIMENTS

Our experiments were carried out using a 4 m long stainless steel tube having an inner-diameter of 49 mm. The tube was divided with a polyester film into two segments of 1 m and 3 m length, respectively. Hydrogen gas was charged as a driving gas in the 1 m long segment, while the remaining 3 m long segment was filled with 99.996% argon gas. Shock waves were produced in the argon gas by breaking the polyester film and reflected at the end wall of the tube. The incident shock waves contain two principal waves whose Mach numbers are 4.8 and 6.7, respectively. The theoretical gasdynamic temperatures in the argon behind the reflected shock waves were estimated to be 5,300 K and 10,000 K, respectively.

The electron and ion temperatures in shock heated argon were measured by a laser light scattering method. Fig.1 shows an arrangement of the measuring apparatus. A Q-switched ruby giant pulse laser having 20 ± 2 MW, 20 nsec duration of half value intensity and 6943 Å wavelength set at the end part of the shock tube was focussed through a sapphire window on the axis of the shock tube.

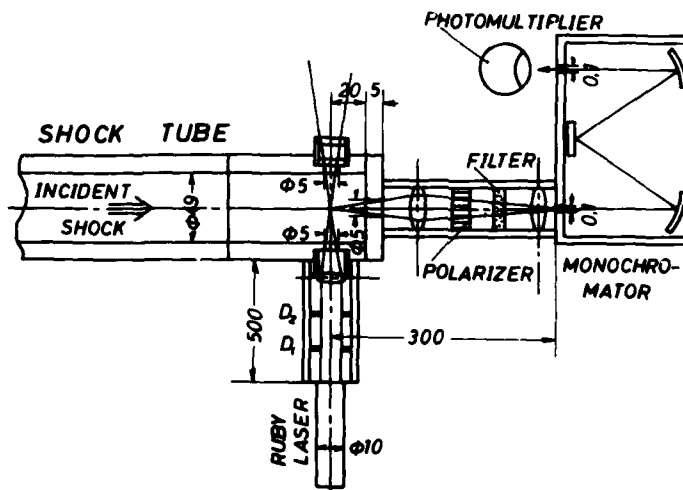


Fig.1. Arrangement of the experimental apparatus for the laser light scattering method.

The emission of the laser beam was triggered by the pressure of the incident shock front through a piezoelectric pressure transducer. Its triggering time was regulated by a delay-circuit in such a way that the laser beam could be emitted at an arbitrary instant after the reflected shock front had passed the measuring point. Thus, it was possible to direct the laser beam to an arbitrary position behind the reflected shock waves.

At the same time, the light of an arbitrary wavelength scattered by the charged particles in argon behind the reflected shock waves in a direction at an angle of 90° to the incident laser beam was observed through a sapphire window at the end plate of the shock tube. The variation of its intensity was measured by a monochromator, a photomultiplier (Hamamatsu TV R466) and an oscilloscope. In some cases, the spectrographs of the scattered light dispersed by the monochromator were recorded directly on photographic films. Light trap diaphragms D_1 , D_2 , a filter and a polarizer were set in the light path in order to eliminate the stray light and luminescence of the shock waves, as shown in Fig.1.

On the other hand, the intensity of several spectrum lines having different wavelength emitted from the shock heated argon gas were measured with the monochromator and the photomultiplier in order to obtain the gas temperature. The monochromator and the photomultiplier were set at the position of the laser for the scattering method. The variation of the intensity of the spectrum lines of the argon was recorded through an oscilloscope, so that the intensity of a spectrum line at an arbitrary position behind the reflected shock front could be obtained.

In addition to the experimental apparatus for the measurement of the spectrum lines a piezoelectric pressure transducer was set at the end plate of the shock tube, so that the instant of the reflection of the incident shock front at the tube end could be marked, while the beginning of the emission in argon was observed. In our experiments we observed the spectrum line of 6043.2 Å wavelength from argon at the theoretical gasdynamic temperature of 3,300 K, 4,200 K and 4,900 K of argon gas having a density of 0.03 kg/m^3 behind the reflected shock waves.

We could measure the period t_E from the reflection of the incident shock front at the tube end to the beginning of the light emission in argon, while the propagation period t_R of the reflected shock front from the tube end to the measuring point could be calculated from the initial condition and the velocity of the incident shock. We took the difference between t_E and t_R as an induction period of light emission. The experiment at each condition was repeated more than 50 times, so that the histograms of the induction period could be obtained. The fluctuation of the incident shock propagation velocity was always kept within $\pm 1.7\%$.

EXPERIMENTAL RESULTS

The laser light scattered in an ionized gas consists of two components: the electron component and the ion component. The spectrum of the electron component has a relatively wide frequency range but low intensity, while that of the ion component has a very small frequency range and high intensity in our cases (ref.4).

1) Electron Temperature

Comparing the spectra obtained from the experiments with those theoretically obtained by W.H.Kegel (ref.5), it is possible to estimate the characteristic parameter

$$\alpha \approx \frac{\lambda_0}{4\pi D \cdot \sin(\theta/2)}, \quad (1)$$

where λ_0 is the wavelength of the incident laser beam, D the Debye

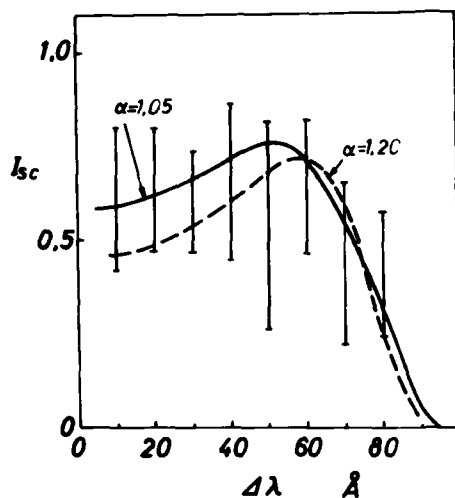


Fig. 2. Spectra of the electron component of the scattered light in argon at 50 μsec after the passage of reflected shock front. Mach number of the incident shock: 6.7, I_{sc} : relative intensity, $\Delta\lambda$: wavelength deviation from that of the laser beam.

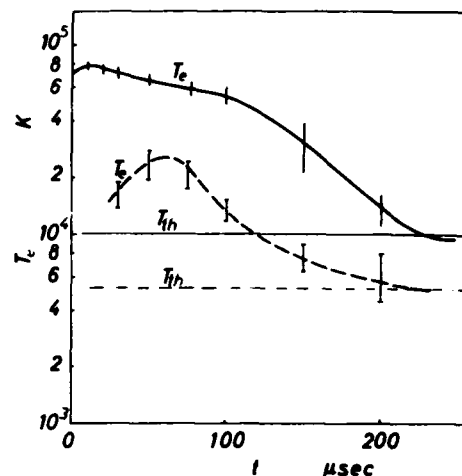


Fig. 3. Measured electron temperature T_e and theoretical gasdynamic temperature T_{th} with respect to the time t after the passage of reflected shock front. Mach number of the incident shock is 6.7 for the solid line and 4.8 for the broken line.

length and θ the scattering angle. In Fig. 2 an example of the theoretically possible spectrum of the measured scattering light corresponding to the maximum and minimum values of α is shown. From the values of α and the spectra we obtained the electron temperature T_e and density by the method developed by W.H. Kegel (ref. 5). Fig. 3 shows the measured electron temperature.

2) Ion Temperature

As the ion component of the scattered light had such a small frequency range that the measurement with the photomultiplier could not be performed to obtain its spectrum, we first took the direct photographs of the scattered light dispersed through the monochromator and analyzed them with a microphotometer. Fig. 4 illustrates an example of the spectra of scattered light analyzed with the microphotometer. It shows both the ion and electron components, but in most cases we observed only the ion component.

We can calculate from these spectra the ion temperature just like the electron temperature (ref. 5) under the consideration of the characteristic parameter

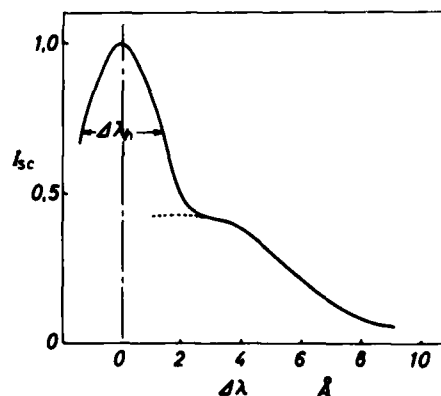


Fig. 4. Spectrum of the scattered light obtained from spectrographs. 3 μsec after arrival of reflected shock front. Mach number of the incident shock is 6.7. $\Delta\lambda_h$: half value width.

and ion mass. As the characteristic parameter in our cases is almost equal to zero, we calculated the ion temperature from the half value width of the intensity $\Delta\lambda_h$. Fig.5 shows the measured ion temperature in argon behind the reflected shock waves whose incident shock waves had a Mach number of 6.7.

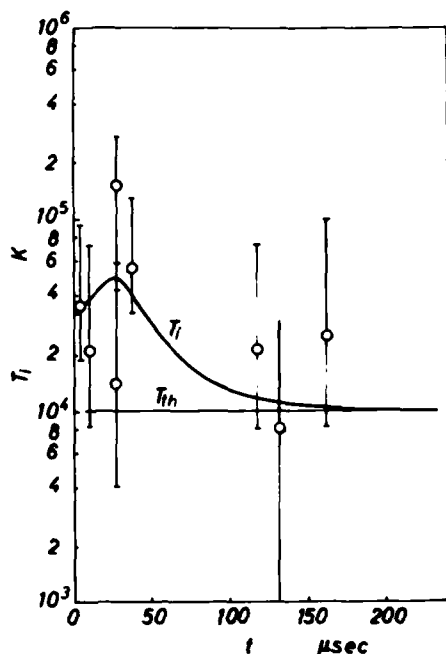


Fig.5(left). Ion temperature T_i measured by the laser light scattering method and theoretical gas-dynamic temperature T_{th} in argon with respect to the time t after passage of the reflected shock front.

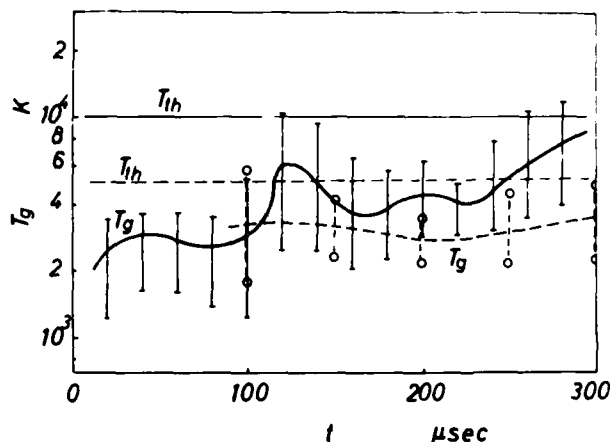


Fig.6. Gas temperature T_g measured by the spectroscopic method. Mach number of the incident shock is 6.7 for the solid line and 4.8 for the broken line.

3) Gas Temperature

We tried to measure the gas temperature of argon behind reflected shock waves by observing the intensity of several spectrum lines emitted from argon under the assumption that the shock heated gas is in an equilibrium.

In our experiments we measured the intensities I of the spectrum lines of 5373.6 Å, 5912.1 Å and 6052.7 Å wavelength, respectively and estimated the gas temperature according to the following equation (ref.3):

$$I = \frac{h\nu}{4\pi} g_n A_{nm} \frac{N(T)}{U(T)} \exp\left(-\frac{E_n}{kT}\right), \quad (2)$$

where h is the Planck's constant, ν the frequency of the spectrum line, g_n the statistical weight, A_{nm} the transition probability of the line, $N(T)$ the gas density, $U(T)$ the partition function, E_n the energy of the n -level of the line and k Boltzmann constant. A_{nm} , g_n and E_n were taken from the Journal of Quantitative Spectroscopy and Radiative Transfer (London, 1961). In order to confirm these values, we compared these values with those measured by the light reversal method in the same argon gas behind reflected shock waves whose incident shock had a Mach number of 4.2. Fig.6 illustrates the measured gas temperature T_g with respect to the time t after the passage of the reflected shock front.

4) Probability of Light Emission

The induction period of light emission in the argon gas behind reflected shock waves fluctuated in a fairly large range. From the results measured more than 50 times we obtained a histogram of the induction period of light emission for each experimental condition. Fig.7 shows an example of such histogram in which t means the induction period and N the frequency.

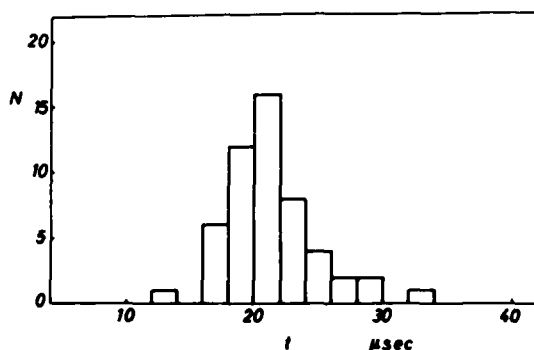


Fig.7. Histogram of induction period of light emission in argon gas behind reflected shock waves. Mach number of the incident shock is 4.3.

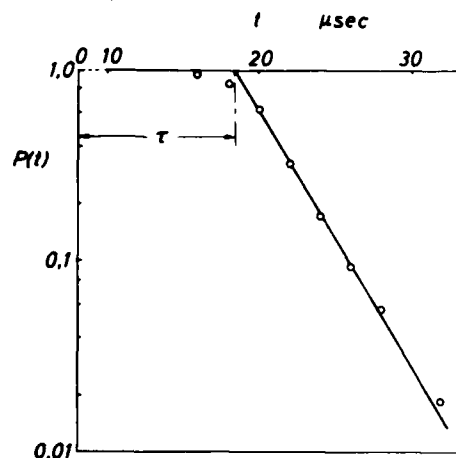


Fig.8. $\ln P(t)$ against the induction period of light emission t at the same condition of Fig.7.

If $q(t)$ is the probability density of light emission, $P(t)$ the probability of light emission whose induction period is longer than t , m the molar number of the shock heated gas from which the light emission is observed (m is constant in this case), and μ the probability of light emission in one mole gas per unit time, we can calculate the light emission probability μ according to the following equations (ref.1):

$$P(t) = \int_t^{\infty} q(t) \cdot dt \quad (3)$$

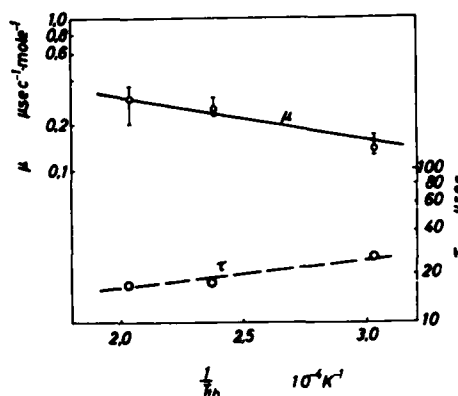
$$m \cdot \mu \cdot P(t) \cdot dt = -dP \quad (4)$$

$$m \cdot \mu = - \frac{d \ln P(t)}{dt} \quad (5)$$

Fig.8 illustrates an example of the relations between $\ln P(t)$ and t , which are almost linear. This result means that the light emission probability μ is constant for time t and the phenomenon of the light emission in a shock heated gas is of a stochastic nature like ignition or nucleation (ref.1,6) which takes place with a certain definite probability under a definite condition. The phenomenon consists of two processes, that is, the initiation process and the development process. The period τ in which no light emission is observed is the development period in which the phenomenon develops to such a state that the light emission becomes observable.

Fig.9 illustrates the logarithm of the light emission probability μ and that of the development period τ with respect to the reciprocal theoretical gasdynamic temperature of the argon.

Fig.9(right). $\ln \mu$ and $\ln \tau$ with respect to the reciprocal theoretical gasdynamic temperature in the argon gas behind reflected shock waves. The density of gas behind the reflected shock waves is always 0.033 kg/m^3 .



DISCUSSION

In Fig.10 the measured electron temperature T_e , ion temperature T_i and gas temperature T_g as well as the theoretical gasdynamic temperature T_{th} in argon behind reflected shock waves whose incident shock has a Mach number of 6.7 are again illustrated in a group with respect to the time t after the passage of the reflected shock front at the measuring point. During the first 100 μsec to 200 μsec both the electron and ion temperatures are much higher than the theoretical gasdynamic temperature, while the measured gas temperature is rather lower than the theoretical one.

1) Gas Temperature

The gas temperature measured by the spectroscopic method is much lower than the theoretical gasdynamic temperature. As explained in the previous section, the light emission in a shock

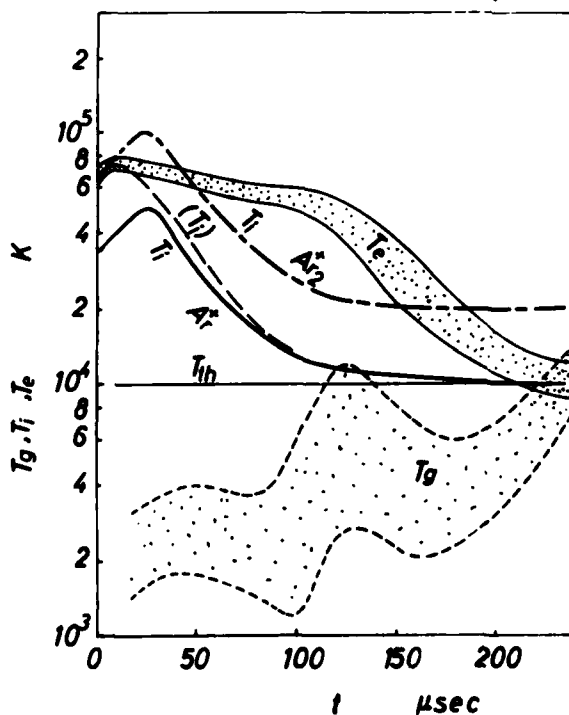


Fig.10

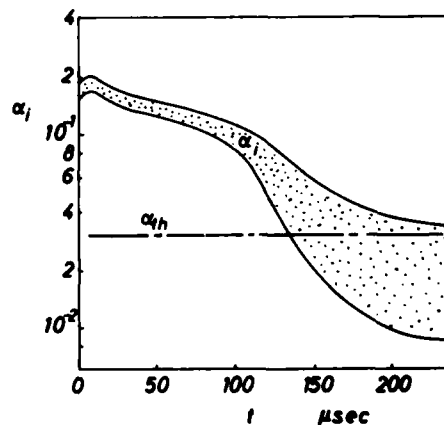


Fig.11. Ionization rate α_i in argon behind the reflected shock waves with respect to the time t after the passage of the reflected shock front. α_{th} : the ionization rate in the equilibrium state according to Saha's equation.

heated gas is a stochastic phenomenon in which a fairly large fluctuation occurs with a certain probability. This light emission consists of two processes: the initiation and the development. During the period of a few hundred microseconds from the beginning of emission to the time in which the whole gas emits light, the gas is not in an equilibrium state. The gas contains two parts, one of which emits light and the other does not emit light. That is, there are high temperature parts and low temperature parts simultaneously. During this period the correct gas temperature cannot be obtained by the spectroscopic method, because some parts of the gas at high temperature emit light, while the other parts of lower temperature absorb light. A value of the gas temperature lower than the average one is thus sometimes obtained by the spectroscopic method.

2) Electron and Ion Temperatures

The electron temperature as well as the ion temperature measured by the laser light scattering method is much higher than the theoretical gasdynamic temperature. Fig.11 illustrates the ionization rate of argon behind reflected shock waves, obtained by the laser light scattering method, in comparison with that obtained theoretically according to Saha's equation. At first the measured value of the ionization rate is much higher than the theoretical one and then approaches it after about 200 μ sec. This means that the ionized argon gas behind reflected shock waves is at first in a non-equilibrium state, as the light emission also suggests. In a shock heated gas, therefore, there must be some very high temperature parts which initiate the ionization.

On the other hand, we have observed in argon gas behind reflected shock waves an ion mass of about twice the value of an argon atom during the first 20 μ sec by the double probe method using a high frequency multistep potential(ref.7). This suggests that some argon atoms associate with each other, forming diatomic argon Ar_2 and ionize. According to the results obtained by the laser light scattering method, the ion temperature is lower than the electron temperature. Considering the association, however, and using the mass of Ar_2 , we obtain the ion temperature shown in Fig.10 as a broken line indicated with Ar_2^+ . This result agrees quite well with the electron temperature during the first 20 μ sec, but after that the ion temperature becomes too high. The associated argon atoms are dissociated again after the ionization producing Ar ions. The ion temperature can thus be calculated from the spectra of the scattered light at first with the mass of associated argon ions Ar_2^+ , then with the mixture of Ar_2^+ and Ar^+ , and finally with the mass of the monatomic Ar^+ . Under such assumption a variation of the ion temperature in argon with respect to the time after passage of the reflected shock front is indicated as a broken line (T_i) in Fig.10.

The anomalously high temperatures of the free electrons and ions in argon behind reflected shock waves are thus caused by the heat released through the association.

Summarizing the results observed in our experiments the processes are explained as follows:

- 1) At first argon atoms in some points behind reflected shock waves associate with each other, releasing some reaction heat
- 2) With the released heat the association develops further.
- 3) The light emission and the ionization of the associated and

monatomic argon are observed in the course of association. The phenomena proceed during this period in a non-equilibrium state and both the ion and electron temperatures become much higher than the average gas temperature.

4) Then the associated argon atoms dissociate again and the state approaches an equilibrium, accompanying the partial recombination of ions and free electrons.

CONCLUSIONS

The results obtained by the laser light scattering method and spectroscopic method show the following phenomena occur in argon gas behind reflected shock waves:

- 1) The electron temperature, ion temperature and gas temperature in argon are different from each other during the first period of a few hundred microseconds after arrival of the reflected shock front; the electron and ion temperatures are much higher than the theoretical gasdynamic temperature, while the gas temperature is apparently lower than the theoretical one.
- 2) The ionization rate in argon gas during the first period is also much higher than that in the equilibrium state.
- 3) The induction period of light emission fluctuates with a certain probability determined by the physical state of the gas.

From these phenomena we concluded as follows:

- 1) The process is irreversible, in which the argon gas is in a non-equilibrium state during the first period of a few hundred microseconds after the arrival of the reflected shock front.
- 2) At first, when the reflected shock front arrives, the argon atoms associate partially with each other and form diatomic molecules, releasing reaction heat.
- 3) The associated argon atoms heated by the reaction heat are ionized and then dissociated, releasing free electrons and monatomic ions.
- 4) Then the recombination of excessive ions with free electrons takes place. The ions and free electrons approach an equilibrium state and thus the argon gas becomes homogeneous.
- 5) The gas temperature measured by the spectroscopic method does not indicate the mean gas temperature, because of the non-equilibrium state and inhomogeneity during the first period. Generally such non-equilibrium states and fluctuating phenomena should occur in irreversible processes. The association of argon atoms is not yet clear and should be further investigated.

REFERENCES

1. K.Terao, Japan.J.Appl.Phys., 16, p.29 (1977).
2. K.Terao, Japan.J.Appl.Phys., 8, p.486(1964).
3. K.Terao, K.Imamura and N.Takasu, Proceedings of the 12th International Symposium on Shock Tubes and Waves, p.548 (1979).
4. H.J.Kunze, Plasma Diagnostics, North Holland (1968), Ch.9.
5. W.H.Kegel, IPP 6/34, Institut f. Plasmaphysik, (1965).
6. K.Terao, F.Hatano and F.Sano, Japan.J.Appl.Phys., 3, p.728 (1964).
7. K.Terao and K.Yamamoto, Proceedings of the Eighth International Shock Tube Symposium, 43 (1971).

NEW EXPERIMENTAL RESULTS UPON IONIZATIONAL
RELAXATION OF A SHOCK HEATED XENON PLASMA

P. VALENTIN, Cl. THENARD, P. MAILLOT

Laboratoire de Thermodynamique, L.A. C.N.R.S. N° 230
Université de ROUEN, B.P. 67 76130 MONT-SAINT-AIGNAN (France)

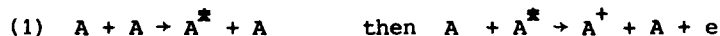
This paper deals with the ionizational relaxation of a shock heated Xenon plasma. The initial pressures are 1.5 and 10 torr, the rate of impurities is below 10^{-3} and the Mach numbers lie within the range 8 to 18. The measurements of the total relaxation time and the velocity are determined by the use of schlieren systems. The growth of the electron density is deduced from the data given by a submillimeter interferometer operating at 890 GHz and by spectrophotometers.

Our experimental results show the products $P_1\tau$ are depending on P_1 , and the increase of the electronic density is much faster than the one given by the theoretical model developed for inert gases [1]. For these reasons this model must be revised and we think that a better agreement could be obtained by the introduction of two temperatures in the electronic velocity distribution.

INTRODUCTION

The ionization process of noble gases excited by normal shock waves has been studied extensively [1 to 7]. The general feature of the mechanisms which happen in the relaxation zone may be described as follows:

Near the upstream region of the shock, ionization is initiated by atom-atom inelastic collisions according to [1]



As reactions



are more efficient than the A-A collisions, they quickly dominate these latter. Equilibrium is reached when the number of electrons is such that the reverse reactions balance the direct ones.

The above mentioned mechanisms seem to explain satisfactorily the experimental results for $M > 12$. But, the inelastic cross sections of reactions (1) and (2) being adjusted according to experiment conditions [4], the present investigation was undertaken in order to try to check such ajustement. For this purpose we have studied plasma of Xenon generated by shock waves for initial pressures 1.5 and 10 torr and for Mach numbers lying within the range 8 to 18.

APPARATUS AND PROCEDURE

The shock tube is composed of surfaced stainless pipe 11 m in length, with a 10 cm internal diameter. It is filled with Xenon N 45 delivered by Air Liquide. The rate of impurities is below 10^{-3} and their ionization energies generally are higher than that of Xenon.

The passage of the shock front at successive positions along the shock tube is detected by schlieren systems. The oscillogramm (Fig. 1) shows the passage of the shock front, the arrival of the luminous front and the contact surface. Thus, the total relaxation time, the velocity of the shock front and their variation along the shock tube are measured accurately (within 2 %).

Near the equilibrium region, electronic density is deduced from the absolute measurement of the continuum in the range 472.2 nm and 486.4 nm. Schluter's coefficients ξ are used in our computation.

To continue the investigation of the relaxation zone, we have carried out electronic density variation measurement using a submillimeter interferometer [9] ($\lambda = 337 \mu\text{m}$) which covers the range of 10^{18} to $5 \cdot 10^{20} \text{ e m}^{-3}$ in our experimental conditions ($P_1 = 1.5 \text{ torr}$), Fig. 2 is an example of the observed signal.

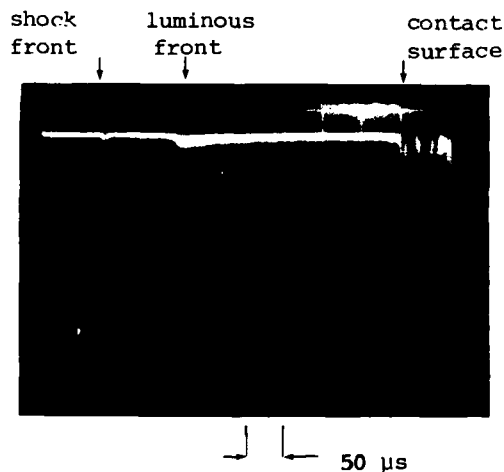


Fig. 1 : Schlieren oscillogramm
 $M = 10$ $P_1 = 1.5 \text{ torr}$

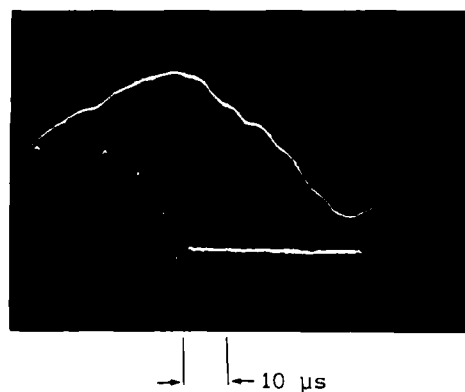


Fig. 2 : Submillimeter interferometer response. The lower trace is the continuation of the upper trace
 $M = 9$ $P_1 = 1.5 \text{ torr}$

It shows the shift of the fringes and the absorption of the electromagnetic wave, from which the effective collision frequencies ν_{eff} and the effective plasma frequencies ω_{peff} can be determined. Using Frost and Phelps's data [8],

Coulombian cross sections and Maxwellian distribution functions, we have computed [9] the theoretical values of ω_{peff} and ν_{eff} as a function of the electronic temperature T_e and the degree of ionisation $\alpha = \frac{N_e}{N_e + N_0}$. In our conditions,

ω_{peff} is equal to $\omega_p = \left(\frac{N_e e^2}{\epsilon_0 m_e} \right)^{1/2}$ and $\nu_{\text{eff}} / \omega \ll 1$. Thus the electronic

density must be easily determined. Fig. 3 is an example of the variation of ν_{eff}/N_0 and N_e versus time for $M = 10$. Unlike the smooth variation of N_e , the effective collision frequency is not a monotone function [6]. Fig. 4 is an attempt at the determination of the variation of T_e from the experimental values and the theoretical results of computation concerning α and ν_{eff}/N_0 . Note that near $\alpha = 10^{-3}$ it is rather difficult to deduce T_e from experimental data (curve with stars) which are furthermore determined with a large uncertainty.

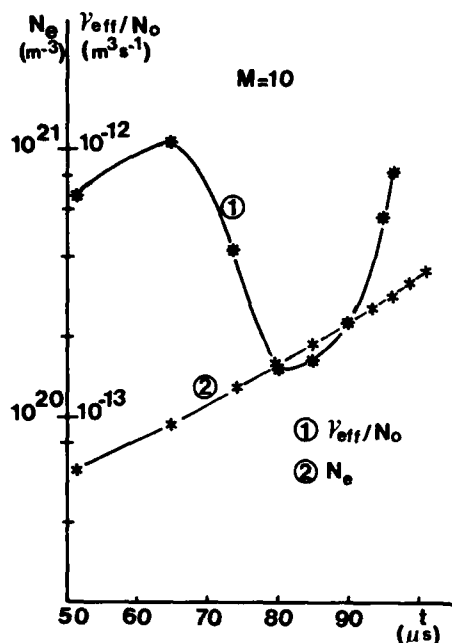


Fig. 3 : Density and effective collision frequency profiles obtained with the sub-millimeter interferometer.

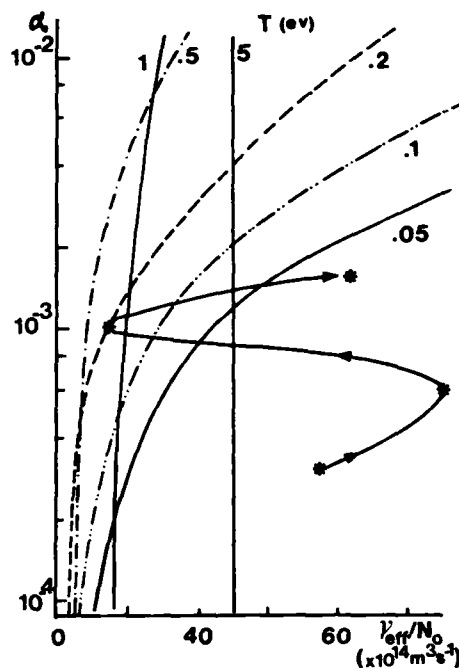


Fig. 4 : An attempt at the determination of the electronic temperature from the experimental values of α and v_{eff}/N_0 .

It must be emphasized that the electronic density gradient is sufficiently weak to allow an accurate measurement of N_e .

THEORETICAL RESULTS, COMPARISON WITH EXPERIMENTAL RESULTS

The flow is assumed to be steady and one dimensional in shock coordinates. In the relaxation region, dissipative and radiative effects are neglected, and moreover, the velocity distributions of the atoms and of the electrons are assumed to be maxwellian. The local characteristic temperatures of these distributions, respectively T_A and T_e , can be determined by means of the Rankine Hugoniot's relations supplemented by the electronic energy balance equation. Using a similar model as the one presented by Wong and Bershader [1] we have computed the growth of the electronic density behind a shock front. We have theoretically verified that the production of electrons by inelastic collisions between atoms is preponderant only during 30 % of the total relaxation time and therefore the products $P_1\tau$ are weakly depending on P_1 and are principally depending on M . Fig. 5 shows the measured values of product $P_1\tau$ as a function of $1/T_{A0}$ or M , for initial pressures 1.5 torr and 10 torr. Solid curves are theoretical curves computed with two values of the inelastic cross sections; for curve (1), they are those of Chubb [5] and for curve (2) they have been increased 10 times. For $M > 14$, there is a reasonable agreement between experimental and theoretical results. This is more doubtful within the range $10 < M < 14$ where the experimental values agree with the computed one using Chubb's cross sections for $P_1 = 10$ torr and these values increased 10 times for $P_1 = 1.5$ torr. When $M < 10$ the discrepancy is complete. Moreover, a further increase of the cross sections is unable to reduce the discrepancy, as a consequence of the concomitant decrease of T_e . Comparing our experimental results with those published by other authors, we can notice that the products $P_1\tau$ are nearly almost the same when P_1 is the same, Roth's results excepted [9]. But their ranges of Mach

number or initial pressure P_1 are often narrow. Without doubt, our results show that the product $P_1\tau$ depends on P_1 .

Fig. 6 compares the experimental electronic growths with the theoretical profiles computed with the Chubb's cross section increased 10 times. The discrepancy is an obvious fact, especially at the end of the relaxation zone where the inelastic eA collisions are theoretically the most efficient to create electrons.

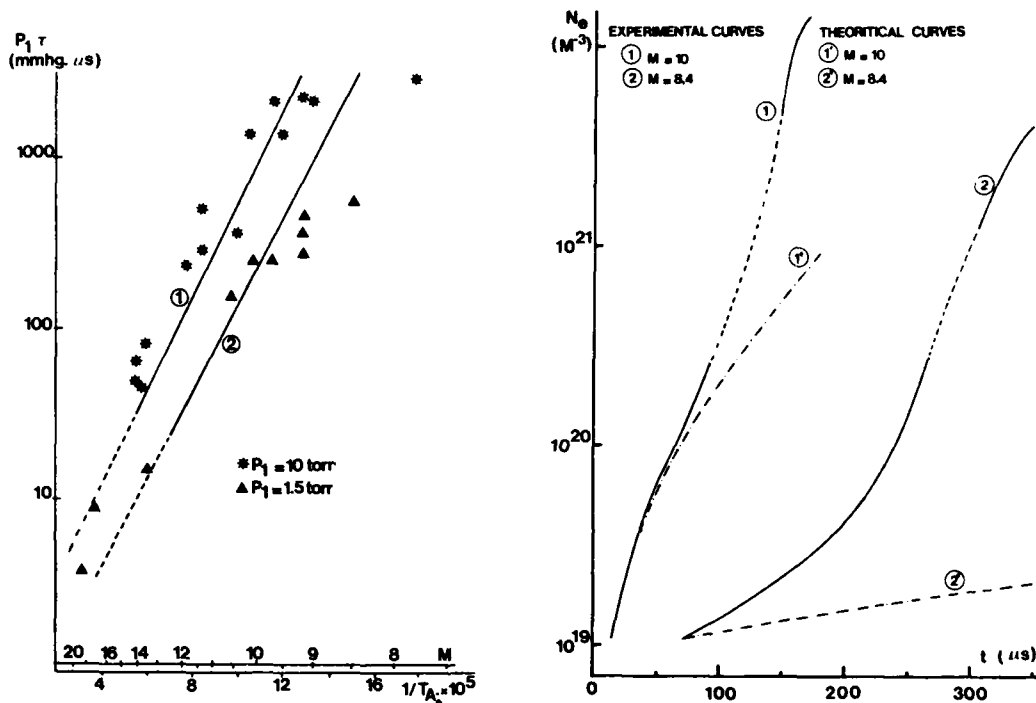


Fig. 5 : $P_1\tau$ product versus $\frac{1}{T_{A0}}$ or M
 1) Theoretical curve computed with Chubb's data .
 2) Theoretical curve computed with Chubb's data increased 10 times

Fig. 6 : Comparison between experimental and theoretical profiles of the electron growth (The cross sections introduced in our computation are those of Chubb increased 10 times).

DISCUSSION

Effects of impurities have been involved to explain the discrepancies between experimental and theoretical results concerning the product $P_1\tau$ [2]. Experiments carried out with other rate of impurities show that they have an important effect upon the ionization rate at the beginning of the relaxation zone, but if the impurity level is less than 1 part in 10^3 , the rate of electron production is not altered in the zone where e-A inelastic collisions are prevailing. Moreover the relative variation of the total ionization time is below 30 %. Therefore, even if the amount of impurities is about 10^{-3} , the effect of these impurities is unable to explain the observed discrepancy concerning the product $P_1\tau$.

We have sought an explanation in looking at phenomena neglected in the above presented theoretical model. The photoexcitation of atoms by resonant lines emitted by the equilibrium zone has been found to have the most important effect upon the rate of ionization.

Fig. 7 and 8 compare the efficiency of this process (curves 4 and 5) with that of collisional processes (curves 2 and 3). The rate of the radiative excitation to the level $1S_4$ and $1S_2$ is computed according to Biberman's scheme [10]. The experimental geometrical size of the plasma is taken into account, which explains that the arrival of the equilibrium zones occurs at a time τ smaller than the theoretical one appearing on curves (2) and (3). However it can be noticed that smaller is the Mach number more important is the effect of the photoexcitation. Nevertheless the total computed rate of electron production is still much smaller than the experimental one (curve 1).

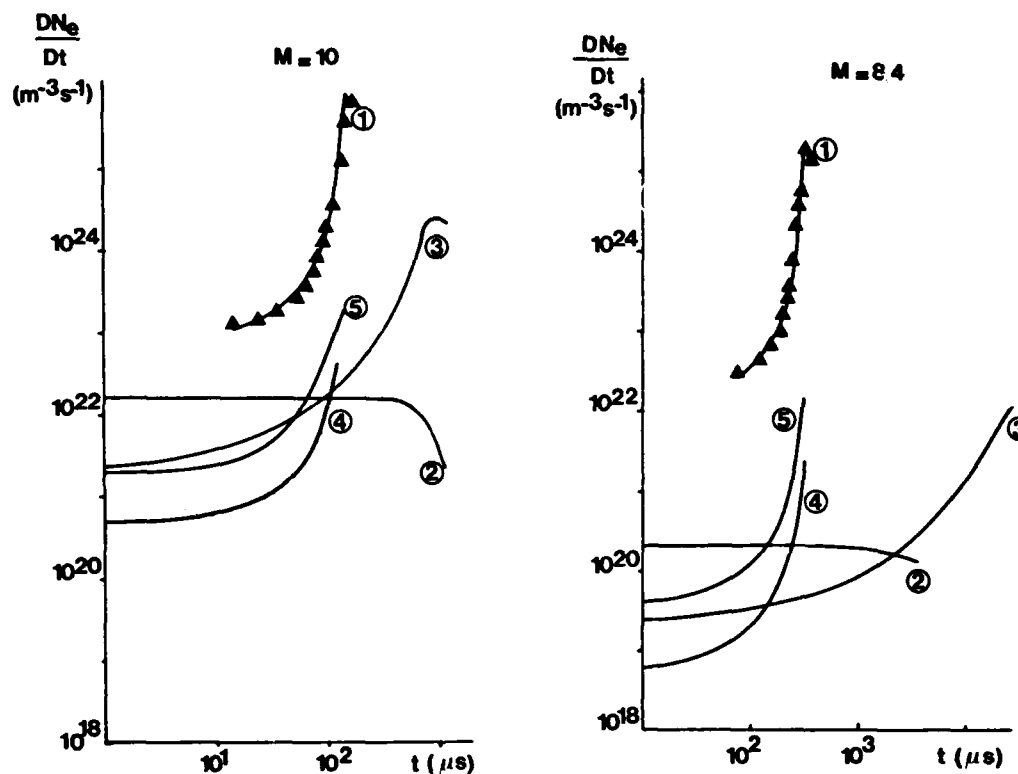


Fig. 7 and 8

Comparison of the efficiency of some processes creating excited atoms

Curve (2) by inelastic A-A collisions

Curve (3) by inelastic e-A collisions

Curve (4) by photoexcitation to the level $1S_4$

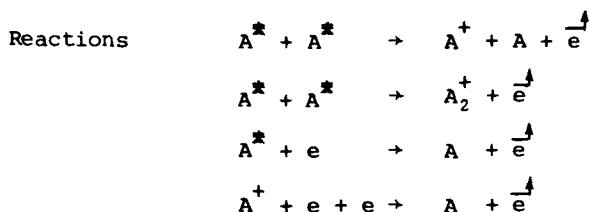
Curve (5) by photoexcitation to the level $1S_2$

Curve (1) Experimental rate of electron production

CONCLUSION

In order to fit experimental and theoretical results concerning the product P_{1T} , many authors change the inelastic cross sections they introduce in their computation. An increase of the A-A inelastic cross section may be justified to allow for the effect of impurities at the beginning of the relaxation zone, but it seems difficult to justify all increase of the e-A inelastic cross section. Moreover we have shown that this procedure is inadequate to explain our experimental results concerning not only the relaxation time but also the profiles of the electron growth.

Consequently we think that nothing but a change in the electron velocity distribution [11] can explain such experimental results.



could be liable to create "hot electrons", i.e, electrons having an energy as high as 4 to 9 eV. We think that the energy of these hot electrons is not immediately distributed to other electrons by elastic e-e collisions and therefore that phenomena involves a total distribution function composed of a maxwellian body like the one calculated previously and a perturbation in the range of higher energy like the one observed in post discharge experiments [12]. Coefficients of overpopulation of electrons in the tail of 20 ($M = 10$) and 400 ($M = 8.4$) enable to check our experimental results. A rough preliminary computed model [13] to understand the formation of this tail is not yet satisfying but we expect better results in the next few months.

References

1. H. WONG, D. BERSHADER, J. Fluid. Mech. 26, 459 (1966)
2. H. PETSCHKE, S.R. BYRON, Ann. Phys., 1270 (1957)
3. J.A. SMITH, Phys. Fluid, 11, 2150 (1968)
4. G.I. KOZLOV, D.I. ROITENBURG, STUPITSKII, Sov. Phys. Tech. 17, 9, 1512 (1973)
5. D.I. CHUBB, Phys. Fluid. 11, 2363 (1968)
6. K.E. HARWELL, R.G. JAHN, Phys. Fluid. 7, 214 (1963)
7. Y. ENOMOTO, J. Sci. Hiroshima Univ. Ser. A, 36, 95 (1972)
8. L.S. FROST, A.V. PHELPS, Phys. Rev. 136, A 1538 (1964)
9. C. THENARD, Thèse d'Etat, Université de Rouen (1980)
10. L.M. BIBERMAN, A.Kh. MNATSAKANYAN, I.T. YAKUBOV, Sov. Phys. USPE 13, 728 (1971)
11. R.H.M. SMITS, M. PRINS, Physica B+2, 2, 262 (1979)
12. P. MONCHICOURT. Thèse d'Etat, Université Paris-Sud (1977)
13. P. RANSON, Thèse d'état, Université d'Orléans (1978).

NUMBER DENSITY OF THE 5s STATES DURING THE
IONISATION RELAXATION OF SHOCK HEATED KRYPTON

Th. Zaengel* and W. Böttcher

Institut für Plasmaphysik
Universität Hannover
Callinstr. 38, D-3000 Hannover, FRG

The number density n_n of the first excited level of krypton has been determined during the ionisation relaxation by time resolved absorption spectroscopy of the Kr I line $1s_5 \rightarrow 2p_9$ at $\lambda = 811.3$ nm. Using a 1 m grating monochromator and a pulsed continuous background light source densities $2 \cdot 10^{15} \text{ m}^{-3} \leq n_n \leq 2 \cdot 10^{18} \text{ m}^{-3}$ could be measured. The electron densities were measured simultaneously with a 4 mm microwave interferometer from $n_e = 2 \cdot 10^{18} \text{ m}^{-3}$ to $n_e = 4 \cdot 10^{19} \text{ m}^{-3}$. We used a diaphragm shock tube of $52 \times 52 \text{ mm}^2$ cross section and 6 m lengths and investigated shocks having Mach numbers ranging from $M = 12$ ($p_1 = 4$ Torr) to $M = 8$ ($p_1 = 40$ Torr). The shock tube was evacuated by a diffusion pump. Gassing introduced an impurity level ranging from 7 ppm ($p_1 = 40$ Torr) to 70 ppm ($p_1 = 4$ Torr). The test gas was Kr 4.0. The experimental results are compared to model calculations in order to deduce effective cross section constants C_{jk} . The reaction kinetics was modelled by a modified two step ladder-climbing model under the assumption of a maxwellian distribution function of the electrons. The excitation cross sections were written as $Q = C_{jk}(E_{rel} - E_{jk})$. The gas flow was calculated in the heat bath approximation using a program by F. Demmig, which takes into account the instability of the shock and boundary layer.

INTRODUCTION

The ionisation relaxation of shock heated rare gases has been investigated many times. Usually the relaxation of the electron density $n_e(t)$ is measured and one tries to reproduce the measurements by model calculations. It has been shown by Harwell and Jahn (ref. 1) that the ionisation rate \dot{n}_e is determined by the effective excitation rate of the first excited levels, which in krypton are the four 5s levels. Although there has been a considerable

*Now with PHILIPS Research Lab., P.B. 1980, 5100 Aachen / FRG

refinement in the gas dynamic and reaction kinetics models (ref. 2,3), there is still a considerable scatter of the excitation cross sections derived from comparison of the measured data with the model calculations.

We believe that the main reason for this situation are impurities which influence the ionisation in the very beginning of the relaxation. We have found changes up to a factor of two by using different krypton bottles all specified by the suppliers to be Kr 4.7, i. e. to contain only 30 ppm impurities (ref. 4). As Kr 4.7 is the purest krypton available commercially, one should have this in mind, when discussing cross sections evaluated from measurements of the ionisation relaxation in krypton.

In the present work we investigate the excitation rates by atom-atom and electron-atom collisions from the 5s levels into higher levels. The effective rate of these processes determines the population density $n_i(t)$ of the 5s levels. Therefore, it is necessary to measure $n_i(t)$. We have done this by time resolved absorption measurements of the Kr I line $1s_5 \rightarrow 2p_9$ at $\lambda = 811.3$ nm. The ionisation rates were measured simultaneously using a 4 mm microwave interferometer.

For the model calculations we used the gasdynamic model of Demmig (ref. 3) and a modified two step ladder climbing model. It was not necessary to use the multi-step model of ref. 3 as we were not interested in the population of higher excited levels. We did not use the much more complicated model of Meyer-Prüßner and Demmig (ref. 5) as we have, up to now, no experimental proof whether strong deviations from a maxwellian electron distribution function really occur.

SHOCK TUBE AND SHOCK SPEED MEASUREMENT

The shock waves are generated in a hydrogen driven diaphragm shock tube of 6 meter length and a quadratic cross section of 52×52 mm², which has already been described in ref. 6. The tube, made of aluminium, is evacuated by an oil diffusion pump to a rest gas pressure of about 10^{-5} Torr before filling it with the test gas. The impurity levels calculated from the measured pressure rise during the first 60 s after shutting off the pumps ranged from 70 ppm ($p_1 = 4$ Torr) to 7 ppm ($p_1 = 40$ Torr). Due to a fast handling system it was always possible to make the measurements during this time interval. The test gas used in the present investigation was Kr 4.0. The most important specified impurities were Xe (60 ppm), N₂ (20 ppm) and H₂O (5 ppm). The location of the absorption measurement x_{m1} is situated 3.217 m behind the diaphragm whereas the beam of the microwave interferometer crosses the tube at $x_{m2} = 3.265$ m behind the diaphragm.

The shock speed is measured by a laser beam deflection method. Eight equidistant beams of He-Ne lasers cross the shock tube perpendicular to the flow direction and will only illuminate the photodiodes if the beams are deflected by the shock. The amplified signals of the diodes start and stop a 7-channel 10 MHz-counter, displaying the times Δt_i between two successive pulses. The maximum error in the determination of the time the shock needs for running from one laser beam to the other is ± 0.2 %. Their distances x_i can be defined with an error of ≤ 0.1 %.

DIAGNOSTICS

The set-up for the absorption measurements is shown in fig. 1. As background light source we used a pulsed capillary discharge developed by Kusch (ref. 7). The flat current pulse of 8 kA and about 200 μ s duration was generated by discharging a matched transmission line. The capillary CP was a 2 mm diameter bore in a lucite plate of 8 mm thickness, which was replaced after each discharge in order to get reproducible light pulses. This discharge emits end-on a reasonably flat pulse (fig. 2) of continuous radiation with a radiation temperature of 36000 K (ref. 7). In order to protect the condensor L_1 from the intense plasma beam exhausted from the capillary a thin glass plate GP is inserted, which had to be replaced after each discharge. L_1 images the capillary into the centerplane of the shock tube ST with a seventeenfold magnification. This plane is imaged by L_2 and L_3 onto the entrance slit MS of the monochromator giving an image of 10 mm diameter. The slit-width being 10 μ m only this part of the radiation which has passed a plasma slab of about 0.4 mm by 35 mm enters the monochromator, i. e. the spatial resolution in the direction of flow is 0.4 mm.

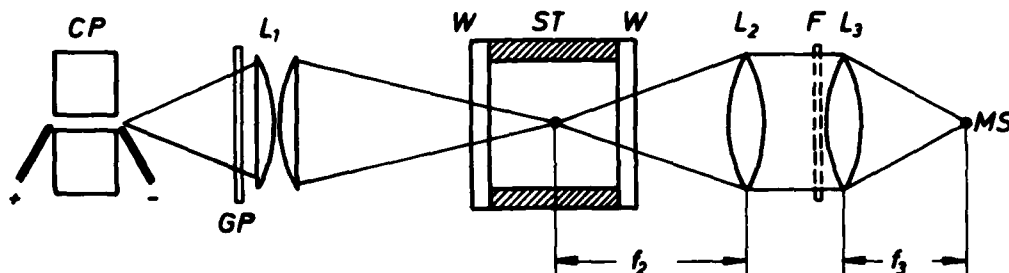


Fig. 1 - Optical set-up (not to scale); $f_1 = 7$ cm; $f_2 = 40$ cm; $f_3 = 12$ cm; W: Windows; F: Filter blocking; $\lambda \leq 680$ nm.

The monochromator was a 1 m grating monochromator (McPherson 2051) with a 1200 line/mm grating, which was used in first order. The lens diameters were chosen so as to illuminate the whole grating area of 102×102 mm² in order to ensure maximum resolution. The measured resolving power at $\lambda = 811.3$ nm using 10 mm high and 10 μ m wide entrance and exit slits was $\lambda/\Delta\lambda = 5.8 \cdot 10^4$. It turned out that it was extremely difficult to set the wavelength scanning system with an accuracy corresponding to the resolving power. The stability was so bad that the adjustment had to be checked immediately before and after each run of the shock tube. A small mirror inserted into the monochromator near to the exit slit focussed a broader band of the continuum near to $\lambda = 811.3$ nm onto a fibre light guide. Thus the emission of the background light source could be monitored (signal R in fig. 2). Both the radiation transmitted at $\lambda = 811.3$ nm (signal T in fig. 2) and the reference continuum were recorded on an oscilloscope (Tectronix 5113) using photomultipliers with extended S 20-cathode (EMI 9659 B). The plasma emission I_e as defined in (4) was determined in a second shock tube run under the same gasdynamic conditions. As the amplitude of the emission signal showed some variations from run to run it was normalized to that part of the absorption oscillogram in which $I_{tr} - I_e \ll I_e$ (i. e. there is 100 % absorption).

The electron density was measured by a schlieren compensated

Mach-Zehnder microwave interferometer working at 70 GHz, which was developed by G. Meinhold (ref. 8). The set-up can measure electron densities from $2 \cdot 10^{18} \text{ m}^{-3} < n_e < 4 \cdot 10^{19} \text{ m}^{-3}$.

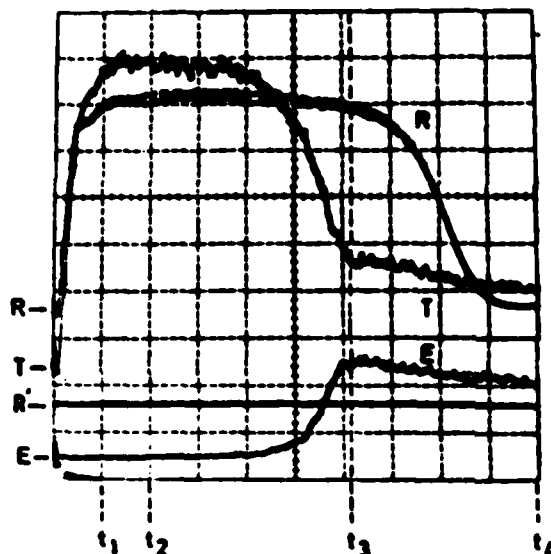


Fig. 2 -

First run:

 $T \equiv I_{tr}$ from equ. (2);

R: reference continuum.

Second run:

 $E \equiv I_e$ from equ. (4);

R' = reference continuum.

 t_2 : arrival of shock front $t_3 \dots t_4$: 100 % absorption $I_0(t) = R(t) \frac{T_{12}}{R_{12}}$ T_{12} : mean value $t_1 \dots t_2$ t : 30 $\mu\text{s}/\text{Div}$

DATA REDUCTION

The radiation $I_{\lambda, tr}(\lambda) d\lambda$ entering the monochromator in the wavelength interval $d\lambda$ is given by

$$I_{\lambda, tr}(\lambda) d\lambda = (I_{\lambda, 0}(\lambda) e^{-\tau(\lambda)} + (1 - e^{-\tau(\lambda)}) S_{\lambda}(\lambda)) d\lambda. \quad (1)$$

If the absorbing plasma is homogeneous along the line of sight, i. e. perpendicular to the flow velocity, $\tau(\lambda) = k(\lambda) \cdot l$ is the optical depth, $S_{\lambda}(\lambda)$ the source function and $I_{\lambda, 0}(\lambda)$ the intensity of the background light source.

The intensity leaving the exit slit is given by

$$I_{tr} = \int_0^{\infty} Z(\lambda) I_{\lambda, tr}(\lambda) d\lambda \quad (2)$$

where $Z(\lambda)$ is the apparatus profile with $\int Z(\lambda) d\lambda = 1$. Combining (1) and (2) one gets

$$I_{tr} = I_{\lambda, 0}(\lambda_0) \int_0^{\infty} Z(\lambda) e^{-\tau(\lambda)} d\lambda + I_e \quad \text{where} \quad (3)$$

$$I_e = \int_0^{\infty} Z(\lambda) (1 - e^{-\tau(\lambda)}) S_{\lambda}(\lambda) d\lambda \quad (4)$$

is the radiation which would leave the monochromator if $I_{\lambda, 0} = 0$, i. e. I_e is the plasma emission without background light source. In writing (3) it was assumed that $I_{\lambda, 0}(\lambda)$ is constant in the small region around λ_0 where $Z(\lambda) \neq 0$.

If the absorption is due to only one line transition the optical depth is connected to the population density n_n of the lower state of this line by

$$\tau(\lambda) = k(\lambda) l = \frac{\pi e^2 \lambda_0^2}{m_e c^2} f_{mn} n_n P_\lambda(\lambda) l. \quad (5)$$

where $P_\lambda(\lambda)$ is the line profile with $\int P_\lambda(\lambda) d\lambda = 1$.

From the measured PMT outputs one gets

$$\frac{I_{tr} - I_e}{I_{\lambda,0}(\lambda_0)} = \int_0^\infty Z(\lambda) e^{-\tau(\lambda)} d\lambda \quad (6)$$

and has to calculate numerically rhs of (6) in order to determine n_n . This can be done only if $Z(\lambda)$, $P_\lambda(\lambda)$, l and f_{mn} are known.

$Z(\lambda)$ has been measured by scanning the monochromator over the emission line of a low pressure krypton discharge lamp emitting a line with a width much smaller than the width of $Z(\lambda)$. The profile was not very constant or reproducible, therefore, always the $Z(\lambda)$ determined for the individual run was used.

The line profile $P_\lambda(\Delta\lambda)$ was taken to be a Voigt profile given by ref. 9:

$$P_\lambda(\Delta\lambda) = \frac{H(\alpha, v)}{\sqrt{\pi} \Delta\lambda_{DO}} \quad v = \Delta\lambda / \Delta\lambda_{DO}; \quad \alpha = \gamma / 2\Delta\lambda_{DO} \quad (7)$$

$$\Delta\lambda = \lambda - \lambda_0; \quad \Delta\lambda_{DO} = \lambda_0 / c_0 \sqrt{2kT_a / m_a}$$

The collision broadening is under the conditions of this report due to van der Waals broadening only. The damping constant γ which gives the full half width of the dispersion profile has been measured by B.-H. Müller similar to the method used by Vaughan (ref. 10). For $\lambda = 811.3$ nm we got with an error of $\pm 20\%$

$$\gamma = 12 \text{ mÅ} (T_a/295)^{0.3} n_a 10^{-18} \text{ cm}^3. \quad (8)$$

According to theory the line shift was taken to be $\Delta\lambda_s = \gamma/2.75$. For the oscillator strength $f_{mn} = 0.5$ was used.

Fig. 3 shows $n_n(x_{m1}, t)$ evaluated for a number of runs. The runs are characterized by the temperature T_{ao} and the groundstate number density n_{ao} obtained from the Rankine Hugoniot equations of an ideal gas using the shock front velocity measured at x_{m1} .

No.	T_{ao}/K	$n_{ao}/10^{24} \text{ m}^{-3}$	No.	T_{ao}/K	$n_{ao}/10^{24} \text{ m}^{-3}$
1136	13310	0.755	1084	9540	1.27
1135	13100	0.757	1087	8840	1.62
1079	11200	0.756	1150	8070	3.69
558	10450	0.844	1091	8390	2.00
565	10350	1.09	1154	7100	4.80
1099	10900	0.504	1093	7860	2.49

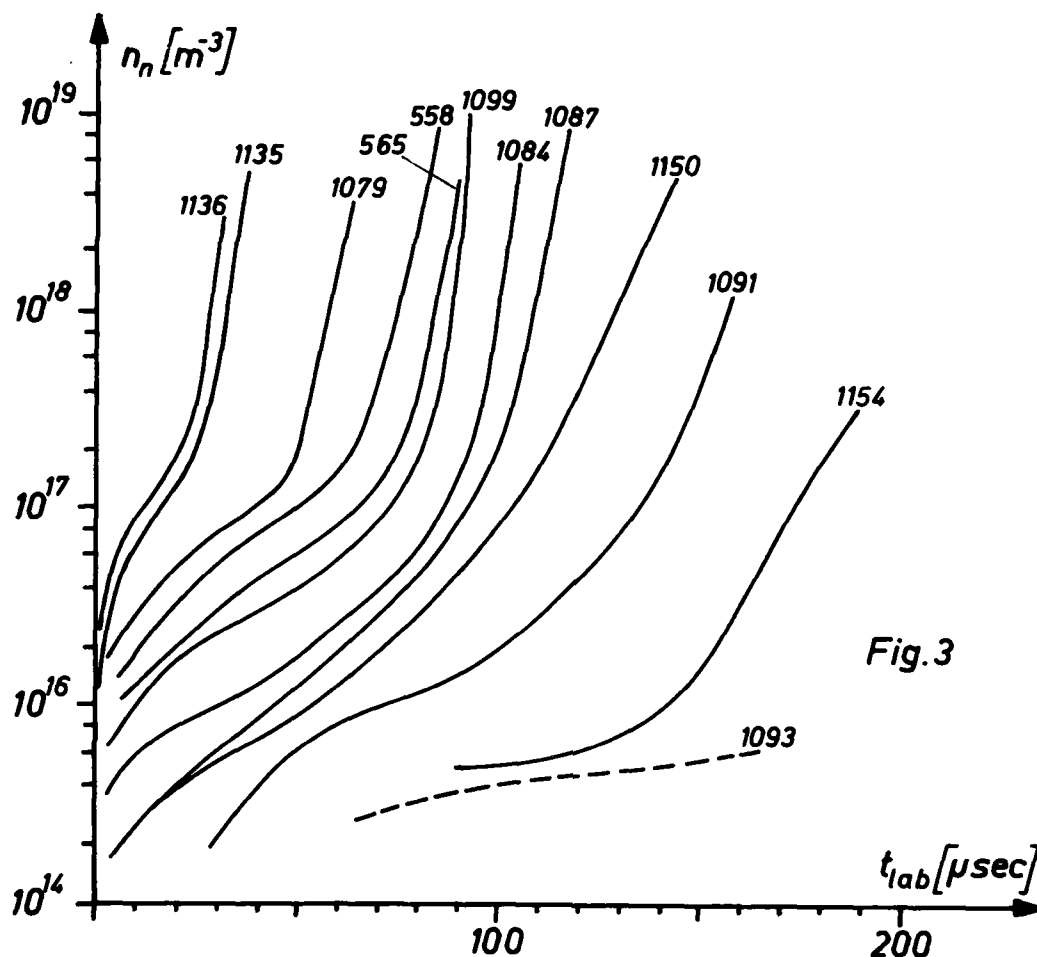


Fig. 3

MODEL CALCULATIONS

For the calculation of the time dependent population densities $n_n(x_{m1};t)$ and the electron densities $n_e(x_{m2};t)$ one has to model the gasdynamic flow as well as the reaction kinetics. Generally both processes interact. In the heat bath approximation, which is used here, this interaction is neglected by setting $n_e = n_i = 0$ in all gasdynamic equations. Most sensitive to this neglect is the caloric equation of state

$$h_p = \frac{5}{2} (n_a + 2 n_e) kT + n_e E_{ion}.$$

The temperature related to h_p is higher if one sets $n_e = 0$. In all our experiments $n_e/n_a \leq 2 \cdot 10^{-3}$. This gives for $E_{ion} = 14$ eV and $kT = 1$ eV a maximum error of + 1.5 % in T . This increases the excitation rate of the first quasilevel by about 15 % which is well within the limits of accuracy of our experiment.

Our gasdynamic model was developed by Demmig and has been described in ref. 3. In the present application we used a program which included the boundary layer as given in ref. 3, but described krypton as an ideal gas, i. e. all collision cross-sections were set to zero. This calculation gives the path $x_F(t)$ of a fluid particle F and $n_a(x_F(t))$ as well as $T_a(x_F(t))$.

Using these data the reaction equations can be integrated along $x_F(t)$ from t_{F0} to t_{FM} . t_{F0} is the time when F enters the shock front. t_{FM} is the time when F passes the point of observation x_m , i. e. $x_m = x_F(t_{FM})$. Doing this for a number of fluid particles produces $n_n(x_{m1}; t)$ and $n_e(x_{m2}; t)$. The advantage of this procedure is that it is easier to use different models of the reaction kinetics.

The reaction kinetics is approximated by a modified two-step ladder climbing model. The first quasilevel QL 1 ($E_1 = 10.18$ eV) is formed by the four 5s states. The second quasilevel QL 2 ($E_2 = 11.99$ eV) by the 5p and 4d states. We assume that the ionisation rate \dot{n}_e is equal to the effective depopulation rate of QL 1, which is described by the collisional rates between QL 1 and QL 2. This assumption is equivalent to the assumption that

$$\frac{dn_e}{dt} \gg \sum_{j=2}^{\infty} \frac{dn_j}{dt}. \quad \text{The rate equations are thus given by}$$

$$\dot{n}_1 + \dot{n}_e = n_a^2 R_{01}^a(T_a) + n_e n_a R_{01}^e(T_e) \quad (9)$$

$$\dot{n}_e = n_1 n_a R_{12}^a(T_a) + n_1 n_e R_{12}^e(T_e) \quad (10)$$

The deexcitation rates as determined by detailed balancing are under our conditions negligible. In calculating the deexcitation rate $2 \rightarrow 1$ it was assumed n_2 is in PLTE with n_e . For the coefficients R_{jk}^p we have chosen the form valid for a Maxwellian distribution and a cross-section given by

$$Q_{jk}^p = C_{jk}^p (E_{rel} - E_{jk}),$$

which gives

$$R_{jk}^p = \alpha_{jk}^p C_{jk}^p (8 kT_p / \pi m_p)^{1/2} (E_{jk} + 2 kT_p) e^{-E_{jk}/kT_p}, \quad (11)$$

where $m_p = 0.5 m_{Kr}$ if $p = a$ and $m_p = m_e$ if $p = e$

$$E_{jk} = \text{excitation energy}; \quad \alpha_{jk}^e = 1; \quad \alpha_{01}^a = 0.5; \quad \alpha_{12}^a = 1;$$

$$E_{rel} = m_p g^2/2 = \text{relative kinetic energy.}$$

The electron temperature T_e was calculated by integration of the electron energy balance (12) along $x_F(t)$:

$$\begin{aligned} \frac{3}{2} \frac{D_0}{Dt} (kT_e) + kT_e \frac{\partial u}{\partial x} &= \frac{3m_e}{m_a} \cdot k (T_a - T_e) (v_{ea} + v_{ei}) - n_a R_{01}^e E_1 \\ &\quad - n_1 R_{12}^e (E_{ion} - E_1 + \frac{3}{2} kT_e). \end{aligned} \quad (12)$$

The elastic electron-ion collision frequency v_{ei} is small compared to v_{ea} . We used the value given by Spitzer in ref. 11.

The elastic electron-atom collision frequency $\nu_{ea}(T_e)$ was approximated for $6000 \text{ K} \leq T_e \leq 15000 \text{ K}$ by

$$\nu_{ea} = n_a \cdot \sqrt{8 kT_e / \pi m_e} \cdot (8.8 \cdot 10^{-24} (T_e - 3000)) m^2. \quad (13)$$

The cross section $Q_{ea}(T_e)$ used here is related to $Q^{1.1}(T_e)$ given by Devoto in ref. 12 by $Q_{ea} = 1.5 Q^{1.1}$.

In order to calculate $n_n(\lambda = 811.3 \text{ nm})$ from the population n_1 of the first quasilevel it is assumed that the population ratios of the four 5s levels are given by Boltzmann relations with $T = T_a$. This results for $7000 \text{ K} \leq T \leq 14000 \text{ K}$ in

$$n_1 = n_n \cdot 1.85 \pm 6 \text{ \%}.$$

RESULTS OF CALCULATION

By variation of the four cross section constants we tried to find a set which reproduced the measured values. The calculated electron densities ($n_e(x_{m2}; t)$) were not sensitive to the choice of $C_{12}^{a,e}$. The values of $C_{01}^{a,e}$ thus represent a fit to our n_e measurements. Using these values we fitted $C_{12}^{a,e}$ to the measured values $n_1(x_{m1}; t)$. The calculated values were mainly determined by C_{01}^a/C_{12}^a and C_{01}^e/C_{12}^e . We found that all measurements can be reproduced by the calculations within $0.4 < n_1(\text{calculated}) / n_1(\text{measured}) < 1.6$ by the set of cross-section constants:

$$\begin{aligned} C_{01}^a &= 0.75 \times 10^{-5} \quad (\pm 10 \text{ \%}) \quad m^2/Ws \\ C_{01}^e &= 6.6 \times 10^{-3} \quad (\pm 30 \text{ \%}) \quad m^2/Ws \\ C_{12}^a &= 7.0 \times 10^{-2} \quad (\pm 10 \text{ \%}) \quad m^2/Ws \\ C_{12}^e &= 1.0 \quad (+ 50 \text{ \%}) \quad m^2/Ws \end{aligned}$$

DISCUSSION OF RESULTS

The most interesting results are the ratios C_{12}^a/C_{01}^e of the cross section constants. We find

$$C_{12}^a/C_{01}^a = 62 \cdot C_{12}^e/C_{01}^e.$$

This implies that during the relaxation the excitation $1 \rightarrow 2$ is still dominated by atom collisions, when the excitation $0 \rightarrow 1$ is already dominated by electron collisions.

The value of C_{01}^e found here is in good agreement with the cross section determined from measurements of the first Townsend coefficient by Specht et al. in ref. 13. For temperatures $6000 \text{ K} < T_e < 10000 \text{ K}$ the rates calculated from this cross section are reproduced by (11) setting $C_{01}^e = 5.4 \cdot 10^{-3} m^3/Ws$.

The electron excitation rate $1 \rightarrow 2$ resulting from our cross section is about a factor of 10 smaller than the rate calculated from the Born cross sections calculated by Hyman in ref. 14. At

present we cannot explain this large difference. We believe that a much more refined model of the reaction kinetics is necessary to answer this problem. We want to emphasize that the present cross sections are fitted to describe the measured time dependence $n_1(x_{m1};t)$ and $n_e(x_{m2};t)$ by the modified two step model.

The results of an improved model should be compared with more reliable experimental data of $n_1(t)$ and $n_e(t)$. We are preparing absorption measurements using a single line CW dye laser as background light source in order to avoid the difficulties of the monochromator and the emission correction. Additionally the range of n_e measurements will be extended to $n_e = 8 \cdot 10^{20} \text{ m}^{-3}$ by using a HCN laser interferometer.

ACKNOWLEDGEMENTS

This work was financially supported by Deutsche Forschungsgemeinschaft. Thanks are due to G. Zimmermann and D. Leseberg who conducted the electron density measurements.

REFERENCES

1. K. E. Harwell and R. G. Jahn, Phys. Fluids 7, 214 (1964).
2. Y. Enomoto, Theor. appl. Mechanics 23, 27 (1975).
3. F. Demmig, Proc. 11th Int. Symp. Shock Tubes, p. 119 (1977).
F. Demmig, Comput. Phys. Commun. 14, 7 (1978).
4. E. Scholle and Th. Reese, unpubl. report IPP, Universität Hannover (1978).
5. R. Meyer-Pruessner and F. Demmig, Proc. 12th Int. Symp. on Shock Tubes, p. 197 (1979).
6. Th. Reese, Proc. 11th Int. Symp. Shock Tubes, p. 441 (1977).
7. H. Kusch, H. Schreiber and H. Ehrich, Z. Naturforsch. 27 a, 693 (1972).
8. G. Meinhold, G. Zimmermann and D. Leseberg, unpubl. reports IPP, Universität Hannover (1975, 1976).
9. G. D. Finn and M. N. Mugglestone, M.N. RAS London 2, 221 (1965) and
K. Hunger, Z. Astrophys. 39, 36 (1956).
10. B.-H. Müller, unpubl. report IPP, Universität Hannover (1976) and
J. H. Vaughan, Phys. Rev. 166, 13 (1959).
11. L. Spitzer, Physics of fully ionised gases Interscience (1956).
12. R. S. Devoto, AIAA J. 7, 199 (1969).
13. L. T. Specht, S. A. Lawton and De Temple, J. Appl. Phys. 51, 166 (1980).
14. H. A. Hyman, Phys. Rev. A 18, 441 (1978).

COLLISIONAL EXCITATION AND IONISATION OF NO BEHIND SHOCK WAVES

H.P. Richarz, A.E. Beylich, H. Grönig

Institut für Luft- und Raumfahrt, Stoßwellenlabor

RWTH Aachen, West Germany

Experimental and theoretical studies of NO γ band emission from shock front-near regions in NO-Xe-mixtures (NO-concentration 5 % - 12 %) are performed. The basis for experiments is an UHV-shock tube ($9 < M_s < 11$; $5,4 \leq p_1/mb \leq 10,2$; i.d. 96 mm).

To interpret the time history of NO γ radiation a detailed theoretical model is set up, including vibrational, chemical, and radiative relaxation processes. The excitation of the NO $A^2\Sigma^+$ state is described by a modified collision theory, considering 11 vibrational levels of the NO $X^2\Pi$ ground state, and 8 vibrational levels of the electronic $A^2\Sigma^+$ state.

γ_0 (2260 Å)-, γ_{10} (2147 Å)-, γ_{20} (2045 Å)-radiation is calculated; the best fit of computed time history to experimental data allows to determine the inelastic cross sectional slopes near the threshold of NO-excitation and -ionisation by Xe and electron impact, respectively. The following cross sectional slope constants are obtained:

$$\begin{aligned} S_{NO-e}^* &= 7,0 \cdot 10^{-17} \text{ cm}^2/\text{eV} \\ S_{NO-Xe}^* &= 1,8 \cdot 10^{-21} \text{ cm}^2/\text{eV} \\ S_{NO-Xe}^+ &= 2,1 \cdot 10^{-22} \text{ cm}^2/\text{eV} \end{aligned}$$

(The excitation is denoted by an asterisk, the ionisation by a plus sign)

Introduction

In connection with spectroscopic studies of the relaxation zone of shock heated NO-Xe mixtures at wave lengths from 2000 - 2300 Å the following phenomena are observed: Up to shock Mach numbers of 5-6 typical absorption records were noticed with a sharp decrease of intensity due to the density jump behind the shock front and a subsequent slight increase according to the vibrational relaxation¹. Heightening the Mach numbers the absorption jump still occurs, followed by a faster intensity gain due to the onset of emission from the heated gas. The time interval between shock arrival and noticeable radiation becomes shorter with increasing Mach numbers. From Mach numbers about 7-8 the emission dominates and no absorption signal is detectable, not even at the shock front: Immediately behind the shock front the radiation intensity rises to a sharp maximum and then decreases quickly to its equilibrium value (e.g. Fig. 1). Similar radiation overshoots were previously observed by other authors^{2,3,4}. In some cases this seems to be due to band emission of carbon radicals like C₂, CN, CH generated by decomposition of impurities (e.g. pump oil, sealing material) in the shock tube. In order to avoid formation of carbon compounds in the present experiments, an all metal sealed UHV (Ultra-High-Vacuum) shock tube is used, where the UHV is generated by an oilfree turbomolecular pump.

Additionally are performed experiments in pure Xenon and in mixtures of Xe with O₂, N₂, and N₂-O₂ in the same Mach number range. In these cases no comparable luminosity close to the shock front is observed. This leads to the conclusion that the strong U.V. emission of NO-Xe mixtures in the front-near region is a specific NO process due to the nonequilibrium excitation of upper electronic states, especially the NO A ²Σ⁺ state (according to the chosen wave length interval).

Experimental method

The experiments were carried out in a 96-mm-i.d. stainless steel UHV shock tube. High pressure section (1,98 m) and low pressure section (6,28 m) are independently to be heated up to temperatures of about 420 °C. The lowest attainable pressure is 10⁻⁸ mb, the combined leak and outgassing rate is generally less than 10⁻⁶ $\frac{\text{mb} \cdot \text{l}}{\text{s}}$.

The speed of the incident shock waves is measured by means of a schlieren method. A laser beam is divided up into four parallel and equidistant beams (Fig. 2), which cross the shock tube normal to the axis. Each of them is focused onto an adjustable knife edge in front of a photo diode. The beam deflection within the incoming shock wave is detected by the photodiodes, which trigger the counters and the oscilloscope. The uncertainty in measured shock speed is less than 1 %.

The center line of the optical test section passes the shock tube axis in a distance of 4,40 m from the diaphragm. For applications in the near ultraviolet fused silica windows are used to extend the spectral range down to about 1650 Å. Time-resolved measurements of the spectral intensity behind the incident shock in the wave length-interval 2000 Å < λ < 2300 Å are obtained by use of a 0,75 m Czerny-Turner grating monochromator (Jarrell-Ash; blaze wave length of grating: 2400 Å), and a photomultiplier (EMI 9635 QB with bialkali photocathode), the quantum efficiency of which is independent of wave length in the spectral range of interest.

A 200 W deuterium lamp (Original Hanau), producing a continuous spectrum in the near U.V., serves as the light source for absorption experiments. Its intensity maximum occurs at 2200 Å, the decrease in intensity at wave length between 2000 Å and 2400 Å is less than 8 %. With absorption measurements the point of maximum emittance is focused onto the entrance slit of the monochromator. In the case of emission measurements the radiating volume element at the shock tube axis is focused onto the entrance slit.

High purity laboratory gases are used: Helium (99,996 % purity, main impurities: Ne, N₂, H₂O) as driver gas; N₂ (99,999 %; Ne, Ar, H₂O), O₂ (99,995 %; N₂, Ar, H₂O), Xe (99,997 %; Kr, N₂), and NO (99,9 %; N₂, N₂O, NO₂) as test gases. All of them are dried prior to application in the shock tube experiments.

Theoretical treatments

At temperatures, at which double ionisation is still negligible, shock heated NO-Xe mixtures essentially contain the following species: Xe, Xe⁺, NO, O₂, N₂, O, N, NO⁺, N⁺, O⁺, N₂⁺, O₂⁺, e, NO₂, and N₂O, according to the equilibrium reactions (1) - (11):

Equilibrium reactions (activation energies in parantheses)	Nonequilibrium reactions
$\text{Xe} \rightleftharpoons \text{Xe}^+ + e \quad (12,13 \text{ eV}) \quad (1)$	$\text{NO}_v'' + M + \Delta E_{v''}^{\text{vib}} \rightleftharpoons \text{NO}_v' + M \quad (12)$
$\text{NO} \rightleftharpoons \text{N} + \text{O} \quad (6,50 \text{ eV}) \quad (2)$	$\text{NO}_v'' + M + \Delta E_{v''}^{\text{D}} \rightleftharpoons \text{N} + \text{O} + M \quad (13)$
$\text{NO} \rightleftharpoons \text{NO}^+ + e \quad (9,26 \text{ eV}) \quad (3)$	$\text{NO}_v'' + M + \Delta E_{v''}^{\text{O}} \rightleftharpoons \text{NO}_v^{\text{O}} + M \quad (14)$
$\text{O}_2 \rightleftharpoons \text{O} + \text{O} \quad (5,12 \text{ eV}) \quad (4)$	$\text{NO}_v'' + M + \Delta E_{v''}^{\text{O}^+} \rightleftharpoons \text{NO}_v^{\text{O}^+} + e + M \quad (15)$
$\text{N}_2 \rightleftharpoons \text{N} + \text{N} \quad (9,76 \text{ eV}) \quad (5)$	$\text{NO}_v'' + M + \Delta E_{v''}^{\text{N}^+} \rightleftharpoons \text{NO}_v^{\text{N}^+} + e + M \quad (16)$
$\text{O} \rightleftharpoons \text{O}^+ + e \quad (13,61 \text{ eV}) \quad (6)$	$\text{NO}_v'' + M + \Delta E_{v''}^{\text{vib}} \rightleftharpoons \text{NO}_v^{\text{vib}} + M \quad (17)$
$\text{N} \rightleftharpoons \text{N}^+ + e \quad (15,53 \text{ eV}) \quad (7)$	$\text{NO}_v'' + h\nu_{v''} \rightleftharpoons \text{NO}_v^{\text{O}^+} \quad (18)$
$\text{N}_2 \rightleftharpoons \text{N}_2^+ + e \quad (15,58 \text{ eV}) \quad (8)$	$\text{N} + \text{O} + 2,77 \text{ eV} \rightleftharpoons \text{NO}^+ + e \quad (19)$
$\text{O}_2 \rightleftharpoons \text{O}_2^+ + e \quad (12,07 \text{ eV}) \quad (9)$	$\text{N}_2 + \text{O}_2 + 1,88 \text{ eV} \rightleftharpoons \text{NO} + \text{NO} \quad (20)$
$\text{NO}_2 \rightleftharpoons \text{NO} + \text{O} \quad (3,11 \text{ eV}) \quad (10)$	$\text{NO} + \text{O} + 1,38 \text{ eV} \rightleftharpoons \text{N} + \text{O}_2 \quad (21)$
$\text{N}_2\text{O} \rightleftharpoons \text{N}_2 + \text{O} \quad (1,68 \text{ eV}) \quad (11)$	$\text{N}_2 + \text{O} + 3,26 \text{ eV} \rightleftharpoons \text{NO} + \text{N} \quad (22)$
	$\text{O}_2 + M + 5,12 \text{ eV} \rightleftharpoons \text{O} + \text{O} + M \quad (23)$
	$\text{N}_2 + M + 9,76 \text{ eV} \rightleftharpoons \text{N} + \text{N} + M \quad (24)$
	$\text{Xe} + M + 8,31 \text{ eV} \rightleftharpoons \text{Xe}^+ + M \quad (25)$
	$\text{Xe}^+ + M + 3,82 \text{ eV} \rightleftharpoons \text{Xe}^+ + e + M \quad (25)$
	$\text{Xe} + e + 12,13 \text{ eV} \rightleftharpoons \text{Xe}^+ + e + e \quad (26)$

At low initial NO-concentrations, reactions (6)-(9) have a very poor influence to the gas composition (e.g. a NO-concentration of 12 % at a temperature of 10000 K provides a number density ratio $n_{\text{O}^+}/n_{\text{Xe}^+}$ of 3 0/00; in consequence of the low O₂-dissociation energy the formation of O₂⁺-ions is unimportant, too). Already at low temperatures the concentrations of NO₂ and N₂O are small compared with that of N₂ and O₂; so the reactions (10),(11) may be neglected in the temperature range of interest.

For the treatment of nonequilibrium phenomena behind the shock wave we assume: 1. Translation and rotation are everywhere in instantaneous equilibrium at a local translation-rotation temperature T. 2. The rate velocity of any chemical reaction is governed by the local gas state.

The approach to equilibrium in shock heated NO-Xe mixtures with

particular respect to the excitation and deexcitation of the different vibrational levels of the electronic $\text{NO } ^2\Sigma^+$ state is determined mainly by the nonequilibrium processes listed above. The vibrational level in the upper energy-state is denoted by v' , the lower one by v'' . M symbolizes atomic or molecular catalysts (in reactions (14)-(17) also an electron), e an electron. Dissociation, excitation, and ionisation are indicated by D , an asterisk, and a plus sign, respectively. The rate constants of reactions (13), (19)-(26), quoted from the literature, are listed in (5) as is a detailed deduction of the mathematical expressions for reactions (12)-(18). The basic ideas will be summarized subsequently.

Reaction (12) characterizes the vibrational relaxation of NO molecules in the $\text{NO } X^2\Pi$ ground state. Under certain conditions (harmonic oscillator, initial nonequilibrium Boltzmann distribution, assumptions 1. and 2. given above) the vibrational relaxation can be described in terms of a local "vibrational" temperature T_v , which is different from the local translational-rotational temperature T ⁶.

Reaction (13) describes the NO dissociation with regard to the vibration. Using the CVD (Coupling of Vibration and Dissociation) model⁶ with its basic assumption, that dissociation can occur with equal probability from any vibrational level, the inherent rate constant, quoted in Table I, is to multiply with

$$\chi(T_v, T) = \frac{1}{N_v} \frac{1 - \exp[-N_v(\Theta_v/T_v - \Theta_v/T)]}{\exp(\Theta_v/T_v - \Theta_v/T) - 1} \frac{\exp(\Theta_v/T_v) - 1}{\exp(\Theta_v/T) - 1} \quad (27)$$

N_v is the number of vibrational levels including the dissociation level, $\Theta_v = hc\omega/k$ is the characteristic vibrational temperature of a harmonic oscillator. (NO : $\Theta_v = 2740$ K, $N_v = 29$)

Reactions (14), (15) and (16) are related to the excitation and the ionisation from the ground state, and the ionisation from the excited state (Fig. 3). We first deal with the transitions from a vibrational level v'' of the ground state to a vibrational level v' of an excited state. It is assumed, that the harmonic oscillator approximation is valid. The minimum excitation energy $\epsilon^* = k\Theta_v^*$ is supposed to be equal to the energy difference of the 0,0-transition; $\Delta\epsilon^* = hc \cdot \omega^* = k\Theta_v^*$ is the energy difference of adjacent vibrational levels in the excited state. The rate of transitions due to collisions that involve a relative transitional energy $\epsilon^* + 1 \cdot \Delta\epsilon^* \leq \epsilon(l) < \epsilon^* + (l+1) \Delta\epsilon^*$ can be expressed in the form

$$\left(\frac{dn_{v''v'}}{dt}\right)(l) = P_{v''v'}^*(l, M) \cdot Z \cdot \frac{Z(l) - Z(l+1)}{Z} \cdot \frac{n_{v''}}{n} \quad (28)$$

Here are $l = 0, 1, 2, \dots$ an integer control variable, $P_{v''v'}^*(l, M)$ the fraction of collisional events, involving an energy $\epsilon(l)$, that results in a transition $v'' \rightarrow v'$. The values of $P_{v''v'}^*$ are in general different for different catalytic particles. Z is the bimolecular collision rate, $[Z(l) - Z(l+1)]/Z$ the fraction of collisions involving an energy $\epsilon(l)$, n the number density of the considered molecules in the ground state, and $n_{v''}/n$ the fraction of molecules in the vibrational level v'' .

At collisional energies $\varepsilon(1)$ only a limited number of vibrational levels in the excited state are within reach. The quantum number of the uppermost level shall be denoted by x^* (Fig. 4). We set

$$P_{v''v'}^*(1, M) = P_{v''}^*(1, M) \cdot q_{v''v'}^{\text{norm}}(1) \quad (29)$$

$P_{v''}^*(1, M)$ is the fraction of collisions with an energy $\varepsilon(1)$, that results in a transition from the vibrational level v'' of the ground state to any attainable level in the excited state ($v' \leq x^*$), $q_{v''v'}^{\text{norm}}(1)$ is a modified Franck-Condon factor and gives the probability of a transition from the given v'' to a certain v' for the specified electronic transition. It obeys the relations

$$q_{v''v'}^{\text{norm}}(1) = q_{v''v'} / \sum_{v'=0}^{x^*} q_{v''v'} ; \quad q_{v''v'}^{\text{norm}}(1) = 0 \quad \text{if } v' > x^* \quad (30)$$

with $x^* = \text{Int}(1 + v'' \Delta \varepsilon / \Delta \varepsilon^*)$. The further process is based on the assumption, that the probability of an electronic transition is independent of the momentary vibrational state of the molecule. This assumption is made in consequence of the Born-Oppenheimer approximation, that postulates complete separation of nuclear and electronic motions. Thus we get

$$P_{v''v'}^*(1, M) = P^*(1, M) q_{v''v'}^{\text{norm}}(1) \quad , \quad (31)$$

$$\left(\frac{dn_{v''v'}^*}{dt} \right) (1) = P^*(1, M) q_{v''v'}^{\text{norm}}(1) Z \frac{Z(1) - Z(1+1)}{Z} \frac{n_{v''}}{n} \quad (32)$$

The excitation or ionisation of an atom of species Y by electron impact or heavy particle collision may be described by the expression

$$\frac{dn_Y^*}{dt} = \frac{n_Y n_M}{\sigma} \int_{v(\varepsilon_Y^*)}^{\infty} \sigma_M^*(v) v f(v) dv \quad (33)$$

Excitation or ionisation from the ground state is denoted by an asterisk, while M indicates the colliding particle. σ , the symmetry factor, is 1 for $M \neq Y$ and 2 for $M \equiv Y$. The Maxwell distribution function $f(v) dv$ is related to the relative velocity v and the reduced mass μ of the colliding pair; the dependence of the excitation (or ionisation) cross section $\sigma_M^*(v)$ on the relative velocities is known as the excitation (or ionisation) function for a number of atoms and molecules. Near the threshold the cross section frequently depends linearly on the energy of relative motion:

$$\sigma_M^*(v) = S_M^*(\varepsilon - \varepsilon_Y^*) ; \quad S_M^* = \text{konst} \quad (34)$$

with $\varepsilon = 1/2 \mu v^2$. Substituting this quantity into (33) we find a relation, that describes the excitation (or ionisation) of a two level system by collisions with particles of thermal energies (i.e. energies, that slightly exceed the threshold potential).

A similar relation may be deduced from (32): At moderate temperatures, if $\Delta \varepsilon^* / \varepsilon^* \rightarrow 0$, and $\Delta \varepsilon / \varepsilon^* \rightarrow 0$, equation (32) describes

approximately a two level system, too, with degenerate energy levels. Summing over v' , v'' , and l leads to

$$\frac{dn^*}{dt} = \sum_{l=0}^{\infty} P^*(l, M) Z \frac{Z(l) - Z(l+1)}{Z} \quad (35)$$

If the summation is replaced by an integral we find by comparison:

$$P^*(l, M) = P^*(M) l \quad \text{with} \quad P^*(M) = \frac{S_M^* k \Theta_v^*}{\sigma_{o, M}},$$

where $\sigma_{o, M}$ denotes the gaskinetic cross section. Taking into account the finite energy differences between adjacent vibrational states a more extensive computation shows that

$$P^*(l, M) = P^*(M) (1 + \alpha^* l) \quad \text{with} \quad P^*(M) = \frac{S_M^* k \Theta_v^*}{\sigma_{o, M} \alpha^*} \quad (36)$$

and $\alpha^* = \alpha^*(\Theta_v^*/T, \Theta^*/T) \sim 2$ at temperatures $T \geq \Theta_v^*$.

Finally the transition rate for collisional induced electronic transitions to a certain vibrational state v' is described by

$$\frac{dn_{v'}^*}{dt} = P^*(M) Z \sum_{l=0}^{\infty} (1 + \alpha^* l) \frac{Z(l) - Z(l+1)}{Z} \sum_{v''} q_{v', v''}^{\text{norm}}(l) \frac{n_{v''}}{n} \quad (37)$$

and is valid for excitation as well as for ionisation, and for transitions between excited states, too, if these states are energetically wide spaced. The Franck-Condon factors of the transitions considered here are taken from (7) ($\text{NO } X^2\Pi, v'' \rightleftharpoons \text{NO } A^2\Sigma^+, v'$) and from (8) ($\text{NO } X^2\Pi, v'' \rightleftharpoons \text{NO}^+ X^1\Sigma^+, v'$). As a result of the nearly identical potential shapes of $\text{NO } A^2\Sigma^+$ state, and $\text{NO}^+ X^1\Sigma^+$ state, resp., these factors are almost equal at corresponding transitions. Thus, ionisation from the excited state is caused with noticeable probability only by transitions with equal values of vibrational quantum numbers. Simultaneous determination of all probabilities ($P^*(M)$, $P^+(M)$, $P^{*+}(M)$), defined by the above theory, is not possible by the results of the experiments performed. We proceed with the following simplifying assumptions: 1. Each atomic and molecular species in the gas mixture possesses the same effectiveness in excitation (or ionisation) of NO. The resulting error is small at low NO concentrations. 2. The ratio of the probabilities of excitation by electrons and by heavy particles is equal to that of ionisation: $P_e^*/P_M^* = P_e^+/P_M^+ = P_e^{*+}/P_M^{*+} = W$.

If these assumptions are valid, the rate constants of reactions (14)-(16) are dependent only on 3 unknown parameters, W , $G = P_e^*/P_e^+$ and P_e^{*+} which may be obtained by the aid of experiments. P_e^+ is found from eq. (36) with the cross section and slope constant S_e^+ given by Tate & Smith⁹.

Reaction (17) corresponds to the vibrational relaxation of the excited NO molecules. Since we ask for the density numbers of the individual vibrational states, we have to set up the master equations for each level. P_{10} , the probability of the collision induced vibrational 1-0 transition in the $\text{NO } A^2\Sigma^+$ state is a

function of T and calculated from the measurements of Roth ¹⁰.

Reaction (18) describes the number density change of NO molecules in the ground state and in the excited state due to radiative transitions. If the gas is optically thin, as in the present case, only the backward reaction of (18) is important. The decrease of population density of a vibrational level v' in an excited electronic state B by spontaneous radiative transitions to a vibrational level v'' in the ground state A may be calculated from

$$dn_{Bv'}/dt = - A(Av'', Bv') n_{Bv'} \quad (38)$$

$A(Av'', Bv')$, the Einstein coefficient for spontaneous emission, is related to the absorption oscillator strength f_{BA} by

$$A(Av'', Bv') = \frac{g_A}{g_B} \frac{8\pi^2 e^2}{m_e c^3} \frac{\nu_{Av'', Bv'}}{\nu_{AB}} f_{BA} q_{v''v'} \quad (39)$$

g_A, g_B are the statistical weights, ν_{AB} is an average frequency for the electronic transition. The values for f_{BA} and ν_{AB} were taken from Huber & Herzberg ¹¹ and Bethke ¹², respectively.

If the condition prevails, that the electron temperature T joins the translational-rotational temperature T , the rate constants of reactions (12)-(26) are functions of n_i, T, T_e, ρ , and t . Supplemented by the conservation of charges and particles the mathematical treatment leads to a system of linear differential equations, that may be integrated in conjunction with the appropriate temperature and density variations, given by the shock conservation equations.

Since the number densities of the individual vibrational levels of the excited NO $A^2\Sigma^+$ state are now known as functions of time (subject to the parameters mentioned above), it is possible to calculate the time history of γ band radiation. The detectable radiation intensity of an emitting self-absorbing gas is given by

$$I_v = \frac{\epsilon_v}{\alpha_v} (1 - e^{-\alpha_v s}) \quad (40)$$

s is the optical path length, ϵ_v and α_v are the emission and absorption coefficients. The mathematical expressions $\epsilon_v = f(f_{BA}, \nu_{AB}, \nu, q_{v''v'}, n_{Bv'}, T)$ and $\alpha_v = f(f_{BA}, \nu, q_{v''v'}, T_v, T)$ are derived with reference to Kivel et al.⁷ and Keck et al.¹³.

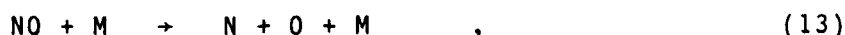
Results and discussion

To gain the optimum matching of computed radiation time histories to the experimental data, the parameters $W, G = p^*/p^+$, and p^{*+} are systematically varied (Fig. 5). From this we obtain the following cross sectional slope constants:

$$\begin{aligned} S_{NO-e}^* &= 7,0 \cdot 10^{-17} \text{ cm}^2/\text{eV} \pm 18 \% \\ S_{NO-Xe}^* &= 1,8 \cdot 10^{-21} \text{ cm}^2/\text{eV} \pm 24 \% \\ S_{NO-Xe}^+ &= 2,1 \cdot 10^{-22} \text{ cm}^2/\text{eV} \pm 24 \% \end{aligned}$$

The variation of P^{*+} by orders of magnitude has no effect on the computed time histories. The comparison of relative maximum intensities of measured and calculated time histories within the indicated wave length interval show a good agreement between experiments and theory.

The initial time history of γ band radiation is mainly ascribed to the excitation of the electronical $\text{NO } A^2\Sigma^+$ state due to collisions of NO molecules in the $\text{NO } X^2\Pi$ ground state with neutral bath-gas particles. The subsequent radiation course is based on the increasing number density of atomic nitrogen and oxygen due to the dissociation process



followed by a short-time rise in production of free electrons by the associative ionisation



The large excitation and ionisation cross sections for electron impact cause the considerable rise of radiation intensity. The final decrease in γ band emission depends on the proceeding decay of excitable NO molecules in the ground state due to reaction (13).

The time lag between shock arrival and occurrence of the intensity maximum is severely affected by changes in the rate constant values of reaction (19). Best fit to the experimental data was obtained by use of the quantity reported by Lin and Teare¹⁴.

References

- 1) Wray, K.L.: J. Chemical Phys. 36, No. 10, 2597, (1962)
- 2) Laporte, O.; Wilkerson, T.D.: J. Opt.Soc.Amer. 50, 1293, (1960)
- 3) Charitis, G.; Doherty, L.R.; Wilkerson, T.D.: J. Chem. Phys. 27, No. 6, 1415, (1957)
- 4) Arnold, J.O.; Nicholls, R.W.: Recent Devel. in Shock Tube Research, Proc. 9th Int. Shock tube Symp., Stanford University, (1973)
- 5) Richarz, H.P.: Diss. RWTH Aachen (1980)
- 6) Wray, K.L.; Teare, J.D.: J.Chem. Phys.36, No. 10, 2582, (1962)
- 7) Kivel, B.; Mayer, H.; Bethe, H. Ann. of Phys. 2, 57, (1957)
- 8) Nicholls, R.W.: J. Phys. B (Proc. Phys. Soc.), Ser. 2, 1, 1192 (1968)
- 9) Tate, J.T.; Smith, P.T.: Phys. Rev. 39, 270, (1932)
- 10) Roth, W.: J. Chem. Phys. 34, No. 3, 999, (1961)
- 11) Huber, K.P.; Herzberg, G.: Molecular Spectra and Molecular Structure, IV. Constants of Diatomic Molecules; van Nostrand N.Y., (1979)
- 12) Bethke, G.W.: J. Chem. Phys. 31, No. 3, 669, (1959)
- 13) Keck, J.C.; Camm, J.C.; Kivel B.; Wentink, T.: Ann. of Phys. 7, 1, (1959)
- 14) Lin, S.C.; Teare, J.D.: Phys. Fluids 6, No. 3, 355, (1963)

Table 1. Forward rate constants k_f

Reaction No.	Catalyst M	Rate constant expression	cm^3/s
(13)	$\text{O}_2, \text{N}_2, \text{Xe}$	$6.62 \cdot 10^{-4} \tau^{-3/2} \exp(-75400/T)$	
	$\text{NO}, \text{N}, \text{O}$	$1.33 \cdot 10^{-2} \tau^{-3/2} \exp(-75400/T)$	
(19)	-	$5.0 \cdot 10^{-11} \tau^{-1/2} \exp(-32500/T)$	
(20)	-	$7.56 \cdot 10^{-1} \tau^{-5/2} \exp(-64600/T)$	
(21)	-	$6.16 \cdot 10^{-15} \tau \exp(-20850/T)$	
(22)	-	$1.16 \cdot 10^{-10} \exp(-38000/T)$	
(23)	$\text{NO}, \text{N}, \text{Xe}$	$5.98 \cdot 10^{-6} \tau^{-1} \exp(-59400/T)$	
	N_2	$1.20 \cdot 10^{-5} \tau^{-1} \exp(-59400/T)$	
	O_2	$5.31 \cdot 10^{-5} \tau^{-1} \exp(-59400/T)$	
	O	$1.49 \cdot 10^{-4} \tau^{-1} \exp(-59400/T)$	
(24)	$\text{NO}, \text{O}_2, \text{O}, \text{Xe}$	$3.19 \cdot 10^{-7} \tau^{-1/2} \exp(-113200/T)$	
	N_2	$7.97 \cdot 10^{-7} \tau^{-1/2} \exp(-113200/T)$	
	N	$6.81 \cdot 10^{-2} \tau^{-3/2} \exp(-113200/T)$	
(25)	$\text{Xe} (\text{NO}, \text{O}, \text{N}, \text{O}_2, \text{N}_2)$	$1.0 \cdot 10^{-16} \tau^{1/2} \exp(-96400/T)$	
(26)	e	$2.6 \cdot 10^{-10} \tau^{1/2} \exp(-140740/T)$	

Forward rate constant k_f and reverse rate constant k_r are related to each other by the principle of detailed balancing: $k_r = k_f/K_c(T)$, where $K_c(T)$ is the equilibrium constant.

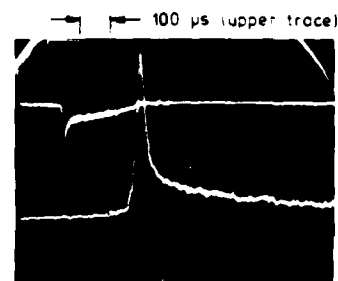


Fig. 1. Emission of NO γ_{10} band
Sample oscillogram
Test conditions:
 $\lambda = 2146.5 \text{ \AA}$
 $10.1 \text{ } \mu\text{m} = 89.9 \text{ } \mu\text{m}$
 $p_1 = 5.6 \text{ mb}$
 $T_1 = 293 \text{ K}$
 $N_6 = 9.96$

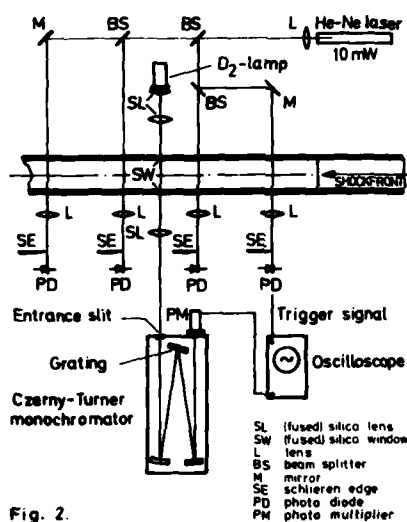


Fig. 2.

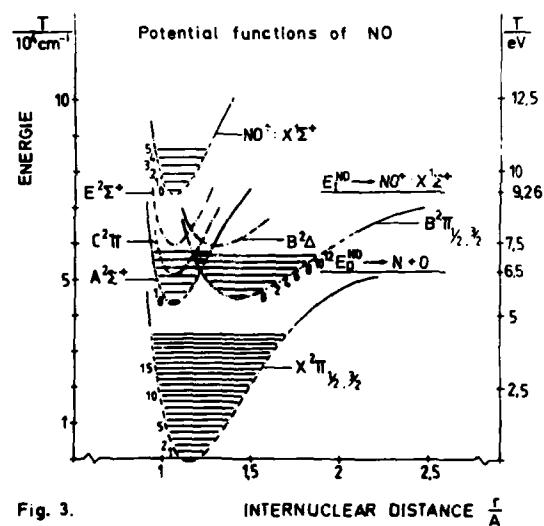


Fig. 3.

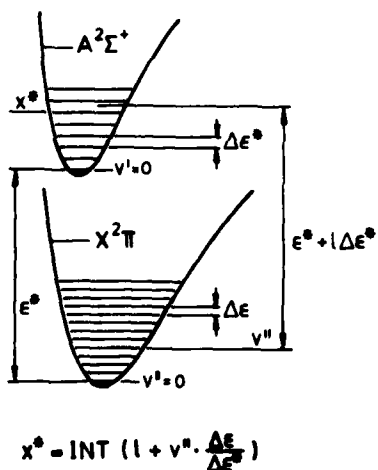


Fig. 4.

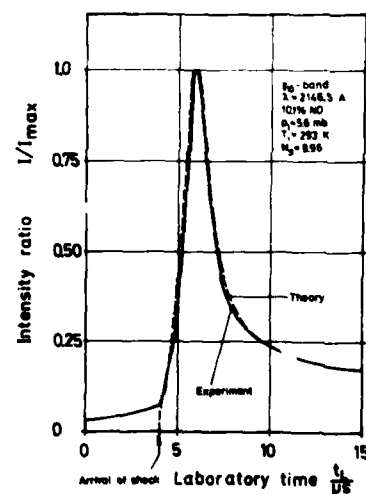


Fig. 5.

THE INVESTIGATION OF IONIZATION PHENOMENA
IN A 800 MM SHOCK-TUBE

Zhu Nai-yi and Li Xue-fen

Institute of Mechanics

Chinese Academy of Sciences, Beijing, P.R.C.

The electron density behind normal shock waves has been measured systematically in a 800 mm dia. shock-tube, over the range of $P_1 = 1 \times 10^{-2} \sim 1$ mmHg, $M_1 = 10 \sim 20$, by the use of the near-free-molecular Langmuir probes, the ordinary microwave transmission, and the special highly sensitive microwave transmission and microwave reflection methods, made by the authors. It is found that the experimental results agree basically with the theoretical equilibrium predictions. The variation of ionization relaxation time with M_1 is obtained, and it is in good agreement with the theoretical predictions over the whole range of our experiment. Moreover, the typical structure of ionization shock wave is given.

INTRODUCTION

The phenomena of ionization in high temperature air have been investigated systematically by many authors (Ref.1,2), and the tables (Ref.3,4) of its thermodynamical properties including the effects of ionization are being used broadly in engineering.

However, it is still a difficult task to exactly measure the electron density in air at high temperature under various conditions. It is well known that there exist the very complicated ionization and many other chemical reactions in high temperature air, and we still do not have a thorough understanding about the mechanism of ionization. The information about ionization of air below three or four thousand degrees Kelvin in the tables of thermodynamical properties being used at present is not quite complete, but the ionization of air in this range of temperature is of great concern in practical engineering problems. Thus, there is the necessity to investigate these phenomena further.

THE EQUIPMENT AND THE APPARATUS

The equipment used is a shock-tube which is 20M long and 800mm in diameter. The structure and operating characteristics of it was given briefly in ref. 5. In order to measure the electron density in air at high temperature, the following apparatus was used:

The Near-Free-Molecular Langmuir Probe

The structure and the operating principle of this type of Langmuir probe is described in ref. 6. Its exposed part is about 2mm long, 0.06mm in diameter, so the capability of its time and spatial-resolution is fairly good, and it is used in our shock-tube to measure the ionized shock structure and the relaxation time of ionization processes.

The Ordinary 3cm And 8mm Microwave Transmissions

These two types of transmission measurement give reliable values of electron density in high temperature air behind the shock wave (Ref.7,8). Its shortcoming is that the spatial-resolution is not very high, thus the results obtained can only be regarded as some mean value. Moreover, the measuring range of these types of transmission is very narrow.

High Sensitivity Microwave Transmission And Reflection

The structure and working principle of this type of transmission and reflection measuring equipment developed by the authors, whose operating wavelengths are 3cm and 8mm, was described in ref 9. The utilization of a crystal oscillator as a microwave source makes the whole apparatus very convenient and compact, and the utilization of mixing type receiver greatly increases the anti-interference ability and the sensitivity of measurement; their sensitivity is one or two orders higher than that of the ordinary apparatus.

RESULTS

The variation of the ionization relaxation time measured by the use of Langmuir probe in the air behind normal shock waves as a function of Mach number M_s is given in Fig 1. The curves on it corresponds to the dissociation neutralization reaction



two values of rate constant are used respectively, for curve I

$$K_e = 3 \times 10^{-3} T^{-3/2} \text{ cm}^3 / \text{ sec} \quad (2)$$

for curve II

$$K_e = 9 \times 10^{-3} T^{-3/2} \text{ cm}^3 / \text{ sec} \quad (3)$$

According to their results of measurement in the reference 10, A. Frohn et al. suggested that the commonly used rate constant in eq. (2) must be increased by a factor of three, which is shown by eq. (3) and by the dotted line in Fig. 1.

However, according to the results obtained by the present authors it is not necessary to make such a change. In our own opinion the rate constant given in eq. (2) is still the best approximation at present.

The variation of the peak values of electron density behind normal shock waves with Mach number, corresponding to $P_1 = 1 \times 10^{-2}$ mmHg, 1×10^{-1} mmHg, 3×10^{-1} mmHg, 1 mmHg, is given in Fig. 2. to 5. These results are obtained using the apparatus listed in section 2 respectively, and are basically in good agreement. This proves that the data obtained are reliable. Also shown in these figures are the theoretical results in the often used tables of thermodynamic properties (Ref. 3, 4). From these figures we can see that the measurements are basically in accord with the theoretical values.

The typical structure of an ionized shock wave is given in Fig. 6.

REFERENCES

1. Shao-Chi Lin, etc., Phys. of Fluids 5 No 12 (1962) 1633.
2. Shao-Chi Lin, etc., Phys. of Fluids 6 No 3 (1963) 355.
3. А.С.Презводителей, Е.В.Смупоченко "Таблицы Термодинамических Функций Воздуха" (1962) А.Н. СССР.
4. N. B. S. AEDC-TR-65-58 (1965).
5. Nai-yi Zhu and Hong-de Li, "Measurements of flow parameters in a 800 shock tube" Acta Mechanica Sinica No 3 (1978) 234.
6. Nai-yi Zhu and Lian-xing Li, "A near-free-molecular Langmuir probe and the investigation of ionization shock structure" Acta Mechanica Sinica Supplement (1981)
7. Nai-yi Zhu and Xue-fen Li, "Measurement of the electron density behind a strong shock using 3 cm microwave transmission" Acta Mechanica Sinica (1981) (to be published).
8. Nai-yi Zhu and Xue-fen Li, "Measurement of the electron density behind a strong shock using 8 mm microwave transmission" (to be published).
9. Nai-yi Zhu and Xue-fen Li, "The high sensitive microwave transmission and reflection" Plasma Letters (1981)
10. A. Frohn and P. C. T. de Boer, Physics of Fluid Supplement 1 (1969) I-54.
11. Y. Manheimer-Timnat and W. Low, J. Fluid. Mech. 6 No 3 (1959) 449.
12. B. Niblett and V. Blackmann, J. Fluid. Mech. 4 No 2 (1958) 191.
13. Т.В.Баменова, Ю.С.Лобастов, "Физическая газодинамика и свойства газов при высоких температурах" (1964) 17.

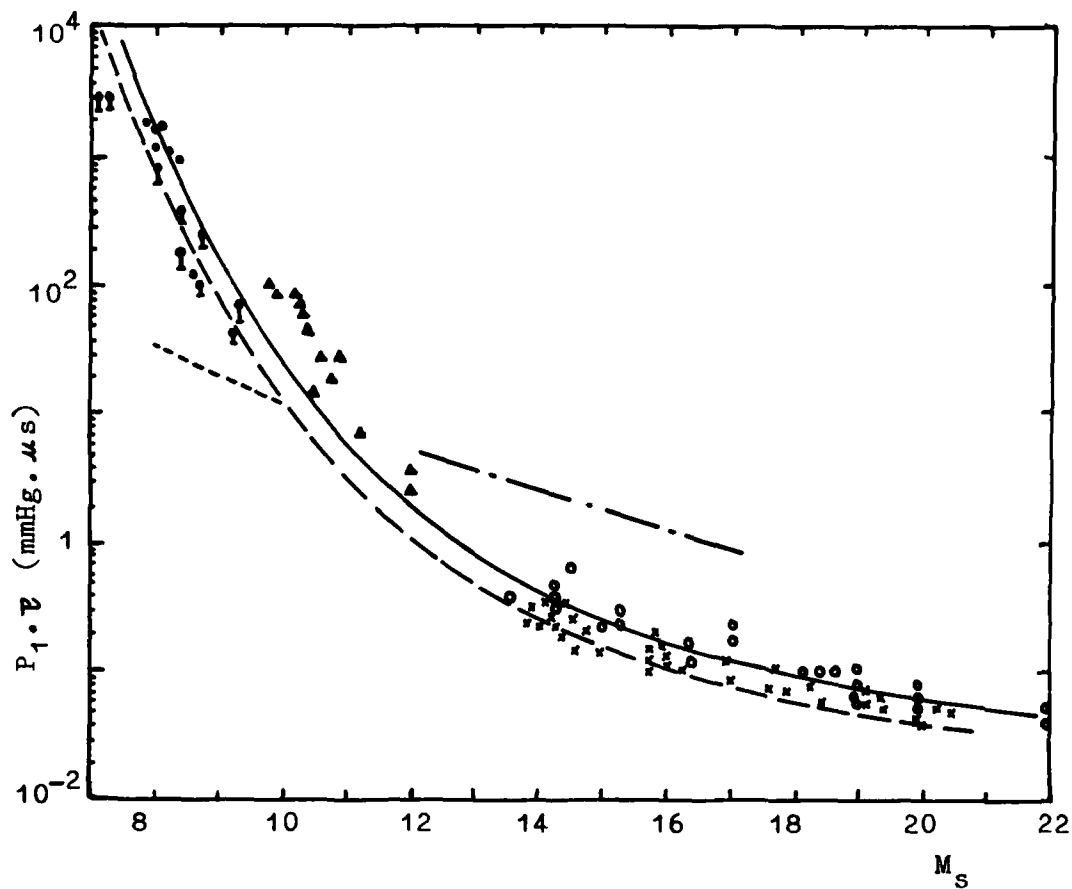


Fig 1. Ionization relaxation times behind normal shock waves in air.

- A. Frohn 10 ;
- × S.C. Lin 1 ;
- ▲ T.B. Bajenova 13 ;
- present results ;
- Y. Manheimer-Timnat 11
- . - B. Niblett 12
- curve I, $K_e = 3 \times 10^{-3} T^{-3/2} \text{ cm}^3/\text{sec}$;
- curve II, $K_e = 9 \times 10^{-3} T^{-3/2} \text{ cm}^3/\text{sec}$.

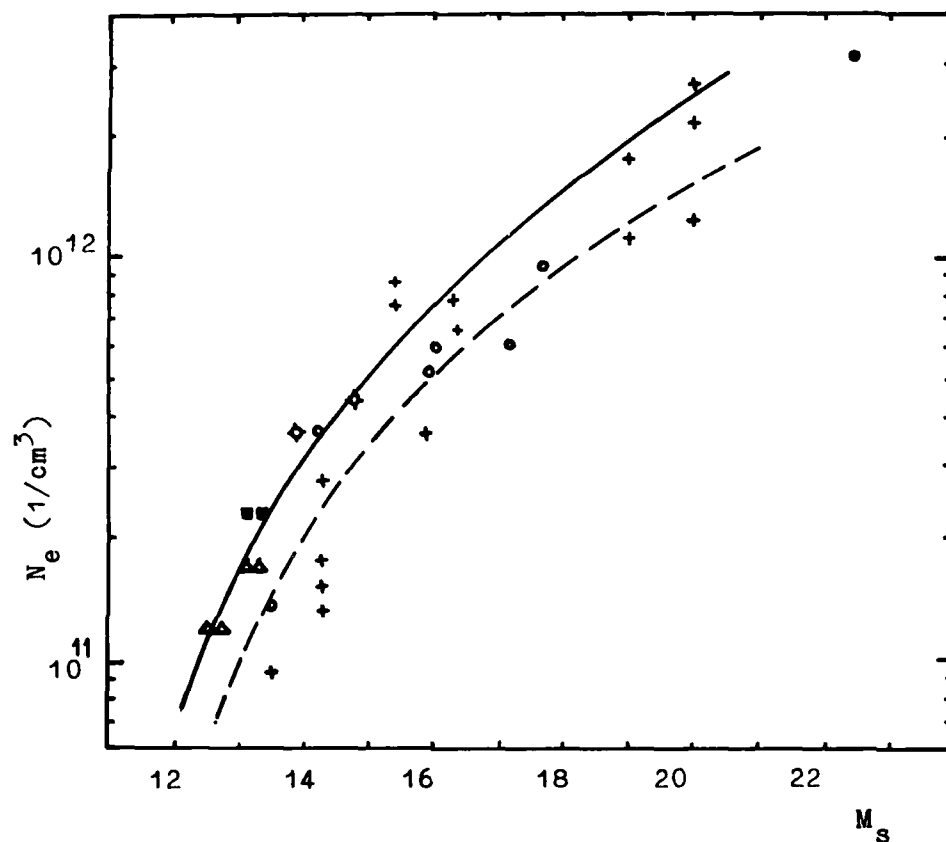


Fig 2. Peak electron density behind normal shock waves in air. $P_1 = 1 \times 10^{-2} \text{ mmHg}$.

- + Near-free-molecular Langmuir probe;
- 3 cm ordinary microwave transmission;
- 8 mm ordinary microwave transmission;
- ◇ 3 cm microwave interferometer;
- △ 3 cm high-sensitive microwave transmission;
- 8 mm high-sensitive microwave reflection;

———— N. B. S. 4 ;

----- A. H. CCCP. 3 .

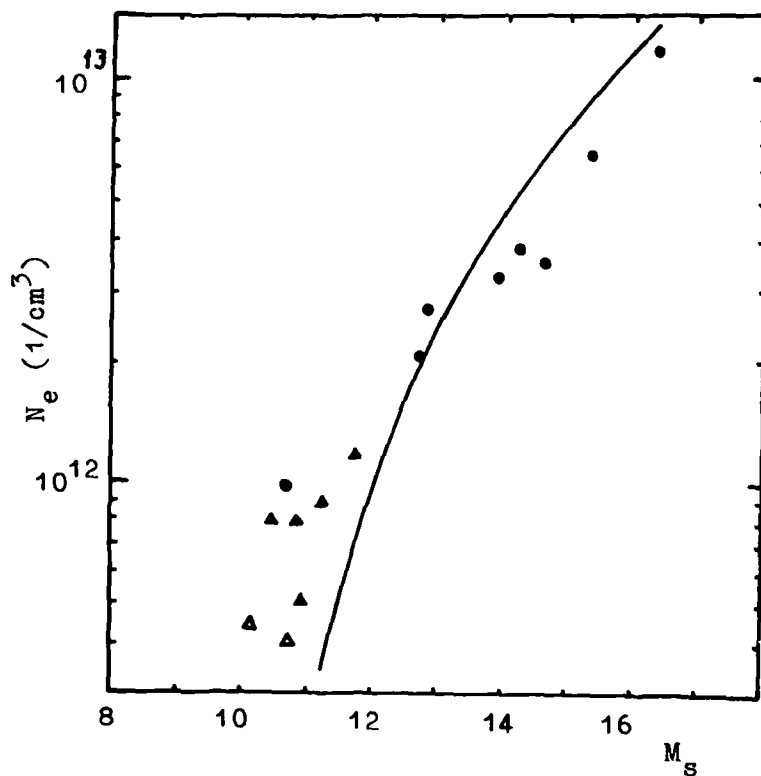
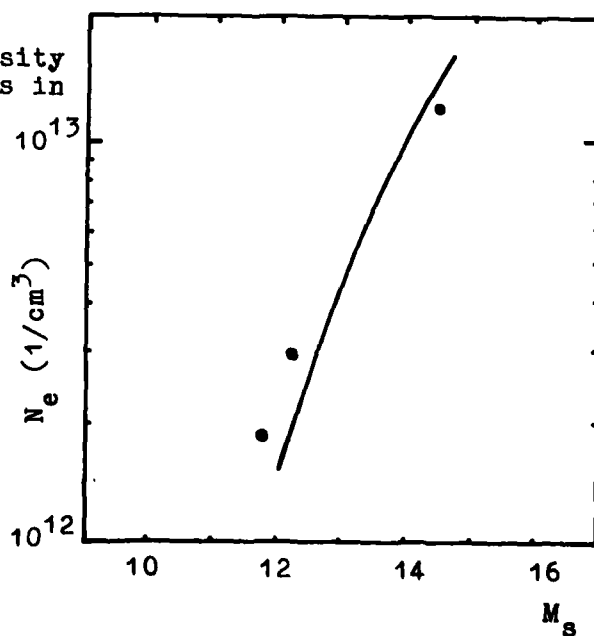


Fig 4. Peak electron density behind normal shock waves in air.

$P_1 = 3 \times 10^{-1}$ mmHg.

• 8 mm ordinary microwave transmission;

— N.B.S. 4



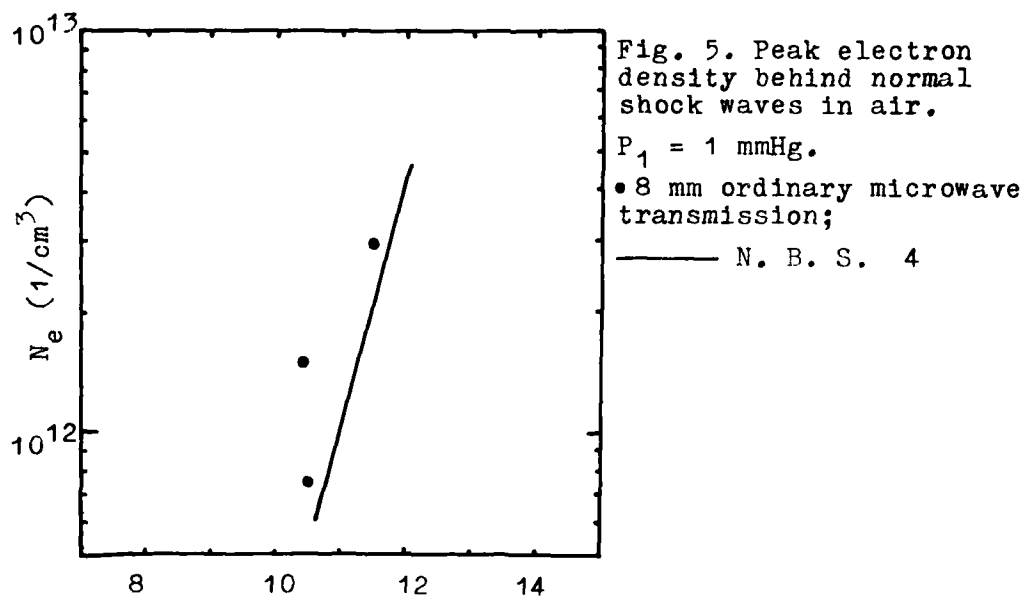
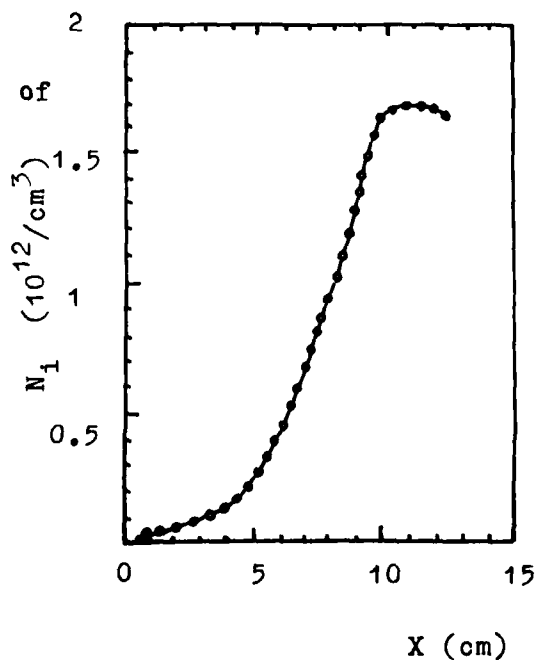


Fig. 6. Typical structure of ionization shock wave

$P_1 = 10^{-2}$ mmHg,

$M_s = 22$.

X is distance behind shock wave.



STUDIES OF THE VIBRATIONAL RELAXATION OF DIATOMIC MOLECULES IN A SHOCK HEATED MOLECULAR BEAM AND ITS APPLICATION TO IONIZATION BY ELECTRON IMPACT

B. Evans^{1†}, S. Ono^{1*}, R.M. Hobson¹, S. Teii^{3*}, A.W. Yau², J-S. Chang³

1. Dept. of Physics and CRESS, York University, Toronto, Canada
2. Herzberg Institute of Astrophysics, NRC, Ottawa, Canada
3. Department of Engineering Physics, McMaster Univ., Hamilton, Canada

The shock heated molecular beam technique was used to obtain vibrationally excited oxygen, nitrogen and carbon monoxide molecules. The vibrational distribution of these diatomic molecules, in argon gas as the "carrier" gas of a shock heated molecular beam, has been calculated by considering atomic recombination and collisional excitation-de-excitation during the expansion. The vibrationally excited molecules, which correspond to vibrational temperatures T_v , in the range 1800 K to 7000 K, are used to examine the role played by vibrational excitation in both direct and dissociative electron impact ionization cross sections, over a range of electron energies from 50-500 eV.

1. Introduction

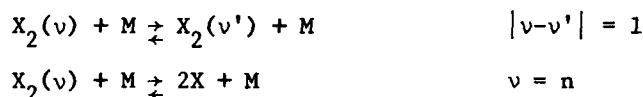
The direct and dissociative ionization cross-section of vibrationally excited molecules by electron impact is not well understood at present. Further understanding of the role of vibrational excitation on the ionization of molecules has increased in importance as a result of recent developments in gaseous lasers, plasma enhanced chemical vapour deposition for the production of solar cells, impurity problems in nuclear fusion research, flame chemistry and the chemistry of planetary atmospheres. There are few previously reported values of such processes leading to ionization. Spence and Dolder¹ suggested that the cross section for dissociative ionization increases in value up to 50% at an electron energy of 200 eV and vibrational temperature of 3100 K using a shock heated molecular beam (SHMB) with mass spectrometer. Crane and Stalker² estimated that the effect of vibrational excitation on total ionization is only less than 30% in Nitrogen at an electron energy above 200 eV and vibrational temperatures ≤ 3100 K using the SHMB with ion sampling by a mass spectrometer. Micheja and Burrow³, using a crossed beam technique, indicated that the effect of vibrational excitation on dissociative ionization is as much as 100% near the threshold for the first three vibrational levels of Nitrogen. Theoretical studies, employing statistical methods, to predict the roles of vibrational excitation in dissociative ionization, have been conducted by Dronin and Gorokhov⁴, Venugopalan⁵ and Jackson et al.⁶. However, these theories only apply to larger molecules or are limited in threshold electron energy. For larger electron energies the calculation has been done only for Hydrogen⁷. More recently, Evans et al.⁸ predicted that the effect of vibrational excitation in dissociative ionization is only less than 29%, even for vibrational temperatures as high as 104 K for oxygen, using a modified reflection method for larger electron energies.

In this paper, direct and dissociative ionization cross-sections of vibrationally excited molecules by electron impact are measured at elevated vibrational temperatures for diatomic molecules. The vibrationally excited molecules were produced by a shock-heated molecular beam technique and the vibrational relaxation in the system was predicted numerically.

2. Vibrational Relaxation in a Shock Heated Molecular Beam

2.1 Method of calculation and the procedure employed

As the molecular plasma is expanded through a nozzle, the translational, rotational and vibrational energy modes come into equilibrium at different rates. The translational and vibrational relaxation times are typically in the order of a few collisions; the vibrational relaxation time is much longer. In the present work, the vibrational distribution function of the molecular beam is computed as a function of time, assuming translational and rotational equilibrium, and using a method similar to that developed in Yau⁹. In particular, the molecule is assumed to consist of N vibrational levels, and the vibrational relaxation of the molecular beam is characterised by the reactions



where $X_2(v)$ is the diatomic molecule in the v th vibrational level and M is the major constituent of the gas. n is used here to indicate the continuum levels.

The first reaction considers collisional excitation and de-excitation while the second reaction considers dissociation and recombination. The diatomic molecule X_2 is assumed to be at sufficiently small concentrations so that $X_2 - X_2$ collisions can be ignored. Excitation and de-excitation is also assumed to occur from only vibrational levels that are adjacent and all are in the ground electronic state.

The time dependent population of the v th level $n_v(t)$, is given by the master equation

$$\frac{dn_v(t)}{dt} = [M] \left\{ \sum_{v'=0}^{n-1} g_{v',v} n_{v'}(t) - \sum_{v'=0}^n g_{vv'} n_v(t) + g_{nv} n_n^2(t) \right\}, v \leq n-1$$

and

$$\frac{dn_n(t)}{dt} = 2[M] \left\{ \sum_{v'=0}^{n-1} g_{v',n} n_{v'}(t) - n_n^2(t) \sum_{v'=0}^{n-1} g_{nv'} \right\}$$

where $g_{vv'}$ is the transition probability from v to v' . As a consequence of detailed balancings

$$\tilde{n}_v g_{vv'} = \tilde{n}_{v'} g_{v'v}; \quad \tilde{n}_v g_{vn} = \tilde{n}_n^2 g_{nv}$$

where \tilde{n}_i is the equilibrium population of the i th state. Also, for a given diatomic molecule X_2 and inert gas M , $g_{vv'}$ is a function of the temperature of the inert gas.

The solution to the master equation is drastically simplified by linearizing the $n_n^2(t)$ term. By defining

$\alpha_n = 1/2 \tilde{n}_n + \Delta$ and $\Delta = n_n(t) - \tilde{n}_n$, we obtain $n_n^2 = \tilde{n}_n^2 + 2\tilde{n}_n \Delta + \Delta^2$, so that near equilibrium, $\Delta \approx 0$, and $n_n^2 \approx 2\tilde{n}_n \alpha_n$ in the above equation. The details of the

linearization procedure and method of numerical solution can be found in Yau⁹.

In order to integrate the above differential equations the change of the gas density with distance in the present SHMB apparatus was plotted as a function of time steps, which were chosen so that the development in time of the density decay was well approximated. The size of the time steps was variable. The initial values at the beginning of the program (i.e. in the shock reflected region) were calculated from the JPL program of Horton and Menard¹⁰. The temperatures, and argon gas density decay in the molecular beam from nozzle to freeze out point (or free molecule point) were obtained from the numerical results of Evans et al¹¹, in which it is assumed that the small admixture of molecular gases in Argon does not affect the neutral beam flow properties.

2.2. Numerical Results

Numerical vibrational population distributions for 1% nitrogen gas seeded in the Argon carrier gas are shown in Fig. 1, for various locations \bar{x} along the axis and downstream of the expansion nozzle at $T_5 = 6000\text{K}$, where T_5 is the temperature in the shock reflected region. Fig. 1 shows that the vibrational population distribution becomes non-Boltzmann almost immediately after the expansion nozzle. Numerical vibrational population distributions at the free molecular point for 1% nitrogen molecules seeded in the Argon carrier gas are shown in Fig. 2 for various shock reflected region temperatures. Fig. 2 shows that none of the vibrational distributions at the free molecular point are Boltzmann like above $T_5 = 3000\text{K}$. The larger concentrations and the depletion of vibrationally excited molecules ($v > 5$) (relative to their equilibrium values) are observed also in Fig. 2 for T_5 larger than and smaller than about 6500K respectively. The survival of molecular nitrogen at the free molecular point with shock reflected temperature are shown in Fig. 3 for various nitrogen partial pressures (expressed as %). It was found that the vibrational population distribution at the free molecular point does not vary significantly over the present range of nitrogen partial pressures. Similar calculations have also been carried out for oxygen or carbon-monoxide mixed with Argon gas. A typical Oxygen result is shown in Fig. 4 for various shock reflected region temperatures. Similar conclusions to those found in the case of nitrogen are found

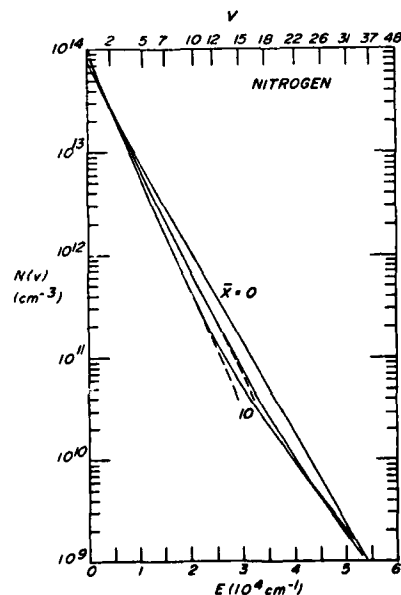


Fig. 1: Numerical vibrational population distributions of nitrogen for various location \bar{x} at $T_5 = 6000\text{K}$

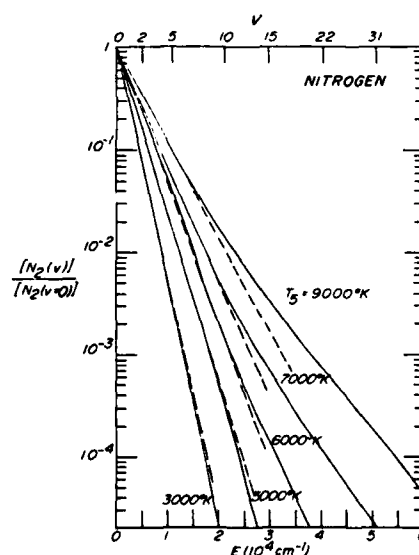


Fig. 2: Numerical vibrational population distributions of nitrogen at free molecular points for various T_5

in the case of O_2 . Oxygen is found to recover its Boltzman distribution for $T_5 \leq 6,200$ K.

Typical vibrational temperature relaxation in the shock heated beam with nitrogen as an additive is shown in Fig. 5, for a range of T_5 , where the gas temperature relaxation is also compared. In these cases the vibrational temperatures are determined from the slopes of the population distribution at small vibrational levels ($v \leq 5$) (since the populations of vibrational levels above about 5 are orders of magnitude smaller than $v \leq 5$). Fig. 5 shows that a highly vibrationally excited molecular beam can be developed in the present apparatus. The resulting vibrational temperature at a free molecular point is shown in Fig. 6 for O_2 , N_2 and CO additives. Fig. 6 also shows that the vibrational temperature at a free molecular point increases nonlinearly with the shock reflected region temperature.

3. Electron Impact Ionization Cross Section Measurements of a Molecule in a High Vibrational State

3.1 Experimental Apparatus and Procedure

A schematic diagram of the shock heated molecular beam apparatus is shown in Fig 7. It is seen to consist of a shock tube section, a beam formation region, ionization and detection sections.

The shock tube consists of a 7.1 m long, polished steel tube of 10 cm internal diameter. The low pressure section is 4.1 m long and the driver section is 3.0 m long. By varying the shock tube diaphragm pressure ratio, diaphragm thickness or the driver and test gases, Mach numbers between 3 and 13 were achieved. The shock wave velocity was measured by up to four platinum thin film gauges and a piezoelectric pressure transducer.

The beam formation section consists of three vacuum chambers; the first separating the nozzle and skimmer, the second between the end of the skimmer and the collimator and the third section past the collimator and containing the molecular beam diagnostics section. The expansion vessels were made of

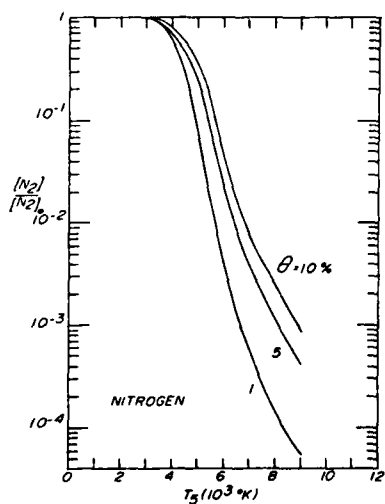


Fig. 3: Survival of molecular nitrogen at the free molecular point with T_5 for various nitrogen partial pressures.

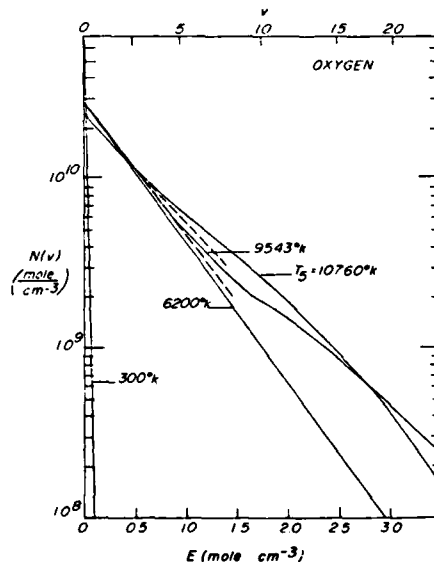


Fig. 4: Numerical vibrational population distributions of oxygen at free molecular point for various T_5 .

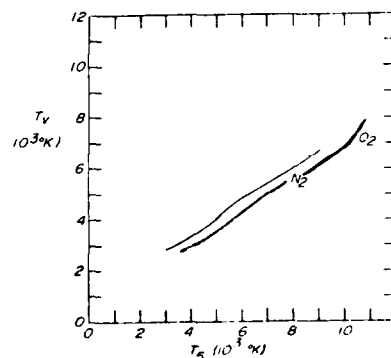
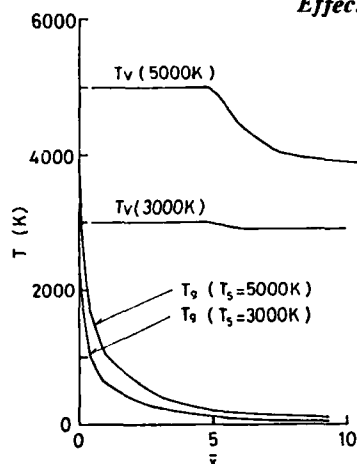


Fig. 5: Vibrational temperature relaxation of nitrogen along the location \bar{x} , Fig. 6: Vibrational temperature at a free molecular point vs T_5 for O_2 , N_2 and CO additives.

2 cm thick, 60 cm internal diameter glass cylinders. (Q.V.F.). The first section, containing the skimmer and collimator was 80 cm long while the second section was 60 cm long. The electron gun, the grid and collector constituted the ionization region. The electrons were obtained by heating a Ba-O coated cathode by a ceramic covered tungsten heater. The heater was held at cathode potential thus avoiding arcs, and was used with a fixed 6.3 V drop, which led to a current of up to 0.85 amps. The cathode voltage could be varied from 0 to 500 volts. From the electron current-voltage characteristic, the electron gun was found to follow the Child-Langmuir space-charge law with a slope of 0.11μ per volts. The electron collector consists of about 150 razor blades (uncoated Shick injector blades) held tightly together and electrically isolated from ground. Due to the sharpness of the blades most electrons are either absorbed on first impact or are reflected back into the blades and then collected. The potential of the collector could be varied from 0 to 500 volts. A coarse copper grid, held over the collector and maintained at ground potential was employed, in order to avoid the collector voltage from accelerating electrons and affecting the collections of ions. From the observed ion signal-electron collector voltage characteristics, the range $100 \leq V \leq 80$ found out to have no effect on collector voltages and large enough to collect most of the electrons.

The positive ion detection section consists of an einzel lens leading to a quadrupole mass-spectrometer and ion counter. The einzel lens consists of three parallel steel plates each with a centre hole diameter of 1 cm. The voltage of the centre plate could be varied from 0-250 volts, positive or negative, with respect to ground. The outer two plates were electrically connected at voltages from 0-250 volts, positive or negative. For the focal lengths used in this experiment, the lens acted as a thin convex lens. It was found by experiment that setting of -142 V for the inside plate and -60 V for the two outside plates of the einzel lens gave the optimum focusing characteristics (i.e. large signal with low signal distortion). The ion detector developed by Joshi et al.¹² was used in the present study.

3.2 Experimental Procedure and Calibration

The ion signal for a given run was obtained by varying the electron energy with a fixed constant voltage applied elsewhere. Thus the intent was to reproduce, as best as possible, the same conditions for differing electron energies at a given vibrational excitation.

For each temperature condition, an argon and neon ionization cross section curve was obtained for the purpose of calibration. The experimentally

derived cross sections were normalized with the argon and neon cross sections from Rapp and Englander-Golden¹³. Since these cross sections should be independent of the vibrational temperature, they were employed as references. The calibrations and normalization procedure follow the usual sequence. The ion signal from the detector (I_+) is related to the cross section (σ) by

$$I_+ = \eta I_- n \ell \sigma$$

where n is the neutral number density, ℓ is the collisional path length of the electrons with the neutrals, I_- is the electron gun current and η is the total collection efficiency, which includes that affected by the following parameters (a) einzel lens (b) transmission through the quadrupole system (c) ion detection system. This leads to a determination of the absolute cross section, σ , for ionization of a seeded gas, by assuming that η is the same for the seeded gas as for argon.

$$\sigma = \frac{I_+(V, N, T) \sigma_A(V)}{I_+(V, A, T) \chi}$$

where $I_+(V, N, T)$ is the ion signal from the detector measured at an electron beam voltage of V for species N at temperature T , $\sigma_A(V)$ is the ionization cross section of argon from Rapp and Englander-Golden¹³ measured at V and χ is the present concentration of molecules in argon. From the argon and neon curves for different shock reflected region temperatures, a weak mass effect and molecular beam property effect on the collection efficiency has been observed.

3.3 Experimental Results and Discussions

The electron ionization reactions for oxygen in the present electron energy ranges and partial pressures are direct and dissociative ionization, as follows:



Typical electron impact measurements reported here in the case of direct ionization of oxygen with $T_v=5300$ K are shown in figure 8 and are compared with results reported by other workers at $T_v=300$ K. Figure 8 shows that the cross sections reported here agree both in order of magnitude and in the shape of the curve with the other results. The effects of vibrational temperature on this cross section are shown in Fig. 9. The latter indicates that the cross section at a vibrational temperature of 2300 K is identical with the present $T_v=300$ K results. The measurements at $T_v=6000$ K shows some small systematic variations of the cross sections. It is also seen to vary for $E \geq 200$ eV. At $E \leq 200$ eV, the maximum in the cross section seems to be shifted towards higher electron energy with increasing vibrational temperatures.

The effects of vibrational temperature on the oxygen electron impact dissociative ionization are shown in Fig. 10 together with the results of Rapp et al¹⁴ at 300 K. Figure 10 shows general correlation with the results of Rapp et al¹⁴. However a more definite shift to higher E is observed in the current measurement of the cross section for dissociative ionization. Finally the σ_{diss} for oxygen is plotted as a function of vibrational temperature and compared with the theoretical predictions of Evans et al⁸ in figure 11, which are strictly only valid for higher values of E . Nevertheless they are seen to be in substantial agreement with the experimental values. The disagreement between these results and the much larger shift determined by Spence and Dolder¹, could well be due to an inadequate allowance for η by these authors. σ_{diss} at $T_v=3000$ K for CO is shown and is compared with the room temperature ($T_v=300$ K) measurements of Rapp et al (1965) in figure 12. Only the case of $CO+e \rightarrow C+O^++2e$ is shown in the figure. It is seen that the increase in σ_{diss} leading to O^+ is about one order of magnitude when the vibrational temperature is increased,

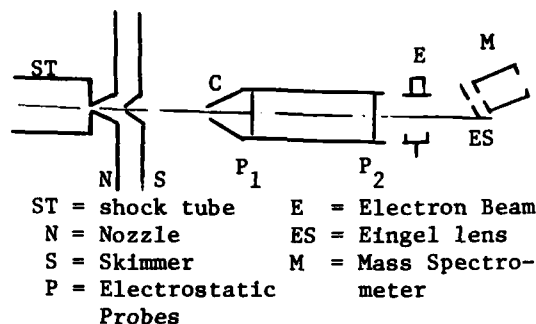


Fig. 7: Schematic of Ionization Cross section measurement apparatus.

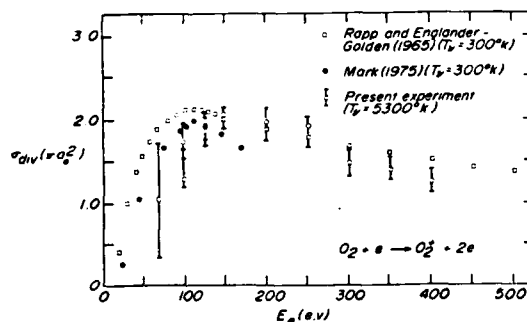


Fig. 8: Direct ionization cross section of oxygen with $T_v = 5300 \text{ K}$.

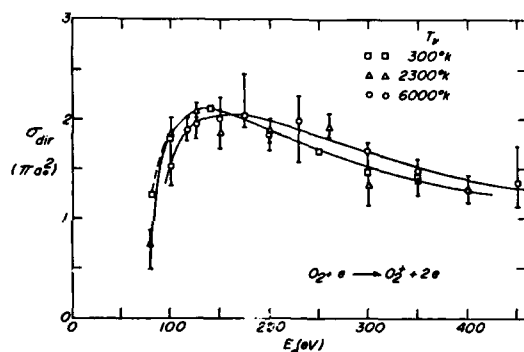


Fig. 9: The effect of vibrational temperature on direct ionization cross section of oxygen.

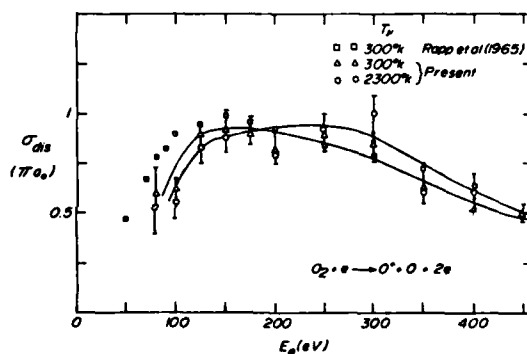


Fig. 10: The effect of vibrational temperature on dissociative ionization cross section of oxygen.

although the same general shape of the curve is maintained.

4. Conclusion

The measurement of ionization cross section by electron impact has been conducted, employing a shock heated molecular beam, and the relaxation of vibrational temperature in the system is predicted numerically. This leads to the following conclusions.

- (1) For shock reflected temperatures, T_5 , larger than 6000 K, the vibrational population distribution at the free molecular (freeze out) point is non-Boltzmann for any mixture ratio with argon.
- (2) For concentrations of seeded molecules less than 10%, the vibrational population distribution was near Boltzmann and independent of partial pressure for $T_5 \leq 3000 \text{ K}$.
- (3) The density of molecules at a free molecular point decreases nonlinearly with an increase in temperature of the reflected region T_5 .
- (4) The vibrational temperature at a free molecular point, increases nonlinearly with the temperature in the shock reflected regions.
- (5) There are some small systematic variations of the cross sections for both dissociative and direct electron impact ionization, with vibrational temperature in the case of homonuclear molecules.
- (6) The experimental results agree with theoretical values obtained using a modified reflection method for the dissociative ionization cross section of oxygen.
- (7) A relatively larger influence of the vibrational temperature on the

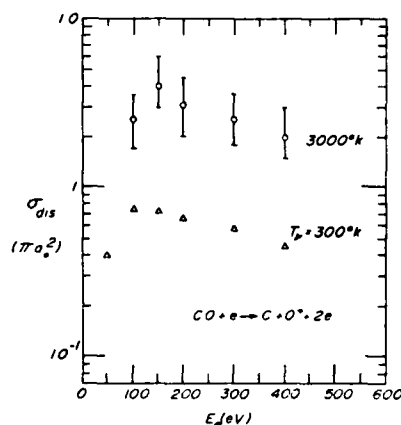


Fig. 11: Comparison of experimental σ_{diss} with theory.

dissociative ionization cross section has been observed for a heteronuclear molecule, i.e. CO in the present case.

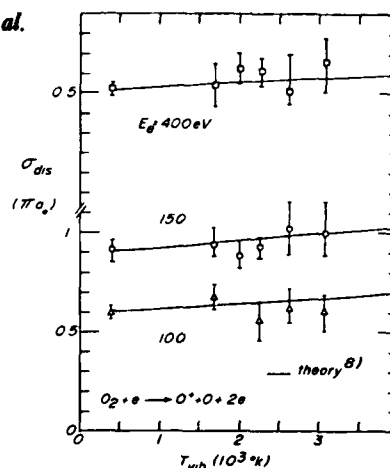


Fig. 12: The effect of vibrational temperature on dissociative ionization cross section of CO.

References

1. D. Spence and K.T. Dolder (1970) *Phys. Fluids* **13**, 88-95.
2. K.C.A. Crane and R.J. Stalker (1977), *J. Phys. D: Appl. Phys.* **10**, 679-95.
3. J.A. Michejda and P.D. Burrow (1977), *Bull. Am. Phys. Soc.*, **22**, 196.
4. A. A. Dronin and L.N. Gorokhov (1972), *High Temp.* **10**, 40-5.
5. M. Venugopalan (1971), "Reaction Under Plasma Conditions", Vol. II, Ch. 11, Wiley-Interscience Co.
6. W.M. Jackson, R.T. Brackmann and W.L. Fite (1974) *Int. J. Mass. Spec. and Ion Phys.* **13**, 237-250.
7. J. K. Cashion (1966), *J. Chem Phys.* **45**, 1663.
8. B. Evans, R.M. Hobson and J.S. Chang (1981), *Bull. Am. Phys. Soc.* (In press)
9. A. W. Yau (1978), Ph.D. Thesis, York University, Toronto.
10. T.E. Horton and W.A. Menard (1969), J.P.L. Technical Report, 32-1350.
11. B. Evans, J.S. Chang, R.M. Hobson, and K. Teshima (1980), *Proceedings of 12th Int. Symp. on Shock Tubes and Waves*, pp. 571-8.
12. S. Joshi, R.H. Prince and T.V. Ward (1975), *Rev. Sci. Instrum.*, **46**, 559.
13. D. Rapp and P. Englander-Golden (1965), *J. Chem. Phys.*, **43**, 1464.
14. D. Rapp, P. Englander-Golden and D.D. Briglia (1965) *J. Chem. Phys.* **42**, 4081.
15. G. Herzberg (1950) "Molecular Spectra and Molecular Structure", vol. II, Van Nostrand Co. Inc., New York.

Acknowledgements

The authors wish to express their appreciation to Drs. R. W. Nicholls, R. H. Prince, Y. Ichikawa, P. Baille, T. Kaneda and S. Matsumura for valuable discussions and comments. This work was partially supported by the National Science and Engineering Research Council of Canada.

* Permanent address: Department of Electrical Engineering, Musashi Inst. of Technology, Tokyo, Japan.

† Present address: DREV, Valcartier, Quebec, Canada.

AD P000277

DISCHARGE FLOW/SHOCK TUBE STUDIES OF SINGLET OXYGEN

Peter Borrell, P.M. Borrell, M.D. Pedley, K.R. Grant and R. Boodaghians

Department of Chemistry, Keele University, Staffordshire, England.

The four modes of using a discharge flow shock tube are discussed with examples drawn from previous work and our own studies of singlet oxygen, ($O_2(^1\Delta_g)$ and $O_2(^1\Sigma_g^+)$). Preliminary results are reported of the temperature dependence of the 'dimol' emission and of the quenching of $O_2(^1\Sigma_g^+)$ by N_2O .

INTRODUCTION

The discharge flow shock tube is a useful means of isolating and studying the elementary reactions of excited chemical intermediates and free radicals, at the high temperatures of interest in flames and combustion. The advantage over the normal shock tube is the separation of the production of the intermediates from the shock heating, which acts simply as a temperature and concentration switch.

Although there was an early study by Benson¹, and allied work using a pulsed discharge by Wray and Teare², the first apparatus in the present form was that of Hartunian, Thompson and Hewitt³ who used an RF discharge to dissociate nitrogen, and studied the temperature dependence of the afterglow recombination reaction. Gross^{4,5,6} and Cohen used the same tube with a microwave discharge to study further chemiluminescent processes. Breen, Quay and Glass^{7,8} then used an RF discharge to study the effect of atoms on vibrational relaxation, and also studied⁹ the reactions of H atoms with N_2O .

We tried experiments with active nitrogen¹⁰ but our recent work has been on studies of singlet oxygen^{11,12}. This has given us an insight into the methods of using the technique and here we review these, taking examples for each from our own and other work.

EXPERIMENTAL

Figure 1 shows a diagram of our apparatus. Purified O_2 is passed over mercury and through the microwave discharge cavity. Mercury removes atomic oxygen and leaves a flow which at 6 torr (~ 700 Pa), contains 5–10% $O_2(^1\Delta_g)$ in O_2 . The concentration of $O_2(^1\Sigma_g^+)$ is about 0.1% of the $O_2(^1\Delta_g)$. The oxygen then flows along the shock tube in the opposite direction to the shock. When studying weak emissions, the direction of flow is important; with the pre-shock flow in the opposite direction to the shock wave, the discharge is closer to the observation station and so the signal/noise ratio is increased.

In the pre-shock flow, $O_2(^1\Delta_g)$ is deactivated both by collision and at the walls so there is a concentration gradient along the tube which we measure with a travelling photomultiplier.

The shock wave is generated by pressure bursting an aluminium diaphragm with He, N_2 or mixed driver gases at 6 atm (~ 600 kPa). The speed, from 0.8 to 1.7 $km\ s^{-1}$ giving temperatures between 600 K and 1850 K, is measured with three laser light screens. The light emission is observed by two photomultipliers (EMI 9658B equipped with filters), and their outputs are stored with transient recorders. The digitised output is then passed to a Hewlett Packard 2647A graphics terminal for storage and analysis.

Our technique differs from those used previously⁷ in the flow direction, the facilities for pre-shock analysis of the concentration gradient, and the use of the whole post-shock emission trace for analysis.

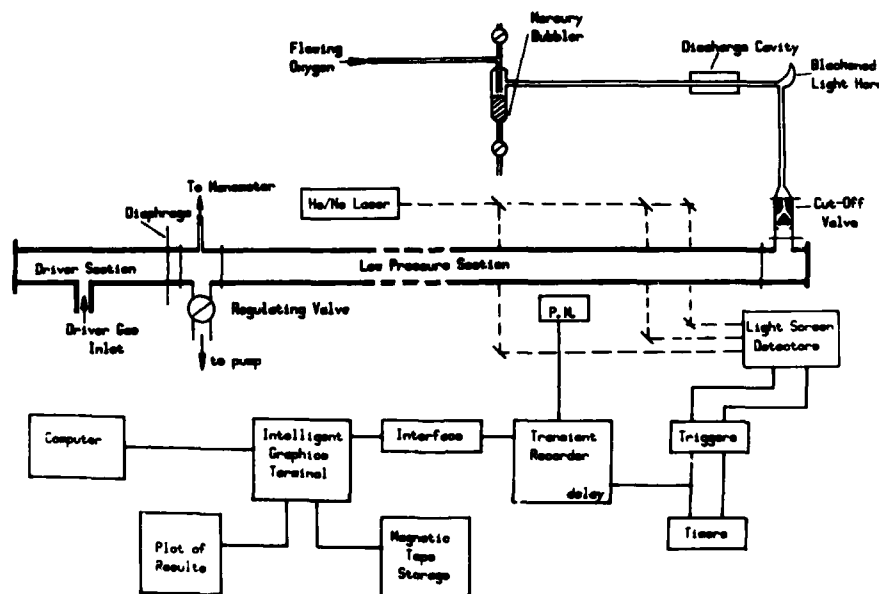


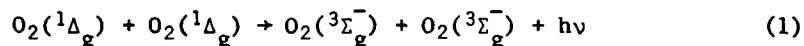
Figure 1. A diagram of the discharge flow/shock tube apparatus.

METHODS FOR USING A DISCHARGE FLOW/SHOCK TUBE

(1) Measurements of chemiluminescent reactions using the shock front compression

For luminescent reactions which occur in the pre-shock flow, shock compression provides a ready way to study changes with density and temperature. The mode was used by Hartunian, Thompson and Hewitt³ and by Gross and Cohen^{4,5} to study the chemiluminescent recombination reactions; $N+N$; $N+O$; and $SO+O$.

We have used it to study the 'dimol' emission reactions¹³ of $O_2(^1\Delta_g)$; in these still unfamiliar processes, two excited molecules lose their energy¹⁴ in a single quantum of radiation ($\lambda=634$ nm):



Now the intensity of a collisional process should be given by

$$634I = kT^{\frac{1}{2}} [O_2(^1\Delta_g)]^2 \quad (2)$$

and so the ratio of post to pre-shock intensity is

$$(634I_2/634I_1) = K(T_2/T_1)^{\frac{1}{2}} (\rho_2/\rho_1)^2 \quad (3)$$

where ρ and T are the density and temperature. K should be unity if equation (2) is valid. Figure 2 shows the variation of K with T for this 634 nm emission.

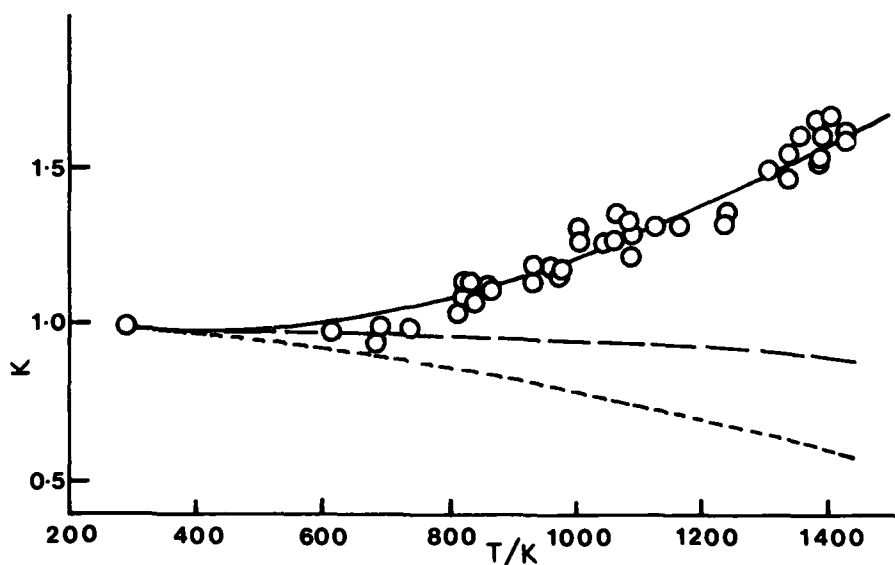


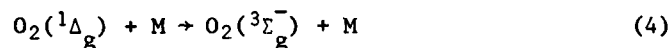
Figure 2. The variation of K (equation 3) with temperature. The points are experimental results. The full line shows the final fit using a model with the normal and first two hot bands; the dotted line shows the contribution of the normal band, and the dashed line the sum of the normal and first hot bands.

At lower temperatures K is close to unity indicating the correct attribution and behaviour, but it does increase systematically. We take the increase to indicate the presence of "hot bands"; emissions from vibrationally excited $O_2(^1\Delta_g)$ molecules. For example the band at 634 nm corresponds to simultaneous transition from $(v'=0, v''=0)$ in the reactants to $(v''=0, v'=0)$ in the products. The following transitions would also occur near 634 nm, $(v'=1, v''=0)$ to $(v''=1, v'=0)$ and $(v'=1, v''=1)$ to $(v''=1, v'=1)$ but these would only be seen at the higher shock temperatures. The line in the figure shows the fit which we have obtained with this model, and using it we have determined the relative transition probabilities for these transitions.¹⁵

(2) Measurements of the change in concentration gradient

Earlier workers³⁻⁷ had noted the gradient but did not need to analyse it. Figure 3 shows a trace¹² for the post-shock emission from $O_2(^1\Delta_g)$. The compression at the shock front (method 1) is evident but it is followed by a decay. Remember that after the front, one sees gas from upstream, in the shock sense, passing the observation point. Now does the fall simply reflect the pre-shock concentration gradient in the tube or is it due to a deactivation process?

The deactivation reaction is:



with a rate constant $k(T_1)$ at the pre-shock temperature, T_1 . If the pre-shock flow rate is f then post-shock decay due to the concentration, c , can be shown to be:

$$c/c_0 = \exp[-k(T_1)W_s(\rho_2-\rho_1)t_\ell/\rho_1f] \quad (5)$$

where t_ℓ is the laboratory time and W_s is the shock velocity.

If there is deactivation at the high temperature then a further factor must be added to the exponent: $-k(T_2)\rho_2 t_\ell/\rho_1$.

The line in figure 3 shows the decay predicted from the pre-shock gradient; the good fit shows that $k(T_2)$ is not measurable in our system.

There are two conclusions from this analysis: since $O_2(^1\Delta_g)$ is not deactivated at high temperature each record of the emission gives us an accurate concentration profile of the pre-shock concentration; it indicates that our tube is working well and gives us confidence in the analysis. Secondly, for a change to be discernable, the ratio $k(T_2)/k(T_1)$ must be about 40 which corresponds to a minimum activation energy of about 15 kJ mol^{-1} .

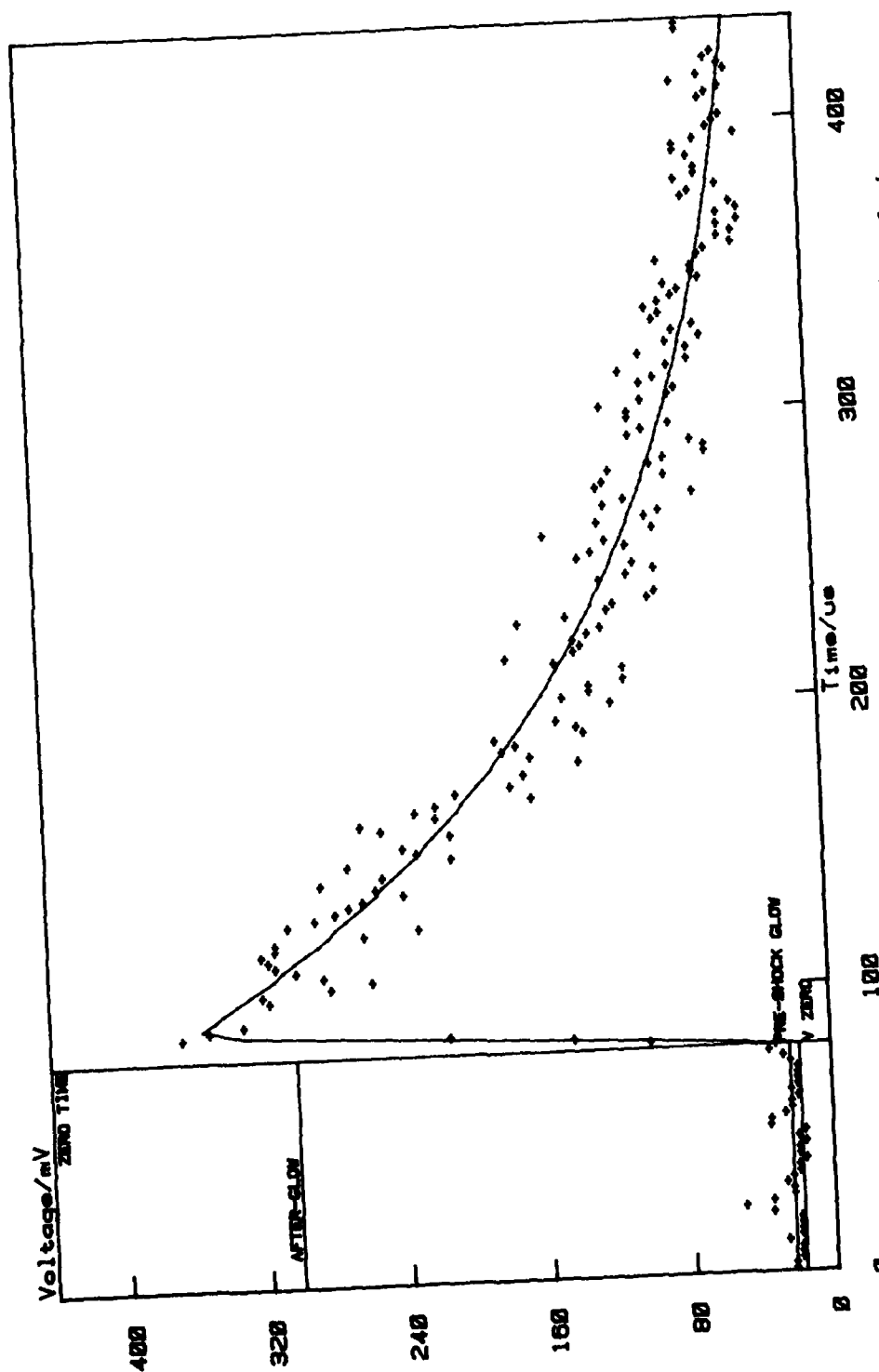


Figure 3. A digitized experimental trace of emission from $O_2(^1\Delta_g)$ as a function of time. The line through the points shows the change predicted from the shock conditions, together with the pre-shock concentration gradient.

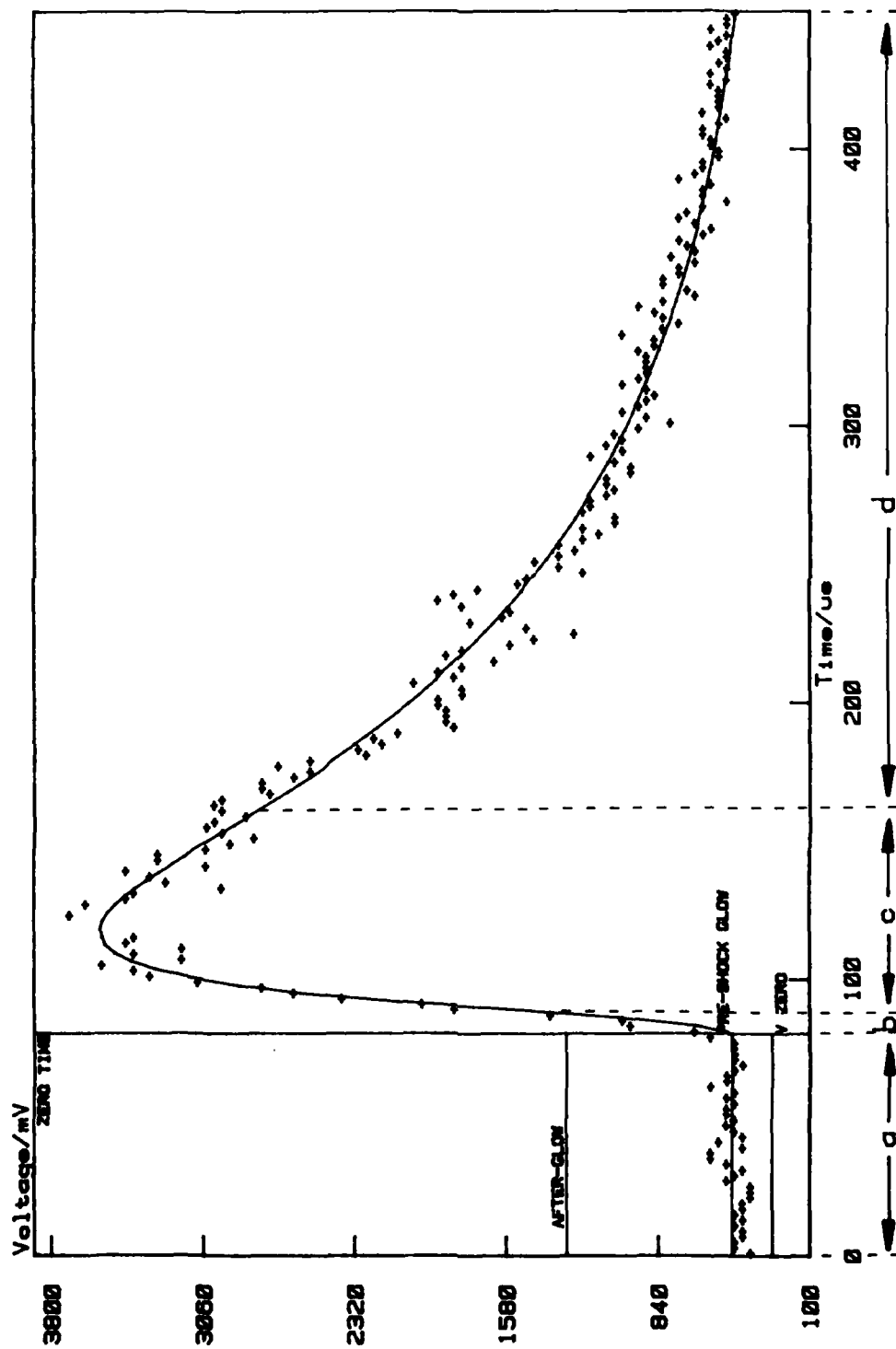


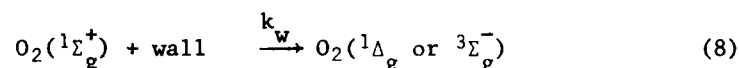
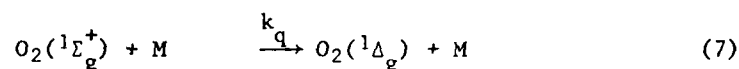
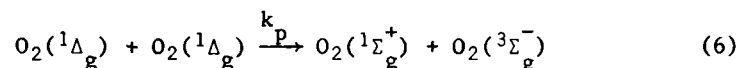
Figure 4. A digitized trace showing the emission from $O_2(1\Sigma_g^+)$ as a function of time. The line through the points shows the fit with equation 10. The letters are referred to in the text and show the various regions.

(3) Adjustment in the steady state after shock heating

Here measurements are made of the enhancement of the emission over that expected from the pre-shock value, and also of the rate of relaxation to the new state.

Figure 4 shows the emission trace for $O_2(^1\Sigma_g^+)$. It can be divided into five regions of which the figure shows four.

(a) The pre-shock emission at 762 nm is from $O_2(^1\Sigma_g^+)$ which is formed in the energy pooling reaction from $O_2(^1\Delta_g)$ and removed by collisional deactivation or at the wall:



At any point in the tube there is a steady state concentration of $O_2(^1\Sigma_g^+)$ determined by its rates of formation and removal at room temperature.

(b) The rise at the shock front is due to the compression, so that :

$$^{762}I_2(t=0) = ^{762}I_1 \rho_2/\rho_1 \quad (9)$$

This is equivalent to mode 1 and can be used to check the pressure dependence of the emission¹². The risetime, characterised by t_s , is due to the optical slitwidth.

(c) A relaxation zone follows the rise; in it the concentration adjusts to the new steady state level determined by reactions (6) and (7) at the high temperature.

(d) The fall in emission is governed by the pre-shock decay of $[O_2(^1\Delta_g)]$ along the tube - i.e. as in mode 2.

(e) Finally, but not shown, there is a fall in emission at the arrival of the contact surface.

The analysis must take all the features in (a) to (d) into account. After integrating the rate equations for reactions (6) to (8) the following expression is obtained for the post-shock emission:

$$^{762}I_2(t) = ^{762}I_1 (\rho_2/\rho_1) \int_{t-t_s}^t \{K + (1-K)\exp[-k_q t]\} \exp(-\alpha t) dt / t_s \quad (10)$$

where α is the constant describing the concentration gradient, k_q is the rate constant for equation (7) at T_2 , and K is the ratio of the high^q and low temperature rate constant ratios:

$$K = \frac{k_p(T_2)/k_q(T_2)}{k_p(T_1)/\{k_q(T_1) + k_w/[M]\}} \quad (11)$$

The wall reaction is neglected at T_2 .

The integration is done numerically, since we take into account the change of density with vibrational relaxation and non-ideal shock behaviour.¹² The analysis is carried out by a combination of interactive computer graphics and non-linear least squares¹⁶ to give α and t_s which can be compared with the known parameters for the system, $k_q(T_2)$ and K which then yield $k_p(T_2)$.

We have made measurements with a number of additives^{12,17} and figure 5 shows some of our results, including preliminary measurements for N_2O as a quencher. An interesting feature of the results is the negative temperature dependence of quenching by CO_2 and N_2O which contrasts with the slow rise with temperature of the rate constants for quenching by O_2 and N_2 .

We have also used this method to study vibrational relaxation¹⁸ of $O_2(^1\Delta_g)$ by studying the 'dimol' emission at 579 nm.

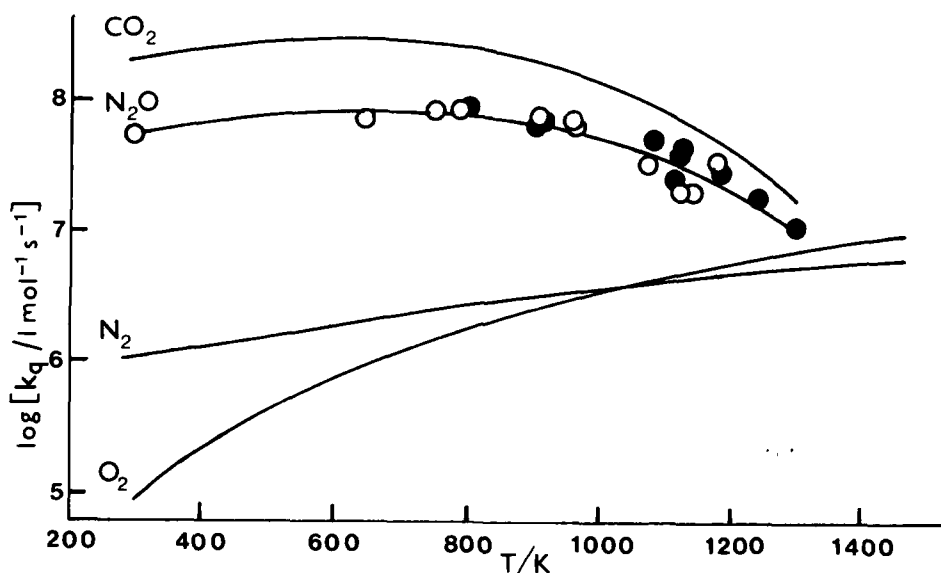


Figure 5. A plot of the rate constants obtained for the quenching of $O_2(^1\Delta_g)$ by various gases. Experimental results for two mixtures with nitrous oxide are shown.

(4) Normal measurements with reactive additives.

Here the discharge is used to generate an intermediate which is used as an additive in a normal shock tube experiment. Breen, Quay and Glass^{7,8} used this mode in their measurements of the vibrational relaxation of O_2 in the presence of atomic oxygen. The atom concentration (up to 1.8%) was measured by the air afterglow from added NO. Then the relaxation time was measured by the laser schlieren technique of Kiefer and Lutz¹⁹.

Glass and Quay⁹ used the same mode to measure the reaction $H+N_2O$, by studying the decay of infrared emission from N_2O in the presence of atomic H ($\sim 0.4\%$).

In both applications the concentration of the atoms was assumed, reasonably, to be constant but if the concentration does change appreciably, then the change must be taken into account (method 2).

CONCLUSION

The examples show the versatility of the discharge flow shock tube for making measurements of the rates of fundamental chemical and spectroscopic processes. As with any method, the reactions to be studied must satisfy certain conditions on rate and temperature dependence, and it is necessary to make thorough pre-shock measurements in order to obtain the best understanding of the post-shock behaviour. It is certainly worthwhile to analyse the whole of the post-shock emission to obtain a full understanding of the processes occurring and reliable values of the rate constants. When this is done the technique provides probably the best method for measuring rates of reactions between 600 and 2000 K.

This work is supported by the Science Research Council.

REFERENCES

1. J.M. Benson, Physical Properties of Active Nitrogen, NACA, TR2293, 1951 (quoted in reference 4).
2. K.L. Wray and J.D. Teare, Proc. Int. Conf. Phys. Electronics & Atomic Collisions, 3rd, Univ. Coll. London 1963, p.1123.
3. R.A. Hartunian, W.P. Thompson & E.W. Hewitt, J. Chem. Phys., **44**, 1765 1966.
4. R.W.F. Gross, J. Chem. Phys., **48**, 1302, 1968.
5. R.W.F. Gross and N. Cohen, J. Chem. Phys., **48**, 2582, 1968.
6. N. Cohen and R.W.F. Gross, J. Chem. Phys., **50**, 3119, 1969.
7. J.E. Breen, R.B. Quay and G.P. Glass, Proc. Internat. Shock Tube Symp., 9th Stanford University Press, 1975, p.375.
8. J.E. Breen, R.B. Quay and G.P. Glass, J. Chem. Phys., **59**, 556, 1973.
9. G.P. Glass and R.B. Quay, J. Phys. Chem., **83**, 30, 1979.
10. P. Borrell, P.M. Borrell and A. Brittain, U.S. Clearing House Fed. Sci. Tech. Inform., AD 1969, 702808.
11. P. Borrell, P.M. Borrell and M.D. Pedley, J. Photochem., **9**, 107, 1978.
12. P. Borrell, P.M. Borrell, M.D. Pedley and K.R. Grant, Proc. Roy. Soc. London, **A367**, 395 1979.
13. P.M. Borrell, P. Borrell and K.R. Grant, J. Chem. Soc., Faraday II, **76**, 1442, 1980.
14. E.W. Gray and E.A. Ogryzlo, Chem. Phys. Letters, **3**, 658, 1969.
15. P. Borrell, P.M. Borrell, K.R. Grant and R. Boodaghians, J. Chem. Soc., Faraday II, (submitted for publication).
16. P. Borrell, Computers and Chemistry, **4**, 131, 1980.
17. P. Borrell, P.M. Borrell and K.R. Grant, Nuovo Cimento (in press).
18. P.M. Borrell, P. Borrell and K.R. Grant, J. Chem. Soc., Faraday II, **76**, 923, 1980.
19. J.H. Kiefer and R.W. Lutz, J. Chem. Phys., **44**, 658, 1966.

AD P000278

ROTATIONAL RELAXATION OF H_2 IN NOZZLE FLOW

Y. MATSUMOTO, H. MATSUI AND T. ASABA

Department of Reaction Chemistry
Faculty of Engineering, University of Tokyo
Bunkyo-ku, Tokyo, 113, Japan

The present investigation was undertaken in order to measure the rotational relaxation rate of molecular hydrogen by monitoring the number density of $n-H_2$ in a state: $v=0$ and $J=1$ in the supersonic nozzle flow, by means of coherent anti-Stokes Raman spectroscopy (CARS). The CARS apparatus was essentially the same type of Régnier and Taran.

As the preliminary experiment the CARS transformation coefficient was measured on wide temperature and pressure range, which was in agreement with the theoretical calculations.

In the experiments of the rotational relaxation, the gas mixture (20% H_2 + 80% Ar) was heated by the reflected shock wave in the temperature range from 2200 to 2650 K and the pressure range from 1.5 to 5 atm and expanded rapidly through the conical nozzle, so that the non-equilibrium conditions between the rotational and the translational degrees of freedom were realized, where concentration of H_2 ($J=1$) was determined by CARS technique.

Experimental results were analyzed by means of the conventional conservation equations of fluid mechanics and the master equations using the rate constants with an exponential energy gap law.

1. Introduction

Unless the system is in the extremely low temperature, molecules distribute in many rotational states. Since the energy gap between adjacent rotational levels increases with the rotational quantum number, the higher levels can relax more slowly than the lower levels. These multilevel features make it difficult to understand the experimental results of the rotational relaxation.

The rotational relaxation of molecular hydrogen has been extensively investigated by means of the various techniques, such

as sound absorption [1-4], shock tube [5-7] and free jet expansion [8,9]. Because the rotational distribution was not measured in these experiments, the deduced results from the experiments were the rotational collision number, Z_R , or the relaxation time τ .

The temperature dependencies of the collision number in these works were not in agreement with each other. These apparent discrepancies were qualitatively explained by Rabitz and Lam [10] who solved the fluid mechanical equations and the master equations by using the theoretically calculated state-to-state rate constants. They concluded that single relaxation time derived from those experiments were expected to yield different behaviours, and this was a result of multilevel natures as well as the differences of initial distributions in the rotational levels.

In this study the concentration of molecular hydrogen in a state, $v=0$ and $J=1$, was monitored directly by CARS (Coherent Anti-Stokes Raman Spectroscopy) to observe the rotational relaxation process in the supersonic nozzle flow. The experimental results confirmed the inference drawn by Rabitz and Lam.

Although CARS has been developed as a powerful nonlinear optical technique and has many advantages [11-13], it was necessary to know how CARS signal intensity depends on the temperature and the total pressure in order to apply this technique to the study of rotational relaxation in molecular hydrogen. Since the technique was developed rather recently and the temperature and the pressure dependence were not known, experiments for obtaining those dependences were performed as the preliminary experiments.

2. Experimental

CARS apparatus was essentially the same as that of Taran et al. [14] and shown in Fig.1. The pumping laser was the giant pulse ruby laser (GRL, about 10MW, 20 nsec.) which worked on a single longitudinal mode and focused in the high pressure cell which contained pure H_2 gas of about 8 atm. to generate the stimulated Raman scattering (SRS). SRS from the high pressure cell at the room temperature worked on $Q_{0,1}(1)$ line [15], so CARS signals were associated with two states of H_2 ; $v=0, J=1$ and $v=1, J=1$. After the first order anti-Stokes radiation was removed by the glass filter, F_1 (Hoya R-64), both GRL and the first order Stokes radiations were overlapped collinearly and focused in the observation point by use of the lens L_3 ($f = 15$ cm). The generated CARS signals were separated by dichroic mirror (DCM) and detected by the photomultiplier (PM, Hamamatsu TV, R106UH) through the appropriate filters and the monochromator by which the stray light was removed.

Since the intensity of CARS depended on that of the pumping laser, CARS signal from the reference cell (RC) which contained H_2 gas at 2 atm. was measured simultaneously.

Each output of the CARS signal was fed into the high speed integrator (INT, Cambera 2005), then displayed on a CRT.

A shock tube was used for measurements of temperature and pressure dependence of CARS intensity. The shock tube was made of aluminum of 60 mm x 60 mm cross section and consisted of about 2 m long low pressure section and 1 m long high pressure one.

The light pulse of GRL was synchronized with the reflected shock wave by use of a delay circuit. The pressure of the reflected

[554]

Matsumoto et al.

shock wave was measured by the well calibrated pressure gauge (Kistler) which was mounted just above the observation point and the temperature was calculated by the conventional way. The measurements of the CARS signal intensity were performed on the gaseous mixtures of hydrogen and argon at 300 ± 5 , 880 ± 50 , 1550 ± 50 K and the total density range of gas was from 1×10^{18} to 2×10^{19} molecules/cm³. The mole fraction of H₂ was 1.0 (300K), 0.7 (880K) and 0.5 (1550K), respectively.

In the experiments of the rotational relaxation, the measurements of CARS signal intensity were performed on H₂ diluted in Ar for the calibration of the optical system at the room temperature.

The shock tube was used with the conical nozzle separated by the diaphragm (Myler 12 μ m thick), as is seen in Fig.2.

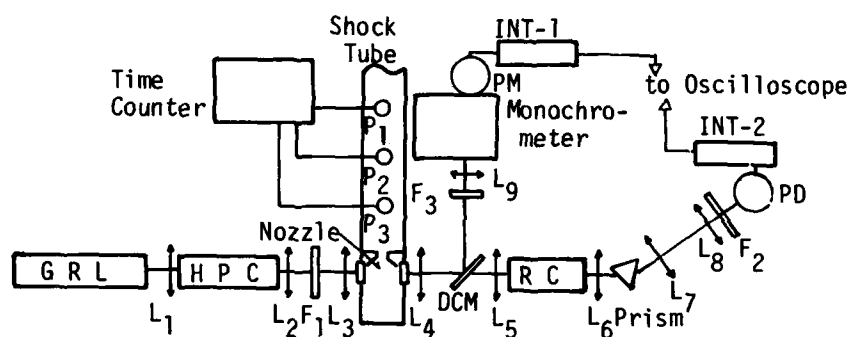


Fig.1 SCHEMATICS of THE EXPERIMENTAL SYSTEMS

GRL: Giant Pulse Ruby Laser, HPC: Stimulated Raman Cell
 RC: Reference Cell, INT: High Speed Pulse Integrator
 L₁~L₉: Lens, F₁~F₃: Filter, DCM: Dichroic Mirror
 P₁~P₃: Piezo Gage, PM: Photomultiplier, PD: Photo Diode

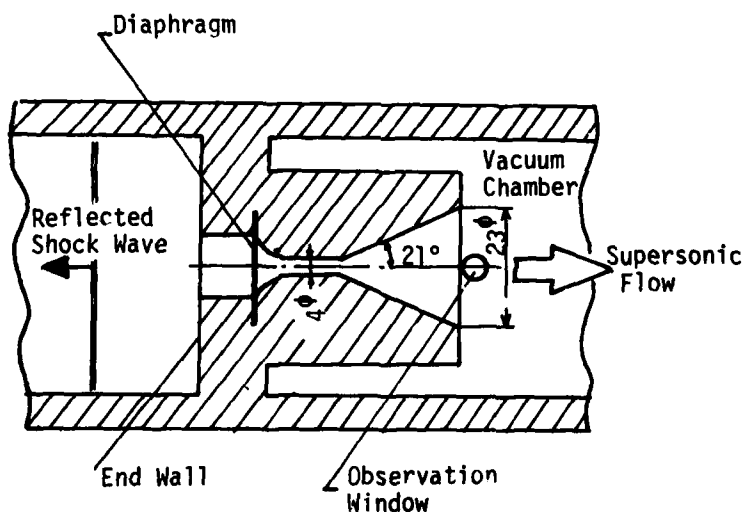


Fig.2 DETAILS of THE NOZZLE SECTION

The shock heated gaseous mixture (20% H₂ + 80% Ar) was expanded through the conical nozzle and was translationally cooled rapidly, but the energy transfer between rotational and translational degrees of freedom was insufficient. In this non-equilibrium condition, the concentration of hydrogen molecules in a state, $v=0$, $J=1$ was monitored by means of the CARS technique. The uniformity of the nozzle-expanding flow was examined by observing the emission from the carbon dioxide molecules which was seeded in Ar + H₂ gas mixture. The duration of the uniform nozzle flow was about 300 μsec. GRL was fired during this period by use of a delay circuit. Experiments were performed at the stagnation temperature and pressure ranging from 2200 to 2650 K and from 1.5 to 4.7 atm, respectively. Reagents gases of H₂ and argon used were of the research grade (99.999% purity).

3. Results and Discussions

CARS process can be described by the third-order nonlinear susceptibility, $\chi^{(3)}$, and the spectrum of the susceptibility is affected by the thermal molecular motions. Therefore, when the temperature and the total pressure of the system are different from those in the calibration procedure, it is necessary to examine how CARS signal intensity depends on these conditions. The detailed description related to this subject was given elsewhere[19], so the theoretical results are described briefly.

CARS signal intensity, $I_3(\omega_3)$, is given as

$$I_3(\omega_3) = \iint d\omega_1 d\omega_2 |\chi^{(3)}(\omega_3; \omega_1, \omega_1, -\omega_2)|^2 I^2(\omega_1) I_2(\omega_2), \quad (1)$$

where $I_1(\omega_1)$ and $I_2(\omega_2)$ are intensity of the pumping laser and Stokes shifted emission, respectively. The expression of the susceptibility, $\chi^{(3)}$, is

$$\chi^{(3)} = c^4 / (\omega_1 \omega_2^3) (d\sigma/d\Omega) N\Delta x F(\omega_3, \omega_0, \gamma; T), \quad (2)$$

where $(d\sigma/d\Omega)$ is the differential cross section of the spontaneous Raman scattering, $N\Delta x$ is the population difference between two states related to Raman transition, ω_0 is the eigen frequency of the Raman active molecule and c is the velocity of light. The spectrum of the susceptibility is determined by the function, F . The functional form of F cannot be expressed analytically and depends of many variables including γ which was the measure of the total number density defined as

$$\gamma = k_B T / (\mu D), \quad (3)$$

where k_B is Boltzmann constant, μ is the reduced mass and D is the diffusion coefficient.

Fig. 3 shows the experimentally obtained CARS signal intensity which was divided by $(N\Delta x)^2$. Calculated results are given in the solid lines and are in good agreement with the experimental results. Therefore, it is possible to evaluate the correction of CARS signal intensity caused by the different conditions of the system from those of the calibration procedure by use of

this theoretical result.

In the experiments of the rotational relaxation, gas mixtures of hydrogen and argon were heated by the reflected shock waves and expanded through the nozzle. In the subsonic part of the nozzle flow, the rotational and vibrational modes were assumed to relax fast enough to follow the translational mode. As the coupling between the translational and rotational modes becomes weak with decrease of the number density in the supersonic part, the non-equilibrium features in the rotational distribution are observed. This process was simulated by coupling the fluid mechanical equations and the kinetic equations.

The expansion flow was treated as quasi-one dimensional stationary flow of cross section area $A(r)$, where r is the distance along the flow.

The relations of fluid mechanics may be derived by considering the following conservation laws,

$$\rho u A(r) = \text{const.}, \quad \text{conservation of mass} \quad (4)$$

$$\rho u \frac{du}{dr} = - \frac{1}{\rho} \frac{dp}{dr}, \quad \text{conservation of momentum} \quad (5)$$

$$C_p T_T + \phi \epsilon_R + \frac{1}{2} \mu u^2 = \text{const.}, \quad \text{conservation of energy} \quad (6)$$

where p is the pressure, u is the velocity of the nozzle flow, ρ is the total number density, ϕ is the mole fraction of H_2 and m is the averaged mass of gas mixture. It should be noted that the energy content of the rotational mode per molecule ϵ_R is separated from that of translation mode i.e. $C_p T_T$ in Eq.(6), where C_p is the translational heat capacity at constant pressure. These equations involve the number density of hydrogen molecules which are

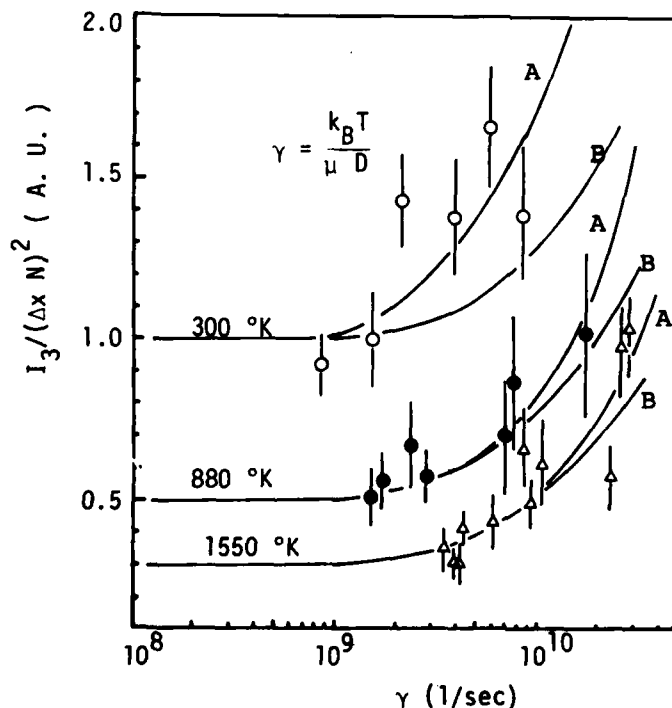


Fig. 3 TEMPERATURE and PRESSURE DEPENDENCE of CARS INTENSITY

Experimental Results behind Reflected Shock Wave:

○ $T = 300 \text{ K}$ (pure H_2)

● $T = 880 \pm 50 \text{ K}$
(0.7 H_2 + 0.3 Ar)

△ $T = 1550 \pm 50 \text{ K}$
(0.5 H_2 + 0.5 Ar)

Solid Lines: Calculation

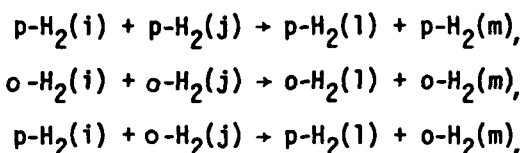
A: FWHM of GRL = 0.015 cm^{-1}

B: FWHM of GRL = 0.01 cm^{-1}

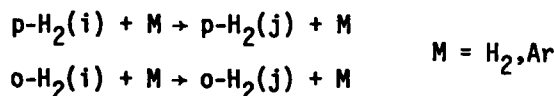
in *i*th rotational state ρ_i ,

$$\rho_i = y_i \rho, \quad (7)$$

where y_i is the mole fraction of the *i*th rotational state. In constructing the master equations the followings can be assumed:
i) The recombination of hydrogen atoms and the vibrational relaxation of H₂ are frozen in the vicinity of the nozzle throat, since their rates are much slower than that of the rotational relaxation.
ii) The R-R process is neglected. Rabitz and his collaborators have extensively studied these processes by means of the effective potential method [10, 17]. They calculated the cross sections over the wide range of energy and showed that the cross section of R-R processes, i.e.



are 1 or 2 orders smaller than that of R-T processes, i.e.



iii) Since the rates of the R-T processes of multi-quantum transition i.e. $|\Delta J| = 4$ are about 2 orders slower than that of transition $|\Delta J| = 2$, R-T processes of double quantum jump are most effective and the other processes can be neglected. The master equations can be written as,

$$u \frac{d y_i}{d r} = \rho \sum_j [-y_i k_{ij} + y_j k_{ji}]. \quad (8)$$

The rate constants of R-T processes have been calculated by Rabitz and Zarur[17] in the H₂-He system and these are well expressed in the exponential gap law,

$$k_{ij} = C_1 g_j \exp(-C_2 |\epsilon_i - \epsilon_j| / k_B T), \quad (9)$$

where C_1 and C_2 are constant and g_j is the degeneracy of *j*th state [18]. This functional form is adopted in our calculations. Eqs. (4), (5), (6) and (8) are numerically solved by use of the method of Gear.

As is shown in Fig.4, calculated results are in good agreement with the experiments, when the parameters in Eq.(9) are chosen as

$$C_1 = 1.5 \times 10^{10} \text{T} \quad (\text{cm}^3/\text{mole. sec.}) \quad \text{and} \quad C_2 = 1.8.$$

These rate constants are smaller than the calculations of Rabitz & Zarur by a factor of about 2 ~ 4 in each transitions. Considering the difference of the collision partner, i.e. He and Ar, it should be noted that the rate constants obtained in the theoretical work by Rabitz & Zarur seems to be reasonable.

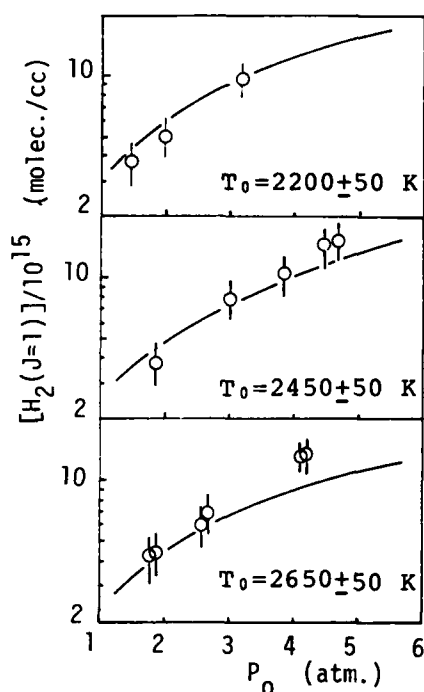


Fig. 4 CONCENTRATION of $o\text{-H}_2(J=1)$ at THE NOZZLE EXIT

T_0 and P_0 are the stagnation temperature and the stagnation pressure, respectively.

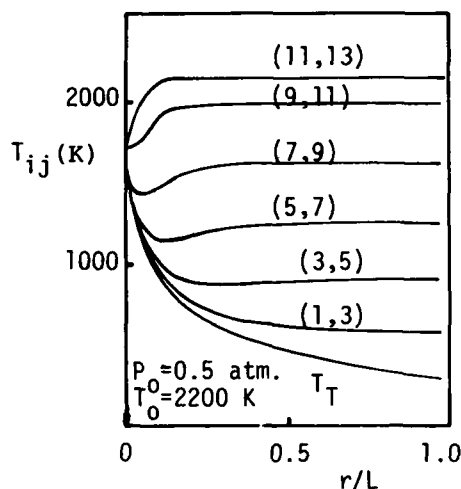


Fig. 5 VARIATIONS of PAIRWISE TEMPERATURES along NOZZLE AXIS

The numbers in the bracket indicate the rotational quantum numbers, i and j .

It is apparent that Maxwell-Boltzmann distribution over the rotational states is not held during the relaxation process, as seen in Fig. 5. Here the pair temperature is defined as

$$T_{ij} = \frac{[\epsilon_j - \epsilon_i]}{k_B \ln[y_i(2j+1)/y_j(2i+1)]} \quad (10)$$

It is clearly seen that the pair temperature depends on the distance from the throat and the higher rotational levels are frozen in the vicinity of the nozzle throat and the lower rotational levels relax faster, as it is expected from the calculation by Rabitz and Lam.

Since the previous investigators measured the indirect quantities to observe the rotational relaxation process, they could only deduce a single relaxation time or collision number using the Bethe-Teller equation,

$$\frac{d}{dt} \epsilon_R(t) = \frac{1}{\tau} [\epsilon_R^\infty - \epsilon_R], \quad (11)$$

where, ϵ_R^∞ is the rotational energy in the equilibrium.

It is obvious from the present experiment that the concept of the rotational collision number in the relaxation of the multi-level system is physically insignificant as Rabitz and Lam have theoretically pointed out.

4. Conclusions

The rotational relaxation process was observed by means of CARS technique and the conclusions are as follows:

i) For the rate constants of R-T process in the H_2 -Ar system, the exponential gap law can predict the present experiments very well and are in good agreement with the theoretical prediction by Rabitz and Zarur.

ii) The concept of the rotational collision number in the rotational relaxation process used conventionally by many investigators is physically insignificant as Rabitz and Lam have pointed out theoretically.

References

1. T. G. Winter and G. L. Hill, J. Acoust. Soc. Am. 42, 848 (1967)
2. R. M. Jonkman, C. J. Prangma, I. Ertas, H. F. P. Knaap and J. J. M. Beenakker, Physica (Utrecht) 38, 441 (1968)
3. J. L. Stewart and E. S. Stewart, J. Acoust. Soc. Am. 24 194 (1952)
4. J. E. Rhodes, Phys. Rev. 70, 932 (1946)
5. C. A. Boitnott and R. C. Warder, Jr., Phys. Fluids 14, 2312 (1971)
6. M. J. Yoder, J. Chem. Phys. 56, 3226 (1972)
7. G. Lemsch and H. Grönig, Proceedings of the 11th International Symp. on Shock Tubes and Waves, p.132 (1977), Univ. Washington Press.
8. R. J. Gallagher and J. B. Fenn, J. Chem. Phys. 60, 3087, 3492 (1974)
9. K. Winkelman, 11th International Symposium on Rarefied Gas Dynamics (1978)
10. H. Rabitz and S. H. Lam, J. Chem. Phys. 63, 3532 (1975)
11. W. M. Tolles, J. M. Nibler, J. R. McDonald and H. B. Harvey, Appl. Spectroscopy 31, 253 (1977)
12. J. P. E. Taran, "Tunable Lasers and Applications", Springer Series in Optical Sciences, Vol.3. p.378 (Springer Verlag, 1976, ed. A. Mooradian, T. Jaeger and P. Stokseth)
13. S. Druet and J. P. E. Taran, "Chemical and Biochemical Applications of Lasers", Vol.4, Chap.5, p.187 (Academic Press, 1979, ed. C. B. Moore)
14. P. R. Régnier and J. P. E. Taran, AIAA J 12, 826 (1974)
15. R. W. Minck, R. W. Terhune and W. Rado, Appl. Phys. Lett. 3, 181 (1963)
16. R. W. DeWitt, A. B. Harvey and W. M. Tolles, "Theoretical Development of Third-Order Susceptibility as Related to Coherent Anti-Stokes Raman Spectroscopy", NRL Memorandum Report No.3260 (1976)
17. G. Zarur and H. Rabitz, JCP. 59, 943 (1973); *ibid.* 61
18. K. Koura, Phys. Fluids, 24, 583 (1981)
19. Y. Matsumoto, H. Matsui and T. Asaba, submitted to Optics Comm.

AD P000279

VIBRATIONAL RELAXATION OF POLYATOMIC MOLECULES IN GAS MIXTURES

Heshel Teitelbaum

Department of Chemistry, University of Ottawa

Ottawa, Ontario, Canada K1N 6N5

Experimental measurements were made of the vibrational relaxation rates of CH_4 and C_2H_4 behind shock waves. The laser schlieren technique was used in order to find the rates at temperatures as low as 330 K. The vibrational relaxation times agreed within 5% of other workers' ultrasonics measurements of pure ethylene and shock tube measurements of pure methane. Precision of better than 1% for individual mixtures allowed for a sensitive test of the linear mixture rule for methane:

$$k = \sum x_i k_i$$

where k_i are the quasi-first order rate constants for the gas by collider i , x_i the mole fraction of the species i in a mixture, and k the overall rate constant for the mixture. It was found that with methane-argon mixtures the linear mixture rule was not strictly obeyed. Distortion from linearity is evident at mole fractions of $\text{CH}_4 < 0.02$, and is most pronounced at the highest temperatures studied (1600 K).

INTRODUCTION

The laser schlieren technique has been instrumental in precise measurements of rates of vibrational relaxation¹ and of the dissociation of diatomic² and triatomic³ molecules in shock waves. Its excellent time resolution has allowed kineticists to probe early reaction times and make conclusions about the involvement of rotational motion during vibrational relaxation⁴ and to detect dissociation-incubation times⁵. Its sensitivity to the thermochemistry of a process allows the unravelling of relatively complicated combustion mechanisms. However much of the work has been confined to simple molecules, and the author wished to see whether larger molecules, especially hydrocarbons, could also be studied. It is known that the vibrational relaxation times of hydrocarbons are very short⁶, so that a successful study would have to be done at temperatures as low as possible and would have to involve high dilutions with inert and inefficient collision partners.

A standard procedure when working with mixtures is to span the range of mole fractions, and to extract from the extremes of the data the influence of the diluent on the vibrational relaxation rate and of the relaxing gas itself on the rate. In that procedure the linear mixture rule is tacitly assumed:

$$k = \sum k_i x_i$$

560

where k_i are the quasi-first order rate constants for relaxation of the gas by collider i , x_i the mole fraction of species i in a mixture, and k the overall rate constant for the mixture. This is purely an empirical rule, which is not really predicted by theoretical calculations^{7,8}. Nevertheless, all experimental tests of the rule up to the present have confirmed it to within experimental error for diatomic relaxation¹ and dissociation². Such tests were limited however by mole fractions which were not less than 0.05; and thus one aim of this work was to extend that range down to mole fractions of 0.005.

EXPERIMENTAL

The apparatus was a rectangular cross-section shock tube equipped with a laser schlieren observation section. It has been described in detail elsewhere¹. One major modification involved stabilization of the gold film resistance strip velocity gauges, so that shock waves with temperatures behind the incident wave as low as 350 K could be studied routinely. We used C_2H_4 (research grade > 99.98% pure), CH_4 (> 99.5% pure), and Ar (prepurified grade > 99.998% pure). Impurities were mainly N_2 , whose efficiency as energy transfer agent for hydrocarbons is known to be small⁶. The C_2H_4 and CH_4 were used initially undiluted, in order to establish the reliability of the shock tube to study hydrocarbon relaxation. Subsequently CH_4 was diluted, and the following mixture compositions were studied: 50%, 25%, 10%, 5%, 2%, 1%, and 1/2%. Table 1 shows the range of experimental conditions for the mixtures.

Table 1. Range of Experimental Conditions for Relaxation of CH_4 in Ar

% CH_4	Initial Pressure (torr)	Incident Shock Temperature (K)	$\Delta\rho/\rho_0$
100.	6.0 - 90.7	340 - 678	0.100 - 1.645
48.85	6.8 - 146	339 - 932	0.073 - 1.558
24.74	6.8 - 154	352 - 1145	0.058 - 1.090
9.91	6.9 - 160	366 - 1416	0.026 - 0.575
4.91	5.0 - 319	387 - 1325	0.016 - 0.258
2.04	7.0 - 322	388 - 1624	0.008 - 0.144
1.15	7.0 - 40.0	648 - 1662	0.016 - 0.081
0.497	6.8 - 21	844 - 1699	0.013 - 0.038

Experiments at elevated mole fractions and relatively high temperatures gave rise to very large perturbations from vibrational equilibrium, as is indicated by the ratio $\Delta\rho/\rho_0$, where ρ_0 is the initial unshocked gas density, and $\Delta\rho$ the change in density during the vibrational relaxation period. For pure ethylene the pressure range was 4.6 - 109 torr, the temperature range 333-551 K, and $\Delta\rho/\rho_0 = 0.170 - 2.09$. However, for both CH_4 and C_2H_4 the relaxation time was so short for these extreme cases (0.3 μ sec in lab coordinates) that the first observation time possible (determined by the extent of the shock front curvature effect to be $\sim 1 \mu$ sec) was already well beyond 3 relaxation units. Thus the experiments can be considered to have occurred under essentially isothermal conditions. The temperatures quoted in table 1 and the relaxation times quoted below correspond to equilibrium or near thermal equilibrium. For experiments under less severe conditions the first observation time possible approached one relaxation unit. For all experiments the temperature change was in the range 1 - 35 K. In principle it is still possible to obtain relaxation times as a function of temperature for each experiment. This was indeed done, but was used only as a diagnostic tool. Because of the large specific heats of hydrocarbons compared to diatomic molecules, and because of the large pressures and hence large rates of relaxation, the schlieren signals tended to be more than adequate in magnitude. The improved sensitivity gave rise to excellent oscillograms even at low temperatures (see fig. 1), and was the reason why low mole fraction mixtures could be studied.

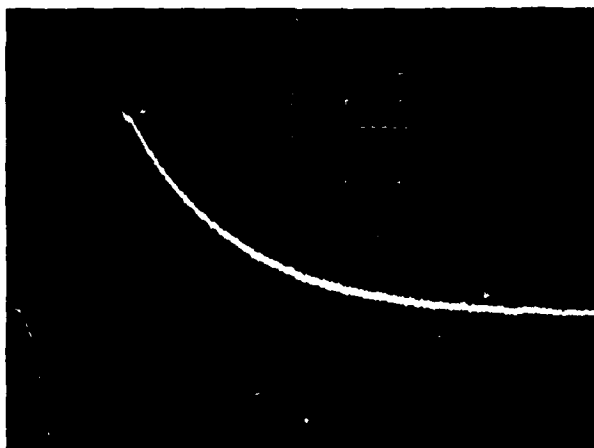


Fig. 1. Oscillogram of laser schlieren signal from vibrational relaxation of pure CH_4 . Initial pressure = 18.3 torr, shock velocity 0.868 mm/usec, $T = 436$ K at thermal equilibrium. Each horizontal division is 1 μs .

Temperatures higher than 1700 were not studied in order to avoid the influence of dissociation. Mole fractions less than 0.005 were not studied in order to avoid the possible interference by boundary layer growth.

Voltage signals obtained from the photodetection system were linearly proportional to laser beam deflections caused by the chemical reaction, and were calibrated with the aid of a rotating mirror. The time resolution of the opto-electronic system was better than 50 nsec.

DATA REDUCTION

The measured voltages were very nearly exponential functions of time. To a first approximation a plot of the logarithm of the voltage as a function of time is linear (correlations > 0.98). The slope of such a plot, especially in nearly isothermal conditions is closely related to the relaxation time in laboratory coordinates. By multiplying with the equilibrium density ratio one converts the result to a gas-particle time scale; by multiplying with the pressure one normalizes the result to one atmosphere; by multiplying with a specific heat ratio $C_p/(C_p - C_{vib})$ one corrects the result for time variation of the translational temperature by a factor which can approach 2 in the extreme cases of this work. This procedure is due to Blackman¹, and is usually quite successful. In assessing this procedure it is worthwhile realizing that it is an approximation. One assumes that the empirical rate law is valid:

$$\frac{d\epsilon}{dt} = \frac{\epsilon_{\infty}(T(t)) - \epsilon}{\tau} \quad (1)$$

Here ϵ is the instantaneous vibrational energy of the gas at time t , T is the translational temperature, and ϵ_{∞} is the equilibrium vibrational energy for temperature T . It can be calculated from the usual quantum statistical mechanical expressions from a knowledge of the fundamental vibration frequencies. C_p is the constant pressure heat capacity (which one can obtain from JANNAF tables¹⁰) and C_{vib} is the contribution by the active modes of vibration to C_p . One assumes that the heat capacity of the gas mixture and the pressure are constants in time, and one ignores the variation in time of bulk flow kinetic energy in the energy flux balance. We used this procedure in order to obtain a good first approximation to τ and to its temperature dependence. However the analysis was refined by using a procedure similar to Kiefer's¹¹ to account for the finite perturbations. It should be stressed that one cannot avoid assuming the validity of eq. (1), nor avoid ambiguities resulting from use of the correction factor $C_p/(C_p - C_{vib})$. The latter arise from the laser

schlieren's basic limitation in having to make assumptions about the thermochemistry of the process. In this case it takes the form of assuming whether the observed relaxation is that of only some (i.e. the slowest) modes or of all modes of vibration (9 for CH_4 , 12 for C_2H_4). In the Blackman procedure it involves estimating C_{vib} ; in a more rigorous procedure it involves estimating ϵ itself. In this work we argue that all modes are relaxing simultaneously with the same time constant (at least near equilibrium). This is justified because it is possible to measure the total amount of energy relaxed during the observation period. This is done by integrating the measured rate of change of density to obtain $\Delta\rho$. It was found that by extrapolating to the time origin, that the measured $\Delta\rho$ is very close to what one would expect when all vibrational modes relax simultaneously. If some early relaxation process were occurring on a shorter time scale one would expect a correspondingly smaller $\Delta\rho$. That this was not so, and that during the observed relaxation zone there was no evidence of more than one different relaxation time, was taken to mean that all modes relax concertedly. Other systems studied in the past led to similar conclusions. It remains however, in principle, a basic ambiguity, since *except* by assuming one relaxation zone one cannot unambiguously assign the measured time variation of τ to either a temperature variation or to a variation in the number of modes relaxing. The basic advantage of the Blackman method is that there is no need for an absolute measure of the density gradient nor of the time origin.

A rigorous procedure due to Kiefer¹¹ makes use of the fact that one measures the rate of change of density at each point in time, and thus one can obtain an estimate of τ at each instant in time. Starting from eq. (1) one can show that

$$p\tau = - \frac{p[1 - d\epsilon_\infty/d\epsilon]}{\frac{d}{dt} \ln(\tau d\epsilon/dt)} \quad (2)$$

In the following: p , ρ , u , T , μ , h are the local pressure, density, gas-particle velocity, temperature, molecular weight, and specific enthalpy respectively. Symbols subscripted with "o" correspond to unshocked variables. Eq. (2) can be simplified if one notes that

$$\frac{d\epsilon}{dt} = \frac{d\epsilon}{d\rho} \frac{d\rho}{dy} \frac{dy}{dt_\ell} \cdot \frac{dt_\ell}{dt} = \frac{d\epsilon}{d\rho} \frac{d\rho}{dy} u_0 \frac{\rho_0}{\rho} \quad (3)$$

where t_ℓ is time in laboratory coordinates.

$$\text{Also} \quad \frac{d\epsilon_\infty}{d\epsilon} = \frac{d\epsilon_\infty}{dT} \frac{dT}{d\rho} \frac{d\rho}{d\epsilon} = C_{\text{vib}} \frac{dT}{d\rho} \frac{d\rho}{d\epsilon} \quad (4)$$

where C_{vib} is the vibrational contribution to the heat capacity of the gas. In Kiefer's original analysis, the factors $dT/d\rho$ and $d\rho/d\epsilon$ were evaluated numerically. Here we give analytical expressions based on a solution of the Hugoniot equations and their derivatives:

$$\rho u = \rho_0 u_0 \quad (5)$$

$$p + \rho u^2 = p_0 + \rho_0 u_0^2 \quad (6)$$

$$h + \frac{1}{2} u^2 = h_0 + \frac{1}{2} u_0^2 \quad (7)$$

$$\text{and} \quad p = \rho \frac{RT}{\mu} \quad (8)$$

$$\text{and} \quad u_0 h = x_0 \cdot (4RT + \epsilon) + (1 - x_0) 5RT/2 \quad (9)$$

where x_0 is the mole fraction of the relaxing component of the mixture, and where we have identified ϵ with all vibrational modes of a non-linear polyatomic molecule. The solution is:

AD-A122 200

PROCEEDINGS OF THE INTERNATIONAL SYMPOSIUM ON SHOCK
TUBES AND WAVES (13TH. (U) CALSPAN ADVANCED TECHNOLOGY
CENTER BUFFALO NY C E TREANDR ET AL. JUL 81

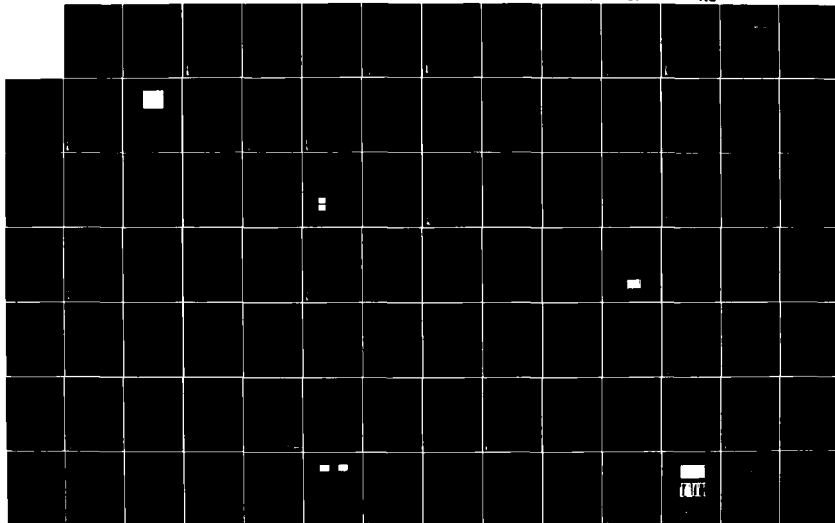
7/10

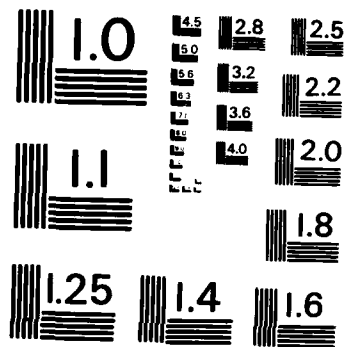
UNCLASSIFIED

AFOSR-TR-82-1031 F49620-81-C-0002

F/G 20/1

NL





MICROCOPY RESOLUTION TEST CHART
NATIONAL BUREAU OF STANDARDS-1963-A

$$u = \rho_0 u_0 / \rho \quad (10)$$

$$p = p_0 + \rho_0 u_0^2 (1 - \rho_0 / \rho) \quad (11)$$

$$RT = [RT_0 + \mu_0 u_0^2 (1 - \rho_0 / \rho)] \rho_0 / \rho \quad (12)$$

$$\frac{d\epsilon}{d\rho} = \frac{\rho_0}{X_0 \rho^2} \left\{ RT_0 (3X_0 + 5)/2 + \mu_0 u_0^2 \left[\frac{1}{2} + (2 + 3X_0/2)(1 - 2\rho_0/\rho) \right] \right\} \quad (13)$$

$$\text{and} \quad \frac{dT}{d\rho} = - \frac{\rho_0}{R\rho^2} [RT_0 + \mu_0 u_0^2 (1 - 2\rho_0/\rho)] \quad (14)$$

The factor $(1 - d\epsilon_\infty/d\epsilon)$ can be rewritten as $\frac{d\epsilon/dT - d\epsilon_\infty/dT}{d\epsilon/dT}$

and thus be recognized as the more exact analogue of the Blackman factor $C_p/(C_p - C_{vib})$. Indeed, if in the denominator of eq. (2), τ and ρ do not vary strongly with time, then eq. (2) reduces exactly to the Blackman form.

Measured voltages are directly proportional to laser beam deflection Δ . Δ is related to the density gradient via

$$\Delta = \kappa D l d\rho/dy \quad (15)$$

where l is the width of the shock tube, D the detector distance to the shock tube, and κ is the Gladstone-Dale constant for the gas mixture. The latter is a mass fraction average over the κ 's of the individual component gases. For argon it is 0.159, for methane 0.628, and for ethylene 0.388 cm³g⁻¹. Thus $d\rho/dy$ is easily determined. One then integrates the measured density gradient backwards in time to a point where the resulting $\Delta\rho$ equals that expected for the whole relaxation process. In this work such time origins were consistently close to the arrival of the shock front at the laser beam (as given¹⁴ by Kiefer's procedure). Such integrations result in precise assignment of ρ to each time-point. From this, the remaining thermodynamic variables (eqs. 10 - 14) can be obtained.

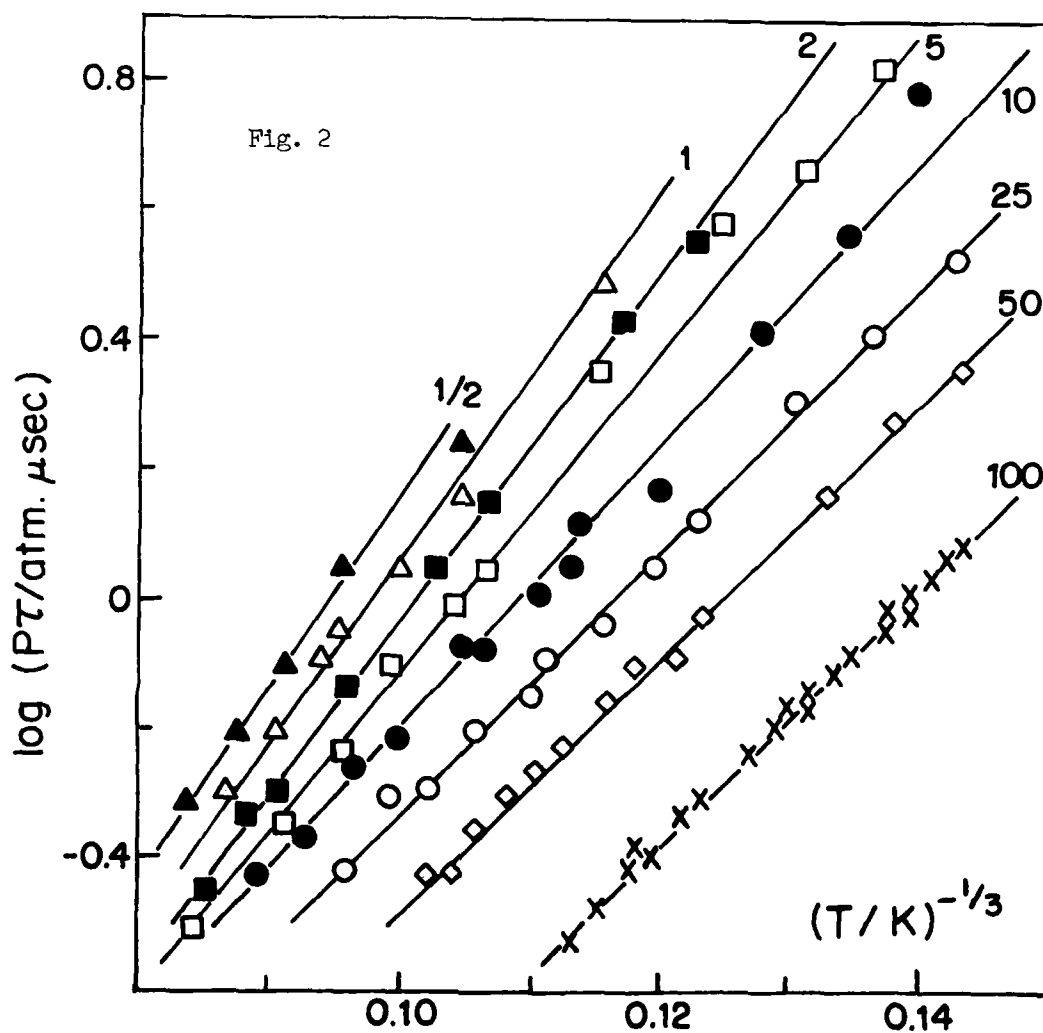
The denominator of eq. (2) is obtained iteratively by determining the slope at time t of a graph of $\ln\tau + \ln(d\epsilon/dt)$ vs t . If the graphs are plotted vs t_ℓ , then the slopes are multiplied by ρ_0/ρ in order to convert to gas-time. As a first approximation one uses the value of τ obtained by the Blackman method. In this work τ was not very temperature dependent, nor did the temperature vary much with time. Therefore the first term in $\ln\tau + \ln(d\epsilon/dt)$ was nearly constant, and the slope was not sensitive to the initial choice of τ . The value of τ determined from eq. (2) was usually not significantly different from the Blackman result, but it was subsequently used as a better approximation in the denominator. One iteration was sufficient in all cases.

One might expect that a procedure which relies on measuring density gradients absolutely would be sensitive to exact measures of calibration factors and of locating the time origin and baseline precisely. However, as seen above, the procedure is still *primarily* a log plot vs time, and only incidentally accounts (but not very sensitively) for modest variation of thermodynamic variables, whose estimation depends not very critically on an exact assignment of the time origin and of the baseline. Thus, as far as time constants are concerned, one need not be very exacting. However $\Delta\rho$ is sensitive to locating the time origin exactly, and here care is indeed needed. Proper location of the time origin involves determining the extent of diffraction of the laser beam interacting with the curved shock front¹⁴. One should also correct for the finite width of the laser beam¹, and correct for non-unidimensional flow behind the shock front¹⁵. A good guide to estimating the extent of the shock front curvature is given by De Boer¹⁶.

One subtle but serious error that can be made is mentioned here. The location of the baseline (i.e. zero-voltage modulation) is crucial to measuring density gradients accurately near equilibrium. It is normally located by ensuring that the oscilloscope sweep is triggered somewhat in advance of shock arrival. However the intrinsic thickness of the baseline, plus the onset of small signals due to boundary layer growth at late times, and even the noise on the signal itself can cause a profound error in a near-zero signal. An odd $\tau(t)$ would result from a point-by-point analysis. In this work the baseline was systematically adjusted by amounts imperceptible to the eye. For each case τ was measured as a function of time. The time variation was attributed to temperature variation. Thus one could measure $\tau(T)$ for each experiment. This was compared to the temperature dependence of τ as given by the results of all experiments analyzed by the Blackman procedure. The baseline was adjusted until the temperature dependences coincided. Such a procedure is valid only if one ascertains from measurements at earlier times (where the baseline does not influence τ) that a single pure relaxation time is involved. It is felt that this procedure fixes the baseline precisely and gives results which are more internally consistent.

RESULTS

Fig. 2 shows the measured relaxation times for CH_4 in mixtures with argon, as a function of temperature. Reproducibility is within 2%. The lines are



two-parameter least square fits, and are labelled with % CH₄. Ethylene relaxes about 4 times faster than methane in the same temperature range. The associated increase in the measuring difficulty is reflected in the poorer precision, as can be seen in figure 3.

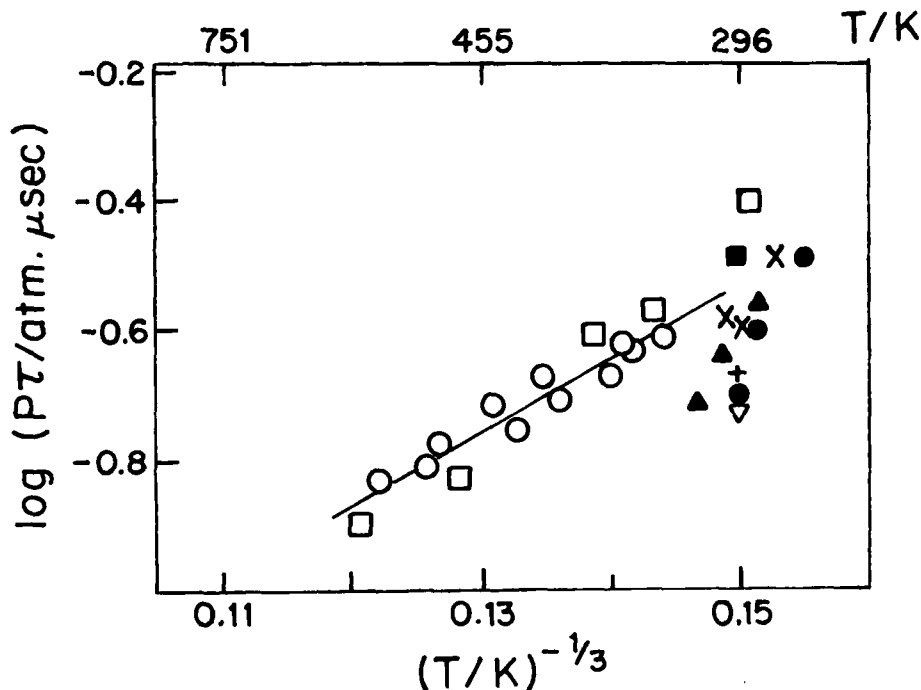


Fig. 3. Vibrational relaxation times of pure C₂H₄: ○ This work; ● McGoubrey¹⁷; X McGrath¹⁸; ▲ Richards¹⁹; □ Corran, Lambert et al²⁰; ▼ Edmonds²¹; ■ Arnold²²; + Nomoto²³. The line is a least squares fit to the data of this work.

In the absence of the present results it would be very difficult to assess the measurements of earlier workers who used ultrasonic dispersion techniques¹⁷⁻²³. The present results confirm those of Lambert²⁰ who took care to use relatively pure ethylene. The author is not aware of any shock tube results with which to compare his results. One can however compare the methane measurements with those of Simpson which are also obtained by the laser schlieren technique²⁴. Agreement is excellent. Fig. 4 shows the results of early workers using ultrasonic dispersion^{25-27, 29, 30}. The latter are less precise than those from the shock tube studies, but they agree on the whole very well with the present results.

DISCUSSION

The precision of the results in fig. 2 allows us to sensitively test the linear mixture rule. For each individual mixture they were fitted to straight lines: $\log p\tau$ vs $T^{-1/3}$. For a given temperature, $1/p\tau$ was interpolated from each mixture line, and plotted as a function of mole fraction in fig. 5. With only 5% measurement uncertainty, the curvatures observed are significant. Deviations from the linear mixture rule is most pronounced at the highest temperatures and at mole fractions < 0.02 . Similar results have recently been observed for N₂O³¹ and for C₂H₆³². Only one other experimental shock tube study showed such behaviour. Glärzer³³ used UV absorption of the individual vibrational states of NO mixed with argon at mole fractions as low as 0.0006. The very strong deviation at $X_{NO} < 0.02$ enabled the extraction of detailed rate constants in the mechanism for the equilibration of NO. In the same way

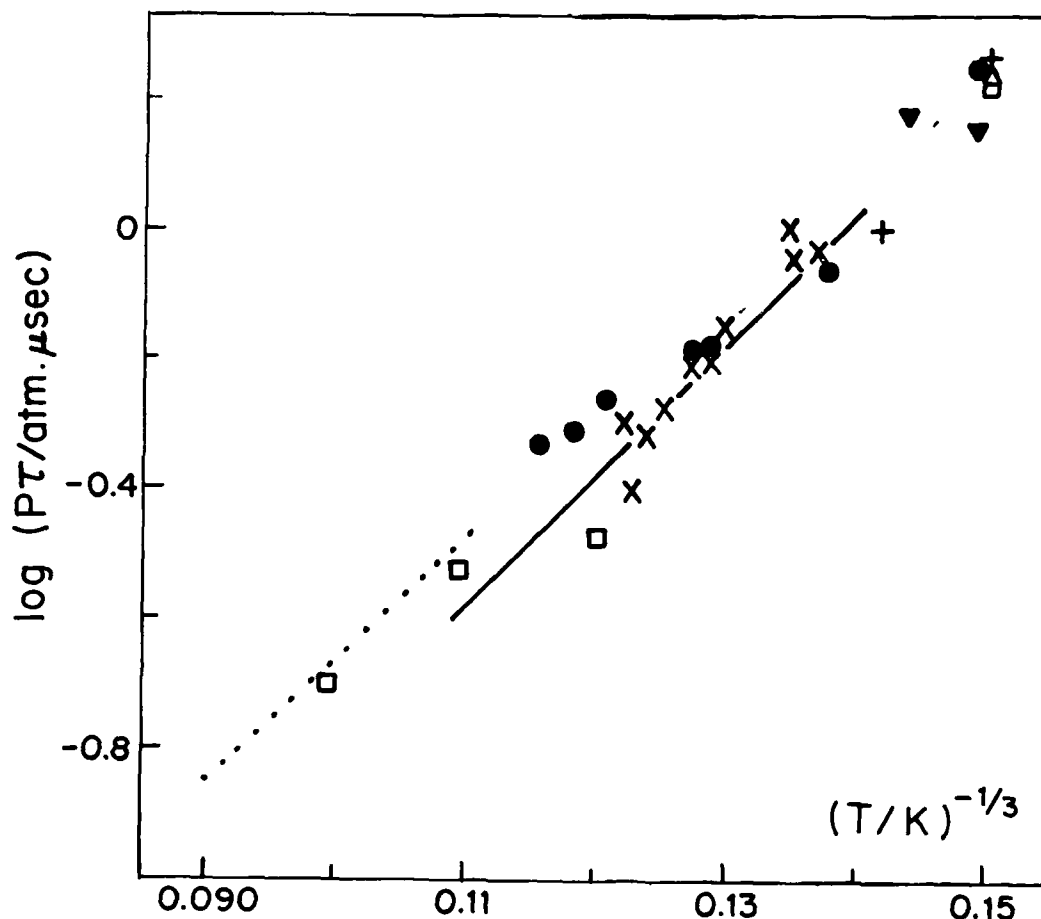


Fig. 4. Vibrational relaxation times of pure CH_4 . — This work (from fig. 2); X Jackson et al.²⁴; \square Hill and Winter²⁵; Richards and Sigafos²⁶; \bullet Eucken and Aybar²⁷; \blacktriangle Moore²⁸; + ∇ Ottrell et al.^{29,30}.

curvature of the present results indicate that it might be possible to extract more information about energy transfer in the CH_4 - Ar system. It is not likely though that the present results have much to do with V-V processes, since the laser schlieren observations are insensitive to such basically thermoneutral reactions.

One need hardly emphasize the errors that are inherent in using linear mixture rules at high dilutions. If one were to extrapolate the low mole fraction end of the curve at 1371 K to $X_{\text{CH}_4} = 1$ one would be in error by a factor of 15. Linearly extrapolating the high mole fraction end of the curve to $X = 0$ would cause an error of a factor of 2. However the error could be substantially larger if, as in the case of NO, even more profound curvature were found to exist at mole fractions less than 0.005.

CONCLUSIONS

It has been demonstrated that the vibrational relaxation rates of polyatomic molecules can be measured in shock tubes, especially if diluted by inert gases. It has also been demonstrated that great care should be exercised when using linear mixture rules in chemical kinetics.

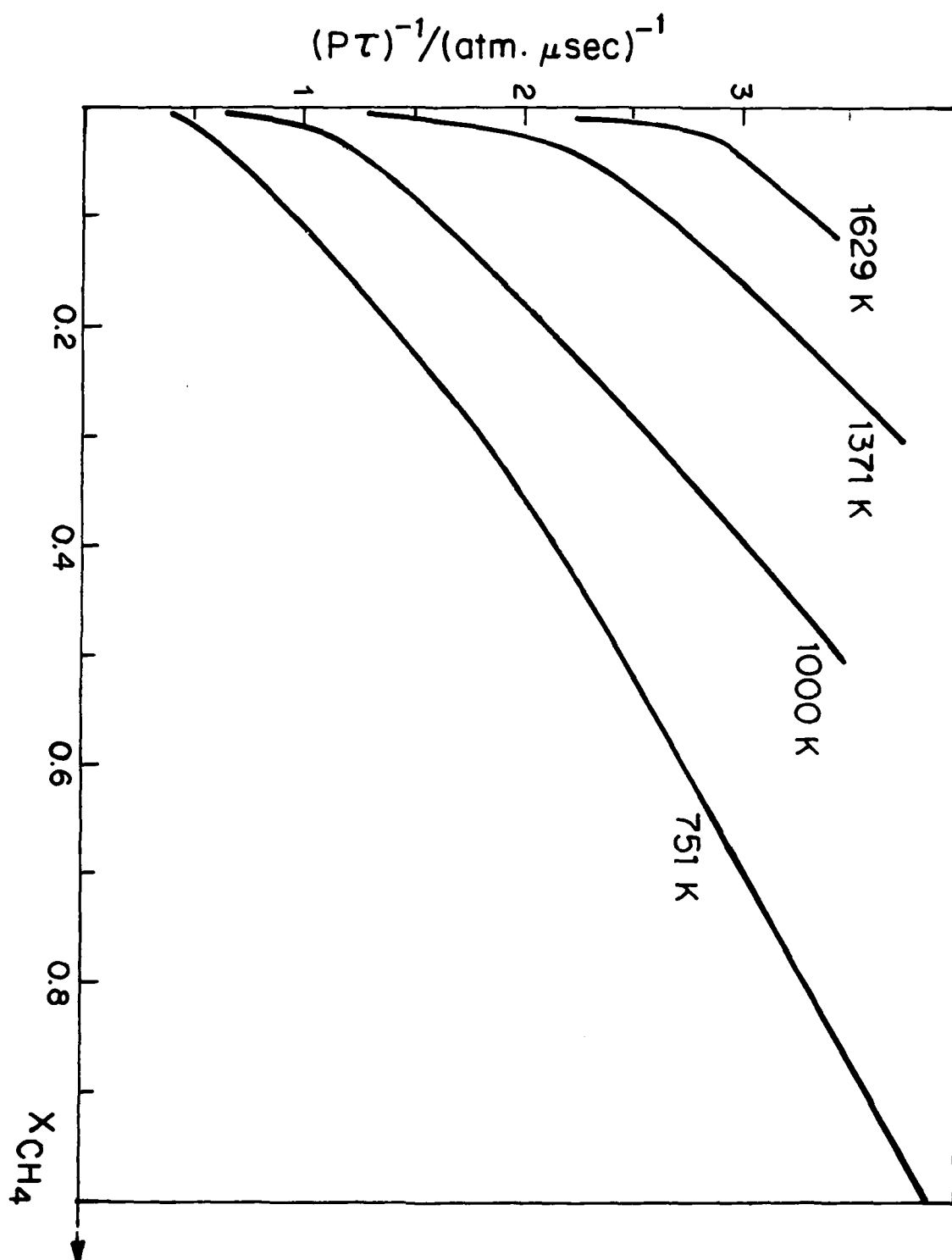


Fig. 5. Non-linear mixture rule for CH_4 -Ar vibrational relaxation. Typical uncertainties are of the order of 5%.

REFERENCES

1. J. E. Dove, H. Teitelbaum. *Chem. Phys.* 6, 431 (1974).
2. W. D. Breshears, P. F. Bird, J. H. Kiefer. *J. Chem. Phys.* 55, 4017 (1971).
3. J. H. Kiefer. *J. Chem. Phys.* 61, 244 (1974).
4. J. E. Dove, H. Teitelbaum. *Chem. Phys.* 40, 87, (1979).
5. J. E. Dove, W. S. Nip, H. Teitelbaum. *Proceedings of 15th Symp. (Internat.) on Combustion*, The Combustion Institute, p. 903, Pittsburgh (1975).
6. T. L. Cottrell, J. C. McCoubrey. *Molecular Energy Transfer in Gases*, London, Butterworths (1961).
7. J. Troe. *Ber. Bunsen Ges. Phys. Chem.* 84, 829 (1980).
8. R. K. Boyd. *Can. J. Chem.* 55, 802 (1977).
9. V. Blackman. *J. Fluid Mech.* 1, 61 (1956).
10. JANAF Thermochemical Tables, NBS, 2nd ed. (1972).
11. J. H. Kiefer. *J. Chem. Phys.* 44, 658 (1966).
12. C.J.S.M. Simpson, T. R. D. Chandler, *Proc. Roy. Soc. A* 317, 265 (1970).
13. J. H. Kiefer, M. Z. Al-Alami, J.-C. Hajduk. *Appl. Optics* 20, 221 (1981).
14. H. Teitelbaum, PhD Thesis, U. of Toronto (1974), App. G.
15. P. C. T. DeBer. *Phys. Fluids* 6, 962 (1963).
16. J. C. McCoubrey, J. B. Parke, A. R. Ubbelohde. *Proc. Roy. Soc. A* 223, 155.
17. W. D. McGrath, A. R. Ubbelohde. *Proc. Roy. Soc.* 227A, 1 (1957).
18. W. T. Richards, J. A. Reid. *J. Chem. Phys.* 2, 206 (1934).
19. P. G. Corran, J. D. Lambert, R. Salter, B. Warburton. *Proc. Roy. Soc.* 244A, 212 (1958).
20. P. D. Edmonds, J. Lamb. *Proc. Phys. Soc. Lond.* 72, 940 (1958).
21. J. W. Arnold, J. C. McCoubrey, A. R. Ubbelohde. *Proc. Roy. Soc.* 248A, 445.
22. O. Nomoto, T. Ikada, T. Kishimoto. *J. Phys. Soc. Japan* 7, 117 (1952).
23. J. M. Jackson, P. A. Lewis, M. P. Skirrow, C.J. S. M. Simpson. *J. Chem. Soc. Faraday Trans II. Chem. Phys.* 75, 1341 (1979).
24. G. L. Hill, T. G. Winter. *J. Chem. Phys.* 49, 440 (1968).
25. I. W. Richards, D. H. Sigafos, *J. Chem. Phys.* 43, 492 (1965).
26. A. Eucken, S. Aybar. *Z. Phys. Chem.* B46, 195 (1940).
27. a) J. T. Yardley, C. B. Moore. *J. Chem. Phys.* 49, 1111 (1968).
b) P. F. Zittel, C. B. Moore. *J. Chem. Phys.* 58, 2004 (1973).
28. T. L. Cottrell, A. J. Matheson. *Trans. Faraday Soc.* 58, 2336 (1962).
29. T. L. Cottrell, P. E. Martin, *Trans. Faraday Soc.* 53, 1157 (1957).
30. J. E. Dove, W. S. Nip, H. Teitelbaum (to be published)
31. J. E. Dove, Y. Grant (to be published)
32. K. Glänzer. *Chem. Phys.* 22, 367 (1977).



AD P000280

VIBRATIONAL RELAXATION AND DISSOCIATION RATE MEASUREMENTS
IN POLYATOMIC MOLECULES

M. Tyaga Raju, S.V. Babu*, Y.V.C. Rao and V. Subba Rao

Department of Chemical Engineering, I. I. T.
Kanpur, 208016, India

✓ Laser schlieren technique has been used to obtain vibrational-vibrational energy transfer and dissociation rates in some polyatomic molecules behind incident shock waves. A series mechanism was postulated in the earlier studies to explain the measured energy transfer rates in SO_2 obtained using the ultrasonic and laser induced fluorescence techniques. Our experimental and calculated results on SO_2 show a double relaxation and energy transfer by a series process at low temperatures and a complex series-parallel process at higher temperatures. Our measurements of the dissociation rates in SO_2 - rare gas mixtures show that the rates depend on the mixture composition. Preliminary experiments in CH_4 -Ar mixtures indicate single exponential relaxation.

INTRODUCTION

Intermolecular and intramolecular energy transfer studies in polyatomic molecules have been widely studied during the past few years. In general, the intramolecular vibrational-vibrational energy transfer rates are quite fast compared to the V-T/R rates such that the vibrational modes attain equilibrium distribution rapidly resulting in the relaxation of energy by a single V-T step involving usually the lowest vibrational mode. However, it has been noticed in some molecules especially when the energy of the lowest vibrational mode is less than the energy difference between it and the next higher mode, more than one relaxation step characterises the process. SO_2 is one such molecule to exhibit such a behaviour. Several experimental techniques have been employed to investigate it. These include ultrasonics, laser induced fluorescence and shock waves. Initial experimental studies were all confined to low temperatures. In a molecule with several vibrational modes there are several pathways for energy transfer: a parallel process where energy passes from translational degrees to different vibrational modes independently, a series process in which the lowest vibrational mode receives energy from translation followed by V-V transfer

*Presently at Clarkson College of Technology, Dept of Chem. Engg. Potsdam, N.Y. 13676.

570

process and finally a more complex series-parallel process where more than one vibrational mode is involved in a V-T process followed by faster V-V processes. Lambert and Salter (1) required two relaxation times to explain their ultrasonic dispersion measurements in gaseous SO_2 . Shields and Anderson (2) calculated energy transfer probabilities from ultrasonic absorption studies in SO_2 - Ar mixtures over a temperature range 300 - 500 K using the series mechanism. Siebert and Flynn (3) used the laser induced fluorescence technique at room temperature to estimate the energy transfer probabilities in SO_2 . Theoretical calculations of Dickens and Linnett (4) at these temperatures are at variance with these experimental results. Further, the thermal dissociation rates of SO_2 obtained by various experimental techniques differed considerably. Hence, a study of vibrational relaxation and dissociation rates have been measured over a wide temperature and composition range.

EXPERIMENTAL

The experimental setup is described elsewhere (5,6). The driver section of the shock tube was 15.3 cm ID and 1.68 m long ss cylindrical tube and the low pressure section a 9.85 cm ID and 5.72 m long honed ss cylindrical tube. The two tubes were joined together by an intermediate tapered ss section which was permanently attached to the high pressure section. The two sections could be locked together or unlocked by means of a coupling device. The driven section could be evacuated to 2×10^{-5} torr by a 4" silicone oil diffusion pump backed by a roughing pump. The combined leak and degassing rate in the low pressure section was measured intermittently and was found to be less than 5×10^{-4} torr/min. The driver section was evacuated by a separate mechanical pump. Shock waves were generated by bursting mylar sheets of 0.005" thickness by a pneumatically operated mechanical plunger. Mixtures of $\text{H}_2 + \text{N}_2$ were used as the driver gas to obtain the required variations in the shock velocity. The shock speed was measured by means of gold resistance thermal gauges mounted flush with the walls of the shock tube. The rise time of the thin film gauges was found to be about a microsecond.

The observation station i.e. the point where the laser beam passed through the shocktube was located 5 cm downstream of the last thin film gauge and 3.5 cm before the end plate. It was ensured that there was no interference from the reflected shock wave. Glass windows of 1" dia. were mounted flush with the wall in plexiglass adaptors which were cleaned regularly with lens paper. The 6328 Å laser beam from a 0.5 mw Spectra Physics model 156 He - Ne laser passed through the shock tube normal to its axis through these windows. The laser beam emerging from the shock tube was reflected by an aluminum coated surface of a quartz prism to fall on a knife edge. The distance between the center of the tube and the prism was 1.35 m and that between the prism and the knife edge was 5.5 m. The quartz prism was mounted on a platform which in turn was fixed on the shaft of a synchronous motor. A straight edge of a razor blade was used as a knife edge. It was mounted such that it could be moved smoothly in a plane perpendicular to the laser beam to cut it along its vertical axis. The light that was not cut off by the knife edge was collected by a 7 cm dia. lens and focussed onto a type HP type 5082 - 4203 pin photodiode. The whole assembly was mounted on a device which could be moved in the X,Y, and Z directions. The diode could be adjusted very precisely to receive all the light collected by the lens. The photodiode output after suitable amplification was fed directly to a Tek type 1A5 plugin amplifier and a Tek type 549 storage oscilloscope which was operated in a single sweep mode and externally triggered with the signal from the thin film gauge just ahead of the observation station. The overall response time of the system was measured by recording schlieren signals in argon which was found to be about 0.12 microsecond.

MATERIALS

A GLC analysis of SO_2 gas used in the experiment showed the presence of about 2% of combined O_2 and N_2 as impurities. A purified sample of SO_2 by repeated freezing, evacuation and melting gave identical results as the cylinder gas. Hence, The cylinder gas was directly used along with high purity Matheson

helium (99.995%) and ultra high purity argon (99.999%) from Indian Oxygen LTD. CH₄ is of Matheson research grade (99.99%) purity.

EXPERIMENTAL RESULTS

Experiments were first conducted in pure CO₂ in the temperature range 600 - 1600 K. The schlieren trace yielded single exponential decay throughout the relaxation region without any observable deviation. The data obtained agreed quite well with other laser schlieren data on CO₂. This ensured satisfactory performance of the experimental setup. Density gradient profiles in incident shock waves were obtained in pure SO₂ in the temperature range 550 - 1200 K. It was noticed that in a semilog plot of intensity versus time the first few points deviate from the straight line drawn through the rest of the points. Such a behaviour was absent in the case of CO₂. The final slopes of such straight lines ignoring the first few points were converted to vibrational relaxation times. The relaxation times were plotted on Landau - Teller plots ($\log P\tau$ vs $T^{-1/3}$) and a least square analysis of the data gave the following equation.

$$P = \exp (- 2.71 + 9.3 T^{-1/3})$$

Mixtures Of Argon In SO₂

Relaxation measurements were carried out in mixtures of SO₂ and argon at different compositions. The density gradient profiles show the same behaviour as in pure SO₂; the initial points deviate from a straight line drawn through the later points. In order to obtain precise information about the nature of this deviation, two oscilloscopes were simultaneously used to obtain the complete time history of the decay of the signal right from the beginning. In the regular experiments, the earlier part of the trace was off scale. For this reason, the vertical scale in one of the scopes was compressed by a factor of five thus obtaining the total trace. On analysis, the trace obtained in 11% SO₂ - Ar mixture at $p_1 = 5.0$ torr yielded two relaxation zones, one fast and one slow with two time constants; $\tau_1 = 0.28$ microseconds and $\tau_2 = 1.04$ microseconds. τ_1 is more than twice the time constant for the system. However, no effort was made to analyse the faster process in view of its closeness to the system constant. It may be surmised that SO₂ does relax with two relaxation times corresponding to a faster and a slower process.

An analysis of the mixture data using the mixture rule

$$\frac{1}{PT_{mix}} = \frac{X}{PT_{SO_2 - SO_2}} + \frac{1 - X}{PT_{SO_2 - M}}$$

where (PT)_{mix} is the relaxation time at 1 atm for the mixture, (PT)_{SO₂-SO₂} is the relaxation time at 1 atm for pure SO₂, (PT)_{SO₂-M} is the relaxation time at 1 atm for SO₂ infinitely diluted in the rare gas M and X is the mole fraction of SO₂ in the mixture. A least square analysis of the data gave the following equations :

$$(PT)_{SO_2 - SO_2} = \exp (- 2.96 + 11.9 T^{-1/3})$$

$$(PT)_{SO_2 - Ar} = \exp (- 4.65 + 40.32 T^{-1/3})$$

$$(PT)_{SO_2 - He} = \exp (- 7.58 + 54.68 T^{-1/3})$$

Energy Transfer Mechanism

Shields and Anderson analysed their ultrasonic absorption data in SO_2/Ar mixtures using the series mechanism in which the lowest vibrational mode of SO_2 is first activated by a fast V - T step followed by the excitation of the ν_1 mode via the $2\nu_2$ mode by a slow V-V step which finally equilibrates with the ν_3 mode by a fast V-V energy transfer process. The results from the laser induced fluorescence studies at room temperature were also in agreement with the above analysis. The present density gradients which show double exponential behaviour confirms two relaxation processes; one a fast and the other a slow process. However, these results cannot substantiate whether the stretching modes received energy through a series, parallel or a complex series/parallel process? It is, in fact impossible to distinguish between these by measuring bulk relaxation rates.

It is to resolve this difficulty that the various energy transfer probabilities have been estimated using the SSH-Tranczos theory in the temperature range 300 - 2000 K (7). In the following, the notation $P_{k-1}^{i-j}(a,b)$ represents the probability that the quantum state of mode a is changed from i to j while that of b is changed from k to l in a collision and states a, b and c refer to the ν_2 , ν_1 , ν_3 modes respectively. The results are shown in fig.1. It can be seen that at low temperatures, $p_{01}^{20}(a,b)$ and $p_{10}^{01}(a)$ alone are significant suggesting that at these temperatures, the energy relaxes via the series process $2\nu_2 \rightarrow \nu_1$ while ν_2 is activated by a V - T process. All this is in agreement with the experimental predictions. However, at and above 1000 K, $p_{10}^{01}(b,a)$ attains values equal to and / or larger than $p_{01}^{20}(a,b)$ while the value of $p_{10}^{01}(b)$ also rises rapidly suggesting that at high temperatures a complex series/parallel mechanism may dominate over a single step i.e. both ν_2 and ν_1 are activated by V - T processes.

Dissociation rates of SO_2 in $\text{SO}_2 + \text{Ar}$ mixtures at different compositions were measured behind incident shock waves over a temperature range of 4000 - 6000 K at initial pressures of 1.0 to 2.5 torr. The recorded signals exhibited two exponentials, a faster one due to vibrational relaxation and a slower one due to dissociation. The density gradient at the point of intersection of these two exponentials was used to obtain the initial dissociation rates. A least squares analysis of the data gave the following empirical relations.

$$k_{\text{SO}_2 - \text{Ar}} = 3.34 \times 10^{15} \exp \left(- \frac{107.6}{RT} \text{ k cal/mole} \right) \text{ cm}^3 / \text{mole sec.}$$

$$k_{\text{SO}_2 - \text{SO}_2} = 5.02 \times 10^{14} \exp \left(- \frac{66.6}{RT} \text{ K cal/mole} \right) \text{ cm}^3 / \text{mole. sec.}$$

which demonstrate a strong dependence of the rate on the composition.

Vibrational relaxation times of CH_4 in $\text{CH}_4 - \text{Ar}$ mixtures have been measured at various compositions over a temperature range 600 - 2000 K at initial pressures 1.0 to 2.5 torr. The schlieren signals exhibited single exponential behaviour till around 1800 K and a double exponential behaviour above this temperature. The double exponential behaviour above 1800 K is supposed to be due to appreciable amount of dissociation of CH_4 at these temperatures. A typical schlieren signal and its semilog plot are shown in fig.2. Similar to all schlieren signals, it shows a sharp positive spike due to the shock front arrival at the observation station followed by a slow decrease. The signals exhibited a single exponential behaviour till about 1800 K which is supposed to be due to vibrational relaxation in methane. The slopes of these lines were measured. The inverse of these slopes are the vibrational relaxation times in the laboratory time scale. The experiments are under progress and the data will be published on completion.

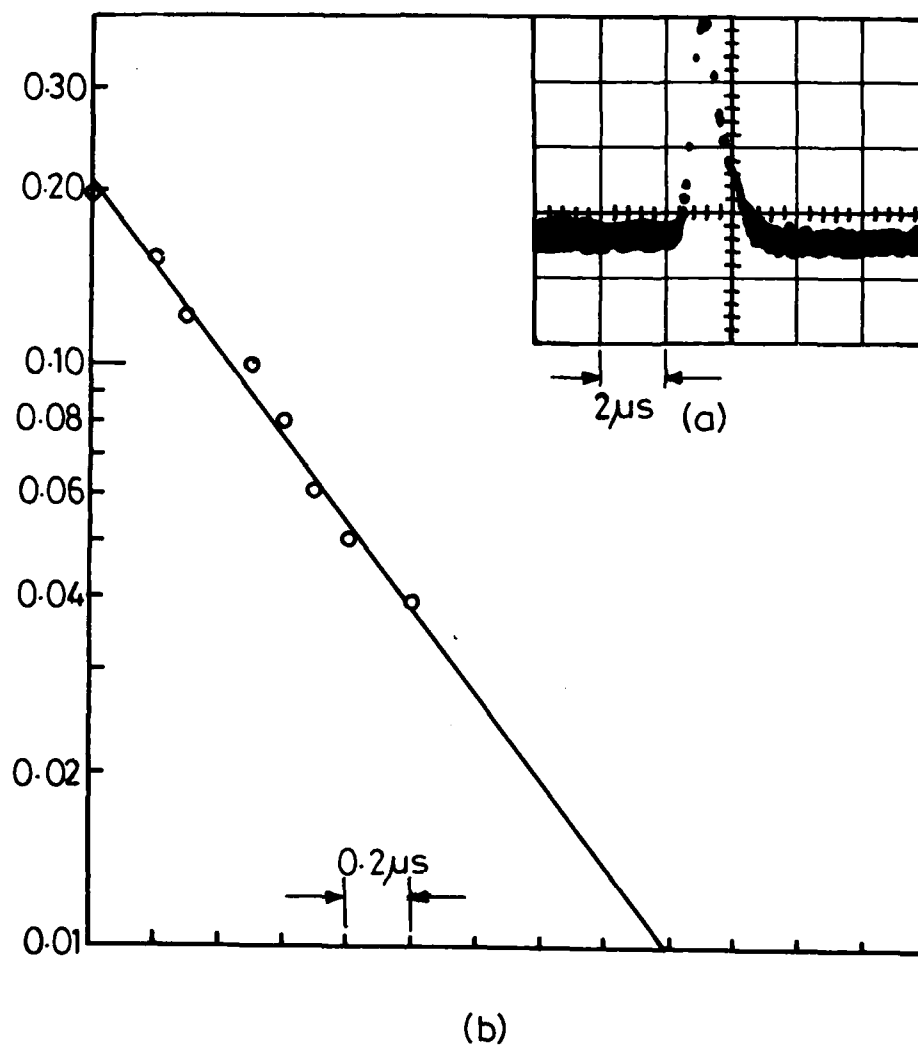


Fig. 2 - (a) A typical schlieren signal in CH₄-Ar mixture.
 CH₄ = 1%, $P_{\text{initial}} = 1$ torr, $U_1 = 108808.52 \text{ cm s}^{-1}$, $T_2 = 120^\circ \text{K}$.
 (b) Semi log Plot of the schlieren signal.

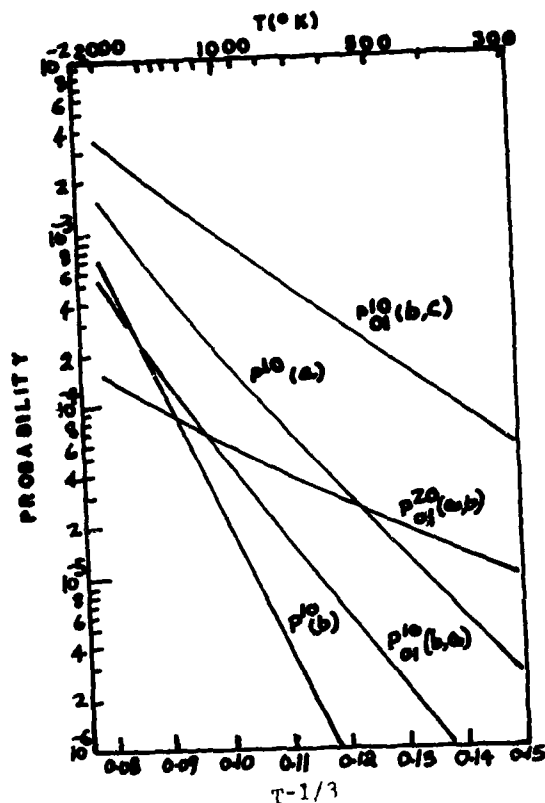


Fig. 1

Temperature dependence of
energy transfer probabilities

References

- (1) J.D. Lambert and R. Salter, Proc. Roy. Soc. A 243 (1957) 78
- (2) F.D. Shields and B. Anderson, J. Chem. Phys. 55 (1971) 2636
- (3) D. Siebert and G. Flynn, J. Chem. Phys. 62 (1975) 1212
- (4) P.G. Dickens and T.W. Linnett Proc. Roy. Soc. A 243 (1957) 84
- (5) V.V.N. Kishore, S.V. Babu, and V. Subba Rao, Chem. Physics 46 (1980) 297
- (6) M. Tyaga Raju, S. V. Babu and V. Subba Rao, Chem. Physics, 48 (1980) 411
- (7) Y.V.C. Rao, Chem. Phys. Letters, 62 (1979) 107

AD P000281

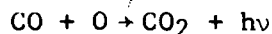
CO + O CHEMILUMINESCENCE: RATE COEFFICIENT
AND SPECTRAL DISTRIBUTION

A. Grillo and M. Slack

Research Department, Grumman Aerospace Corporation
Bethpage, New York 11714

ABSTRACT

Radiative combination of atomic oxygen and carbon monoxide



has been investigated at temperatures in the vicinity of 3000 K. The absolute spectral intensity of the chemiluminescence continuum was measured between 2400 and 7000 Å. An overall photon production rate coefficient of $I_0 = 4(\pm 4) \times 10^5 \text{ cm}^3 \text{ mole}^{-1} \text{ sec}^{-1}$ was obtained in the presence of argon. Combined with room temperature data our results yield a rate coefficient $I_0 = 6.0 \times 10^5 \exp(-1280/T) \text{ cm}^3 \text{ mole}^{-1} \text{ sec}^{-1}$ in the temperature range 300 to 3000 K. The influence of selected third bodies upon the chemiluminescence was also investigated.

INTRODUCTION

Chemiluminescence from the radiative combination of atomic oxygen and carbon monoxide

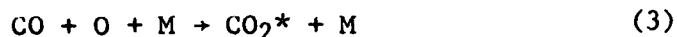


is often observed in the spectra of flames (Refs 1 and 2) and has been used as a diagnostic to measure the atomic oxygen concentration in combustion processes (Refs 3 and 4). High temperature rate coefficient measurements of this chemiluminescent reaction exhibit considerable scatter (Ref. 5) and no study has been conducted on the influence of third bodies at elevated temperatures. The objective of the present investigation was to measure the rate coefficient and spectral distribution for Reaction 1 at temperatures around 3000 K and to determine the influence of selected third bodies.

The emission intensity I from Reaction 1 has been observed (Ref. 5) to follow the second order dependence

$$I = I_0 [CO] [O] \quad (2)$$

which is compatible with the following mechanism



A steady-state analysis yields

$$I = k_3 k_4 [CO] [O] [M] / (k_4 + k_5 [M]) \quad (6)$$

and for $k_5 [M] \gg k_4$ this gives

$$I_0 = k_3 k_4 [CO] [O] / k_5 \quad (7)$$

which leads directly to Eq. 2 with $I_0 = k_3 k_4 / k_5$ in units of $\text{cm}^3 \text{ mole}^{-1} \text{ sec}^{-1}$. Note that while the intensity is independent of the concentration of the third body collision partner M, it has been observed to depend on the nature of the third body (argon, oxygen and nitrogen).

EXPERIMENTAL TECHNIQUE

Mixtures of CO - N₂O - argon were heated behind reflected shock waves in a conventional 3.81 cm i.d. stainless steel shock tube, which has been previously described (Refs. 6 and 7). Upon shock heating the N₂O rapidly dissociates to yield O atoms. Our approach was to measure the spectral distribution of the absolute intensity (A_λ) from Reaction 1, which when converted to a spectral rate and integrated yields the total photon production rate coefficient (I_0). Experimental conditions in the reflected shock region were typically 3000 K at a pressure of 3 atm; 3000 K was selected to facilitate comparison with previous data.

The CO was 99.99% pure, the argon diluent was 99.999% pure and the nitrous oxide was 99.99% pure. Gases were supplied by Matheson and used without further purification. Details of the gas handling, shock velocity measurement, and experimental procedures have been described previously (Ref. 6).

Absolute spectral intensity (A_λ) of the chemiluminescence continuum was measured between 2400 and 7000 Å, using narrow band interference filters (bandwidth ~100 Å) and an EMR 547 E-05M-14 photomultiplier whose cathode quantum efficiency was calibrated against NBS standards. An oscillogram of emission at 3000 Å is shown in Fig. 1. The radiating volume was carefully defined by a series of apertures and baffles. Concentrations of the shock heated CO and O were computed from the measured incident shock velocity and initial mole fractions of CO and N₂O. It is tempting to assume that the N₂O dissociates completely and rapidly to N₂ and O, and to equate the initial O atom concentration with the initial shock heated N₂O concentration. However, that assumption overpredicts the O atom concentration and would result in an underprediction of A_λ . We computed the time dependent O atom concentration in

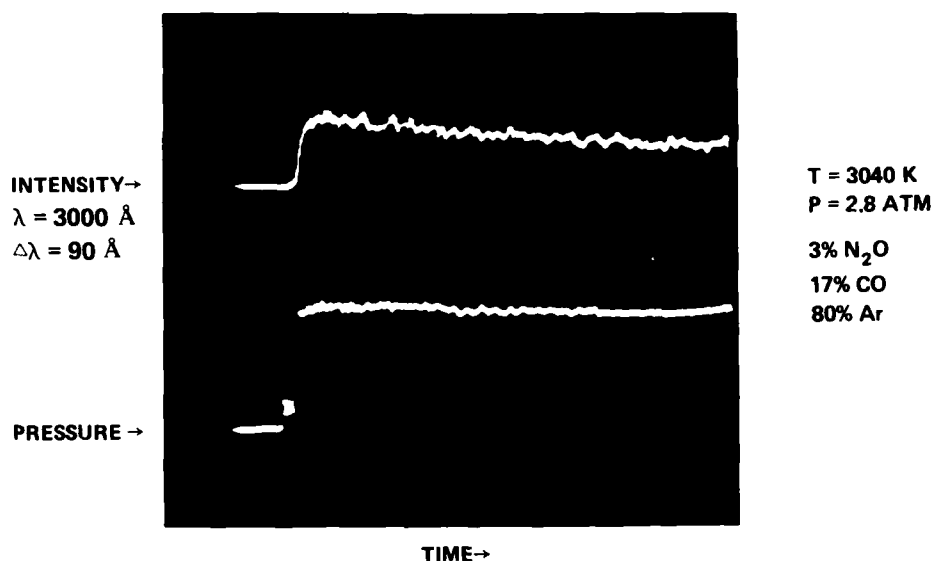


Figure 1. Sample CO + O Chemiluminescence Intensity and Pressure Records

CO-N₂O-argon mixtures using an 8 reaction model of N₂O dissociation (see Table 1), together with the standard CO/O₂ reactions. From the measured intensity, the known radiating volume and the computed reactant concentrations, the absolute spectral intensity per unit volume per unit concentration of O and CO was obtained.

TABLE 1 Nitrous Oxide Decomposition Mechanism

Reaction	Rate Coefficient ^a	Source
N ₂ O+M = N ₂ +O+M	$5 \times 10^{14} \exp(-29000/T)$	Ref. 19
N ₂ O+O = NO+NO	$4.1 \times 10^{13} \exp(-12350/T)$	Ref. 20
N ₂ O+O = N ₂ +O ₂	$4.4 \times 10^{13} \exp(-12350/T)$	Ref. 20
O ₂ +M = O+O+M	$1.8 \times 10^{18} T^{-1} \exp(-59380/T)$	Ref. 5
N ₂ +O = NO+N	$7.6 \times 10^{13} \exp(-38000/T)$	Ref. 19
NO+O = N+O ₂	$1.5 \times 10^9 T \exp(-19500/T)$	Ref. 19
NO+O ₂ = NO ₂ +O	$1.7 \times 10^{12} \exp(-23400/T)$	Ref. 19
NO ₂ +M = NO+O+M	$1.1 \times 10^{16} \exp(-33000/T)$	Ref. 19

^a Units: cm³ mole⁻¹ sec⁻¹

The majority of experiments were conducted with a mixture of 17 mole% CO and 3.0 mole% N₂O in an argon diluent. The influence of N₂ was investigated by working in a nitrogen diluent; other gas influences were investigated by addition to the argon diluent.

A basic test of the relationship in Eq. 2 was conducted at temperatures close to 3000 K and at a wavelength of 3000 Å. The results in Fig. 2 clearly demonstrate that the intensity is proportional to the product of O and CO concentrations for our experimental conditions.

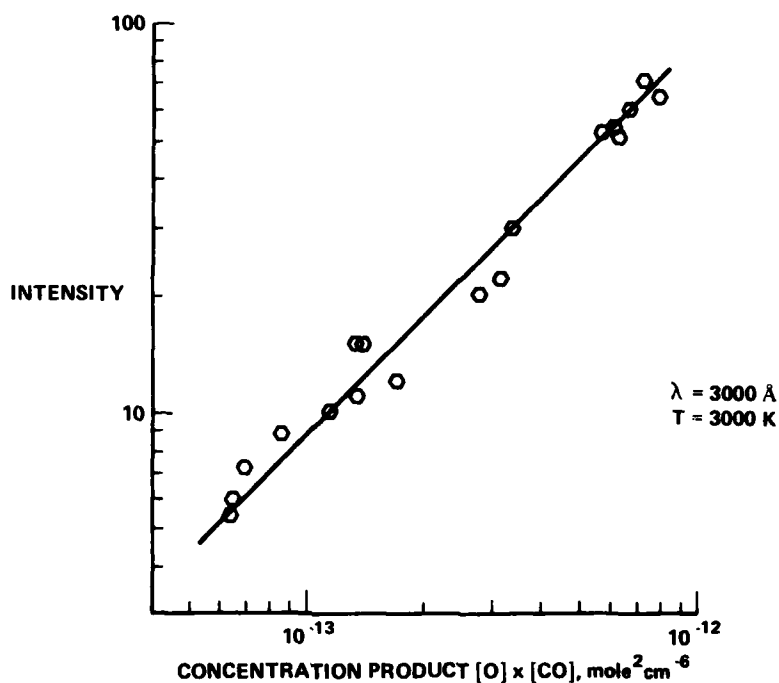


Figure 2. Experimental Confirmation of the Relationship $I \sim [O] \times [CO]$

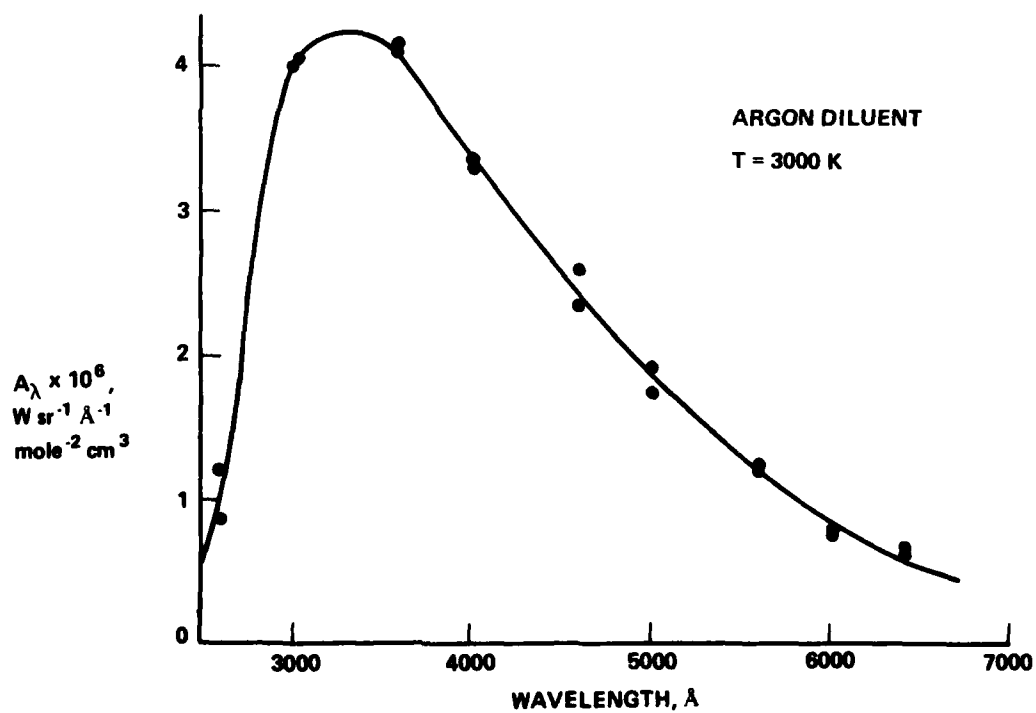


Figure 3. Absolute Spectral Intensity Distribution from CO+O Chemiluminescence Measured at 3000 K in an Argon Diluent

RESULTS

Our measurements at 3000 K of the absolute spectral intensity A_λ between 2400 and 7000 Å are shown in Fig. 3. The intensity was observed to peak about 3300 Å, and decays more rapidly at lower wavelengths than it does at longer wavelengths. Based on the recombination energy, no chemiluminescence would be expected below 2260 Å.

The A_λ data in Fig. 3 was converted to spectrally dependent rate coefficients for Reaction 1; integration yields a total rate coefficient for Reaction 1 of

$$I_0 = 4(\pm .4) \times 10^5 \text{ cm}^3 \text{ mole}^{-1} \text{ sec}^{-1} \quad (8)$$

at 3000 K in the presence of argon.

The influence of other diluents (or additives) on A_λ was investigated at 3000 Å. Changing from an argon to a nitrogen diluent had no effect on A_λ . Similarly, the addition of CO_2 in percentages up to 10% had a negligible influence on A_λ . In marked contrast, the addition of H_2 , in mole percentages ranging from 0.1 to 5, caused a reduction in the observed intensity (e.g. a 50% decrease in intensity for 0.5% H_2). This influence of H_2 is attributed to the competing and conflicting effects of (1) O atom removal by reactions with H_2 , (2) possible quenching of the chemiluminescence by hydrogenous species, and (3) thermal emission of OH in the 3064 Å band. Measurements at wavelengths other than the 3000 Å band filter could eliminate the last concern, but decoupling the first two effects would require analysis beyond the scope of the present investigation.

DISCUSSION

Earlier work on $\text{CO} + \text{O}$ chemiluminescence is discussed and compared with the current results.

Rate Coefficients

The rate coefficient I_0 and its temperature dependence have been investigated in discharge flow experiments, in a flow discharge shock tube, in a shock tube, in a stirred discharge flow study, in a flame, and in a reaction vessel. Fig. 4 presents an Arrhenius plot of these I_0 measurements.

Clyne and Thrush (Refs. 8 and 9) measured I_0 in a discharge flow tube between 200 and 300 K. The proportionality of Eq. 2 was established, and I_0 was found to be dependent on the nature of the third body M (see Table 2), but independent of the pressure of the third body.

Hartunian et al. (Ref. 10) employed a flow discharge shock tube to measure the ratio of chemiluminescent intensities across a weak shock in a CO/O_2 mixture and obtained $I_0 = 10^6 \exp(-1260/T) \text{ cm}^3 \text{ mole}^{-1} \text{ sec}^{-1}$ between 350 and 1600 K. This rate coefficient is based on a ratio involving I_0 from Clyne and Thrush, and is therefore dependent on the accuracy of their data.

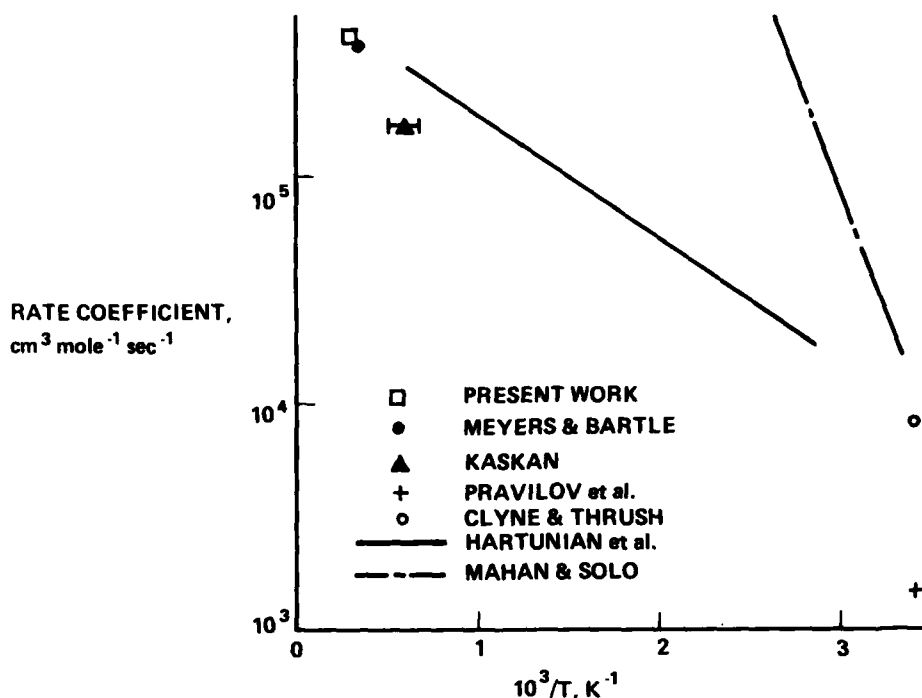


Figure 4. Rate Coefficients for the Reaction $\text{CO} + \text{O} \rightarrow \text{CO}_2 + \text{h}\nu$ in an Argon Diluent (References cited in text).

Meyers and Bartle (Ref. 11) made absolute spectral intensity measurements from shock heated O, CO and argon mixtures at pressures between 0.5 and 1.0 atm and at temperatures of 2679 and 2943 K. They used shock heated ozone as the source of O atoms. The spectral intensity at 2943 K was reduced to a rate constant of $3.80 \times 10^5 \text{ cm}^3 \text{ mole}^{-1} \text{ sec}^{-1}$ in the presence of argon; at 2679 K a rate constant of 3.83×10^5 may be obtained.

In a stirred discharge flow reactor at temperatures between 300 and 530 K, Mahan and Solo (Ref. 12) investigated radiative recombination and also the overall rate of recombination of CO and O to form CO_2 . Their rate coefficient for Reaction 1, $I_0 = 1.4 \times 10^{11} \exp(-4790/T)$ has an activation energy which is incompatibly high with respect to all other data.

Kaskan (Ref. 13) investigated CO + O chemiluminescence in premixed $\text{CO}/\text{H}_2/\text{air}$ and $\text{CO}_2/\text{H}_2/\text{air}$ flames. In the temperature range 1500 to 1900 K, Kaskan estimates a rate constant of $1.63 \times 10^5 \text{ cm}^3 \text{ mole}^{-1} \text{ sec}^{-1}$, which is low compared to the results of Hartunian et al.

Pravilov et al (Ref. 14) measured I_0 at 293 K, using a reaction vessel into which mixtures of CO, O and He were introduced, and obtained $1.5 \times 10^3 \text{ cm}^3 \text{ mole}^{-1} \text{ sec}^{-1}$ in excess helium. This is low compared to the results of Clyne and Thrush (Ref. 8) at the same temperature.

Our own measurements are in good agreement with the early work of Meyers and Bartle, and with the results of Hartunian et al. (see Fig. 4). Combining our measurements (Eq. 8) with these high temperature results and the room temperature data of Clyne and Thrush, we obtain the following rate coefficient

$$I_0 = 6.0 \times 10^5 \exp(-1280/T) \text{ cm}^3 \text{ mole}^{-1} \text{ sec}^{-1} \quad (9)$$

for Reaction 1 in the presence of argon, and over the temperature range 300 to 3000 K.

Spectral Distribution

In systems containing O and CO, the accompanying radiation from 2500 to 7000 Å appears in low resolution as a continuous background or continuum. At high resolution, the continuous background has been resolved (Ref. 15) into a dense rotational fine structure having no underlying continuum.

Meyers and Bartle (Ref. 11) measured the absolute spectral intensity A_λ in low resolution (~ 200 Å) between 2500 and 7986 Å, at two temperatures, 2679 and 2943 K. The intensity does not exhibit a discernible temperature dependence over the small temperature interval of the two sets of data. A comparison in Fig. 5 shows the good agreement between our present data and the earlier work of Meyers and Bartle.

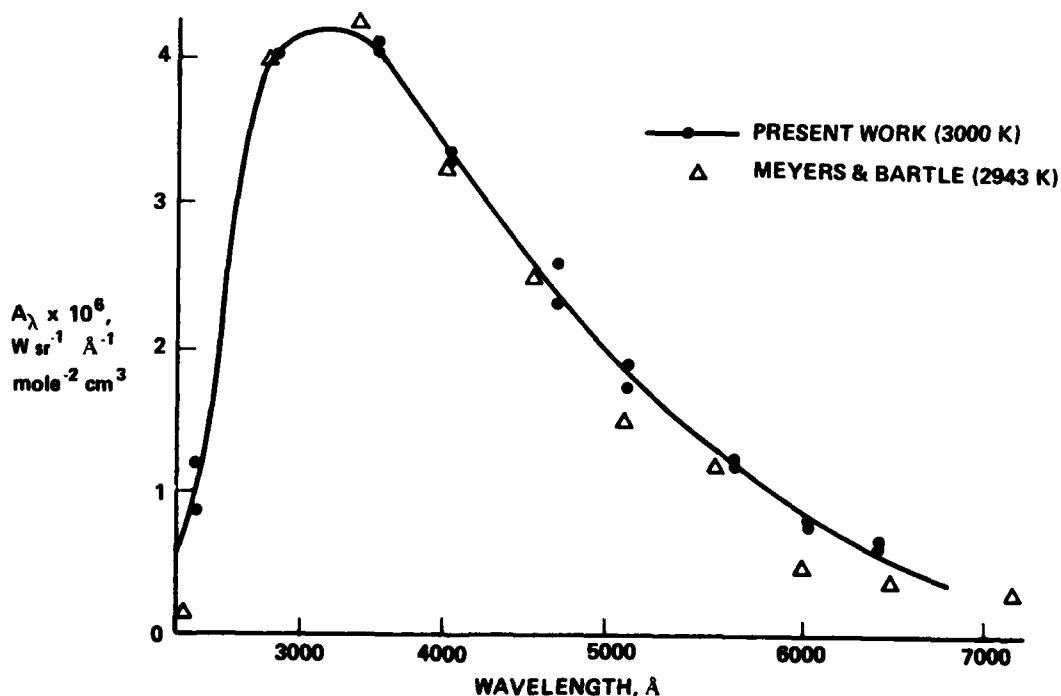


Figure 5. Absolute Intensity Distribution for CO + O Chemiluminescence; Comparison of Present Work and Data of Meyers and Bartle (Ref. 11).

Vanpee et al. (Ref. 16) have measured spectral intensities from a CO/H₂/O₂ flame and their data, while in relative, rather than absolute units, confirms the spectral distributions in Figs. 3 and 5.

Pravilov et al. have measured the chemiluminescence spectrum for CO + O combination at room temperature (293 K) in an He diluent (Ref. 14). Comparison with Fig. 3 shows that at room temperature the peak intensity is two orders of magnitude lower and is shifted about 800 Å toward the red.

Diluent and Additive Effects

The influence of different diluents upon the chemiluminescence has been the subject of only two previous investigations at room temperature, which produced conflicting results (see Table 2). Clyne and Thrush (Ref. 8) found that I_O increased in the presence of N₂ and O₂, relative to Ar; I_O decreased in the presence of He and Ne. Pravilov et al. (Ref. 17) found I_O independent of diluents (He, Ar and N₂).

TABLE 2 Third Body/Diluent Influences

Diluent	Rate Coefficient (cm ³ mole ⁻¹ sec ⁻¹)		
	Present Work (T = 3000K)	Clyne & Thrush (T = 293K)	Pravilov (T = 293K)
Argon	4x10 ⁵	8x10 ³	1.5x10 ³
N ₂	4x10 ⁵	11.2x10 ³	1.5x10 ³
O ₂	---	12.0x10 ³	0.5x10 ³ *
CO ₂	4x10 ⁵	---	---

* P_{O₂} = 1.0 Torr.

In the present investigation at 3000 K we found that A_λ at 3000 Å was the same for N₂ and argon diluents; the addition of CO₂ and small mole fractions of H₂O to the argon diluent also had no effect on A_λ. Our N₂ and argon diluent data is in agreement with the observations of Pravilov et al. (Ref. 17).

A systematic qualitative study of the influence of added H₂ on CO/air and CO/O₂ flame emission was conducted by Weston (Ref. 1). Hydrogen was observed to reduce the chemiluminescence continuum as recorded on spectral plates between 2500 and 6000 Å. These results are consistent with the present observations of the influence of H₂, and an investigation by Gaydon (Ref. 18). In all cases analysis is required to decouple the influence of O atom removal by reactions with H₂, and the possible influence of quenching by hydrogenous species. Note that Weston also studied the influence of gaseous H₂O on CO/O₂ flame emission and found that H₂O, like H₂, markedly reduced the observed CO + O chemiluminescence.

CONCLUSIONS

A rate coefficient for the radiative combination of carbon monoxide and oxygen atoms (Reaction 1) has been measured at 3000 K in an excess of argon or nitrogen and the results (Eq. 8) are in good agreement with earlier measurements by Meyers and

and Bartle (Ref. 11). Serious differences remain between room temperature rate coefficients, both with respect to magnitude and influence of diluents.

REFERENCES

1. F. R. Weston, Proc. Roy. Soc. A109, 176 (1925).
2. A. Gaydon and H. Wolfhard, "Flames: Their Structure, Radiation and Temperature," 4th Edition, Chapman & Hall, London (1979).
3. C. T. Bowman, "Proceedings of 15th Symposium (International) on Combustion, Combustion Institute Pittsburgh (1975), p. 869.
4. A. Dean and R. Johnson, Combust. Flame 37, 109 (1980).
5. D. L. Baulch et al., "Evaluated Kinetic Data for High Temperature Reactions : Vol 3," Butterworths, London, (1976).
6. M. Slack, Combust. Flame 28, 54 (1977).
7. A. Grillo, R. Reed, and M. Slack, J. Chem. Phys. 70, 1634 (1979).
8. M. Clyne and B. Thrush, Proc. Roy. Soc. A269, 404 (1962).
9. M. Clyne and B. Thrush, "Proceedings of Ninth Symposium (International) on Combustion" Combustion Institute, Pittsburgh (1963), p. 177.
10. K. A. Hartunian, W. P. Thompson, and E. W. Hewitt, J. Chem. Phys. 44, 1765 (1966).
11. B. Meyers and E. Bartle, J. Chem. Phys. 47, 1783 (1967).
12. B. Mahan and R. Solo, J. Chem. Phys. 37, 2669 (1962).
13. W. Kaskan, Combust. Flame 3, 39 (1959).
14. A. Pravilov et al., Zh. Fiz. Khim. 52, 1863 (1978).
15. J. H. Callomen and A. C. Gilby, J. Chem. Soc. 1471 (1963).
16. M. Vanpee, K. Cashin and R. Mainiero, Combust. Flame 33, 99 (1978).
17. A. Pravilov et al., Kin. Katal. 19, 1115 (1978).
18. A. Gaydon and F. Guedney, Trans. Farad. Soc. 51, 894 (1955).
19. D. L. Baulch et al., "Evaluated Kinetic Data for High Temperature Reactions: Vol. 2," Butterworths, London (1973).
20. J. P. Monat, R. K. Hanson and C. H. Kruger, Comb. Sc. & Tech. 16, 21 (1977).

AD P000282

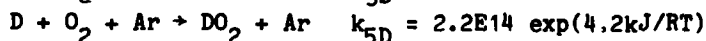
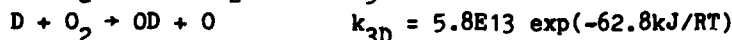
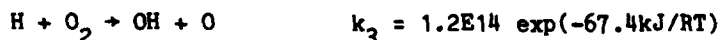
RESONANCE ABSORPTION MEASUREMENTS OF ATOM CONCENTRATIONS IN REACTING GAS MIXTURES. 9. MEASUREMENTS OF O ATOMS IN OXIDATION OF H₂ AND D₂

KRISHNA M. PAMIDIMUKKALA and GORDON B. SKINNER

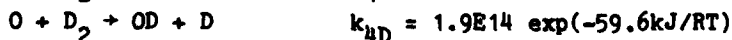
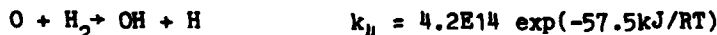
Department of Chemistry, Wright State University

Dayton, Ohio 45435, U.S.A.

Resonance absorption spectroscopy has been used to measure oxygen atom concentrations in shock heated H₂-O₂-Ar and D₂-O₂-Ar mixtures. Rich, lean and stoichiometric compositions have been studied in the temperature range 1000 - 2500 K. Under all conditions studied, the hydrogen-oxygen reaction could be adequately described by a small number of elementary reactions, and the rate constants could be deduced for several of them. From data on rich and stoichiometric mixtures we found (units of mole⁻¹ cm³ s⁻¹ for reaction 3 and mole⁻² cm³ s⁻¹ for reaction 5)



The kinetic isotope effect for reaction 3 was found to be 1.4 at 1500K, while that for reaction 5 was 2.0 in the 1000-1200K range. Both of these values are smaller than those found earlier from H and D measurements. Data from very lean H₂-O₂-Ar and D₂-O₂-Ar mixtures are consistent with the rate coefficients (units of mole⁻¹ cm³ s⁻¹).



which are close to values that we have determined from O atom measurements in N₂O-H₂-Ar and N₂O-D₂-Ar mixtures. The isotope effect for reaction 4 from the above equations is 2.6 at 1500K, compared to 1.7 from our N₂O experiments.

INTRODUCTION

Over the past few years there has been growing interest in measuring atom concentrations in reacting gas mixtures in shock tube experiments. Measurements of H and D atom concentrations in the oxidation of H₂ and D₂ have been reported from this laboratory and elsewhere^{2,3}, but there have been no experimental data available on the measurement of O atoms in these reactions. The present work has the aim of measuring O atom concentrations in the oxida-

tion of H_2 and D_2 by O_2 , evaluating rate constants of some of the elementary reactions involved, and comparing the results with those obtained from H and D measurements.

EXPERIMENTAL

All the data were obtained using a 7.6 cm diameter stainless steel shock tube which has been described elsewhere. The resonance absorption spectroscopic technique was used for measuring O atom concentrations. The source of radiation was a microwave discharge lamp (source B), the construction details of which are given in Ref. 5. In all experiments the operational conditions of the discharge lamp were maintained constant: 2.5 torr lamp gas pressure, gas concentration 0.1% O_2 in He, and 40 watts microwave power. The discharge lamp was calibrated for analysis of oxygen atoms by a procedure similar to that used for H and D. Typical calibration curves for two temperatures are given in Fig. 1.

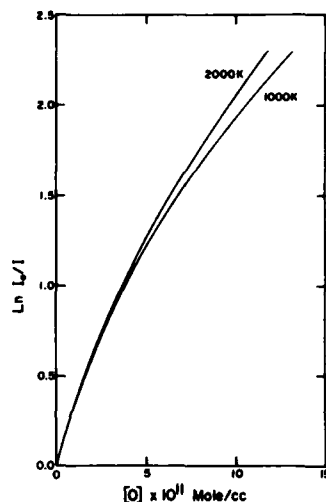


Fig. 1. Calibration curves for analysis of oxygen atoms obtained from line shape measurements.

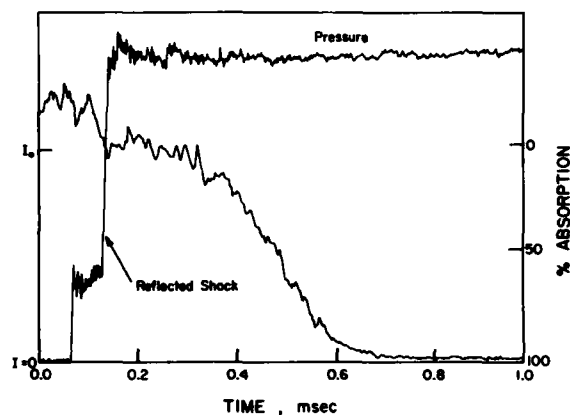


Fig. 2. Transmitted intensity, as attenuated by oxygen atoms in shock tube, as a function of time for mixture 1a at 1116 K and 2.36 atm.

Oxygen atom concentrations were measured behind reflected shock waves at a distance of 2 cm from the end plate, close enough so that side wall effects were minimal. Test times varied from 200 to 2000 microseconds. In each experiment the pressure and the intensity of the lamp, as attenuated by oxygen atoms in the shock tube, were recorded as a function of time on a digital storage oscilloscope and then transferred to a strip chart recorder. The atom concentrations were then evaluated from the oscillograms using calibration curves. Representative pressure and intensity traces are given in Fig. 2.

MATERIALS

For making up sample gas mixtures we used Airco Research grade argon having total hydrocarbon, hydrogen and oxygen impurities less than 2 ppm. Matheson ultra high purity hydrogen (99.999%) and oxygen (99.99%) were used, each containing less than 1 ppm hydrocarbons. Deuterium was also from Matheson, 99.5 atom % pure. For driver gas we used Airco helium (99.995%) and argon (99.999%) while for the discharge lamp gas we used Airco Grade 5 helium (99.999%) and the O_2 listed above. No further purification of the gases was attempted except for making mixture 1(a) in which the argon was further purified by allowing it to pass through a trap containing 4A and 4B type molecular sieves cooled to dry ice temperature. The molecular sieves were expected to remove remaining hydrocarbon and water impurities. In this case the gas samples were introduced into the shock tube via a hole (2 mm dia)

drilled at an angle through the end plug in such a way that the hole was very close to the shock tube wall and did not affect the gas dynamics appreciably. In all other experiments the gas samples were introduced near the diaphragm.

RESULTS

The gas mixtures studied and the individual experimental details for each mixture are listed in Tables 1 and 2 for H_2-O_2 and D_2-O_2 , respectively. As expected for H_2 and D_2 oxidation reactions, it was found that the O atom concentrations increased exponentially with time after a short initial period. The temperature range studied for each mixture was limited at the lower end by the detection limit. At the lowest temperatures there was about a 15% decrease of intensity over the total test time of 2030 μ s.

The logarithms of the oxygen atom concentrations were plotted against time, and the slope, $d\ln[O]/dt$, was calculated for each experiment. In many experiments, the first two points, at the shortest times, fell below the experimental curve, but not enough detail was observable to show how the exponential curve was approached. A representative plot of $\ln [O]$ vs. time is shown in Fig. 3. All experiments displayed essentially the same features. In Tables 1 and 2 we have listed the slope, k_1 , and $[O]$ extrapolated to zero time for each experiment for H_2-O_2 -Ar and D_2-O_2 -Ar mixtures.

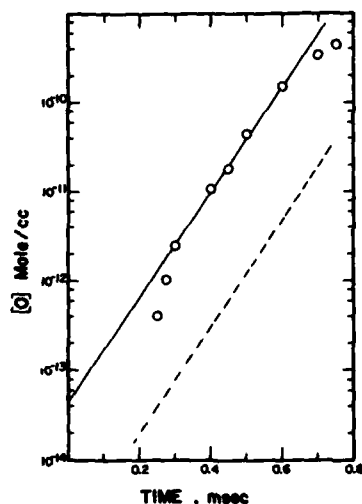
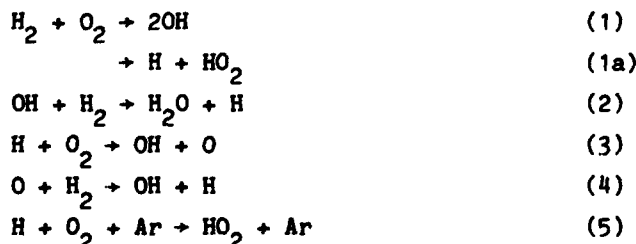


Figure 3. Measured O atom concentrations for mixture of 1% H_2 , 0.5% O_2 in argon at 1116 K, 2.36 atm. total pressure. O, measured concentrations; — Line drawn through data to obtain slope of graph; ---, curve calculated using the data of Table 3.

DISCUSSION

Previous measurements on H and D have indicated that a kinetic mechanism consisting of reactions 1-5 provides an adequate description of the hydrogen-oxygen chemistry under our experimental conditions.



There is still uncertainty about the relative importance of the reactions (1) and (1a). It was pointed out by Jachimowski and Houghton and confirmed by our H and D measurements that it is hard to distinguish between these two reactions experimentally because they lead to the same kinetic

Table 1. Experimental Data and Calculations for Formation of Oxygen Atoms in H_2-O_2 -Ar Mixtures.

Temp., K	Press., Atm	Expt. Slope,* s ⁻¹	[O] as t + 0 mole cm ⁻³	Expt. Slope Calc. Slope	k ₁ , Calc., mole ⁻¹ cm ³ s ⁻¹
Mixture 1 1% H ₂ , 0.5% O ₂					
1012	2.18	8.90E03	8.4E-14	1.25	2.9E05
1018	2.41	6.99E03	1.6E-13	0.86	5.2E05
1036	2.38	9.75E03	4.1E-14	1.05	1.6E05
1061	2.21	1.09E04	3.9E-14	1.01	1.9E05
1061	2.32	1.03E04	5.7E-14	0.96	2.6E05
1074	2.31	1.23E04	4.4E-14	1.02	2.3E05
1097	2.34	1.22E04	7.5E-14	0.86	4.4E05
1135	2.31	1.55E04	8.0E-14	0.88	6.1E05
1298	2.27	3.15E04	1.5E-14	0.86	2.9E05
1325	2.19	3.10E04	1.9E-14	0.75	4.3E05
Mixture 1a. 1% H ₂ , 0.5% O ₂					
1056	2.19	9.21E03	6.8E-14	0.94	3.2E05
1075	2.59	1.06E04	8.3E-14	0.80	3.8E05
1112	2.37	1.28E04	5.2E-14	0.86	3.3E05
1116	2.36	1.38E04	4.3E-14	0.91	2.8E05
1200	2.28	2.14E04	2.9E-14	1.02	3.3E05
1216	1.93	1.88E04	6.0E-14	0.88	8.8E05
1245	2.13	2.56E04	1.6E-14	0.81	2.5E05
1275	1.81	3.49E04	7.9E-15	1.10	1.7E05
1342	1.68	2.80E04	1.4E-14	0.85	4.4E05
1438	1.48	3.87E04	2.7E-14	1.08	1.4E06
1515	1.36	3.81E04	1.4E-14	0.90	1.1E06
Mixture 2. 2% H ₂ , 0.2% O ₂					
1031	2.33	5.34E03	1.3E-14	1.20	1.2E05
1057	2.37	6.31E03	8.5E-14	1.20	9.4E05
1081	2.48	6.92E03	1.1E-14	1.10	1.4E05
1110	2.35	8.19E03	1.3E-14	1.25	2.1E05
1203	2.00	1.38E04	7.4E-15	1.10	2.4E05
1277	2.36	2.03E04	2.8E-15	1.04	1.1E05
1322	2.18	2.14E04	3.7E-15	0.99	2.1E05
1410	2.05	2.28E04	1.7E-15	0.89	1.5E05
1429	2.21	1.75E04	5.2E-15	0.99	4.6E05
Average ratio for mixtures 1, 1a and 2				0.96	
Mixture 3. 50 ppm H ₂ , 5000 ppm O ₂					
1287	2.29	2.58E03	1.4E-12	0.91	2.5E07
1389	2.17	3.86E03	1.1E-12	1.12	3.3E07
1488	2.14	3.81E03	2.0E-12	0.93	9.2E07
1539	2.16	4.25E03	2.4E-12	0.95	1.3E08
1593	2.07	4.25E03	2.3E-12	0.91	1.6E08
1637	1.95	5.57E03	1.5E-12	1.18	1.3E08
1710	2.30	7.80E03	8.8E-13	1.29	7.9E08
1956	1.96	7.24E03	2.1E-12	1.15	4.2E08
Average ratio for mixture 3				1.04	

* slope is $d \ln [O] / dt$.

Table 2. Experimental Data and Calculations for Formation of Oxygen Atoms D_2 - O_2 -Ar Mixtures.

Temp., K	Press., Atm	Expt. Slope, s ⁻¹	[O] as $t \rightarrow 0$, mole cm ⁻³	Expt. Slope Calc. Slope	k_1 , Calc., mole ⁻¹ cm ³ s ⁻¹
Mixture 1. 1% D_2 , 0.5% O_2					
1003	2.41	5.94E03	1.7E-13	0.99	1.7E05
1009	2.38	6.11E03	2.3E-13	0.98	2.5E05
1021	2.38	6.82E03	1.7E-13	1.00	2.0E05
1024	2.34	6.70E03	1.0E-13	0.97	1.2E05
1045	2.33	7.69E03	3.1E-13	0.96	4.5E05
1055	2.25	9.16E03	1.4E-13	1.09	2.3E05
1071	2.21	8.77E03	1.7E-13	0.97	3.2E05
1081	2.22	8.88E03	1.6E-13	0.93	3.2E05
1107	2.22	1.13E04	3.0E-13	1.00	7.2E05
1295	2.25	1.95E04	2.0E-13	1.08	1.4E06
1312	2.31	2.61E04	6.5E-13	1.01	4.9E05
Mixture 2. 0.1% D_2 , 0.05% O_2					
1421	1.74	3.63E03	7.2E-13	1.13	1.2E08
1495	1.88	4.12E03	3.7E-13	0.99	7.6E07
1565	1.82	5.46E03	1.9E-13	1.12	5.2E07
1614	1.69	5.89E03	2.3E-13	1.17	8.1E07
1646	1.73	6.28E03	2.6E-13	1.08	2.0E08
1699	1.94	6.62E03	5.0E-13	0.97	2.0E08
1893	2.00	8.17E03	9.2E13	1.03	6.2E08
1918	1.62	9.35E03	5.6E-13	0.96	4.9E08
2346	1.27	1.20E04	9.8E-13	1.15	2.7E09
2465	1.16	1.10E04	1.2E-12	0.97	4.3E09
Mixture 3. 2% D_2 , 0.2% O_2					
1125	1.79	7.45E03	9.0E-16	1.51	7.5E03
1231	1.81	7.84E03	1.9E-14	0.97	3.0E05
1252	1.79	8.13E03	3.4E-14	0.92	6.0E05
1286	2.09	1.36E04	6.0E-15	1.13	1.1E05
1394	1.71	1.67E04	2.2E-15	1.18	8.2E04
1440	2.24	2.00E04	1.4E-14	0.97	4.8E05
1472	2.04	2.15E04	7.8E-15	1.01	3.4E05
1546	1.91	2.33E04	1.3E-14	0.98	7.9E05
1576	1.86	2.81E04	4.3E-15	1.15	3.0E05
Average ratio for mixtures 1, 2 and 3				1.03	
Mixtures 4. 0.2% D_2 , 0.4% O_2					
1001	2.51	2.84E03	6.8E-13	0.74	8.2E05
1042	2.62	4.11E03	6.4E-13	0.76	1.0E06
1113	2.29	8.02E03	2.3E-13	1.08	6.9E05
1124	2.45	7.71E03	6.5E-13	0.93	1.9E06
1127	2.16	8.02E03	3.9E-13	1.06	1.4E06
1145	2.35	9.18E03	4.8E-13	1.03	1.7E06
1195	2.36	1.05E04	4.8E-13	0.95	2.3E06
1263	2.30	1.47E04	2.0E-13	1.01	1.5E06
1285	2.22	1.61E04	1.6E-13	1.07	1.4E06
1311	2.14	1.64E04	2.1E-13	1.03	2.1E06
Average ratio for mixture 4				0.98	

Mixture 5. 50 ppm D₂, 5000 ppm O₂

1374	2.67	1.34E03	1.6E-12	0.86	1.4E07
1393	2.62	1.77E03	1.4E-12	1.06	1.4E07
1434	2.48	1.80E03	1.4E-12	1.09	1.7E07
1493	2.42	1.91E03	2.3E012	1.06	3.6E07
1544	2.42	2.03E03	2.4E-12	1.02	4.6E07
1587	2.35	2.27E03	2.0E-12	1.09	1.6E08
1656	2.40	1.95E03	5.8E-12	0.84	1.6E08
1671	2.11	2.20E03	2.6E-12	1.05	8.8E07
1703	2.14	2.81E03	2.0E-12	1.27	7.4E07
1774	2.17	3.45E03	1.5E-12	1.41	6.7E07

Average ratio for mixture 5

1.08

* Slope is $\text{dln } [O]/\text{dt}$ Table 3. Kinetic Data for H₂-O₂ and D₂-O₂ Reactions.

Reactions	Arrhenius Parameters		Reference
	A*	E, kJ	
1. H ₂ + O ₂ → 2OH	1.7E13	205.6	7
2. OH + H ₂ → H ₂ O + H	1.0E14	27.2	See text
	5.2E13	27.2	9
3. H + O ₂ → OH + O	1.2E14	67.4	this work
	1.1E14	67.4	1
4. O + H ₂ → OH + H	4.2E14	57.5	See text
	2.3E14	57.5	11
	2.2E14	57.5	10
5. H + O ₂ + Ar → HO ₂ + Ar	4.5E14	-4.2	this work
	4.4E14	-4.2	1
1D D ₂ + O ₂ → 2OD	1.1E13	205.6	1
2D OD + D ₂ → D ₂ O + D	4.7E13	29.3	See text
3D D + O ₂ → OD + O	5.8E13	62.8	this work
	1.6E13	62.8	1
4D O + D ₂ → OD + D	1.9E14	59.6	See text
	1.6E14	59.6	11
5D D + O ₂ + Ar → DO ₂ + Ar	2.2E14	-4.2	this work
	1.0E14	-4.2	1

* Units of A, mole⁻¹ cm³ s⁻¹ for Reactions 1-4; mole⁻² cm⁶ s⁻¹ for Reaction 5.

behavior after a very brief initial period. In the present study we had hoped to distinguish between them in specific experiments with mixture 1a in which the impurities were expected to be exceptionally low, but without success.

After a brief initial period, reactions 2 to 5 reach the partial equilibrium state in which concentrations of H, OH and O maintain a constant ratio to one another. Under these conditions we obtain the following relationship for [O]:

$$[O] = [O]_0 \frac{\exp(2k_3 - k_5[Ar])[O_2] t}{C} \quad (\text{I})$$

$$\text{where } [O]_0 = \frac{k_1[O_2]}{k_4} \text{ or } [O]_0 = \frac{k_3 k_{1a}[O_2]}{k_2 k_4} \quad (\text{II})$$

$$C = \frac{k_3 [O_2]}{k_4 [H_2]} + \frac{2k_3 [O_2]}{k_2 [H_2]} + 1 \quad (III)$$

In these equations [H₂] and [O₂] are the initial concentrations of the mixture, since all of our measurements were taken during the induction period of the reaction.

We have carried out numerical integration of reactions 1 through 5 using the rate coefficients given in Ref. 1 as a first approximation, calculating the slopes, $d \ln [O]/dt$, at each temperature. Since $C \approx 1$ for rich and stoichiometric mixtures, the slope of the graph of $\ln [O]$ versus time was determined mainly by reactions 3 and 5, reaction 5 contributing significantly only below 1200 K. Accordingly, rate coefficients k_3 and k_5 were adjusted to get the best fit to the experimental data. The kinetic data that gave the best match to the data of Table 1 are listed in Table 3. The results obtained from O atom measurements are essentially the same as those from H atom measurements.

For the deuterium analogs of reactions 3 and 5 we found rate constants somewhat higher than the values reported in Ref. 1. At 1500 K the isotope effect for reaction 3 was found to be a factor of 1.4 while for reaction 5 at 1000 - 1200 K it is 2.0. These effects seem more reasonable than the values of 4.5 and 4.4 that we obtained earlier, in light of both the nature of the reaction and also earlier experimental results^{3,8}.

Although rate coefficients k_3 and k_5 could be obtained from the rich and stoichiometric mixtures, not enough details could be obtained from these mixtures for reactions (2) and (4). At extremely low concentrations of H₂ where C is no longer close to 1, reactions (2) and (4) become important. The slope, for lean mixtures, is given by

$$\frac{d \ln [O]}{dt} = \frac{2k_3 [O_2] k_2 k_4 [H_2]}{k_3 [O_2] (k_2 + 2k_4) + k_2 k_4 [H_2]} \quad (IV)$$

For mixtures such as 50 ppm H₂, 5000 ppm O₂

$$k_3 [O_2] (k_2 + 2k_4) \gg k_2 k_4 [H_2] \quad (V)$$

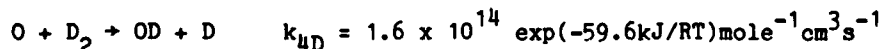
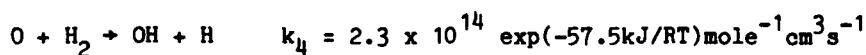
and thus,

$$\frac{d \ln [O]}{dt} = \frac{2k_2 k_4 [H_2]}{k_2 + 2k_4} \quad (VI)$$

However, the expression cannot be simplified to give rate constants for a single reaction since k_2 and $2k_4$ are not very different throughout our experimental range. It does appear from the rate constants determined by Gardiner et al.⁹ for reaction 2 and by Schott, Getzinger and Seitz¹⁰ for reaction 4, as used in our earlier paper, that $2k_4$ will be less than k_2 except at the top of our range.

The rate coefficients for reactions 2, 4, 2D and 4D listed in our earlier paper¹ led to smaller calculated O atom concentrations than we observed. We obtained good agreement with our data by leaving the Arrhenius activation energies unchanged while increasing the A factors by about 40%, to the values listed in Table 3 of this paper.

We have recently¹¹ measured rate constants for reactions 4 and 4D by following the O atom concentration changes in shock-heated mixtures of 20 ppm N₂O and 100 ppm H₂ (or D₂) in argon. These rate constant expressions are



and are considered to be within about 30% since the O atom concentrations were determined mainly by reactions 4 or 4D, with minimal interference from other reactions. Accordingly, we consider that the rate constants for reactions 4 and 4D actually lie between the values given in Table 3 and those listed above, perhaps a little closer to the latter values. The isotope effect of reaction 4 from the N_2O studies is about 1.7 at 1500 K., compared to 2.6 as determined from the present work.

It seems that, in spite of our precautions, there were some H- or O-atom-producing impurities that initiated H_2 and D_2 oxidation. This is probably the reason why our estimates of k_1 , listed in Tables 1 and 2 are erratic in many experiments as shown in Fig. 4. However, in some of the experiments, particularly for reaction mixture 1a in which the impurities are expected to be low, our values came close to the curve of Jachimowski and Houghton⁷, confirming that their k_1 (or k_{1a}) is a good one.

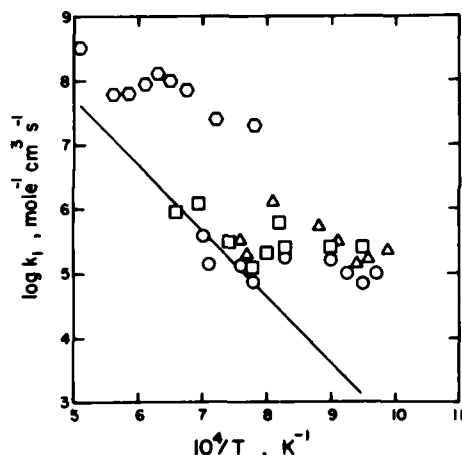


Figure 4. Rate constants for $\text{H}_2 + \text{O}_2 + 20\text{H}$ calculated from experimental data: Δ , 1% H_2 , 0.5% O_2 ; \square , 1% H_2 , 0.5% O_2 , (Mix. 1a); \circ , 2% H_2 , 0.2% O_2 ; \circ , 50 ppm H_2 , 5000 ppm O_2 ; —, equation of Jachimowski and Houghton⁷.

REFERENCES

1. C.-C. Chiang and G.E. Skinner, Proceedings of the 12th International Symposium on Shock Tubes and Shock Waves, p. 629 (1980).
2. A.L. Myerson and W.S. Watt, J. Chem. Phys., **49**, 425 (1968).
3. D. Appel and J.P. Appleton, Symposium (Int.) on Combustion, **15**, 701 (1975).
4. C.-C. Chiang, A. Lifshitz, G.B. Skinner and D.R. Wood, J. Chem. Phys., **70**, 5614 (1979).
5. A. Lifshitz, G.B. Skinner and D.R. Wood, Rev. Sci. Instrum., **49**, 1322 (1978).
6. K.M. Pamidimukkala, A. Lifshitz, G.B. Skinner and D.R. Wood, J. Chem. Phys., To be published.
7. C.J. Jachimowski and W.M. Houghton, Comb. Flame, **17**, 25 (1977).
8. S.C. Kurzius and M. Boudart, Comb. Flame, **12**, 477 (1968).
9. W.C. Gardiner, W.G. Mallard, M. Morinaga, J.H. Owen, W.T. Rawlins, T. Takeyama and B.F. Walker, Symposium (Int.) on Combustion, **14**, 61 (1973).
10. G.L. Schott, R.W. Getzinger and W.A. Seitz, Int. J. Chem. Kinet., **6**, 921 (1974).
11. K.M. Pamidimukkala and G.B. Skinner, To be published.

This research was supported by the U.S. Department of Energy under Contract DE-AC02-76ER02944.

AD P000283

DIRECT MEASUREMENTS OF O-ATOM REACTIONS

WITH HCN AND C₂H₂ BEHIND SHOCK WAVES

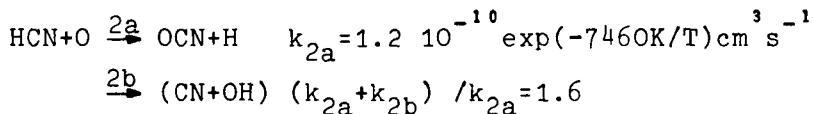
P. ROTH, R. LÖHR

Fachgebiet Strömungstechnik

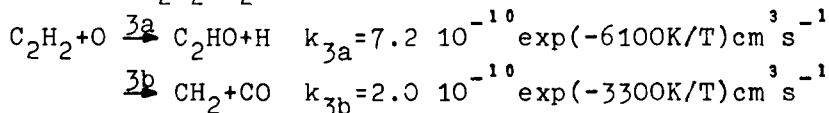
Universität GH Duisburg, D-4100 Duisburg, W. Germany

High temperature reactions of O-atoms with HCN and C₂H₂ have been studied behind reflected shock waves in the temperature range 1500 K \leq T \leq 2600 K. The O-atoms were generated by the known fast decomposition of N₂O. The time dependent behaviour of the O-atoms in the post shock reaction zone and the generation of H-atoms have been measured by resonance absorption spectroscopy (ARAS). Because of the sensitivity of this experimental technique initial concentrations of reactants in the ppm region are sufficient.

The interpretation of the HCN/N₂O measurements in terms of rate coefficients can be given by the two-channel-reaction



For the C₂H₂/N₂O reaction system the reactions



are dominant in the low concentration reaction system and the interpretation of measured H- and O-atom profiles by the given rate coefficients is easy to do and unequivocal.

INTRODUCTION

High temperature O-atom reactions are central to the general process of hydrocarbon oxidation kinetics. The isolation and determination of individual rate coefficients is difficult because of the normally complex reaction systems. It has been shown (for example, ^{1, 2, 3}) that the atomic resonance absorption spectrophotometry (ARAS) in connection with shock tube technology is a good and successful approach to kinetic data acquisition. For the direct time dependent measurements of H- and / or O-atom concentra-

tions behind reflected shock waves, initial concentrations of reactants in the ppm region are needed. Because of this very high dilution the number of elementary reactions which determine basically the overall high temperature reaction behaviour is low. In most cases a simple kinetic interpretation of measured time dependent atom concentrations is possible.

In this paper the ARAS-method is applied to investigate the high temperature reaction behaviour of O-atoms with HCN and C_2H_2 . HCN is known to be an intermediate in the NO formation kinetics and was first proposed by Fenimore⁴ and measured by Bachmeier, Eberius and Just⁵ in rich hydrocarbon flames. The rate coefficient of the HCN + O reaction has been measured by Davies and Thrush⁶ using flow reactor technique. Their low temperature results are



$$k = 8.6 \times 10^{-12} \exp(-4075 \text{ K}/T) \text{ cm}^3 \text{ s}^{-1} \quad 470 \text{ K} \leq T \leq 575 \text{ K}$$

Direct measured high temperature rate coefficients are not known. The linear Arrhenius extrapolation of the rate coefficient from low to high temperatures can lead to considerable errors. Similar reactions are known to show significant non-Arrhenius behaviour.

The reaction of O-atoms with C_2H_2 is an important step in many hydrocarbon combustion systems. At low temperatures it has been extensively studied in flow reactors by different experimental techniques (for example ^{7 8 9 10}). Several free radicals were observed as primary and secondary products. At flame conditions the removal of C_2H_2 mostly occurs by reactions with O and OH. Fenimore and Jones¹¹ and Vandooren and van Tiggelen¹² deduce rate coefficients from their flame measurements. In shock tube experiments^{13 14} the O+ C_2H_2 reaction could not be directly measured. This elementary reaction is included in the overall C_2H_2 oxidation mechanism.

In order to study the reaction behaviour of O-atoms with HCN and C_2H_2 at temperatures $T > 1500 \text{ K}$ we measured H- and O-atom concentrations in highly diluted HCN/ N_2 O-Ar and C_2H_2 / N_2 O-Ar systems. The O-atoms were generated by the known fast decomposition of N_2O .

EXPERIMENTAL

Extreme purity is essential if a shock tube is to be used to obtain kinetic measurements on low concentration systems. The UHV-apparatus consists of a diaphragm-shock tube, a mixing and storage bottle for the gas mixtures, and an optical system for the detection of O- and H-atoms by the atom resonance absorption spectroscopy (ARAS)³.

The internal surface of the stainless steel shock tube (internal diameter 7.9 cm) is specially prepared for high vacuum purposes. The tube can be heated and is evacuated via a special end plate valve by a forepump, turbomolecular pump, and liquid nitrogen-cooled titanium-sublimation pump to pressure down to about 10 mbar. As molecular sieves prevent the forepump oil from entering the tube, the residual gas is practically free of hydrocarbons. The leak-plus-outgassing rate is of the order of 8×10^{-10} mbar per minute. Only very pure gases are used. The argon has a purity of 99.9999 %, with N_2 being the main impurity. The present experiments have been carried out with mixtures manometrically prepared with calibrated diaphragm-type pressure gauges. Using metal seals

(Au, Ag, Cu) the mixing system can be heated and evacuated by a second pumping unit to pressures of $p \approx 10^{-8}$ mbar.

The optical detection system consists of a microwave-excited discharge lamp, the absorption zone in the shock tube being separated on both sides by two thin MgF₂-windows, a 1m McPherson vacuum UV monochromator, and a special solar-blind photomultiplier. The corresponding spectral lines H α = 121,6 nm, OI = 130,5 nm are excited in a gas mixture of He with 2% H₂ or O₂ that passes through the lamp at a pressure of 6 mbar. The risetime of the detection system is less than 20 μ s for a signal to noise ratio of about 15. Experiments with argon alone at high temperature, up to 3000 K, showed negligible absorption signals due to impurities or their secondary products, and so highly diluted mixtures can be investigated up to this temperature. A more detailed description of the experimental setup is given elsewhere³.

The optical measurement technique is a line emission - line absorption method with the spectral shape of the emitter line not being known in detail and supposed to be mainly influenced by self-reversion³. So calibration experiments have to be made to find out the correlation between measured absorption and concentration. The calibration procedure for H-atoms can only be performed on the basis of kinetic properties. For O-atom calibration the partial equilibrium of O-atoms which can be realized behind shock waves in Ar/N₂O mixtures have been used.

RESULTS

The shock tube experiments have been performed using gas mixtures with various initial concentration ratios of reactants highly diluted in Ar. The temperature range of both series of experiments was somewhat different, the pressures are approximately 1.7 bar.

HCN/N₂O : 25/5, 25/25, 50/10,
50/50, 100/20, 200/40 ppm/ppm
1700 K \leq T \leq 2500 K

C₂H₂/N₂O : 10/10, 25/25, 15/100
ppm/ppm, 1500 K \leq T \leq 2575 K

Because of the different sensitivity of the H- and O-atom resonance absorption (factor of about 10 in concentration) and the special experimental arrangement it was not possible to measure both atom concentrations simultaneously. The absorption experiments have been performed independently with temperatures of the H-atom measurements being at the lower part of the given temperature ranges.

The general behaviour of the O-atom absorption signals is similar in the HCN/N₂O and C₂H₂/N₂O case.

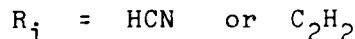
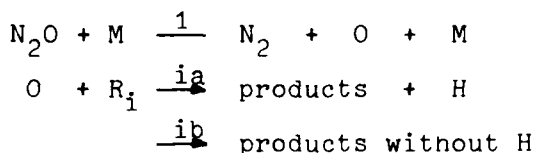
Figure 1. Absorption signals behind shock waves
a) O-atom absorption in C₂H₂/N₂O-Ar mixtures 100 μ s²/div
b) H-atom absorption in HCN/N₂O-Ar mixtures 100 μ s /div

An example is shown in fig. 1, upper part. After shock arrival the production of O-atoms from N_2O begins immediately and the absorption increases. The atoms formed react with HCN or C_2H_2 and the absorption reaches a maximum value. Then it decreases because of the consumption of N_2O and the resulting reduction in the O-atom production rate.

An example of measured H-atom absorption typical for both C_2H_2 and HCN systems is given in the lower part of fig. 1. The early signal increase after shock arrival indicates that H-atoms are one of the direct products of the O-atom attack on C_2H_2 or HCN.

DISCUSSION

Because of the high dilution the reaction behaviour of the HCN/ N_2O and C_2H_2 / N_2O systems will be determined by only a few elementary reactions.² The known pyrolytical decomposition of N_2O and secondary reactions of O-atom with HCN or C_2H_2 will be most important. A direct decomposition of HCN and C_2H_2 is of minor importance under the present experimental conditions. The beginning of the reactions can be kinetically modelled in the following way.



A simple analytical solution of the time dependent atom concentrations in the reaction zone behind shock waves can be derived from the above reaction scheme if the concentration R_i is assumed to be nearly constant.

$$\frac{[O]}{[N_2O]_0} = \frac{c_1}{c_1 - c_i} \{-\exp(-c_1 t) + \exp(-c_i t)\} \quad (1)$$

$$\frac{[H]}{[N_2O]_0} = \frac{c_{ia}}{c_i} \left\{ 1 + \frac{c_i}{c_1 - c_i} \exp(-c_1 t) - \frac{c_1}{c_1 - c_i} \exp(-c_i t) \right\} \quad (2)$$

$$c_1 = k_1 [Ar]$$

$$c_i = k_i [R_i]_0 = (k_{ia} + k_{ib}) [R_i]_0$$

$$c_{ia} = k_{ia} [R_i]_0$$

$$k_1 = 2.4 \times 10^{-9} \exp(-30800 \text{ K}/T) \text{ cm}^3 \text{ s}^{-1}$$

The quantities c_i and c_{ia} are identical if the reaction channel ia only of the proposed mechanism is important. The given rate coefficient k_1 has been taken from reference².

For every individual O-atom experiment the quantity c_i or k_i ($i = 2$ HCN, $i = 3$ C₂H₂) has been varied to fit the measured concentrations by equation (1). A good rendering of the O-atom maximum is a specially used criterion. Two examples are given in fig. 2.

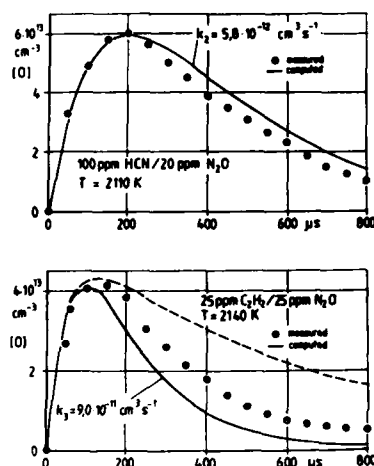


Figure 2. Measured and computed O-atom concentration (simple kinetic model)

- a) HCN/N₂O-Ar mixture $k_2 = 5.8 \times 10^{-12} \text{ cm}^3 \text{ s}^{-1}$
 b) C₂H₂/N₂O-Ar mixture $k_3 = 9.0 \times 10^{-11} \text{ cm}^3 \text{ s}^{-1}$

— C₂H₂ = const

---- C₂H₂ ≠ const

In the upper part computed and measured concentrations of the HCN/N₂O system are shown using $k_2 = 5.8 \times 10^{-12} \text{ cm}^3 \text{ s}^{-1}$. After the maximum the measurement lies below the computed curve. This was found in all other HCN/N₂O experiments and is attributed to the influence of secondary reactions. An example of measured and computed O-atom concentrations in the C₂H₂/N₂O system is shown in the lower part of fig. 2. The rate coefficient k_3 which fits the measured maximum value is much higher than in the other case. The condition of nearly constant C₂H₂-concentration assumed in equation (1) is not satisfied. The dashed line in fig. 2 (lower part) represents a computation in which C₂H₂ is not assumed to be constant. The difference in the measured O-atom concentration must be explained by additional reactions which have to be taken into account for a complete description of the reaction behaviour of the system. For all O-atom measurements in the HCN/N₂O and C₂H₂/N₂O systems the individual rate coefficients have been determined based on the simplified reaction scheme. The mean value of k_2 and

k_3 can be given in simple Arrhenius form.

$$k_2 = 1.9 \times 10^{-10} \exp(-7460 \text{ K}/T) \text{ cm}^3 \text{ s}^{-1} \quad 15$$

$$k_3 = 7.3 \times 10^{-10} \exp(-4600 \text{ K}/T) \text{ cm}^3 \text{ s}^{-1} \quad 16$$

The H-atoms measured in both reaction systems have been fitted in a similar way by using equation (2) of the simple kinetic model. The coefficients c_2 and c_3 are known from the O-atom experiments and the only fitting parameter in both cases is the reaction channel ratio $c_{ia}/c_i = k_{ia}/k_i$. Two examples are shown in fig. 3.

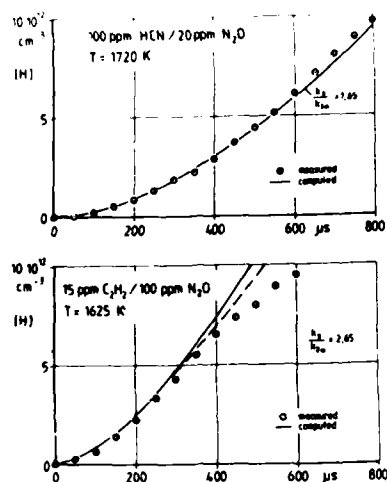


Figure 3. Measured and computed H-atom concentration (simple kinetic model)

a) HCN/N₂O-Ar mixture

$$\frac{k_2}{k_{2a}} = 1.65$$

b) C₂H₂/N₂O-Ar mixture

$$\frac{k_3}{k_{3a}} = 2.65$$

In the upper part an H-atom concentration profile measured in the HCN/N₂O system is shown together with the computed profile using a ratio $c_2/c_{2a} = k_2/k_{2a} = 1.65$. The agreement between experiment and calculation is remarkably good. The given ratio of rate coefficients for these individual experiments is greater than 1. This means that the decrease of the O-atom production rate and the increase of H-atoms cannot be explained by only one reaction channel 2a. In the lower part of fig. 3 an example of a measured H-atom concentration profile in the C₂H₂/N₂O reaction system is given. The drawn line represents the time behaviour computed from equation (2) using a coefficient ratio $k_3/k_{3a} = 2.65$. The dashed line gives the result of an additional computation with C₂H₂ ≠ const. At times $t > 300 \mu\text{s}$ the measurement lies below the computed curves. This must be explained by further reactions not included in the simple reaction model.

By analysing all H-atom experiments in the described way individual reaction channel ratios k_{ia}/k_i under different experimental conditions could be determined. In the case of the HCN/N₂O reaction system a channel ratio.

$$\frac{k_2}{k_{2a}} \approx 1.6 \quad 1700 \text{ K} \leq T \leq 2200 \text{ K}$$

independent on temperature was found¹⁵. From the measurements in the C₂H₂/N₂O system a temperature dependent mean value of the ratio k_3/k_{3a} could be derived and given in simple Arrhenius form¹⁶.

$$\frac{k_3}{k_{3a}} = 1.03 \times \exp(1500 \text{ K/T})$$

All data interpretations are based on the above given simple kinetic reaction model.

A better fit of measured H- and O-atom concentrations especially at later times can only be achieved by additional reactions. Reactions of products with the initial molecules and reactions of products with other products have to be considered. In the HCN/N₂O system the reaction scheme given in Tab. 1 has been proposed with suitable rate coefficients.

Reaction	Rate coefficient cm ³ s ⁻¹
N ₂ O + M $\xrightarrow{1}$ N ₂ + O + M	2.4x10 ⁻⁹ exp(-30 800 K/T)
HCN + O $\xrightarrow{2a}$ OCN + H	1.2x10 ⁻¹⁰ exp(- 7 460 K/T)
$\xrightarrow{2b}$ (CN + OH)	0.7x10 ⁻¹⁰ exp(- 7 460 K/T)
OCN + O \longrightarrow CO + NO	3x10 ⁻¹¹
OCN + H \longrightarrow CO + NH	3x10 ⁻¹¹
CN + O \longrightarrow CO + N	3x10 ⁻¹¹
CN + OH \longrightarrow OCN + N	3x10 ⁻¹¹
N ₂ O + H \longrightarrow N ₂ + OH	1.3x10 ⁻¹⁰ exp(- 7 600 K/T)
HCN + OH \longrightarrow CN + H ₂ O	10 ⁻¹²

Table 1. Kinetic Data for the HCN/N₂O Reaction System

Reaction	Rate coefficient cm ³ s ⁻¹
N ₂ O + M $\xrightarrow{1}$ N ₂ + O + M	2.4x10 ⁻⁹ exp(-30 800 K/T)
C ₂ H ₂ + O $\xrightarrow{3a}$ C ₂ HO + H	7.2x10 ⁻¹⁰ exp(- 6 100 K/T)
$\xrightarrow{3b}$ CH ₂ + CO	2.0x10 ⁻¹⁰ exp(- 3 300 K/T)
CH ₂ + O \longrightarrow CH + OH	1.5x10 ⁻¹⁰
\longrightarrow HCO + H	0
CH ₂ + H \longrightarrow CH + H ₂	5.0x10 ⁻¹¹
C ₂ HO + H \longrightarrow CH ₂ + CO	5.0x10 ⁻¹¹
CH ₂ + C ₂ H ₂ \longrightarrow C ₃ H ₄	1.5x10 ⁻¹¹
C ₂ H ₂ + OH \longrightarrow products	1.0x10 ⁻¹⁰ exp(- 7 000 K/T)

Table 2. Kinetic Data for the C₂H₂/N₂O Reaction System

In Tab. 2 the kinetic data used in the C_2H_2/N_2O reaction system are shown. The computer simulations were performed to determine whether or not the preliminary estimates of the rate coefficients k_2 and k_{2a} or k_3 and k_{3a} , given above, must be modified, if a more detailed reaction scheme is used. The measurements and computer simulations are not sufficient to determine further rate coefficients. For both reaction systems, a nearly perfect fit in most cases, and at least a satisfactory fit in some cases was achieved. An example is shown in fig. 4. In all cases the influence

of the additional reactions on the computed H- and O-atom concentrations are relatively weak. Because of the good agreement between experiment and calculation, found in all cases, the estimates of the rate coefficients k_i and k_{ia} are confirmed by the computer simulations^{15, 16}.

In fig. 5 the rate coefficient k_{2a} obtained in the HCN/ N_2O reaction system is shown together with the low temperature results of Davies and Trush⁶. The non-Arrhenius behaviour of the rate coefficient is obvious. In fig. 6 results of the present shock tube measurements on $C_2H_2 + O$ reactions together with available results obtained by various experimental techniques are summarized. The room temperature values and the recommended extrapolation of Jones and Bayes¹⁰ for k_{3a} fits the present results if non Arrhenius behaviour of k_{3a} is assumed.

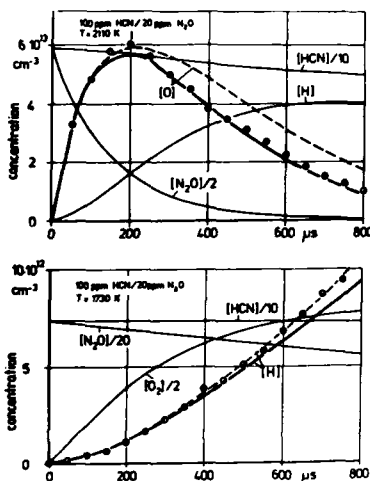


Figure 4. Measured and computed H- and O-atom concentration profiles in the HCN/ N_2O reaction system using the reaction scheme of Tab. 1

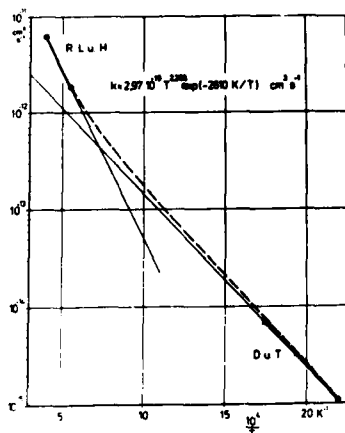


Figure 5. Rate coefficients of the reaction $HCN + O \rightarrow OCN + H$.

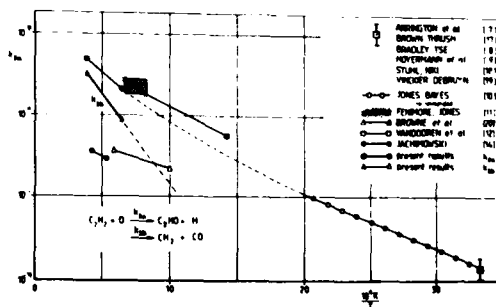



Figure 6. Rate coefficients of the reaction $C_2H_2 + O$.

ACKNOWLEDGEMENTS

The authors wish to thank Dr. Dan Dolan, University of Minnesota, for helpful discussion. The financial support of the Deutsche Forschungsgemeinschaft is gratefully acknowledged.

REFERENCES

1. P. Roth, Th. Just, Ber. Bunsenges. Phys. Chem. 81, 572 (1977)
 2. P. Roth, Th. Just, Ber. Bunsenges. Phys. Chem. 79, 682 (1975)
 3. P. Roth, U. Barner, R. Löhr, Proceedings of the 12th International Symposium on Shock Tubes and Waves, p. 621 (1979)
 4. C. P. Fenimore, 13th Symp.(Int.) on Combustion, p. 373, The Combustion Institute, Pittsburgh 1971
 5. F. Bachmeier, K.H. Eberius, Th. Just, Comb. Sci. and Techn. 7, 77 (1973)
 6. F. B. Davies, B.A. Thrush, Trans. Faraday Soc. 64, 1836 (1968)
 7. C.A. Arrington, W. Brenner, G.P. Glass, J.V. Michael, H. Niki, J. Chem. Phys. 43, 525 (1965)
 8. J.N. Bradley, R.S. Tse, Trans. Faraday Soc. 65, 2685 (1969)
 9. K. Hoyerman, H.G. Wagner, J. Wolfrum, Z. Physik. Chem. NF 36, 193 (1969)
 10. I.T.N. Jones, K.D. Bayes, 14th Symp.(Int.) on Combustion, p. 277, The Combustion Institute, Pittsburgh 1973
 11. C.P. Fenimore, G.W. Jones, J. Chem. Phys. 39, 1514 (1963)
 12. J. Vandooren, P.J. Van Tiggelen, 16th Symp.(Int.) on Combustion p. 1133, The Combustion Institute, Pittsburgh 1976
 13. G.P. Glass, G.B. Kistiakowski, J.V. Michael, H. Niki, 10th Symp.(Int.) on Combustion, p. 513, The Combustion Institute, Pittsburgh 1965
 14. C.J. Jachimowski, Comb. and Flame 29, 55 (1977)
 15. P. Roth, R. Löhr, H.D. Hermanns, Ber. Bunsenges. Phys. Chem. 84, 835 (1980)
 16. R. Löhr, P. Roth, Ber. Bunsenges. Phys. Chem. 85, 153 (1981)
 17. J.M. Brown, B.A. Thrush, Trans. Faraday Soc. 63, 630 (1967)
 18. F. Stuhl, H. Niki, J. Chem. Phys. 55, 3954 (1971)
 19. C. Vinckier, W. Debruyne, 17th Symp.(Int.) on Combustion, p. 623, The Combustion Institute, Pittsburgh 1978
 20. W. G. Browne, R. P. Porter, J.D. Verlin, A.H. Clark, 12th Symp.(Int.) on Combustion, p. 1035, The Combustion Institute, Pittsburgh 1969.
- 

AD P000284

THE EFFECT OF MINUTE QUANTITIES OF IMPURITIES ON SHOCK
TUBE KINETICS. THE REACTION $H_2 + D_2 \rightarrow 2HD$

Assa Lifshitz and Menashe Bidani

Department of Physical Chemistry, The Hebrew University
Jerusalem, Israel

Harvey F. Carroll

Department of Physical Sciences, Kingsborough
Community College of CUNY, Brooklyn, NY, USA

An ultra-clean 2 in I.D. single pulse shock tube coupled to an atomic resonance absorption detection system was constructed in order to determine H atom concentration by Lyman- α absorption. The shock tube with its LiF windows was baked to 300°C and pumped down to $\sim 10^{-7}$ torr under this baking temperature. Ultra-pure argon could be shock heated to ~ 2500 K with no spurious H atom absorption. The system was constructed in order to study the kinetics of chemical reactions, which are strongly catalyzed by H atoms, under the conditions where no such atoms are detected. The tube fulfilled the function of a single pulse shock tube but at the same time provided the knowledge whether or not H atoms were present in the hot gas. Specifically, the role of H atoms in the $H_2 + D_2$ exchange reaction was studied. Mixtures of hydrogen and deuterium diluted in argon were shock heated to 1375-1760 K; samples were then taken from the tube and analyzed mass spectrometrically for the ratio $[HD]/[D_2]$. 1400 K was the highest temperature at which no spurious H atom absorption was observed in a shocked mixture of 1% H_2 -1% D_2 . Under the conditions of no absorption, no (or $\leq 1\%$) HD conversion was obtained. At higher temperatures, Lyman- α absorption was detected and more HD conversion was observed. A comparison between these results and results obtained previously in less clean systems suggests that the high HD conversion observed in the past was strongly influenced by hydrogen atoms generated from impurities. The existence of a molecular mechanism in the H_2 - D_2 exchange reaction is thus highly doubtful.

INTRODUCTION

One of the major advantages of the shock tube over the conventional oven heating is the homogeneous conditions under which a chemical reaction can be studied at high temperatures. As the heating is gas dynamic, heat does not flow across the tube walls; they remain cold and prevent heterogeneous catalysis. This behavior was very often stressed when chemical kinetic studies in shock tubes were presented. The question of an uncontrolled homogeneous catalysis was but very little discussed, although it might create severe problems, as severe as in the case of heterogeneous catalysis. Impurities in the shock tube, depending upon their nature and quantity, can produce upon

shock heating active fragments which might then participate in the main reaction. This is in particular true when an unreactive chemical system is subjected to contaminants which can easily be decomposed by the shock wave to produce active radicals or atoms. These can later homogeneously catalyze the studied chemical reactions.

The most common contaminants are leaked oxygen, water, and pump oil as well as hydrocarbon impurities in the carrier gas. The latter two create the more undesirable situation. Although the commonly used pumping systems can easily reduce the pressure in the tube to a suitably low level ($\sim 10^{-5}$ torr), some hydrocarbon oil molecules are always able to make their way through the trap and become absorbed on the shock tube walls. They are later stripped off during the shock process and decompose in the hot gas. Their decomposition, together with that of the hydrocarbon impurities in the carrier gas, leads to the production of H atoms, one of the most chemically active species.

The oxidation of carbon monoxide and the exchange reaction between hydrogen and deuterium are only two of many examples where chemical reactions are strongly catalyzed by very small concentrations of hydrogen atoms.

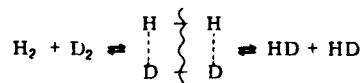


Clearly, in order to study the clean molecular processes:



the condition where no hydrogen atoms are present in the reaction system must be established. We shall later show that such conditions do not at all exist in conventional shock tubes.

It was already shown fifteen years ago that when a mixture of hydrogen and deuterium highly diluted in argon is shock heated in a conventional single pulse shock tube to the temperature range 1100–1300 K, a considerable conversion to deuterium hydride (HD) occurs with an activation energy of ~ 40 kcal/mole^{1,2,3}. Since this temperature range and activation energy are much lower than what is required to dissociate molecular hydrogen to hydrogen atoms, the production of HD could not be explained on the basis of an atomic displacement mechanism (reactions 3 & 4) in view of the apparently very low concentration of H atoms in the system. A molecular mechanism (reaction 6) and a 4-center transition state H_4 was therefore suggested in order to explain the experimental observations.



It should be emphasized that the ruling out of the 3-center atomic displacement route (reactions 3 & 4) was based on a *calculated* value of H atoms

assuming two sources: the self dissociation of the hydrogen molecule and the known leak rate of oxygen. No attempt was ever made to actually determine the H atom concentration in the hot gas.

When a 4-center transition state H_4 was suggested as an intermediate in the H_2 - D_2 exchange¹, attempts were made by a number of theoreticians to calculate a reaction path on the H_4 potential energy surface that would switch atoms but at energies less than a single H_2 dissociation. However, no matter what structure was assigned to the H_4 complex such a path could never be calculated⁴⁻⁶. The reaction barrier was always above the H_2+2H asymptote. (An H_4 intermediate was later suggested^{7,8} but the temperature at which the reaction was studied was too high to allow the formation of such a complex.)

Serious objections were therefore raised^{9,10} to the proposed H_4 transition state claiming that the main source of H atoms was not the dissociation of molecular hydrogen but shock dissociation of hydrogen containing impurities such as pump oil, for which the activation energy is much lower.

In order to clarify this and other points, we decided to study the exchange reaction between H_2 and D_2 in a single pulse shock tube and at the same time to determine the H atom profile directly, using Lyman- α absorption at 1215.67 Å. The goal was to achieve the conditions where no absorption of H atoms around 1400 K would be observed and at the same time to find out whether exchange has occurred. The work described in this article is part of this effort.

EXPERIMENTAL

In order to achieve the conditions where no spurious H atom absorption at Lyman- α would be observed due to impurities, an ultra clean single pulse shock tube was constructed. It was 2 in I.D. made of electropolished seamless stainless steel tubing. The driven section was 4 m long and the driver had a variable length up to 2.7 m. All parts of the shock tube were cleaned with trichlorethylene and methylene chloride prior to their assembly. The only rubber or plastic material in the high vacuum system was the Viton O-rings in the Al gate valves.

Pieces of the shock tube were connected with copper gaskets, except for the last half of the driven section, which used gold gaskets to ensure smoothness in the region of the formed shock wave. Shock speed for temperature calculations was measured with flush mounted Model 6QP 500 Vibrometer quartz transducers. An additional transducer to record the pressure - time history was mounted in line with the optical path.

The vacuum system consisted of a 4" diffusion pump charged with Dow Corning 705 oil and two Varian 4" Long-Life LN_2 Cryotrap separated by a 1 m, 4 in I.D. curved pipe. Roughing was done by a mechanical pump located 2.5 meters away from the shock tube port and trapped with LN_2 and a 5 Å molecular sieve; all this to prevent back streaming of pump oil into the shock tube. The bakeable gas handling and mixing manifold was made of stainless steel and used Nupro metal seal bellows valves. The pressure was read by Schaevitz diaphragm type pressure transducers. A schematic diagram of the pumping system is shown in Figure 1.

Diaphragms used were 0.3 mm aluminum, scored with a knife edge to ensure a clean burst. Dry nitrogen was used to fill the shock tube when changing diaphragms and kept flowing at positive pressure while the shock tube was open.

The test gas for the exchange studies was composed of 1% Matheson

Research Grade hydrogen (99.9995%) and 1% Matheson C.P. Grade deuterium (99.5%) diluted in Matheson Grade argon (99.9995%). Prior to preparation, the storage tank and gas handling system were baked to 300°C under high vacuum. All gases were passed through previously baked under vacuum Merck 5 Å Molecular Sieve beads in a trap cooled with ethanol and LN₂ (about -100°C). All connecting tubings were flamed under vacuum if they had been open to the air. The test gas was prepared in an 8 liter stainless steel tank at 100 psia.

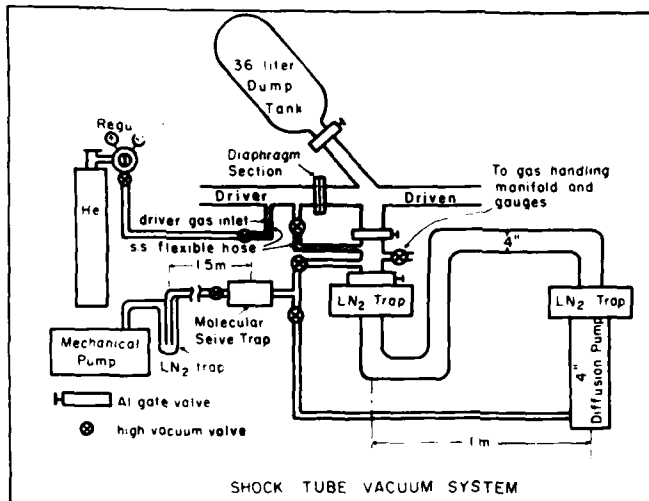


Figure 1. A schematic diagram of the pumping system of the ultra clean shock tube. Note the long distance between the pumps and the shock tube port.

The object of all the precautions taken was to keep the system clean and minimize the production of spurious H atoms upon shock heating. When these were not taken, for example, when the 99.9995% argon was used without further purification, some Lyman- α absorption was noticed already at 1500 K. It was also found that the test gas had to be introduced into the shock tube through the end block and not through the diaphragm section as is usually done. Doing so, minute traces of pump oil located near the diaphragm were swept out of the tube during the introduction of the test mixture rather than into the tube.

In order to be able to bake the shock tube with its LiF windows to 300°C, a novel double window system shown in Fig. 2 was designed¹¹. This design was necessary since unlike quartz or glass, a gold gasket cannot be used to make the vacuum seal as the pressure needed would crush the window. Epoxy is most commonly used to seal these windows, but it begins to decompose at

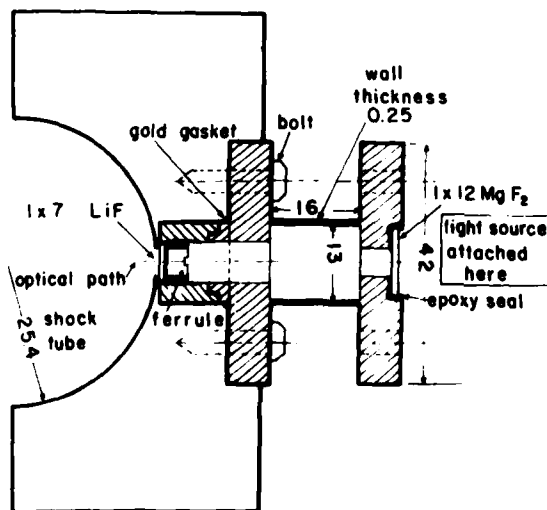


Figure 2. The end block of the tube with its double window arrangement. The system is baked to 300°C.

about 150°C, thus limiting the baking temperature. In this design, the windows on the walls of the shock tube are flush mounted and held in place by a metal ferrule. They are not vacuum tight and are not epoxied in. The second window which provides the vacuum seal is epoxied in place and is separated from the shock tube by a thin walled (0.25 mm) stainless steel tube to minimize heat transfer to the epoxy seal. On the other side of the shock tube the thin walled tube is replaced by thin bellows. It provides a flexible connection to the monochromator and allows for slight changes in position owing to the shock tube expansion upon baking. This system has been baked repeatedly to 300°C at 5×10^{-7} torr overnight with no decomposition of the epoxy.

With the shock tube and double window just described, baked overnight to 300°C under 5×10^{-7} torr, very good performance was obtained. Matheson Grade argon which was further purified with a 5 Å molecular sieve at $\sim 100^\circ\text{C}$ could be shock heated to ~ 2500 K without showing any H atom absorption at Lyman- α . 1% H_2 in argon purified as above could be shock heated to 1500 K with less than 5% peak absorption. These conditions were found satisfactory and suitable for the $\text{H}_2 + \text{D}_2$ exchange studies.

The spectrometric system attached to the shock tube consisted of the Lyman- α radiation source, the optical cell (the shock tube with its double window system), the monochromator and the extreme solar blind photo multiplier. The light source is a conventional one made of 13 mm O.D. quartz tube through which 1% H_2 in helium is flown at 2-3 torr. The Ophthos Evanson microwave cavity received 50 watts power from a KIVA 2.45 GHz generator. A McPherson Model 218 0.3 m scanning monochromator is attached to the opposite side of the end block. An EMR Model 542G-08-18-03900 extreme solar blind photomultiplier, operated at 3000 V picks up the signal and feeds it to a Model 805 Biomation Waveform Recorder modified for two channel operation. Signals are displayed on an oscilloscope and recorded on an X-Y recorder. The Lyman- α signal at 1215.67 Å had a signal to noise ratio of over 10 to 1. The response time of this arrangement was 50 μsec . Typical synchronized pressure and absorption traces are shown in Figure 3.

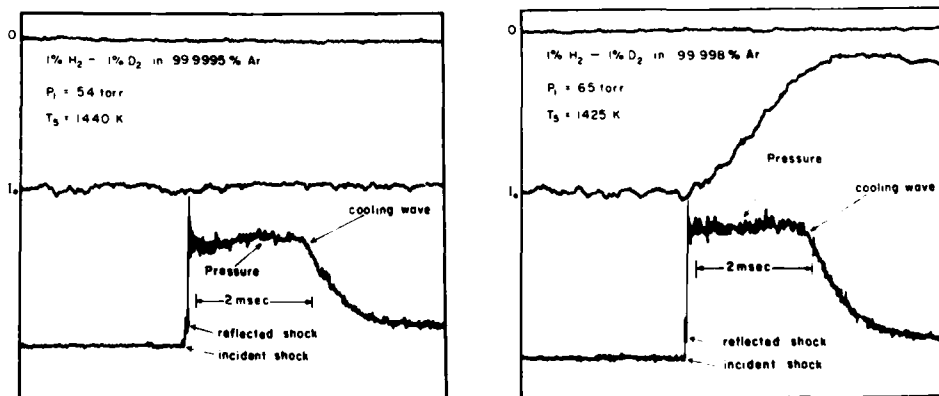


Figure 3. Synchronized pressure and Lyman- α absorption traces. A mixture of 1% H_2 -1% D_2 in 99.998% argon shows considerable absorption around 1400 K.

RESULTS AND DISCUSSION

A number of shocks were run over the temperature range 1370-1760 K with an initial pressure $p_1 \sim 60$ torr. For each shock the Lyman- α absorption was recorded using the spectrometric system described earlier. In addition, a 50 ml sample was collected from the end block of the driven section for mass spectral analysis. Analyses for H_2 , HD and D_2 were done on an ATLAS MAT CH4

mass spectrometer. Dwell times were approximately 2 msec.

A summary of the experimental results is given in Table I. It shows the shock temperature, the percent absorption at the peak of the absorption trace and the percent conversion expressed as $\{[HD]/[D_2]\}_t - \{[HD]/[D_2]\}_0$. Although the data are somewhat scattered they give a clear picture, in particular when compared to shocks run previously in conventional (rather than ultra clean) single pulse shock tubes.

The exchange results obtained in the present study (L, B & C 1980) are shown in comparison with four previous studies. They are expressed in a graphical form as $[HD]_t/[HD]_{eq}$ plotted against the temperature and are shown in Figure 4. The differences in the extent of exchange in the five different

Table I

Results of the Exchange Tests in the Ultra Clean Shock Tube

Shock No.	Shock Temperature K	Peak Absorption in Percent	$\{[HD]/[D_2]\}_t - \{[HD]/[D_2]\}_0$
1	1370	~0	0.8
2	1420	~6*	1.8
3	1430	25*	3.6
4	1440	~0	3.1
5	1495	~6	2.5
6	1505	~5	1.5
7	1580	~5	6.4
8	1610	16	10.3
9	1710	15	15
10	1715	17	26
11	1760	57	27

*unpurified argon

studies are striking. In the early studies of Bauer & Ossa¹ and Lifshitz & Burcat² a few percent conversion to HD were already obtained at 1100 K whereas in the present study a temperature of 1500 K was necessary to observe the same extent of exchange. When looked at from another angle, at around 1400 K, no (or less than 1%) exchange was obtained in the present study, whereas in the two earlier studies mentioned above, 35-50% exchange was observed at that temperature. The only difference between the present (L, B & C 1980) and the earlier studies (B & O 1966, B & L 1967) is the cleanliness of the systems used. In the present study, an ultra-clean shock tube has been used and no absorption of Lyman- α radiation was detected at 1400 K (see Table I). In the previous studies, relatively unclean tubes have been used, and no purification of the gases was attempted. Since no H atom detection systems were coupled to these tubes, no information is available as to how many H atoms were present in the hot gas. However, Lifshitz and Frenklach examined the Lyman- α absorption in a mixture of 1% D₂-1% H₂ in prepurified argon (99.998%) using the same tube used by Lifshitz and Burcat ten years earlier. Under the same pumping conditions and similar overall experimental conditions, almost complete absorption of the Lyman- α radiation was observed around 1400 K. This clearly indicates a high concentration of H atoms, probably sufficient to bring the exchange close to equilibrium via the $H + D_2 \rightarrow HD + D$ chain.

In all the studies performed the extent of HD production was strongly dependent on the cleanliness of the shock tube used. The study of Lifshitz

and Frenklach (1976)¹² was performed in a relatively clean tube but not as clean as the present one. Extents of exchange were higher than the ones in the present study but considerably lower than the ones reported in the two early studies. (See Figure 4.)

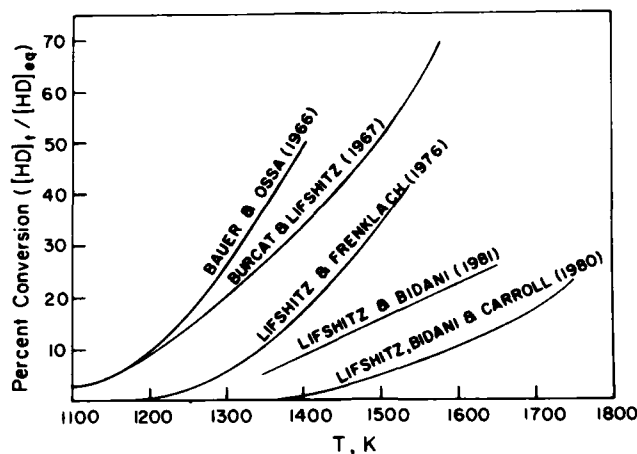


Figure 4. A comparison between five exchange studies. The extent of exchange is determined by the cleanliness of the tube.

Actually, Figure 4 represents also a plot of $[HD]_t/[HD]_{eq}$ vs. percent absorption of the Lyman- α radiation, except that the percent absorption scale is different for each study. In the three later studies, where Lyman- α absorption was followed, the extent of exchange was higher for higher optical densities. The percent absorption for a given mixture and tube conditions was always found to increase with temperature. This suggests that the concentration of H atoms increases with temperature. The X axis in Figure 4 may be very well replaced by H atom concentration for a given study.

The only conclusion that can be drawn from this analysis even before carrying out any calculations is that the exchange was due to impurities that generated hydrogen atoms upon shock heating.

Supporting evidence to what has already been concluded is found in the rate law which was deduced in many H/D shock tube exchange studies^{1,2,13-15}. In almost all cases, a strong third body effect was observed (effect of the argon diluent). It was interpreted as the participation of the argon in vibrationally exciting the exchange partners. We believe that the strong dependence of the exchange rate on the concentration of the third body was related to its function in stripping off the absorbed pump oil impurities from the shock tube walls and dissociating them as well as the hydrocarbon impurities in the argon, with the consequent production of hydrogen atoms.

One should also mention the exchange studies performed by Kern et al.,¹⁶ who determined the time profile of the HD in a TOF mass spectrometer coupled to their shock tube. They found a rate law in which $[HD]_t$ was proportional to t^2 . Since the concentration of the hydrogen atoms increases linearly with time and since $d[HD]/dt$ is proportional to $[H]_t$, a quadratic time dependence for $[HD]_t$ must show up.

Additional supporting evidence for the radical chain mechanism can be obtained by the following simple calculation. For this mechanism, at low extents of reaction, the concentration of $[HD]_t$ is given by:

$$[HD]_t = [H][D_2]k_3t \quad I$$

On the assumption that the mechanism is indeed a chain reaction mechanism

(reactions 3 and 4) let us calculate what should be the H atom concentration, and what should be the equivalent Lyman- α absorption in order to obtain the same extent of exchange observed by Bauer & Ossa¹ or Lifshitz & Burcat².

At 1400 K, $k_3 = 1.25 \times 10^{12} \text{ cm}^3 \text{ mole}^{-1} \text{ sec}^{-1}$. For a 2 msec reaction time (common to 2 in single pulse shock tubes), 10% exchange will require (Eq. I) an average concentration of H atoms of $4 \times 10^{-11} \text{ mole/cc}$. For 50% extent of exchange the value will be somewhat higher than $2 \times 10^{-10} \text{ mole/cc}$. In an optical path of 2 in with a conventional atomic resonance light source, the latter will cause at 1400 K some 80% absorption of Lyman- α radiation depending upon the specific calibration curve chosen^{12,17}. In view of the Lifshitz and Frenklach measurements of Lyman- α absorption in a conventional single pulse shock tube, such absorption (and even higher) would certainly be observed in the Bauer & Ossa or Lifshitz & Burcat experiments, if atomic resonance detection systems were attached to their tubes.

CONCLUSIONS

On the basis of the exchange rates obtained in this study and their comparison with previous exchange studies, it is believed that the exchange between two hydrogen molecules observed in the past is the result of homogeneous H atom catalysis. The formation of a 4-center transition state is therefore very doubtful.

ACKNOWLEDGEMENTS

The authors wish to thank Professor S. H. Bauer for continuous interest in this work and for many helpful discussions during the construction phase and the performance of the exchange experiments. This work was supported by a grant from the U.S.-Israel BiNational Science Foundation. Professor S. H. Bauer served as the American cooperative investigator for this grant. This research was also supported (in part) by a grant from the PSC-BHE Research Award Program of the City University of New York.

REFERENCES

1. S. H. Bauer and E. Ossa, *J. Chem. Phys.*, **45**, 434 (1966).
2. A. Burcat and A. Lifshitz, *J. Chem. Phys.*, **47**, 3079 (1967).
3. D. Lewis and S. H. Bauer, *J. Am. Chem. Soc.*, **90**, 5390 (1968).
4. D. M. Silver and R. M. Stevens, *J. Chem. Phys.*, **59**, 3378 (1973), and literature cited.
5. N. J. Brown and D. M. Silver, *J. Chem. Phys.*, **68**, 3607 (1978).
6. N. J. Brown and D. M. Silver, *J. Chem. Phys.*, **72**, 3869 (1980).
7. J. S. Wright, *Chem. Phys. Lett.*, **6**, 476 (1970), *Can. J. Chem.*, **53**, 549 (1975).
8. D. A. Dixon, R. M. Stevens and D. R. Herschbach, *Faraday Discuss. Chem. Soc.*, **62**, 110 (1977).
9. F. Kaufman, *Ann. Rev. Phys. Chem.*, **20**, 62 (1969).
10. S. W. Benson, Private Communication.
11. A. Lifshitz, M. Bidani and H. F. Carroll, *Rev. Sci. Instrum.*, **52**, 622 (1981).
12. A. Lifshitz and M. Frenklach, *J. Chem. Phys.*, **67**, 2803 (1977).
13. A. Lifshitz, C. Lifshitz and S. H. Bauer, *J. Am. Chem. Soc.*, **87**, 143 (1965).
14. A. Burcat, A. Lifshitz, D. Lewis and S. H. Bauer, *J. Chem. Phys.*, **49**, 1449 (1968).
15. W. S. Watt, P. Borrell, D. Lewis and S. H. Bauer, *J. Chem. Phys.*, **45**, 444 (1966).
16. R. D. Kern and G. G. Nika, *J. Phys. Chem.*, **25**, 1615, 2541 (1971).
17. Th. Just, in *Shock Waves in Chemistry*, A. Lifshitz, editor, Marcel Dekker Inc., New York, p. 279 (1981).

AD P 000 285

MOLECULAR BEAM TECHNIQUE FOR RECORDING
CHEMICAL SPECIES BEHIND INCIDENT SHOCK WAVES

ST. ARNDT and A. FROHN

Institut für Thermodynamik der Luft- und Raumfahrt, Universität
Stuttgart, Pfaffenwaldring 31, 7000 Stuttgart 80, Germany



It is the purpose of the present paper to develop a molecular beam technique for recording continuously the concentration of chemical species behind the incident shock wave in a shock tube. The sample is drawn through a diverging nozzle located at the end of the low pressure section of the shock tube. The inlet diameters of the nozzles are 1-4 mm. It is assumed that the expansion is so fast that freezing of chemical reactions occurs. With a skimmer a molecular beam is formed which is analyzed with a quadrupole mass filter. Preliminary experiments were performed with N_2 and binary mixtures of N_2 and O_2 at initial pressures between 1 mbar and 10 mbar and at Mach numbers ranging from $M_0 = 6$ to $M_0 = 12$. Experimental results are compared with intensities which are determined theoretically assuming a Maxwellian distribution function behind the incident shock.

INTRODUCTION

The experimental setup used in this paper is similar to devices, first proposed by Skinner^{1,2,3}. In his experiments the molecular beam was drawn from the gas heated by the reflected shock wave. The important difference is, that in our case the gas sample is drawn continuously from the flow behind the incident shock wave, thus a nearly undisturbed sampling is possible. The shock tube has been coupled directly to the molecular beam system without using a second diaphragm, which would disturb the flow. Pressure differences occurring between the low pressure section of the shock tube and the vacuum chambers of the molecular beam system are compensated by differential pumping. In the low pressure section pressures between one and ten millibar are used. Behind the expansion nozzle pressures lower than 10^{-4} millibar are obtained by a high pumping capacity. As a consequence of this high pressure difference the nozzle flow starts without delay.

EXPERIMENTAL CONFIGURATION

In Figure 1 the principle of the molecular beam apparatus is shown.

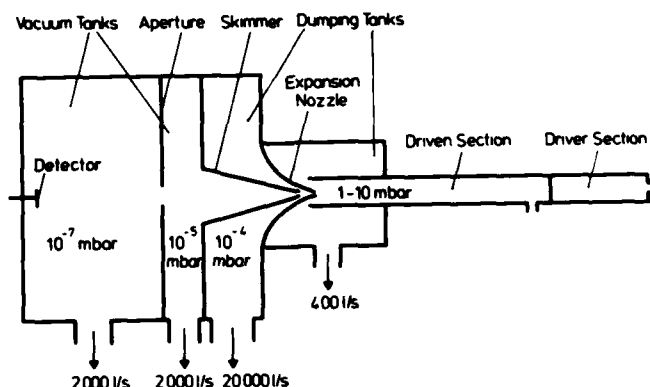


Fig.1 Schematic diagram of molecular beam apparatus

The low pressure section of the shock tube ends in a dumping tank so that most of the incident gas expands into this tank. The gas sample needed for the measurement is drawn through a supersonic nozzle located at the end of the dumping tank. This nozzle cuts out the sample from the core of the flow behind the incident shock wave and expands it within a few microseconds. Freezing of the chemical reactions occurs. Behind this nozzle there is a skimmer whose entrance diameter is in the order of some mean free paths of the molecules at this point. Thus a molecular beam is formed. The position of this skimmer is variable in axial direction and behind the skimmer there is an aperture in order to keep the ambient pressure for the molecular beam as low as possible. Thus in the detector chamber a vacuum of approximately 10^{-7} millibar is obtained and interference of reflected molecules with the beam is avoided. Because in all measurements only the core of the flow is used, no disturbance by boundary layer effects can occur as it is the case for measurements behind reflected shock waves, in which the gas sample is drawn through the thermal boundary layer on the end plate of the shock tube. The molecular beam is analyzed by means of a quadrupole mass filter, which is movable in three directions. In each run the concentration of only one mass is measured, because the duration of flow is in the order of some hundred microseconds.

The exchangeable tips of both nozzles were produced galvanically to get an extremely sharp nozzle entrance and a very smooth inner surface. The tips of the expansion nozzle have diameters between one and four millimeters and the entrance diameters of the skimmer are between two and five millimeters. The length of the shock tube is 8 m and the inner diameter is 38 mm. The vacuum tank of the molecular beam system has a volume of 0.7 m^3 . Shock tube and first dumping tank are built in UHV-technique to ensure that the test gas could not be impurified.

FEATURES OF THE MOLECULAR BEAM

The distance between the expansion nozzle and the skimmer defines the freezing time of the reactions. The known relation for the collision number leads to a number ϵ that is characteristic for the process of freezing. When

$$\epsilon = \int_{t_f}^{\infty} n \sigma \bar{c} dt ,$$

where t_f is the freezing time, becomes very small, the process of freezing is finished. The freezing time in the experiments carried out is in the order of one microsecond. By determination of the width of the radial beam intensity profile in the molecular beam one can find out, whether the nozzles are well positioned. Figure 2 shows a characteristic axial density profile in the molecular beam behind the last orifice, whose diameter was ten millimeters.

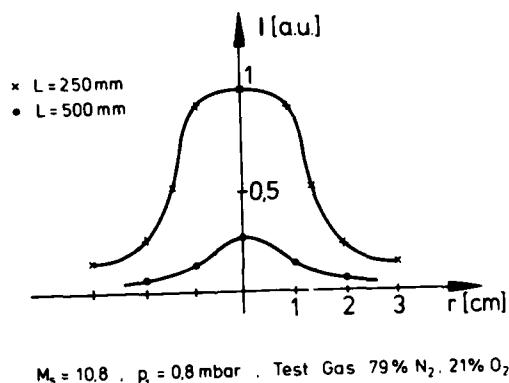


Fig.2 Radial density distribution in the molecular beam for different distances L between skimmer and detector

It can be seen, that the duration of flow in the molecular beam is much longer than the flow in the shock tube, which is caused by the molecular velocity distribution of the particles in the shock tube. Figure 3 shows a typical ion profile in air measured with a Langmuir probe in the shock tube and Figure 4 shows the corresponding ion current in the molecular beam measured with a Faraday cup.

Assuming a Maxwellian velocity distribution for the molecules in the flow behind the shock wave and using the flow variables after the expansion as initial conditions one can derive an analytical expression for the particle current in the molecular beam. The calculation takes into account the geometry of the experimental setup and the shape and length of the density profile of the particles in the flow behind the shock wave.

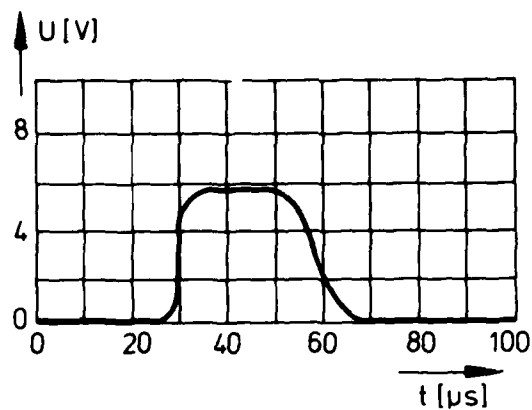


Fig.3 Ion profile in the shock tube

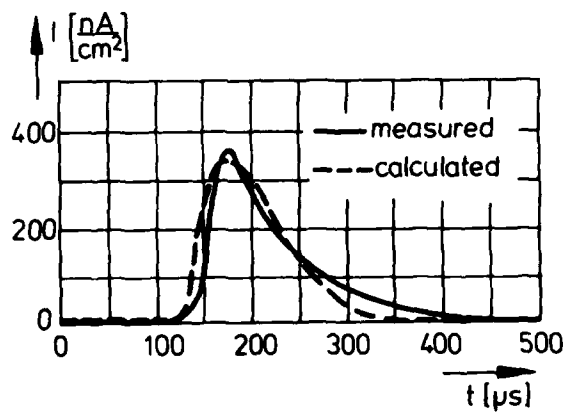


Fig.4 Ion profile in the molecular beam.

Experimental conditions:
 Test Gas 79 % N_2 , 21 % O_2 ;
 $M_s = 10,8$; $p_1 = 0,8$ mbar;
 Ions: NO^+ .

For the particle current in the molecular beam the following result is found:

$$I_1(t) = B \left[\left(\frac{x_1}{2} + \frac{u}{c_m} \right) \exp(-x_1^2) + \alpha (1 - \operatorname{erf} x_1) \right] \quad \text{for } t \leq t_1$$

and

$$I_2(t) = B \left[\left(\frac{x_1}{2} + \frac{u}{c_m} \right) \exp(-x_1^2) - \left(\frac{x_2}{2} + \frac{u}{c_m} \right) \exp(-x_2^2) + \frac{2\alpha}{\sqrt{\pi}} \int_{x_1}^{x_2} e^{-c^2} dc \right] \quad \text{for } t > t_1$$

where t_1 is the length of the ion profile in the shock tube and

$$B = \frac{e A u n_0^2}{\sqrt{\pi}} \quad ; \quad \alpha = \frac{\sqrt{\pi}}{4} + \frac{u^2}{c_m^2} \cdot \frac{\sqrt{\pi}}{2}$$

$$x_1 = \frac{L}{c_m t} - \frac{u}{c_m} \quad ; \quad x_2 = \frac{L}{c_m (t - t_1)} - \frac{u}{c_m} \quad .$$

The two expressions for $I_1(t)$ and $I_2(t)$ give the arrival conditions at the detector for molecules which are in the volume $A \cdot u \cdot t_1$ in the flow behind the incident shock wave, when t_1 is the duration of flow in the shock tube, u the flow velocity and A the entrance area of the skimmer. As the calculation not only includes the mass dependent particle current with respect to time but also the mass dependent radial intensity distribution the measured concentration profiles in the molecular beam can be corrected by comparison with the calculated profiles. The comparison between a measured and a calculated ion profile in the molecular beam is shown in Figure 4 for NO^+ . Figure 5 shows an example of a neutral density profile in the molecular beam.

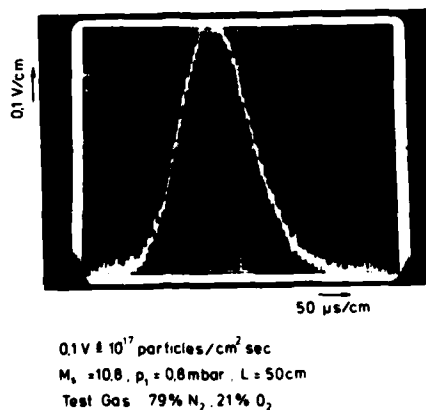


Fig.5 Density profile of NO in the molecular beam

Measurements of the beam concentration under various conditions have shown, that the measured beam intensity is a function of the distance between nozzle and skimmer as it is shown in Figure 6. At very short nozzle-skimmer distances the intensity decreases rapidly.

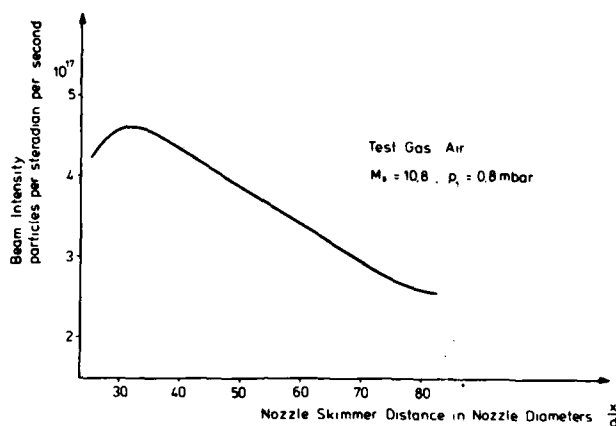


Fig.6 Beam intensity in dependence of the skimmer position

Figure 7 shows particle energies, measured in the molecular beam. The shock Mach numbers in the range between $M_s = 8$ and $M_s = 12$ were chosen because of the reactions which are investigated. Higher and of course lower particle energies are available.

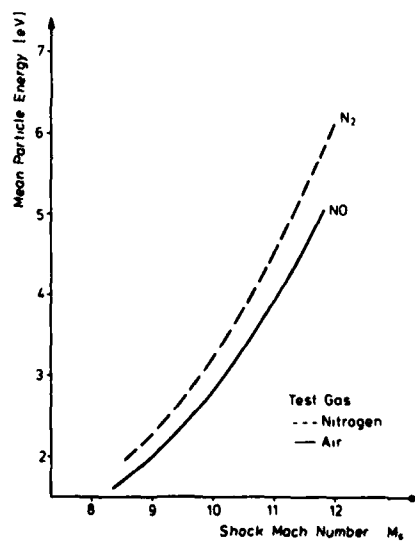


Fig.7 Particle energies in the molecular beam

Previous measurements at the well known high temperature system N_2-O_2 have shown, that it is possible to measure with the described experimental setup continuously the concentrations of reaction products that originate behind incident shock waves. In the system N_2-O_2 thermal ionization occurs, where the ion NO^+ dominates. Thus the system can be used to calibrate the mass filter so that absolute concentration measurements become possible. As the transformation of the density profile in the shock tube to the density profile in the molecular beam is given by an analytical expression the time dependent particle concentrations can be measured in the molecular beam.

ACKNOWLEDGEMENT

The authors acknowledge the support provided for this project by the "Deutsche Forschungsgemeinschaft".

REFERENCES

1. G.T.Skinner, Phys.Fluids 4, 1172 (1961)
2. T.V.Jones and M.A.Byrne, 6th Rarefied Gas Dynamics. 1311 (1969)
3. D.Spence and K.T.Dolder, Phys.Fluids 13, 88 (1970)

AD P 000286

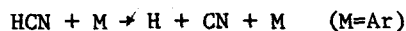


SHOCK TUBE STUDY OF THE THERMAL DECOMPOSITION OF HYDROGEN CYANIDE

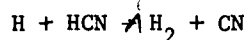
Attila Szekely, Ronald K. Hanson and Craig T. Bowman

High Temperature Gas Dynamics Laboratory
Department of Mechanical Engineering
Stanford University
Stanford, CA 94305

The decomposition rate of hydrogen cyanide,



has been determined in the temperature range 3570 - 5036 K using a shock tube technique. HCN - Ar mixtures (3 - 142 ppmv HCN) were heated by incident shock waves at post-shock pressures of 0.17 - 0.29 bar, and CN emission from the $\text{B}^2\Sigma^+ \rightarrow \text{X}^2\Sigma^+$ system near 388 nm was used to monitor the time-varying CN concentration. Interferences from secondary reactions, including:



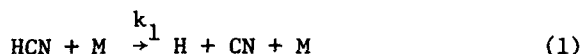
were minimized by using low initial HCN mole fractions. An important feature of the present experiments is that the emission records extend to long enough times for the HCN to be converted completely to CN, thereby making the emission intensity traces self-calibrating. The experimental data are closely fit by the Arrhenius expression

$$k_1 = 10^{(14.61 \pm 0.11)} \exp[(-44740 \pm 1060/T)] \text{ cc/mol-sec}$$

The present rate coefficient data, together with data at lower temperatures (2200 - 3300 K) by Roth and Just [1] and Roth [2], have been analyzed using unimolecular reaction rate theory.

I. INTRODUCTION

The kinetics of hydrogen cyanide are of current interest in studies of pollutant formation from the combustion of fuels containing organically bound nitrogen. As a first step in a program to investigate the pyrolysis and oxidation of HCN, an experimental study of the unimolecular decomposition of hydrogen cyanide:



was undertaken.

The only prior determination of k_1 is due to Roth and Just [1], who measured the rate coefficient in the temperature range 2200–2700 K using H-atom resonance absorption. Subsequent studies by Roth [2] have extended this range to 3300 K. The present experiments, based on an alternative measurement scheme, using CN emission, provide data in the temperature range 3570–5036 K. The combined temperature range of these three studies is nearly 3000 K, thereby enabling an accurate assessment of the temperature dependence of the rate coefficient and contributing to a better understanding of the unimolecular decomposition of small molecules.

II. EXPERIMENTAL

The experiments were carried out behind incident shock waves in a 15-cm internal diameter stainless steel shock tube. Diaphragms made of Lexan, 1.0 to 1.8 mm thick, were ruptured by increasing the driver gas (He) pressure until the plastic was punctured by a fixed crossed-knife device located downstream. Prior to each run, the shock tube was evacuated with a diffusion pump to a pressure of 6×10^{-6} torr or lower, with a combined leak and outgassing rate typically less than 3×10^{-5} torr/min.

Two sets of experiments were conducted, with hydrogen cyanide supplied by two different manufacturers. Scientific Gas Products supplied a mixture of 3.19% HCN in krypton, with an estimated level of impurities of less than 20 ppmv, the main impurity being water. Airco Industrial Gases supplied an analyzed mixture containing 1.01% HCN, <5.4 ppmv CO_2 , <2 ppmv H_2O , <1 ppmv O_2 , <0.2 ppmv SO_2 , and the balance argon. Mixtures of HCN in Ar were prepared by partial pressures immediately before each run in a stainless steel tank and mixed with an externally-driven stirring rod. Initial pressures in the test section were in the range 2–6.5 torr, with HCN mole fractions of 3 to 142 ppmv. Post-shock pressures varied from 0.17 to 0.29 bar.

The progress of the decomposition reaction was monitored by measuring CN-radiation in the violet ($\text{B}^2\Sigma^+ \rightarrow \text{X}^2\Sigma^+$) system around 388 nm, using a Bausch and Lomb 1/4-meter monochromator with a spectral bandwidth of 16 nm, coupled to a Dumont 7664 photomultiplier tube. The radiation profile was recorded on a Nicolet Explorer III digital oscilloscope with a resolution of 0.5 μs /data point. The spatial resolution of the optical system was varied from 3 to 6.5 mm by adjusting the entrance and/or exit slits of the monochromator or by changing the horizontal width of a slit placed between the shock tube and the monochromator. Additionally, the electronic response time of the system was varied in the range 1.5–2.5 μs by using low-pass filters with different cut-off frequencies. In this way adequate ratios of chemical reaction time to shock transit time and electronic rise time could be

achieved, while maintaining a good signal to noise ratio. A typical experimental trace of CN emission intensity as a function of laboratory time is shown in Fig. 1.

III. DATA REDUCTION

In all the experiments, very small concentrations of HCN were used, so that:

1. the heated gas is optically thin, and
2. the post-shock temperature is essentially constant during the test time employed for rate coefficient determination (< 400 sec).

If V is the output voltage of the detector and I the intensity of spontaneous emission incident on the detector, within the spectral bandwidth of the monochromator, then:

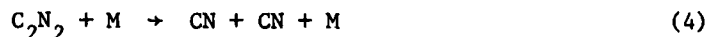
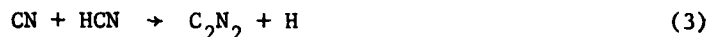
$$V \propto I \propto [\text{CN}]L\phi(T)$$

where $[\text{CN}]$ is the time-dependent CN concentration, L the shock tube diameter and $\phi(T)$ a function of temperature which takes into account the CN spectroscopy and the optical arrangement. Since T is essentially constant throughout an experiment,

$$V = \text{const.} \times [\text{CN}]$$

and the CN concentration time history is given by the V vs. time record.

The rate coefficient, k_1 , was determined by matching measured and calculated histories of $[\text{CN}]/[\text{CN}]_{\text{max}}$, where $[\text{CN}]_{\text{max}}$ is the maximum $[\text{CN}]$ concentration attained within a given experiment. The following five-reaction mechanism was employed in the analysis:



Forward and reverse reactions were included, the rate constants used being given in Table I. A sensitivity study showed that CN formation is dominated by Reaction (1) for the initial HCN concentrations employed. The influence of the other reactions is negligible for a range of reasonable values of the rate coefficients (See Figs. 2 and 3). The presence of a CN emission plateau in all experiments, together with a consistent, concentration-independent $V_{\text{max}}/[\text{HCN}]_0$ vs. T curve, confirms the fact that CN-removing reactions play only a minor role within the reaction times of interest. Table II lists the experimental conditions and the determined k_1 -values for all the runs. The tabulated k_1 -data were fit to an Arrhenius expression in the temperature range 3570 - 5036 K, Fig. 4. The best least-squares fit to the data is given by:

$$k_1 = 10^{(14.61 \pm 0.11)} \exp[(-44740 \pm 1060)/T] \text{ cc/mol-sec}$$

corresponding to an activation energy of 372.1 kJ/mol, significantly lower than the endothermicity of the reaction ($\Delta H_{T=98}^\circ = 502.3 \text{ kJ/mol}$ [3]; see discussion).

IV. DISCUSSION

The low initial HCN concentrations used in the present study were chosen so as to minimize the contribution of secondary reactions, especially (3), to the removal of HCN. Experiments in progress suggest a value of k_3 of about $3 \times 10^{13} \text{ cc/mol-sec}$ in the temperature range 3500 - 4200 K. For the lower limit of the temperature range of the present experiments, reaction (3) limits the initial HCN concentration to several tens of ppmv if significant kinetic interference is to be avoided.

The fact that experiments performed with HCN from two different sources are in excellent agreement indicates that impurities present in the gases did not affect the determination of the rate coefficient. The effect of impurities such as H_2O and O_2 in the test mixture, due to leaks and outgassing, was investigated analytically and found to influence the determination of k_1 only minimally.

A reported source of error in determining kinetic parameters by monitoring radiation from electronically excited CN is the possibility that $\text{CN}(\text{B}^2\Sigma^+)$ is not in equilibrium with $\text{CN}(\text{X}^2\Sigma^+)$ [4]. If $\text{CN}(\text{B}^2\Sigma^+)$ is not in equilibrium with $\text{CN}(\text{X}^2\Sigma^+)$, however, then it should only differ from the equilibrium value, $\text{CN}(\text{B}^2\Sigma^+)_e$, by a temperature and pressure-dependent factor which is given by a combination of collisional activation and deactivation and radiative quenching rate coefficients. Since both T and P are essentially constant throughout the present experiments, the ratio $[\text{CN}(\text{B}^2\Sigma^+)]/[\text{CN}(\text{B}^2\Sigma^+)]_{\text{max}}$ should be equivalent to $[\text{CN}]/[\text{CN}]_{\text{max}}$ at all times.

For the present experimental conditions, reaction (1) is within the low pressure, second order regime. According to weak-exchange process theory [5],

$$k_1 = \beta_c k_1^{\text{s.c.}} \quad (6)$$

where β_c is the weak-collision factor, and $k_1^{\text{s.c.}}$ is the strong-collision rate coefficient. $k_1^{\text{s.c.}}$ can be computed using methods outlined in [5]. For our conditions, the values of β_c range from about 0.02 at 5000 K to 0.04 at 3600 K, which is within the range for experimentally determined β_c 's for the decomposition reactions of other small molecules [5]. In addition, the temperature dependence of β_c over the temperature range 2200 - 5000 K was determined, using the present experiments together with those reported in [1-2]. The individual β_c - values together with a best least-squares fit:

$$\beta_c = 10^{(6.75 \pm 0.42)_T - (2.27 \pm 0.12)} \quad (7)$$

are plotted in Fig. 5. The temperature exponent is in reasonable agreement with the value suggested by Rabinovitch and coworkers [7,8] in the weak-collision limit. Fig. 6 shows the present k_1 -values, the data of Refs. 1 and 2 and a plot of k_1 vs. T obtained by using Equation (6) with β_c given by Equation (7).

ACKNOWLEDGEMENTS

The authors wish to thank Prof. Dr.-Ing. P. Roth, Universität Duisburg, for providing us with additional unpublished data on the decomposition of hydrogen cyanide. This work was supported by the U. S. Department of Energy under Contract DE-AM03-76F00326, P. A. 68.

REFERENCES

1. Roth, P., Just, Th., Ber. Bunsenges. Phys. Chem. 80, 171 (1976).
2. Roth, P., Private Communication, 1981.
3. Handbook of Chemistry and Physics, 57th Edition, Chemical Rubber Company Press, Cleveland, Ohio (1977).
4. Fueno, T., Tabayashi, K., Kajimoto, O., J. Phys. Chem, 77, 575 (1973).
5. Troe, J., J. Chem. Phys. 66, 4758 (1977).
6. Luther, K., Troe, J., Seventeenth Symposium (International) on Combustion (The Combustion Institute, Pittsburgh, 1979), p. 535.
7. Tardy, D. C., Rabinovitch, B. S., Chem. Rev. 77, 369 (1977).
8. Rabinovitch, B. S., Keil, D. G., Burkhalter, J. F., Skinner, G. B. Proc. 10th Int. Shock Tube Symp. (The Shock Tube Research Society, Japan, 1975), p. 579.
9. Baulch, D. L., Drysdale, D. D., Horne, D. G., Lloyd, A. C., Evaluated Kinetic Data for High Temperature Reactions, Vol. 1, 1972.

TABLE I

Reaction	Rate Coefficient*	Reference
$\text{HCN} + \text{M} \rightarrow \text{H} + \text{CN} + \text{M}$	$4.07 \times 10^{14} \exp(-44740/T)$	Present experiments
$\text{H} + \text{HCN} \rightarrow \text{H}_2 + \text{CN}$	2×10^{12}	Estimate
$\text{CN} + \text{HCN} \rightarrow \text{C}_2\text{N}_2 + \text{H}$	3×10^{13}	Estimate (based on experiments in progress)
$\text{C}_2\text{N}_2 + \text{M} \rightarrow 2\text{CN} + \text{M}$	$[3.51 \times 10^{12}/5!] T^{1/2} (63160/T)^5 \times \exp(-63160/T)$	4
$\text{H}_2 + \text{M} \rightarrow 2\text{H} + \text{M}$	$2.2 \times 10^{14} \exp(-48310/T)$	9

* cc/mol-sec

TABLE II

Run #	T(K)	P ₂ (bar)	X _{HCN} ^o (ppmv)	k ₁ (cc/mol-sec)
1	3570	0.26	2.7	1.74×10^9
2	3613	0.26	17.0	1.82×10^9
3	3650	0.22	3.5	1.74×10^9
4	3730	0.25	36.0	2.56×10^9
5	3770	0.22	3.0	2.78×10^9
6	3770	0.26	142.0	2.54×10^9
7	3776	0.25	73.0	2.94×10^9
8	3800	0.25	17.0	3.42×10^9
9	3840	0.22	60.0	3.50×10^9
10	4020	0.19	27.0	5.88×10^9
11	4039	0.29	72.0	6.47×10^9
12	4065	0.31	19.0	7.00×10^9
13	4120	0.29	17.0	7.80×10^9
14	4220	0.26	36.0	9.00×10^9
15	4275	0.23	12.0	9.07×10^9
16	4355	0.20	19.5	1.50×10^{10}
17	4545	0.20	22.0	2.60×10^{10}
18	4580	0.19	15.0	1.92×10^{10}
19	4820	0.19	20.0	3.00×10^{10}
20	4920	0.18	22.0	5.35×10^{10}
21	4920	0.18	22.2	5.35×10^{10}
22	5036	0.17	39.0	6.05×10^{10}

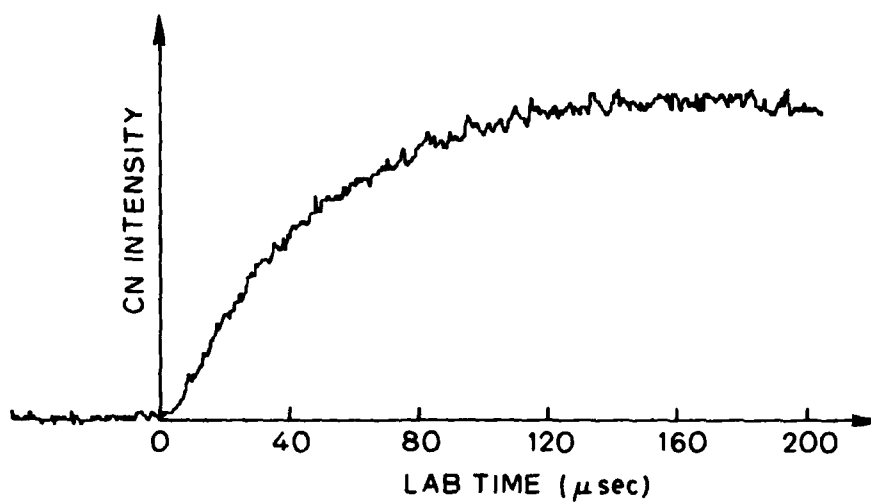


Fig. 1. CN-emission intensity profile (Run 15).

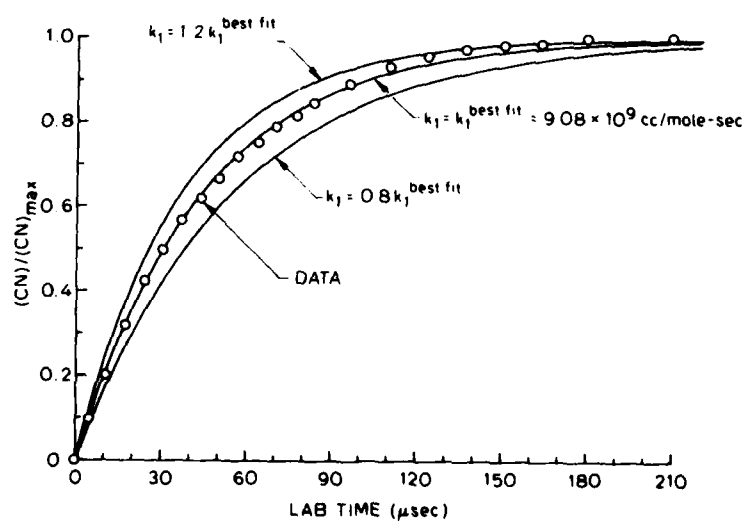


Fig. 2. Comparison of measured and calculated $[CN]/[CN]_{max}$ profiles (Run 15).

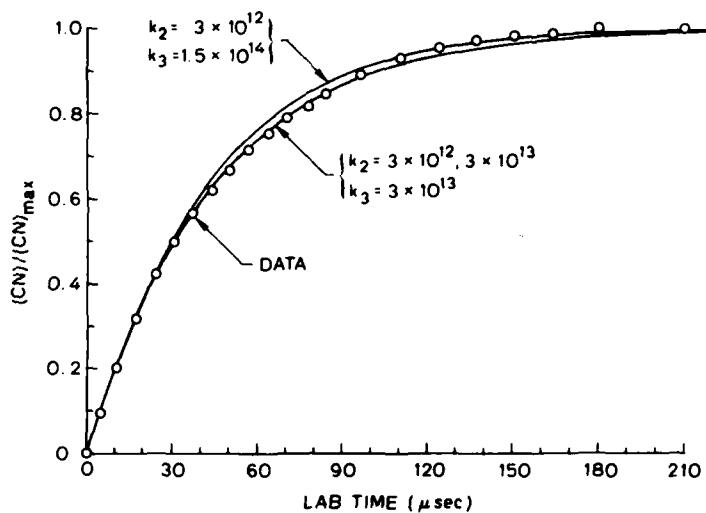


Fig. 3. Sensitivity of $[CN]/[CN]_{\max}$ to other rate coefficients (Run 15).

The two curves corresponding to $k_2 = 3 \times 10^{12}$ and $k_2 = 3 \times 10^{13}$ are indistinguishable.

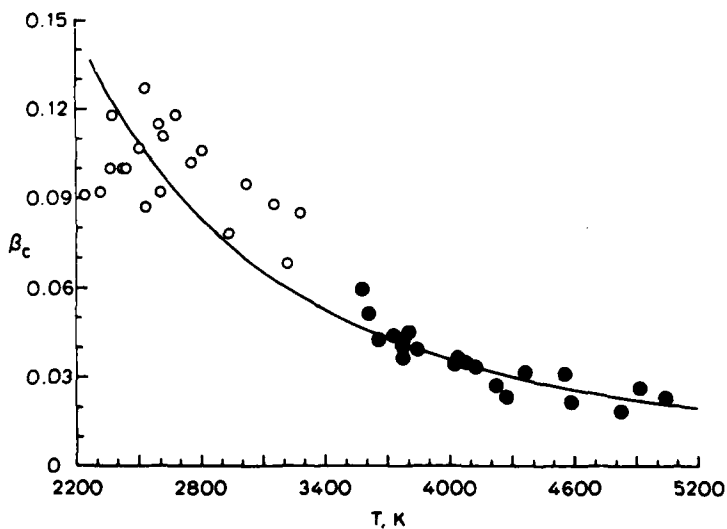


Fig. 4. β_c vs. T for present experiments (●) and those of [1-2] (○). The line is a least-squares fit to the data given by $\beta_c = 10^{6.75} T^{-2.27}$.

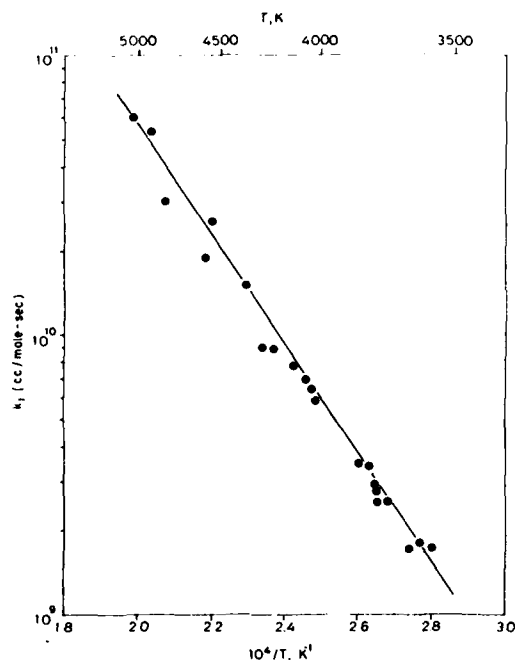


Fig. 5. Arrhenius plot of k_1 : $\text{HCN} + \text{M} \rightarrow \text{H} + \text{CN} + \text{M}$

$$k_1 = 10^{14.61} \exp(-44740/T) \text{ cc/mol-sec}$$

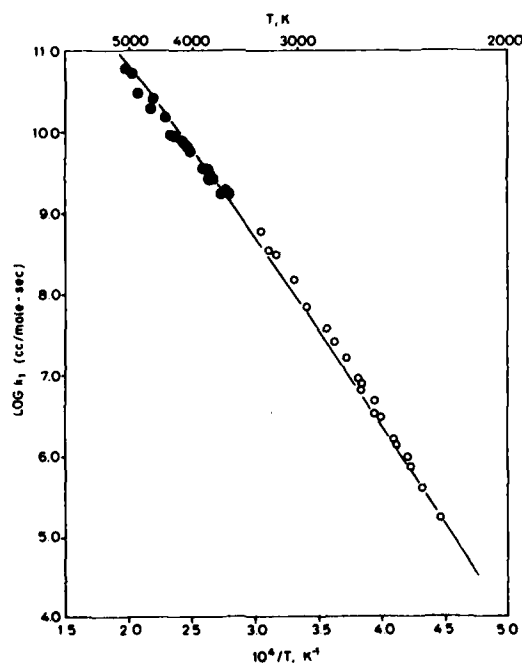


Fig. 6. Comparison between experimentally determined k_1 -values (● present experiments, ○ [1-2]) and k_1 given by Eq.(6), with β_c given by Eq.(7).



AD P000287

DECOMPOSITION OF HYDROGEN AZIDE IN SHOCK WAVES

G. Dupré*, C. Paillard*, J. Combourieu*, N.A. Fomin†, R.I. Soloukhin†

*Centre National de la Recherche Scientifique et Université, Orléans, FRANCE.

†Heat and Mass Transfer Institute, Minsk, U.R.S.S.

The thermal decomposition of hydrogen azide dilute in argon has been studied in the pressure region from 55 to 200 Torr, between 850 and 2000 K. The evolution of species such as HN_3 , $\text{NH}({}^1\Delta)$, $\text{NH}({}^3\Sigma^-)$, NH_2 and N_3 was monitored behind incident shock waves using emission techniques. At temperatures T_2 lower than 1250 K, the fast consumption of HN_3 was preceded by an induction period which became negligible at higher temperatures. For $T_2 > 1250\text{K}$, the apparent rate constant of the decomposition process, determined from HN_3 half-life, was found to be of first order in both HN_3 and Ar. With mixtures containing 0.5 mol % HN_3 and $1250 < T_2 (\text{K}) < 1400$, our investigation yielded an expression which is in good agreement with that of Kajimoto et al. in the same temperature and dilution ranges, but at higher pressures. However in opposite to Kajimoto et al.'s results, $\text{NH}({}^1\Delta)$ was found to be the principal product of primary reaction step whereas $\text{NH}({}^3\Sigma^-)$, NH_2 and N_3 appeared to be secondary products. At $T_2 > 1450\text{K}$, the activation energy was much lower than that determined by Demin et al. at higher pressures. With mixtures containing 2 mol % HN_3 , the rate constants were higher.

INTRODUCTION

Previous studies have brought some information about the general characteristics of the explosive decomposition of hydrogen azide, HN_3 , when a laminar flame as well as a detonation take place (1-4). This gaseous compound is very endothermic and able to sustain a flame at very low pressures and in highly dilute mixtures. The mechanism of explosive decomposition is complex and its study has shown that HN_3 is a source of NH radicals and vibrationally excited nitrogen molecules (5).

Thermal decomposition of HN_3 dilute in argon has been already studied in shock tubes with monitoring by spectroscopic techniques (6,7) but the data reported by the different authors are in disagreement on several points. In the low temperature range studied by Zaslonko et al. (8), the reaction is essentially a chain process with a rather extensive induction period followed by a rapid decomposition of HN_3 . The appearance of a vibrational non-equilibrium during decomposition, due to the formation of vibrationally excited nitrogen molecules and the transfer of energy to HN_3 molecules, would explain that the reaction order and the activation energy varied with pressure between 1 and 6 atm. At lower pressures, the order would be equal to 2. According to Kajimoto et al. (7)

the reaction rate was of first order in both HN_3 and Ar in the 600-2200 Torr pressure range, and the primary step yielded to the formation of N_2 and $\text{NH}({}^3\Sigma^-)$, whereas, for Zaslonko et al., $\text{NH}({}^1\Delta)$ was the first radical produced.

Because of these uncertainties, we have reinvestigated, in a large temperature range and for two distinct mixtures but at lower pressures, the thermal decomposition of shock-heated HN_3 dilute in Ar, using infrared, visible and ultra-violet emissions with the aim of precisizing HN_3 pyrolysis.

EXPERIMENTAL.

Details of the preparation of gaseous HN_3 have been given previously (9). Briefly, HN_3 was obtained from the reaction of concentrated orthophosphoric acid with sodium azide at 40°C . Mass spectra did not reveal any presence of impurities in the prepared azide.

Mixtures of HN_3 diluted to 98 and 99.5 mol.% with Argon were heated behind incident shock waves to temperatures of 850 to 2000 K and postshock pressures of 0.04 to 0.25 atm.

The shock tube which consisted of separate elements carefully joined in line, was entirely made of glass with an inner diameter of 22 ± 0.1 mm. The driver and driven sections were 1.15 m and 2.15 m long respectively, separated with a diaphragm which was made of a Terphane sheet of 5 μm thickness and placed in a quick-change mount. Prior to diaphragm bursting, the shock tube was evacuated down to a pressure of 10^{-3} Torr, then filled with Helium in the driver section and with the gaseous mixture in the driven section.

The optical setup consisted - of a series of plane windows, 10 mm dia., mounted on a flat-milled piece of glass tube, and made of quartz or KRS 5 according to the spectral region of interest, - of one cooled InSb detector with a maximum spectral response near 4.67 μm frequency - of photomultipliers type RCA 1P 21 and Hamamatsu R 928 for visible and UV radiations - of narrow bandpass-filters chosen to follow species such as HN_3 : 4.67 μm , $\text{NH}({}^1\Delta)$: 326.5 nm (HBW: 9.3 nm), $\text{NH}({}^3\Sigma^-)$: 338.1 nm (HBW: 9.1 nm), NH_2 : 600 nm (HBW: 9.33 nm), N_2 : 270 nm (HBW: 9.7 nm) and one 210 nm filter (HBW: 13 nm). The optical signals were amplified with a high speed electrical device and recorded on oscilloscopes simultaneously with pressure. A series of piezoelectric gauges (Model LEM 20H48 and 20H47), flush with the inside wall and equally spaced over a 0.7 m distance along the driven section, could determine the precise time at which the incident shock front passed along the observation windows and also measure the incident speed and wave deceleration. Since all circuit elements had a fast response, no significant errors could be attributed to electronic sources.

Incident shock parameters were computed in the conventional way from incident shock velocities and gas initial conditions with taking the heat capacity of hydrogen azide into account and the growth of a laminar boundary layer behind the shock front (10).

RESULTS.

a) Time histories of the IR, visible and UV emission records.

The feature of HN_3 (ν_2), $\text{NH}({}^1\Delta)$, $\text{NH}({}^3\Sigma^-)$, N_2 and NH_2 emissions, so as the 210 nm emission is drawn with respect to particle time in Fig. 1 and 2 for 0.5 and 2% HN_3 molar fractions, in the whole range of temperature studied. Time zero is representative of the shock wave arrival, determined by the rapid pressure jump. Each vertical column corresponds to experiments made at similar shock temperatures. Distinct experiments are noted with dotted and solid lines.

The 4670 nm radiation, I_{ν_2} , corresponds to the molecular vibration frequency ν_2 of the antisymmetric oscillator of the HN_3 molecule. I_{ν_2} increased during a non negligible lapse of time τ_v which is attributed to vibrational relaxation, then it reached a maximum value $I_{\nu_2}^0$. At low temperatures, the rapid

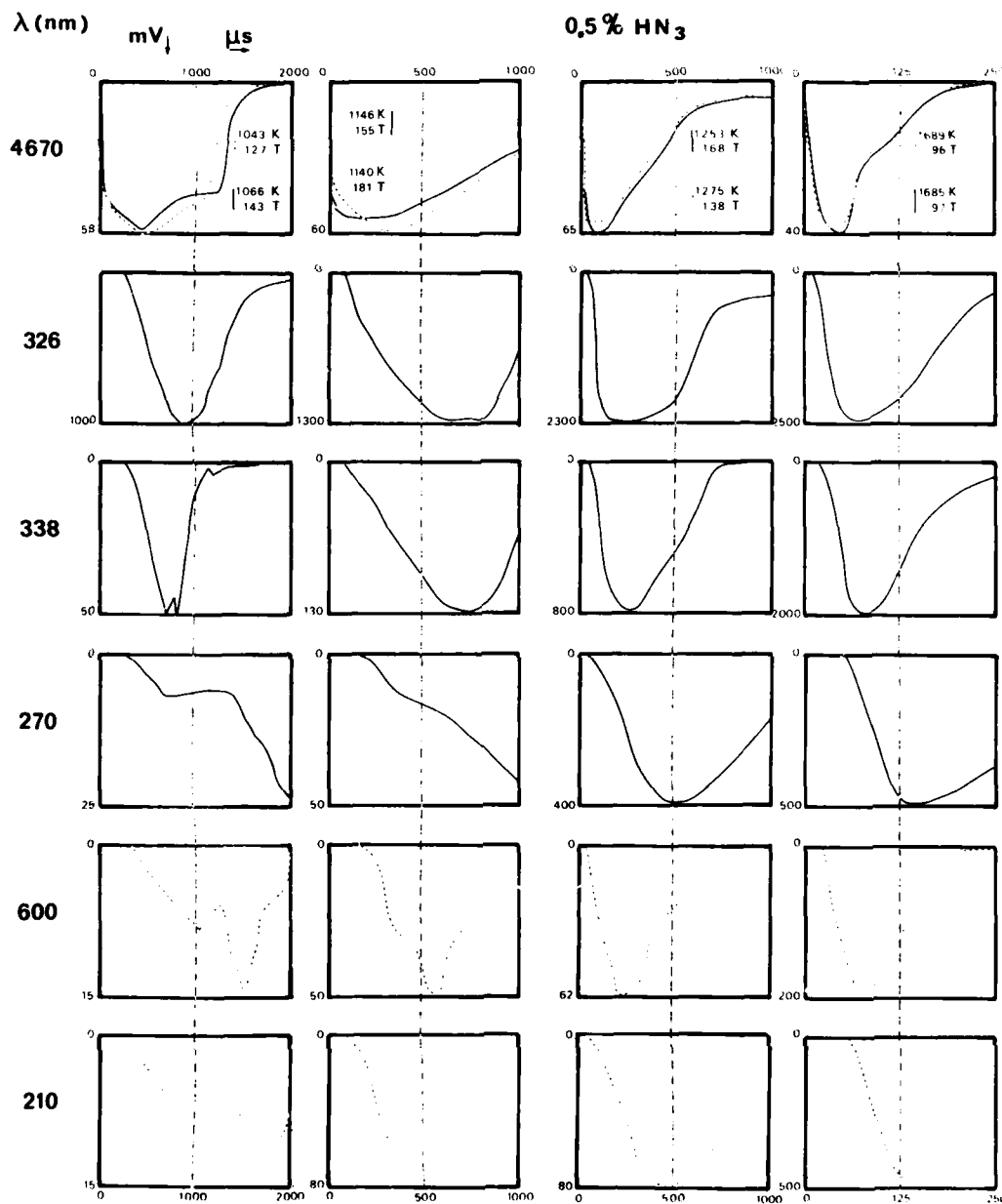


Figure 1: Typical records of IR, visible and UV emissions behind the incident shock.

Mixture {0.005 HN₃ + 0.995 Ar}

Particle times (on x-axis), shock temperatures (K) and pressures (T=Torr) noted inside frames are calculated without taking into account boundary layer effects.

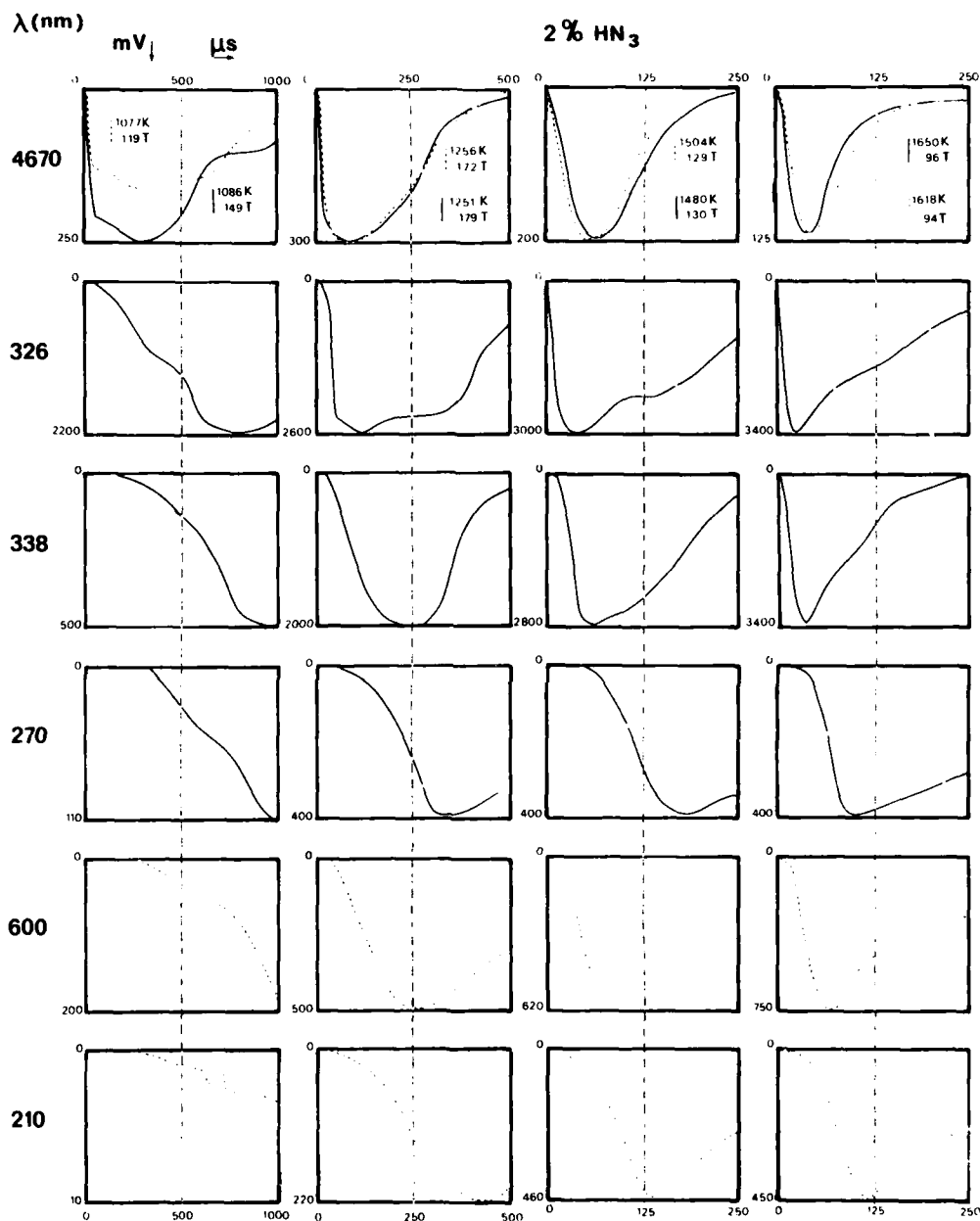


Figure 2: Typical records of IR, visible and UV emissions behind the incident shock.

Mixture (0.02 HN_3 + 0.98 Ar)

Particle times (on x-axis), shock temperatures (K) and pressures (T=Torr) noted inside frames are calculated without taking into account boundary layer effects.

decrease of the infrared signal was observed after a rather long delay depending on temperature and pressure, which corresponds to the induction lag, τ_{ind} , as defined by Zaslonko et al. (8). During this lag, the emission intensity increased owing to activation of HN_3 (ν_2) by active centers such as vibrationally excited N_2 molecules. Accumulation of such centers up to a well-determined concentration would be the cause of the rapid acceleration of the reaction (11).

Observation of NH emission signals showed that no stationary state was obtained simultaneously for both states of NH radicals. In the general case, $\text{NH}(^3\Sigma^-)$: 338 nm appeared noticeably delayed with respect to the formation of $\text{NH}(^1\Delta)$: 326 nm and almost at the same time as NH_2 : 600 nm. $\text{NH}(^3\Sigma^-)$, NH_2 and N_3 radicals are found to be produced in secondary reactions. At the far UV wavelength $\lambda = 210$ nm, the species emitting after a very long lapse of time could not be attributed to HN_3 molecule as Kajimoto et al. did for the 206.2 nm absorption (7).

b) Induction period.

The fast consumption of HN_3 is preceded at low temperatures by a long induction period as shown above. As the kinetic scheme of the decomposition process is a complex one, τ_{ind} depends not only on temperature but also on the concentration of the components. According to Zaslonko et al. (8), this dependence can be represented by the following expression:

$$\log \left\{ \tau_{ind} [\text{HN}_3]^{1.68} [\text{Ar}]^{-0.64} \right\} = \frac{8200}{T_2} - 9.27$$

(τ_{ind} in μs , $[\text{HN}_3]$ and $[\text{Ar}]$ in mol.l^{-1}), deduced from experiments performed between 900-1300 K, 0.4-2.5 atm and for 1-5.4 mol.% HN_3 in Ar.

HN_3 molar fraction	T_2 (K)	P_2 (Torr)	τ_{exp} (μs)	$\tau_{calc.}$ (μs)
0.02	1238	159	1031	995
	1335	199	130	279
0.005	1223	197	890	9804
	1341	197	164	2764

Table 1: Comparison between experimental and calculated (8) induction periods.

In the present study, measurements of induction periods have been made for similar temperatures and dilutions but at lower pressures (Table 1). The experimental values, τ_{exp} , compared with those calculated from Ref. (8), τ_{calc} , showed that the expression given above is only valid for the mixture containing 2 mol.% HN_3 at the lowest temperature.

c) Effect of vibrational non-equilibrium.

Under thermodynamic equilibrium conditions, the assumption of a Boltzmann distribution of molecules over the vibrational levels yields the Arrhenius law for the chemical reaction rate constant. If the vibrational relaxation time, τ_v , and the chemical reaction time, τ_r , are on the same order of magnitude, then the vibrational temperature of the reacting molecules, T_v , may differ from the translational temperature, T . Thereafter, the reaction rate constant appears to be dependent on vibrational temperature (12) and a certain degree of vibrational non-equilibrium is to be expected during the course of the reaction.

The following competing processes will lead to deviations in the Boltzmann vibrational distribution of the initial HN_3 molecules: (i) decomposition of the HN_3 molecule after the total amount of stored vibrational energy has reached the activation level, the lower vibrational levels being depopulated in this case; (ii) selective pumping of the antisymmetric mode ν_2 of HN_3 due to a quasi-resonant V-V exchange with vibrationally excited nitrogen molecules; (iii) non-resonant vibrational exchange with the reaction products; (iv) various V-V, V-V' and V-T relaxation processes.

The measurement of the infrared radiation at $4.67 \mu\text{m}$ wavelength was used for studying non-equilibrium phenomena and especially deviations from equilibrium with respect to one of the vibrational degrees of freedom, such as vibrational relaxation times at high temperatures.

1) Vibrational Boltzmann distribution.

According to Ref.13, the equilibrium emission intensity, $I_{\nu_2}^0$, normalized to HN_3 concentration ρ is, for the case of an optically thin layer, proportional to the vibrational energy of the mode ν_2 , that is:

$$\frac{I_{\nu_2}^0}{\rho} = K \frac{h\nu_2}{\exp \frac{h\nu_2}{kT_v} - 1}$$

where h is the Planck constant, k the Boltzmann constant and K , a constant factor proper to the apparatus.

If assumption is made of a Boltzmann distribution in the mode ν_2 , then:

$$\frac{I_{\nu_2}}{\rho} = \left[\exp \frac{h\nu_2}{kT_2} - 1 \right]^{-1}$$

as T_v equals T_2 which is the initial translational temperature behind the incident shock wave. The validity of the optically thin layer approximation, which is essential for the determination of concentration of chemical species to be proportional to the emission intensity, is verified by the data given in Fig.3 displaying the dependence with temperature of $I_{\nu_2}^0/\rho$ normalized to a reference $I_{\nu_2}^0/\rho'$, for both mixtures studied.

It is clearly seen that the data for the 0.5 mol.% HN_3 mixture (black dots) practically coincide with the corresponding values for a molar fraction of 2 % (white dots). Therefore, a deviation of the function:

$$\varphi = \frac{I_{\nu_2}^0}{\rho} \cdot \frac{\rho'}{I_{\nu_2}^0} \frac{\exp \frac{h\nu_2}{kT_2} - 1}{\exp \frac{h\nu_2}{kT_2'} - 1}$$

from unity will evidence a difference between the distribution function and the Boltzmann one. Fig.4a and 4b display the temperature dependence of the function φ for both mixtures. Analysis of these data showed that at $T_2 > 1000 \text{ K}$, $\varphi < 1$, which demonstrated an evident disturbance of a Boltzmann energy distribution in the mode ν_2 of HN_3 . A similar conclusion was made in Ref.12 for the monomolecular decomposition of the N_2O molecule.

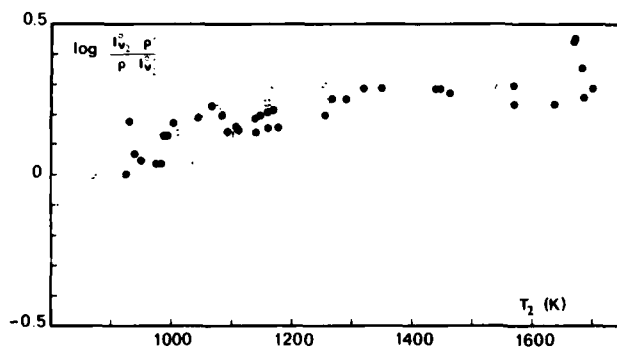


Figure 3: Logarithm of experimental $I_{v_2}^0 / \rho$ normalized to a reference $I_{v_2}^0 / \rho^*$ versus shock temperature.

● : Mixture {0.005 HN_3 + 0.995 Ar}
○ : Mixture {0.02 HN_3 + 0.98 Ar}

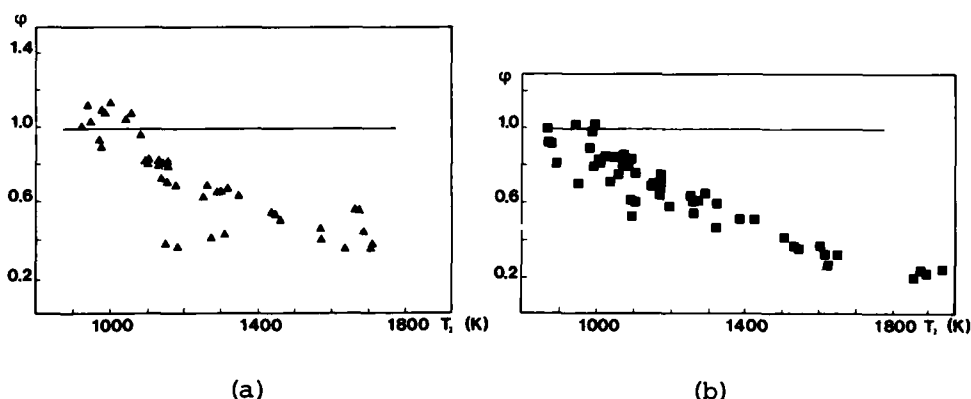


Figure 4: Variation of the factor ϕ , determined from experimental 4.67 μm emission intensities, with shock temperature. Comparison with Boltzmann distribution in the v_2 mode of HN_3 molecule.

(a): \blacktriangle : Mixture {0.005 HN_3 + 0.995 Ar}

(b): \blacksquare : Mixture {0.02 HN_3 + 0.98 Ar}

2) Vibrational relaxation

The relaxation time, τ_V , of the antisymmetric vibration of $\text{HN}_3(v_2)$ has been studied from emission at 4.67 μm for both 0.5 and 2 mol.% HN_3 mixtures in the whole temperature (850–1800 K) and pressure (50–200 Torr) ranges. The logarithm of the product $\tau_V \cdot P_2$ was plotted versus $T_2^{-1/3}$ in Fig. 5. The Landau-Teller plot was found to be approximately linear. Relaxation times had been also calculated by Zaslonko et al. (14) using the SSH theory for the system {0.025 HN_3 + 0.975 Ar} at $T_2 = 1050$ K and $P_2 = 4.2$ atm. τ_V , equal to 0.8 μs , was smaller than the value estimated from our results ($\tau_V = 1.6$ μs), but of the same order of magnitude.

At the highest temperatures, $T_2 > 1600$ K, the relaxation times were not negligible with respect to the HN_3 half-life, which was thus difficult to estimate from the 4.67 μm emission.

The effect of vibrational relaxation on the overall rate constant value of HN_3 decomposition is possibly one of the reasons of discrepancy between the data obtained by the various authors (6,7), as the set of processes (i-iv) can yield different vibrational distributions of reacting molecules in every particular case. To study the effect of vibrational relaxation on the chemical kinetics in more detail, a direct control of the molecular states of populations is needed.

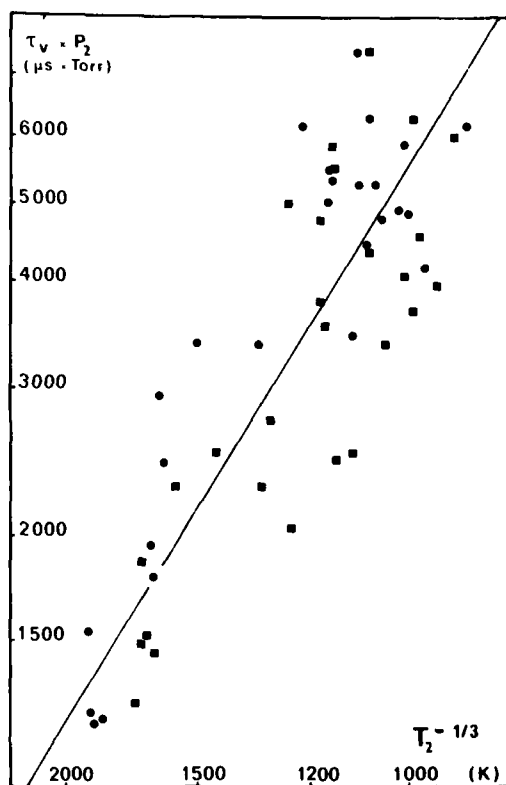


Figure 5: Logarithmic Landau-Teller plot of the product of vibrational relaxation time into shock pressure, versus shock temperature raised to the $-1/3$ power.

- : Mixture {0.005 HN_3 + 0.995 Ar}
- : Mixture {0.02 HN_3 + 0.98 Ar}

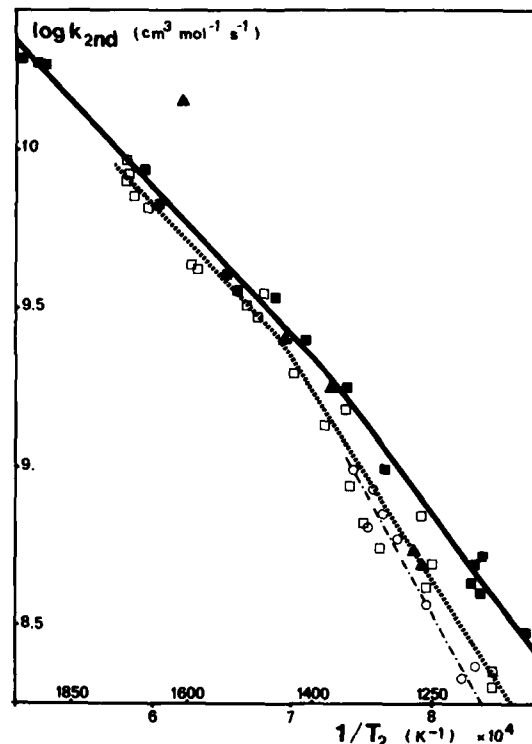


Figure 6: Logarithmic Arrhenius plot of the apparent second-order rate constants of HN_3 decomposition, versus inverse shock temperature.

- : {0.02 HN_3 + 0.98 Ar}
- : {0.005 HN_3 + 0.995 Ar}
- : this work
- : Kajimoto et al's results
- ▲ : Zaslonko et al's results

d) Rate of HN_3 decomposition

At temperatures higher than 1250 K, the induction period became short with respect to HN_3 half-life $t_{1/2}$. HN_3 decay rates were determined by monitoring the 4.67 μm emission decrease, from measurements of the particle time at which the infrared signal is half-reduced.

In the range $1250 < T_2 \text{ (K)} < 2000$, our investigation yielded an apparent rate constant, k_{2nd} , of first order in both HN_3 and Ar.

The logarithm of k_{2nd} was plotted against inverse shock temperature for both mixtures in Fig. 7 and compared with results of other authors. The rate constants given by Zaslonko (11) were deduced from HN_3 half-life times by monitoring absorption at 290 nm. Their values plotted in Fig. 7 correspond to the experimental data initially expressed in s^{-1} and converted into second-order rate constants according to the expression:

$$k_z = \frac{10^{11.5}}{[\text{Ar}]} \cdot \exp(-20000/T) \text{ cm}^3 \text{ mol}^{-1} \text{ s}^{-1}$$

Results reported by Kajimoto et al. (7) were obtained from the analysis of the initial portion of the HN_3 absorption curve at 206 nm.

With the mixture containing 0.5 mol.% HN_3 and $1250 < T_2 \text{ (K)} < 1400$,

k_{2nd} determined in the present work were in good agreement with Kajimoto's values, determined in similar temperature and dilution ranges but at higher pressures. A least-squares best fit to our data yielded to the following Arrhenius expression:

$$k_{2nd} = 5.5 \cdot 10^{-13} \exp(-14\,000/T) \text{ cm}^3 \text{ mol}^{-1} \text{ s}^{-1}$$

However, in comparison with the rate constant k_K given by Kajimoto:

$$k_K = 7.6 \cdot 10^{-14} \exp(-18\,200/T) \text{ cm}^3 \text{ mol}^{-1} \text{ s}^{-1}$$

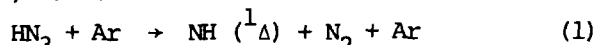
the preexponential factor and the activation energy were found to be lower in the present work.

For experiments conducted at $T_2 > 1450 \text{ K}$, we found that the activation temperature decreased to a much lower value than that determined at higher pressures (15):

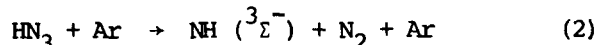
$$k'_{2nd} = 2.2 \cdot 10^{-12} \exp(-9750/T) \text{ cm}^3 \text{ mol}^{-1} \text{ s}^{-1}$$

With the mixture containing 2 mol.% HN_3 , k_{2nd} was found to be higher. The difference could be due to the reaction exothermicity although the energy release was limited by the presence of intermediate species and partly converted into N_2 vibrational excitation. Furthermore, the mechanism consisted of chain reactions. Therefore the Arrhenius law was not valid and experimentally a variation of the activation energy with temperature was observed.

From our experiments, the predominant pathway for HN_3 decomposition was the formation of $\text{NH}({}^1\Delta)$ radicals:

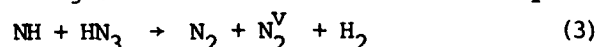


as suggested also by Zaslanko, even though $\text{NH}({}^3\Sigma^-)$ could be produced through the reaction:



or through a spin exchange reaction with HN_3 . This result disagrees with the primary process proposed by Kajimoto, corresponding to the triplet pathway.

NH radicals initially formed will fastly react with HN_3 producing NH_2 and N_2 radicals. Another process is the exothermic reaction (3) ($\Delta H = -189 \text{ kcal mole}^{-1}$), leading to the formation of vibrationally excited products:



The presence of N_2^{V} in the reacting mixture will accelerate the decomposition rate as the energy transfer from N_2^{V} to HN_3 will proceed effectively by way of resonant V-V transfer (11).

REFERENCES

1. Laffitte P., Hajal I. and Combourieu J., 10th Symp. (Intern.) Combust., 79, 1965.
2. Paillard C., Dupré G. and Combourieu J., Adv. Mass Spectrometry, Vol. 8, Heyden, 1943, 1980.
3. Paillard C., Dupré G. and Combourieu J., J. Chim. Phys., 70, 811, 1973.
4. Paillard C., Dupré G., Lisbet R., Combourieu J., Fokeev V.P. and Gvozdeva L.G., Astr. Acta, 6, 227, 1979.
5. Rozenberg A.S., Arsen'ev Yu.N. and Voronkov V.G., Fiz. Gor. Vzor., 6, 302, 1970.
6. Zaslanko I.S., Kogarko S.M. and Mozhukhin E.V., Kinet. Katal., 13, 829, 1972.
7. Kajimoto O., Yamamoto T. and Fueno T., J. Phys. Chem., 83, 429, 1979.
8. Zaslanko I.S., Kogarko S.M. and Mozhukhin E.V., Fiz. Gor. Vzor., 9, 339, 1973.
9. Dupré G., Paillard C. and Combourieu J., Dynamic Mass Spectrometry, Vol. 4, Heyden, 233, 1976.
10. Strehlow R.A. and Belford R.L., AAE Tech. Rept. No. 69-1, Univ. Illinois, Urbana, 1969.
11. Zaslanko I.S., Kogarko S.M., Mozhukhin E.V., Dokl. Akad. Nauk. SSSR, 210, 1127, 1973.
12. Zuev A.P. and Tkachenko B.K., Zh. Tekh. Fiz., 3, 1321, 1980.
13. Dicus J.C., J. Chem. Phys., 32, 1262, 1960.
14. Zaslanko I.S., Kogarko S.M., Mozhukhin E.V., Mukoseev Yu.K., Kinet. Katal., 16, 1111, 1975.
15. Demin A.I., Zaslanko I.S., Kogarko S.M. and Mozhukhin E.V., Kinet. Katal., 14, 283, 1973.

7

1

Part VI: TWO PHASE FLOW AND CONDENSATION

AD P000288

THE RELAXATION ZONE BEHIND NORMAL SHOCK WAVES IN A REACTING DUSTY GAS

PART 1. MONATOMIC GASES

Gabi Ben-Dor and Ozer Igra

Department of Mechanical Engineering

Ben-Gurion University of the Negev, Beer Sheva, Israel

The conservation equations for a suspension composed of an ionized gas and small solid dust particles are formulated and solved numerically. Such flows can be found downstream of strong normal shock waves propagating into dusty gases. The solution indicates that the presence of the dust significantly affects the post-shock flow field. Owing to the dust, the relaxation zone will be longer than in the pure plasma case; the equilibrium values for the suspension pressure and density will be higher than the dust-free case, while the obtained values for the temperature, degree of ionization and velocity will be lower. The numerical solution was executed for shock Mach numbers ranging from 10 to 17. It was found that the thermal relaxation length for the plasma decreases rapidly with increasing shock Mach number, while the thermal relaxation length for the suspension mildly increases with increasing M's. The kinematic relaxation length passes through a pronounced maximum at $M=12.5$. Throughout the investigated range of Mach numbers, the kinematic relaxation length is longer than the suspension thermal relaxation length.

I. Introduction

The interest in the gas dynamic behavior of a gas particle suspension grew in the past two decades due to its application to many flow fields. Some typical examples are: metalized propellants for rockets, jet type dust collectors and blast waves in a dusty atmosphere. General descriptions of such flows can be found in Soo's book¹ and in the reviews of Marble² and Rudinger³. In the present work, the flow field which develops downstream of a strong normal shock wave, propagating into a dusty argon gas, has been formulated and solved numerically. The basic difference between a homogeneous, ideal gas and a dusty reacting gas is that in the latter the flow thermodynamics and kinematic properties exhibit a continuous change through a much thicker layer, called the relaxation zone. In the considered flow, a leading shock discontinuity produces sudden changes in the flow properties to be followed by the relaxation zone, throughout which the flow properties adjust from their frozen value (at the shock front) toward an appropriate equilibrium condition. Downstream of a strong shock wave (high shock Mach number), the post-shock frozen temperature is high enough to promote excitation of the internal degrees of freedom. For a dust-free gas, a relaxation zone will prevail, downstream of the shock front, throughout which the gas/plasma passes from its frozen state

to an appropriate post-shock equilibrium state⁴. At the far end of the relaxation zone, equilibrium among the various constituents of the plasma (atoms, ions and electrons) is reached. However, in the considered case, due to the presence of the dust, two relaxation mechanisms exist simultaneously. The first, responsible for reaching equilibrium state among the plasma components, is the collisional-radiative interactions between the plasma elements; the second, responsible for generating equilibrium between the post-shock plasma and the dust, is the viscous and heat transfer interactions between the dust and the gaseous phase of the suspension.

The analysis of the relaxation zone in an ideal (non-reacting)-gas is well known. (For example see the pioneering works of Carrier⁵, Kriebel⁶ and Rudinger⁷). The aim of the present work is to cover the case of shock wave propagation into a dusty real gas (high shock Mach numbers).

II. Theoretical Background

The present work deals with a monatomic gas (argon). When this gas is exposed to strong normal shock waves, due to the elevated post-shock temperature, the gas becomes partially ionized, i.e., it can be considered as a mixture of atoms, ions, and electrons. Appleton and Bray⁸ presented a general formulation for the conservation equations for reacting gases (plasmas). Assuming a steady, inviscid, non-diffusive one-dimensional flow without electromagnetic fields, and that the dust particles fulfill the following conditions (Marble², Carrier⁵, Kriebel⁶ and Rudinger^{3,7}):

- 1) all solid particles are rigid inert small spheres uniformly distributed in the gas/plasma,
 - 2) the volume of the particles in the suspension is neglected,
 - 3) the interaction between the solid particles can be neglected,
 - 4) ahead of the normal shock wave, the dust particles are in a state of equilibrium with the gas,
 - 5) the particles are too large to experience a Brownian motion in the gas/plasma,
 - 6) aside from the viscous interaction between the gas/plasma and the solid particles, the gas phase can be regarded as inviscid,
 - 7) the weight of the particles, and the buoyancy forces are negligibly small, compared to the viscous drag forces, and that
 - 8) the temperature within the particles is uniform,
- results in the following conservation equations for the suspension:

continuity (plasma)

$$u \frac{dn_a}{dx} + u \frac{dn_e}{dx} + (n_a + n_e) \frac{du}{dx} = 0 \quad (1)$$

momentum (plasma)

$$T \frac{dn_a}{dx} + (T + T_e) \frac{dn_e}{dx} + \frac{m_a}{k} (n_a + n_e) \frac{du}{dx} + (n_a + n_e) \frac{dT}{dx} + \frac{dT_e}{dx} = - \frac{m_a}{k} n_u (n_a + n_e) \frac{dv}{dx} \quad (2)$$

energy (plasma)

$$- \frac{1}{n_a + n_e} \left[\frac{5}{2} n_e T_e + (n_a + n_e) T \right] \frac{dn_a}{dx} + \frac{1}{n_a + n_e} \left[\left(\frac{3}{2} n_a - n_e \right) T_e - (n_a + n_e) T \right] \frac{dn_e}{dx} + \frac{3}{2} (n_a + n_e) \frac{dT}{dx} + \frac{3}{2} n_e \frac{dT_e}{dx} = \frac{1}{ku} \left(Q_{\text{rad}} - \frac{dn_e}{dt} I \right) - \frac{m_a n}{k} (n_a + n_e) \left(v \frac{dv}{dx} + C \frac{dr}{dx} \right) \quad (3)$$

continuity (electron gas)

$$u \frac{dn_e}{dx} + n_e \frac{du}{dx} = \frac{dn_e}{dt} \quad (4)$$

energy (electron gas)

$$\frac{3}{2} u T_e \frac{dn_e}{dx} + \frac{5}{2} T_e n_e \frac{du}{dx} + \frac{3}{2} n_e u \frac{dT_e}{dx} = (Q_e - \frac{dn_e}{dt} I) + 3 n_e \frac{m_e}{m_a} (v_{ei} + v_{ea}) (T - T_e) \quad (5)$$

The terms dv/dx and $d\tau/dx$ arise from the gas-particle momentum and heat exchange. They can be expressed as follows⁷:

$$\frac{dv}{dx} = - \frac{3}{4} \frac{m_a (n_a + n_e)}{Dd} C_D \frac{(v-u)^2}{v}, \quad \frac{d\tau}{dx} = \frac{Nu}{Pr} \frac{6\mu}{D^2 d \delta} \frac{T-\tau}{v} + \frac{6\epsilon\sigma}{CDd} \frac{T^4 - \tau^4}{v} \quad (6)$$

where n_a , n_e , m_a and m_e are the atom and electron number densities and the atom and electron masses, respectively. T , T_e and u are the heavy particles (atom and ions), the electron gas temperatures and the plasma velocity, respectively. k , Q_{rad} , dn_e/dt , I , Q_e , v_{ei} and v_{ea} are the Boltzmann constant, the plasma radiation losses, the rate of electron production, the atom's ionization potential, the electron gas radiation losses, and the collision frequencies between electron-ions and electron-atoms, respectively. The distance measured downstream from the shock front is x . v , τ , C , D , d are the velocity, the temperature, the heat capacity, the diameter and the density of the solid particles, respectively. C_D is the drag coefficient. Nu , Pr , ϵ , μ , σ and δ are the appropriate Nusselt and Prandtl numbers (based on the diameter of the particles), the emissivity of the dust particles, the gas viscosity, the Stefan-Boltzmann constant and the ratio of the solid/gas specific heat capacities, respectively. The ratio between the dust and the gas rates of mass flow is η .

It should be noted that while introducing the dust particles into the plasma, it is probable that at the higher temperatures reached behind strong shock waves the dust will ablate and/or chemically react with the gaseous phase of the suspension. However, the inclusion of such processes into the conservation equations would constitute a significant complication of their solution. As a first step in the analysis of ionizing shocks in a dusty gas these processes will be neglected even though they may be significant mechanisms. It is therefore assumed that the dust particles are inert. Based on this assumption and the fact that the dust particles are much larger than the plasma atoms (5μ as compared to $10^{-4}\mu$), the only effective interaction between the two phases can be via viscous and heat transfer mechanisms.

In order to solve equations (1) to (6) the parameters Q_{rad} , dn_e/dt , v_{ei} , v_{ea} , Q_e , C_D , Pr , Nu and μ must be expressed in terms of the following seven flow variables: n_a , n_e , u , v , T , T_e and τ . This can be found in Refs. 9 and 10.

III. Numerical Technique

The expressions for dv/dx and $d\tau/dx$ [Eq. (6)] were inserted into Eqs. (2) and (3). As a result, a set of five nonlinear simultaneous differential equations (1 to 5), with five unknowns dn_a/dx , dn_e/dx , du/dx , dT/dx and dT_e/dx was obtained. This set was then rewritten in a compact form: $AX=B$ where A , X and B represent the appropriate matrices.

By finding the inverse matrix A^{-1} , which fulfills the condition $A^{-1}A=I$, the value of the derivatives was found from: $X=A^{-1}B$; then a numerical integration scheme was carried out.

The Eulerian integration scheme was adopted due to the length (timewise) of the computer program, which could not allow other schemes. However, in order to overcome the inaccuracy problem associated with the Eulerian scheme, the step-size was checked in every iteration. A step size was chosen which resulted in values deviating by less than 0.1% from values computed with a step size twice as large.

The initial conditions, immediately behind the shock front were set as follows: $u=u_f$, $T=T_f$, $n_a=\rho_f/m_a$, $n_e=0.001 n_a$, $T_e=(T_f+T_o)/2$, $v=u_o$, $\tau=T_o$, where subscript "f" denotes the frozen values obtained immediately behind the shock front and subscript "o" indicates the unshocked state ahead of the shock wave. Note that the initial values of n_e and T_e were set arbitrarily. It was shown by Liu¹⁰ that the initial values of n_e and T_e influence only the very beginning of the relaxation zone. Further down the relaxation zone, the values of n_e and T_e converge to one value, independent of their initial value. The integration was carried out until an equilibrium was reached, i.e., until the end of the relaxation zone. The suggested numerical scheme is much faster than the finite elements scheme used by Liu¹⁰. In the present scheme, the derivatives of the various suspension properties are analytically calculated, before a numerical integration is carried out.

IV. Results and Discussion

In order to demonstrate the dust effect on the flow properties in the relaxation zone, the conservation equations (1 to 6) were solved with and without dust. The solution was conducted for a typical shock tube generated argon plasma, i.e., $M=15$, $P_o=5$ torr and $T_o=300$ K. The following dust parameters were used: $d=1.5$ g/cm³, $C=10^7$ erg/g/K, $\epsilon=1$, $D=0.0005$ cm. The solution was carried out for two different dust concentrations, $\eta=0.1$ and 0.2 . The results obtained for the dust-free case ($\eta=0$) are in good agreement with those of Liu¹⁰.

The pressure variations in the relaxation zone are shown in Fig. 1. As expected, the dust presence causes the pressure to increase in the relaxation zone. (As will be shown shortly, the dust particles experience deceleration throughout the relaxation zone. This in turn, results in an increase in the plasma pressure.) It is also apparent from Fig. 1 that as the dust concentration grows the suspension pressure increases. It should be noted that the relaxation zone length for the dusty gas is greater than that appropriate to the dust-free case.

The variation of the degree of ionization α , in the relaxation zone, is shown in Fig. 2. Since the dust particles absorb part of the thermal energy generated by the strong shock wave, it is expected that the dust-free case will have higher values of α , as is evident from Fig. 2. Increasing the dust concentration will increase the amount of heat absorbed by the solid phase of

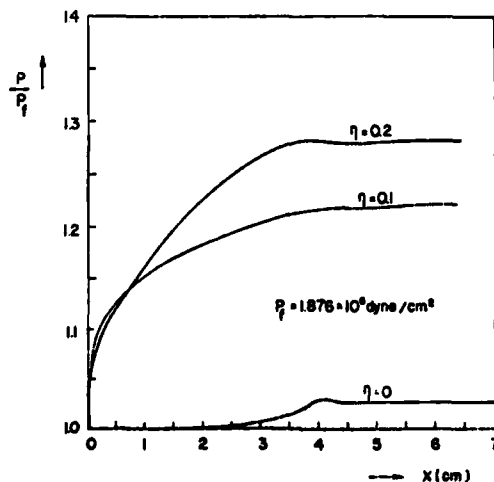


Figure 1: The variation of the pressure with distance behind the shock front

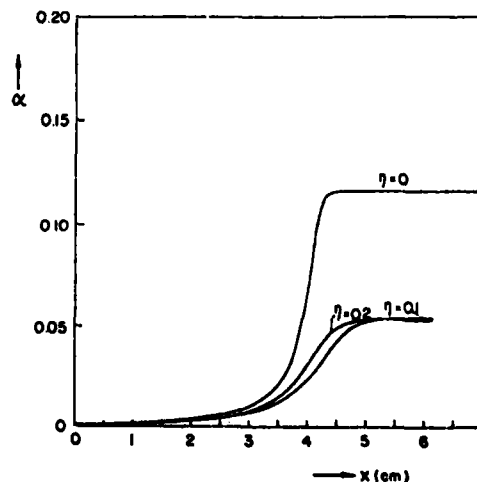


Figure 2: The variation of the degree of ionization with distance behind the shock front.

the suspension and thereby decrease the degree of ionization as is apparent from Fig. 2. The reduction in α due to the dust is quite significant, about 54% at the rear end of the relaxation zone (Fig. 2).

When dealing with temperature, unlike in the dust-free case, there are three different temperatures to equalize: the dust temperature τ , the atom and ion temperature T , and the electron gas temperature T_e . The results for $\eta=0$, $\eta=0.1$ and $\eta=0.2$ are shown in Fig. 3. Fig. 3 is similar to Liu's findings¹⁰; it suggests that for the pure argon case the relaxation zone length is about 4.5 cm and the equilibrium temperature is 12530 K. It is evident from Fig. 3 that for $\eta=0.1$ the extent of the relaxation zone (for T_e to reach T) increases to about 5.5 cm and the equilibrium temperature is reduced to 11390 K. The reduction in the equilibrium temperature is due to the presence of the dust particles which absorb significant amounts of the post-shock thermal energy. Recall that the dust initial temperature is only 300 K. Increasing the dust concentration will result in a faster decrease in T and a slower increase in τ , as is evident from Fig. 3. The difference in the electron temperature and the equilibrium temperature for the different η 's, is very small. The fact that a 9% reduction in the equilibrium temperature (from the $\eta=0$ to the $\eta=0.1$ case) corresponds to a 54% reduction in α should not be surprising, since the ionization rate constant exponentially depends on the temperature.

The minimum in T_e at the beginning of the relaxation zone (Fig. 3) is a direct result of the initial value chosen for T_e . Immediately behind the shock front the number density of the free electrons is negligibly small, consequently, it is quite artificial to assign a temperature T_e to a gas at that state. Unlike Liu¹⁰ who smeared out the minimum in T_e and extrapolated the curve smoothly, here the actual shapes of the T_e -curve, as calculated, are drawn. This is a more accurate presentation in the sense that the derivatives of our curves at any given location behind the shock front satisfy Eqs. (1) to (6) while those of Liu do not. It should be remembered, however, that Liu has shown that the values of T_e converge to the same value, shortly behind the shock front, independently of the initial value chosen for T_e ¹⁰.

Knowing how P , T , T_e and α vary in the relaxation zone it is easy to estimate how ρ will behave. From the equation of state we have $P = \rho R(\alpha T_e + T)$ where R is the gas constant. It was shown that the introduction of dust causes P to increase and α and T to decrease in the relaxation zone. Therefore, it is expected that the dust presence will cause the density to increase, as is confirmed by the results shown in Fig. 4.

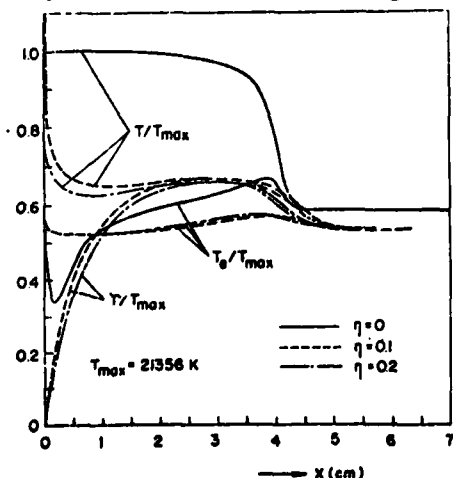


Figure 3: The variation of the temperatures with the distance behind the shock front.

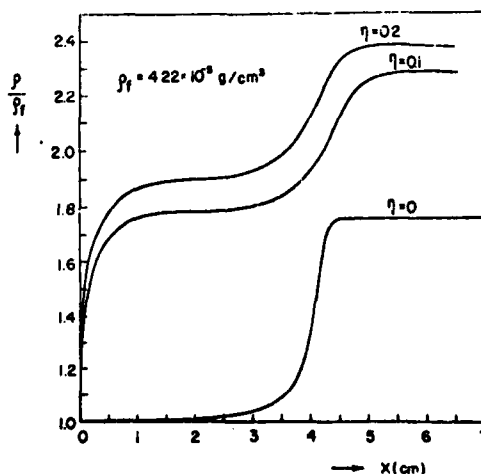


Figure 4: The variation of the density with distance behind the shock front.

The kinematic behavior of the considered flow is shown in Fig. 5. The velocity changes, for the dust-free case ($\eta=0$) are the same as those reported by Liu¹⁰, i.e., almost a constant flow velocity throughout most of the relaxation zone, to be followed by a rapid velocity drop close to the rear end of the relaxation zone. Using "sterile" momentum considerations could lead to a wrong conclusion that the plasma velocity u , for a dusty gas, will be higher than that appropriate to a dust-free gas. Recall that the solid particles enter the relaxation zone with a very high velocity (the shock wave velocity) which reduces to a relatively low equilibrium velocity via viscous interaction. However, for a steady, one-dimensional flow $\rho u = \text{constant}$. As shown previously, the equilibrium post-shock density for a dusty gas is significantly higher than that of an appropriate dust-free gas, therefore a lower equilibrium velocity should be expected for the dusty plasma. This fact is confirmed in Fig. 5. It is also apparent from this figure that the relaxation zone length of the dusty plasma is significantly longer than the appropriate pure gas case. Note also that the higher the concentration is, the shorter is the relaxation length. Comparing the results shown in Fig. 5 with those of the previous figures indicates that the kinematic relaxation length is longer than the thermal one.

In summary, the introduction of dust causes the relaxation length to increase, it also results in an increase in the equilibrium values of the plasma pressure and density and a decrease in the plasma temperature, degree of ionization and velocity, as compared with the appropriate dust-free case.

It is of interest to check how the plasma transport coefficients change in the relaxation zone. Fig. 6 illustrates the changes experienced by the plasma viscosity as a function of the distance measured downstream from the shock front. In order to fully comprehend this figure, the plasma viscosity dependence upon temperature was evaluated, for atmospheric pressure (see Fig. 7). The dashed line corresponds to the commonly used expression $\mu = AT^{0.76}$. As can be seen in Fig. 7, this expression is good only for the range $T < 9000$ K. When T exceeds 9000 K, ionization becomes significant and its contribution to μ via α , cannot be neglected anymore. It is apparent from Fig. 7 that the viscosity reaches a maximum at a temperature of 12000 K. At temperatures lower or higher than this value there is a significant reduction in μ . The present numerical solution ($P_0 = 5$ torr, $T_0 = 300$ K and $M = 15$) suggests a frozen temperature of about 21000 K and an equilibrium value around 12000 K (see Fig. 3). Therefore it can be expected that the plasma viscosity will increase through-

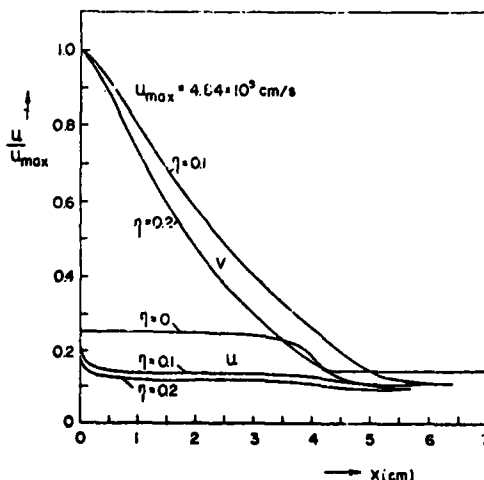


Figure 5: The variation of the velocities with distance behind the shock front

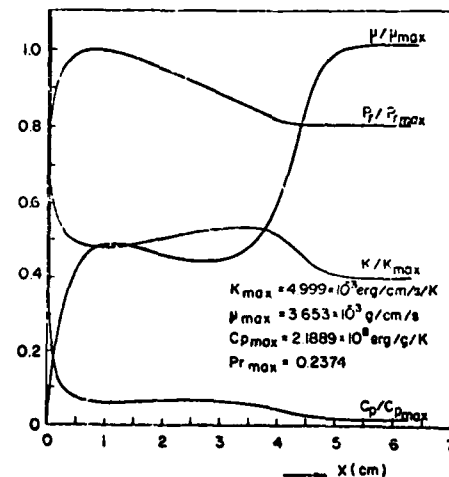


Figure 6: The variation of the transport coefficients with distance behind the shock front

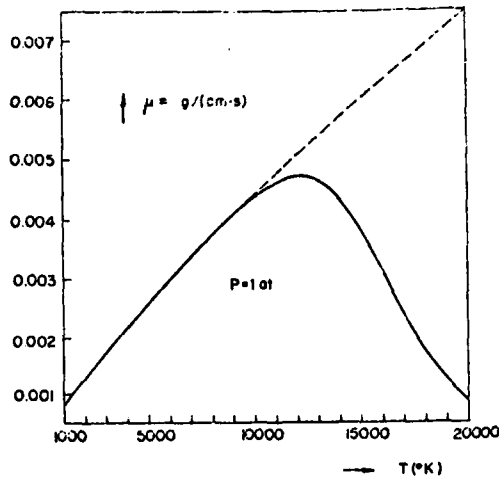


Figure 7: Viscosity dependence on temperature

out the relaxation zone, reaching its maximum value towards its rear end. This is confirmed by Fig. 6, hence it is expected that most of the particles' deceleration will take place at the rear part of the relaxation zone, where μ is large and so are the viscous forces.

The thermal conductivity of the plasma is also shown in Fig. 6. It suggests that K decreases with increasing the distance measured from the shock front. The variation in the plasma specific heat capacity at constant pressure C_p , and its Prandtl number, Pr , throughout the relaxation zone are also shown in Fig. 6. It should be mentioned here, that the values of μ , K , C_p and Pr , appearing in Fig. 6, were normalized by the appropriate maximum value reached in the relaxation zone.

The three major conditions required for obtaining a state of equilibrium in the shocked suspension are:

- 1) Reaching a unique temperature for the plasma, i.e., $T=T_e$. This is reached via collisional-radiative processes among the various plasma components.
- 2) Equilibrating the temperature of the plasma and the solid dust particles, i.e., $T=\tau$. This is reached by convective and radiative heat transfer between the two phases of the suspension.
- 3) Obtaining one velocity for the entire suspension, i.e., $v=u$. This is reached via viscous interaction between the plasma and the solid dust particles.

It is of interest to compare the lengths required for reaching each of the above mentioned processes. For this purpose the following three relaxation lengths were defined:

- (i) Thermal relaxation length for the plasma - L_{T_e} , where L_{T_e} is the distance, measured downstream of the shock front, at which $|T-T_e|/T \leq 0.02$.
- (ii) Thermal relaxation length of the suspension - L_τ , where L_τ is the distance at which $|T-\tau|/T \leq 0.02$.
- (iii) Kinematic relaxation length for the suspension - L_v , where L_v is the distance at which $|v-u|/v \leq 0.02$.

The behavior of these three relaxation lengths, for various shock Mach numbers is shown in Fig. 8. (For all values M the following suspension parameters were used: $P_0=5$ torr, $T_0=300$ K, $d=1.5$ g/cm³, $C=10^7$ erg/g/K, $\epsilon=1$, $D=0.0005$ cm and $\eta=0.02$.) It is apparent from Fig. 8 that L_{T_e} monotonically decreases with increasing shock Mach number. This behavior should be expected since the most effective mechanism for reaching a unique plasma temperature, in a relatively dense plasma, is collisions, and the most effective energy-

transfer-collisions are the electron-electron collisions. For the high Mach number cases the degree of ionization is relatively high and therefore there are enough free electrons to establish an equilibrium plasma temperature fairly rapidly. This is not the case for the low Mach number case ($M \leq 12$), where α is low, and so is the number density of the free electrons. In such a case T_e will lag behind T for a relatively long time (distance) as is evident from Fig. 8. Unlike L_{T_e} , L_T mildly increases with increasing M 's. This behavior is due to the fact that with increasing M the initial difference between T and τ increases. (The initial value of τ is 300 K while that of T increases with M .) It is of interest to note that at high values of M ($M > 16$), L_{T_e} approaches L_T indicating that a unique thermal relaxation length, for the entire suspension, could be obtained for such cases.

The behavior of L_V is more peculiar. It is suggested in Fig. 8 that a pronounced maximum exists in L_V at $M=12.5$. The dominant parameter affecting the dust deceleration is the plasma viscosity. As mentioned earlier (Fig. 7), the viscosity strongly depends on the plasma temperature and its degree of ionization. In Fig. 9 the variation of μ , with distance measured from the shock front is shown (M appears as a parameter). The values of μ are normalized by the maximum viscosity μ_{\max} , appropriate to $M=12$. It is evident from Fig. 9 that the lowest μ is obtained for $M=12.5$. The closest neighbors are the μ 's of $M=12$ and $M=13$. In light of these facts the behavior of L_V (Fig. 8) is self-explanatory. It should also be noted that throughout the investigated range of M , L_V was always greater than L_T , in accordance with the findings of Igra and Ben-Dor for the ideal gas case¹¹.

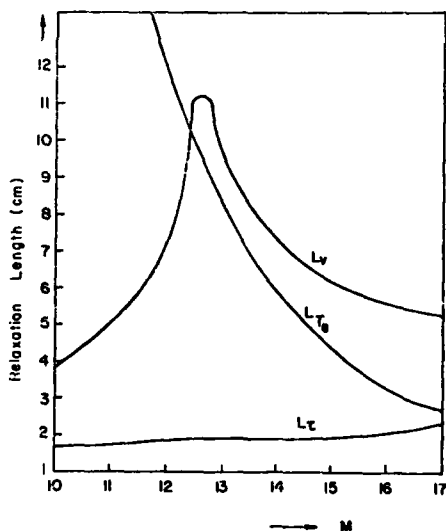


Figure 8: The dependence of the various relaxation lengths on the shock wave Mach number.

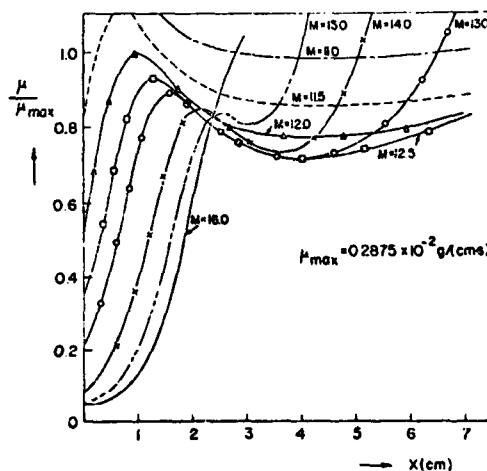


Figure 9: Viscosity variation with distance as a function of the incident shock wave Mach number

V. Conclusions

The conservation equations for ionizing shocks in a dusty gas were formulated and solved numerically to obtain the variation of the thermodynamic and kinematic properties throughout the relaxation zone.

The solution indicated that the introduction of dust into the plasma strongly affects the relaxation zone which develops downstream of the shock front. Owing to the dust, a longer relaxation zone develops; at its rear end the suspension pressure and density are higher than those appropriate to dust-free gas. On the other hand, the equilibrium values for the suspension tem-

perature, velocity and degree of ionization are lower than those appropriate to the pure gas. As the shock wave Mach number increases, the plasma and the suspension thermal relaxation lengths approach each other, to result in a common value. Throughout the investigated range of M , the kinematic relaxation length was found to be longer than the thermal relaxation lengths.

The proposed numerical code can be used for different gases and for various types of particles. It can also be extended to cover non-uniformly sized particles and curved shocks.

Acknowledgements

The authors wish to thank their colleague Dr. J.J. Gottlieb of the Institute of Aerospace Studies, University of Toronto, for suggesting this subject and providing a detailed literature survey. Thanks are also offered to Mr. Y. Klein for his assistance with the computer work.

References

1. S.L. Soo, Fluid Dynamics of Multiphase Systems. (Blaisdell Publishing Co., Waltham, Mass., 1967).
2. F.E. Marble, Ann. Rev. Fluid Mech. 2, 397 (1970).
3. G. Rudinger, Applied Mech. Rev. 26, 273 (1973).
4. I.I. Glass and W.S. Liu, J. Fluid Mech. 84, 55 (1978).
5. G.F. Carrier, J. Fluid Mech. 4, 376 (1958).
6. A.R. Kriebel, J. Basic Engng. Trans. ASME D86, 655 (1964).
7. G. Rudinger, Phys. Fluids 7, 658 (1964).
8. J.P. Appleton and K.N.C. Bray, J. Fluid Mech. 20, 659 (1964).
9. S. Knoos, J. Plasma Phys. 2, 207 (1968).
10. W.S. Liu, University of Toronto, Institute for Aerospace Studies, UTIAS Report, 198 (1975).
11. O. Igra and G. Ben-Dor, Israel J. Tech. 18, 159 (1980).

AD P000289

SHOCK WAVE STRUCTURE IN GAS-PARTICLE MIXTURES

AT LOW MACH NUMBERS

G.KÖNIG and A.FROHN

Institut für Thermodynamik der Luft- und Raumfahrt, Universität

Stuttgart, Pfaffenwaldring 31, 7000 Stuttgart 80, Germany

The shock wave structure in gas-particle mixtures has been investigated by measuring density profiles of the gas and number density profiles of the particles for shock Mach numbers below $M_s = 1.2$. The measured profiles are compared with theoretical results. The experiments have been performed with a vertically mounted shock tube. For the generation of weak shock waves the usual diaphragm has been replaced by a pneumatic valve. A laser differential interferometer was used to measure the gas density and the number density of the particles was determined by extinction measurements. As gas-particle mixtures MgO-smoke and SiO₂-dust are used with mean particle diameters of 0.6 μm and 1.5 μm . The loading ratio of the particles in the gas was below 10^{-2} . For the calculations the gasdynamic shock and the relaxation zone are treated separately. Standard drag coefficient and heat conduction for steady flow are assumed to describe the gas-particle interaction.

INTRODUCTION

The shock wave structure in a particle-laden gas has been treated theoretically in a number of papers¹⁻⁷. These papers include effects such as finite particle volume in the mixture, influence of particle size distribution and decay of shock wave strength in heavily laden gas. In all these papers it has been assumed that the shock can be separated into an unsteady gasdynamic shock followed by a steady relaxation zone due to acceleration and heating of the particles. This treatment is possible when the molecular shock transition due to viscosity and heat conduction is much faster than the macroscopic shock transition in the relaxation zone. It can be expected that the separation becomes invalid for small particles and weak shock waves. The continuous transition in weak shock waves has been investigated by Hamad⁸.

Only few experimental results for shock waves in particle-laden gases have been published⁹⁻¹³. Effective drag coefficients for the particles are determined by Selberg and Nicholls and by

Rudinger with shock tube experiments. The particle diameters ranged from 29 μm to 450 μm and the loading ratios of the particles from 0.05 to 0.36. In both papers it is found that the measured drag coefficient is much higher than the standard drag coefficient for a single sphere. Oota, Tajima and Morii measured the decay of a shock wave in a heavily laden gas. The diameters of the single particles ranged from 3 μm to 9 μm and extremely high loading ratios of 2 have been reached. These authors measured the shock structure in the gas but the comparison with the theory is difficult because of agglomeration. For the experimental investigations mentioned pressure transducers, light scattering and rotating drum camera have been used. In the present paper the structure of weak shock waves is investigated. For the experiments small particles and low loading ratios are used. With optical measuring techniques a high spatial resolution is obtained.

THEORY

The structure of the shock wave is determined by the continuity, the momentum and the energy equations. When the particle cloud can be described by continuum variables these equations have the form

$$\frac{d}{dx}(\zeta_G u_G) = 0, \quad (1)$$

$$\frac{d}{dx}(\zeta_P u_P) = 0, \quad (2)$$

$$\zeta_G u_G \frac{du_G}{dx} = F_{Px} - \frac{dp_{xx}}{dx}, \quad (3)$$

$$\zeta_P u_P \frac{du_P}{dx} = -F_{Px}, \quad (4)$$

$$\zeta_G u_G \frac{de_G}{dx} = F_{Px}(u_P - u_G) - p_{xx} \frac{du_G}{dx} - \frac{dq_x}{dx} + Q_P, \quad (5)$$

$$\zeta_P u_P \frac{de_P}{dx} = -Q_P. \quad (6)$$

Here ζ represents the concentration, i.e. mass of the gas or the particles per unit volume of the system, e the inner energy, u the velocity, p_{xx} a component of the stress tensor and q_x a component of the heat flux vector. The subscripts G and P refer to gas and particles. The quantities F_{Px} and Q_P represent the interaction force and the heat transferred between particles and gas. Contributions of the particles to the stress tensor and to the heat flux vector are neglected. Mass transfer between gas and particles and chemical reactions are not considered. The continuity equations (1) and (2) can be integrated immediately. The result is

$$\zeta_G u_G = \zeta_{G1} u_1 = m, \quad (7)$$

$$\zeta_P u_P = \zeta_{P1} u_1 = \beta m, \quad (8)$$

where m is the mass flow rate of the gas and β is the mass flow ratio of the particles in the gas. The subscript '1' refers to the known equilibrium state ahead of the shock. Eliminating F_{Px}

and Q_p from equations (3) to (6) one obtains two equations which after integration take the form

$$u_G + \beta u_p + p_{xx}/m = P/m \quad \text{and} \quad (9)$$

$$(e_G + u_G^2/2) + \beta(e_p + u_p^2/2) + p_{xx}u_G/m + q_x/m = E \quad (10)$$

with the integration constants P/m and E . Introducing the well known relations

$$e_G = c_v T_G, \quad e_p = c T_p,$$

$$p_{xx} = p - \frac{4}{3} \eta \frac{du_G}{dx}, \quad q_x = -\lambda \frac{dT_G}{dx} \quad \text{and}$$

$$p = \rho_G R_G T_G,$$

the equations (9) and (10) can be written as

$$\frac{4}{3} \frac{\eta}{m} \frac{du_G}{dx} = u_G + \beta u_p + \frac{R_G T_G}{(1-\phi)u_G} - \frac{P}{m}, \quad (11)$$

$$\frac{\lambda}{m} \frac{dT_G}{dx} = c_v T_G + \frac{u_G^2}{2} + \beta(c T_p + \frac{u_p^2}{2}) + u_G(\frac{P}{m} - u_G - \beta u_p) - E. \quad (12)$$

In equation (11) the concentration of the gas ζ_G has been expressed by the temperature of the gas T_G and the volume fraction of the particles ϕ .

By elimination of F_{px} and Q_p two equations have been lost. These equations are replaced by the momentum equation and the energy equation for a single particle which are

$$m_p u_p \frac{du_p}{dx} = -\frac{m_p}{\zeta_p} F_{px} - \frac{m_p}{\rho_p} \frac{dp_{xx}}{dx} \quad \text{and} \quad (13)$$

$$m_p u_p \frac{de_p}{dx} = -\frac{m_p}{\zeta_p} Q_p, \quad (14)$$

where m_p is the mass of a particle and ρ_p is the density of the particle material. In these equations it has been assumed that the physical properties are constant in the particle volume. The force F_{px} can be expressed by the empirical drag coefficient C_D and the heat Q_p is expressed by the Nusselt number Nu . Together with equations (3) and (4) equations (13) and (14) take the form

$$(1-\phi)u_p \frac{du_p}{dx} = C_D \frac{3}{4} \frac{\rho_G}{\sigma_p} (u_G - u_p)^2, \quad (15)$$

$$u_p \frac{dT_p}{dx} = Nu \frac{6}{\sigma_p^2} \frac{\lambda}{c \rho_p} (T_G - T_p), \quad (16)$$

where σ_p is the actual particle diameter. For numerical calculations the empirical coefficients C_D and Nu must be known as functions of Reynolds number and Prandtl number.

Difficulties occur in the integration of the autonomous differential equations (11), (12), (15) and (16) because the equilibrium states in front and behind the shock are singularities of the system. General solutions are therefore not known. Solutions for special cases have been given by different authors¹⁻⁸. Rudinger⁴ for example assumed that the shock transition can be treated as an unsteady gasdynamic shock followed by a relaxation zone. Neglecting the coefficients of viscosity η and the heat conductivity λ in equations (11) and (12) he obtained two algebraic equations. Assuming that u_p and T_p are constant these equations yield the Rankine-Hugoniot conditions for the gasdynamic shock. Now the integration of the equations (15) and (16) is straight forward. Polydisperse particle distributions can be taken into account by replacing the size distribution by different classes of particle size. For low Mach numbers analytical solutions have been given by Hamad⁸. For $M_s \rightarrow 1$ the equations (15) and (16) become linear relaxation equations and together with the equations (11) and (12) analytical solutions are developed by series expansions.

EXPERIMENTS

Measurements have been performed with a shock tube which is shown schematically in Fig.1. As low pressure section a glass tube was used with an inner diameter of 26 mm and a length of 3 m. The glass tube allows optical measurements without disturbing the gas flow. The usual shock tube diaphragm has been replaced by a special valve which opens the high pressure section independently of the pressure difference between high and low pressure section. With this valve which has been described in detail elsewhere¹ it is possible to produce very weak shocks of variable strength.

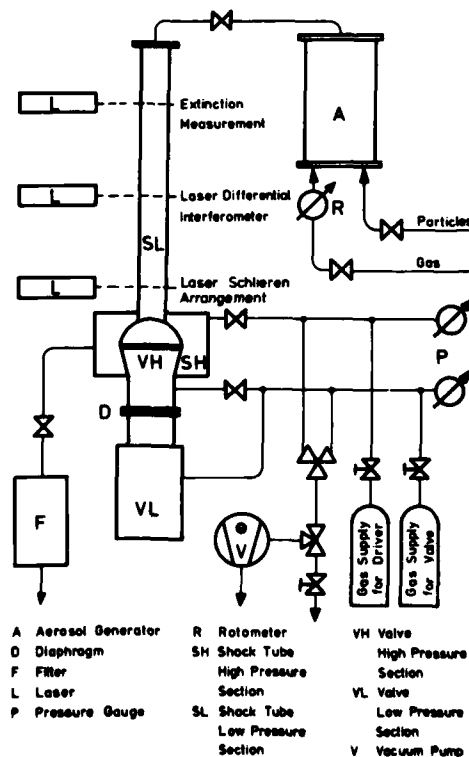


Fig. 1
Experimental setup

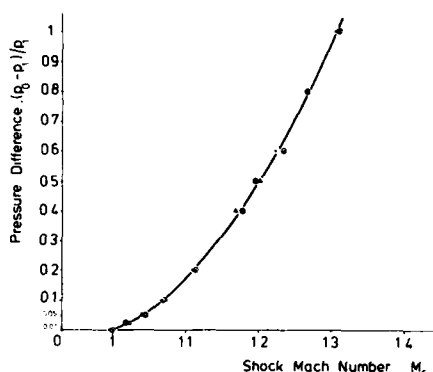


Fig. 2 Measured shock Mach number M_s as a function of pressure difference between high and low pressure section. Instead of a diaphragm the valve of Ref. 14 has been used between high and low pressure section.

In Fig. 2 the measured shock Mach number is plotted against the pressure difference between high and low pressure section. Here the shock Mach number has been determined from the travelling time of the shock front which was measured with two laser-schlieren systems having a distance of 18.6 mm.

The density profile of the gas across the shock was measured by a laser differential interferometer¹⁵. The light intensity I can be related to the density of the gas ρ_G by the equation

$$\frac{I}{I_{\max}} = \cos^2 \left[\frac{\pi l_I}{\lambda_{\text{vac}}} \left(\frac{\rho_G}{\rho_{G1}} - 1 \right) (n_1 - 1) + \frac{\phi}{2} \right], \quad (17)$$

where I_{\max} is the maximum intensity, l_I is the effective path length of the laser beams in the shock tube, λ_{vac} is the vacuum wave length of the laser light and $\phi/2$ is the phase shift. For actual measurements equation (17) has been linearized for $\phi = 3\pi/4$. One obtains the relation

$$\frac{\Delta I}{I_{\max}} = \frac{1}{k} \frac{\Delta \rho_G}{\rho_{G1}} \quad \text{with} \quad \frac{1}{k} = \frac{\pi l_I}{\lambda_{\text{vac}}} (n_1 - 1), \quad (18)$$

where k is the inverse sensitivity of the interferometer. By experiments in pure gases it has been found, that an effective path length l_I of approximately 0.41 mm gives a suitable sensitivity. The number density profile of the particles has been determined by the extinction of a laser beam¹⁶. The experimental setup is shown in Fig. 3. The laser beam was split in order to perform difference measurements. By this arrangement the noise of the laser light was reduced so that transmittance changes of 1/1000 could be detected. Using Bouguer's law

$$f/f_0 = \exp(-n_p a E l_E), \quad (19)$$

the transmittance f/f_0 of the dispersion can be used to determine the number density n_p of the particles when the projected area a of the particles is known. In equation (19) E is the extinction coefficient and l_E is the path length of the laser beam in the dispersion i.e. the inner diameter of the shock tube. For determination of the mass flow rate \dot{m} equation (19) is used in its original form. For the evaluation of the extinction profiles across the shock equation (19) has been linearized so that the change of the transmittance is proportional to the change of

the number density:

$$\frac{\Delta f}{f_1} = \epsilon_1 \frac{\Delta n_p}{n_{p1}} \quad \text{where} \quad \epsilon_1 = -n_{p1} a E l_E = \ln \frac{f_1}{f_0} \quad (20)$$

As the sensitivity ϵ_1 cannot be changed very much by the extinction arrangement it depends mostly upon n_{p1} . That means for low particle number densities and low shock Mach numbers no extinction profiles could be measured. The signals of the optical systems

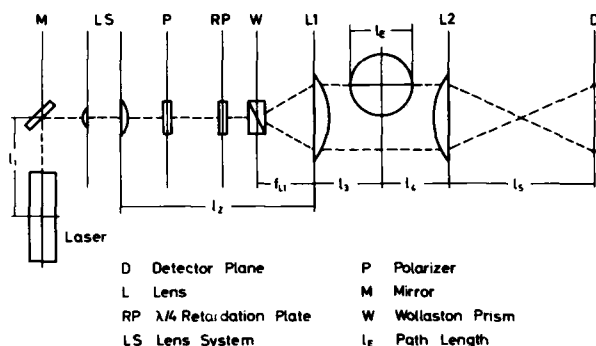


Fig. 3
Extinction
arrangement

were recorded by pin-diodes in connection with an oscilloscope or a transient recorder. The finite width of the laser beam together with the electrical circuit gave a rise time for the signals of approximately 1 μ s. This corresponds to a spatial resolution of 0.4 mm.

The gas-particle mixtures were generated in a separate chamber and then filled in the shock tube. As particle material MgO particles and SiO₂ powder are used with mean diameters of approximately 0.6 μ m and 1.5 μ m. The MgO-spike was produced by burning Mg-metal while SiO₂ particles were dispersed by a rotating propeller. The loading ratio β of the particles in the gas was below 10^{-2} so that the interferometric measurements were not disturbed. The particles were dispersed in air or nitrogen at the pressure of one bar and at room temperature.

RESULTS

Fig. 4 shows an experimental profile of the gas density and the particle number density across the shock at a Mach number $M_s = 1.13$ and a particle loading ratio of $\beta = 2.3 \cdot 10^{-3}$ in an MgO-air dispersion. The unsteady density change in the gasdynamic shock is represented in Fig. 4a by a rise time in the signal of about 1 μ s. Behind this steep density change no further density rise can be observed. The number density profile of the particles shown in Fig. 4b starts with sharp rise at the beginning and approaches then its equilibrium value. In Fig. 5 a number density profile is shown for SiO₂-N₂ dust at the same Mach number and the same loading ratio as in Fig. 1. One recognizes a larger rise time caused by the larger particles. In the case of SiO₂-particles the extinction signal is more irregular as in the case of MgO-particles for it is difficult to disperse the larger particles sufficiently uniform. In Table 1 the measured density changes for gas and for particles are compared with the Rankine-Hugoniot condition. For this comparison



Fig.4 Experimental density profiles of gas and of particles in MgO-air dispersion at a Mach number $M_s = 1.13$ and a loading ratio $\beta = 2.3 \cdot 10^{-3}$; $\sigma_p = 0.6 \mu m$, $Re = 3.16$.

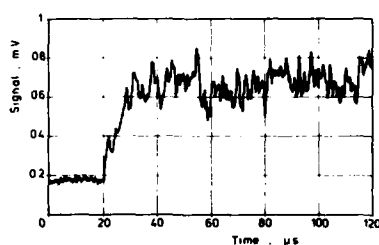


Fig.5 Experimental number density profile of particles in SiO₂-N₂ dispersion at $M_s = 1.13$ and $\beta = 2.3 \cdot 10^{-3}$; $\sigma_p = 1.5 \mu m$, $Re = 7.77$.

the Mach number was determined from the travelling time of the shock front. The experimental profiles from Fig.4 and Fig.5 are in good agreement with theoretical profiles for mean particle diameters of $0.6 \mu m$ and $1.5 \mu m$. In the theoretical calculations it has been assumed that gasdynamic shock and relaxation zone can be separated. The empirical coefficients C_D and Nu are evaluated by the equations

$$C_D = \frac{24}{Re} + \frac{4}{Re^{1/3}} \quad \text{and} \quad (21)$$

$$Nu = 2 + 0.6 Pr^{1/3} Re^{1/2} \quad (22)$$

DISPERSION	THEORY		EXPERIMENT	
	gasdynamic shock	total shock	gas	particles
MgO - air	1.2206	1.2238	1.20	1.28
SiO ₂ - N ₂	1.2206	1.2236	1.23	1.33

Table 1: Comparison of Rankine-Hugoniot condition with measured density ratios across the shock for gas and for particles in profiles of Fig.4 and Fig.5; $M_s = 1.13$
 $\beta = 2.3 \cdot 10^{-3}$

Experimental profiles of the gas density for very low shock Mach numbers are shown in Fig.6 and Fig.7 together with theoretical results. Here the travelling time of the shock front can not be measured with sufficient accuracy to determine the shock Mach number. Using the Rankine-Hugoniot condition the Mach number is determined from the measured gas density change.

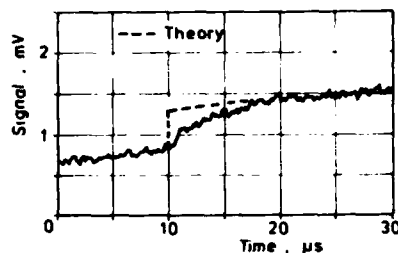
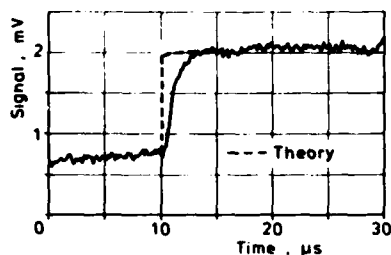


Fig.6 Experimental density profiles of gas in $\text{SiO}_2\text{-N}_2$ dispersion together with calculated profiles.

a: $M_s = 1.03$, $\beta = 3 \cdot 10^{-3}$, $\sigma_p = 1.5 \mu\text{m}$, $Re = 1.69$;
b: $M_s = 1.01$, $\beta = 2 \cdot 10^{-3}$, $\sigma_p = 1.5 \mu\text{m}$, $Re = 0.56$.

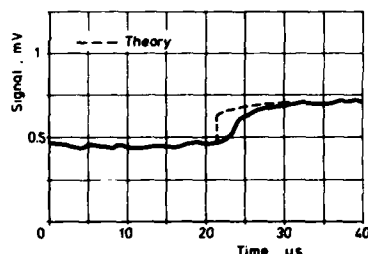


Fig.7 Experimental density profile of gas in MgO-air dispersion together with a calculated profile for $M_s = 1.01$ and $\beta = 5.8 \cdot 10^{-3}$; $\sigma_p = 0.6 \mu\text{m}$, $Re = 0.23$.

In Fig.6 it can be seen how the profile becomes flatter when the Mach number decreases from $M_s = 1.03$ to $M_s = 1.01$. At the higher Mach number $M_s = 1.03$ first deviations between the theoretical curve and the measurement occur whereas at $M_s = 1.01$ the measured profile shows significant deviations from the theory. The profile of Fig.7 is obtained for $M_s = 1.01$ and for a higher loading ratio of $\beta = 5.8 \cdot 10^{-3}$. In contrast to the theory the experimental profile is completely smooth in this case. No gasdynamic shock can be found.

CONCLUSIONS

The theory based on a gasdynamic shock is in good agreement with the experiments for shock Mach numbers above 1.1 and for not too high loading ratios. It should be emphasized that the density profile of the particles depends significantly on the relation $C_p(Re)$.

For very weak shock waves the shock Mach number had to be determined from the measured density change across the shock. In spite of the experimental errors connected with this procedure it was found that the concept of a gasdynamic shock becomes invalid for shock Mach numbers below 1.03 and loading ratios above $2 \cdot 10^{-3}$. For the future it is planned to compare experimental results for low Mach numbers with the continuous solutions of Hamad⁸.

REFERENCES

1. Carrier, G.F., J.Fluid Mech. 4, 376 (1958)
2. Rudinger, G., Phys.Fluids 7, 658 (1964)
3. Marble, F.E., Ann.Rev.Fluid Mech. 2, 397 (1970)
4. Rudinger, G., AIAA J. 3, 1217 (1965)
5. Varma, T.D., Chopra, N.K., ZAMM 18, 650 (1967)
6. Kriebel, A.R., Trans.ASME Ser.D 86, 655 (1964)
7. Bhutani, O.P., Chandran, P., Int.J.Engng.Sci. 15, 537 (1977)
8. Hamad H., Frohn A., ZAMP 31, 66 (1980)
9. Selberg, B.P., Nicholls, J.A., AIAA J. 6, 401 (1968)
10. Rudinger, G., Trans.ASME Ser.D 92, 165 (1970)
11. Oota, E., Tajima, K., Morii, H., Bull.JSME 19, 384 (1976)
12. Hamad, H., König, G., Frohn, A., Proceedings of the ICHMT-1978 Int.Seminar, Dubrovnik, 647 (1979)
13. König, G., Frohn, A., Proceedings of the Int.Symp.Flow Visualization, Bochum 560 (1980)
14. Garen, W., Synofzik, R., Frohn, A., AIAA J. 12, 1132 (1974)
15. Smeets, G., George, A., ISL-Report No. 28/73, Deutsch-Französisches Forschungsinstitut, Saint-Louis (1973)
16. Hodgkinson, J.R., Aerosol Science ed. C.N.Davies, Academic Press, New York (1966)

AD P 000290

CROSS-SECTIONAL CONCENTRATION OF PARTICLES DURING SHOCK PROCESS
PROPAGATING THROUGH A GAS-PARTICLE MIXTURE IN A SHOCK TUBE

Eisuke Ota, Kiyohiro Tajima and Shigeki Suzuki

Department of Mechanical Engineering

Waseda University, Tokyo, Japan

Shock wave-forms in a gas-particle mixture are discussed according to the following investigations. A shock tube of 70 mm internal diameter is used for the experiments by dispersing glass spheres into atmospheric air in the driven section. Pressure, particle velocity and particle number are measured. Mach number of the shock wave is less than 1.5, mass flow ratio of the phases ranges from 0.1 to 0.5, and diameters of the particles are 30 and 50 ~~mm~~ *microns*.

(1) Since the relaxation length of the flow is very large, the wave system in the shock tube should be treated as non-steady accounting for the shock wave decay. A method of characteristics is applied, and the results agree well with the measurements in the leading zone of the wave. However, a higher increase of pressure than the experimental wave form is still observed in the rear part of the wave.

(2) Particle drag, measured by streak recordings, gives a satisfactory continuation of Rudinger's law, and seems to increase with the particle diameter. Effects of the drag law to the shock wave form are indicated.

(3) The number density of particles near the tube wall is found by almost 50 % lower than the density at the center. Such a cross-sectional concentration of particles is expected to be induced by the wall boundary layer. Introducing a lift force due to the velocity shear and an impaction force between particles, trajectories and density distribution are estimated. However, the iterative procedure of analysis approaching the experimental wave form is not yet completed.

INTRODUCTION

Recent developments in two-phase fluid dynamics have solved, both by theoretical and by experimental investigations, various problems in engineering applications. The scientific interests are frequently directed to unsteady phenomena, where the most characteristic behaviors are related to transfers of mass, momentum and energy between phases constituting the flow system, and where time constants of transfer are large in compared with time scales of the flow. The assumption of averaged continuum is usual in mathematical treatments of the dispersed systems, and equations describing the conservation laws for each phases are coupled by laws of transfer processes. However, there arise many difficulties in the modelings and in the analyses. Discussions on averagings in time or in space, effects due to averagings in mass and momentum, and stability

153

of numerical analyses are the fundamental problems. Furthermore, universal laws describing the transfer processes within the dispersed structure have not been established so far. A shear layer will also make the situations complicated.

Shock tubes are the most convenient tools to obtain basic knowledges about the flow. In the present paper, a mixture of air and solid particles is used as the driven medium. The process of relaxing non-equilibriums in velocity and in temperature is concerned by initiating the flow by a shock front. Since the studies made by Carrier[1], Kriebel[2] and Rudinger[3], the relaxation zone, as an internal structure of the two-phase shock wave, is usually treated quasi-stationary. However, in case of large particle diameters, thickness of the zone is so large that the stationary relations are no more applicable to unsteady problems. The leading shock front and the relaxation zone constitute a system of unsteady motions. Interactions between the flow and a boundary layer will modify the system. The mechanism might be related not to a mass sink, but probably to transmitting of particles out of the layer, or a concentration.

SHOCK TUBE EXPERIMENTS

The shock tube used is schematically shown in Fig.1. It is vertically mounted with the driver section in the lower part. The driven section of 5.6 m long is constituted with a pure air section of 2 m long and the upper part of dispersed mixture. The internal diameter is 70 mm. As illustrated in the wave diagram, a plane shock front is formed in the air section, and is incident to decay through the mixture. By this arrangement, boundary conditions of the two phase flow are simplified, and confusions due to interactions of contact surface and expansion wave generated by the operation are successfully avoided. The particles are fed through an injection valve and dispersed into the tube by driving a suction fan connected to the top end of the shock tube. Then the valve is slid to open the tube. Atmospheric air is sucked in through the port I to suspend the particles, and is exhausted out from port O at the top end. Both

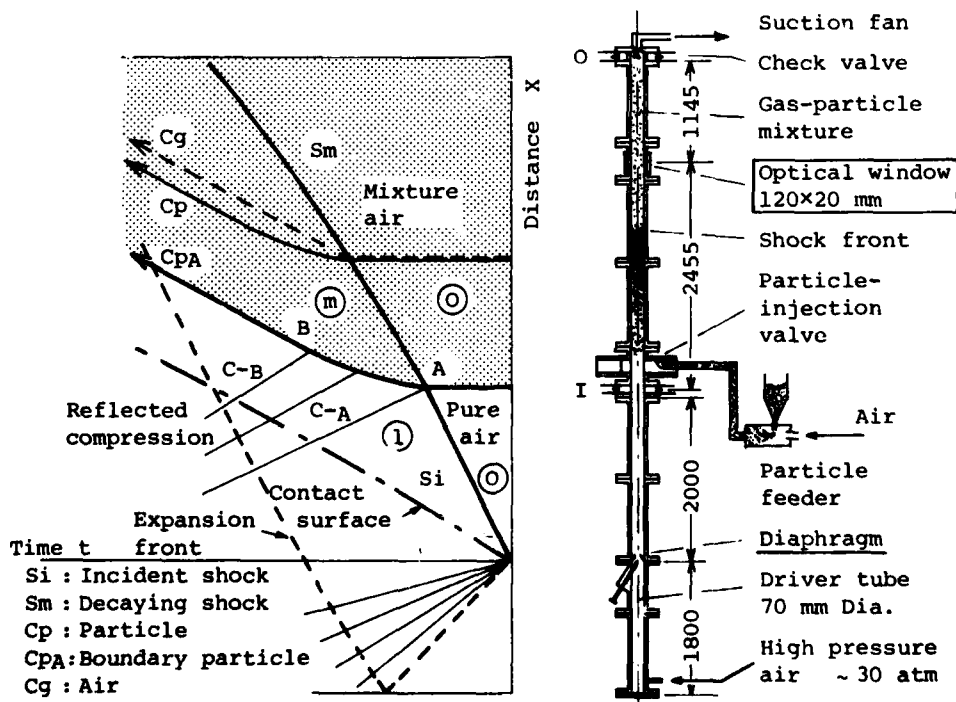


Fig.1 Schematics of the shock tube and wave diagram operating with a gas-particle mixture.

of the ports are equipped with a check valve and a particle filter. After the passing of a shock front, the valves are shut off by the pressure increase, so that almost all of the particles are conserved within the tube. The sediment at the bottom is collected for weighing, and the loading ratio averaged over the test section is obtained. The particles are glass beads of 30 and 50 μm nominal diameters. The specific weight is 2.5, and the specific heat is 0.25 $\text{kgf/kg}^\circ\text{K}$. In the early stage of the investigation, a powder of white carbon is used [4]. However, the diameter is so small, i.e. 5-9 μm , that some difficulties arose due to coalescence.

Shock velocity of the incident wave, local velocity during the decay, wave form of pressure, particle trajectories and particle number are measured. The data are taken at a section 2.5 m downstream of the incidence. Typical recordings are shown in Fig.2, where M_{si} and M_{sm} denote Mach numbers of the incident and the decaying shock front based on sound speed of air. Mass flow ratio of particles to air is indicated by η . It is clearly observed in the pressure signals that the wave is initiated by a discontinuous jump, which is found well agree with the Rankine-Hugoniot condition of air. The further increase shows the relaxation process. As the particle diameter D increases, the relaxation becomes considerably longer, e.g. 200 μsec for $D \approx 10 \mu\text{m}$ and more than 5 msec for 50 μm . It should also be noted that, as the mass flow ratio increases, the leading front becomes weak, and the wave in the extremity takes a continuous wave-form. The streak schlieren pictures in Fig.2(a) are not so clear as usual recordings because of cloudy situation of the fields. Velocities of particles are measured by using a micro-optical reader, and the accelerations are determined by polynomial fittings. Particle number is obtained by counting light pulses. A light beam of a He-Ne laser is focused at a measuring point, and the light signals scattered by particles in crossing the sampling volume are collected by a photo-multiplier. The optical arrangement and the output signals are shown in Fig.2(c). The volume is measured to be 100 μm in diameter and 1 mm in length. Two systems are used; one is focused at the center, $r=0$, and the other is at 5 mm from the tube wall, or at 80 % of the radius R . The density of the pulse near the wall is considerably lower than the density at the center. The pulse numbers during an interval of 0.5 msec at every shock tube run are averaged over ten runs to express the number density of particles.

UNSTEADY ONE-DIMENSIONAL ANALYSIS AND DISCUSSIONS OF WAVE-FORMS

In the mathematical formulation, volume interaction is neglected, since volume fraction of particles is estimated less than 1 %. The interactions due to drag force and heat transfer between the phases are taken into account. Then, the system of equations for the averaged continuum takes the simplest form as follows.

$$\frac{\partial \rho}{\partial t} + \frac{\partial}{\partial x} \rho u = 0, \quad \frac{\partial \sigma}{\partial t} + \frac{\partial}{\partial x} \sigma u_p = 0 \quad \dots (1a, 1b)$$

$$\frac{\partial}{\partial t} (\rho u + \sigma u_p) + \frac{\partial}{\partial x} (\rho u^2 + \sigma u_p^2) + \frac{\partial p}{\partial x} = 0 \quad \dots (2)$$

$$\frac{\partial}{\partial t} [\rho (c_v T + \frac{1}{2} u^2) + \sigma (c \tau + \frac{1}{2} u_p^2)] + \frac{\partial}{\partial x} [\rho u (c_p T + \frac{1}{2} u^2) + \sigma u_p (c \tau + \frac{1}{2} u_p^2)] = 0 \quad \dots (3)$$

$$\frac{\partial}{\partial t} u_p + u_p \frac{\partial}{\partial x} u_p = \frac{3\rho}{4Dd} C_D |u - u_p| (u - u_p), \quad \frac{\partial \tau}{\partial t} + u_p \frac{\partial \tau}{\partial x} = \frac{6\mu}{D^2 d} \frac{Nu}{Pr} (T - \tau) \quad \dots (4a, 4b)$$

In the equations, ρ : density of gas, σ : mass of particles per unit volume of the mixture, u and u_p : velocities of gas and particles, p : pressure, T and τ : temperatures of gas and particles, c_p and c_v : specific heats of gas, c : specific heat of particle material, D : particle diameter, d : density of particle material, μ : viscosity of gas, Nu : Nusselt number, Pr : Prandtl number, Re : Reynolds number of particle, and $\delta = c/c_p \approx 1$. Ideal gas laws are applied for the gas phase.

(White Carbon, 5-9 μm)
KISTLER-201B

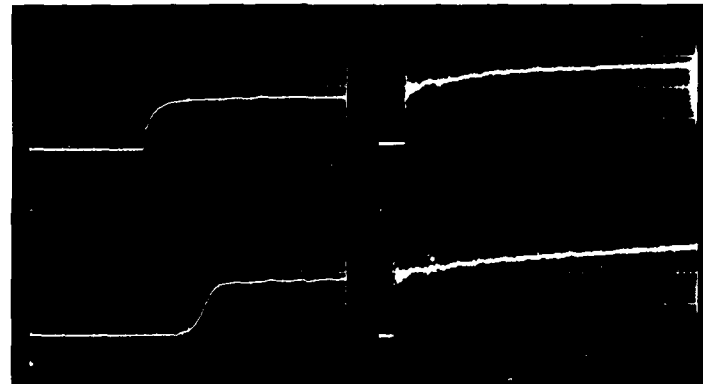
(Glass Beads)
KISTLER-603A

$M_{sm} = 1.16$
 $\eta = 1.0$
10 psi/div
200 μs /div

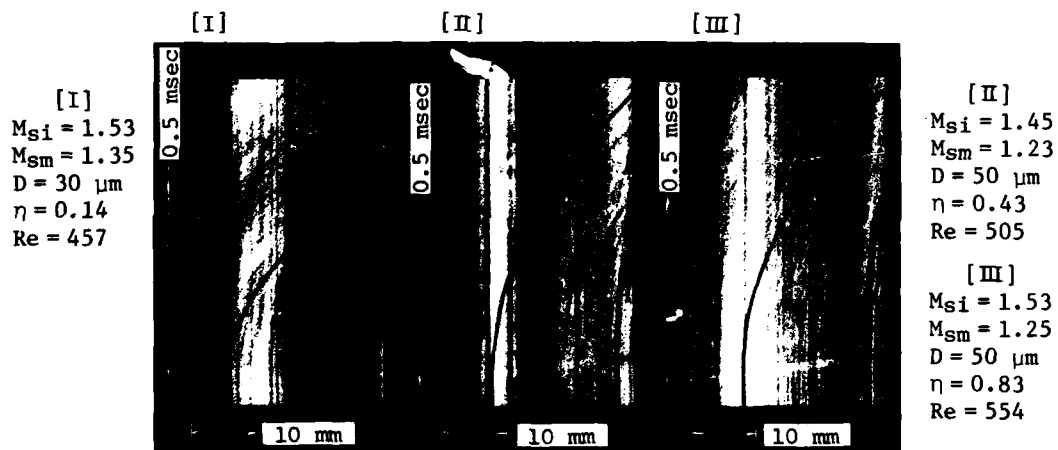
$M_{sm} = 1$
 $\eta = 1.7$
10 psi/div
200 μs /div

$M_{sm} = 1.26$
 $D = 26 \mu\text{m}$
 $\eta = 0.19$
5 psi/div
500 μs /div

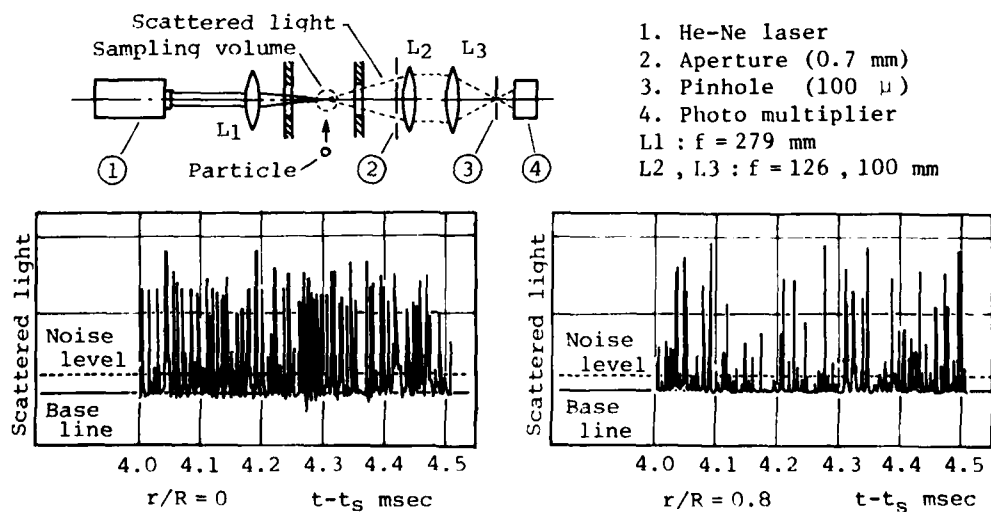
$M_{sm} = 1.29$
 $D = 50 \mu\text{m}$
 $\eta = 0.51$
5 psi/div
500 μs /div



(a) Pressures of two-phase shock wave



(b) Streak schlieren pictures showing trajectories of particles.



(c) Scattered light signals; $D = 50 \mu\text{m}$, $\eta = 0.3$, $M_{sm} = 1.3$

Fig.2 Typical recordings of two phase experiment in shock tube

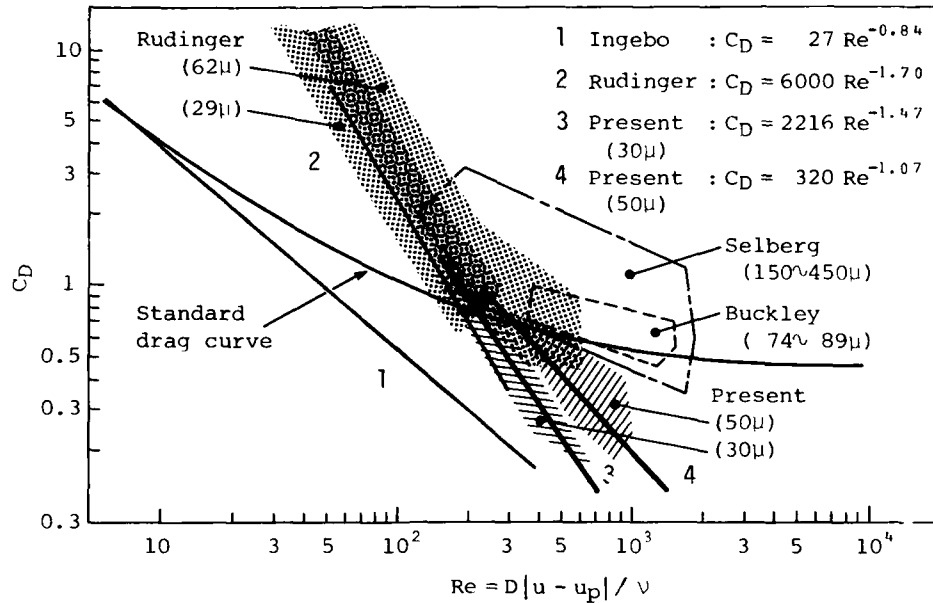


Fig. 3 Drag coefficient of particles in dispersed mixture of air. The data except 1 are obtained by shock tubes.

The wave motion corresponding to the diagram in Fig.1 is analyzed using the method of characteristics [4]. The initial and the boundary conditions are prescribed as follows;

- The region 0 is at a constant state and at a uniform dispersion, i.e. $u = u_p = 0$, $p = p_0$, $T = \tau = T_0$ and $\eta = \eta_0$.
- Given the velocity U_{si} of the incident front at section of incidence x_0 , the trajectory of shockfront is to be determined using the Rankine-Hugoniot relations and the frozen condition for the air and the particle respectively.
- Along the path C_{pA} of boundary particle, the air follows the simple wave relation, and the number of particle is infinitesimal, i.e. $\sigma = 0$.

The laws of drag and heat transfer give significant differences in the calculated waveforms. Three correlations of drag, as compared in Fig.3, and the Knudsen-Katz formula of heat transfer, i.e. $Nu = 2 + 0.6Pr^{1/3} Re^{1/2}$, are used. The Ingebo's law takes the lowest drag for dispersed systems. The present data are obtained by a similar method as made by Rudinger[5]. Using steady equations of mass and momentum, values of C_D and Re are determined from pressure data and velocity and acceleration of particles. The data at 0.1 msec after the front are used in order to avoid the effect of unsteady propagation of the leading shock front. A considerable amount of scatter exists in the results due to a random appearance of particle trajectories in the streak pictures. The C_D data in Fig.3 seem to increase as the particles become large, probably due to differences in interaction distance between particles. No reasonable correction is found to express the effect at this stage. The present value obtained for 30 μ m particles is found close to the result of Rudinger.

The changes of waveforms during the shock wave decay are typically shown in Fig.4. The incident shock front of $M_{si} = 1.6$ decays over a distance of more than 10 meters to a steady front of $M_{se} = 1.27$. The final Mach number is identical with the value predicted by an effective gas model, where the incident wave is transmitted through a gas specified with "effective" values of gas constant and specific heat ratio. The terminal waveforms coincide with the stationary shock waveforms calculated with the value of M_{se} . As the mass flow ratio increases, the terminal shock front becomes weak as stated before. Fig.4(c) indicates the

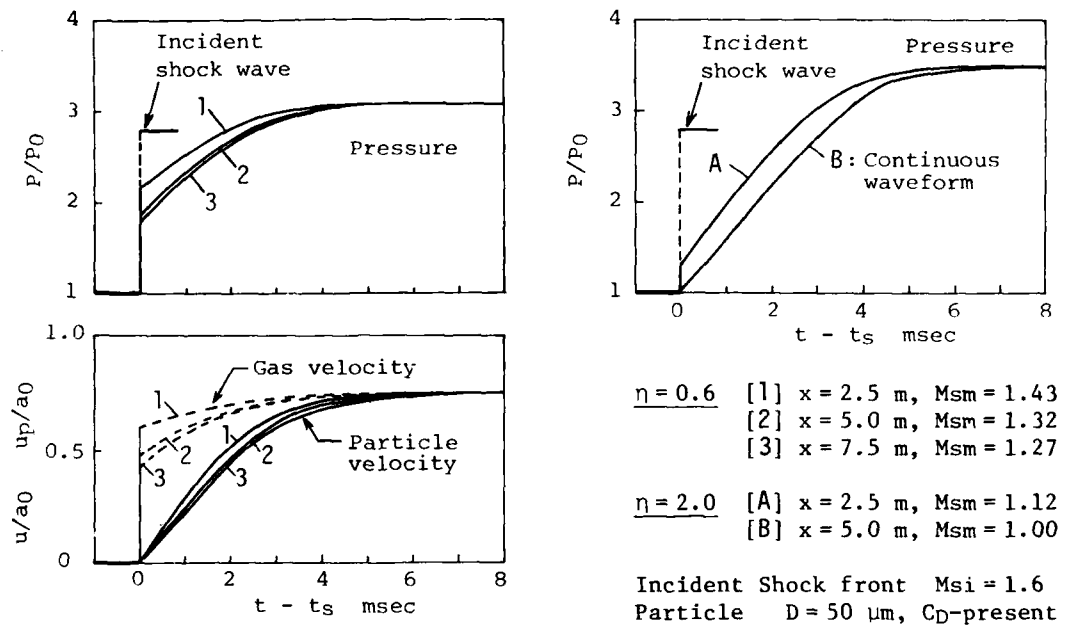


Fig. 4 Processes showing the decay of a shock front and local waveforms calculated at distance x from the incidence.

process whereby a continuous waveform is realized. It should be remarked that the shock wave continues to decay so long as the steady waveform at the local shock Mach number exceeds the local unsteady waveform.

Experimental pressure and particle velocity are compared with the results of analyses in Fig.5. In the velocity diagram, ten readings from the streak pictures are shown in a form of histogram for every 100 μ sec. The pressures calculated by stationary wave equations exhibit considerably higher increase than the experimental results. This is because the shock wave is decaying at the section of measurements. Such unsteady effect does not appear so clearly in the velocity as in the pressure. The unsteady pressures related to the present correlation of drag seem to agree well with the leading part of the experimental profiles. However, a considerable amount of deviation arises in the rear part, in accordance with an experimental evidence that the final pressure, which does not depend on the descriptions of the transfer processes, is lower than the predicted. The other two correlations take lower values of drag force than the present correlation in the experimental range of Re number. Then, the decay of shock front, the pressure increase and the particle acceleration are calculated less gradual, and the rate of pressure increase becomes similar to the results of the experiments. It is still premature to find out the most suitable correlation among the three, because of the presence of various uncertainties and assumptions in the formulation of the flow, e.g. non-uniform initial dispersion, inter-particle actions and two-dimensional motions.

A FUNDAMENTAL CONSIDERATION OF BOUNDARY LAYER EFFECT

The measurement of particle number reveals that the number density near the tube wall is considerably lower than the density at the center axis. Typical results are shown in Fig.6. At the center, i.e. $r = 0$ mm, the density increases similarly with the result of unsteady analysis, while the density at $r = 28$ mm seems almost constant and is 50 % lower than the center flow density at the end of the process. Such concentration of particles may be expected due to an effect of wall boundary layer. In an usual shock tube flow, the growth of the boundary layer acts as a mass sink in a shock fixed co-ordinate system so that the

AD-A122 200

PROCEEDINGS OF THE INTERNATIONAL SYMPOSIUM ON SHOCK
TUBES AND WAVES (13TH. (U) CALSPAN ADVANCED TECHNOLOGY
CENTER BUFFALO NY C E TREANDOR ET AL. JUL 81

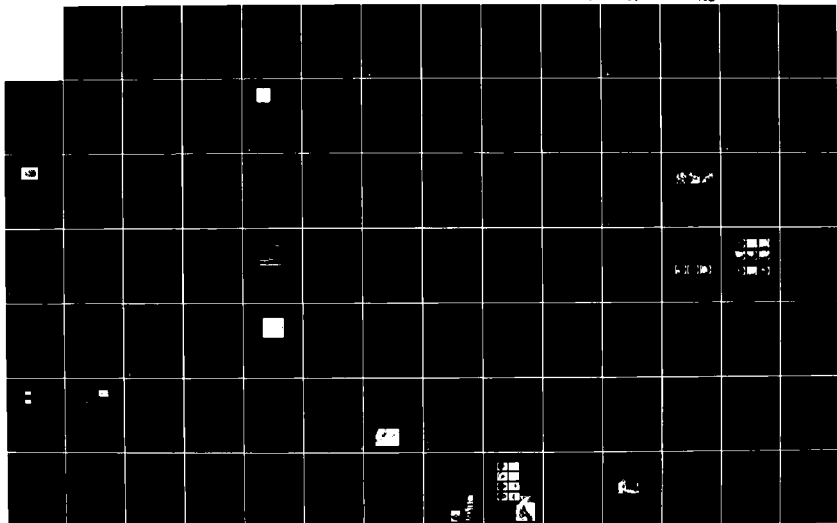
8110

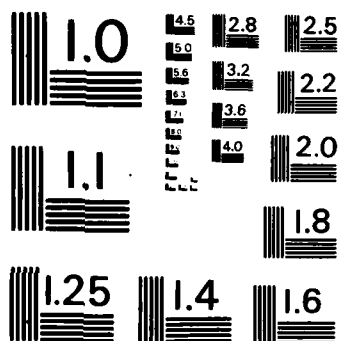
UNCLASSIFIED

AFOSR-TR-82-1031 F49629-81-C-0002

F/G 20/1

NL





MICROCOPY RESOLUTION TEST CHART
NATIONAL BUREAU OF STANDARDS-1963-A

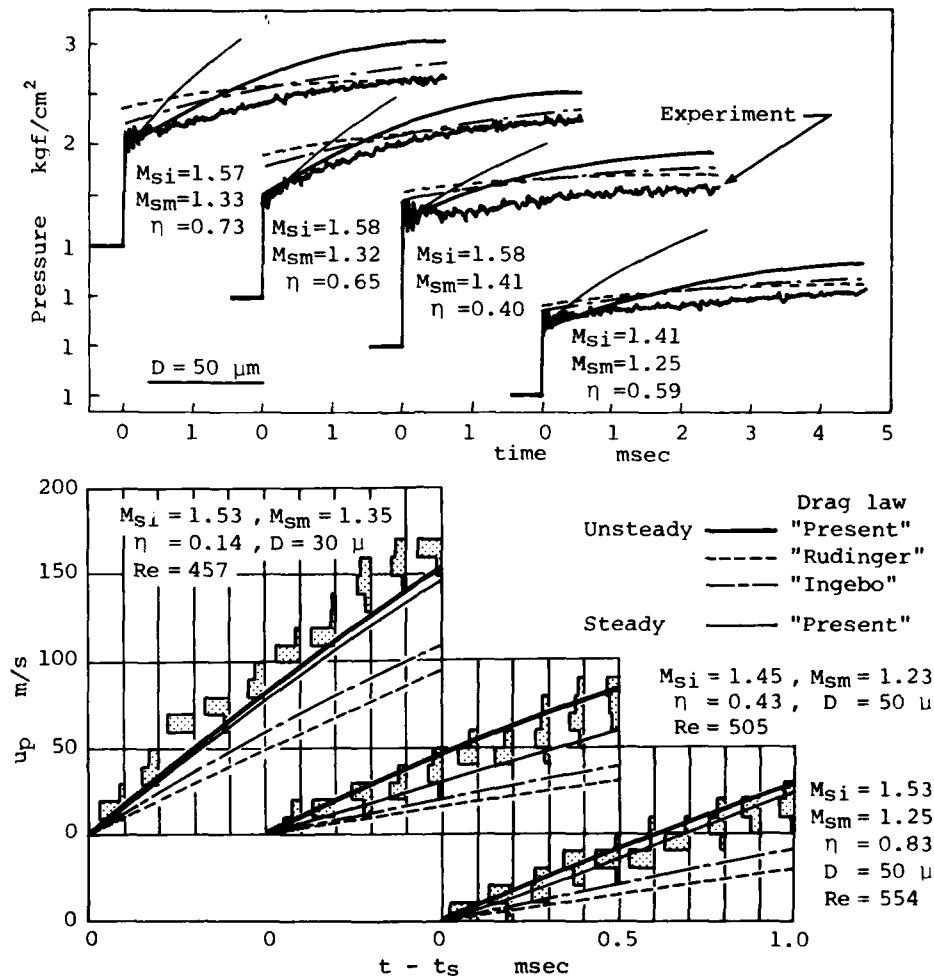


Fig. 5 Comparison of measured and calculated profiles of pressure and particle velocity. Various C_D data are used.

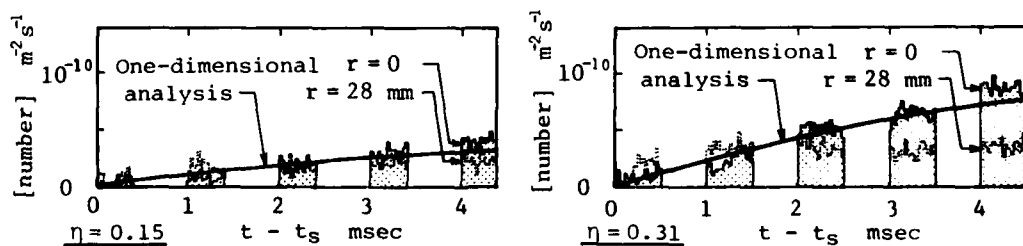


Fig. 6 Number density of particles showing the cross-sectional concentration. $M_{Sm} = 1.31$ and $D = 50 \mu m$.

pressure increases with distance from the shock front. In the present case, the particles in the boundary layer receive a lift force due to the velocity shear of the gas flow and move away from the tube wall [6], so that the structures of one-dimensional wave are modified through a somewhat different mechanism.

Two-phase boundary layers are treated by various authors [7] using the method of momentum integral relations. In the early stage of the present study, the interaction problem of boundary layer flow and the external tube flow is intended to solve iteratively accounting for the displacement effect. The system

is constituted with equations of continuity, motion and energy describing the external flow of gas phase, a momentum integral relation of the two phase boundary layer, and equations of motion and energy of particles with external forces of lift and drag. The interaction is introduced in the continuity equation by adding a normal velocity term as the mass sink, which is related to the displacement thickness by the integral relation of continuity of the boundary layer. However, the method is found unsuccessful because that particles in the boundary layer completely fly out to interact with free stream particles at different velocities and phase densities, so that the concept of displacement effect is no more applicable for the external flow correction. Basic knowledges about the behaviors and the concentration of particles must be required. The following procedure is executed as a preliminary investigation.

- (1) Boundary layer profiles of velocity and temperature in a shock fixed coordinate are calculated by numerically integrating the momentum integral relation. The one-dimensional waveforms are used as conditions at the edge of the layer. It is assumed that the particles are absent from the layer, and that the velocity and the temperature are expressed by third order polynomials.
- (2) A Lagrangian cell of particle phase, which is located initially behind the shock front, is represented by a particle (i), and the trajectory and the phase density are obtained by integrating the following equations;

$$u_p \frac{d}{dx} u_p = F \mu (u - u_p), \quad u_p \frac{d}{dx} v_p = E \rho (u - u_p) \sqrt{v \frac{\partial u}{\partial y}} + F \mu (v - v_p) \dots (5a, 5b)$$

$$u_p \frac{d}{dx} \sigma = -\sigma \left[\frac{\partial}{\partial x} u_p + \frac{\partial}{\partial y} v_p \right], \quad \dots \dots \dots (5)$$

and Eq.(4b), where, d/dx denotes a differentiation along the i -th trajectory. u and v are velocity components in the direction of x and y . Drag and lift forces take the most simple forms, so that $F \equiv 3A/(4D^2d)$ and $E \equiv -3a/(4\pi Dd)$.

- (3) When more than two trajectories intersect each other, a force of impaction acted to the reference particle by the others (r) is added to the right hand sides of Eqs.(5). It is expressed as $\sum F_{ir} (\vec{u}_p^r - \vec{u}_p^i)$, see Soo[8], and the fraction impacted is taken as unity in the calculation.

- (4) Density $\tilde{\sigma}$ and velocities of particle phase at a point of intersection are determined as $\sum_i \sigma^i$, $\sum_i \sigma^i u_p^i / \tilde{\sigma}$ and $\sum_i \sigma^i v_p^i / \tilde{\sigma}$ respectively.

In Fig.7, trajectories of representative particles and the density profiles are shown. The thickness of the boundary layer and the highly concentrated layer are calculated very thin in compared with the tube diameter and the experimental data, so that the external flow must be affected only slightly. Nevertheless, it is clearly seen that the boundary layer influences the flow through transmitting particles crossed the shock front and generating a high density zone outside of the layer. The thickness reaches several times the boundary layer thickness. Such non-uniform distribution of particle density modifies the gas flow in the second step of the iterative procedure. However, an assumption of thin layer neglecting the normal gradient of pressure will be no more valid. Profiles of pressure and gas velocity are estimated by assuming parallel stream tubes. As indicated in the figure, the normal gradient of pressure is almost two hundreds times the axial gradient, so that a normal motion of particles and gas must be induced toward the center. The procedure obtaining the two-phase profiles are not completed at this stage, and a reasonable method of analysis must be developed to execute the second step. The experimental results of particle number indicate that, in contrary to the estimated, the density near the wall is considerably rarefied. The difference may be partly due to the modeling of the interaction of particles from the boundary layer with the free stream particles. If a complete momentum mixing is assumed, then the free stream particles are expected to be more deflected, and the particle phase is rarefied near the edge of the boundary layer. Of course the real situation is much complicated, and the complete modeling may be very difficult.

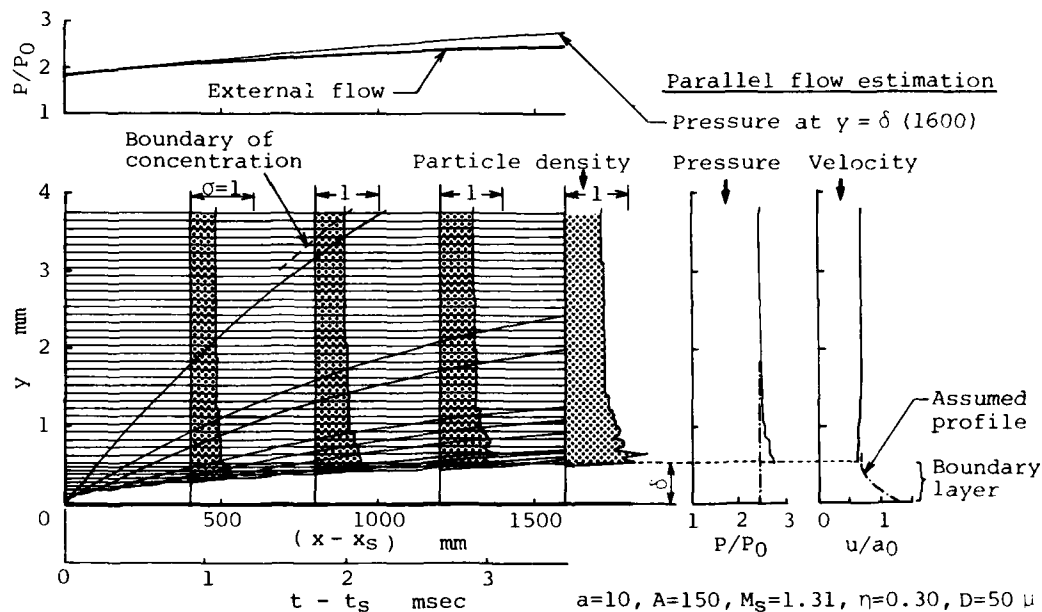


Fig. 7 Trajectories and phase density of particles induced by boundary layer. Interaction between particles appears slightly.

CONCLUDING REMARKS

Structures of shock waves in solid particle and gas mixtures are discussed by experiments and analyses. Effects of unsteady propagation of shock front initiating the process are made clear. Several drag laws, including results of the present measurement, are used to describe the momentum transfer between the particles and the gas, but discrepancies arise significantly between the waveforms in experiments and in analysis. Among various uncertainties, the boundary layer effect is concerned, since the mechanism of interaction with the external flow is not made clear for the two phase flow. The usual concept of displacement effect is found no more suitable, and the interaction takes place through a cross-sectional concentration of particles. The particles incoming to the boundary layer are transmitted out into the external flow by an action of lift force induced by velocity shear. Though the iterative procedure of analysis is not completed at yet, and though the concentrated layer is unexpectedly thin, an induced inward flow is estimated to arise so that the experimental profiles of the two phase flow may be approached.

The authors are greatly indebted to Mr. H. Katsuta, the former student of the graduate school of Waseda University, for the drag force measurement, and to Mr. A. Fujimoto, the graduate student, for a considerable part of the computation. They would also be grateful to Mr. R. Okutsu, Mr. S. Kuramochi, Mr. H. Matsuoka, Mr. M. Mochizuki and Mr. M. Mori, the graduate student, for the help in preparing the manuscript.

REFERENCES

- [1] Carrier, G.F., *J. Fluid Mech.*, Vol. 4, Part 4 (1958), 376.
- [2] Kriebel, A.R., *Trans. ASME, Ser. D*, 86-4 (1964), 655.
- [3] Rudinger, G., *Phys. Fluids*, 7-5 (1964), 658.
- [4] Outa, E., et al., *Bulletin JSME*, 19-130 (1976), 384.
- [5] Rudinger, G., *Trans. ASME, Ser. D*, 92-1 (1970), 165.
- [6] Bracht, K., Thesis, Dr.-Ing., Ruhr-Universität Bochum (1978).
- [7] Jain, A.G. and Ghosh, A., *Z. Flugwiss. Weltraumforsch.*, 3 (1979), Heft 1, 29.
- [8] Soo, S.L., "Fluid Dynamics of Multiphase Systems", Ginn, Lexington, MA (1967).

AD P000291

MOTION OF SMALL PARTICLES IN A FIELD OF OSCILLATING SHOCK WAVES*

G. Rudinger¹, K.H. Chou² and D.T. Shaw²

State University of New York at Buffalo

Buffalo, New York 14260

Small particles (near 1 μm) suspended in a gas are difficult to remove by conventional separation equipment. A promising technique is to expose the suspension to a field of high-intensity standing sound waves in which the motion of particles relative to one another leads to collisions and agglomeration. The resulting increase in the average particle size then facilitates particle removal by conventional means. Experiments indicate marked increase in the agglomeration rate if the intensity of the oscillations becomes so high that the sound waves steepen to form oscillating shock waves. Particles also exhibit a strong tendency to drift to the nearest velocity node. The drift velocity in a field of oscillating shock waves is evaluated as affected by the frequency and amplitude of the oscillations and by the particle relaxation time. The results are compared with those for a hypothetical field of sinusoidal sound waves and indicate that the drift velocity can be considerably larger for oscillating shock waves than for standing sine waves. Times required for particles to drift from a point close to a loop to the nearest node are computed for several cases and are consistent with preliminary experimental observations.

Introduction

Many industrial processes produce a gas with small suspended particles which must be removed before the gas can be used or exhausted into the atmosphere. Conventional separation equipment, such as cyclones, loose efficiency if the particles are smaller than a few μm , but acoustic agglomeration is a promising technique to overcome this difficulty.^{1,2} Inability of the particles to follow rapid gas oscillations leads to formation of agglomerates for which average removal by conventional means becomes practicable.

*Work supported in part by the United States Department of Energy

¹Department of Mechanical and Aerospace Engineering

²Department of Electrical Engineering

If the wave intensity is increased, sinusoidal sound waves become distorted and eventually develop into oscillating shock waves. Observations in standing-wave field have shown that particles drift toward the nearest velocity node, where the resulting increase in concentration enhances the agglomeration rate. For a complete understanding of agglomeration, it is therefore important to be able to predict particle drift. Drift in a field of standing sinusoidal waves has been analyzed previously^{1,3,4}; it had also been pointed out that drift is affected by distortion of the wave form¹, but apparently no investigations of particle drift in a field of oscillating shock waves have been made.

Experiments

Experiments were performed in a vertical plexiglass test tube of 75 mm diameter and 1.5 m length. A loudspeaker assembly was connected to the top of the tube, and the bottom was closed. It was loaded with an aerosol (NH_4Cl , $D_p = 0.2\text{--}0.5\mu\text{m}$, $\rho_p = 1.58\text{g/cm}^3$) at a concentration of 40 g/m³. Sound pressure levels and wave forms were recorded by a calibrated microphone, and the size of the agglomerated particles was determined by sampling and electron micrographs. Details are given elsewhere.⁵

Initially, the particles formed a dense cloud, but some time after turning on the sound, the cloud became much more transparent except near the nodes indicating reduction of the number density between the nodes as result of agglomeration and drift. Shock waves were formed when the sound pressure level exceeded approximately 160 dB, and agglomeration and drift became much more rapid at still higher intensities. The marked increase of the agglomeration rate after formation of shock waves had previously been observed by Temkin.⁶ At about 170 dB, and a frequency of 0.5 kHz, the experiment was essentially completed within approximately 10 s after turning on the sound. Samples of the agglomerated particles indicated typical particle sizes of 10 to 20 μm . Acoustic pressure levels are generally expressed in dB, and the relationship to other measures of shock strength, outlined in the Appendix, indicates that these shocks are much weaker than those usually considered in gas dynamics.

Analysis

Analysis of particle motion in the oscillating flow field is based on the often made assumptions that the particle is spherical and that the velocity of the particle relative to that of the gas is small enough that Stokes drag is sufficiently accurate. Forces on the particle associated with the distortion of the flow field by an accelerating particle are neglected, because the particle density is about three orders of magnitude larger than the gas density; for small particles, gravity also is insignificant compared with viscous drag as long as their settling velocity is much smaller than the velocities of interest⁷. The equation of particle motion is then given by

$$(\pi D_p^3 \rho_p / 6)(du_p/dt) = 3\pi D_p \mu (u - u_p) \quad (1)$$

where D_p , ρ_p and u_p are the particle diameter, material density and velocity, u and μ are the velocity and viscosity of the gas, and t is time. After division by the mass of the particle, this equation becomes

$$du_p/dt = (u - u_p)/\tau \quad (2)$$

where $\tau = \rho_p D_p^2 / 18\mu$ is the particle relaxation time, and u is defined as the gas velocity at the location of the particle. Since the particle moves in an oscillating flow field, u must be described as a function of x and t before Eq. (2) can be solved. The following description of the field of oscillating shocks is based on the one given by Temkin.⁸ A wave diagram for one cycle is shown in Fig. 1, where shock waves oscillate between $x = 0$ and $x = L$. For the present analysis, it is immaterial whether these points represent physical boundaries or nodes of higher-mode oscillations. These shock waves are so weak that their velocity is practically equal to the speed of sound c in the gas. They have a constant strength that is conveniently expressed by $\Delta u/c$, where Δu is the velocity change across the shock, or simply by Δu , since only constant values of c will be considered (see Appendix). It is evident from Fig. 1 that the frequency f , or cycle time $1/f$, and the distance L between nodes are related by $L = c/2f$. The shock waves thus divide the flow field for each cycle into two regions: region I, which lies behind a shock wave traveling in the direction of increasing x , and region II where it travels in the opposite direction. Within each region, the flow velocity is not a function of time but varies linearly with x between 0 and Δu as shown in Fig. 2; it is positive in region I and negative in region II. The heavy lines indicate the distribution for a shock traveling to the right.

It is convenient to introduce the dimensionless variables $U = u/\Delta u$, $U_p = u_p/\Delta u$, $\xi = x/L$ and $\theta = t/\tau$. Velocities in regions I and II then are given by

$$U_I = \xi \quad \text{and} \quad U_{II} = \xi - 1 \quad (3)$$

The shock trajectories shown in Fig. 1 can be expressed as

$$S_1: \xi = 2f\tau\theta; S_2: \xi = 2(1-f\tau\theta); S_3: \xi = 2(1+f\tau\theta) \quad (4)$$

In Eq. (2), u is a function of the particle position x , and $u_p = dx/dt$, and, in dimensionless variables, Eq. (2) becomes therefore

$$d^2\xi/d\theta^2 + d\xi/d\theta - K\xi = 0 \quad \text{for region I} \quad (5a)$$

$$d^2\xi/d\theta^2 + d\xi/d\theta - K\xi = -K \quad \text{for region II} \quad (5b)$$

where $K = \tau\Delta u/L = 2f\tau\Delta u/c$ is a dimensionless constant. The solution of Eqs. (5) is given by

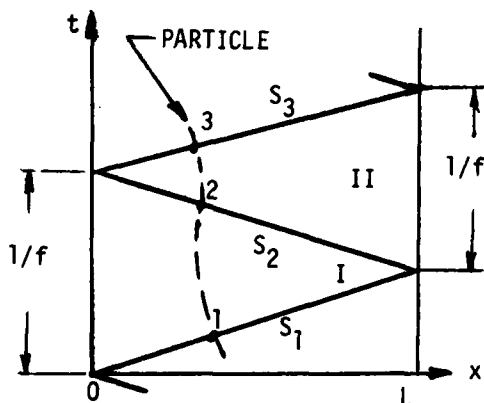


Fig. 1 Wave diagram for oscillating shocks (S_1, S_2 and S_3) and a particle trajectory (broken line).

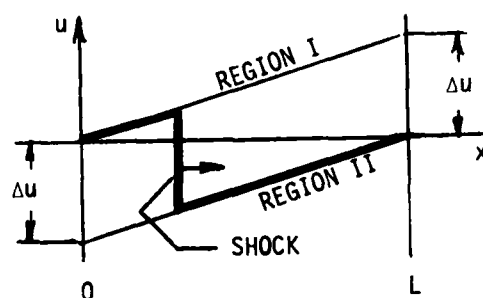


Fig. 2 Velocity distribution in regions I and II. Heavy line indicates distribution for a shock traveling to the right.

$$\xi = A_1 e^{\alpha_1 \theta} + A_2 e^{\alpha_2 \theta} \quad (6)$$

where α_1 and α_2 are the roots of $\alpha^2 + \alpha - K = 0$. The integration constants A_1 and A_2 must be found from prescribed initial conditions for regions I and II. A particle trajectory is indicated in Fig. 1 as a broken line and intersects the three shocks at points 1, 2 and 3. For region I, ξ_1 can be arbitrarily selected and the corresponding dimensionless time is $\theta_1 = \xi_1/2f\tau$. The initial value of the derivative $(d\xi/d\theta)_1 = KU_{p1}$ at point 1 is not known beforehand, but a close approximation can be obtained, because drift during one cycle and the amplitude of the particle oscillations are so small that the particle trajectory can be approximated by $\xi = \xi_1 = \text{const}$. Since U then is also constant within each region, the solution of Eq. (2) becomes a simple exponential. The particle velocity at points 2 and 3 is determined by

$$U_{p2} - U_I = (U_{p1} - U_I) e^{-(\theta_2 - \theta_1)} \quad \text{for region I}$$

$$U_{p3} - U_{II} = (U_{p2} - U_{II}) e^{-(\theta_3 - \theta_2)} \quad \text{for region II}$$

where U_I and U_{II} are given by Eq. (3); the time intervals follow from Fig. 1 as $\theta_2 - \theta_1 = (1 - \xi)/f\tau$ and $\theta_3 - \theta_2 = \xi_1/f\tau$. If one eliminates U_{p2} from these equations and sets $U_{p3} = U_{p1}$, according to the foregoing assumptions, the initial velocity is found as

$$\left(\frac{d\xi}{d\theta}\right)_1 = KU_{p1} = K\left[\xi_1 - \frac{1 - \exp(-\xi_1/f\tau)}{1 - \exp(-1/f\tau)}\right] \quad (7)$$

One can then evaluate A_1 and A_2 in Eq. (6) and obtain the equation of the particle trajectory in region I as

$$\xi = \xi_1 - \frac{K}{\alpha_1 - \alpha_2} \left\{ \frac{(1 + \alpha_2)U_{p1} - \xi_1}{\alpha_1} [e^{\alpha_1(\theta - \theta_1)} - 1] - \frac{(1 + \alpha_1)U_{p1} - \xi_1}{\alpha_2} [e^{\alpha_2(\theta - \theta_1)} - 1] \right\} \quad (8)$$

Since $\theta_2 = (2 - \xi_2)/2f\tau$ from Fig. 1, Eq. (8) can be solved for $\xi = \xi_2$ by iteration; differentiation of Eq. (8) and substitution of the result then yields also $(d\xi/d\theta)_2$. In the next step, Eq. (5b) can be solved for region II in the same manner. The initial conditions are now given by ξ_2 , θ_2 and $(d\xi/d\theta)_2$. Intersection of the trajectory with shock 3 yields ξ_3 and θ_3 , and the drift velocity for this cycle is therefore

$$u_D = (x_3 - x_1)/(t_3 - t_1) = (L/\tau)(\xi_3 - \xi_1)/(\theta_3 - \theta_1) \quad (9)$$

Since the difference between ξ_3 and ξ_1 is quite small, a high accuracy (6 significant figures) is needed to obtain meaningful results. In an attempt to improve the initial approximation for $(d\xi/d\theta)_1$, the results for point 3 were used as starting values for another cycle but led to no significant changes in u_D . The drift velocity is always found to be directed toward the nearest node, where it must be zero. It also must be zero at the loop point, $\xi = 0.5$, because of the symmetry of the flow field, but this location is not stable, because the slightest deviation starts the drift toward the nearest node. The drift time from loop to node is taken as

$$\Delta t = L \int_{0.495}^{0.005} d\xi/u_D \quad (10)$$

where the limits are somewhat arbitrarily selected because $u_D = 0$ at $\xi = 0$ and 0.5 . Values of U_D were computed for several values of ξ_1 (Fig. 3), and Δt then was determined numerically.

It is of interest to compare the results with those for standing sinusoidal waves of equal maximum velocity change. Such waves are purely hypothetical, since they would steepen immediately to form oscillating shock waves, but the comparison indicates the extent to which shock waves are more or less effective in driving particles toward the nodes. For a standing sine wave, one has

$$u = (\Delta u/2) \sin(\pi x/L) \sin \omega t \quad (11)$$

where $\omega = 2\pi f$. Substitution into Eq. (2) leads to

$$d^2\xi/d\theta^2 + d\xi/d\theta - (K/2) \sin \pi \xi \sin \omega \tau \theta = 0 \quad (12)$$

Marble⁴ solved this equation by a series expansion in terms of the small parameter $K/2$ and obtained the drift velocity at ξ as

$$u_D = - \frac{\Delta u^2}{16c} \frac{\omega \tau}{(1 + \omega^2 \tau^2)} \sin 2\pi \xi \quad (13)$$

Thus, the maximum drift velocity is obtained for $\omega \tau = 1$ and at $\xi = 0.25$, that is, at the center between loop and node. A more elaborate theory by Dukhin³ (see also ref. 1) accounts for forces resulting from the distortion of the flow field by the particle, but the results become identical to Marble's if $(2/3)[(\rho_p/\rho)/\omega \tau]^{1/2} \gg 1$, where ρ is the gas density. This condition is reasonably satisfied for the present study, since $\rho_p/\rho = 0(10^3)$ and $\omega \tau \approx 1$ in the range of main interest. Drift times for sinusoidal oscillations are obtained by substituting Eq. (13) into Eq. (10); integration then yields

$$\Delta t = 1.322c/fu_{Dmax} = 2.115 c^2/f\Delta u^2. \quad (14)$$

Results and Discussion

The following examples are based on particle relaxation times between 0.01 and 1.0 ms and frequencies of 0.5 and 1.0 kHz. The speed of sound is always taken as 347 m/s, and shock strengths are specified by velocity changes Δu between 10 and 40 m/s. As seen in the Appendix, the corresponding sound pressure levels range from somewhat below 160 dB to about 170 dB and are typical for acoustic agglomeration work. As the analysis in the preceding section shows, drift velocities do not depend on f and τ separately but only on the product $f\tau$. However, the frequency also enters explicitly into calculations of drift times.

Variations of the drift velocity between loop ($\xi = 0.5$) and node ($\xi = 0$) are shown in Fig. 3 for $u = 40$ m/s and for the six combinations of f and τ identified in the caption. Solid lines refer to oscillating shocks and broken lines to standing sinusoidal waves. Effects of varying f and τ are indicated separately to demonstrate the effect of those variables directly. In general, the shocks produce significantly larger drift velocities than sine waves -- three times as large in case (c) --, but the difference becomes smaller as f and τ increase. For the largest values of f and τ , the difference actually reverses, case (d). For sinusoidal waves, the maximum is always at the center between loop and node ($\xi = 0.25$), but for shock waves, it is increasingly shifted toward the node as f and τ decrease. This shift was a completely unexpected finding.

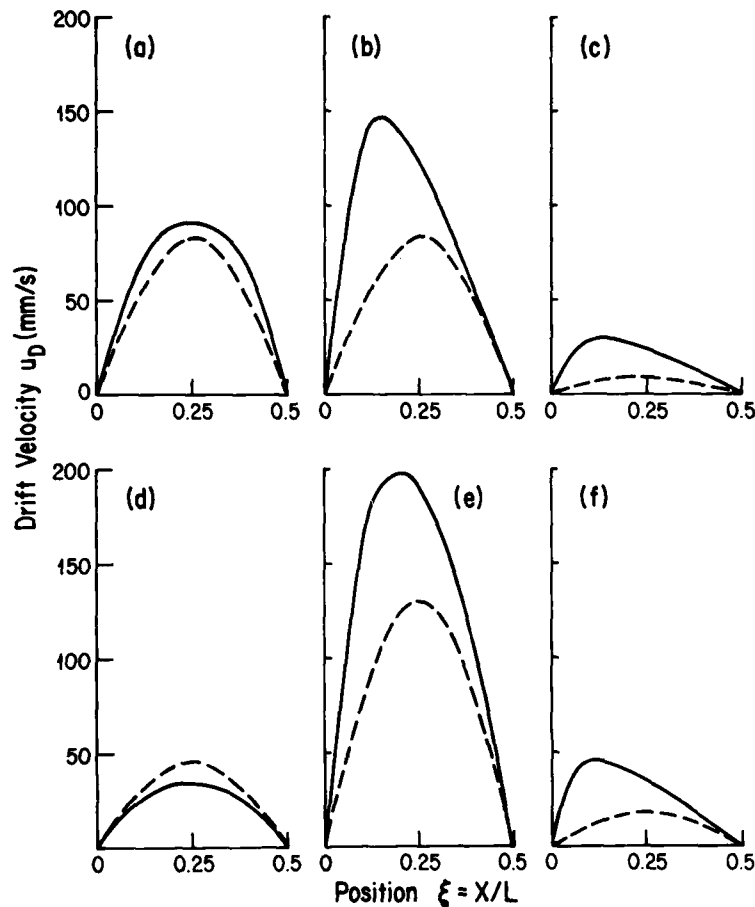


Fig. 3 Variation of drift velocity (taken as positive) for $\Delta u = 40$ m/s, for oscillating shocks (solid lines) and standing sine waves (broken lines).

f (kHz)	τ (m/s)		
	1.0	0.1	0.01
0.5	(a)	(b)	(c)
1.0	(d)	(e)	(f)

The marked increase of u_D at $\xi = 0.25$ with increasing shock strength is shown in Fig. 4. A scale for $\omega\tau$ is provided at the top of the figure. It shows that all maxima lie at $\omega\tau = 1$, as in the case of sinusoidal oscillations indicated by Eq. (16), although the analysis involves only f and not ω . For sinusoidal oscillations, Eq. (13) gives a simple relationship between $u_{Dc}/\Delta u^2$ at $\xi = 0.25$ and $\omega\tau$ or $f\tau$ which is shown in Fig. 5 as the solid curve. Data from Fig. 4 also are entered with different symbols identifying different values of Δu . These fall almost exactly on a single curve. The small residual scatter is believed to be a consequence of the increasing shift of the maximum of u_D at small values of $f\tau$. This figure again shows the much larger drift velocities produced by oscillating shocks except for high values of $f\tau$. The curves actually cross over at about $\omega\tau = 4$, but the reason for this behavior is not clear. If the solid curve is enlarged by a constant factor of 1.52 to match the shock data at their maximum, the broken

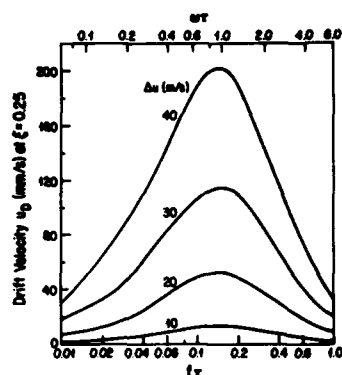


Fig. 4 Effect of shock strength (Δu) on drift velocity (taken as positive) at $\xi = 0.25$.

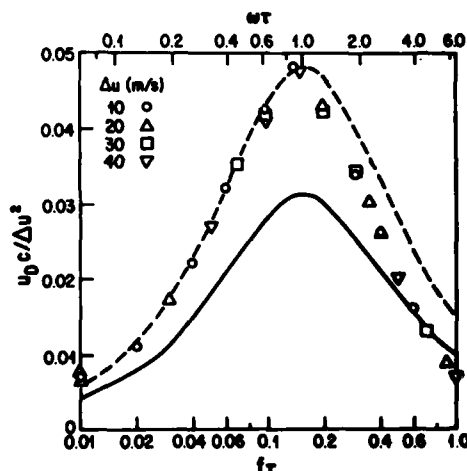


Fig. 5 Drift velocity parameter (taken as positive) at $\xi = 0.25$. Symbols refer to shock waves of various strength and solid line to standing sine waves; broken line represents solid line multiplied by 1.52 to match shock data at maximum.

line is obtained. It lies close to the data points for $\omega\tau < 1$ but is considerably higher for $\omega\tau > 1$.

The time required for a particle to drift from a point close to a loop ($\xi = 0.495$) to a point close to the nearest node ($\xi = 0.005$) is indicated in Table 1 for both oscillating shocks and standing sine waves for the six combinations of f and τ considered and for $\Delta u = 40$ m/s (about 170 dB). Also listed are the maximum values of the drift velocity from Fig. 3 and the diameters of NH_4Cl particles in air computed from τ . The values for $f = 0.5$ kHz thus correspond to the described experiments. It can be seen that computed travel times of several seconds are consistent with the observed particle sizes of several μm . A more quantitative agreement could not be expected because of the limited data available from the preliminary experiments.

In summary, it can be seen that oscillating shock waves produce drift velocities toward the nearest node that are almost exactly proportional to Δu^2 . These velocities are about 1.5 times larger than those produced by standing sound waves for $\omega\tau < 1$, but this ratio gradually decreases for larger values of $\omega\tau$ and falls below 1.0 at about $\omega\tau = 4$. The reason for this result is not clear at this time. Also, the unexpected shift of the maximum of u_d toward the node is not yet understood. These questions would require further investigation.

Table 1. Drift times for $\Delta u = 40$ m/s and $c = 347$ m/s

f(kHz)	τ (ms)	f τ	D_p (μ m)	u_{Dmax} (mm/s)		Δt (s)	
				Shocks	Sine Waves	Shocks	Sine Wave
1.0	1.0	1.0	14.7	33	45	13	10
	0.1	0.1	4.6	196	130	2.4	3.5
	0.01	0.01	1.5	45	18	11	25
0.5	1.0	0.5	14.7	92	83	9	11
	0.1	0.05	4.6	146	82	7	11
	0.01	0.05	1.5	30	9	32	101

Appendix: Relationship between dB notation and shock strength

In acoustics, it is customary to measure sound pressure levels in dB, which are defined as $9 \text{ dB} = 20 \log_{10} p_{rms} + 74$, where p_{rms} is the rms-value of the pressure amplitude in dyn/cm^2 . The change from maximum to minimum pressure is therefore given by $\Delta p = 2^{3/2} p_{rms}$ and represents also the pressure change across the corresponding shock wave. For a shock in atmospheric air ($p_{atm} \approx 10^6 \text{ dyn/cm}^2$), the pressure ratio is therefore $P = 1 + \Delta p/p_{atm}$. Thus, a pressure level in dB is readily converted to P and, with the aid of standard shock equations, also to the shock Mach number M_S and relative velocity change $\Delta u/c$. The following table lists a few examples and values for Δu for $c = 347$ m/s.

Table 2. Measures of shock strength

dB	P	M_S	$\Delta u/c$	Δu (m/s)
160	1.056	1.024	0.040	13.9
165	1.100	1.042	0.068	23.6
170	1.178	1.074	0.120	41.6
175	1.316	1.127	0.200	69.4

References

1. E.P. Mednikov, Acoustic Coagulation and Precipitation of Aerosols. Transl. from the Russian by C.V. Larrick, Consultants Bureau, New York, 1965.
2. D.T. Shaw, Recent Developments in Aerosol Science. Wiley-Interscience Publ. New York, Chapter 13, pp. 279-319, 1978.
3. S.S. Dukhin, Theory of drift of an aerosol particle in a standing acoustic wave. Kolloid Journal, 22, 133-135, 1960 (transl. from Kolloidny Zhurnal).
4. F.E. Marble (unpublished), included in M. Gerstein, Final technical report on combustion instability. Rept. No. SN1800, 1965, Dynamic Science Corp., Monrovia, California 91016. (AD623847)
5. K.H. Chou, P.S. Lee and D.T. Shaw, Application of acoustic agglomeration to hot gas cleanup in pressurized fluidized-bed combustors. AIAA Paper No. 81-0394, 1980.
6. S. Temkin, Droplet agglomeration induced by weak shock waves. Physics of Fluids, 13, 1639-1641, 1970.
7. G. Rudinger, Fundamentals of Gas-Particle Flow. Handbook of Powder Technology (J.C. Williams and T. Allen, editors), Vol. 2, Elsevier Scientific Publishing Co., Amsterdam, 1980.

8. S. Temkin, Propagating and standing sound waves. Journal of the Acoustical Society of America, 45, 224-227, 1969.
9. P.M. Morse, Vibration and Sound, McGraw-Hill Book Co., New York, 1948, p. 226.

Acknowledgements

The authors wish to thank U.P. Wen and T. Osman for their assistance by programming the computer and obtaining the numerical data.

AD P000292

SHOCK TUBE MEASUREMENTS OF IR RADIATION
IN HOT GAS/PARTICLE MIXTURES*

V. S. Calia, W. Konopka, R. A. Reed and R. A. Oman

Grumman Aerospace Corporation

Bethpage, New York 11714

A shock tube technique has been employed to establish a broad data base for the validation of computer codes that predict IR radiation in high temperature aerosols. Accurate control of particle and gas temperatures and concentrations across a wide range of conditions is provided in the reflected shock zone of a shock tube. Particles up to 10 μ m diameter equilibrate within a small fraction of available test time, making parameter control independent of thermal lag predictions. Optical thicknesses for either gas or particle components can be provided as high as 4. Temperature calculations supported by measurements indicate that the equilibrium aerosol temperature can be predicted to within $\pm 5\%$ in the temperature range 1000 to 2000 K if the particle loading is restricted to roughly 20% by mass. Independent measurements of particle concentration by multi-spectral extinction and laser Doppler velocimetry demonstrate that the particle cloud is uniform in space and time and that agglomeration is negligible. Examples of data are presented for C, Al_2O_3 and melted Al_2O_3 particles at various optical depths, in transparent and IR active gases, under conditions of multiple scattering. The results provide new determinations of optical properties at high temperature and a well-controlled data set for the investigation of two-phase radiation transport and heterogeneous combustion processes.

INTRODUCTION

This work is motivated by the need for improved radiative transport diagnostics of thermophysical properties in gas-particle flows and heterogeneous combustion processes.

* Work was supported by AFRPL under contract FO4611-79-C-0017.

While significant progress has been made in the understanding of radiation transport in hot gas systems, predictive tools and diagnostic techniques for two-phase gas-particle systems are less well developed¹. Two-phase systems present an impressive array of problems including particle formation processes and size distributions, coupled gas-particle emission, absorption, and scattering, and, in some cases, non-equilibrium between gas and particle temperatures and velocities^{1,2}. The development of computer codes to handle this combination of problems requires well characterized data sets to test their ability to treat simultaneously the spectral details of multiple scattering and emission/absorption by the gas and particles. Of fundamental importance in such validation is the ability to determine all of the experimental parameters, with special emphasis on the accurate determination of gas and particle temperature. The sensitivity of prediction/validation to temperature errors is essentially the same as the sensitivity of the Planck function which in the mid-IR (2 - 5 μm) goes like T^{-3} for $T \sim 1500$ K. Analysis shows that the sensitivity of two-phase radiance to particle concentration, size, and scattering phase function is slower than linear for simple cylindrical geometries.

There are two fundamental aspects of two-phase radiative transport codes that must be verified: particle optical properties and two-phase radiative transport models. The need for experimental particle measurements arises from uncertainties in the temperature variation of particle optical properties, from the nonspherical shape of many aerosol particles, and from possible differences in optical properties between the bulk and powdered samples. The need for two phase radiative transfer measurements arises from entirely new band modeling methods required for two-phase flows with multiple scattering³. These fundamental code modules require investigation over a full range of optical depths (dimensionless length measured in photon mean free paths) from thin to thick. In the optically thin limit only single scattering occurs, and the experiments in this regime are important for the verification of particle emission/scattering laws. In the optically thick limit the multiple scattering gas/particle interactions depend only upon the local properties of the medium, and experiments in this regime test the validity of multiple scattering models independent of geometric effects. In the regime of intermediate optical depth, the multiple scattering gas/particle interaction depends both on the properties of the medium and the large scale spatial structure of the test media. Experiments in this most important regime test realistic multiple scattering problems in geometrically complex flow fields.

To obtain the needed data base an extensive experimental program was carried out at Grumman in the reflected zone of a conventional shock tube. The advantage of this approach is the high degree of control afforded over such test conditions as flow geometry, particle size and type, gas composition, tracer constituents, and aerosol temperature. Quantitative accuracy criteria for experiment control were selected based on a desired net predictive accuracy goal of 30% in aerosol radiance. To meet this specification and to ensure gas/particle equilibrium conditions in the test aerosol the particle mass fraction and nominal diameter were restricted to .20 and 10 μm , respectively.

The specific test conditions for our experiments were chosen to maximize the impact of selected two-phase transport effects and do not necessarily pertain to the operational characteristics of actual combustor systems. Test aerosols investigated employed 1, 3, and 9 μm diameter Al_2O_3 particles as representative of purely scattering type particles and 0.4 μm diameter C and 3 μm diameter ZrC emissive particles in various combinations of inert and IR-active gases, in the temperature range from 1200 to 3000 K. The concentrations of particles and gases were varied independently to cover a wide range of optical thickness and scattering/extinction ratios. CO and CO_2 test gases were used to test differing two-phase emission models for diatomic and polyatomic molecules, respectively.

The following sections of this paper first briefly describe the experimental technique and then give selected results.

AEROSOL GENERATION

The code validation experiments were carried out in the reflected zone of a conventional shock tube. Particles were introduced into the test gas by entrainment in the gas flow behind the incident shock wave. To illustrate the introduction method a schematic wave-particle diagram is shown in Fig. 1. Prior to the test, the particles are distributed on a mid-plane plate located near the driven section end wall (roughly 5 shock tube diameters away). When the incident shock wave passes the particle pile the particles are continuously entrained in the post-shock flow and rapidly spread across the shock tube. Subsequent interaction with the turbulent, stagnant gas behind the reflected shock further distributes the particles to form the test medium. This same technique has been successfully employed by Seeker et al.⁴ in coal ignition studies.

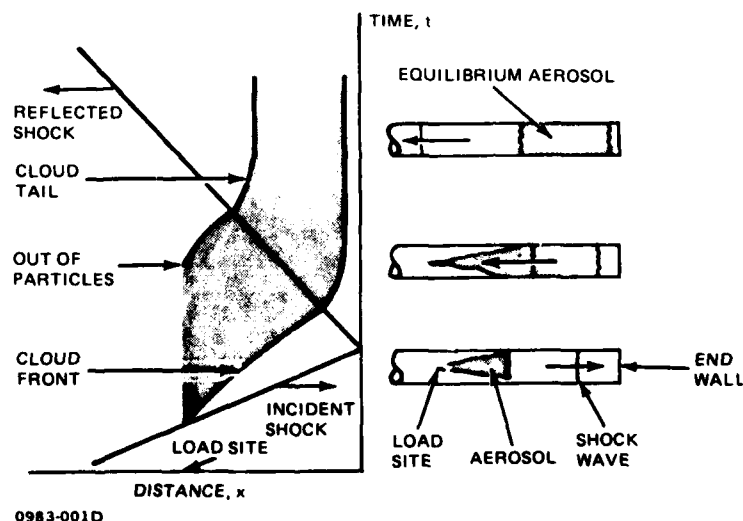


Figure 1. Illustration of Spatial and Temporal Development of an Aerosol Cloud in a Shock Tube. Behind the incident shock the particles spread with roughly 20° total included angle (measured from glow photographs). Mean velocity turbulence levels behind the incident shock (10 to 15 m/sec, LDV) and in the stagnation zone (20 to 30 m/sec, LDV) help to produce the uniform test medium.

The success of this approach is due to a combination of factors:

1. Operation in the reflected zone of the shock tube produces an equilibrium aerosol in which two-phase radiative transport is decoupled from particle/gas fluid dynamic interactions.
2. For particle diameters below $10\text{ }\mu\text{m}$ analysis⁵ and experiment show that thermal relaxation times are sufficiently short to permit pulsed ($\sim 2\text{ ms}$) shock tube experiments with complete assurance of thermal equilibrium, permitting accurate prediction of gas/particle temperature.
3. The simple particle loading method produces well mixed, uniform aerosols at least two tube diameters in length so that cloud edge effects on the measured radiation are minimized.
4. The generated aerosols are relatively free of particle agglomerates; agglomerates are undesirable because they behave like particles with unpredictable size distribution.
5. Gas and particle concentrations and temperature in the test aerosol can be independently varied over wide ranges with tight control over all aerosol properties.

The test aerosol is uniform in space and time as demonstrated by laser Doppler and multi-wavelength extinction measurements of the particle concentration at a variety of longitudinal and radial positions within the cloud. These data (Table 1, Figs. 2 & 3) are internally consistent and show the aerosol to be uniform for a minimum of two shock tube diameters. The aerosol cloud is also relatively free of agglomerates. Agglomeration can be detected by enhanced laser extinction at long wavelengths where agglomerates have substantially larger optical cross sections than single particles. Comparisons of LDV particle counts with extinction data at 0.26, 0.63, 3.39, and $10.6\text{ }\mu\text{m}$ showed no large or systematic differences.

TABLE 1. COMPARISON OF EXTINCTION AND LDV PARTICLE NUMBER DENSITY MEASUREMENTS IN Al_2O_3 AEROSOLS.

Test Condition	Method	Measurement Station, cm	Particle Density, $10^5/\text{cm}^3$
MACH NO. = 1.8 N_2 CARRIER GAS $3\text{ }\mu\text{m}$ DIA Al_2O_3	LDV	29	7.1
	$3.4\text{ }\mu\text{m}$ EXTINCTION	41	6.4
	$3.4\text{ }\mu\text{m}$ EXTINCTION	25	6.6
	$10.6\text{ }\mu\text{m}$ EXTINCTION	25	7.6
MACH NO. = 2.35 Ar CARRIER GAS $3\text{ }\mu\text{m}$ DIA Al_2O_3	$3.4\text{ }\mu\text{m}$ EXTINCTION	25	2.4
	$.63\text{ }\mu\text{m}$ EXTINCTION	29	3.0

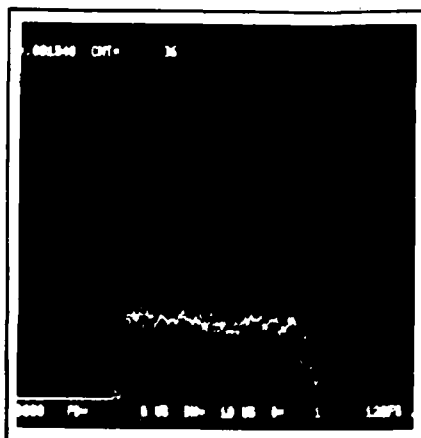
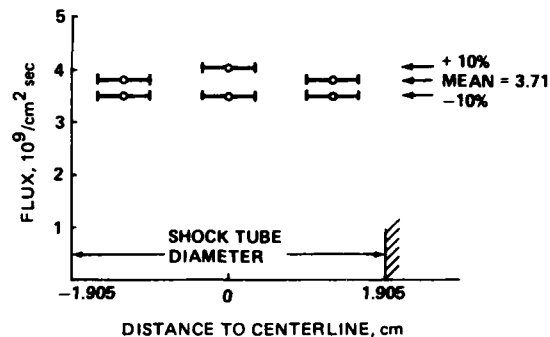


Figure 2. LDV Particle Flux vs Time in $\text{Al}_2\text{O}_3/\text{N}_2$ Aerosol. Temporal uniformity of the aerosol is demonstrated by a constant particle flux ($1.2 \times 10^9/\text{cm}^2/\text{s}$) over the 2 ms steady flow time; sample time is 10 μs .



0983-003D

Figure 3. Radial Survey of LDV Particle Flux in $\text{Al}_2\text{O}_3/\text{N}_2$ Aerosol. Spatial uniformity of the test aerosol is shown by the insensitivity of the flux level to radial position. Each point represents a separate run. Mean flux level corresponds to 1.03×10^6 particles/ cm^3 .

The particle concentration in the test aerosol is varied for a given particle type and incident shock strength by simply adjusting the initial gas pressure in the shock tube, ie, it was empirically determined in this work that particle concentration is nominally a linear function of the ratio of gas density behind the incident shock to particle diameter. This functionality holds even when the local gas Mach number is slightly supersonic if the initial gas density is adjusted for the anticipated jump conditions.

Analysis⁵ and measurements of the temporal variation of radiation (see Fig. 4) indicate that the particles equilibrate with gas conditions in less than 1 ms if the particles (Al_2O_3 , ZrC , & C) are restricted to a maximum diameter of about 10 μm . The equilibrium temperature can be predicted to sufficient accuracy ($\pm 5\%$) from the one dimensional shock tube equations using the usual measurements of incident shock wave speed and measurements of the particle concentration and nominal size to estimate particle loading. For low mass loading ($\leq 3\%$) the pure gas predictions provide the desired accuracy, a fact that has been employed by many investigators^{6,7,8} of two-phase phenomena in shock tubes. With increased mass loading the loss of heat from gas to particles and, for our continuous entrainment process, variable particle residence time behind the incidence shock, must be accounted for. A small region of the cloud near the load site will be in nonequilibrium (the extent of the nonequilibrium region depends on heating rates and particle type and size). Comparisons of detailed one-dimensional calculations⁹ (as well as much simpler steady flow analysis in shock-fixed coordinates) with temperature measurements indicate that the desired accuracy can be achieved if the particle to gas mass concentration is restricted to about 20% in the temperature range 1000-2000 K, Fig. 4. Spurious waves generated from the particle load plates and the windows are a major concern in the experiments. Calibration runs using SO_2 tracer gas and UV thermometry were employed to ensure that our test conditions were not influenced by such interactions.

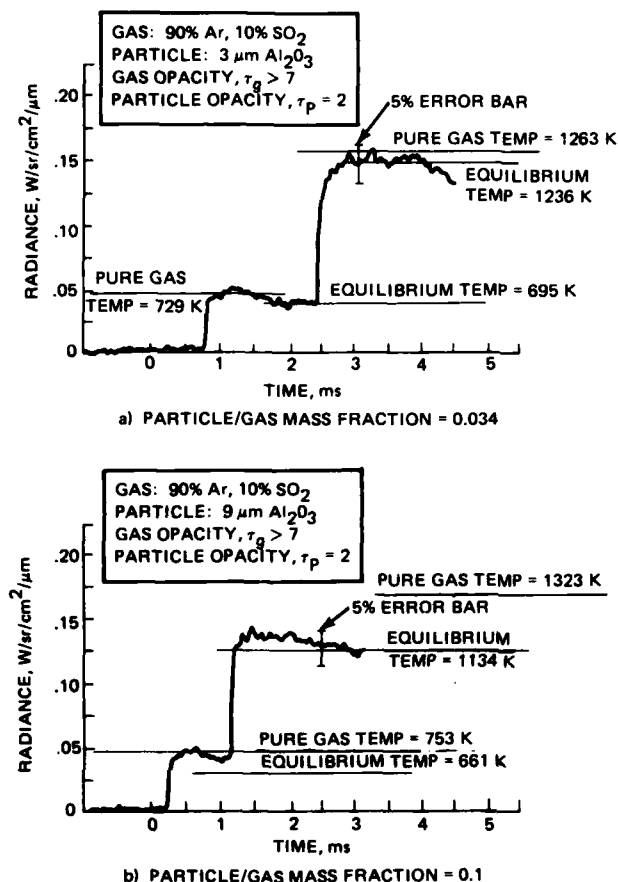


Figure 4. Aerosol Temperature Inferred from IR Radiance Measurements. Aerosol temperature was monitored from IR radiance measurements at 7.3 μm, where the ν_3 SO₂ fundamental and the LWIR absorption of Al₂O₃ combine to make the aerosol nearly black (emissivity > 0.95). The error bars indicate the spread in radiance associated with a 5% temperature error.

SAMPLE RESULTS

The previous section of this paper discussed the generation and characterization of uniform high temperature aerosols at equilibrium in the stagnation zone of a conventional shock tube. The controlled uniform flow aerosols can be used directly to test radiative transport exclusive of flow effects, or as a source for flows to test coupled two-phase flow and radiative effects. The experimental work to date has been concerned with the first of these two alternatives. Tests have been configured for code validation of multiply scattering media and for particle optical properties. Radiation measurements have been made on both an in-band and on a line-resolved basis using a variety of photometers and spectrometers. In the following sample results are presented.

Optical radiation diagnostics of carbon and soot aerosols are important for the design and understanding of a wide variety of coal and hydrocarbon fueled combustors. The specification of particle size distributions and soot/carbon optical properties remains a major practical consideration for such systems, so that it is generally not possible to identify with precision the role of two-phase multiple scattering from measurements on actual systems. Shock tube experiments with particles of controlled size distribution and chemical composition provide tests at a reduced level of complexity which display these effects more clearly.

Figure 5 shows the spectral emissivity of $0.4 \mu\text{m}$ diameter amorphous carbon particle clouds as a function of optical depth τ . The emissivity approaches an asymptotic limit for large τ substantially below the value of unity for a pure absorber, and the emission is non-gray. These are consequences of multiple scattering and depend upon both particle optical properties and medium geometry. Reference to the work of Bauer and Carlson¹⁰ indicates that the role of geometry is significant in our experiments, so that this data will provide useful tests of prediction techniques for complex combustor geometries. We note that our data contradicts MacGregor's¹¹ conjecture of a long wavelength cutoff in the emission spectrum of small particles ($\lambda(\text{cutoff}) = \sqrt{2}\pi d_p$, d_p = particle diameter) which for our nominal $0.4 \mu\text{m}$ carbon corresponds to $1.8 \mu\text{m}$.

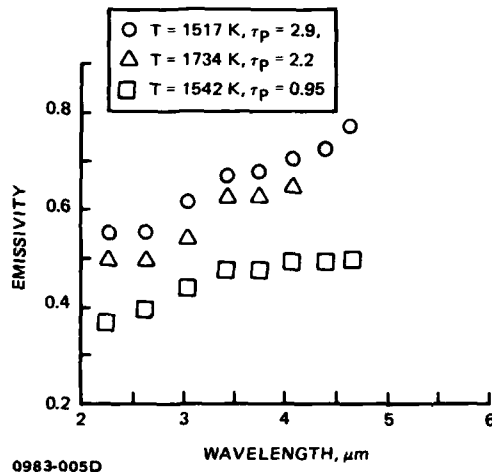


Figure 5. Spectral Emissivity of a Carbon Aerosol.

The spectral emissivity of $0.4 \mu\text{m}$ diameter amorphous carbon is non-gray in the mid-IR. The absolute values of cloud emissivities indicate that the particles have significant scattering cross section and cannot be described using a pure absorption model. The carrier gas is Ar and τ_p is the particle optical depth.

Radiant heat transfer analysis in two-phase media requires a knowledge of the hemispherical emissivity. Our measurements in Al_2O_3 aerosols with CO_2 and CO as IR-active gases indicate that specification of this quantity requires appropriate two-phase analysis under certain conditions. In particular, the presence of scattering particles in an emitting medium acts to reduce the medium emissivity $\epsilon(\theta)$ for small angles θ ($\theta = 90^\circ$ for the perpendicular). This behavior is well known in the analysis of plane parallel atmospheres (limb darkening) and is related to the increased reflectivity of certain solid surfaces near grazing incidence. Fig. 6 shows the angle dependent emissivity of a $\text{CO}_2/\text{Al}_2\text{O}_3$ aerosol, normalized by the value expected from the CO_2 alone without scattering. The emissivity vs θ curve exhibits a characteristic knee near 30° , related to the width of the particle forward scattering lobe, below which two-phase effects cause an appreciable reduction in emissivity. These data will test the ability of new two-phase band models to properly describe multiple scattering in three-dimensional geometries.

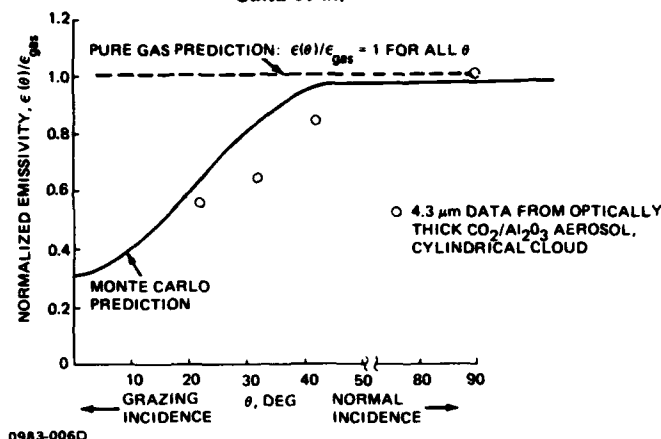


Figure 6. Angle Dependence of Aerosol Cloud Emissivity. The addition of scattering Al_2O_3 particles to CO_2 in controlled aerosols tests the ability of alternate two-phase techniques to accurately predict the observed reduction in $\epsilon(\theta)$.

Measurements of melted Al_2O_3 illustrate the use of the shock tube aerosol technique to determine particle optical properties. Prior measurements of this material above and below the melt point (2320 K) yielded contradictory results. In particular, Mularz and Yuen¹² disputed the discontinuous jump in particle emissivity associated with the solid to liquid phase change reported by Carlson¹³ and by Gryvnak and Burch¹⁴. Our own measurements (Fig. 7) exhibit a discontinuity at the melt point, with the mid-IR emissivity of the liquid phase at least one order of magnitude greater than for the solid phase. We attribute the observations of Mularz and Yuen¹² to thermal lag between the gas and particles. In particular, examination of their emission versus temperature data reveals a characteristic plateau region near the melt point which we attribute to temperature arrest of particles undergoing solidification ($\Delta H/C \sim 900\text{K}$). The present measurements are the first mid infrared data for this material, and a complete analysis will be published elsewhere. Preliminary analysis of particle emission cross sections from our data, shown in Fig. 7, indicates a temperature-independent particle emissivity near 0.5 between 2500 - 3000 K. This observation also suggests the possible use of Al_2O_3 as a fiducial temperature indicator in high temperature flows, analogous to the use of thermal phase change paints.

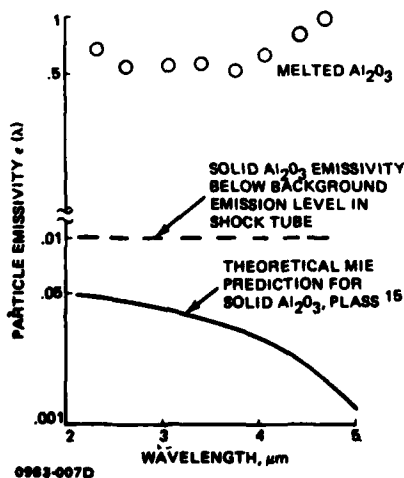


Figure 7. Emissivity of Melted Al_2O_3 . The mid-IR emissivity of a form Al_2O_3 jumps discontinuously at the melt point (2320 K) to a high temperature independent value near 0.5 between the melt point and 3000 K.

CONCLUSIONS

The shock tube aerosol generation technique employed provides a unique means of systematically studying complex two-phase radiative transfer effects with tight control over aerosol properties. Tests are conducted with a known particle size and type and controlled gas composition and flow geometry, leading to considerable simplification in experiment design. Particles equilibrate rapidly with the shock heated gas well within the available test time and produce a well defined temporally and spatially uniform aerosol free from agglomerates. Initial application of this technique has produced a comprehensive validation data base to aid in development of new two-phase radiative transport codes and new data on the optical properties of melted Al_2O_3 particles.

REFERENCES

1. McGregor, W., Presented at 17th Aerospace Sciences Meeting, Paper No. 79-0084, New Orleans, LA, January 15-17, 1979.
2. Viskanta, R., Advances in Heat Transfer VIII, Academic Press, N.Y. 1964.
3. Malkmus, W., Photon Research Associates, to be published in J. Quant. Spectrosc. Radiat. Transfer.
4. Seeker, W. R., Wegener, T., Lester, W., and Merklin, J.F., Proc. 17th Int'l Symp. Combustion, p 155, 1979.
5. Oman, R. A., Konopka, W., and Calia, V.S., Proc. of 2nd Multiphase Flow and Heat Trans Workshop, Miami Beach, Florida, April 1979; also Grumman Research Department Memorandum RM-686J, April 1979.
6. Lowenstein, A.I., and C. W. Von Rosenberg, Jr., Proc. of 11th Int'l Symp. on Shock Tubes & Waves, p. 366, 1977.
7. Nettleton, M.A., and Stirling, R., Proc. Roy. Soc. A300, p. 62, 1967.
8. Nicholls, R.W., Parkinson, W.H., and Reeves, E.M., Appl. Optics, Vol. 2, No. 9, p. 919, 1963.
9. Marconi, F., Rudman, S., and Calia, V.S., Presented at AIAA 13th Fluid & Plasma Dynamics Conference, Paper No. AIAA-80-1448, July 14-16, 1980, Snowmass, Colorado; to be published in AIAA Journal.
10. Bauer, E. and Carlson, D.J. J. Quant. Spectrosc. Radiat. Transfer, 4, p. 363, 1974.
11. McGregor, W., J. Quant. Spectrosc. Radiat. Transfer, 19, p. 659, 1978.
12. Mularz, E.J. and Yuen, M.C., J. Quant. Spectrosc. Radiat. Transfer 12, p. 1553, 1972.
13. Carlson, D.J., Proc. 10th Int'l Symp. Combustion, p. 1413, 1965.
14. Gryvnak, D.A. and Burch, D.E., J. Optical Soc. Am., 55, p. 625, 1965.
15. Plass, G. N. Applied Optics 4, p. 1616, 1965.

AD P00293

STUDY OF BINARY NUCLEATION IN A LUDWIEG TUBE

R.A. Zahoransky and S.L.K. Wittig

Lehrstuhl und Institut für Thermische Strömungsmaschinen

Universität Karlsruhe, D-7500 Karlsruhe 1, West Germany

In extending earlier studies, the nucleation of ethanol-water mixtures is analyzed using Ludwig tube flow in combination with a differential interferometer and high speed photographic diagnostics. Excellent agreement with calculations employing binary nucleation theory is obtained for alcohol-rich mixtures whereas for high water concentrations differences between experiment and theory are observed. This is attributed to the characteristic change of the surface tension. The importance of the expansion rate is demonstrated.

INTRODUCTION

As discussed in a previous paper¹, interest has grown in recent years in the utilization of binary mixtures as working fluids in Clausius-Rankine cycles at relatively low upper temperature levels^{2,3}. Solar systems and waste heat recovery may be mentioned as typical examples. In general, the fluid is expanded within the turbine across the saturation line to achieve high efficiencies and large enthalpy differences. It is well known, that after crossing the dew point in a fast turbine expansion process the thermodynamic equilibrium is not obtained. After reaching a certain state of supersaturation the metastable state of the vapor collapses in a sudden homogeneous nucleation. Markable effects due to the sudden phase change and droplet formation on efficiency performance and reliability of the low pressure end stages of the turbine are observed⁴.

With exception of a small number of original experiments⁵, no information is available on binary nucleation over the whole range of mixture concentration at high cooling rates as experienced in turbomachinery and other technical applications.

Another motivation concerns questions regarding homogeneous binary nucleation in meteorological processes. Using binary nucleation theory, it has been shown that certain pollutants in the atmosphere such as sulfuric acid may trigger vapor condensation even if the water vapor would be superheated in its isolated state⁶.

In extending our earlier measurements¹ within the expansion fan of a shock tube, the present study incorporates the short duration flow of a Ludwig tube. Ethanol/water-mixtures were of primary interest because water-alcohol systems seem to be of predominant technical importance and water-ethanol permits a first access to a comparison between theory and experiments as their basic thermal data are available in the temperature range of interest.

THEORY

The generally accepted theory of homogeneous binary nucleation was developed by Neumann and Döring⁷ and extended by Reiss⁸ and is based on the classical nucleation theory. The basic equation derived for the binary nucleation rate is in analogy to the unary condensation:

$$I = C \exp(-\Delta G^*/(kT)) \quad (1)$$

with

ΔG^* the critical free energy for isothermal nucleus formation from the vapor phase
 k the Boltzmann constant
 T the temperature
 C the frequency factor

For the isothermal difference of Gibbs' free energy it is found:

$$\Delta G = n_1(\mu_{1l} - \mu_{1g}) + n_2(\mu_{2l} - \mu_{2g}) + 4\pi r^2 \sigma + (4/3)\pi r^3(p - p_\infty) \quad (2)$$

with

μ_{1l}, μ_{2l} molecular chemical potential in the liquid phase, component 1, 2
 μ_{1g}, μ_{2g} molecular chemical potential in the gas phase
 n_1, n_2 number of molecules in the nucleus
 r nucleus radius
 σ surface tension
 p total vapor pressure
 p_∞ saturation pressure of the mixture at cluster composition

The last term in Eq.(2) is considerably smaller compared to the other portions and will be neglected in the following considerations. In plotting ΔG as a function of n_1 and n_2 it can be shown that in general a saddle point is obtained as illustrated in Fig.1. The direction of the main condensation process, therefore, is predetermined. The relevant critical parameters n_1^* and n_2^* can be derived from the saddle point conditions:

$$\left. \frac{\partial \Delta G}{\partial n_1} \right|_{n_2} = \left. \frac{\partial \Delta G}{\partial n_2} \right|_{n_1} = 0 \quad (3), (4)$$

with the requirement $\left(\frac{\partial^2 \Delta G}{\partial n_1 \partial n_2} \right)^2 - \frac{\partial^2 \Delta G}{\partial n_1^2} \frac{\partial^2 \Delta G}{\partial n_2^2} > 0 \quad (5)$

The preexponential factor can be calculated following Reiss⁸

$$C = \frac{\beta_1 \beta_2}{\beta_1 \sin^2 \phi + \beta_2 \cos^2 \phi} (N_1 + N_2) S Z \quad (6)$$

with

$$\beta_i = \frac{P_i}{\sqrt{2\pi m_i kT}} ; \quad i = 1, 2 \quad \text{collision rate} \quad (7)$$

p_i partial pressure in the vapor phase
 m_i molecular weight
 N_i molecular concentration in the vapor phase

$S = 4\pi r^2$ surface area of the cluster at the saddle point (8)

$Z = \sqrt{-P/Q}$ Zeldovich factor (9)

$$P = \frac{\partial^2 \Delta G}{\partial n_1^2} \cos^2 \phi + 2 \frac{\partial^2 \Delta G}{\partial n_1 \partial n_2} \cos \phi \sin \phi + \frac{\partial^2 \Delta G}{\partial n_2^2} \sin^2 \phi \quad (10)$$

$$Q = \frac{\partial^2 \Delta G}{\partial n_1^2} \sin^2 \phi - 2 \frac{\partial^2 \Delta G}{\partial n_1 \partial n_2} \cos \phi \sin \phi + \frac{\partial^2 \Delta G}{\partial n_2^2} \cos^2 \phi \quad (11)$$

ϕ is the angle between the n_1 -ordinate and the projected direction of the main condensation path across the saddle point. It can be calculated according to

$$\operatorname{tg}^2 \phi + (R d_B - d_A) \operatorname{tg} \phi - R = 0 \quad (12)$$

where R is the correction factor proposed by Stauffer⁹

$$R = \beta_2 / \beta_1 \quad (13)$$

$$d_A = - \frac{\partial^2 \Delta G}{\partial n_1^2} / \frac{\partial^2 \Delta G}{\partial n_1 \partial n_2} ; \quad d_B = - \frac{\partial^2 \Delta G}{\partial n_2^2} / \frac{\partial^2 \Delta G}{\partial n_1 \partial n_2} \quad (14), (15)$$

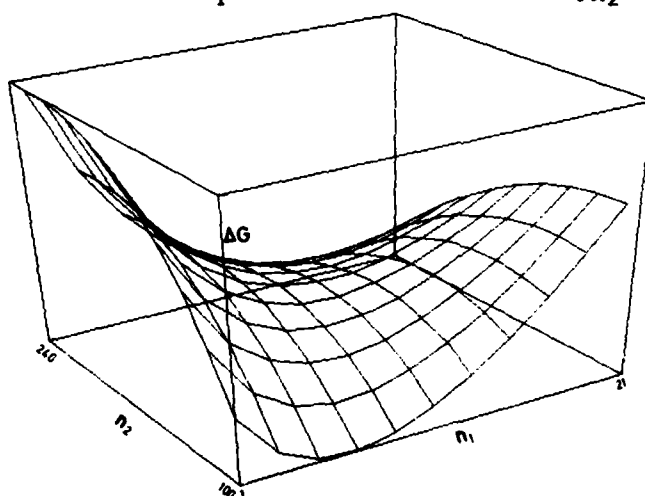


Fig.1 Free energy ΔG for cluster formation from the vapor phase

$T = 293.15 \text{ K}$

$I = 10^6 \text{ m}^{-3} \text{ s}^{-1}$

$a_1 = 0.20, a_2 = 1.91$

Critical values
(saddle point):

$n_1^* = 11, n_2^* = 168$

Water/ethanol mixture

Ideal gases were assumed which is of sufficient accuracy for the present study with relatively low normalized pressures. The surface tension and the density of the liquid phase were obtained by polynomial approximation with respect to the mole fraction of the alcohol and the temperature. The phase equilibrium in the temperature range of interest was approximated by the NRTL equation with 6 coefficients¹⁰.

EXPERIMENTAL

The expansion of the superheated vapor into the two phase region was accomplished in a Laval nozzle of a Ludwig tube. By proper choice of the initial state within the driver it was possible to position the onset of nucleation during the first stationary flow cycle within the supersonic section of the Laval nozzle. The flow field upstream, therefore, is not affected and unsteady effects are eliminated if the conditions of the local critical heat addition are considered. This, to our experience,

seems to be the main advantage in comparison to nucleation studies in the unsteady expansion fan of the driver section of a shock tube¹.

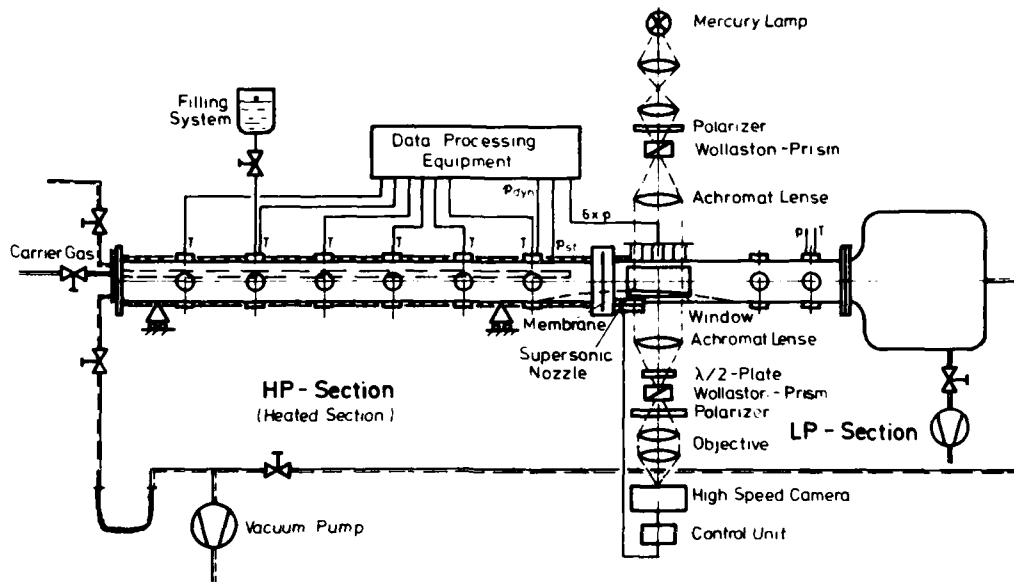


Fig.2 Schematic of Ludwig tube

Fig.2 illustrates the schematic of the experimental setup. In principle it is derived from our earlier expansion tube¹. The binary mixture to be studied is prevaporized and superheated within the driver itself. To guarantee an almost isothermal nucleation process as required by the classical nucleation theory as described by Eq.(2), the vapor is diluted by a noncondensable carrier gas such as nitrogen. To secure a perfect mixing of the carrier gas and the vapor, the inert gas is added by a concentric perforated distribution tube with the length of the driver section.

The convergent section of the nozzle begins slightly upstream of the diaphragm and the throat of the nozzle is located closely to the membrane. Quartz windows are used in the supersonic domain of the nozzle within the driven section for the optical measurements. The onset of condensation characterized by heat addition and a change of the density can be detected by a differential interferometer. A high speed camera is used to record the fringe shift. The pressure distribution within the divergent part of the nozzle is monitored by three piezoelectric pressure transducers. In a sequence of preliminary experiments using noncondensable gases it was possible to determine the nozzle's effective cross-section. Variations of the total pressure throughout the steady flow cycles can be neglected as the driver length to its diameter ratio was chosen to be about fifty as suggested by Ludwig¹¹. The static pressure recorded during the steady flow, therefore, was constant.

MEASUREMENTS AND ANALYSIS

Because of the relatively small diameter of the achromatic lenses of the differential interferometer, it was impossible to

view the whole divergent section of the nozzle. It, therefore, was necessary to preestimate the onset of nucleation. These initial experiments were performed in utilizing the expansion fan in the high pressure section of a conventional heated shock tube, thus saving large amounts of high speed film material. As mentioned, the setup of the tube and the measurement procedure were described in our earlier paper¹. The high cooling rates as required in modeling steam turbine flow, however, were only achieved in the nozzle experiments. The initial states of the expansion were set such that the phase change was obtained in the temperature range of 263 K to 293 K, the range of interest in low temperature steam turbine application. As indicated, all property values of the H_2O/C_2H_5OH mixture over the whole range of mixture composition are available in this temperature interval.

The p, T diagram of Fig.3 shows a comprehensive comparison of our preliminary calibration experiments with pure water vapor in the Ludwig tube with our own shock tube results as well as with those by other groups at higher pressures and temperatures. The good agreement supports the assumption that the results obtained from the Ludwig tube for binary mixtures are quite accurate and of good reproducibility.

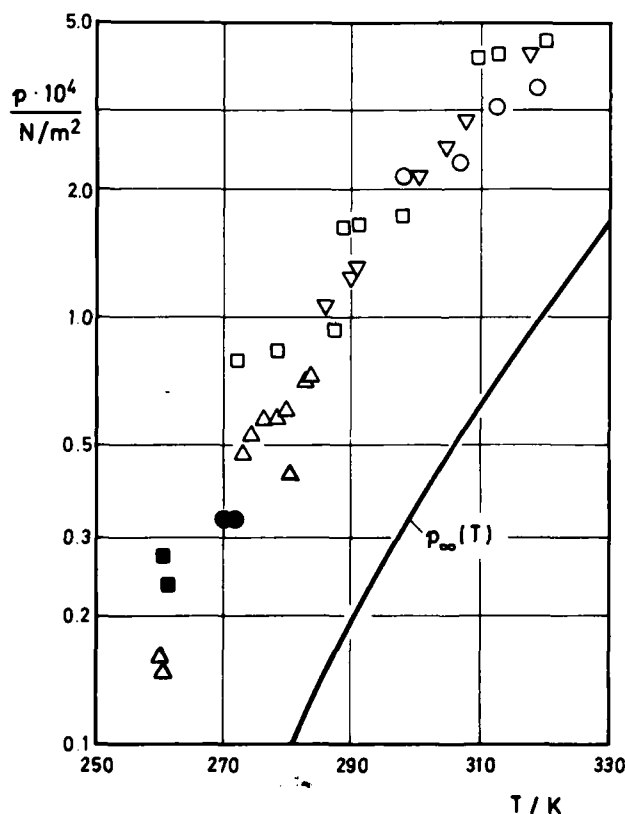


Fig.3 State of homogeneous nucleation of pure water vapor

○ Wittig et al.¹

□ Gyarmathy and Meyer¹⁶

▽ Barschdorff¹⁷

△ Barschdorff¹⁸

Present study:

● Shock tube experiments

■ Ludwig tube experiments

An interferogram of the supersonic flow with condensation for a water/ethanol mixture is shown in Fig.4. Due to the sudden heat addition the fringe shift is induced. Thus, the state at onset of condensation can be easily determined from the gasdynamic relations of the nozzle flow. The particular characteristics of

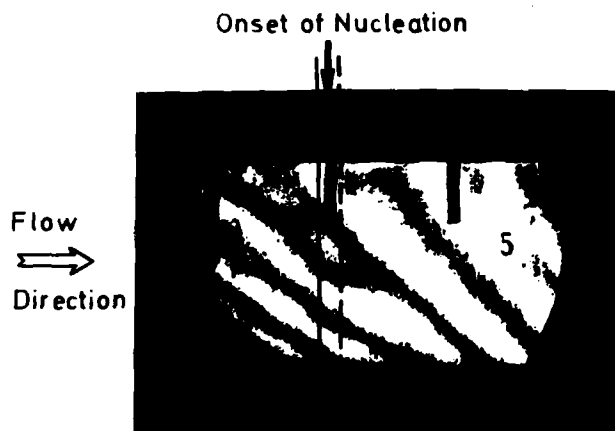


Fig.4 Interferogram of the supersonic flow field with binary nucleation taken with the high speed camera at 1500 frames/s.

the differential interferometer image was taken into account in the analysis of the interferograms.

In Fig.5 all experimental results - it is the state of nucleation within the a_1, a_2 plane - are plotted. Here a_1, a_2 are the activities of water and alcohol which are defined as the ratio of the partial vapor pressure to the saturation pressure of the pure fluids. The full lines represent the theoretical results at -10°C , 0°C and 20°C respectively for a nucleation rate of 10^{15} or $10^{10} \text{ cm}^{-3}\text{s}^{-1}$. The last rate was derived from shock tube experiments; for nozzle flow with considerably higher cooling rates, rates up to 10^{15} are to be expected. In comparing Fig.5 and 6 of the experimentally determined onset of condensation - these are the experiments in the cloud chamber, in the expansion tube and in the Ludwig tube of this study - a shift of the critical activities to higher values with increasing cooling rates is observed. The experimental values with pure alcohol vapor

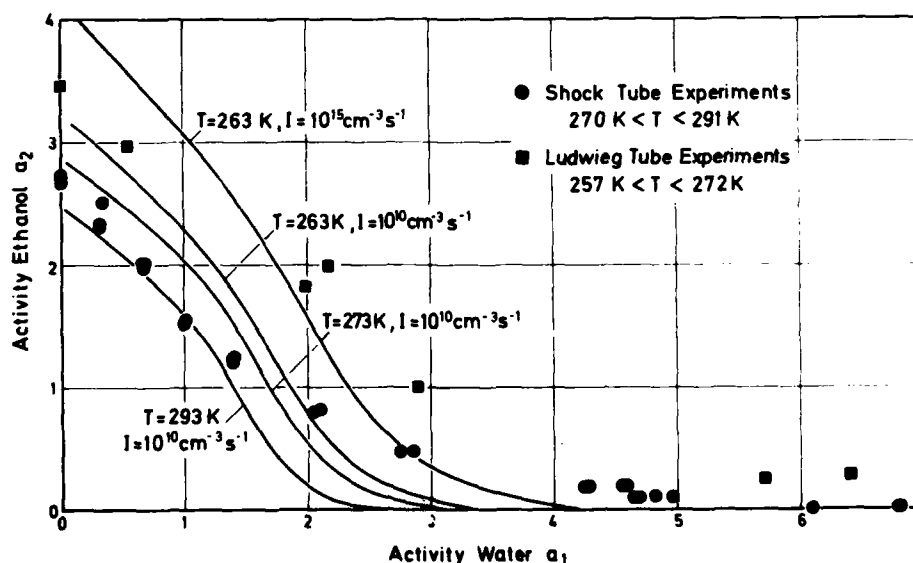


Fig.5 Homogeneous binary nucleation of water/ethanol mixture

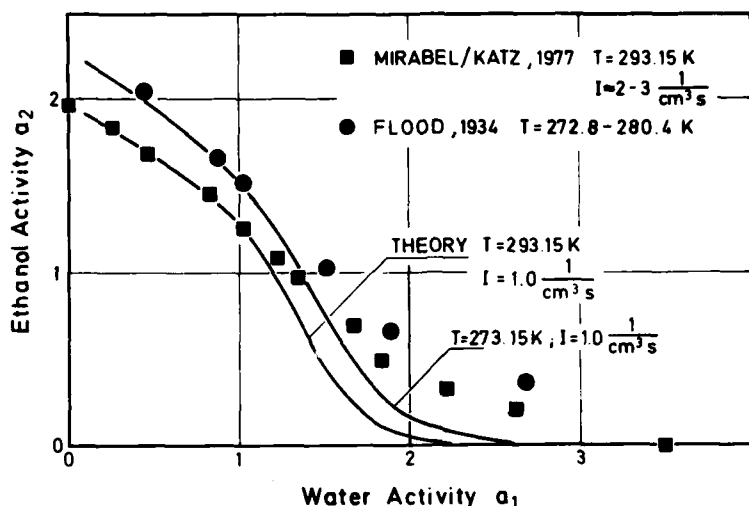


Fig.6 Comparison of theory with earlier experiments

($x = 0$) and with alcohol rich vapors demonstrate excellent agreement with theory. Significant deviations to the theory are evident with water-rich mixtures - a tendency which has been observed in the original cloud chamber experiments of Flood in 1934¹² and in the newer study by Mirabel and Katz in 1977¹³ with extremely low cooling rates.

DISCUSSION

Deviations of experimental results with pure water from the classical homogeneous nucleation theory have been frequently discussed (see for example¹⁴). Generally, it is assumed that the main source for these deviations can be found in the use of the bulk surface tension. It appears to be plausible that extremely small critical droplets - in the present case one cluster contains less than 100 molecules ($r < 10 \text{ \AA}$) - will have a different effective surface tension than the macroscopic value. In addition, for water/alcohol mixtures the strong gradient of the macroscopic surface tension $\partial\sigma/\partial x$ for $x \rightarrow 0$ will be of dominant influence for the nucleation process as can be seen from Eqs.(3) and (4). The behaviour of σ versus x is illustrated in Fig.7 for some selected temperatures. This strong gradient of the bulk surface tension is explained by the enrichment of the alcohol on the liquid's surface¹⁵. Such an enrichment over the surface area, however, is impossible for small critical clusters which contain a few alcohol molecules (see Table 1) only in the concentration region under consideration¹³. It seems that in water rich clusters the macroscopic surface tension as well as its first and second derivatives with respect to the mole fraction of the second mixture component is not relevant for the condensation process.

For a better understanding of the influence of the surface tension which must be regarded as the main source of the deviations we are planning to study selected alcohol/alcohol mixtures. Here, a linear change of the macroscopic surface tension with respect to the mole fraction is generally found. Deviations, therefore, as observed with water/alcohol mixtures between theory and experiments should not exist.

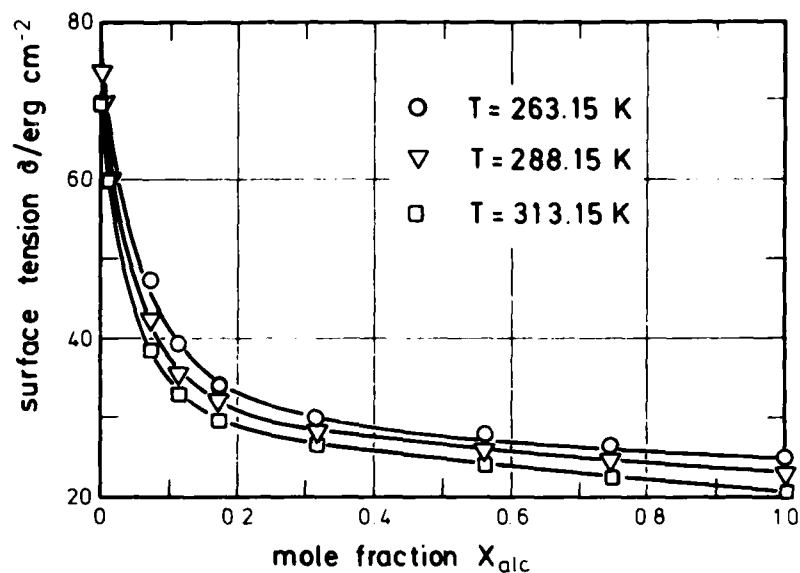


Fig.7 Surface tension of the water/ethanol mixture

a_1 Wat.	a_2 Alc.	x^*	n_1^*	n_2^*	r^* Å	$\frac{\Delta G^*}{kT}$	ϕ	Z	$C/10^{24}$ cm ⁻³ s ⁻¹
0.1	2.73	0.975	1.8	71.8	11.8	37.4	1.54	0.01	17.3
0.2	2.64	0.949	3.9	72.7	11.9	38.1	1.51	0.02	34.5
0.4	2.49	0.891	8.8	72.0	11.9	38.8	1.44	0.04	68.4
0.6	2.33	0.823	15.0	69.8	11.9	39.1	1.34	0.08	100.2
0.8	2.16	0.742	23.1	66.3	11.8	39.4	1.21	0.12	127.3
1.0	1.96	0.639	34.4	60.9	11.7	39.5	1.02	0.18	143.2
1.2	1.73	0.503	51.3	51.9	11.4	39.4	0.76	0.23	132.9
1.4	1.42	0.355	71.7	39.4	11.1	39.0	0.49	0.20	87.9
1.6	1.06	0.257	84.1	29.1	10.7	38.5	0.33	0.14	52.3
1.8	0.72	0.200	88.8	22.2	10.3	38.1	0.24	0.11	34.2
2.0	0.45	0.164	89.5	17.5	10.0	37.8	0.19	0.09	24.6
2.4	0.15	0.119	86.4	11.7	9.5	37.3	0.13	0.07	16.0
2.8	0.04	0.092	81.2	8.3	9.1	37.0	0.09	0.05	12.0

Table 1: Quantities characterizing the saddle point for $I = 10^{10}$ cm⁻³s⁻¹ at 273 K (theory)

ACKNOWLEDGEMENTS

Thanks are due to Dr.-Ing. W. Studziński and to Mr. G. Spiegel for their help in performing the experiments and their assistance with the calculations.

REFERENCES

1. S.L.K. Wittig, R.A. Zahoransky, S.S. Kim and D.E. Wurcz, Proc. of the 12th Int. Symp. on Shock Tubes and Waves, Jerusalem, 437 (1979)
2. A. Buch, Energie 3, 91 (1978)
3. J. Heeren, Energie 4, 135 (1978)
4. W. Traupel, Therm. Turbomaschinen I, Springer Verlag Berlin, Göttingen, Heidelberg (1958)
5. P.P. Wegener and B.J.C. Wu, Faraday Disc. Chem. Soc. 61, 77 (1976)
6. C.S. Kiang and D. Stauffer, Faraday Symp. Chem. Soc. 7, 26 (1974)
7. K. Neumann und W. Döring, Z.phys.Chemie A 186, 203 (1940)
8. H. Reiss, J.Chem.Phys. 18, 840 (1950)
9. D. Stauffer, J.Aerosol Sci. 7, 319 (1976)
10. H. Renon, L. Asselineau, G. Cohen and C. Rimbault, Calcul sur ordinateur des équilibres liquid-vapeur et liquide-liquide, Editions Technip, Paris (1971)
11. H. Ludwig, AGARD Rep. No. 143 (1957)
12. H. Flood, Z.phys.Chemie A 170, 286 (1934)
13. P. Mirabel and J.L. Katz, J.Chem.Phys. 67, 1697 (1977)
14. P.P. Wegener, Nonequilibrium Flows, P.P. Wegener, ed. Marcel Dekker, New York and London, Chap. 4 (1969)
15. E.A. Guggenheim, Thermodynamics, 4th ed. (1959)
16. G. Gyarmathy and H. Meyer, VDI Forschungsheft 508 (1965)
17. D. Barschdorff, Forsch.Ing.-Wes. 37/5, 146 (1971)
18. D. Barschdorff, Phys.Fluids 18/5, 529 (1975)

AD P000294

INVESTIGATIONS OF HOMOGENEOUS NUCLEATION IN Fe, Si, Fe/Si,
FeO_x, and SiO_x VAPORS AND THEIR SUBSEQUENT CONDENSATION

John R. Stephens and S. H. Bauer

Department of Chemistry

Cornell University, Ithaca, New York 14853

Critical pressures vs temperatures for avalanche condensation of homogeneously nucleated Fe, Si, Fe/Si, FeO_x and SiO_x vapors are reported. In favorable cases (Fe, Si, Fe/Si), limits to the homogeneous cluster formation rates were obtained. Mixtures of 0.1 to 2.5% Fe(CO)₅ and/or SiH₄ in Ar, N₂O/Ar or H₂/N₂O/Ar were heated behind reflected shocks to temperatures above the boiling point of the condensed phase. Condensation which occurred in the subsequent expansion fan was monitored by light scattering and turbidity of the sample. All the systems showed substantial supersaturation ratios relative to their equilibrium vapor pressures, ranging from a factor of less than 10 for Fe to several orders of magnitude for SiO_x. The condensation temperatures and pressures are in substantial disagreement with those predicted by classical and Lothe-Pound theories for the measured flux rates. The results illustrate the difficulties in predicting the condensation sequence of solids from terrestrial or stellar atmospheres assuming thermodynamic equilibrium.

INTRODUCTION

Homogeneous nucleation and cluster growth rates in supersaturated metal and metal oxide vapors, and characteristics of the resultant condensates, are important for stratospheric chemistry in which aerosols of meteoric origin can affect the stratospheric ozone balance (ref. 1), in astrophysics, where homogeneously nucleated dust affects the thermal balance in some stars (ref. 2), and in some industrial processes such as the production of pure silicon from SiH₄ (ref. 3). Although much effort has been devoted to the study of homogeneous nucleation of organic (ref. 4,5) and inorganic (ref. 6) supersaturated vapors, as well as binary systems (ref. 7) which condense under low supersaturation conditions, relatively little work has been carried out on the nucleation of refractory systems. In our laboratory critical pressures vs temperature were determined for Bi, Pb, Fe, and Si (ref. 8,9); the enthalpy of condensation vs cluster size was determined for Fe

clusters (ref. 10); and initial growth rates for these metals studied (ref. 11). The results in these investigations were found to be in disagreement with classical nucleation theory, and a kinetic-molecular formalism has been proposed to describe the nucleation kinetics of these highly supersaturated systems (ref. 12).

Reported here are critical pressures vs temperature for the systems Fe, Si, Fe/Si, FeO_x , and SiO_x , and cluster flux rates for the metal vapors. Improvements in the experimental system allowed simultaneous determination of critical pressures and cluster fluxes in the expansion fan following reflected shocks. The bi-metallic Fe/Si system was chosen for study as an example of binary nucleation which exhibits significant nonideality in the bulk liquid. The iron oxide and silicon oxide systems are quite different; iron oxide condensates are believed to be formed from the major gas phase species $\text{Fe(g)} + \text{O}_2$ (ref. 13), while the silicon oxide condensation requires the reaction $\text{SiO(g)} + \text{H}_2\text{O} \rightarrow \text{SiO}_2(\text{l,s})$ (ref. 13). The morphology and crystalline phases present in the condensates were determined by electron microscopy.

EXPERIMENTAL

The shock tube technique used was similar to that employed in refs. 8 and 9, with the improvements noted below. Mixtures of 0.1 to 2.5% Fe(CO)_5 , SiH_4 with H_2 and/or N_2O in Ar were heated behind reflected shocks in a 2" diameter brass shock tube. The onset of rapid homogeneous nucleation and cluster growth which took place in the subsequent expansion wave were determined by monitoring the intensity of scattered light and turbidity of the sample. The absolute scattered intensity was calibrated by introducing freon-22 into the tube prior to each shock experiment.

The samples were prepared from triple distilled Fe(CO)_5 and/or high purity SiH_4 , and ultra high purity H_2 , diluted with ultra high purity Ar. Concentrated samples were prepared (~2.5% Fe(CO)_5 or SiH_4) and sequentially diluted to the required concentration. SiH_4 , Fe(CO)_5 and N_2O concentrations were confirmed by quantitative infrared absorption analysis, with an accuracy of approximately $\pm 15\%$. Samples below 0.1% SiH_4 or Fe(CO)_5 frequently showed loss by absorption of the metal precursors onto the shock tube walls, resulting in anomalously low condensation temperatures. Samples were introduced into the driven section of the shock tube at pressures ranging from 20 to 60 torr. Driver pressures at the diaphragm pressure break points ranged from 85 to 135 psi. Hydrogen was used for the driver gas.

The incident shock speeds were measured using Kistler 601 pressure transducers, one adjacent to the observation windows, located 88 mm from the end wall, with one transducer in the end wall. The side wall pressure transducer was recessed 0.030" and its face sealed with Dow Corning RTV, flush with the tube wall to reduce temperature effects on the transducer. The side wall transducer was calibrated quasi-statically and dynamically to 10KHz; these calibrations agreed within 2%. Pressure readings behind incident and reflected Ar shocks using the above calibrations agreed to within 10% of the pressure values calculated using the NASA Shock Program (ref. 14). Temperatures behind the reflected shock varied from 2400 to 4500°K. High temperatures behind the reflected shock well in excess of the gas-liquid equilibrium temperatures were required to fully vaporize all transient clusters which were generated behind the incident shock.

It is critical that the windows through which the Argon-ion laser beam enters and leaves the shock tube be scatter free. The window configuration used in this study is a significant improvement over that used previously; it is illustrated in Fig. 1.

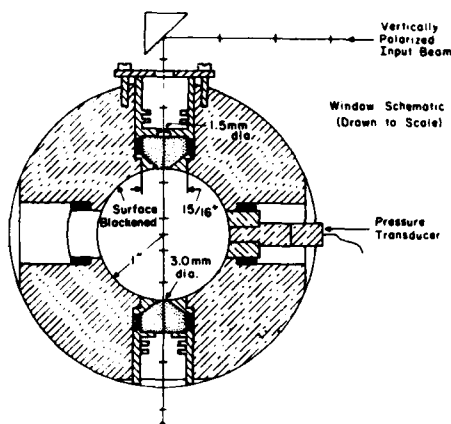


Figure 1
Schematic of the Shock
Tube Window Configuration

The semi-conical, anti-reflection coated quartz windows fitted flush to the tube wall enhanced the signal-to-noise by a factor of 10 for calibration of the absolute scattering intensity, and reduced the sensitivity to tube oscillations to insignificant levels. Improved linearity of the scattering signal was achieved by amplifying the phototube current with an op-amp operating in the charge to voltage mode. The incident laser beam was chopped at 30 kHz, resulting in a time resolution of 30 microseconds in the scattering and absorption signals. Thermal emission from the shocked gas resulted in a strong low frequency (1 kHz) scattering signal. The scattering and emission signals were separated by passing the scattering phototube output through a multiple pole Butterworth high-pass filter with a cut-off frequency (-3db) of 7 kHz. The onset of significant scattering by clusters was clearly visible in the filtered traces.

Samples of the condensates were collected on transmission electron microscope (TEM) sample grids held in a plug inserted in the shock tube wall several centimeters downstream from the window. Electron micrographs were taken with JEOL-100B and JEOL-200X microscopes at magnifications of 100,000 times and selected area electron diffraction patterns were obtained to aid in identifying the phases present in the condensates.

RESULTS

1. A summary of the samples investigated is presented in Table 1.

The critical pressures for avalanche condensation vs temperature for the Fe, Si, Fe/Si, FeO_x and SiO_x systems are shown in Figs. 2-6, wherein the metal or metal oxide partial pressures are plotted, assuming the monoatomic metal or the monoxide is the metal bearing species. Plots of $\log P$ vs T at avalanche condensation, as opposed to the usual $\ln S_c$ (S_c = supersaturation ratio) allows several related systems to be superposed so that their condensation relationships may be seen, and avoids compression along

TABLE 1. Typical Initial and High Temperature (2200°K) Compositions

System	Initial (Mole %)		Equilibrium (Mole %) at ~2200°K
Fe	Fe(CO) ₅ Ar	1 99	Fe(0.95); CO(4.8); Ar(94)
Si	SiH ₄ Ar	1 99	Si+Si ₂ +Si ₃ (0.46); H ₂ (1.9); Ar(97.5)
Fe/Si 1:1	Fe(CO) ₅ SiH ₄ Ar	0.5 0.5 99	Fe(0.43); Si(0.48); CO(2.4); H ₂ (0.95); Ar(96)
Fe/Si 1:2	Fe(CO) ₅ SiH ₄ Ar	0.25 0.50 99.25	Fe(0.24); Si(0.48); CO(1.2); H ₂ (0.13); Ar(96.3)
FeO _x O/Fe=1.8	Fe(CO) ₅ N ₂ O Ar	0.70 1.20 98.1	Fe(0.61); FeO(0.05); CO(2.2); CO ₂ (1.1); O ₂ (0.35x10 ⁻³); N ₂ (1.17); O(3.1x10 ⁻⁴); Ar(94.8)
FeO _x O/Fe=6.2	Fe(CO) ₅ N ₂ O Ar	1.0 6.23 92.8	Fe(0.31); FeO(0.65); CO(0.33); CO ₂ (4.4); O ₂ (0.40); N ₂ (5.9); O(1.35x10 ⁻²); Ar(88)
SiO _x O/Si=1.42	SiH ₄ N ₂ O Ar	0.87 1.21 97.9	SiO(0.86); SiO ₂ (9.8x10 ⁻⁴); H ₂ O(0.33); O ₂ (5.1x10 ⁻⁶); H ₂ (1.36); N ₂ (1.2); O(4.9x10 ⁻⁵); H(5.3x10 ⁻²); OH(1.7x10 ⁻³); At(96.2)
SiO _x O/Si=1.60	SiH ₄ N ₂ O Ar	1.1 1.74 97.2	SiO(1.07); SiO ₂ (2.2x10 ⁻³); H ₂ O(0.62); O ₂ (2.18x10 ⁻⁵); H ₂ (1.50); N ₂ (1.70); O(1.2x10 ⁻⁴); H(6.7x10 ⁻²); OH(3.9x10 ⁻³); Ar(95.0)
SiO _x O/Si/H ₂ 3.1/1/1.63	SiH ₄ N ₂ O H ₂ Ar	1.1 3.44 1.81 93.6	SiO(1.08); SiO ₂ (7.2x10 ⁻³); H ₂ O(2.26); O ₂ (2.5x10 ⁻⁴); O(4.3x10 ⁻⁴); H ₂ (1.64); H(7.2x10 ⁻²); N ₂ (3.36); OH(1.4x10 ⁻²); Ar(91.6)

the P axis. The data points are plotted with representative error bars shown as crosses; these include errors in measuring the initial shock speed, uncertainties introduced in calculating the temperature behind the reflected shocks assuming frozen or equilibrium chemistry for the incident and reflected shocks, and nonlinearities in the pressure transducers and oscilloscopes. The ratios of temperatures post reflected shock to the points of condensation were determined from the ratio of pressures at the condensation point and immediately behind the reflected shocks. Temperature dependent γ 's were used. This dependence was most significant for the SiO_x and FeO_x systems. Lower limits for the cluster fluxes for selected shocks are shown in the graphs for the Fe, Si, and Fe/Si systems. Predictions of classical nucleation theory, with flux as a parameter, are plotted together with the experi-

mental data. The assumptions used in the classical calculations are discussed for each system below.

Figure 2 shows the critical condensation pressures for Fe vs T superposed on the Fe equilibrium solid-liquid-gas phase diagram. The present data indicated by the crosses confirm the results reported previously (ref. 8). The condensation pressure

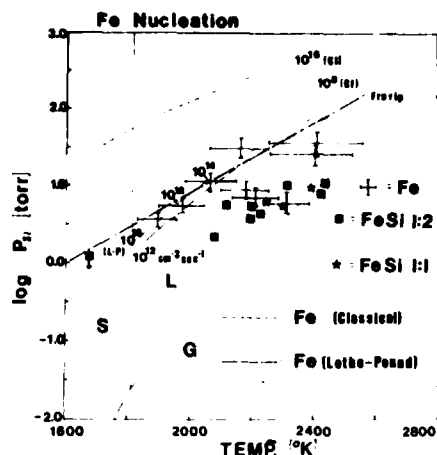


Figure 2

Critical (log) pressures vs temperatures for Fe and Fe/Si condensation and predictions of classical and Lothe-Pound theories. Previous results (ref. 8) are shown. The three Fe points on the lower right are believed to be anomalous due to oxygen contamination.

is typically 10-100 times the equilibrium vapor pressure at a given temperature. Also shown are the classical and Lothe-Pound theoretical predictions based on bulk properties given in ref. 8. Iron condenses at high temperatures and lower pressures at a given flux than estimated from the classical theory. The critical condensation pressures obtained for the Fe/Si system (1:1 Fe/Si and 1:2 Fe/Si) are also shown in Fig. 3. The sum of Fe and Si metal pressures were plotted vs T. Lower limits to the fluxes, and predictions based on binary classical nucleation theory were included, taking into account the reduced activity of Fe and Si in

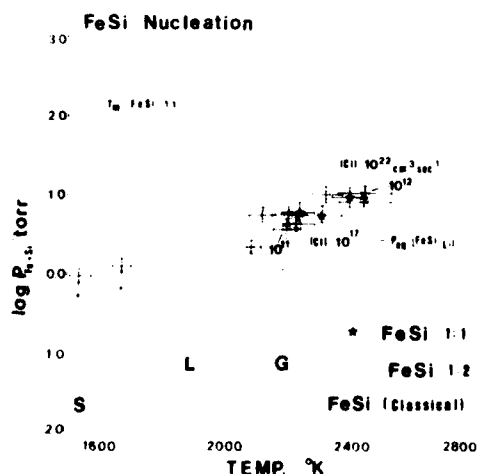


Figure 3

Critical (log) pressures vs temperatures for Fe/Si condensation, and predictions of binary classical nucleation theory. Points with arrows are upper limits because of possible loss of precursors to the shock tube walls.

the binary melt (ref. 15).

The optical properties of Fe/Si melts were estimated from

the d.c. resistance of FeSi_2 solid above the semiconductor-metal transition temperature at $\sim 1210^\circ\text{K}$, using the Drude free electron theory, assuming the optical constants at the laser wavelength were similar to these at the zero frequency limit (ref. 16,17). The 1:1 and 1:2 Fe/Si systems exhibit the same condensation pressures vs temperature. Both systems condense at slightly higher temperatures than pure Fe metal, reflecting the lowered activity in the liquid phase. Electron micrographs of typical condensates are shown in Fig. 7.

Figure 4 is a plot of $\log P$ vs T for Si, superposed on the Si equilibrium P-T phase diagram. Also shown is the best fit of Si condensation pressures previously reported (ref. 9), and lower limit to cluster fluxes estimated by Tabayashi and Bauer for incident shocks. We believe in ref. 9 the reflected shock temperatures were not sufficiently high to vaporize the clusters formed

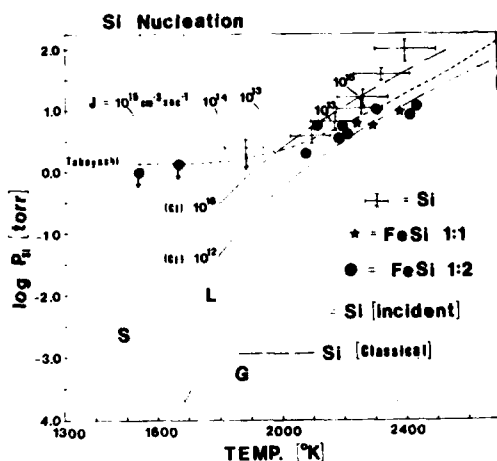


Figure 4

Critical (log) pressures vs temperatures for Si and Fe/Si and predictions of classical nucleation theory for Si nucleation. Previous results (ref. 9) are shown. Points with arrows indicate upper limits because of possible loss of SiH_4 to the shock tube walls.

in the incident shock, resulting in inhomogeneous condensation. The low temperature portion of the previous data was not confirmed in this study due to loss of SiH_4 from $\leq 0.1\%$ SiH_4 samples to the shock tube walls. This led to low infrared band intensities and anomalously low condensation temperatures. The lower limits to Si flux determined in reflected shocks in this study are similar to those measured in ref. 9 using incident shocks. The Fe/Si system also shown condenses at nearly the same temperature as the pure Si system, with somewhat higher condensation temperatures at high pressures.

Figure 5 shows condensation pressures vs temperature for the FeO_x system. The pressures assume the major gaseous component is Fe; this is based on vaporization studies of iron oxide melts (ref. 13). Vapor pressures were calculated from the pressure of Fe over FeO (ref. 18). Two series of shocks were carried out with $\text{N}_2\text{O}/\text{Fe}(\text{CO})_5$ ratios of 1.75 and 6.23. The oxygen-rich system condensed at slightly higher temperatures than the oxygen poor system. The crystalline phases identified in the condensates were FeO with $\gamma\text{Fe}_2\text{O}_3$ and/or Fe_3O_4 for the oxygen-rich system, with $\gamma\text{Fe}_2\text{O}_3$ and/or Fe_3O_4 occurring in the oxygen-poor condensates. Many euhedral grains were seen in the condensates (Fig. 7). Cluster formation rates were not calculated due to uncertainties in the optical properties of the initial FeO_x clusters formed.

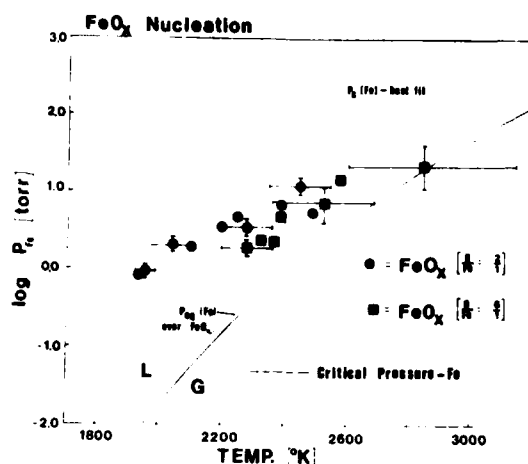


Figure 5

Critical (log) pressures vs temperatures for FeO_x condensation, at two different O/Fe ratios. The critical pressures vs temperature for metallic iron are also shown.

Condensation pressures vs temperature for $\text{SiH}_4/\text{N}_2\text{O}$ and $\text{SiH}_4/\text{N}_2\text{O}/\text{H}_2$ systems are plotted in Fig. 6 for three different O/Si ratios. The "silicon pressure" is predominantly SiO(g) (ref. 13). SiO pressures vs T were calculated from JANAF data (ref. 18). The major oxygen bearing gas phase species in these systems are SiO and H_2O . Hydrogen was added to the oxygen-rich system to ensure formation of H_2O rather than allow free oxygen at high temperatures. The three ratios of O/Si used were 1.43, 1.58, and 3.10. Cluster fluxes were not calculated due to uncertainties in the optical properties of the initial clusters formed. The scatter and error bars in these data are significantly larger than the

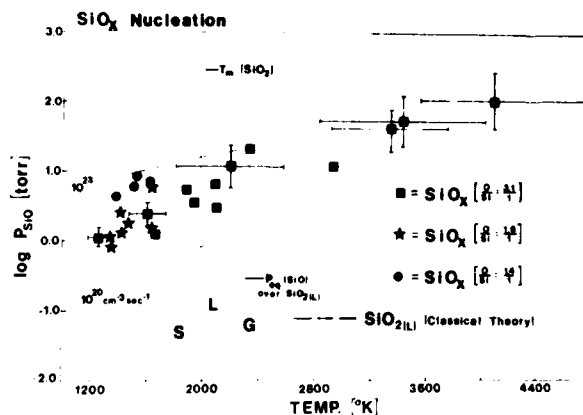


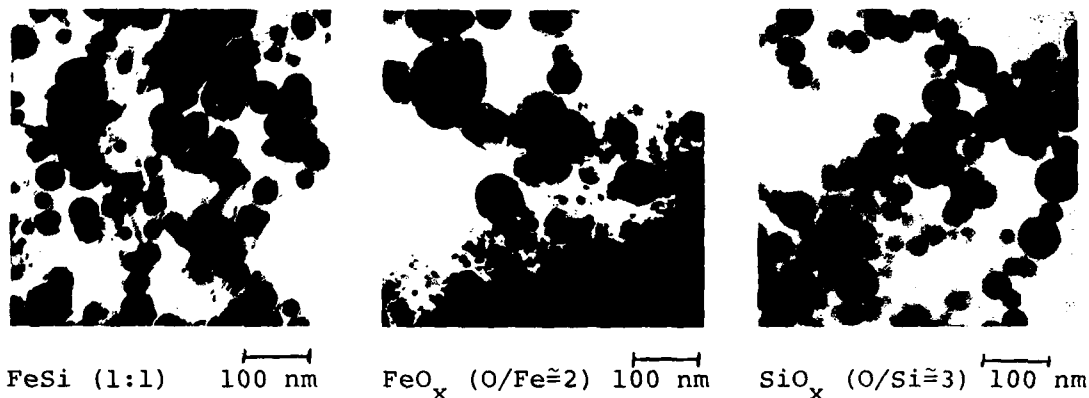
Figure 6

Critical (log) pressures vs temperatures for SiO_x condensation at three O/Si ratios. Predictions of simple classical nucleation theory are shown. The assumptions used in calculating the theoretical predictions are discussed in the text.

other systems, due to the large pressure ratios required for condensation, and large differences between the frozen and equilibrium shock conditions, for the concentrated samples used. Despite these uncertainties, the silicon oxide shows much greater temperature dependence than the other systems. An increase in the condensation temperature with oxygen content at a given (SiO) pressure is indicated. For the classical theory estimates, we assumed that rapid reaction of SiO(g) and H_2O forms $\text{SiO}_2(l)$ the most stable condensed phase, on the cluster surface. For reasonable cluster flux limits, similar to the other systems studied 10^{13} - 10^{15} ($\text{cm}^{-3} \text{sec}^{-1}$), condensation takes place at pressures

three orders of magnitude greater than predicted. The slope of the critical pressure vs temperature curve, however, is correctly predicted. Electron micrographs of the SiO_x condensates (Fig. 7) show the condensates to consist of spherical grains. The low oxygen condensates show an amorphous (presumably SiO_2) phase plus Si metal. The high oxygen condensates contain only an amorphous (SiO_2) phase.

Figure 7. Electron Micrographs of the Condensates



CONCLUSIONS

The above data clearly show that the classical nucleation theory is inadequate for describing the nucleation of refractory species which exhibit high supersaturation ratios prior to condensation. These results are in accord with recent condensation studies of several low temperature systems, for example propanol and water, in which the experimental results are similar to the classical theory under low flux conditions (~ 1 cluster/ cm^3 sec) but show systematic deviations from the classical predictions, under higher flux conditions 10^6 – 10^9 (clusters/ cm^3 sec) (ref. 19). The deviations are both in high and low temperature directions. In systems exhibiting high levels of supersaturation, or under high flux conditions, a more realistic kinetic-molecular formalism such as outlined by Bauer and Frurip (ref. 12) is needed to correctly address nucleation phenomena.

The three binary systems Fe/Si, SiO_x , and FeO_x show varying degrees of complexity, and illustrate features which should be incorporated in any comprehensive theory. The binary system Fe/Si is the simplest of the three. No change in speciation is required for the gas to liquid transition since Fe and Si exhibit complete miscibility (ref. 15). However, the nonideality of the binary liquid is manifest in slightly higher condensation temperatures than for the pure phases. The implication is that binary clusters are more stable than pure clusters (heat release on mixing). A higher enthalpy of vaporization leads to a smaller critical size nucleus; i.e. such binary systems condense earlier. The oxides require simultaneous reaction and nucleation for the condensation to occur. For the classical nucleation calculation we assumed fast reaction on the cluster surfaces of the major gas phase species to form the condensed phase. This assumption implies that the condensation should be independent of the composition of the gaseous species present in excess. Perhaps for both systems, and particularly for FeO_x , the condensation temperature shows an explicit oxygen dependence, indicating that the rate of surface

reactions, or at least the formation of the stable condensed oxide, is not faster than the diffusion rate of gas phase species to the clusters. Species specific-real time spectroscopy techniques to probe the reacting, condensing system will help to elucidate the mechanism of such cluster formation.

The above experiments have implications for modeling the condensation of dust in astronomical environments. Much of the literature in this field has been devoted to calculating equilibrium condensation temperatures of refractory phases, such as Fe/Mg silicates and iron (Review, ref. 20). The present data indicate that even under well characterized laboratory conditions, equilibrium calculations clearly do not represent actual condensation behavior of the system; for example, in SiO_2 , supersaturations of three orders of magnitude were found. Classical nucleation calculations are also inadequate to correctly describe astronomical condensation processes. Only systematic, controlled nucleation experiments using species-specific real time probes, coupled with a kinetic-molecular nucleation theory, will allow meaningful data to be obtained which can be applied to astronomical condensation.

ACKNOWLEDGMENT

This work was supported by the National Science Foundation under Grant No. DMR-78/0307.

REFERENCES

1. D.M. Hunten, R.P. Turco, and O.B. Toon, *J. Atmos. Sci.* **37**, (6), 1342 (1980).
2. P.G. Martin, *Cosmic Dust: Its Impact on Astronomy*, (Clarendon Press, Oxford, England), 1978.
3. F.C. Eversteijn, *Phillips Res. Rep.* **26**, 134 (1971).
4. J.L. Katz, P. Mirabel, C.J. Scoppa II, and T.L. Virkler, *J. Chem. Phys.* **65**, 382 (1976).
5. C. Becker, *J. Chem. Phys.* **72**, 4579 (1980).
6. B.N. Hale and P.L.M. Plummer, *J. Atmos. Sci.* **31**, 1615 (1974).
7. C. Flageallet, N. Cao Dinh, and P. Mirabel, *J. Chem. Phys.* **72**, 544 (1980).
8. D.J. Frurip and S.H. Bauer, *J. Phys. Chem.* **81**, 1001 (1977).
9. K. Tabayashi and S.H. Bauer, in *Proceedings of the 12th International Symposium on Shock Tubes and Waves*, Jerusalem, July 16-19, 1979 (Magnes Press, The Hebrew University, Jerusalem, Israel), 409 (1979).
10. H.J. Freund and S.H. Bauer, *J. Phys. Chem.* **81**, 994 (1977).
11. D.J. Frurip and S.H. Bauer, *J. Phys. Chem.* **81**, 1007 (1977).
12. S.H. Bauer and D.J. Frurip, *J. Phys. Chem.* **81**, 1015 (1977).
13. K.A. Gingerich, in *Current Topics in Materials Science* **6** (E. Kaldis, Ed.), (North Holland Publ.), 345 (1980).
14. S. Gordon and B. McBride, *NASA Spec. Publ.* #273, (1971).
15. R. Hultgren, P.D. Desai, D.T. Hawkins, M. Gleiser, and K.K. Kelley, *Selected Values of the Thermodynamic Properties of Binary Alloys* (American Society for Metals), 1973.
16. U. Birkholz and J. Schelm, *J. Physica Status. Solidi* **34**, K177 (1970).
17. U. Birkholz, H. Finkenrath, J. Naegele, and N. Uhle, *Phys. Stat. Sol.* **30**, K81 (1968).
18. D.R. Stull and H. Prophet, (Eds.) *"JANAF Thermochemical Tables, 2nd ed."* Dow Chemical Co., Midland, Michigan, 1970.
19. P.E. Wagner and R. Strey (Personal Communication), 1980.
20. S.S. Barshay and J.S. Lewis, *Ann. Rev. Astron. Astrophys.* **14**, 81 (1976).

AD P000295

CONDENSATION KINETICS OF IRON AND SILICON IN THE VAPOR PHASE

J. STEINWANDEL,* TH. DIETZ, V. JOOS AND M. HAUSER

INSTITUT FÜR PHYSIKALISCHE CHEMIE

Universität Stuttgart, Stuttgart, W. Germany

Atomic vapors of iron or silicon were generated by shock heating the compounds $\text{Fe}(\text{CO})_5$ or SiH_4 in the incident shock wave of a 12.7 cm diameter shock tube. The initial concentrations of the compounds in argon in the driven section of the tube (driver gas He) were sufficiently low that ideal shock tube operation and an isothermal condensation reaction can be assumed. Varying shock wave temperature and initial compound concentration we produced supersaturated states between incident and reflected shock wave. The atomic vapors condensed to form small clusters of the two elements. The rate of formation of these "droplets" was detected using atomic and molecular spectroscopy and light scattering respectively. Because the surface tension loses its proper meaning for particles of atomic dimensions, classical nucleation theory cannot be used for comparison with the experiments. Therefore, it was tried to describe the condensation on the basis of a new hypothesis omitting the use of the surface tension.* Rate constants for condensation could be derived from this simple model involving collision theory and using a constant number density of growing particles.

Introduction

The so-called classical nucleation theory was developed by Volmer and Weber [1], Becker and Doering [2], Zeldovich [3], Frenkel [4] and others. These authors use a thermodynamic and kinetic model to derive a theoretical steady-state nucleation rate for the "critical" nuclei. These particles are produced in the supersaturated system and they are assumed to be in a metastable equilibrium with the supersaturated vapor before condensation occurs. The classical work involves two fundamental approximations which do not hold for condensation studies in shock tubes of the type discussed here.

- 1) It is assumed that the condensing systems contains a constant number of monomers during the reaction time with the nuclei removed from the system upon reaching the critical size. The mass of the removed nuclei is replenished by an equal mass of monomer. These arguments are valid in open systems like experiments in supersonic nozzles, see Wegener [5], but not

* Now at Department of Engineering and Applied Science, Yale University, New Haven, CT, USA.

- necessarily in closed systems like Wilson cloud chambers and shock tubes.
- ii) The classical theory uses the macroscopic surface tension for the calculation of the reversible work of formation of a droplet in the supersaturated vapor.

According to Gibbs, the use of the surface tension is artificial when a bulk liquid cannot be assumed. In other words, vapor pressure and surface tension for atoms or dimers cannot be defined by bulk approaches in situations as discussed in this paper. Here condensation is a phenomenon which must be described without the use of such assumptions by invoking the methods of chemical kinetics.

Figure 1 schematically shows the experimental arrangement. The He-driven high-temperature shock tube has a uniform diameter of 12.7 cm, a diameter large enough to avoid wall reactions. The length of the driver and driven sections is 3.6 m and 5.4 m respectively. Shock speed is measured by using three platinum resistance gauges and recorded by a digital counter and the marker channel of a transient recorder (Maurer). The first two gauge signals are used for triggering the digital counter and an oscilloscope, while the third signal from the incident shock wave triggers the two-channel transient recorder, which is operated in a pre-trigger mode recording the pre-history of the measurement. Attenuation of the incident shock wave speed is less than 1% per m in all experiments. The gases used (He and Ar) were of 99.9997% purity to avoid reactions with nitrogen or oxygen. SiH_4 is used as a doped gas at 2% by vol. in pure argon. This gas is mixed with the flowing carrier gas for homogeneous distribution in the driven section to final concentrations of less than 1% by vol. in the carrier gas.

The $\text{Fe}(\text{CO})_5$ is introduced into the test section by saturating an argon bypass with the compound, and mixing again as in the case of SiH_4 described above, to final concentrations of about 1%. A Xenon-high-pressure arc (XBO 450-1) with high-stabilized power supply is used as light source for absorption and turbidity measurements.

The Iron Condensation Results

The incident shock-wave temperatures of these experiments were about $1000 \text{ K} \leq T \leq 1700 \text{ K}$ at initial Fe-atomic concentrations $2 \text{ to } 4 \times 10^{14} \text{ cm}^{-3}$. The supersaturations, $x = p/p_\infty$, where p is the initial Fe partial pressure and p_∞ is the saturation pressure of the bulk iron phases at these temperatures were about $2.2 \leq \ln x \leq 20.2$. Figure 2 shows a typical analog signal of the transient recorder. The top trace shows transient absorption of the Fe I resonance line at $\lambda = 385.991 \text{ nm}$ wavelength. The signal is obtained using the method of integral absorption spectroscopy described by Naumann and Michel [6] for alkaline-earth atoms and by Steinwandel et al. [7] for transition metal atoms. In close approximation, the slit function of both monochromators are triangular. The bandwidth of the monochromator (Zeiss M4 GII) was set to 0.2 nm for the Fe I measurements. The photomultiplier received signals of integral absorption $20\% \leq A \leq 50\%$. The M4 GII was operated at maximum dispersion of the prisms.

The atomic density rises immediately with the arrival of the incident shock, because the $\text{Fe}(\text{CO})_5$ decomposes completely in the front of the shock wave. It is important to notice from the fast disappearance of the Fe I absorption signal that the condensation reaction starts at once without delay. The low plateau shows stray extinction of condensate particles which evaporate completely in the front of the reflected shock wave. The bottom trace taken at $\lambda = 389.00 \text{ nm}$ outside the collision-broadened Fe-spectral line shows no significant signal. Therefore, we can assume that our interpretation of the Fe-I-resonance signal is correct and no significant impurities are present. The rectangular marks are the signals from the platinum gauges. Table 1 shows experimental results at various temperatures (supersaturation) and initial concentrations n_0 of iron atoms with various condensation half-value times $\tau_{1/2}$.

All decay curves of the atomic absorption are of the same hypobolic type

shown in the transient. No indication of anything like a delay in the time to establish nucleation is seen. The condensation is likely to be a collision-controlled phenomenon and many small particles with a diameter < 1 nm are produced. Figure 3 shows some detected condensation half life times versus the degree of supersaturation.

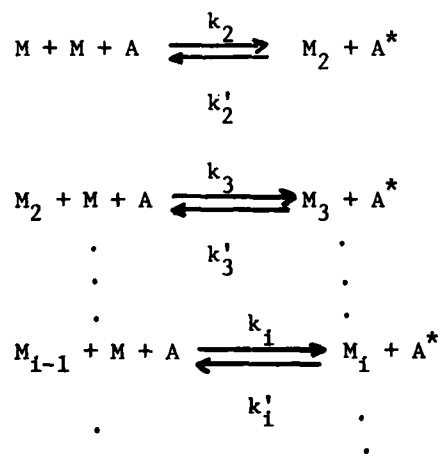
The Silicon-condensation Results

In order to clarify condensation kinetics by new experimental methods we did silicon condensation experiments in the temperature range $2000 \text{ K} \leq T \leq 3000 \text{ K}$ at supersaturations which were produced by thermal decomposition of SiH_4 behind the incident shock wave. In these experiments we could not detect any absorption of the 251, 61 nm Si I-resonance line. In this case the decomposition of SiH_4 is the rate determining process and the mechanism of decomposition will be presented in a subsequent paper. We were able to detect the Si_2 molecule by time-resolved absorption spectroscopy during the condensation using the X-H-band system of the molecule (Herzberg [8]). The dimer is present immediately behind the incident shock wave.

To obtain further information, condensation of stray-extinction at two different wavelengths was detected and a typical experiment is shown in Fig. 4. As in the case of iron, the condensation starts immediately without any delay. But condensation as well as the evaporation in the reflected wave are much slower compared to the iron experiments. In the case of silicon the number density of the droplets and the number of atoms in the cluster are larger compared to iron. These conclusions are partly based on a new kinetic description of the condensation.

Kinetics of Particle Growth

Condensation is a multistep reaction which can be described by the following reaction scheme starting from the monomers,



Using the classical description of homogeneous nucleation, a critical cluster equilibrium has to be assumed in the reaction scheme. But as denoted, we have not been able to find a steady of nucleation and therefore, we further assume multistep oligomerisation.

A first general approach using a hierarchy of kinetic differential equations starting with small oligomers is far too underdetermined to be soluble. Under the assumptions of a constant number density of particles that are able to grow and using the relation between number of atoms in the cluster and cluster radius — the clusters are assumed to be spherical — the following final formula can be derived

$$t = \frac{1}{a^2 n \bar{v}} \left[\ln \frac{(R-a)(a^2+ar+r^2)}{(r-a)(a^2+aR+R^2)} + \frac{1}{\sqrt{3}} \left(\operatorname{atn} \frac{2r+a}{a\sqrt{3}} - \operatorname{atn} \frac{2R+a}{a\sqrt{3}} \right) \right], \quad (1)$$

where R is the average instantaneous radius of the growing particle, \bar{v} the relative gas velocity of the particles; r is the radius of one particle at time zero and t the condensation time; a , the parameter of growth kinetics is defined by

$$a^3 = r_1^3 \cdot \frac{n_0}{n}, \quad (2)$$

where n_0 means the initial monomer density and n the growing particle density.

Figure 5 shows a calculation of the function $R(t)$ and it can be seen that after a certain time condensation ceases. The number density and the cluster radii determine the scattering of light and we used the general Mie-theory for calculating turbidity coefficients σ_{ext} [9].

The stray-extinction measurements at two different wavelengths allow the determination of the radii. Good consistenc of our theoretical model with the experiments is achieved by identifying the disposable parameter n of growing particles with that of *silicon dimers* from the dimerisation equilibrium



by extrapolating the JANAF-values [10], the final cluster radii in the experiment shown in Figure 4 was determined to be ≤ 1 nm. The iron experiments also agree with the assumptions described above assuming iron dimers as growing particles.

Finally, concerning the classical theory of homogeneous nucleation, we believe that it's application in the case of silicon and iron condensation is invalid.

References

1. M. Volmer and A. Weber, Zeitschr. f. phys. Chem. A 170, 273 (1934).
2. R. Becker and W. Doering, Ann. Phys. 24, 719 (1935).
3. J. Zeldovich, J. Exptl. Theoret. Phys. (USSR) 12, 525 (1942).
4. J.F. Frenkel, Kinetic Theory of Liquids (Oxford University Press, New York 1946).
5. P.P. Wegener and B.J.C. Wu, Advanc. in Coll. and Interface Sci. 7 325-417 (1977).
6. F. Naumann and K.W. Michel, Z. Phys. 255, 348 (1972).
7. J. Steinwandel et al., Z. Naturforsch. 35A (1980).
8. G. Herzberg, Spectra of Diatomic Molecules, New York 1951.
9. H.C. Van de Hulst, Light Scattering by Small Particles, John Wiley, New York 1957.
10. JANAF, NSRDS-NBS 37, Washington 1971.

T [K]	n_{Fe} [cm^{-3}]	$\ln(p/p_{\infty})$	$\tau_{1/2}$ [μsec]
980	$2.1 \cdot 10^{14}$	20.2	16.2
1075	$4.5 \cdot 10^{14}$	18.8	24.4
1190	$4.9 \cdot 10^{14}$	13.8	32.4
1220	$3.8 \cdot 10^{14}$	12.6	40.4
1380	$2.7 \cdot 10^{14}$	8.4	45.4
1500	$2.4 \cdot 10^{14}$	5.7	80.8
1605	$2.7 \cdot 10^{14}$	3.3	96.0

Table 1: Some iron-condensation experiments.

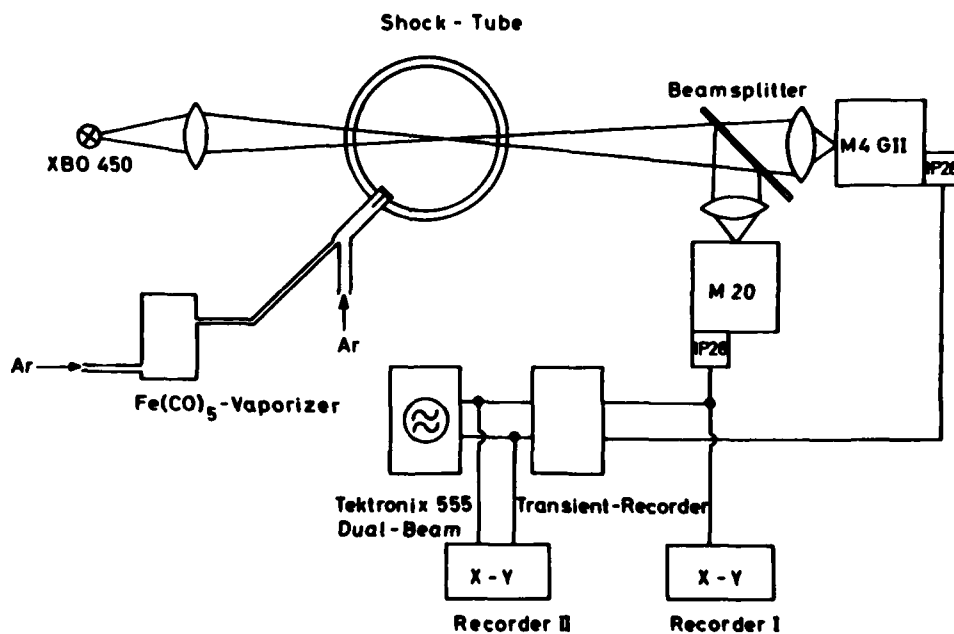


Figure 1: Schematic diagram of the experimental arrangement.

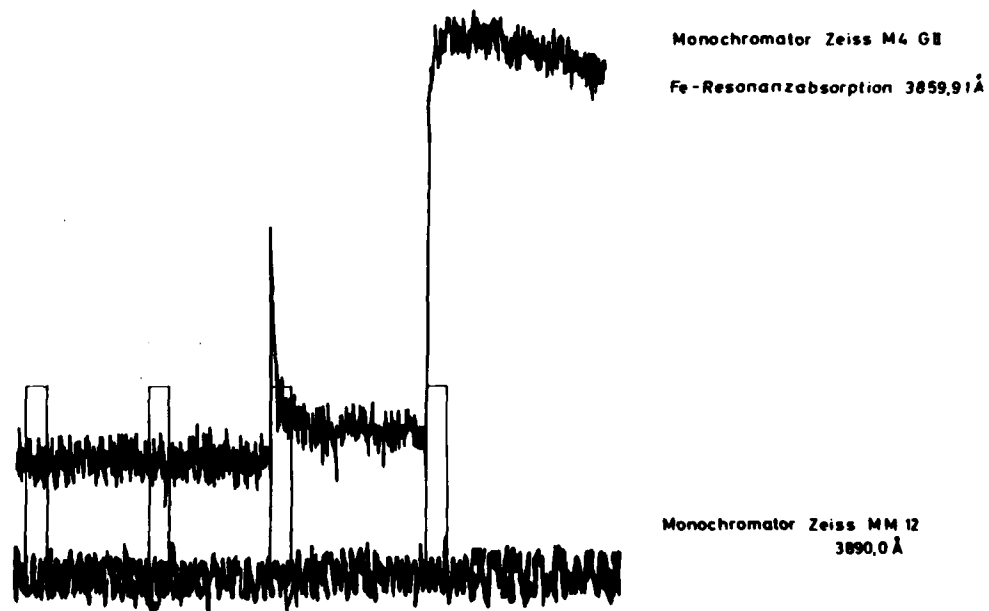


Figure 2: Analog signal of the transient recorder.
Iron-condensation (Fe-atomic line
spectroscopy 385.991 nm).

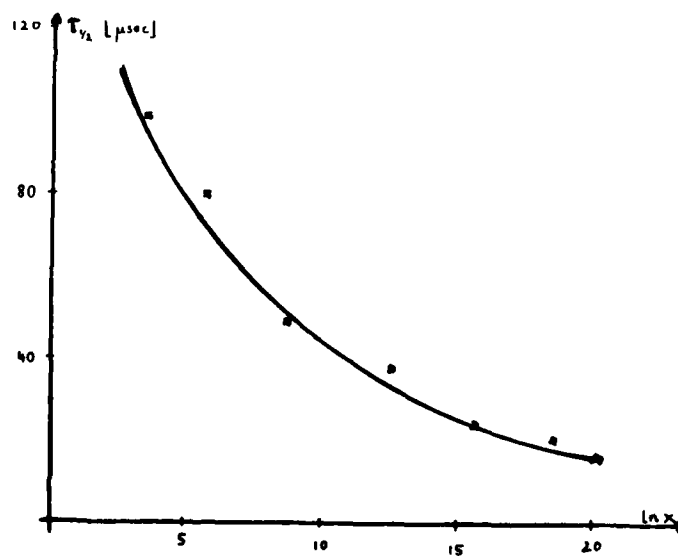


Figure 3: Detected iron-condensation times vs. degree of supersaturation.

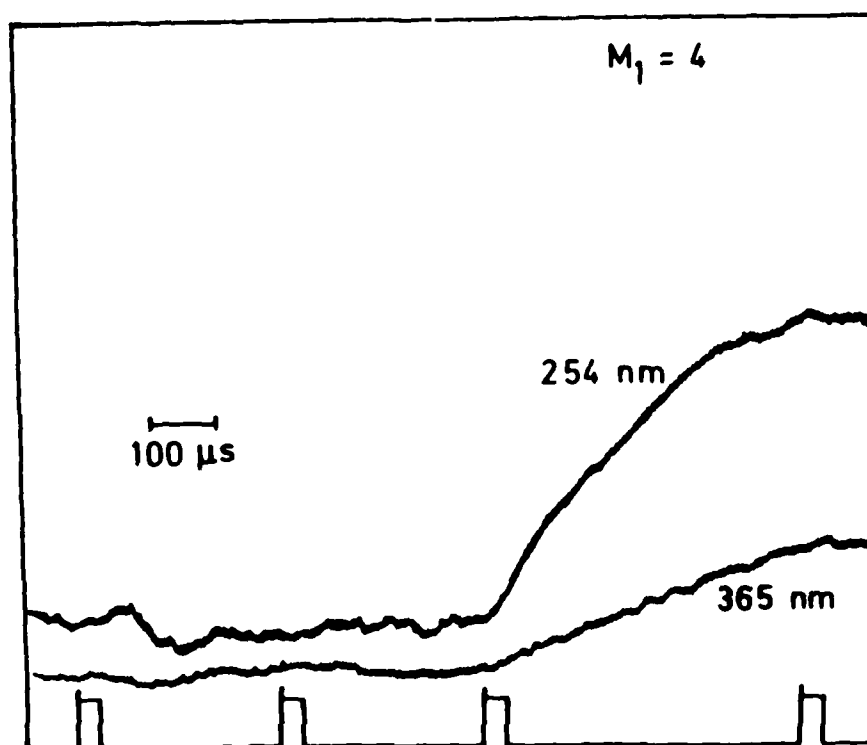


Figure 4: Analog signal of the transient recorder. Silicon condensation experiment. Turbidity measurements of the growing clusters.

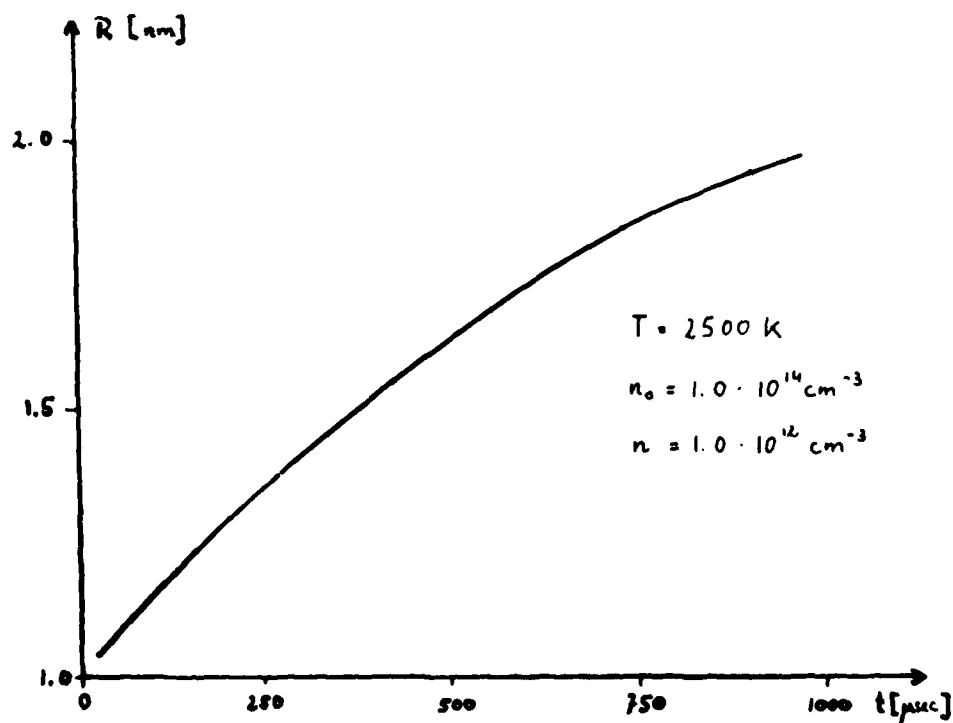


Figure 5: Cluster Radius R as a function of observation time. Calculations on the basis of the condensation model.

SHOCK-TUBE SIMULATION EXPERIMENT OF SUPERSONIC CONDENSATION FLOW ACCOMPANYING A SHOCK WAVE

HAKURO OGUCHI, KATSUSHI FUNABIKI
AND TORU ITO*

*The Institute of Space and Astronautical Science
Komaba, Meguro-ku, Tokyo, Japan*

AD P000296

Recently, the senior author (H.O.) presented an analysis, based upon the kinetic theory, for one-dimensional strong condensation problem, in which condensation rate is so large that the normal flow velocity directed onto an interface attains supersonic. According to the results, a stationary shock may appear far ahead of the condensing interphase. The existence of similar shock can also be predicted by simple wave theory, if shock wave is considered to reflect on the wall allowed to suck fluid. Such a wall may therefore simulate condensing interphase. From this point of view, we conducted simulation experiment of supersonic condensation flow accompanying a shock wave, by means of a shock tube. The shock tube driven by fast-acting valve enables us to take a series of shadowgraphs at any moments desired. The reflected shock speed slows down for greater amount of suction or for smaller contraction of end wall, and eventually becomes stationary at rest. This critical condition of stationary reflected shock is found to be well predicted by the simple wave theory. In much increase of suction, the shock is swallowed into the end wall. These processes are also similar to wave propagation processes in a supersonic nozzle with varying contraction of the diffuser.

INTRODUCTION

In the past decade, the condensation problem has been analysed from the kinetic point of view. The strong condensation problem was first analysed by Kogan et al. (ref.1) based upon the kinetic model and thereafter by Hatakeyama et al. (ref.2) based upon the moment method. These analyses, however, retained only the cases when the flow directed onto the condensing interface is subsonic. Recently, the senior author (H.O.) and Hatakeyama extended the non-linear analysis to the cases of much stronger condensation,

*present address: Kawasaki Heavy Industry Ltd., Gifu-C., Japan.

when the flow directed onto the interphase attains supersonic beyond the sonic (ref.3) According to their results, there appears a stationary shock wave ahead of the interface, so that the large condensation rate is fed by the pressure rise behind the shock wave. For simplicity, the analysis has been carried out for the one-dimensional geometry; that is, an infinitely plane interface is considered.

This similar flow situation may be seen in the reflection process of the incident shock from the wall allowed to suck the fluid. In fact, as shown later on, the simple wave theory also suggests the existence of the reflected shock wave stationary relatively to the wall, if adequate amount of fluid is sucked at the end wall. In the shock tube research, there were many investigations on the interaction problem of the shock wave with the porous wall, grid and wire mesh, which allow the fluid suction or passage. The interaction mechanism was studied from the various view points; for example, one may cite the references 4 - 8. If our attention is focused on the behavior of the reflected shock, the greater incident shock Mach numbers are likely to slow down the propagation speed of the reflected wave (ref.6) and also the greater amount of fluid passage or suction to do so (ref.8). In the continuum version of the problem, the wall allowed to suck the fluid may simulate a condensation interface, so far as the wave propagation induced by the condensation is concerned. Apparently, there is difference in flow structure near the interface from that near the wall. From the point of view mentioned above, we conducted a simulation experiment of one-dimensional supersonic condensation problem, focusing our attention to the shock wave propagation. In this experiment, the shock tube driven by a fast-acting valve was employed in some improvement of the previous one (ref.9).

EXPERIMENTAL APPARATUS: SHOCK TUBE

In Figure 1 is shown the schematic diagram of the shock tube used in the present experiment. The shock tube is driven by actuating a free piston MP through an auxiliary valve AP, in place of a conventional diaphragm breaking. The auxiliary valve is also operated by actuating a small free piston. The driver section of the tube is about 5 liters in capacity and its maximum tolerable pressure is about 30 kg/cm. The driven tube made of stainless steel is a circular tube of about 5 m long and 50 mm in dia. and the test section with a rectangular cross section 50 x 50 mm is equipped. The test section is connected through a reservoir to the vacuum system. In order to change smoothly the cross section from circular to rectangular, a distant section is inserted in between.

The operation and performance of this type of shock tube have already been reported in some detail (ref.9). We note here that the previous driven mechanism (ref.8) has been improved so as to be able to simultaneously supply gases into the driver section as well as the auxiliary piston section from a common high pressure storage. This modification results in further feasibility for the operation. As can be seen from the figure, a free piston MP is contrived to quickly move back and forth responding the movement of an auxiliary free piston, which can be followed by on-off switching of small magnetic valve, equipped outside of the driver section. Namely, if the valve V1 is opened with closed V2, the gas is supplied into the driver section and then both main and auxiliary piston shunt to stop the flow from the driver section into the driven tube and also the flow from the main piston cylinder to the

atmosphere. Then, the pressure in the driver section is raised up to a pressure desired. If the other magnetic valve V2 is opened, the gas behind the auxiliary piston is released into the atmosphere. With the auxiliary piston moved back, the gas behind the main piston is also released through the drain tube into the atmosphere. Consequently, the operation can be made simply by a snap action. Both operational feasibility and reproducibility of this type of shock tube are quite satisfactory, as previously reported in ref.9.

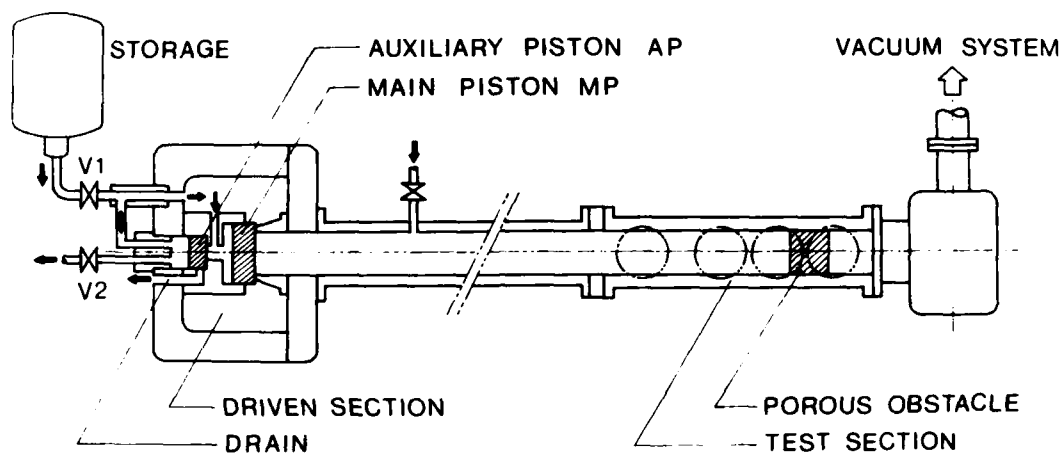


Figure 1. Schematic of the shock tube.

THEORETICAL ASPECT OF THE PROBLEM

So far the surface condensation problem has been analysed from the kinetic approach by many investigators. For simplicity, to clarify the characteristic nature pertinent to the flow induced by surface condensation we consider a steady, one-dimensional flow of the vapor condensing on an infinitely plane interphase. In the initial stage of the analytical study, the cases when the condensation rate is small were analysed on a linearized version. In the cases of weak condensation, the condensation rate increases with difference of the ambient pressure at infinity from the surface pressure. The velocity of the induced flow directed onto the interphase increases with condensation rate. Consequently, the induced flow velocity also increases with pressure difference. This is likely to be valid unless the normal velocity at infinity attains sonic speed. By the non-linear analysis based on the moment method (ref.3), it is found that in increasing the condensation rate the normal velocity eventually attains supersonic beyond the sonic. On the contrary to the subsonic cases, in the supersonic cases the difference of the ambient pressure from the surface decreases with condensation rate. Such large condensation rate, however, is fed by the pressure rise behind the shock wave which necessarily appears in the field ahead of the kinetic region adjacent to the interphase. The kinetic analysis clarifies the detail of the flow structure including the shock wave as well as the kinetic layer.

In the present paper, we concerns with a shock-tube simulation of the continuum version of one-dimensional condensation flow accompanying a shock wave. Suppose that a condensing plane interface is inserted normal to the wall in a shock tube. In the condensable vapor within the shock tube, the incident shock propagates toward the interface and reflects back from the interface. For greater condensation rate, the reflected shock slows down in propagation. If we identify the major effect of condensation on the flow with that due to the suction of the flow at the boundary, the condensing interface may be taken in place by the porous boundary which is enabled to suck the flow. If so, the flow concerned is schematically illustrated as shown in Figure 2; that is, the interface is replaced by a plate with an orifice. If the flow at the orifice is assumed sonic, the quasi one-dimensional analysis leads the relation of the reflected shock Mach number $M_r = u_r/a_2$ to the contraction ratio A^*/A , for fixed flow Mach number $M_2 = u_2/a_2$ and specific heats ratio γ . As for the symbols, u is the flow or shock velocity relative to the wall, a the sonic speed, M the Mach number referred to a_2 , A and A^* the cross section of the shock tube and orifice, respectively, and the subscript 2 refers to quantities pertinent to the flow behind the incident shock. Using the shock and isentropic flow relations, we obtain after some manipulation

$$\frac{A^*}{A} = (M_2^2)^{(\gamma+1)/2(\gamma-1)} G^{1/(\gamma-1)} \left[\frac{(\gamma-1)M^2 + 2}{M\{(\gamma-1)M^2 - (\gamma+1)MM_r\}} \right] \quad (1)$$

where

$$F = \frac{\gamma-1}{\gamma+1} \left[\frac{(\gamma-1)M^2+2}{(\gamma+1)M^2} \left(1 + \frac{M_r}{M_2}\right) - \frac{M_r}{M_2} \right]^2 + \frac{2\{2\gamma M^2 - (\gamma-1)\}\{(\gamma-1)M^2+2\}}{(\gamma+1)^3 M^2 M_2^2}$$

$$G = \frac{(\gamma+1)^{\gamma+1} M^{2\gamma}}{[(\gamma-1)M^2+2]^\gamma [2\gamma M^2 - (\gamma-1)]}$$

and M is the flow Mach number relative to the reflected shock; that is,

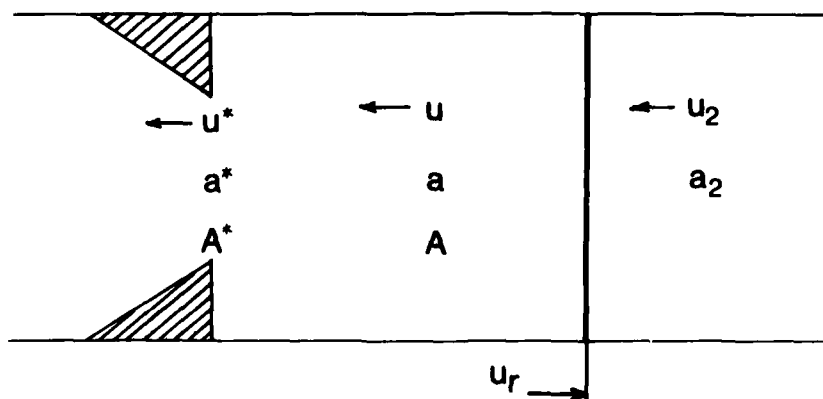


Figure 2. Reflection of the shock wave from an orifice plate.

$$M = (u_2 + u_r)/a_2 = M_2 + M_r$$

For given M_2 and A^*/A for a specific gas, Eq.(1) yields the reflected shock Mach number M_r . From the definition, when $M_r = 0$, the reflected shock is stationary relatively to the wall. For that case, $M = M_2$ and thus A^*/A reduces to a function of M only; that is, Eq.(1) reduces to

$$\frac{A^*}{A} = [(\gamma+1)M^2]^{-(\gamma+1)/2(\gamma-1)} [(\gamma-1)M^2+2]^{1/2} [2\gamma M^2-(\gamma-1)]^{1/(\gamma-1)} \quad (2)$$

This relation is the one previously derived by Lukasiewicz (ref. 10) for the supersonic diffuser problem. The contraction ratio A^*/A given by Eq.(2) is the maximum diffuser contraction permissible for a supersonic nozzle of Mach number M . This situation of the flow corresponds to that of a supersonic condensation flow accompanying a stationary shock wave ahead of the condensing interface. The results of quasi one-dimensional analysis above derived will be compared with the experiment later on.

EXPERIMENTAL RESULTS AND DISCUSSION

The measurements mainly consist of taking a flash shadowgraph and recording the incident shock speed by means of a couple of pressure transducers mounted flush with the tube wall. As previously noted, the shock tube in this experiment has an excellent reproducibility of the shock Mach number from run to run, so that the flash shadowgraph was able to take at any moment desired. According to this characteristics, the reflected shock speed was able to measure from a series of flash shadowgraphs under a fixed incident shock speed. It is noted that the reflected shock speed could not precisely be measured from the records of the pressure gauges mounted at the wall, because the foot of the reflected shock wave is disturbed due to the interaction with the wall boundary layer induced by the incident shock.

In Figure 3 are presented the data obtained by the measurements mentioned above, for the cases of comparatively larger contraction, say $A^*/A = 0.18, 0.31, 0.57$. The incident shock Mach number M_s is about 3.0 and the test gas is nitrogen. In this figure, x is measured toward upstream from the end wall and t_r the time from the instant when the incident shock has just arrived at the end wall. As can be seen from the figure, the speeds of the reflected shock wave are nearly constant during propagation toward upstream for a fixed contraction. Also a typical example of shadowgraph is shown in Figure 4.

In this experiment, our attention is focused on the cases of much smaller contraction; for example, $A^*/A = 0.85$ and 0.93 . For such smaller contractions, the geometries of the contraction were chosen from a view point of structural tolerance. The schematic of the contractions are shown in Figure 5. The similar experiments were conducted for these contractions. As an example, for $A^*/A = 0.93$, a series of shadowgraphs are shown in Figure 6 for $M_s = 3.0$ and 3.7 . It is worthwhile noting that the reflected shock is nearly plane except the foot near the wall, despite the two dimensional geometry of the contraction. Furthermore, it can be seen that the reflected shock speed very much slows down and,

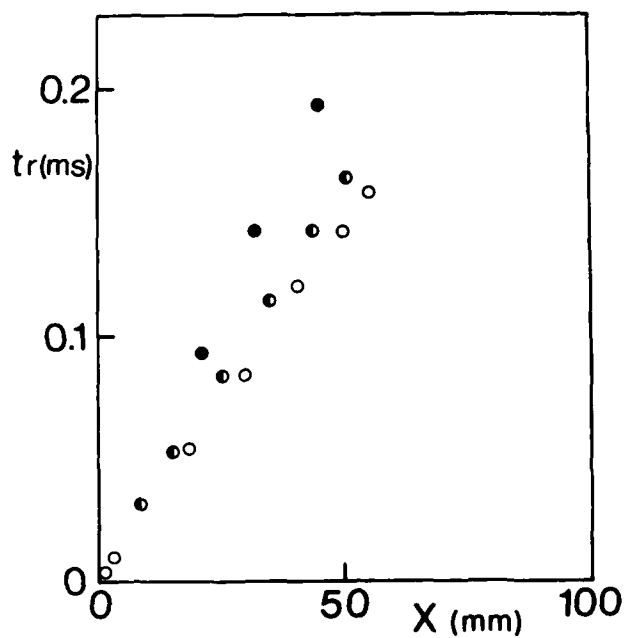
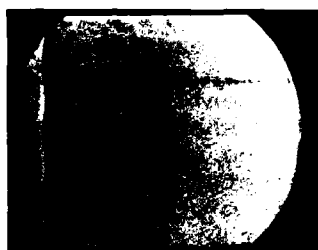


Figure 3. Propagation of reflected shock wave.

- $A^*/A = 0.18$
- ◐ $A^*/A = 0.31$
- $A^*/A = 0.57$



$t_r = 12 \mu s$



$t_r = 52 \mu s$



$t_r = 142 \mu s$

Figure 4. A series of shadowgraphs.

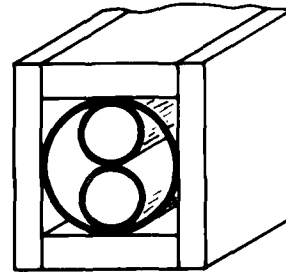
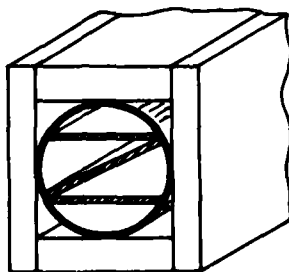
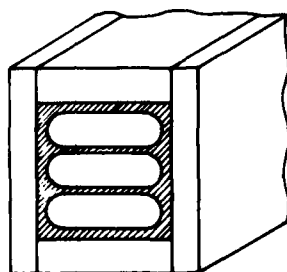
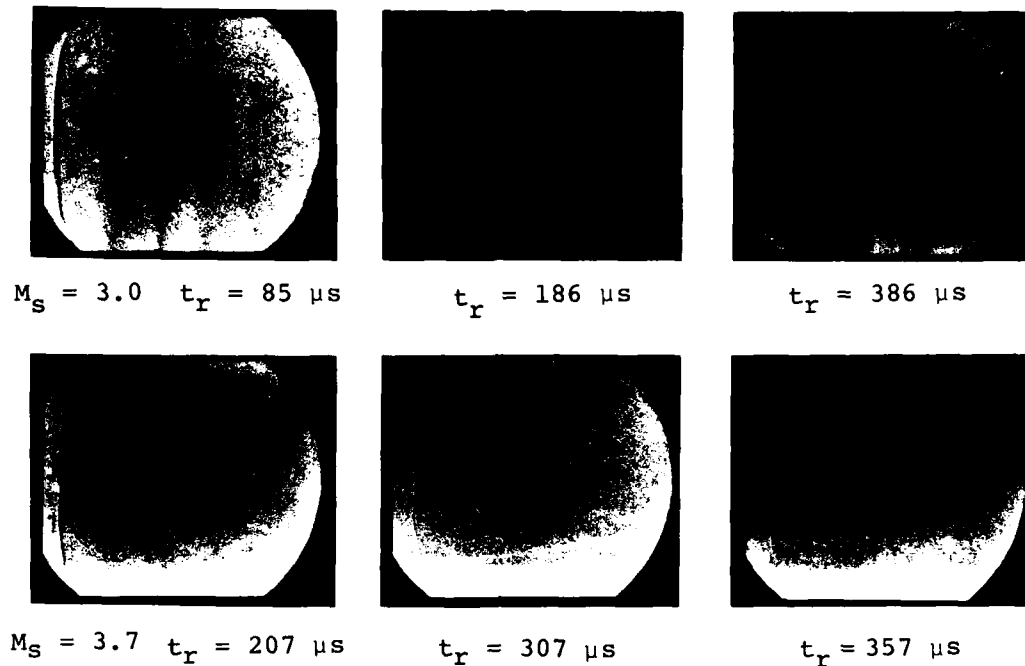
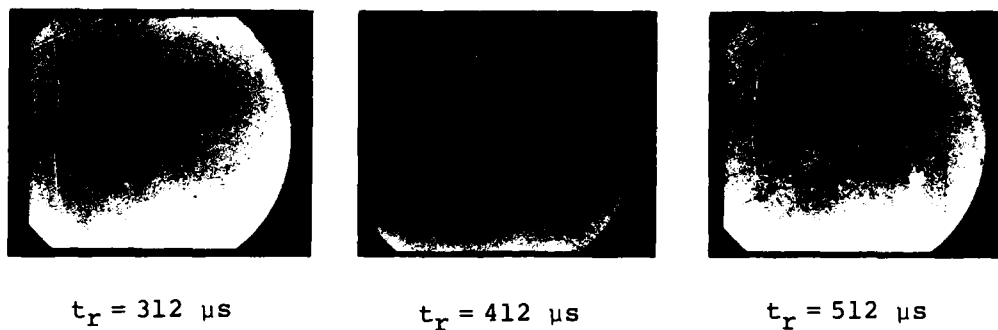


Figure 5. Various geometries of contraction.

Figure 6. Reflection of the shock wave for $A^*/A = 0.93$, N_2 .Figure 7. Stationary reflected shock wave for $M_s = 3.9$, $A^*/A = 0.93$, N_2 .

especially, for the case of $M_s = 3.9$ the reflected shock may be regarded as nearly stationary relative to the wall (see Figure 7). This situation resembles that of the supersonic condensation flow accompanying a stationary shock wave ahead of the interphase, upon which all the mass of incoming flow is condensed. The situation can also be regarded as that of the supersonic nozzle flow ahead of the maximum contraction diffuser.

To examine how the geometry of contraction does affect on the propagation and formation of the reflected shock, two other geometries of $A^*/A = 0.93$ were tested. From comparison with these, it can be seen that the difference in geometry provides no appreciable difference in the propagation speed of the reflected shock wave, while there appears somewhat difference in the time needed to establish a plane reflected shock.

All of the data shown above are pertinent to the case of

N_2 as the test gas. The similar experiment has also been conducted for the case of CO_2 as the test gas. The Mach number of reflected shock is plotted against the incident shock Mach numbers in Figures 8 and 9, respectively, for N_2 and CO_2 . In these figures, the full lines indicate the results from Eq.(1), which is derived from quasi one-dimensional analysis. The agreement of the experiment is remarkable. From this fact the assumption of quasi one-dimensionality is likely to be assured in application to the present shock tube problem.

Finally, we note from the shadowgraphs for the case of much smaller contraction $A^*/A = 0.95$ that in either case of N_2 and CO_2 the shock propagating toward upstream disappears as if the shock is swallowed toward the contraction, in other words, the supersonic flow starts throughout the tube ahead of the contraction. From this fact it can be said that the shock wave disappears for the contraction below the critical, for which only the stationary shock wave can exist. In simulation to the condensation problem, we may conclude that the shock wave disappears even in supersonic condensation for the stronger condensation rate beyond the critical, for which the stationary shock wave can exist ahead of the interface.

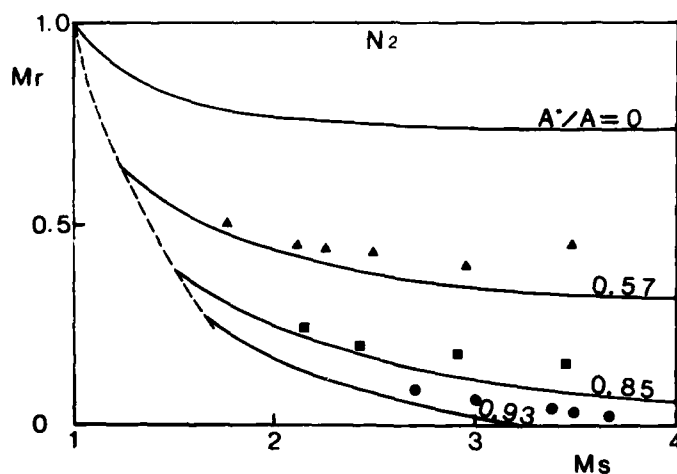


Figure 8.
 M_r versus M_s for various A^*/A ; full lines from simple wave theory Eq.(1) for N_2 .

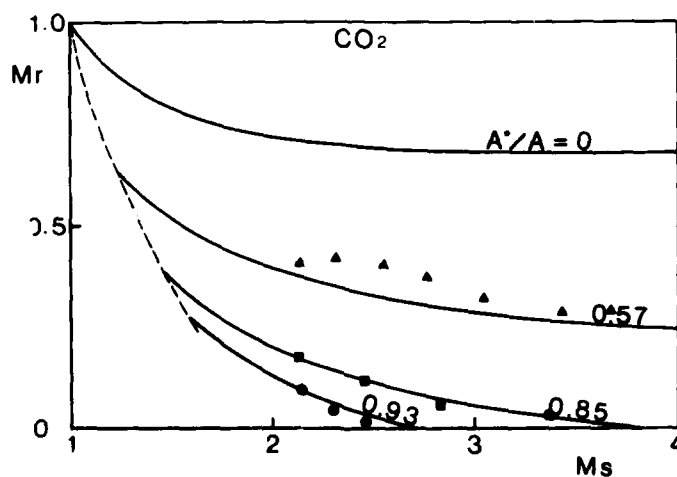


Figure 9.
 M_r versus M_s for various A^*/A ; full lines from simple wave theory Eq.(1) for CO_2 .

References

1. M. N. Kogan and N. K. Makashev, *Fluid Dynamics*, 6, 913 (1974).
2. M. Hatakeyama and H. Oguchi, in "Rarefied Gas Dynamics", Vol.2, ed. by R. Campargue, Commissariat A L'energie Atomique, Paris, p. 1293 (1979).
3. H. Oguchi and M. Hatakeyama, Proceedings of 12th International Symposium on Rarefied Gas Dynamics, "Rarefied Gas Dynamics", ed. by S. Fisher, AIAA, New York (1981) (to be published).
4. K. O. Tong, C. J. Knight and B. N. Srivastava, *AIAA Journal*, 18, 1298 (1980).
5. J. E. Bowman and G. B. F. Niblett, *Proc. Phys. Soc., Sec. B*, 68, 1003 (1955).
6. D. S. Dosanjh, NACA TN 3680 (1956).
7. W. G. Cornell, *Trans. American Soc. Mech. Eng.*, 80, 791 (1958).
8. H. Oguchi, K. Funabiki and S. Sato, Proceedings of the 10th International Shock Tube Symposium, p. 386 (1975).
9. K. Maeno and H. Oguchi, *J. de Physique*, 41, Colloque C9, C9 (1980).
10. J. Lukasiewicz, *J. Aero. Sci.*, 20, 617 (1953).

AD P000297

EXPERIMENTS IN SHOCK LIQUEFACTION

G. Dettleff^{*)}, G.E.A. Meier^{**)} and H.-D. Speckmann^{**) ,}
P.A. Thompson^{***)} and C. Yoon^{***)}

^{*)} Present address: DFVLR-AVA Göttingen, Bunsenstr. 10,
D-3400 Göttingen, FRG

^{**)} Max-Planck-Institut für Strömungsforschung, Böttinger Str. 4-8,
D-3400 Göttingen, FRG

^{***)} Rensselaer Polytechnic Institute, Troy, N.Y. 12181, USA

The liquefaction shock wave, a compression shock which converts vapour into liquid, has been experimentally produced as the reflected shock at the closed end of a shock tube in test fluids with many molecular degrees of freedom. Measurements of pressure, temperature, index of refraction and shock velocity confirm the existence of the shock and its general conformity to classical Rankine-Hugoniot conditions, [1] - [5].

Normal and stereoscopic photography confirms the existence of a clear liquid phase and reveals small two-phase torus-form vortex rings, which are formed in or near the shockfront and move in the same direction as, but less rapidly than the shock wave, i.e., the rings move away from the closed end of the shock tube.

If the fluid behind the shock is a mixture of droplets and vapour (partial liquefaction) evidence of shock splitting at the phase boundary is found, i.e. the shock consists of a system of two diverging compression waves.

INTRODUCTION

The liquefaction shock is a shock compression (produced, for example, in a shock tube), in which the upstream state of the test fluid is gaseous and the downstream state is liquid.

Contrary to the well-known condensation shock in expanding gas flows, the state behind the liquefaction shock can be fully wet, i.e. all inflowing gas will completely condense.

The physical background of this new phenomenon [1] is the condensation behaviour of retrograde gases (Fig.1). The isentropic compression of the gas or saturated vapour of a regular fluid (air, water) will not change the gaseous state of aggregation (a). In the case of a retrograde fluid with its different shape of the

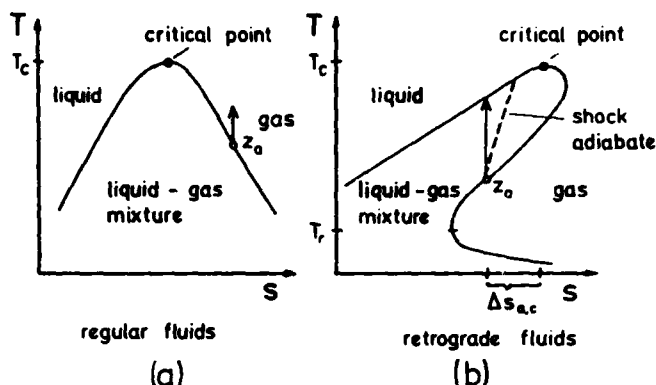


Figure 1. Temperature - entropy diagramme for regular (a) and retrograde (b) fluids.

saturation line in a temperature - entropy diagramme (b) the isentropic compression of a gas can lead to a mixture or liquid state. An essential difference between a regular and a retrograde fluid is the ability of retrograde liquids to store the released heat of vapourisation.

A shock compression with an associated entropy increase $\Delta s < \Delta s_{a,c}$ (Fig.1b) can accomplish the phase transition if the ideal-gas^c heat capacity c_v^o exceeds a limiting value: $c_v^o \geq 40 \cdot R$, where R is the universal gas constant. This has been shown theoretically by Thompson and Sullivan in 1975 [1].

In a following study Dettleff, Thompson, Meier, and Speckmann [2] showed that the shock liquefaction can be verified experimentally in a shock tube. The initial state 0 of the test fluid (Fig.2) and the Mach number M_s of the incident shock wave (I) were coordinated such that partial or complete liquefaction occurred behind the reflected shock wave (R) in the state 2.

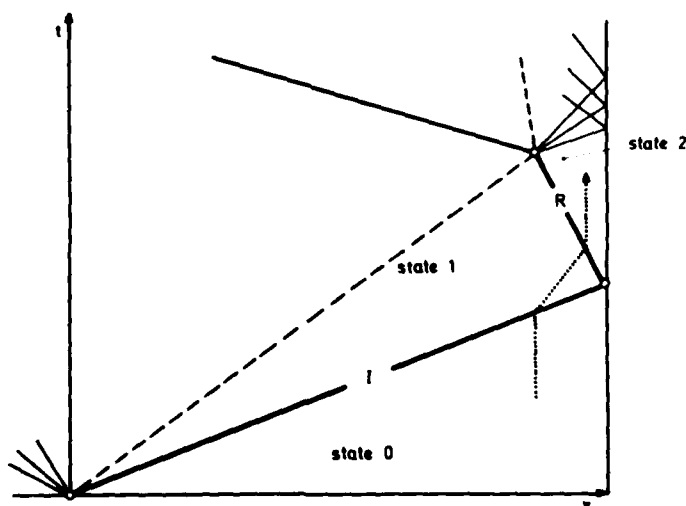


Figure 2. Schematic x-t diagram for the shock tube flow (test section).

Measurements of the shock velocity, pressure, temperature, and density in the state 2 were performed, using C₈F₁₆ (ISC designation PP3) in most cases as test fluid. The results of pressure and temperature measurements are shown in Fig.3.

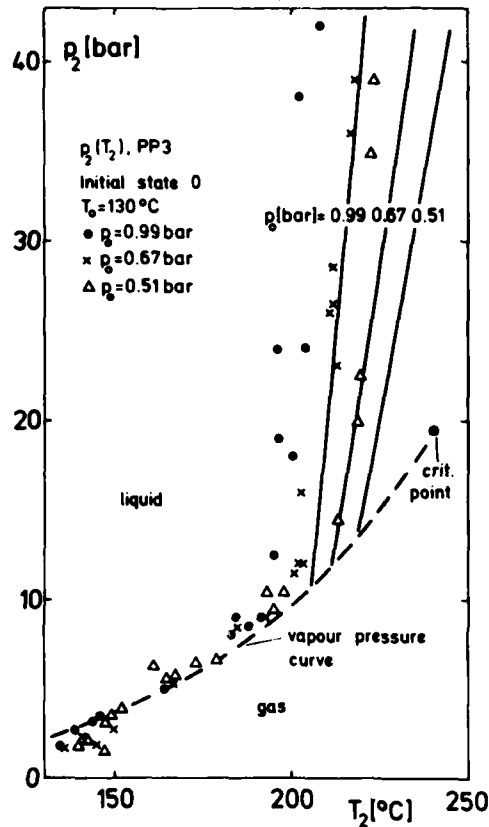


Figure 3. Results of pressure and temperature measurements behind the liquefaction shock wave, state 2. Theoretical curves calculated by [3].

The initial state 0 of the test fluid is unchanged while the Mach number M_s of the incident shock is increased leading to states 2 of partial and complete liquefaction behind the reflected shock.

More experimental results have been published in [2],[4],[5].

PHOTOGRAPHIC OBSERVATIONS

The present subject of investigation is the structure of the shock front where the phase transition takes place. Photographic observations of the liquefaction region between the reflected shock and the end wall of the test section show that the complete liquefaction is associated with the production of small rings (Fig.4). Detailed observations, especially by means of stereoscopic photography show that the smaller rings (with a diameter smaller than approximately 1 mm) are concentrated in a layer of about 1 - 2 mm thickness in or immediately behind the shock front. A few of them are left behind in the liquid between the endwall of the tube and the reflected shock, increasing in diameter. In Fig.5 the relation between the ring diameter and the distance Δx (distance ring-shock front) is shown. By means of the double-flash technique, the movement of these larger rings

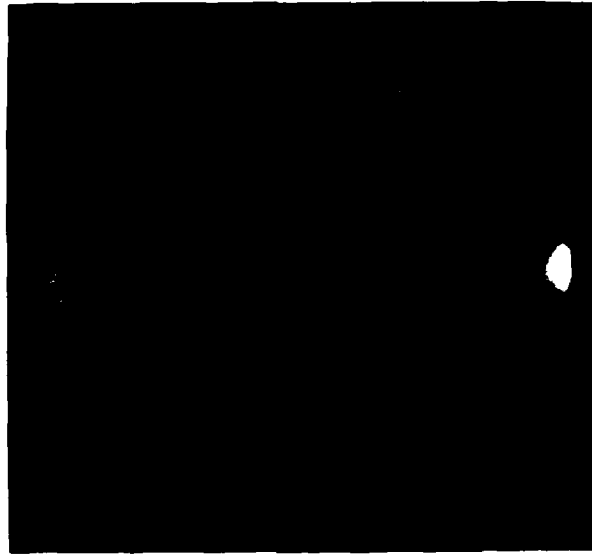


Figure 4. Photographic observation of the liquefaction region. PP3, $T_0 = 130^\circ\text{C}$, $p_0 = 0.67$ bar, $M_s = 2.4$, 0.55 ms after reflection, diameter of the window 50 mm. View direction see Figure 5.

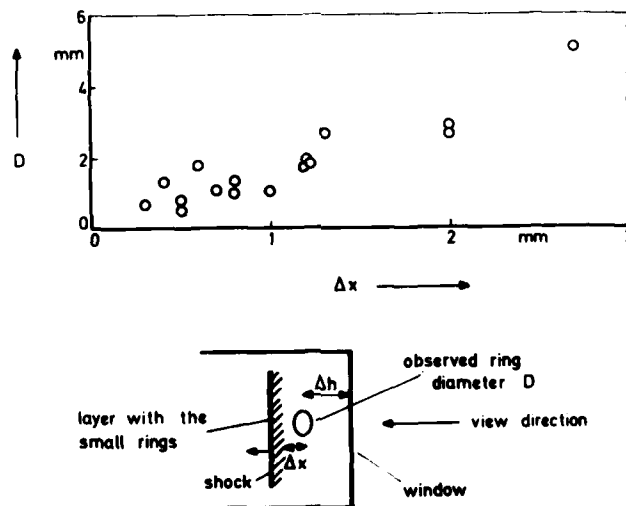


Figure 5. Spatial distribution of the rings in the liquefaction region. Relation between the ring diameter D and the distance Δx (ring-shock front).

has been observed. They move in the same direction as the reflected shock but their velocity v_T is smaller and depends strongly on the ring diameter D (Fig. 6).

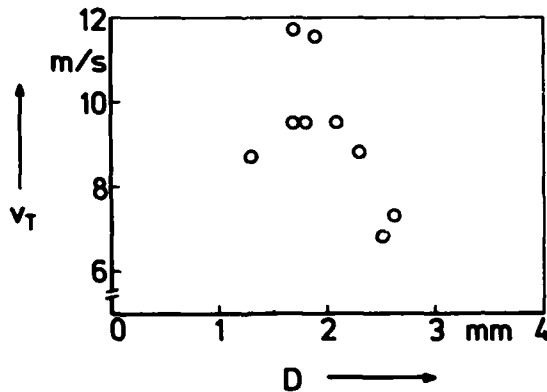


Figure 6. Translational velocity v_T of the rings in dependence on the ring diameter D .

The observed kinematic behaviour of the larger rings suggests that they are vortex rings, the core being the visible white torus which we assume is filled with a mixture of gas and liquid. The measured quantities allow an estimate of the circulation Γ of the vortices:

$$\Gamma = \frac{2\pi \cdot v_T \cdot D}{\ln \frac{4D}{d_t}}$$

$$\approx 0.05 \frac{\text{m}^2}{\text{s}}$$

with d_t the core diameter. The above equation is strictly valid only for $d_t/D \ll 1$ [6]. This estimate agrees very well with another [2] with different assumptions concerning the pressure distribution inside and outside the vortex core.

SHOCK INSTABILITY

An inherent property of retrograde fluids is that the isentrope in a pressure-volume diagram passes through the mixture region and that the isentrope has a discontinuity in slope where it intersects the saturation line (Fig. 7). This deflection can cause an instability of the shock wave when it lies between the upstream and downstream state of the shock compression [1].

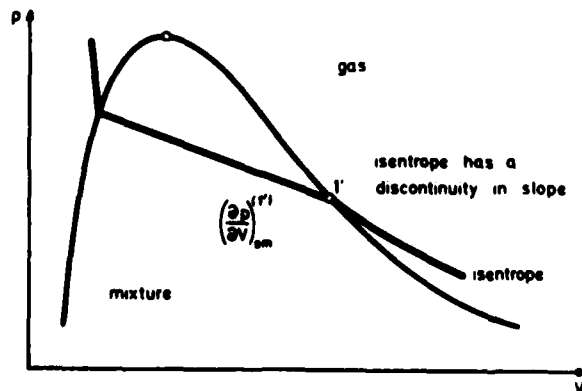
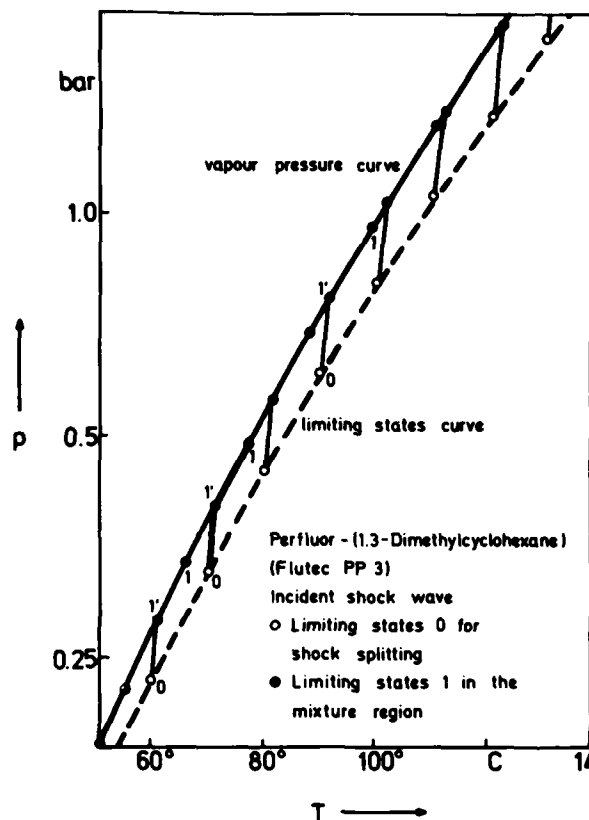


Figure 7. Pressure-volume diagram of a retrograde fluid with discontinuity in the slope of the isentrope at the phase boundary.

We have checked the behaviour of the liquefaction shock wave at the phase boundary and found that shock splitting can occur. It is assumed that the intermediate state 1' (Fig.7) at the phase boundary is known. Then from the known slope $(\partial p / \partial V)^{(1')}_{sm}$ of the isentrope at the phase boundary in the mixture and from the shock adiabat the limiting upstream state 0 and downstream state 1 for which shock splitting is possible can be determined. In Fig.8 the results of the calculation of limiting

states for the incident shock wave are shown.



First experiments have been performed to verify the theoretically predicted shock splitting. Using a laser beam perpendicular to the tube axis (Fig.9) two waves have been detected. We found that the fluid in the state between the two shocks allows the transmission of the light while the intensity decreases behind the second wave indicating the presence of a gas-liquid mixture. Obviously the phase transition takes place within the front of the second wave.

Figure 8. Limiting states for shock splitting, (incident shock) in PP3.

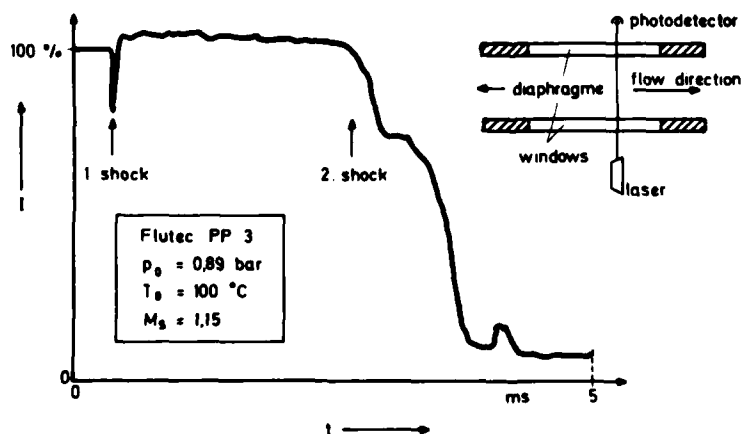


Figure 9. Splitting of the incident shock in PP3. Measurement of the transmitted light intensity I .

In the case of the reflected shock we found that the intensity histories show the same qualitative behaviour. Pressure measurements show that two compression waves can be reflected when the phase boundary is between the upstream and downstream state (Fig.10). When the Mach number of the incident wave is changed (initial state 0 fixed) the pressure of the intermediate state is almost invariable. With increasing Mach number the first pressure jump decreases and the second increases. The first compression wave is steep while the second has a thickness of about 1 mm. We are aware that bifurcation of the reflected

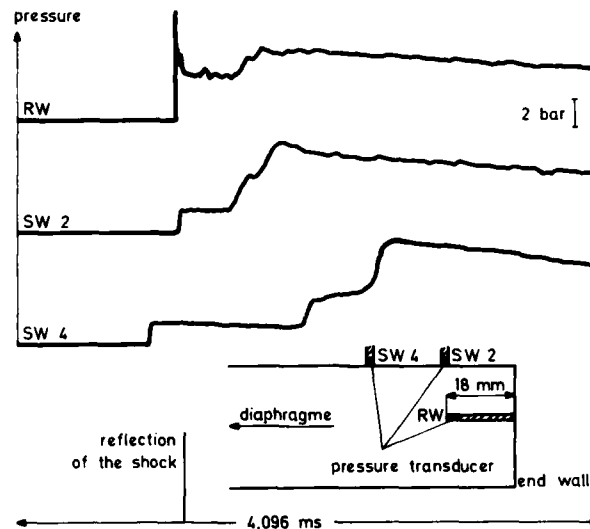


Figure 10. Pressure history of the reflected shock. Partial liquefaction in state 2. Phase boundary lies between upstream and downstream state. PP3, $T_0 = 130^\circ\text{C}$, $p_0 = 0.7\text{ bar}$, $M_s = 1.65$.

shock due to boundary layer interaction must be expected [7]. But two pressure jumps have also been observed on the axis of the tube, detected by means of a pressure transducer which has been introduced through the endwall. They occur at the same time as those detected at the wall (position SW2). If the Mach number is decreased and the downstream state becomes gaseous only one reflected wave is observed, though bifurcation should still occur.

Under conditions where shock splitting can be expected, a laser beam which is reflected from the inner side of the window in the end wall shows intensity oscillations immediately after the reflection of the shock (Fig.11). Outside of the expected shock splitting region (gaseous state 2) they are not detected. We conclude that the intensity oscillations are due to density oscillations behind the reflected shock.

The oscillations do only occur shortly after the reflection. This could be an indication of the establishment of a split shock system (the incident wave is stable) though a clear physical reason is not yet obvious.

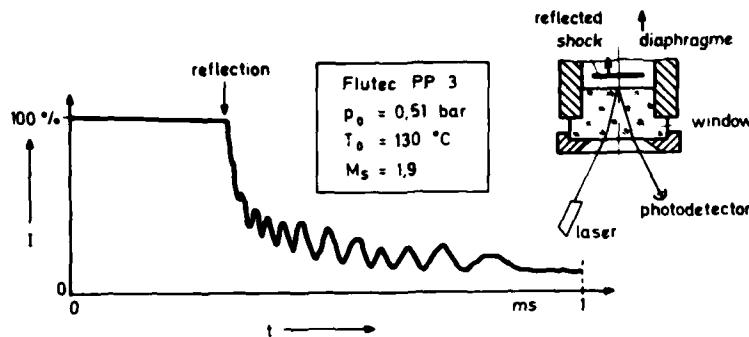


Figure 11. Measurement of the reflected light intensity. Partial liquefaction in state 2. Phase boundary lies between upstream and downstream state.

CONCLUSION

Summarizing, it can be stated that shock splitting of liquefaction shock waves is evident. The stereoscopic investigation shows that the observed rings are produced in a shock front of about 1 mm thickness and that their behaviour coincides with that of vortex rings.

References

- [1] P. A. Thompson and D. A. Sullivan, "On the possibility of complete condensation shock waves in retrograde fluids." *J. Fluid Mech.*, **70**, 639-649 (1975).
- [2] G. Dettleff, P. A. Thompson, G. E. A. Meier, H.-D. Speckmann, "An experimental study of liquefaction shock waves." *J. Fluid Mech.*, Vol. 95, Part 2, 279-304 (1979).
- [3] D. A. Sullivan, "Computer subroutines for the computation of thermodynamic properties and processes." Max-Planck-Institut für Strömungsforschung, Bericht 110 (1977).
- [4] G. Dettleff, "Experimente zum Nachweis der Verflüssigungsschlagwelle in retrograden Gasen." Dissertation, Georg-August-Universität Göttingen (1978).
- [5] H.-D. Speckmann, "Spontane Kondensation retrograder Gase durch Verdichtungsstöße." Diplomarbeit, Georg-August-Universität Göttingen (1978).
- [6] D. W. Sallet and K. Kraemer, "Translational velocity of vortex rings." 50 Jahre Max-Planck-Institut für Strömungsforschung, Göttingen (1975).
- [7] M. Honda, K. Takayama, O. Onodera, Y. Kohama, "Motion of reflected shock waves in shock tube." In: *Modern Developments in Shock Tube Research* (ed. G. Kamimoto), Shock Tube Research Society, Japan (1975).

AD P000298

SHOCK PROPAGATION IN LIQUID-GAS MEDIA

T. Fujiwara and T. Hasegawa

Department of Aeronautical Engineering
Nagoya University, Nagoya 464, Japan

Shock wave propagation in bubbled liquids is studied from experimental and theoretical points of view. The third-order partial differential equation derived through acoustic approximation is used to analyse subsequent behaviors of initially semi-infinite-step or square pressure pulses. The solutions are obtained in closed forms using the Laplace transformation.

The 7.5 to 15 atm He or N₂ is used to generate a shock wave in an initially atomospheric liquid-bubble system, where nitrogen, Ar, He, Ar-diluted oxyhydrogen or stoichiometric oxyhydrogen bubbles of about 4 to 10 mm dia. are introduced into water or glycerin liquid. Attenuation or dispersion of the shock wave is observed by pressure transducers, whereas the motion of a bubble is visualized using a high-speed framing camera. The motion is monitored during its several-cycle oscillation corresponding to the 1.5 msec duration of the light source and the framing speed 100,000 f/sec. In glycerin the top of the bubble quickly becomes flat when the bubble diameter exceeds minimum during the first compression-expansion oscillation. This flattened top remains unchanged in the later processes while the bottom of the bubble stretches, its lower half elongated, and finally the bubble splits into a larger and a smaller ones. The attenuation of the oscillation is found faster in glycerin than in water. The above-mentioned deformation is not observed in water where oscillation is in good agreement with the theoretical analysis until the complete breakup of the bubble into many fine ones is triggered by the start of Rayleigh-Taylor instability. Ar-diluted oxyhydrogen bubbles in glycerin at $p_4 = 15$ atm are the only ones successful to indicate the reaction during the maximum bubble compression.

INTRODUCTION

Shock propagation and associated bubble motion in a bubbled liquid have been studied by several workers, from the viewpoint of water hammer action of a shock wave (refs. 1,2), where attention has been focused on the propagation velocity and structure of the shock wave. On the other hand, the individual behaviors of a bubble have been analysed in the field of cavitation and explosives. In connection with the mechanism of detonation propagation in

porous condensed explosives, several different possibilities are proposed to explain the formation of heterogeneous hot spots during the passage of front shock wave (ref. 3); adiabatic compression, shock wave formation due to the compression of porous pockets or bubbles (ref. 4), formation of micro jets in a bubble caused by large pressure difference at the interface between condensed substance and gas, etc.

In this study, the behavior of a bubble after being compressed by a propagating shock wave is observed in a shock tube filled with a liquid: The bubble gas species, the liquid materials and the pressure ratio p_4/p_1 are changed in order to observe their influences on the motion of the bubble.

The observed results are compared with a theoretical prediction taking account of liquid viscosity and nonlinear bubble oscillation under the influence of several different temporal pressure profiles.

The influence of the bubble exothermicity is observed using stoichiometric and Ar-diluted oxyhydrogen mixtures and compared with inert bubbles.

The acoustic approximation is applied to a weak shock wave propagating in a bubbled liquid to yield the solution in a closed form. The propagation and dispersion of the shock wave are shown for the two initial conditions: step-shaped and square-shaped pressure pulses.

ACOUSTIC THEORY OF SHOCK PROPAGATION IN BUBBLED LIQUIDS

One-dimensional propagation of pressure waves in a liquid with homogeneously distributed gas bubbles can be analysed taking account of heat transfer between the bubbles and the surrounding liquid. This problem has already been analysed considering such heat transfer and additionally the viscous effect caused by the relative motion between a bubble and a liquid, where the dispersion relation is shown (ref. 5) and a qualitative description is given to the wave propagation when a step-shaped pressure profile is applied initially (ref. 6).

Assuming that (i) the relative motion between a bubble and a liquid, the scattering of sound waves, the mass transfer, the deformation and oscillation of a bubble, the surface tension and the gravity are neglected, (ii) the temperature of the liquid remains unchanged due to its large heat capacity, and (iii) the gas is perfect and the temperature in a bubble is uniform, the acoustic approximation of flow equations leads to the final form

$$\frac{\partial}{\partial t} \left(\frac{1}{a_{ad}^2} \frac{\partial^2 p}{\partial t^2} - \frac{\partial^2 p}{\partial x^2} \right) + \frac{1}{\tau_0} \left(\frac{1}{a_e^2} \frac{\partial^2 p}{\partial t^2} - \frac{\partial^2 p}{\partial x^2} \right) = 0, \quad (1)$$

$$\tau_0 = \frac{1 - \beta_0 + \gamma \beta_0}{\gamma} \frac{d_0^2}{Nu \alpha_g}, \quad \gamma = \frac{C_{p2}}{C_{p1}}, \quad \alpha_g = \frac{k_g}{\rho_{g0} C_{p1}}, \quad (2)$$

$$a_{ad}^2 = \frac{(1 - \beta_0 + \gamma \beta_0) \rho_{g0}}{\rho_0 \left(\frac{\beta_0}{R^* T_{g0}} + \frac{\rho_{g0}}{\rho_{l0}} \frac{1 - \beta_0}{a_f^2} \right)}, \quad d_0 = \text{bubble diameter}, \quad (3)$$

$$a_e^2 = \frac{\rho_{g0}}{\rho_0 \left(\frac{\beta_0}{R^* T_{g0}} + \frac{\rho_{g0}}{\rho_{l0}} \frac{1 - \beta_0}{a_f^2} \right)}, \quad (4)$$

where τ_0 indicates the characteristic time of heat transfer, a_{ad} and a_e the adiabatic and isothermal sound velocities, γ the specific heat ratio, and α_g the thermal diffusivity. β_0 denotes the void fraction, $Nu = d_0 q / k_g (T_g - T_l)$ the Nusselt number, q the heat flux through bubble surface, ρ_{g0} and ρ_{l0} the initial mass densities of gas and liquid, $\rho_0 = \beta_0 \rho_{g0} + (1 - \beta_0) \rho_{l0}$, R^* the gas const, T_{g0} the initial gas temperature and a_f the sound velocity of liquid.

It is noted that Eq.(1) is identical with the wave equation for a gas undergoing chemical reactions or relaxation of internal degrees of freedom, where an asymptotic solution is obtained for an initially step-shaped pressure pulse (ref. 7). Eq.(1) gives the following equation for a wave propagating to the positive direction of x (ref. 8):

$$\frac{\partial}{\partial t} \left(\frac{1}{a_{ad}} \frac{\partial p}{\partial t} + \frac{\partial p}{\partial x} \right) + \frac{1}{\tau_0} \left(\frac{1}{a_e} \frac{\partial p}{\partial t} + \frac{\partial p}{\partial x} \right) = 0, \quad (5)$$

which provides the exact solutions using the Laplace transformation:

(a) Initial condition; step-shaped pressure pulse. The exact solution is

$$p(x, t) = \Delta p_0 \exp \left[-\frac{x}{a_{ad} \tau_0} \left(\frac{a_{ad}}{a_e} - 1 \right) \right] \times \left\{ E \left(t - \frac{x}{a_{ad}} \right) + \int_0^{t - \frac{x}{a_{ad}}} e^{-\frac{\xi}{\tau_0} \sqrt{\frac{A x}{\xi}}} I_1 \left(2 \sqrt{A x \xi} \right) d\xi \right\}, \quad (6)$$

$A = \left(\frac{a_{ad}}{a_e} - 1 \right) / a_{ad} \tau_0^2$, $E(t)$ =step function, $I(x)$ =modified Bessel.

(b) Initial condition; square-shaped pressure pulse. The exact solution is

$$p(x, t) = \Delta p_0 \exp \left[-\frac{x}{a_{ad} \tau_0} \left(\frac{a_{ad}}{a_e} - 1 \right) \right] \times \left\{ \left[E \left(t - \frac{x}{a_{ad}} \right) + \int_0^{t - \frac{x}{a_{ad}}} e^{-\frac{\xi}{\tau_0} \sqrt{\frac{A x}{\xi}}} I_1 \left(2 \sqrt{A x \xi} \right) d\xi \right] + \left[E \left(t - t_w - \frac{x}{a_{ad}} \right) + \int_0^{t - t_w - \frac{x}{a_{ad}}} e^{-\frac{\xi}{\tau_0} \sqrt{\frac{A x}{\xi}}} I_1 \left(2 \sqrt{A x \xi} \right) d\xi \right] \right\} \quad (7)$$

The two solutions (6) and (7) are illustrated for a air-water system in Figs.1 and 2. In Case (a) a nearly step-shaped wave head propagates during $t \leq \tau_0$ with the adiabatic sound velocity a_{ad} . At $t > \tau_0$, the wave front becomes attenuated and the effect of dispersion clearly emerges. At $t = 50 \tau_0$, the

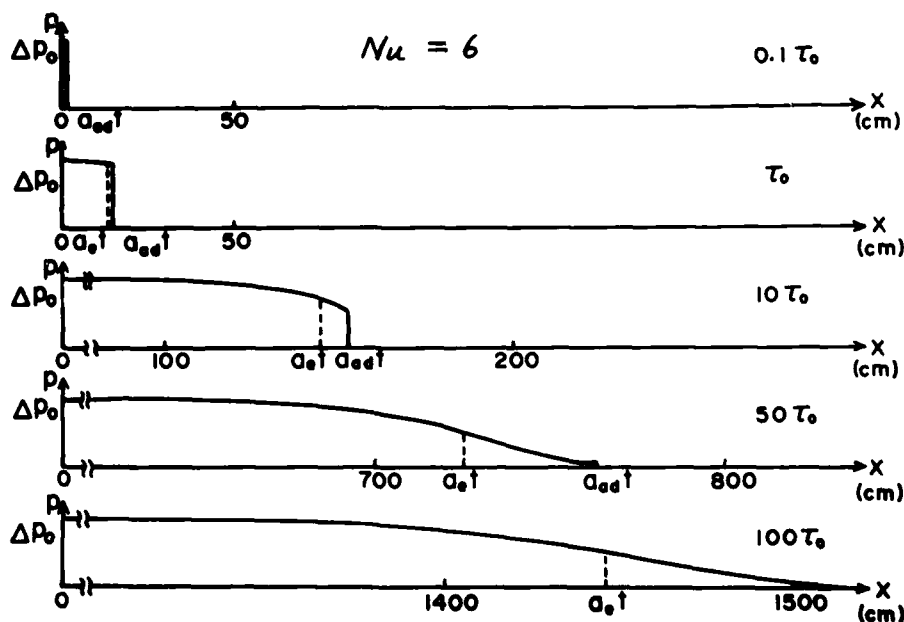


Fig.1 Case (a) Initial condition; step-shaped pressure pulse. Evolution of the pressure profile is shown for the parameters; $p_0 = 1$ atm, $T_0 = 300$ K, $\beta_0 = 0.3$, $d_0 = 1$ mm, $a_{ad} = 23.3$ m/sec, $a_e = 22.0$ m/sec, $\tau_0 = 6.75$ ms.

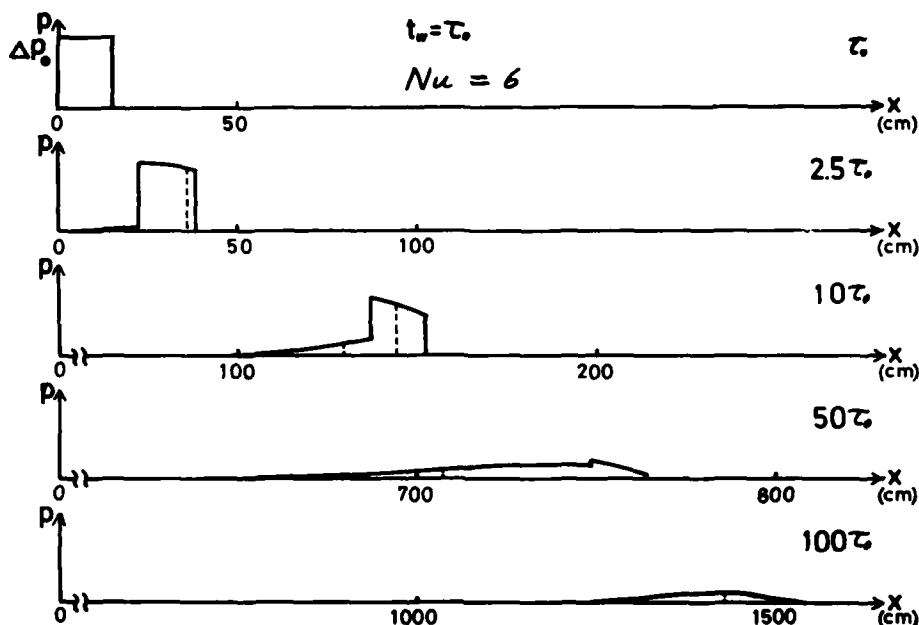


Fig.2 Case (b) Initial condition; square-shaped pressure pulse. Evolution of the pressure profile is shown for the parameters; $p_0=1$ atm, $T_0=300$ K, $\beta_0=0.3$, $d_0=1$ mm, $a_{ad}=23.3$ m/sec, $a_e=22.0$ m/sec, $\tau_0=6.75$ msec, $t_w=\tau_0$.

complete dispersion prevails.

ANALYSIS OF BUBBLE OSCILLATION

Assuming that the interbubble distance is sufficiently large, the motion of a bubble caused by the interaction with an incident shock wave is treated independently. The following simplifications are made: (i) The gas in the bubble is thermodynamically uniform, obeying the perfect gas law. (ii) The temperature of the liquid is unchanged, while the viscosity of the liquid is taken into account. (iii) The heat transfer through gas-liquid interface is retained in the formulation while the mass transfer, typically evaporation, condensation and dissolution are neglected. Then the motion of a spherical bubble of radius R is governed by

$$\text{Mass: } \frac{d}{dt} \left(\rho_g \frac{4}{3} \pi R^3 \right) = 0, \quad (8)$$

$$\text{Momentum (ref.9): } R \frac{d^2 R}{dt^2} + \frac{3}{2} \left(\frac{dR}{dt} \right)^2 + 4\nu \frac{1}{R} \frac{dR}{dt} = \frac{p_g - p_\infty}{\rho_l}, \quad (9)$$

$$\text{Energy: } \frac{d}{dt} \left(\rho_g \frac{4}{3} \pi R^3 C_g T_g \right) = - \frac{Nu k_g (T_g - T_l)}{2R} 4\pi R^2 - \left(p_g - \frac{4\mu}{R} \frac{dR}{dt} \right) \frac{d}{dt} \left(\frac{4}{3} \pi R^3 \right), \quad (10)$$

where ν denotes the kinematic viscosity of the liquid. After some manipulations, these equations can be reduced to the following in dimensionless forms:

$$\frac{d^2 \tilde{R}}{d\tilde{t}^2} = - \frac{3}{2} \frac{1}{\tilde{R}} \left(\frac{d\tilde{R}}{d\tilde{t}} \right)^2 - \frac{1}{Re} \frac{1}{\tilde{R}^2} \frac{d\tilde{R}}{d\tilde{t}} - \frac{1}{M^2} \frac{\tilde{p}_\infty - \tilde{p}_g}{\tilde{R}}, \quad (11)$$

$$\frac{d\tilde{T}_g}{d\tilde{t}} = - \frac{3}{2} \gamma \frac{Nu}{Re} (\tilde{T}_g - 1) \tilde{R} - 3(\gamma - 1) \tilde{p}_g \tilde{R}^2 \frac{d\tilde{R}}{d\tilde{t}} + 12 \frac{\nu}{C_g T_{g0} t_0} \tilde{R} \left(\frac{d\tilde{R}}{d\tilde{t}} \right)^2, \quad (12)$$

$$Re = \frac{R_0^2}{4\nu t_0}, \quad M^2 = \frac{R_0^2}{t_0^2 \rho_0 / \rho_g}, \quad \tilde{p}_g = \frac{\rho_g C_g R_0^2}{t_0 k_g}, \quad \tilde{t} = \frac{t}{t_0}, \quad \tilde{R} = \frac{R}{R_0}. \quad (13)$$

Eqs. (11) and (12), together with Eq. (8) and the equation of state, are utilized to solve \hat{R} , \hat{T}_2 , \hat{P}_2 and $\hat{\rho}_2$. Temporal behaviors of the radius, temperature, pressure and density of the bubble can be calculated if the far-field pressure \hat{P}_{∞} in the liquid is prescribed a priori. However an experimentally observed bubble is under strong confinement in a shock tube, and accordingly such far-field pressure can not be obtained in reality. Instead, the pressure measured in the same plane as the window for bubble observation is interpreted as \hat{P}_{∞} .

EXPERIMENTAL

As illustrated in Fig. 3, the present vertical shock tube consists of a 44.5-cm-long driver section separated by plastic diaphragms from a 154-cm-long test part with 50 mm x 50 mm square cross section. In the test tube either pure water or glycerin is filled up to 70 cm below the diaphragms, while the remaining volume filled with atmospheric air. The selected pressures in the driver section are twofold, 7.5 and 15 atm, using either nitrogen or helium. The lower end of the test tube is equipped with a 0.8 mm i.d. syringe in order to produce a column of bubbles from a vessel pressurized up to 2 - 3 atm. Shock tube firing is made in synchronization with the signal of steady bubble formation. The arrival of a shock wave and the oscillatory pressure behaviors caused by the motion of bubbles are measured using the two Kistler 601A pressure transducers mounted in the same cross section as the observation window. The motion of a bubble is observed with high temporal resolution using a high-speed framing camera Nikon-Uemura Type at about 100,000 f/sec and a Xenon flash lamp with a duration 1.2 msec. In order to study the influence of internal degrees of freedom and exothermicity on the amplitude of oscillation, instability of the bubble and extent of maximum compression, the bubble gas species are changed among nitrogen, Ar, He, stoichiometric and Ar-diluted oxyhydrogen.

(i) Shock propagation in pure liquid: As shown in Fig. 4, substantial decrease of shock propagation velocity was observed due to the wall deformation (ref. 10); 956 m/sec in water, 36 % reduction from its sound velocity 1500 m/sec, and 1093 m/sec in glycerin, 45 % reduction from 1986 m/sec. As obtained in Figs. 1 and 2, the dispersion caused broadened wave profiles, the rise time being increased from 600 μ sec at Location 1 to 1500 μ sec at Location 2 in water, and from 120 μ sec at Location 1 to 280 μ sec at Location 2 in glycerin, during the passage of 459 mm. It is considered that the high viscosity of glycerin (1500 times water value) works to suppress the dispersion. The second rise of the pressure at Location 1 occurring about 1.4 msec later in both water and glycerin can be explained

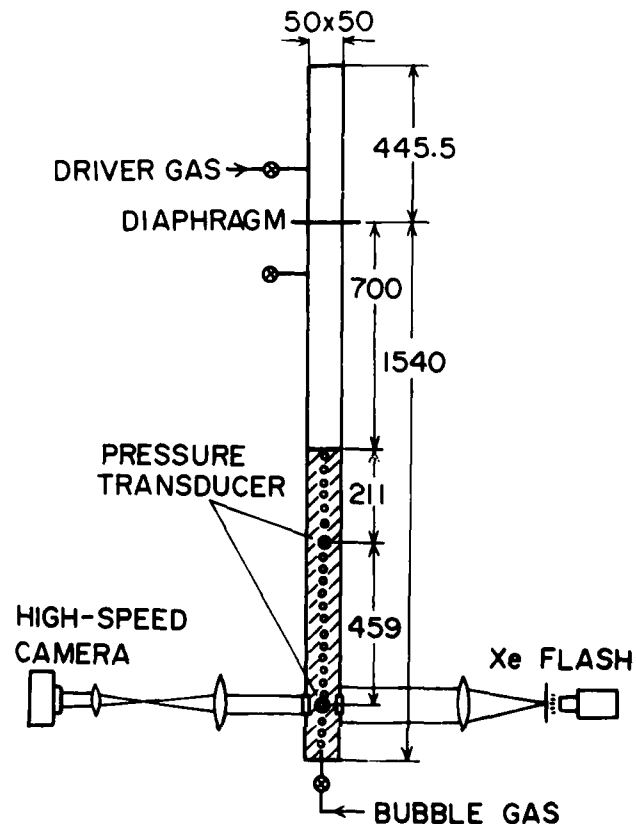


Fig. 3 Sketch of Shock Tube and Measurement System

Driver Pressure ; $P_4 = 7.5$ atm (N_2)
 Test Pressure ; $P_1 = 1.0$ atm (air)
 Time Scale ; 200 μ sec/div

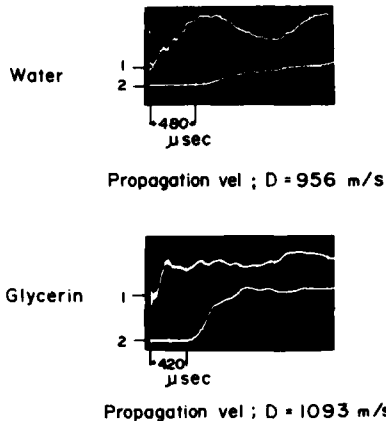


Fig.4 Pressure profile of shock wave in water and glycerin with no bubbles.

by the arrival of the shock wave reflected at the contact surface, as shown in Fig.5. On the other hand, shock reflection at the tube bottom end did not occur to a detectable extent, mainly due to dispersion and attenuation.

(ii) Bubble motion in water: As shown in Table 1, bubble gases were either nitrogen or stoichiometric oxyhydrogen for the two shock strengths $p_4=7.5$ and 15 atm. For any combination of the parameters, the bubble motion was close to cyclic during the first two periods. Meanwhile, a double-disc-shape instability appeared immediately after the bubble diameter exceeded the first minimum and started growing. After the first two cycles of oscillation, the instabilities spread over the entire bubble and, as a result, the oscillatory motion deviated from periodic one, as shown in Fig.6. The initial periodic motion is in good agreement with the theoretical result using Eqs.(11) and (12), along with the far-field pressure variation $\bar{p}_{\infty}(t)$. In fact, this far-field pressure was assumed to be a step function shown in Fig.6, because the wall pressure recorded a similar profile throughout water-bubble experiments.

Although the two shock strengths $p_4/p_1=7.5$ and 15 were used, appreciable increase of the pressure was not obtained at the observation section due to high attenuation and dispersion; this caused failure to impart a large amount of energy to a bubble during the first compression stage. Minimum diameter ratio R/R_0 never became smaller than 0.6 and the gas temperature was at most 554 K which was insufficient to ignite a stoichiometric oxyhydrogen in less than 100 μ sec.

It may be interesting to note that as soon as a bubble surface was infected by Rayleigh-Taylor instabilities completely, the instabilities developed rapidly and disintegration into numerous fine bubbles occurred within 1 msec.

(iii) Flattened top of bubble in glycerin: Glycerin-bubble experiments were performed for more combinations of the parameters, as indicated on Table 1. It was already seen that glycerin is more efficient to compress a bubble due to its smaller dispersion, as shown in Fig.4. Indeed the pressure peak reached more than 10 atm in comparison with 2 atm for water, when $p_4/p_1=15$ was used. Instead, glycerin's high viscosity made it impossible to control the bubble radius under

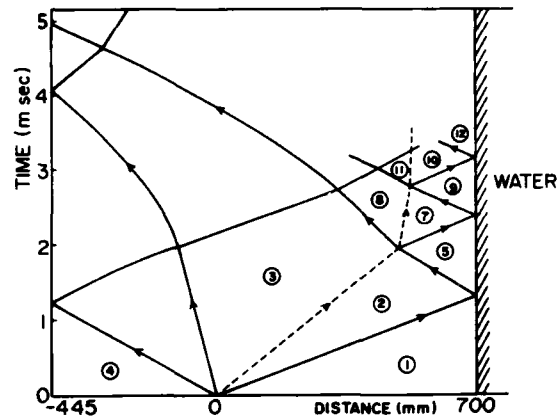


Fig.5 Shock wave diagram in the gas column of shock tube test section.

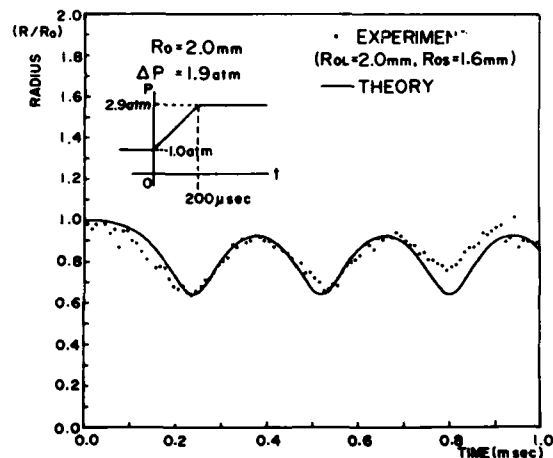


Fig.6 Temporal behavior of bubble radius. $p_4=7.5$ atm (N_2). Bubble; N_2 . Liquid; water. Bubble size; $R_{OL}=2.0$ mm.

Driver Pressure ; $P_4 = 15 \text{ atm (He)}$ Test Pressure ; $P_1 = 1 \text{ atm (Air)}$ Bubble ; $R_{L0} = 4.56 \text{ mm}$ $R_{T0} = 5.00 \text{ mm}$ 90% Ar + 10% ($\text{H}_2 + 2\text{O}_2$)

Liquid ; Glycerin

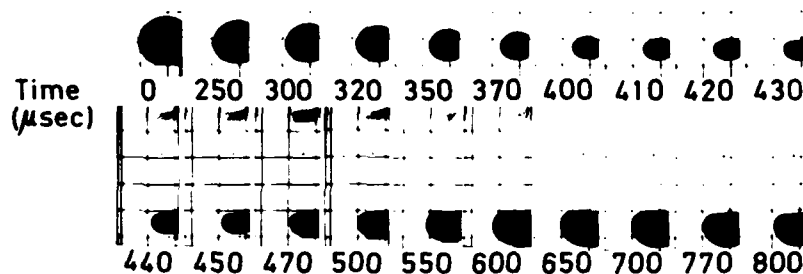
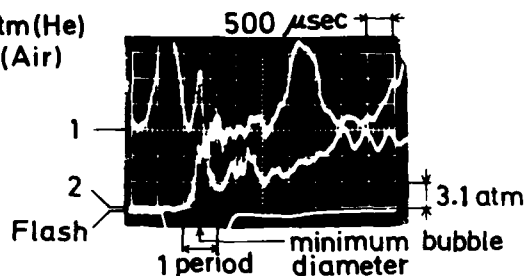


Fig. 7 Bubble motion in glycerin and simultaneous pressure oscillograph. Bubble; 0.9Ar+0.1(H_2+2O_2), initially ellipsoid (longitudinal rad. 4.56, transverse rad. 5.00 mm). Sequentially shown are the shadowgraphs of a bubble during the first period of oscillation. The behaviors of the pressure at Location 1 and 2 are shown on the oscillogram.

(Initial) (1st minimum)

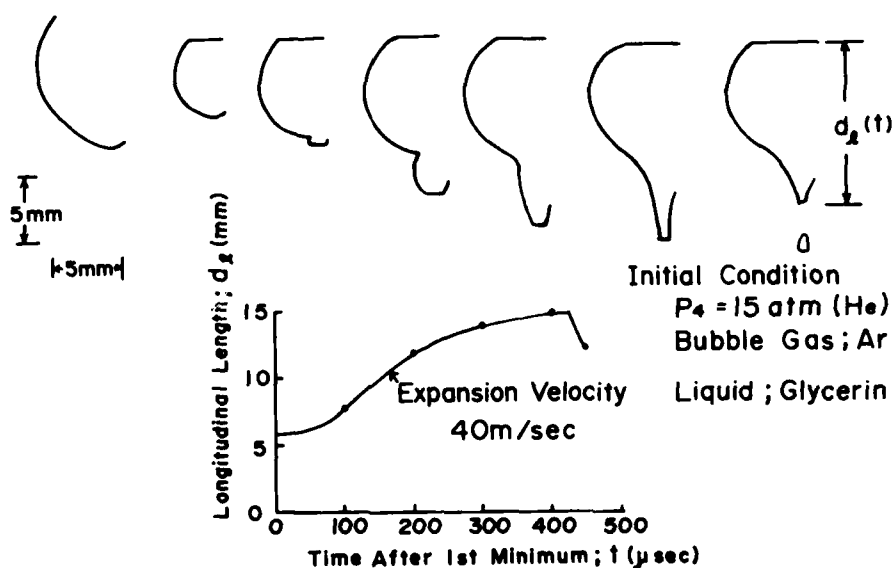
 $t = -530 \quad 0 \quad 100 \quad 200 \quad 300 \quad 400 \quad 450 (\mu\text{sec})$ 

Fig. 8 Deformation and splitting of a bubble in glycerin. Initial condition; a vertically long ellipsoidal bubble (longitudinal rad. about 5 mm) containing pure Ar, driver gas pressure 15 atm (He). The shock wave arrives at $t = -530 \mu\text{sec}$ and gives the maximum compression of the bubble at $t = 0$. The maximum stretching velocity of the bubble in vertical direction reaches 40 m/sec, due to the growth of the bottom bulge.

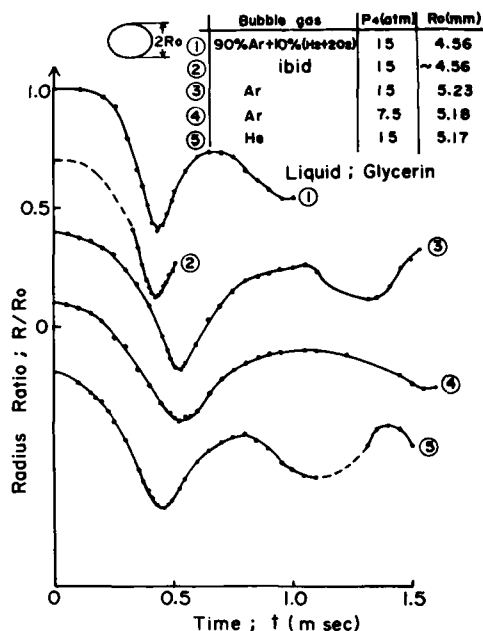


Fig.9 Temporal variation of longitudinal radius of a bubble for several combinations of parameters.

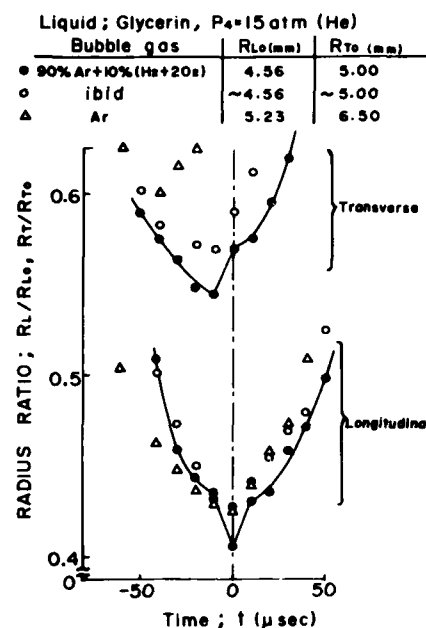


Fig.10 Bubble radius oscillation near its first minimum. Transverse and longitudinal radii are compared for non-spherical bubbles.

4 mm, which caused the bubble oscillation of rather long period. As observed in Fig.7, the shadowgraphs of a bubble during the first period of oscillation showed sudden flattening of the top at about $t=430 \mu\text{sec}$, right after the instant of minimum radius. This flat top remained throughout the subsequent oscillation process, indicating that there was always a flow downward. Considering that the images were shadowgraphs, it is natural to conclude that the actual bubble had top-hollow structure only the outline of which was seen. Interestingly, stable and attenuating oscillation continued retaining nearly the same shape, even if a small bubble was puffed out at the second or third period of oscillation (11,12).

(iv) Parachute-type instability in glycerin: Immediately after the first minimum radius, a certain bubble posed a parachute-shape instability, as seen in the sketch of Fig.8. After ejecting a microbubble, it rebounded to a flat shape and then a double-disc-type instability similar to the one in water appeared rapidly and grew into higher-frequency instabilities. In fact, this parachute type was the only one leading to an irregular bubble shape in glycerin.

(v) Comparison among various bubble motions in glycerin: Five different cases are compared in Figs.9 and 10, where attention was focused on a bubble containing Ar-diluted oxyhydrogen. According to a simple calculation, 0.55 compression gave the temperature 922 K and the pressure 18.5 atm, yielding the induction time $56 \mu\text{sec}$ for the gas. It is speculated that the shorter periods of oscillation appearing on No.1 and No.2 curves of Fig.9 and the very short-time change of radius shown in Fig.10 might be the outcome of exothermic reaction. It is also noted that a He bubble in Fig.9 oscillated with a shorter period even if the other parameters were almost identical to Ar bubbles.

(vi) Bubble oscillation in glycerin; theory and experiment: As seen in Figs.11 and 12, the experimentally observed bubble oscillation in glycerin differed from water counterpart in (a) faster attenuation, (b) non-linear behavior, and (c) at least two high peaks in $\hat{p}_{\infty}(t)$. In order to obtain the best fit with observation, the finite-rise step, saw-tooth, or periodic exponential profiles was assumed for the far-field pressure. Figs.11 and 12 show that although sufficient attenuation was not given, the latter two profiles provided far better agreement with the observed period than the step profile which was successful for water.

Liquid: Water (pressure profile is nearly a step with finite rise time)

p_4 : atm(gas)	Bubble gas	Bubble radius	Observed phenomena
7.5 (N ₂)	N ₂	1 - 2.5 mm	Periodic oscillation during the first two cycles and then instability dominates. Double-disc instability appears at the first minimum radius. $R/R_0 > 0.6$.
15 (N ₂)	N ₂	1 - 2.5 mm	
15 (N ₂)	2H ₂ +O ₂	about 2 mm	
12-15 (He)	2H ₂ +O ₂	about 2 mm	ibid. No reaction.

Liquid: Glycerin (pressure profile has at least two high peaks)

p_4 : atm(gas)	Bubble gas	Bubble radius	Observed phenomena
7.5 (N ₂)	N ₂ , Ar	4 mm	Regular spherical oscillation.
15 (He)	N ₂	4 - 5 mm	When parachute-shape deformation sporadically appears, bubble splitting is followed by instability growth into double-disc and further. Otherwise, no instability grows, although a micro-bubble is thrown out during oscillation. Bubble top flattens and remains unchanged during the entire process.
15 (He)	Ar	4 - 5 mm	
15 (He)	0.9Ar+0.1 (H ₂ +2O ₂)	4 - 5 mm	
15 (He)	He	4 - 5 mm	ibid. Sudden flattening of bubble top appears at the first minimum radius. Shorter-period oscillation.

Table 1. List of Experimental Conditions and Respective Results

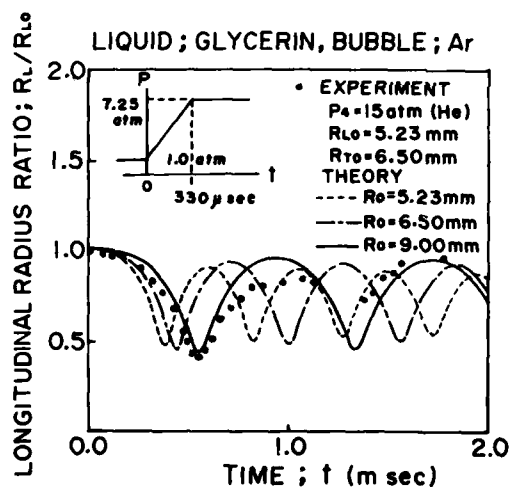


Fig.11 Experimental and theoretical bubble oscillation in longitudinal direction. P_{t00} = step profile.

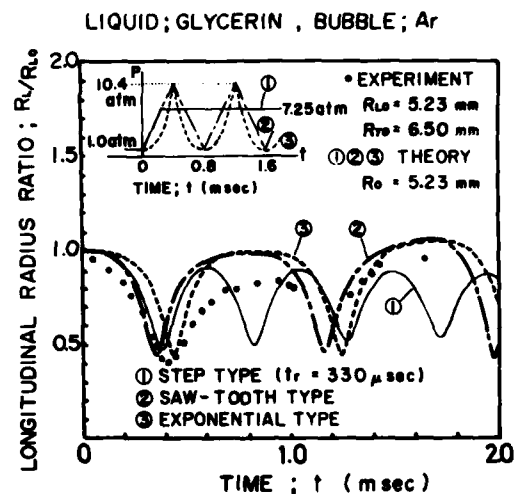


Fig.12 Experimental and theoretical bubble oscillation in longitudinal direction. P_{t00} = periodic profile.

References

1. L. van Wijngaarden, *Ann. Rev. Fluid Mech.* **4**, 369 (1972)
2. Y. Mori et al., *Int. J. Multiphase Flow* **2**, 139 (1975)
3. M. M. Chaudhri and J. E. Field, *Proc. Roy. Soc. London* **A340**, 113 (1974)
4. C. L. Mader, *Phys. Fluids* **8**, 1811 (1965)
5. Din-Yu Hsieh and M. S. Plesset, *Phys. Fluids* **4**, 970 (1961)
6. L. Noordzij and L. van Wijngaarden, *J. Fluid Mech.* **66**, 115 (1974)
7. B. T. Chu, *Wright Air Development Center TN-57-213*, 1957.
8. G. B. Witham, *Commun. Pure Appl. Math.* **12**, 113 (1959)
9. M. S. Plesset and A. Prosperetti, *Ann Rev. Fluid Mech.* **9**, 145 (1977)
10. H. Kawada et al., *Trans. Japan Soc. Aero. Space Sci.* **16**, 195 (1973)
11. G. Rudinger and L. M. Somers, *J. Fluid Mech.* **7**, 161 (1960)
12. M. W. Evans et al., *Phys. Fluids* **5**, 651 (1962)

7

1

Part VII: ENVIRONMENTAL AND ENERGY RELATED APPLICATIONS

1

1

AD P000299

A COMPARISON OF MEASURED AND COMPUTED ENERGY EXCHANGER PERFORMANCE

William J. Thayer III and John F. Zumdieck

Mathematical Sciences Northwest, Inc.

Bellevue, Washington 98004

Measurements and numerical modeling of energy exchanger flow and performance have been carried out to characterize controlling processes and to maximize the efficiency of a small test device. An energy exchanger is a rotating, axial flow wave machine in which unsteady gasdynamic processes are used to directly transfer work between initially high and low pressure streams. A laboratory scale energy exchanger was developed and tested under steady flow conditions to study sensitivity to a number of flow and configuration parameters. This machine operated at a pressure ratio of approximately 2.5 and transferred approximately 100 kW of power between two impedance matched streams. Measurements were made of both overall flow and performance parameters and of flow details during tests. These data were used to evaluate the work transfer efficiency, η_{eff} , which is related to a turbine and compressor efficiency product, and equivalent adiabatic turbine and compressor efficiencies. Tests demonstrated a maximum work transfer efficiency of 74 percent, equivalent compressor and turbine efficiencies of 75 and 97 percent, respectively, and showed the sensitivity of these efficiencies to the controlled parameters. Test results have largely verified a computer model of energy exchanger flow, provided a clear understanding of dominant flow processes, and led to expectations of 80 to 85 percent transfer efficiencies in future energy exchangers.

I. INTRODUCTION

The energy exchanger transfers work from an expanding high pressure gas stream to another initially lower pressure gas stream which is compressed. These functions are analogous to those of a mechanically coupled gas turbine and compressor. However, the transfer of work between these streams is fluid dynamic, and shaft work is not a required transfer mechanism. Since the energy exchanger transfers the potential for doing work from one gas stream to another, it could equally well be called a "pressure exchanger" or "work exchanger." The term "energy exchanger" was coined by Hertzberg (Ref. 1) in his early work to apply unsteady gasdynamic processes to power cycles.

Energy exchangers are gasdynamic wave machines similar to those patented by Seippel in 1946. Many applications of wave machines have been

73)

PRECEDING PAGE

proposed since that time. These have included applications to internal combustion engine supercharging, hypersonic wind tunnel test facilities, chemical processing, high temperature compression, and other transfer processes between gas streams. The development and application of wave machines has recently been extensively reviewed by Rose (Ref. 2). Several new applications of the energy exchanger to power generation cycles have recently been studied by Mathematical Sciences Northwest, Inc. (Ref. 3). These applications included its use as a high pressure, high temperature top stage for a gas turbine topping-steam bottoming cycle using coal derived fuels, use as a high temperature air compressor for a coal burning MHD power plant, and use as a "dirty" gas expander/air compressor for pressurized, fluidized bed (PFB) fired coal burning power plants. The energy exchanger offers distinct advantages in terms of overall plant efficiency, simplicity, and durability relative to gas turbines in PFB cycles using conventional compressors, turbines, and gas clean-up techniques (Ref. 3). These studies show that operation of the energy exchanger at work transfer efficiencies of 75 percent or higher is required for effective application of this technology in power generation applications (Ref. 3). As discussed below, results of testing and computer modeling indicate that the energy exchanger will operate at efficiencies of this level or higher when this technology is further developed and implemented in large scale devices.

Energy exchangers can be configured with one expansion/compression cycle per revolution of the rotor as was the test machine in Figure 1. A number of long narrow gas passages, which behave very much like shock tubes, are mounted on the periphery of a rotating drum. Two gas streams flow steadily into the rotor through ports in the stationary endwalls, transfer power by means of the steady port flows and a pressure wave system which is repetitively established in each tube, and then flow steadily into the outlet ports. Motion of the tubes past the stationary inlet and outlet ports and regions of closed endwall is used to establish the unsteady flow processes within the rotating tubes of wave machines. Low pressure gas, called the "driven" stream after shock tube nomenclature, enters the rotor through a large port, is compressed by pressure waves within the rotor tubes, and leaves the rotor at high pressure through the smaller driven stream outlet port in Figure 1. A continuous stream of high pressure gas, called the "driver" stream, enters the rotor through a small inlet port, transfers its power to the driven stream through unsteady flow processes on the rotor, and exhausts

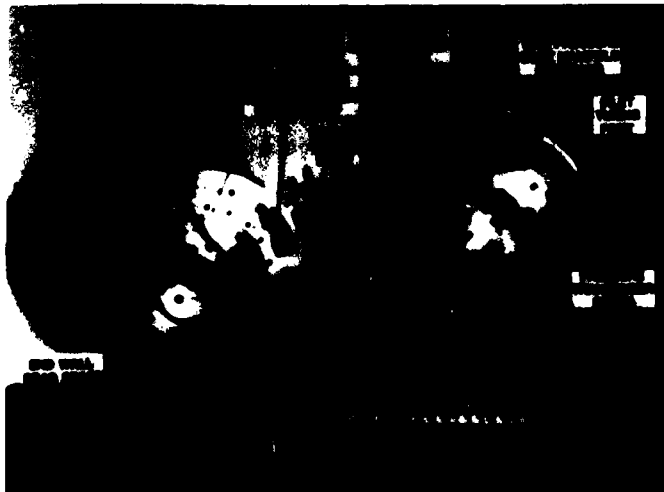


Figure 1: Energy Exchanger Rotor, Inlet and Outlet Endwall, and Port Assemblies.

from the rotor through a low pressure port. The operation of the energy exchanger and other wave machines is described in considerable detail in Reference 3. Through the use of proper rotor, port, and endwall configurations and operating conditions, work transfer between the driver and driven streams can be made very efficient. Both the experiments and code projections discussed below indicate that energy exchangers can have high efficiencies and other favorable operating characteristics which will make these machines very useful in power generation applications.

This paper extends the preliminary test and computational results presented in Reference 4 to the most recent test data and computations (Ref. 3). Since the earlier paper, the test energy exchanger has been reconfigured, and tests have been conducted for an expanded range of conditions. The clearances between the rotor and stationary inlet and outlet ports were reduced to minimize leakage. Wave management ports have been used to cancel undesired reflections of compression and expansion waves, improve inlet and outlet flow uniformity, and reduce associated losses. In addition, port width, rotor speed, and flow conditions have been varied to identify conditions of highest efficiency and to determine sensitivities to flow parameter variations. Additional instrumentation, including pressure transducers mounted on the rotor, was used to identify flow problems and mechanisms which govern the energy exchanger work transfer efficiency. The net effect of the configuration and operating parameter changes has been to increase the transfer efficiency to 74 percent.

The energy exchanger flow code, which was described in the earlier paper (Ref. 4) and in Reference 3, has been used to calculate internal flow conditions and overall performance for a range of configurations and operating conditions of the test energy exchanger. As discussed in Section IV, computed energy exchanger flows agree very well with overall performance measurements and with detailed measurements of flow property variations during each tube rotation. This agreement has verified that the dominant mechanisms have been adequately modeled and has provided confidence in the accuracy of the code for projecting energy exchanger performance in other operating and machine size regimes. Computations indicate that energy exchangers with throughput and operating conditions comparable to the test device could operate at transfer efficiencies of 80 percent if relatively minor changes were made in the basic wave system and configuration. Similar calculations indicate that large scale energy exchangers could operate with efficiencies to approximately 85 percent at conditions similar to those tested.

II. ENERGY EXCHANGER FLOW CODE

The projections of energy exchanger performance discussed below were made using a computer program which was developed to model energy exchanger flows (Ref. 3). The flow within tubes on the energy exchanger rotor was modeled using the one dimensional unsteady flow equations. Terms were included to calculate friction and heat transfer processes using correlations for steady, turbulent pipe flows. The one dimensional unsteady tube flow equations were solved numerically using the flux correlated transport technique. This technique is accurate and stable in regions of high property gradients, such as shock waves and interfaces between different gases, and allows calculations to be carried out over many cycles. Thus, operational transients and approach to steady state operation of the energy exchanger can be accurately calculated. The internal, unsteady tube flow equations were coupled to steady flow equations governing the external manifold and endwall leakage flows at the rotor boundaries. All of the inlet port flows external to the rotor were treated as regions of uniform, specified total pressure and temperature with losses due only to leakage when the tubes were fully open to the ports. The outlet ports were treated as regions of uniform, specified

static pressure. Leakage to atmosphere through the clearance regions between the rotor and endwalls was treated using the steady flow equations governing compressible gas flow with friction. The boundary condition equations were treated independently as required in each port and blank endwall region and in transition regions between ports and between ports and endwall regions. Losses due to transient pressure imbalances between adjacent external and internal regions were evaluated using a quasi-steady flow formulation and the assumption of no recovery of dynamic head. This energy exchanger flow code is believed to model the dominant flow processes with sufficient accuracy that projections of performance and evaluations of configuration and operating parameter dependence can be dependably made. This will be apparent in comparisons with test results as discussed in Section IV.

The efficiency with which the energy exchanger extracts work from the driver stream and transfers it to the driven stream is represented by the work transfer efficiency, η_{EE} . This efficiency was defined as the ratio of the increase in expansion work ideally extractable from the driven stream as it is processed by the energy exchanger to the expansion work ideally extractable from the incoming driver stream. For the test energy exchanger this can be expressed as

$$\eta_{EE} = \frac{\dot{W}_{id2} - \dot{W}_{id1}}{\dot{W}_{id1} + \dot{W}_{id3}} \quad (1)$$

where $\dot{W}_{i(n)}$ is the work rate which could be generated by expansion through an ideal turbine from the state of interest to a reference pressure (ambient pressure for all tests and computations). The subscripts d1, d2, D1, and D2 refer to the driven inlet and outlet streams and driver inlet and outlet streams, respectively. The subscripts D3 and D4 refer to the inlet and outlet streams for the wave management ports, respectively. For ideal gases with constant specific heats, the ideal expansion work terms can be written as

$$\dot{W}_{in} = \dot{m}_n c_{pn} T_n \left(1 - \frac{P_a}{P_{on}}^{\gamma_n - 1/\gamma_n} \right) \quad (2)$$

where \dot{m}_n , c_{pn} , T_n , γ_n , and P_{on} are, respectively, the mass flow rate, specific heat, temperature, specific heat ratio, and stagnation pressure of the stream of interest and P_a is the reference pressure. The work and efficiency terms were evaluated in the code by suitably integrating computed flow properties across the inlet and outlet ports.

III. ENERGY EXCHANGER TEST APPARATUS

Tests were conducted using a laboratory scale energy exchanger and test facility (Ref. 3) which were developed to demonstrate high efficiency, to provide data for code verification, and to provide a better understanding of dominant energy exchanger flow mechanisms and losses. The energy exchanger which was used for testing is shown partially assembled in Figure 1. It was designed on the basis of ideal one-dimensional flow calculations using the method of characteristics before the flow code described above had been developed. This energy exchanger transferred approximately 100 kW from the driver stream to the driven stream. The argon driver stream and 80% argon-20% helium driven stream had matched acoustic impedances to simplify the wave system by which power was transferred. The expanding driven stream entered the rotor at a pressure of 25.3 kPa (36.9 psia) and temperature of 525 K and left the rotor at approximately ambient pressure. The work done by this stream was largely used to compress the driven stream from approximately ambient conditions through a pressure ratio of approximately 2.5. Mass flow rates of the driver and driven streams were in the range of 0.8-1.1 kg/sec.

In addition, two small port flows were used during some tests to cancel pressure waves at critical rotor locations and thus provide more uniform port flows, better pressure recovery, and higher transfer efficiency. These wave management ports were located near the driven gas inlet and outlet ports and required approximately 25 and 80 gm/sec of flow, respectively, to cancel the principal expansion waves. The energy exchanger rotor was 40 cm long, 45 cm in diameter, and had 100 tubes in the annular region between 32.75 and 40.25 cm diameter. Only 40 percent of the ideal maximum endwall periphery was used for gas flow in the test energy exchanger, as is evident in Figure 1. Large regions of blank endwall were incorporated for instrumentation and to permit the energy transfer rate to be increased. The clearance between the rotor and the stationary flow ports was reduced from 0.033 cm (0.013 inch) in the earlier tests (Ref. 4) to 0.010-0.013 cm (0.004-0.005 inch) in the tests reported here. The design rotor speed was 1960 rpm, and tests were conducted for a speed range to 10 percent above and below this value.

All tests were carried out at steady state operating conditions. The test facility which was developed for this program operated for six seconds during each test. Gases and thermal energy for each test were stored in pressure vessels and storage heaters, respectively. Prior to each test, the rotor and all inlet and outlet ports and piping were heated to constant temperatures corresponding to steady state conditions. This ensured that test conditions did not change during each test. Steady flow conditions were established during the first second of each test by using an appropriately designed valving and flow system. These conditions were maintained during the remainder of each test by the programmed opening of control valves. This facility made possible relatively low cost, repeatable testing of the energy exchanger at steady state conditions.

Flow meters, thermocouple probes, and pressure transducers were used to monitor inlet and outlet mass flow rates, pressures and temperatures at low velocity regions upstream of the inlet manifolds and downstream of the outlet diffusers. The energy exchanger work transfer efficiency, η_{EX} , as defined by Equations (1) and (2), and the equivalent compressor, η_{CE} , and turbine, η_{TE} , efficiencies were evaluated from these data using equations given in Reference 3. Leakage was calculated as the difference between the measured total inlet and outlet mass flow rates. Twenty-four pressure transducers located on the inlet and outlet endwalls were used to measure steady pressures at various fixed angular locations of the tube rotation. In addition, three pressure transducers were installed in one rotor tube at locations near the inlet, at the centerplane, and near the outlet. They were used to measure the time varying pressure throughout the tube rotation. Signals from these high frequency response transducers were transferred from the rotor to stationary external amplifiers and data recording equipment through a low noise slip ring assembly. Gas samples were taken from the outlet port regions where the interfaces between driver and driven gases left the rotor and were analysed using a gas chromatograph. These data were used to monitor interface locations and to determine the degree of mixing between streams.

The entire test control, data acquisition, and data reduction sequence was carried out using a PDP-11 minicomputer system. The steady state flow data were measured, digitized, and stored in computer memory every 1/30 second throughout each test. The high frequency data from the pressure transducers mounted on the rotor and a timing/position signal were measured, digitized, and stored at 25 μ sec intervals for 0.2 second periods during each test. Four channels of a transient digitizer were used to acquire and store this data for transfer to and reduction by the minicomputer after each test. All data from each test were permanently stored on floppy disks after each test. Computations to determine efficiency, mass flow rates and leakage, pressure distributions, and histories were carried out shortly after each test.

IV. TEST RESULTS AND COMPARISONS WITH CODE CALCULATIONS

Testing of the energy exchanger was conducted for several configurations and over a range of operating conditions. Configuration changes included variation of the clearance between rotor and endwalls, incorporation of wave management ports near the driven gas inlet and outlet ports, and increasing the area of the main driven stream outlet port. Operating parameters which were varied during the test program included driver and driven gas inlet pressures, driven gas outlet pressure, rotor speed, and flow rates through the wave management ports. The energy exchanger flow code was used to compute detailed flow parameters and overall performance of a number of test conditions. The data are discussed and compared with computations in this section.

Overall Performance Data and Computations

The major configuration changes had significant effects on the work transfer efficiency and flow through the energy exchanger. Decreasing the clearance between the rotor and stationary manifold faces reduced the leakage from approximately 12 percent of the total input flow rate to 3-4 percent as predicted by the leakage model, and provided a substantial efficiency improvement. This may be seen by comparing the lower two curves of Figure 2, where the dependence of the energy exchanger work transfer efficiency, η_{EE} , on the driven stream outlet pressure, P_{D2} , is shown. The low leakage tests, for which data is shown in Figure 2, were conducted at a driver inlet total pressure of 2.71 atm, driven stream inlet stagnation pressure of 1.08 atm, and a driver outlet pressure of 1.00 atm. The rotor speed of 1790 rpm gave a higher efficiency than the design speed of 1960 rpm. Both inlet and outlet wave management ports were closed for these tests. The maximum efficiency was approximately 70 percent for driven outlet pressures in the range of 2.2 to 2.4 atm for the low clearance configuration, approximately 11 efficiency points higher than the high leakage case. The mass flow rate into the driven outlet manifold decreased continuously as the pressure was raised for both configurations, and caused a decrease in efficiency as the pressure ratio was increased. It should be pointed out that the test energy exchanger had no mechanical or thermal problems operating at the low rotor-manifold clearance once the device had been properly aligned. No contact occurred during the rapid pressurization and flow transients of the tests, although some motion of the manifolds could be detected.

A second configuration change was suggested by exercising the unsteady flow code on the test energy exchanger and closely related geometries. Since

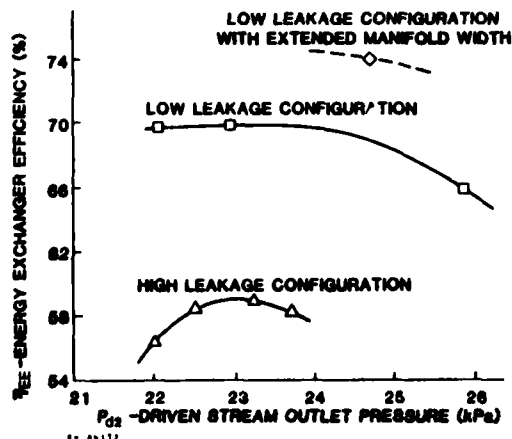


Figure 2: Comparison of Energy Exchanger Efficiency Variation with Backpressure for Low and High Leakage Configurations.

decreased driven stream outflow rates were observed experimentally at high back pressures (see Figure 2), the possibility of increasing this flow rate by extending the high pressure outflow manifold was evaluated. An 11 percent increase in mass flow rate and efficiency was predicted to result from a 15 percent increase in this manifold width. Unfortunately, resources were not available to disassemble the test device, fabricate a new high pressure outflow manifold, diffuser, and ducting, and reassemble and realign the test device. To examine the effectiveness of increased manifold width, the outlet wave management port was operated in conjunction with the main high pressure port to provide matched recovery flow conditions in the low velocity ducts downstream of the device. This increased the outflow area by 22 percent, substantially more than that predicted as optimal by the code. For this condition an 8 percent improvement in efficiency was predicted. The measured high pressure outflow rate increased by approximately 10 percent and provided an efficiency rise to $\eta_{EE} = 74$ percent, as shown in the uppermost curve in Figure 2. Tests were conducted at only one condition for this configuration due to the difficulty in matching flows and to the lateness in the test program of this test series. However, higher efficiencies could be expected if tests were conducted to optimize performance with respect to back pressure and speed.

A comparison of measured and computed energy exchanger efficiency is made in Figure 3 for the range of pressure ratios of the driven and driver streams used in the low leakage tests of Figure 2. Here PR_C is the ratio of the driven outlet stagnation pressure, P_{od2} , to the driven inlet stagnation pressure, P_{od1} , and PR_T is the ratio of the driver inlet stagnation pressure, P_{od1} , to the driver outlet static pressure, P_{D2} , which was nearly ambient. Variation in this ratio of compression to expansion pressure ratios was accomplished experimentally by varying the backpressure of the driven outlet stream while maintaining all other parameters at approximately constant conditions. The experiments showed that efficiency was relatively constant at pressure ratios less than approximately 0.8. At higher pressure ratios the efficiency dropped off quite rapidly due to a decrease in mass flow rate into the constant width, high pressure outlet manifold. The relative magnitude of the computed work transfer efficiency is in quite good agreement with the experimental data, although the code predicted a drop in efficiency at lower pressure ratios which was not observed in experiments. The difference between predicted and measured efficiencies is believed to be due to variable pressure and reversed flow conditions which occurred in portions of the manifolds under certain operating conditions. These nonuniform flow conditions became greater at the lower pressure ratios. Fortunately, the actual device performance seemed to be less sensitive to these nonuniformities than was predicted. Since constant conditions were assumed to exist across the manifolds in the

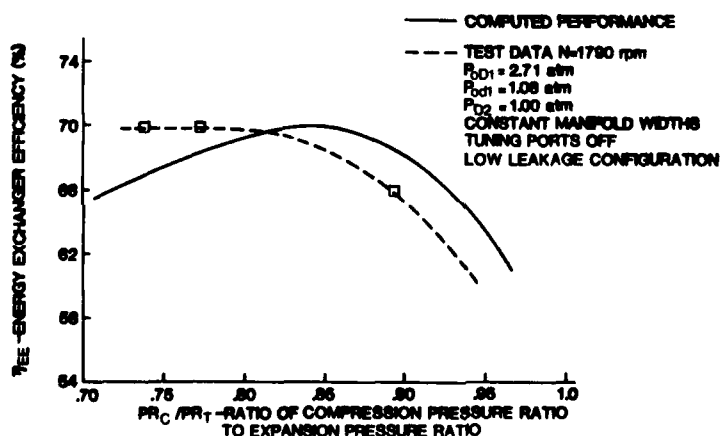


Figure 3: Comparison of Computed and Measured Energy Exchanger Efficiency.

computer model, discrepancies between experiments and the code are not surprising at conditions which produced nonuniform external flows. Upgrading of the code to include a two dimensional manifold flow model would be very desirable to better model actual flow conditions. However, the general agreement between the predicted and measured efficiencies gives enough credibility to the code that predictions can reasonably be made to determine effects of device configuration and operating parameter changes.

Performance projections have been made for energy exchangers which could transfer approximately 100 kW as did the test machine to determine the configuration and maximum efficiency which could be expected. These projections indicate that using an optimal driver outlet port width and location could increase the efficiency to approximately 76 percent. If, in addition, the blank endwall regions were reduced from that used in the test device to the minimum required for operation, leakage would decrease to approximately 1 percent of the total flow and improve the efficiency by 3 to 4 efficiency points. Changing the low pressure port widths and locations slightly to optimize real energy exchanger operation would improve efficiency by almost one efficiency point, moving the high pressure ports relative to one another is projected to have a similar effect. The energy exchanger code indicates that the combined effect of all of these changes would provide a transfer efficiency of 80 percent for an optimized, 100 kW size energy exchanger.

A few additional calculations have been made to evaluate the potential efficiency of large energy exchangers. Devices considered were similar to the optimized small energy exchanger and operated at similar conditions but were scaled up to handle 100 to 1000 times more flow. Projections indicate that work transfer efficiencies as high as 85 percent may be feasible for such large scale devices.

Detailed Flow Measurements and Computations

Very good agreement can also be shown between measured and computed pressures within the rotor tubes as they rotate through repetitive cycles. These comparisons are made for tests at conditions both without (Figure 4) and with (Figure 5) flow through the wave management ports. Computed and measured pressures at the inlet end of the rotor are shown as a function of tube angular position, θ , through one rotation. The zero angle location was designated to be at the start of the low pressure, driver gas exhaust port. Pressures measured at fixed locations on the inlet manifold plane are also shown as discrete data points on these figures. Pressures measured continuously on the rotor and at the adjacent endplane are in very good agreement, although some electrical noise is evident for the on-rotor data. Agreement between computed and measured pressure histories is quite good in the active portion of the cycle (i.e., $\theta < 160^\circ$). Comparison of Figures 4 and 5 demonstrates the effectiveness of the wave management ports in cancelling pressure disturbances.

The efficiency data, the pressure data from endwall and on-rotor transducers, and the computed flow properties led to a greatly increased understanding of the operation and performance of real energy exchangers and of the dominant wave mechanisms. Principal waves and loss mechanisms have been identified and are discussed in detail in Reference 3. In the later portion of the test program when the code was operational and its accuracy established, similar predictions guided changes in device operation to optimize performance. Additional calculations were used to predict performance improvements which would be expected to derive from changes in the test device configuration and scale.

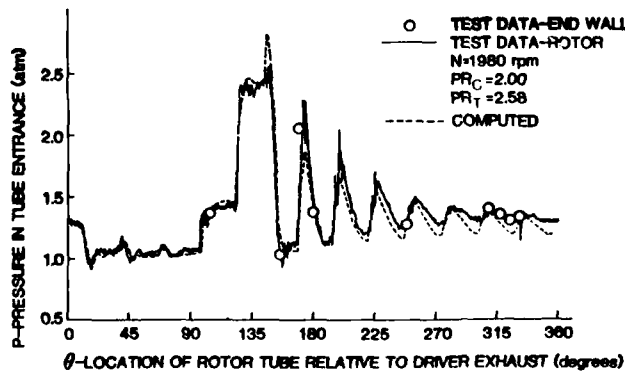


Figure 4: Comparison of Measured and Computed Pressure History Without Wave Management.

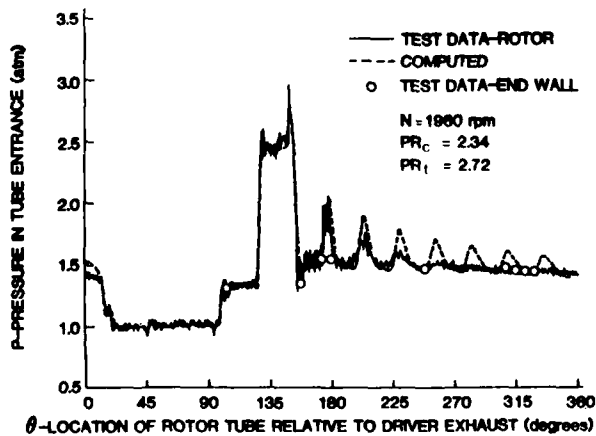


Figure 5: Comparison of Measured and Computed Pressure History With Wave Management

ACKNOWLEDGEMENTS

The work described in this paper was sponsored by the Department of Energy Basic Energy Sciences Division under Contract DE-AC06-78-ER01084.

REFERENCES

1. Weatherston, R.C. and Hertzberg, A., "The Energy Exchanger: A New Concept for High Efficiency Gas Turbine Cycles," ASME Journal of Engineering for Power, 1966.
2. Rose, P.H., "Potential Applications of Wave Machinery to Energy and Chemical Processes," Shock Tubes and Shock Waves. Proceedings of the 12th International Symposium on Shock Tubes and Waves, A. Lifshitz and J. Rom, Editors, The Magnes Press, 1980.
3. Thayer, W.J. III et al., Energy Exchanger Performance and Power Cycle Evaluation-Experiments and Analysis, Final Report DOE/ER/01084-1, April 1981.
4. Thayer, W.J. III et al., Measurements and Modeling of Energy Exchanger Flow, Energy to the 21st Century, Proceedings of the 15th Intersociety Energy Conversion Engineering Conference, Seattle, WA., August 1980, p. 2368.

AD P000300

Flow Fields Produced by Pipeline Explosions

D.G. Edwards R.M. Smith

University of Surrey, Stag Hill

Guildford, England.

Abstract The accidental bursting of a high-pressure gas pipeline has been modelled both in the laboratory using a special variant of shock tube with a wall-mounted diaphragm and by computation.

The effect of bursting time and driver gas properties on the flow at various points in the vicinity of the burst has been studied and recommendations have been drawn up in relation to hazard avoidance.

Introduction

The increasing concern over the past decade with industrial health and safety has led to a requirement for a greater understanding of the hazards eg. in the nuclear power and petro-chemical industries resulting from the explosion of pipelines containing gas or vapour at high pressure.

The present work makes use of a variant of the shock tube to simulate the bursting of such a pipeline.

Pressure measurements both inside the pipe and in the vicinity of the bursting diaphragm, augmented by schlieren photography of the emerging flow field have given an insight into the basic nature of the flow and have established its resemblance both to gun muzzle flows and starting flows of short-duration rockets. Computer modelling has reproduced several of the main flow features and has provided good quantitative predictions of peak over-pressure at various points in the flow field. Regions of particular potential hazard in the context of pipe explosion are identified. Information is also presented on the influence of fracture rate on peak blast over-pressure, and on the decay rate of the blast with distance from the burst for a variety of high-pressure driver gases.

2.1 Shock-Tube Pipeline Explosion Simulator

The shock tube used for the simulation of the pipeline explosions is of 2-inch square internal cross section and has a special test-section with a 2-inch square aperture cut through the tube wall. A diaphragm is initially clamped over this aperture by means of a special flange.

The diaphragms used to date have been of half-hard aluminium, their bursting pressure and petal formation controlled by milled diagonal grooves.

These typically range from 25% to 75% of the basic sheet thickness and give bursting pressures consistent to $\pm 6\%$, in addition to producing reliable petalling.^{(1,2)*}

The shock-tube is mounted on trestles with its axis 4ft above the laboratory floor and a vertical wooden board 8ft square is attached to the trestles as shown in figure 1. The diaphragm clamping flange fits flush into a hole in the wooden board, the arrangement serving to simulate a burst just below ground-surface.

2.2 Conventional Shock-Tube

Information on the bursting characteristics of diaphragms similar to those used in the blast simulator was obtained from the same shock tube used in the conventional mode. Glass end-windows allowed direct spark photography of the bursting diaphragms for opening-rate measurements. Slit windows in the side-walls adjacent to the diaphragm clamping flange allowed opening-rate measurements by means of a light-beam/photomultiplier technique. The results are shown in figure 2.

Finally, a pair of schlieren windows extending across the full depth of the tube and forming the actual diaphragm clamping surface at their upstream edges, allowed flow visualisation of the earliest portion of the shock formation process.

The diaphragms used for this work were grooved in an H-configuration so as to produce two equal flaps on bursting, and thus generate an almost two-dimensional starting flow. The results are shown in Plate 1.

2.3 Experimental Measurements

The experiments carried out were aimed principally at:

- a) determining the pressure history both in the environment adjacent to the burst, and inside the shock-tube and
- b) obtaining qualitative information on the nature of the external flow-field produced by the burst.

Two approaches were used to determine the pressure histories. The first was based on the use of free-mounted blast gauges while the second involved the introduction of a large splitter-plate on the flow centre-line (figure 1) so facilitating the use of pressure transducers in the more orthodox wall-mounted mode. In each case, pressure-sensing elements of both the piezo-resistive and piezo-electric types were used. It proved necessary to isolate the latter from mechanical vibration of the mounting probe or splitter plate, by the use of a soft suspension which gave a natural frequency of less than 10Hz.

The piezo resistive gauge elements were substantially insensitive to mechanical vibration but their signal-to-noise ratio and resonant frequencies fell short of those of the piezo-electric types.

A further pressure transducer was symmetrically wall-mounted in the shock tube immediately opposite the diaphragm aperture, so as to indicate the stagnation pressure of the diaphragm flow.

Qualitative information on the development of the external flow-field in the vicinity of the bursting diaphragm was obtained by conventional delayed-spark schlieren photography.

* Numbers in parentheses relate to references

3. Computer Modelling

The flow in the pipe interior has been computer-modelled using a two-dimensional Eulerian finite-difference code (3), and the same code in axisymmetric form has been applied to the external flow-field. The properties of the two-varying flow fields were conservatively matched at the diaphragm interface. The external field was modelled over an axial distance of 1.0m and a radius of .5m, using a grid of cells with dimensions of .025m square. The calculations were advanced in time-steps of not more than 5.0×10^{-6} to ensure stability in the finite-difference equations.

4. Diaphragm Opening Time

The simplest model of the opening process of a metal diaphragm assumes that the petals are freely hinged at their roots and that throughout the opening process, a pressure equal to the shock tube driver pressure acts normal to the petal inside surface. If the pressure downstream of the petal is ignored, this gives an opening time t , for the triangular petals used in the present work of

$$t = (\pi \rho_d t_d L / 2 p_d)^{1/2} \quad 3.1$$

where t_d is the diaphragm thickness, ρ_d the diaphragm material density, and $2L$ the petal-root width.

Significant departures from the simplifying assumptions described above occur in practice. These are due mainly to:

- the reduction in pressure applied to the petals as the primary rarefaction strengthens during petal folding,
- the reduction in pressure of the petals associated with the kinetic energy increase in the flow accelerating towards the progressively increasing aperture and
- the bending resistance of the petal edges. These factors together with the initial deflection of the pressurised diaphragm represented as a petal angle Θ are incorporated in a realistic opening time analysis.

At a given instant in the diaphragm opening process, it is assumed that a quasi-steady flow accelerates from the tail of the primary rarefaction to sonic velocity at the point of exit from the diaphragm region.

This allows the calculation of a time-varying moment M_g on the diaphragm petals which is given by:

$$M_g = \frac{2}{3} L^3 p^* \int_0^{L \sec \Theta_0} (p/p^* - 1) (y/L) d(y/L), \quad 3.2$$

where p^* is the quasi-steady critical pressure.

Equating mass flows at the tail of the rarefaction and at the diaphragm exit gives:

$$\rho_R u_R = \rho^* a^* (1 - \cos \Theta / \cos \Theta_0) \quad 3.3$$

It is convenient to express the properties behind the rarefaction wave in terms of the tail slope N in the $x - t$ plane, (4) - $N = (1/a_4) dx/dt$ and N is then related to Θ by.

$$\begin{aligned} & (1+N(1-(\gamma_4-1)N/2))^{2/(\gamma_4-1)} \times (1+(\gamma_4-1)N^2/2)^{-(\gamma_4+1)/2(\gamma_4-1)} \\ & = 1 - \cos\theta / \cos\theta_0 \end{aligned} \quad 3.4$$

Combining the results of equations 3.2 to 3.4 to give the value of p^* , the moment M_0 is calculated as a function of θ .

When such calculations are combined with evaluations of the bending resistance of the petal edges, the resulting equation of petal motion is:

$$\begin{aligned} \ddot{\theta} = \cos^3\theta_0 / (\rho_d t_d) & \left[4 p^* / L \int_0^{L \sec\theta_0} (p/p^* - 1)(y/L) d(y/L) \right. \\ & \left. - 3 t_d^2 \delta_d / L^3 \ln(\cos\theta_0 + 1 + \cos^2\theta_0)^{1/2} \right] \quad 3.5 \end{aligned}$$

The second item in the square brackets represents the effect of root bending stiffness. Integration of the angular acceleration equation gives the results shown in figure 2.

5. Results

5.1 Diaphragm Opening Rate

The effect of root bending stiffness is seen to increase the overall opening time by some 40% compared with the freely-hinged case. Experimental measurements of petal motion obtained, as outlined in section 2 show that although the initial petal motion is less rapid than predicted, the overall opening times are well estimated, from equation 3.5. Plate 1 shows one of the multi-spark diaphragm opening pictures from which the θ vs time values were determined.

5.2 Schlieren Studies

Plate 1 also shows a sequence of single-spark schlieren photographs of the flow emerging from a folding 2-flap diaphragm. The initial diaphragm pressure ratio was 15.1. A well defined central supersonic jet appears on most of the frames with a distinct taper downstream associated with the unsteady nature of the exit region and the progressive increase in initial jet width with time.

In the earliest pictures the coalescing compressions from which the shock will shortly form are also well defined ahead of the contact region.

Plate 2 shows corresponding results for the flow emerging into the atmosphere from a folding 4-flap square diaphragm. Two sequences of pictures are shown, one taken using nitrogen as the driver gas, the other with helium as driver.

In neither case has the compression wave system ahead of the contact surface coalesced into a single blast wave, though the helium results demonstrate the more rapid coalescence. The plume of driver gas is of course three dimensional and its internal features are masked by the turbulent eddying exterior. However, the general form of the plume differs markedly from its shock-tube counterpart but is quite similar to that shown in Plate 3. This was produced by the firing of a short duration rocket-motor.(6) The flow-fields produced by such devices have been well understood for several decades.(5) Figure 3 illustrates schematically their most important features. These include an expanding supersonic jet of propellant gas terminated downstream in a rearwards-facing Mach disc and flanked by oblique shocks, the above shock system providing the appropriate thermodynamic changes to match conditions at the extremities of the plume to those produced in the atmosphere by the receding blast wave. The similarity in the exterior shapes of these plumes is an indication of a further resemblance in the two wave systems underlying them.

5.3 Measured and Computed Pressure Histories

The wall stagnation pressure history shown in Figure 4 shows that following an initial pressure reduction from p_4 resulting from the arrival of the primary expansion from the diaphragm, a brief period of mechanical vibration of the tube walls occurs followed by a period in excess of 4.0ms of virtually constant pressure. External blast wave measurements may be made throughout this period without loss of uniformity in driver conditions through the arrival of the reflected rarefaction wave.

The measured level is slightly higher than both the value predicted by the theory in Section 4 and the computed results. This is almost certainly due to vena contracta at the aperture leading to a slight over-estimate of the effective fully open area.

The axial pressure histories shown in figure 5 illustrate several important flow features. Firstly, the compression front is characterised by a relatively shallow gradient. The pressure rise time is of the same order as the diaphragm opening time and the corresponding schlieren photographs confirm the finite extent of the coalescing compression wave system.

Almost as soon as peak pressure is attained a pressure drop occurs, over a time scale appreciably shorter than the original rise. This represents the effect of the Mach disc which is seen to travel downstream to each successive gauge station in turn weakening as it does so. At the first station the pressure drop at the Mach disc far exceeds the rise caused by the blast, and might indeed represent the more serious hazard in a real pipeline explosion. The large-amplitude pressure fluctuations which arise at each station after the passage of the Mach disc may be linked with the persistence within the plume of driver gas of the disturbances which gave rise to the secondary wavelets visible in many of the schlieren photographs.

Several of the flow features described above are reproduced in the corresponding computer predictions. The peak blast over-pressures are mainly in good accord with measured values and the Mach disc is quite well represented though the suction peak at the first gauge station is of only half the measured magnitude.

Figure 6 shows a typical trace obtained from the gauges arranged in a column at right angles to the flow centre-line. The record at position 1 is essentially as discussed in connection with figure 5 but the traces from position 2 exhibit a pronounced double peak with a repeatable time interval between. The feature is consistent with the motion over the transducer face of the following flow features:

- a) the primary blast wave giving the first peak
- b) the Mach disc, giving the ensuing steep pressure reduction
- c) the oblique shock at the edge of the plume giving the rapid pressure recovery followed by a more gradual tailing off.

The third record from a gauge at a greater distance from the flow centre-line does not show the double-peak feature. This indicates that the oblique shock lies between the two transducer locations 2 and 3.

5.4 Effect of Opening Rate

A striking feature of the results relating blast pressure to diaphragm opening rate is the very rapid decrease in pressure occurring as the opening rate decreased. This feature, which is illustrated by the results shown in Figure 7, was observed at each of the transducer stations and would appear to have considerable significance in the general context of explosion hazard. The indication is that a ductile type of pipe fracture extending over a time period which is long compared with L/a_4 is likely to produce lower blast-over pressure than the sudden shattering of the walls of a brittle pipe. The further indication is that this effect will extend to a distance in excess of five pipe diameters from the burst.

5.5 Effect of Driver-Gas Sound Speed

As in the case of the simple shock tube, it is anticipated that with helium as the driver gas, the blast over-pressure should be greater, for the same p_4 and diaphragm opening time than with air or nitrogen as driver. Carbon dioxide on the other hand should prove a weaker blast than air again under corresponding conditions. All these predictions were confirmed in the present experiments though the differences in blast amplitude and velocity were not especially great.

Figure 8 shows that the peak blast pressure ratio p_2/p_4 when plotted against the dimensionless distance parameter $\frac{x}{L} \frac{a_0}{a_4}$, collapses towards the curve:

$$p_2/p_4 = 18.0 \left(\frac{x}{L} \frac{a_0}{a_4} \right)^{-1.65}$$

6. Conclusions

- a) The flow field produced by a diaphragm bursting in unconfined space has been found to display many important features in common with gun muzzle flows eg. Mach disc barrel shocks and the same distinctive plume shape. An understanding of these features is essential in the assessment of near-field hazards caused by pipe explosions.
- b) Computer predictions of many of the above features are in good accord with experimental observations.
- c) Speed of rupture has an important influence on peak blast over-pressure. Ductile fractures simulated by slowly-opening diaphragms give much-reduced blast amplitudes compared with fast fractures.
- d) A scaling law concerning axial blast decay shows that the pressure diminishes approximately in proportion to the one-sixth power of distance over the first few pipes diameters of travel.
- c) The peak suction some 2 diameters downstream of the diaphragm is considerably in excess of the peak over-pressure and could provide the major source of hazard in a pipeline explosion

REFERENCES

1. A J Armstrong and R Watson "Bursting characteristics of thin metal diaphragm in shock tubes. ASME prep (65-WA/MET-16) (1965)
2. D G Edwards "The bursting pressure of metal diaphragms in square-section shock-tubes" Aero JRAES Vol 74 No 709 (1970)
3. R A Gentry, R E Martin and B J Daly, "An Eulerian Differencing Code for Compressible Flow Problems". Jour Comp Phys 1 8.7 (1966)
4. I I Glass and J Gordon Hall "Shock tubes" UTIA Review No 12 (1958)
5. C Cranz and B Glatzel "Die Ausstromung Von Gasen Be Hohen Anfangsdrucken" Ann der Physik Vol 43 (1914)
6. D G Edwards and A Hillman "Computation of Rocket Blast Fields" 5th International Symposium on Ballistics ENSAE Toulouse (April 1980)

Acknowledgments

The authors wish to thank the Science Research Council UK for their support for this work under Grant GR/A/0074.5

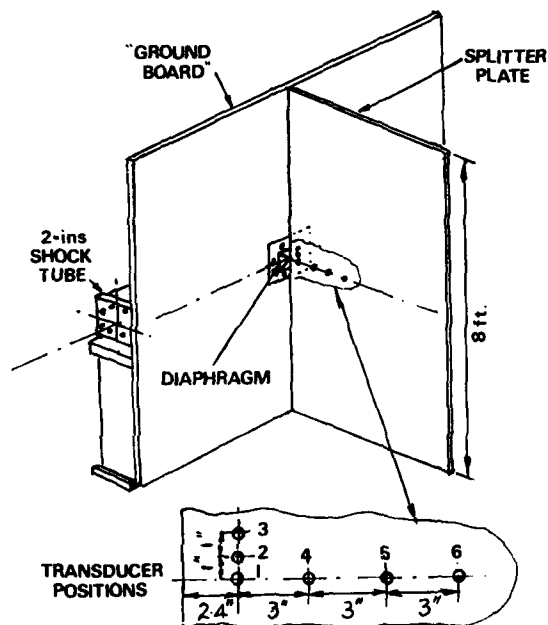


Fig1 LABORATORY BLAST SIMULATOR

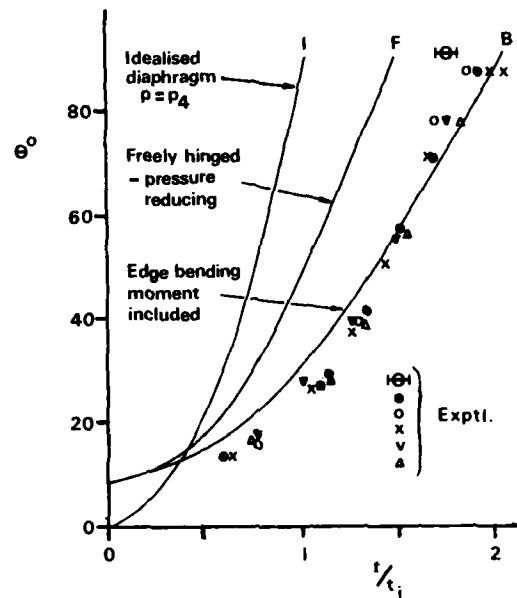


Fig2 DIAPHRAGM PETAL MOTION

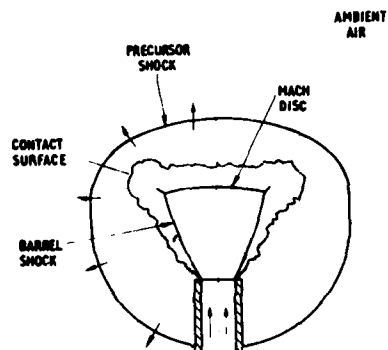


Fig3 ROCKET STARTING FLOW

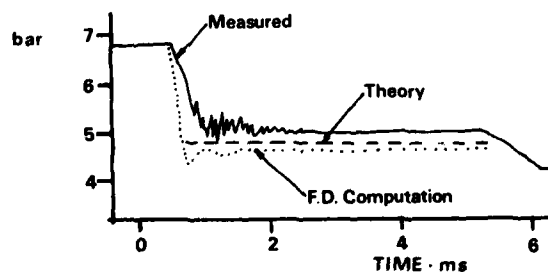


Fig4 WALL STAGNATION PRESSURE

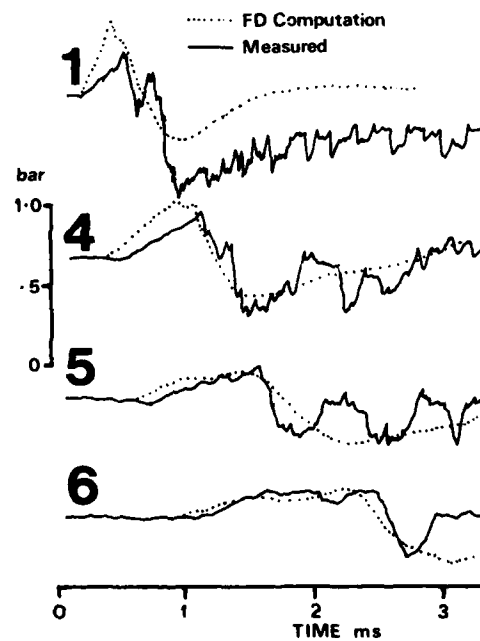


Fig5 AXIAL PRESSURE HISTORIES

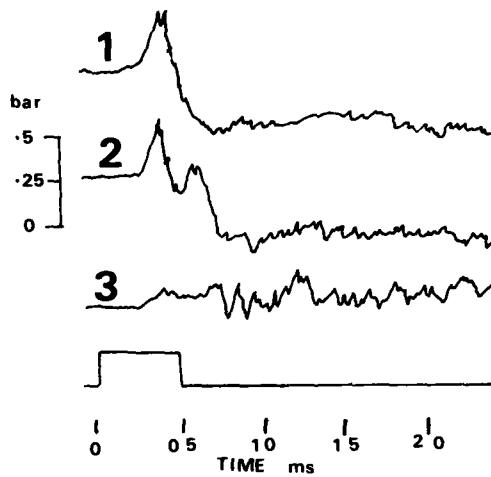


Fig 6 PRESSURE HISTORIES AT DIFFERENT LATERAL POSITIONS

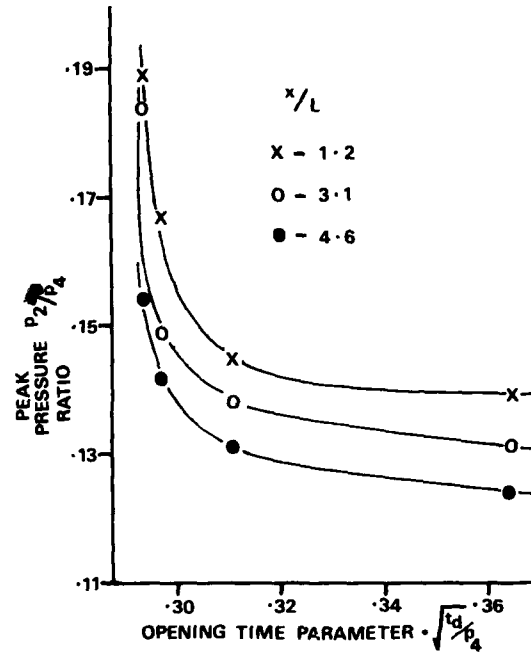


Fig 7 EFFECT OF OPENING TIME ON BLAST PRESSURE

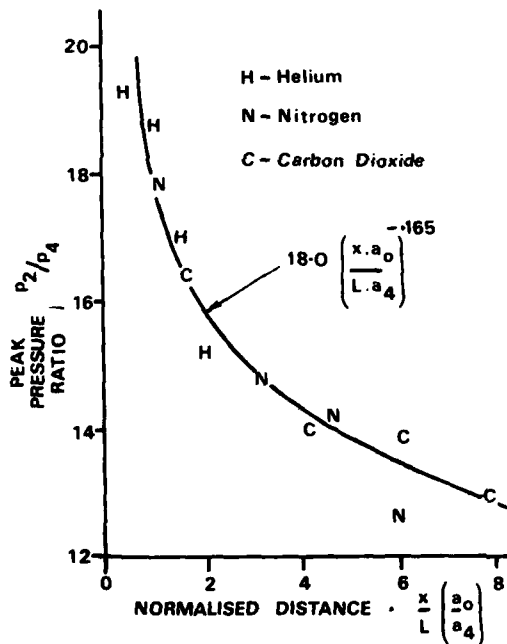


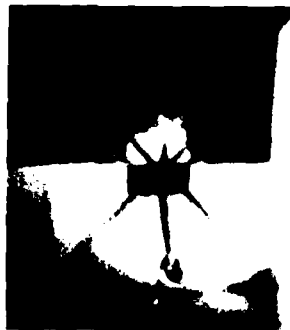
Fig 8 EFFECT OF AXIAL DISTANCE ON BLAST PRESSURE

INITIAL FLOW IN A SHOCK TUBE



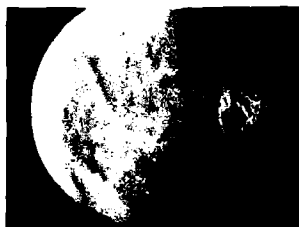
— PLATE 1 —

MULTI-SPARK PICTURE OF DIAPHRAGM BURST (10 kHz)



[752]

Edwards and Smith



140 μ s



125 μ s



285 μ s



200 μ s



425 μ s

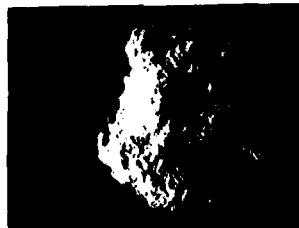


360 μ s



550 μ s

NITROGEN DRIVER



500 μ s

HELIUM DRIVER

PLATE 2 - DEVELOPMENT OF
EXHAUST FLOW FROM
BURST SIMULATOR

PLATE 3 - ROCKET STARTING FLOW



AD P 000301

STUDIES ON MECHANICAL AND AERODYNAMICAL
BLAST-ATTENUATION DEVICES

L.Z.Dumitrescu, A.Mitrofan and S.Preda

INCREST-National Institute for Scientific and
Technical Creation 77962 Bucharest, Romania

Protection of personnel and/or equipment in enclosures against strong blasts involves the use of fast-action valves to shut off ventilation inlets and other openings. Such a device was submitted to shocks up to 5 atms in a large shock-tube facility and after redesign adequate strength was demonstrated.

It was also found that the incident pressure jump is transmitted, with little attenuation, through the valve, during the closing process (2-10 msec), and means to reduce it were sought. To this purpose, a simple model of the relevant wave phenomena was developed and experimental simulations were performed in a small shock-tube. Various types of devices, mainly based on diffraction effects, were investigated, showing that simple but effective solutions can be developed.

Finally, the dangers of focalisation effects of the primary blast are recalled, in the case of improperly designed geometries at the valve inlet.

Introduction

There are various circumstances in which personnel and/or equipment have to be protected, in enclosures, against strong blasts. One common feature is the use of some kind of fast-action valves, to shut off ventilation inlets and other openings, under the action of the blast itself. In this connection, three main problem areas are to be dealt with: (i) to provide and check the mechanical strength of the valves; (ii) to ascertain whether the main blast impulse is properly attenuated and, if necessary, to take further measures to reduce it; and (iii) to ensure, by adequate aerodynamic design of the surrounding structures, that focalisation of the main blast will not occur, overstressing the valves and other inlets.

This paper presents some experiments carried out at the INCREST, in the course of a program which addressed the above subjects; it should be pointed out that the application field of the results is quite diversified, including protection against explosions in coal mines and steam power plants, a.s.o.

Development of a fast-closing valve

Various types of valves designed for this application are described in the literature (e.g.ref.1); they have to fulfill a number of conflicting requirements: adequate strength to resist the maximum design impact loads (ranging from 1 to over 20 atms), positive closure under the action of much weaker shocks (typically 0.05 atm), low aerodynamic resistance (head loss) in the open position, foolproof operation, minimal attendance and maintenance.

One such valve, of the venetian-blind type, has been subjected to tests in the large shock-tube of the INCREST (figure 1). This facility, described at the XII-th Symposium², has a length of 170 m, 900 mm ID and a design overpressure of 22 atms.

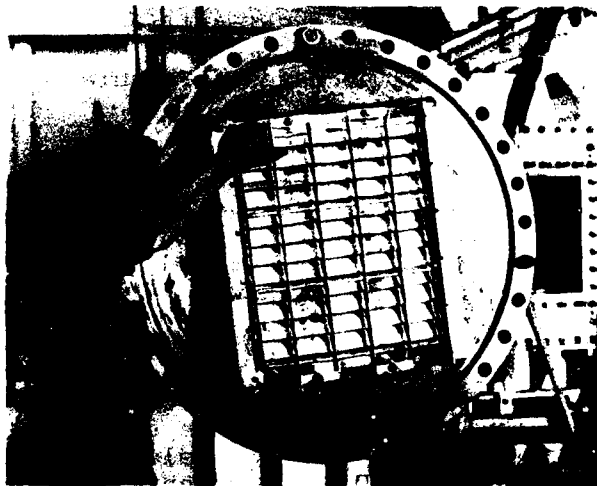


Figure 1.
Installation of
the valve for
testing in the
shock-tube.

To obtain the required shock strength, the driver length of the tube was charged to 10.5 atms; scribed mild steel diaphragms (two 1 mm sheets) were used, which gave very consistent results. The measuring equipment was standard, with a counter chronometer to measure the shock speed (and subsequently to compute the reflected shock overpressure); pressure transducers monitored the upstream and downstream events (figure 2). The duration of the reflected shock pressure plateau was over 50 msec's, quite sufficient to check the operation of the valve.

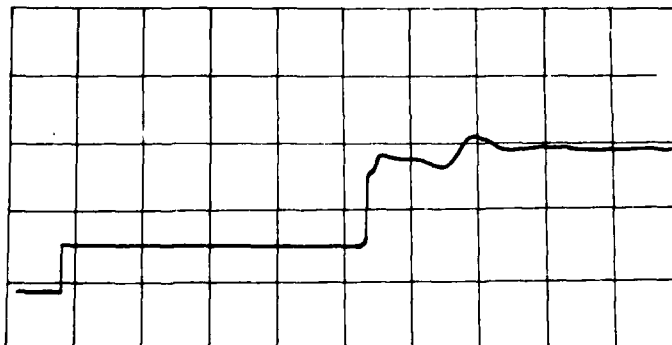


Figure 2.
Oscilloscope re-
cording of the
primary and reflec-
ted shock, upstream
of the valve. Time
base, 1 msec/sq.

The first series of tests showed that the designers of the valve had grossly underestimated the severity of the shock loads, and a complete redesign was necessary before producing a satisfactory piece of equipment.

This experience prompted the decision to submit, on a routine basis, samples of production valves, to the same check in our facility, and no further troubles were encountered with the new design.

As mentioned above, the pressure rise downstream of the valve was also recorded, showing that the closing duration of the blinds was short, but finite (about 10 msecs for a 0.5 atm shock, diminishing to about 2 msecs for the strongest blast) and that, during this period, the primary shock could pass, with little attenuation, through the device. On the recording of figure 2, this closing process is also discernible on the upstream pressure trace. Since, very often, behind the valves there may be equipment subjected to damage (such as sieves, filters a.s.o.), a study was undertaken, to find means for further reducing the severity of the transmitted impulse.

A model for the wave process associated with the operation of the valve

First, it should be pointed out that the typical pressure signature of a strong blast (figure 3) shows a decay with a time constant of the order of a second.

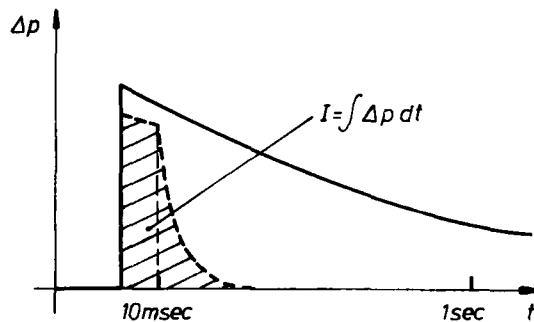


Figure 3. The primary and transmitted pressure impulse.

The effects of the blast on a structure depend on its peak overpressure, but also on the total impulse I . Now, as mentioned above, the duration while the valve is open is much shorter and, therefore, the transmitted impulse is greatly reduced, although the primary shock jump may not be significantly attenuated. In view of the above, it seemed reasonable to replace, for the purposes of our study, the real blast shape with a normal shock, followed by a constant pressure plateau, of a duration covering by some margin the closing time of the valve.

A simplified model of the wave train generated downstream of the valve may then be conceived by assuming that, during the first instants, while the valve is open, the primary shock is transmitted as such, and it is convenient to imagine a piston, whose motion produces the shock (figure 4).

The valve closure is then equivalent to stopping the piston,

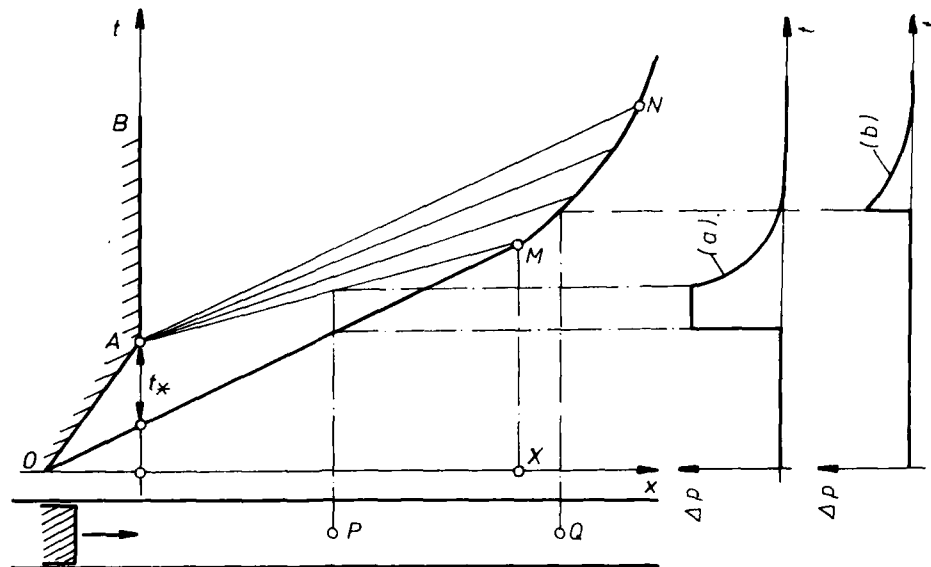


Figure 4. Wave diagram modelling the closing sequence of the valve
 OAB-piston path; OMN-primary shock; AMN-expansion wave;
 t_* -time lag of valve closure; (a)-pressure variation at station P; (b)-ditto, at Q.

which generates an expansion wave that propagates downstream, eventually to catch up with the shock; the time evolution of the overpressure at a point in the downstream duct, as sketched in figure 4 (a), is very similar to actual recordings.

Of course, the strength of the transmitted shock depends on the area of the downstream duct, relative to the free passage area of the valve itself, a point to be discussed later; here we note that the wave diagram sketched above is very similar to the description of events in a shock-tube having a short driver chamber and operated at low to moderate Mach numbers. This remark allowed us to undertake an experimental study of various means for reducing the strength of the transmitted impulse.

The efficiency of shock-attenuating configurations

Our problem is then the following: given a pressure pulse of the shape shown in figure 4 (a), to find means for reducing: (i) its peak overpressure; (ii) the total impulse; and (iii) the initial pressure gradient. On the other hand, constraints are imposed by the requirements of low steady-flow head loss, limited occupied space, and low cost.

1. A first idea would be to make use of viscous dissipation, and frequently various types of filters (sieves, pebble beds a.s.o.) are installed, which could serve the purpose. However, these might produce considerable head losses and, sometimes, the problem of protecting the filters themselves to excessive loads may arise.

2. Another, conceptually simple solution is to reduce the shock intensity by expanding the flow in a large buffer chamber.

The method is effective, but may be costly to implement; one should also be careful to protect objects placed along the centerline of the valve, inside the chamber, since experience shows that the blast is far from decaying spherically, and quite sizeable overpressures may be recorded along the flow direction, even at some distance from the outlet.

3. Our attention was then directed to using the shock diffraction as a possible mechanism for dissipating the impulse energy. The idea would be to fragment the primary shock through multiple diffractions inside a suitably-configured structure; thus, the requirement of smearing the main shock front is achieved; then, vortices and turbulence would act and dissipate the overall energy of the pulse.

This concept originated from a reassessment of a series of experiments carried out some 15 years ago³; it was found then, that when a shock wave was propagating through a duct having a sharp 90 degs. bend, a complicated diffraction pattern developed, resulting in the transmitted shock being replaced by a train of lower-amplitude waves. By contrast, in a rounded bend, the shock passed almost unaffected.

Starting from the above considerations, a series of experiments was undertaken, in a small shock-tube (length 4 m, ID 56 mm, charging pressure 1 atm), with a variable-length driver chamber, mounting various shapes of obstacles at the downstream end. It was assumed that, in the relevant range of parameters, the pressure level, as well as Mach and/or Reynolds number simulation are not essential. Diagnostic tools included pressure recordings and Schlieren pictures. In figure 5, some of the models tested are sketched.

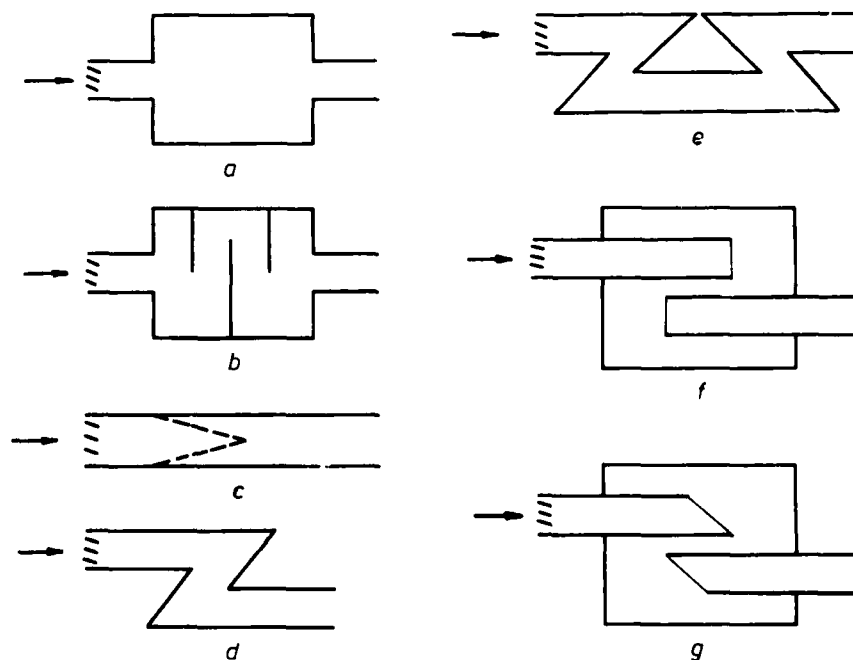


Figure 5. Various types of shock-attenuation configurations.

AD-A122 200

PROCEEDINGS OF THE INTERNATIONAL SYMPOSIUM ON SHOCK
TUBES AND WAVES (13TH. (U) CALSPAN ADVANCED TECHNOLOGY
CENTER BUFFALO NY C E TREADOR ET AL. JUL 81

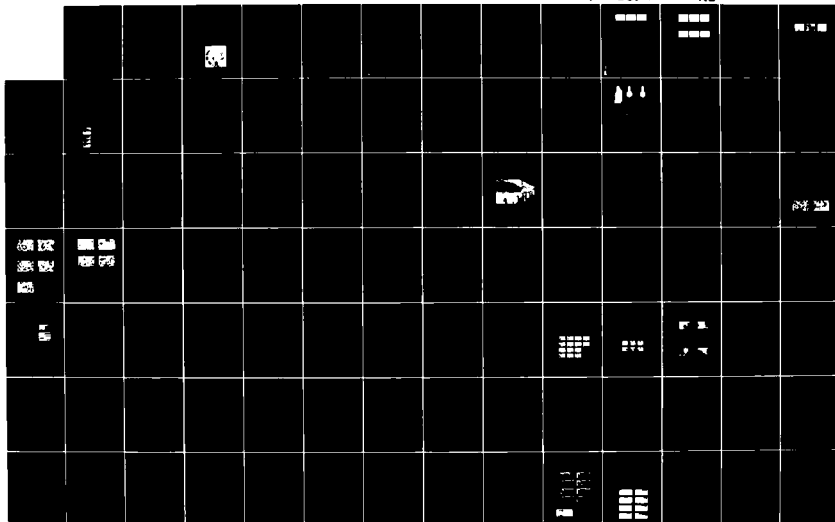
9/10

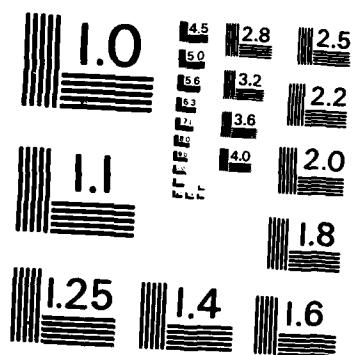
UNCLASSIFIED

AFOSR-TR-82-1031 F49629-81-C-0002

F/G 20/1

NL





MICROCOPY RESOLUTION TEST CHART
NATIONAL BUREAU OF STANDARDS-1963-A

The method is effective, but may be costly to implement; one should also be careful to protect objects placed along the centerline of the valve, inside the chamber, since experience shows that the blast is far from decaying spherically, and quite sizeable overpressures may be recorded along the flow direction, even at some distance from the outlet.

3. Our attention was then directed to using the shock diffraction as a possible mechanism for dissipating the impulse energy. The idea would be to fragment the primary shock through multiple diffractions inside a suitably-configured structure; thus, the requirement of smearing the main shock front is achieved; then, vortices and turbulence would act and dissipate the overall energy of the pulse.

This concept originated from a reassessment of a series of experiments carried out some 15 years ago³; it was found then, that when a shock wave was propagating through a duct having a sharp 90 degs. bend, a complicated diffraction pattern developed, resulting in the transmitted shock being replaced by a train of lower-amplitude waves. By contrast, in a rounded bend, the shock passed almost unaffected.

Starting from the above considerations, a series of experiments was undertaken, in a small shock-tube (length 4 m, ID 56 mm, charging pressure 1 atm), with a variable-length driver chamber, mounting various shapes of obstacles at the downstream end. It was assumed that, in the relevant range of parameters, the pressure level, as well as Mach and/or Reynolds number simulation are not essential. Diagnostic tools included pressure recordings and Schlieren pictures. In figure 5, some of the models tested are sketched.

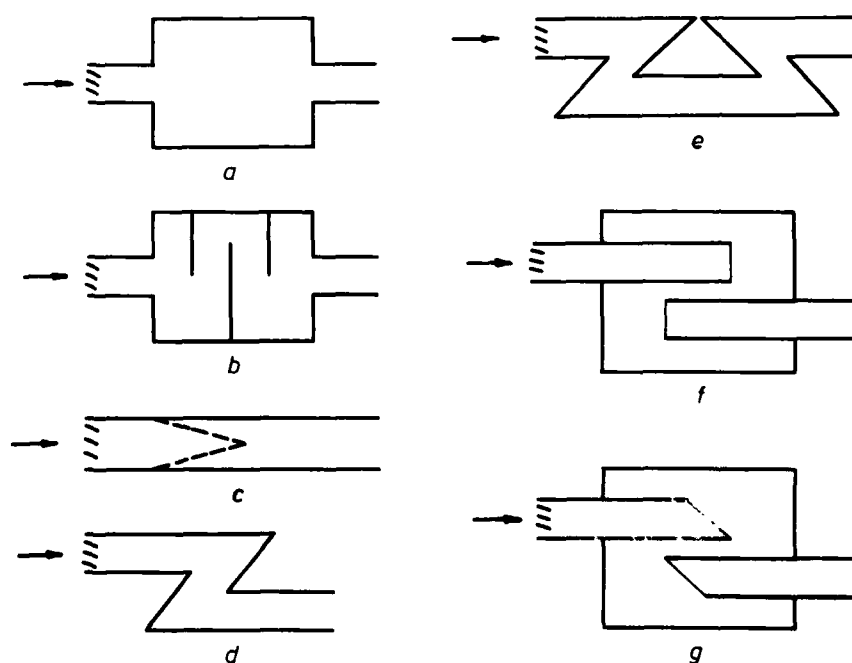


Figure 5. Various types of shock-attenuation configurations.

(a) The first model simulated a small buffer chamber, having an enlarged area three times that of the duct. Results showed that, although at the exit of the chamber some attenuation of the primary shock is present, very soon the shock reshapes itself and little advantage remains. This self-stabilizing property of shock waves is, incidentally, the main explanation of the working principle of the shock-tube.

(b) Better results are obtained if one inserts a number of baffles inside the buffer chamber. These generate a series of diffractions of the primary wave, while the sharp edges of the baffles give birth to a number of vortices, which contribute to dissipation.

(c) Going further along these lines, it was tried to induce a thorough fragmentation of the shock, by inserting in the duct a cone, having a large number of small perforations; it was found, however, that the shock reestablished itself quickly, without any significant attenuation, so that this configuration had to be abandoned.

(d) Much improved attenuation was produced by configurations generating large-scale diffraction patterns and concentrated eddies; an example is a couple of sharp bends having turning angles of over 90 degs (actually, 135 degs were tried), forming a Z traject. The Schlieren picture of figure 6 shows the complicated wave structure into which the primary shock is broken. As a result, the initial shock front is substantially smeared, as may be seen in figure 7.



Figure 6. The diffraction pattern in a couple of sharp 135 degs. bends.



Figure 7. Pressure recording downstream of the sharp bends of figure 6.

(e) This solution may be further improved, e.g. by placing in series two such configurations, in a double Z pattern. Such a structure is easy to build and does not induce unacceptable head losses in steady flow.

(f) By applying the same concepts, one may also improve the efficiency of buffer chambers without increasing their volume, by not letting the valve to discharge directly into the chamber, but providing two lengths of tubing inside the chamber, at the inlet and outlet, as shown in figure 5, f.

(g) Even further attenuation and broadening of the shock front is obtained by bevelling the ends of the tubings described above. Such a design is also relatively easy to implement, even in existing sites, and should be recommended.

4. In addition to these various configurations based on diffraction processes, another, very simple solution has been investigated. Referring back to figure 4, one may see that the primary shock, after being transmitted through the valve, will eventually be caught by the expansion wave generated at the valve closure; thereafter, the shock will be gradually eaten up by the expansion (figure 4, (c)). Therefore, it suffices to provide, downstream of the valve, a tubing of the requested length, to take advantage of this process. The catch-up distance, X , is readily computed and, in the M_s range relevant to our problem, is of the order of 10 to 15 times $a_0 t_*$, where a_0 is the sound speed, and t_* the closing time of the valve. Experiments in the shock-tube fully confirmed these considerations. In view of its simplicity, this solution is, perhaps, the most practical, in addition producing low head losses, little structural design problems, a.s.o. In case a sufficient length cannot be accommodated, one may combine this solution with one of the above, e.g. by placing at the tube end, a Z or double Z bend (figure 8).

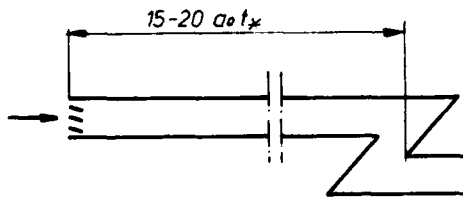


Figure 8. An efficient configuration for reducing the strength of the transmitted shock.

Finally, it should be pointed out that, in most cases the intensity of the transmitted shock is somewhat reduced with regard to the primary blast, by the mere fact that the downstream duct has usually, a larger cross-section than the free passage area of the valve in the open position.

Prevention of focalisation effects

We now turn our attention to phenomena taking place at the entrance to the valve, when it is struck by the blast. It should be pointed out that the direction from which the blast could arrive is seldom known exactly and, therefore, a worst case has to be considered, namely that of frontal impingement. If the valve is mounted flush with a plane wall (or the ground), the peak overpressure would correspond to that behind the reflected shock, and

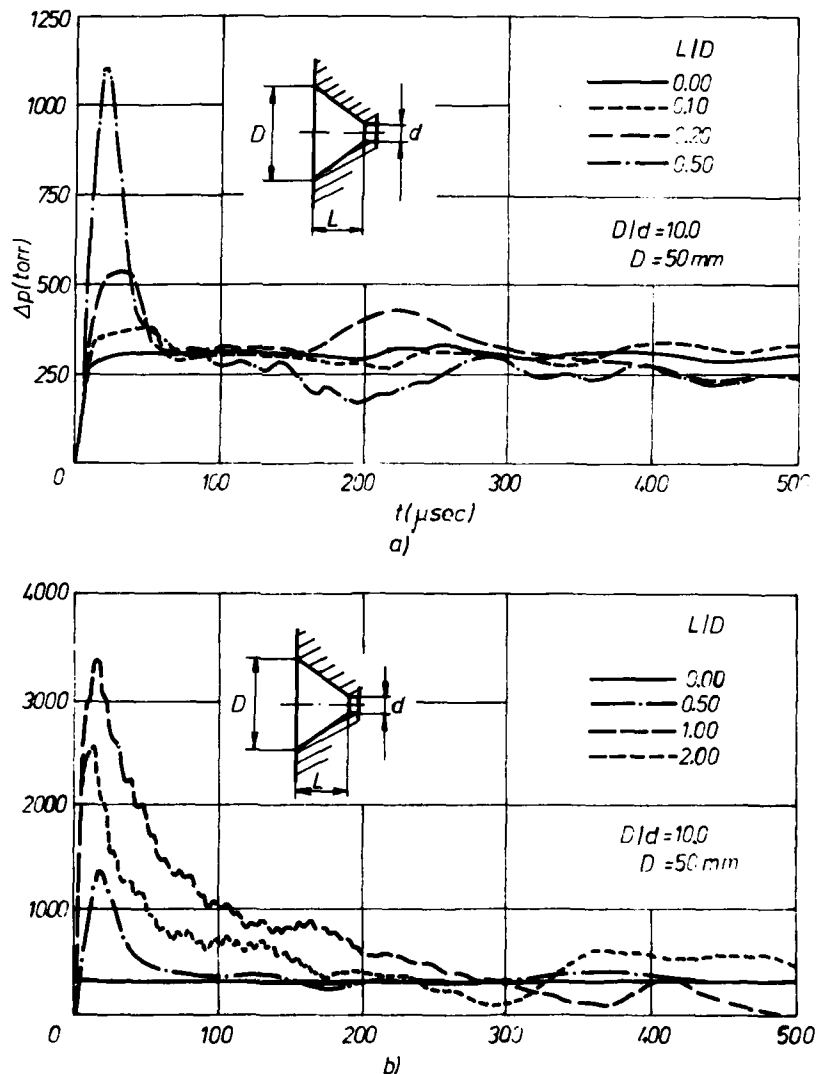


Figure 9. Amplification of shock waves in conical cavities.
a - The effects of shallow cavities.
b - The effect of deeper cavities.

this would be the intensity of the transmitted pulse through the valve, while open. However, the geometry of the inlet may produce important effects.

In this connection, we recall here some results of a former experimental study⁴, on the overpressure produced at the end-wall of a shock-tube, if a cylindrical recess is present. It was found that even very shallow cavities ($L/D=0.02$) produced visible pressure peaks, while the presence of a longer tubing ($L/D=1.0$) doubled the reflected shock overpressure.

Even more drastic is the effect of a conical cavity, as shown in figure 9: for a ratio $L/D=0.2$ the pressure jump is doubled, while at $L/D=2.0$ a tenfold amplification is found. Unfortunately, it is not uncommon to see such configurations in actual sites.

Bearing these in mind, one should take care to avoid geometries which might produce focalisation effects. The simplest way is to mount the valves flush with the walls; one may also use some form of protection, following the ideas discussed in the preceding section, e.g. by installing a properly-designed buffer chamber in front of the valves.

Finally, one should mention that, in some instances, the severity of blast loadings may depend on large-scale features of the terrain and/or structures present⁵, and some sort of model testing of the whole site might be warranted. A large facility, like the one mentioned, would be useful in such a project.

Conclusions

The shock-tube proves itself again to be a versatile tool, enabling a large variety of subjects to be investigated, and systematic application of concepts related to wave propagation and diffraction leads to the development of solutions to a problem with manifold practical implications.

References

1. Bergman, S.G.A., Rapid-closing anti-blast valves, Report 104:3, Royal Swedish Fortification Administration Research Dept. (1972).
2. Dumitrescu, L.Z., Proceedings of the XII-th International Symposium of Shock Tubes and Waves, p.137-146 (1979).
3. Dumitrescu, L.Z., Proceedings of the Royal Aeronautical Society Centenary Congress in conjunction with the V-th ICAS Congress, London, p.187-205 (1966).
4. Dumitrescu, L.Z., Cercetări în tuburile de șoc (Studies in Shock-Tubes, in Romanian), p.277-286, Editura Academiei, Bucharest (1969).
5. Brode, H.L., Proceedings of the XII-th International Symposium on Shock Tubes and Waves, p.31-47 (1979).

RESPONSE OF A ROOM SUBJECTED TO SIMULATED SONIC BOOMS*

N. N. Wahba, I. I. Glass and R. C. Tennyson

Institute for Aerospace Studies, University of Toronto

Toronto, Canada

The response of a room of plaster-wood construction with an open window subjected to sonic-boom loading was investigated both analytically and experimentally. First, the pressure variations inside the room were predicted analytically by viewing the room as a Helmholtz resonator. The UTIAS Travelling-Wave, Horn-Type, Sonic-Boom Simulator was then used to generate sonic booms in order to check the analysis. The measured room pressures were in good agreement with the predicted results. The room overpressures in some cases were found to be twice as great as that in the incident sonic booms. Second, the structural response of the room walls due to the pressure loading was also predicted analytically and the results compared to experiments using strain gauges. The agreement between analysis and experiment was very satisfactory. The effect of various physical parameters such as sonic-boom duration, room volume and window area were investigated. Third, the statics and dynamics of a cracked plaster-wood wall were investigated using a finite-element method and checked experimentally.

The analysis and experimental data can be useful in assessing structural damage caused by supersonic-aircraft overflights.

INTRODUCTION

Sonic boom is the transient pressure wave experienced by an observer exposed to the shock-wave system created by a supersonic aircraft. The sonic boom has an overpressure signature that resembles a letter N, as illustrated in Figure 1. Therefore, it is often called an N-wave. This wave can be defined by the peak overpressure p_0 , total duration τ and risetimes of the front and tail waves t_r and t_f , respectively. Typical values of the peak overpressure, duration and risetimes are 100 N/m^2 , 200-300 ms and 1-5 ms, respectively, for a current supersonic transport (SST) aircraft such as the Anglo-French Concorde, Soviet TU-144 or a large military bomber like the B-58.

*This work was supported by Transport Canada Research and Development Centre, the Natural Sciences and Engineering Council and the U.S. Air Force under Grant AFOSR-77-3303.

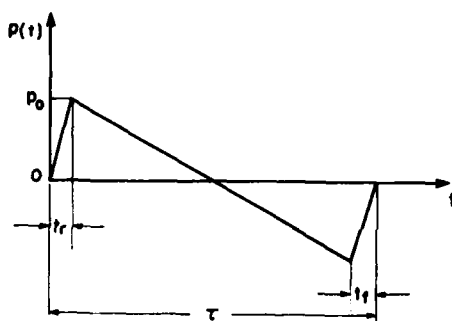


Figure 1. Typical N-wave pressure signal.

A shorter fighter aircraft such as the F-16 produces a sonic boom with a duration correspondingly shorter at about 100 ms.

As a building is subjected to a sonic boom, pressure disturbances are transmitted into the interior of the building through open windows and doors and through its structural elements according to their flexibilities and sound transmissibilities. Theoretical studies of the dynamic response of buildings to sonic-boom loading have been limited to very idealized mathematical models such as a single degree of freedom system, beams or isotropic homogeneous plates (Refs. 1-5). However, these simplified models cannot accurately represent the detailed response of a typical house (Ref. 6) owing to a lack of representation of many factors such as the coupling between the structural elements, the interaction of the air cavities and the structure of the buildings as well as a lack of knowledge of the mode shapes, natural frequencies and structural damping of the elements.

Several overflight tests were conducted in St. Louis (Refs. 7, 8), Oklahoma City (Refs. 9-11), White Sands (Refs. 10, 11) and Edward Air Force Base (Ref. 12) using military aircraft to generate sonic booms. The objective of these tests was to study the reaction of communities to sonic-boom exposure. Respondents had a negative attitude toward the sonic boom. One of the serious concerns was the possibility of building damage due to sonic-boom loadings. The graph in Figure 2 illustrates the various types of reported damage mentioned in complaints and indicates their frequencies as a percentage of the total (Ref. 7). Although plaster cracks were reported most frequently (about 43% of the total), many cases were considered to be doubtful. The reported damage was considered possibly valid in only about 20% of the cases investigated (Ref. 8). In plaster walls for example, the situation is complicated because plaster never appears as a single structural element. However, the existence of a large number of stress concentrations do exist in corners and at the junctions of ceiling and walls.

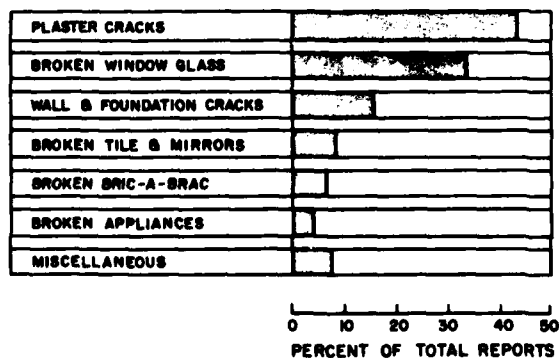


Figure 2. Bar graph showing types of damage due to sonic booms reported in complaints (but not validated) in the Greater St. Louis area. Percentage values of abscissa are based on a total of 3,114 complaints for which data were available (Ref. 7).

Overflights proved to be disadvantageous mainly because of the substantial organization involved and associated costs. Consequently, laboratory tests were conducted in the UTIAS Travelling-Wave Horn-Type Sonic-Boom Simulator (Ref. 13), where fatigued plaster panels of relatively small area (40cm x 40cm) were first subjected to sonic booms to test the so-called "life-time" concept produced by weathering and stress cycling. The results showed that panels of this type could withstand sonic booms for centuries without cracking (Ref. 14).

The objective of the present program was to obtain both analytical and experimental data for an actual plaster-wood room subjected to controlled sonic-boom loading. The purpose was to study the possibility of damage arising from resonance conditions.

SIMULATED SONIC BOOMS

The UTIAS Travelling-Wave Horn-Type Sonic-Boom Simulator (Refs. 13-16) was used to generate sonic booms. The simulator consists essentially of a steel-reinforced concrete horizontal pyramidal horn (25m long with a 3m square base). A unique dual flap-type mass-flow valve is installed near the apex of the horn to regulate the release of stored air from a high-pressure reservoir into the horn. This sudden discharge creates a travelling N-wave that propagates to the large end of the pyramid. The design, operation and performance of the sonic boom-simulator are described in Ref. 16. The open base of the horn is covered with a recoiling porous-piston reflection-eliminator to minimize the undesirable reflection of the sonic-boom signals from the open end of the horn. A full scale test room is linked to the horn interior by a 1.8m x 3.6m cutout. This cutout is sealed with a 1.9cm thick wooden board to permit various sizes of openings. The inner dimensions of the room are as follows: 2.42m high, 4.1m long and 3.2m wide. The walls and ceiling of this room are made of plaster-wood construction. A schematic diagram of the sonic-boom simulator is shown in Figure 3.

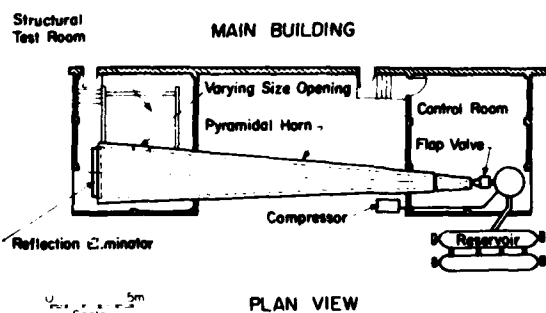


Figure 3. Plan view of travelling-wave sonic-boom simulator.

The peak overpressure and duration of the simulated boom can be controlled independently such that either one is less than, equivalent to, or greater than that obtained for an actual aircraft. Figure 4 shows oscilloscope pressure traces of simulated sonic booms for three different durations (100, 190 and 285ms) measured at a distance of 21.3m from the apex of the horn. There are weak pressure perturbations superimposed on the N-wave resulting from the fact that the base of the horn and the reflection eliminator are enclosed in a room which includes the test room. Therefore, the wave leaving the horn is partially reflected from the walls and propagates back into the horn through the porous piston. Furthermore, as the room air responds according to the wave leaving the horn, much like a Helmholtz resonator, additional pressure perturbations follow the reflected wave into the horn.

PRESSURES INSIDE A ROOM SUBJECTED TO SONIC BOOMS

The pressure induced in a room by a sonic boom incident on an open window

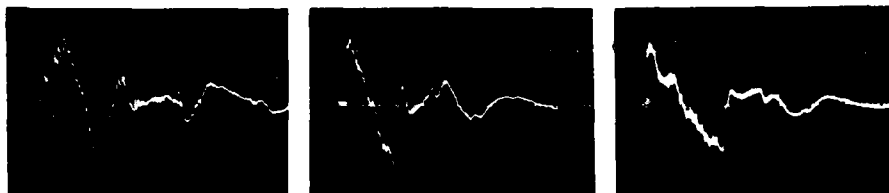


Figure 4. Overpressure vs time for varying simulated sonic boom duration. Vertical scale: 54 (N/m²)/div.

(a) $\tau = 100\text{ms}$, time base 50ms/div; (b) $\tau = 190\text{ms}$, 100ms/div; (c) $\tau = 285\text{ms}$, 100ms/div.

was investigated both analytically and experimentally in some detail (Ref. 17). The room was assumed to be a rigid enclosure of volume V having a window with an opening of area A . It was found that the low frequency components of the sonic boom which contain most of the acoustic energy dominate the interior pressure profile. Based on a Fourier transform analysis it was proved that the frequency components from 0 up to $(30/2\pi\tau)$ Hz contain 94% of the total energy of an N-wave. Although the high-frequency components of the sonic boom are of importance in the study of "startle effects" in humans and animals, they are unimportant for structural response. The different types of energy dissipation associated with the window, the air, the structure and the absorbing surfaces of the room were taken into account. It was found that the system can be represented by a second order differential equation given by

$$\left(\frac{1}{2\pi\bar{\tau}}\right)^2 \left(\frac{d^2 p_r}{dT^2}\right) + \left(\frac{\zeta}{\pi\bar{\tau}}\right) \left(\frac{dp_r}{dT}\right) + p_r = p(t) \quad (1)$$

where p_r is the room pressure and T is the normalized time ($T = t/\tau$). Therefore, the room pressure is governed by two parameters: the damping ratio ζ and the period ratio $\bar{\tau}$ ($= \tau/t_n$ where t_n is the natural period of the system). Both the damping ratio and the period ratio were related to the physical properties of the system such as the room volume V , window area A , and the average absorption coefficient of all surfaces of the room α_m . The analysis showed that the system should be frequency dependent. Therefore, an analytical method based on a Fourier transform was developed to find the pressure-time histories of the room. The room pressure has the appearance of a damped sine wave and decays rapidly as the damping increases (higher value of α_m , smaller room volume or window area). For a lightly damped system ($\alpha_m = 0$), the room overpressures were found to be twice as great as that in the incident sonic boom when the natural period of the system and the duration of the N-wave are equal.

The concept of a Helmholtz resonator was confirmed experimentally by showing the room pressure was nearly uniform everywhere. Figure 5 shows the pressure signatures measured at three different positions in the room. It can be seen that the three signatures are almost identical.

Sonic booms of the type shown in Figure 4 served as incident waves. Five window sizes ranging from 0.09m² to 0.93m² were investigated. Figure 6 illustrates the pressure-time history for a 0.9m x 0.3m opening subjected to incident waves of 100, 190 and 285ms duration. Comparisons between the predicted and measured pressures for various window sizes are shown in Figure 7. Satisfactory agreement between analysis and experiment was obtained in terms of signature form, phase and amplitude. The predicted pressure oscillations appear to decay faster and have lower amplitudes than the experimental values owing to the omission in the analysis of the perturbations following the N-wave.

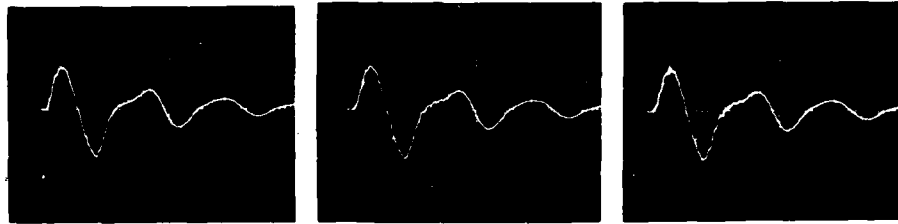


Figure 5. Room overpressure vs time for varying interior locations. $\tau = 190\text{ms}$, window $0.3\text{m} \times 0.3\text{m}$, vertical scale $54 \text{ (N/m}^2\text{)}/\text{div}$, time base $100 \text{ ms}/\text{div}$. (a) At the centre of the room; (b) at the centre of rear wall; (c) at the centre of side wall.

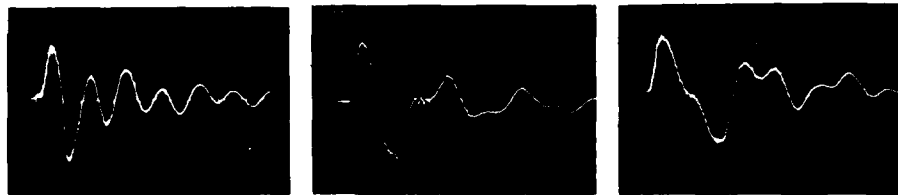


Figure 6. Overpressure vs time at centre of room for various simulated sonic booms. Window $0.9\text{m} \times 0.3\text{m}$, vertical scale $54 \text{ (N/m}^2\text{)}/\text{div}$, time base $100\text{ms}/\text{div}$. (a) $\tau = 100\text{ms}$ ($\bar{\tau} = 0.76$); (b) $\tau = 190\text{ms}$ ($\bar{\tau} = 1.45$); (c) $\tau = 285\text{ms}$ ($\bar{\tau} = 2.18$).

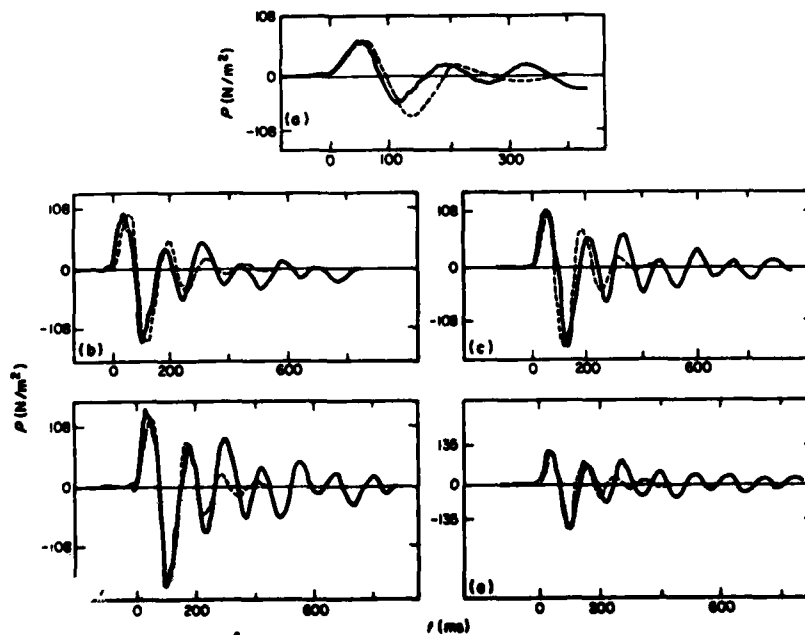


Figure 7. Comparison of predicted and measured pressures inside room for various window sizes. $\tau = 100\text{ms}$; ——— experiment, - - - theory. Window sizes: (a) $0.3\text{m} \times 0.3\text{m}$; (b) $0.9\text{m} \times 0.3\text{m}$; (c) $0.6\text{m} \times 0.6\text{m}$; (d) $0.9\text{m} \times 0.6\text{m}$; (e) $1.5\text{m} \times 0.6\text{m}$.

DYNAMIC RESPONSE OF A PLASTER-WOOD WALL TO SONIC BOOMS

The test room is linked to the horn interior by a cutout as shown in Figure 3. The inner surfaces of the walls and the ceiling of this room are made of plaster while their outer surfaces are made of 1.0cm thick plywood nailed to wooden framing joists (8.9cm x 3.5cm) for the walls and (19.5cm x 3.8cm) for the ceiling. The distance between centrelines of two consecutive joists is 40.0cm. The room has a light-weight wooden door which was kept closed throughout the experiments. The wall facing the opening was chosen for the structural response study. Figure 8(a) shows a schematic diagram of this wall and the locations where 1.27cm strain gauges were mounted. Figure 8(b) illustrates the various materials forming the wall cross-section.

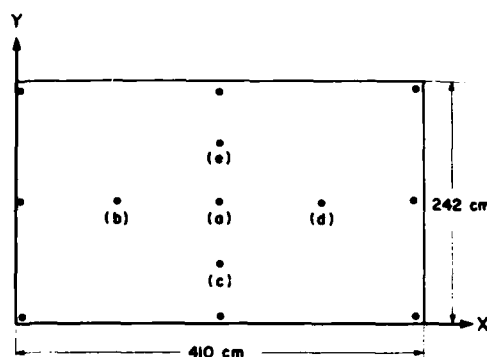


Figure 8(a). Schematic diagram of the plaster-wood wall indicating the positions of strain gauges.

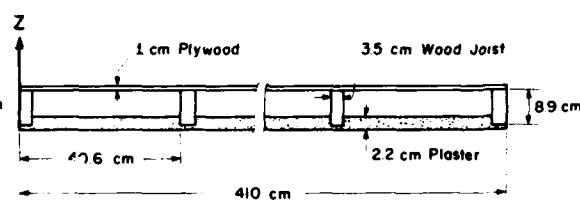


Figure 8(b). Cross-section of the plaster-wood wall.

The elastic constants, such as modulus of elasticity and Poisson's ratio for each material, were determined experimentally with the use of strain gauges installed on a cantilever beam specimen deflected by a tip load. The stress generated at the mounting point of the gauge may be calculated by simple beam theory. The plaster was considered an isotropic material while the plywood and the wooden joists were assumed to be orthotropic and hence the elastic constants were determined both parallel and perpendicular to the fibres. The structural damping of the wall was estimated by exciting the natural modes of the wall using a loudspeaker and measuring the resulting steady-state strains.

Two different methods of analysis were adopted. In the first method, the deflections were expressed by a double trigonometric function series in space variables (X,Y) and generalized coordinates as function of time. In the second method, the finite-element technique was used to predict the dynamic response. Lagrange's equations were then used to develop the following equation of motion in a matrix form

$$[M] \left\{ \frac{d^2 q}{dt^2} \right\} + [C] \left\{ \frac{dq}{dt} \right\} + [K] \{q\} = \{F\} \quad (2)$$

where [M], [C] and [K] are the mass, damping and stiffness matrices, respectively. They were evaluated using the density, dimensions and elastic constants for each individual material as well as the damping constant of the wall. The load vector {F} was derived from the external work done by the room pressure applied on the wall, and the unknown vector {q} represents the generalized coordinates. Solving Eq. (2) gives the natural frequencies and deflections of the wall and hence the strains ϵ and the stresses σ can be determined.

A series of tests was conducted to verify the analysis. Strains in both the X and Y directions were measured at the locations indicated in Figure 8(a).

A sample of the measured room pressures (the upper traces) and the corresponding measured strains ϵ_{yy} (the lower traces) is illustrated in Figure 9. It can be seen that both room pressure and strain have the same appearance of a damped sine wave and their amplitudes increase as the window size increases. Note that the strain signals were inverted to show the correspondence between them and the loading-pressure signals.

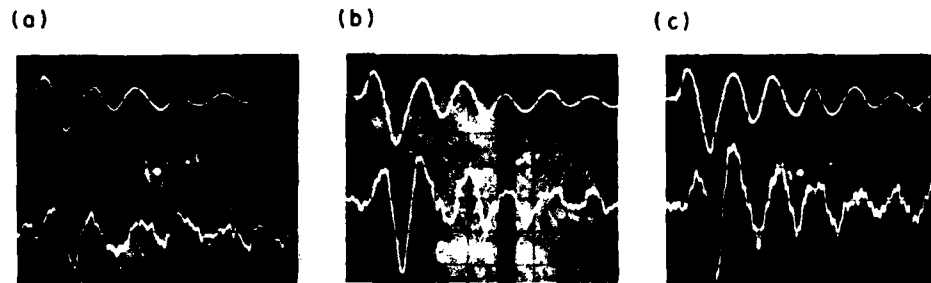


Figure 9. Room overpressure and strains at the centre of the wall vs time for varying window sizes; time base 100ms/div, upper traces (150 N/m²)/div, lower traces (10 $\mu\text{m/m}$)/div.

(a) Window 0.37m²; (b) window 0.56m²; (c) window 0.93m².

While the largest strains were measured at the centre of the wall, very small strains were obtained along the wall edges. This justifies the assumption of considering the wall as a simply-supported plate. Due to the double symmetry of the wall, the measured strains at (b) and (c) are similar to those at (d) and (e), respectively. Strains in the horizontal direction ϵ_{xx} were found both analytically and experimentally to be very small all over the plaster surface. The agreement between the measured and predicted strains at various locations for different window sizes is very satisfactory as shown in Figure 10.

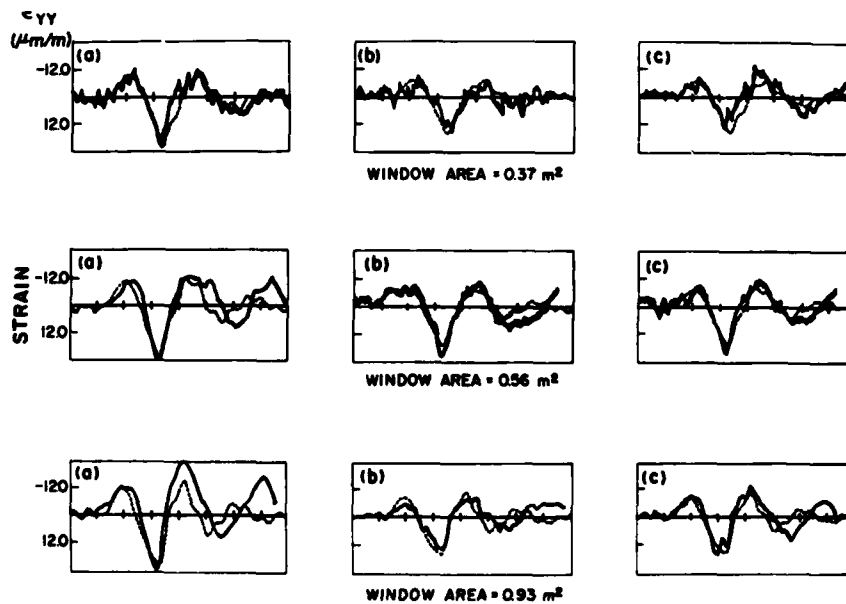


Figure 10. Comparison between predicted and measured strains in different locations for various window sizes. $\tau = 100\text{ms}$, ——— experiment, --- theory, time base 50ms/div.

Since the primary interest of this work was to study the possibility of damage in such a plaster-wood construction due to sonic-boom loadings, stresses were evaluated along the thickness of the wall. Figure 11 shows the resulting strains and stresses in both the X and Y directions, calculated at the centre of the wall where the largest stresses were found. It should be mentioned that the N-wave duration and window size were chosen in order to achieve a resonance condition for the room as an acoustic system. Consequently, higher loadings can be provided. Due to the compatibility of the deflections, the strains are continuous throughout the thickness of the wall, unlike the stresses which have different values at the interface between the materials due to the change in elastic constants.

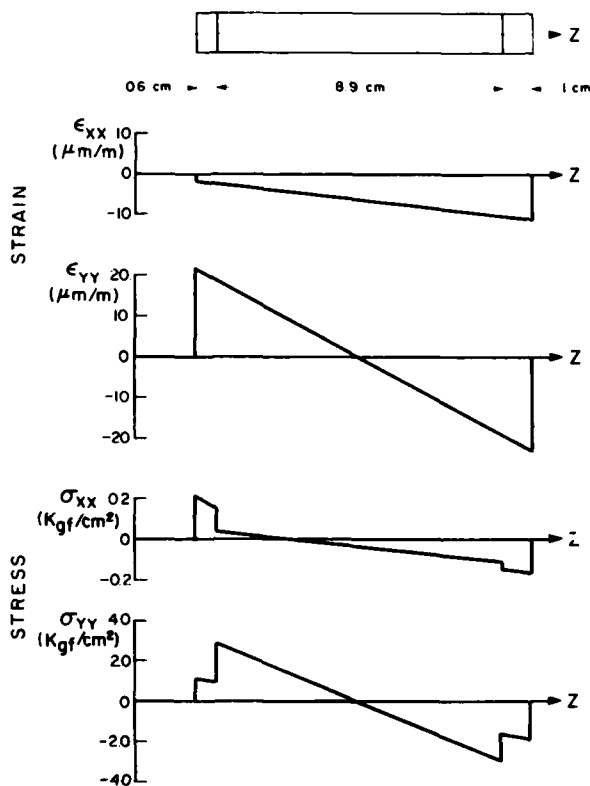


Figure 11. Strains and stresses calculated at the centre of the wall throughout the thickness.

Although the situation considered herein is critical since the room is acoustically at resonance, the stresses produced due to an N-wave having an overpressure of 150 N/m^2 amount to only 7% of the yield stress of the plaster. Therefore, one can conclude that no damage is expected for such structures under these loadings.

DYNAMIC RESPONSE OF A CRACKED PLASTER-WOOD WALL TO SONIC BOOMS

In many cases, structural failures under loading conditions are frequently attributed to the growth of cracks. During the past two decades, several investigators have given their attention to predicting accurately the stresses in the immediate neighbourhood of the crack tip, as the fracture of a structure is mainly governed by this stress field. Williams (Ref. 18) has shown that the stresses near the crack tip tend to infinity in a way which is proportional to the reciprocal of the square root of the distance from the crack tip. The strength of the singularity, which is referred to as the stress intensity factor, depends on the magnitude of the loading forces and the configuration of the structure including the crack size. For complicated structures and

loadings such as a plaster-wood wall under sonic-boom loading, no analytical solutions are available owing to the inherent difficulties in evaluating the crack tip stresses. Therefore, numerical methods, such as the finite-element technique, are appropriate in such cases. The details of the analysis and the results will be published elsewhere (Ref. 19).

A horizontal crack of 19cm length was artificially introduced in the plaster. Strain gauges were then mounted in the immediate vicinity of the crack tip along the crack direction. Figure 12 shows the room pressure as well as the strains measured at the centre of the wall and also at distances of 0.6cm, 1.25cm and 2.9cm from the crack tip. The size of the window in this experiment was 0.93m^2 and subjected to an N-wave having a duration of 100ms. The room pressure and strains have a similar signature form. However, strains measured near the crack tip are about nine-fold larger in magnitude than those measured at the centre of the wall. [Note that the largest strain of the uncracked wall was measured at the centre of the wall and there was no significant change in the strain at (a) after introducing the crack.] It can also be seen that the strains decrease rapidly as the distance from the crack tip increases. Using these measured results, the stress intensity factor was computed. Subsequently, an experiment was conducted to estimate the critical stress-intensity factor for the plaster at which a crack starts growing by applying a pure cylindrical bending moment to a square plate of plaster. Using this value of the critical stress-intensity factor, it was concluded that this type of cracked plaster-wood wall could withstand an N-wave having an over-pressure up to 400 N/m^2 without crack propagation. The work in this area is being continued and extended to investigate various crack situations and sonic-boom loading conditions.

CONCLUSIONS

The response of a room of plaster-wood construction with an open window subjected to sonic-boom loading was investigated. The N-wave pressure signatures were generated in the UTIAS Travelling-Wave, Horn-Type, Sonic-Boom Simul-

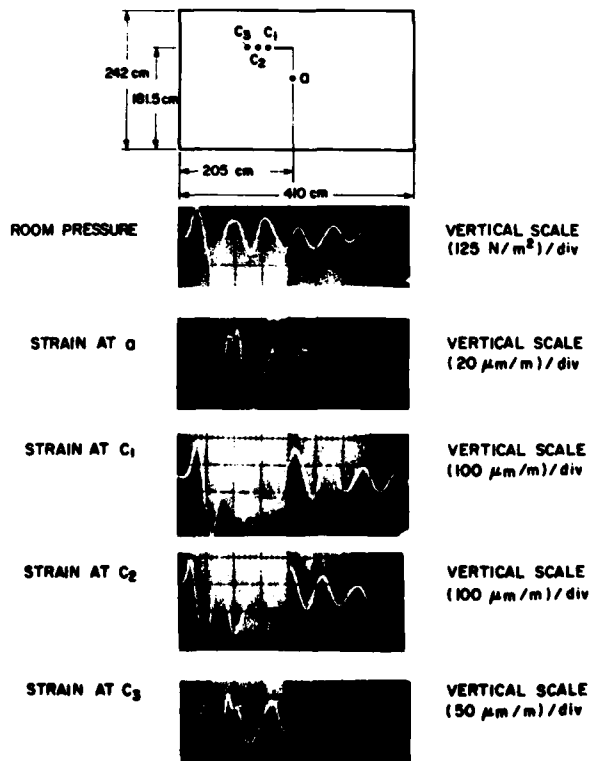


Figure 12. Time histories of room pressure and corresponding strains measured at the centre of the wall and in vicinity of crack tip. Window size 0.93m^2 , $\tau = 100\text{ms}$, time base $100\text{ms}/\text{div}$.

ator. It was observed that if the dimensions of the room are small in comparison to the wavelength of the sonic boom, then the room acts as a Helmholtz resonator since the low-frequency components of the sonic boom contain most of the acoustic energy. This was confirmed experimentally by showing that the room pressure was nearly uniform everywhere. The room overpressures in some cases were found to be twice as large as those in the incident sonic boom. The pressure-time histories of the room were predicted using a Fourier transform method and the results were found to be in good agreement with test data.

The structural response of the room walls, due to the pressure loading, was predicted analytically using a series solution for the deflection as well as using a finite-element technique. The agreement between analysis and experiment was very satisfactory for the range of sonic-boom durations, room volumes, window areas and wall absorptivity investigated. In general, it was found that the stresses produced in the wall were very small (within 7% of the yield stress of the plaster).

After introducing a wall crack, strains at the centre of the wall were not observed to change significantly. However, strains measured in the vicinity of the crack tip increased as expected about nine-fold compared to those measured at the centre of the wall. These strains showed the tendency to be proportional to the reciprocal of the square root of the distance from the crack tip. It was found that such a type of cracked plaster-wood wall would withstand a sonic boom having an overpressure up to 400 N/m^2 without crack propagation. It is worth mentioning that this value is about four times the overpressure produced by current supersonic transports under normal conditions. It should not be inferred from this result that so-called superbooms or spiked booms would cause crack propagation. As noted, most of the energy is in the low-frequency range and the spikes would add very little energy to the total. Consequently, the entire boom would have to contain the energy found in a 400 N/m^2 normal N-wave, which is usually not encountered, before crack propagation would occur.

ACKNOWLEDGEMENT

We wish to thank Dr. J. J. Gottlieb and Dr. J. S. Hansen for their valuable comments and discussions.

REFERENCES

1. M. J. Croker, R. R. Hudson, *J. Sound & Vibration* 9, 454-468, 1969.
2. D. H. Cheng, J. E. Benveniste, NASA CR-1281, 1969.
3. G. Koopmann, R. M. Orris, *J. Sound & Vibration* 19, 373-377, 1971.
4. J. E. Benveniste, D. H. Cheng, *J. Aircraft* 4, 494-498, 1967.
5. A. Craggs, NASA CR-1175; also NASA CR-1176, 1968.
6. B. L. Clarkson, W. H. Hayes, *J. Acoust. Soc. Amer.* 51, 742-757, 1972.
7. C. W. Nixon, H. H. Hubbard, NASA TN D-2705, 1965.
8. C. W. Nixon, P. N. Borsky, *J. Acoust. Soc. Amer.* 39, S51-S58, 1966.
9. D. A. Hilton, V. Huckel, R. Steiner, D. J. Maglieri, NASA TN D-2539, 1964.
10. T. H. Higgins, 70th Mtg. Acoust. Soc. Amer., St. Louis, 1965.
11. R. L. Sharpe, G. Kost, *Amer. Soc. Civil Engng. Struct. Div. Jour.* 97, 1157-1174, 1971.
12. "Sonic Boom Experiments at Edwards Air Force Base", Interim Rep., Contract AF 49(638)-1758 by Stanford Res. Inst. for the National Sonic Boom Evaluation Office, 1967.
13. I. I. Glass, H. S. Ribner, J. J. Gottlieb, *CAS J.* 18, 235-246, 1972.
14. B. R. Leigh, R. C. Tennyson, I. I. Glass, *CAS J.* 21, 352-360, 1975.
15. J. J. Gottlieb, *Prog. Aerospace Sci.* 17, 1-66, 1976.
16. J. J. Gottlieb, W. Czerwinski, N. N. Wahba, R. E. Gnoyke, 12th Int. Symp. on Shock Tubes & Waves, Jerusalem, 276-287, July 16-19, 1979.
17. N. N. Wahba, I. I. Glass, R. C. Tennyson, *J. Sound & Vibr.* 68, 259-279, 1980.
18. M. L. Williams, *Trans. ASME, J. Appl. Mech.* 24, 109-114, 1957.
19. N. N. Wahba, Univ. of Toronto, Ph.D. Thesis (to be published).

AD P000303

SHOCK DIFFRACTION COMPUTATIONS OVER COMPLEX STRUCTURES

Andrew Mark
Ballistic Research Laboratory
U.S. Army Armament Research and Development Command
Aberdeen Proving Ground, Maryland 21005

and

Paul Kutler, Chief
Applied Computational Aerodynamics Branch
NASA Ames Research Center
Moffett Field, California 94035

This work contains the results of a study aimed at the development of two- and three-dimensional numerical procedures for computing the flowfield generated by the interaction of a blast wave and a rigid body. A number of numerical procedures were applied to two-dimensional problems including both implicit and explicit algorithms. Each was tried on the blast wave-cylinder interaction problem. MacCormack's method with added fourth-order dissipation yielded the best results and was then applied to the blast wave-truck interaction problems in two dimensions. MacCormack's method was also used in three dimensions to determine the flowfield that results when a blast wave strikes a rectangular parallelepiped at an arbitrary angle. Both the two- and three-dimensional computations were compared with experiments in a number of ways. Two dimensional density contours show qualitative agreement for shock front location and Mach stem formation with spark shadowgraphs taken in a shock tube. Pressure-time histories indicate good quantitative agreement between theory and experiment both in two- and three-dimensions.

INTRODUCTION

The accurate prediction of the effects of blast waves encountering vehicles and structures is essential in the design, survivability, and hence effectiveness of these configurations. Detailed experimental blast wave interaction data is both costly and difficult to obtain. Moreover, these experiments frequently do not provide a complete picture of the blast wave interaction flowfield. Actual experiments, in fact, only yield pressure data at a few selected points on the models. As a consequence essential design parameters are often difficult to define.

Design information for the kind of blast wave-vehicle encounter as pictured in Fig. 1 may be obtained experimentally in several ways. In one approach a large explosive charge is detonated near an instrumented vehicle or structure enabling direct measurements to be taken. This approach, while realistic, is costly, results in few data points, and frequently provides little understanding of the important flowfield phenomena. Another approach is to place a model of

the target inside a shock tube. In this case, better control can be provided and the experimental cost is less. Nevertheless, the experiments are still limited in their range of applicability as a result of scaling, shock tube wall effects, realistic wave shapes and flow duration.

As an alternative to the experimental description of the blast wave interaction phenomenon, one can use computational fluid dynamics. This is the approach adopted here. Accurate finite difference simulations offer the possibility of providing design data at a relatively low cost. Such a simulation provides a complete flowfield description that is essential to a fundamental understanding of the fluid mechanics and a necessity for an effective structural design. The numerically generated flowfield data can then be integrated to yield other vital information such as the total loads, center of pressure, and overturning moments.

In the past second-order finite-difference procedures have been used by Kutler, et al. (See References 1 and 2) to solve simple shock-diffraction problems involving both regular and Mach reflections of the incident shock. In these cases all discontinuities were fit, i.e., treated as sharp discontinuities. Blast wave encounter problems with two-dimensional wedges and three-dimensional cones in supersonic flight have been solved by Kutler, et al. (See References 3 and 4) again using second-order finite-difference procedures. In these instances a "shock-capturing" philosophy was employed and resulted in an accurate description of the so-called "shock-on-shock" problem.

In the present paper, these "shock-capturing" flowfield simulation techniques have been adapted to the blast-wave interaction problem. Only inviscid flow problems have been considered, but both complex two-dimensional and simple three-dimensional geometric configurations have been used as targets.

GOVERNING EQUATIONS

Several assumptions are made in the present study of blast wave encounters with targets. The first is that the blast wave is assumed to be planar relative to the target and that conditions behind the wave can be adequately and consistently described. Secondly, viscous effects are ignored. Finally, any effects which result from radiative heating on the target are assumed negligible, and a perfect gas equation of state is employed.

Under the above assumptions, the governing partial differential equations are the unsteady Euler equations. To permit the mapping of two- or three-dimensional complicated physical regions into rectangular or cubical computational domains respectively, the following independent variable transformation is employed:

$$\tau = t; \quad \xi = \xi(t, x, y, z); \quad \eta = \eta(t, x, y, z); \quad \zeta = \zeta(t, x, y, z) \quad (1)$$

Because the above transformation maps the body and outer boundary surfaces onto constant coordinate lines and planes, application of the boundary condition procedures is facilitated. The above transformation also permits the clustering of grid points in the vicinity of the body.

Under this transformation, the governing partial differential equations in strong conservation law form become

$$q_\tau + E_\xi + F_\eta + G_\zeta = 0 \quad (2)$$

where the flux vectors E , F , G of Eq. (2) assume the form

$$E = \begin{bmatrix} \rho U \\ \rho uU + \xi_x p \\ \rho vU + \xi_y p \\ \rho wU + \xi_z p \\ (e + p)U - \xi_t p \end{bmatrix} \quad F = \begin{bmatrix} \rho V \\ \rho uV + \eta_x p \\ \rho vV + \eta_y p \\ \rho wV + \eta_z p \\ (e + p)V - \eta_t p \end{bmatrix} \quad G = \begin{bmatrix} \rho W \\ \rho uW + \zeta_x p \\ \rho vW + \zeta_y p \\ \rho wW + \zeta_z p \\ (e + p)W - \zeta_t p \end{bmatrix} \quad (3)$$

where $U = \xi_t + u\xi_x + v\xi_y + w\xi_z$, $V = \eta_t + u\eta_x + v\eta_y + w\eta_z$, and $W = \zeta_t + u\zeta_x + v\zeta_y + w\zeta_z$ are the contravariant velocity components without metric normalization.

In the conserved variables of Eq. (2) p represents the pressure, ρ the density, u , v , and w the three Cartesian velocity components, and e the total energy per unit volume. For an ideal gas, the pressure, density, and velocity components are related to the energy by the following equation:

$$e = \frac{p}{\gamma - 1} + \rho \frac{u^2 + v^2 + w^2}{2} \quad (4)$$

The metrics required by Eq. (3) in general are not known analytically and must be evaluated numerically. Details for this procedure are given in Reference 5.

NUMERICAL ALGORITHMS

The transformed governing equations (Eq. (2)) were solved by both explicit and implicit finite-difference procedures. These schemes included MacCormack's⁶ explicit method with an additional fourth-order dissipation term, Beam and Warming's^{7,8} implicit method in the delta-form, and Steger and Warming's⁹ explicit upwind scheme. MacCormack's scheme captured the shock within the least number of grid points and consumed the least amount of machine time, and therefore, it is the only procedure presented here. The others can be found in Reference 5.

MacCormack's method is a second-order, noncentered predictor-corrector scheme and appears as follows:

$$\left. \begin{aligned} \bar{q} &= q^n - \Delta t (\Delta_\xi E^n + \Delta_\eta F^n + \Delta_\zeta G^n) \\ q^{n+1} &= \frac{1}{2} [\bar{q} + q^n - \Delta t (\nabla_\xi \bar{E} + \nabla_\eta \bar{F} + \nabla_\zeta \bar{G}) + \epsilon D^n] \end{aligned} \right\} \quad (5)$$

where \bar{E} implies that the flux vector E is evaluated using elements of the predicted value \bar{q} , and Δ and ∇ are the standard forward and backward difference operators. The quantity D represents a fourth-order dissipation term in all three directions whose effect is governed by the dissipation constant ϵ .

GRID GENERATION

The generalized coordinate transformation given by Eq. (1) permits the use of grids based not only on standard coordinate systems such as cylindrical or spherical but also numerically generated grids such as those obtained by solving elliptic partial differential equations. In this study both analytically and numerically determined grids were used to discretize the physical regions of interest.

For two-dimensional targets consisting of cylinders and rectangles, an analytically described mesh based on a cylindrical-like coordinate system is employed (see Figs. 2a and 2b). Points can be clustered near the body for better resolution by using an exponential function.

In order to discretize an arbitrary two-dimensional shape such as a truck and its surrounding flowfield, a numerically generated grid was used (see Fig. 2c). The partial differential equations used for this process are elliptic and satisfy a maximum principle. The technique for generating these grids was obtained from R. L. Sorenson at NASA's Ames Research Center and was a result of a paper by Steger and Sorenson.¹⁰ Details of the mesh generation procedure can be found in that paper, but suffice it to say that the method can treat arbitrary bodies and outer boundaries with clustering near the body.

For the three-dimensional problem, the flowfield resulting from the interaction of a blast wave and a rectangular parallelepiped was desired. Discretization of this flowfield was accomplished using a spherical-type grid as shown in Fig. 3.

BOUNDARY AND INITIAL CONDITIONS

Two types of computational boundaries were considered; those across which there is no mass flow (impermeable surfaces) and those across which there is mass flow (permeable surfaces). Impermeable boundaries include solid walls, planes of symmetry, and slip surfaces whereas permeable boundaries include shock waves, porous walls, and inflow or outflow boundaries.

In the blast wave interaction problems of interest here, boundary condition procedures are required at the body, the planes of symmetry, and along the outer boundary. For inviscid flows, the boundary condition at the surface of a body requires flow to be tangent to the body. This implies that the velocity component V of Eq. (3) must be equal to zero at the body. In order to simulate this numerically, the image plane concept is used. By employing this concept, an image line of nodal points is established which falls one mesh interval inside of the body (see Figs. 2 & 3). Flow variables along this line are obtained by use of the flow variables at the body and the adjacent flowfield interior points, both at the previous time step. The flow variables for the new time step at the body can now be obtained by the same numerical algorithm that was used for the interior points, and hence with the use of the implicit procedure, the body points are also updated implicitly. The details of this procedure for both the two- and three-dimensional cases are given in Reference 5.

To numerically simulate the ground plane (plane of symmetry) in both the two- and three-dimensional problems, the reflection principle is employed. In this approach the pressure, density, energy, and tangential velocity components, are treated as even functions with respect to the ground plane while the normal velocity component is treated as an odd function.

RESULTS AND DISCUSSIONS

In this section numerical results are presented which describe the interaction of a blast wave with a body. In two-dimensions, a comprehensive set of results is presented for the blast wave-cylinder interaction while partial results are presented for the blast wave-truck interaction. In three-dimensions partial results are also presented for the blast wave parallelepiped interaction problem.

Numerical and experimental results for the blast wave-cylinder interaction problem are presented in several ways. In Fig. 4a computed pressure-time histories are compared with experimental results obtained by Pearson et al.¹¹ at the Ballistic Research Laboratory. The inset in each figure depicts the measuring

station of the transducer. The blast wave passes over the cylinder from left to right. In each case, the smooth curve is the computed result while the oscillatory curve is the measurement. The oscillations represent excursions from true values due to transducer ringing, local unsteadiness due to model oscillations, general flow anomalies, etc. A sample of the more interesting cases with significant wave structure are shown ($\theta = 45^\circ, 135^\circ, 180^\circ$). All the locations (except for 180°) have a similar structure. A sharp rise in the pressure signifies the arrival of the incident blast wave at the measuring station. This is followed by an exponential-like decay and a second, more "smeared" jump to a plateau value. The delays from $t = 0$ on the abscissa represent the time before the shock arrived at the sampling station. The results can be more fully explained with the help of Figs. 4b, computed isopycnics, and 4c, spark shadowgraphs (obtained by Vandromme¹²). Interesting results develop as the shock encounters the cylinder and passes over it. A triple point and Mach Stem appear partway up the windward side of the cylinder as is clearly seen in both the computed isopycnics and the shadowgraphs. The contact surface emanating from the triple point (as seen in Fig. 4c) is not reproduced in the isopycnic plots of 4b. This is because of inadequate resolution of the computational grid. Better results would be obtained with an increase in the number of grid points or an adaptive gridding scheme. As the primary shock continues toward the rear of the cylinder, it eventually reflects and is propagated upstream. As this reflected shock arrives at a measuring station, it gives rise to the second "smeared" jump in Fig. 4a. The smeared nature of the jump is manifest in viscous effect near the surface which now begin to make their effects felt. The discrepancy in the pressure amplitude in the bottom figure of 4a and the latter half of the top two figures is also attributable to viscous effects. These effects were neglected in the computation.

The interaction of a blast wave with a truck for intermediate times is shown in Fig. 5 in the form of pressure contours. For this case the grid size consisted of 32 points in the j -direction (along the body) and 25 points in the k -direction (normal to the body). The blast wave had a strength of 34.5 kPa overpressure. Figure 5a shows the reflected blast wave from the front of the truck while Fig. 5b shows a reflected wave from the windshield. In Fig. 5c the blast wave is beginning to expand over the cab of the truck while the reflected waves from the front and windshield move away from the vehicle. This particular calculation does demonstrate the versatility of the arbitrary body mesh generator and shock-capturing ability of MacCormack's method for computing complicated flowfields.

The three-dimensional interaction of a blast-wave with a rectangular parallelepiped was computed using MacCormack's method with fourth-order smoothing. For this calculation the grid consisted of 54 points in the j -direction or around the body, 24 points in the k -direction, and 16 points in the l -direction, or between the body and the outer boundary (see Fig. 3).

Numerical results were obtained for which experimental data was available. The experimental data was obtained by placing pressure gages at various positions on the model and recording the time histories of the pressure as it was struck by the blast wave (see Fig. 3).

The initial conditions for this case consisted of a blast wave Mach number of 1.14, freestream pressure of 101.33 kPa, and angle of incidence α of 52.5° . The distance r_{bw_i} from the origin to the blast wave (see Fig. 3) was 4.91.

The results of this first calculation are shown in Fig. 6 where the pressure in kilo-Pascals is plotted as a function of time in milliseconds for three stations. The solid dots shown on each of the curves in Fig. 6 is the experimental data. The agreement is acceptable and can be made much better with better grid resolution.

REFERENCES

1. Kutler, P. and Shankar, V. S. V., "Diffraction of a Shock Wave by a Compression Corner; Part I-Regular Reflection," presented at the AIAA 9th Fluid and Plasma Dynamics Conference, San Diego, CA, July 14-16, 1976. AIAA Journal; Vol. 15, No. 2, February 1972, pp. 197-203.
2. Shankar, V., Kutler, P., and Anderson, D. A., "Shock Wave by a Compression Corner; Part II-Single Mach Reflection," AIAA Paper 77-89, presented at the AIAA 15th Aerospace Sciences Meeting, Los Angeles, CA, January 24-26, 1977. AIAA Journal, Vol. 16, No. 1, pp. 4-5, January 1978. Also NASA Technical Memorandum TM-73, 178.
3. Kutler, P. and Sakell, L., "Two-Dimensional, Shock-on-Shock Interaction Problem," AIAA Journal, Vol. 13, No. 3, pp. 361-367, March 1975.
4. Kutler, P. and Sakell, L., "Three-Dimensional, Shock-on-Shock Interaction Problem," AIAA Journal, Vol. 13, No. 10, pp. 1360-1367, October 1975.
5. Kutler, P. and Fernquist, A. R., "Computation of Blast Wave Encounter with Military Targets," Flow Simulations, Inc. Report No. 80-02, April 1980.
6. MacCormack, R. W., "The Effect of Viscosity in Hypervelocity Impact Cratering," AIAA Paper 69-354, Cincinnati, Ohio, 1969.
7. Beam, R. and Warming, R. F., "An Implicit Factored Scheme for the Compressible Navier-Stokes Equations," AIAA Paper 77-645, 1977.
8. Warming, R. F. and Beam, R., "On the Construction and Application of Implicit Factored Schemes for Conservation Laws," SIAM-AMS Proceedings, Vol. 11, Proceedings of the Symposium on Computational Fluid Mechanics, New York, 1977.
9. Steger, J. L. and Warming, R. F., "Flux Vector Splittings of the Euler Equations in Conservation Law Form," NASA TM 78605, July 1979.
10. Steger, J. L. and Sorenson, R. L., "Automatic Boundary Clustering in Grid Generation with Elliptic Partial Differential Equations," submitted to the Journal of Computational Physics.
11. Pearson, R. J., Wisniewski, H. L. and Szabados, P. D., "Synergism in Nuclear Thermal/Blast Loading," Proceedings of the 7th International Symposium on Military Application of Blast Simulation, Ralston, Alberta, Canada, July 1981.
12. Vandromme, D., "Contribution to the Study of a Diffraction Pattern of a Plane Shock Wave Around a Cylinder," Secondary Thesis, Von Karman Institute for Fluid Dynamics, June 1980.

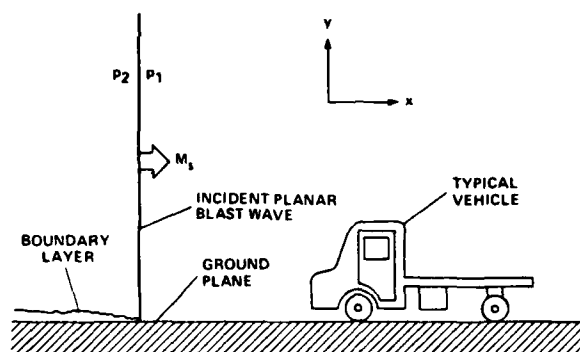


Figure 1. Blast Wave-Vehicle Interaction Problem

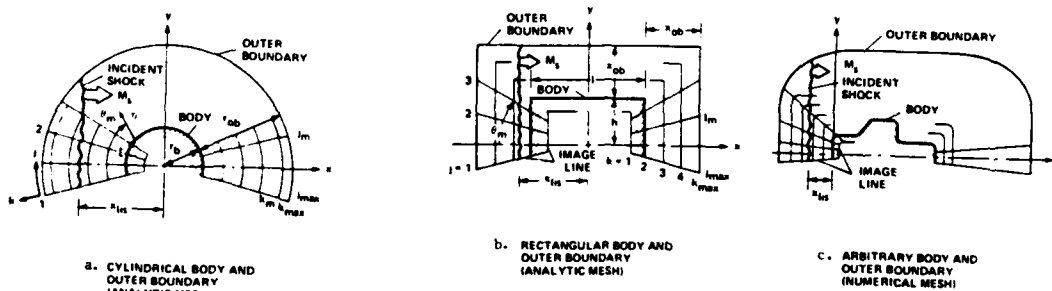


Figure 2. Description of Grids Used in Two-Dimensional Problem

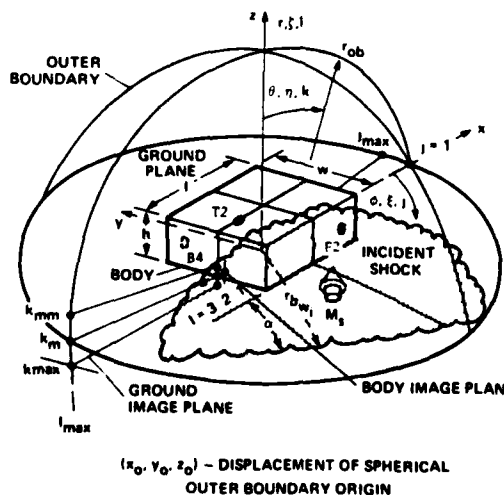
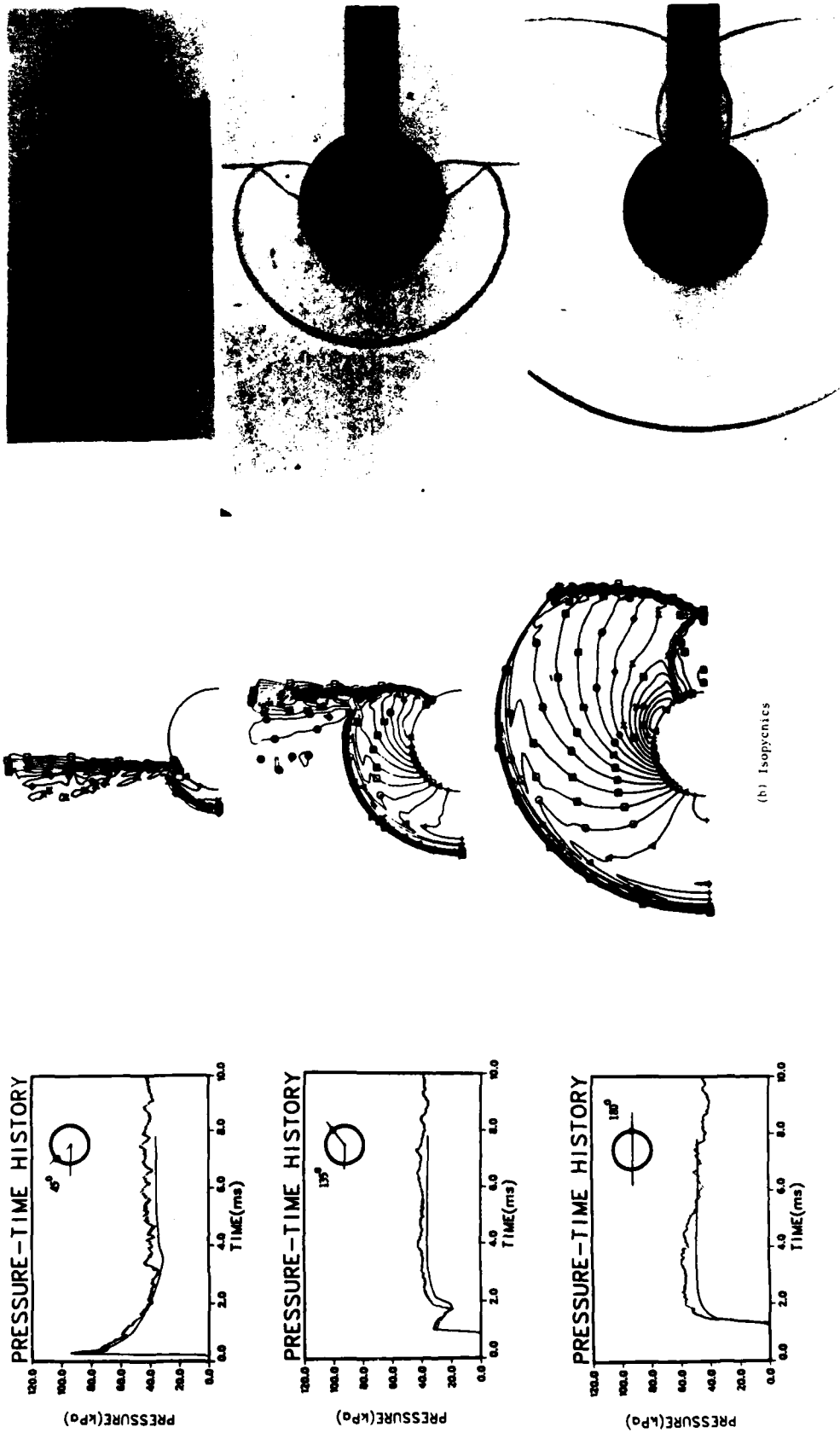


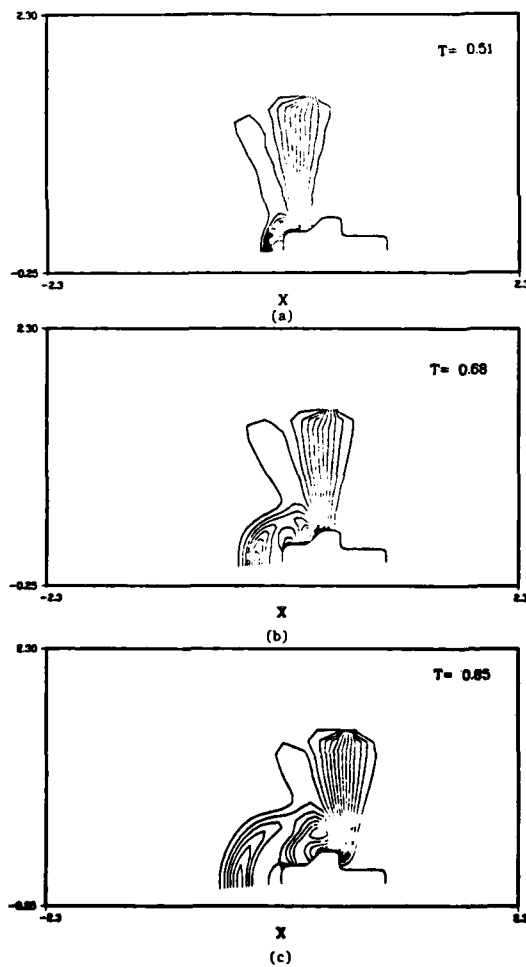
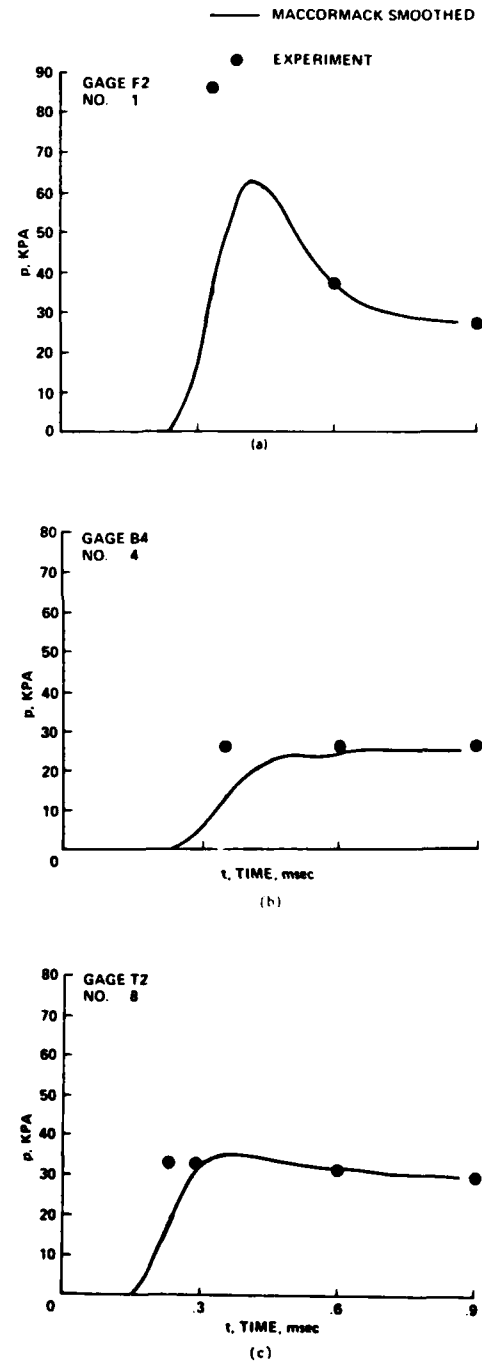
Figure 3. Description of Grid Used in Three-Dimensional Problem



(c) Spark Shadowgraphs by Vandromme¹²

Figure 4 Last Wave-Cylinder Encounter; $M_s = 1.17$.

(a) Pressure-Time History for Shock Strength of 43 kPa.

Figure 5. Pressure Contours of Blast Wave-Vehicle Interaction; $M_s = 1.14$ Figure 6. Surface Pressure Distribution on a Rectangular Parallelepiped as a Function of Time for Various Gage Positions; $M_s = 1.13$, $\alpha = 52.5^\circ$.

AD P000304

SIMULATION OF BLAST FIELDS BY HYDRAULIC ANALOGY

J.L. Stollery, K.C. Phan and K.P. Garry

College of Aeronautics

Cranfield Institute of Technology
Cranfield, Bedford, England.

The blast wave emanating from the rear of most shoulder-launched recoilless weapons can be literally deafening. To reduce the blast overpressure a number of different silencers have been proposed. The cost of field trials on the actual weapon is considerable so the hydraulic analogy has been used to investigate over 70 configurations, and to try to understand the various mechanisms that reduce the overpressure at the relevant 'ear position'. Measurements have also been made using a ~~1 1/2" diameter~~ 32mm air-driven, open-ended shock-tube fitted with a variety of silencers and exhausting into the atmosphere. Comparisons have been made between the two-dimensional hydraulic analogy and the three-dimensional shock tube results in order to check the validity and utility of the analogy. The hydraulic analogy has also been used to simulate the effects of one or more reflecting surfaces when firing recoilless weapons in rooms, streets and passageways. As might be expected the position of any reflecting walls is critical and can sometimes greatly magnify the peak overpressure experienced by the operator.

INTRODUCTION

The objective of our study is to suggest practical means of reducing the blast wave noise emanating from the rear of shoulder-launched weapons. The real flow has not been duplicated but instead two separate simulation techniques have been adopted. In the first of these the water analogy was used to obtain a qualitative assessment of over 70 different silencer configurations. By measuring the water wave signatures the relative noise levels at the gunner's ear position could be estimated and the most effective silencers selected.

Although the water table provides a quick, simple inexpensive facility for preliminary assessment the analogy to gas flow is not exact. Moreover the gas flow we wish to study here is three-dimensional whereas the water table only simulated two-dimensional

conditions. Hence the hydraulic tests were supplemented by firings of an open-ended shock tube, with and without some of the most promising silencer shapes as found from the water-table. Thus the work falls naturally into the two separate but inter-related programmes described below.

NOTATION

c	caliber, i.e. diameter of shock tube or width of the channel
d	local water depth
d_0	undisturbed water level
N	sound pressure level
P	pressure
P_0	atmospheric pressure
ΔP	$(P - P_0)$
P_{ref}	acoustic reference pressure, $2 \times 10^{-5} \text{ Nm}^{-2}$
x	distance downstream of the mouth or exit
X	x/c
γ	ratio of the specific heats of a gas

THE WATER TABLE PROGRAMME

The 'wave generator' was held down on the 9' x 4' (2.7m x 1.2m) water table from above. The 'gun' was simulated by a 12" (30cm) long channel 1.2" wide (3cm) divided by a spring-loaded sluice gate into a 'high pressure' and 'low pressure' region. The table was filled to the optimum depth of 0.19" (0.48cm) at which level the wave propagation velocity is least dependent on wavelength (Ref.1). The reservoir behind the sluice gate was normally filled to a height of 0.63" (1.6cm). Sudden release of the gate generated an hydraulic jump analogous to the blast wave from the rear of a shoulder-launched weapon. The water wave propagated down the channel, through any silencer, and then diffused from the mouth of the channel, out over the bed of the water table.

The wave signature at any station was measured using a Wayne Kerr capacitance proximity probe and the signals were recorded using a U.V. recorder. Full details of the facility, equipment, calibration and measuring techniques are all given in Ref.2.

A large number of silencers were tested, all manufactured from the same thickness of 'Perspex' sheet as the main channel (0.08", 2mm). The silencers tried fell into 8 categories, namely extensions, baffles, flares, shields, perforations, cups, boxes and snouts. There are of course an enormous number of combinations of these types which are possible and many of these were tried. Some of the combinations tested are shown in Fig.1.

The wave signature was usually measured at each of 132 grid stations, paying particular attention to the point B5 which is approximately the position of the gunner's ear. From the signature the maximum wave height was measured, converted into a maximum pressure using the water to gas analogy relationship

$$(d/d_0)^2 = (P/P_0)$$

and this in turn was converted to the noise level in decibels using the formula

$$N(\text{dB}) = 20 \log_{10} \left[\frac{P - P_o}{P_{\text{ref}}} \right] ,$$

where N is the sound pressure level. From the grid measurements noise contours were constructed.

Considering just peak measurements at the B5 station, the basic tube (no silencer) produced a wave corresponding to 171dB. A straight extension to the basic tube of two and four calibers reduced this noise level to 168 and 166dB respectively. Such a reduction is to be expected since effectively the ear is being placed further from the source of the blast wave (i.e. the end of the tube) and the blast wave must decay with distance. The effect of perforating the basic tube was less obvious. It had been thought that perforations might break up the single blast wave into a series of smaller, weaker waves reaching the ear over a longer period. In this way the noise might be 'smeared out' and its intensity reduced. The actual effect was entirely the opposite. The perforations effectively placed the blast wave closer to the ear and the more of the tube that was perforated the greater was the noise level. Perforating a length of just one caliber raised the noise level by 5dBs.

Flaring the end of the tube had little effect but a slight contraction (negative flare) gave a 1dB noise reduction. Shields were only effective when increasing the overall length of the tube and then no better than a straight extension. Isolated baffles were only marginally beneficial. The first significant noise reductions were obtained using cups and boxes. Replacing the last two calibers of channel length by a box 3c wide, gave a 5dB reduction and further benefits were obtained by increasing the overall length (i.e. adding the box to the end of the 'basic tube'). Some of the best configurations are shown in Fig.2 where an overall increase in length of 3 calibers has been accepted.

The greatest reduction in maximum noise level (around 12dB, see Fig.2f) was achieved using a large box enclosing a partly perforated tube plus a snout. This compares with a reduction of 5dB achieved from a simple 3 caliber extension of the basic tube (Fig.2b).

For a number of configurations the complete noise field was plotted in the form of 'isobars' based on the maximum values of wave height measured at any station. Fig.3a shows that for the basic (unsilenced) tube the emerging blast wave acts like a cylindrical source moving away from the mouth of the tube. Fig.3b shows comparable measurements in air using a large shock tube (Ref.5). The similarities are obvious though the air data are three-dimensional and hence the 'noise' decays more rapidly.

Fig.4 is a plot of the water table 'noise' contours around one of the most successful silencer configurations. Comparison with Fig.3a shows that the wave emerging from the end of the tube is considerably reduced in strength. The subsequent isobar patterns are similar though some shielding is provided by the external shape of the silencer box.

In an attempt to understand the way in which the silencers reduced the wave strength a number of shadowgraph pictures were taken. The pictures are not as clear as we should like because (a) the 'Perspex' walls of the tube do not show up well and (b) there are a number of capillary waves which tend to confuse and complicate the pattern. Nevertheless the spread of the 'blast wave' and the formation of the vortices at the mouth of the tube are made clearly visible, as is the very complex nature of the flow development within the silencers. Many of the pictures are given in Ref.8.

The last part of the water table programme simulated the effect of firing a weapon in a confined space. It is of course extremely simple to place walls of any number and shape on the table. Fig.5 shows the 'pressure' trace at the gunner's station when firing from a room with and without a front wall. Comparison with the unconfined trace shows clearly the effect of the reflected waves from the walls. Depending on the geometry it is quite possible for two or more reflected waves to coalesce to produce noise levels considerably more intense than that produced by the initial blast wave. For example the third peak in Fig.5a is more than double that of the first. Removal of the front wall (Fig.5b) makes the first and third peak levels roughly equal but introduces a large negative pressure level. From the times of the peaks, the known geometry and wave speed plus a visual watch of the water table flow pattern it was easy to confirm that the peaks do refer to reflections of the initial blast wave from the various walls.

The utility of the water analogy is ultimately dependent on its ability to predict what happens in the real situation. One of the reasons for making water table measurements was to test computer programs for two-dimensional unsteady flow of the analogous gas with $\gamma = 2$. Details of these calculations are given in Ref.3. Experimentally we are stretching (perhaps overstretching) the analogy and hoping to find useful silencer configurations for three-dimensional blast waves in air from two-dimensional flows on a water table though similar work elsewhere (Ref.4) has proved very helpful. In order to assess the utility of the analogy more clearly, a complementary programme of measurements in air was undertaken.

THE SHOCK TUBE PROGRAMME

A simple 32mm diameter open-ended shock tube has been modified to take a number of silencers. Pressure measurements are made using a number of 'Kulite' and 'Endevco' piezo-resistive transducers built into slender 'lollipop' mountings. The pressure signature is stored digitally then displayed graphically using a pen recorder. Typical pressure records at the gunner's station with and without a silencer are shown in Fig.6. The pressure records at all other stations are similar, except within a conical zone of 15° semi-angle surrounding the axis of the shock tube with the origin at the mouth. In this region the first pressure peak is followed a little later by a second, larger one which in turn is followed immediately by an even larger negative pressure pulse. These effects are thought to be due to jet impingement on the transducer and its stand and are subject to further investigation. In plotting Fig.7, only the first pressure peak measured along the centreline

has been used in the comparison with data from the water table and from other shock tubes (Refs.5 and 6) and from a small rocket motor rig (Ref.7). It is obvious that no simple scaling of the type

$$\frac{\Delta P}{P_0} = k \left(\frac{x}{c} \right)^n$$

is capable of correlating the data. A more useful characteristic length may be the size of the 'shock bottle' or other jet dimension.

All the measurements were made when driving the shock tube with air at a gauge pressure of 80 psi. The diaphragm pressure ratio was therefore 6.4 which theoretically should generate a shock Mach number of 1.47 with a pressure behind the shock of 34 psia. The pressure actually measured just inside the mouth of the tube by a wall mounted transducer was 32 psia.

A number of silencers have been tested and overpressures measured at the gunner's station. The reduction in noise level is listed in Table 1 which also gives the water table results. The agreement in the order of effectiveness is striking. It would appear that the relative merits of the various silencers, as indicated by the water table tests, are confirmed by the shock tube tests in air. Moreover particular effects such as the sensitivity of the noise level to the number and position of baffles are faithfully reproduced. Thus Fig.8 shows the effect of the position of a single external baffle as measured in the 'real' and 'analogous' facilities.

One additional feature has been tried. The silencers have been lined with absorbent material. So far the only noticeable effect has been the reduction of some of the high frequency components of the noise. Further tests are underway.

CONCLUSIONS

Measurements of analogous noise level using a two-dimensional water table facility are relatively simple, quick and inexpensive. A large range of silencer configurations can be tested in conditions of both confined and unconfined space.

Measurements using an open-ended shock tube in air are more complex, more time-consuming and considerably more expensive.

Comparisons between the two sets of measurements suggest that the water table results can predict the relative merits of the various configurations. The hydraulic analogy is also very useful in drawing attention to the wave reflection and refraction effect both inside complex silencer geometries and from outside walls.

The most significant difference between the two sets of tests is the pressure signature in the region of the jet behind the gun. In the shock tube tests the jet remains relatively discreet and, within this zone, jet impingement on the transducer and its support are thought to distort the pressure signature after the passage of the initial blast wave. In the water table tests

the flow expands rapidly at the mouth forming two vortices. This rapid spread may be more representative of the high pressure flow exhausting from a real weapon.

ACKNOWLEDGEMENTS

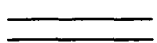
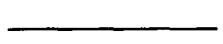
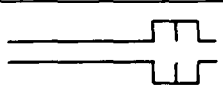
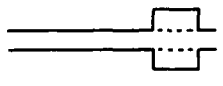
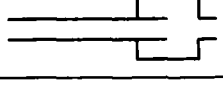
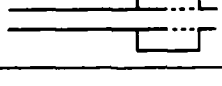
This work has been carried out with the support of the Procurement Executive, Ministry of Defence.

REFERENCES

1. E.V. Laitone, J.Aero.Sci. Vol.19, No.4 (April 1952).
2. K.P. Garry, College of Aeronautics Report 8003 (1980).
3. J.M.R. Graham and R. Hillier, Imperial College, Dept. of Aero Note, (September 1979).
4. H.J. Sneek, Benet Weapons Lab., Watervliet, Report WVT-TR-75043 (July 1975).
5. G.P. Beichler and L.P. Grady, Ballistics Research Lab., Maryland, Technical Note No.843.
6. S.I. Cowley, College of Aeronautics M.Sc. thesis (June 1960).
7. L. Pennelegion and J.F. Grimshaw, Proceedings of the 12th International Symposium on Shock Tubes and Waves, Jerusalem (July 1979).
8. K.C. Phan, College of Aeronautics Memo 8101 (1981).

TABLE 1

Noise level at the Gunner's Ear (Station B5)
(A comparison between the water table and shock tube results)

G e o m e t r y	Water Table		Shock Tube	
	$\Delta P(\text{dB})$	Improve- ment (dB)	$\Delta P(\text{dB})$	Improve- ment (dB)
Basic Tube 	171.0	-	154.0	-
Basic Tube + 3c ext. 	166.5	-4.5	149.1	-4.9
N 022/3 	161.6	-9.4	146.3	-7.7
N 006/3 	161.3	-9.7	145.5	-8.5
N 023/2 	158.5	-12.5	144.2	-9.8
N 024/2 	158.3	-12.7	143.3	-10.7

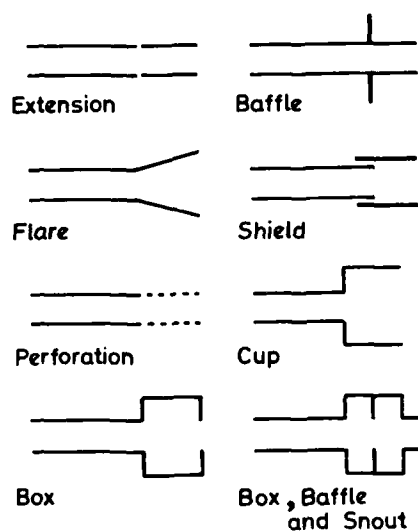


Fig. 1 Classification of silencer geometries

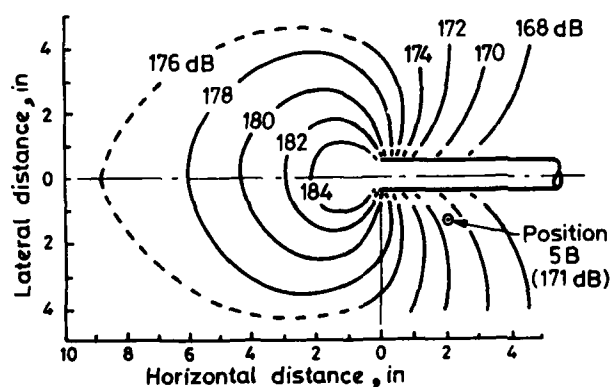


Fig. 3a Noise contours around the basic tube

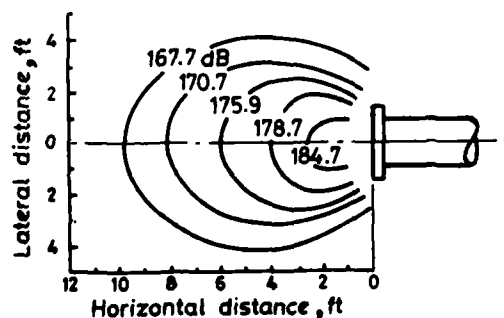


Fig. 3b Results from a 2ft diameter shock tube (Ref. 5 $P_4 = 50\text{psi}$)

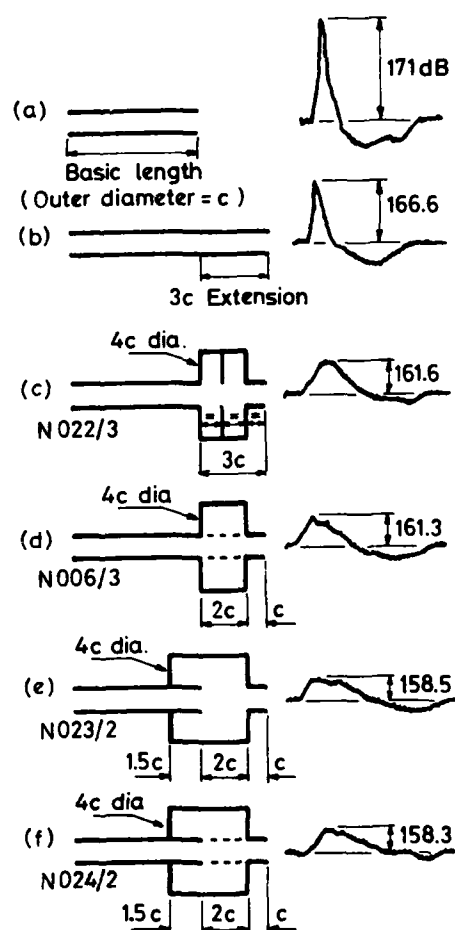


Fig. 2 Some effective silencers (pressure-time trace recorded at B5)

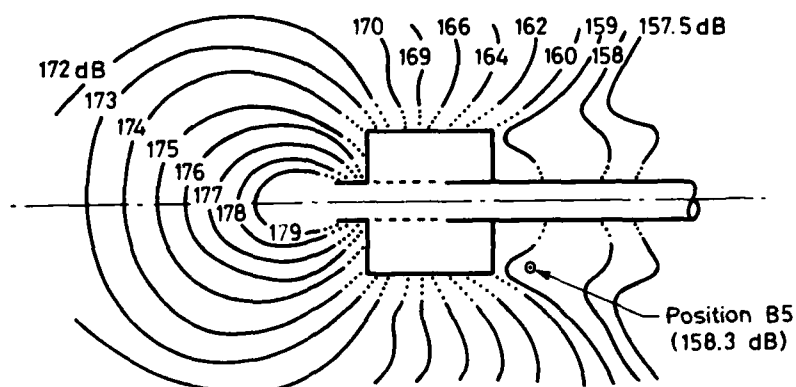


Fig.4 Noise contours around N O24/2

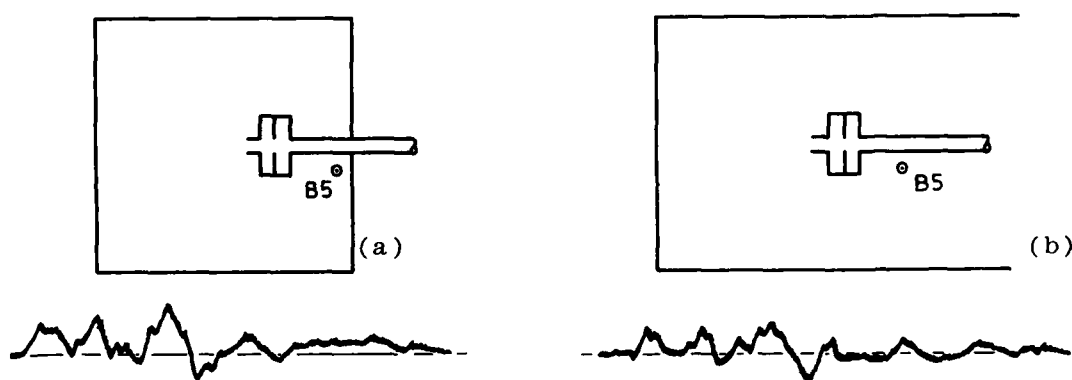


Fig.5 Pressure wave reflections from enclosing walls

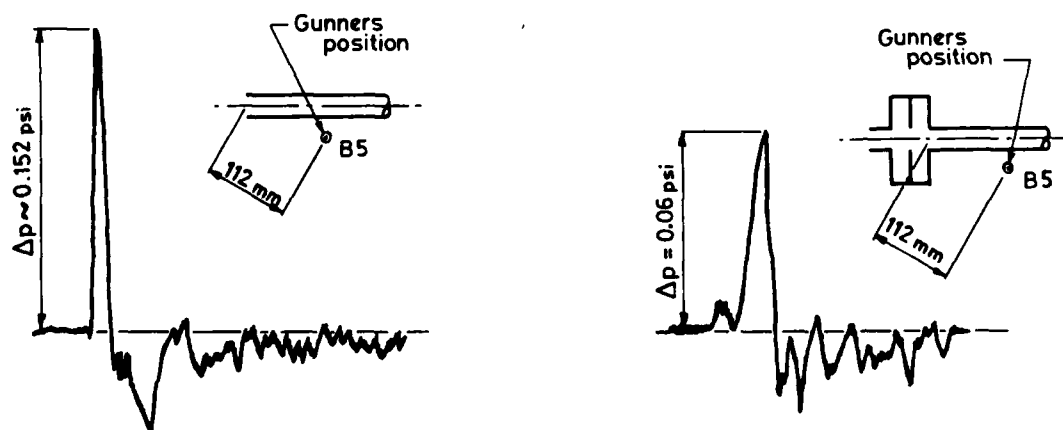


Fig.6 Pressure measurements at the gunner's station, with and without a silencer

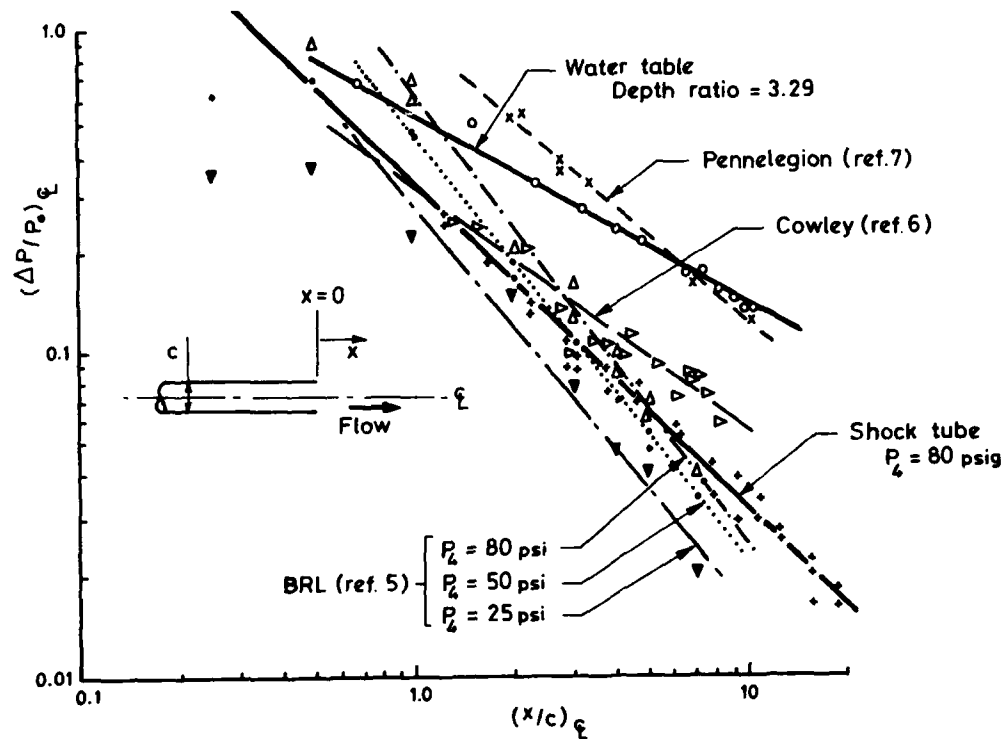


Fig. 7 Peak pressure along the centre-line

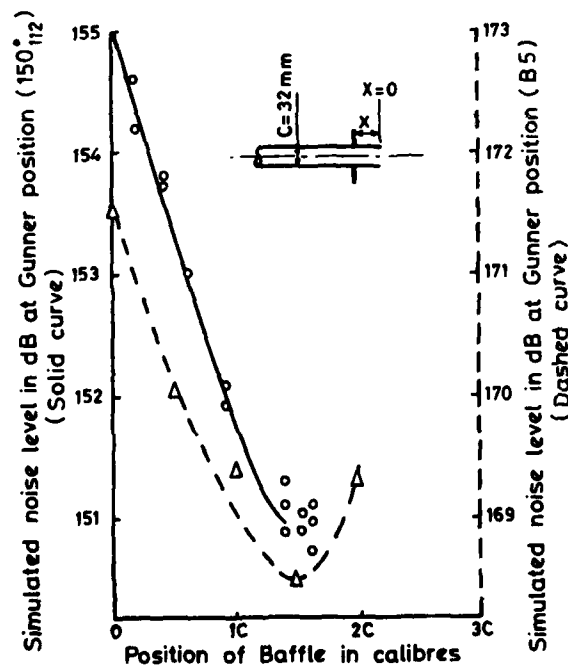


Fig. 8 Effect of baffle position on noise level at gunner's station

AD P000305

FAST PYROLYSIS OF PULVERIZED LIGNITE IN A SINGLE-PULSE SHOCK-TUBE

H.J. FRIESKE, E. SEELBACH, G. ADOMEIT

Institut für Allgemeine Mechanik

Technische Hochschule Aachen, Germany

A single-pulse-shock tube, with a newly developed instrumentation such that high pressure pulses of reproducible and preselectable length could be produced, is used to investigate the influence of pressure, temperature, particle size, and variable test times on the gaseous volatile matter at heating rates up to 10^6 K/s. After quenching of the sample by the expansion wave the final composition of the gaseous products is analysed using gas chromatography and mass-spectrometry. The quenched lignite particles are collected and analysed chemically and by scanning electron microscopy to detect compositional and physical changes. The concentrations of the following products CH_4 , C_2H_6 , C_3H_8 , C_6H_{14} , C_2H_4 , C_3H_6 , C_4H_8 , C_2H_2 , CO , CO_2 , H_2 , O_2 , N_2 have been measured. These data confirm that the dependencies observed in the past, when going from low to medium heating rates, are continued to high heating rates.

Introduction

When coal is heated it undergoes a series of chemical and physical reactions, decomposing in volatile matter and solid residue. If this is performed in an inert atmosphere this process is called pyrolysis. It is particularly important for the production of liquids and gases from coal by application of heat only /1/, but it also accompanies all other thermal coal-processes.

In the past different types of pyrolysis experiments of coal have been performed with heating rates ranging from 10^{-2} K/s to 10^5 K/s. The results of these studies show that the heating rate is a very important parameter leading to different products and different product quantities /2/. Several investigations achieved medium heating rates, ranging up to 10^4 K/s by means of the electric grid technique /3,4,5,6/. The pressure has been varied in these experiments from vacuum to 100 bar and the peak temperature achieved was 1200 K. These apparatus allow analyses of the volatile products as well as the residual char. A disadvantage appears to be the ambiguous influence of catalytic cracking on the hot metal screens. A further type of pyrolysis experiments with increased heating rates is the entrained flow technique using a laminar flow of an inert gas at up to 2200 K and atmospheric pressure /7/. The coal particles are entrained in this flow and heated up with a maximum rate of 10^5 K/s. Still higher heating rates may be achieved with the shock tube. This and some other advantages stimulated various investigations of coal dust. NETTLE-

TON, et al. /8/ used it to investigate ignition phenomena of particles in the size range typical of coal dust burners. WOODBURN, et al. /9/ employed a vertical shock tube with fluidized coal particles to study the hydrogenation with volatile catalysts. LOWENSTEIN, et al. /10/ employed spectroscopy to obtain information on the heating process of the particles, the evolution of the volatiles and the formation of soot.

An analysis of the product formation was not performed in these investigations. This is one of the reasons why the present investigation was undertaken; the single-pulse shock-tube giving the possibility of a detailed analysis of the reaction products after freezing and also of varying the length of the heating period. Lignite was chosen as the first substance to be investigated because of the lack of data pertaining to high heating rates /11/.

Experimental Equipment

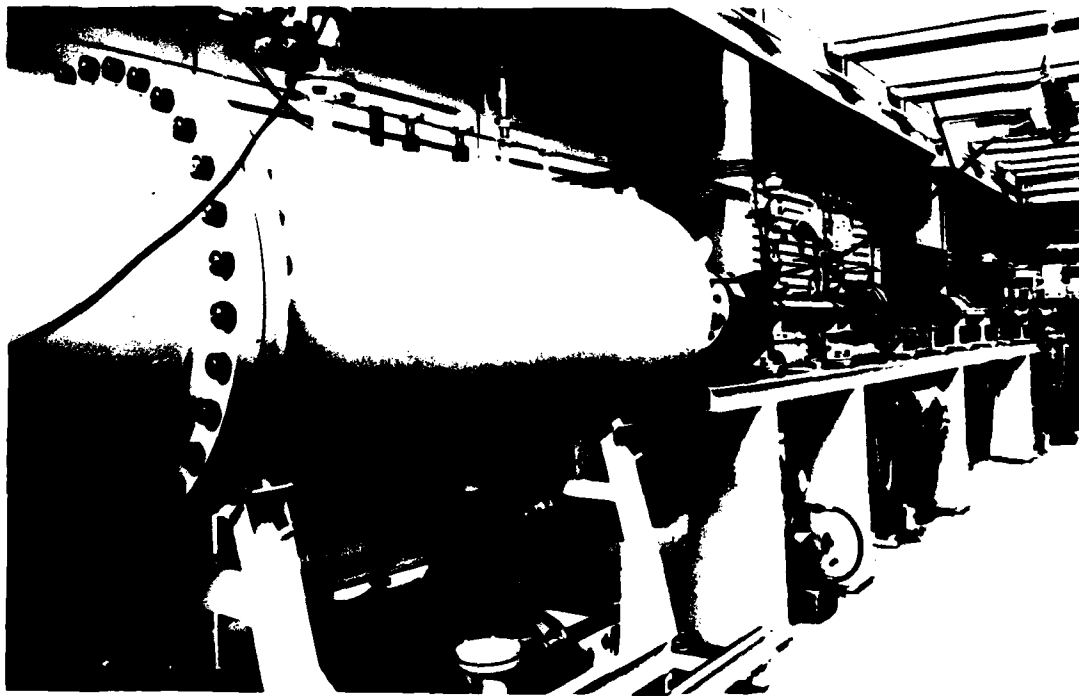


Fig. 1 : Photograph of single-pulse shock-tube

The single-pulse shock-tube, shown in Fig. 1 and represented schematically in Fig. 2, consists of a driver section DS (2 m), a low pressure section LPS (6.44 m) with a circular cross section of 87 mm inside diameter, and a dump tank DT (3 m³) /12,13/. The dump tank is connected to the driver section by a double diaphragm system DDS, which is pressurized to a medium value in order to distribute the load over both diaphragms D21 and D22. The diaphragm D21 consists of polyester and is opened by the exploding wire EW at distinct times depending upon the desired duration of the single pulse. The opening of the diaphragm D21 causes the break of diaphragm D22 as soon as it is reached by the expansion wave. The reproducibility of the time lag was checked and found to be satisfactory. For the double diaphragm system and the driver section helium was used, whereas for the low pressure section a gas mixing tank GMT allows preparation of suitable gas mixtures with the pressure p_1 .

Diagnostics

After freezing the pyrolysis gas-coaldust-mixture by expanding the gas into the dump tank two gas probes are sampled by operating a solenoid valve SV at a preset time interval after expansion. One of these probes, collected in an evacuated glass bulb GB(MS), is analysed directly by a quadrupole mass-spectrometer to obtain the concentrations of CO, CO₂, H₂, O₂ and N₂. The second probe is collected in a glass bulb with moveable piston PI(GC), to increase the pressure to atmospheric value after sampling. It is analyzed in a WARNER CHILCOT gas chromatograph equipped with a FID and an aluminium oxide 80/100 mesh column, 6 ft x 1/8" to obtain the fractions of the hydrocarbons.

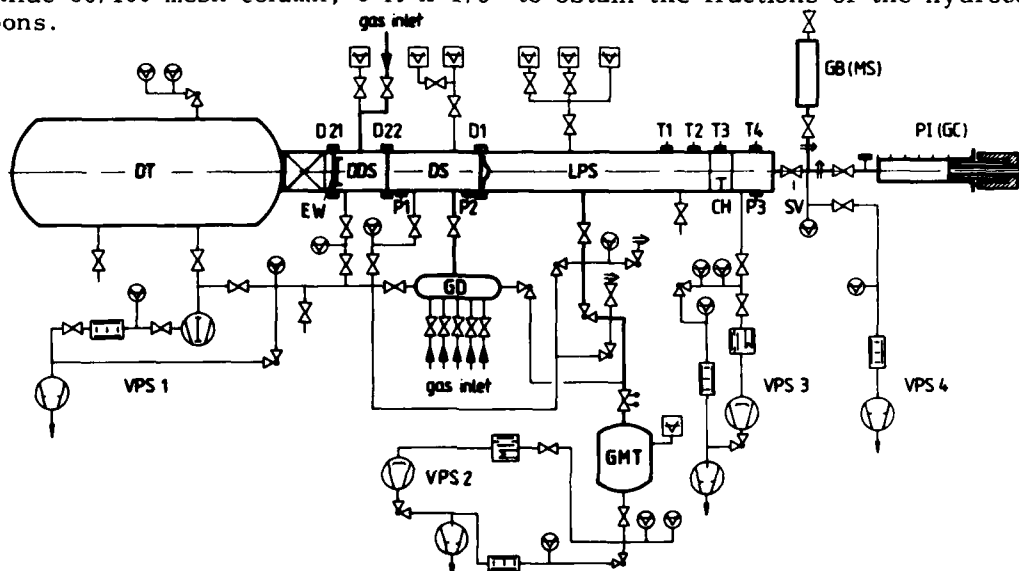


Fig. 2 : Schematic representation of single-pulse shock-tube

The pyrolyzed lignite particles are collected and analyzed, either by ultimate analysis or by a detailed analysis of the products of a further pyrolysis performed in a FISCHER curie point pyrolyzer 9425. Furthermore the collected lignite particles were investigated by scanning electron microscopy. Some of these photomicrographs are shown in Fig. 7 to Fig. 17.

Electronic Instrumentation

The time dependent pressure is measured at three locations by PCB piezo-crystal pressure transducers with built in MOS FET voltage resistance converters. The temperature variation is measured near the shock tube end wall using a thin film gauge T4 with a directly coupled preamplifier. The pressure and the thin film gauge signals are displayed on two dual channel oscilloscopes S1 and S2 with delay time bases. When the diaphragm D1 is burst the current-carrying trigger wire TW ruptures at the time $t = 0$. This trigger wire is a double enameled copperwire with 0.02 mm diameter laying in a loop across the diaphragm D1. The trigger unit TU generates a low impedance trigger signal and is able to check the insulation of the wire. This signal is applied to the trigger input of the oscilloscopes and the control units. The incident shock wave velocity and the attenuation are calculated from the time intervals between the rise of the signals of the thin film gauges. T1 starting the electronic counter EC1, T2 stopping the electronic counter EC1 and also starting EC2, and T3 stopping the counter EC2. Preamplifiers C1, C2, C3, with a built-in adjustable comparator, are directly plugged onto the thin film gauge assembly. Two outputs provide the amplified signal and the comparator signal.

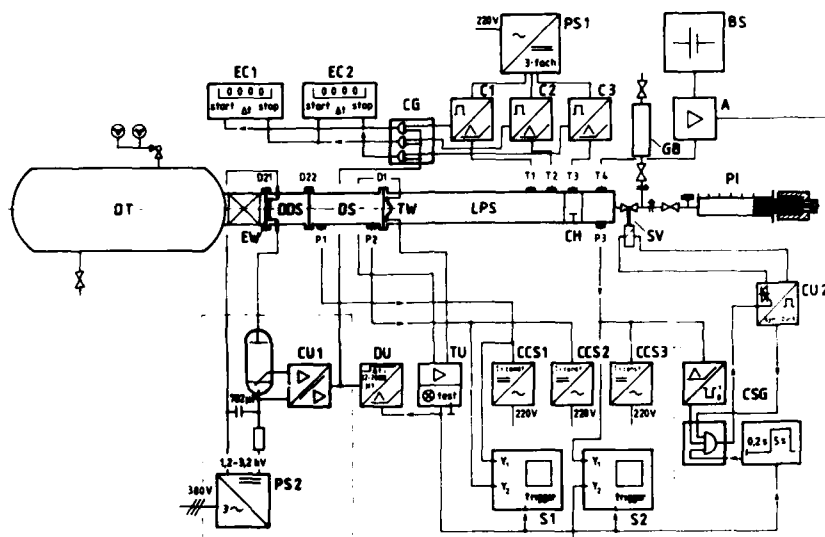


Fig. 3 : Electrical instrumentation

Several controls provide a reproducible, safe and reliable operation of the shock tube. All control functions are initiated by the rupture of the trigger wire TW. After a time lag from 2 to 2000 μ s, which may be preset in 2 μ s steps, a pulse from the delay unit DU causes the control unit CU1 to fire the ignitron and to open the diaphragm D21 by wire explosion. The same pulse blocks the input signal of the electronic counters EC1 and EC2 by closing the gate CG for 200 μ s to avoid starting the electronic counters EC1 and EC2 by interferences due to high energy capacitor discharge.

Gas samples are taken after the experiment by actuating the solenoid valve SV. The AC-operated magnet is able to open and close the valve within half a line cycle (10 ms). In order to prevent interferences due to high switching currents, the magnet has to be switched at zero crossing line voltage. The switched line cycles have to be an integer number. For reproducible sampling the delay after triggering and the opening time must be preset with an uncertainty smaller than 20 ms. A safety circuit has to prevent the opening if the pressure in the shock tube is higher than 0.5 bar due to a malfunction of the shock tube to avoid damage of the connected glass bulbs. To fulfill these demands the control unit CU2 and control signal generator CSG have been designed. The unit CU2 switches the valve by means of a triac and derives a pulse train from the line voltage. These 30 ms pulses are rising with every second zero crossing of the line. The control unit CSG combines these signals logically "and" with the signal "1" for a pressure < 0.5 bar derived from the P3-signal, and a "1" for the 5 s pulse starting 0.2 s after the trigger event. The "and" gate output fires the triac.

Power Supplies

A regulated high voltage power supply PS2 charges the capacitor that stores the energy for the exploding wire. The voltage is adjustable from 1.2 to 3.2 kV corresponding to a stored energy from 560 to 4000 Joule. The pressure transducers are fed from three constant current sources CCS1, CCS2, CCS3. Each part of a triple power supply PS1 is connected to one of the comparator-amplifiers C1, C2, C3. The power for the amplifier A is supplied by a battery set.

The small signals from the pressure and temperature gauges can only be used for evaluation and triggering if one can suppress ripple, noise and interference to a sufficiently low level. This pertains particularly to the disturbance caused by the exploding wire. The major part of the energy for wire explosions is released in less than 20 μ s corresponding to a peak power of about 100 MW. By a careful design of the medium pressure chamber, the discharge circuit, the grounding procedure of the control units, and the installation of the different transducer in the shock tube the interference can be kept at a tolerable level. The medium pressure chamber had to be equipped with an internal insulation to prevent the arc from flashing over to the tube. The wire EW, the shielded discharge power line and the enclosure for the PS and CU unit must not be connected to any part of the experimental setup. The power has to be supplied from a separated power line.

Near the downstream end of the shock tube a central grounding point was chosen to which the ground of the measuring and control units were connected. Every unit has its own power supply with a separation transformer. Interconnections between the different units are performed by means of optocouplers. Transducers were installed electrically insulated to the shock tube to avoid any ground loop in the measuring and control system. The line power is fed through a line filter. In this manner an excellent suppression of ripple and interference was achieved. The high energy capacitor discharge left only a small peak on the pressure trace which serves as a mark for the start of the wire explosion. Because of the sensitivity of the counters to this mark the unit CG blocks the electronic counters during the discharge.

Experimental Results

The pyrolysis of lignite particles of a mean diameter 10 μ m and 70 μ m has been investigated in first experiments at three different pressure levels. The temperature has been kept within certain limits. The length of the pressure pulse behind the reflected shock waves was varied in three steps from about 100 μ s to about 1800 μ s. The gas and particle samples were analyzed as described in Section 2. Some of the results are shown in Figs. 4, 5 and 6. The lignite investigated is Rheinische Braunkohle:

Proximate analysis (wt. %)		Ultimate analysis (wt. %, daf)	
Moisture	12.1	Carbon	71.8
Ash	3.91	Hydrogen	4.83
Volatile matter	44.6	Nitrogen	.73
Fixed carbon	39.5	Sulphur	.31
		Oxygen (by difference)	22.3

The results which are shown in Fig. 4a and Fig. 5a were obtained at pressures of 6.6 bar and 6.2 bar. The relative mass fractions ΔM_{rel} of the products are qualitatively the same for both particle sizes. For the largest pyrolysis time the detailed product concentration by percentage of weight are compiled in the table below.

Table I

Product	CH ₄	C ₂ H ₆	C ₆ H ₁₄	C ₂ H ₄	C ₃ H ₆	C ₄ H ₈	C ₂ H ₂	CO ₂	CO	H ₂
A(wt. %)	.9	.23	.17	.8	.29	.11	8.5	6.5	77	4.3
B(wt. %)	2.7	0.5	1.6	2.4	.48	.16	13.5	4.4	69.7	4.6

A : Particle diameter 10 μ m, pressure p_5 = 6.6 bar, duration time = 1550 μ s

B : Particle diameter 70 μ m, pressure p_5 = 6.2 bar, duration time = 1890 μ s.

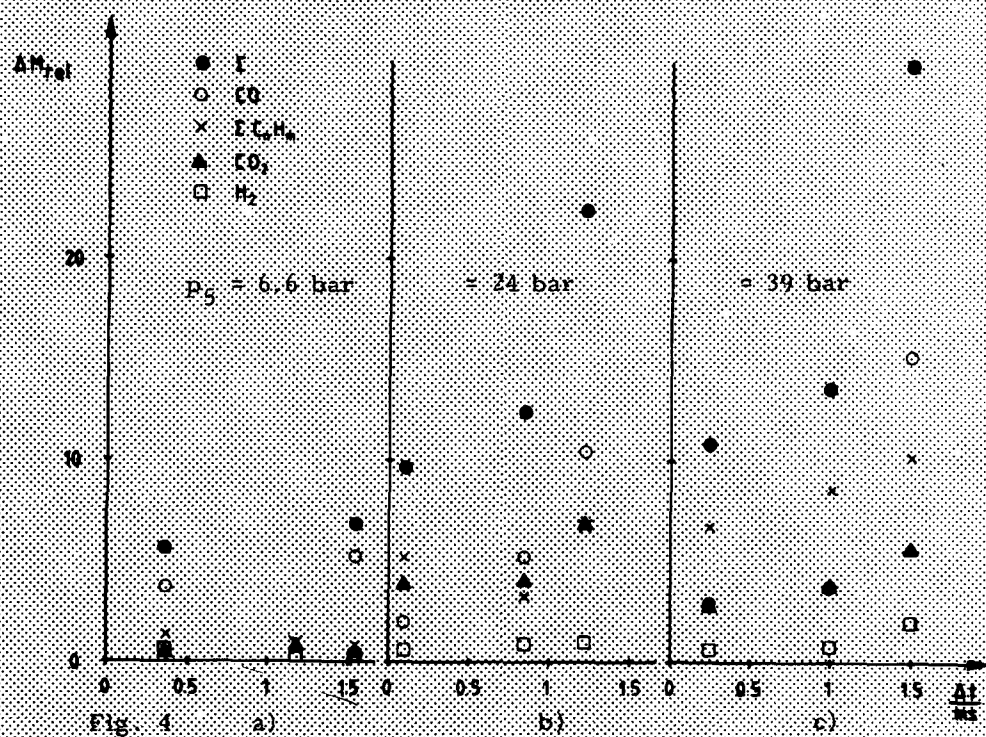


Fig. 4 a) $T_5 = 3250 \text{ K}$, $h_r \text{ rate} = 600 \cdot 10^4 \text{ K/s}$, mean diameter $\approx 10 \mu m$; argon
 b) $\approx 2910 \text{ K}$, $\approx 500 \cdot 10^4 \text{ K/s}$
 c) $\approx 2960 \text{ K}$, $\approx 490 \cdot 10^4 \text{ K/s}$

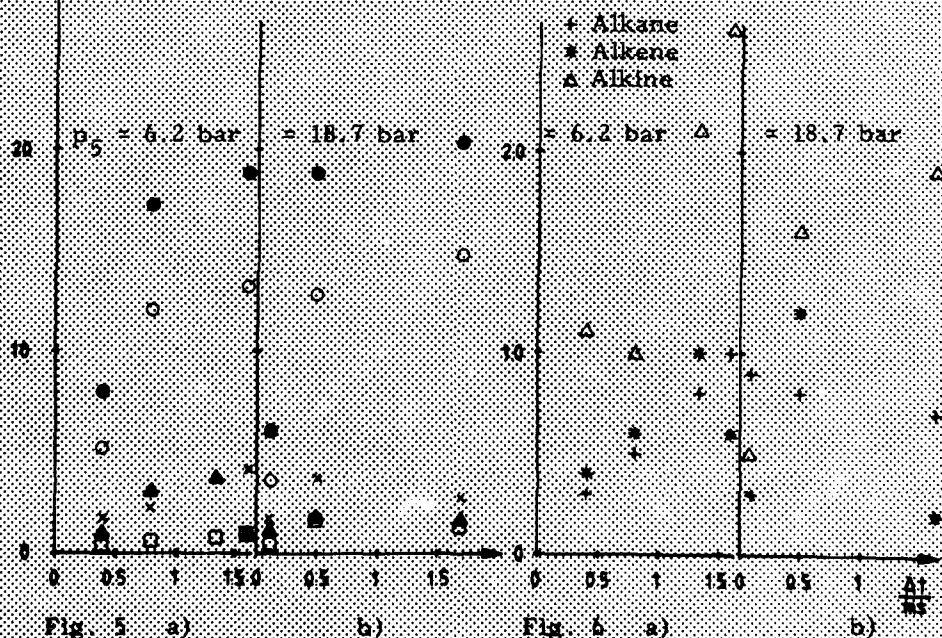


Fig. 5 a) $T_5 = 3700 \text{ K}$, $h_r \text{ rate} = 26 \cdot 10^4 \text{ K/s}$, mean diameter $\approx 70 \mu m$; argon
 b) $\approx 3700 \text{ K}$, $\approx 26 \cdot 10^4 \text{ K/s}$
 Fig. 6 a) $\approx 3700 \text{ K}$, $\approx 26 \cdot 10^4 \text{ K/s}$
 b) $\approx 3700 \text{ K}$, $\approx 26 \cdot 10^4 \text{ K/s}$

P. MASEK investigated the pyrolysis of the same lignite at a much lower heating rate of 5 K/min. His final temperature was 1300 K and the pressure was 1.0 bar. The distribution of his gaseous pyrolysis products is the following: CH_4 : 10.7; CO_2 : 66.0; CO : 19.8; H_2 : 3.6. One can see that the mass concentration of hydrogen is of the same order. The ratio of CO/CO_2 is 0.30, which is a value considerable below the ratio of 13.84 obtained in our experiments. The major hydrocarbon components in our experiment are C_2H_2 with 8.5 % resp. 13.5 % and CH_4 with 0.9 resp. 2.7 %. MASEK measured CH_4 as the only hydrocarbon with the considerably higher value of 10.7 %.

At medium heating rates of 1000 K/s the pyrolysis of lignite was investigated by SUUBERG, et al. /6/ at atmospheric pressure, a final temperature of 1300 K and isothermal holding times of 2 to 10 s. They obtained a CO/CO_2 ratio of 1.85. These CO/CO_2 ratios are compiled again in Table II. It is seen that with increasing heating rate the yield of CO increases continuously.

Table II

	MASEK	SUUBERG, et al.	this work	
	lignite	lignite	lignite	
heating rate	.083 K/s	10^3 K/s	$610 \cdot 10^4$ K/s	$26.5 \cdot 10^4$ K/s
pressure	atmosph.	atmosph.	6.6 bar	6.2 bar
CO/CO_2	.30	1.85	13.84	

Results obtained by pyrolyzing coal at low and high heating rates /14/ were compared by JÜNTGEN and van HEEK /5/. They found that the hydrogen concentration is nearly independent of the heating rates whereas CH_4 decreases by one order of magnitude, and C_2H_2 is formed only at high heating rates. These results show the same dependence which was described above for lignite. Considering the pressure influence it is observed that the total yield of gases and of CO increases with pressure. This is in accordance with observations made by SUUBERG, et al. /6/.

Scanning Electron Microscopy

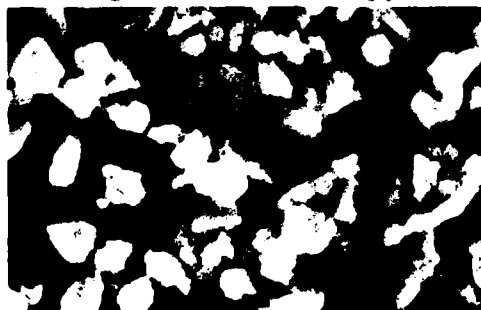


Fig. 7 : Unshocked lignite particles
magnification = 300

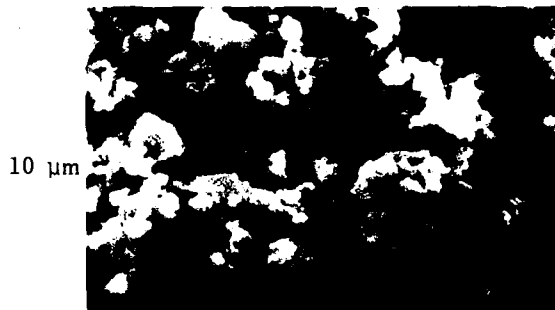


Fig. 8 : Shocked lignite particles
magnification = 300
 $p_5 = 6.2$ bar; $T_5 = 2720$ K
heating rate = $600 \cdot 10^4$ K/s
argon

Shock heated as well as the original lignite particles were investigated by scanning electron microscopy /9,10/. All pyrolyzed particles were subjected to maximum pulse lengths. Figure 7 is a micrograph of the original 10 μm particles, Fig. 8 a micrograph of the same material after shock heating. The appearance has changed drastically, particles of a much smaller size dominating the micrograph. They are agglomerated either to chains or to lumps. Of the original

material only a few larger ones appear to have remained.



Fig. 9 : Unshocked lignite particles
magnification = 300



Fig. 10 : Shocked lignite particles
magnification = 300
 $p_5 = 6.2$ bar; $T_5 = 2720$ K
heating rate = $88 \cdot 10^4$ K/s
argon

Figures 9 and 10 show $30 \mu\text{m}$ particles. In Fig. 10 the same small sized particles are seen, which have also been formed in the pyrolysis of the $10 \mu\text{m}$ particles. They either form their own clusters or they stick to the surface of the original particles, which appear to be affected only in a surface layer.



Fig. 11 : Unshocked lignite particles
magnification = 100



Fig. 12 : Shocked lignite particles
magnification = 100
 $p_5 = 22.6$ bar; $T_5 = 2480$ K
heating rate = $23 \cdot 10^4$ K/s
argon

Micrographs of the $70 \mu\text{m}$ particles are represented in Fig. 11 and 12. The same observations discussed with respect to the $30 \mu\text{m}$ particles appear to hold except that the separate agglomerates of the very small sized particles observed in Fig. 9 and 10 can hardly be seen.



Fig. 13 : Unshocked lignite particles
magnification = 30

Figures 13 to 17 show $120 \mu\text{m}$ particles. Figure 13 shows the original material, Fig. 14 and 16 the shock heated particle, the first in an argon atmosphere, the second in nitrogen. Also the temperature and pressures differ. In contrast to the smaller particles the size has changed strongly, particularly of the particles heated in nitrogen. Figures 15 and 17 have a magnification of 100 and demonstrate this effect more clearly.



Fig. 14 : Shocked lignite particles
magnification = 30
 $p_5 = 22.6$ bar; $T_5 = 2480$ K
heating rate = $7.9 \cdot 10^4$ K/s
argon



Fig. 15 : Shocked lignite particles
magnification = 100
 $p_5 = 22.6$ bar; $T_5 = 2450$ K
heating rate = $7.9 \cdot 10^4$ K/s
argon

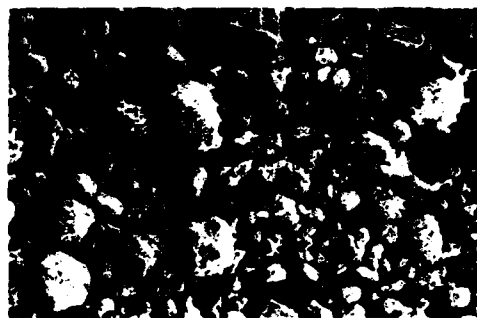


Fig. 16 : Shocked lignite particles
magnification = 30
 $p_5 = 5.5$ bar; $T_5 = 1710$ K
heating rate = $5.3 \cdot 10^4$ K/s
nitrogen



Fig. 17 : Shocked lignite particles
magnification = 100
 $p_5 = 5.5$ bar; $T_5 = 1710$ K
heating rate = $5.3 \cdot 10^4$ K/s
nitrogen

Comparing these micrographs with the investigations of bituminous and high volatile bituminous coal [9,10] the most obvious common feature is the formation of a surface with a strongly disrupted structure. The change of the original particle size and the formation of the very small separate clusters is not described.

Conclusions

The instrumentation of a single-pulse shock-tube was developed such that high pressure-pulses of reproducible and preselectable length could be produced. These characteristics are needed to investigate the pyrolysis of coal particles at high heating rates and high pressures. To achieve this goal the double diaphragm system DDS, separating the driver section from the dump tank had to be opened completely within a time interval short compared to the desired pulse length. At the high pressures desired this was only possible with a wire explosion of sufficiently high energy. The time delay between the rupture of the first diaphragm D1 and the double diaphragm system could be controlled precisely after developing a suitable triggering device. Particular care had to be devoted to avoid electrical interference of this discharge with the measuring and control units. Special grounding, shielding and filtering procedures had to be observed. Furthermore coincidence checks had to be used to rule out any spurious operations. First experiments were performed with this single-pulse shock-tube to investigate the pyrolysis of lignite particles of mean diameters 10 μ m, 30 μ m, 70 μ m, and 120 μ m, at pressures p_5 ranging from 5.5 to 39.0 bar and temperatures T_5 ranging from 1470 to 3250 K in a background atmosphere consisting of argon and nitrogen.

The analysis of the gaseous volatile matter shows that the dependencies observed when going from low to medium heating rates are continued to high heating rates. This concerns the increase of CO yield compared to CO₂, the decrease of CH₄ and the appearance of C₂H₂ at significant concentrations with high heating rates. An increase in the amount of gaseous volatile matter with pressures was observed above the value given by SUUBERG, et al. This dependence appears to become particularly pronounced for smaller lignite particles.

The scanning electron microscopy shows, that as a result of pyrolysis, small sized particles of about 2 µm diameter are formed which either agglomerate separately or adhere to the surface of the original particles.

- The pyrolysis process seems to affect the 10 µm particles entirely. After pyrolysis of this sample hardly any particles of original shape are left.
- Larger particles - 30 µm, and 70 µm - are affected in a surface layer. They keep their shape more or less.
- The largest 120 µm particles however disintegrate again, apparently by mechanical loading.

Acknowledgements

This work is supported by the DEUTSCHE FORSCHUNGS-GEMEINSCHAFT. We are grateful to RHEINISCHE BRAUNKOHLLENWERKE AG for preparing the lignite samples and to the GEMEINSCHAFTSLABOR FÜR ELEKTRONENMIKROSKOPIE of the Technische Hochschule Aachen for performing the scanning electron microscopy investigations.

References

- /1/ JUNTGEN, H., van HEEK, K.H.
Meeting on Coal Fundamentals, Stoke Orchard (1977)
- /2/ JUNTGEN, H., van HEEK, K.H.
Brennstoffchemie Nr. 6, Band 50 (1969), p. 172
- /3/ ANTHONY, D.B., HOWARD, J.B., MEISSNER, H.P., HOTTEL, H.C.
Rev. Sci. Instrum. Vol. 45 (1974), p. 992
- /4/ ANTHONY, D.B., HOWARD, J.B., HOTTEL, H.C., MEISSNER, H.P.
15th Symposium on Combustion Pittsburg, Pa. (1975), p. 1303
- /5/ KOCH, V., van HEEK, K.H., JUNTGEN, H.
Dynamic Mass Spectrometry, Heyden & Son Ltd., London (1970), p. 15
- /6/ SUUBERG, E.M., PETERS, W.A., HOWARD, J.B.
17th Symposium on Combustion, University of Leeds, England (1978)
- /7/ KIMBER, G.M., GRAY, M.D.
Combustion and Flame, Vol. 11 (1967), p. 360
- /8/ NETTLETON, M.A., Stirling, R.
Proc. Roy. Soc. London, 300 (1967), p. 62
- /9/ WOODBURN, E.T., EVERSON, R.G., KIRK, A.R.M.
Fuel, Vol. 53 (1974), p. 38
- /10/ LOWENSTEIN, A.I., von ROSENBERG (Jr.), C.W.
11th Symposium on Shock Tubes and Waves, Seattle (1977), p. 366
- /11/ MASEK, P.
Dissertation, RWTH Aachen (1981)
- /12/ GLICK, H.S., SQUIRE, W.S., HERZBERG, A.
5th Symposium on Combustion, Reinhold (1955), p. 393
- /13/ WITTIG, S.L.K.
Dissertation, RWTH Aachen (1967)
- /14/ SCHULTZ, J.L., SHARKEY, A.G. Jr.
Carbon, Vol. 5 (1967), p. 57

AD P000306

SHORT RESIDENCE-TIME PYROLYSIS AND
OXIDATIVE PYROLYSIS OF BITUMINOUS COALS

S.L. Szydlowski, D.C. Wegener, J.F. Merklin, and T.W. Lester

Kansas State University

Manhattan, KS 66506

The devolatilization of two U.S. bituminous coals during short residence times in inert and oxidizing atmospheres was investigated in a single-pulse shock tube.

Methane, ethane, and ethene yields exhibited maxima from 1300 to 1500 K; however, acetylene yields increased with temperature over the entire temperature range. The yields were affected by residence times shorter than 1 msec.

Pseudo first-order rate-constants were determined using a decomposition model, first order in the amount of substance yet to be evolved. Activation energies for light hydrocarbon production ranged from 79 to 123 kJ/mole, depending on the atmosphere. Associated preexponential

factors are 5×10^5 to $3 \times 10^7 \text{ sec}^{-1}$. A scheme using multiple parallel reactions with distributed parameters did not provide significantly better correlation. The relative smallness of the activation energies with respect to those representative of a chemically controlled process, the lack of better correlation with a multiple parallel reaction scheme, and the influence of atmosphere on the activation energy suggest that the production of these constituents from coal before ignition is governed, in part, by physical processes.

* It is suggested that

INTRODUCTION

In several recent papers(1-2), we have reported on the short residence-time evolution of light hydrocarbons from pulverized bituminous coals. In conjunction with measurements of the ignition and burnout kinetics of these coals, these data supported the theory that, even at heating rates in excess of 10^6 K/sec , a significant fraction of the total light-hydrocarbon volatiles can evolve prior to particle ignition.

In analyzing these data, we were perplexed that much of the existing kinetic information on the formation of hydrocarbons was

inadequate to predict the levels of lower hydrocarbons within the very short times available behind the reflected shock wave in a single-pulse shock-tube. The most reliable data on individual species evolution from American bituminous coals have been provided by Suuberg, et al. (3), while the most complete information on the qualitative and quantitative volatile yields from a wide range of American coals has been reported by Solomon (4). Both sets of experimenters used electrically heated grids (5), within which were sandwiched small amounts of pulverized coal. Heating rates were adjusted to between 1000 K/sec after it was ascertained that heating rate had no observable influence on product distribution or yield. The heating rates and the maximum temperatures (1373 K) at which kinetic data could be obtained are lower than the heating rates (10^5 - 10^6 K/sec) and maximum particle temperatures (in excess of 2000 K) that are to be expected in pulverized coal flames (6).

To start to clarify the discrepancy between published kinetic data and our observed hydrocarbon yields, three bituminous coals were shock heated in nitrogen, air, and argon for varying dwell periods (0.3 to 3 msec), over a temperature range of approximately 1000 to 1900 K. The unreacted solid and evolved gases and liquids were cooled at rates in excess of -10^5 K/sec by the reflected rarefaction fan. In this paper we report on the techniques used to collect the stable products of reaction and to infer pseudo first-order rate-coefficients from the product yields.

APPARATUS AND PROCEDURE

The general technique for studying the ignition and oxidation of pulverized coal in shock tubes, as well as the construction of the single pulse tube, have been covered previously (1,2,7-9). To facilitate collection of solid and liquid products of reaction, a new test section, 27 cm in length and 5.7 cm inside diameter, was constructed in which removable aluminum liners (5.08 cm inside diameter) were placed. The test section, shown schematically in Fig. 1, contains two access ports. The port 7.66 cm downstream from the isolation ball valve is used to introduce the coal sample. The gaseous products of reaction are vented through the other.

Helium (Airco, 99.995% purity) was used as the driver gas in all experiments. The length of the driver section was varied between 1 and 3 m by means of a variable length end plug to change the nominal dwell time behind the reflected shock wave. For periods of less than 1 msec, the driver section was shortened by approximately 1.5 m. The coals were shock heated in atmospheres of argon (Matheson, 99.999% purity), nitrogen (Airco extra dry 99.5% purity), or air (Matheson, zero with total hydrocarbons less than 2 ppm). To minimize contamination, all gases were filtered through activated charcoal and molecular sieve 5A to remove moisture and hydrocarbons. A molecular sieve foreline trap was installed on the vacuum line to absorb contaminants from the roughing and oil diffusion pumps. Shocks were initiated by the mechanical rupture of aluminum diaphragms (for tests in argon), and by overpressure rupture of mylar diaphragms (for all other tests).

Three different U.S. bituminous coals were used in the experiments. In the argon tests, from which solid residue and liquid samples were collected, 40 ± 0.8 mg of an Illinois #6 coal that had been sieved to -400 U.S. mesh were used. In the other experiments, 20 ± 0.4 mg of coal were used. Properties of the

coals tested are listed in Table 1. All coals were stored in a dessicator until immediately before their use in a test. The coal sample was introduced into the shock tube by means of a dispersion plate suspended from a saddle block fitted flush to the inner diameter of the shock tube liner (see Fig. 1). It has been shown previously (7) that this dispersion technique produces a reasonably uniform suspension along an axial distance of 10cm. Moreover, in a series of recent tests with $\text{Al}_2\text{O}_3/\text{N}_2$ aerosols,

Oman, et al. (10) have determined via Laser Doppler Velocimetry that the radial distribution of particles is surprisingly uniform across the test section.

Immediately after the diaphragm rupture, the ball valve (see Fig. 1) was closed, isolating the test section from the rest of the shock tube. The test section was isolated for one hour to allow the gaseous products to approach a uniform compensation axially. A 75 cm^3 gas sample was extracted through a $2 \mu\text{m}$ stainless steel filter into a previously evacuated stainless steel bottle. Lower hydrocarbons ($\text{C}_1\text{-C}_4$) were analyzed by a Tracor Model 560 gas chromatograph equipped with dual flame ionization detectors. The determination of the thermodynamic conditions behind the reflected shock wave is covered in Szydlowski (11). Further experimental details may also be obtained in Seeker (9), Vaughn (12), or a series of recent papers (1,2,7,8).

RESULTS

Hydrocarbon yields ($\text{C}_1\text{-C}_4$) were analyzed in the various test gases over a temperature range of approximately 1000 to 1900 K, with nominal residence times of 0.3 to 3.0 msec, and under total pressures of $0.8 \pm 0.2 \text{ MPa}$. The qualitative results for all test gases are similar to those exhibited in Fig. 2 for Illinois #6 pyrolysis in N_2 . Ethylene yields as a fraction of the as-received coal mass are greater than methane yields up to approximately 1600 K for N_2 . Unlike previous experiments with relative rapid heat-up at lower temperatures (see particularly Suuberg, et al. (3,13) and Solomon (4)) the yields of aliphatic gases all exhibit maxima with temperature. Above this, they decrease in favor of acetylene. The total lower-hydrocarbon gas-yields asymptotically approach (see Fig. 3) a constant value for the experiments in nitrogen, indicative of an equilibrium being established among the gases. On the other hand, in the argon runs, the total hydrocarbon yields begin to decrease, even as acetylene continues to increase. The hydrocarbon yields determined for the Pittsburgh seam ($3.3 \mu\text{m}$) coal in air are equivalent to those obtained in nitrogen up to 1263 K, at which point ignition was observed. More can be found relating to this last point in Seeker (9) and Seeker, et al. (1).

The yields obtained in argon were obtained for residence times between 1 and 3 msec (solid symbols) and 0.3 msec (open symbols). Within the data scatter, the yields are equivalent for times greater than 1 msec, lower for the very short residence time runs. The influence of the diluent gas on methane yields is illustrated in Fig. 4, along with the methane yields from pyrolysis of a Pittsburgh seam coal as reported by Suuberg, et al. (3) and Tyler (14). The first experiments were conducted in a heated grid apparatus in which the coal volatiles were ejected into a cold bath of helium while the second experiments

were conducted (with the same Pittsburgh seam coal sample) in a fluidized bed of sand in which the volatiles were ejected into a hot helium gas environment. Although both experimenters quote heating rates of 10^4 K/sec (recall the Suuberg experiments found no influence of heating rate on product yield or distribution), the temperature histories were different as were the residence times to which the coal and volatiles were exposed to elevated temperatures (one second or longer). The cooling rates were nominally 200 K/sec for the MIT work, but were not quoted for the Tyler experiments.

In the shock tube experiments, the residence times for the argon runs were 1 msec, and for the other atmospheres, 1.4 msec. The rates of heatup and cooling will be discussed in the subsequent section. Although the heating rates are slightly different for the argon tests and the tests conducted with diatomic gases, the yields of methane, as shown in Fig. 3, are equal to within the range of data scatter up to 1300 K.

The yields continue to increase in the nitrogen experiments up to 1600 K. Insofar as the yields are nearly equivalent below 1300 K, the influence of diluent gas appears not to be merely one of heating rate, but rather one of third body influence.

DISCUSSION

The shock tube is a well established instrument with which to generate accurate kinetic information for high-temperature gas-phase reactions. The generation of usable kinetic data for heterogeneous reactions is not as certain. The principal difficulty is the finite heat-up rate and quench that complicate the analysis of data. To establish the heat-up characteristics of polydisperse particle suspensions behind the reflected shock, Seeker conducted a number of optical pyrometry measurements (9). The response of the 4.1 μ m Illinois #6 coal sample to reflected shock waves at temperatures between 1205 and 1226 K is shown in Fig. 5. The heating from the incident shock conditions proceeds at a rate of approximately 3×10^6 K/sec and the particle suspension relaxes quickly to a temperature very close to the initial reflected shock gas temperature. For all cases in these experiments, the particle mass loading was maintained at less than 5% of the reflected shock gas density. In similar experiments, Seeker determined that the cooling rate of the particle suspension agreed very closely with that predicted from the pressure history, assuming an isentropic expansion.

In determining kinetic information from the pyrolysis yields, we assumed that the hydrocarbon gas yields could be correlated with a decomposition model, first order in product remaining to be evolved. It is well known (see for instance Anthony and Howard (15) or Suuberg, et al. (3)) that such kinetics are only crude and often inadequate representations of the multiple reactions leading to each observed product; nonetheless, we have found that a multiple reaction sequence as described by Anthony, et al. (16) does not correlate our data significantly better than a single reaction model. It is clear from companion studies on benzene and toluene pyrolysis in our laboratories (see for instance Vaughn (12) and Vaughn, et al. (17)) that the lighter hydrocarbon yields result not only from the coal, but also from the ring rupture of light tars and aromatic constituents. Suuberg, et al. (3) have also pointed out that mass transfer within the particle must also be exerting an influence on the apparent kinetics; however, the rapid heat-up and small particle

sizes used in these experiments minimized, but did not eliminate, this influence.

Bearing these concerns in mind, the first order rate expression used is

$$\frac{dV}{dt} = k_0 \exp(-E_0/RT) (V^* - V) \quad (1)$$

where V is the yield as a fraction of the as-received mass of the coal loading, V^* is the maximum yield realized under the available reaction time and temperature, and k_0 and E_0 are the first estimates of the Arrhenius parameters, uncorrected for finite-rate heating or cooling. Integration yields

$$\frac{V^* - V}{V^*} = \exp[-k_0 t \exp(-E_0/RT)] \quad (2)$$

where t is the nominal dwell time behind the reflected shock. Suuberg, et al. (13) have shown that for a constant heating-rate, the yield is

$$\frac{V^* - V}{V^*} = \exp[-(k_0 RT^2/mE_0) \exp(-E_0/RT)] \quad (3)$$

where m is the heating rate. We may define an equivalent time at the final temperature required to produce the yields obtained under the constant heat-up to that final temperature. Doing so,

$$\exp[-k_0 \exp(-E_0/RT) \Delta t] = \exp[-(k_0 RT^2/mE_0) \exp(-E_0/RT)] \quad (4)$$

where Δt is the time required. Simplifying, we obtain

$$\Delta t = RT^2/mE_0. \quad (5)$$

The time, obtained from the oscilloscope recording of the pressure trace and used to obtain the initial estimates of k_0 and E_0 in

Eq. (2), includes the time required to heat the suspension to the final gas temperature; however, the equivalent time is less than this and the corrected time for reaction at the final temperature is calculated from,

$$t' = t - \frac{T_5 - T_0}{m} + \Delta t \quad (6)$$

where t' is the corrected dwell time and T_0 is the particle temperature entering the reflected shock wave. Using this analysis resulted in reductions of from approximately 150 to 400 μsec for the argon shocks, 120 to 300 μsec for the shocks with the small Pittsburgh seam and Illinois #6 in nitrogen, and 425 to 750 μsec for the large Pittsburgh seam. Only one iteration was required for the small coal samples; two were required for the larger Pittsburgh seam sample. The kinetic parameters for the four coals are tabulated in Table 2 and shown on an Arrhenius plot in Fig. 6. The kinetics are about one order of magnitude greater than the simple first order models for light hydrocarbon production by Solomon (4) and for CH_4 (Suuberg, et al (3)). In

the multiple reaction model of Suuberg, et al., only one reaction is sufficient to correlate appearances of C_2H_6 from the pyrolysis of Pittsburgh seam coal; with an assumed first-order preexponen-

tial factor of 10^{13} sec^{-1} and a resulting activation energy of 230.1 kJ/mole, the results of Suuberg and the current tests are in good agreement between 1000 and 1100 K. Correcting the data for finite rate quench would adjust the rate constants by somewhat smaller amounts than does the finite heating-rate correction; this was not performed, however, insofar as the heating rate correction produced a better fit to the rate data than did either the uncorrected kinetic coefficients or the inclusion of finite-rate quench corrections.

It should be emphasized that the shock tube technique produces light hydrocarbon yields that are a result of both primary and secondary reactions; whereas, the electrically heated grid work of Suuberg, et al. (3) and Solomon (4), through the use of a cold bath gas, quench the secondary reactions. Nevertheless, the shock tube is useful for studying short residence-time pyrolysis behavior in a particle suspension undergoing heating rates commensurate with those found in utility boilers. With sufficiently rapid heating rates, we have also demonstrated that lower-hydrocarbon yields comparable to those obtained at much longer residence times at slower heating rates can be obtained. It is not clear that the decreased gaseous volatile yields from pyrolysis of Illinois #6 in argon vis a vis nitrogen, are due to a third body mechanism; however, the decrease of methane at a lower temperature in argon than in nitrogen may be indicative that the vibrationally hot radical fragments from decomposition of the coal or aromatic constituents above 1300 K are not able to stabilize as lower molecular weight hydrocarbons, but repolymerize to form, eventually, soot or repolymerize with the char. More complete experiences with solid and liquid characterization in various atmospheres, including isotopically labeled gases, are now underway to determine to what extent third body stabilization is important in high temperature pyrolysis of various coals.

ACKNOWLEDGEMENTS

Acknowledgement is made to the donors of the Petroleum Research Fund, administered by the American Chemical Society, for partial support of this work. D.C.W. thanks the Kansas Engineering Experiment Station for financial support through a Graduate Research Assistantship.

REFERENCES

1. W.R. Seeker, D.C. Wegener, T.W. Lester and J.F. Merklin Seventeenth Symposium (International) on Combustion (The Combustion Institute, Pittsburgh, 1979) p. 155.
2. W.R. Seeker, and T.W. Lester, Western States Meeting, The Combustion Institute, Boulder, CO, 1978.
3. E.M. Suuberg, W.A. Peters, and J.B. Howard Seventeenth Symposium (International) on Combustion (The Combustion Institute, Pittsburgh, 1979) p. 117.
4. P.R. Solomon, Pulverized Coal Combustion: Pollutant Formation and Control, edited by A.F. Sarofim, G.B. Martin, W.S. Lanier and T.W. Lester (U.S. Government Printing Office, Washington, in press) Chap. 3.
5. D.B. Anthony, J.B. Howard, H.P. Meissner and H.C. Hottel, Rev. Sci. Instrum., **45**, 992 (1974).
6. A.F. Sarofim and J.M. Beer. See ref. 4, Chap. 4.

7. W.R. Seeker, T.W. Lester and J.F. Merklin, Rev. Sci. Instrum. 51, 1523 (1980).
8. T.W. Lester, W.R. Seeker and J.F. Merklin Eighteenth Symposium (International) on Combustion (The Combustion Institute, Pittsburgh, 1981) in press.
9. W.R. Seeker, Ph.D. dissertation, Kansas State University, 1979.
10. R.A. Oman, W. Konopka and V.S. Calia, Proceedings of the Second Multiphase Flow and Heat Transfer Workshop, Miami Beach, FL, 1979.
11. S.L. Szydlowski, M.S. Thesis, Kansas State University, 1979.
12. S.N. Vaughn, Ph.D. dissertation, Kansas State University, 1980.
13. E.M. Suuberg, W.A. Peters and J.B. Howard, Ind. Eng. Chem. Process Design Dev. 17, 37 (1978).
14. R.J. Tyler, Fuel, 59, 218 (1980).
15. D.B. Anthony and J.B. Howard, A.I. Ch.E.J., 22, 625 (1976).
16. D.B. Anthony, J.B. Howard, H.C. Hottel and H.P. Meissner, Fifteenth Symposium (International) on Combustion (The Combustion Institute, Pittsburgh, 1975) p. 1303.
17. S. N. Vaughn, T. W. Lester and J. F. Merklin, this Symposium.

Table 1. Coal Properties

Analysis	Component	Pitts. Seam	Ill. #6 (1)	Ill. #6 (2)
Proximate*	Ash	6.4	12.7	10.3
	Volatile Matter	35.5	34.4	37.8
	Moisture	1.9	4.4	2.1
	Fixed Carbon	56.2	48.5	49.8
Ultimate**	H	5.6	5.3	5.2
	C	82.2	75.0	77.3
	N	1.7	1.3	1.4
	O	9.3	14.6	12.3
	S	1.2	3.8	3.8
Number Mean Diameter***		3.3 μ m 14.9 μ m	4.1 μ m	7.3 μ m
Mass Mean Diameter		13.0 μ m 24.8 μ m	15.5 μ m	18.4 μ m

*Analysis by Hazen Research, Inc., Golden CO

**Ultimate Analysis by Galbraith Laboratories, Inc., Knoxville TN

***Size analysis determined by Coulter Counter and microscopy

Table 2. Pseudo first-order rate-constants* for the formation of lower hydrocarbons from the pyrolysis of bituminous coals.

Coal	Uncorrected		Corrected	
	k_o	E_o	k'	E'
Illinois 6(Ar)	7.5×10^5	88.4	1.6×10^6	92.8
Illinois 6(N ₂)	3.3×10^5	75.4	5.2×10^5	78.8
Pittsburgh Seam (3.3)	2.1×10^7	120.2	3.3×10^7	123.3
Pittsburgh Seam (14.9)	1.2×10^7	94.1	7.6×10^6	107.8
Pittsburgh Seam (composite)	-----	-----	1.7×10^7	116.8

* Units for k_o and k' are sec^{-1} and for E_o and E' kJ/mole.

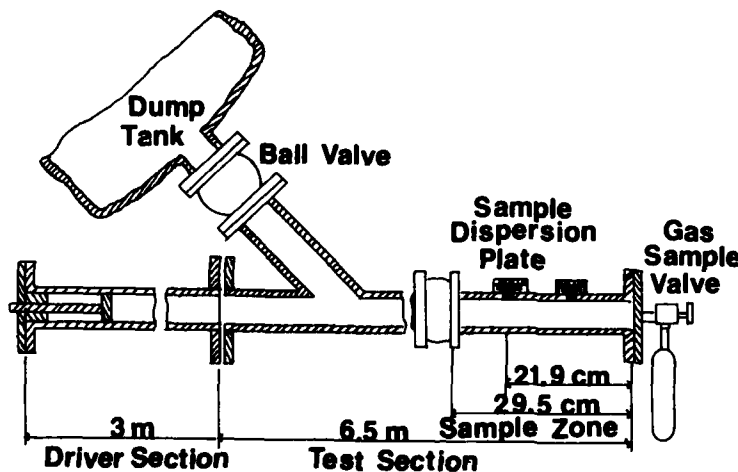


Fig. 1. Schematic of KSU Shock Tube.

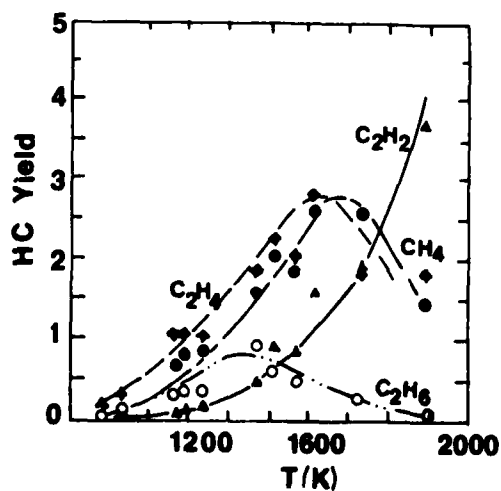


Fig. 2. Light hydrocarbon yield as a function of temperature.

filled circles - CH₄
open circles - C₂H₆
filled diamonds - C₂H₄
filled triangles - C₂H₂

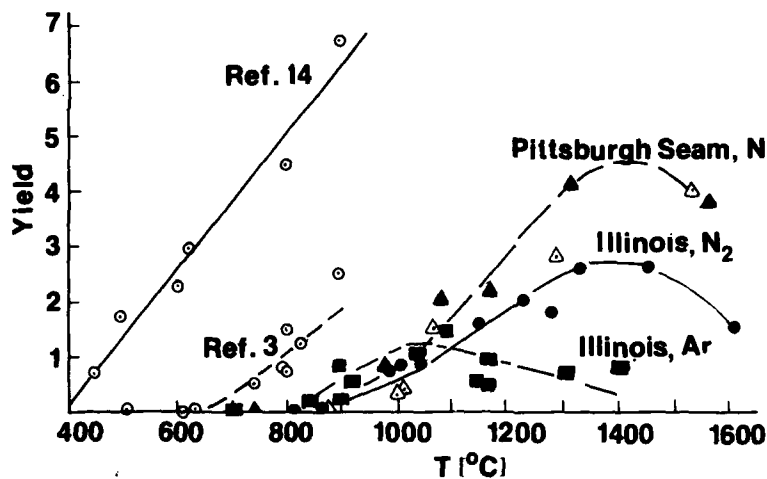


Fig. 4.
Comparison of
Methane yields
(%, as received)
as a f (T).

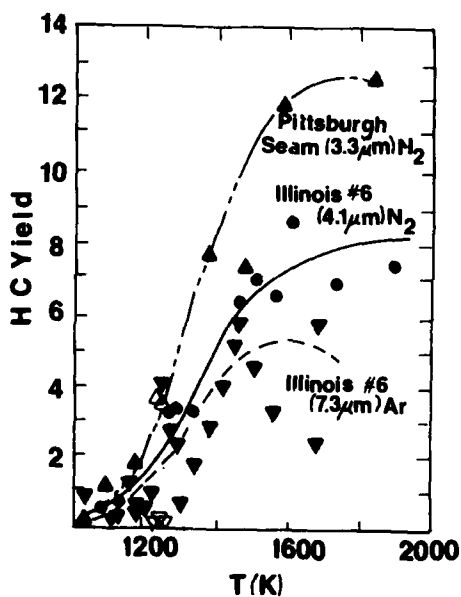


Fig. 3. Hydrocarbon Yields
(%), as a f (T).

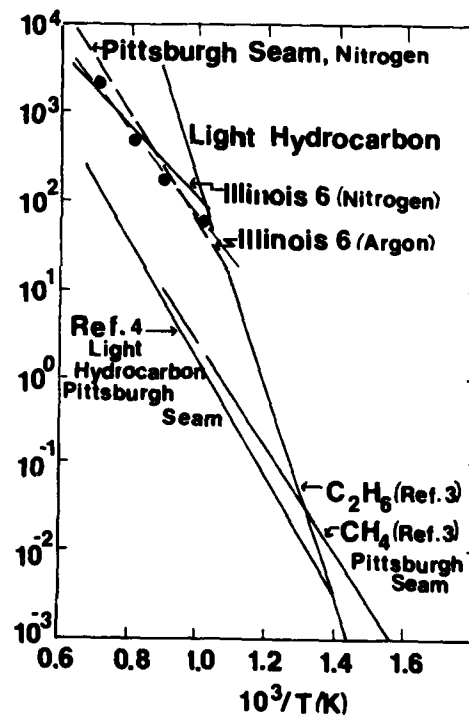
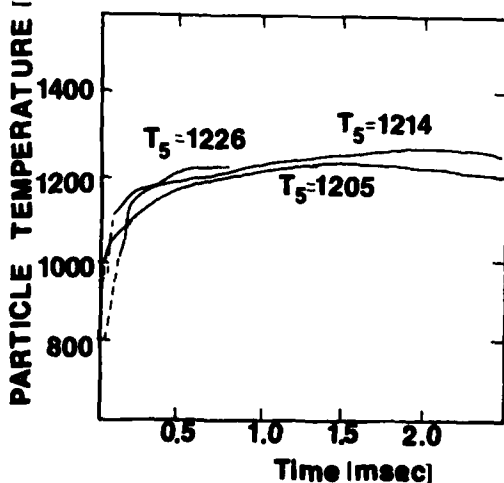


Fig. 6. Comparison of first
order rate constants for
hydrocarbon evolution.

Fig. 5. Particle temperature
as a f (time) after reflected
shock.

SHOCK WAVE IGNITION OF PULVERIZED COAL

E.A. Ural, M. Sichel, and C.W. Kauffman

Department of Aerospace Engineering, The University of Michigan

Ann Arbor, Michigan 48109

AD P000302

Heating and ignition delay times behind an incident shock of small clouds of coal dust-particles of three different size ranges were measured in a shock tube. Four different compositions of O₂-N₂ mixtures were used as the oxidizer and the incident shock Mach number varied from 4.1 to 4.8. Observed delay times were in the range 10 to 150 μ sec, decreasing with increasing Mach number and O₂ concentration. The theoretical analysis is based on the numerical solution of the one-dimensional transient heat equation for a single spherical particle. Particle acceleration has an important effect on heat transfer and is considered in the model. Heating due to gas phase and heterogeneous reactions is represented with appropriate volumetric or surface source terms. The results show that volatilization is insufficient to account for the short delay times observed. The main mechanism for ignition in these short times appears to be heterogeneous surface reaction both on the outside and within the porous particle. This conclusion is also supported by the tests conducted with char and graphite. After making the necessary corrections for the electro-optical system performance theoretically calculated heating and ignition delays agreed well with the experimental measurements.

INTRODUCTION

Combustion of pulverized solid fuels in gaseous oxidizers is fairly well understood. However, recent interest in dust explosions has focused attention on a new aspect of this problem. In explosive combustion, processes are so rapid compared to conventional applications that they usually lie well beyond the range of validity of presently available theories and experimental data. Explosive combustion of dust-oxidizer mixtures occurs either as a deflagration in a confined space, or as a detonation. Detonation, although less frequent, is more hazardous because of its higher overpressures and propagation velocities. The detonability of coal-air mixtures is still controversial. However, such mixtures with excess oxygen or methane, and some agricultural dust-air mixtures have been observed to detonate in laboratory experiments as well as in practice.

The structure of a detonation consists of a leading shock followed by an induction and reaction zone. The end of the induction zone is characterized by the ignition of the fuel, while burnout or quenching characterizes the end of

the reaction zone. The initiation and propagation of detonations depend mainly on the induction zone thickness¹. To understand the quantitative nature of two phase detonations it is thus necessary to carry out experiments designed to simulate the flow behind the leading shock of a detonation wave. Obviously the ideal experiment would be to study the detonation itself in a long tube. However this may not always be feasible as it would require very large tube diameters to eliminate the influence of confinement². To simulate the flow field through the induction zone, shock tube studies should be sufficient and are much simpler to carry out. Several shock tube investigations of coal dust ignition already exist in the literature (e.g. Ref. 3). In these studies mixing the dust with the oxidizer has been a problem; thus, the incident shock was utilized to disperse the dust, and the dust was then ignited by the reflected shock. Such studies thus fail to account for the high convective flow velocities experienced by the particles in the induction zone of a detonation.

This paper presents briefly an experimental and theoretical investigation of the ignition delays of small coal-dust clouds behind incident shock waves. The experimental apparatus and procedure are first delineated then experimental results are presented. A theoretical analysis based on a simplified model of the ignition process is then described and the results are compared to the experimental measurements. The details can be found in Ref. 11.

EXPERIMENTAL APPARATUS AND PROCEDURE

A conventionally designed horizontal shock tube was used in the incident shock mode for the experiments. The test section is filled with gas of the desired composition and pressure. The driver is filled with high pressure helium and a nichrome wire is exploded with a large capacitor discharge to break the upstream diaphragm stack. A shock then propagates through the test section creating a high speed flow of increased pressure and temperature. In the test section, a cloud generator (Fig. 1) employing a solenoid actuated

impulse mechanism generates a slowly settling cloud of dust prior to the arrival of the incident shock. The tip of the rod where the dust is lightly packed is designed to introduce some shear which provides for better cloud dispersion.

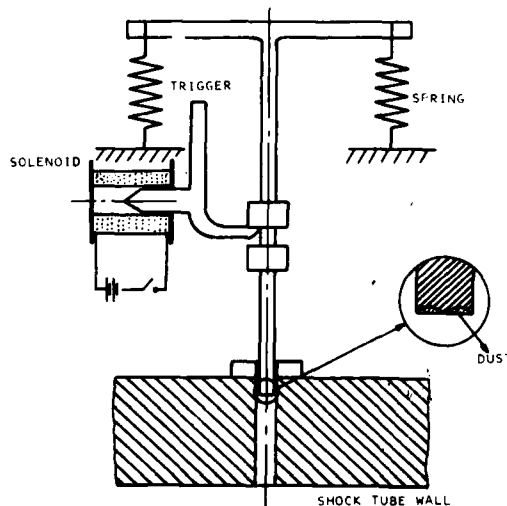


Figure 1. Sketch of the Cloud Generator

Synchronization of shock and the cloud so that they meet in the observable volume defined by the two windows is crucial. Therefore it is necessary to introduce a time delay between the pulses for the solenoid and the nichrome wire. A series of tests were conducted to optimize this time delay, and a success probability of approximately 2/3 is achieved. For that reason, a spark shadowgraph of the cloud is photographed on a polaroid film for each run right before the arrival of the shock. These photographs are used in accepting or discarding the runs

on the basis of cloud location and dispersion. Figure 2(a) shows a typical example of such a photograph. For a run to be acceptable the cloud should be in the light region projected by the windows and should not have large particle agglomerations. As seen in Fig. 2(b), after the collision with the shock the smaller agglomerations are shattered providing a fairly uniform

distribution. However, small particles are observed to shed from the larger agglomerations with a stripping type of behavior. In the latter case most of the particles are attached to the agglomeration which keeps them cooler during most of the test time so that the results will not be representative of the real cloud-flow interaction. Indeed the ignition times observed with large agglomerations present were considerably larger than those observed for a fully dispersed cloud.

Just upstream of the observation window two pressure switches 0.305 m apart are used to measure the wave speed. A pressure transducer located opposite the cloud generator marks the start of the interaction between the cloud and the flow. The end of the test time is determined by the arrival of either the expansion wave or of the contact surface at the cloud and is determined by a thermocouple. Because of the acceleration of the cloud, the cloud-flow interaction is observed with an RCA 931B photomultiplier viewing the entire length of the test section windows. The signals from the pressure transducer, thermocouple and photomultiplier are recorded on Polaroid film with a chopped, dual beam Tektronix oscilloscope in the single sweep mode. A typical trace is shown in Fig. 2(c).

EXPERIMENTAL RESULTS

In the experiments, Eastern Kentucky bituminous pulverized coal was used. In Table I the ASTM proximate and ultimate analyses of this coal are given. Control runs were also made with high purity electrode graphite and with the char obtained from the proximate analysis of the same coal as that used in the tests. All dusts were dessicated first and sieved to provide size ranges of 53/74, 37/53 and less than 37 microns. Tests were carried out in nitrogen-oxygen mixtures with oxygen volume percentages of 0, 21, 50 and 100%, initially at 33 kiloPascals. The Mach numbers employed were in the range 4.1 to 4.8. Contamination of the tube is monitored periodically using runs without particles, and the tube is cleaned when needed. For each acceptable run two delay times were determined from the oscilloscope trace of the photomultiplier. Time zero is taken as the moment of collision of the shock with the cloud as marked by a

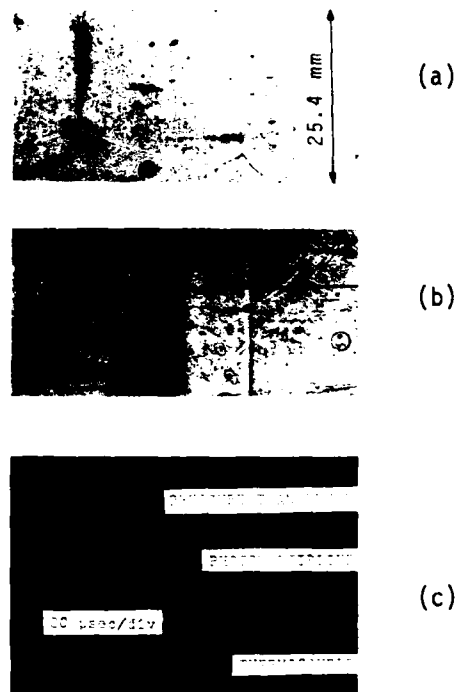


Figure 2. Typical Cloud (a) before, (b) after the shock wave. (c) Typical scope record.

TABLE I. ANALYSIS OF DESSICATED COAL SAMPLE

Proximate Analysis (as fired)

Inherent Moisture	= 1.1%
Volatile	= 28.0%
Ash	= 26.8%
Sulphur	= 1.3%
Fixed Carbon	= 42.8%

Ultimate Analysis (moisture free)

C	= 58.5%
H	= 3.9%
N	= 1.2%
O	= 8.0%
S	= 1.3%
Ash	= 27.1%

rapid change in the pressure transducer signal. The heating delay is taken as the time at which the photomultiplier output first starts to change, while the ignition delay is taken as the time at which the photomultiplier output shows a sharp increase.

Delay times in the range of 10 to 150 μsec were observed. Experiments resulting in delay times of less than 10 μsec were discarded due to limitations in the time resolution of the experimental arrangement. The time required for the shock wave to sweep through the cloud imposes a more stringent condition on temporal resolution than the bandwidth of the electronics. From Fig. 2(a) it can be seen that a typical cloud has a dimension of less than 5 mm in the flow direction which yields a 3 to 4 μsec sweep time for the incident shock strengths used in the experiment.

The heating and the ignition delay data measured in the experiments are displayed in the Arrhenius plots of Figs. 3 and 4, respectively. The delay times are plotted against the non-dimensional reciprocal static-temperature of the post-shock gases. The Mach number of the incident shock is also indicated on the abscissa. As is to be expected, the delay times tend to decrease with increasing oxygen concentration and increasing incident shock Mach number or flow temperature. The particle size dependence of the delay times is so small as to be indistinguishable within the experimental scatter.

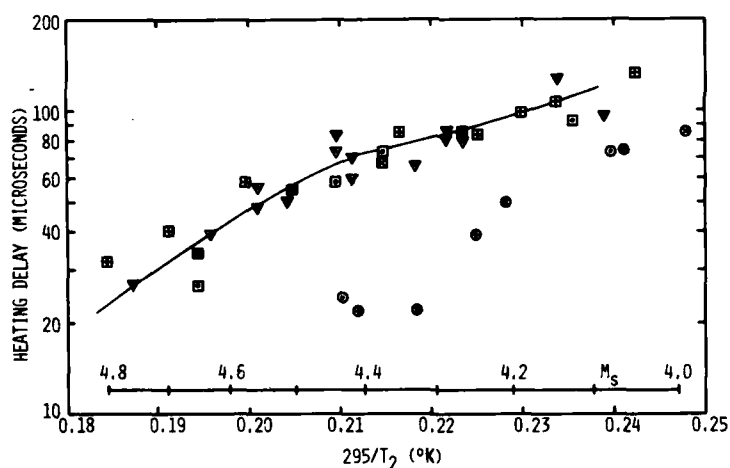


Figure 3. Heating Delays (line shows the theory for nitrogen)

LEGEND

DUST

COAL

LT37

37/53

53/74

GRAPHITE

CHAR

TEST GAS

$X_{O_2} = 0.9$

$X_{O_2} = 0.21$

$X_{O_2} = 0.5$

$X_{O_2} = 1.0$

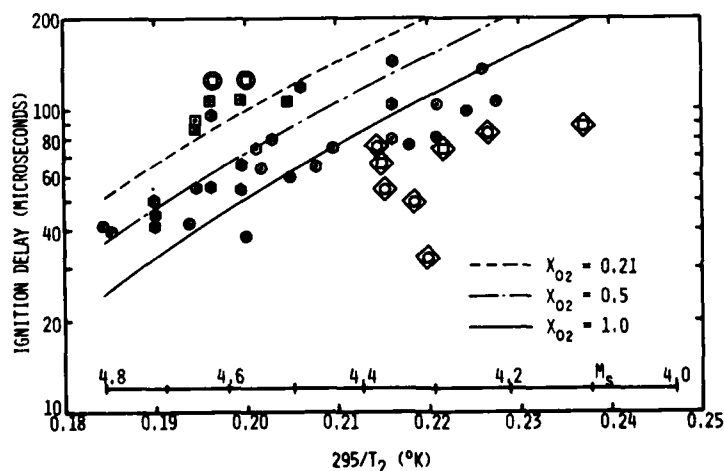


Figure 4. Ignition Delays (lines show the theory)

As seen in Fig. 4, the photomultiplier detects radiation even for particles in pure nitrogen. This set of data was therefore interpreted as representing the particle heating delay, namely the time required for the particle surfaces to reach a temperature sufficiently high to emit detectable thermal radiation. It is seen in Fig. 3 that the heating delays are about the same for pure nitrogen and the 21% oxygen mixture. However, the heating delays are much shorter for mixtures of higher oxygen content. As will be discussed below, this effect may be due to the ignition of smaller particles or sharp particle edges prior to the observed heating delay time. In that sense the term "heating delay" is a misnomer.

It can be seen from Table I that the volatile content of the coal used here is 28% of the total mass or 39% of the combustible mass. It is also known that for most applications, the early stages of coal combustion are governed by the release and combustion of volatiles for coals of this much volatile content. To determine the influence of volatiles for the shock wave ignition, graphite and char were tested. The graphite used is high purity electrode graphite which has no volatiles and a very small porosity. Char particles, on the other hand, were obtained from the proximate analysis of the coal dust used in the above tests and so they had a negligible volatile content, but high porosity. The results, also shown in Fig. 4, indicate that under the same experimental conditions char ignites sooner than coal while the graphite ignites later. The behavior of the char supports the hypothesis that heterogeneous reactions are the dominant factor in shock ignition. The increased ignition delay of the graphite is probably due to its lack of porosity, and supports the idea that in the case of the coal and char particles heterogeneous reactions are not confined to the surface but also occur in the outer layers of the porous particle structure.

THEORETICAL ANALYSIS

Interpretation of the above data requires a detailed analysis of the interaction between the flow and the dust cloud, and of the performance of the electro-optical system.

After the incidence of the shock wave the cloud is in a supersonic, high temperature and high pressure flow. The mean free path of the post shock gases is of the order of 0.05 microns so that the relative flow will be in the continuum or near-continuum regime for most particles. It has been observed that the shock impact disperses the initial cloud (Fig. 2b). In part this dispersion is a consequence of the particle size distribution since the smaller particles accelerate more rapidly. In the simplified analysis presented here it is therefore assumed that the particles are so widely spaced that interactions between the particles can be neglected and a single particle model is valid. Initially particles are in a supersonic flow so that a bow shock stands upstream of each particle. The bow shock causes an additional increase in the pressure and temperature. Because of the high flow velocity around the particle, pressure also varies considerably over the surface. If the particle is porous, like coal or char, there may thus be a flow of gas into and through the particle.

Particle heating starts at the instant of shock impact. However, as the particle accelerates the relative convective velocity decreases reducing the rate of heat transfer to the particle, and eventually the bow shock disappears. The time required for the particle surface to reach a threshold temperature that is high enough for the particle cloud to first excite the electro-optical system is defined as the heating delay period. When the right conditions are achieved, the exothermic oxidation reactions occurring near the particle surface will result in a rapid temperature rise, which causes a sudden increase in the photomultiplier signal thus indicating the end of the ignition delay period. Due to the high convective velocity around the particle the Biot

number for coal particles is of order unity; hence, convection is not the only process limiting the rate of heat transfer. Temperature variations within the particle must also be considered.

Since a small cloud is being observed in this experiment the radiative heat transfer among the particles will be negligible as opposed to a full fledged combustion wave where there is a big variation of particle surface temperature across the wave. Also, in the ignition studies, particle temperatures are relatively low during most of the pre-ignition period so that radiative heat loss to the shock tube walls as well as the temperature dependence of the thermal properties of the particles can be neglected.

In order to establish a simple mathematical model it would be helpful to know in advance whether the ignition occurs on the surface or in the gas phase. Preliminary studies indicated that for shock Mach numbers between 4.1 to 4.8 the observed ignition delay times are too short for significant devolatilization to occur. According to the Bazdorch and Hawksley model⁴ less than 3% of the volatile content is released within the delay times observed here, when the highest rate constant from Anthony and Howard⁵ is used and the particles are assumed to reach the post-shock static-temperature instantaneously. This suggests that less than 1% of the heated coal mass is volatilized prior to ignition. Due to the large temperature gradient at the surface volatiles will be generated only in a thin outer layer of the particle. At the same time the inward flow mentioned earlier will tend to carry these volatiles into the particle interior where it is too cool for reaction. Hence the actual ignition would appear to be due to surface reactions. This conclusion is also supported by the shock tube experiments of Hwang and Kathiresan³.

A crucial problem is now establishing the surface area available for heterogeneous reaction. For most industrial applications the porous flow of volatiles within coal particles is now recognized to be important for accurate devolatilization modeling. In shock ignition, however, the porous flow of oxidizer into and through the particle becomes important. An order of magnitude analysis using Darcy's equation gives porous flow time-scales of the order of the observed ignition delay times, for typical particle sizes. This flow will obviously expose the pore structure to fresh oxidizer and make the internal surface available for heterogeneous reaction. As also observed in the experiments with char and graphite, the internal surface area will thus be an important parameter governing the shock wave ignition. The unsteady energy equation for porous media, however, reveals that the contribution of this flow to heat transfer is small compared to conduction in the solid medium.

Although the actual shapes of coal particles are random in nature and far from spherical they are assumed to be spherical in the analysis. Furthermore, it is assumed that the convective heat transfer to the particle can be represented by an average heat flux calculated from the instantaneous recovery temperature and the surface-average film-conductance. This assumption leads to a spherically symmetric temperature distribution. Although the uniform heat flux assumption is not necessary, replacing the particles by spheres introduces so much error that a detailed analysis of the convection about the sphere is not justified.

The energy equation for the particle is then reduced to

$$\frac{\partial T}{\partial t} = \frac{a}{r^2} \frac{\partial}{\partial r} \left(r^2 \frac{\partial T}{\partial r} \right) + \frac{u'''(r,t)}{\rho_c C} \quad 0 \leq r < R \quad t > 0 \quad (1)$$

The source term u''' accounts for the internal heterogeneous reaction and is given by

$$u'''(r,t) = Q S_1 \rho_c P_{O_2} A \exp [-E/RT(r,t)] \quad (2)$$

where S_i and Q are the internal surface area and the heat of combustion per unit mass, respectively. The particle motion is governed by the equation

$$\frac{4}{3} \pi R^3 \rho_c \frac{dV}{dt} = C_D \frac{1}{2} \rho_2 \pi R^2 (V_2 - V_p)^2 \quad (3)$$

where the subscript 2 denotes the flow properties of the gas behind the incident shock wave. The drag coefficient C_D has been determined as a function of Mach and Reynolds numbers using the empirical correlations of Walsh⁶. As discussed above, at the particle surface the spherically symmetric boundary condition

$$k_c \frac{\partial T}{\partial r}(R, t) = h(t) [T_r(t) - T(R, t)] \quad (4)$$

is used. The heat transfer coefficient h and the recovery temperature T_r vary with time as the particle accelerates, and this variation has a significant effect on the heat transfer. The heat transfer coefficient depends on the instantaneous Mach, Reynolds and Prandtl numbers and is calculated using an empirical correlation⁷. The recovery temperature is represented by $T_r = T_3 + \bar{r} (T_{03} - T_3)$, where T_3 and T_{03} are the static and stagnation temperatures just behind the bow shock on the axis of symmetry, respectively, and both are time dependent. The value 0.92 is taken for the recovery factor \bar{r} from Ref. 8 for near continuum flow as the Knudsen number based on the particle boundary layer thickness is less than 0.05. Finally, assuming that the exchange of momentum and heat between the gas and the particles have negligible effect on the gas flow, conventional shock relations complete the formulation.

A finite difference scheme is developed to solve the resulting set of equations. The surface reaction rate for carbon and the thermal properties for bituminous coal are taken from Refs. 4 and 9, respectively. The internal surface area per unit mass, S_i , has been determined using the data of Gan et al.¹⁰ for the carbon content of the coal particles as given in Table I. The variation of computed particle surface temperature with time is shown in Fig. 5 for 37-micron coal particles in Mach 4.7 flows with four different gas compositions.

A sensitivity analysis has been carried out to set a bound to the contribution of the volatiles to the particle ignition behavior. In the first of the two limiting cases considered the volatiles, once evolved, are assumed to burn immediately at the point of evolution. This effect is taken into account

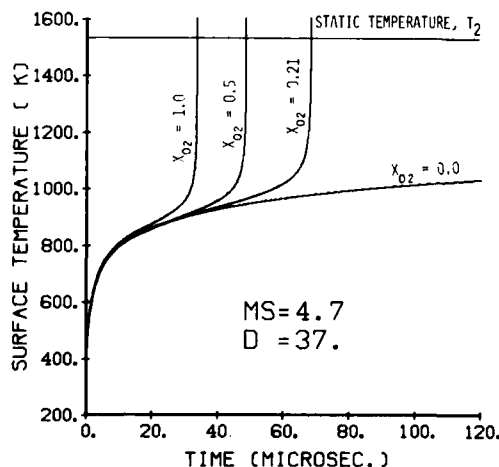


Figure 5. Calculated Surface Temperature

by an additional heat source term in Eq. (1). In the second case volatiles, once evolved, are assumed to migrate to the surface and burn there instantaneously. Thus the contribution will be through the addition of a surface heat source term to the boundary condition (4), which involves the integral of the volatilization rate over the particle volume. The contribution of volatiles, although more in the second case than in the first, is insignificant in both cases. When the heterogeneous reaction term is deleted from the computation the time required for particles to achieve the static flow temperature is more than twice that calculated considering heterogeneous reaction only, even when the oxidizer is air.

COMPARISON OF THEORY AND EXPERIMENT

An accurate correlation of the calculated surface temperature curves and the measured heating and ignition delays requires a quantitative study of the electro-optical system behavior. In this section a simplified model to interpret the photomultiplier output is presented and then it is used to compare the experimental and theoretical results.

The photomultiplier output is approximately proportional to the light flux incident on the photosensitive surface. The constant of proportionality, the spectral sensitivity, varies with the wavelength; whereas the light flux depends on the intensity and the angle of incidence of the light. While a cloud of dust particles is traversing the field of view the incident light flux received by the photomultiplier will vary with time because the angle of incidence changes with the particle location, and the intensity changes with the particle surface temperature and the distance between the particle and the photomultiplier. To account for all these features, the electro-optical system output V_{pm} , is assumed to be proportional to the spectral response S_λ , the view factor S_α , and the total particle surface area A_p as viewed by the photosensitive surface. Then it follows that

$$V_{pm} \propto S_\lambda S_\alpha A_p \quad (5)$$

The spectral response is defined as

$$S_\lambda = \int_0^\infty \epsilon_\lambda(\lambda, T_w) E_{b\lambda}(\lambda, T_w) R_\lambda(\lambda) d\lambda \quad (6)$$

where ϵ_λ , $E_{b\lambda}$ and R_λ are the spectral emissivity of the particles, the black body spectral power given by the Planck's law and the spectral sensitivity of the photomultiplier, respectively. If the variation of ϵ_λ within the bandwidth of the photomultiplier is negligible

$$S_\lambda = \bar{\epsilon} s_\lambda(T_w) = \bar{\epsilon} \int_0^\infty E_{b\lambda}(\lambda, T_w) R_\lambda(\lambda) d\lambda \quad (6a)$$

where the bar indicates the average quantity. Taking $R_\lambda(\lambda)$ from the manufacturer's specifications for the photomultiplier $s_\lambda(T_w)$ is computed numerically as a function of the particle surface temperature. The view factor, on the other hand, degenerates into a directional sensitivity curve, as the characteristic cloud dimension is much less than the optical pathlength. Therefore S_α has been taken as the photomultiplier anode voltage $V(x_p)$ as a function of cloud location x_p , measured by moving a small incandescent lamp through the test section. Thus the photomultiplier output is

$$V_{pm} \propto \bar{\epsilon} s_\lambda(T_w) V(x_p) A_p \quad (5a)$$

By definition, experimental heating delays correspond to a minimum detectable light flux on the photosensitive surface which is a constant threshold value. Therefore, if $\bar{\epsilon} A_p$ is assumed to be constant for the same type and size of particles then $s_\lambda(T_w) V(x_p)$ must also be a constant at the end of the heating delay time. The theoretical model presented in the previous section is used to determine the times required for various Mach numbers to make $s_\lambda V$ a constant whose value is chosen to give the best fit to the experimental data. Results for heating delays in nitrogen are shown in Fig. 3 for 37 micron particles.

Experimental ignition delays were identified by a sharp increase in the photomultiplier output. It is seen in Fig. 5 that after the oxidation becomes

significant there is a similar rapid increase also in the calculated surface temperature. As the spectral response increases exponentially with the temperature this term dominates the directional sensitivity term in this regime, and therefore the ignition delay data corresponds to a constant particle surface temperature. The theoretical ignition delay times calculated this way are not sensitive to the value of this constant since the surface heating rates are very high. The theoretical ignition delay times are displayed in Fig. 4 for 37 micron particles in 3 different gas compositions.

Particle size dependence of the experimental delay times are more moderate than predicted by the present theory¹¹. At the coarse end of the particle size spectrum this is attributed to the irregular particle shapes and the non-symmetry of the temperature distribution within the particle. Depending on the local radius of curvature, particle edges as well as the vicinity of the stagnation points of the flow will heat up faster and ignite while the other parts of the particle are still cool. On the other hand, for the fine particles the porous flow and consequently the internal reaction will be less than anticipated by the present theory, therefore resulting in longer actual delay times. The success of the single spherical-particle analysis thus depends on the choice of the representative particle size which must result in an effect equivalent to the real particles. The representative size of 37 microns here yields good agreement between experiment and theory.

CONCLUSIONS

Experimental measurements of heating and ignition delay times for the shock ignition of Eastern Kentucky bituminous coal have been made. The experimental results and the theoretical calculations show that volatilization is not significant for the short delay times observed. The main mechanism of ignition appears to be heterogeneous reaction both on the outside and within the porous particles. Therefore internal surface area rather than the volatile content becomes a key parameter governing the shock wave ignition. This conclusion is also supported by the shorter delays observed for char since it has a much lower volatile content and more internal surface area than coal. A simple theoretical model based on an overall first-order heterogeneous reaction-rate without adjusting any parameters provided results in good agreement with the measurements.

ACKNOWLEDGMENT

This work was partially supported by the National Science Foundation (Dr. R.E. Rostenbach, Project Monitor) under grant ENG-7622958. The useful suggestions, comments and questions of Professors J.A. Nicholls and C. Hermance are gratefully acknowledged. The authors would also like to thank Mr. F.G. Campau and R.E. Habermos of Detroit Edison who furnished the coke samples and the analysis of the coal.

REFERENCES

1. Lee, J.H., *Ann. Rev. Phys. Chem.* 28, 1977, pp. 75-104.
2. Moen, I.O., Donato, M., and Lee, J.H., *18th Symp. (Int'l) on Comb.*, 1980.
3. Hwang, C.C. and Kathiresan, M., *Central States Section, The Combustion Institute*, April 1977.
4. Field, M.A., Gill, D.W., Morgan, B.B., and Hawksley, P.G.W., *BCURA* 1967.
5. Anthony, D.B. and Howard, J.B., *AIChE J.* 22, July 1976, pp. 625-656.
6. Walsh, M.J., *AIAA J.* 13, 1975, pp. 1526-1528.
7. Fox, T.W., Rackett, C.W., and Nicholls, J.A., *Proc. 11th Int'l Symp. on Shock Tubes and Waves*, 1977.
8. Schaaf, S.A. and Chambre, P.L., *Princeton Univ. Press*, 1961.
9. Bazdorch, S., Gregory, D.R., and Field, M.A., *Fuel* 43, 1964, pp. 267-280.
10. Gan, H., Nandi, S.P., and Walker, P.L., Jr., *Fuel* 51, 1972, pp. 272-277.
11. Ural, E.A., Ph.D. Thesis, The University of Michigan, 1981.

AD P000308

A STUDY ON THE IGNITION OF A FUEL DROPLET
IN HIGH TEMPERATURE STAGNANT GAS

Yoshio YOSHIKAWA, Michio TOMITA and the late Haruo KAWADA

*Department of Mechanical Engineering, Tokyo Institute of Technology
Ohokayama, Meguro-ku, Tokyo, 152, Japan*

ABSTRACT

This study aimed to clarify the effects of the fuel vapor, which had evaporated in advance and formed combustible mixture around the condensed phase, on the ignition of a fuel droplet under the gas dynamic compression. A soap bubble was utilized to make a heterogeneously distributed fuel vapor pocket in oxidizer gas which offered a model of the vapor cloud around the fuel droplet. Induction periods for the onset of strong emission were measured for fuel droplets, and the models and their ignition processes were examined precisely by means of the interferometric measurement of the fuel concentration field.

The ignition delays of a fuel droplet and a pocket show nearly the same value in the temperature ranges of experiments. Moreover, the results of the interferometric measurement shows that the ignition process of a droplet is nearly the same as that of a pocket. In both cases the ignition (flame) first appears in outer end of the vapor cloud where the fuel concentration is very low, then it spreads into inner part of the cloud. This result shows that the flame first appears at the point where the ignition delay shows its minimum in the system.

1. Introduction

When there is a fuel droplet or spray in air, part of fuel evaporates and forms combustible mixture around the condensed phase if the fuel has sufficient vapor pressure. The ignition process of this system under the gas dynamic compression is a problem of great physical importance, for it constitutes a basis for the understanding of the combustion process of spray and film detonations. This process is considered to be different from that of a cool fuel droplet suddenly introduced into fuel free high temperature air. In fact, the ignition-lags of a fuel droplet[1] and spray[2] behind reflected shock waves were found to be fairly shorter than those observed in furnaces. These differences are surmised to come from the effects of the fuel vapor which has evaporated in advance and has formed combustible mixture around the condensed phase. Therefore, this study aimed to clarify the effects of the fuel vapor on the ignition process of a fuel droplet.

In this work, a soap bubble was utilized to make a heterogeneously distributed fuel vapor pocket in oxidizer gas which offered a model of the vapor

cloud around the fuel droplet. Induction periods for the onset of emission were measured for fuel droplets, and the models and their ignition processes were examined precisely by means of the interferometric measurement of the fuel concentration field.

2. Experimental Setup

A specially designed shock tube was employed, which is shown in Fig. 1, in which two oppositely facing shock waves of equal strength collided with each other at the center of the test section and produced a high temperature stagnant gas region. This condition is just the same as that behind reflected shock wave but there is no end wall of a shock tube. Four pressure transducers are equipped to trigger the light source for high speed interferometric photography, to measure the shock speed of the incident shock wave and to follow the pressure at the center of the test section. Induction times for the onset of emission are measured using a photomultiplier tube at the center of the test section. There is a 100 mm diameter optical glass window also at its center through which high speed interferometric photographs are taken.

A soap bubble was utilized to make a heterogeneously distributed fuel vapor pocket in oxidizer gas which offered a model of the vapor cloud around the fuel droplet. This soap bubble and the fuel droplet are hung at the center of the test section of the shock tube which are shown in Fig. 2. The droplet is hung by a small metal hemisphere (1 mm diameter) at the tip of a needle of a syringe, on the other hand, the soap bubble is sustained by a cone (5 mm diameter) at the tip of a needle. Ethylene glycol is added to the soap suds so

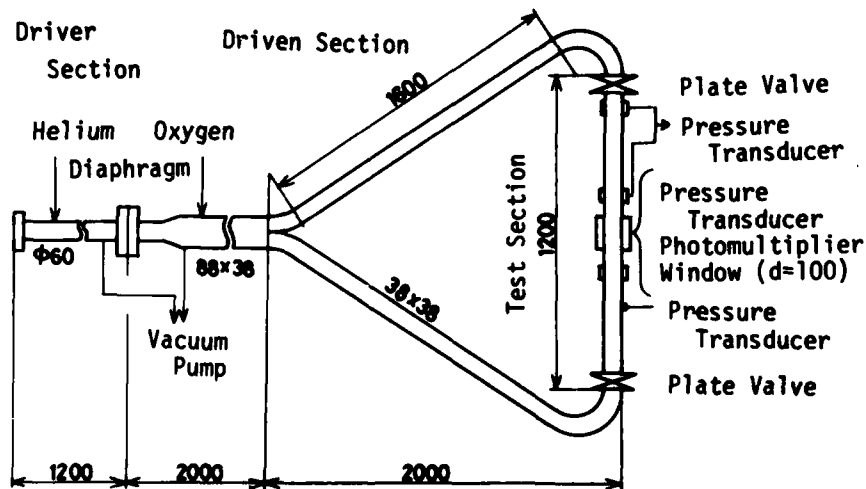


Fig. 1 Shock Tube

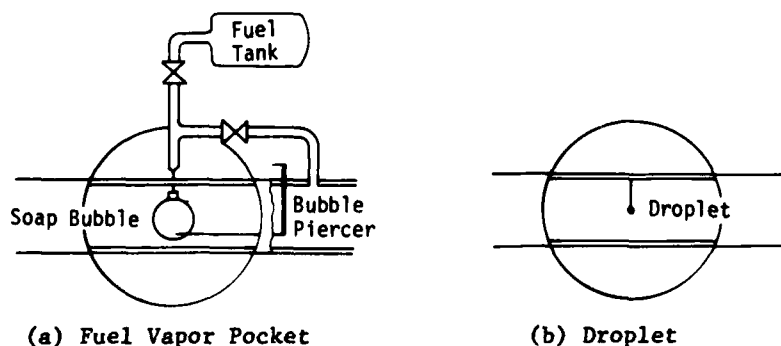


Fig. 2 Test Section

that the bubble is stable under the low pressure condition of the initial state in the shock tube.

Normal alkanes were used as representatives of fuels. These were n-pentane and n-hexane for the model of the vapor cloud and n-decane, n-dodecane and n-tetradecane for the droplet. Pure oxygen or air and helium were used as the oxidizer and driver gases whose pressures were 2.0-6.7 kPa (15-50 Torr) and 0.6-1.1 MPa (6.0-11 atm) respectively. From these conditions, the temperature and the pressure of the stagnant region ranged from 1200-2600 K and from 200-500 kPa (2-5 atm) respectively.

3. Results and Discussions

3-1. The Whole Process of the Ignition of a Fuel Droplet

The ignition process of a n-decane droplet was observed by means of a high speed camera and a photomultiplier tube. An example of the results is shown in Fig. 3. These photographs were picked out from a sequence of photographs taken every 29 μ sec. The number "0" in the emission history indicates the time of the collision of incident shock waves which means the establishment of the high temperature stagnant gas region. Hereafter, time is measured from this time. Other numbers show the released times of corresponding photographs. Experimental conditions are shown in the figure. The emission

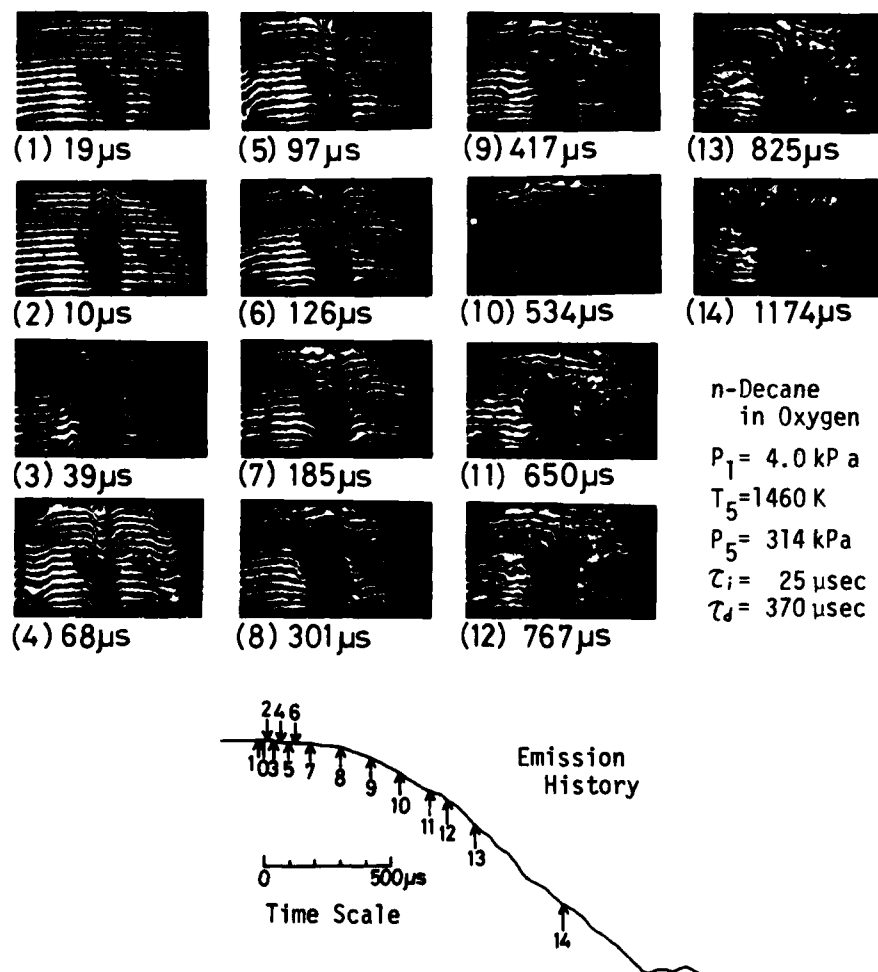


Fig. 3 Whole Process of the Ignition of a Fuel Droplet

history shows a weak jump at 20 μ sec between Photos. 2 and 3. It shows a plateau for about 100 to 200 μ sec, then increases exponentially to its maximum. Correspondingly, Photo. 2 shows upward shift of fringes which represents the compressed fuel vapor cloud while they turn downward in Photo. 3, that is, the cloud has burnt between these photographs. Photos. 4 to 8 show mild evaporation and combustion of fuel, then the definition of droplet becomes obscure in Photos. from 9. All of these processes are considered to be important steps in the ignition of a fuel droplet, however, this study mainly concerns initial ignition process of fuel vapor as the first step of the study on the ignition process of a fuel droplet.

3-2. Fuel Concentration Distribution in the Fuel Vapor Pocket

Temporal changes of fuel concentration distribution after the soap bubble had been ruptured were observed by means of interferometric photography. The result is shown in Fig. 4. These photographs were taken every 10 msec. Photograph *a* was released just before the rupture of bubble. It was done by a needle which appears at lower right in the photograph. The fuel vapor diffused rapidly as shown in Photos. *b* to *f*. It is deduced from this result that the equivalence ratio at the center of the test section has already decreased to less than 2. On the other hand, calculation of unsteady-state molar diffusion shows that the equivalence ratio is 2 at 10 sec. Therefore, the mixing in this study is far faster than molar diffusion, which is attributable to the flow induced by ruptured soap bubble. It takes 1 to 3 sec from the rupture of the bubble to the collision of the shock waves in usual run, so that the shock waves compress the fuel vapor pocket after the completion of the mixing by the flow but before the effect of molar diffusion becomes significant.

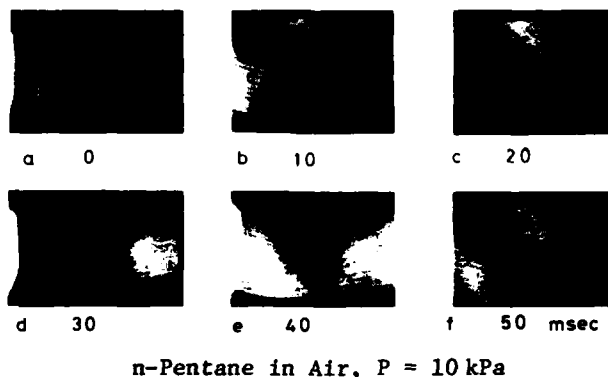


Fig. 4 Diffusion of the Fuel Vapor in a Pocket

3-3. Fuel Concentration Distribution in the Ignition Process

Figures 5 and 6 show concentration distributions in the ignition processes of the pocket and the droplet. Downward shifts of fringes correspond to increases in refractive index (*i.e.* in the concentration of fuel) in these photographs. Therefore, the fuel concentrations show their maxima at the center of the test section in these photographs and decrease as increasing the distance from the center. The distributions of the equivalence ratio and the temperature in the stagnant region behind reflected shock waves are deduced under the following assumptions: (1) The field is one dimensional, (2) properties behind reflected shock waves are just the same as those obtained when the mixture is compressed by a pair of incident and reflected shock waves up to the pressure behind the reflected shock wave calculated in fuel free oxidizer gas from the measured speed of the incident shock wave, (3) the concentration of fuel is zero at the end of the tail of the fringe. The

first assumption is satisfied everywhere except in the region just behind reflected shock waves where boundary layers interact with them. Therefore, the end of the tail in assumption (3) is defined at the inner end of this region. Regarding the second assumption, secondary pressure waves are generated when a shock wave propagates into a region where there is a concentration distribution. However, they are weak in gas mixture because the difference in acoustic impedance is small between gases. Moreover, a rarefaction wave is

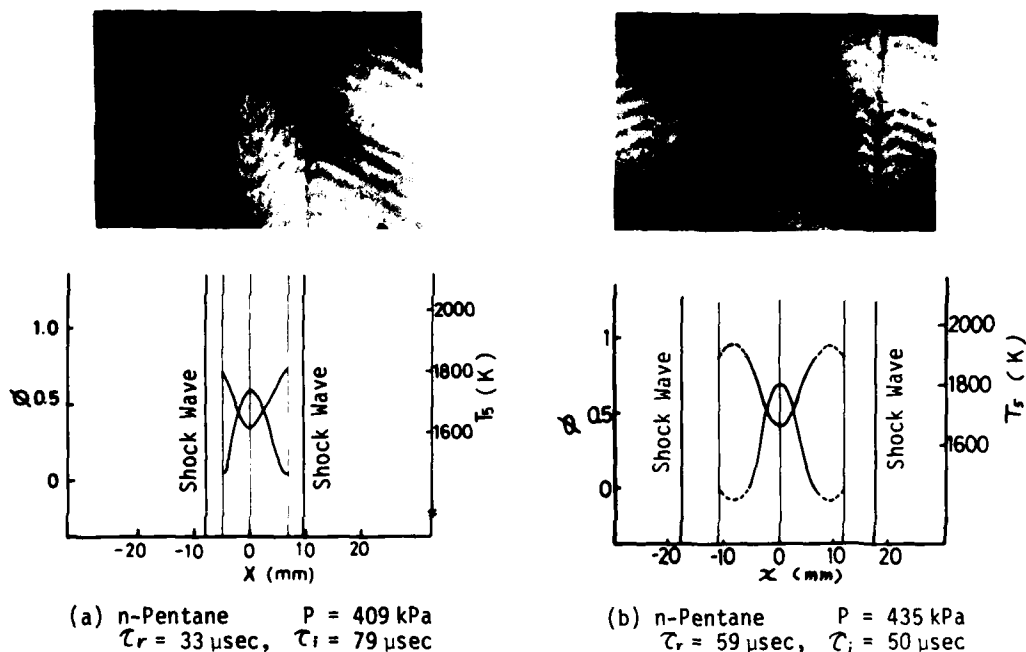


Fig. 5 Fuel Concentration Distributions for a Pocket

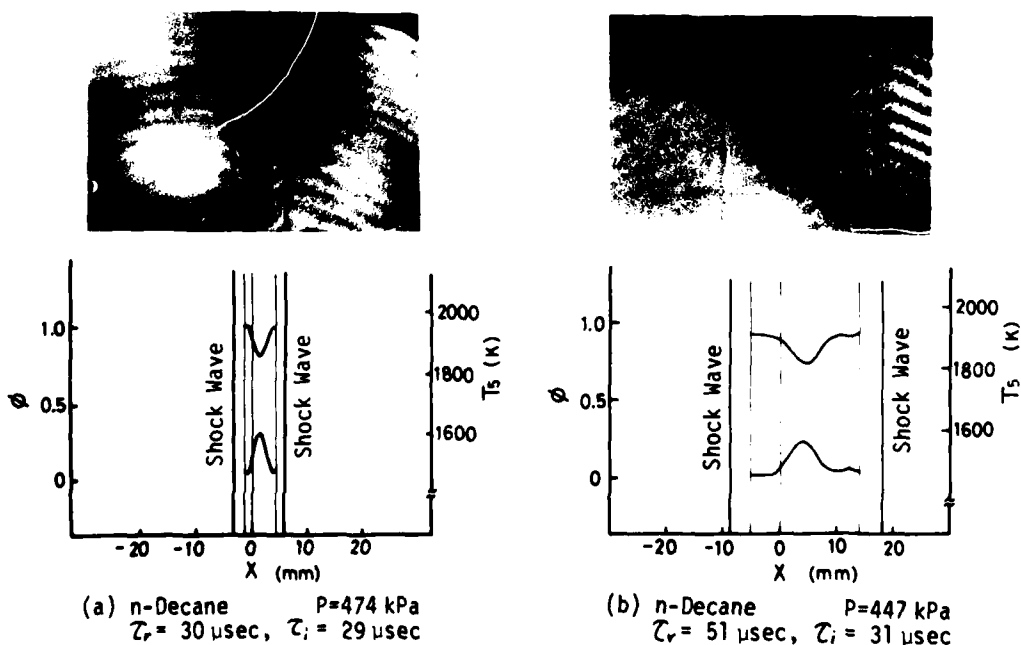


Fig. 6 Fuel Concentration Distributions for a droplet

generated as a secondary wave by a reflected shock wave in the region where a compression wave has been generated by a incident shock wave. Therefore, this assumption is considered to be a good approximation in this study. The third assumption was confirmed by integrating the concentration distribution obtained under these assumptions. The amount of fuel estimated by the integration agrees fairly well with that in the soap bubble for the case of the fuel vapor pocket. On the other hand, the concentration of fuel at the center of the test section is lower than one calculated from the saturated vapor pressure of the fuel at initial temperature for the case of a droplet. However, the integrated sum of fuel evaporated is about 10% of initial droplet and the error is considered to be small if it is assumed that the latent heat for evaporation has been supplied from the droplet. Deduced distributions of the equivalence ratio and the temperature are also shown in Fig. 5 and 6.

τ_r indicates the released time of the photograph in these figures and τ_i represents the ignition delay in the same mixture. Photographs (b) in these figures were both released short times after the onsets of emission in which fringes were disturbed at the outer end of the tails. These disturbances are considered to show the existence of flame. On the other hand, Photo. (a) in Fig. 5 was released just after the onset of emission in which there was not any distinguishable signal in fringes. These results show that the ignition process of a droplet is nearly the same as that of a fuel pocket. In both cases the ignition (flame) first appears in outer end of the vapor cloud where the fuel concentration is very low, then it spreads into inner part of the cloud. Considering the resolution of fringe shift, the equivalence ratio at the ignition point was estimated to be smaller than 0.01 in oxygen and to be smaller than 0.05 in air. The ignition delays of several saturated higher hydrocarbons from butane to octane were examined in a previous work[3]. The result showed that ignition delays of lean mixtures with oxygen (and inert gas) strongly depended on temperature but were independent of fuels and their concentrations except ones of extremely lean mixtures. Therefore, it is concluded that the flame first appears at the point where the ignition delay shows its minimim in the system.

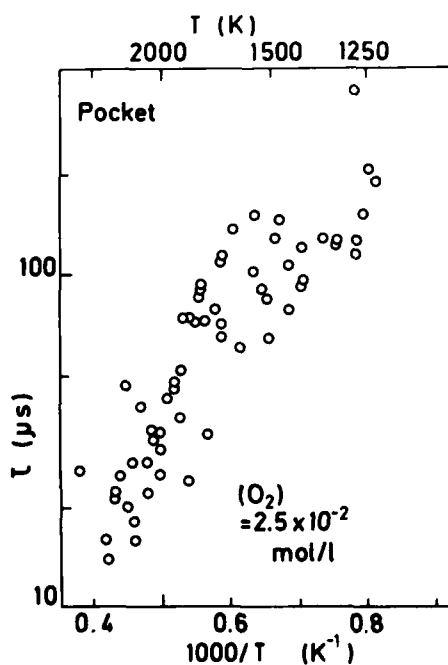


Fig. 7 Ignition delay of a n-Hexane Vapor Pocket

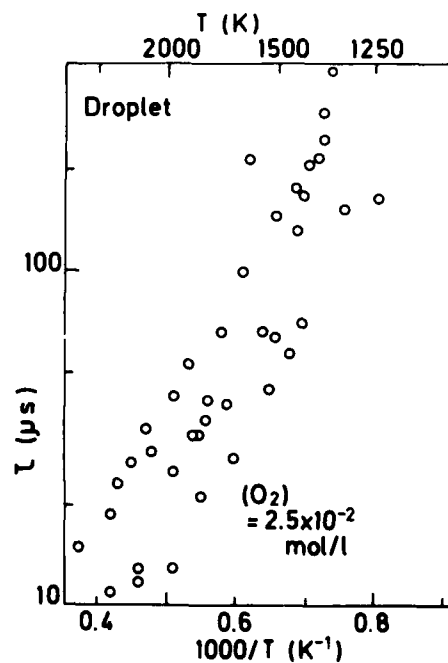


Fig. 8 Ignition delay of a n-Tetradecane Droplet

Evaporation and oxidation of the body of a fuel droplet follow the ignition and combustion of the fuel vapor cloud around it and are considered to be controlled by the combustion of the cloud. These processes are being studied now and the result will be reported in the near future.

3-4. Ignition Delays of a Fuel Pocket and a Droplet

The ignition delay is defined here as a time interval between the collision of incident shock waves and the weak jump in the emission history which is shown in Fig. 3. Therefore, this induction time corresponds to the onset of reaction in outer end of the vapor cloud. The ignition delays of a fuel vapor pocket and a fuel droplet were measured for wide temperature ranges. The results for a n-hexane vapor pocket and a n-tetradecane droplet are shown in Figs. 7 and 8 in which ignition delays have been normalized to a typical experimental condition of oxygen concentration under the assumption that the ignition delay is inversely proportional to oxygen concentration. This assumption is based on the result of the previous work[3] in which ignition delays of homogeneous mixtures of hydrocarbon fuels and oxygen were studied. Using the least square method, these ignition delays have been represented by straight lines, which are shown in Fig. 9. The results for a n-pentane vapor pocket and n-decane and n-dodecane droplets coincide respectively with those for a n-hexane vapor pocket and n-tetradecane droplet. Therefore, they have been included respectively in the ignition delays of a pocket and a droplet in the figure. The result for the homogeneous mixture[3] is also shown in it.

The temperature dependency of the ignition delay of a pocket is slightly smaller than that of a droplet but they show nearly the same values. On the other hand, the ignition delay of the homogeneous mixture is more than an order of magnitude shorter than those studied here and the temperature dependency is about twice. The induction time in the homogeneous system consists only of delays of chemical origin but those in the heterogeneous systems, such as a vapor pocket and a droplet studied here, include ones of physical origin as well. The ignition first appears in outer end of the vapor cloud, as men-

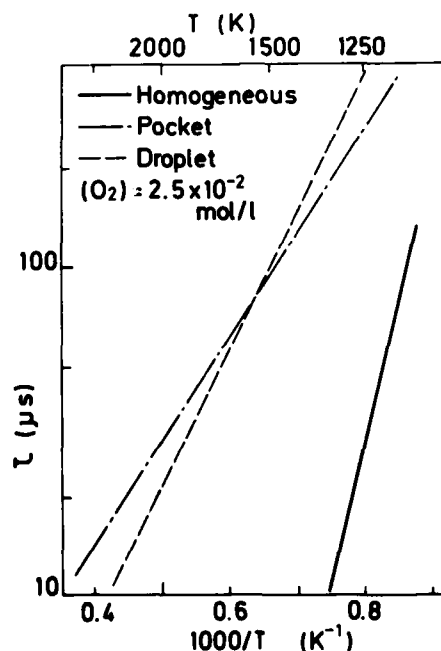


Fig. 9 Ignition Delays of a Fuel Vapor Pocket, a Fuel Droplet and Homogeneous Mixture

tioned in section 3-3, the chemical process is considered to be the same as that in homogeneous system. Therefore, the difference between these systems is considered to be in physical processes. The most dominant physical delay is surmised here to be the time required for reflected shock waves to arrive at outer end of the vapor cloud. Although the physical processes of heat transfer, evaporation and diffusion are really important in the processes of combustion of condensed phase, they participate only in later processes and are controlled by the combustion of vapor cloud around the condensed phase.

4. Conclusions

The ignition processes of a fuel droplet and its model were studied precisely and the observations were made;

(1) A heterogeneously distributed fuel vapor pocket in oxidizer gas formed by means of a soap bubble offers a good model of the vapor cloud around a fuel droplet.

(2) The ignition (flame) first appears in outer end of the vapor cloud where the fuel concentration is very low.

(3) This process is independent of the existence of condensed phase.

(4) The ignition process of the body of a droplet proceeds in the burnt gas of the vapor cloud and is controlled by the ignition and combustion processes of the cloud.

[References]

- [1] H. KAWADA, *et al.*, *Acta Astronautica*, Vol. 1 (1974), 753.
- [2] K. MIYASAKA and Y. MIZUTANI, *16th Symp. (Int.) on Comb.* (1976), 639.
- [3] Y. YOSHIKAWA, *et al.*, *Bulletin of the JSME*, Vol. 21(1978), 486.

AD P 000309

SHOCK INITIATED IGNITION IN HEPTANE-OXYGEN-ARGON MIXTURES

Alexander Burcat

Aeronautical Engineering Department
Technion - Israel Institute of Technology, Haifa 32000, Israel

Richard F. Farmer and Richard A. Matula

College of Engineering, Louisiana State University
Baton Rouge, Louisiana 70803

The ignition of heptane in mixtures containing oxygen and argon was studied behind reflected shock waves in 56 mm i.d. and 26 mm i.d. single-pulse shock tubes. The measurements covered the temperature range 1100-1700 K and reflected shock pressures varying from 2 to 12 atmospheres. The experimental results of 140 shocks, whose ignition delay times were measured at the end plate in the large shock tube, can be correlated by the relationship

$$\tau = 6.3 \times 10^{-12} \exp(+35300/RT) [C_7H_{16}]^{0.2} [O_2]^{-1.1} [Ar]^{0.6} \text{ sec}$$

In the 26 mm shock tube, the detection point was located ~80 mm from the end plate and the induction times were correlated by different parameters. These parameters were influenced by gas dynamic effects caused by the combustion process. Previous results are discussed in view of this behavior.

INTRODUCTION

Heptane is considered as a very important hydrocarbon. It is the largest constituent of kerosine and in some cases may reach up to 25% of the kerosine distillate. Therefore heptane is considered as a good representative of kerosine and studying its ignition and oxidation has always been of great practical interest.

A large number of investigations dealing with the oxidation of heptane were carried out. Even though these investigations are limited to shock tubes and high temperature flow reactors the subject is well covered¹⁻⁶. Most of the papers deal with n-heptane by comparing it to other fuels¹⁻⁴, but some are devoted entirely to n-heptane oxidation⁵⁻⁶.

This investigation is in line with earlier ignition and kinetic studies of methane⁷, ethane⁸, propane⁹, and ethylene¹⁰, whose aim was to establish a well-defined overall correlation and on the basis of which detailed kinetic mechanisms have been published¹¹⁻¹³. An additional purpose was to compare ignition delay data obtained at the end plate to data obtained on the side wall of the tube. A detailed kinetic mechanism on n-heptane was reported by Williams⁶ and his scheme was considered in this study.

EXPERIMENTAL

Two different shock tubes were employed in this research. The Technion shock tube was stainless steel, 54 mm in diameter with a 4 meter long driven section. The tube was described in literature¹⁴. The shock speed was calculated from time intervals obtained between two Kistler piezoelectric transducers 200 mm apart. The time intervals were measured to $\pm 0.1 \mu\text{sec}$. A third Kistler 603A transducer located at the end plate was used to record the pressure-time history of the experiment. The signal of the pressure was fed into a Biomation 805 transient recorder on which the ignition delay times were recorded with 2% accuracy.

The LSU tube was a 26-mm glass single-pulse shock tube⁴. In this tube pressure was measured with a Kistler 603A piezoelectric transducer located 79.5 mm from the end plate of the shock tube. The output of the transducer was recorded from a Tektronix 561A oscilloscope on Polaroid film. The ignition delay times were signified by the onset of the ignition pressure and could be read with 5-10% accuracy. Incident shock speeds were measured using piezoelectric pressure transducers to trigger the start and stop channels of interval timers. Transient times between transducers 20 inches apart were measured to $\pm 1 \mu\text{sec}$.

In both shock tubes the materials used were "Merck" spectrochemical n-heptane, Matheson 99.95% pure oxygen and 99.99% pure argon. Airco helium was used as the driving gas. All materials were used without further purification. The n-heptane vapors were used to prepare mixtures in stainless steel tanks at 5 atmospheres pressure. The mixtures were allowed to mix for a minimum of 24 hours before use.

The enthalpies of n-heptane for the calculation of the reflected shock temperature were taken from API Project 44¹⁵ and extrapolated to the 1000-2600 K range with the use of Wilhoit's polynomials¹⁶. The oxygen enthalpies were taken from JANAF tables¹⁷ and the argon enthalpies from NASA SP 3001 tables¹⁸. The reflected shock temperatures were calculated using the standard conservation equations and the ideal gas equation of state assuming frozen chemistry.

RESULTS

Table I represents the 15 series run with the 6 different mixtures of n-heptane-oxygen-argon at the different pressure and temperature conditions. The mixtures were made in such a way as to permit direct delineation of the power dependencies of the ignition delay times investigated. The general overall ignition delay equation was assumed

$$\tau = 10^{-x} \exp(+E/RT) [C_7H_{16}]^a [O_2]^b [Ar]^c \text{ sec}$$

In each shock performed in a mixture of known concentration the ignition delay time τ and the reflected temperature T_3 are recorded. The experiments were spread over the temperature range in such a way as to permit maximum accuracy to the parameters evaluated, according to the method used in former investigations⁷⁻¹⁰. Approximately 280 shocks were recorded half of which were Technion results, and half were LSU results.

Of the 140 shocks performed at the Technion, 113 are represented in Figure 1 and 2 as $\log \tau$ vs $1/T_3$. The a and b dependencies of heptane and oxygen respectively are presented in Fig. 1 by groups C-E and C-F. In Fig. 2 the overall, as well as the argon dependency, are presented by groups B-D and D-G, respectively.

TABLE I

DETAILS OF GROUPS OF EXPERIMENTS OF n-HEPTANE-OXYGEN-ARGON-MIXTURES
TECHNION EXPERIMENTS

Series	Concentrations % mole C_7H_{16} O_2		No. of exp.	T_5 K range	P_1 torr	Average $C_5 \times 10^5$ moles/cc	Symbol
A	1	11	13	1239-1419	100	4.1	•
B	1	11	19	1273-1788	50	2.2	◻
C	0.5	11	20	1247-1530	100	3.6	◊
D	1	11	17	1220-1570	200	8.4	△
E	2	11	17	1265-1635	100	5.2	▲
F	0.5	2.8	18	1443-1759	100	3.6	◊
G	3	33.1	16	1143-1464	50	3.6	x

LSU EXPERIMENTS

A	2	11	17	1189-1342	100	6.0	◊
B	0.5	11	19	1205-1320	100	3.6	x
C	0.5	2.8	19	1366-1582	100	3.6	•
D	1	11	16	1261-1450	50	2.1	△
E	1	11	15	1159-1288	200	8.0	■
F	1	11	15	1163-1331	100	3.9	v
G	3	33.1	20	1087-1200	50	4.1	◻
H	0.61	6.7	15	1222-1389	100	3.5	▲

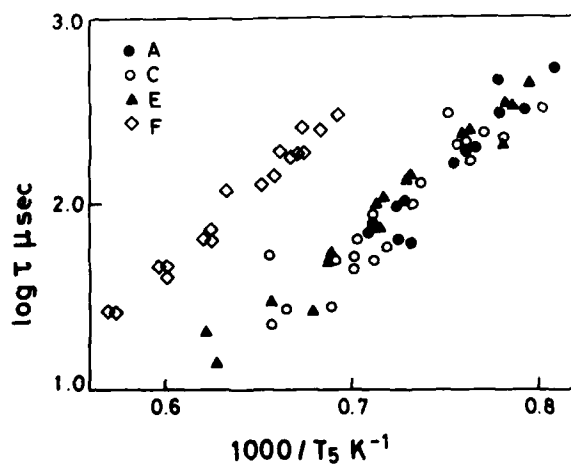


Fig. 1:
Log τ vs $1/T_5$
showing graphi-
cally the
heptane and
oxygen power
dependencies.

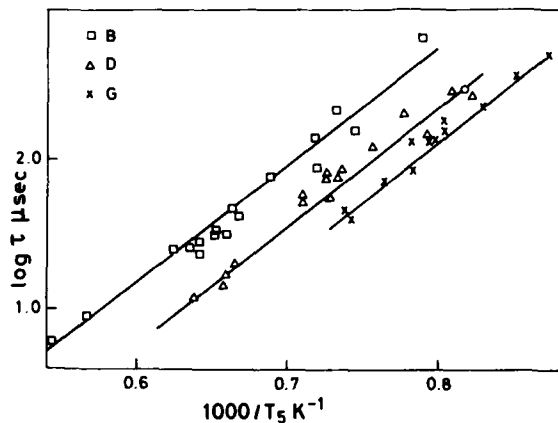


Figure 2:
Log τ vs $1/T_5$ showing the overall and the argon power dependencies.

All 113 experiments were treated with a student t statistical program published elsewhere¹⁹. The values obtained for 99 shocks with a 2σ spread around the central value were

$$\tau = 6.3 \times 10^{-12} \exp\left(\frac{35300 \pm 1900}{RT}\right) [C_7H_{16}]^{0.2} [O_2]^{-1.1} [Ar]^{0.6} \text{ sec}$$

A similar value within the same error limit was obtained for 110 shocks with a 3σ spread around the central value. These values can be verified graphically on Figures 1 and 2 as explained in earlier articles^{7,9}.

Figure 3 is a plot of $\log \tau / ([C_7H_{16}]^{0.2} [O_2]^{-1.1} [Ar]^{0.6})$ vs $1/T_5$ for 110 points showing the 3σ spread around the evaluated statistical line.

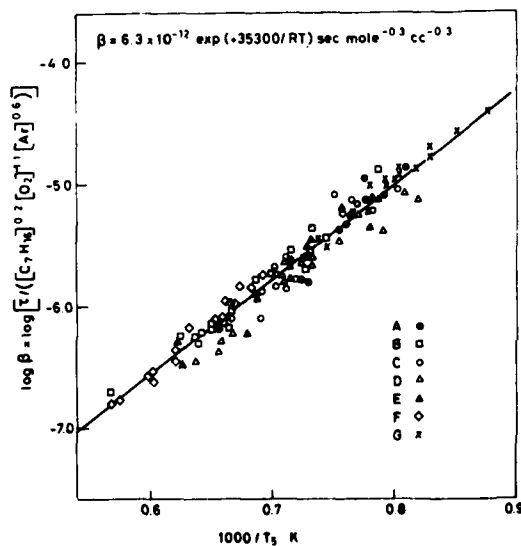


Figure 3:
A plot of $\log \beta$ vs $1/T_5$ for all the Technion ignition delay experiments.

Of the 8 groups of experiments performed at LSU, 128 shocks were included in the statistical analysis and they are presented in Figure 4 with a 30 spread.

The result of the statistical correlation for the 128 shocks whose ignition was measured 80 mm downstream from the end plate of the driven section is

$$\tau = 1.2 \times 10^{-20 \pm 1.3} \exp\left(\frac{56000 \pm 4300}{RT}\right) [C_7H_{16}]^{0.7 \pm 0.2} [O_2]^{-2.0} [Ar]^{0.17 \pm 0.22} \text{ sec}$$

In Figure 4 $\log \tau / ([C_7H_{16}]^{0.7} [O_2]^{-2.0})$ vs $1/T_5$ is drawn for all 128 experiments and the above correlation line is shown.

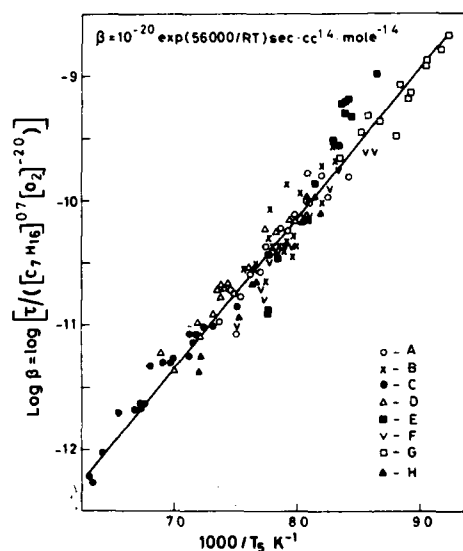


Figure 4:

A plot of $\log \beta$ vs $1/T_5$ for data gathered 79 mm away from the end plate (LSU data).

Table 2 gives details of 3 representative shocks of each group of the Technion experiments.

Table 3 shows a comparison between shocks run at the Technion and at LSU having approximately the same pressure and temperature conditions, in mixtures of the same concentrations. From the comparison it is clear that the experiments measured at the side wall away from the end plate have shorter ignition delay times than those measured at the end plate. This is true in all cases despite the scatter of the results.

DISCUSSION

In this research two series of experiments are presented, the Technion data performed in the conventional way with the ignition delay time measured at the end wall, and those performed at LSU in a small diameter tube with the pressure transducer located 79 mm from the end plate.

The differences found in the ignition delay correlation are dramatic.

a) The activation energy is 56 kcal compared to 35.3 on the end plate.

b) The power dependencies are also drastically increased: $a = 0.7$ compared to 0.2, $b = -2.0$ compared to -1.10 and $c = 0$ compared to 0.6. These differences are caused by the location of the diagnostic transducer. The ignition is measured away from the end plate in a region raised to the T_5 temperature at different times before the event. If the ignition occurs at

the end plate until it reaches the transducer, the time will be shorter than the natural time on the end plate. This is caused by the fact that once a flame is started at the end plate it is driven forward by the burned gases and by the additional reflected waves coming from the narrow tube walls causing turbulence. Thus the flame becomes turbulent arriving to the detection transducer earlier than it normally should have. This should be the explanation for the different parameters obtained. Of course the "correct" values should be the ones measured at the end wall while the ones measured 79 mm downstream show the influence of the gasdynamics of a turbulent flame.

TABLE 2
THREE REPRESENTATIVE SHOCKS FROM EACH SERIES OF EXPERIMENTS
PERFORMED AT THE TECHNION

Series	Shock No.	Composition %		P_1	P_5	T_5	ρ_5 / ρ_1	U_5	τ
		C_7H_{16}	O_2	torr	atm	K		mm/ μ sec	μ sec
A	6	1	11	116	4.66	1260	7.27	.3778	323
	10	1	11	105	5.17	1410	7.95	.3913	70
	14	1	11	103	4.52	1323	7.56	.3835	170
B	22	1	11	50	2.03	1268	7.30	.3785	647
	29	1	11	70	3.15	1341	7.64	.3851	155
	37	1	11	50	3.08	1602	8.75	.4077	25
C	41	0.5	11	100	3.81	1311	6.62	.4014	200
	45	0.5	11	101	3.51	1245	6.37	.3946	330
	57	0.5	11	100	4.81	1503	7.30	.4206	27
D	64	1	11	200	9.23	1361	7.73	.3869	87
	65	1	11	200	8.34	1286	7.39	.3801	200
	75	1	11	200	11.81	1565	8.61	.4046	12
E	88	2	11	100	5.01	1257	9.08	.3470	452
	90	2	11	101	7.95	1595	11.24	.3714	14
	93	2	11	100	6.17	1401	10.04	.3578	95
F	105	0.5	2.8	100	5.17	1661	7.10	.4460	44
	114	0.5	2.8	99	4.07	1443	6.50	.4242	303
	118	0.5	2.8	100	4.43	1509	6.69	.4310	190
G	123	3	33.1	53	4.42	1342	14.17	.3189	39
	136	3	33.1	55	3.25	1137	11.83	.3063	490
	138	3	33.1	51	3.70	1254	13.19	.3135	142

Oppenheim et al.^{3,20} have suggested that ignition causes definite misreadings of the measurement. This is perfectly true because Oppenheim did his measurements a few centimeters from the end plate and he encountered the same problems that were encountered in the shocks performed at LSU.

Comparison of the n-heptane parameters with those found previously for other parafins⁷⁻⁹ shows the following similarities and differences: a - the argon power dependency previously found in other parafins to be zero, is here 0.6; b - the oxygen power dependency is the same as in methane⁷, ethane⁹

and propane⁸; c - the fuel power dependency is small as in the other cases. The very weak power dependence of the fuel was traditionally explained as a result of a mechanism where the first initiating reaction is the decomposition of the fuel followed by a branching reaction involving no fuel molecule, $H + O_2 \rightarrow OH + O$, and the following steps being the reactions of the O and OH radicals with the fuel parent-molecule.

TABLE 3
IGNITION DELAY TIME COMPARISON BETWEEN TECHNION
AND LSU EXPERIMENT SETS

Concentration % C_7H_{16}	O_2	P_1 torr	LSU Experiments		Technion Experiments	
			TK	τ μ sec	T K	τ μ sec
0.5	2.8	100	1576	18	1579	115
			1526	65	1530	128
			1445	180	1443	303
1	11	50	1428	30	1428	87
			1365	90	1368	213
			1261	500	1268	647
1	11	100	1331	30	1323	170
			1288	95	1286	457
			1261	135	1261	323
1	11	200	1288	15,15,40	1287	200
			1240	85	1234	291
2	11	100	1313	95	1309	244
					1317	231
			1255	285	1257	452
3	33.1	50	1200	145	1205	224,238
			1176	220	1174	347
			1137	220	1137	490

The activation energy obtained at the Technion, 35.3 kcal/mole, is the exact value of the lean mixture of Coats and Williams⁶. In our research the activation energy was the same for lean and rich mixtures. The high activation energy, 45.2 kcal/mole for rich mixtures, found by Williams, is undoubtedly caused by the location of his observation point 12.5 mm from the end plate. The LSU experiments show that higher activation energies are obtained this way and the richer the mixture the higher the activation energy.

Williams⁶ also could not correlate his experiments but proposed a relationship

$$\tau = [C_7H_{16}]^{1.42} \exp(+35300/RT)$$


which is very puzzling. Again, the experiments made at LSU indicate the possibility of a high fuel power-dependency to be obtained if the location of the detection station is away from the end plate.

The kinetic scheme of Coats and Williams⁶ assumes a pyrolytic degradation of heptane as well as a degradation of heptane to heptyl radical C_7H_{15} . The real oxidation occurs to C_2 molecules and radicals. They ignore any oxidation possible between radicals or molecules like C_3H_7 , etc., known to be of great importance¹². Coats²¹ chose $C_7H_{16} \rightarrow C_5H_{11} + C_2H_5$ to be the first reaction in the kinetic scheme rather than the other two possibilities $C_7H_{16} \rightarrow C_6H_{13} + CH_3$ and $C_7H_{16} \rightarrow C_4H_9 + C_3H_7$, on the basis that it has the minimal endothermicity among the three reactions. However, since the source for these data²² is highly unreliable for this kind of comparison, the choice looks like a purely arbitrary one and so it was presented⁶. The table of rate constants given in the article⁶ is insufficient to reconstruct the kinetics since a large number of important reactions was omitted, for example, $H_2 + O \rightarrow H + OH$, which is as important as $H + O_2 \rightarrow O + OH$. The rate constants are similar to those gathered by Bahn²³ and can be adjusted to fit the oxidation kinetics. Thus, although Coats' full scheme²¹ is arbitrarily chosen, it is a fair scheme and it reproduces, after some adjustments, the oxidation of heptane.

ACKNOWLEDGMENTS

The authors wish to thank Mr. Uwe Brinkmann, summer visiting student from the University of Hannover at the Technion, and Mr. Raphael Espinoza from LSU for performing part of the shock tube experiments. Thanks are extended to Prof. Daniel Weihs and especially to Prof. Assa Lifshitz for valuable discussions.

REFERENCES

1. C.R. Orr, 9th Combustion Symposium, 1034 (1963).
 2. S.M. Kogarko and A.A. Borisov, *Bull. Acad. Sci. USSR*, **8**, 1255 (1960).
 3. D.J. Vermeer, J.W. Meyer and A.K. Oppenheim, *Comb. and Flame*, **18**, 327 (1972).
 4. A. Burcat, R.C. Farmer, R.L. Espinoza and R.A. Matula, *Comb. and Flame*, **36**, 313 (1979).
 5. G.S. Levinson, *Comb. and Flame*, **9**, 63 (1965).
 6. C.M. Coats and A. Williams, 17th Combustion Symposium, 611 (1979).
 7. A. Lifshitz, K. Scheller, A. Burcat and G.B. Skinner, *Comb. and Flame*, **16**, 311 (1971).
 8. A. Burcat, R.W. Crossley, K. Scheller and G.B. Skinner, *Comb. and Flame*, **18**, 115 (1972).
 9. A. Burcat, A. Lifshitz, K. Scheller and G.B. Skinner, 13th Comb. Symp. 745 (1971).
 10. J.A. Baker and G.B. Skinner, *Comb. and Flame*, **19**, 347 (1972).
 11. G.B. Skinner, A. Lifshitz, K. Scheller and A. Burcat, *J. Chem. Phys.*, **56**, 3853 (1972).
 12. G.J. Jachimowski, *Comb. and Flame*, **29**, 55 (1977).
 13. D.B. Olson and W.C. Gardiner, *J. Phys. Chem*, **81**, 2514 (1977).
 14. A. Burcat, *Comb. Sci Technol.*, **21**, 169 (1980).
 15. American Petroleum Institute, Project 44, issued by Thermodynamic Research Center, Texas A & M University, College Station, Texas.
 16. R.C. Wilhoit, *TRC Current Data News* **3**, #2 (1975).
 17. JANAF Thermochemical Tables NSRDS-NBS 37 (1971), D.R. Stull and H. Prophet editors.
 18. B.J. McBride, S. Heibel, J. Ehlers and S. Gordon, "Thermodynamic Properties to 6000 K for 210 Substances", NASA SP-3001 (1963).
 19. M. Frenklach, Ph.D. Thesis. The Hebrew University of Jerusalem, Israel, 1975.
 20. J.W. Meyer and A.K. Oppenheim, 13th Combustion Symposium, 1153 (1971).
 21. C.M. Coats, Dissertation, The University of Leeds (1978).
 22. G.S. Bahn, Approximate Thermochemical Tables, NASA CR-2178 (1973).
 23. G.S. Bahn, "Theoretical Autoignition and Combustion of Several Fuels", NASA CR-2455 (1974).
- 

AD P000310

AN EXPERIMENTAL AND ANALYTICAL INVESTIGATION OF HIGH
TEMPERATURE IGNITION OF ETHANOL

K. Natarajan* and K. A. Bhaskaran

Department of Mechanical Engineering

Indian Institute of Technology, Madras-600 036, India

An experimental and analytical investigation of the ignition of ethanol-oxygen-argon mixtures behind reflected shock waves was carried out over the temperature range 1300-1700K at pressures of 1.0 and 2.0 atm and equivalence ratios of 0.5, 1.0 and 2.0. In the experimental investigation, ignition was identified by the emission of visible light in a shock tube. The time interval between the arrival of the incident shock at the end flange and the subsequent ignition indicated by the first visible light emission was reckoned as the ignition delay. The experimental ignition delay (τ) data were found to correlate with initial ethanol and oxygen concentrations (mole/cc) and with initial temperature (K) by the relationship:

$$\tau = 1.0 \times 10^{-15} \exp(159.8 \text{ kJ/RT}) [\text{C}_2\text{H}_5\text{OH}]^{0.1} [\text{O}_2]^{-0.75} [\text{Ar}]^{-0.25}$$

A 56 step kinetic model for ethanol oxidation in the above temperature range was assembled using published rate coefficient data wherever available and estimated data for the reactions which have not been studied. Theoretical ignition delays were evaluated from the concentration profiles, based on the time at which the OH and CO₂ concentrations reach a value of 2×10^{-9} mole/cc individually compared with the experimental ignition delay data of Cooke et al. [1] which were based on emissions from OH and CO₂.

INTRODUCTION

Methanol and ethanol have the potential to be widely used as practical fuels for transport applications. They are replenishable fuels with reduced pollutant emissions. When compared to methanol, little is known about the combustion mechanism of ethanol at high temperatures. Fundamental aspects of the combustion of ethanol will be helpful in developing a better understanding of energy utilization and pollutant formation.

Experimental information on the high temperature ignition of ethanol is scant. Mullins [2] measured ignition delays of a number of alcohols burning with air in the temperature range 1050-1300K and obtained their activation energies. Cooke et al. [1] measured ignition delays of stoichiometric ethanol-

* Permanent address: A. C. College of Technology, Perarignar Anna University of Technology, Madras-600 025, India.

oxygen-mixtures, diluted with 95% argon, in the temperature range of 1330–1670K and in the pressure range of 200–300 Torr using incident shock waves. Their ignition delay data were based on emissions from OH, CH and CO₂.

EXPERIMENTAL INVESTIGATIONS

A stainless steel shock-tube of 71 mm inside diameter and 14 mm wall thickness, with 3 m long driver section and 5 m long test section was used in this investigation. Aluminium foils of 0.075 mm thickness were used as diaphragm material. A pneumatically operated plunger was used to rupture the diaphragm for any given driver pressure. The end flange of the test section was equipped with a glass window and a piezoelectric pressure transducer. A photomultiplier tube (RCA 931-A) kept in line with the window received the light emitted through a lens system. Fig. 1 gives a schematic diagram of the experimental set-up. A detailed description of the experimental set-up is given in ref. [3].

High purity (99.99%) ethanol, oxygen and argon were used for preparing the test gas mixtures. Hydrogen was used as the driver gas. The test gas mixtures were prepared manometrically using the law of partial pressures and stored in an aluminium cylinder of 25 liters capacity at 2 atm pressure. The mixtures were prepared at least 24 hr prior to use to ensure a thorough mixing of gases. Ethanol was obtained in vapor form by injecting a calculated quantity of liquid ethanol into the mixing chamber under vacuum, through a rubber seal fixed on top of it, using a microsyringe. The partial pressure of ethanol in the mixing chamber was kept below its vapor pressure at room temperature so that it remained as vapor. Table I gives the composition of the mixtures used in this investigation.

TABLE I TEST GAS MIXTURE COMPOSITION

Mixture No.	Mole fraction			ϕ
	C ₂ H ₅ OH	O ₂	Ar	
1.	0.0143	0.0857	0.90	0.5
2.	0.025	0.075	0.90	1.0
3.	0.040	0.060	0.90	2.0

From the measured incident shock velocities extrapolated to the end wall, the reflected shock parameters were computed using one dimensional shock equations. All the ignition delay measurements were carried out behind the reflected shock. The time interval between the arrival of the incident shock at the end flange (detected by the pressure transducer) and the subsequent ignition indicated by the first visible light emission (as detected by the photomultiplier tube RCA 931-A) was reckoned as the ignition delay.

EXPERIMENTAL RESULTS

Ignition delays of C₂H₅OH-O₂-Ar mixtures (Ar=90%) were measured in the temperature range 1300–1700K at pressures of 1.0 ± 0.2 and 2.0 ± 0.2 atm and equivalence ratios of 0.5, 1.0 and 2.0 ($\phi = 3.0 [C_2H_5OH] / [O_2]$).

Figures 2 and 3 show the variation of ignition delay with $1/T$ for $\phi=0.5$, 1.0 and 2.0 at pressures 1.0 ± 0.2 atm and 2.0 ± 0.2 atm.

An ignition delay correlation accounting for temperature, pressure and composition is a convenient way of expressing all the experimental data. For the temperature and concentration ranges covered in this investigation, the ignition delay time of C₂H₅OH-O₂-Ar mixture was found to be represented by:

$$\tau = 1.0 \times 10^{-15} \exp(159.8 \text{ kJ/RT}) [C_2H_5OH]^{0.1} [O_2]^{-0.75} [Ar]^{-0.25}$$

where, the concentrations are in mole/cc, temperature is in Kelvin, the activation energy is in kJ/mole and the ignition delay is in seconds.

A plot of $\tau [C_2H_5OH]^{-0.1} [O_2]^{0.75} [Ar]^{0.25}$, the correlation parameter as a function of $1/T$ is shown in Fig. 4 for all the experimental data. Figure 4 also shows the experimental data of Cooke et al. [1]. The apparent activation energy for ethanol oxidation, reported by Cooke et al. [1] and Mullins and Penner [4] are 143 and 176 kJ/mole respectively, whereas the present investigation yields a value of 159.8 kJ/mole.

ANALYTICAL INVESTIGATIONS

Based on the available reaction kinetic studies of methanol [1,5-10] and acetaldehyde, [11,12] a 56-step reaction mechanism for ethanol oxidation (in the temperature range considered) is proposed. The oxidation mechanism and the forward rate coefficients are presented in Table II. The reactions listed involve 26 species and argon. Essentially, the kinetic model consists of the pyrolytic and oxidative reactions of C_2H_5OH , reactions forming and removing the stable products CH_3CHO , CH_2O , H_2 , CO , CO_2 , CH_4 , C_2H_4 and C_2H_2 , and reactions of the radical species CH_3CHOH , CH_3CO , CH_2OH , CH_3 , CHO , H , O , OH , HO_2 , C_2H_3 , C_2H , CH_2 and CH . To avoid an excessively complicated kinetic scheme, the initiation steps generating CH_2CH_2OH or CH_3CH_2O as an alternative to CH_3CHOH and steps generating CH_2CHO as an alternative to CH_3CO have not been included. As far as possible, data were drawn from currently accepted values quoted in the literature. With the exception of reactions (21), (47) and (48), all other reactions were assumed to be in equilibrium, their reverse rate coefficients being calculated from the equilibrium constant for each reaction.

In the high temperature range considered here, the thermal decomposition of ethanol [reaction (1)] has been suggested as the most likely initiation reaction [1]. In the proposed mechanism, reaction (1) was assumed to be bimolecular. The computed ignition delay times are found to be strongly dependent on this reaction rate. Computer runs made assuming this reaction as unimolecular showed a very high temperature inversion.

As the fuel continues to decompose, the methyl and hydroxymethyl radicals produced in the initiation phase slowly build up a radical pool. These radical species, particularly H , O and OH , accelerate the destruction of fuel molecules. The second major phase of the induction period consists mostly of chain branching steps leading to the consumption of the fuel and major intermediate species like CH_3CHO , CH_2O , CHO , C_2H_6 , C_2H_4 , C_2H_2 , CO and H_2 . The principal fuel reactions are (2), (3) and (4) with the largest contribution provided by reaction (4). The computations show that the rate of reaction (5) has negligible impact on the ethanol disappearance rate.

The CH_3CHOH radical formed in reactions (2)-(5) is assumed to react via reactions (6) and (7). Reaction (6) is highly significant in the present mechanism and is assumed to be bimolecular. It provides an important source for H atoms and is significant both in fuel rich and lean conditions.

Stable intermediates like CH_3CHO , CH_2O and HCO are mainly responsible for degenerate branching reactions. The acetaldehyde concentrations encountered in ethanol oxidation is found to be higher than other intermediates. In these calculations, the largest contribution to the acetaldehyde consumption comes from reaction (12). The acetaldehyde decomposition by reaction (8) comes next in importance. The reaction between the methyl radical and formaldehyde [reaction (31)] is found to be very significant in the present system. Amongst the formyl radical reactions, its rapid decay by reaction (32) is found to be highly significant. Its reaction with molecular oxygen also plays an important role. These reactions are largely responsible for CO production.

Computations show that the oxidation of CH_3 by O atoms through reactions (16) and (17) is more important than its molecular oxidation [reaction (20)]. A substantial fraction of the methyl radicals recombine to form ethane through reaction (21).

In the present mechanism C_2H_6 removal is allowed only via the overall oxidation process [reaction (48)]. Ethylene consumption proceeds mostly through reaction (51). In addition, reaction (49) is of some importance. Vinyl radicals decompose yielding acetylene through reaction (53), which also provides an important source of H atoms. Acetylene reacts primarily with O atoms through reaction (54).

Reactions (36)-(46) form the $\text{CO-H}_2\text{-O}_2$ mechanism which is a central feature of the oxidation mechanisms of all hydrocarbon fuels. OH attack on CO [reaction (36)] is found to be the major path for the production of CO_2 .

ANALYTICAL RESULTS

Using the law of mass action, the law of conservation of energy for constant-volume adiabatic combustion and the ideal gas equation, the values of concentration of all the species, temperature and pressure at various intervals during the reaction were calculated by numerically integrating the system of equations by a variable stepsize, fourth-order Runge-Kutta method. Theoretical ignition delays at various temperatures and pressures were evaluated from the concentration profiles, based on the time at which the hydroxyl (OH) concentration reaches a value of 2×10^{-9} mole/cc. Cooke and Williams [13] have shown that the onset of ignition defined as a rise of the main hydroxyl emission peak to 5% of its maximum value, is equivalent to a hydroxyl ground state concentration of 2×10^{-9} mole/cc in both methane and ethane ignition. From the concentration profiles, the times at which CH and CO_2 concentrations reach a value of 2×10^{-9} mole/cc individually were also evaluated.

Figures 5 and 6 show the computed concentration, pressure, and temperature profiles for the stoichiometric $\text{C}_2\text{H}_5\text{OH-O}_2\text{-Ar}$ mixture at an initial temperature of 1500K and pressure of 2.0 atm.

Figure 7 shows a comparison of the computed values of ignition delay based on OH and CO_2 concentrations with the experimental ignition delay data of Cooke et al. [1], which were based on OH and CO_2 emissions. It is likely that the uncertainties in the quoted rate coefficients together with the existence of alternative reaction paths, not included in the present mechanism, are responsible for the relatively small differences between computed and observed results. The computed values of ignition delay based on CH concentration were much longer compared to the experimental ignition delay data of Cooke et al. [1] which were based on CH emission. This fact indicates that the present mechanism is not yet complete with respect to reactions involving the radical CH.

The experimental ignition delay data of the present investigation at 2.0 atm are not in good agreement with the computed data obtained using the present kinetic model. Many of the rate coefficients related to ethanol were extrapolated from low temperature data and the acetaldehyde mechanism reported by Beeley et al. [11] was used without any modifications. The mechanism needs further modification before it can be used for higher pressures and temperatures.

ACKNOWLEDGEMENT

The authors express their gratitude to Dr. D. L. Baulch, University of Leeds, England, for providing information on rate coefficient data.

TABLE II KINETIC MODEL FOR ETHANOL OXIDATION
(Temperature range: 1300-1700K)

Reaction	ΔH°_{298} (kJ/mole)	Forward rate coefficient ($\text{cm}^3\text{mol}^{-1}\text{s}^{-1}$ unless stated) Act. energies in kJ/mole)	Reference
1. $\text{C}_2\text{H}_5\text{OH}+\text{M}=\text{CH}_2\text{OH}+\text{CH}_3+\text{M}$	360.1	$3.00\text{E } 18\exp(-315.92/\text{RT})$	This work
2. $\text{C}_2\text{H}_5\text{OH}+\text{O}=\text{CH}_3\text{CHOH}+\text{OH}$	-53.9	$6.70\text{E } 12\exp(-6.32/\text{RT})$	14
3. $\text{C}_2\text{H}_5\text{OH}+\text{H}=\text{CH}_3\text{CHOH}+\text{H}_2$	-62.2	$4.40\text{E } 12\exp(-19.12/\text{RT})$	15
4. $\text{C}_2\text{H}_5\text{OH}+\text{OH}=\text{CH}_3\text{CHOH}+\text{H}_2\text{O}$	-125.5	$3.00\text{E } 13\exp(-24.94/\text{RT})$	Estimated
5. $\text{C}_2\text{H}_5\text{OH}+\text{CH}_3=\text{CH}_3\text{CHOH}+\text{CH}_4$	-64.7	$3.98\text{E } 12\exp(-40.57/\text{RT})$	16
6. $\text{CH}_3\text{CHOH}+\text{M}=\text{CH}_3\text{CHO}+\text{H}+\text{M}$	131.1	$5.00\text{E } 13\exp(-91.45/\text{RT})$	Estimated
7. $\text{CH}_3\text{CHOH}+\text{O}_2=\text{CH}_3\text{CHO}+\text{HO}_2$	-65.9	$1.00\text{E } 13\exp(-23.28/\text{RT})$	Estimated
8. $\text{CH}_3\text{CHO}=\text{CH}_3+\text{CHO}$	355.6	$4.00\text{E } 14\exp(-335.50/\text{RT})\text{s}^{-1}$	17
9. $\text{CH}_3\text{CHO}=\text{CH}_3\text{CO}+\text{H}$	359.2	$5.00\text{E } 14\exp(-367.80/\text{RT})\text{s}^{-1}$	18
10. $\text{CH}_3\text{CHO}+\text{O}=\text{CH}_3\text{CH}+\text{OH}$	-68.5	$1.00\text{E } 13\exp(-16.72/\text{RT})$	11
11. $\text{CH}_3\text{CHO}+\text{H}=\text{CH}_3\text{CO}+\text{H}_2$	-76.7	$8.70\text{E } 13\exp(-28.97/\text{RT})$	11
12. $\text{CH}_3\text{CHO}+\text{OH}=\text{CH}_3\text{CO}+\text{H}_2\text{O}$	-140.0	$5.25\text{E } 13\exp(-9.99/\text{RT})$	19
13. $\text{CH}_3\text{CO}=\text{CH}_3+\text{CO}$	60.3	$2.00\text{E } 10\exp(-62.70/\text{RT})\text{s}^{-1}$	20
14. $\text{CH}_2\text{OH}+\text{M}=\text{CH}_2\text{O}+\text{H}+\text{M}$	122.7	$2.50\text{E } 13\exp(-121.34/\text{RT})$	8
15. $\text{CH}_2\text{OH}+\text{O}_2=\text{CH}_2\text{O}+\text{O}_2$	-74.4	$1.00\text{E } 12\exp(-25.10/\text{RT})$	7
16. $\text{CH}_3+\text{O}=\text{CH}_2\text{O}+\text{H}$	-293.1	$8.00\text{E } 13$	21
17. $\text{CH}_3+\text{O}=\text{CH}+\text{H}_2\text{O}$	-42.6	$1.00\text{E } 14$	22
18. $\text{CH}_3+\text{H}=\text{CH}_2+\text{H}_2$	21.5	$7.24\text{E } 14\exp(-63.2/\text{RT})$	23
19. $\text{CH}_3+\text{OH}=\text{CH}_2\text{O}+\text{H}+\text{H}$	134.6	$2.00\text{E } 16\exp(-114.73/\text{RT})$	21
20. $\text{CH}_3+\text{O}_2=\text{CH}_2\text{O}+\text{O}+\text{H}$	205.3	$7.00\text{E } 12\exp(-107.20/\text{RT})$	21
21. $\text{CH}_3+\text{CH}_3=\text{C}_2\text{H}_6$	-376.0	$2.00\text{E } 13$	24
22. $\text{CH}_3+\text{CH}_3=\text{C}_2\text{H}_4+\text{H}_2$	-239.1	$1.00\text{E } 16\exp(-133.60/\text{RT})$	25
23. $\text{CH}_2+\text{O}_2=\text{CHO}+\text{OH}$	-302.2	$1.00\text{E } 14\exp(-15.5/\text{RT})$	26
24. $\text{CH}_2+\text{O}_2=\text{CO}_2+\text{H}+\text{H}$	-342.8	$4.00\text{E } 13\exp(-9.2/\text{RT})$	27
25. $\text{CH}+\text{O}_2=\text{CHO}+\text{O}$	-301.4	$1.00\text{E } 13$	28
26. $\text{CH}_4+\text{H}=\text{CH}_3+\text{H}_2$	2.6	$7.24\text{E } 14\exp(-63.10/\text{RT})$	29
27. $\text{CH}_4+\text{OH}=\text{CH}_3+\text{H}_2\text{O}$	-60.8	$1.50\text{E } 06\text{T}^{2.13}\exp(-10.20/\text{RT})$	30
28. $\text{CH}_2\text{O}+\text{O}=\text{CHO}+\text{OH}$	-50.0	$1.82\text{E } 13\exp(-12.90/\text{RT})$	31
29. $\text{CH}_2\text{O}+\text{H}=\text{CHO}+\text{H}_2$	-58.3	$3.30\text{E } 14\exp(-43.90/\text{RT})$	31
30. $\text{CH}_2\text{O}+\text{OH}=\text{CHO}+\text{H}_2\text{O}$	-121.6	$7.60\text{E } 12\exp(-0.7/\text{RT})$	31
31. $\text{CH}_2\text{O}+\text{CH}_3=\text{CHO}+\text{CH}_4$	-60.8	$2.20\text{E } 13\exp(-21.53/\text{RT})$	16
32. $\text{CHO}+\text{M}=\text{CO}+\text{H}+\text{M}$	63.9	$1.50\text{E } 14\exp(-61.40/\text{RT})$	33
33. $\text{CHO}+\text{H}=\text{CO}+\text{H}_2$	-372.0	$2.00\text{E } 14$	34
34. $\text{CHO}+\text{OH}=\text{CO}+\text{H}_2\text{O}$	-435.3	$1.00\text{E } 14$	35
35. $\text{CHO}+\text{O}_2=\text{CO}+\text{HO}_2$	-133.1	$4.20\text{E } 13\exp(-30.90/\text{RT})$	11
36. $\text{CO}+\text{OH}=\text{CO}_2+\text{H}$	-104.5	$2.32\text{E } 12\exp(-23.85/\text{RT})$	36
37. $\text{CO}+\text{HO}_2=\text{CO}_2+\text{OH}$	-264.4	$2.00\text{E } 14\exp(-96.14/\text{RT})$	37
38. $\text{HO}_2+\text{H}=\text{OH}+\text{OH}$	-160.0	$2.50\text{E } 14\exp(-7.90/\text{RT})$	38
39. $\text{HO}_2+\text{OH}=\text{H}_2\text{O}+\text{O}_2$	-302.2	$5.00\text{E } 13\exp(-4.18/\text{RT})$	39
40. $\text{HO}_2+\text{HO}_2=\text{H}_2\text{O}_2+\text{O}_2$	-177.9	$1.00\text{E } 13\exp(-4.18/\text{RT})$	39
41. $\text{H}_2\text{O}_2+\text{M}=\text{OH}+\text{OH}+\text{M}$	215.0	$1.26\text{E } 17\exp(-190.37/\text{RT})$	38
42. $\text{O}_2+\text{H}=\text{OH}+\text{O}$	70.7	$2.00\text{E } 14\exp(-70.25/\text{RT})$	38
43. $\text{H}_2+\text{O}=\text{OH}+\text{H}$	8.3	$2.20\text{E } 14\exp(-57.32/\text{RT})$	40
44. $\text{H}_2+\text{OH}=\text{H}_2\text{O}+\text{H}$	-63.3	$2.90\text{E } 14\exp(-45.97/\text{RT})$	41
45. $\text{OH}+\text{OH}=\text{H}_2\text{O}+\text{O}$	-71.6	$5.50\text{E } 13\exp(-29.26/\text{RT})$	41
46. $\text{H}+\text{O}_2+\text{M}=\text{HO}_2+\text{M}$	-197.1	$150\text{E } 15\exp(+4.18/\text{RT})\text{cm}^6\text{mol}^{-1}\text{s}^{-1}$	38
47. $\text{C}_2\text{H}_6=\text{CH}_3+\text{CH}_3$	376.0	$8.00\text{E } 12\exp(-294.30/\text{RT})\text{s}^{-1}$	21
48. $\text{C}_2\text{H}_6+\text{OH}=\text{C}_2\text{H}_5+\text{H}+\text{H}_2\text{O}$	73.6	$6.50\text{E } 13\exp(-5.60/\text{RT})$	42
49. $\text{C}_2\text{H}_4+\text{O}=\text{CH}_3+\text{CHO}$	-112.3	$2.26\text{E } 13\exp(-11.30/\text{RT})$	43
50. $\text{C}_2\text{H}_4+\text{H}=\text{C}_2\text{H}_3+\text{H}_2$	9.6	$6.92\text{E } 14\exp(-60.70/\text{RT})$	44
51. $\text{C}_2\text{H}_4+\text{OH}=\text{C}_2\text{H}_3+\text{H}_2\text{O}$	-53.7	$1.00\text{E } 14\exp(-14.60/\text{RT})$	45
52. $\text{C}_2\text{H}_4+\text{OH}=\text{CH}_3+\text{CH}_2\text{O}$	-62.2	$3.00\text{E } 12$	46
53. $\text{C}_2\text{H}_3+\text{M}=\text{C}_2\text{H}_2+\text{H}+\text{M}$	164.8	$1.00\text{E } 15\exp(-91.50/\text{RT})$	44
54. $\text{C}_2\text{H}_2+\text{O}=\text{CH}_2+\text{CO}$	-201.2	$6.30\text{E } 13\exp(-16.70/\text{RT})$	32
55. $\text{C}_2\text{H}_2+\text{OH}=\text{C}_2\text{H}+\text{H}_2\text{O}$	24.0	$6.30\text{E } 12\exp(-29.30/\text{RT})$	32
56. $\text{C}_2\text{H}+\text{O}=\text{CH}+\text{CO}$	-297.6	$5.00\text{E } 13$	47

For computing equilibrium constants most of the thermochemical data were taken from JANAF Thermochemical Tables [48]. For the species C_2H_5OH , CH_3CHOH , CH_3CO , CH_2OH , C_2H_6 , C_2H_3 and H_2O_2 , the data were taken from Ref. [49].

REFERENCES

1. Cooke, D.F., Dodson, M.C. and Williams, A., *Combust. Flame* **21**, 233 (1971).
2. Mullins, B.P., *Fuel* **32**, 451 (1953).
3. Bhaskaran, K.A., Shock tube study of the effect of dimethyl hydrazine on the ignition delay of Hydrogen-Air mixtures, Ph.D. thesis, Indian Institute of Technology, Madras, 1971.
4. Mullins, B.P., and Penner, S.S., *Explosions, Detonations, Flammability and Ignition*, Pergamon Press, London, 1959.
5. Bowman, C.T., *Combust. Flame* **25**, 343 (1975).
6. Aronowitz, D., Naegeli, D.W., and Glassman, I., *J. Phys. Chem.* **81**, 2555 (1977).
7. Aronowitz, D., Santoto, R.J., Dryer, F.L., and Glassman, I., *17th Symp. (Int.) on Comb.*, 633 (1978).
8. Westbrook, C.K., and Dryer, F.L., *Combustion Science and Technology* **20**, 125 (1979).
9. Kenichi Ito and Toshiki Yano, *4th Symp. (Int.) on Alcohol Fuels Technology*, 683 (1981).
10. Natarajan, K., and Bhaskaran, K.A., *Combust. Flame* (in press).
11. Bealey, P., Griffiths, J.P., Hunt, B.A., and Williams, A., *16th Symp. (Int.) on Comb.*, 1013 (1976).
12. Colket III, M.B., Naegeli, D.W., and Glassman, I., *16th Symp. (Int.) on Comb.*, 1023 (1976).
13. Cooke, D.F., and Williams, A., *16th Symp. (Int.) on Comb.*, 757 (1971).
14. Ayub, A.L., and Roscoe, J.M., *Can. Chem.* **57**, 1269 (1979).
15. Aders, W.K., and Wagner, H.G., *Ber. Bunsenges, Phys. Chem.* **77**, 712 (1973).
16. Kerr, J.A., and Parsonage, M.L., *Evaluated Kinetic Data on Gas Phase Hydrogen Transfer Reactions of Methyl radicals*, Butterworths (1976).
17. Colket III, M.B., Naegeli, D.W., and Glassman, I., *Int. J. Chem. Kinet.* **7**, 223 (1975).
18. Kerr, J.A., *Chem. Rev.* **60**, 469 (1966).
19. Huie, R.E., and Herron, J.J., *Progress in Reaction Kinetics* **8**, 3 (1975).
20. Benson, S.W., and O'Neal, E.E., *Kinetic Data on Unimolecular reactions*, NSRDS-NBS report 21 (1970).
21. Bhaskaran, K.A., Frank, P., and Just, Th., *15th Symp. (Int.) on Shock Tubes and Waves*, 503 (1979).
22. Kuratani, K., *Bulletin of the Institute of Space and Aeronautical Science, University of Tokyo*, Vol. II, No. 4 (1975).
23. Olson, D.B. and Gardiner, W.C. Jr., *Combust. Flame* **32**, 151 (1978).
24. Walker, R.W., *Reaction Kinetics and Energy Transfer*, Vol. 2, p.161, S.P.R. Chemical Society (1977).
25. Roth, P., and Just, Th., *Ber. Bunsenges, Physik. Chem.* **83**, 577 (1979).
26. Benson, S.W., and Hengen, G.R., *J. Phys. Chem.* **71**, 1735 (1967).
27. Warnatz, J., *18th Symp. (Int.) on Comb.* (1980) (in press).
28. Jachimowski, C.J., *Combust. Flame* **19**, 347 (1977).
29. Roth, P., and Just, Th., *Ber. Bunsenges, Physik. Chem.* **79**, 682 (1975).
30. Zellner, R., *J. Phys. Chem.* **83**, 18 (1979).
31. Dean, A.M., Johnson, R.L., and Steiner, D.C., *Combust. Flame* **37**, 41 (1980).
32. Vandooran, J., and Van Tiggelen, P.J., *16th Symp. (Int.) on Comb.*, 1133 (1976).
33. Schecker, H.G., and Jost, W., *Ber. Bunsenges, Physik. Chem.* **73**, 521 (1969).
34. Niki, H., Daby, E.E., and Weinstock, B., *12th Symp. (Int.) on Comb.*, 277 (1967).
35. Bowman, C.T., *Combustion Science and Technology* **2**, 161 (1970).
36. Vandooran, J., Peeters, J., and Van Tiggelen, P.J., *15th Symp. (Int.) on Comb.*, 745 (1974).
37. Vardanyan, I.A., Sachyan, G.A., and Nalbandyan, A.R., *Int. J. Chem. Kinet.* **7**, 23 (1975).
38. Baulch, D.L., Drysdale, D.D., Horne, D.G., and Lloyd, A.C., *Evaluated Kinetic Data for High Temperature Reactions* Vol. I, Butterworths, London, 1973.
39. Lloyd, A.C., *Int. J. Chem. Kinet.* **6**, 169 (1974).
40. Schott, G.L., Getzinger, R.W., and Seitz, W.A., *Int. J. Chem. Kinet.* **6**, 921 (1974).
41. Gardiner, W.C., Mallard, W.G., McFarlane, M., Morinaga, K., Over, J.H., Tawlings, W.T., Takeyama, T., and Walker, B.F., *14th Symp. (Int.) on Comb.*, 61 (1973).
42. Smets, B., and Peeters, J., *Second European Combustion Symposium*, 38 (1975).
43. McLain, A.G., and Jachimowski, C.J., *Chemical Kinetic modeling of propane oxidation behind shock waves*, NASA Ind.-8501 (1977).
44. Just, Th., Roth, P., and Damm, R., *16th Symp. (Int.) on Comb.*, 961 (1976).
45. Baldwin, R.R., Simmons, R.F., and Walker, R.W., *Trans. Faraday Soc.* **62**, 2486 (1966).
46. Kerr, J.A., and Rajajckzack, E., *Third Supplementary Tables of Bimolecular Gas Reactions*, Dept. of Chemistry, University of Birmingham (1977).
47. Browne, W.G., Porter, R. P., Verlin, J.D., and Clark, A.H., *12th Symp. (Int.) on Comb.*, 1035 (1976).
48. Stull, D.R., and Prophet, H. (Ed.), *JANAF Thermochemical Tables* NSRDS-NBS 37, Dow Chemical Company, Michigan (1971).
49. Bain, G.S., *Approximate Thermochemical Tables for some C-H and C-H-O species*, NASA Report CR-2178 (1973).

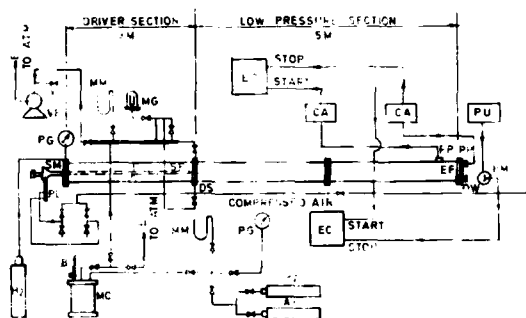
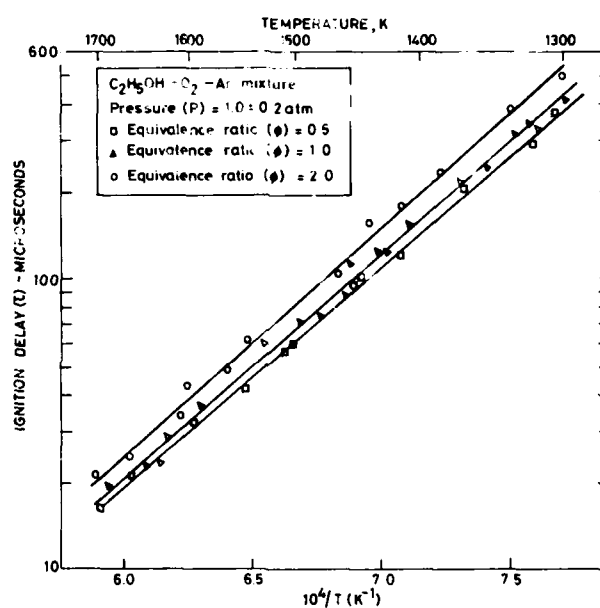
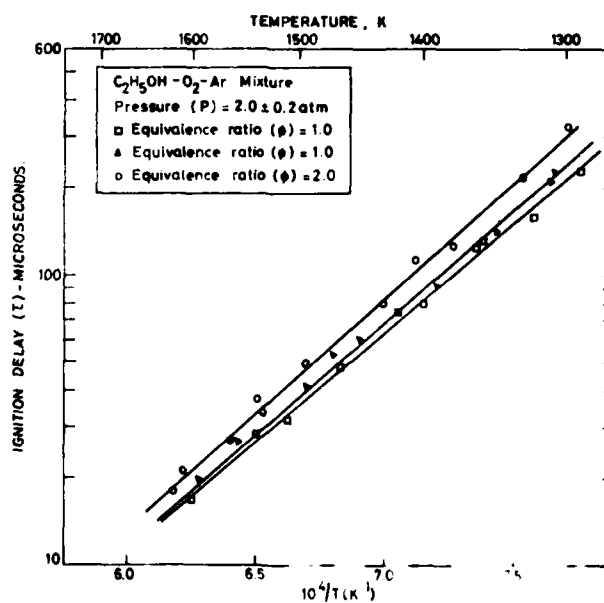


FIG 1 SCHEMATIC DIAGRAM OF THE EXPERIMENTAL SET-UP

FIG 2 EXPERIMENTAL IGNITION DELAY DATA FOR $C_2H_5OH-O_2-Ar$ MIXTUREFIG 3 EXPERIMENTAL IGNITION DELAY DATA FOR $C_2H_5OH-O_2-Ar$ MIXTURE

High Temperature Ignition of Ethanol

[841]

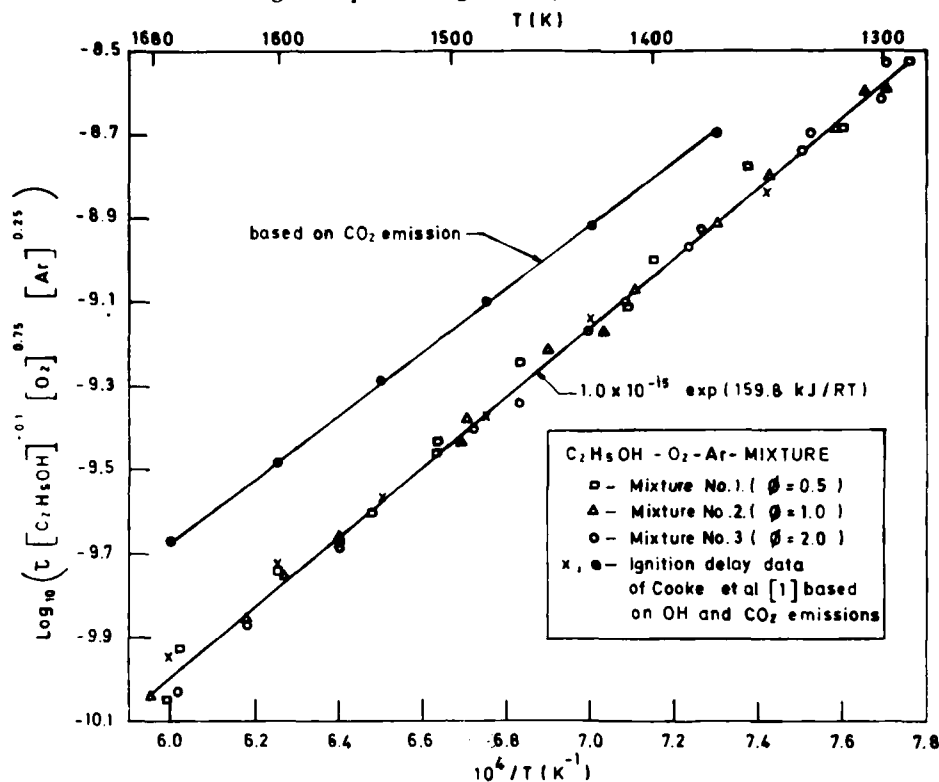


FIG. 4. CORRELATION OF EXPERIMENTAL IGNITION DELAY (sec.) WITH INITIAL POST-SHOCK TEMPERATURE (K) AND CONCENTRATIONS (mole/cc) OF $\text{C}_2\text{H}_5\text{OH}$, O_2 AND Ar.

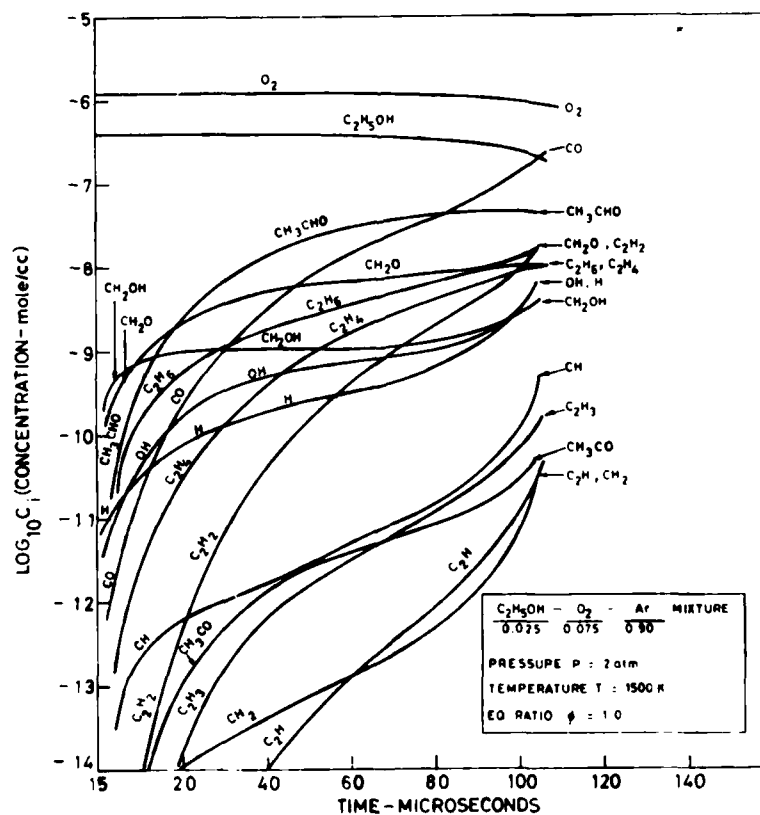


FIG. 5. COMPUTED CONCENTRATION PROFILES

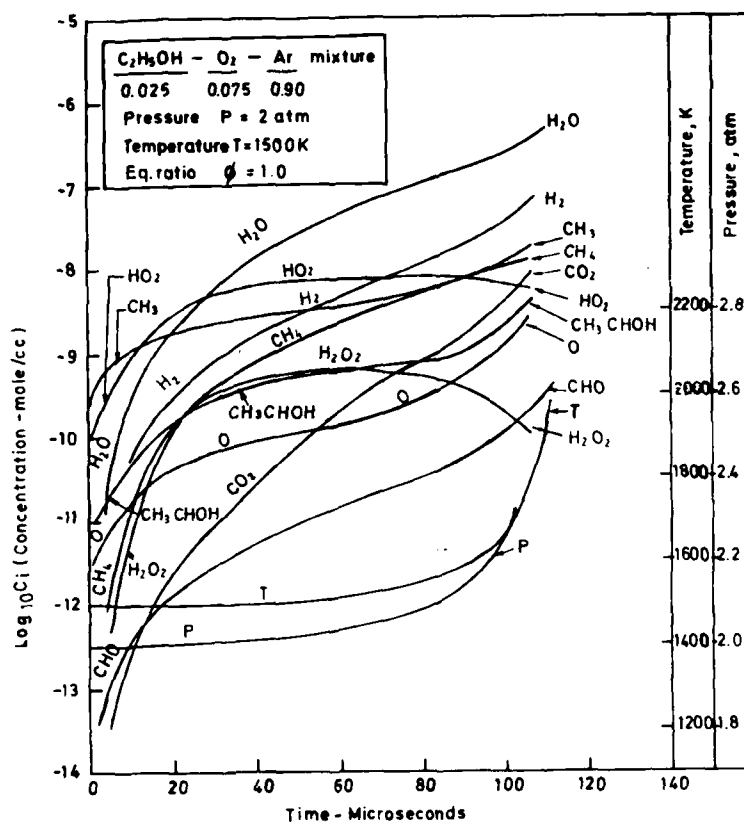


FIG. 6. COMPUTED CONCENTRATION, TEMPERATURE AND PRESSURE PROFILES.

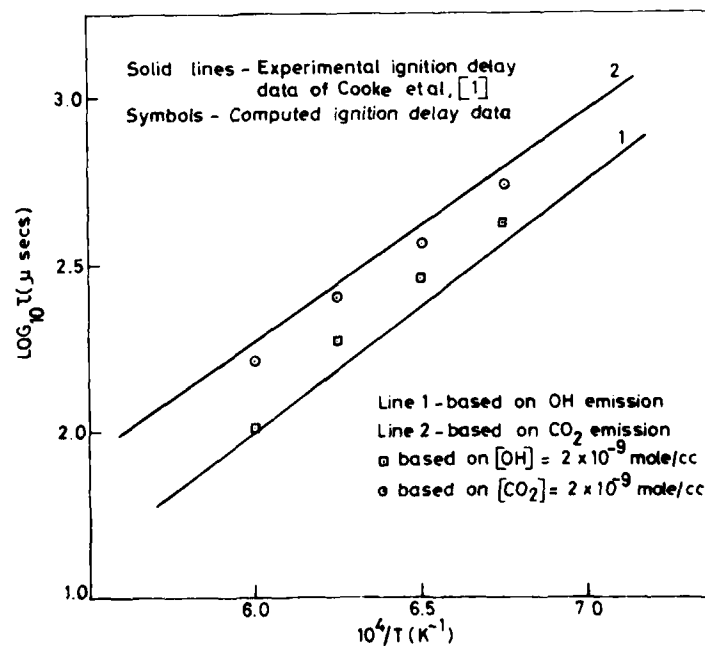


FIG. 7. COMPARISON OF COMPUTED IGNITION DELAY DATA WITH EXPERIMENTAL DATA OF COOKE et al [1]

AD P000311

A STUDY ON THE HYDROGEN-OXYGEN DIFFUSION FLAME IN HIGH SPEED FLOW

S. Takahashi, Y. Yoshizawa, T. Minegishi, the late H. Kawada

Mechanical Engineering Laboratory, Ibaraki prefecture, Japan
Dep. of Mech. Engg., Tokyo Institute of technology, Tokyo, Japan

A new type of apparatus was adapted to the study on the diffusion flame in high speed flow with the use of a shock tube /detonation tube combination. The flows behind the incident shock wave propagating into O₂-Ar mixture and the burned gas behind the detonation wave traveling into a fuel-rich H₂-O₂-Ar mixture were used to produce a fuel flow and an oxidizer flow respectively. The burned gas was issued through a nozzle in parallel to the oxidizer flow and two-dimensional flow field was established at the test section of the shock tube. The process from the starting of the flows to the formation of a diffusion flame was investigated by the pressure measurements in both tubes and by schlieren and interferometric photography. Also the ignition distances of the diffusion flames in quasi-steady state were measured from direct photography. As a result, a detonation tube was shown to be a useful device for producing a high speed and high temperature flow and it was confirmed that the ignition distance is greatly influenced by both velocity difference and hydrogen concentration.

INTRODUCTION

With the requirement for the increasingly faster flight of airplanes, the development of supersonic combustion technology has become one of important subjects in combustion engineering. Various methods of flame holding such as bluff-body, recessed wall, piloted flame and so on have been devised and developed to stabilize a flame in high speed flow. Those methods are used to hold a flame mainly in a premixed gas flow and are not necessarily adequate for the application to supersonic combustion. Recently the supersonic combustion techniques by a diffusion flame have received attention. The flow fields in these combustion systems are considerably complex due to the existence of a shock pattern and a turbulent mixing process. While numerous studies (1)~(5) have been conducted in this field, they have not given enough information to design a combustor of a scramjet engine. On executing an experiment of such supersonic combustion using a steady flow, a huge experimental facility is needed because a large amount of high temperature air flow must be supplied. Moreover, it may be difficult to vary the experimental conditions over a wide range employing a steady flow apparatus.

The detonation tube, as well as the shock tube, is considered to be a simple and convenient device to produce a high temperature gas flow. Behind a

steadily propagating detonation wave, a uniform gas flow of high temperature is formed and also its physical conditions can be evaluated from the characteristic values at Chapman-Jouguet point. Moreover, the use of a detonation tube has the additional advantage that the starting time of a flow can be regulated easily with an electric circuit by firing the detonable mixture in the detonation tube.

In this work, a new type of apparatus was designed for the study on the diffusion flame with the use of a shock tube/detonation tube combination. The detonation tube served as a generator of a fuel flow of high temperature and the shock tube acted as a short duration wind-tunnel of an oxidizer flow. This paper reports the structure of the apparatus and the flow characteristics in both tubes and presents the preliminary results obtained by optically observing the diffusion flame.

EXPERIMENTAL APPARATUS AND PROCEDURE

The experimental apparatus employed in this study consisted of a shock tube and a detonation tube, which were arranged in parallel to each other and connected with a bent-tapered nozzle at the test section of the shock tube as shown in Fig. 1. The shock tube served as a short duration wind-tunnel and the incident shock wave propagating into $O_2(20\%)$ -Ar(80%) mixture generated an oxidizer flow. The shock tube was a conventional one with a 70mm i.d., 3m-long driver section and a 43 mm square, 6 m long driven section. A test section with two glass windows was installed at the downstream end of the driven section and was connected to a dump-tank across a plate valve. A needle in the driver section, which was driven by a solenoid, was used to synchronize the rupture of the diaphragm(1) with the photographing by a high speed camera. On the other hand, the detonation tube produced a fuel flow. The burned gas behind a detonation wave propagating into a fuel-rich H_2 - O_2 -Ar mixture was issued through the nozzle in parallel to the oxidizer flow in the shock tube. The detonation tube was a circular pipe with 32.9 mm i.d. and 1.75 m length. One end of the detonation tube was closed and the other end was connected to the nozzle across the diaphragm(2).

An igniting plug was equipped on the detonation tube near the diaphragm(2) and a circular pipe with numerous holes was inserted into the detonation tube to accelerate the transition from a deflagration wave to a detonation wave.

Two pressure transducers were equipped on the test section and at the location of 2.05 m upstream from its center. The former signal was employed to monitor the pressure change in the test section and the latter signal acted as the signal source for triggering the spark ignitor. The timing of the firing is regulated using a delay circuit so that both the oxidizer flow and the fuel flow may start at almost the same time. Also, both the signals were utilized for the measurement of shock wave velocity which determines the flow conditions of the oxidizer flow. Another pressure transducer was equipped at the closed end of the detonation tube, which enabled us to ascertain whether the complete transition to a detonation wave was established.

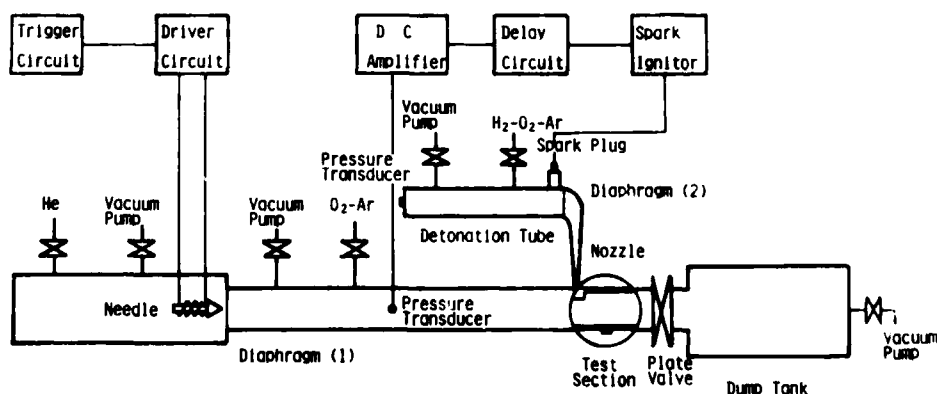


Fig. 1. Experimental apparatus

The test section is shown in Fig. 2. The nozzle, which was curved downward from the joint with the detonation tube, was introduced into the shock tube along the upper wall of the test section. The cross section of the nozzle was contracted to a 43 mm x 2 mm rectangle at its exit and a two-dimensional parallel flow field was formed in the test section.

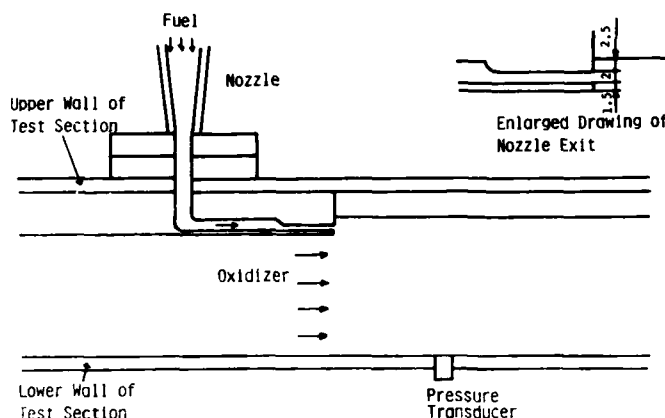


Fig. 2. Test section and nozzle

Each run was shot in the following way. After the driver and driven section of the shock tube, the detonation tube, and the dump-tank were evacuated, pressurized helium, the oxidizer mixture, the fuel mixture and air were introduced into these tubes to the desired pressure respectively. The pressure in the dump-tank was kept at the same level with that in the driven section, and the plate valve is opened. The diaphragm(1) was ruptured by the needle when the framing speed of the high speed camera has reached to around 5000 pps and a shock wave propagated into the driven section. In the already mentioned way, the mixture in the detonation tube was fired with the igniting plug. As a result, the diaphragm(2) ruptures due to the pressure rise in the detonation tube and the burned gas behind the detonation wave issued into the test section through the nozzle in parallel to the oxidizer flow. Schlieren, interferometric and direct photography were employed to observe the flow field.

FLOW CONDITIONS

While the use of a detonation tube has some advantages in producing a high temperature flow, it should be noted that the fuel flow conditions can not be chosen arbitrarily. The strength of the mixture used to produce a fuel flow must be chosen so that the transition time to a detonation wave becomes short compared with the characteristic time, which is defined as the ratio of the detonation tube length to the velocity of the detonation wave. This imposes a severe restriction on the experimental conditions of the fuel flows. In addition, there is a correlation between the temperature and the velocity, and neither can be varied independently. Four kinds of the mixture ($H_2:O_2:Ar=3:1:2$, $3:1:3$, $5:2:3$ and $4:1:2$) were used and their initial pressure was fixed at 700 Torr. Under these experimental conditions, it was confirmed from the pressure measurements that smooth transition to a detonation wave took place. The flowing conditions of fuel were evaluated based on the relationship of isentropic flow and the properties of the mixture at the Chapman-Jouguet point. Namely, the characteristic values at the Chapman-Jouguet point were determined from the composition and the pressure of the initial mixture, and flowing conditions of the downstream from the Chapman-Jouguet point were calculated under the conditions that the flow is isentropic and the sonic flow is established at the nozzle exit. On the other hand, the flowing conditions of oxidizer were determined from the measurement of the incident shock wave velocity in usual way.

The flowing conditions of the oxidizer and of the fuel at the nozzle exit are listed in Table 1. The temperature and Mach number of the oxidizer flow were varied over the range from 600 K to 1150 K and from 0.89 to 1.23 respec-

tively. The temperature and velocity of the fuel flow at the nozzle exit were in the narrow range from 2140 K to 2360 K and 1150 m/s to 1190 m/s respectively. The mole fraction of hydrogen could be changed in the relatively wide range from 0.15 to 0.31.

Table 1. Flow conditions of oxidizer and fuel

Run NO.	Oxidizer Flow				Fuel Flow				Velocity* Parameter	Concen.** Parameter
	Press. MPa	Temp. K	Velocity m/s	Mach NO.	Press. MPa	Temp. K	Velocity m/s	H ₂ %		
1	0.057	1150	770	1.23	0.31	2270	1130	19.6	0.19	2.32
2	0.062	1000	680	1.18	"	"	"	"	0.25	1.83
3	0.065	890	610	1.12	"	"	"	"	0.30	1.54
4	0.080	750	520	1.03	"	"	"	"	0.37	1.06
5	0.071	600	400	0.89	"	"	"	"	0.48	0.98
6	0.052	1070	720	1.20	0.29	2140	1050	16.4	0.19	2.66
7	0.061	990	670	1.17	"	"	"	"	0.22	2.12
8	0.062	850	590	1.10	"	"	"	"	0.28	1.80
9	0.078	740	510	1.01	"	"	"	"	0.35	1.58
10	0.071	600	400	0.89	"	"	"	"	0.45	1.86
11	0.057	940	650	1.15	0.31	2360	1150	15.4	0.28	1.68
12	0.062	1000	680	1.18	0.29	2180	1190	31.1	0.27	3.39

* Velocity parameter $= (U_f - U_o) / (U_f + U_o)$

** Concentration parameter $= (\rho_f \cdot X_{H_2} / M_f) / (\rho_o \cdot X_{O_2} / M_o)$

CHARACTERISTICS OF FUEL AND OXIDIZER FLOW

The flowing conditions listed in Table 1 are valid under the conditions that the flow in the nozzle is steady and the oxidizer flow is not influenced by the existence of the fuel flow. In order to investigate whether these conditions were satisfied, the pressure measurements were made at the test section and at the nozzle prior to the observation of diffusion flame. In Fig. 3, the pressure change in the nozzle (upper trace) and in the test section (lower trace) are shown. The first rise on the both traces represents the issue of the burned gas into the nozzle and the test section. The pressure in the nozzle, then, gradually increases and reaches a certain level. The pressure at this time was 0.54 MPa, which coincided well with the evaluated value. It is considered that the steady flow has been established at this time. This steady state is broken by the propagation of the detonation wave, which has reflected at the closed end of the detonation tube, into the nozzle. The time required for the establishment of the steady state and the duration of the steady state are estimated to be 0.7 ms and 1.0 ms respectively. On the other hand, the pressure in the test section is kept constant for 0.8 ms after showing the temporary fluctuation due to the issue of the burned gas as well as the pressure in the nozzle. Then the gradual increase is observed and followed by the large jump due to the arrival of the reflected detonation wave.

Another pressure measurement in the test section made clearer the characteristics of the oxidizer flow. Three traces in Fig. 4 are the signals of the pressure transducers which were equipped on the test section at intervals of 200 mm. The symbols A, B, C and D indicate the commencement of the fuel flow, the incident shock wave, the compression wave and the reflected detonation wave

respectively. It was found from these traces that the steady flow of the oxidizer lasted for about 0.9 ms until it was interrupted by the compression wave which propagated upstream. Such a compression wave was observed even when Ar was used for the shock tube flow instead of O₂-Ar mixture. Therefore, it is considered that the compression wave does not result from the interaction of the fuel flow and the oxidizer flow, but from the characteristics of the shock tube flow. Although the period in which both of the flows were steady was short in this work, earlier start of the fuel flow will make the duration of the steady state longer.

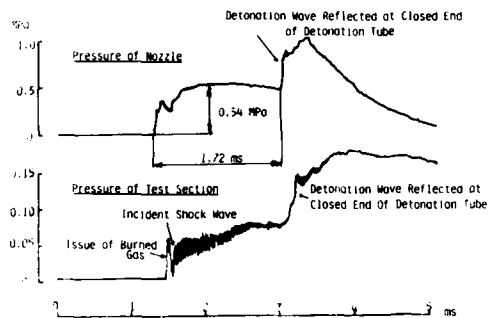


Fig. 3 Pressure changes in the test section and nozzle.

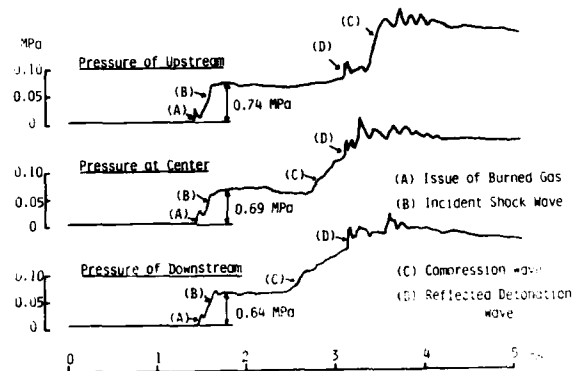


Fig. 4 Pressure changes in the test section.

OBSERVATION OF FLOW FIELD

Figs. 5 and 6 are typical schlieren and interferometric photographs taken to observe the flow field. The pressure change in the test section is also shown in Fig. 5. The figures under these photographs represent the elapsed time from the issue of the burned gas into the test section and the numbers on the pressure trace correspond to those of the photographs. These sequential photographs clarify the flow pattern and the formation process of the diffusion flame. In the first photograph of Fig. 5, the burned gas has been just issued and the mixing region has not been formed yet over the whole region of the test section. The photographs (1)-(3) show the process from the starting of the flows to the establishment of a steady flow. Two oblique shock waves originate from the upper and lower tip of the nozzle exit with the starting of the fuel flow. The former reflects at the upper wall of the test section and propagates across the fuel flow into the free stream of the oxidizer flow. The latter propagates directly into the free stream of the oxidizer. A rarefaction wave also originates from lower tip of the nozzle exit. After reflecting at the upper wall, the rarefaction wave interacts with the oblique shock wave reflected at the upper wall in the free stream of the oxidizer flow, which results in a single oblique shock wave in the oxidizer flow. The shock pattern shows little change in the photographs (3)-(4). This means that a steady flow has been established. After 1.05 ms, it is observed that the shock pattern is disturbed from the downstream by a compression wave. This compression wave corresponds to the one detected by the pressure measurement in the test section.

Fig. 6 is the interferometric photograph of the flow field in a steady state. From the narrow spacing and the large shift of the fringes in the vicinity of the nozzle exit, the fuel flow is found to rapidly expand immediately after issued into the test section. On the contrary, the oblique shock waves bring about slight deceleration and temperature rise to the both flows. The fringes are almost vertical in the fuel and the oxidizer flow except the mixing region. Although the fringe shift of the mixing region is large in the neigh-

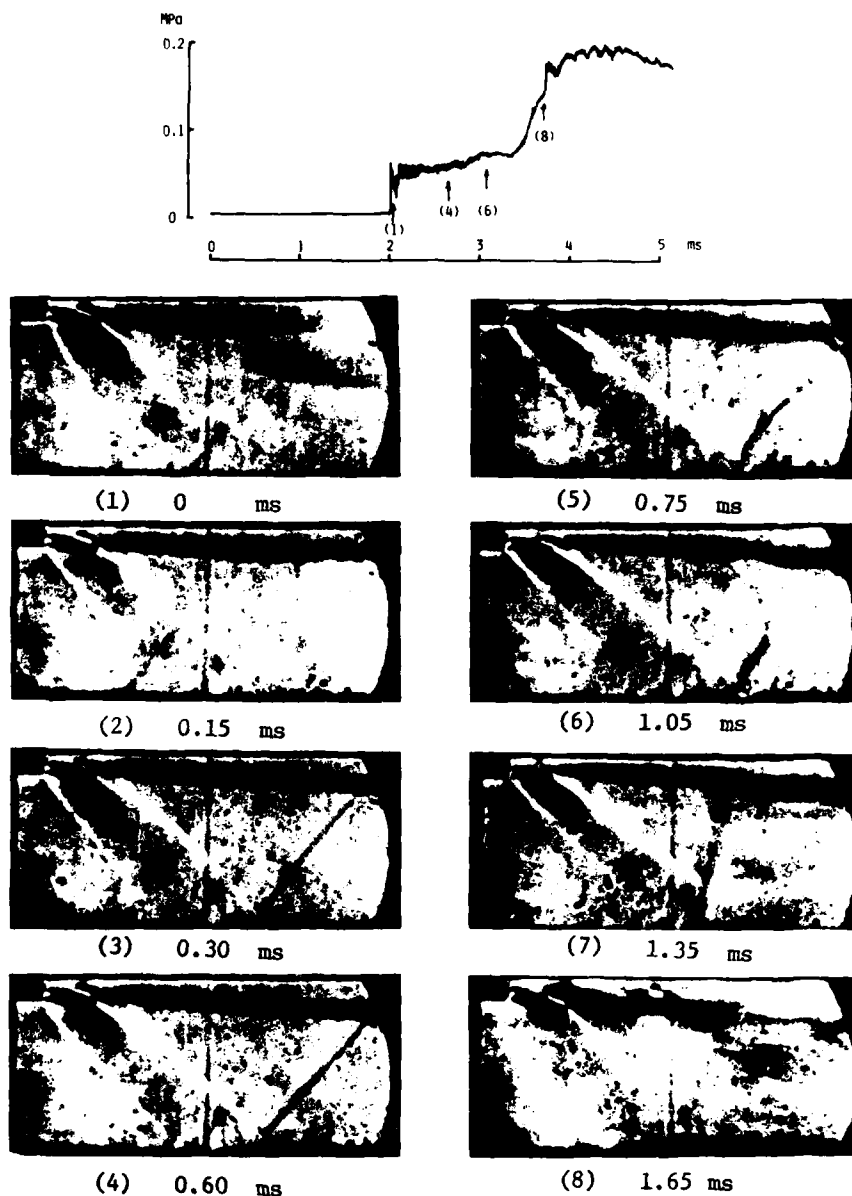


Fig. 5 Schlieren photographs showing typical flow pattern.



Fig. 6 Interferometric photograph showing the steady flow field.

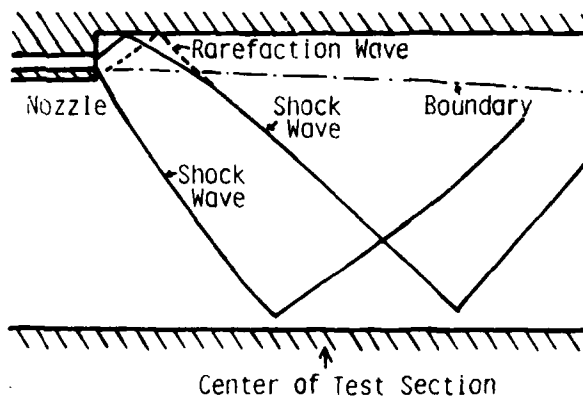


Fig. 7 Schematic drawing of flow field.

borhood of the nozzle exit, it gradually decreases as the mixing of the fuel flow and the oxidizer flow proceeds. These facts suggest that the flow conditions of the fuel change rapidly from those calculated due to the expansion in the test section. It may not be adequate to use the flowing conditions evaluated at the nozzle exit in discussing the properties of the diffusion flame. If the experimental conditions are chosen so that the pressure at the nozzle exit agrees with that of the oxidizer flow, it will be capable of producing the same flowing conditions with those calculated. Fig. 7 is a schematic drawing of the flow pattern which was synthesized from these observations.

OBSERVATION OF DIFFUSION FLAME

Fig. 8 is the direct photographs which show the formation process of a diffusion flame. The figures under the photographs indicate the elapsed time from the issue of the burned gas. Since the fuel is issued before the oxidizer flow starts, the early issued portion of the fuel almost reaches the opposite side of the test section as shown in the first photograph. In the second photograph, the whole mixing region is brightening. The emission, however, does not mean the formation of a diffusion flame because the fragment of the diaphragm burns with its exposure to the surrounding high temperature gas. As the fuel flow approaches its steady state, the ignition point moves downstream. It then stays at a distance apart from the nozzle for a short time and turns back upstream with the passage of the compression wave. In this way, a steady diffusion flame appears to exist, though its duration is short. Therefore, the effect of the velocity difference between the fuel and oxidizer flow and the hydrogen concentration on the ignition distance have been investigated based on the direct photographs of the steady diffusion flame.

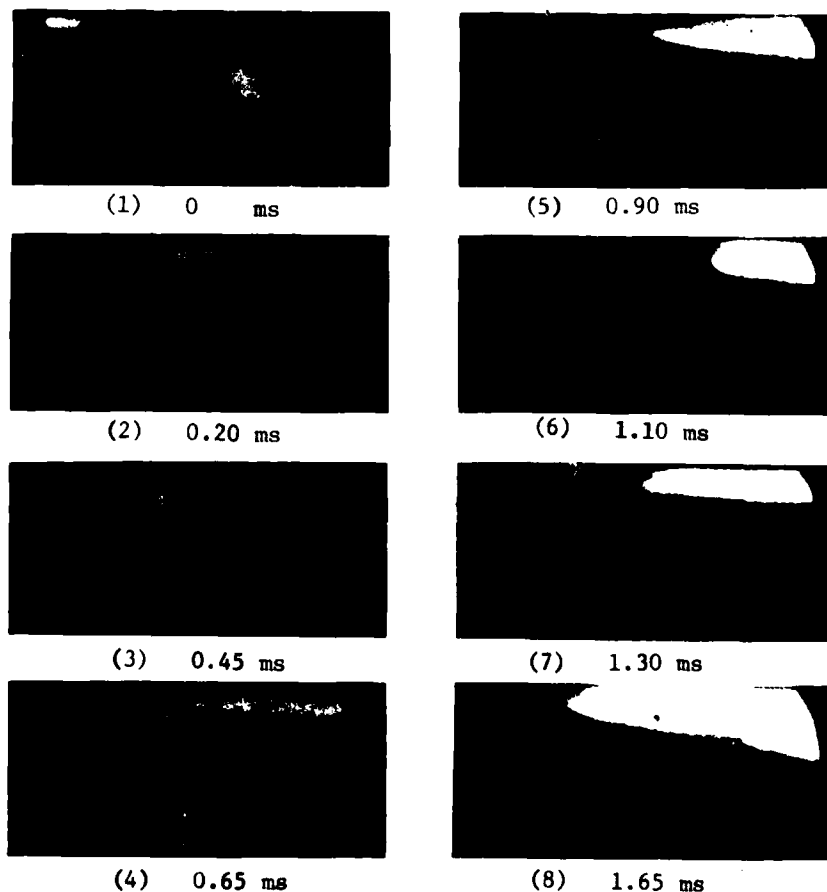
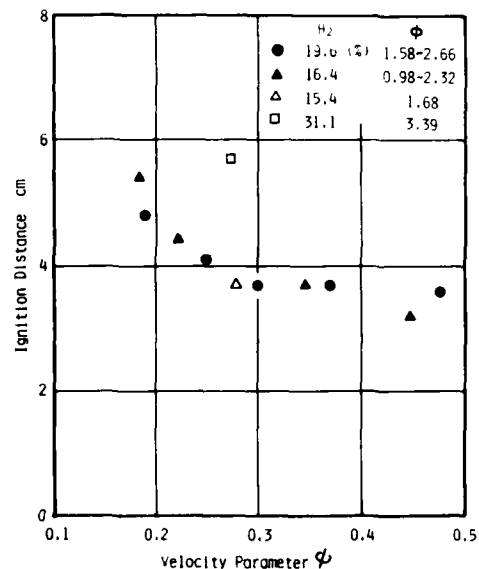


Fig. 8 Direct photographs showing the formation of a diffusion flame.

Each effect can be seen in Fig.9. Velocity parameter ψ is defined as $(U_f - U_o) / (U_f + U_o)$ and stands for a measure of the magnitude of the velocity difference between the both flows. On the other hand, concentration parameter ϕ is defined as $(P_f \cdot X_{H_2} / M_f) / (P_o \cdot X_{O_2} / M_o)$ and represents the over-all mole ratio of hydrogen to oxygen. The change of the velocity parameter ψ was caused mainly by the oxidizer velocity, because the velocity of the fuel flow could not be varied over a wide range as described above. Fig.9 shows a general trend that the ignition distances become shorter as the velocity difference increases. The temperature of the oxidizer flow decreases with the increase of ψ due to a correlation between the temperature and the velocity of the oxidizer flow. Therefore, it may be concluded that the velocity difference greatly influences the ignition distance of the diffusion flame. The effect of hydrogen concentration can be seen by comparing the experimental points of different hydrogen concentration. In the range of hydrogen fraction from 0.15 to 0.20 hydrogen concentration has little effect on the ignition distance. On the contrary, in the case of the higher hydrogen concentration (0.31), the outstanding increase of the ignition distance was found. These experimental results seem to suggest that the ignition distance increases rapidly when the concentration parameter exceeds 2.5.



AD P000312

EXPERIMENTAL INVESTIGATION OF SHOCK INITIATED
METHANE-COMBUSTION NEAR A WALL

R. Keiper, J. H. Spurk

Institut für Technische Strömungslehre
Technische Hochschule Darmstadt
6100 Darmstadt, West Germany

Methane-Air mixture in Argon heat bath is ignited by shock, reflected from the endwall of shock tube.

Using focused laser beams ($\lambda=633$ nm) in conjunction with a Mach-Zehnder Interferometer the time dependent density (index of refraction) in the boundary layer (space resolution ca. 0.1 mm) and outside the boundary layer is observed. Methane absorption is measured with a focused Helium Neon laser beam at 3.391 microns. Surface temperature of the endwall is measured by thin film gauges.

Experiments are compared with numerical prediction based on Bowman's reaction scheme including Zel'dovich mechanism. Agreement between experimental density profiles and numerical prediction is very good. Methane absorption outside the boundary layer agrees well with computation based on isobaric combustion. Measurements in the boundary layer, albeit with insufficient space resolution, are in accord with the predicted trends.

1) Introduction

Combustion processes are strongly coupled to the dynamics of the flow and, especially near a wall, to the diffusion and conduction process. Since all combustion systems have walls where major contributions of pollutants are formed, this zone is of special interest.

We report here on an investigation of this zone which consists of the boundary layer forming at the endwall of a shock tube, when an air-methane mixture diluted by argon, is ignited by the shock reflected from the endwall. While the coupling to the outside flow is rather weak in our case, and one may deplore this lack of realism for the application, it is this fact which makes the flow amenable to computation and to detailed experimental investigation. The computation taking into account the time dependence of the outside flow caused by sidewall boundary layers,

and the combustion process outside the boundary layer, have been reported in [1]. We give here an account of the experimental work, results of which have been used for comparison in [1].

2) Density profiles and surface temperature at the wall.

The experiments were carried out in a stainless steel shock tube of round 100-mm diameter crosssection and a length of 10 m. The shock tube has an insert, which serves as test section, and has a square crosssection of 55x55 mm. Windows installed in the sidewalls allow (interferometric) observation of the flow near the endwall. The tube is filled with a mixture of methane, argon, oxygen and nitrogen with the mole fractions $X_{CH_4} = 0.0325$, $X_{O_2} = 0.162$, $X_{N_2} = 0.0993$ and $X_{Ar} = 0.7062$ to initial pressure of 7 mbar. Shock waves with Mach number of about 3.2 heat the test gas to about 2000 K upon reflection from the endwall.

Two laser beams ($\lambda = 633$ nm) (Figure 1) are used to measure the index of refraction i) in the boundary layer at varying distances from the endwall, ii) outside the layer at a distance of 14 mm from the endwall. The beams are passed through a Mach-Zehnder Interferometer where each beam is split in a reference beam and a beam traversing the test section. The beam outside the boundary layer has a radius of about 1.5 mm. The beam in the boundary layer is focused on the centerline of the test section to a waist radius of about 0.08 mm at the e^{-2} intensity point and the beam radius is practically constant across the test section. A circular stop is placed just outside the window, which was found to reduce the effect of beam refraction in the boundary layer. At the exit of the interferometer the reference beam and test section beam emerge superimposed and their combined intensity will vary according to

$$I(t) = I_0 \cos^2\left(\frac{\delta(t)}{2}\right) \quad (1)$$

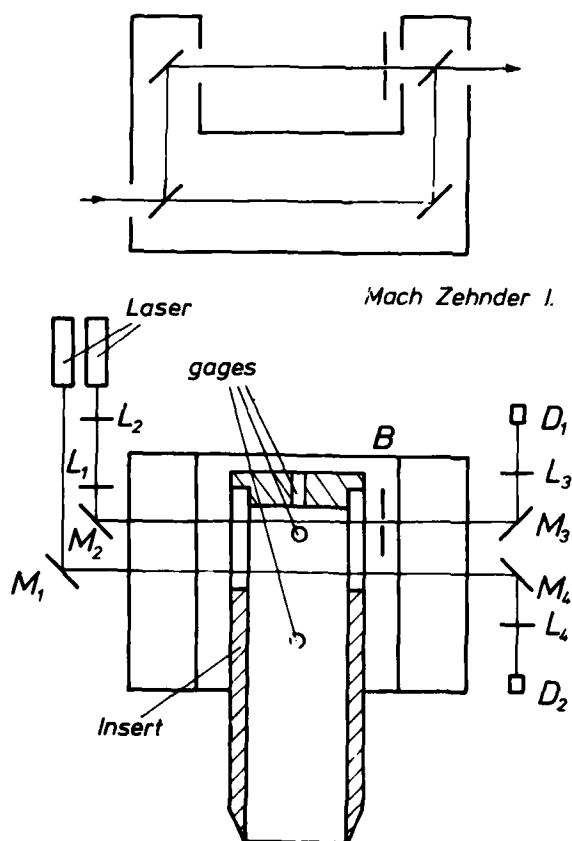


Figure 1: Set-up for density measurement

AD-A122 200

PROCEEDINGS OF THE INTERNATIONAL SYMPOSIUM ON SHOCK
TUBES AND WAVES (13TH. (U) CALSPAN ADVANCED TECHNOLOGY
CENTER BUFFALO NY C E TREANDR ET AL. JUL 81

10/10

UNCLASSIFIED

AFOSR-TR-82-1031 F49629-81-C-0002

F/O 20/1

NL

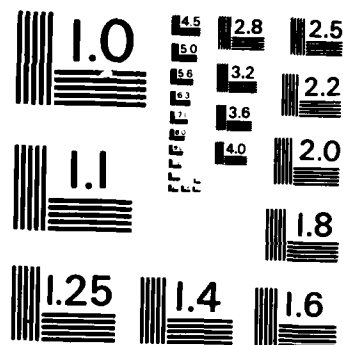
END

DATE

FILED

2 83

DTIC



MICROCOPY RESOLUTION TEST CHART
NATIONAL BUREAU OF STANDARDS-1963-A

from which the phase $\delta(t)$ may be gotten.

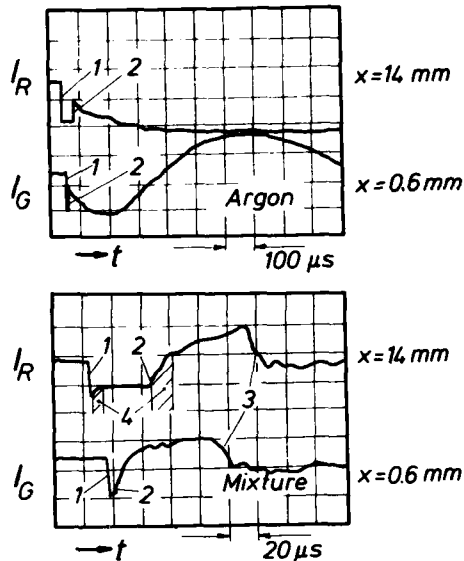


Figure 2: Typical intensity traces

1 incident shock, 3 combustion
2 reflected shock, 4 relaxation

bances behind the initial shock, these are amplified by the reflected shock and lead to an increase in density [2].

The intensity trace I_G in the boundary layer at 0.6 mm from the endwall does not resolve the incident and reflected shock. Due to the increase of density within the growing boundary layer at the endwall, the intensity change behind the shock is much larger; the intensity goes to zero at about 200 μsec and to maximum intensity at about 700 μsec . The intensity trace for the test with combustible mixture shows behind the incident shock a relaxation zone (note the difference in time scale) which is due to vibrational relaxation of the methane component, and behind the reflected shock a relaxation zone, which we attribute to the vibrational relaxation of the oxygen component. The intensity is not constant after the vibrational excitation is reached, but continues to change due to the density increase caused by the sidewall boundary layers. Following this change, there is a rapid decrease of intensity which is due to the decrease of density during combustion. The time between the reflected shock and onset of the combustion is the ignition delay time. This time can also be read off the pressure traces, of which typical examples are shown in Figure 3. The upper trace is again for a test in pure argon; the lower trace is for a test with combustible mixture, and it shows that the combustion process causes an increase in pressure. This behavior is in good agreement with characteristics computation of the inviscid flow outside the boundary layer [1].

The change of index of refraction with time (integrated over the length of the beam in the test section L) is related to the change of phase by

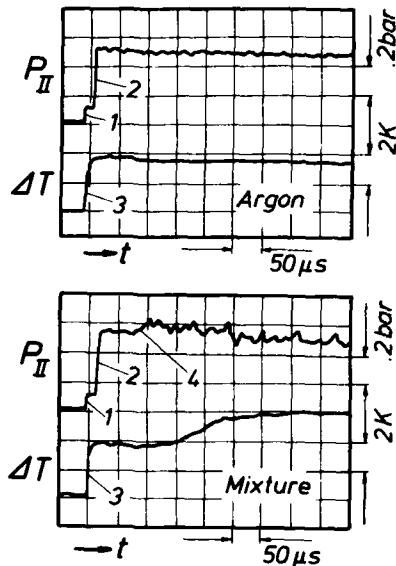


Figure 3: Typical pressure and wall temperature histories
 1 incident shock
 2 reflected shock
 3 temperature jump
 4 combustion

wall smaller than 0.3 mm. Similarity tests of the experimental argon data and comparison with the exact solution indicate a spatial resolution of the optical system of about 0.1 mm. (By these means misalignments of the beam of less than 0.05 mm could be detected.)

Figure 4 shows a comparison of the density histories of three tests with the numerical prediction [1]. In the absence of combustion there is a change of density outside the boundary

$$n(t) - n(o) = \frac{\lambda}{L} \frac{\delta(t) - \delta(o)}{2\pi} \quad (2)$$

where λ is the observing wavelength.

From the change of index of refraction we compute the density change from

$$n(t) - 1 = K\rho(t) \quad (3)$$

since the Gladstone-Dale-Constant $K = \sum K_i \rho_i / \rho$ is almost constant, even for the burnt mixture as the numerical computation shows. Here K_i is the specific refractivity of the i -th component, ρ_i its partial density.

Extensive tests were made in pure argon, where the boundary layer is selfsimilar and an exact solution exists. The tests show, that the effect of refraction precludes measurement of density histories for distances from the end-

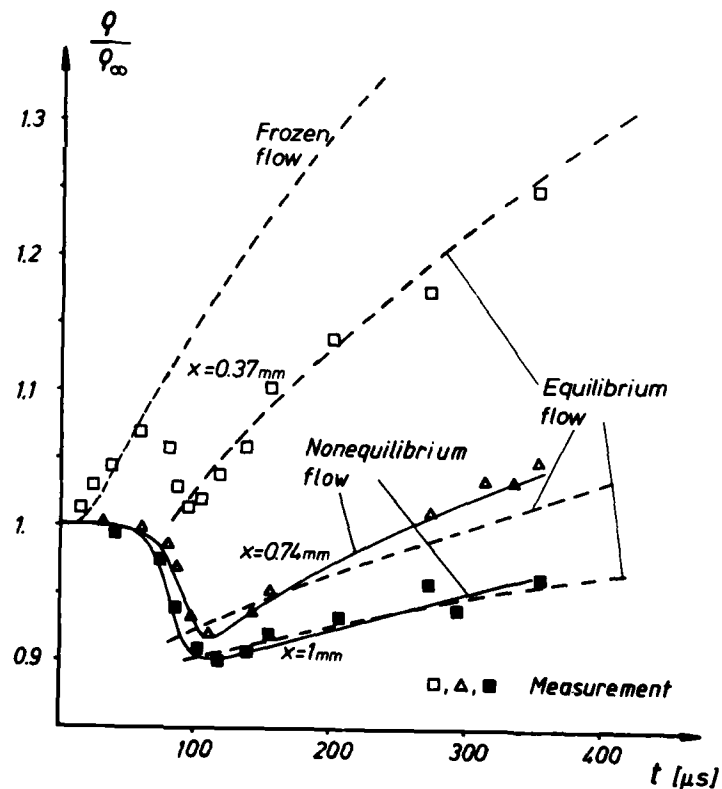


Figure 4: Comparison of measured and computed density histories
 (Computation are based on $T(t=0) = 2017 \text{ K}$, $p(t=0) = 0.52 \text{ bar}$)

layer as discussed above. In order to eliminate this effect the density in the boundary layer is referred to this slowly varying density. In this sense, the boundary layer without combustion or before the combustion sets in, is a quasisimilar boundary layer {1}. The tests at $x = 0.74$ mm and $x = 1.00$ mm have the same shock velocities and therefore the same initial conditions. The numerical computations were based on these test conditions. The agreement between the prediction and the experiments is very good. The test with $x = 0.37$ mm has a different shock velocity so that the experiments cannot immediately be compared with the above mentioned computations. However, here too, the experimental trace follows the curve for frozen flow until the flame reaches the measuring positions and caused a decrease of density. The experimental points then approach the curve for equilibrium flow.

Figure 5 shows the ignition delay time versus equilibrium temperature behind the shock, computed on the basis of Bowman's reaction mechanism {3} including Zel'dovich mechanism {9} assuming homogeneous isobaric conditions. Also shown are experimental delay times. The triangles represent typical delay times taken from the pressure near the endwall and the squares are delay times from the density traces measured 14 mm from the endwall. Our experimental results are in good agreement with Skinner's interpolation formula, evaluated for the concentrations of our mixture {4}. In order to make experimental and theoretical delay times agree, we have changed the preexponential factor in the start reaction $\text{CH}_4 + \text{M} \rightarrow \text{CH}_3 + \text{H} + \text{M}$ from Bowman's value of 1.4×10^{17} to 6.7×10^{17} .

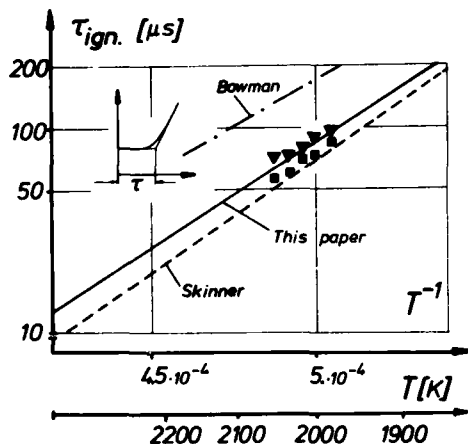


Figure 5: Ignition delay time.

The lower traces show the temperature for a test with combustible mixture, from which the heat transfer rate may be computed. Alternatively, one may compute the temperature change at the surface of the endwall from the theoretical heat transfer, and compare it immediately to the measured temperature distribution, as is done in Figure 6. The computations are based on a noncatalytic wall. Agreement during ignition delay time $\tau_{\text{ign}} < t$ is quite good, but larger differences especially in the slope of the temperature curve are apparent for later times.

While these differences may be caused by catalytic action of the endwall, it may also be due to the fact that Bowman's reaction mechanism does not correctly describe the reaction in the

This value was determined on the basis of extensive characteristic computation of the outer flow in which the pre-exponential factor was varied to give best agreement between measured and computed pressure.

Figure 3 also shows temperature traces, which represent the surface temperatures of (thin film) heat gages mounted in the endwall of the tube. The upper trace, for a test in pure argon, shows the jump in temperature and the subsequent constant wall temperature associated with the similarity nature of this boundary layer.

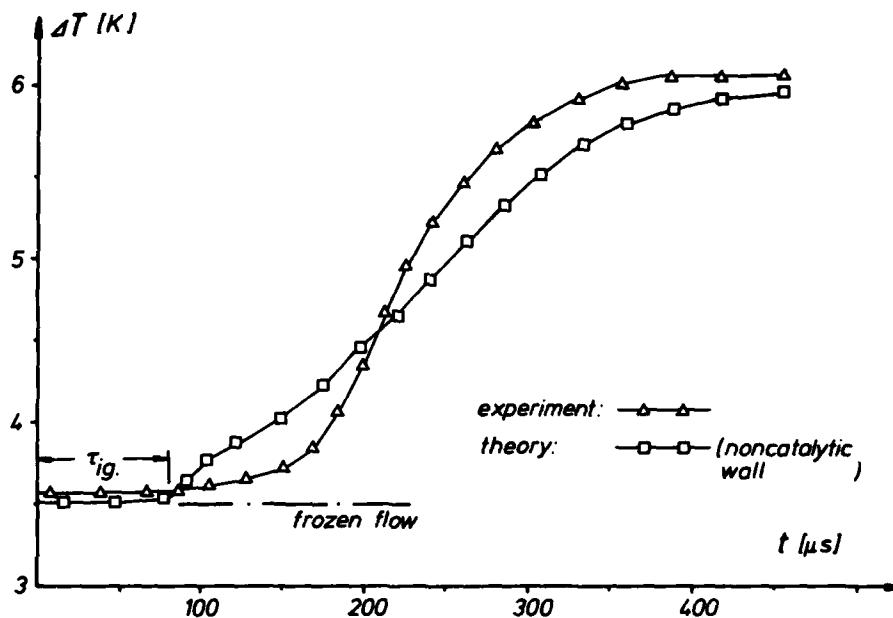


Figure 6: Wall temperature history (computations are based on $T(t=0) = 2017 \text{ K}$, $p(t=0) = 0.52 \text{ bar}$)

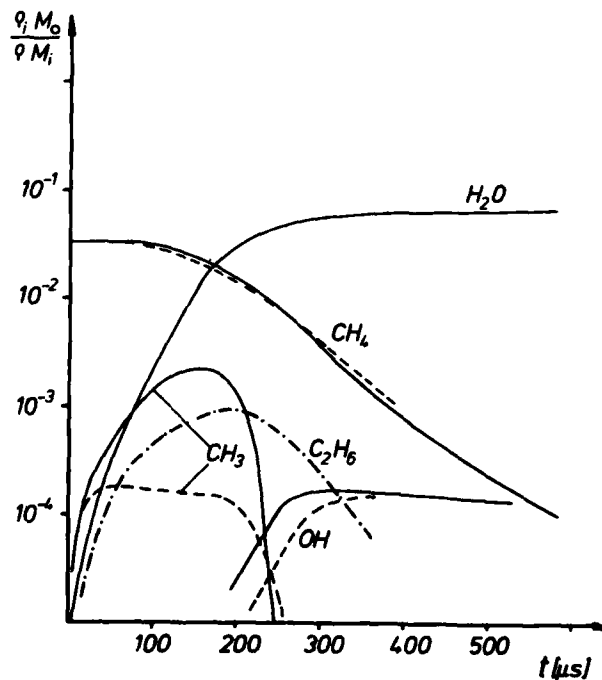


Figure 7: Wall concentrations (solid line based on Bowman [3], broken lines with inclusion of Warnatz reactions [5])

cold portion of the boundary layer. Warnatz [5] has proposed a scheme which includes C_2 -hydrocarbon reactions and which should be better suited for the cold portion of the boundary layer. Some of his reactions (Table 1) were therefore included in our numerical computations. There was almost no change in predicted heat transfer and no change in ignition delay time. The most noteworthy changes occurred in the concentrations near the wall. These changes are shown in Figure 7, where some concentrations at the wall are shown as a function of time.

3) Absorption Measurements.

Despite some difference in heat transfer rates between theory and experiment, the results show, that the overall behaviour of the boundary

Reaction				A{cm,Mol,s}	n	E{cal/Mol}
1		C_2H_6	.4	E + 53	-12	16 200 ¹⁾
2	$CH_3 + CH_3 \rightleftharpoons$	$C_2H_5 + H$.8	E + 15	0	26 512
3		$C_2H_4 + H_2$.1	E + 17	0	32 005
4	H \rightleftharpoons	$C_2H_5 + H_2$.54	E + 3	3.5	5 207
5	$C_2H_6 + O \rightleftharpoons$	$C_2H_5 + OH$.3	E + 8	2	5 111
6	OH \rightleftharpoons	$C_2H_4 + H$.63	E + 7	2	645
7	$C_2H_5 \rightleftharpoons$	$C_2H_4 + H$.14	E + 39	-7	59 500 ¹⁾
8	$C_2H_4 + O \rightleftharpoons$	$CH_3 + HCO$.2	E + 14	0	2 293
9	OH \rightleftharpoons	$CH_3 + H_2CO$.7	E + 36	-7	9 100 ¹⁾

Table 1: Reaction scheme for higher hydrocarbons

(1) Value for 1 bar)

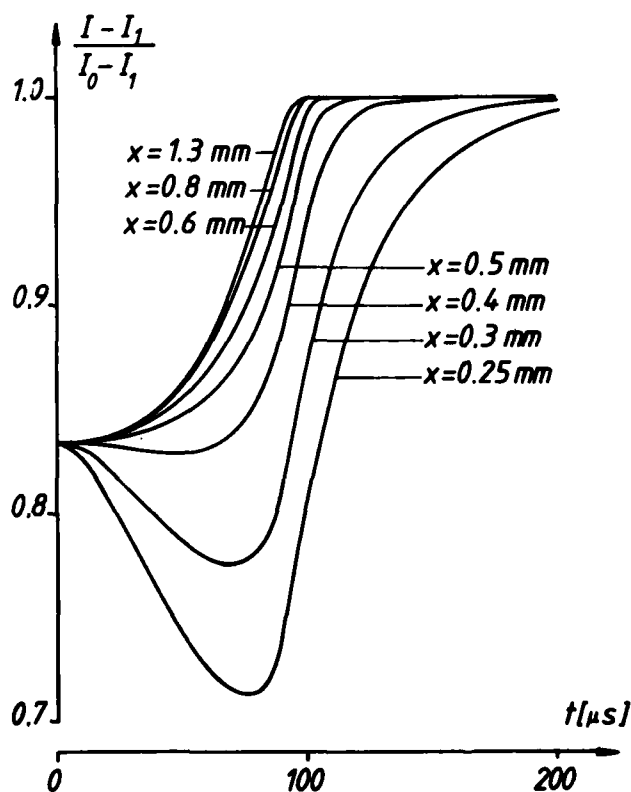


Figure 8: Intensity ratio in the boundary layer for methane absorption (same condition as Fig. 4)

layer is well predicted by the numerical computation. For more detailed information, it is necessary to measure concentrations in the boundary layer. Since the 3.39 μ m He-Ne-Laser line is absorbed by gaseous hydrocarbons, especially methane, diagnostic methods, using the absorption of this line, have found application in flow field studies and kinetics experiments. The use of the method in boundary layer flow requires a narrow beam to give sufficient spatial resolution. Attention must also be paid to problems of beam refraction, since here, one is dealing with absorption near the center frequency, where the index of refraction of the absorbing species can become quite large, and depends on the line profile and therefore on the physical conditions.

We report here on some experiments of preliminary nature, which

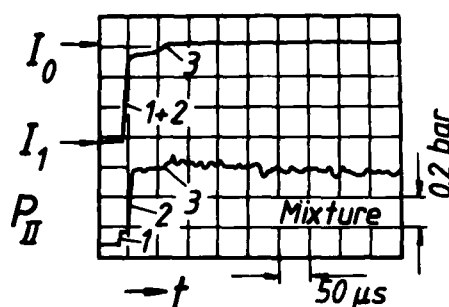


Figure 9: Intensity trace at
 $x = 1.3$ mm
 1 incident shock
 2 reflected shock
 3 combustion

were done to investigate the feasibility of this technique for boundary layer work. The experimental set-up for the absorption measurement was similar to the set-up in figure 1 but without the interferometer. Additional stops on the detector side and a filter were used to eliminate signals from emission. The beam was split into two beams by a splitter plate; one beam passed the test section and the other was used as reference beam and subtracted from the test beam in order to reduce effects of sawtooth-like intensity variation which are particular to the laser used. Since the beam

is normal to the windows, the reflected beam entered the laser and caused a bothersome modulation of the beam intensity. No special effort was made in these tests to obtain high spatial resolution, the beam having a waist radius of about 0.12 mm in the center of test section and a radius of 0.25 mm at the windows. In order to get an idea of what to expect from these measurements we have plotted in Figure 8 the theoretical intensity $(I - I_1)/(I_0 - I_1)$ as a function of time for various distances from the wall for a typical test condition. I_1 is the ratio of transmitted to incident intensity after filling the shock tube. (Our measurement gave a value of $I_1 \approx 0.9$ at 7 mbar pressure, while the computed value based on the absorption coefficient at room temperature according to [6] gave $I_1 \approx 0.895$.) I_0 is the ratio of intensity ($=1$) after combustion is completed and all methane is consumed. I is the intensity ratio during combustion computed from the boundary layer solution and using the temperature fit to the absorption coefficients of references [6], [7].

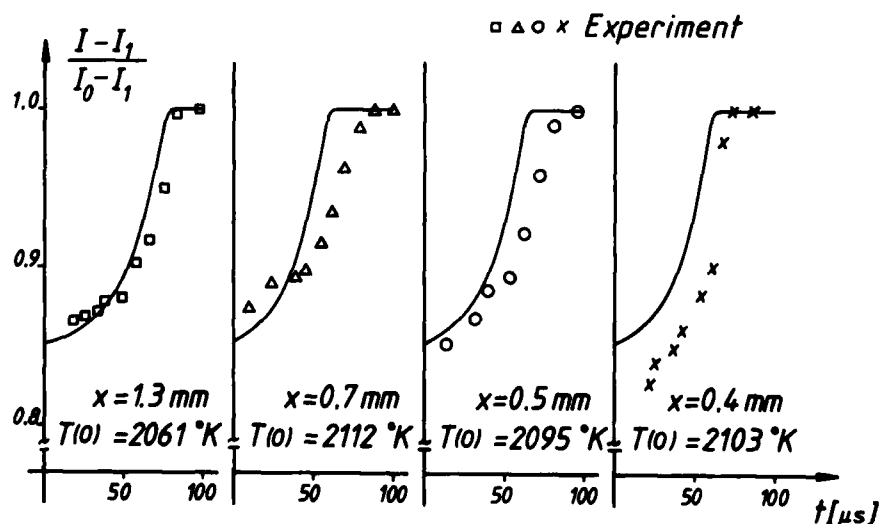


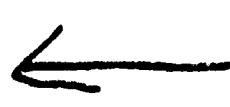
Figure 10: Experimental intensity histories for methane absorption (Theoretical curve is the history outside the boundary layer)

As Figure 8 shows, the intensity behaviour in the boundary layer does not differ much from the behaviour outside the boundary layer ($x=1.3$ mm for the time interval in fig. 8) until distances very close to the wall are reached. The intensity ratio $(I-I_1)/(I_0-I_1)$ can also be formed from the experimental intensity traces such as are shown in Figure 9, where a large change in intensity can be seen across the shock and relatively small changes during combustion. In these experiments there was no beam refraction noticeable. In Figure 10, we show experimental intensity histories $(I-I_1)/(I_0-I_1)$ for various wall distances. The theoretical curve, based on the absorption data of ref [8], are the intensity histories outside the boundary layer, computed for the physical conditions of the corresponding experiment. This preliminary data did not warrant the more expensive boundary layer computation. Because of the poor resolution and still considerable uncertainty of the absorption coefficient at high temperature, no quantitative comparison is appropriate; qualitatively, however, the experiments bear out the results of the numerical computations, namely, that there is little difference between the intensity curves in the boundary layer and outside the boundary layer.

4) Concluding remarks.

Density measurement of high spatial and temporal resolution were made in a reacting boundary layer. The measurements show that the overall boundary layer behaviour is correctly predicted by Bowman's reaction scheme if the start reaction is slightly changed to give the measured ignition delay times. The difference in measured and computed surface temperatures suggests catalytic action of the wall rather than inapplicability of the reaction scheme. Measurements of methane absorption are feasible and are also in accord with prediction.

5) References:

- 1) Keiper, R., Spurk, J.H., to appear J. Fluid Mech.
 - 2) Rudinger, G., Phys. of Fluids 4, 1961, p. 1463
 - 3) Bowman, G.T., 15th Symp. (Int.) on Combustion, 1974, p. 869
 - 4) Skinner, G.B., J. Chem. Phys. 56, 1972
 - 5) Warnatz, J., 18th Symp. (Int.) on Combustion, Waterloo/Canada, 1980
 - 6) Olson, D.B. et. al., Applied Spectroscopy, 1978, 32, p. 489
 - 7) Mallard, W.G. et. al., J. Quant. Spectrosc. Radiat. Transfer, 1978, 20, p. 135
 - 8) Olson, D.B. et. al., Comb. and Flame, 1978, 32, p. 151
 - 9) Nelson, H.F., AIAA J. 14, 1976, p. 1177
- 

AD P000313

A SINGLE PULSE SHOCK TUBE STUDY OF SOOT FORMATION FROM BENZENE PYROLYSIS

Stephen N. Vaughn, Thomas W. Lester and Joseph F. Merklin

Kansas State University

Manhattan, KS 66506

Vapor phase benzene diluted in argon has been pyrolyzed in a single pulse shock tube fitted with an in-line, fullport ball valve to facilitate post shock gas sampling. The disappearance of benzene has been shown to be second order with respect to benzene concentration, and the rate constant (over the temperature range of 1300-2300 K) is best described by

$$k = 4.0 \times 10^{14} \exp(-19250/T) \text{ mol}^{-1} \text{ cm}^3 \text{ sec}^{-1}.$$

Product analyses have shown the major products to be acetylene and styrene with trace amounts of diacetylene, methane, vinylacetylene and toluene also detected. Gravimetric analysis of the solid residue has been achieved using a removable liner in the end section of the shock tube. Recovery of solid and gas species was found to be 85-95% of the original reactant mass with increasing temperature until c. 1900 K at which time the fractional soot yields remain constant at 0.8 to 2700 K.

INTRODUCTION

The phenomenon of soot formation has been studied since the early nineteenth century. Recently, the production of soot from hydrocarbon combustion has become of importance from both a pollutant and a performance point of view. When synthetic fuels are introduced in the future, to augment or replace petroleum fuel, the soot formation problem will certainly worsen (1). The high aromatic content of synthetic fuels is responsible for this increased soot formation.

The pyrolysis of aromatic and substituted aromatic compounds has been studied over a wide range of temperatures and carbon atom concentrations. Benzene has been studied frequently, but most of the work has been performed at lower temperatures. The study of Scully and Davies (2) on the soot formation from a number of aromatic hydrocarbons indicated that the yield of soot

appears to be closely connected to the stability of the aromatic ring and the effect of substitutions on that stability.

There is significant evidence for suggesting there are two chemical pathways for the production of soot from benzene. One pathway at low temperatures ($T < 1400$ K) is via biphenyl as the first intermediate (3,4). There also have been arguments that biphenyl is the first major product from the pyrolysis of benzene at higher temperatures. Asaba and Fujii studied benzene pyrolysis in a single pulse shock tube in the temperature range, 1400 - 1900 K and have suggested that biphenyl is an intermediate, based on optical absorptions at 300 nm and 650 nm (5). Graham, et al. reported a rapid decrease in the soot yield from benzene pyrolysis above 1700 K. They ascribed this behavior to a competition between two pathways of benzene disappearance. One, they term "fast" and the other through ring rupture to acetylene, they described as "slow" (6).

EXPERIMENTAL

Benzene (Fisher, Certified Grade) was used without any further purification. Benzene mixtures were made by injecting a known amount of liquid benzene into an evacuated stainless steel bottle (500 cc) and then adding either nitrogen (Matheson, Zero Grade) or argon (Matheson, 99.999%) as a diluent. Mixture concentration was determined by gas chromatographic analysis. The only impurity was toluene ($\sim 0.1\%$).

Test gases were heated by the reflected shock wave in a 5.0 cm i.d. stainless steel shock tube which has been previously described (7). A number of modifications have been made. The shock tube has been fitted with an in-line, full-port ball-valve to facilitate post shock gas sampling (see Fig. 1). The experimental section was constructed with a removable aluminum liner so solid samples can be collected, weighed and analyzed.

Batch gas samples were taken by expanding the reaction zone mixture into a previously evacuated 75 cc stainless steel bottle equipped with a gas-tight three-way valve fitted with a rubber septum on one of its ports. The contents were analyzed on a Tracor (Model 560) gas chromatograph equipped with dual flame ionization detectors. C_1 - C_4 hydrocarbons were analyzed with 182 cm x 4 mm i.d. glass columns packed with carbosieve B. For C_6 and higher hydrocarbons, 3% OV-103 on Supelocoport (Supelco Inc) and for polycyclic aromatic hydrocarbons, SP 2100 columns were used.

An alternate experimental section was constructed that has a removable aluminum liner. This end section has two top plugs for sample introduction. Gas sampling and venting are done via taps in the end flange. The removable liner may be used in one of two ways, that is, the entire liner may be removed from the shock tube and any condensed products adhering to the inside surface may be removed with a suitable solvent, or a specially modified liner, cut into three sections, along with a thick disk fitted against the end flange, may be tared and reweighed after the shock to determine the mass of solid product present. Qualitative analyses were made on the solid residue. The residue on the liner was extracted with cyclohexane and samples were analyzed by gas chromatography and mass spectrometry (Varian Model EM 600).

The second analysis technique using the removable liners has proven to be more successful. Two of the three short cylinders and the 1.2 cm thick end plug are very carefully weighed prior to insertion into the shock tube on a (Mettler, Model H) analytical balance. Numerous blank runs have indicated that the total weight of the three pieces may be reproducibly determined to within ± 0.2 mg of the original mass after shock tube insertion, and shock heating (without any reactant present). When not in use, the modified liner sections are stored in a vacuum desiccator and the interior of the balance has containers of desiccant present. Exposure to air is strictly minimized as most of the difficulty with this technique arises from water absorption.

RESULTS AND DISCUSSION

The pyrolysis of vapor phase benzene was studied over the temperature range of 1300-2700 K. The initial benzene concentration was varied from 0.4 - 1.25 $\mu\text{mole}/\text{cm}^3$, the reaction time which was corrected for the finite cooling rate was varied from 0.1 - 3.0 msec, the total pressure at the reaction zone was varied from 0.4 - 1 MPa. After shock heating, the products and any unreacted benzene was trapped within the reaction chamber by shutting an in-line ball valve. Gas samples were obtained and analyzed by gas chromatography. By determining the amount of unreacted benzene that was contained within the reaction chamber the fractional decomposition could be determined. Other kinetic parameters were determined by measurement of the incident shock velocity (which may be used to calculate T_5 and P_5 , the reaction temperature and pressure respectively) and the transient pressure (which also measures the reaction dwell time). The initial benzene concentration at reaction conditions was calculated from the ideal gas law using the calculated values of T_5 and P_5 and the measured molar concentration of benzene in test gas.

Once the unreacted fraction of benzene has been determined, it may be used along with the other reaction parameters to calculate a disappearance rate constant based on an assumed reaction order. The general form for the integrated rate expression for benzene may be written either as (8)

$$[C_6H_6]_t^{1-n} - [C_6H_6]_o^{1-n} = (n-1)k_n t \quad n \neq 1 \quad (1)$$

or

$$\ln[C_6H_6]_t - \ln[C_6H_6]_o = -k_1 t, \quad n = 1 \quad (2)$$

where n is the reaction order, k is the reaction rate constant, and the subscripts "t" and "o" refer to the time, t , or the initial value, respectively.

Global reaction order and Arrhenius parameters for the decomposition of benzene were determined based on the measured disappearance of benzene. Rate constants were determined by assuming reaction orders and using the appropriate integral rate equations. The best fit to the data was found by assuming that the reaction was second order in benzene concentration. The

rate constant is

$$k = 4.0 \times 10^{14} \exp(-160/RT) (\text{cm}^3 \text{ mole}^{-1} \text{ sec}^{-1}), \quad (3)$$

where the energy of activation is in kJ/mole. Reported values for experimentally determined activation energies range from 125 kJ/mole (5) to 321 kJ/mole (9) and reaction orders of 1, 3/2, and 2. The Arrhenius plot is shown in Fig. 2, and compared with other reported values (see Fig. 3). The results of Hou and Palmer (10) were obtained using a flow reactor. We are in agreement with the flow reactor studies and disagree with the two shock tube studies. This difference may be due to the difficulty in determining the reaction temperature in shock tubes. Asaba and Fujii note only that they calculated the temperature in the "ordinary way" and no information is available on the method used by Mar'Yasin and Nabutovskii. It is likely that flow reactor studies have determined the reaction temperature more accurately than is possible in a shock tube study. We have made a significant effort to insure as accurate temperature determination as possible by measuring both the incident and reflected shock velocities. The temperature is then calculated based on the incident and reflected shock velocities, as suggested by Tschuikow - Roux et al. (11)

Two major gas phase products were detected, acetylene and styrene, along with a number of other products found in trace amounts. These trace products were determined to be methane, ethylene, and a C_4 compound that was identified by a mass spectrometric analysis to be primarily diacetylene with a smaller contribution from vinylacetylene. Quantitative analysis was possible only on the two major products observed. The yields of acetylene and styrene as a function of temperature are shown in Fig. 4. The reaction time was held relatively constant at 2.0 ± 0.5 msec, the initial concentration of benzene was $1.0 \pm 0.4 \mu\text{mole cm}^{-3}$ and the total reaction pressure was 0.7 ± 0.1 MPa.

Acetylene was detected in all experiments that were run above about 1400 K, its yield quickly increased with increasing temperature until a broad maximum (at 20% by mass of the reactant) at about 1650 K. As the reaction temperature was further increased, the yield of acetylene was observed to slowly decrease so that at 2300 K the acetylene yield had decreased to about 70% of the maximum yield.

Also shown in this figure are data points under the prescribed conditions that correspond to the equilibrium yield of acetylene as calculated by Bauer and Duff (12). The experimentally determined acetylene yields agree quite closely with these calculated thermodynamic equilibrium values. This is an indication that the acetylene yields are nearly at equilibrium under the conditions studied.

The striking feature of the yield of styrene is the narrow temperature region for which it is observed. No styrene was detected in any experiments conducted above 1750 K. The styrene behavior is suggestive of that of a reactive intermediate that is produced early in the reaction and then is consumed in the formation of further products. Other gas phase products were

detected but not measured quantitatively, the concentrations were always less than 1% by weight of the original amount of reactant.

The modification of the reaction chamber in our shock tube permits us to measure quantitatively the amount of soot formed in an experiment. The results are also plotted in Fig. 5, together with an estimated material balance. The balance was obtained by summing the measured yields of soot, acetylene, styrene and the amount of remaining benzene. Between 85 and 95 percent of the initial reactant may be accounted for at all temperatures. Probable errors include neglect of any hydrogen gas formed (may represent up to 5% of the total mass) and the loss of small particles that remain in suspension.

The soot fraction was extracted with cyclohexane or benzene and this extract was analyzed by gas chromatography and mass spectrometry. Stable high molecular weight products with molecular weights of 178, 202, 278 and 350 amu were detected by mass spectrometer analysis of an extract of the soot residue. The first two species have been identified by gas chromatography as phenanthrene and pyrene. Of particular interest is that there are large gaps between the highest molecular weights observed, corresponding to the addition of fragments containing six carbon atoms to the previous species. An important species conspicuous by its absence is biphenyl. It has been observed as a major product in the pyrolysis of benzene at lower temperatures (3), but as the temperature increases the yield of biphenyl decreases (10).

Two sets of experiments were conducted to determine the effect of temperature and soot formation. In Set I the initial benzene concentration was $(8 \pm 4) \times 10^{-7}$ mole cm^{-3} , while in Set II the concentration was $(1.1 \pm 0.3) \times 10^{-7}$ mole cm^{-3} . In the course of this phase of experimentation, the temperature was varied from 1400 - 2700 for each set of reactant concentrations. The reaction time was fixed at 2.0 ± 0.5 msec. One-half hour after the reactant was shock heated the excess gas in the experimental section was slowly vented off and the liner sections were removed and carefully reweighed. Soot mass was determined by the measured difference between initial and final liner weights. The yield of soot as a function of temperature is shown in Fig. 6. The fractional soot yield increases from zero at 1400 K to a maximum of ca. 0.8 at 2000 K and higher temperatures. Note that there are several data points at temperatures greater than ca. 2000 K that indicate a decrease in soot yields with increasing temperature. This effect has been determined to be caused by a slower settling rate for soot formed at higher temperatures. Thus not all of the soot produced at higher temperatures will be collected on the liner after a wait of one-half hour. Experiments in which the delay between heating and sample collection was extended to 16 hours indicate a great increase in observed soot. Similar experiments at lower temperatures have demonstrated little or no effect on soot yields.

Suspended soot samples were collected for transmission electron microscopy and it was observed that the soot particles were composed of a large number of spherical units forming long chains. The individual spherical units were about 25 nm in diameter and measurements of the chains indicate a rather wide range of lengths of about 0.5 - 10 μm .

In an effort to obtain information concerning the time frame during which the formation of soot occurs a series of experiments was conducted in which the reaction dwell time was varied between < 0.1 msec and 2.5 sec. Experimental conditions were arranged so that two temperatures (1650 ± 50 K and 1850 ± 50 K) were examined. Initial benzene concentrations were constant at $(0.6 \pm 0.2) \times 10^{-6}$ mole cm^{-3} .

The results obtained at 1650 ± 50 K indicate that the fractional soot yields range from a minimum of 0.11 ± 0.05 at a dwell time of less than 0.1 msec to a maximum of 0.50 ± 0.07 after a dwell time of 2.5 msec. These data as well as results obtained for selected intermediate dwell times are shown in Fig. 7.

Similarly, Fig. 7 shows the fractional soot yields as a function of dwell time for a reaction temperature of 1850 ± 50 K. At this temperature the fractional soot yields range from 0.26 ± 0.05 at a dwell time of less than 0.1 msec to a maximum of 0.59 ± 0.08 after a dwell time of 2.0 msec.

From these results it is evident that there is significant conversion to soot even at the shortest dwell times. It is further evident that the reactions leading to soot are not effectively quenched. Hence the reactions have low activation energies. To analyze the gross behavior of these soot formation steps, we assumed that the formation of soot from radical fragments arising from ring rupture may be considered as a free-radical chain-polymerization. Using this kinetic model we estimate the energy of activation to be 25 kJ/mole and the frequency factor to be $10^{9.9}$ $\text{mol}^{-1} \text{cm}^3 \text{sec}^{-1}$. Both the activation energy and the frequency factor are typical of values observed for radical-molecule reactions (12).

SUMMARY

The overall rate of benzene disappearance has been determined to be second order with respect to benzene concentration and the rate constant may be best expressed as $k = 4.0 \times 10^{14} \exp(-19,250/T) \text{ mol}^{-1} \text{cm}^3 \text{sec}^{-1}$ over the temperature range of 1300 - 2300 K. Comparisons of this study with other similar studies have demonstrated good agreement with flow reactor studies but are in poor agreement with two shock tube studies.

Soot formation has been studied by use of a liner that may be removed from the shock tube after each shock for solvent extraction of solid products or for gravimetric determination of fractional soot yields. Measurements of soot yields in this way, when coupled with gas phase analysis, have resulted in an 85-95% recovery of the original reactant mass over the rather wide temperature range studied (1300 - 2300 K). The good material balance thus obtained lends credibility to the soot determination technique. Qualitative disagreement is observed between a previous study in which the fractional soot yields were determined optically after 2.5 msec (6) and the present study. This previous study found a steady decrease in fractional yields with increasing temperature until at 2200 K no soot is observed, whereas in the present study steadily increasing fractional soot

yields have been observed to plateau (at ca 0.8) up to quite high reaction temperatures (e.g., 2700 K). The observed differences at high temperatures may be readily explained, however, since it has been demonstrated here that much of the soot produced under these conditions is formed during the cooling period.

ACKNOWLEDGEMENTS

Support of this research from Project Squid, Office of Naval Research, and the Kansas Engineering Experiment Station is gratefully acknowledged.

REFERENCES

1. J.P. Longwell, Sixteenth Symposium (International) on Combustion (The Combustion Institute, Pittsburgh, PA, 1977) p. 1.
2. D.B. Scully and R.A. Davies Comb. Flame, 9, 1985 (1965).
R.A. Davies and D.B. Scully, Comb. Flame, 10, 165 (1966).
3. C.T. Brooks, S.J. Peacock and B.G. Reuben, J.C.S. Faraday I, 75, 652 (1979).
4. C.R. Kinney and R.S. Slysh, Proceedings of the Fourth Conference on Carbon (Pergamon Press, New York, 1960) p.301.
5. T. Asaba and N. Fujii, Thirteenth Symposium (International) on Combustion (The Combustion Institute, Pittsburgh, 1973) p. 433.
6. S.C. Graham, J.B. Homer and J.L.J. Rosenfeld, Proc. Roy. Soc. (London), 344A, 259 (1975).
7. W.R. Seeker, T.W. Lester and J.F. Merklin, Rev. Sci. Instrum., 51, 1523 (1980).
8. O. Levenspiel, Chemical Reaction Engineering, 2nd. Ed. (John Wiley and Sons, N.Y., 1972) p. 41.
9. I.L. Mar'Yasin and Z.A. Nabutobskii, Kinetica i Kataliz, 10, 983 (1969).
10. K.C. Hou and H.B. Palmer, J. Phys. Chem., 69, 863 (1965).
11. E. Tschuikow-Roux, J.M. Simmie, and W.J. Quiring, Aero Acta, 15, 511 (1970).
12. R.E. Duff and S.H. Bauer, Los Alamos Report LA-2556, TID-4500 16th. Ed. (1961).
13. J. Nicholas, Chemical Kinetics (Harper and Row, London, 1976) p. 54.

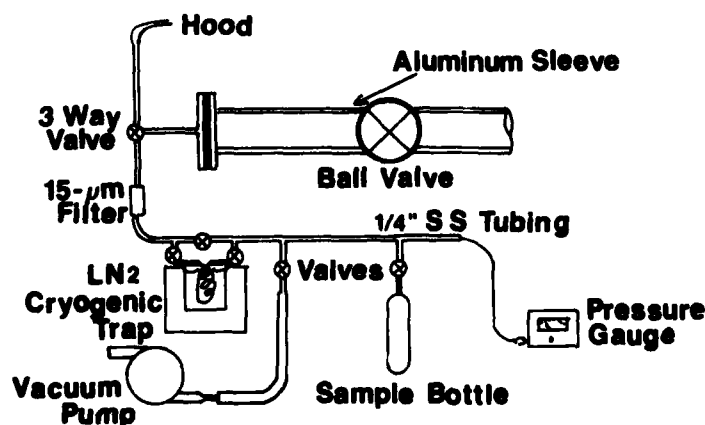


Fig. 1. Post Shock Sample Collection System.

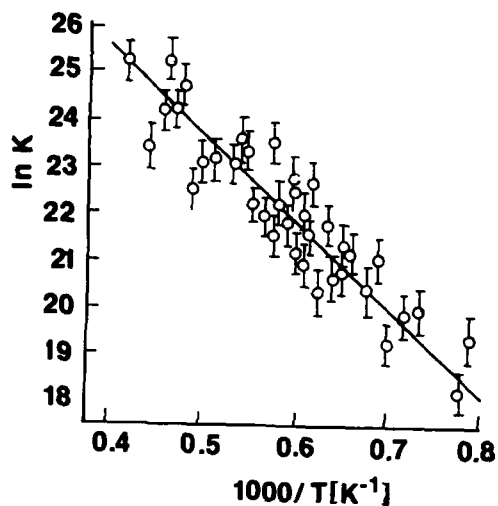


Fig. 2. Arrhenius Plot.

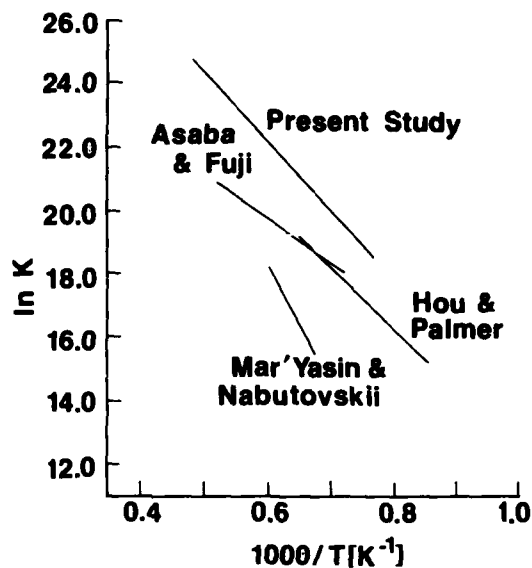


Fig. 3. Comparison of Second Order Arrhenius Plots.

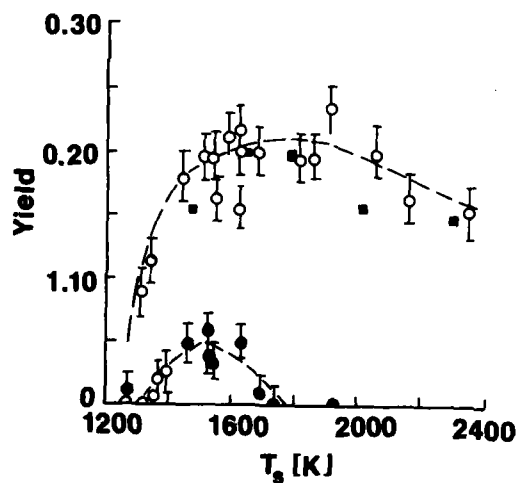


Fig. 4. Yields of Acetylene (open circles) and Styrene (filled circles) as a function of temperature. Squares are calculated equilibrium acetylene yields from (12).

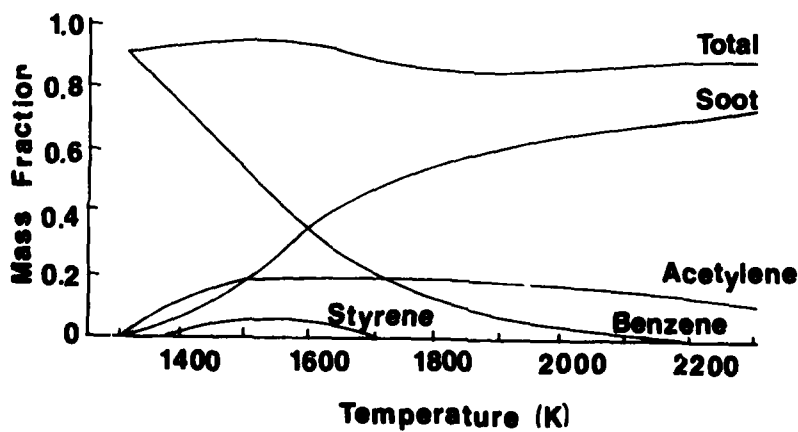


Fig. 5. Material Balance on a mass basis.

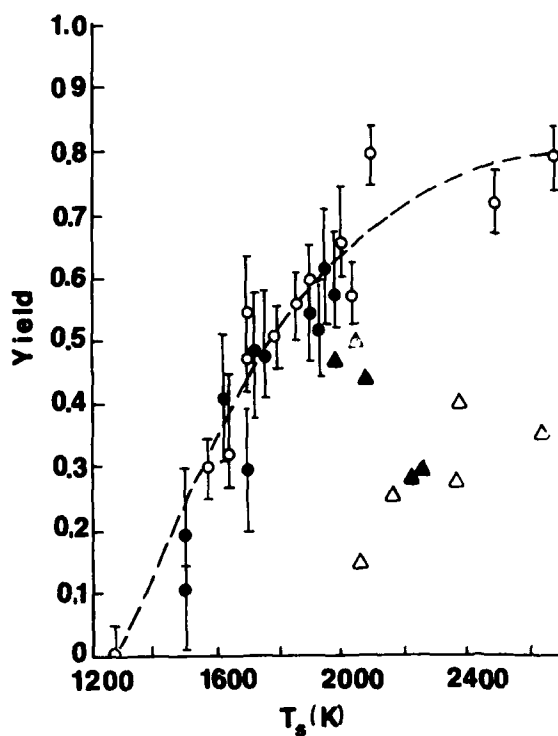


Fig. 6. Soot yields as a function of temperature.

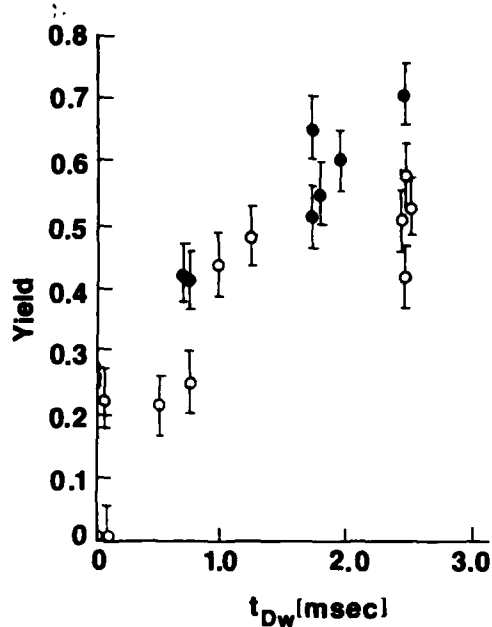


Fig. 7. Soot yields as a function of dwell time.

$[C_6H_6] = 0.6 \times 10^{-6}$ moles cm^{-3}

$P_5 = 0.8$ MPa

$T_5 = 1650$ K (open circles)

$T_5 = 1850$ K (filled circles)

AD P000314

RATES AND MECHANISMS OF FORMALDEHYDE PYROLYSIS AND OXIDATION*

J. M. Kline and S. S. Penner

Energy Center and Department of Applied Mechanics and Engineering
Sciences, University of California, San Diego, La Jolla, CA 92093

Pyrolysis and oxidation rates of formaldehyde have been measured behind reflected shock waves for $1200 \leq T, ^\circ K \leq 2200$ and $1.8 \leq p, \text{atm} \leq 2.7$, in mixtures of $\text{CH}_2\text{O}/\text{Ar}$ and of $\text{CH}_2\text{O}/\text{N}_2\text{O}/\text{CO}/\text{Ar}$, respectively. Concentrations of CH_2O were monitored by absorption of HeXe laser radiation at $3.508 \mu\text{m}$, as well as by CH_2O emission in the infrared. Emissions from CO_2 , H_2O , and CO-O recombination radiation were monitored in the oxidation experiments; CO emission was monitored during pyrolysis.

To account for pyrolysis at late times, it was necessary to allow for direct reaction between H_2 and CH_2O . The 19-step reaction mechanism describes our observed oxidation rates satisfactorily.

1. INTRODUCTION

Formaldehyde (CH_2O) is an intermediate in the oxidation of methane and other hydrocarbons.¹⁻⁴ We have previously studied N_2O pyrolysis;⁵ in reactions with CH_2O , N_2O serves as an O-atom source. Formaldehyde and nitrous oxide are gas-phase products of the decomposition of solid propellant fuels.^{6,7}

Pyrolysis of CH_2O has been studied in the shock-tube,⁸⁻¹¹ with other thermal techniques,¹²⁻¹⁶ and in photolysis.¹⁷⁻²⁰ Formaldehyde oxidation has also been studied in the shock-tube^{8, 21} and by other methods.²² The rates of elementary steps involving CH_2O or CHO have been inferred from shock-tube studies of CH_4 oxidation,^{3, 23, 24} flow-reactor studies of C_2H_4 oxidation,^{25, 26} CH_3CHO oxidation,²⁷ CH_4 flame studies,⁴ and hydrogen²⁸⁻³¹ and carbon monoxide³²⁻³⁵ oxidation. The rate of the

*This research was supported by the U.S. Office of Naval Research under Contract No. N00014-79-C-0261 (monitored by Lt. Richard S. Miller). Details concerning our studies may be found in the Ph.D. thesis of J. M. Kline, University of California, San Diego, 1981.

819

reaction between N_2O and H , which couples the N_2O and CH_2O pyrolyses, has been evaluated.^{21,36-38} A recent study of CH_4 and C_2H_6 oxidation³⁹ has yielded results that are consistent with the mechanisms and rate constants determined in studies of the CH_2O/N_2O system. Several pertinent reviews have also been published.⁴⁰⁻⁴⁴

2. EXPERIMENTAL PROCEDURE

2.1 Determination of Initial CH_2O Concentrations

The initial CH_2O concentration for each test was calculated from observed absorption of $3.508\mu m$ radiation from an HeXe laser. Calibration experiments were performed⁴⁵ in a small cell at $300^\circ K$ to determine the off-peak spectral absorption coefficient for an isolated line in the CH_2O spectrum, using the HeXe laser light source. Pure CH_2O was used to define the line strength (S), the collision-broadened half-width for self-broadening ($b_{C,F}^O$) per unit pressure, and the displacement of the laser frequency from the line center ($\Delta\omega$). Mixtures of CH_2O with Ar and N_2O were employed to determine the collision-broadened half-widths for Ar ($b_{C,Ar}^O$) and N_2O (b_{C,N_2O}^O). The observed spectral absorption coefficients of CH_2O are described by the Voigt profile⁴⁶

$$P_{|\xi|} = P' \frac{a}{\pi} \int_{-\infty}^{\infty} \frac{\exp(-y)^2}{a^2 + (\xi - y)^2} dy,$$

where $P' = (S/\omega_0)(mc^2/2\pi kT)^{1/2}$, $a = b\sqrt{\ln 2}/b_D$, $b_D = (2kT\ln 2/mc^2)^{1/2}\omega$, $b_C = b_{C,F}^O P_F + b_{C,Ar}^O P_{Ar} + b_{C,N_2O}^O P_{N_2O}$, $\xi = (\Delta\omega/\omega_0)(mc^2/2kT)^{1/2}$, $\Delta\omega = \omega - \omega_0$, ω_0 is the frequency at the line center, ω is the frequency of the laser radiation, and the other symbols have their usual meaning. We found⁴⁵ $S = 0.690 \text{ cm}^{-2}\text{-atm}^{-1}$, $b_{C,F}^O = 0.578 \text{ cm}^{-2}\text{-atm}^{-1}$, $b_{C,Ar}^O = 0.0419 \text{ cm}^{-2}\text{-atm}^{-1}$, $b_{C,N_2O}^O = 0.106 \text{ cm}^{-2}\text{-atm}^{-1}$, and $\Delta\omega = 5.04 \times 10^{-3} \text{ cm}^{-1}$.

In our shock tube experiments, $X_F P_{|\xi|} = -\ln(V/V_0)/p\ell$ was measured at known total pressure p ; X_F denotes the CH_2O mole fraction, V_0 the unattenuated laser signal voltage, V the laser signal voltage attenuated by CH_2O absorption in the shock tube prior to passage of the incident shock, ℓ the optical pathlength of the shock tube. It is convenient to find X_F from a plot of $X_F P_{|\xi|}$ vs. p for various X_F .⁴⁵

2.2 Determination of CH_2O Concentration-Time Histories

Our shock-tube facilities are described in Ref. 47. After passage of reflected shock waves, the CH_2O concentration was determined from absorption and emission data. In absorption, we use the relation $X_F = -\ln(V/V_0)/P_{|\xi|} p\ell$. We use the subscript i to identify conditions immediately after passage of the reflected shock wave when $X_{F,0}$ is the initial mole fraction of CH_2O ; the system is nearly isothermal and isobaric until substantial amounts of formaldehyde have disappeared. The CH_2O concentration history is determined from $X_F/X_{F,0} = [\ln(V/V_0)/\ln(V_1/V_0)] \times [(P_{|\xi|} p)_1 / (P_{|\xi|} p)]$.

Formaldehyde emission measurements were performed at $3.5\mu m$ with $\text{FWHM} = 0.039\mu m$. For emission, $V = B^O(\omega, T)K[1 - \exp(-P_{\omega} X_F p\ell)] \approx B^O(\omega, T)K P_{\omega} X_F p\ell$ for $P_{\omega} X_F p\ell \ll 1$; $X_F/X_{F,0} = V/V_1$ for an isothermal and isobaric system at low optical depth.

2.3 Comparison of CH₂O Concentration-Time Histories Derived from Absorption and Emission Measurements

When the CH₂O mole-fraction histories are determined simultaneously from absorption and emission data, three types of results may be observed: the two mole-fraction curves coincide (case 1) when both measurement techniques provide accurate concentration determinations; mole fractions derived from absorption are higher (case 2) when emission data are accurate but absorption occurs by both CH₂O and other species; the concentrations calculated from emission data are higher (case 3) when the absorption data are accurate while emission is observed from CH₂O and other species. For 17 tests, 8 were found to behave as in case 1, 8 (weakly) as in case 3, and 1 as in case 2. We conclude that concentrations of CH₂O should preferably be determined from absorption data, although emission and absorption data were generally found to be in acceptable agreement.

3. RESULTS OF PYROLYSIS AND OXIDATION EXPERIMENTS

3.1 Description of Observations

Twenty-four pyrolysis experiments were performed on CH₂O/Ar mixtures for $1246 \leq T, ^\circ K \leq 2021$, $1.8 \leq p, \text{atm} \leq 2.7$, with CH₂O mole fractions $0.022 \leq X_F \leq 0.13$; 35 oxidation experiments were performed on CH₂O/N₂O/Ar and on CH₂O/N₂O/CO/Ar mixtures with $1380 \leq T, ^\circ K \leq 2123$, $1.8 \leq p, \text{atm} \leq 2.5$, $0.009 \leq X_F \leq 0.062$, and $0.019 \leq X_{N_2O} \leq 0.06$.

3.2 Qualitative Observations Concerning CH₂O Pyrolysis and Oxidation Rates

The temporal behavior of pyrolysis and oxidation rates at low temperatures is summarized by Fig. 1.

The times $t_{0.95}$, $t_{0.5}$, and $t_{0.1}$ are defined as times when the remaining mole fraction of formaldehyde equals 0.95, 0.5, and 0.1 of the initial value, respectively. Examination of our data shows that, for $T \leq 1500^\circ K$, the initial rates of pyrolysis and oxidation (as measured by $t_{0.95}$) are nearly the same; at later times, pyrolysis leads to more rapid decomposition of CH₂O than oxidation. For $T \geq 1500^\circ K$, the initial rates of oxidation are somewhat greater than the rates of pyrolysis; for $t > t_{0.95}$, the rates of pyrolysis and oxidation are approximately equal. Thus, the presence of N₂O appears to decrease the "postinduction" CH₂O decomposition rates for $T \leq 1500^\circ K$; it does not significantly affect the "postinduction" CH₂O decomposition rates for $T \geq 1500^\circ K$.

3.3 Shock-Tube Test Times

In order to verify that measurements of $t_{0.95}$, $t_{0.5}$, and $t_{0.1}$ are meaningful, we have calculated shock-tube test times according to the procedure of Price⁴⁸ and Hooker.⁴⁹ All of the calculated test times are more than a factor of three longer than the test times used by us.

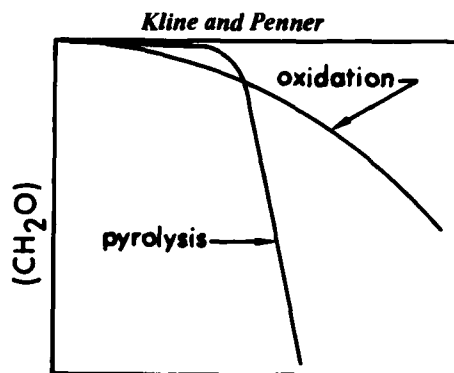


Fig. 1 Schematic diagram showing the observed formaldehyde concentrations as functions of time during pyrolysis and oxidation at the same pressure and low temperature. After (H) reaches a steady state value, the rate of pyrolysis is determined by the 4-step Rice-Herzfeld mechanism and is subsequently strongly increased when H production accelerates formaldehyde decomposition. Initially, oxidation occurs more rapidly than pyrolysis because of contributions from the elementary steps involved in the 19-step mechanism. However, the product hydrogen is now less effective in accelerating formaldehyde decomposition because it is removed not only by an overall reaction with formaldehyde but also by reaction with N_2O , O, OH, etc. As the result, removal of formaldehyde by pyrolysis proceeds more rapidly than removal during oxidation at late times for low temperatures ($T \lesssim 1600^\circ K$). The "induction times" to which we refer during pyrolysis correspond to the regime when the 4-step mechanism applies.

4. COMPARISONS OF PREVIOUS AND PRESENT INVESTIGATIONS ON CH_2O PYROLYSIS AND OXIDATION

In the work of Schecker and Jost³ and of Dean et al,¹⁰ CH_2O concentrations were monitored after shock heating by emission at $3.5\mu m$. Gay et al⁸ used a time-of-flight mass spectrometer to determine the concentrations of CH_2O and other species.

The presence of an "induction period" in CH_2O pyrolysis is shown by Gay et al⁸ in their Fig. 2; we have found that the temperature dependences of these times are nearly identical to those observed by us. The absolute values of the "induction times" in Ref. 8 are 5-7 times longer than ours for tests performed at total pressures approximately 6-7 times lower than ours. Thus, the "induction times" t_i of Ref. 8 are consistent with apparent "induction times" observed by us if $t_i \propto (M)^{-1}$, where (M) represents the total gas concentration.

The presence of an "induction period" in CH_2O pyrolysis has been reported also by Schecker and Jost³ and by Dean et al.¹⁰ Just⁵⁰ measured H-atom concentrations by resonance absorption for $X_F \lesssim 50ppm$; for $X_F = 6 \times 10^{-4}$, absorption was measured at 1730A. Just⁵¹ noted that the data of Dean et al¹⁰ could be modeled by the mechanism of Ref. 11 with a slight change in one rate constant.

Gay et al⁸ reported that the presence of O_2 "greatly accelerated" the initial disappearance of CH_2O . This summary statement is qualitatively consistent with our observations at elevated temperatures.

4.1 Mechanism and Rates for CH₂O Pyrolysis

As was noted in Section 3.1, we observed slow initial CH₂O decomposition rates, which are well described by the four-step Rice-Herzfeld mechanism $\text{CH}_2\text{O} + \text{M} \xrightarrow{k_1} \text{CHO} + \text{H} + \text{M}$, $\text{CH}_2\text{O} + \text{H} \xrightarrow{k_2} \text{CHO} + \text{H}_2$, $\text{CHO} + \text{M} \xrightarrow{k_3} \text{CO} + \text{H} + \text{M}$, $\text{CHO} + \text{H} \xrightarrow{k_4} \text{CO} + \text{H}_2$. Numerical integrations (with the computer program of Bittker and Scullen⁵²) have been performed for this 4-step mechanism for our experiments. The calculations refer to constant enthalpy and volume, which correspond to conditions prevailing behind the reflected shock waves. The rate constants for the initial calculations were taken from Dean et al.²¹ The results of the numerical integrations were used to determine the times $t_{0.95}$, $t_{0.5}$, and $t_{0.1}$ (cf. Sec. 3.2). Agreement between observed and calculated values for $t_{0.95}$ was found to be acceptable, whereas large discrepancies occurred for $t_{0.5}$ and $t_{0.1}$, except at the highest temperatures ($T \geq 2000^\circ\text{K}$). Thus, the 4-step mechanism is inadequate to describe either our observations of pyrolysis rates or those of other investigators who have noted "induction times". A satisfactory empirical fit to our data is obtained if we assume that pyrolysis is effectively autocatalytic, with formaldehyde decomposition accelerated by the presence of H₂ in such a manner that the following overall decomposition rate is observed: $(\dot{\text{CO}}) = (\dot{\text{H}}_2) = -(\text{CH}_2\text{O}) = k_{\alpha}(\text{CH}_2\text{O})(\text{H}_2)$ corresponding to a nearly thermoneutral overall reaction with $k_{\alpha} = 2.4 \times 10^{13} \exp(-16,400/RT)$;* the direct decomposition of CH₂O into CO and H₂ on collision with another molecule has been proposed previously, albeit with rate constants having activation energies two⁴ to four^{50,51} times larger than we require. The value $k_2 = 1.00 \times 10^{14} \exp(-10,500/RT)$ was used because it provided a good fit to early time data; this value for k_2 is about one-third of that of Dean et al.²¹ Results for $T = 1480$ and 2000°K are shown in Fig. 2. The observed good agreement is representative of fits to measured pyrolysis results which we have obtained.

4.2 Mechanism and Rates for CH₂O Oxidation by N₂O

Our observations on oxidation of CH₂O by N₂O are reasonably well accounted for by numerical calculations using the 19-step mechanism of Dean et al.²¹ We used the rate constants of Dean et al.,²¹ except for the reactions of N₂O with M and O for which we used our rate constants from Ref. 5; if we had used the values from Ref. 21, no substantial changes would be observed. The results of computer calculations were also used to determine $t_{0.95}$, $t_{0.5}$ and $t_{0.1}$. These values were plotted as functions of $10^4/T(^{\circ}\text{K})$ and compared with least-squares fits to our measured values; agreement was generally observed to fall within one standard deviation.

When the 19-step mechanism is augmented by the overall process $\text{CH}_2\text{O} + \text{H}_2 \xrightarrow{k_{\alpha}} \text{CO} + 2\text{H}_2$ with k_{α} derived from pyrolysis measurements (Sec. 4.1), agreement with observations becomes poor at low temperatures but is good at high temperatures (see Fig. 3). Addition of the direct reaction $\text{N}_2\text{O} + \text{H}_2 \xrightarrow{k_{\gamma}} \text{N}_2 + \text{H}_2\text{O}$ provides minor improvement. These calculations show that the many rate constants in the 19-step mechanism have been adjusted to describe the CH₂O-N₂O oxidation processes and that the addition of other processes will require modifications in the reaction system if it is to fit also for $T \lesssim 1600^\circ\text{K}$ and large CH₂O concentrations.

*Rate constants are in cm³/mole-sec.

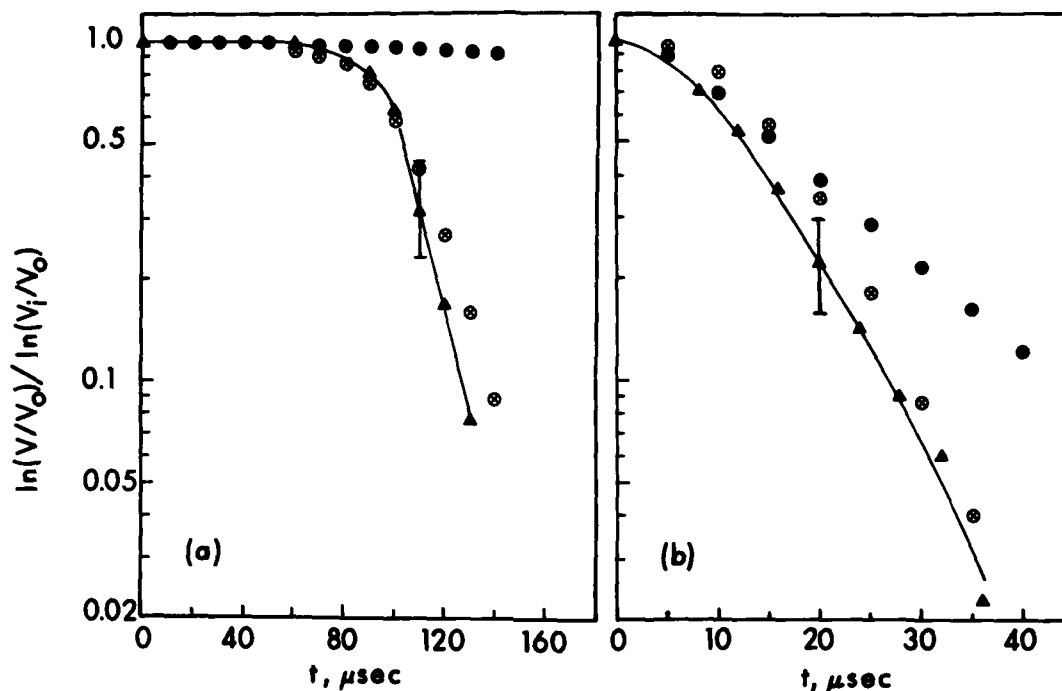


Fig. 2 The ratios of the logarithm of the observed to the logarithm of the initial transmissivity (in laser absorption) are shown as functions of time during pyrolysis for (a) $T_5=1480^\circ\text{K}$, $p_5=2.43$ atm, $X_{F,0}=0.0393$ and (b) $T_5=2000^\circ\text{K}$, $p_5=1.91$ atm, $X_{F,0}=0.0308$. The lines are drawn through the experimental data (Δ) for which representative error bars are indicated. The calculated results shown for the 4-step (\bullet) and 5-step mechanisms (\otimes) have been obtained by using the measured temperature dependence for the spectral absorption coefficient of CH_2O at $3.508\mu\text{m}$.

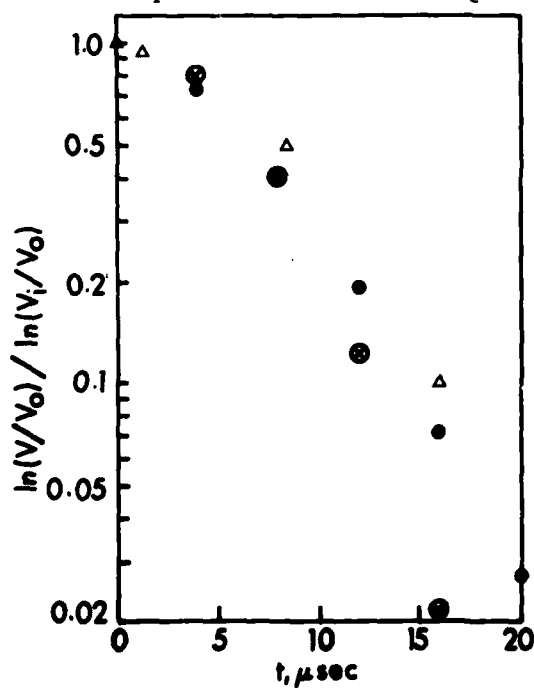


Fig. 3 The ratios of the logarithm of the observed to the logarithm of the initial transmissivity averaged over many tests (Δ) are shown as a function of time during oxidation for $T_5=1930^\circ\text{K}$. The calculated results shown ($p_5=2.16$ atm, $X_{F,0}=0.0612$, $X_{N_2O,0}=0.0282$) for the 19-step (\bullet) and 20-step (\otimes) mechanisms have been obtained by using the measured temperature dependence for the spectral absorption coefficient of CH_2O at $3.508\mu\text{m}$.

Pyrolysis measurements at late times require introduction of an additional rate constant, which does not destroy agreement with observed oxidation rates for $T \geq 1800^\circ\text{K}$.

5. CONCLUSIONS

Our experiments were performed in the temperature range $1200 \leq T, ^\circ\text{K} \leq 2200$, with relatively high initial CH_2O concentrations. We have found that for pyrolysis, with $T \leq 1700^\circ\text{K}$, the 4-step mechanism does not account for the observed CH_2O -time histories while the 5-step mechanism does. For higher temperatures, the differences between the 4- and 5-step mechanisms become smaller and probably fall within experimental error for $T \geq 1900^\circ\text{K}$. For initial CH_2O mole fractions $\leq 1\%$, the 4-step mechanism agrees with experimental observations for $T \geq 1600^\circ\text{K}$. The work of Gay et al.⁸ was performed at temperatures and CH_2O mole fractions similar to ours. Their data (cf. Fig. 1 of Ref. 8) are also modeled by the 5-step mechanism with a revised value for k_α .

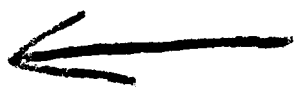
For oxidation of CH_2O by N_2O with $T \geq 1600^\circ\text{K}$, both the 19- and 20-step mechanisms provide acceptable agreement with experiments. For $T \leq 1600^\circ\text{K}$, the 19-step mechanism is better than the 20-step mechanism but reevaluation of the rate constants or the addition of other elementary steps (e.g., steps involving the HO_2 radical) might well change this conclusion. It should be noted that low-temperature oxidation rates have not been observed previously with as high formaldehyde concentrations as were used by us.

Further work in this field should emphasize direct measurements of reaction processes between formaldehyde and hydrogen. Definitive studies must involve time-dependent measurements of reaction intermediates (e.g., H_2 , OH , O) occurring during pyrolysis and oxidation. We do not regard the empirically determined direct reaction between CH_2O and H_2 as a likely elementary step.

REFERENCES

1. W. C. Gardiner, Jr., and D. B. Olson, *Ann. Rev. Phys. Chem.* **31**, 377 (1980).
2. C. K. Westbrook and F. L. Dryer, 18th Symp. (Int.) on Combustion. The Combustion Institute, Pittsburgh, Pennsylvania (in press).
3. C. T. Bowman, 15th Symp. (Int.) on Combustion, pp. 869-882. The Combustion Institute, Pittsburgh, Pennsylvania (1975).
4. J. Peeters and G. Mahnen, 14th Symp. (Int.) on Combustion, pp. 133-146. The Combustion Institute, Pittsburgh, Pennsylvania (1973).
5. K. G. P. Sulzmann, J. M. Kline, and S. S. Penner, Proc. 12th Int. Symp. on Shock Tubes and Waves, pp. 465-475. The Magnes Press, Jerusalem, Israel (1980).
6. A. J. B. Robertson, *Trans. Faraday Soc.* **45**, 85 (1949).
7. B. Suryanarayana, R. J. Graybush, and J. R. Autera, *Chem. Ind.*, p. 2177 (1967).
8. I. D. Gay, G. P. Glass, G. B. Kistiakowsky, and H. Niki, *J. Chem. Phys.* **43**, 4017 (1965).

9. H. G. Schecker and W. Jost, *Ber. Bunsenges. Phys. Chem.* **73**, 521 (1969).
10. A. M. Dean, B. L. Craig, R. L. Johnson, M. C. Schultz, and E. E. Wang, 17th Symp. (Int.) on Combustion, pp. 577-586. The Combustion Institute, Pittsburgh, Pennsylvania (1979).
11. K. A. Bhaskaran, P. Frank, and Th. Just, Proc. 12th Int. Symp. on Shock Tubes and Waves, pp. 503-513. The Magnes Press, Jerusalem, Israel (1980).
12. R. D. Klein, M. D. Scheer, and L. J. Schoen, *J. Am. Chem. Soc.* **78**, 50 (1955).
13. W. R. Brennen, I. D. Gay, G. P. Glass, and H. Niki, *J. Chem. Phys.* **43**, 2569 (1965).
14. A. A. Westenberg and N. deHaas, *J. Phys. Chem.* **76**, 2213 (1972).
15. A. A. Westenberg and N. deHaas, *J. Phys. Chem.* **76**, 2215 (1972).
16. C. J. Chien and D. J. McKenney, *Can. J. Chem.* **56**, 992 (1972).
17. J. R. McNesby, M. D. Scheer, and R. Klein, *J. Chem. Phys.* **32**, 1814 (1960).
18. J. P. Reilly, J. H. Clark, C. B. Moore, and G. C. Pimentel, *J. Chem. Phys.* **69**, 4381 (1978).
19. R. Atkinson and J. N. Pitts, Jr., *J. Chem. Phys.* **68**, 3581 (1978).
20. R. B. Klemm, *J. Chem. Phys.* **71**, 1987 (1979).
21. A. M. Dean, R. L. Johnson, and D. C. Steiner, Combustion and Flame **37**, 41 (1980).
22. M. D. Scheer, 5th Symp. (Int.) on Combustion, pp. 435-446. Reinhold, New York (1955).
23. T. Asaba, K. Yoneda, N. Kakihara, and T. Hikita, 9th Symp. (Int.) on Combustion, pp. 193-200. Academic Press, New York (1963).
24. C. T. Bowman, *Combust. Sci. & Tech.* **2**, 161 (1970).
25. H. Niki, E. E. Daby, and B. Weinstock, 12th Symp. (Int.) on Combustion, pp. 277-288. The Combustion Institute, Pittsburgh, Pennsylvania (1969).
26. N. Washida, R. I. Martinez, and K. D. Bayes, *Z. Naturf.* **29A**, 251 (1974).
27. M. B. Colket, D. W. Naegeli, and I. Glassman, 16th Symp. (Int.) on Combustion, pp. 1023-1039. The Combustion Institute, Pittsburgh, Pennsylvania (1977).
28. I. M. Campbell and B. A. Thrush, *Trans. Faraday Soc.* **64**, 1265 (1968).
29. W. C. Gardiner, Jr., W. G. Mallard, M. McFarland, K. Morinaga, J. H. Owen, W. T. Rawlins, T. Takeyama, and B. F. Walker, 14th Symp. (Int.) on Combustion, pp. 61-75. The Combustion Institute, Pittsburgh, Pennsylvania (1973).
30. G. L. Schott, Combustion and Flame **21**, 357 (1973).
31. G. L. Schott, R. W. Getzinger, and W. A. Seitz, *Int. J. Chem. Kinet.* **6**, 921 (1974).
32. W. E. Wilson and J. T. O'Donovan, *J. Chem. Phys.* **47**, 5455 (1967).
33. M. C. Lin and S. H. Bauer, *J. Chem. Phys.* **50**, 3377 (1969).
34. A. M. Dean and G. B. Kistiakowsky, *J. Chem. Phys.* **53**, 830 (1970).
35. A. M. Dean and D. C. Steiner, *J. Chem. Phys.* **66**, 598 (1977).
36. H. Henrici and S. H. Bauer, *J. Chem. Phys.* **50**, 1333 (1969).
37. C. P. Balakhnine, J. Vandooren, and P. J. Van Tiggelen, Combustion and Flame **28**, 165 (1977).
38. A. M. Dean, D. C. Steiner, and E. E. Wang, Combustion and Flame **32**, 73 (1978).

39. A. M. Dean and R. L. Johnson, *Combustion and Flame* **37**, 109 (1980).
40. F. Kaufman, *Can. J. Chem.* **47**, 1917 (1969).
41. H. Gg. Wagner, 14th Symp. (Int.) on Combustion, pp. 27-36. The Combustion Institute, Pittsburgh, Pennsylvania (1973).
42. D. L. Baulch, D. D. Drysdale, D. G. Horne, and A. C. Lloyd, Evaluated Kinetic Data for High Temperature Reactions, Vol. 1. CRC Press, Cleveland, Ohio (1972).
43. D. L. Baulch, D. D. Drysdale, and D. G. Horne, Evaluated Kinetic Data for High Temperature Reactions, Vol. 2. Butterworths, London, England (1973).
44. D. L. Baulch, D. D. Drysdale, J. Duxbury, and S. J. Grant, Evaluated Kinetic Data for High Temperature Reactions, Vol. 3. Butterworths, London, England (1976).
45. J. M. Kline and S. S. Penner, *J. Quant. Spectrosc. & Radiat. Transfer* **24**, 185 (1980).
46. S. S. Penner, Quantitative Molecular Spectroscopy and Gas Emissivities. Addison-Wesley, Reading, Massachusetts (1959).
47. W. M. Heffington, G. E. Parks, K. G. P. Sulzmann, and S. S. Penner, 16th Symp. (Int.) on Combustion, pp. 997-1101. The Combustion Institute, Pittsburgh, Pennsylvania (1977).
48. M. L. Price, Ph.D. Thesis, University of California, San Diego (1970).
49. W. J. Hooker, *Physics Fluids* **4**, 1451 (1961).
50. Th. Just, Shock Waves in Chemistry (edited by A. Lifshitz). Marcel Dekker, New York (in press).
51. Th. Just, 17th Symp. (Int.) on Combustion, pp. 584-585. The Combustion Institute, Pittsburgh, Pennsylvania (1979).
52. D. A. Bittker and V. J. Scullen, General Chemical Kinetics Computer Program for Static and Flow Reactions, with Application to Combustion and Shock-Tube Kinetics, National Aeronautics and Space Administration, Washington, DC (1972). (NASA Technical Note TN-D-6586, available as N72-15126 from the National Technical Information Service, Springfield, VA 22151.)
- 

SHOCK WAVES IN CHEMISTRY AND PHYSICS

A Brief Tribute to John N. Bradley

John N. Bradley, Professor of Chemistry at the University of Essex died in February 1981. A shock tube enthusiast, he would have contributed a paper to this meeting and it is therefore fitting that we should pay tribute to his memory.

John Bradley was best known for his book, "Shock Waves in Chemistry and Physics", which he wrote in the early sixties. It gave the chemist or physicist, without a knowledge of fluid mechanics, critical introduction to the theory and practice of shock tubes. In particular the book pointed out the possibilities and limitations of the technique and as such provided an excellent survey, not only for practitioners like ourselves, but also for chemists and physicists in general. The book was extremely influential because of the time of its appearance and it contributed substantially to the application of shock techniques in chemistry and physics.

John Bradley was a graduate of the University of Birmingham where he obtained his doctorate for photochemical work. He then went to work with Professor George Kistiakowsky at Harvard where he took up shock tube work and participated in the first attempts to extract samples for mass spectroscopic analysis in a time-resolved regime.

He returned to England to take a position at the University of Liverpool where, among other things, he developed a combined flash-photolysis/shock tube technique. This was not an easy experiment and he was ahead of his time. Now the use of a laser to produce photochemical decomposition in a shock heated gas would circumvent many of the problems associated with a broad-band flash lamp.

In the middle sixties he became Professor and Head of the Department of Chemistry at the new University of Essex and at that time he was one of the youngest Chairmen in the country. Chairman of a developing department is more than a full-time job but his research continued unabated. In recent years he concentrated on the mechanism of pyrolysis of hydrocarbons and on oxidation, studying these most complicated systems with single-pulse shock techniques combined with computational modeling of the multi-reaction mechanisms. He developed his own sensitivity analysis before it became fashionable.

John Bradley was not just a shock tube man: he had wide ranging interests in Chemistry, and worked at various times on photochemistry, laser applications, and surface chemistry.

John had a full life outside his profession. He was a keen sailor both in dinghies and cruisers and he took part in the grueling, demanding, and at times dangerous, 'Round-Britain' race. He was a keen squash player and indeed he died following a vigorous squash game.

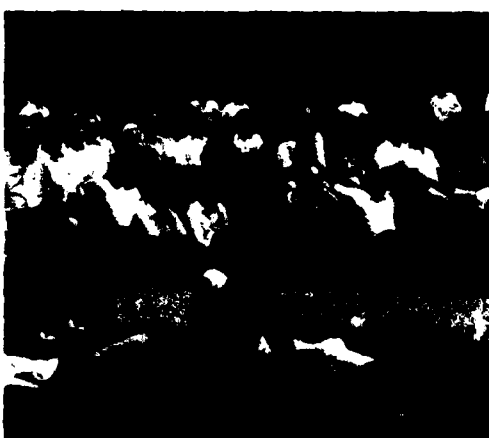
He attended many of these meetings, and was a member of the Advisory Committee - had he lived he would have contributed a paper this afternoon on "Chemically Enhanced Shock Waves and Detonations in Ethylene Oxide-Oxygen-Argon Mixtures". It is sad that he is missing from our ranks.

However, John Bradley was a cheerful friend of many here and he would not have wanted me, in paying this tribute, to cast a note of gloom over what has been a most successful meeting.

So I shall conclude by saying that we who knew John personally and those of us who knew him through his book and his work are privileged to have been in contact with a vigorous, able and good colleague. We remember him with honour and with pleasure.

July 1981

Peter Borrell
Department of Chemistry
Keele University





AUTHOR INDEX

Adomeit, G. 790
Akamatsu, T. 244
Amr, Y.M. 280
Arndt, St. 610
Asaba, T. 552

Babu, S.V. 570
Bauer, S.H. 691
Ben-Dor, G. 326, 637
Bernstein, L. 150
Bershader, D. 200
Beylich, A.E. 519
Bhaskaran, K.A. 834
Bidani, M. 602
Boodaghians, R. 543
Book, D. 376
Boris, J. 376
Borrell, P. 543
Borrell, P.M. 543
Bötticher, W. 271, 510
Bowman, C.T. 617
Briones, R.A. 159
Brocher, E. 209
Brudi, K. 167
Burcat, A. 826
Butler, G.W. 454

Calia, V.S. 673
Cann, M.W.P. 98, 431
Cantello, M. 479
Carroll, H.F. 602
Catherasoo, C. 392
Cavero, A. 297
Chang, J-S. 535
Chou, K.H. 664
Chung, K. 297
Combourieu, J. 626

Dannenberg, R.E. 124
Deckker, B.E.L. 216, 253
Deguchi, M. 116
Demmig, F. 271
Dettleff, G. 716
Dietz, Th. 700
Donati, V. 479
Dumitrescu, L.Z. 753
Dunn, M.G. 32
Dupré, G. 626

East, R.A. 367
Edwards, D.G. 744
Egawa, M. 141
Elabdin, M.N. 385
Elaouazi, M. 209
Erdmann, W. 185
Evans, B. 535
Farmer, R.F. 826
Fomin, N.A. 626
Fontaine, B. 470
Forestier, B. 470
French, R.P. 81
Frieske, H.J. 790
Frohn, A. 610, 646
Fry, M. 376
Fujimura, K. 244
Fujiwara, T. 411, 724
Funabiki, K. 707

Garen, W. 167
Garifo, L. 479
Garry, K.P. 781
Gladstone, D. 420
Glass, I.I. 3, 307, 342, 762
Glenn, H.D. 191
Gotoh, J. 326
Graham, J.M.R. 402
Grant, K.R. 543
Grillo, A. 576
Grönig, H. 519

Hall, J.G. 280
Hanson, R.K. 617
Hasegawa, T. 724
Hauser, M. 700
He, B.P. 107
Hesselink, L. 392
Hillier, R. 402
Hindelang, F.J. 132
Hirose, T. 141
Hirschberg, A. 289
Hobson, R.M. 535
Holst-Jensen, O. 342
Honma, H. 342
Hornung, H.G. 176, 262
Houwing, A.F.P. 176
Hozaka, M. 495

Igra, O. 637
Inger, G.R. 227
Ito, T. 707
Iwamoto, J. 216

Joos, V. 700
Just, Th. 54

Kaitoh, H. 495
Kamei, M. 141
Kauffman, C.W. 809
Kawada, H. 818, 843
Keiper, R. 851
Keough, D.D. 191
Kim, Y.W. 89
Kline, J.M. 869
Knapp, K. 132
Kobayashi, H. 141
Kolodner, P. 486
König, G. 646
Konopa, W. 673
Kratz, H.R. 191
Krech, R.H. 462
Kudian, A.K. 307
Kuhl, A. 376
Kulkarny, V.A. 159, 392
Kutler, P. 772

La Rocca, A.V. 479
Lensch, G. 167
Lester, T.W. 800, 860
Li, X. 528
Liang, P-Y. 200
Lifshitz, A. 602
Löhr, R. 593

Maillot, P. 504
Mark, A. 772
Matsui, H. 552
Matsumoto, Y. 552
Matsushita, M. 244
Matula, R.A. 826
Meier, G.E.A. 716
Menin, R. 479
Merklin, J.F. 800, 860
Merzkirch, W. 185
Minegishi, T. 843
Mitrofan, A. 753

- Natarajan, K. 834
 Neemeh, R.A. 385
 Nicholls, R.W. 98, 431

 Oguchi, H. 707
 Oman, R.A. 673
 Ono, S. 535
 Onorato, M. 479
 Outa, E. 655
 Owren, J.H. 124

 Paillard, C. 626
 Pamidimukkala, K.M. 585
 Pedley, M.D. 543
 Penner, S.S. 869
 Phan, K.C. 781
 Picone, M. 376
 Plett, E.G. 420
 Powell, H.N. 297
 Preda, S. 753
 Pugh, E.R. 462

 Rao, Y.V.C. 570
 Raymonda, J.W. 438
 Reddy, N.M. 235
 Reed, R.A. 673
 Reese, Th. 271
 Richarz, H.P. 519
 Roth, P. 593
 Rudinger, G. 664
 Rushmore, W.L. 438
 Russell, D.A. 454

 Saito, T. 307
 Sandeman, R.J. 176
 Schultz-Grunow, F. 352
 Seelbach, E. 790
 Seiler, F. 317
 Sentman, L.H. 438
 Shaw, D.T. 664
 Shin, J.B. 98, 431

 Shwartz, J. 159
 Sichel, M. 809
 Skinner, G.B. 585
 Slack, M. 576
 Smith, R.M. 744
 Soga, K. 21
 Soloukhin, R.I. 626
 Speckmann, H.-D. 716
 Spurr, J.H. 851
 Stalker, R.J. 81
 Steinwandel, J. 700
 Stephens, J.R. 691
 Stollery, J.L. 781
 Stott, G.T. 150
 Strehlow, R.A. 69
 Stricker, J. 447
 Sturtevant, B. 392
 Subba Rao, V. 570
 Subbiah, M. 438
 Sugimura, T. 411
 Suzuki, S. 655
 Swift, R.P. 191
 Szekely, A. 617
 Szydlowski, S.L. 800

 Tajima, K. 655
 Takahashi, N. 116
 Takahashi, S. 843
 Takayama, K. 326
 Taki, S. 411
 Taylor, J.R. 262
 Teii, S. 535
 Teitelbaum, H. 560
 Tennyson, R.C. 762
 Teranaka, Y. 141
 Terao, K. 495
 Teshima, K. 116
 Thayer, W.J. 735
 Thenard, Cl. 504
 Thompson, P.A. 716
 Tilleman, M. 447

 Tittsworth, J. 376
 Tomita, M. 818
 Townend, L.H. 367
 Tsuboi, T. 141
 Tsumita, Y. 342
 Tyaga Raju, M. 570

 Ural, E.A. 809

 Valentin, P. 504
 van Dongen, M.E.H. 289
 Vaughn, S.N. 860
 Vrugt, P.J. 289

 Wada, I. 21
 Wahba, N.N. 762
 Waiter, S.A. 41
 Walenta, Z. 335
 Wegener, D.C. 800
 White, B.S. 392
 Willems, J.F.H. 289
 Wittig, S.L.K. 682
 Wray, A.A. 200, 358
 Wu, J.H.T. 385

 Xu, X.J. 107

 Yablonovitch, E. 486
 Yau, A.W. 535
 Yoon, C. 716
 Yoshikawa, K.K. 358
 Yoshizawa, Y. 818, 843

 Zaengel, Th. 510
 Zahoransky, R.A. 682
 Zelazny, S.W. 438
 Zhao, M.X. 107
 Zhu, N. 528
 Zhuang, F.G. 107
 Zumdieck, J.F. 735

PREVIOUS PROCEEDINGS OF THE SHOCK TUBE SYMPOSIA

Proceedings of the First Shock Tube Symposium, held at MIT, 26-27 February 1957, sponsored by Air Force Special Weapons Center. Headquarters, Air Force Special Weapons Center, Air Research and Development Command, Kirtland Air Force Base, New Mexico, SWR-TM-57-2, AD No. 467201.

Proceedings of the Second Shock Tube Symposium, 5-6 March 1958, sponsored by Air Force Special Weapons Center. Headquarters, Air Force Special Weapons Center, Air Research and Development Command, Kirtland Air Force Base, New Mexico, SWR-TM-58-3, AD No. 211239.

Proceedings of the Third Shock Tube Symposium, 10-12 March 1959, held at Fort Monroe, Virginia, sponsored by Air Force Special Weapons Center, Headquarters, Air Force Special Weapons Center, Air Research and Development Command, Kirtland Air Force Base, New Mexico, SWR-TM-59-2, AD No. 230333.

Proceedings of the Fourth Shock Tube Symposium, 18-20 April 1961, BRL Report No. 1160, February 1962, AD No. 274039.

Proceedings of the V International Shock Tube Symposium, published by the U.S. Naval Ordnance Laboratory, White Oaks, Silver Spring, Maryland, May 1966, AD No. 484600.

High Temperature and Short Duration Flows. Proceedings of the VI International Shock Tube Symposium, R.J. Emrich, O. Laporte and H. Reichenbach, eds., The Physics of Fluids Supplement I, 1969.

Shock Tubes. Proceedings of the VII International Shock Tube Symposium, I.I. Glass, editor, University of Toronto Press, Toronto 1970.

Shock Tube Research. Proceedings of the VIII International Shock Tube Symposium, J.L. Stollery, A.G. Gaydon and P.R. Owen, eds., Chapman and Hall, London, 1971.

Recent Developments in Shock Tube Research. Proceedings of the IX International Shock Tube Symposium, D. Bershader and W. Griffith, eds., Stanford University Press, Stanford, 1973.

Modern Developments in Shock Tube Research. Proceedings of the X International Shock Tube Symposium, G. Kamimoto, editor, Shock Tube Research Society, Japan, 1975.

Shock Tube and Shock Wave Research. Proceedings of the XI International Symposium on Shock Tubes and Waves. B. Ahlborn, A. Hertzberg and D. Russell, eds., University of Washington Press, Seattle, 1978.

Shock Tubes and Waves. Proceedings of the XII International Symposium on Shock Tubes and Waves. A. Lifshitz and J. Rom, eds., The Magnes Press, The Hebrew University, Jerusalem, 1980.